ERDC TR-13-12

US Army Corps
of Engineers®
Engineer Research and
Development Center

ERDC
INNOVATIVE SOLUTIONS
for a safer, better world

Mississippi Coastal Improvements Program; Evaluation of Barrier Island Restoration Efforts

Ty V. Wamsley, Elizabeth S. Godsey, Barry W. Bunch,
Raymond S. Chapman, Mark B. Gravens, Alison S. Grzegorzewski,
Bradley D. Johnson, David B. King, Rusty L. Permenter,
Dorothy H. Tillman, and Michael W. Tubman

September 2013

Engineer Research and Development Center

The US Army Engineer Research and Development Center (ERDC) solves the nation's toughest engineering and environmental challenges. ERDC develops innovative solutions in civil and military engineering, geospatial sciences, water resources, and environmental sciences for the Army, the Department of Defense, civilian agencies, and our nation's public good. Find out more at www.erdc.usace.army.mil.

To search for other technical reports published by ERDC, visit the ERDC online library at http://acwc.sdp.sirsi.net/client/default.

ERDC TR-13-12
September 2013

Mississippi Coastal Improvements Program; Evaluation of Barrier Island Restoration Efforts

Ty V. Wamsley, Raymond S. Chapman, Mark B. Gravens,
Alison S. Grzegorzewski, Bradley D. Johnson,
David B. King, Rusty L. Permenter, and Michael W. Tubman

Coastal and Hydraulics Laboratory
US Army Engineer Research and Development Center
3909 Halls Ferry Road
Vicksburg, MS 39180-6199

Barry Bunch and Dorothy Tillman

Environmental Laboratory
US Army Engineer Research and Development Center
3909 Halls Ferry Road
Vicksburg, MS 39180-6199

Elizabeth S. Godsey

USACE, Jacksonville District
400 W Bay Street
Jacksonville, FL 32202

Final report

Prepared for US Army Corps of Engineer District, Mobile
109 Saint Joseph Street, Mobile Alabama 36602

Abstract

A comprehensive numerical modeling study was undertaken to support the barrier island restoration plan as part of the Mississippi Coastal Improvements Program. Hydrodynamic, wave, sediment transport, and water quality numerical modeling was conducted to evaluate the effect of Camille Cut closure on circulation and water quality of Mississippi Sound; the combined effect of Camille Cut and Katrina Cut closures on circulation and water quality of Mississippi Sound; reduction of storm wave energy at the mainland Mississippi coast as a result of closing Camille Cut; and optimization of nearshore placement of sand in the littoral zone. Water quality modeling of Mississippi Sound was conducted to determine potential impacts from proposed actions in the Ship Island area using the Curvilinear Hydrodynamic 3D model (CH3D) and the water quality model (CE-QUAL-ICM). Although water quality changes were observed for the alternatives modeled, the impact of Ship Island degradation or restoration does not significantly alter system wide circulation and water quality conditions. The changes in storm wave energy at the mainland Mississippi coast as a result of Ship Island degradation and restoration were quantified through the application of an integrated coastal storm modeling system (CSTORM-MS). Results indicate that the closure of Camille Cut and Ship Island restoration have the potential to reduce storm waves at the mainland coast. The C2SHORE model was applied to numerically predict the morphological response and sand fate for a selection of proposed alternatives. Results indicate that the Camille Cut restoration fill survives higher-frequency storms (such as the 1-yr and 10-yr events), but is breached during the lower-frequency 500-yr event modeled. Potential impacts of nearshore borrow areas were assessed with the spectral nearshore wave transformation model STWAVE and shoreline change model GENESIS. Scenarios included borrow areas offshore of Ship Island, Horn Island, and West Dauphin Island and were evaluated over a period of 20-years. The expected shoreline impacts are site-specific, with both prograding and eroding shoreline areas predicted.

Contents

Figures and Tables

Figures

Tables

Preface

This report describes numerical modeling and field data collection study conducted in support of the Mississippi Coastal Improvements Program's barrier island restoration project. The work was conducted at the request of the Mobile District (SAM), USACE. Elizabeth S. Godsey was the primary engineering point of contact at the District. The study was funded by the Mississippi Coastal Improvements Program and was conducted at the US Army Engineering Research and Development Center (ERDC), Coastal and Hydraulics Laboratory (CHL) and Environmental Laboratory (EL), Vicksburg, MS, during the period October 2009 – June 2012.

The work performed at CHL was under the general supervision of Dr. Ty V. Wamsley, Chief, Coastal Processes Branch, James P. McKinney, Chief, Field Data Collection Branch, and Bruce A. Ebersole, Chief, Coastal Flood and Storm Protection Division. The Director of the Coastal and Hydraulics Laboratory was Dr. William D. Martin. The work performed at Environmental Laboratory (EL) was under the general supervision of Dr. Dorothy Tillman, Chief, Water Quality and Contaminant Modeling Branch, and Warren Lorentz, Chief, Environmental Processes and Effects Division. The Director of the Environmental Laboratory was Dr. Beth Fleming.

COL Kevin J. Wilson was the Commander of ERDC, and Dr. Jeffery P. Holland was Director.

Unit Conversion Factors

Multiply	By	To Obtain
cubic feet	0.02831685	cubic meters
cubic yards	0.7645549	cubic meters
degrees Fahrenheit	(F-32)/1.8	degrees Celsius
feet	0.3048	meters
inches	0.0254	meters
miles (nautical)	1,852	meters
miles (U.S. statute)	1,609.347	meters

1 Introduction[1]

The Mississippi mainland coast is bordered on the south by Mississippi Sound. Five barrier islands form the southern boundary of Mississippi Sound 10 to 15 miles to the south of the mainland. From west to east, the islands are Cat, Ship, Horn, Petit Bois, and Dauphin (Figure 1-1). All of Petit Bois, Horn, and Ship islands and part of Cat Island are within the Gulf Islands National Seashore under the jurisdiction of the National Park Service (NPS).

Figure 1-1. Mississippi barrier islands.

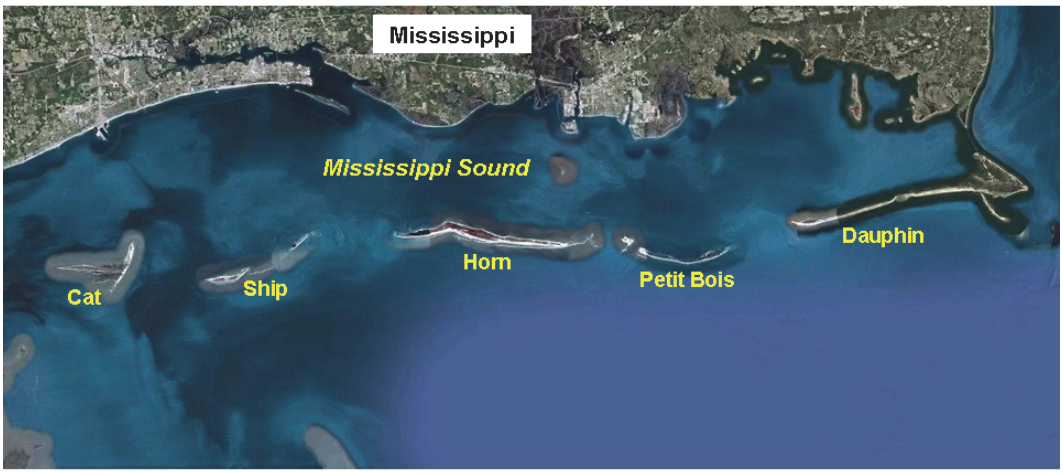

In 1969, Hurricane Camille breached Ship Island. The breach, known as Camille Cut, has existed with varying amounts of natural rebuilding between later storms as documented by Schmid and Yassin (2004). Camille Cut was significantly widened from approximately 2500 m to 5800 m by Hurricane Katrina in 2005. Hurricane Katrina also created a 2000-m-wide breach in Dauphin Island, known as Katrina Cut. These breaches provide a conduit for hurricane surge and offshore oil spills to propagate toward the mainland shore.

After Hurricane Katrina, it became widely accepted by the public that if the Mississippi barrier islands had been in a “pre-Hurricane Camille” condition, there would have been much less storm damage during Katrina. The State’s Hurricane Recovery Program included a massive restoration of

[1] Written by Ty V. Wamsley, Coastal and Hydraulics Laboratory, US Army Engineer Research and Development Center, Vicksburg, MS.

the barrier islands. During completion of the US Army Corps of Engineers' Mississippi Coastal Improvements Program Comprehensive Report, the Mississippi barrier islands were subject to several different design concepts for storm damage reduction including total restoration to the pre-Camille condition. Computer modeling of storm damage reduction benefits from island restoration suggested that storm surge reduction was not large, but other benefits would be obtained from simply maintaining the existence of the islands (USACE 2009). The benefits include reduction of storm wave damage to the mainland coast and environmental benefits associated with maintaining Mississippi Sound as an estuary. A plan was developed to restore Ship Island to ensure its continued existence. The Comprehensive Barrier Island Restoration Plan was coordinated with the NPS and includes direct sand placement in the breach of Ship Island, additional sand placed into the local littoral zone, and changes in the Regional Sediment Management Practice.

Restoration of Ship Island was selected for construction. Hydrodynamic, wave, sediment transport, and water quality numerical modeling is required to support final engineering and design as well as the development of a Supplemental Environmental Impact Statement. The purpose of this report is to evaluate the following:

- Effect of Camille Cut closure on circulation and water quality of Mississippi Sound;
- Combined effect of Camille Cut and Katrina Cut closures on circulation and water quality of Mississippi Sound;
- Reduction of storm wave energy at the mainland Mississippi coast as a result of closing Camille Cut; and
- Optimization of nearshore placement of sand in the littoral zone.

Evaluation of the circulation, water quality, and storm wave energy will be achieved through comparison of results for four alternative conditions including a Base condition (post Hurricane Katrina), With-project (Camille Cut closed), Degraded (Ship Island lowered to below mean sea level across the entire island footprint), and a Cumulative condition which includes Camille Cut closed, Katrina Cut closed, and navigation channels deepened to authorized depths.

Chapter 2 documents a field data collection conducted to support numerical modeling efforts and to provide baseline data so that changes

resulting from the reconstruction of Ship Island can be quantified during project monitoring. Data collected includes waves on both the seaward and sound side of Ship Island, current velocities and flow through the cuts and passes around Ship and Dauphin islands, and water quality information at strategic locations.

Chapter 3 documents circulation modeling conducted to quantify the relative changes in circulation within Mississippi Sound resulting from the Ship Island restoration. A combination of a two-dimensional ADCIRC model and a three-dimensional numerical hydrodynamic model (CH3D-WES) was applied and provided hydrodynamic input to the water quality and sediment transport models discussed in Chapters 6 and 7, respectively.

Chapter 4 documents the wave modeling approach required to provide radiation stress gradients for the hydrodynamics used to force the water quality and sediment transport models. This chapter provides an overview of the numerical wave model STWAVE and documents model validation in the Gulf of Mexico and within Mississippi Sound.

Chapter 5 documents water quality modeling conducted to understand the existing water quality within Mississippi Sound and to quantify the relative changes in the water quality and flushing capacity resulting from the island breach closure.

Chapter 6 documents storm wave sensitivity modeling. Closure of Camille Cut will result in reduction of transmitted wave energy to the mainland Mississippi coast. Relative changes resulting from the barrier island restoration are quantified through application of an integrated coastal storm modeling system.

Chapter 7 documents simulation of waves and currents coupled with a sediment transport model to predict transport pathways for the purpose of optimizing the location of nearshore sand placement.

Chapter 8 documents a sensitivity analysis conducted to examine the impact of dredged borrow areas on sediment transport and shoreline change.

A summary of the findings and conclusions from the study are documented in Chapter 9.

2 Field Data Collection[1]

The field data collection encompassed areas within the Mississippi Sound and Gulf of Mexico surrounding Ship and Dauphin islands, which are shown in Figure 1-1. The Mississippi Sound is located north of the barrier islands, separating them from the mainland shores of Mississippi and Alabama, and has a relatively flat bathymetry. The extent of the current study area around Ship Island is defined by current measurement transect lines shown in Figure 2-1. They stretch from Cat Island, west of Ship Island, (TL-3), across Ship Island Pass to the western end of Ship Island, across Camille Cut (TL-1), and across Little Dog Keys Pass (west) and Dog Keys Pass (east) to Horn Island (TL-2). Ship Island Pass is cut by a navigation channel that extends from the Gulf of Mexico, through the Pass very close to the western end of Ship Island, north to Gulfport, Mississippi. At Ship Island, it has a maximum depth of approximately 12 m. Little Dog Keys Pass is an unmaintained pass with a maximum depth of approximately 11 m, while Dog Keys Pass is the navigation channel leading from the Gulf to Biloxi, passing very close to the western end of Horn Island, and has an unmaintained maximum depth at Horn Island of approximately 11 m. The maximum depth of Camille Cut is approximately 4 m.

Figure 2-1. Current measurement transect lines in the Ship Island study area.

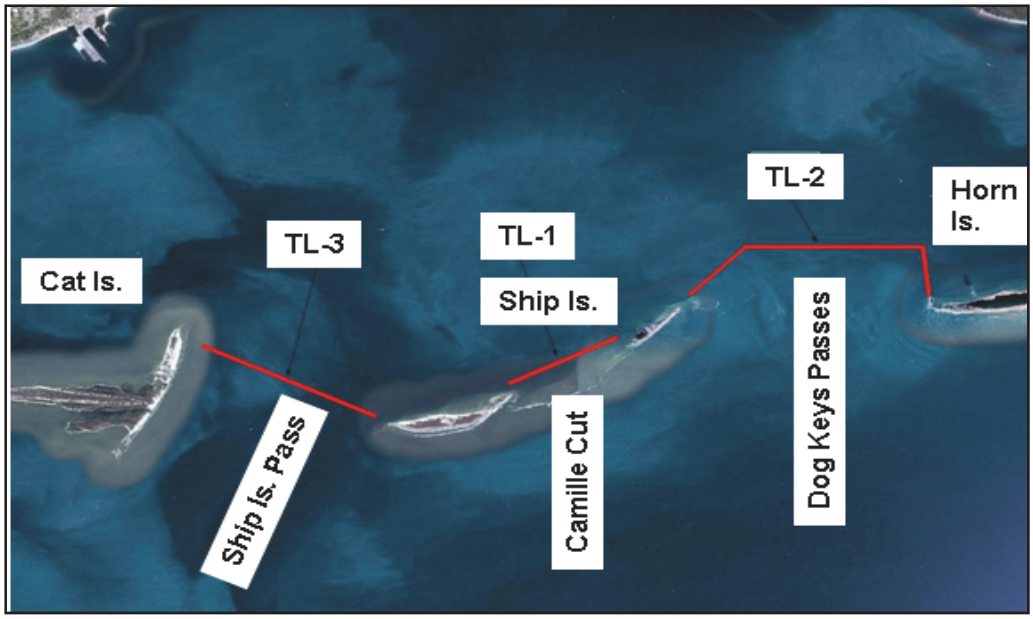

[1] Written by Michael W. Tubman, Coastal and Hydraulics Laboratory, US Army Engineer Research and Development Center, Vicksburg, MS.

The current measurement transect lines around Dauphin Island are shown in Figure 2-2. They extend from Petit Bois Island on the west, across Petit Bois Pass to the western end of Dauphin Island (TL-4), across Katrina Cut (TL-5), and from Dauphin Island north to the mainland across Pass Aux Herons (TL-6). A natural channel runs through Petit Bois Pass close to the western end of Dauphin Island and has a maximum depth of approximately 6 m. The maximum depth of Katrina Cut was approximately 2 m. Katrina Cut has been closed with a temporary rock structure since 2010. Pass Aux Herons goes from the Mississippi Sound into Mobile Bay. The Intracoastal Waterway goes through it with a depth of approximately 4 m.

Figure 2-2. Current measurement transect lines in the Dauphin Island study area.

2.1 Field data collection and monitoring plan

The field data collection and monitoring plans call for measuring baseline conditions and changes resulting from the possible reconstruction of Ship and Dauphin islands. Specifically, the plan was formed to meet the following goals:

- Provide wave climatology in the vicinity of Ship Island;
- Measure current velocities and transport in the cuts and passes through and around Ship and Dauphin islands; and
- Determine baseline water quality at strategic locations.

Two internal recording wave and water-level gauges were deployed, one inside the Mississippi Sound north of Camille Cut, and the other south of Camille Cut in the Gulf. An image of the wave gauge and the locations of both gauges are as shown in Figures 2-3 and 2-4.

Figure 2-3. Wave gauge mounted on trawler resistant pod.

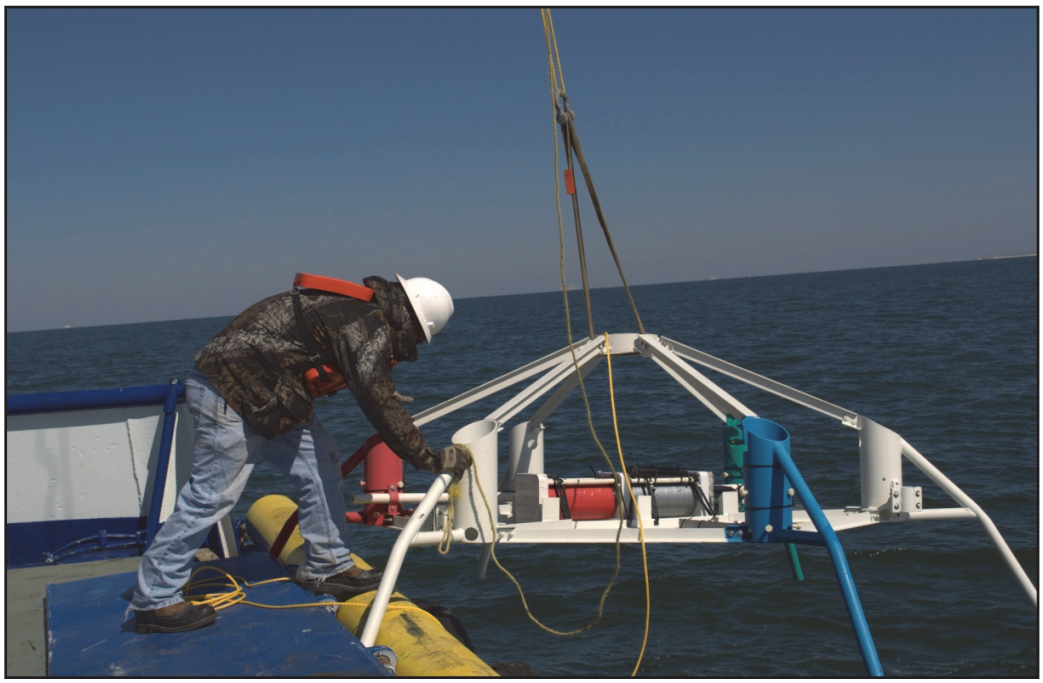

Figure 2-4. Wave gauge deployment locations.

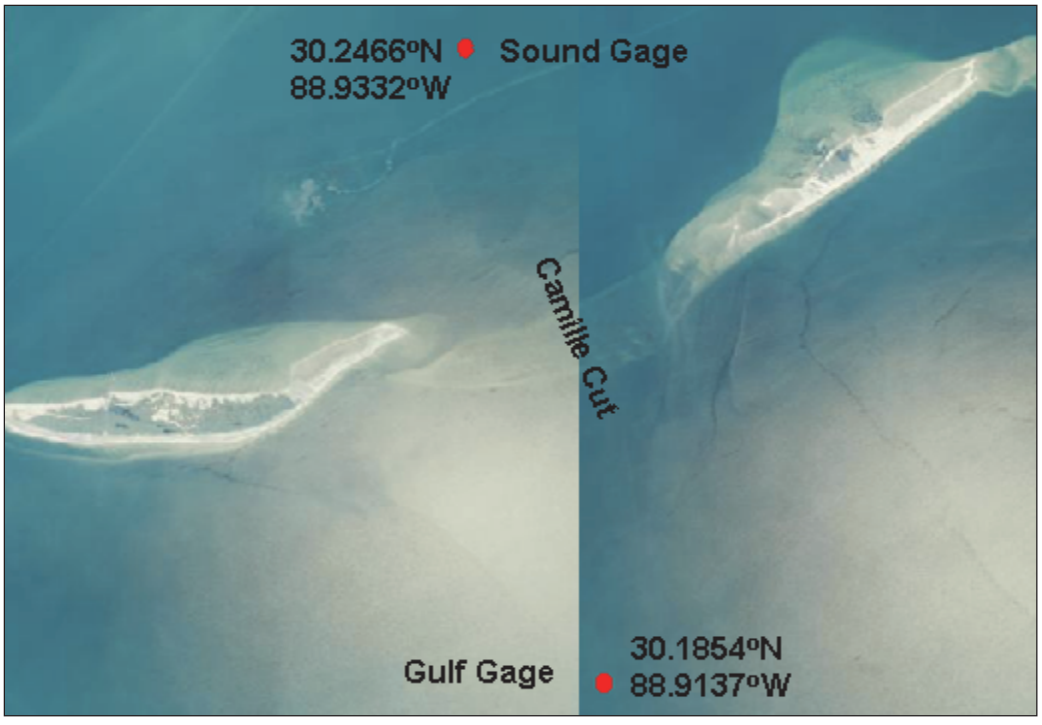

Current velocities were measured during two 10-hour vessel-mounted acoustic Doppler current profiler (ADCP) surveys along the six survey lines shown in Figures 2-1 and 2-2 (TL-1 through TL-6) that crossed Camille and Katrina Cuts, Pass Aux Heron and Ship Island, Dog Key and Petit Bois passes. With vessel transit times to-and-from the sites, this resulted in 12 hour days for three survey crews.

One-liter water samples at eleven sites and three depths were collected while the survey crews were on site for the current surveys and brought back to ERDC for water-quality analysis. Unfortunately the water quality samples were not filtered in the field and preserved with sulfuric and nitric acid, so water quality analyses could not be performed. Separate one-liter samples at each location and depth were taken and brought back to ERDC where their salinities were determined.

2.1.1 Wave measurements

Two Civil Tek internally-recording, directional wave gauges were deployed on March 4, 2010 near Ship Island to provide the wave climatology data. Each gauge consists of three Paroscientific quartz pressure transducers and a data acquisition, processing and storage unit. Components of each gauge are mounted on a steel, trawler-resistant pod having six legs, which sits on the seafloor (Figure 2-3). Alternate legs of the pod hold one of the three pressure transducers; forming an equilateral triangle 1.83 m (6 ft) on a side. Data acquisition, processing and storage unit calculates significant wave height (*Hmo*) and wave period and direction at the peak of the energy spectrum from the one-hertz pressure measurements made every hour. Mean water elevation is also calculated every hour, and the calculated parameters are stored internally in flash memory.

The locations of the gauge deployments are shown in Figure 2-4. Each gauge pod was lowered to the seafloor with a crane on the back deck of the Tyson B deployment vessel (Figure 2-5). Divers then jetted three 3-m-long pipes into the seafloor near the legs of each pod and clamped them to the pod legs to hold them in place.

The wave gauges were recovered on July 15, 2010. The northern gauge, deployed in the Sound, recorded valid data for the entire 143-day deployment. However, the gauge deployed in the Gulf developed an electronic problem on April 30 and recorded only 67 days of valid data.

Figure 2-5 Wave gauge and pod being lowered to the seafloor from the Tyson B.

Plots of significant wave height (*Hmo*), and period and wave direction at the peak of the energy spectra, are in Appendix A. Tables 2-1, 2-2, and 2-3 show the percent occurrence of waves in *Hmo*-period bands for all Sound measurements, all Gulf measurements, and Sound measurements taken during the same period as the Gulf measurements (i.e., March 4 to April 30). Tables 2-4, 2-5, and 2-6 show the percent occurrence of waves in *Hmo*-direction bands for the same time periods.

The direction convention is the direction the waves are coming from. Tables 2-7, 2-8 and 2-9 show the percent occurrence in period-direction bands. In all cases, the total percentage is less than 100 percent by a small amount (less than 2.0 percent) to account for waves that are below gauge threshold.

The predominant wave direction at both gauges was southeast (i.e., 135 to 165 degrees true). At the Sound gauge, for the period March 4 to July 15, 2010, 42.40 percent of the waves were from the southeast. At the Gulf gauge, for the period March 4 to April 30, 2010, 46.3 percent were from the southeast. For the March 4 to April 30 period at the Sound gauge, there were fewer waves from the southeast than at the Gulf gauge, 36.31

Table 2-1. Percent occurrence of waves at the wave gauge in the Mississippi Sound in *Hmo*-period bands for March 4 to July 15, 2010.

Peak Period (s)	*Hmo* (m)											
	0.0-0.2	0.2-0.4	0.4-0.6	0.6-0.8	0.8-1.0	1.0-1.2	1.2-1.4	1.4-1.6	1.6-1.8	1.8-2.0	<2.0	Total
2-3	15.25	21.68	12.83	3.77	0.53	0.03	0.00	0.00	0.00	0.00	0.00	54.09
3-4	4.68	5.62	2.60	2.92	0.72	0.22	0.15	0.00	0.00	0.00	0.00	16.91
4-5	4.89	0.63	0.41	0.00	0.00	0.00	0.00	0.00	0.00	0.00	0.00	5.93
5-6	4.05	0.88	0.06	0.03	0.00	0.00	0.00	0.00	0.00	0.00	0.00	5.02
6-7	5.96	1.32	0.25	0.00	0.00	0.00	0.00	0.00	0.00	0.00	0.00	7.53
7-8	3.67	0.85	0.06	0.03	0.00	0.00	0.00	0.00	0.00	0.00	0.00	4.61
8-9	2.20	0.82	0.00	0.00	0.00	0.00	0.00	0.00	0.00	0.00	0.00	3.02
>9	0.69	1.10	0.09	0.00	0.00	0.00	0.00	0.00	0.00	0.00	0.00	1.88
Total	41.39	32.90	16.30	6.75	1.25	0.25	0.15	0.00	0.00	0.00	0.00	98.99

Table 2-2. Percent occurrence of waves at the wave gauge in the Gulf of Mexico in *Hmo*-period bands for March 4 to April 30, 2010.

Peak Period (s)	*Hmo* (m)											
	0.0-0.2	0.2-0.4	0.4-0.6	0.6-0.8	0.8-1.0	1.0-1.2	1.2-1.4	1.4-1.6	1.6-1.8	1.8-2.0	<2.0	Total
2-3	3.74	5.87	4.48	1.98	0.44	0.29	0.07	0.00	0.15	0.07	0.00	17.09
3-4	3.74	3.52	4.77	7.04	4.33	2.05	0.59	0.37	0.22	0.00	0.00	26.63
4-5	8.36	1.76	1.17	1.61	2.05	1.32	0.51	0.51	0.29	0.00	0.00	17.58
5-6	3.89	0.73	1.91	1.54	1.17	1.39	0.44	0.37	0.15	0.00	0.00	11.59
6-7	5.50	1.83	1.39	1.69	1.17	0.29	0.44	0.29	0.44	0.15	0.00	13.19
7-8	3.08	1.25	0.66	0.44	0.44	0.07	0.00	0.00	0.15	0.00	0.00	6.09
8-9	1.61	0.37	0.95	0.95	0.37	0.59	0.22	0.00	0.22	0.00	0.07	5.35
>9	0.66	0.00	0.22	0.66	0.22	0.07	0.00	0.00	0.00	0.00	0.00	1.83
Total	30.58	15.33	15.55	15.91	10.19	6.07	2.27	1.54	1.62	0.22	0.07	99.35

Table 2-3. Percent occurrence of waves at the wave gauge in the Mississippi Sound in *Hmo*-period bands for March 4 to April 30, 2010.

Peak Period (s)	*Hmo* (m)											
	0.0-0.2	0.2-0.4	0.4-0.6	0.6-0.8	0.8-1.0	1.0-1.2	1.2-1.4	1.4-1.6	1.6-1.8	1.8-2.0	<2.0	Total
2-3	12.69	23.40	15.11	5.06	0.73	0.07	0.00	0.00	0.00	0.00	0.00	57.06
3-4	4.40	3.52	2.49	4.33	1.39	0.51	0.15	0.00	0.00	0.00	0.00	16.79
4-5	5.06	0.59	0.29	0.00	0.00	0.00	0.00	0.00	0.00	0.00	0.00	5.94
5-6	3.45	0.73	0.15	0.00	0.00	0.00	0.00	0.00	0.00	0.00	0.00	4.33

Peak Period (s)	*Hmo* (m)											
	0.0-0.2	0.2-0.4	0.4-0.6	0.6-0.8	0.8-1.0	1.0-1.2	1.2-1.4	1.4-1.6	1.6-1.8	1.8-2.0	<2.0	Total
6-7	5.14	1.61	0.07	0.00	0.00	0.00	0.00	0.00	0.00	0.00	0.00	6.82
7-8	3.37	0.88	0.00	0.00	0.00	0.00	0.00	0.00	0.00	0.00	0.00	4.25
8-9	1.17	0.51	0.00	0.00	0.00	0.00	0.00	0.00	0.00	0.00	0.00	1.68
>9	0.95	0.22	0.00	0.00	0.00	0.00	0.00	0.00	0.00	0.00	0.00	1.17
Total	36.23	31.46	18.11	9.39	2.12	0.58	0.15	0.00	0.00	0.00	0.00	98.04

Table 2-4. Percent occurrence of waves at the wave gauge in the Mississippi Sound in *Hmo*-direction bands for March 4 to July 15, 2010.

Hmo (m)	Wave Direction (°T)											
	345-015	015-045	045-075	075-105	105-135	135-165	165-195	195-225	225-255	255-285	285-315	315-345
0.0-0.2	0.69	0.38	0.41	1.44	2.60	23.60	3.98	1.00	1.44	4.27	1.19	0.38
0.2-0.4	0.82	0.78	1.63	4.77	3.04	13.96	1.38	0.94	2.07	1.66	1.00	0.82
0.4-0.6	0.69	0.72	1.54	2.35	2.26	3.61	0.28	0.19	1.51	1.76	0.75	0.66
0.6-0.8	0.25	0.16	0.41	1.10	0.97	1.07	0.09	0.13	0.31	1.22	0.69	0.35
0.8-1.0	0.00	0.06	0.13	0.00	0.06	0.16	0.03	0.03	0.16	0.44	0.06	0.13
1.0-1.2	0.00	0.00	0.00	0.03	0.06	0.00	0.00	0.00	0.03	0.09	0.00	0.03
1.2-1.4	0.00	0.00	0.00	0.00	0.00	0.00	0.00	0.03	0.00	0.03	0.00	0.00
1.4-1.6	0.00	0.00	0.00	0.00	0.00	0.00	0.00	0.00	0.00	0.00	0.00	0.00
1.6-1.8	0.00	0.00	0.00	0.00	0.00	0.00	0.00	0.00	0.00	0.00	0.00	0.00
1.8-2.0	0.00	0.00	0.00	0.00	0.00	0.00	0.00	0.00	0.00	0.00	0.00	0.00
>2.0	0.00	0.00	0.00	0.00	0.00	0.00	0.00	0.00	0.00	0.00	0.00	0.00
Total	2.45	2.10	4.12	9.69	8.99	42.40	5.76	2.32	5.52	9.47	3.69	2.37

Table 2-5. Percent occurrence of waves at the wave gauge in the Gulf of Mexico in *Hmo*-direction bands for March 4 to April 30, 2010.

Hmo (m)	Wave Direction (°T)											
	345-015	015-045	045-075	075-105	105-135	135-165	165-195	195-225	225-255	255-285	285-315	315-345
0.0-0.2	0.22	0.29	0.51	0.15	7.70	19.08	0.00	1.10	0.95	0.00	0.07	0.51
0.2-0.4	0.51	0.22	1.54	0.22	3.30	5.50	0.15	1.32	0.81	0.37	0.66	0.73
0.4-0.6	0.22	0.00	0.73	0.22	2.49	6.09	0.73	1.47	0.44	1.69	1.25	0.22
0.6-0.8	0.22	0.22	0.15	0.51	2.79	6.97	1.83	0.22	0.66	1.69	0.22	0.44
0.8-1.0	0.00	0.00	0.00	0.00	2.57	3.96	1.17	0.37	0.66	1.47	0.00	0.00
1.0-1.2	0.07	0.00	0.00	0.07	1.83	1.91	0.29	0.44	0.51	0.95	0.00	0.00

Hmo (m)	Wave Direction (°T)											
	345-015	015-045	045-075	075-105	105-135	135-165	165-195	195-225	225-255	255-285	285-315	315-345
1.2-1.4	0.00	0.00	0.00	0.00	0.51	1.03	0.15	0.15	0.00	0.44	0.00	0.00
1.4-1.6	0.00	0.00	0.00	0.00	0.22	0.88	0.15	0.22	0.00	0.07	0.00	0.00
1.6-1.8	0.00	0.00	0.00	0.00	0.37	0.81	0.29	0.00	0.07	0.07	0.00	0.00
1.8-2.0	0.00	0.00	0.00	0.00	0.07	0.07	0.00	0.00	0.07	0.00	0.00	0.00
>2.0	0.00	0.00	0.00	0.00	0.00	0.07	0.00	0.00	0.00	0.00	0.00	0.00
Total	1.24	0.73	2.93	1.17	21.85	46.37	4.76	5.29	4.17	6.75	2.20	1.90

Table 2-6. Percent occurrence of waves at the wave gauge in the Mississippi Sound in *Hmo*-direction bands for March 4 to April 30, 2010.

Hmo (m)	Wave Direction (°T)											
	345-015	015-045	045-075	075-105	105-135	135-165	165-195	195-225	225-255	255-285	285-315	315-345
0.0-0.2	0.95	0.29	0.29	1.69	2.64	20.32	3.89	0.59	1.32	2.86	0.88	0.51
0.2-0.4	1.39	1.17	1.76	4.18	3.82	12.18	0.66	0.51	1.83	1.47	1.25	1.25
0.4-0.6	0.95	1.03	1.69	1.76	2.49	2.64	0.15	0.44	1.91	2.13	1.54	1.39
0.6-0.8	0.29	0.00	0.15	0.88	0.95	1.10	0.22	0.22	0.66	2.64	1.54	0.73
0.8-1.0	0.00	0.00	0.00	0.00	0.07	0.07	0.07	0.07	0.37	1.03	0.15	0.29
1.0-1.2	0.00	0.00	0.00	0.07	0.15	0.00	0.00	0.00	0.07	0.22	0.00	0.07
1.2-1.4	0.00	0.00	0.00	0.00	0.00	0.00	0.00	0.07	0.00	0.07	0.00	0.00
1.4-1.6	0.00	0.00	0.00	0.00	0.00	0.00	0.00	0.00	0.00	0.00	0.00	0.00
1.6-1.8	0.00	0.00	0.00	0.00	0.00	0.00	0.00	0.00	0.00	0.00	0.00	0.00
1.8-2.0	0.00	0.00	0.00	0.00	0.00	0.00	0.00	0.00	0.00	0.00	0.00	0.00
>2.0	0.00	0.00	0.00	0.00	0.00	0.00	0.00	0.00	0.00	0.00	0.00	0.00
Total	3.58	2.49	3.89	8.58	10.12	36.31	4.99	1.90	6.16	10.42	5.36	4.24

Table 2-7. Percent occurrence of waves at the wave gauge in the Mississippi Sound in period-direction bands for March 4 to July 15, 2010.

Peak Period (s)	Wave Direction (°T)											
	345-015	015-045	045-075	075-105	105-135	135-165	165-195	195-225	225-255	255-285	285-315	315-345
2-3	2.26	1.85	3.40	7.87	6.42	9.89	4.13	1.94	4.36	7.53	2.34	2.09
3-4	0.19	0.22	0.66	1.76	1.10	7.41	1.19	0.35	1.13	1.66	0.88	0.28
4-5	0.00	0.00	0.06	0.00	0.63	4.36	0.16	0.03	0.03	0.25	0.41	0.00
5-6	0.00	0.03	0.00	0.00	0.28	4.58	0.03	0.00	0.00	0.03	0.06	0.00

Peak Period (s)	Wave Direction (°T)											
	345-015	015-045	045-075	075-105	105-135	135-165	165-195	195-225	225-255	255-285	285-315	315-345
6-7	0.00	0.00	0.00	0.00	0.19	7.29	0.06	0.00	0.00	0.00	0.00	0.00
7-8	0.00	0.00	0.00	0.00	0.19	4.42	0.00	0.00	0.00	0.00	0.00	0.00
8-9	0.00	0.00	0.00	0.03	0.09	2.76	0.13	0.00	0.00	0.00	0.00	0.00
>9	0.00	0.00	0.00	0.03	0.09	1.69	0.06	0.00	0.00	0.00	0.00	0.00
Total	2.45	2.10	4.12	9.69	8.99	42.40	5.76	2.32	5.52	9.47	3.69	2.37

Table 2-8. Percent occurrence of waves at the wave gauge in the Gulf of Mexico in period-direction bands for March 4 to April 30, 2010.

Peak Period (s)	Wave Direction (°T)											
	345-015	015-045	045-075	075-105	105-135	135-165	165-195	195-225	225-255	255-285	285-315	315-345
2-3	0.73	0.66	2.86	0.88	0.88	2.20	0.51	2.28	2.20	1.47	0.95	1.46
3-4	0.51	0.07	0.07	0.29	5.50	5.36	3.67	2.79	1.90	4.77	1.25	0.44
4-5	0.00	0.00	0.00	0.00	9.38	6.82	0.58	0.22	0.07	0.51	0.00	0.00
5-6	0.00	0.00	0.00	0.00	4.04	7.56	0.00	0.00	0.00	0.00	0.00	0.00
6-7	0.00	0.00	0.00	0.00	1.83	11.37	0.00	0.00	0.00	0.00	0.00	0.00
7-8	0.00	0.00	0.00	0.00	0.22	5.87	0.00	0.00	0.00	0.00	0.00	0.00
8-9	0.00	0.00	0.00	0.00	0.00	5.36	0.00	0.00	0.00	0.00	0.00	0.00
>9	0.00	0.00	0.00	0.00	0.00	1.83	0.00	0.00	0.00	0.00	0.00	0.00
Total	1.24	0.73	2.93	1.17	21.85	46.37	4.76	5.29	4.17	6.75	2.20	1.90

Table 2-9. Percent occurrence of waves at the wave gauge in the Mississippi Sound in period-direction bands for March 4 to April 30, 2010.

Peak Period (s)	Wave Direction (°T)											
	345-015	015-045	045-075	075-105	105-135	135-165	165-195	195-225	225-255	255-285	285-315	315-345
2-3	3.21	2.34	3.67	7.41	7.57	9.02	3.37	1.75	4.69	6.97	3.38	3.65
3-4	0.37	0.15	0.22	1.03	0.73	6.31	0.81	0.15	1.47	3.23	1.76	0.59
4-5	0.00	0.00	0.00	0.00	0.95	4.48	0.22	0.00	0.00	0.15	0.15	0.00
5-6	0.00	0.00	0.00	0.00	0.22	3.96	0.00	0.00	0.00	0.07	0.07	0.00
6-7	0.00	0.00	0.00	0.00	0.29	6.38	0.15	0.00	0.00	0.00	0.00	0.00
7-8	0.00	0.00	0.00	0.00	0.29	3.96	0.00	0.00	0.00	0.00	0.00	0.00
8-9	0.00	0.00	0.00	0.07	0.00	1.32	0.29	0.00	0.00	0.00	0.00	0.00
>9	0.00	0.00	0.00	0.07	0.07	0.88	0.15	0.00	0.00	0.00	0.00	0.00
Total	3.58	2.49	3.89	8.58	10.12	36.31	4.99	1.90	6.16	10.42	5.36	4.24

compared to 46.3 percent, and more waves from the southwest to northwest (i.e., 225 to 345 degrees true) than at the Gulf gauge, 26.18 compared to 15.02 percent. The biggest difference in terms of wave direction at the two gauges for the concurrent measurement period (March 4 to April 30) was in the wider southeast direction band of 105 to 165 degrees true, which at the Gulf gauge included 68.22 percent of the waves, and at the Sound gauge included only 46.43 percent of the waves. At the Gulf gauge, for the March 4 to April 30 period the direction with the largest waves (*Hmo* greater than 0.4 m) was the southeast (21.79 percent from 135 to 165 degrees true), at the Sound gauge for the same period there were slightly more waves that were larger from the west (6.09 percent from 255 to 285 degrees true) than from the southeast (4.25 percent from 135 to 165 degrees true). However, for the Sound gauge during the total deployment (March 4 to July 15), there were slightly more waves that were larger from the southeast (4.84 percent from 135 to 165 degrees true) than from the west (3.54 percent from 255 to 285 degrees true). For all directions, the Gulf gauge measured larger waves. During the March 4 to April 30 period 45.91 percent of the waves at the Gulf gauge had *Hmo*s less than 0.4 m, while for the same time period at the Sound gauge, 67.69 percent had *Hmo*s less than 0.4 m.

The mean water elevations measured at the gauges are shown in Appendix B. The plotted elevations are referenced to the record mean elevations and show the diurnal nature of the tides in the study area.

2.1.2 Current measurements

Current velocities were measured with 1,200 kHz Work Horse ADCPs manufactured by Teledyne RD Instruments. During data collection, the ADCP measures vessel velocity and water velocity. Measurements of vessel velocity are of velocity relative to the seafloor and were used to correct the current velocity measurements for movement of the survey vessel. GPS measured vessel positions were recorded with ADCP data.

The ADCP measures current velocities in cells that extend from near surface to near bottom. In Ship Island and Petit Bois Passes, where the water is deeper and the survey vessel was subjected to more wave induced motions, the size of the cells was 0.5 m to improve the statistical stability of the measurements. At the other locations, the cell size was 0.25 m to improve vertical resolution.

Three vessels conducted the current measurement transect surveys: the *Mr. George* (7.62- m length), the *Madison Gail* (21.03-m length), and the *Scully* (9.14-m length). The *Madison Gail*, being a larger vessel, was used to survey Ship Island and Petit Bois Passes while the other two vessels surveyed the more protected survey lines across Camille and Katrina Cuts (the *Mr. George*), and Dog Keys Passes and Pass Aux Heron (the *Scully*).

Current surveys were conducted in the vicinity of Dauphin Island on March 25, 2010, and in the vicinity of Ship Island on March 31, 2010. Due to the generally shallow depths and lack of significant vertical density stratification in Camille and Katrina Cuts, the current directions should not vary significantly with depth. Therefore, depth averages are best calculated by simply averaging the speeds in the vertical without considering direction, and calculating depth-averaged directions from vertical averages of unit vectors having the measured directions. This was done for survey lines across the cuts. The results for Camille Cut are shown in Figures 2-6. In the figures, the speeds are plotted as positive values when the depth-averaged directions are greater than, or equal to, 248 degrees true and less than 68 degrees true, and as negative values when they are less than 248 degrees true and greater than, or equal to, 68 degrees true. This sign convention can be interpreted as flood, positive speeds, and ebb, negative speeds because there are no currents parallel to Ship Island (orientation 248 to 68 degrees) that aren't captured in the ebb and flood flow through Camille Cut. This can be seen in Figure 2-7 where the currents for survey 10 are plotted in quadrants. In the figure, the bottom plot shows the current speeds as positive if the directions are in the quadrant between 293 and 23 degrees, and negative if they are in the quadrant between 113 and 203 degrees. If the current directions are not in these north-south quadrants representing flow through Camille Cut, they are plotted with zero speed and appear in the top plot. In the top plot, the current speeds are positive if the directions are in the quadrant between 23 and 113 degrees, and negative if they are in the quadrant between 203 and 293 degrees. These quadrants represent flow along the orientation of the north shore of Ship Island. This can be seen in Figure 2-7, except at the ends of the Camille Cut transect, the flow is all ebb through Camille Cut. At the ends of the transect lines, the alongshore flow comes into the area of the Cut and is captured by the ebb flow through the Cut in the center of the survey line. This is the predominant pattern for all but the first two Camille Cut surveys.

Figure 2-6. Current measurements across Camille Cut for Surveys 0 and 01 along transect line TL-1.

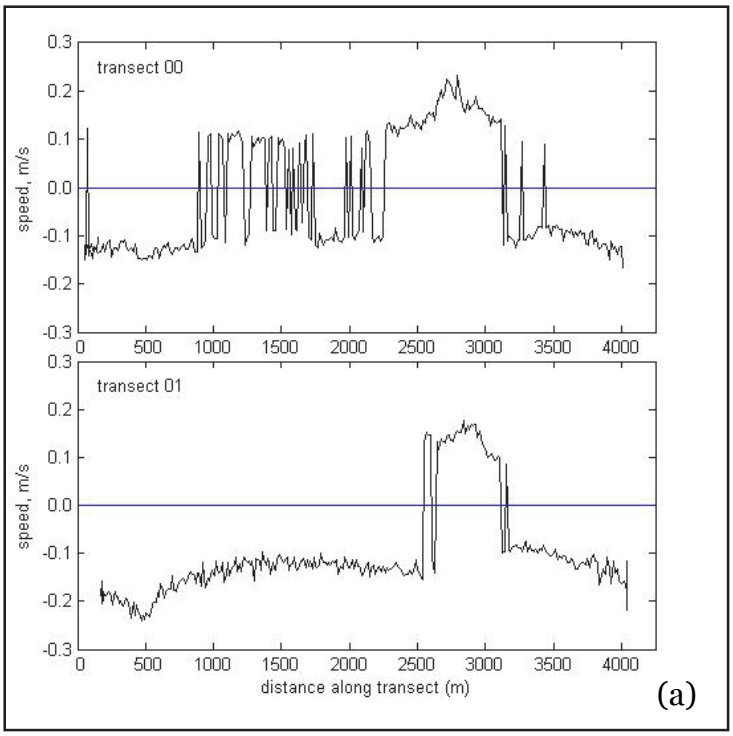

Current measurements across Camille Cut for Surveys 02 and 03 along transect line TL-1.

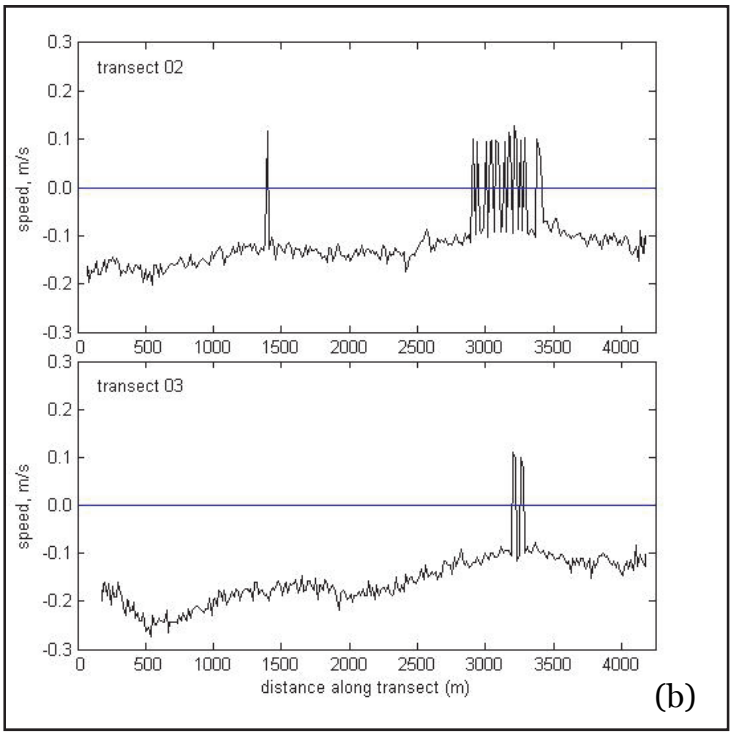

Figure 2-6. (continued) Current measurements across Camille Cut for Surveys 04 and 05 along transect line TL-1.

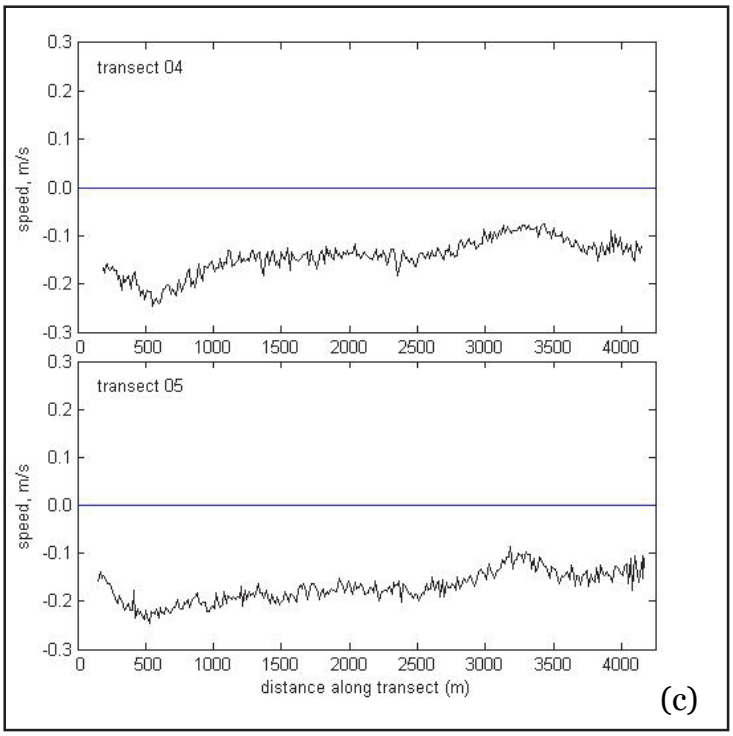

Current measurements across Camille Cut for Surveys 06 and 07 along transect line TL-1.

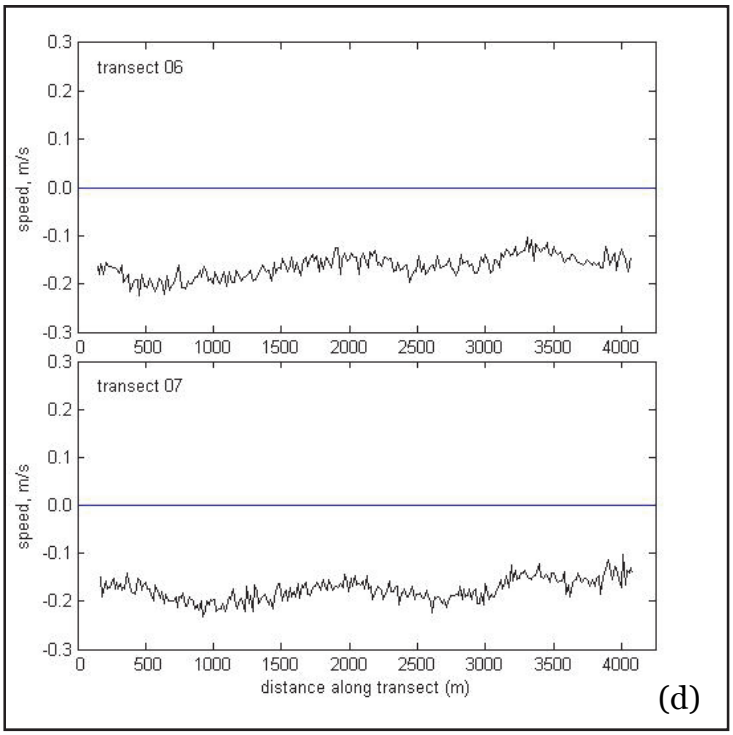

Figure 2-6. (continued) Current measurements across Camille Cut for Surveys 08 and 09 along transect line TL-1.

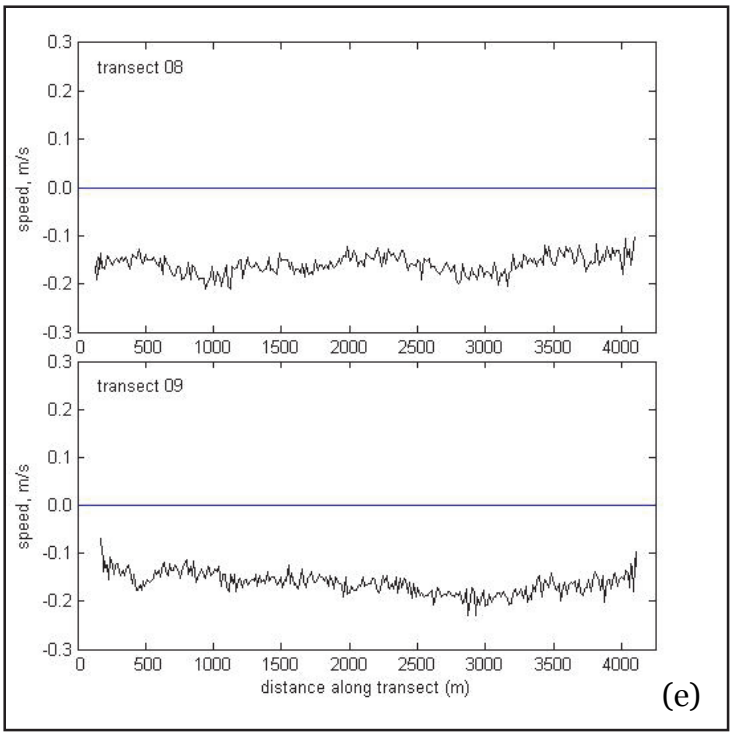

Current measurements across Camille Cut for Surveys 10 and 11 along transect line TL-1.

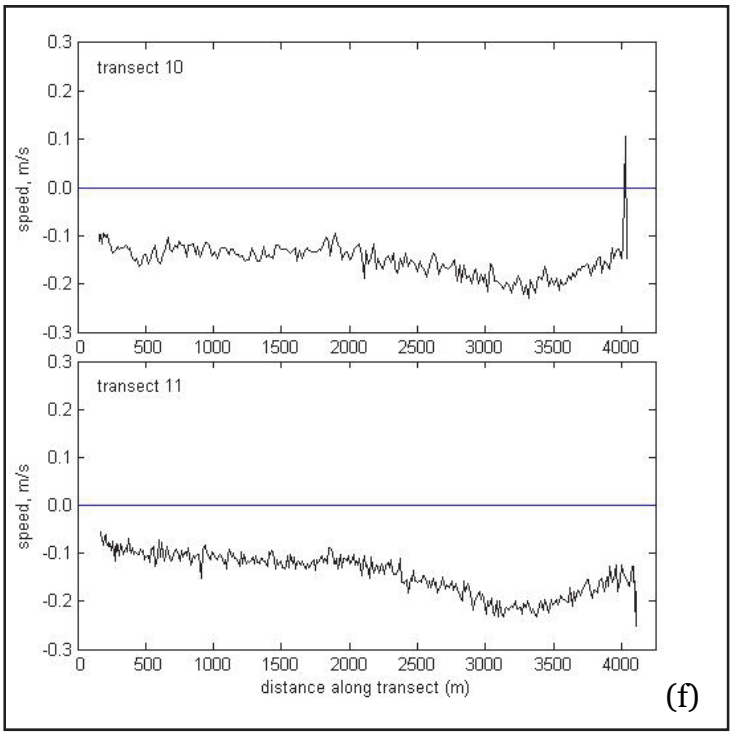

Figure 2-6. (concluded) Current measurements across Camille Cut for Survey 12 along transect line TL-1.

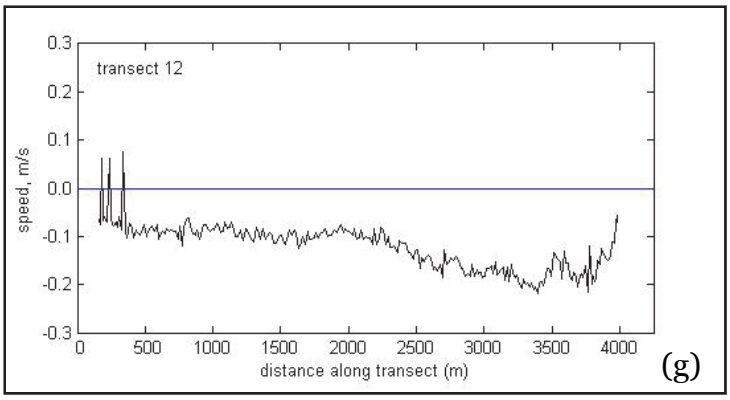

Figure 2-7. Current measurements across Camille Cut for Survey 10 along transect line TL-1, plotted in quadrants.

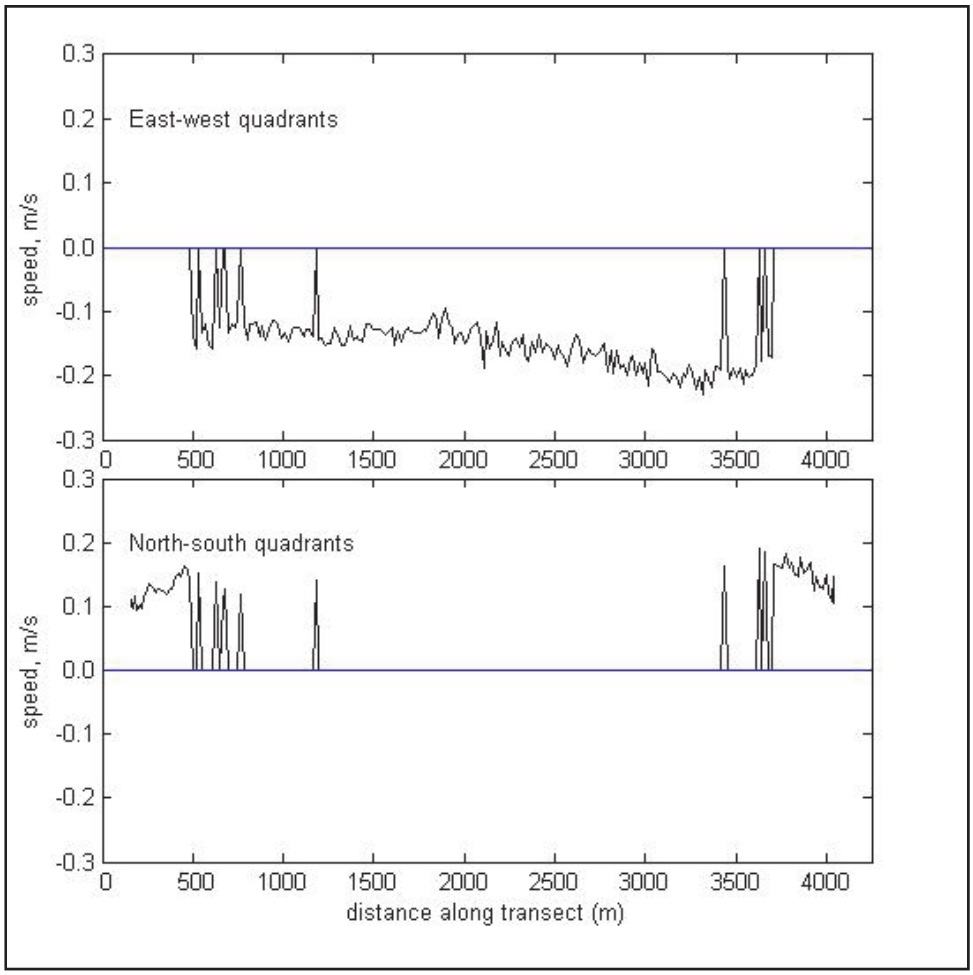

The plots of the currents across Camille Cut in Figures 2-6 and 2-7 show a clear ebb pattern during the survey, with the exception of the first two times the transect was surveyed. During these two times, there is some flood flow

centered at approximately 2750 m across the survey line. In these surveys, alongshore flow at the ends is captured in ebb flow to either side of the flood flow. Therefore the sum of the positive and negative depth-averaged currents for the two quadrants represented in the figures, multiplied by the cross-sectional areas the currents pass through, is expected to be the net flow trough Camille Cut in every case.

In Katrina Cut, currents along the current measurements survey lines are not simple ebb and flood. They are shown in Figure 2-8, categorized in quadrants, similar to what was done for Figure 2-7. In Figure 2-8, the quadrants are 315-45 and 135-225, representing flow through Katrina Cut, and 45-135 and 225-315, representing flow along the north shore of Dauphin Island. In Figure 2-8, flow appears to be predominantly in the north quadrant (positive currents along the bottom *x*-axis of the plot), indicating flood flow through Katrina Cut. In Figure 2-8, there appears to be some ebb flow near the center and on the eastern side of the Cut (negative currents along the bottom *x*-axis of the plot). However, during the other surveys along the transect lines, there appears to be predominantly eastward flow (45 to 135, positive currents along the top *x*-axis of the plots) representing alongshore flow that does not get captured by flow through Katrina Cut.

Figure 2-8. Current measurements across Katrina Cut for Survey 1 along transect line TL-5.

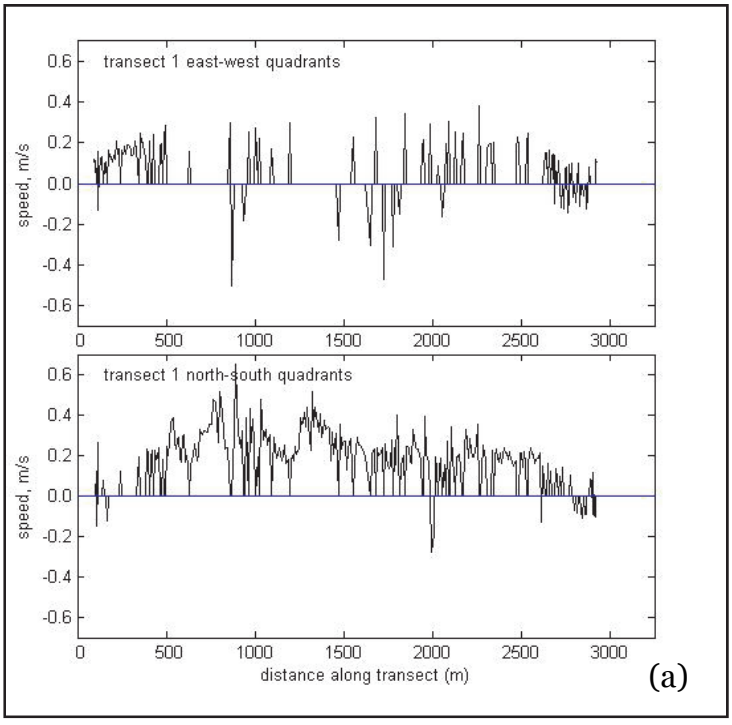

Figure 2-8. (continued) Current measurements across Katrina Cut for Survey 2 along transect line TL-5.

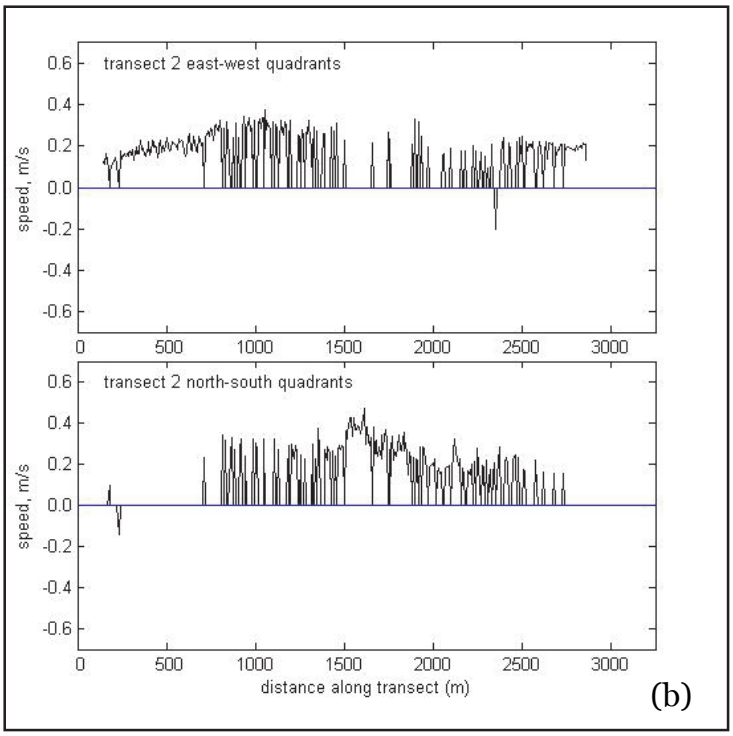

Current measurements across Katrina Cut for Survey 3 along transect line TL-5.

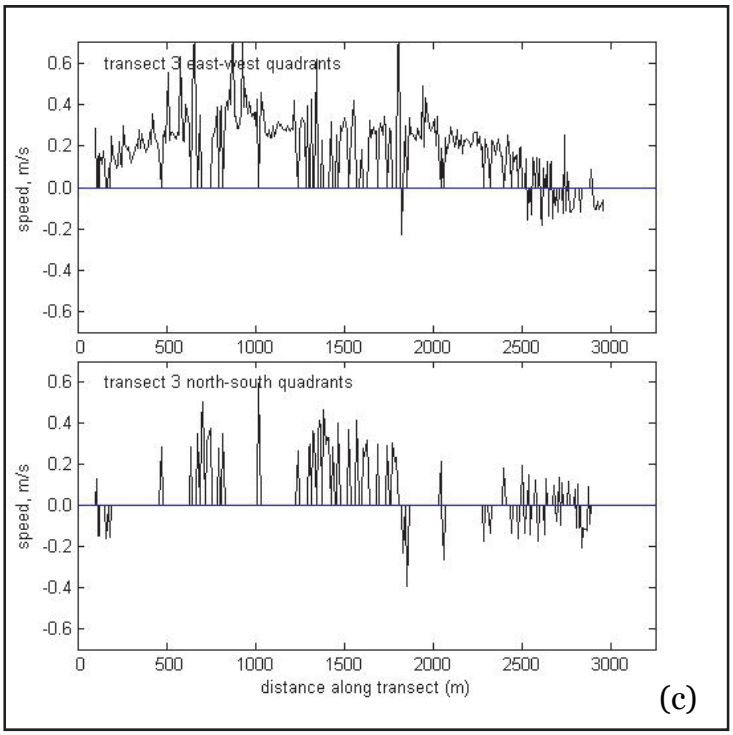

Figure 2-8. (continued) Current measurements across Katrina Cut for Survey 4 along transect line TL-5.

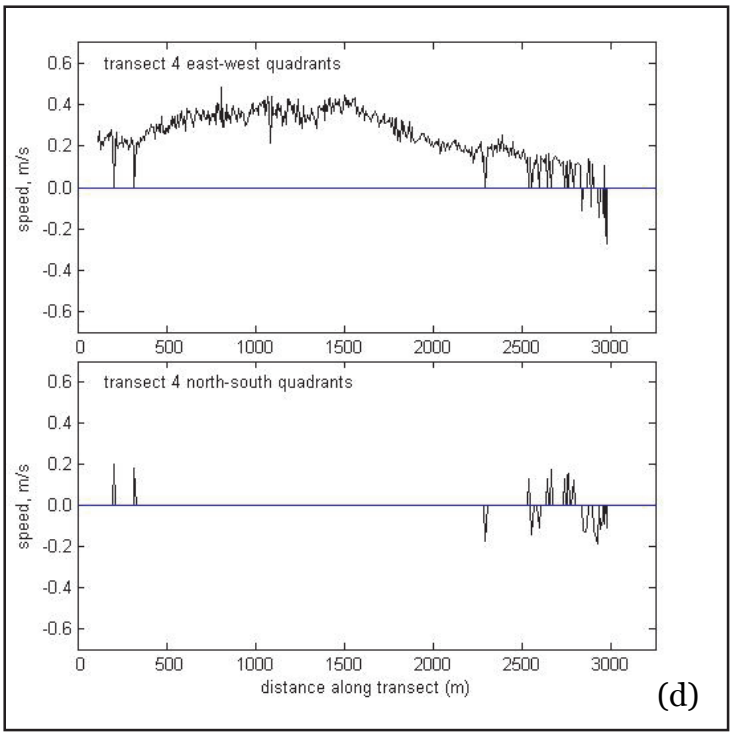

Current measurements across Katrina Cut for Survey 5 along transect line TL-5.

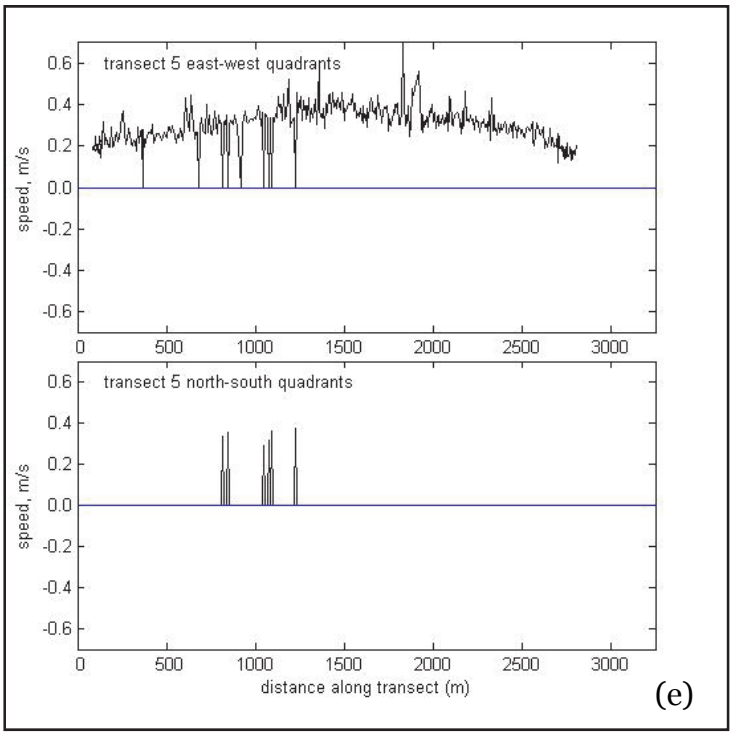

Figure 2-8. (continued) Current measurements across Katrina Cut for Survey 6 along transect line TL-5.

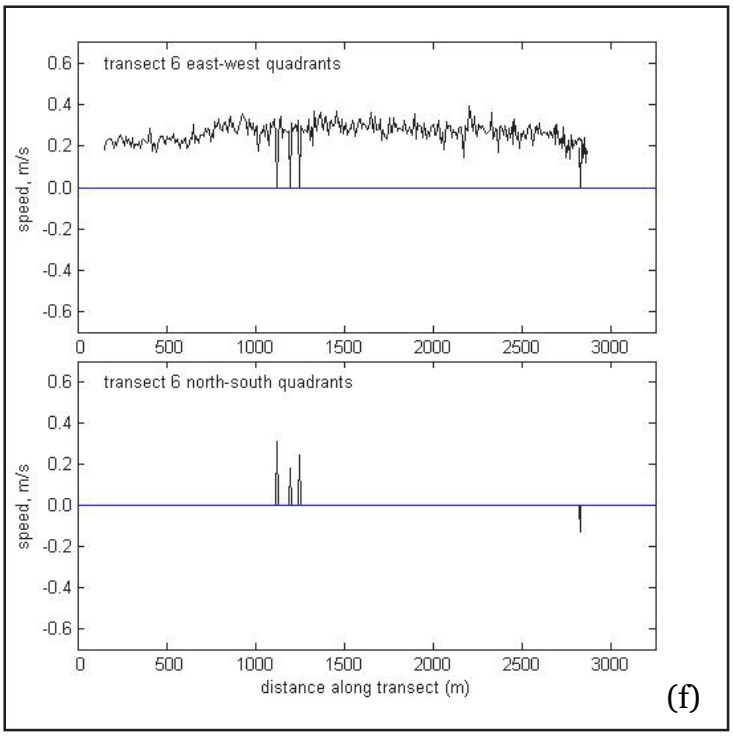

Current measurements across Katrina Cut for Survey 7 along transect line TL-5.

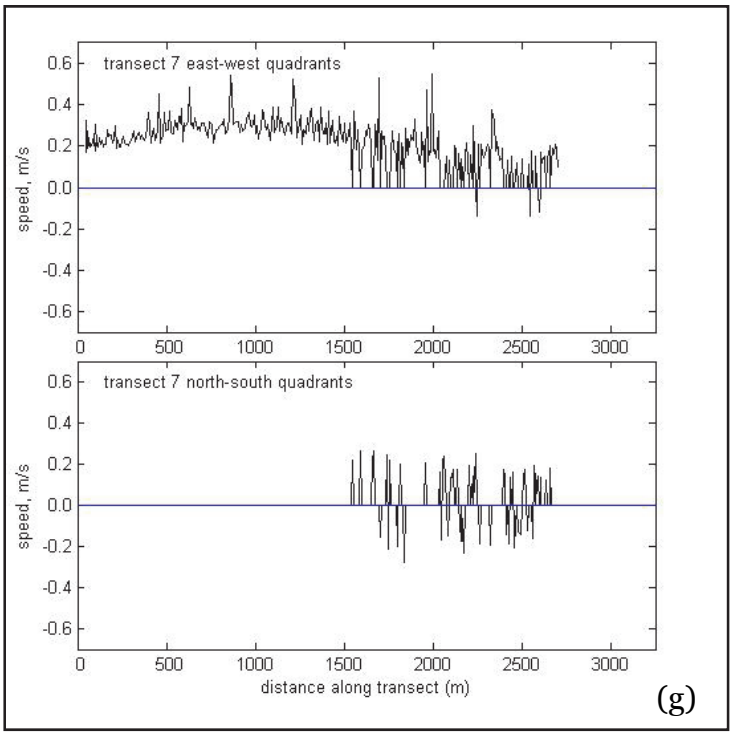

Figure 2-8. (continued) Current measurements across Katrina Cut for Survey 8 along transect line TL-5.

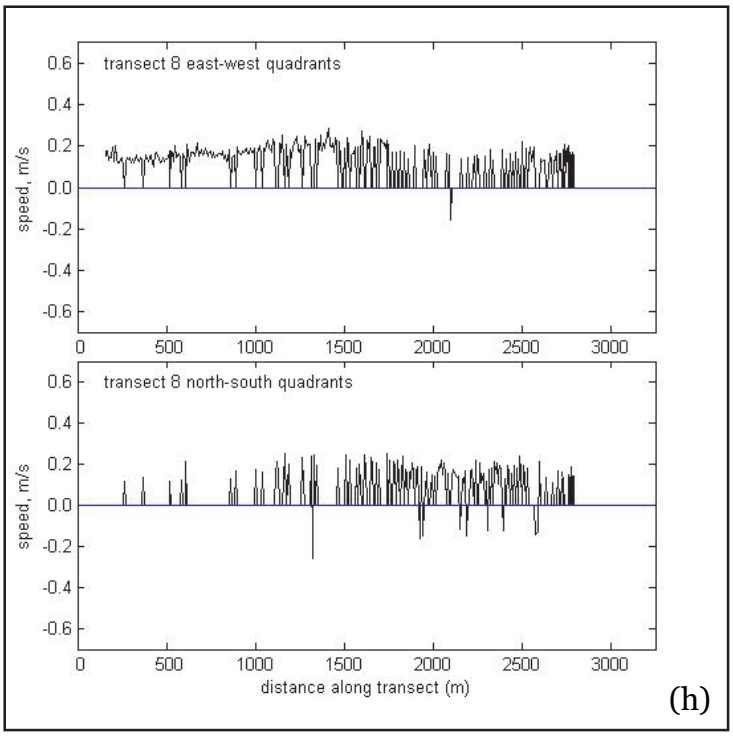

Current measurements across Katrina Cut for Survey 9 along transect line TL-5.

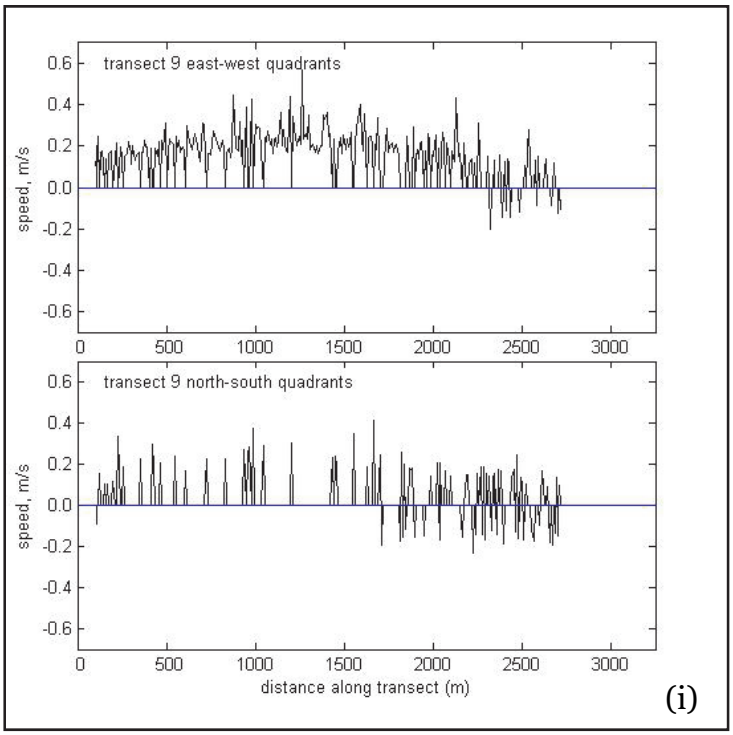

Figure 2-8 (continued) Current measurements across Katrina Cut for Survey 10 along transect line TL-5.

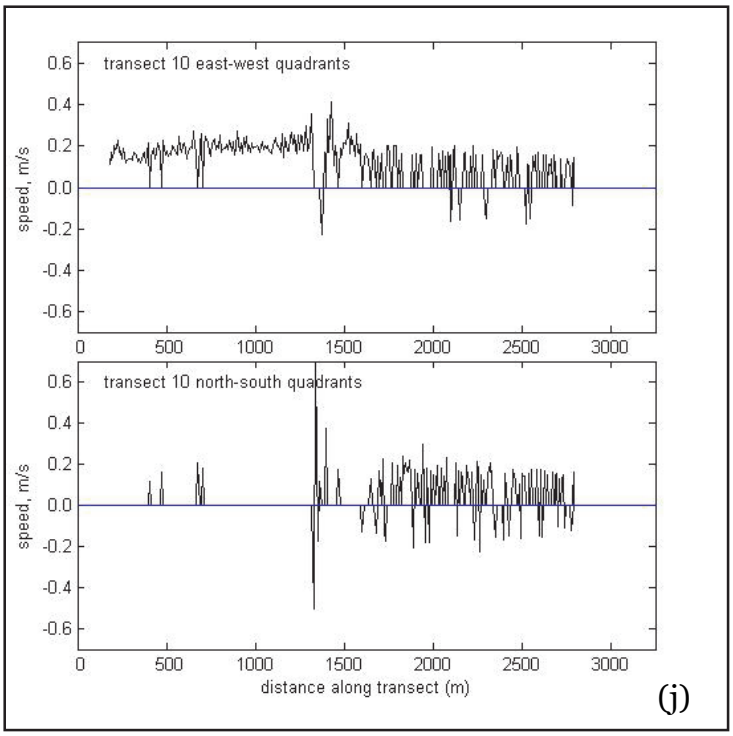

Current measurements across Katrina Cut for Survey 11 along transect line TL-5.

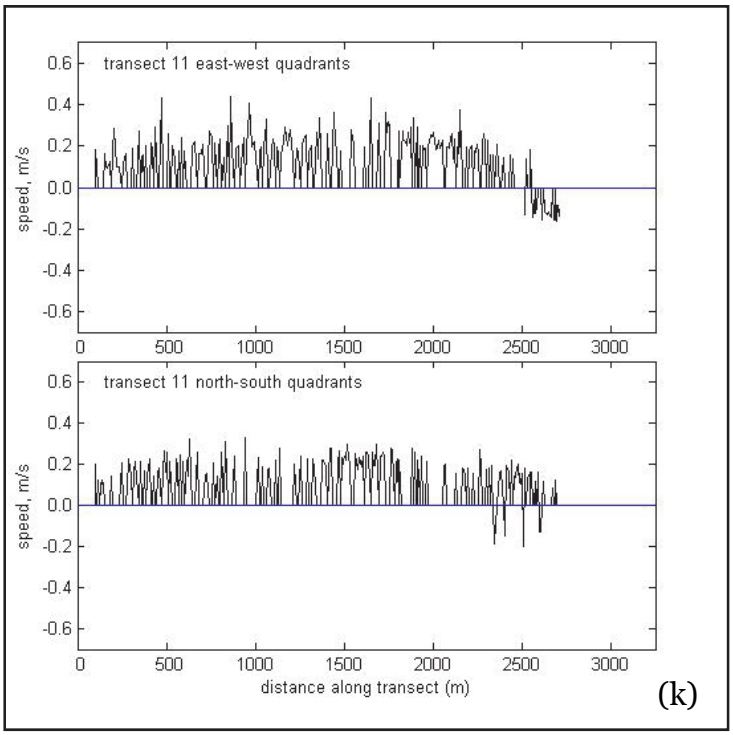

Figure 2-8 (continued) Current measurements across Katrina Cut for Survey 12 along transect line TL-5.

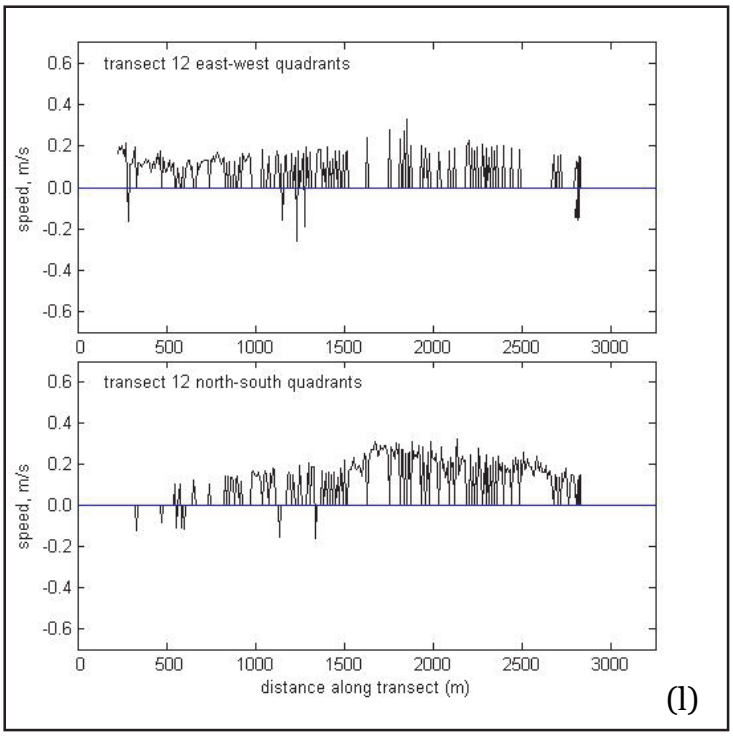

Current measurements across Katrina Cut for Survey 13 along transect line TL-5.

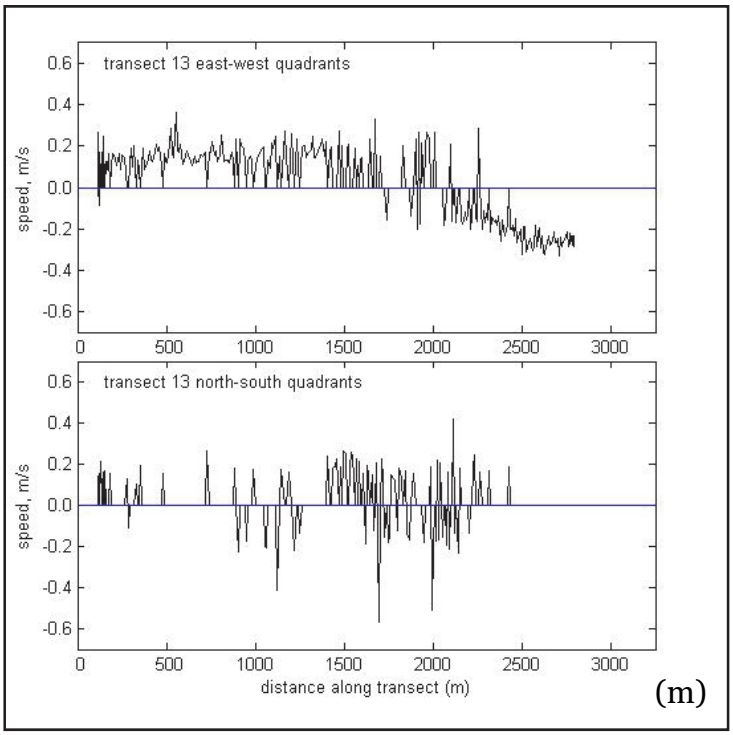

Figure 2-8. (continued) Current measurements across Katrina Cut for Survey 14 along transect line TL-5.

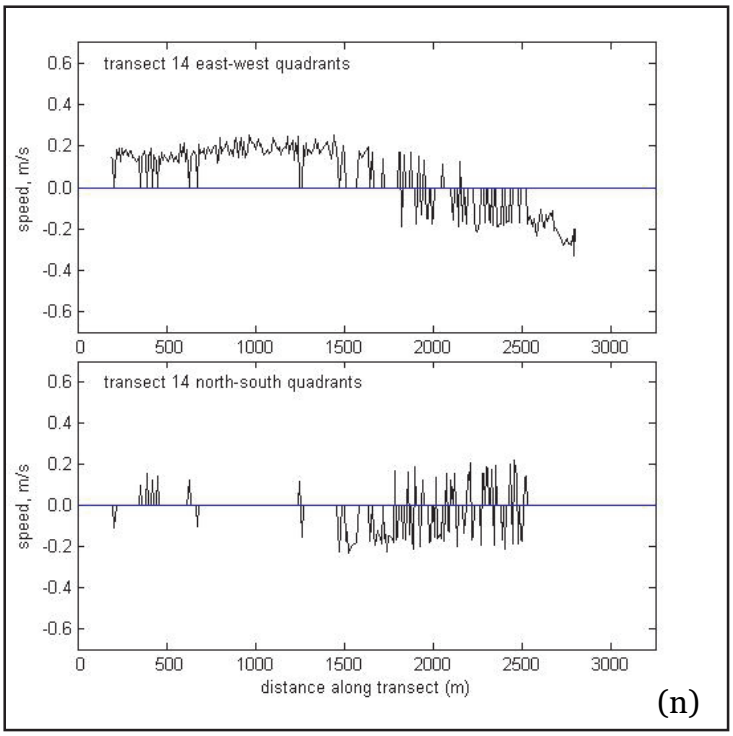

Current measurements across Katrina Cut for Survey 15 along transect line TL-5.

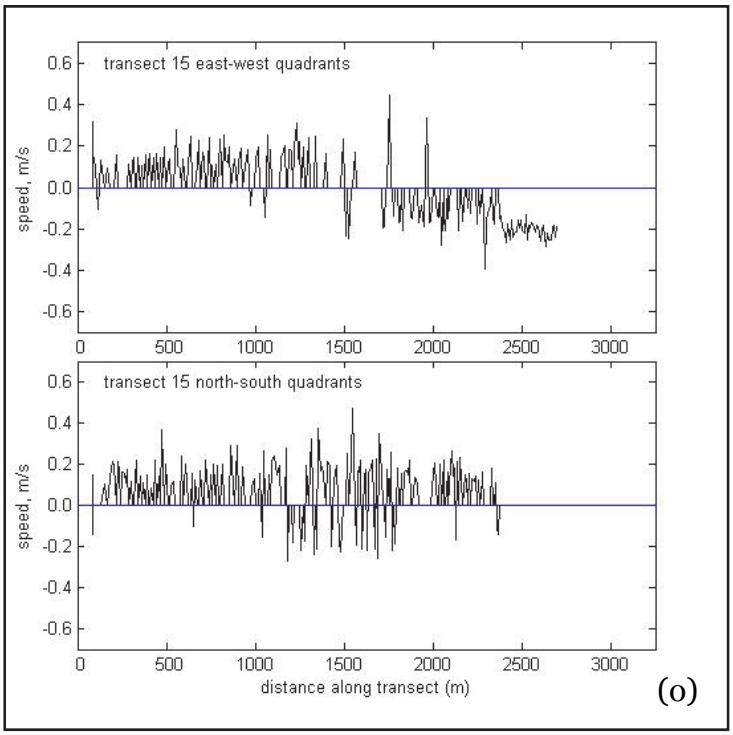

Figure 2-8. (continued) Current measurements across Katrina Cut for Survey 16 along transect line TL-5.

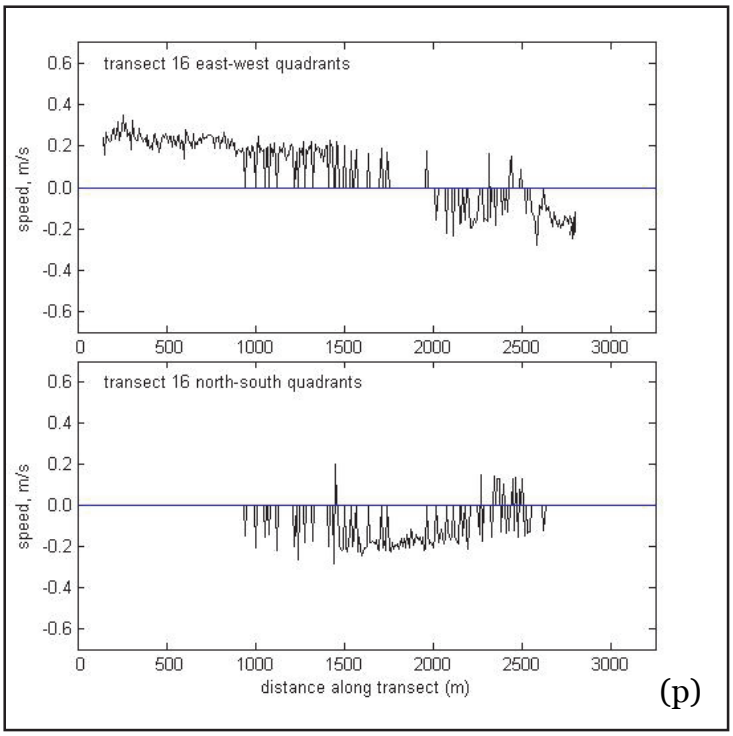

Current measurements across Katrina Cut for Survey 17 along transect line TL-5.

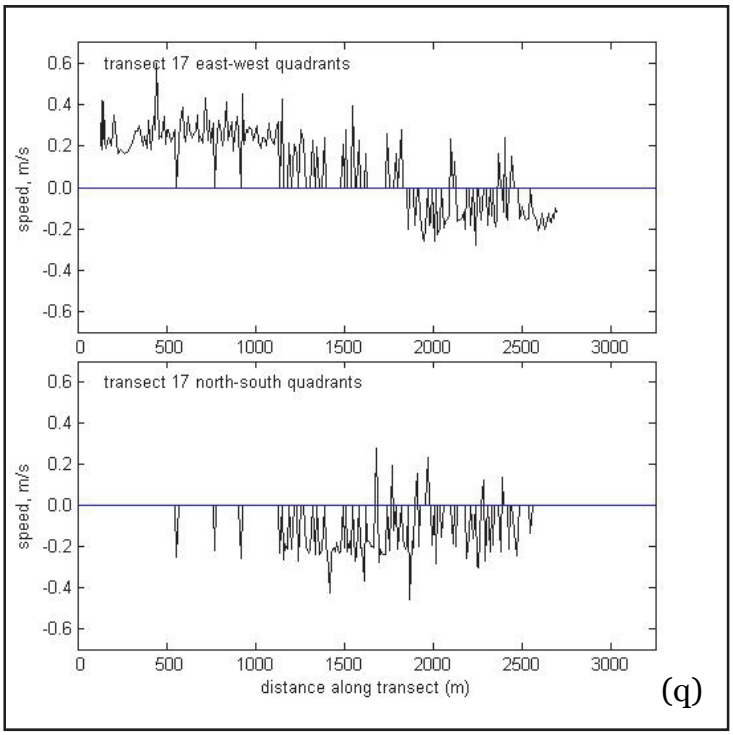

Figure 2-8. (concluded) Current measurements across Katrina Cut for Survey 18 along transect line TL-5.

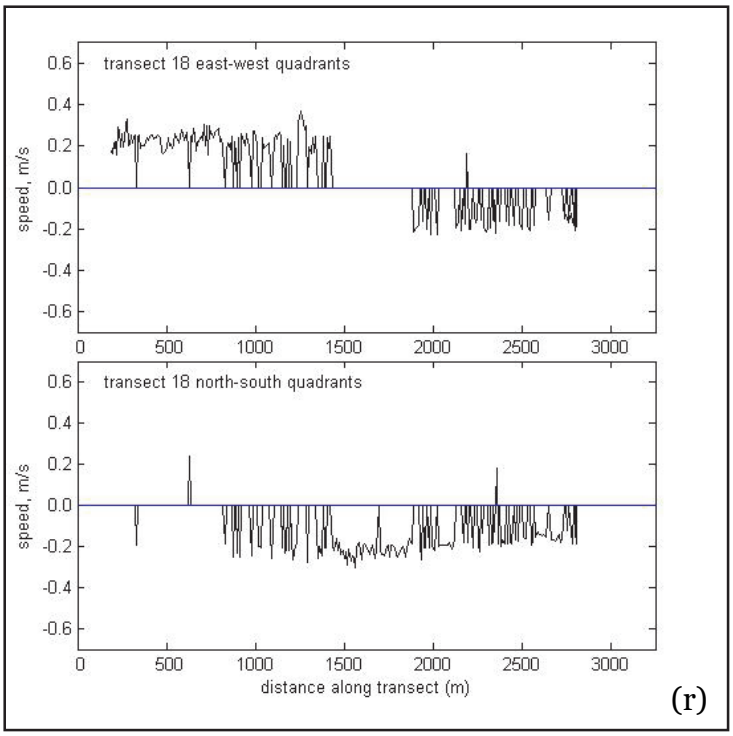

Current measurements across Katrina Cut for Survey 19 along transect line TL-5.

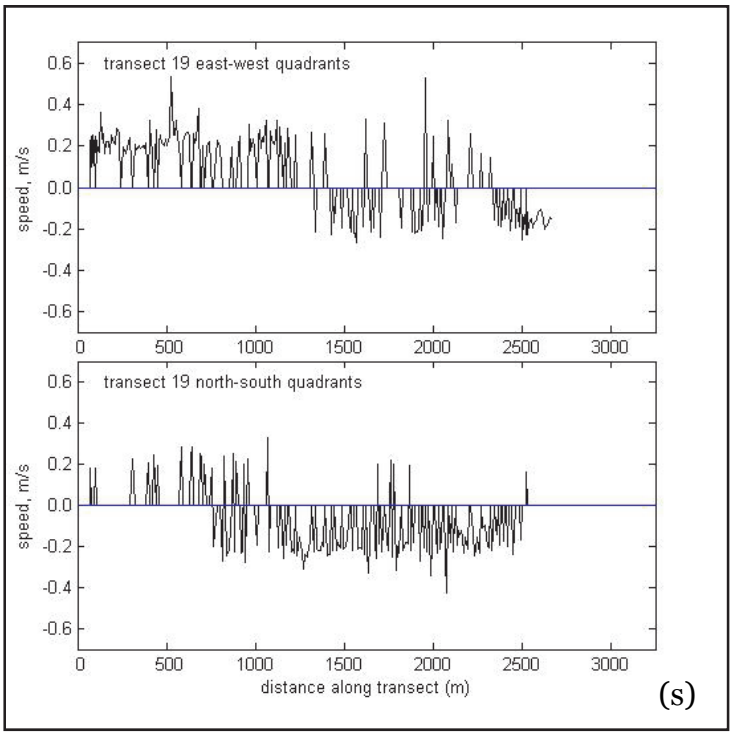

The position of the vessel track was chosen to be as close to the Cut as possible, but in deep enough water where currents could be reliably surveyed with the ADCP without vessel induced velocities masking the real currents (as can happen in very shallow water). Unfortunately, it appears from these data that the north-south flow expected for flow through Katrina Cut is not strong enough in all cases to be clearly distinguishable from the east-west currents along Dauphin Island on its north shore.

Start times for each survey across lines TL-1 (Camille Cut) and TL-5 (Katrina Cut) are given in Tables 2-10 and 2-11. For Camille Cut, net flow through the Cut can be calculated, and is also given in Table 2-10.

Table 2-10. Start times of the current measurements surveys for Camille Cut and net flow through Camille Cut on March 31, 2010.

Surveys of TL-1	0	1	2	3	4	5	6
Time (GMT)	16:35	17:09	17:54	18:29	19:05	19:41	20:18
Net ebb flow (m^3/sec)	158	1147	1198	2140	3329	2899	2908
Surveys of TL-1 continued	7	8	9	10	11	12	
Time (GMT)	20:48	21:24	21:56	22:33	23:04	23:46	
Net ebb flow (m^3/s)	3181	2918	3087	2607	2366	1625	

Table 2-11. Start times of the current measurements surveys for Katrina Cut on March 25, 2010.

Surveys of TL-5	1	2	3	4	5	6	7
Time (GMT)	14:38	15:15	17:01	17:22	17:57	18:22	18:46
Surveys of TL-5 continued	8	9	10	11	12	13	14
Time (GMT)	19:08	19:30	19:52	20:15	20:37	20:58	21:18
Surveys of TL-5 continued	15	16	17	18	19		
Time (GMT)	21:38	21:57	22:18	22:34	22:55		

Cross sections of current speeds along the transects across Ship Island and Dog Keys Passes, and stick plots of depth-averaged current velocities in the shallower Petit Bois Pass and Pass Aux Herons are in Appendix C.

Start times of the surveys, and net flows are given in Table 2-12 and 2-13. Data in Tables 2-10 through 2-13, show that Camille Cut and Dog Keys Passes are both ebbing at 16:41, while flood transport continues in Ship

Table 2-12. Start times of the current measurements surveys and net flow for Ship Island and Dog Keys Passes on March 31, 2010 and Petit Bois Pass on March 25, 2010.

Ship Island Pass								
Surveys of TL-3	1	2	3	4	5	6	7	8
Time (GMT)	14:53	15:58	17:09	18:17	19:26	20:38	21:49	22:55
Net flow (m^3/sec)	flood 10476	Flood 8089	flood 6850	flood 5285	flood 2830	ebb 4111	ebb 5016	ebb 10319
Dog Keys Passes								
Surveys of TL-2	1	2	3	4	5	6	7	
Time (GMT)	12:37	14:10	15:55	17:41	19:37	21:36	23:50	
Net flow (m^3/sec)	flood 8770	flood 8127	flood 2670	ebb 2448	ebb 11624	ebb 14924	ebb 9430	
Petit Bois Pass								
Surveys of TL-4	1	2	3	4	5	6	7	8
Time (GMT)	14:49	15:39	16:23	17:13	17:57	18:47	19:25	20:04
Net flow (m^3/sec)	flood 6843	flood 9552	flood 9571	flood 3371	flood 2125	flood 2324	flood 2213	flood 2077
Surveys of TL-4 continued	9	10	11					
Time (GMT)	20:43	21:22	21:59					
Net flow (m^3/sec)	flood 2604	flood 1810	ebb 2071					

Table 2-13. Start times of the current measurements transects survey lines for Pass Aux Herons and flow into and out of the Mississippi Sound through the Pass on March 25, 2010.

Pass Aux Herons								
Surveys of TL-6	1	2	3	4	5	6	7	8
Time (GMT)	13:41	14:13	14:46	15:16	15:49	16:21	16:52	17:16
Net flow (m^3/sec)	into 535	into 129	out 293	out 650	out 1125	out 1250	out 1037	out 1317
Surveys of TL-4 continued	9	10	11	12	13	14	15	16
Time (GMT)	17:48	18:20	18:57	19:30	20:08	20:38	21:13	21:46
Net flow (m^3/sec)	out 2361	out 2204	out 1697	out 1679	out 1079	out 723	out 603	out 500
Surveys of TL-4 continued	17	18	19					
Time (GMT)	22:17	22:50	23:20					
Net flow (m^3/sec)	out 523	out 393	out 174					

Island Pass until 20:38. At the eastern end of the Mississippi Sound, the flow is into the Sound through Petit Bois Pass and out of the Sound through Pass Aux Heron until 21:59, when Petit Bois Pass begins ebb transport, while the flow through Pass Aux Herons continues out of the Sound into Mobile Bay until 23:20.

2.2 Water samples

Seven water samples were taken near Ship Island and brought back to ERDC were their salinities were determined. Samples were also taken for water quality analyses, but they were not filtered and preserved in the field, and the analyses were not conducted. Near Dauphin Island, four samples were taken for salinity analysis. The locations of the water samples are shown in Figures 2-9 and 2-10. The locations and salinities are given in Table 2-14.

2.3 Summary

Two directional wave gauges were deployed on March 4, 2010 and recovered on July 15, 2010. They were located on the north side of Katrina Cut, in the Mississippi Sound, and on the south side of Katrina Cut in the Gulf of Mexico. The gauge in the Sound recorded valid data for the entire duration of the deployment. The Gulf gauge stopped recording valid data on April 30, 2010, as the result of a problem with the electronics. These wave data show that the predominant wave direction were waves from the southeast (135 to 165 degrees true) at both gauges. This was also the direction for the largest waves at both locations. In comparison to the Gulf gauge, the waves measured at the Sound gauge were significantly smaller.

Current measurements show that maximum depth-averaged ebb currents through Camille Cut on March 31, 2010 were about 0.25 m/sec and maximum ebb flow was 3087 m^3/sec. Flow through Katrina Cut was evident in the current measurements across Katrina Cut, but the survey lines were too far north of the Cut to quantitatively differentiate the flow through the Cut from the along-shore flow on the north side of Dauphin Island. Ebb flow through Camille Cut and Dog Keys Passes on March 31 began approximately four hours before the flood flow in Ship Island Pass changed to ebb. The maximum measured flood and ebb transports through Ship Island Pass were 10476 and 10319 m^3/sec, respectively. The maximum measured ebb flow through Dog Keys Passes was 14924 m^3/sec. Near Dauphin Island, on March 25, 2010, the flow was out of the Mississippi Sound (ebb) through

Figure 2-9. Water sample locations near Ship Island.

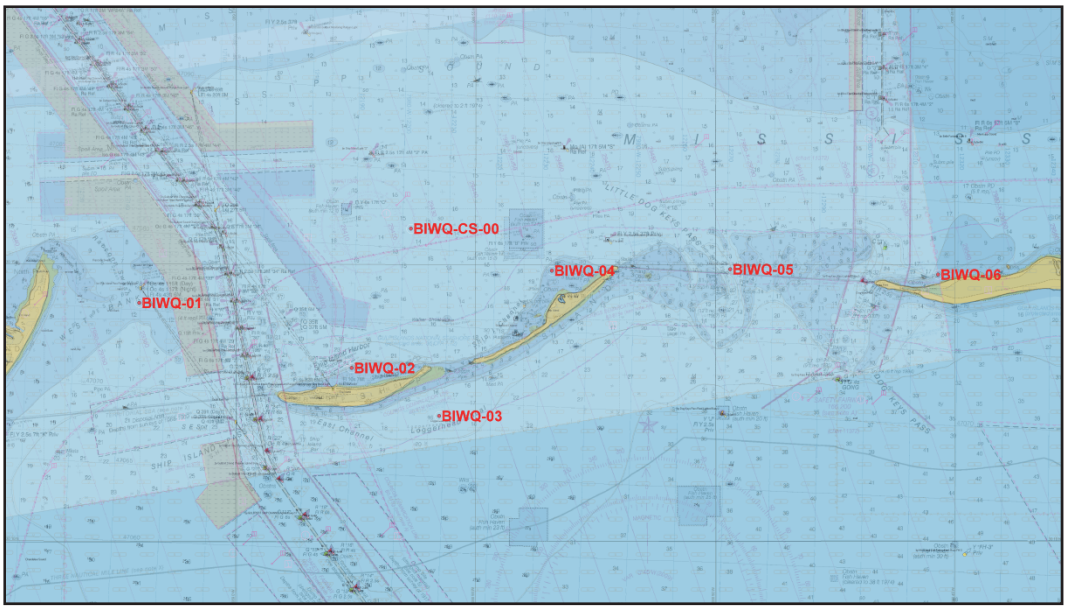

Figure 2-10. Water sample locations near Dauphin Island.

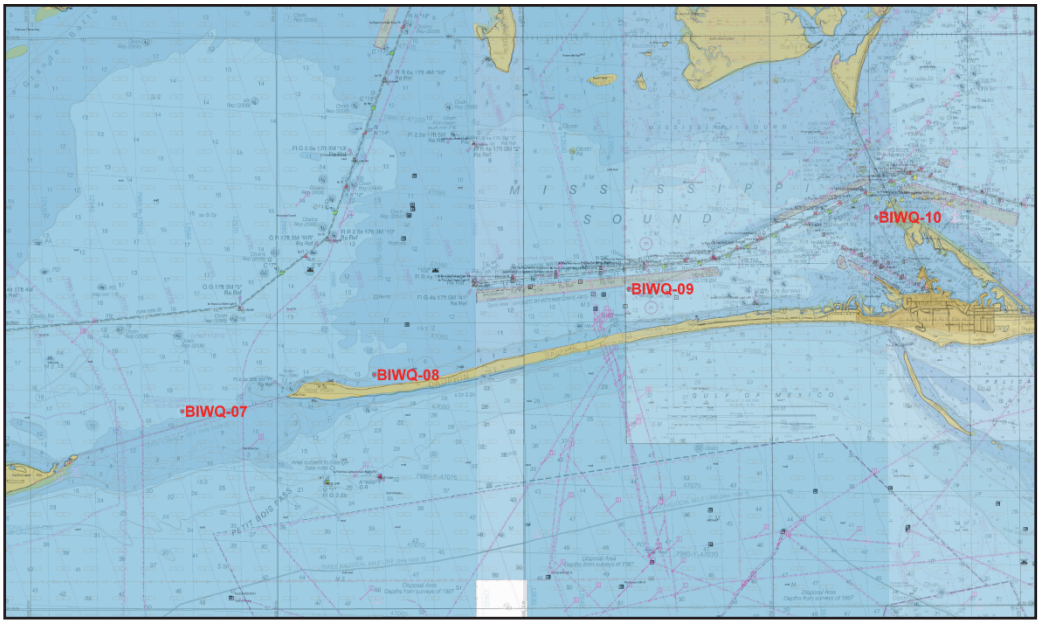

Table 2-14. Water sample locations and salinities.

Station name	latitude °N	longitude °W	depth(m)/salinity (ppt)
BIWQ-CS-00	30.26074	88.93915	0.31/24.5 2.24/26.7 4.88/27.3
BIWQ-01	30.23833	89.03361	0.31/26.5 1.83/28.7 3.66/29.8
BIWQ-02	30.21879	88.95972	0.31/24.1 1.07/24.3 2.13/27.0
BIWQ-03	30.20441	88.92929	0.31/26.0 3.05/29.4 5.49/33.3
BIWQ-04	30.24816	88.89014	0.31/23.0 0.91/24.1 1.83/24.3

Station name	latitude °N	longitude °W	depth(m)/salinity (ppt)
BIWQ-05	30.24856	88.82818	0.31/28.7 3.05/29.2 6.10/30.6
BIWQ-06	30.24694	88.75583	0.31/29.0 1.07/28.9 2.13/29.5
BIWQ-07	30.22458	88.36532	0.31/22.0 2.50/26.0 4.42/29.4
BIWQ-08	30.23500	88.30056	0.31/19.3 2.13/23.6 3.66/26.2
BIWQ-09	30.25972	88.21472	0.31/14.4 1.98/18.3 3.35/21.2
BIWQ-010	30.28020	88.13108	0.00/12.3 1.83/13.2 3.05/14.3

Pass Aux Herons and into the Sound through Petit Bois Pass for approximately the first seven hours of the survey. During the last survey across Petit Bois Pass, the currents began to ebb while current was still flowing out of the Sound into Mobile Bay through Pass Aux Herons. The maximum measured flood flow through Petit Bois Pass was 9571 m^3/sec. The maximum flow through Pass Aux Herons was 2361 m^3/sec.

The water samples were not adequately processed to produce useful water quality information. Salinities were measured and the ranges of salinities for the water samples were 12.3 to 33.3 ppt. The lowest salinities were measured in the eastern part of the Sound near Dauphin Island (Stations BIWQ-08, 09, and 10). The lowest were in Pass Aux Herons, 12.3 to 14.3 ppt, and increased to the west, where they were 19.3 to 26.2 ppt in the Sound near the western end of Dauphin Island. The highest measured salinities were in the Gulf, south of Ship Island, 26.0 to 33.3 ppt. In the Sound north of Ship Island (Stations BIWQ-00, 02 and 04), the range of measured salinities were 23.0 to 27.3 ppt. The maximum salinity measured in the passes was 30.6 ppt near the bottom in Dog Keys Pass.

3 Circulation Modeling[1]

In an effort to quantify the relative changes in circulation within Mississippi Sound resulting from proposed Ship Island restoration alternative configurations, a combination of two-dimensional (2D) ADCIRC model (Luettich et. al. 1992) and a three-dimensional (3D) CH3D-WES model (Chapman et. al. 1996) were applied. These models were primarily applied to provide hydrodynamic input to the water quality model CE-QUAL-ICM (Bunch et al. (2003) and Bunch et al. (2005)).

3.1 ADCIRC grid, model forcing and calibration

An ADCIRC simulation of the Mississippi Sound with Ship Island represented in the grid in the condition that existed prior to Hurricane Katrina, as shown in National Oceanic and Atmospheric Administration (NOAA) Nautical Chart 11373 (1998), was performed for the period March 12 through September 18, 1998 using an existing grid shown in Figure 3-1.

Figure 3-1. ADCIRC grid.

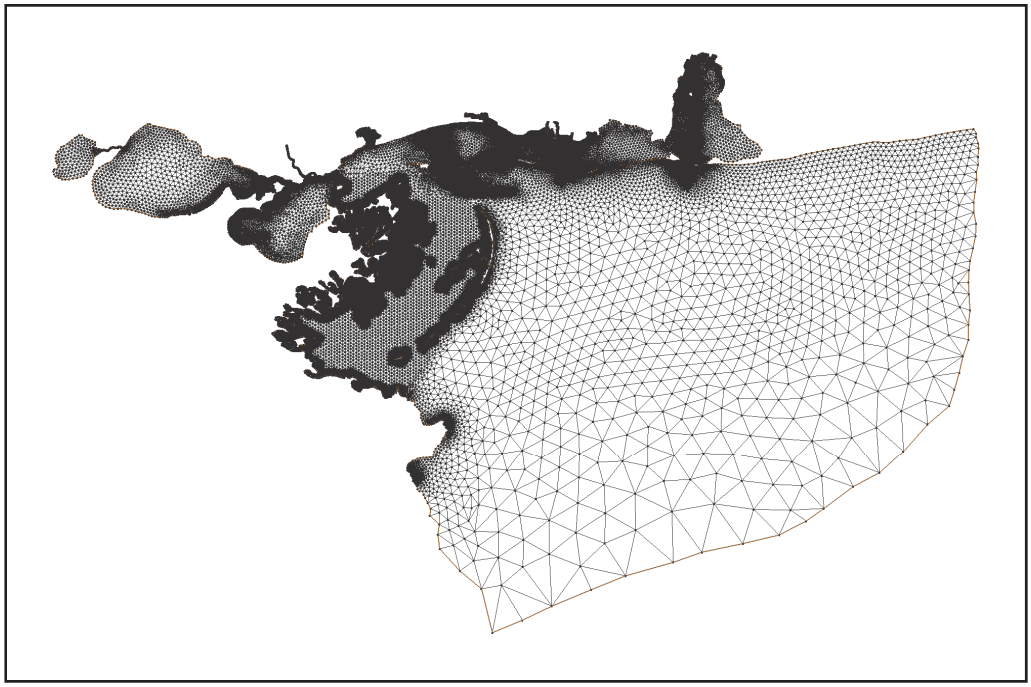

[1] Written by Raymond S. Chapman, Coastal and Hydraulics Laboratory, US Army Engineer Research and Development Center, Vicksburg, MS.

Model forcing consisted of wind and tidal constituent inputs. The grid had been previously calibrated using in-house Coastal and Hydraulics Laboratory (CHL) current and water level data taken in Ship Island Pass (30o 13.7' N, 89o 0.7' W) from January 22 to April 9, 2004. The results for March 12 through September 18, 1998 simulation were verified by comparing the ADIRC calculated water levels with water level measurements made by NOAA at Waveland (Station No. 8747766, 30o 16.9' N, 89o 22' W), and measurements made by the Corps of Engineers at Dauphin Island (DPIA1, 30o 14.88' N, 88o 4.38' W) shown in Figure 3-2 (Bunch et al. 2005 and Chapman et al. 2006).

Figure 3-2 Waveland, MS and Dauphin Island, AL gauge locations.

Tidal forcing was applied to the grid by imposing tidal water-level variations along its open- ocean boundary. Seven tidal constituents (i.e., K1, O1, Q1, M2, S2, N2, and K2) from the East Coast 2001 Data Base of Tidal Constituents (Mukai et. el. 2002) were applied in the simulations. Hourly wind speeds and directions were available for most of the March to September simulation period from NOAA National Data Buoy Center (NDBC) Stations DPIA1 on the eastern end of Dauphin Island and B42007 located 41 km south-southeast of Biloxi (30o 5.4' N, 88o 46.14' W). Wind data is not complete for the entire period at B42007. When wind data was not available for B42007, wind information from the Corps of Engineers Wave Information Study (WIS) hindcasts at Station 145, about 1.8 km west of B42007, was used in place of the missing data (Figure 3-3).

Figure 3-3. NDBC buoy and WIS model locations.

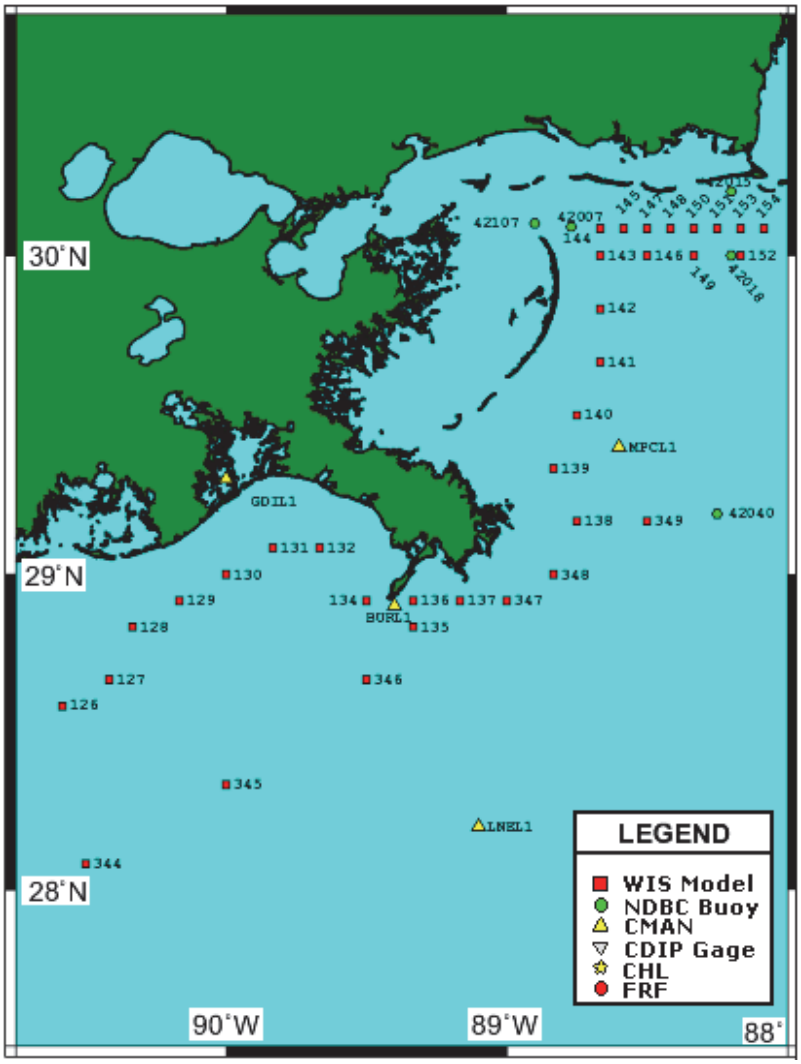

Winds were applied to the ADCIRC grid by using winds from B42007 (and WIS Station 145 where necessary) from the western most grid boundary over to Pascagoula, and winds from DPIA1 from about half way between Petit Bois Island and Dauphin Island over to the eastern grid boundary. In between the two, a linear interpolation of the wind speeds and directions was used. Winds were uniform in the onshore-offshore direction.

Water-level elevations calculated by ADCIRC along the CH3D open-ocean boundary provided the tidal forcing for CH3D. Figure 3-4 shows an example of the ADCIRC simulated elevations used by CH3D. A total of four simulations were made to provide CH3D tidal forcing, all for March 12 through September 18, 1998. The first simulation was with Ship Island as it was in 1998, the second was with Ship Island as it exists today after Hurricane

Katrina, the third was a degraded Ship Island condition, and the fourth was with a proposed restored Ship Island. The only changes made in the grid for each configuration were to Ship Island. Other areas were not changed.

Figure 3-4. ADCIRC generated elevations at CH3D forcing node 3 for March 13 to April 18, 1998.

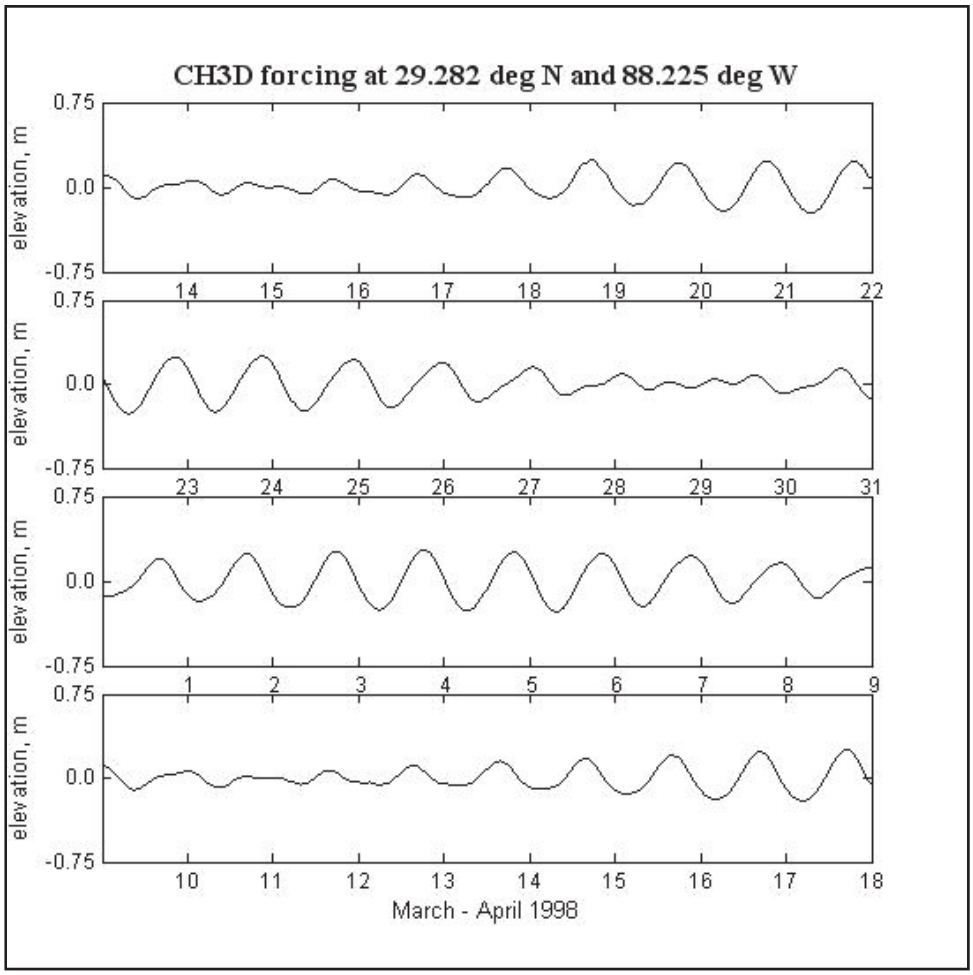

Figure 3-5 shows the grid and bathymetry around Ship Island for the 1998 condition and the post-Katrina condition. The post-Katrina condition is based on the 2008 – 2009 surveys conducted by the United States Geological Survey (USGS) (Buster and Morton 2011) and the US Army Corps of Engineers, Mobile District. The Degraded condition, shown in Figure 3-6, was created by placing all of the Ship Island area underwater at a depth of approximately 2-m. Figure 3-6 shows the restored condition, which includes filling the cut between East and West Ship Islands and the nearshore region of East Ship Island with upwards of 22 million cubic yards of sandy material. The fill template for Camille Cut breach closure consists of an averaged approximate 3,280-m equilibrated island width at an

Figure 3-5. The grid around Ship Island for the 1998 condition (top) and the Post-Katrina condition (bottom).

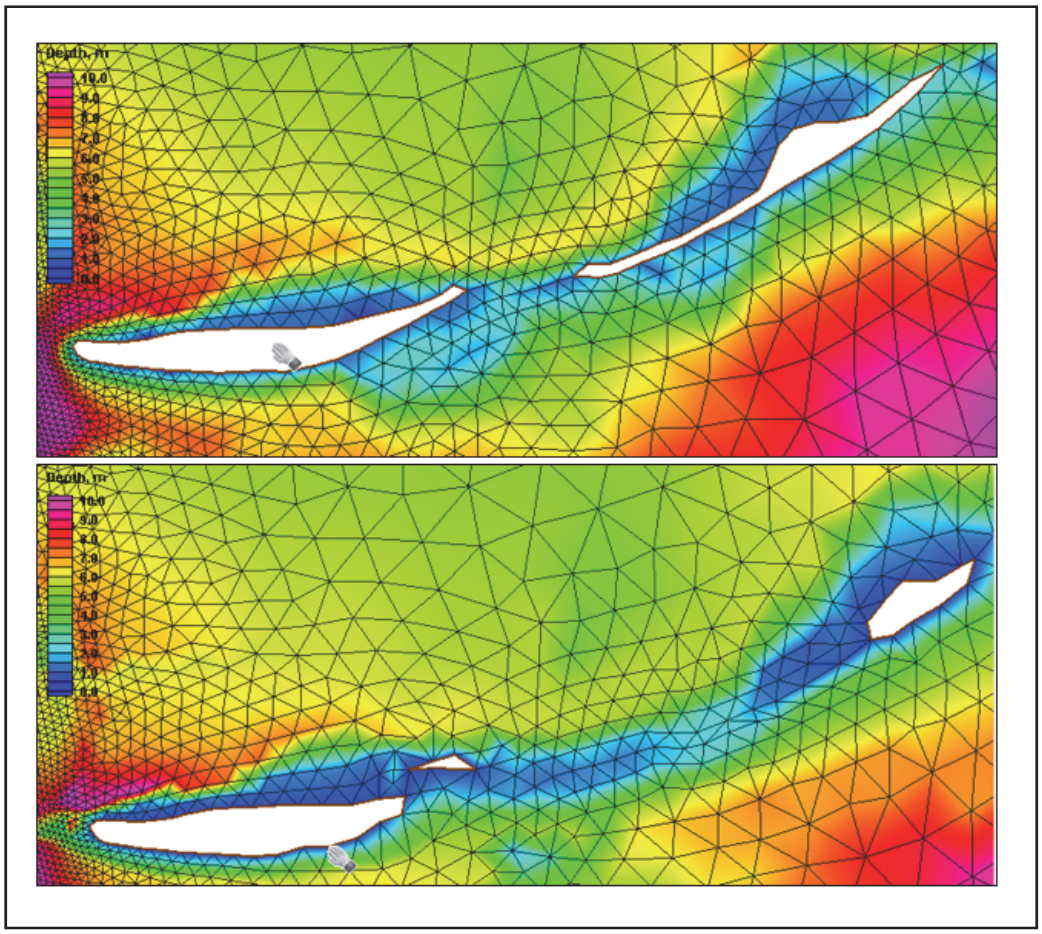

elevation of approximately 2.4-m NAVD88. The feeder berm template along East Ship consists of fill placed between elevations of approximately +0.3 to -4.6-m NAVD88. Finally, a Cumulative Ship Island alternative grid was developed based on inclusion of the proposed restored conditions, closure of Katrina Cut breach in Dauphin Island and construction of authorized channel dimensions at Gulfport and Pascagoula Federal Navigation projects.

Results of the simulation with Ship Island in its 1998 condition (Figure 3-5, top) for May 15 to June 15, 1998, are plotted with observed water levels at Dauphin Island and Waveland in Figures 3-7 and 3-8, respectively. These plots show good agreement at both the Dauphin Island and Waveland gauges when considering that the meteorological forcing data used were input files of opportunity and not a project specific and analyzed climatology (IPET 2008; Cox and Cardone 2007). In addition, atmospheric pressure forcing was not applied in these simulations.

Figure 3-6. The grid around Ship Island for the degraded condition (top) and the restored condition/cumulative (bottom).

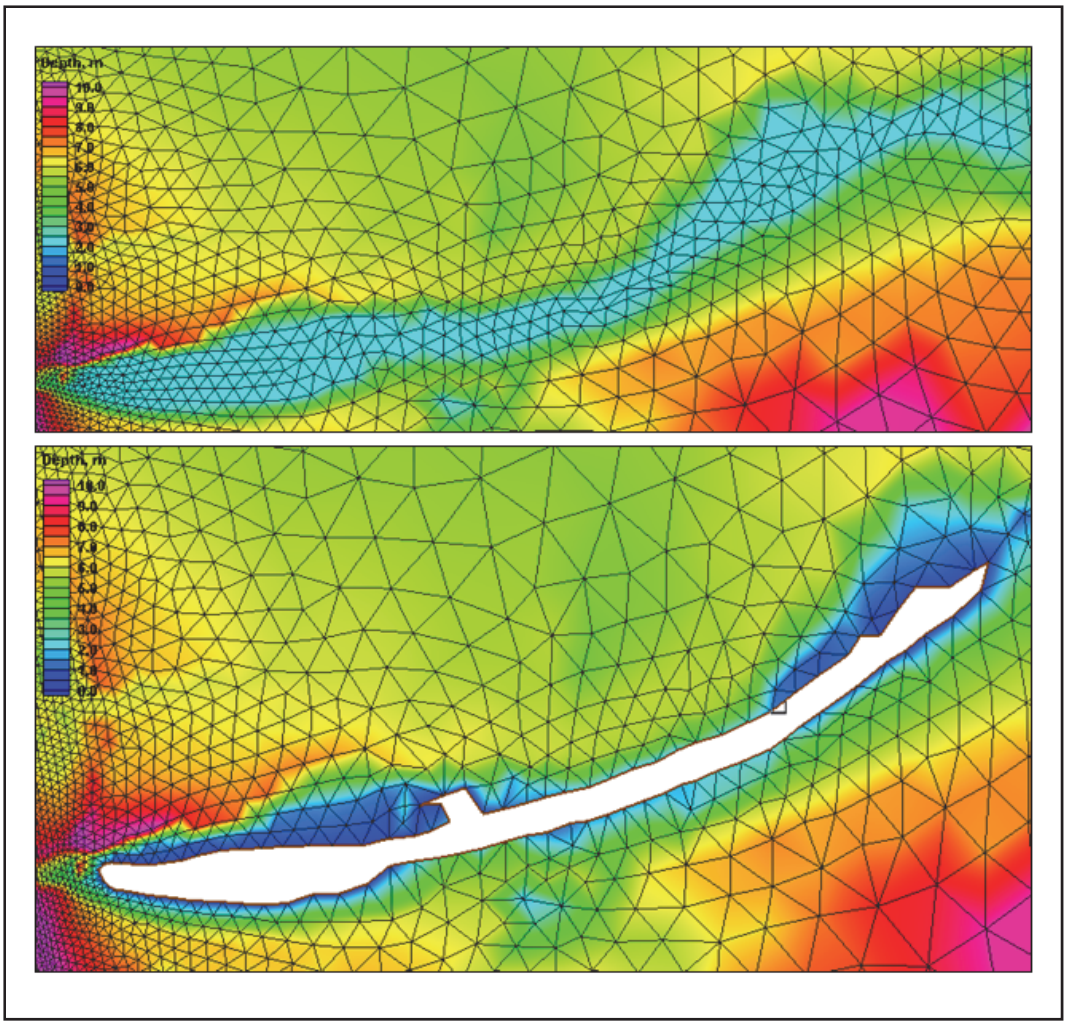

Figure 3-7. Comparison of ADCIRC simulated water levels (red lines) with measured water levels (black lines) at Dauphin Island.

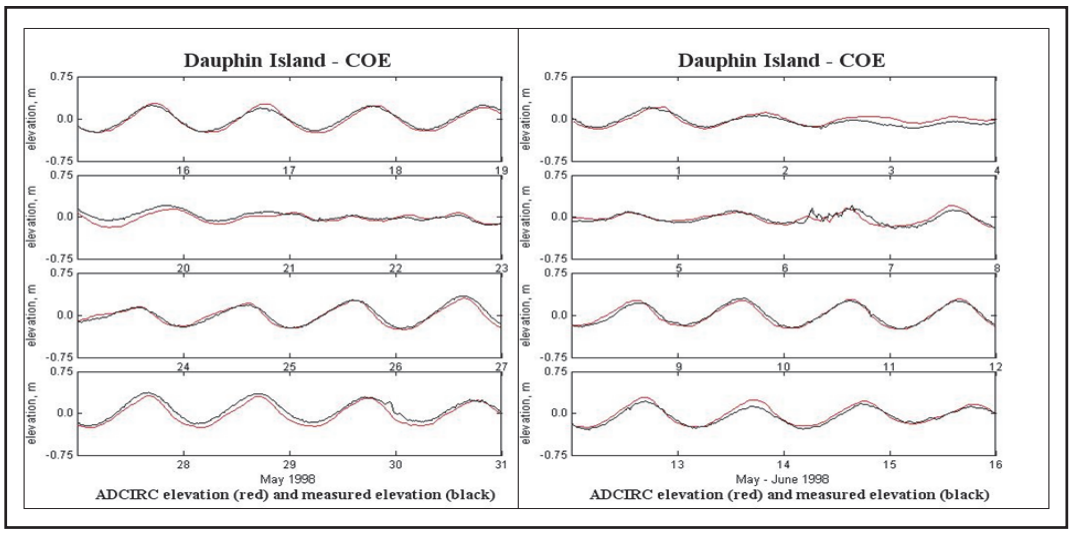

Figure 3-8. Comparison of ADCIRC simulated water levels (red lines) with measured water levels (black lines) at Waveland.

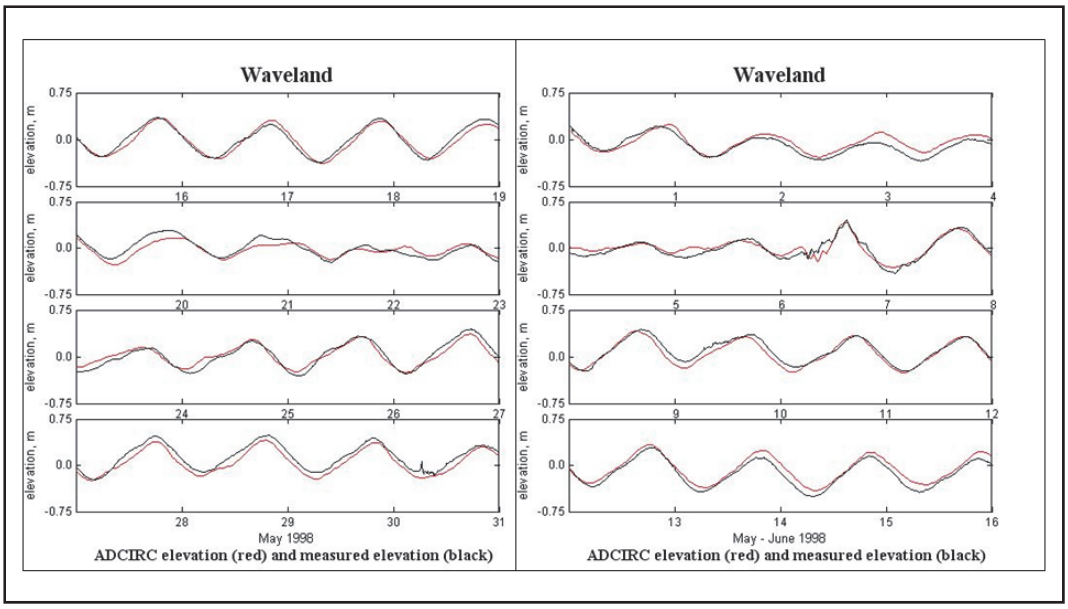

3.2 CH3D hydrodynamic simulations

The modeling approach taken to perform near-field, nested CH3D simulations utilizing ADCIRC tidal boundary forcing has been described in detail in Bunch et al. (2003) and Bunch et al. (2005). Hydrodynamic input data developed for MS Sound Hydrodynamic and Salinity Sensitivity Modeling Project (Chapman et al. 2006) were utilized. In addition, radiation stress gradient forcing was applied utilizing output from STWAVE (Smith et al. 1999). A description of the STWAVE modeling is provided in Chapter 4. The base CH3D grid developed for this study is shown in Figure 3-9.

Model calibration consisted of ensuring that a correct representation of tide and wind driven exchange within the sound was simulated. As with ADCIRC simulations, calibration of CH3D was based on the six month time period between March and September of 1998. A tidal prism and storm event calibration was performed comparing ADCIRC, CH3D, and NOAA predicted water surface elevations at Dauphin Island, Alabama (Figures 3-10) and observed water surface elevations at Waveland, Mississippi (Figures 3-11). It is seen in these figures that the water surface elevation is tracked well at both locations, where the phase consistency is shown in Figure 3-10, and the response to storm wind forcing is shown in Figure 3-11. Again, much of the differences seen in the model data comparisons can be attributed to the lack of site specific wind and atmospheric pressure forcing.

Figure 3-9. CH3D Grid.

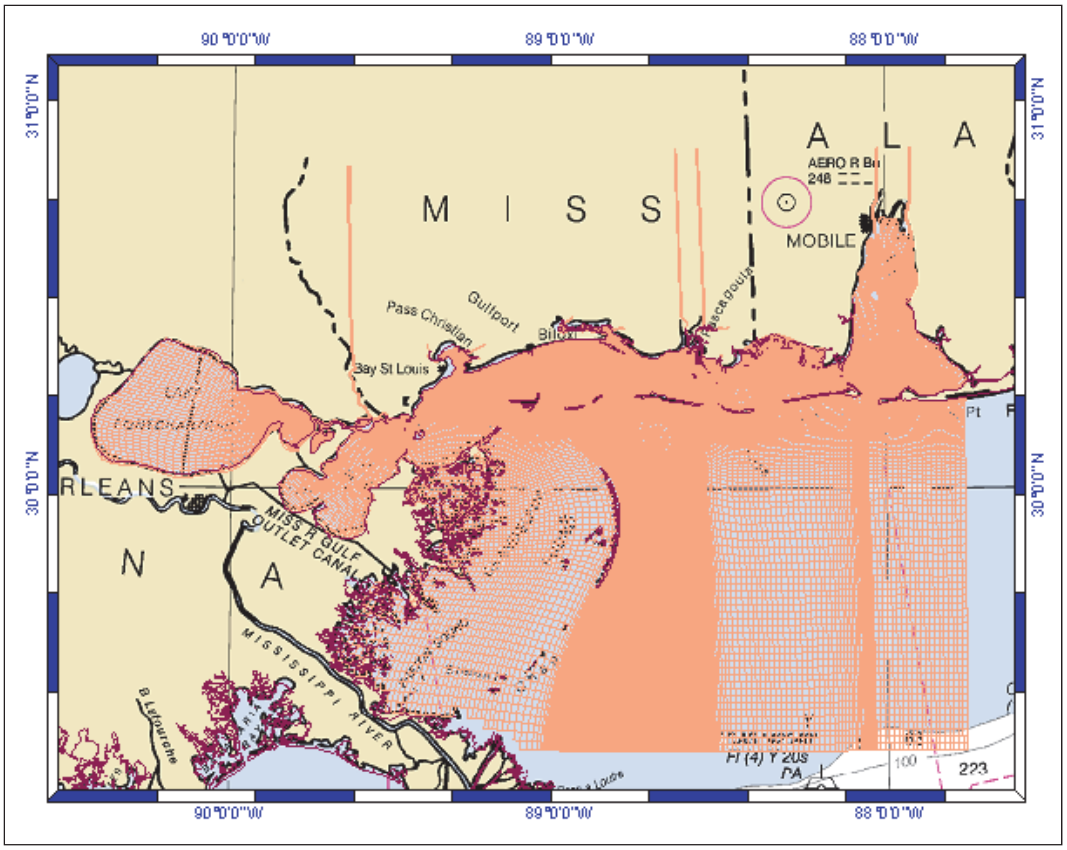

Figure 3-10. Comparison of Observed water surface level with ADCIRC and CH3D predictions at Dauphin Island, AL.

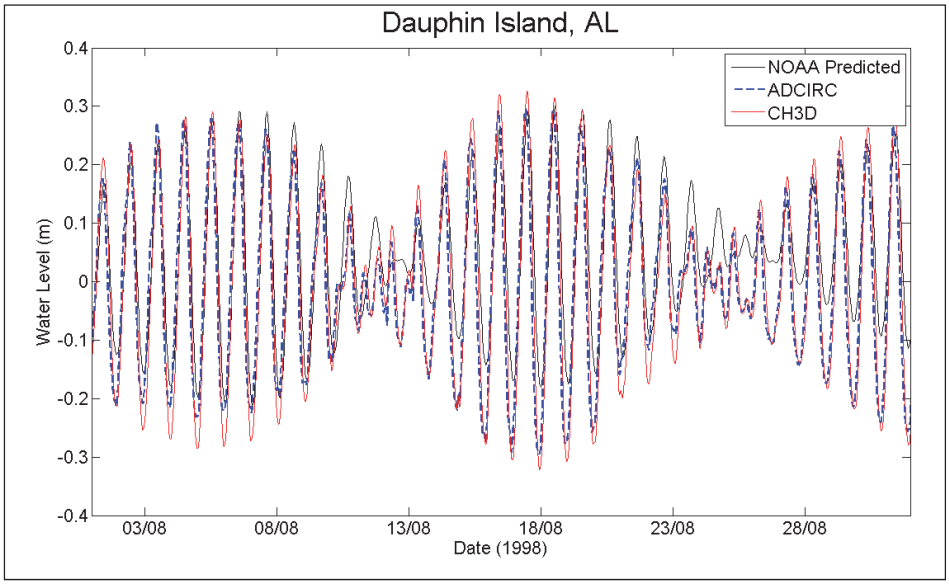

Figure 3-11. Comparison of Observed water surface level with ADCIRC and CH3D predictions at Waveland, MS.

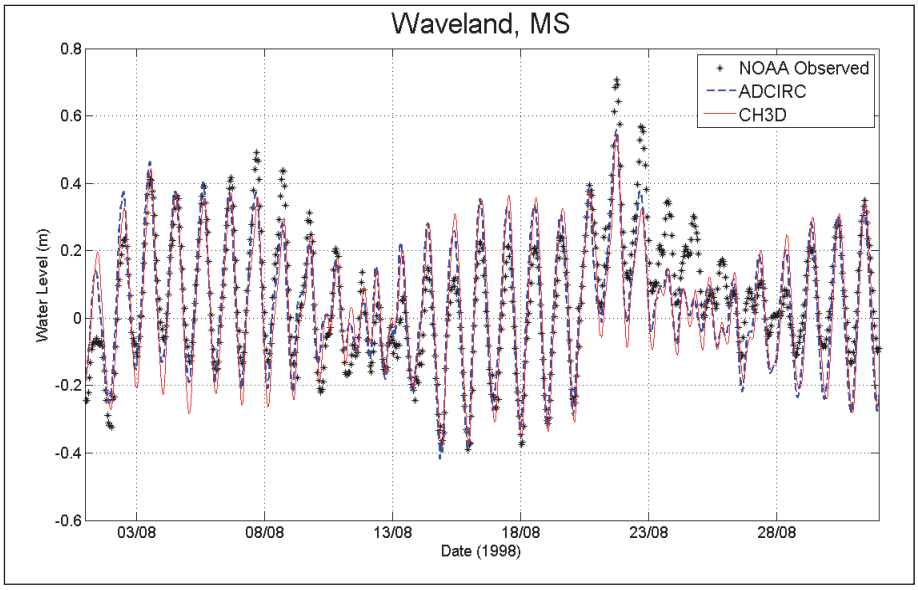

Subsequent to model calibration, hydrodynamic input files were generated for CE-QUAL-ICM. As described above, five alternative grids were developed, simulations performed and input hydro files generated.

4 Nearshore Wave Modeling[1]

This chapter provides an overview of the nearshore numerical wave modeling approach and documents the wave model validation in the Gulf of Mexico and within Mississippi Sound. The nearshore wave modeling was required to provide radiation stress gradients for the 3D circulation model CH3D (Chapter 3). To assess the nearshore wave model performance, a verification hindcast for the time period April-May 2010 was performed to coincide with a period of wave data collected by ERDC at two sites in the vicinity of Ship Island (Chapter 2).

STWAVE (Smith et al. 2001; Smith 2007) solves the steady-state wave action balance equation along piecewise, backward-traced wave rays on a Cartesian grid. STWAVE utilized 40 frequency bins, on the range 0.05-0.83 Hz and increasing in bandwidth linearly ($\Delta f/f$ = 0.02), along with 72 directional bins of a constant width of 5.0 degrees. The parallel, full-plane version of STWAVE (henceforth referred to as STWAVE-FP) was applied at 200 m resolution in a nearshore domain that is 185 km x 170 km in spatial extent, as shown in Figure 4-1.

Figure 4-1. STWAVE-FP Existing Post-Katrina wave domain for April-June 2010 simulations.

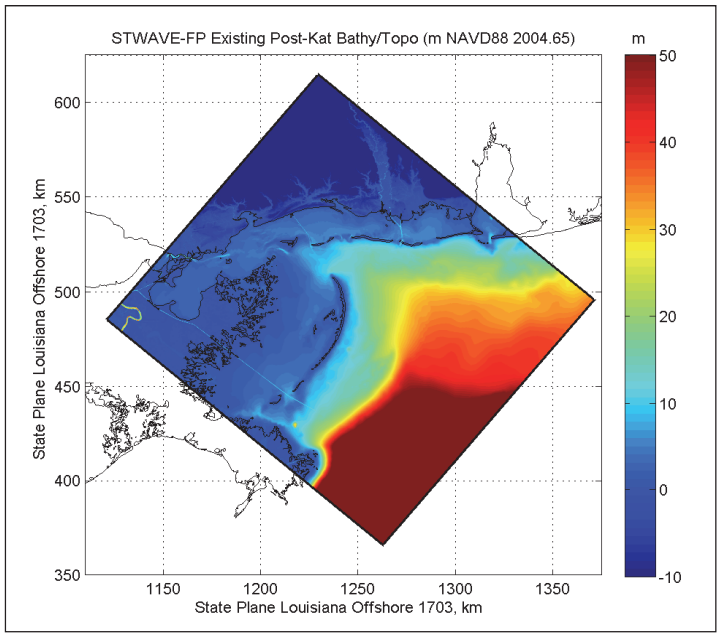

[1] Written by Alison Sleath Grzegorzewski, Coastal and Hydraulics Laboratory, US Army Engineer Research and Development Center, Vicksburg, MS.

The STWAVE-FP nearshore wave modeling supported two main tasks during this project:

- The STWAVE-FP model was applied for the period March-September 1998 so that the resulting radiation stress gradients could be applied within the 3D circulation model (Chapter 3). Radiation stress gradients are the flux of momentum which is lost by breaking waves. When the waves break, the momentum is transferred to the water column, forcing nearshore currents or changes in water level. The effect on currents (and in turn circulation) may be important in the water quality circulation model application (Chapter 5).
- The STWAVE-FP model was coupled with ADCIRC and forced with Watershed Assessment Model (WAM)/Planetary Boundary Layer (PBL) WAM/PBL for the storm wave modeling sensitivity study (Chapter 6). The purpose of the storm wave modeling was to examine the wave changes which resulted from a degraded and restored Ship Island condition when compared to the existing post-Katrina Ship Island condition.

4.1 STWAVE grid bathymetry/topography

The STWAVE-FP grid bathymetry and topography were interpolated from the sl15v3 ADCIRC mesh. The circulation model ADCIRC covers a large domain including the entire Gulf of Mexico and the Atlantic Ocean eastward to the 60 degrees West longitude line. The high-resolution ADCIRC mesh includes over 2.0 million nodes and over 4.0 million elements. The mesh bathymetry and topography were compiled from many sources, including: ETOPO1 in deep water (Amante and Eakins 2009), Coastal Relief DEMS (NOAA 2008), recent surveys by the Corps of Engineers and NOAA in the nearshore, as well as lidar surveys. Additional details on the ADCIRC sl15v3 mesh development and validation can be found in Bunya et al. 2010. For the pre-Katrina condition, the ADCIRC mesh and STWAVE-FP grid were updated with additional data collected by the Joint Airborne LIDAR Bathymetry Technical Center of Expertise (JALBTCX). The hydrographic and topographic data were collected by the CHARTS system along the northern Gulf of Mexico, spanning from Ship Island, MS, to Dauphin Island, AL during the period 4/24/2004 to 5/5/2004. For the existing post-Katrina condition, the ADCIRC mesh and STWAVE-FP grid were updated with additional detailed post-Katrina bathymetry derived from USGS data taken June 2008 and June 2009 combined with EAARL LIDAR (Brock et al. 2007).

4.2 Boundary conditions

4.2.1 Wind fields

The STWAVE-FP wind fields were spatially and temporally variable and interpolated from the ADCIRC modeling domain for both the 1998 and 2010 modeling simulation periods. The March-September 1998 ADCIRC simulation used wind fields from the NOAA National Data Buoy Center (NDBC) Stations DPIA1 on the eastern end of Dauphin Island and B42007 located 41 km south-southeast of Biloxi (30° 5.4' N, 88° 46.14' W). The wind data were not available for the entire March-September 1998 period at B42007. Therefore, when wind data were not available at B42007, wind information from the Army Corps of Engineers Wave Information Study (WIS) hindcasts at Station 145, approximately 1.8 km west of B42007, was used in place of the missing measurements. Additional information about the WIS data can be obtained from the website http://wis.usace.army.mil/. The reader is also referred to Chapter 3 for additional details.

The April-May 2010 ADCIRC simulation used wind fields modeled by the Air Force Combat Climatology Center (AFCCC) on a 37 × 33 grid between 90.5778°W and 87.3240°W in longitude and 27.8353°N and 31.0099°N in latitude, with spatial resolution of 0.0986° in longitude and 0.0858° in latitude. The temporal resolution of the Air Force wind data are 1.0 hour. To assess the Air Force wind fields, the archived measured wind data from the NOAA NDBC Station #42040 was compared with the AFCCC data in 2010 (Figure 4-2). NDBC Station #42040 is located approximately 120 km south of Dauphin Island, AL (29°12'45" N 88°12'27" W) and the winds are measured 10 m above sea level. In addition, wind measurements from the NOAA National Ocean Service (NOS) Station at Gulfport Outer Range (GPOM6 #8744707) were also compared with the AFCCC wind data in 2010 (Figure 4-3). The Gulfport Outer Range Station is located north of West Ship Island in Mississippi Sound at 30°13'48" N 88°58'55" W and the winds are measured at 13.7 m above the site elevation. The station wind speed values were adjusted to 10 m wind speeds for comparison with the AFCCC wind data using the 1/7 exponential power law. The root-mean-square-error (RMSE) is 2.0 m/sec at NDBC Station #42040 and the RMSE is 2.8 m/sec at NOS Station at Gulfport Outer Range, i.e. the modeled AFCCC wind data show good agreement with the measured wind data during the April-May 2010 period.

Figure 4-2. Comparison of Air Force wind speeds with measured NOAA NDBC Station #42040 wind speeds.

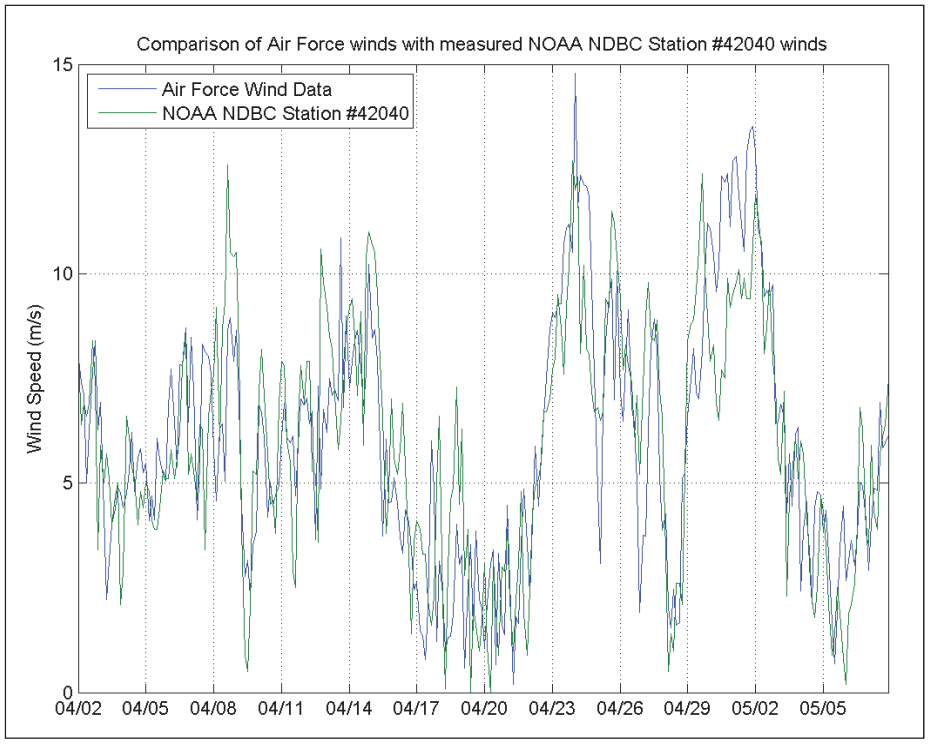

Figure 4-3. Comparison of Air Force wind speeds with measured NOAA NOS Gulfport Outer Range wind speeds.

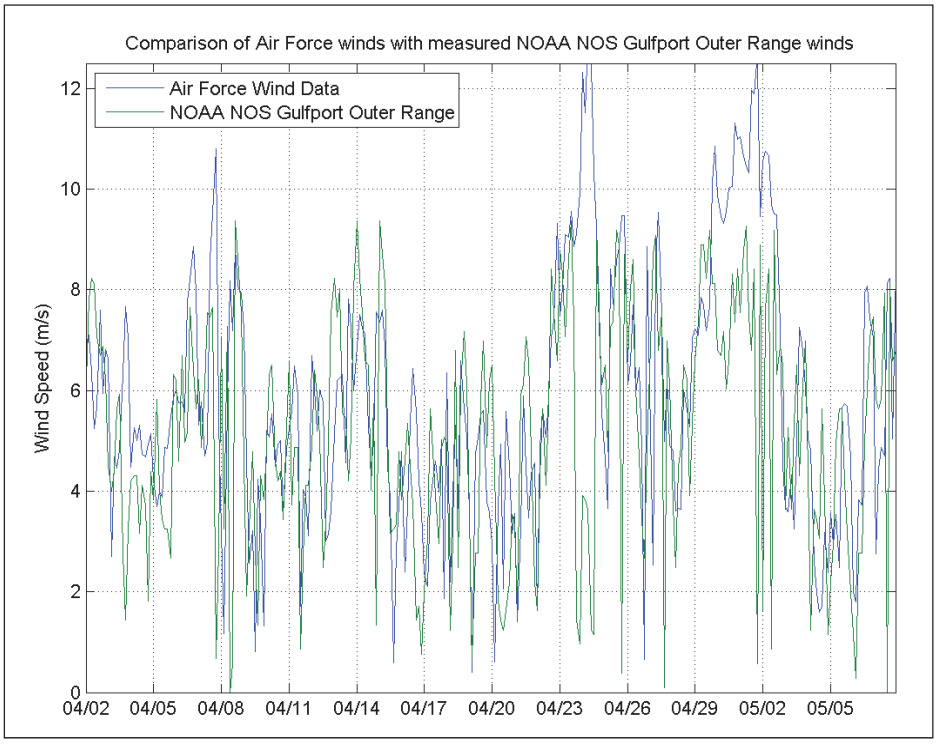

4.2.2 Tides

Tidal water level adjustments were spatially and temporally variable within the STWAVE-FP model and were interpolated from the ADCIRC model output for both the 1998 and 2010 modeling simulation periods. Seven tidal constituents were used during the ADCIRC simulations: K1, O1, Q1, M2, S2, N2, and K2. The reader is referred to Chapter 3 for additional details.

4.2.3 Offshore spectra

Directional wave spectra from the NOAA NDBC Station #42040 that is located approximately 120 km south of Dauphin Island, AL (29°12'45" N 88°12'27" W) were applied along the offshore boundary in STWAVE-FP. The NDBC Station #42040 is located in a depth of approximately 165 m. Additional information about the NDBC data can be obtained from the website http://www.ndbc.noaa.gov/.

4.3 STWAVE-FP validations

Field measurements are a critical asset for understanding wave processes and improving and validating nearshore wave models, such as STWAVE-FP. The validation of STWAVE-FP was performed with the ERDC-field data collected during March-July 2010 at Ship Island. In addition, STWAVE-FP has been validated during Hurricane Gustav in 2008 as briefly described below and in more detail in Smith et al. 2010.

4.3.1 Hurricane Gustav 2008 validation

Hurricane Katrina (2005) brought severe storm damage to the Northern Gulf of Mexico due to waves and storm surge. Unfortunately, wave measurements during hurricanes are extremely difficult to obtain. However, during Hurricane Gustav in 2008, many nearshore wave measurements were made in Southeastern Louisiana and these data were used to evaluate the STWAVE-FP nearshore wave model in both open and protected coastal areas. The methodology and results are discussed in detail in Smith et al. 2010.

Prior to Hurricane Gustav in 2008, the Corps of Engineers, Coastal and Hydraulics Laboratory (CHL) deployed six bottom-mounted wave gauges east and south of New Orleans in depths of 0.5-1.2 m. A joint effort between the University of Notre Dame and the University of Florida involved the

deployment of an additional 20 bottom-mounted wave gauges in depths of 1.4-14 m, mainly in the vicinity of the coastal regions southeast and southwest of New Orleans, LA.

Figure 4-4 provides a summary of the peak-to-peak comparisons of the maximum modeled versus measured wave heights at all gauges with the two STWAVE-FP domains used for the study. The average percent error is -1.0 percent (model overestimation). The root-mean-square-error is 0.6 m or approximately 25 percent. Comparisons of modeled frequency spectra under the strongly forced storm conditions that existed during Gustav showed fair agreement with the measured data, although the measured spectra showed more complexity in the spectra shape than the STWAVE-FP model results.

Figure 4-4. Peak-to-peak wave height comparison for Hurricane Gustav 2008 wave gauges and STWAVE-FP, from Smith et al. 2010.

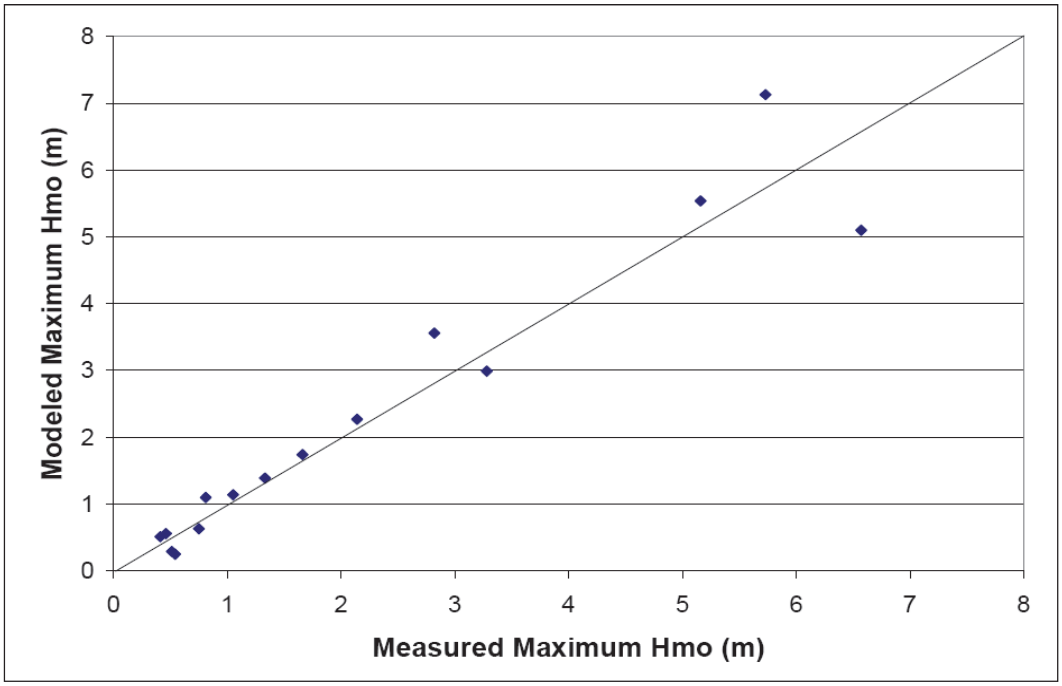

4.3.2 2010 validation

ERDC deployed two Civil Tek internally-recording, directional wave gauges on March 4, 2010 at two locations in the vicinity of Ship Island, as shown in Figure 4-5. The Mississippi Sound gauge was deployed in a depth of 5 m and the Gulf of Mexico gauge was deployed in a depth of 7.6 m. The two gauges were recovered on July 15, 2010. While the gauge deployed in the Mississippi Sound recorded valid data for the entire 143-day deployment,

the gauge deployed in the Gulf of Mexico developed an electronic problem on April 30, 2010 and recorded only 67 days of valid data. The reader is referred to Chapter 2 for additional details regarding the field data collection efforts and results. The NOAA NDBC Station #42040 (located approximately 120 km south of Dauphin Island) was offline until April 2010, and an absence of other available deepwater wave data exists in the area for use along the offshore model domain during March 2010. Therefore, the wave comparisons shown in this chapter are provided for the time period beginning in April 2010, when offshore wave data were available from the NOAA NDBC Station #42040.

Figure 4-5. Location map showing the two 2010 ERDC wave gauge deployment locations near Ship Island.

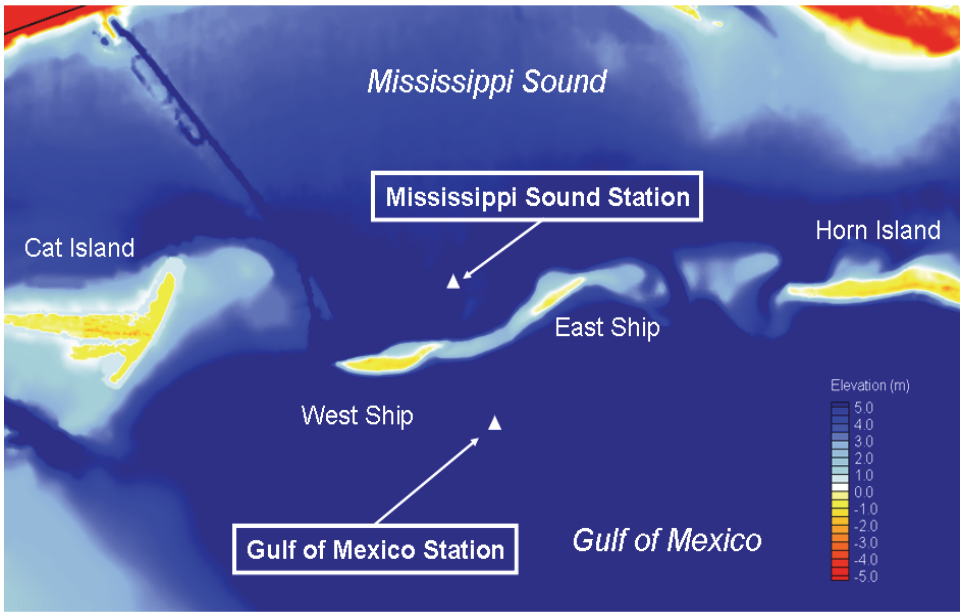

4.3.2.1 Time-series figures at the Gulf of Mexico station

Figures 4-6 through 4-8 show time-series comparisons for the measured versus STWAVE-FP modeled zero-moment wave height, peak wave period, and wave direction at the Gulf of Mexico station. While a small over-prediction of wave height and under-prediction of peak wave period is observed, the STWAVE-FP model is able to reproduce these parameters within good agreement. Quantitative measures of the STWAVE-FP model performance are provided in Table 4-1 in the Summary and Conclusions section of this chapter. The comparison of modeled versus measured wave direction in Figure 4-8 shows very good agreement between STWAVE-FP and the measurements, showing waves being predominantly propagated from the southeast at the Gulf of Mexico station.

Figure 4-6. Time-series of measured and modeled *Hmo* (m) at the Gulf of Mexico station.

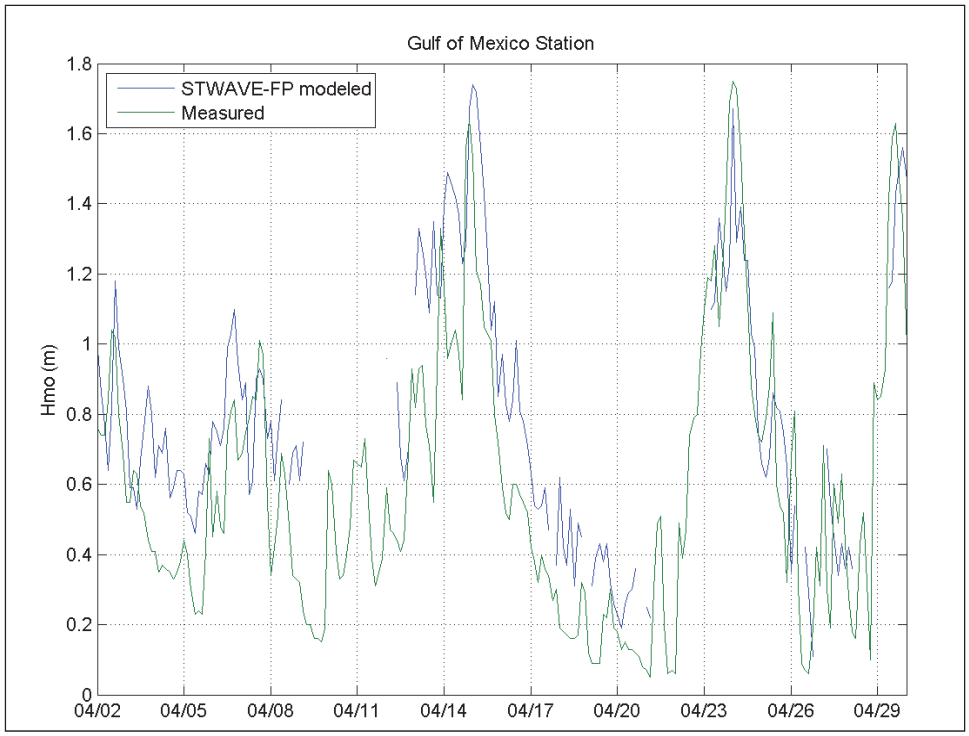

Figure 4-7. Time-series of measured and modeled *Tp* (sec) at the Gulf of Mexico station.

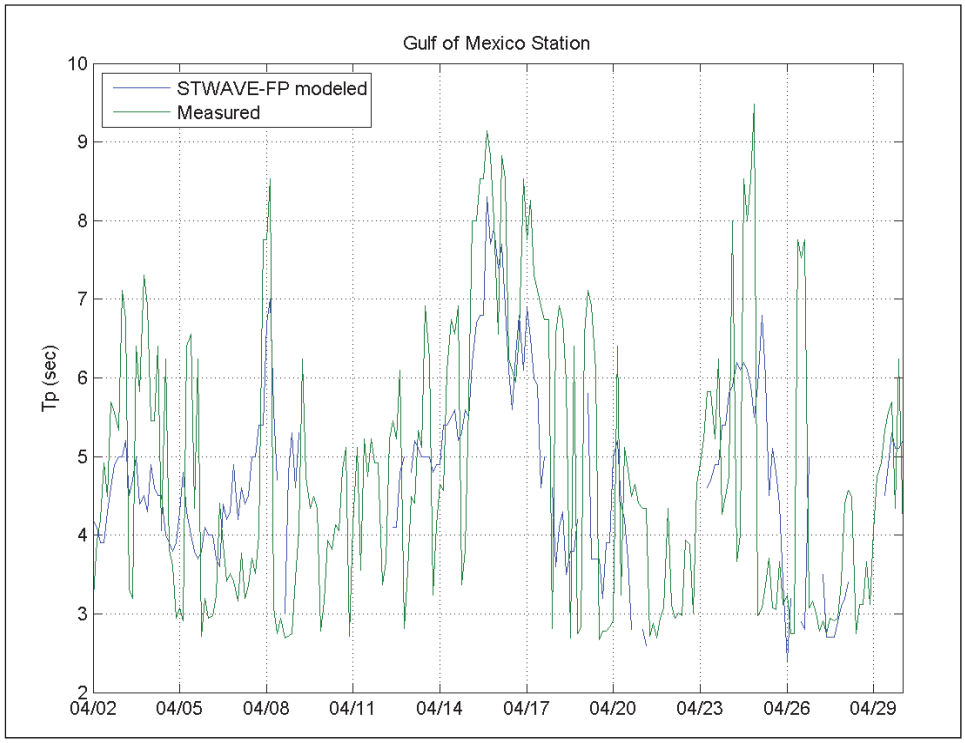

Figure 4-8. Time-series of measured and modeled direction (degrees clockwise from North) at the Gulf of Mexico station.

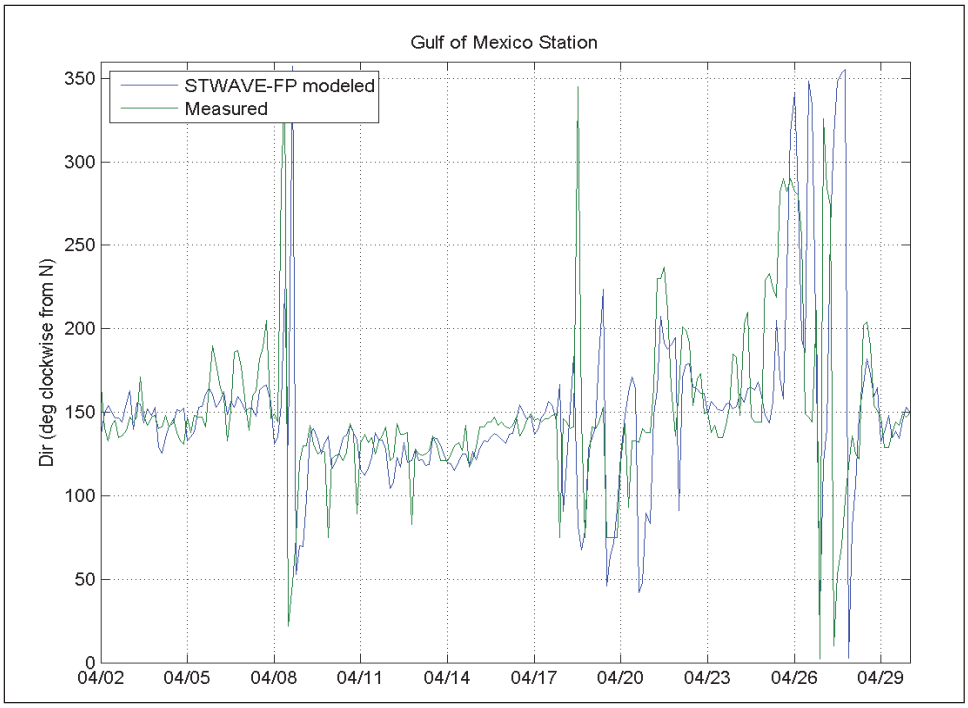

Table 4-1. Performance of STWAVE-FP for wave height.

Measure of Performance	Gulf of Mexico Station	Mississippi Sound Station
Root-mean-square-error, RMSE	0.27 m	0.23 m
Scatter index, SI	0.45	0.76
Model performance index, MPI	0.58	0.74
Operational performance index, OPI	0.23	0.22
Bias	0.16 m	0.16 m

4.3.2.2 Time-series figures at the Mississippi Sound station

Figures 4-9 through 4-11 show time-series comparisons for the measured versus STWAVE-FP modeled zero-moment wave height, peak wave period, and wave direction at the Mississippi Sound station. A more pronounced pattern of over-prediction of wave height is observed at this station. In addition, an over-prediction of peak wave period is observed at this station. It is possible that the bathymetrical inaccuracies account for some of the discrepancies between measurements and model predictions. Depth-limited and steepness-induced wave breaking processes are important in the numerical model simulations; therefore, accurate bathymetry is critical. Quantitative measures of the STWAVE-FP model performance are provided in Table 4-1.

Figure 4-9. Time-series of measured and modeled *Hmo* (m) at the Mississippi Sound station.

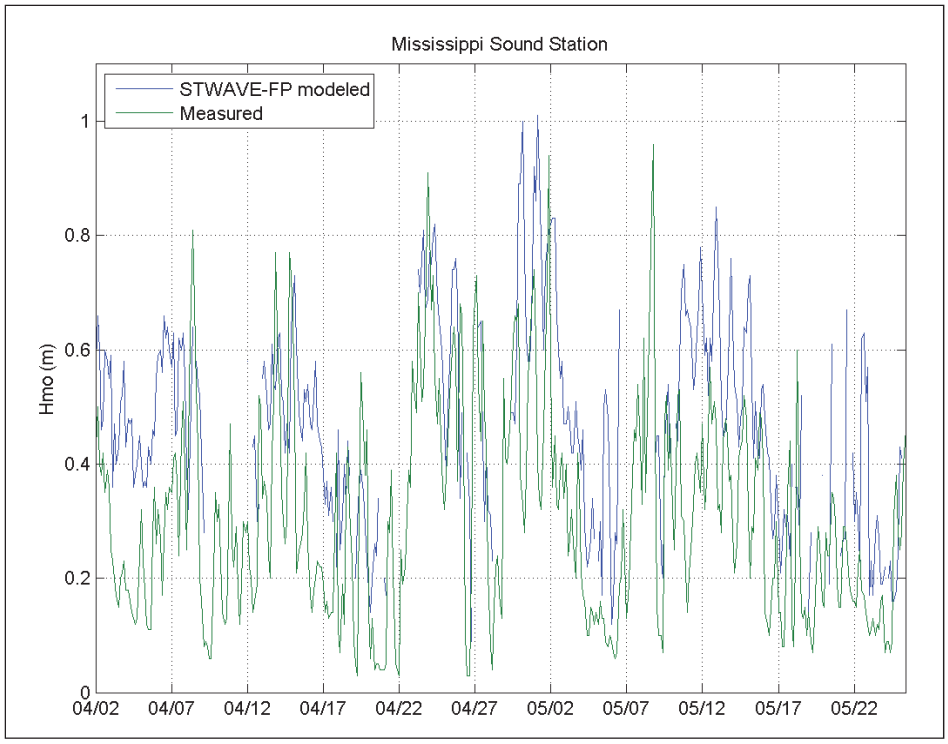

Figure 4-10. Time-series of measured and modeled *Tp* (sec) at the Mississippi Sound station.

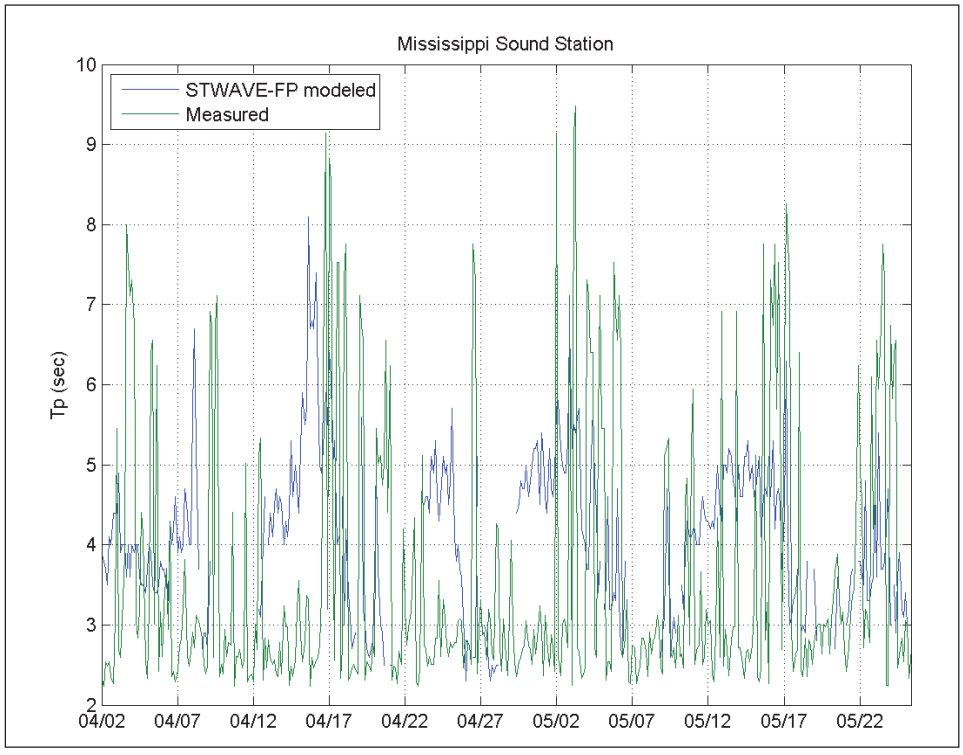

Figure 4-11. Time-series of measured and modeled direction (degrees clockwise from North) at the Mississippi Sound station.

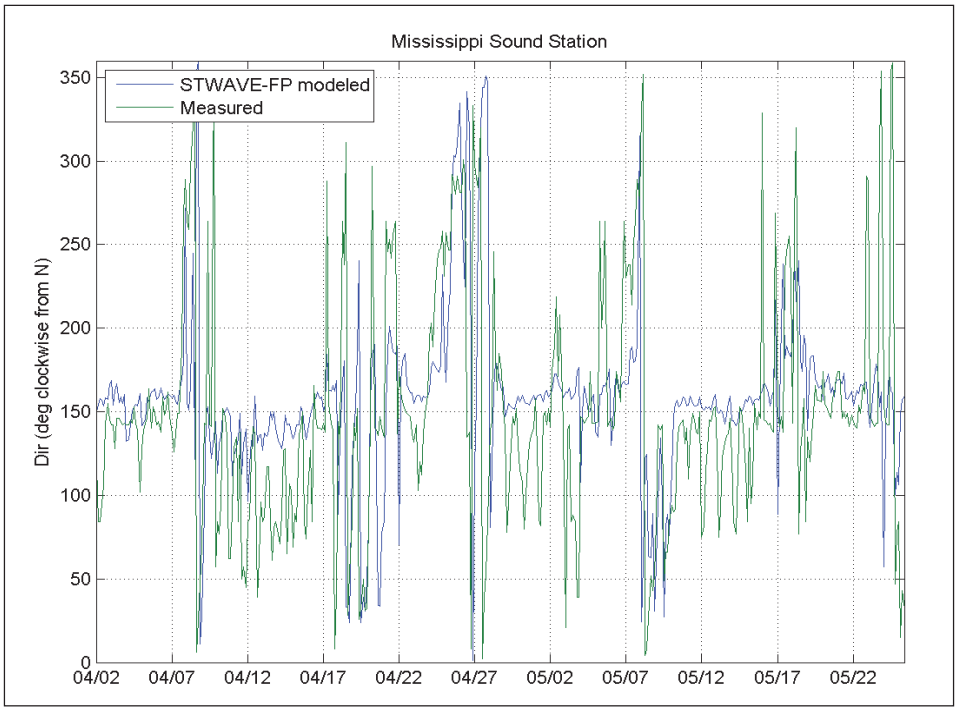

Another explanation for the observed differences between measured versus modeled wave heights and periods are related to the pressure gauges and the peak periods near or at the high-frequency cut-off for the spectral analysis. The high-frequency peaks in the spectra near the cut-off can be a result of amplification of noise due to large values of the pressure response function (applied to account for the depth attenuation of short-period wave components). Wave height in such situations may be either over-estimated (due to amplification of noise) or under-estimated (due to truncation of the energetic part of the spectrum). Wave periods would generally be under-estimated. In most applications, these truncated spectra would be disregarded for model verification, but for this application they provide valuable information about what was not measured. The direction comparison of measured versus modeled wave direction in Figure 4-11 shows excellent agreement between STWAVE-FP and the measurements, showing waves predominantly propagating from the southeast.

4.3.2.3 Wave height reduction factor

A wave height reduction factor, defined as the ratio of wave height at the Gulf of Mexico station to the wave height at the Mississippi Sound station, was computed for the measured and modeled waves. The wave height reduction factor clearly demonstrates the attenuation in wave heights

across Ship Island, from the exposed waves at the Gulf of Mexico station to the more sheltered waves at the Mississippi Sound station in both the model and the measurements. The average wave height reduction factor predicted by the model is 0.67, whereas the average wave height reduction factor observed in the measured data is 0.64.

4.3.2.4 Histograms for the Gulf of Mexico station

Figures 4-12 through 4-17 show histograms for the measured and STWAVE-FP modeled zero-moment wave height, peak wave period, and wave direction at the Gulf of Mexico station. Both the measured (Figure 4-12) and the modeled (Figure 4-13) histograms for wave heights show that the vast majority of wave heights are *Hmo* < 1.0 m for the Gulf of Mexico station. While the measured waves (Figure 4-14) show the most frequently occurring peak periods as *Tp* = 3-4 sec, the modeled waves (Figure 4-15) show the most frequently occurring peak periods as *Tp* = 4-5 sec. Both the measured and modeled waves show excellent agreement for wave direction, with the predominant direction of wave propagation from the southeast, 135 degrees clockwise from the North (Figures 4-16 and 4-17). Overall, STWAVE-FP is shown to model the measurements with very good agreement for the Gulf of Mexico station. Quantitative measures of the STWAVE-FP model performance are provided in Table 4-1.

4.3.2.5 Histograms for the Mississippi Sound station

Figures 4-18 through 4-23 show histograms for the measured and STWAVE-FP modeled zero-moment wave height, peak wave period, and wave direction at the Mississippi Sound station. Both the measured (Figure 4-18) and the modeled (Figure 4-19) histograms for wave heights show that the vast majority of wave heights are *Hmo* < 0.6 m for the Mississippi Sound station. While the measured waves (Figure 4-20) show the most frequently occurring peak periods as *Tp* = 2-3 sec, the modeled waves (Figure 4-21) show the most frequently occurring peak periods as *Tp* = 3-5 sec. Both the measured and modeled waves show very good agreement for wave direction, with the predominant direction of waves propagating from the southeast to the south, i.e. 90-180 degrees clockwise from North (Figures 4-22 and 4-23). Overall, STWAVE-FP is shown to model the measurements with reasonable agreement at the Mississippi Sound station. Quantitative measures of the STWAVE-FP model performance are provided in Table 4-1.

Figure 4-12. Histogram of the measured *Hmo* (m) at the Gulf of Mexico station.

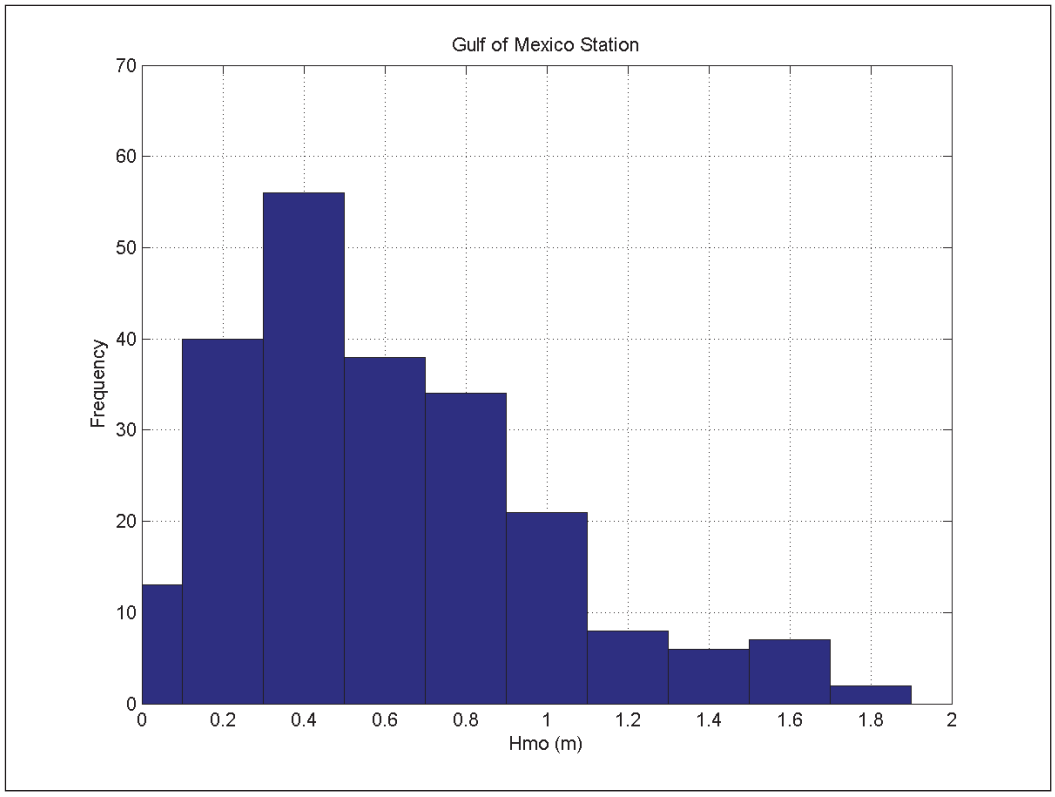

Figure 4-13. Histogram of the modeled *Hmo* (m) at the Gulf of Mexico station.

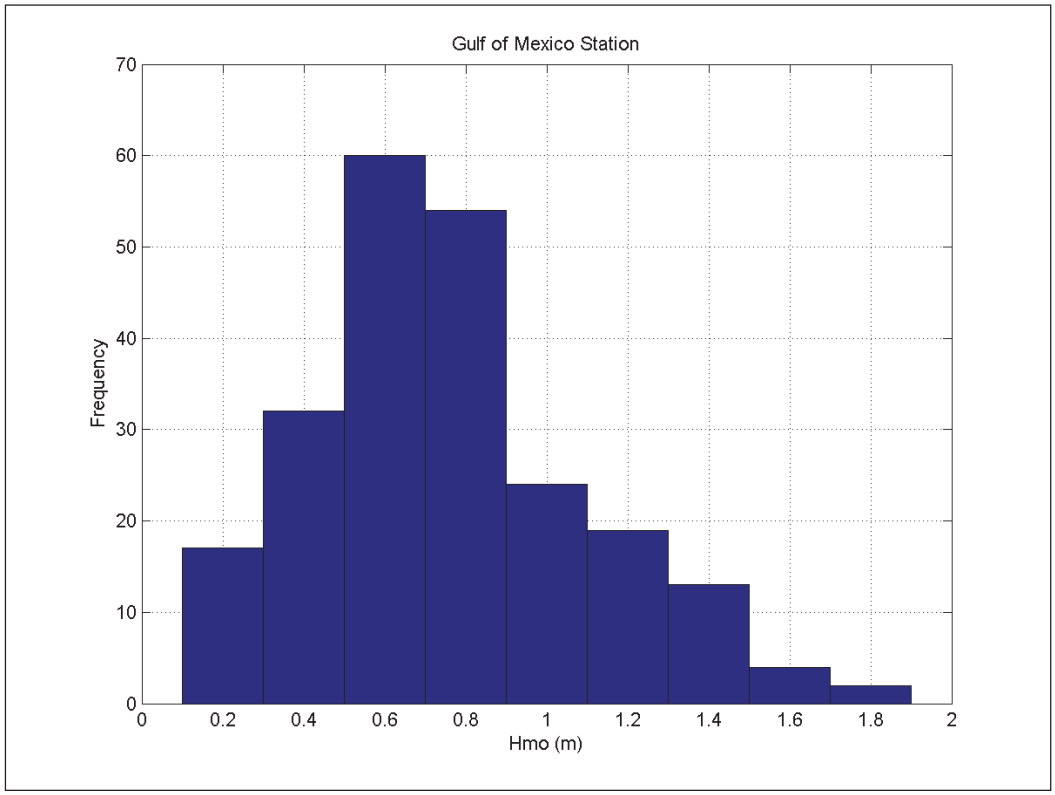

Figure 4-14. Histogram of the measured *Tp* (sec) at the Gulf of Mexico station.

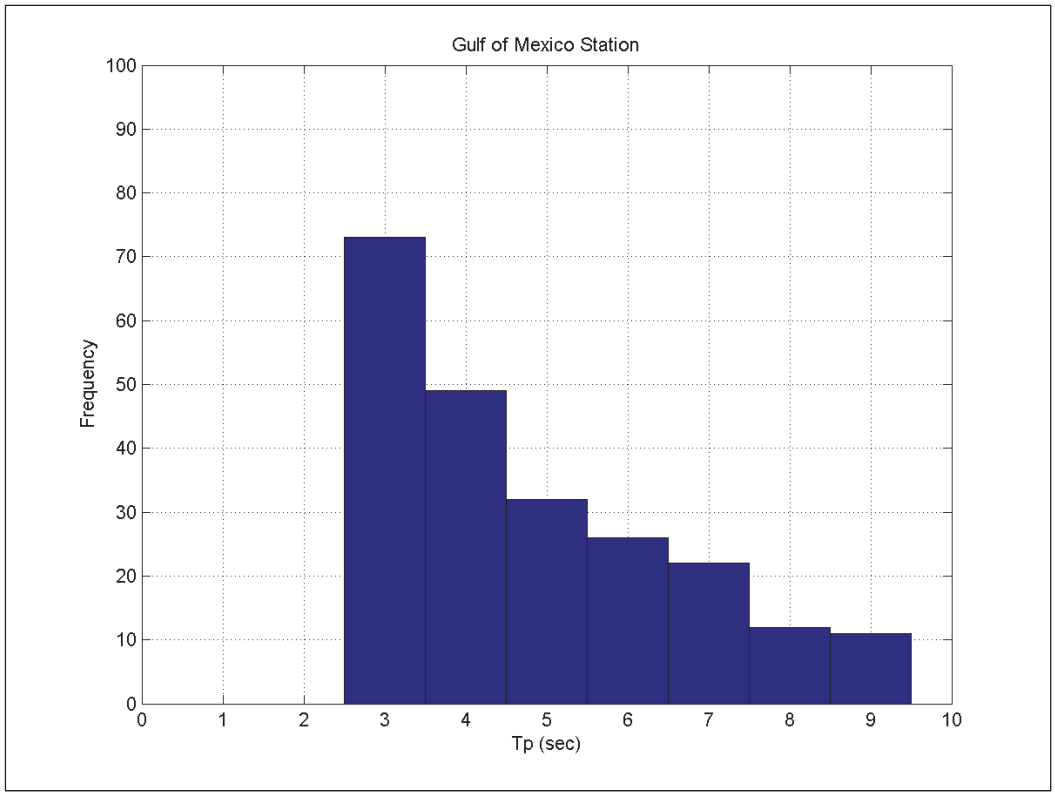

Figure 4-15. Histogram of the modeled *Tp* (sec) at the Gulf of Mexico station.

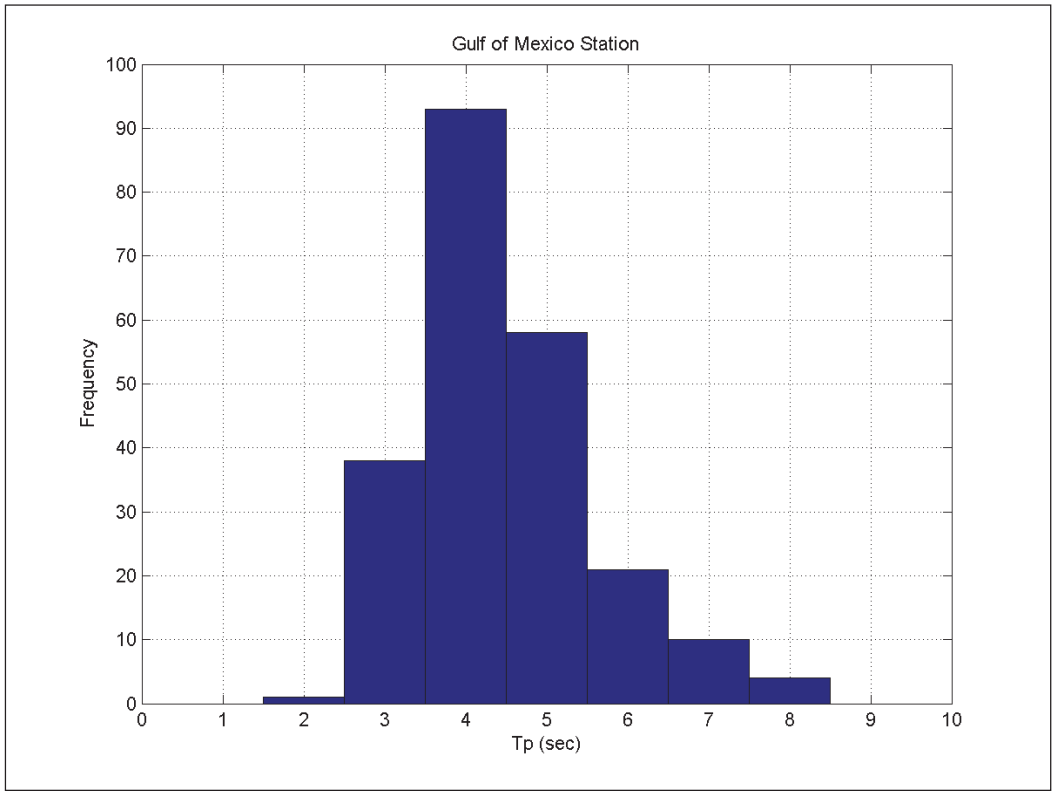

Figure 4-16. Histogram of the measured direction (clockwise from North) at the Gulf of Mexico station.

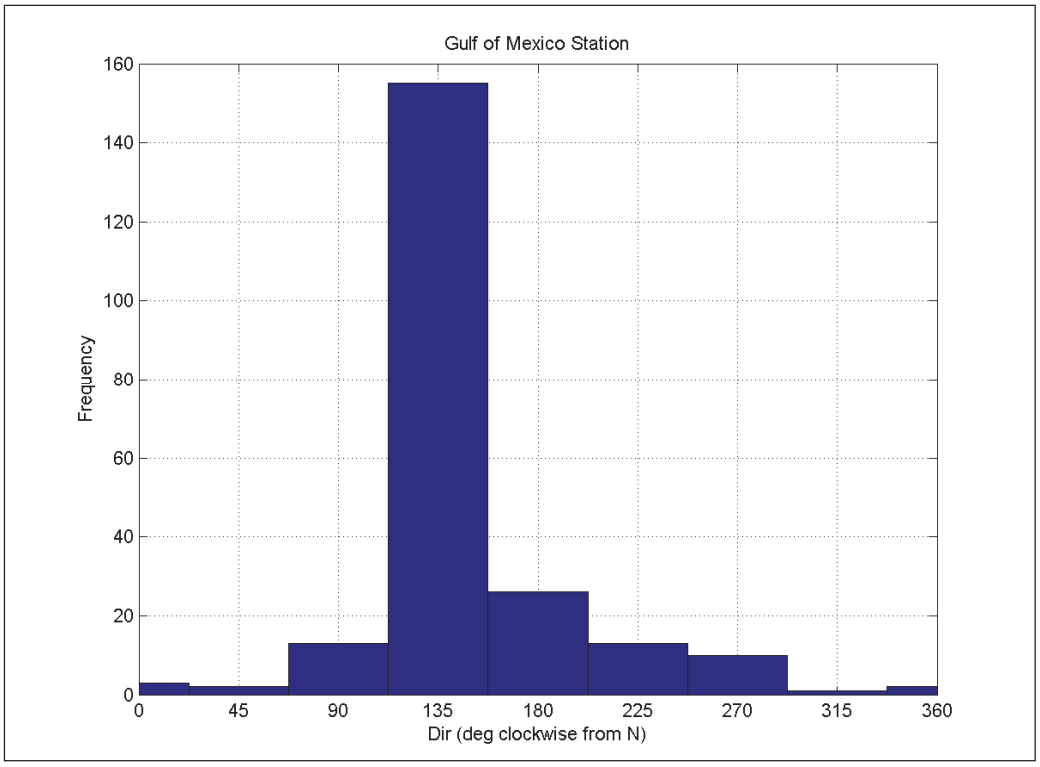

Figure 4-17. Histogram of the modeled direction (clockwise from North) at the Gulf of Mexico station.

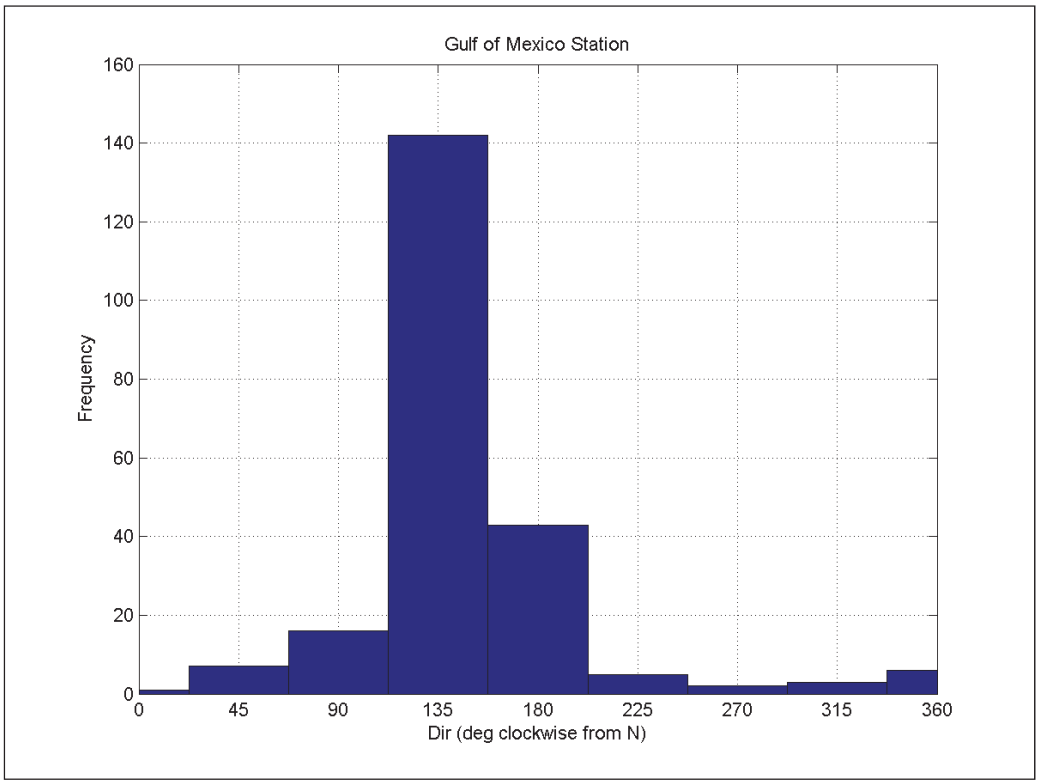

Figure 4-18. Histogram of the measured *Hmo* (m) at the Mississippi Sound station.

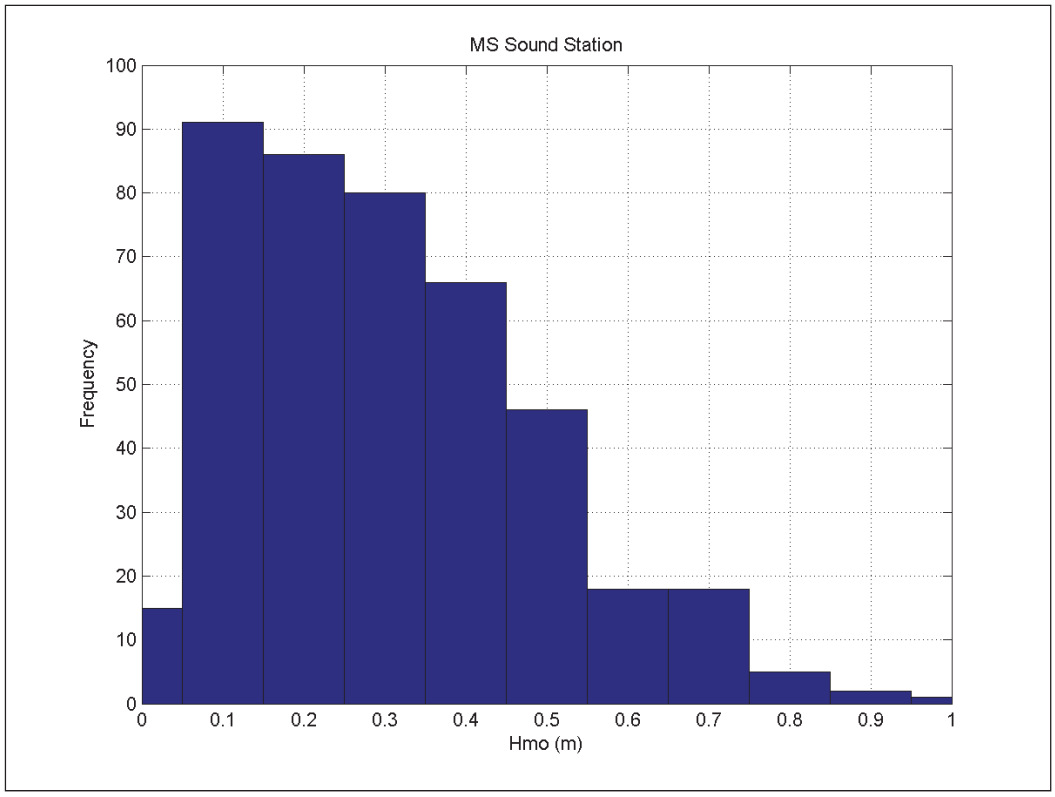

Figure 4-19. Histogram of the modeled *Hmo* (m) at the Mississippi Sound station.

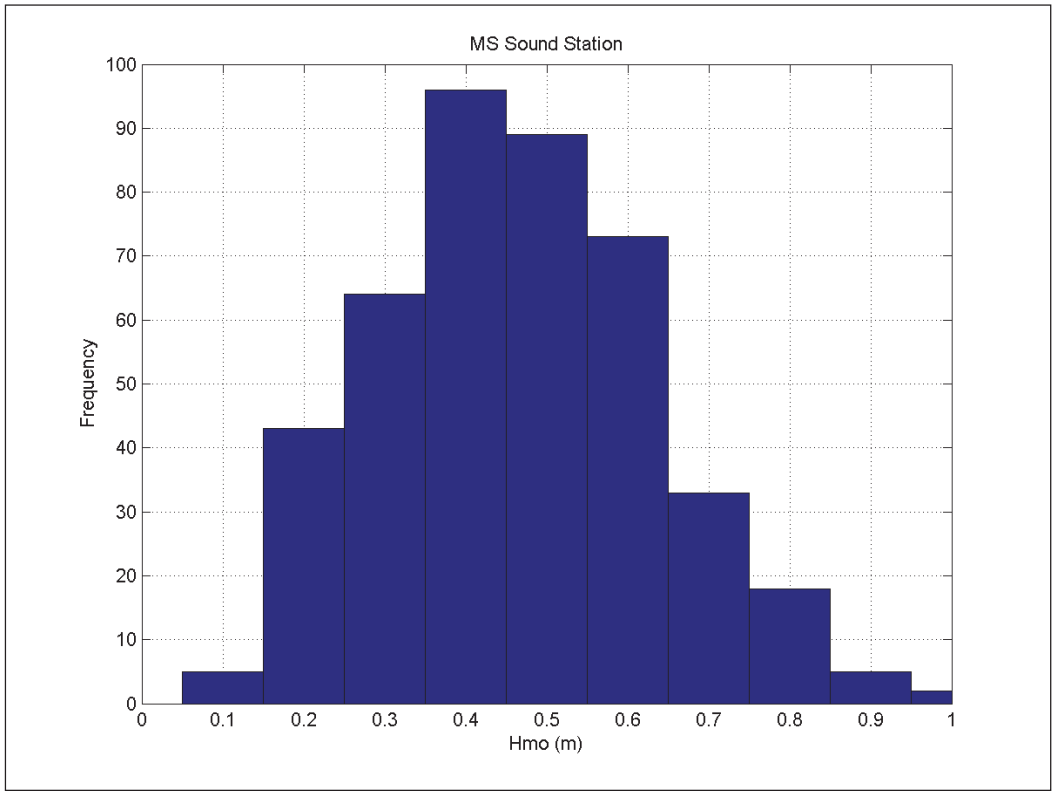

Figure 4-20. Histogram of the measured *Tp* (sec) at the Mississippi Sound station.

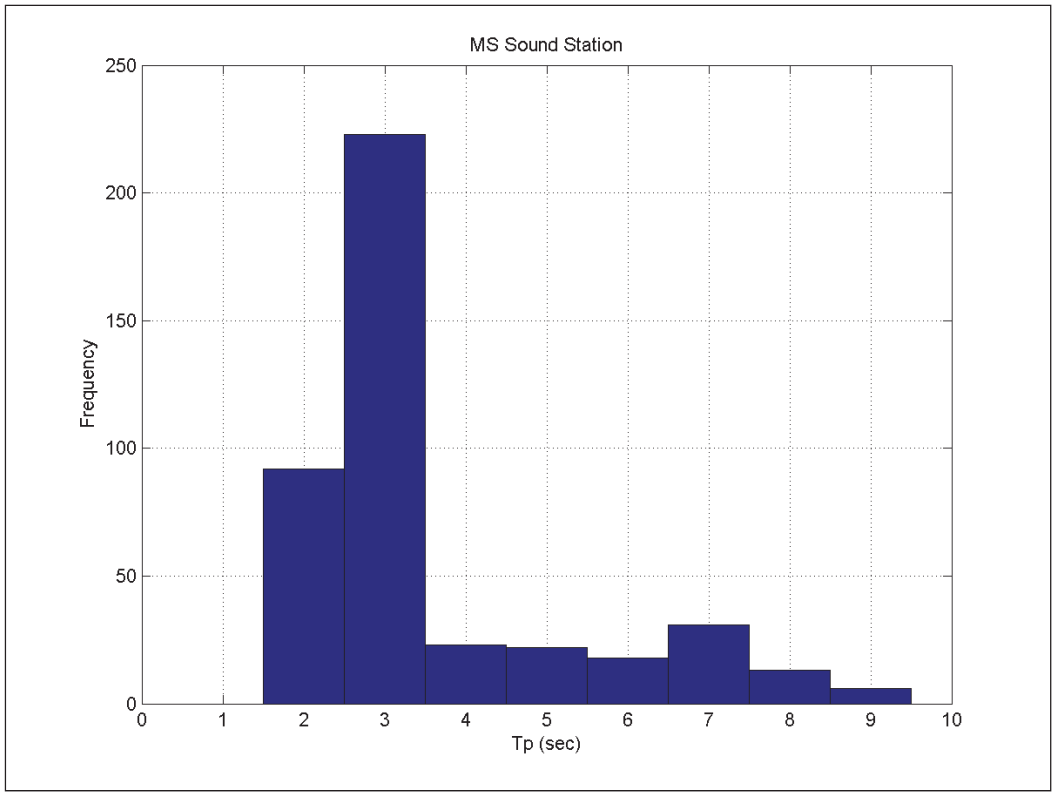

Figure 4-21. Histogram of the modeled *Tp* (sec) at the Mississippi Sound station.

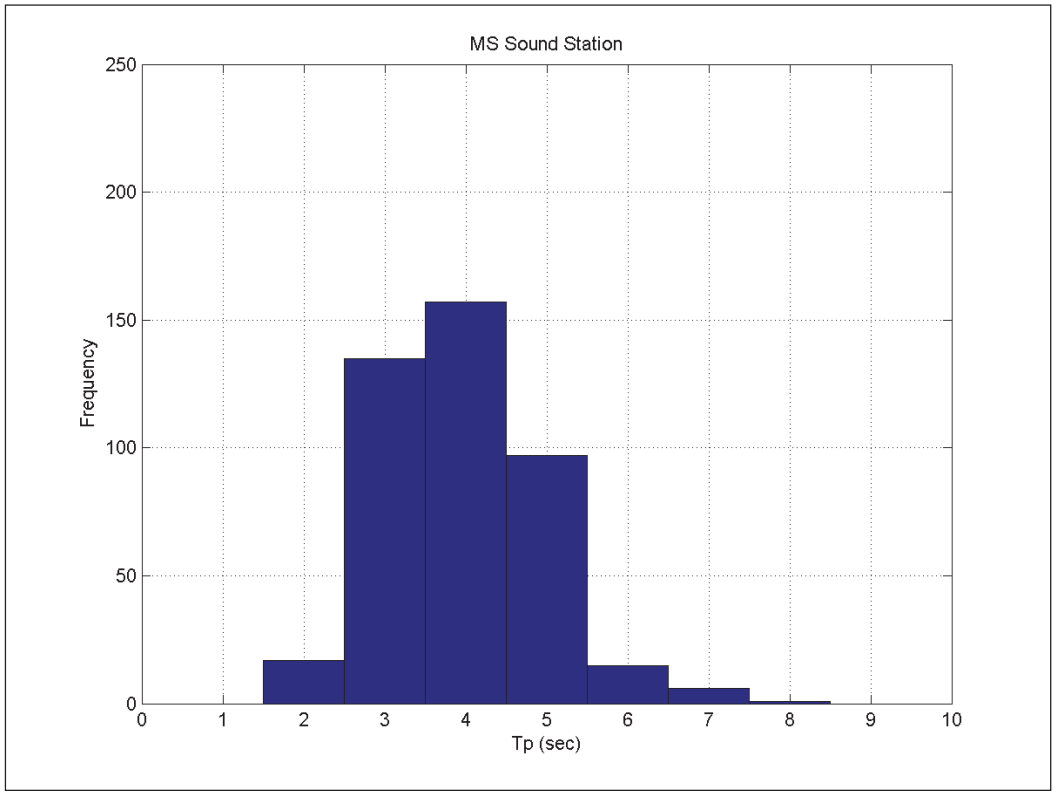

Figure 4-22. Histogram of the measured direction (degrees clockwise from North) at the Mississippi Sound station.

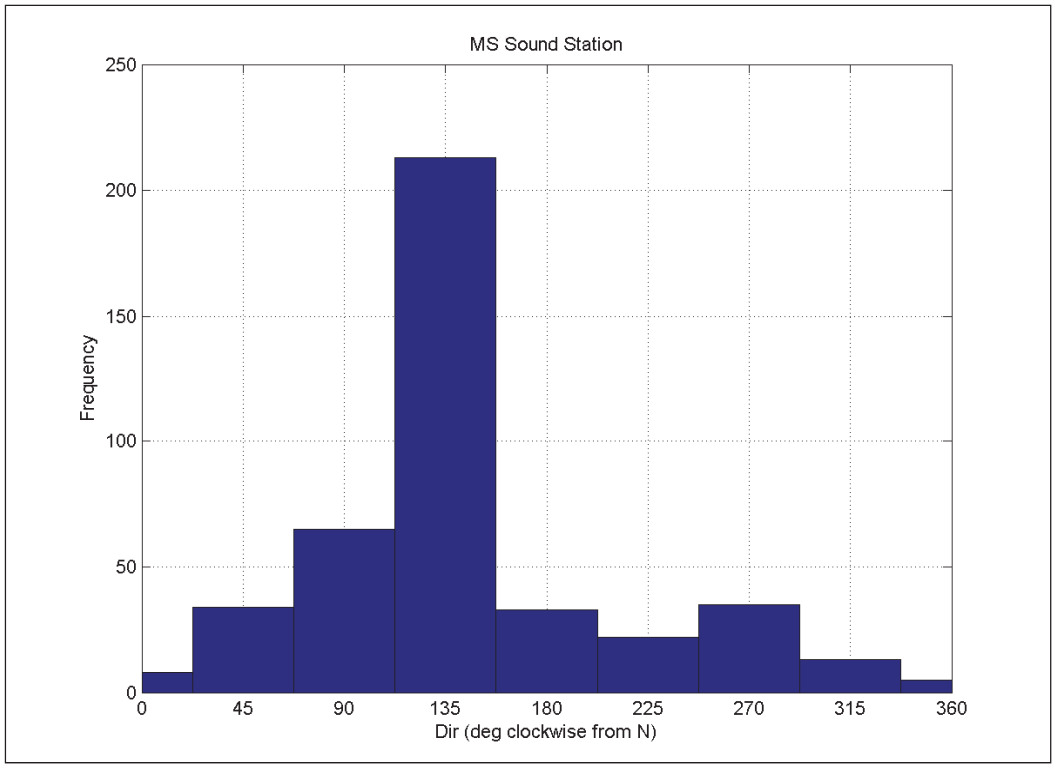

Figure 4-23. Histogram of the modeled direction (degrees clockwise from North) at the Mississippi Sound station.

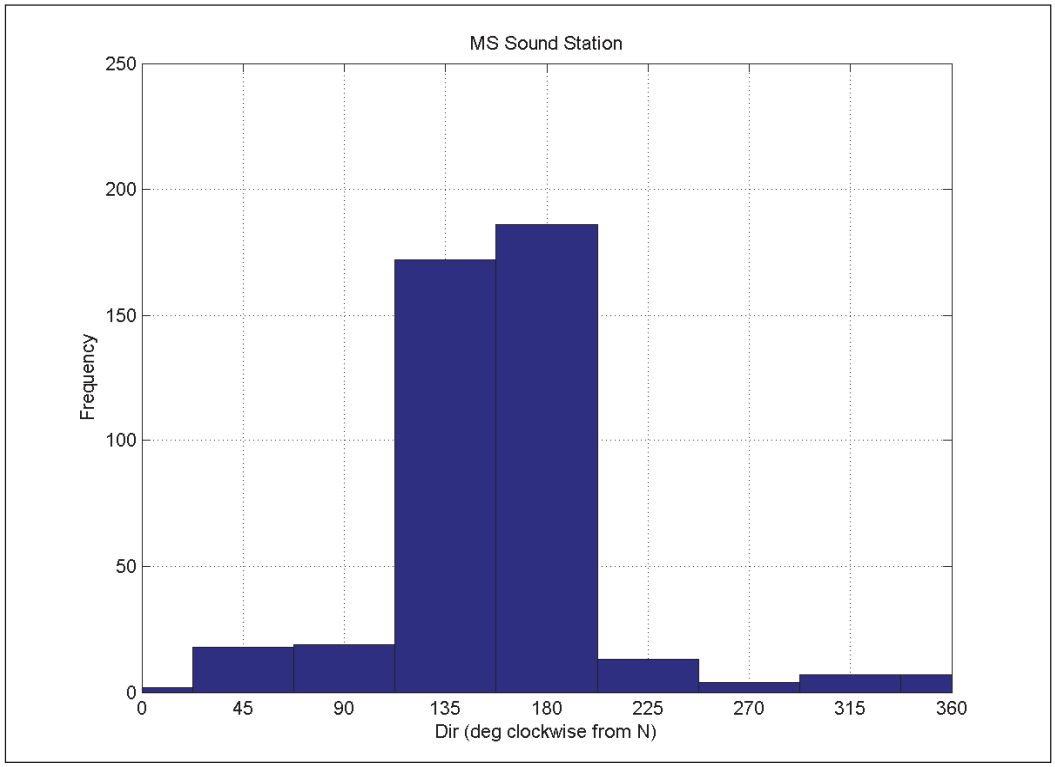

4.3.3 Additional measures of model performance

To quantify the predictive capability of STWAVE-FP, the root-mean-square-error (RMSE) was computed at the Gulf of Mexico and Mississippi Sound stations. The RMSE of the wave height is 0.27 m at the Gulf of Mexico station and 0.23 m at the Mississippi Sound station. To quantify the performance of ocean wave models, a scatter index (SI) is sometimes used (Zambreski 1989, 1991; Komen et al. 1994; Romeiser 1993), which is defined as the *RMSE* normalized with the mean observed value. The *SI* for the wave height is 0.45 at the Gulf of Mexico station and 0.76 at the Mississippi Sound station.

As discussed by Ris et al. (1999), this scatter index may appear to understate the skill of the wave model, as it tends to be large in some coastal applications. The reason is that the RMSE of the wave height is normalized with the mean observed wave height, which is usually rather small in coastal regions (0.6 m and 0.3 m at the Gulf of Mexico station and Mississippi Sound station, respectively). Therefore, the SI attains high values of 0.45 and 0.76 at the Gulf of Mexico station and Mississippi Sound station, respectively, due to being normalized by the small mean observed waves.

Ris et al. (1999) proposed two alternative model performance indices to supplement the standard *RMSE* and *SI* calculations, referred to as the model performance index (*MPI*) and the operational performance index (*OPI*).

The model performance index (*MPI*) is considered to better diagnose the modeling performance and indicates the degree to which the model reproduces the observed changes of the waves, where *MPI* is defined as 1 minus the *RMSE* normalized with the root-mean-square (*RMS*) of the observed changes. The definition of *RMS* of the observed changes is identical to that of *RMSE*, except that all computed values are replaced by the observed incident values. For a perfect model, *RMSE* = 0 and the value of the *MPI* = 1, whereas *MPI* = 0 for a model that (erroneously) predicts no changes (*RMSE* = *RMS* of the observed changes). The *MPI* for the wave height is 0.58 at the Gulf of Mexico station and 0.74 at the Mississippi Sound station.

The more predictive operational performance index is defined as the *RMSE* normalized with the incident observed values. It is predictive and operational in the sense that for a given value of the *OPI* (presumably a

characteristic of the model and its implementation for a particular region), an error estimate can be made on the basis of incident wave conditions, prior to the computations. The *OPI* for the wave height is 0.23 at the Gulf of Mexico station and 0.22 at the Mississippi Sound station.

To determine the systematic part of the model performance, the bias is also considered. The bias is simply the mean error, defined as the STWAVE-FP model results minus the observations. The bias for the wave height is 0.16 m at the Gulf of Mexico station and 0.16 m at the Mississippi Sound station.

4.4 Summary and conclusions

This chapter provided an overview of the nearshore numerical wave modeling approach and documented the wave model validation in the Gulf of Mexico and within Mississippi Sound. The STWAVE-FP nearshore wave modeling supported two main tasks during this project: the STWAVE-FP model was applied for the period March-September 1998 so that the resulting radiation stress gradients could be applied within the 3D circulation model (Chapter 3). In addition, the STWAVE-FP model was coupled with ADCIRC and forced with WAM/PBL for the storm wave modeling sensitivity study (Chapter 6).

Field measurements are a critical asset for understanding nearshore wave processes and improving and validating nearshore wave models. The validation of STWAVE-FP was performed with the ERDC-field data collected during March-July 2010 at two stations near Ship Island, one station in the Gulf of Mexico and one station in Mississippi Sound (Figure 4-5). In addition, STWAVE-FP has been validated during Hurricane Gustav in 2008, as briefly described herein, and in more detail in Smith et al. 2010.

To quantify the predictive capability of STWAVE-FP, measures of model performance such as root-mean-square-error, scatter index, model performance index, operational performance index, and bias were computed for wave height at the Gulf of Mexico station at and the Mississippi Sound station. These values are summarized in Table 4-1.

In summary, the STWAVE-FP model compared with good agreement to the measurements, overall. The wave model also predicted the attenuation in wave heights across Ship Island rather well, from the exposed waves at the Gulf of Mexico station to the more sheltered waves at the Mississippi Sound station. The average wave height reduction factor predicted by the model is

0.67, whereas the average wave height reduction factor observed in the measured data is 0.64, where the wave height reduction factor is defined as the ratio of wave height at the Gulf of Mexico station to the wave height at the Mississippi Sound station.

5 Water Quality Modeling[1]

Focus of the water quality effort of this study was to understand existing water quality within the Mississippi Sound and to quantify relative changes in the water quality and flushing capacity resulting from proposed actions. A 3D water quality model was applied in concert with the combined wave and current numerical model (CH3D). A 3D model was determined to be necessary due to existing deep-draft channels and vertical structure of salinity and temperature within the Sound. CE-QUAL-ICM was applied to quantify dissolved oxygen, salinity, temperature, total suspended solids, nutrients, and chlorophyll *a* ("Chl *a*") pre and post project for the various proposed alternatives selected. Calibration of CE-QUAL-ICM was conducted through comparison to existing data. Five scenarios were evaluated and include: Base conditions ("Pre Katrina"), "Post-Katrina," "Restored," Without Project ("Degraded") and "Cumulative" (With Project, Katrina Cut Closure, and authorized channel dimensions).

5.1 Water quality model description

CE-QUAL-ICM (ICM) is a flexible, widely applicable, state-of the-art eutrophication model. Initial application was to Chesapeake Bay (Cerco and Cole 1994). Since the initial Chesapeake Bay study, the ICM model code has been generalized with minor corrections and model improvements. Subsequent additional applications of ICM included the Delaware Inland Bays (Cerco et al. 1994), Newark Bay (Cerco and Bunch 1997), the San Juan Estuary (Bunch et al. 2000), Florida Bay (Cerco et al. 2000), St. Johns River (Tillman et al. 2004) and Port of Los Angeles (Bunch et al. 2003a and 2003b; Martin et al. 2008; and Tillman et al. 2008). Each model application employed a different combination of model features and required addition of system-specific capabilities.

General features of the model include:

- Operational in one-, two-, or three-dimensional configurations;
- Thirty-six state variables including physical properties;

[1] Written by Barry W. Bunch and Dorthy H. Tillman, Environmental Laboratory, US Army Engineer Research and Development Center, Vicksburg, MS.

- Sediment-water oxygen and nutrient fluxes may be computed in a predictive sub-model or specified with observed sediment-oxygen demand rates (SOD);
- State variable may be individually activated or deactivated;
- Internal averaging of model output over arbitrary intervals;
- Computation and reporting of concentrations, mass transport, kinetics transformations, and mass balances;
- Debugging aids include ability to activate and deactivate model features, diagnostic output, volumetric and mass balances; and
- Operates on a variety of computer platforms. Coded in ANSI Standard FORTRAN F77.

ICM is limited by not computing the hydrodynamics of the modeled system. Hydrodynamic variables (i.e., flows, diffusion coefficients, and volumes) must be specified externally and read into the model. Hydrodynamics may be specified in binary or ASCII format and are usually obtained from a hydrodynamic model such as the CH3D_WES model (Johnson et al. 1991).

5.2 Conservation of mass equation

The foundation of CE-QUAL-ICM is the solution to the three-dimensional mass-conservation equation for a control volume. Control volumes correspond to cells on the model grid. CE-QUAL-ICM solves, for each volume and for each state variable, the equation:

$$\frac{\delta V_j C_j}{\delta t} = \sum_{k=1}^{n} Q_k C_k + \sum_{k=1}^{n} A_k D_k \frac{\delta C}{\delta x_l} + \Sigma S_j \tag{5.1}$$

where:

V_j = volume of j^{th} control volume (m^3)
C_j = concentration in j^{th} control volume ($g\ m^{-3}$)
t, x = temporal and spatial coordinates
n = number of flow faces attached to j^{th} control volume
Q_k = volumetric flow across flow face k of j^{th} control volume ($m^3\ s^{-1}$)
C_k = concentration in flow across face k ($g\ m^{-3}$)
A_k = area of flow face k (m^2)
D_k = diffusion coefficient at flow face k ($m^2\ s^{-1}$)
S_j = external loads and kinetic sources and sinks in j^{th} control volume (gs^{-1})

Solution of Equation 5-1 on a computer requires discretization of continuous derivatives and specification of parameter values. The equation is solved explicitly using upwind differencing or the QUICKEST algorithm (Leonard 1979) to represent C_k. The time step, determined by stability requirements, is usually five to fifteen minutes. For notational simplicity, transport terms are dropped in reporting of kinetics formulations. For this study, the parallel version of ICM was used for computational purposes.

5.3 State variables

CE-QUAL-ICM incorporates 36 state variables in the water column including physical variables, multiple algal groups, and multiple forms of carbon, nitrogen, phosphorus, and silica (Table 5-1). Two zooplankton groups known as microzooplankton and mesozooplankton, are available and can be activated when desired.

Table 5-1. Water quality model state variables.

Temperature	Salinity
Fixed Solids	Cyanobacteria
Diatoms	Other Phytoplankton
Zooplankton 1	Zooplankton 2
Labile Dissolved Organic Carbon (DOC)	Refractory Dissolved Organic Carbon
Labile Particulate Organic Carbon	Refractory Particulate Organic Carbon
Ammonium (NH4)	Nitrate + Nitrite Nitrogen (NO3)
Urea	Labile Dissolved Organic Nitrogen (DON)
Refractory Dissolved Organic Nitrogen	Labile Particulate Organic Nitrogen
Refractory Particulate Organic Nitrogen	Total Phosphate (Tp)
Labile Dissolved Organic Phosphorus (DOP)	Refractory Dissolved Organic Phosphorus (DOP)
Refractory Particulate Organic Phosphorus	Labile Particulate Organic Phosphorus
Particulate Inorganic Phosphorus	Chemical Oxygen Demand (COD)
Dissolved Oxygen (DO)	Particulate Biogenic Silica
Dissolved Silica	Internal Phosphorus Group 1
Internal Phosphorus Group 2	Internal Phosphorus Group 3
Clay	Silt
Sand	Organic Sediments

Of the state variables listed above, 15 variables with observed data available were activated during calibration. The variables activated are listed in Table 5-2.

Table 5-2. Active water quality model state variables.

Temperature	Salinity
Fixed Solids	Other Phytoplankton
Labile Dissolved Organic Carbon (DOC)	Labile Particulate Organic Carbon (POC)
Nitrate + Nitrite Nitrogen (NO3)	Ammonium (NH4)
Labile Dissolved Organic Nitrogen (DON)	Labile Particlate Organic Nitrogen (PON)
Total Phosphate (Tp)	Labile Dissolved Organic Phosphorus (DOP)
Labile Particulate Organic Phosphorus (POP)	Dissolved Oxygen (DO)
Dissolved Silica	

5.4 CE-QUAL-ICM grid

Computational grids for the Mississippi Sound study are shown in Figure 5-1. Characteristics of all grids for water quality runs are listed in Table 5-3. Water quality grids have the same number of cells as the hydrodynamic grid described in Chapter 3 except along the ocean boundaries. Cells along the ocean boundary were removed because of differences in how ICM handles flows at ocean boundaries. CH3D specifies a water surface elevation or head condition at the ocean boundary while ICM requires a flow for the face along the boundary. Removing cells along the ocean boundary has no impact upon water quality computations on the interior of the grid.

5.5 Data requirements

The following data were required for an application of ICM:

- Bathymetry
- Comparison (observed) data
- Initial conditions
  - Temperature
  - Water quality constituents
- Boundary conditions
  - Inflow/outflow
  - Temperature
  - Water quality
- Meteorology

Figure 5-1. Mississippi Sound computational grids for all simulation scenarios indicated below the plot. (Sheet 1 of 5)

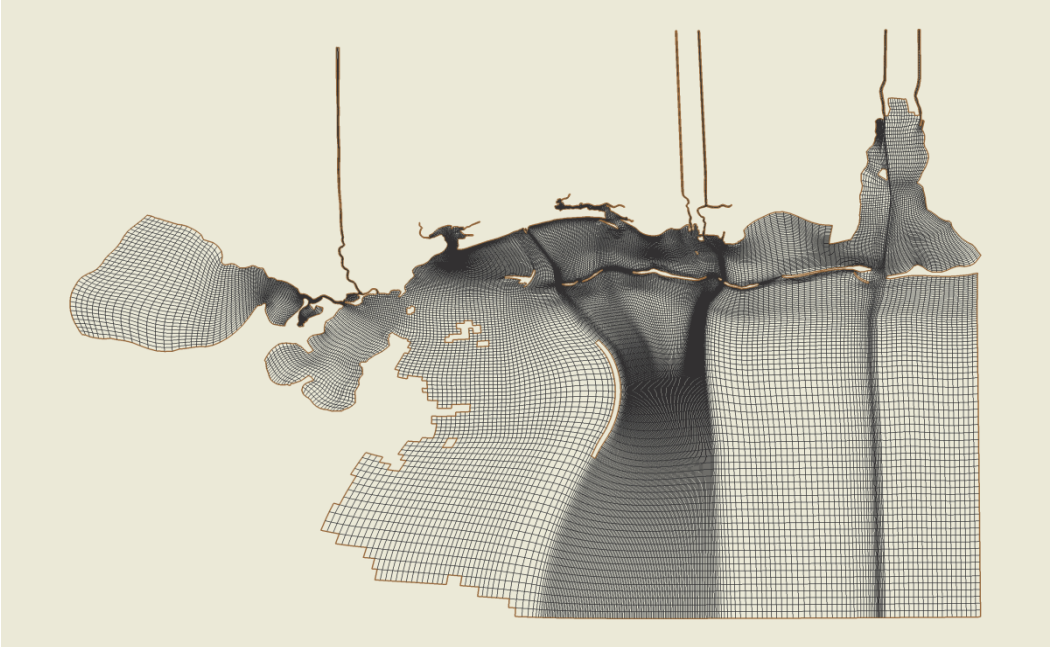

Pre-Katrina

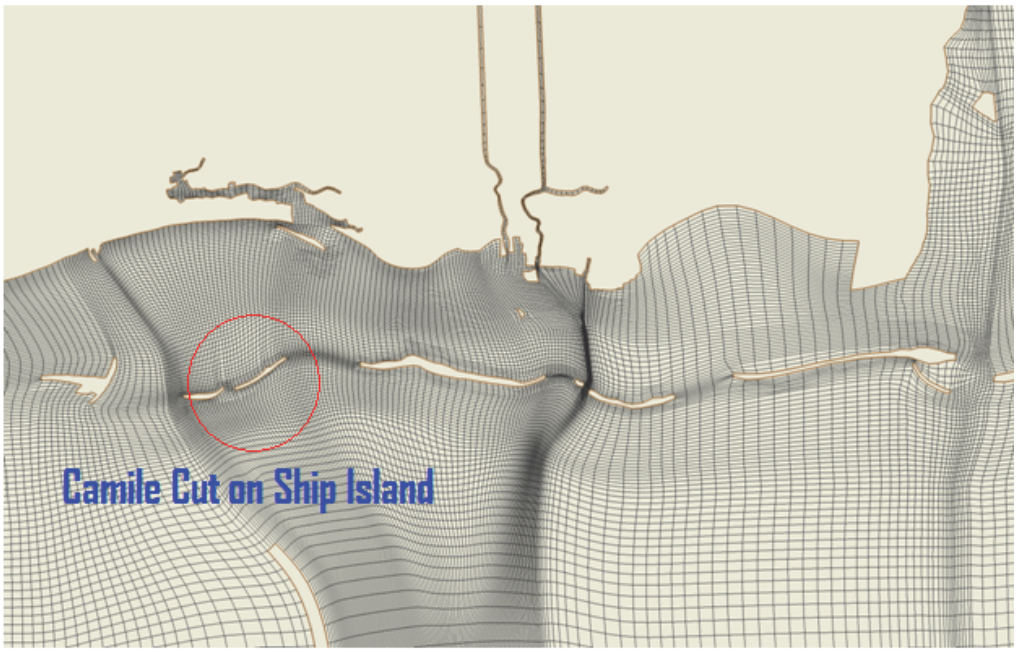

Inset of Pre-Katrina showing cut

Figure 5-1. (Sheet 2 of 5).

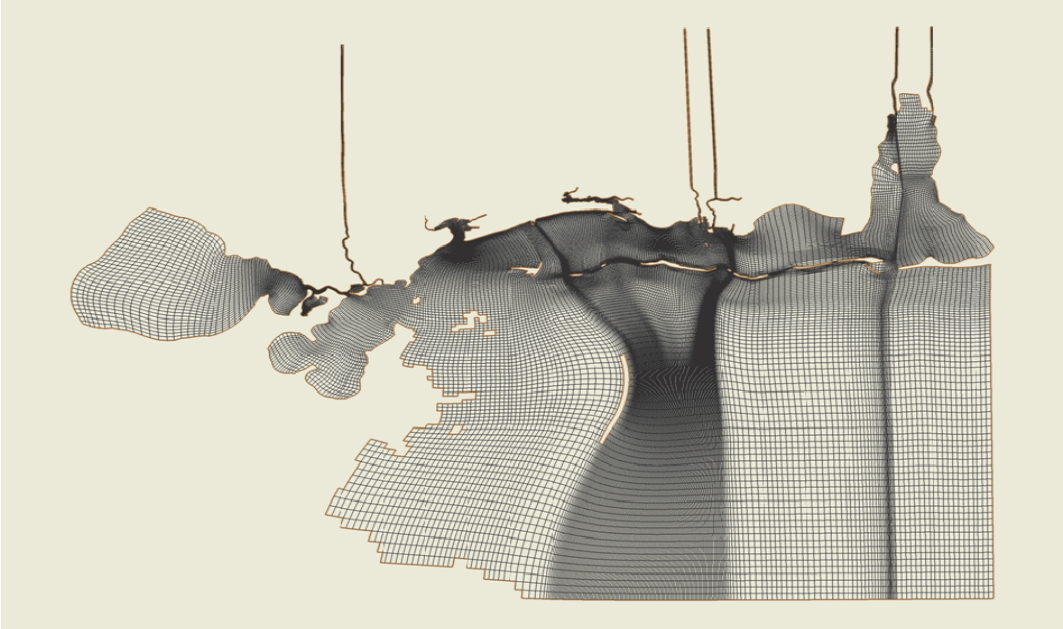

Post-Katrina

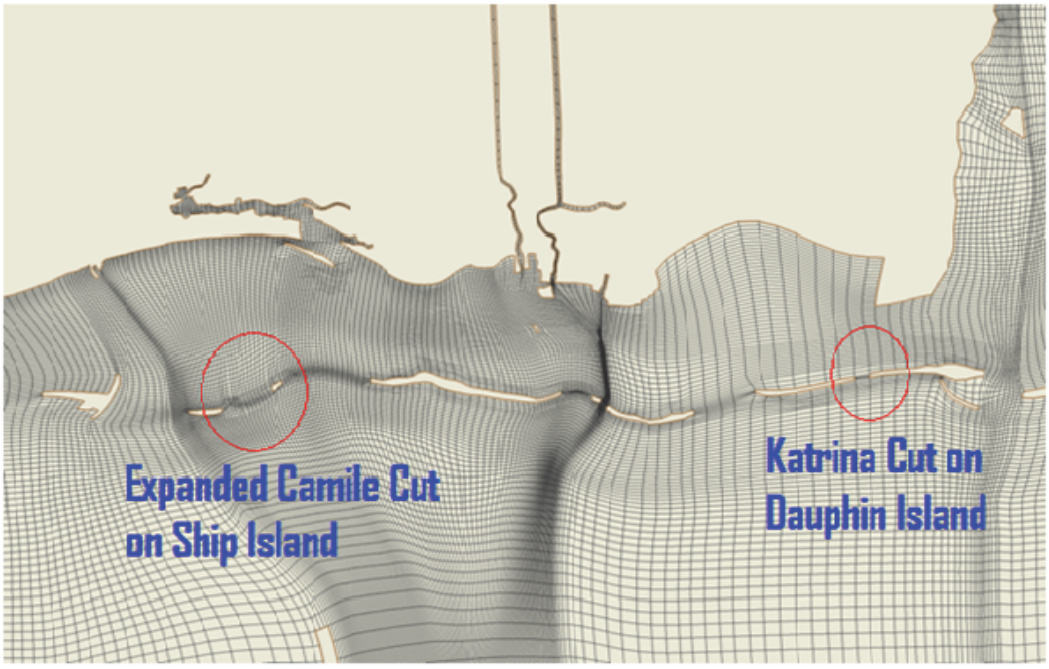

Inset of Post-Katrina Conditions showing modifications from Pre-Katrina

Figure 5-1. (Sheet 3 of 5).

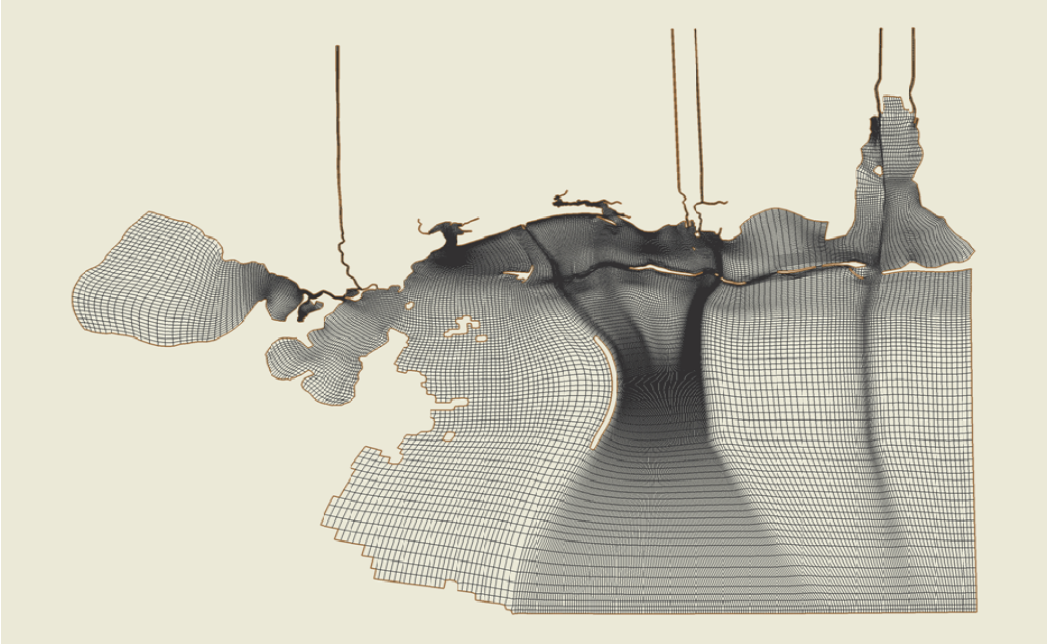

Degraded

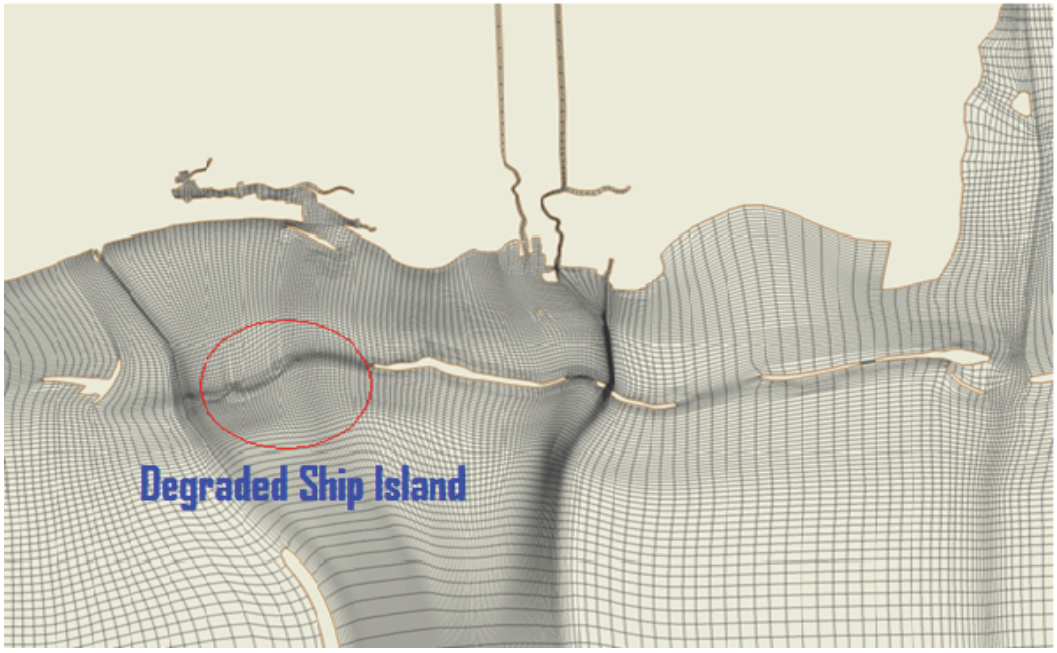

Inset of Degraded showing modifications from Pre-Katrina

Figure 5-1. (Sheet 4 of 5).

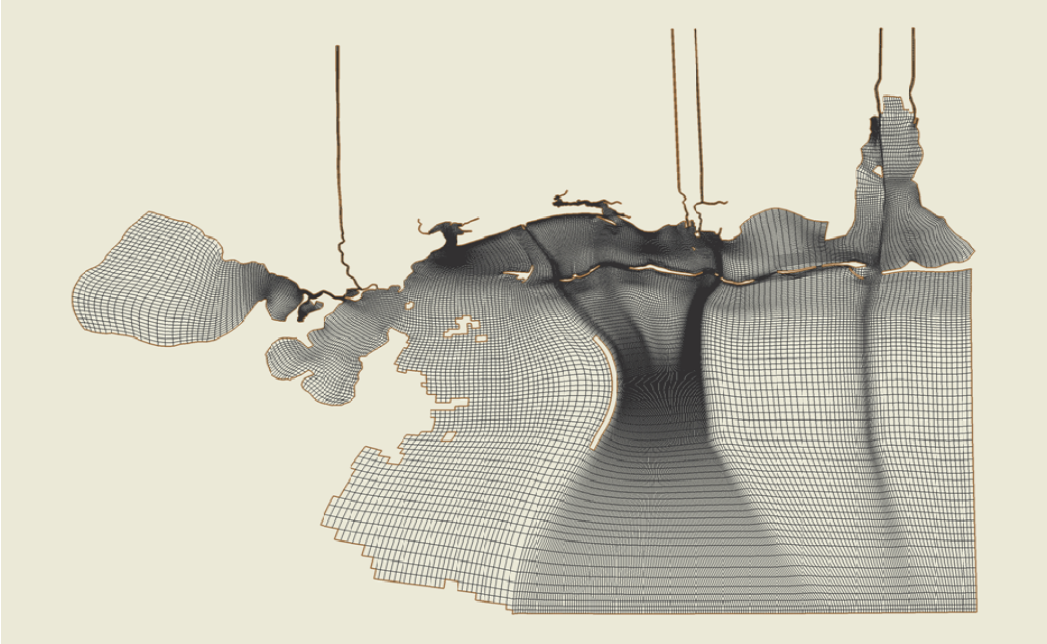

Restored

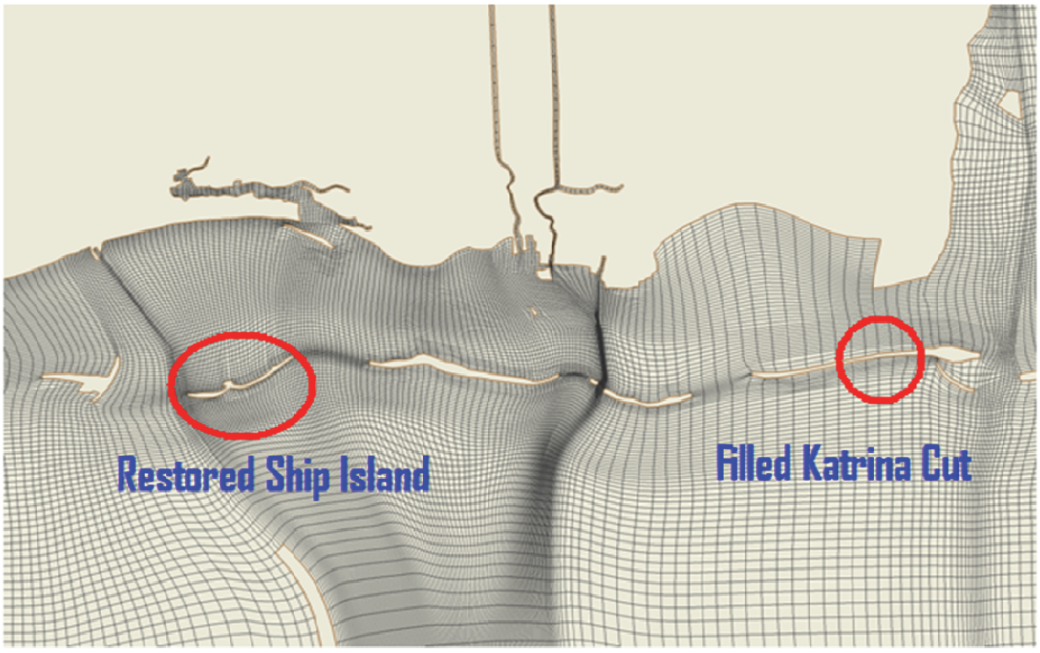

Inset of Restored showing modifications to Pre-Katrina

Figure 5-1. (Sheet 5 of 5).

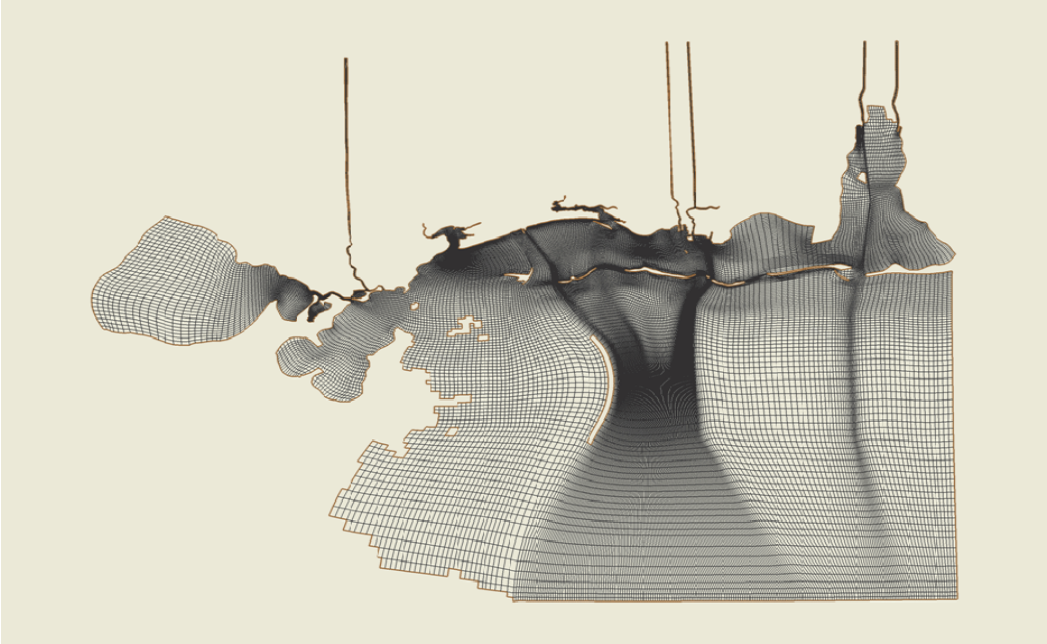

Cumulative

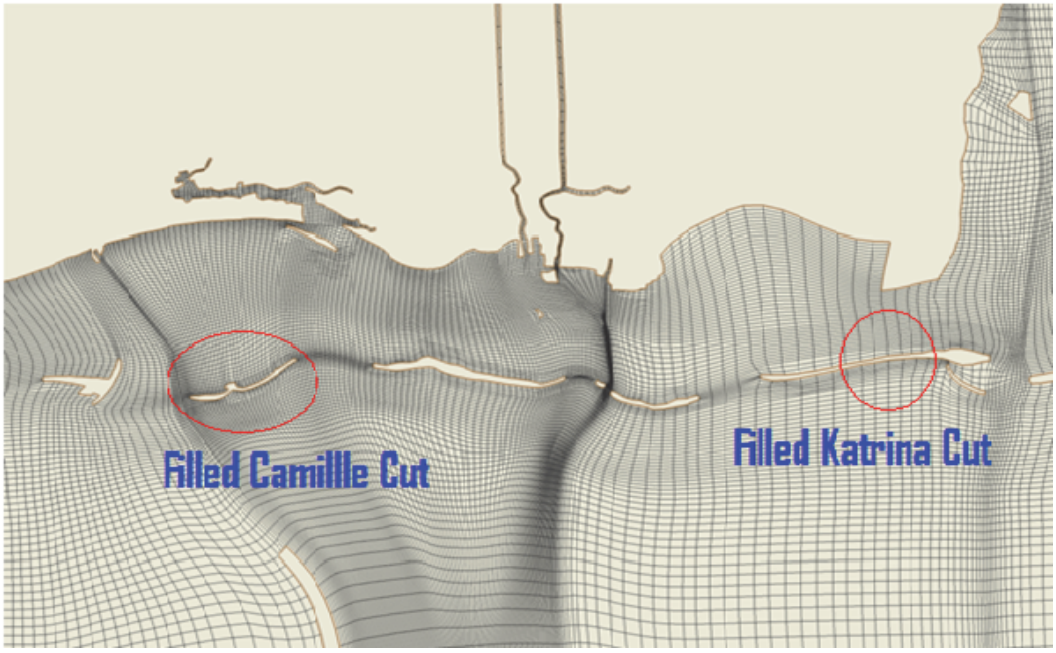

Inset of Cumulative showing modifications from Pre-Katrina

Table 5-3. Water quality grid characteristics for water quality runs.

Number of Grid Cells and Flow Faces	Pre- Katrina	Post-Katrina	Restored	Degraded	Cumulative
Total Cells	196820	197150	196740	197355	196725
Surface Cells	39364	39430	39348	39471	39345
Total Flow Faces	544951	545970	544692	546639	544660
Total Horizontal Flow Faces	387495	388250	387300	388755	387280
Surface Horizontal Flow Faces	77499	77650	77460	77751	77456

These data set initial conditions at the start of a model run and provide time-varying inputs that drive the model during the course of a simulation.

Initial and boundary conditions and comparison data all provide different functions in water quality modeling. Comparison data have no effect on model performance and are used only to assess model performance. Initial and boundary conditions are of greater importance because they directly influence model predictions. Unfortunately, boundary conditions are rarely determined with a frequency that most modelers consider sufficient to accurately describe the forcing functions that are ultimately responsible for observed temperature and water quality conditions. For this study, comparison and boundary data from the Mississippi Department of Environmental Quality (MS DEQ) were collected at most on a quarterly basis for the years 1996 through 2002. This limited the boundary data to two or three points during the calibration period.

5.6 Observed data for calibration

The MS DEQ provided observed data that were used for setting water quality initial and boundary conditions during calibration. Initial conditions for the water column were specified as uniform for all layers based on observed data closest to the simulation start day (April 1, 1998) and are listed in Table 5-4. To provide a more realistic initial condition (spatially varied) in the study area, ICM was run for one month with the uniform initial conditions discussed above. From this run, water quality conditions were output to a file and applied as initial conditions for the remaining calibration runs.

Table 5-4. Initial conditions.

Constituent	Calibration/Scenario Values
Temperature (^{o}C)	18.7
Salinity (ppt)	10.0
Dissolved Organic Carbon (g/m^3)	7.0
Dissolved Oxygen (g/m^3)	8.3
Ammonium (g/m^3)	0.12
Nitrate-Nitrite (g/m^3)	0.02
DIP (g/m^3)	0.16

5.6.1 Initial and boundary conditions

Initial conditions for the water column were specified as uniform for all layers based on observed data closest to the simulation start day (April 1, 1998). Values used for each water quality constituent are listed in Table 5-4.

Water quality boundary conditions specified along the ocean and river boundaries were uniform for each layer (see Tables 5-5 through 5-11). There were nine river inflow points modeled in CH3D and ICM: 1) Pearl River, 2) Jourdan River, 3) Wolf River, 4) Biloxi River, 5) East Pascagoula, 6) West Pascagoula, 7) Escatawpa River, 8) Alabama River and 9) Tombigbee River. Water quality boundary conditions were available for all rivers except the Pearl, Alabama, and Tombigbee. Boundary conditions for the Pearl River were set to values used for the Jourdan River and a beach monitoring station at Pass Christian since they were in the same vicinity. Boundary conditions for the Alabama and Tombigbee rivers were set to values used for the Pascagoula River. Variables used for boundary conditions for rivers were not always collected on the same dates and at the same frequency, which is required by ICM. Thus, to use all possible dates of observed data, missing values were interpolated or assumed constant when necessary. Flow boundary conditions used in the CH3D modeling are discussed in Chapter 3.

Observed water quality boundary conditions for the river boundaries were available for the state variables temperature, salinity, dissolved oxygen (DO), ammonium, and nitrate-nitrite. The other constituent boundary conditions were handled similar to Dortch et al. (2007) by estimating values from related observed data such as total organic carbon (TOC), total Kjeldahl nitrogen (TKN), total phosphorus (*Tp*), orthophosphate

Table 5-5. Southern Ocean boundary conditions.

Date	Constituent	Calibration value
4/01/98	Temperature (°C)	18.7
4/01/98	Salinity (ppt)	34.0
4/01/98	DOC (g/m^3)	7.0
4/01/98	DO (g/m^3)	8.3
4/01/98	Ammonium (g/m^3)	0.24
4/01/98	Nitrate-Nitrite (g/m^3)	0.9
4/01/98	TIP (g/m^3)	0.005
4/01/98	Chlorophyll (ug/L)	7.0
4/15/98	Temperature (°C)	20.1
4/15/98	Salinity (ppt)	34.0
4/15/98	DOC (g/m^3)	7.0
4/15/98	DO (g/m^3)	8.8
4/15/98	Ammonium (g/m^3)	0.1
4/15/98	Nitrate-Nitrite (g/m^3)	0.02
4/15/98	TIP (g/m^3)	0.03
4/15/98	Chlorophyll (ug/L)	7.0
4/30/98	Temperature (°C)	23.6
4/30/98	Salinity (ppt)	34.0
4/30/98	DOC (g/m^3)	6.0
4/30/98	DO (g/m^3)	8.1
4/30/98	Ammonium (g/m^3)	0.1
4/30/98	Nitrate-Nitrite (g/m^3)	0.06
4/30/98	TIP (g/m^3)	0.06
4/30/98	Chlorophyll (ug/L)	7.0
5/14/98	Temperature (°C)	26.2
5/14/98	Salinity (ppt)	34.0
5/14/98	DOC (g/m^3)	4.0
5/14/98	DO (g/m^3)	7.9
5/14/98	Ammonium (g/m^3)	0.1
5/14/98	Nitrate-Nitrite (g/m^3)	0.02
5/14/98	TIP (g/m^3)	0.02
5/14/98	Chlorophyll (ug/L)	7.0
5/30/98	Temperature (°C)	30.4
5/30/98	Salinity (ppt)	34.0
5/30/98	DOC (g/m^3)	6.0
5/30/98	DO (g/m^3)	8.3
5/30/98	Ammonium (g/m^3)	0.16

Date	Constituent	Calibration value
5/30/98	Nitrate-Nitrite (g/m^3)	0.02
5/30/98	TIP (g/m^3)	0.21
5/30/98	Chlorophyll (ug/L)	7.0
6/30/98	Temperature (^{o}C)	28.9
6/30/98	Salinity (ppt)	34.0
6/30/98	DOC (g/m^3)	4.0
6/30/98	DO (g/m^3)	7.9
6/30/98	Ammonium (g/m^3)	0.13
6/30/98	Nitrate-Nitrite (g/m^3)	0.02
6/30/98	TIP (g/m^3)	0.065
6/30/98	Chlorophyll (ug/L)	7.0
7/25/98	Temperature (^{o}C)	33.6
7/25/98	Salinity (ppt)	34.0
7/25/98	DOC (g/m^3)	6.0
7/25/98	DO (g/m^3)	8.9
7/25/98	Ammonium (g/m^3)	0.1
7/25/98	Nitrate-Nitrite (g/m^3)	0.02
7/25/98	TIP (g/m^3)	0.02
7/25/98	Chlorophyll (ug/L)	7.0
8/26/98	Temperature (^{o}C)	31.0
8/26/98	Salinity (ppt)	34.0
8/26/98	DOC (g/m^3)	1.0
8/26/98	DO (g/m^3)	5.5
8/26/98	Ammonium (g/m^3)	0.15
8/26/98	Nitrate-Nitrite (g/m^3)	0.02
8/26/98	TIP (g/m^3)	0.075
8/26/98	Chlorophyll (ug/L)	7.0
9/21/98	Temperature (^{o}C)	29.2
9/21/98	Salinity (ppt)	34.0
9/21/98	DOC (g/m^3)	5.0
9/21/98	DO (g/m^3)	6.0
9/21/98	Ammonium (g/m^3)	0.38
9/21/98	Nitrate-Nitrite (g/m^3)	0.02
9/21/98	TIP (g/m^3)	0.145
9/21/98	Chlorophyll (ug/L)	7.0

Table 5-6. Eastern Ocean boundary conditions.

Date	Constituent	Calibration Value
4/01/98	Temperature (^{o}C)	18.7
4/01/98	Salinity (ppt)	0.1
4/01/98	DOC (g/m^3)	7.0
4/01/98	DO (g/m^3)	8.3
4/01/98	Ammonium (g/m^3)	0.24
4/01/98	Nitrate-Nitrite (g/m^3)	0.09
4/01/98	TIP (g/m^3)	0.005
4/01/98	Chlorophyll (ug/L)	7.0
4/15/98	Temperature (^{o}C)	20.6
4/15/98	Salinity (ppt)	0.4
4/15/98	DOC (g/m^3)	4.0
4/15/98	DO (g/m^3)	8.1
4/15/98	Ammonium (g/m^3)	0.12
4/15/98	Nitrate-Nitrite (g/m^3)	0.16
4/15/98	TIP (g/m^3)	0.02
4/15/98	Chlorophyll (ug/L)	7.0
4/30/98	Temperature (^{o}C)	23.6
4/30/98	Salinity (ppt)	11.5
4/30/98	DOC (g/m^3)	6.0
4/30/98	DO (g/m^3)	8.1
4/30/98	Ammonium (g/m^3)	0.1
4/30/98	Nitrate-Nitrite (g/m^3)	0.06
4/30/98	TIP (g/m^3)	0.06
4/30/98	Chlorophyll (ug/L)	7.0
5/14/98	Temperature (^{o}C)	26.2
5/14/98	Salinity (ppt)	17.9
5/14/98	DOC (g/m^3)	4.0
5/14/98	DO (g/m^3)	7.9
5/14/98	Ammonium (g/m^3)	0.1
5/14/98	Nitrate-Nitrite (g/m^3)	0.02
5/14/98	TIP (g/m^3)	0.02
5/14/98	Chlorophyll (ug/L)	7.0
5/30/98	Temperature (^{o}C)	30.4
5/30/98	Salinity (ppt)	34.0
5/30/98	DOC (g/m^3)	6.0
5/30/98	DO (g/m^3)	8.3
5/30/98	Ammonium (g/m^3)	0.16

Date	Constituent	Calibration Value
5/30/98	Nitrate-Nitrite (g/m^3)	0.02
5/30/98	TIP (g/m^3)	0.2
5/30/98	Chlorophyll (ug/L)	7.0
6/30/98	Temperature (^{o}C)	28.9
6/30/98	Salinity (ppt)	22.8
6/30/98	DOC (g/m^3)	4.0
6/30/98	DO (g/m^3)	7.9
6/30/98	Ammonium (g/m^3)	0.13
6/30/98	Nitrate-Nitrite (g/m^3)	0.02
6/30/98	TIP (g/m^3)	0.065
6/30/98	Chlorophyll (ug/L)	7.0
7/25/98	Temperature (^{o}C)	33.5
7/25/98	Salinity (ppt)	22.3
7/25/98	DOC (g/m^3)	1.0
7/25/98	DO (g/m^3)	8.9
7/25/98	Ammonium (g/m^3)	0.11
7/25/98	Nitrate-Nitrite (g/m^3)	0.02
7/25/98	TIP (g/m^3)	0.075
7/25/98	Chlorophyll (ug/L)	7.0
8/26/98	Temperature (^{o}C)	31.0
8/26/98	Salinity (ppt)	22.8
8/26/98	DOC (g/m^3)	6.0
8/26/98	DO (g/m^3)	6.8
8/26/98	Ammonium (g/m^3)	0.14
8/26/98	Nitrate-Nitrite (g/m^3)	0.02
8/26/98	TIP (g/m^3)	0.03
8/26/98	Chlorophyll (ug/L)	7.0
9/21/98	Temperature (^{o}C)	29.2
9/21/98	Salinity (ppt)	22.7
9/21/98	DOC (g/m^3)	5.0
9/21/98	DO (g/m^3)	6.0
9/21/98	Ammonium (g/m^3)	0.38
9/21/98	Nitrate-Nitrite (g/m^3)	0.02
9/21/98	TIP (g/m^3)	0.145
9/21/98	Chlorophyll (ug/L)	7.0

Table 5-7. Pearl River boundary conditions.

Date	Constituent	Calibration value
4/01/98	Temperature (^{o}C)	18.7
4/01/98	Salinity (ppt)	0.1
4/01/98	DOC (g/m^3)	12.0
4/01/98	DO (g/m^3)	8.3
4/01/98	Ammonium (g/m^3)	0.24
4/01/98	Nitrate-Nitrite (g/m^3)	0.09
4/01/98	TIP (g/m^3)	0.005
4/01/98	Chlorophyll (ug/L)	7.0
4/15/98	Temperature (^{o}C)	20.1
4/15/98	Salinity (ppt)	2.4
4/15/98	DOC (g/m^3)	7.0
4/15/98	DO (g/m^3)	8.8
4/15/98	Ammonium (g/m^3)	0.1
4/15/98	Nitrate-Nitrite (g/m^3)	0.16
4/15/98	TIP (g/m^3)	0.03
4/15/98	Chlorophyll (ug/L)	7.0
4/30/98	Temperature (^{o}C)	21.3
4/30/98	Salinity (ppt)	6.0
4/30/98	DOC (g/m^3)	5.0
4/30/98	DO (g/m^3)	7.9
4/30/98	Ammonium (g/m^3)	0.16
4/30/98	Nitrate-Nitrite (g/m^3)	0.03
4/30/98	TIP (g/m^3)	0.025
4/30/98	Chlorophyll (ug/L)	7.0
5/14/98	Temperature (^{o}C)	26.2
5/14/98	Salinity (ppt)	8.5
5/14/98	DOC (g/m^3)	4.0
5/14/98	DO (g/m^3)	7.9
5/14/98	Ammonium (g/m^3)	0.1
5/14/98	Nitrate-Nitrite (g/m^3)	0.02
5/14/98	TIP (g/m^3)	0.02
5/14/98	Chlorophyll (ug/L)	7.0
5/30/98	Temperature (^{o}C)	31.1
5/30/98	Salinity (ppt)	11.3
5/30/98	DOC (g/m^3)	5.0
5/30/98	DO (g/m^3)	6.2
5/30/98	Ammonium (g/m^3)	0.19

Date	Constituent	Calibration value
5/30/98	Nitrate-Nitrite (g/m^3)	0.02
5/30/98	TIP (g/m^3)	0.13
5/30/98	Chlorophyll (ug/L)	7.0
6/30/98	Temperature (^{o}C)	33.5
6/30/98	Salinity (ppt)	19.3
6/30/98	DOC (g/m^3)	4.0
6/30/98	DO (g/m^3)	8.7
6/30/98	Ammonium (g/m^3)	0.17
6/30/98	Nitrate-Nitrite (g/m^3)	0.02
6/30/98	TIP (g/m^3)	0.015
6/30/98	Chlorophyll (ug/L)	6.6
7/25/98	Temperature (^{o}C)	29.8
7/25/98	Salinity (ppt)	20.3
7/25/98	DOC (g/m^3)	3.0
7/25/98	DO (g/m^3)	5.0
7/25/98	Ammonium (g/m^3)	0.13
7/25/98	Nitrate-Nitrite (g/m^3)	0.02
7/25/98	TIP (g/m^3)	0.025
7/25/98	Chlorophyll (ug/L)	7.0
8/26/98	Temperature (^{o}C)	30.2
8/26/98	Salinity (ppt)	21.5
8/26/98	DOC (g/m^3)	6.0
8/26/98	DO (g/m^3)	3.7
8/26/98	Ammonium (g/m^3)	0.1
8/26/98	Nitrate-Nitrite (g/m^3)	0.02
8/26/98	TIP (g/m^3)	0.05
8/26/98	Chlorophyll (ug/L)	7.0
9/21/98	Temperature (^{o}C)	28.3
9/21/98	Salinity (ppt)	10.0
9/21/98	DOC (g/m^3)	9.0
9/21/98	DO (g/m^3)	5.8
9/21/98	Ammonium (g/m^3)	0.2
9/21/98	Nitrate-Nitrite (g/m^3)	0.03
9/21/98	TIP (g/m^3)	0.05
9/21/98	Chlorophyll (ug/L)	7.0

Table 5-8. Jourdan River boundary conditions.

Date	Constituent	Calibration value
4/01/98	Temperature (^{o}C)	18.7
4/01/98	Salinity (ppt)	0.1
4/01/98	DOC (g/m^3)	12.0
4/01/98	DO (g/m^3)	8.3
4/01/98	Ammonium (g/m^3)	0.24
4/01/98	Nitrate-Nitrite (g/m^3)	0.9
4/01/98	TIP (g/m^3)	0.005
4/01/98	Chlorophyll (ug/L)	7.0
4/15/98	Temperature (^{o}C)	21.4
4/15/98	Salinity (ppt)	0.3
4/15/98	DOC (g/m^3)	8.0
4/15/98	DO (g/m^3)	7.2
4/15/98	Ammonium (g/m^3)	0.13
4/15/98	Nitrate-Nitrite (g/m^3)	0.06
4/15/98	TIP (g/m^3)	0.085
4/15/98	Chlorophyll (ug/L)	7.0
4/30/98	Temperature (^{o}C)	23.6
4/30/98	Salinity (ppt)	11.5
4/30/98	DOC (g/m^3)	6.0
4/30/98	DO (g/m^3)	8.1
4/30/98	Ammonium (g/m^3)	0.1
4/30/98	Nitrate-Nitrite (g/m^3)	0.06
4/30/98	TIP (g/m^3)	0.06
4/30/98	Chlorophyll (ug/L)	7.0
5/14/98	Temperature (^{o}C)	26.2
5/14/98	Salinity (ppt)	17.9
5/14/98	DOC (g/m^3)	4.0
5/14/98	DO (g/m^3)	7.9
5/14/98	Ammonium (g/m^3)	0.1
5/14/98	Nitrate-Nitrite (g/m^3)	0.02
5/14/98	TIP (g/m^3)	0.02
5/14/98	Chlorophyll (ug/L)	7.0
5/30/98	Temperature (^{o}C)	30.5
5/30/98	Salinity (ppt)	23.3
5/30/98	DOC (g/m^3)	5.0
5/30/98	DO (g/m^3)	6.3
5/30/98	Ammonium (g/m^3)	0.1

Date	Constituent	Calibration value
5/30/98	Nitrate-Nitrite (g/m^3)	0.02
5/30/98	TIP (g/m^3)	0.025
5/30/98	Chlorophyll (ug/L)	7.0
6/30/98	Temperature (^{o}C)	31.5
6/30/98	Salinity (ppt)	2.9
6/30/98	DOC (g/m^3)	4.0
6/30/98	DO (g/m^3)	5.8
6/30/98	Ammonium (g/m^3)	0.11
6/30/98	Nitrate-Nitrite (g/m^3)	0.02
6/30/98	TIP (g/m^3)	0.075
6/30/98	Chlorophyll (ug/L)	6.6
7/25/98	Temperature (^{o}C)	29.8
7/25/98	Salinity (ppt)	20.4
7/25/98	DOC (g/m^3)	3.0
7/25/98	DO (g/m^3)	5.0
7/25/98	Ammonium (g/m^3)	0.13
7/25/98	Nitrate-Nitrite (g/m^3)	0.02
7/25/98	TIP (g/m^3)	0.025
7/25/98	Chlorophyll (ug/L)	7.0
8/26/98	Temperature (^{o}C)	31.1
8/26/98	Salinity (ppt)	10.0
8/26/98	DOC (g/m^3)	8.0
8/26/98	DO (g/m^3)	6.2
8/26/98	Ammonium (g/m^3)	0.24
8/26/98	Nitrate-Nitrite (g/m^3)	0.03
8/26/98	TIP (g/m^3)	0.015
8/26/98	Chlorophyll (ug/L)	7.1
9/21/98	Temperature (^{o}C)	25.6
9/21/98	Salinity (ppt)	0.03
9/21/98	DOC (g/m^3)	23.0
9/21/98	DO (g/m^3)	6.2
9/21/98	Ammonium (g/m^3)	0.1
9/21/98	Nitrate-Nitrite (g/m^3)	0.08
9/21/98	TIP (g/m^3)	0.095
9/21/98	Chlorophyll (ug/L)	7.0

Table 5-9. Wolf Creek boundary conditions.

Date	Constituent	Calibration value
4/01/98	Temperature (^{o}C)	18.7
4/01/98	Salinity (ppt)	0.1
4/01/98	DOC (g/m^3)	12.0
4/01/98	DO (g/m^3)	8.3
4/01/98	Ammonium (g/m^3)	0.24
4/01/98	Nitrate-Nitrite (g/m^3)	0.9
4/01/98	TIP (g/m^3)	0.005
4/01/98	Chlorophyll (ug/L)	7.0
4/15/98	Temperature (^{o}C)	21.4
4/15/98	Salinity (ppt)	0.03
4/15/98	DOC (g/m^3)	8.0
4/15/98	DO (g/m^3)	9.6
4/15/98	Ammonium (g/m^3)	0.27
4/15/98	Nitrate-Nitrite (g/m^3)	0.03
4/15/98	TIP (g/m^3)	0.015
4/15/98	Chlorophyll (ug/L)	10.0
4/30/98	Temperature (^{o}C)	23.6
4/30/98	Salinity (ppt)	11.5
4/30/98	DOC (g/m^3)	6.0
4/30/98	DO (g/m^3)	8.1
4/30/98	Ammonium (g/m^3)	0.10
4/30/98	Nitrate-Nitrite (g/m^3)	0.06
4/30/98	TIP (g/m^3)	0.06
4/30/98	Chlorophyll (ug/L)	7.0
5/14/98	Temperature (^{o}C)	26.2
5/14/98	Salinity (ppt)	17.9
5/14/98	DOC (g/m^3)	4.0
5/14/98	DO (g/m^3)	7.9
5/14/98	Ammonium (g/m^3)	0.1
5/14/98	Nitrate-Nitrite (g/m^3)	0.02
5/14/98	TIP (g/m^3)	0.02
5/14/98	Chlorophyll (ug/L)	7.0
5/30/98	Temperature (^{o}C)	30.5
5/30/98	Salinity (ppt)	23.3
5/30/98	DOC (g/m^3)	5.0
5/30/98	DO (g/m^3)	6.3
5/30/98	Ammonium (g/m^3)	0.1

Date	Constituent	Calibration value
5/30/98	Nitrate-Nitrite (g/m^3)	0.02
5/30/98	TIP (g/m^3)	0.065
5/30/98	Chlorophyll (ug/L)	7.0
6/30/98	Temperature (^{o}C)	30.2
6/30/98	Salinity (ppt)	2.9
6/30/98	DOC (g/m^3)	1.0
6/30/98	DO (g/m^3)	6.2
6/30/98	Ammonium (g/m^3)	0.11
6/30/98	Nitrate-Nitrite (g/m^3)	0.05
6/30/98	TIP (g/m^3)	0.035
6/30/98	Chlorophyll (ug/L)	6.6
7/25/98	Temperature (^{o}C)	29.8
7/25/98	Salinity (ppt)	20.4
7/25/98	DOC (g/m^3)	3.0
7/25/98	DO (g/m^3)	5.0
7/25/98	Ammonium (g/m^3)	0.13
7/25/98	Nitrate-Nitrite (g/m^3)	0.02
7/25/98	TIP (g/m^3)	0.025
7/25/98	Chlorophyll (ug/L)	7.0
8/26/98	Temperature (^{o}C)	32.6
8/26/98	Salinity (ppt)	2.7
8/26/98	DOC (g/m^3)	8.0
8/26/98	DO (g/m^3)	7.2
8/26/98	Ammonium (g/m^3)	0.21
8/26/98	Nitrate-Nitrite (g/m^3)	0.04
8/26/98	TIP (g/m^3)	0.03
8/26/98	Chlorophyll (ug/L)	8.0
9/21/98	Temperature (^{o}C)	24.1
9/21/98	Salinity (ppt)	0.03
9/21/98	DOC (g/m^3)	10.0
9/21/98	DO (g/m^3)	5.8
9/21/98	Ammonium (g/m^3)	0.1
9/21/98	Nitrate-Nitrite (g/m^3)	0.06
9/21/98	TIP (g/m^3)	0.02
9/21/98	Chlorophyll (ug/L)	10.0

Table 5-10. Biloxi River boundary conditions.

Date	Constituent	Calibration value
4/01/98	Temperature (^{o}C)	20.3
4/01/98	Salinity (ppt)	1.1
4/01/98	DOC (g/m^3)	6.0
4/01/98	DO (g/m^3)	8.1
4/01/98	Ammonium (g/m^3)	0.15
4/01/98	Nitrate-Nitrite (g/m^3)	0.11
4/01/98	TIP (g/m^3)	0.065
4/01/98	Chlorophyll (ug/L)	7.0
4/15/98	Temperature (^{o}C)	21.3
4/15/98	Salinity (ppt)	8.8
4/15/98	DOC (g/m^3)	8.0
4/15/98	DO (g/m^3)	7.9
4/15/98	Ammonium (g/m^3)	0.10
4/15/98	Nitrate-Nitrite (g/m^3)	0.02
4/15/98	TIP (g/m^3)	0.95
4/15/98	Chlorophyll (ug/L)	10.0
4/30/98	Temperature (^{o}C)	23.8
4/30/98	Salinity (ppt)	10.8
4/30/98	DOC (g/m^3)	5.0
4/30/98	DO (g/m^3)	7.5
4/30/98	Ammonium (g/m^3)	0.10
4/30/98	Nitrate-Nitrite (g/m^3)	0.03
4/30/98	TIP (g/m^3)	0.03
4/30/98	Chlorophyll (ug/L)	7.0
5/14/98	Temperature (^{o}C)	26.2
5/14/98	Salinity (ppt)	17.9
5/14/98	DOC (g/m^3)	4.0
5/14/98	DO (g/m^3)	7.9
5/14/98	Ammonium (g/m^3)	0.1
5/14/98	Nitrate-Nitrite (g/m^3)	0.02
5/14/98	TIP (g/m^3)	0.02
5/14/98	Chlorophyll (ug/L)	7.0
5/30/98	Temperature (^{o}C)	31.0
5/30/98	Salinity (ppt)	12.5
5/30/98	DOC (g/m^3)	5.0
5/30/98	DO (g/m^3)	7.0
5/30/98	Ammonium (g/m^3)	0.18

Date	Constituent	Calibration value
5/30/98	Nitrate-Nitrite (g/m^3)	0.02
5/30/98	TIP (g/m^3)	0.08
5/30/98	Chlorophyll (ug/L)	7.0
6/30/98	Temperature (^{o}C)	28.6
6/30/98	Salinity (ppt)	17.5
6/30/98	DOC (g/m^3)	5.0
6/30/98	DO (g/m^3)	6.2
6/30/98	Ammonium (g/m^3)	0.25
6/30/98	Nitrate-Nitrite (g/m^3)	0.02
6/30/98	TIP (g/m^3)	0.70
6/30/98	Chlorophyll (ug/L)	7.0
7/25/98	Temperature (^{o}C)	33.1
7/25/98	Salinity (ppt)	12.1
7/25/98	DOC (g/m^3)	5.0
7/25/98	DO (g/m^3)	7.6
7/25/98	Ammonium (g/m^3)	0.15
7/25/98	Nitrate-Nitrite (g/m^3)	0.02
7/25/98	TIP (g/m^3)	0.03
7/25/98	Chlorophyll (ug/L)	6.0
8/26/98	Temperature (^{o}C)	32.5
8/26/98	Salinity (ppt)	19.1
8/26/98	DOC (g/m^3)	8.0
8/26/98	DO (g/m^3)	7.8
8/26/98	Ammonium (g/m^3)	0.15
8/26/98	Nitrate-Nitrite (g/m^3)	0.02
8/26/98	TIP (g/m^3)	0.035
8/26/98	Chlorophyll (ug/L)	6.0
9/21/98	Temperature (^{o}C)	26.6
9/21/98	Salinity (ppt)	2.7
9/21/98	DOC (g/m^3)	15.0
9/21/98	DO (g/m^3)	5.3
9/21/98	Ammonium (g/m^3)	0.57
9/21/98	Nitrate-Nitrite (g/m^3)	0.04
9/21/98	TIP (g/m^3)	0.095
9/21/98	Chlorophyll (ug/L)	7.0

Table 5-11. East and West Pascagoula River, Escatawpa River, Alabama River, and Tombigbee River boundary conditions.

Date	Constituent	Calibration value
4/01/98	Temperature (^{o}C)	20.3
4/01/98	Salinity (ppt)	1.1
4/01/98	DOC (g/m^3)	6.0
4/01/98	DO (g/m^3)	8.1
4/01/98	Ammonium (g/m^3)	0.15
4/01/98	Nitrate-Nitrite (g/m^3)	0.11
4/01/98	TIP (g/m^3)	0.065
4/01/98	Chlorophyll (ug/L)	7.0
4/15/98	Temperature (^{o}C)	21.3
4/15/98	Salinity (ppt)	8.8
4/15/98	DOC (g/m^3)	8.0
4/15/98	DO (g/m^3)	7.9
4/15/98	Ammonium (g/m^3)	0.10
4/15/98	Nitrate-Nitrite (g/m^3)	0.02
4/15/98	TIP (g/m^3)	0.95
4/15/98	Chlorophyll (ug/L)	10.0
4/30/98	Temperature (^{o}C)	23.8
4/30/98	Salinity (ppt)	10.8
4/30/98	DOC (g/m^3)	5.0
4/30/98	DO (g/m^3)	7.5
4/30/98	Ammonium (g/m^3)	0.10
4/30/98	Nitrate-Nitrite (g/m^3)	0.03
4/30/98	TIP (g/m^3)	0.03
4/30/98	Chlorophyll (ug/L)	7.0
5/14/98	Temperature (^{o}C)	26.2
5/14/98	Salinity (ppt)	17.9
5/14/98	DOC (g/m^3)	4.0
5/14/98	DO (g/m^3)	7.9
5/14/98	Ammonium (g/m^3)	0.1
5/14/98	Nitrate-Nitrite (g/m^3)	0.02
5/14/98	TIP (g/m^3)	0.02
5/14/98	Chlorophyll (ug/L)	7.0
5/30/98	Temperature (^{o}C)	31.0
5/30/98	Salinity (ppt)	12.5
5/30/98	DOC (g/m^3)	5.0
5/30/98	DO (g/m^3)	7.0

Date	Constituent	Calibration value
5/30/98	Ammonium (g/m^3)	0.18
5/30/98	Nitrate-Nitrite (g/m^3)	0.02
5/30/98	TIP (g/m^3)	0.08
5/30/98	Chlorophyll (ug/L)	7.0
6/30/98	Temperature (^{o}C)	28.6
6/30/98	Salinity (ppt)	17.5
6/30/98	DOC (g/m^3)	5.0
6/30/98	DO (g/m^3)	6.2
6/30/98	Ammonium (g/m^3)	0.25
6/30/98	Nitrate-Nitrite (g/m^3)	0.02
6/30/98	TIP (g/m^3)	0.70
6/30/98	Chlorophyll (ug/L)	7.0
7/25/98	Temperature (^{o}C)	33.1
7/25/98	Salinity (ppt)	12.1
7/25/98	DOC (g/m^3)	5.0
7/25/98	DO (g/m^3)	7.6
7/25/98	Ammonium (g/m^3)	0.15
7/25/98	Nitrate-Nitrite (g/m^3)	0.02
7/25/98	TIP (g/m^3)	0.03
7/25/98	Chlorophyll (ug/L)	6.0
8/26/98	Temperature (^{o}C)	32.5
8/26/98	Salinity (ppt)	19.1
8/26/98	DOC (g/m^3)	8.0
8/26/98	DO (g/m^3)	7.8
8/26/98	Ammonium (g/m^3)	0.15
8/26/98	Nitrate-Nitrite (g/m^3)	0.02
8/26/98	TIP (g/m^3)	0.035
8/26/98	Chlorophyll (ug/L)	6.0
9/21/98	Temperature (^{o}C)	26.6
9/21/98	Salinity (ppt)	2.7
9/21/98	DOC (g/m^3)	15.0
9/21/98	DO (g/m^3)	5.3
9/21/98	Ammonium (g/m^3)	0.57
9/21/98	Nitrate-Nitrite (g/m^3)	0.04
9/21/98	TIP (g/m^3)	0.095
9/21/98	Chlorophyll (ug/L)	7.0

phosphorus (PO_4), and total suspended solids (TSS). For example, organic nutrients and organic carbon loads from the river are assumed to be in the dissolved form. Specifically, TOC was assumed to be comprised of solely dissolved organic carbon (DOC), and particulate organic carbon (POC) was assumed to be zero. Similarly, total organic nitrogen (TON) was assumed to be dissolved organic nitrogen (DON), and particulate organic nitrogen (PON) was assumed to be zero. The TON was computed by subtracting NH_4 from TKN. The PO_4 was assumed to represent total inorganic phosphorus (Total Phosphate), the model state variable. There were only a few PO_4 values for 1998, but data from 1998 and other years indicated that *Tp* was approximately equal to PO_4, or there was little or no organic phosphorus in the stream. Thus, total phosphate values were assigned the *Tp* values, and zero concentrations were set for dissolved and particulate organic phosphorus (DOP and POP). Inorganic suspended solids (ISS), a model state variable, was assumed to equal TSS; thus, there was little or no organic suspended solids, which is consistent with the other assumptions for organic carbon and nutrients. Atmospheric loads were turned on in the model and values were set consistent with Dortch et al. (2007). These values are listed in Table 5.12.

A uniform sediment oxygen demand (SOD) of 0.25 gm O_2 m^{-2} day^{-1} was specified over the entire study area except on the rivers modeled. An SOD rate of 1.5 gm O_2 m^{-2} day^{-1} was used on most of the rivers based on observed SOD collected during the 1997 Escatawpa River Study.

Table 5-12. Atmospheric Loads (kg/day) from Dortch et al. (2007).

NH4	NO3	LDOP
0.230	0.34	0.35

5.6.2 Meteorological data

Meteorological data measured at Mobile airport for the calibration period (1998) was obtained from the Air Force Combat Climatological Center. Daily values for cloud cover, dry bulb temperature, dew point temperature, and wind speeds were used in the heat exchange program (Eiker 1977) to compute heat exchange coefficients, solar illumination, fractional day length, and equilibrium temperature. Bunch et al. (2003) compared meteorological data at Mobile and Keesler Air Force base to see if major differences occurred. Graphs are included in Appendix D for the meteorological conditions at these two locations for the 1995-2000 periods. Since

differences were minimal, it was decided to use Mobile airport data for this study.

5.6.3 Kinetic rates

Appendix D contains ICM kinetic (the rate of change in a biochemical or other reaction) rate files used in this study. Complete descriptions of kinetic processes in ICM can be found in Cerco and Noel (2004).

5.7 Calibration

Calibration was accomplished through an iterative process that included running ICM, comparing model output to observed data, and modifying kinetic rates until statistical comparisons were acceptable. Model performance was evaluated using three forms of graphical comparison: time-series plots, scatter plots, and percent cumulative distribution plots. In addition, three statistics, mean error (*ME*), absolute-mean-error (*AME*) and root-mean-square-error (*RMSE*), were calculated to further evaluate model performance. Presentation of model results is limited to constituents where observed data were available. For instance, although total phosphate is turned on as a state variable with boundary and initial conditions estimated from *Tp*, output results for this variable will not be presented since there were no observed data.

The *RMSE* is an indicator of the deviation between predicted water quality values and observed values. A value of zero would indicate no variation between the observed and predicted. The *ME* indicates on average how the model is doing. For example, a positive *ME* indicates the model is under predicting while a negative *ME* indicates the model is over-predicting (predictions exceed observed). A value of zero for *ME* would also indicate complete agreement between predicted and observed. The *AME* indicates how far, on the average, computed values are from observed values. An *AME* of 0.5 °C means that the computed temperatures are, on the average, within ± 0.5 °C of the observed temperatures. Each statistic was calculated for all stations where observed data were available; data were not distinguished by layer, thus providing an overall model performance. Equations for *ME*, *AME,* and *RMSE* are:

$$ME = \frac{\Sigma(O - P)}{n} \tag{5.2}$$

where

ME = mean error
O = observation
P = model prediction
n = number of observations;

$$AME = \frac{\Sigma|O-P|}{n} \tag{5.3}$$

where:

AME = mean error; and

$$RMSE = \sqrt{\frac{\Sigma(O-P)^2}{n}} \tag{5.4}$$

where:

$RMSE$= root-mean-square-error.

Values for each statistic are presented on time-series plot for each water quality constituent where observed data were available.

Time-series' plots of model output and observed data demonstrate model performance over time and provide indications of interactions between modeled parameters. Time-series plots were generated for stations sampled by the MS DEQ shown in Figure 5-2.

Scatter plots provide a synopsis of overall model performance, such as over/under predicting or missing high/low values while percent cumulative distribution plots present how distribution of predicted values compare with observed. Data for all layers where observed data were available were used in creating the scatter and cumulative distribution plots.

ICM model results consisted of value outputs every three hours from the start of the simulation for all constituents modeled for all cells in the water quality grid. To evaluate model performance, constituent concentrations were output for cells in locations where observed data were monitored. Points to consider when viewing the plots are: 1) model output represents

Figure 5-2. Observed station locations.

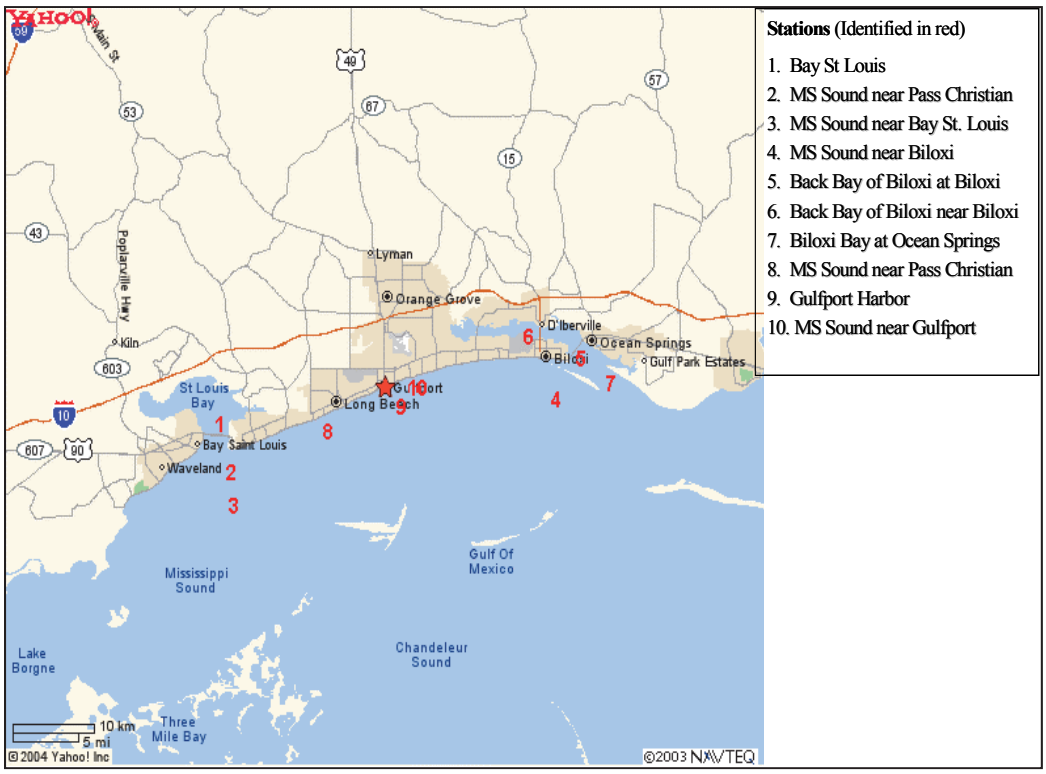

values for concentrations averaged every three hours, whereas the observed data are instantaneous measurements and 2) parameters such as dissolved oxygen and salinity depending on location exhibit strong patterns that are influenced by diurnal effects or tidal action, respectively, which may not be captured in model outputs due to the output frequency and give the appearance that the model is over- or under-predicting observed data.

5.8 Calibration results and discussion

Time-series calibration results are shown in Appendix E (Figures E-1 through E-60). Results are presented for all stations for which observed data were available (see Figure 5-2). Circles represent observed data while a solid line represents model results. Each figure contains two plots for a constituent - one for surface results and one for bottom results. Table 5-13 includes the *AME* target value for all observed data and the *AME* model statistic for all stations and water quality constituents. The *AME* target value is described by Smith et al. (2010) as a good indicator of model performance. It is calculated as 10 percent of the range of observed data:

$$Target = (maximum\,observed - minimum\,observed) * 0.1 \qquad (5.5)$$

Table 5-13. Model *AME* values (left) versus Target *AME* values (right)

Station	Temperature		Salinity		DO		NH_4		No_2+No_3		TOC		Tp	
Combined Stations	1.28	1.36	4.99	3.26	1.09	0.75	0.06	0.14	0.02	0.07	1.46	0.7	0.20	0.19

Temperature. ICM is reproducing the observed temperature time-series data at surface and bottom layers accurately (see Appendix E). Temperature patterns increase from spring to summer and begin to decrease as fall approaches. The *AME* value is below the target *AME* value. From the figures, the *ME* indicates that differences in model predictions are usually less than observed data which is also indicated in the scatter plot (Figure 5-3). The model domain covers a large area and the meteorological data used as a forcing function is from the Mobile airport. These conditions may not represent the whole domain thus introducing some error. Most of the discrepancies between predicted and observed temperatures are likely due to comparing model result output in three hourly averaged intervals to observed data collected at specific times. Temperatures are influenced by the time of day the data were taken and can change several degrees over the course of a day.

Salinity. ICM is capturing the trends in salinity over the simulation period (Appendix E). Observed and model data show trends of lower salinity values in the spring increasing to higher values in the summer period. Spring rains keep salinity levels along the coast line low and as summer approaches, salinity levels rise. Salinity values collected diurnally for some days at some stations (e.g. Figure B-2) had values ranging from approximately 13 ppt to 28 ppt. When calculating the statistics, diurnally collected observed data were averaged then compared to model output. Generally, ICM underpredicts salinity values by 3.72 ppt (see *ME* on Figure 5-3). The *RMSE* indicates the model values range from +/- 8.0 ppt of the observed value. When compared to the salinity results from Bunch et al. 2003, the present ICM application predicts similar salinity values. More frequent salinity boundary conditions and better handling of initial conditions would improve model results for salinity. Because the domain of the model grid is farther away from land, it takes longer for ocean boundary conditions to penetrate pass the barrier islands thus taking longer for initial conditions to be replaced. If the model was spun up for 60 days and conditions at the end of this run were used as initial conditions, model results for the early part of the simulation would improve.

Figure 5-3. Scatter (upper) and Cumulative Distribution percent (lower) plots of calibration results for all water quality constituents. (Sheet 1 of 6)

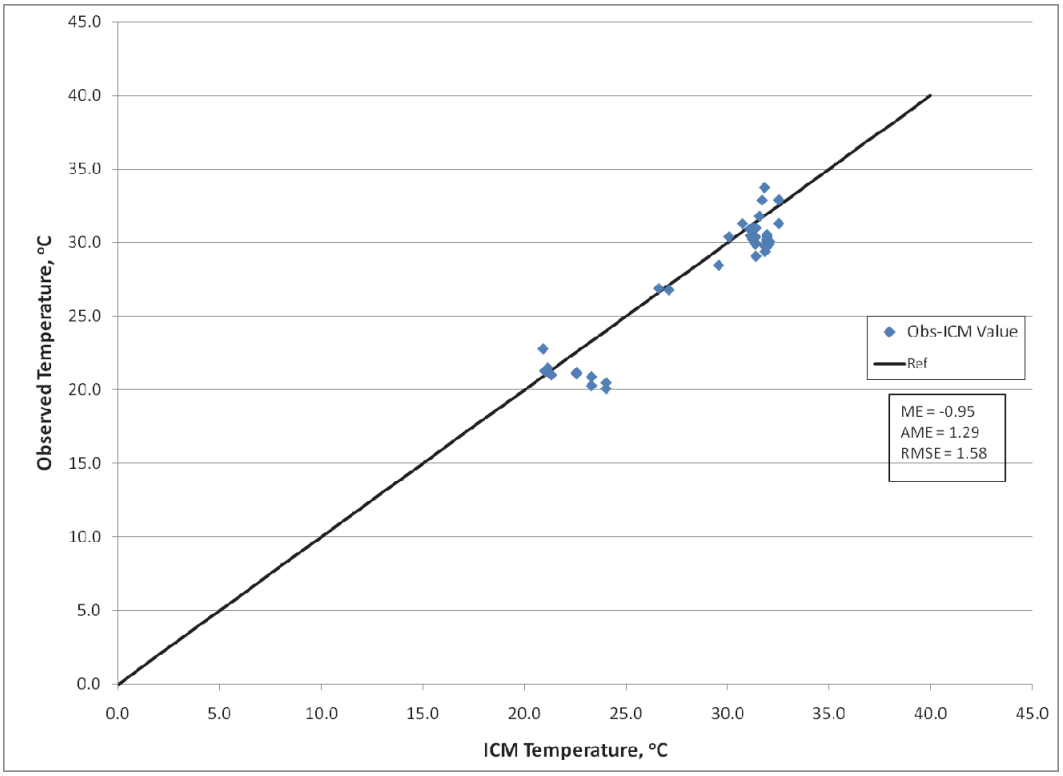

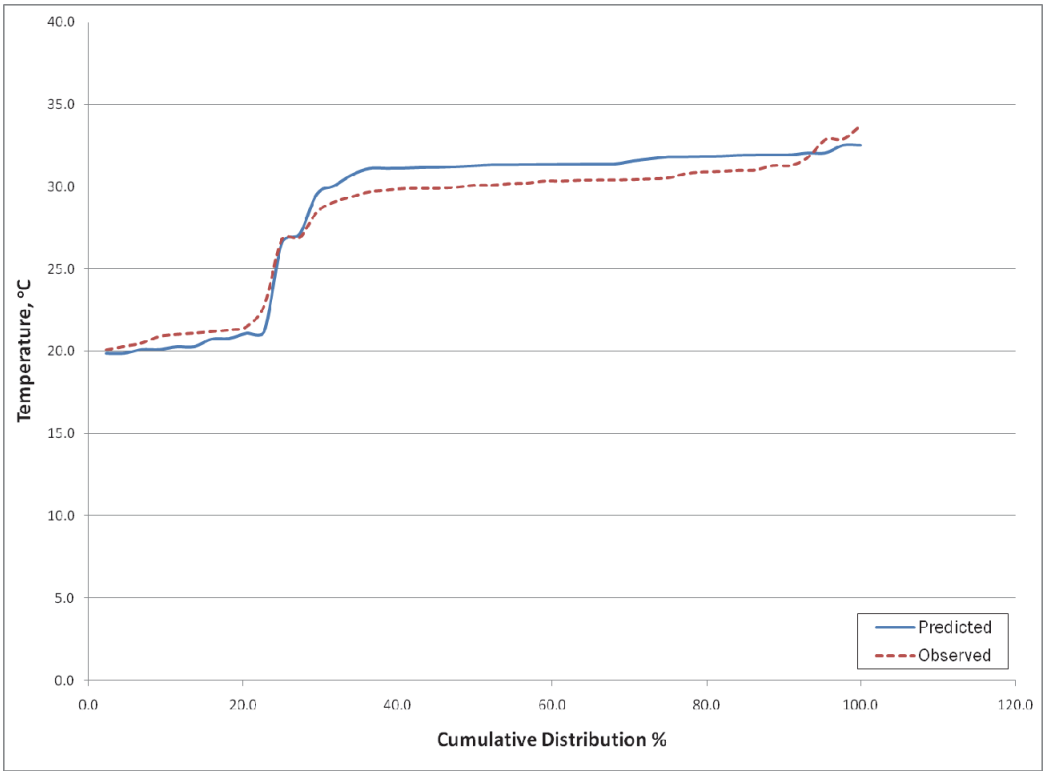

Figure 5-3. (Sheet 2 of 6).

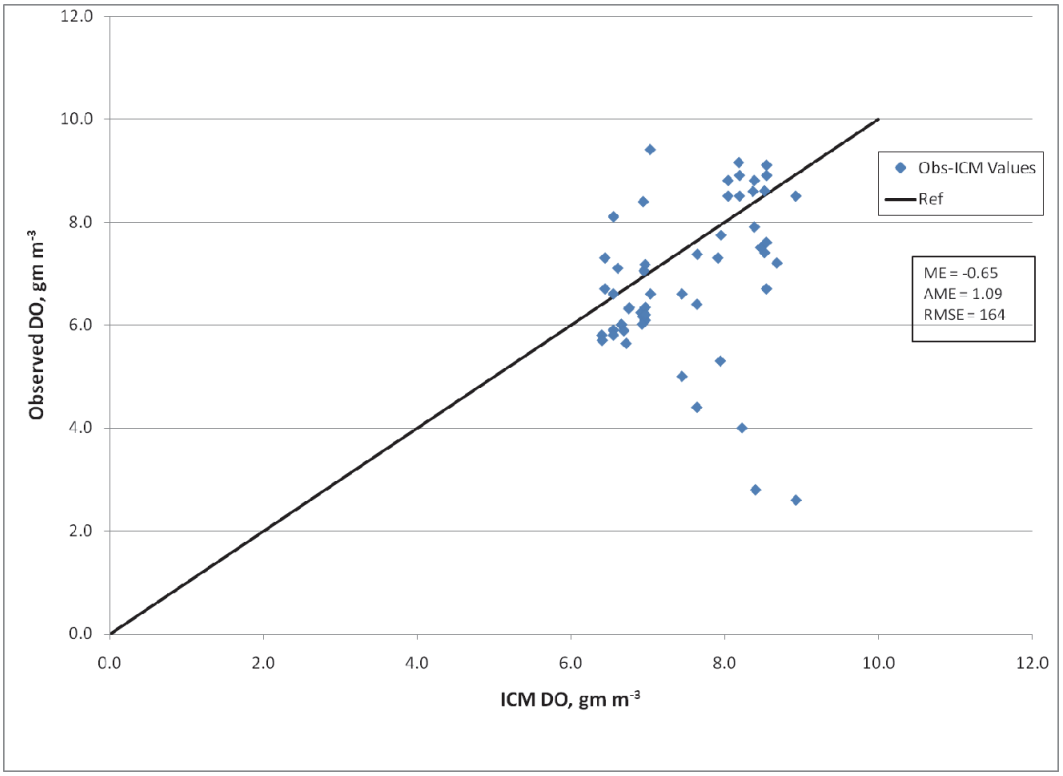

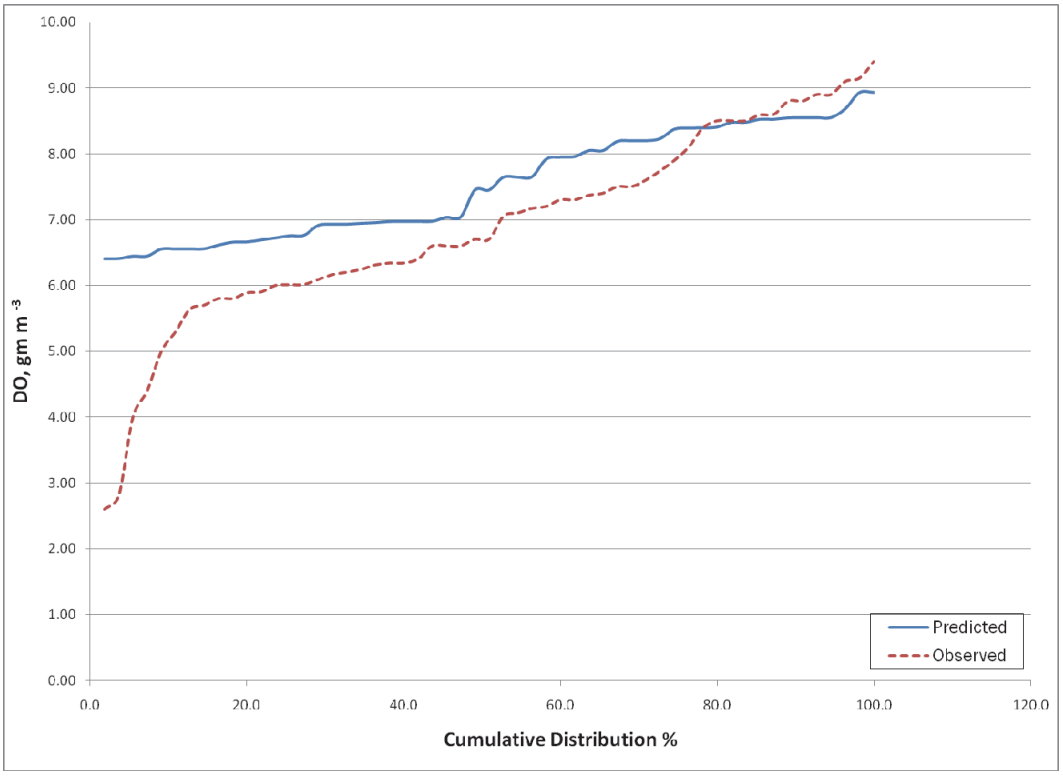

Figure 5-3. (Sheet 3 of 6).

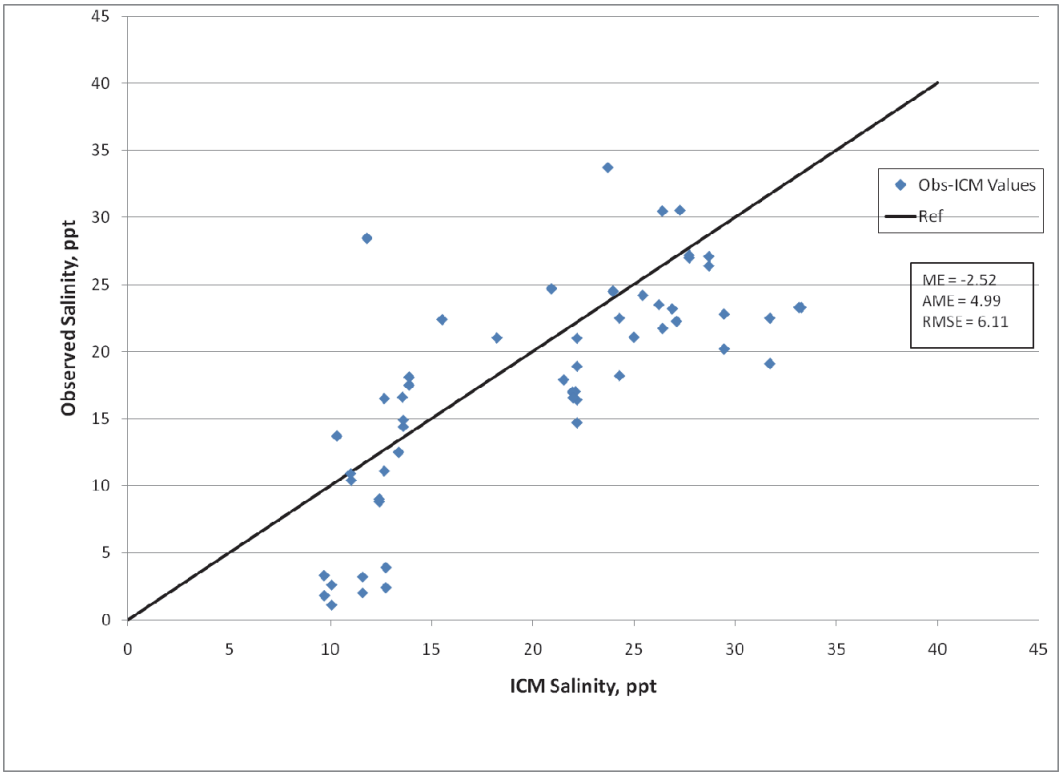

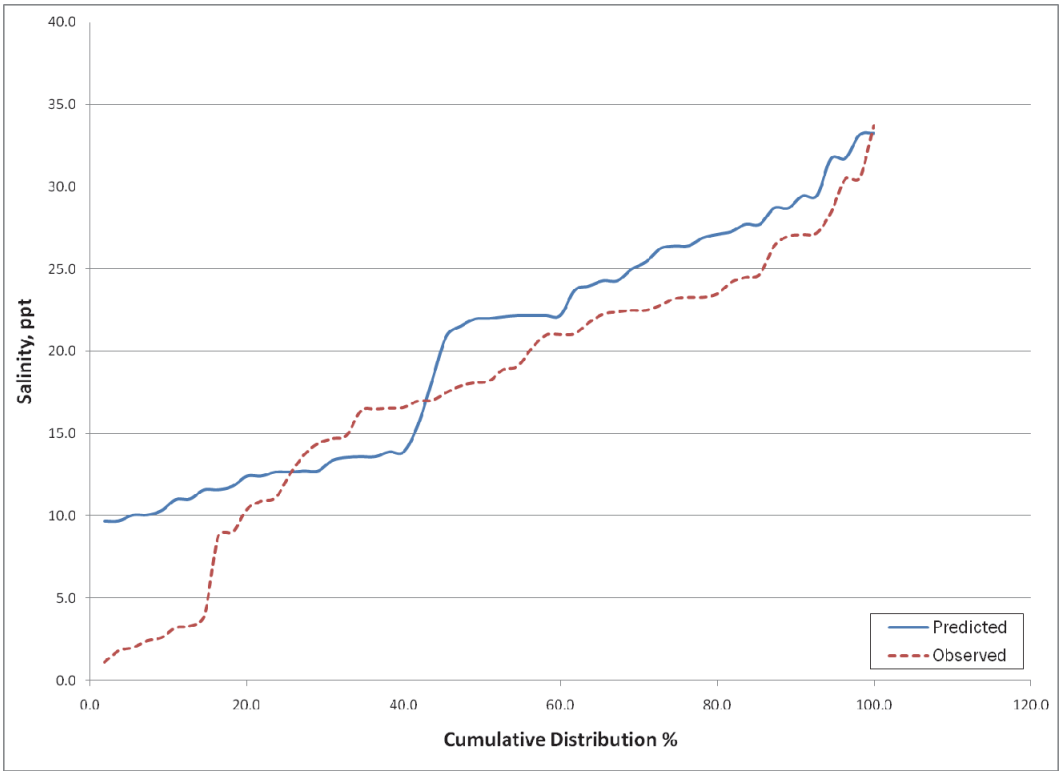

Figure 5-3. (Sheet 4 of 6).

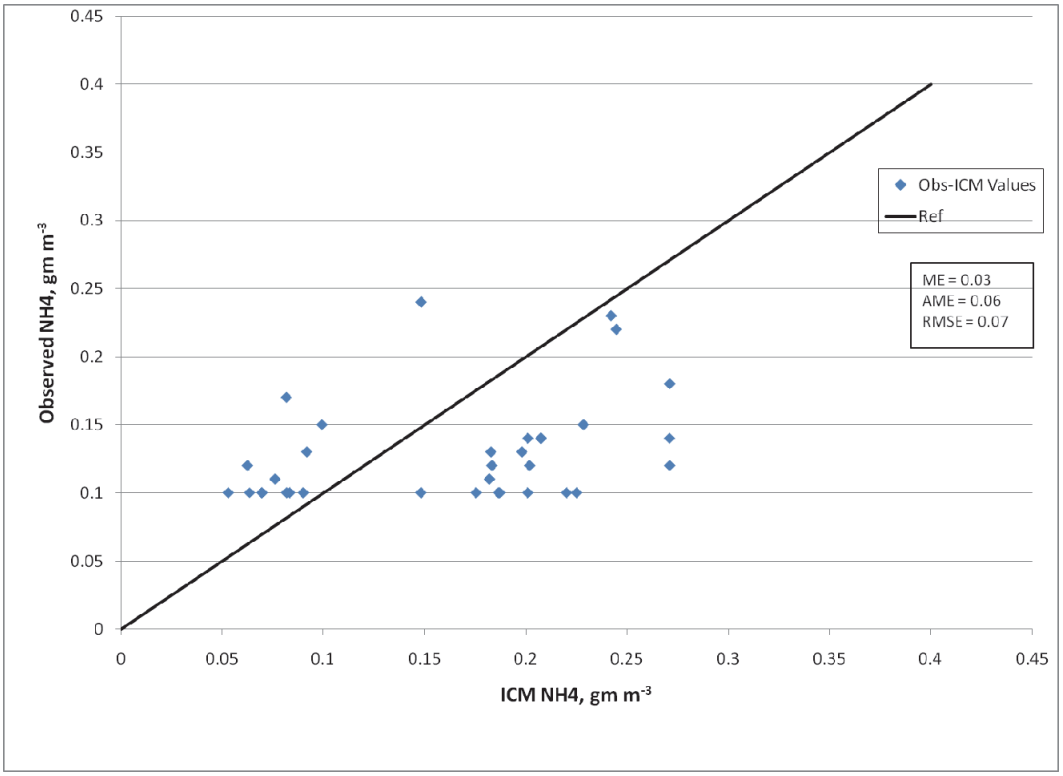

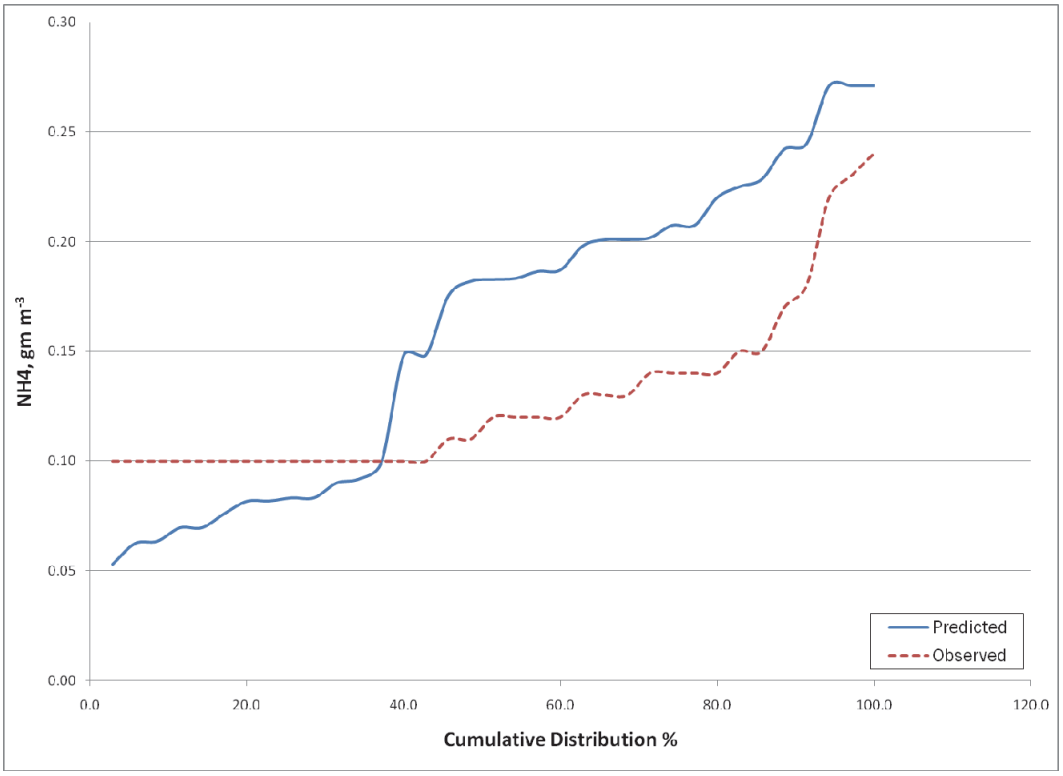

Figure 5-3. (Sheet 5 of 6).

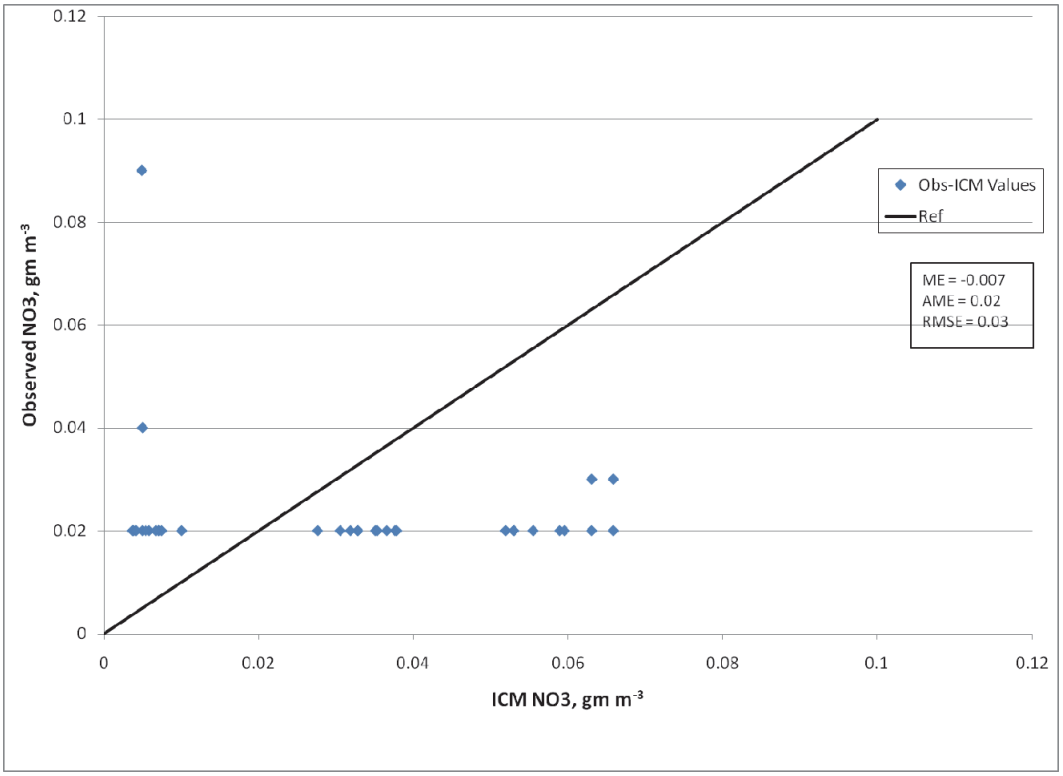

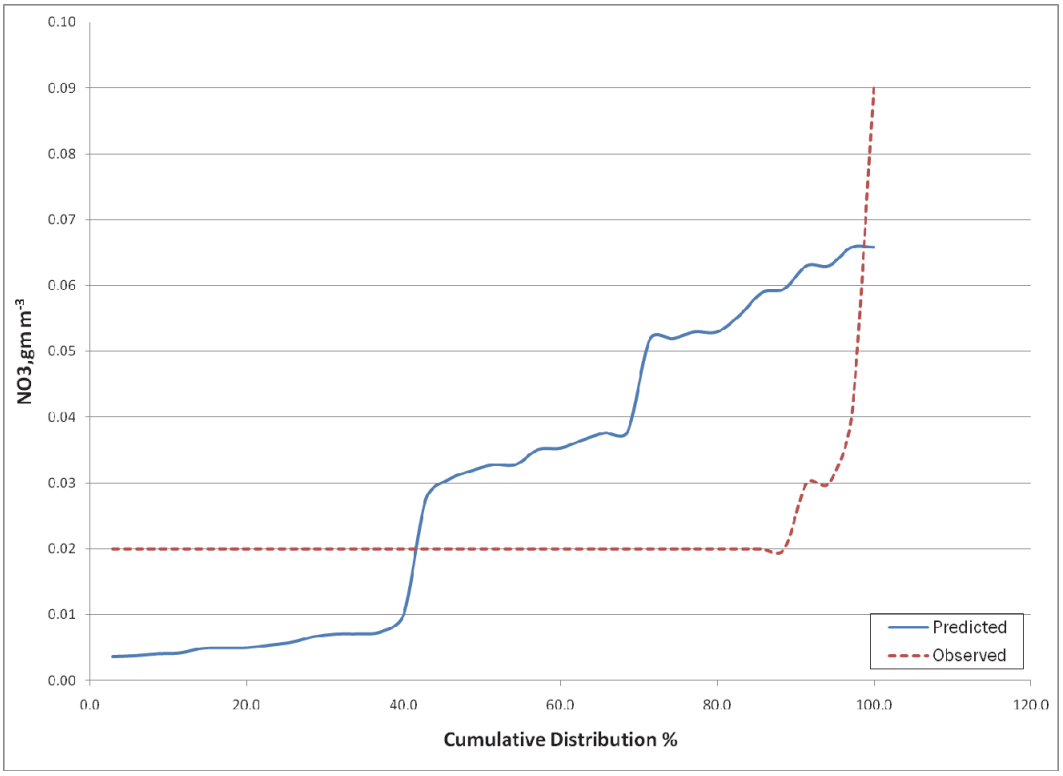

Figure 5-3. (Sheet 6 of 6).

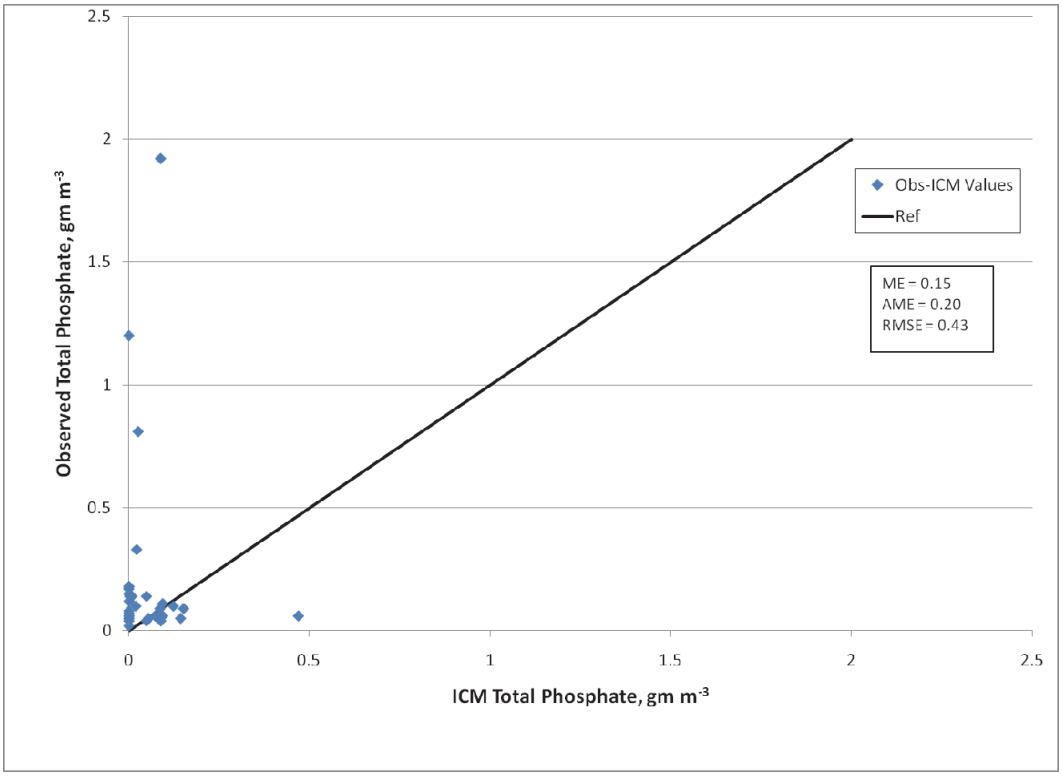

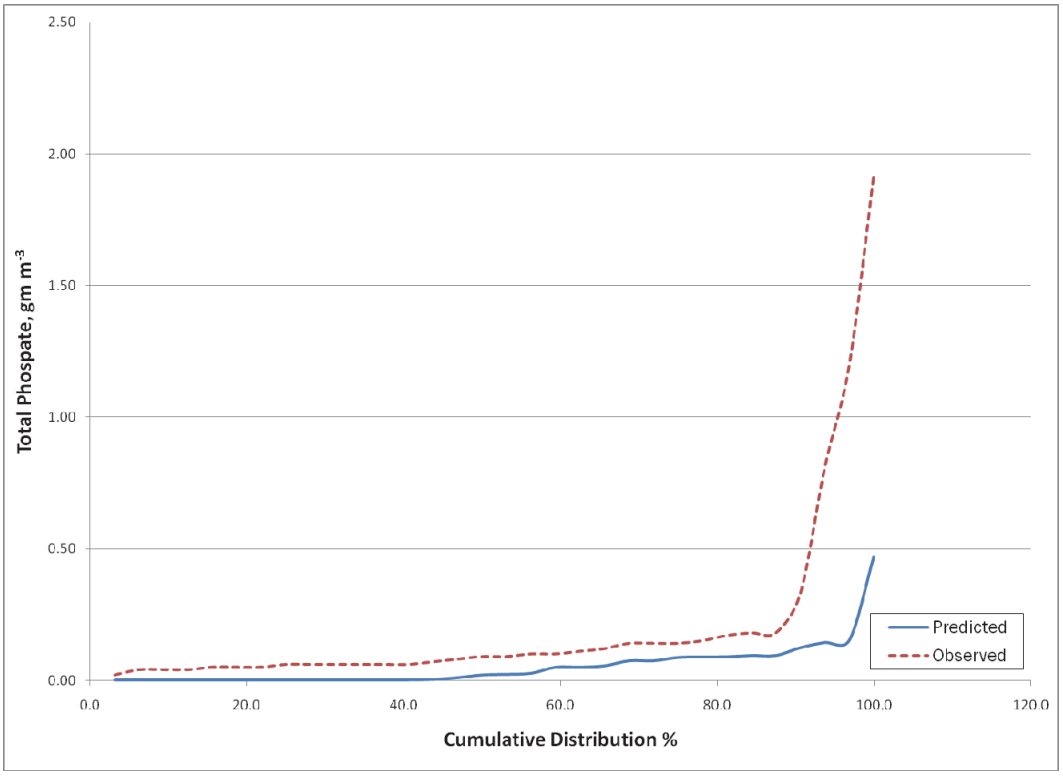

Dissolved Oxygen. The ICM is capturing the trend of the slow decline in DO concentrations from spring to the end of summer with the bottom layer showing a steeper decline at some stations (see figures in Appendix E for DO). Model performance (Figure 5-3) shows ICM has a tendency to over-predict DO concentrations below 6.6 gm m^{-3}, which occurs less than 45 percent of the time. Most of the values in this range were sampled in the bottom layer where ICM is unable to predict the very low DO values at stations in the back-bay locations (i.e., station 5 and 6). It was decided that too much vertical mixing is occurring in this area because the same winds are applied over the open ocean as well as the bay area in CH3D. Sensitivity runs increasing SOD rates were conducted but only slightly improved the DO values. For values greater than 6.6 gm m^{-3}, ICM under-predicts DO concentrations indicated by a *ME* of –1.17 gm m-3. The inability of ICM to accurately predict the DO concentrations above saturation is due to the lack of sufficient calibration data to determine if algal concentrations are being reproduced accurately. Observed data for algae were not available during the calibration period, thus ICM may not be predicting the chlorophyll concentrations adequately. Algal dynamics can increase or decrease DO through photosynthesis or respiration. Diurnal effects to DO are also missing in the predicted data but not in the observed. Observed data collected diurnally around simulation days 104 through 107 were averaged to get an equivalent value for comparison to model output during this time period. This may have introduced some error in the statistics.

Nutrients. Of the nutrients modeled, only ammonia (NH_4) and nitrate-nitrite (NO_3) had observed data available for comparison to model output. Comparisons for only these two constituents will be shown and discussed. Time-series plots for NH_4 and NO_3 (see Appendix E) indicate that ICM is generally producing trends in data behavior. Both observed and model values for NH_4 and NO_3 show very little variation in concentration levels throughout the simulation period. Most values are in the detention limit range. One of the most noticeable increases in NH_4 concentration occurs for the bottom layer at Station 6. Since ICM is unable to predict the low DO at this station due to over mixing; the release of NH_4 from the sediments will not be triggered. This in turn affects the NO_3 at this layer and station.

The *AME* values show good agreement for all stations (Table 5-13) to the target *AME* of 0.14 for NH_4 and 0.07 gm m^{-3} for NO_3. Most observed concentrations of these two constituents are measured at the detection levels. However when concentration levels increase later in the simulation,

the ICM model results follow this trend in constituent behavior. The scatter plot (Figure 5-3) and *ME* (Table 5-13) indicate that for the observed data available ICM consistently under predicts NH_4 and NO_3 for the lower concentration levels and compare favorably in the upper levels. With algae being modeled and no way to determine if predictions are comparable to observed, there is some uncertainty of algal growth impacts to nutrient levels.

As discussed previously, observed values of total phosphate were not available only observed total phosphorus (*Tp*). It was assumed that most of the *Tp* was available as total phosphate. Figure 5-3 indicates that this assumption was reasonable given that ICM was able to predict most of the lower levels of total phosphate as seen in Figure 5-3. The calculated *AME* value of 0.2 is only slightly higher than the target *AME* range of 0.19 (Table 5-13).

5.8.1 Scenario results and discussion

Presentation and discussion of scenario runs includes results for base (Pre-Katrina), Post-Katrina, Degraded, Restored, and Cumulative conditions. Scenario results were presented as time-series plots. Time-series plots were the main visual means to analyze water quality in the areas of interest. Animations were generated for each scenario run to help identify areas of interest. Similar to calibration, model results for plotting were output every three hours after start of the simulations.

Since changes in DO, Chlorophyll a, and salinity were key constituents that signal changes to water quality, plots of these comparing all scenario results to base results will be presented and discussed. Time-series plots of water quality constituents of interest were generated for all ten stations where observed data were available (Figure 5-2) and seven additional locations within the Ship Island study area. Locations of stations were selected to determine impacts of different modifications to Ship Island. Of the observed stations used during calibration, scenario results from Station 2 (northwest around the Pearl River), Station 5 (slightly northeast around Pascagoula), and Station 10 (beach area immediately north of Ship Island) will only be discussed and presented in this section. Figures showing scenario results at other calibration stations (Figure 5-2) and additional stations around Ship Island can be found in Appendix E. In each figure legend, simulation runs are identified by their scenario name (i.e, Pre-Katrina (base), Post-Katrina, Degraded, etc). In addition to comparison of time-series of base to scenario

results of selected water quality constituents, the maximum percent change between base and each scenario results was calculated over the simulation period as an indicator of detrimental change. Maximum (upper number) and minimum (lower number) percent change values are listed in Table 5-14 for DO, Chlorophyll *a*, and salinity for Stations 2, 5, and 10.These numbers represent the greatest change during the simulation period for a three hour averaged period. A positive number indicates scenario concentrations were higher than "Pre" (base) concentrations and a negative number indicates scenario concentrations were lower than "Pre."

Table 5-14. Maximum percent change for dissolved oxygen, chlorophyll *a*, and salinity.

Station #	DO Max & Min % Change				Chlorophyll Max & Min % Change				Salinity Max & Min % Change			
	1*	2*	3*	4*	1	2	3	4	1	2	3	4
2	1.67 -0.18	4.02 -3.42	1.84 -0.31	1.50 -1.85	15.04 -3.71	23.09 -14.64	21.10 -3.15	12.11 -4.09	2.16 -8.42	34.12 -13.90	2.90 -8.76	1.43 -8.41
5	8.85 -1.59	9.28 -5.28	9.50 -1.56	9.29 -1.44	48.95 -14.08	45.28 -26.42	51.23 -11.17	49.53 -13.13	7.72 -15.24	16.57 -19.56	8.17 -14.77	8.02 -10.99
10	5.52 -4.53	5.05 -5.52	5.61 -5.16	5.53 -4.81	40.12 -36.37	36.23 -34.90	41.47 -36.45	40.71 -38.13	16.22 -14.83	23.39 -16.21	17.91 -13.00	16.90 -8.72
Katrina Cut - Station 7, Figure 5.7	4.52 -14.87	2.70 -5.25	7.25 -14.34	5.61 -14.91	38.92 -87.42	25.62 -78.69	39.80 -86.76	43.41 -87.46	102.87 -21.83	17.72 -24.51	98.54 -34.54	102.81 -21.89

* 1=((Post – Pre)/Pre)*100

2=((Cumulative – Pre)/Pre)*100

3==((Degraded – Pre)/Pre)*100

4==((Restored – Pre)/Pre)*100

Negative sign indicates scenario value less than "Pre" (base) value

From Figures 5-4 through 5-6, all water quality constituents show changes in water quality from base ("Pre") to some degree. Beginning with the minimum percent change in DO concentrations, results for the "Cumulative" scenario showed that the largest reduction in DO concentrations from "Pre" conditions was about 5.52 percent at Station 10. This translates into a change of DO concentration from ≈7.75 to 7.3 mg/L. A similar reduction was seen at Station 5. At Station 2, the DO concentration reduction was around 3.43 percent for the "Cumulative" scenario. Although decreases in DO concentrations occurred, the largest was considered insignificant and well within state standards in ocean waters. The maximum percent change in DO concentrations indicating an increase in DO values from "Pre" occurred at Station 5 and was ≈9.0 percent for all scenarios. This

Figure 5-4. Comparison of DO, Chlorophyll, and Salinity at Station 2 for all scenario results (continued).

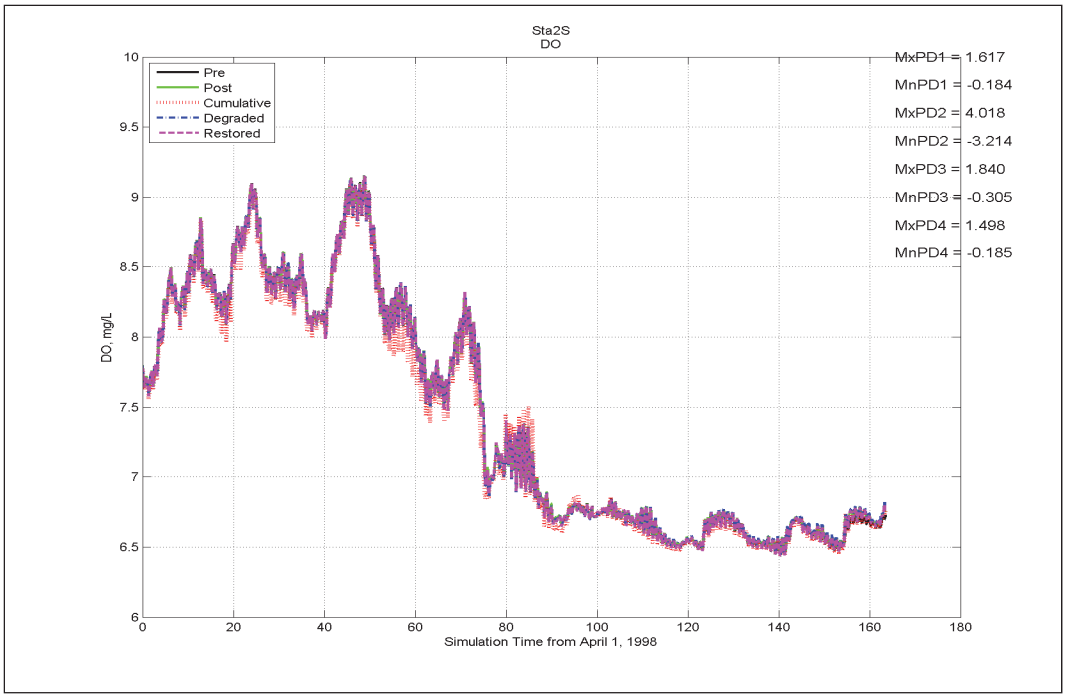

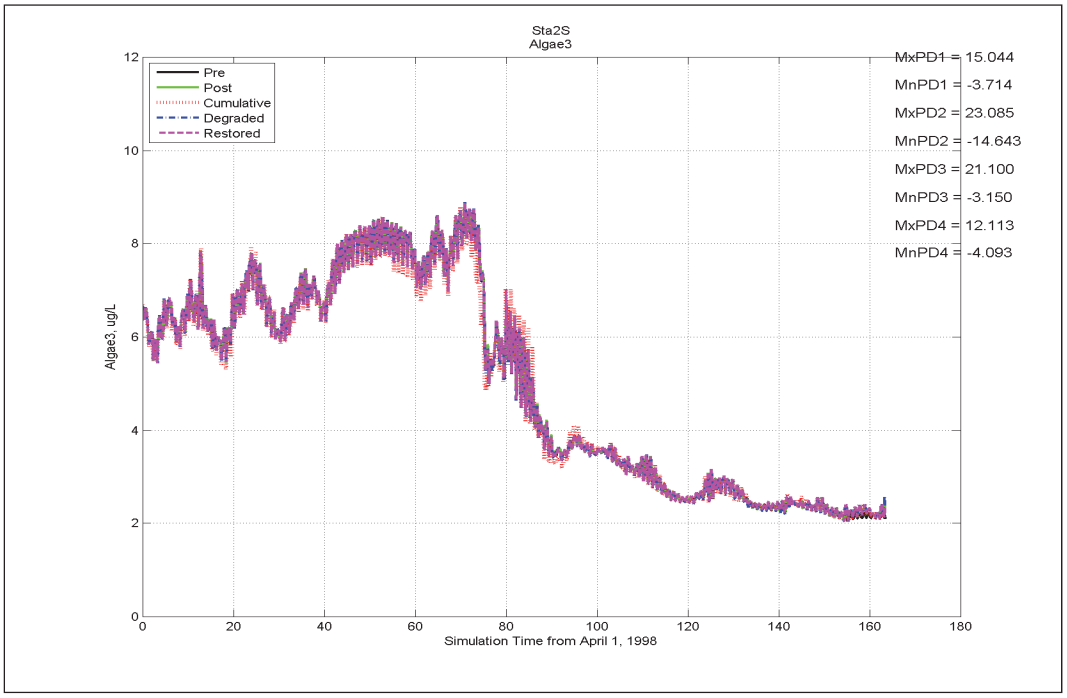

Figure 5-4. Concluded.

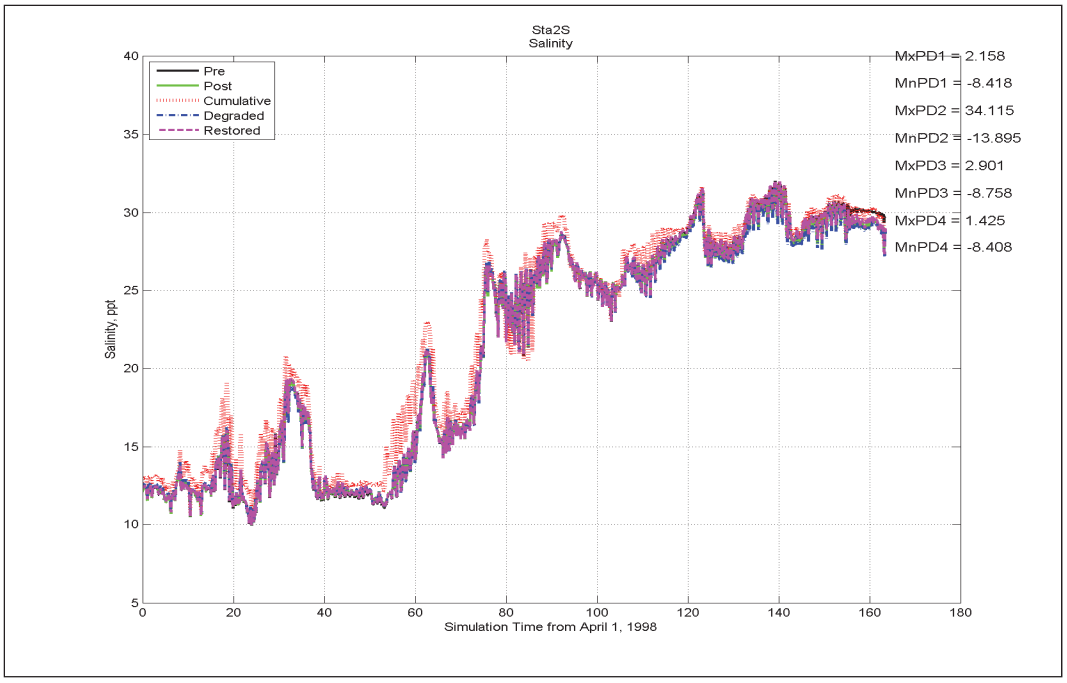

Figure 5-5. Comparison of DO, Chlorophyll, and Salinity at Station 5 for all scenario results (continued).

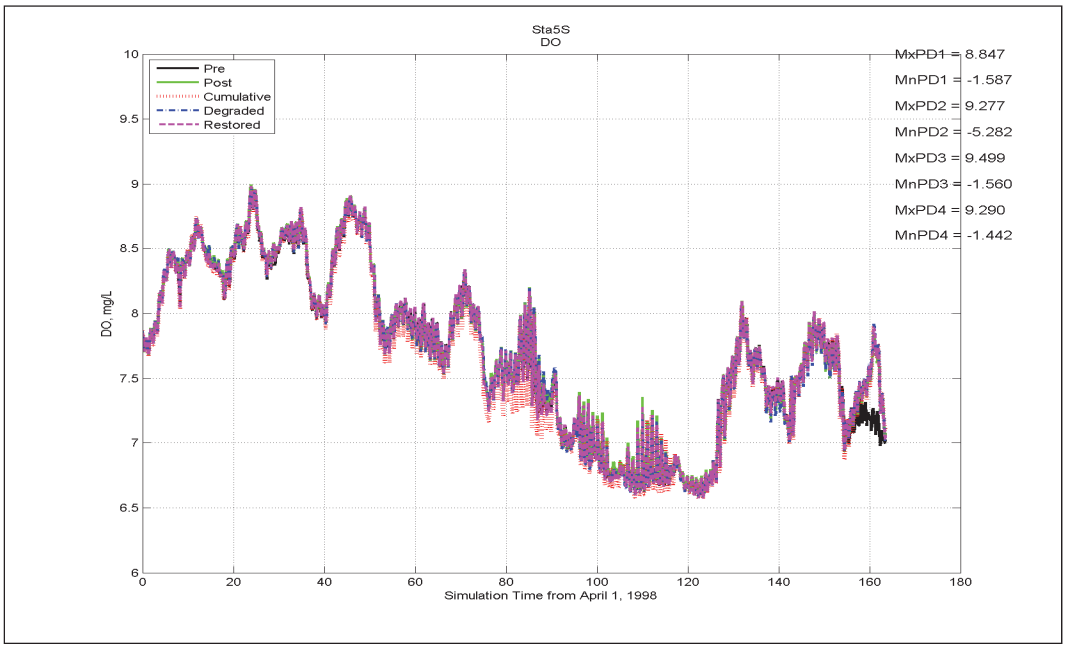

Figure 5-5. Concluded.

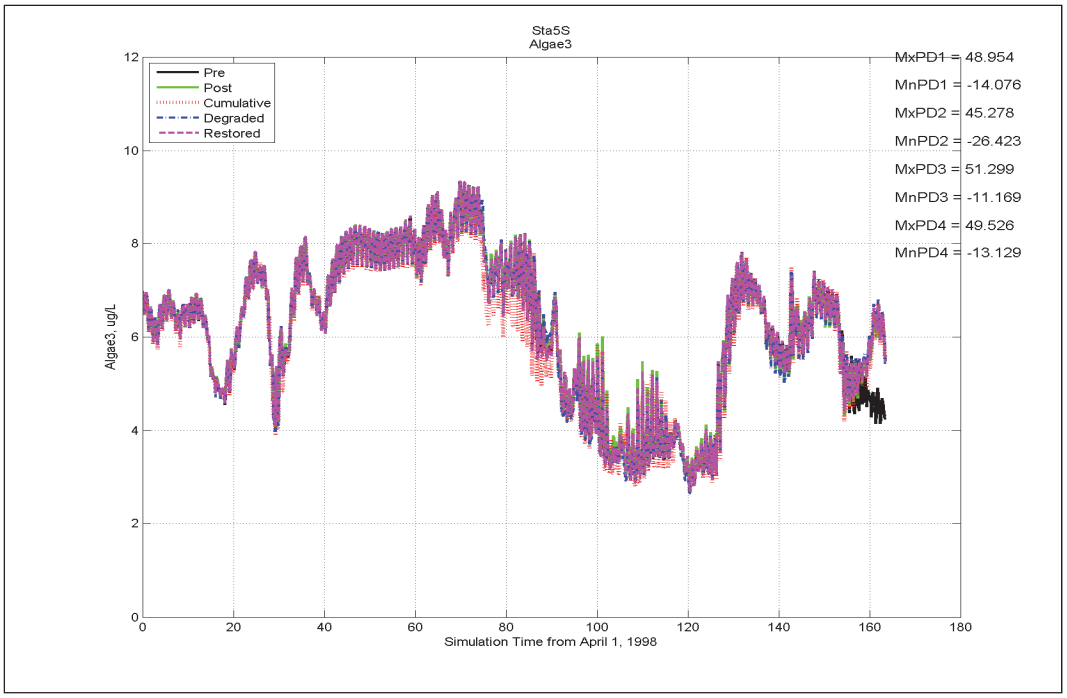

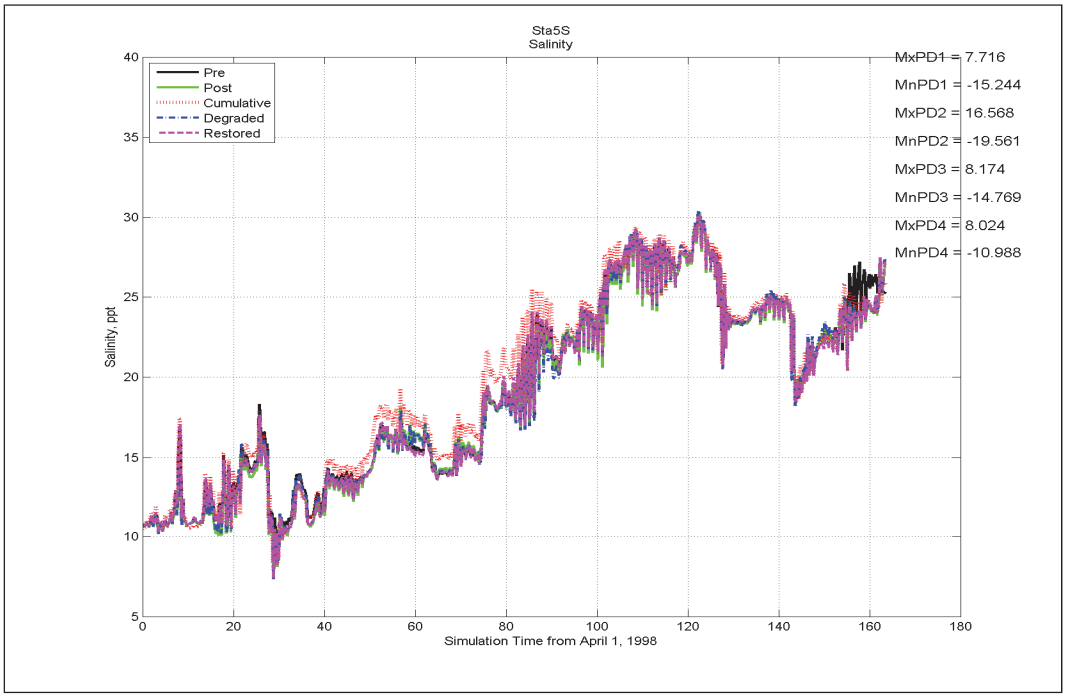

Figure 5-6. Comparison of DO, Chlorophyll, and Salinity at Station 10 for all scenario results all (continued).

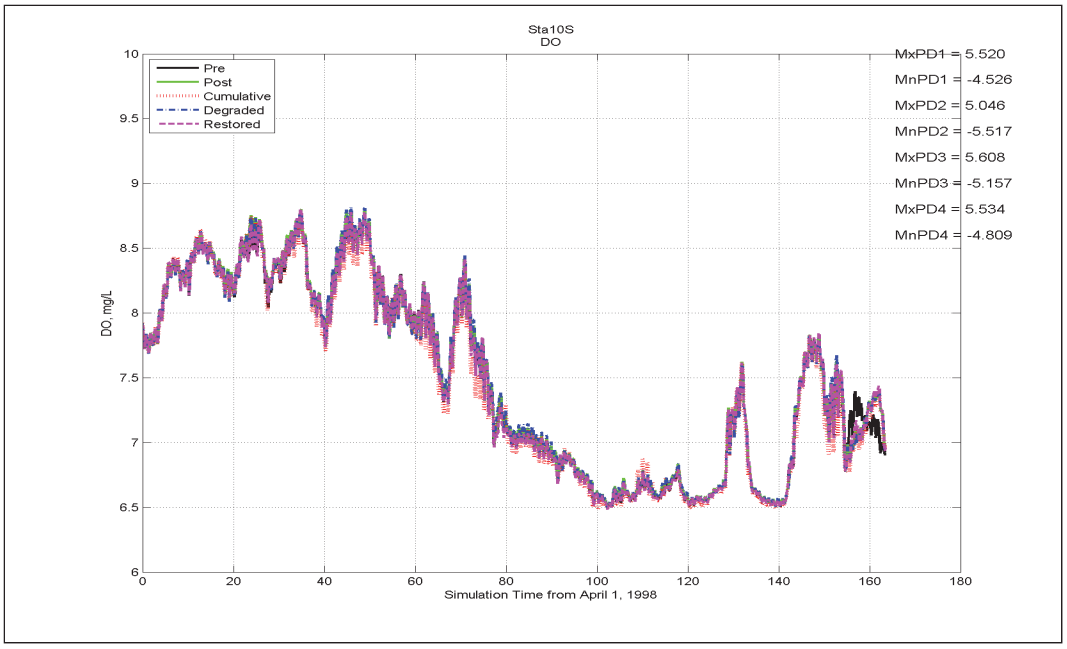

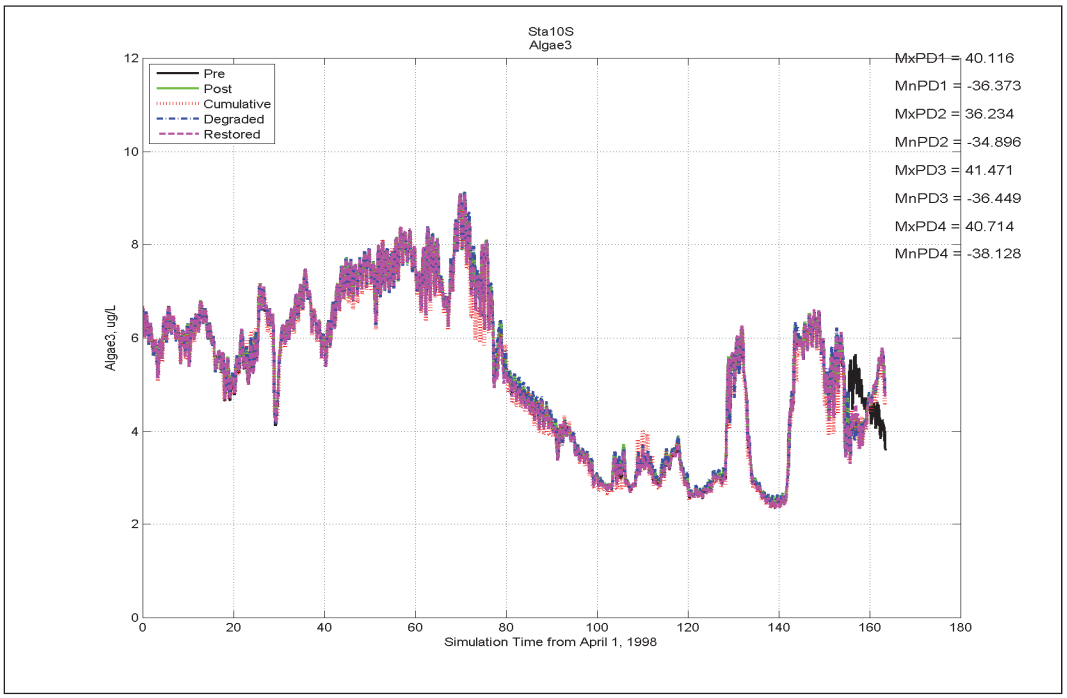

Figure 5-6. Concluded.

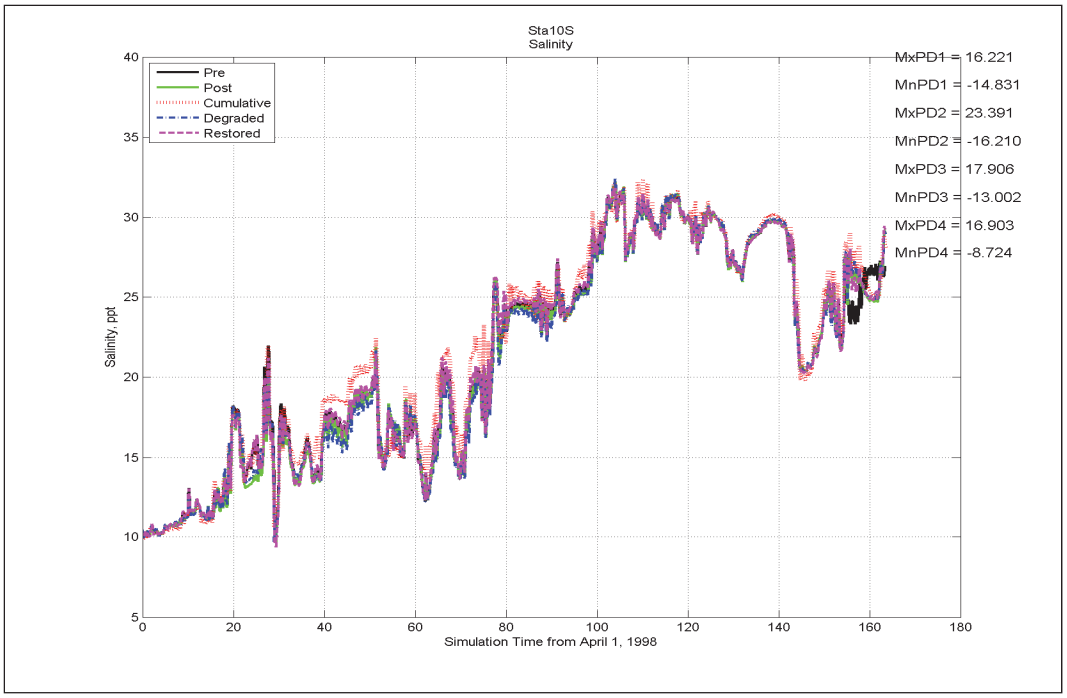

improvement would be like going from a value of 8.0 mg/L to 8.72 mg/L. This occurred toward the end of the simulation around simulation day 160. Station 10 results showed DO concentrations from all scenarios increased about 5.5 percent; a little over half as much as at Station 5. Station 2 showed even less of an increase as the other two stations. During the same time period as the maximum percent change in DO occurred (simulation day 160), chlorophyll *a* concentrations for all scenarios increased by 40 to 50 percent over "Pre" conditions at Stations 5 and 10. At Station 2, the increase was only half as much as the other two stations. With increased chlorophyll *a*, more photosynthesis produced additional DO resulting in the increased DO values. All salinity scenario results for maximum and minimum percent changes had similar values except results for the "Cumulative" scenario. Maximum and minimum percent change of salinity values for the "Cumulative" scenario show the largest maximum (34.12 percent) at Station 2 and lowest minimum (-19.56 percent) at Station 5. At Station 2, salinity increased from ≈11.85 ppt ("Pre" conditions) to 15.89 ppt ("Cumulative" conditions) on simulation day 55. At the same time, DO and chlorophyll values were reduced about ≈2.09 percent and 3.75 percent, respectively. Although DO and Chlorophyll *a* were also reduced, these were not the greatest reductions in DO and chlorophyll *a* concentrations at this station. The greatest reduction for these two constituents actually occurred on simulation day 74 showing that changes to these constituent concentra-

tions are not entirely dependent on salinity concentration but are impacted by changes to nutrient levels as well. Although to some extent DO saturation is affected by salinity increases, changes to DO concentration were affected more by reduction in chlorophyll *a* concentrations. Chlorophyll *a* concentrations are in turn affected by nutrient and light levels. As demonstrated here, increase in salinity concentration indicates circulation changes which do impact nutrient levels resulting in lower chlorophyll *a* concentrations thus impacting DO. The minimum percent change in salinity occurred at Station 5 toward the beginning of the simulation (simulation day 29). "Cumulative" salinity value on this day was 8.99 ppt while the "Pre" salinity was 11.18 ppt. This indicates circulation changes as higher salinity water does not reach Station 5 as quickly as before.

In the area of modifications (see Figure 5-7), the largest differences between salinity for "Pre" and scenario results occurs on the land side of the transect that crosses the Katrina cut (Station 7 in Figure 5-7). It is important that while Station 7 is within the domain of the model used for this study it is far removed from Ship Island and any remediation efforts there. The changes observed at Station 7 are the result of direct breach of Dauphine Island from Hurricane Katrina. This station was presented in the report because it indicated the greatest differences between "Pre" and all other scenario comparisons.

Figure 5-7. CE-QUAL-ICM water quality ship Island stations.

All scenarios show close to 100 percent maximum increase in salinity values except for the "Cumulative" scenario. The maximum percent change calculated for DO, chlorophyll, and salinity (Figure 5-8) occurred at different simulation times at this station. Salinity has the greatest percent change of ≈103 percent change for "Restored" and "Post " with "Degraded" slightly less at ≈99 percent compared to "Pre" at simulation day 7.25. This is a salinity change from 12.53 ppt to 25.41 ppt. With the Katrina Cut in place, higher salinity water from the ocean side is entering faster into the landside of the Barrier Islands. With the higher salinity water and change in circulation, DO concentrations have been reduced from 8.25 mg/L to 7.06 mg/L for both "Restored" and "Post" and 7.09 mg/L for "Degraded." This resulted from a reduction in chlorophyll *a* (6.14 mgm/L to 2.5 mgm/L) for the three scenarios caused by changes in nutrient concentrations with increases in salinity affecting DO saturation.

Appendix E contains time-series figures of water quality simulation results for all stations surrounding Ship Island (Figure 5-7). Percent difference values are denoted on each figure for the maximum and minimum predicted values minus the Pre-Katrina condition results. Within the immediate Ship Island area, water quality conditions for the restored case are always closer to those of Pre-Katrina than they are to Post-Katrina. Percent differences in the Degraded and Post-Katrina conditions are similar to each other. This is reasonable as both contain the most open water conditions at Ship Island. Comparison of maximum/minimum percent differences between Cumulative and Pre-Katrina conditions and Restored and Pre-Katrina showed similar results. This indicates that there is little difference in the conditions of the Restored and Cumulative cases in the vicinity of Ship Island. Therefore, one can conclude that the Cumulative or Restored case is closer to Pre-Katrina conditions than they are to Post-Katrina. This is based upon direct comparison of Post-Katrina and Pre-Katrina conditions which are a good indicator of what comparisons of Cumulative and Restored cases are to Post-Katrina.

Water Quality Hydrodynamics. Changes to bathymetry have the potential to alter circulation patterns to a degree that water quality conditions are impacted. Water quality in a system is a function of loadings, processes, and flows. Hydrodynamic data files used for water quality model simulations were processed and flow histories determined for various locations in the system, Figure 5-9. Figures 5-10 through 5-15 show the time-series of flows at these transects. The patterns for all cases are very

Figure 5-8. Comparison of DO, Chlorophyll, and Salinity at Station 7(Figure 5-7) for results from simulations representing "Pre", "Post", "Restored", "Degraded," and "Cumulative" conditions (continued).

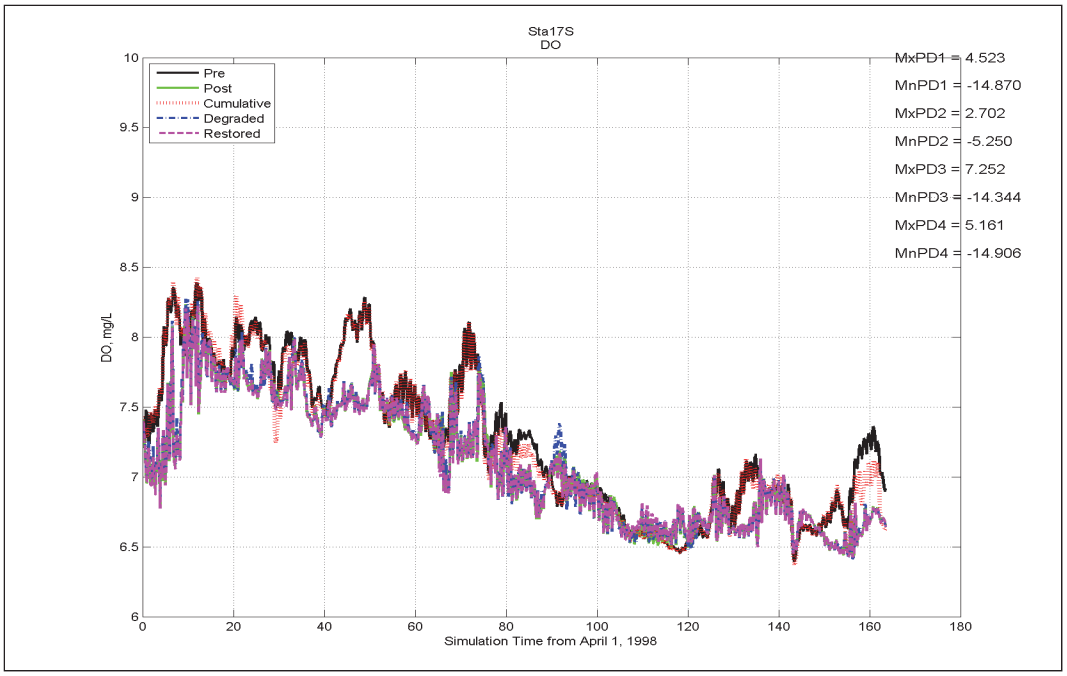

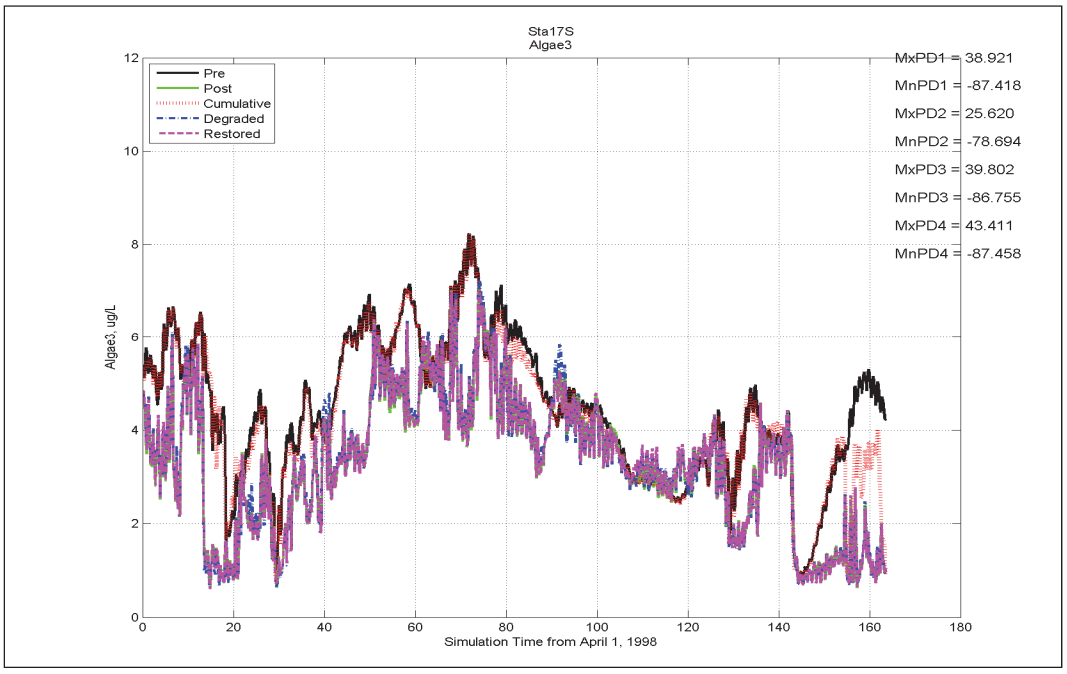

Figure 5-8. Concluded.

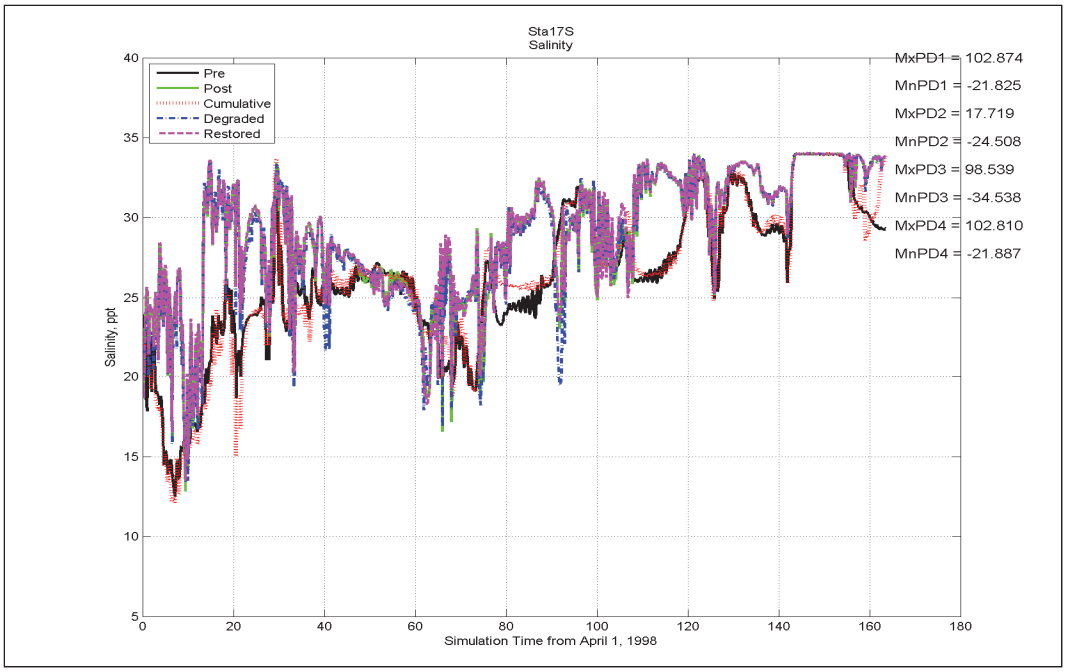

Figure 5-9. CEQUAL-ICM water quality model net flow transects.

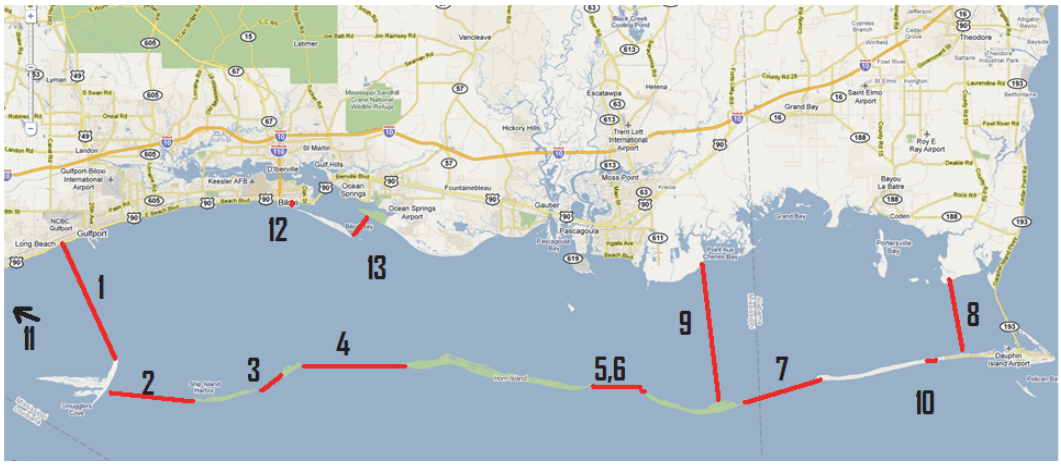

Figure 5-10. Scenario flows through Camille Cut.

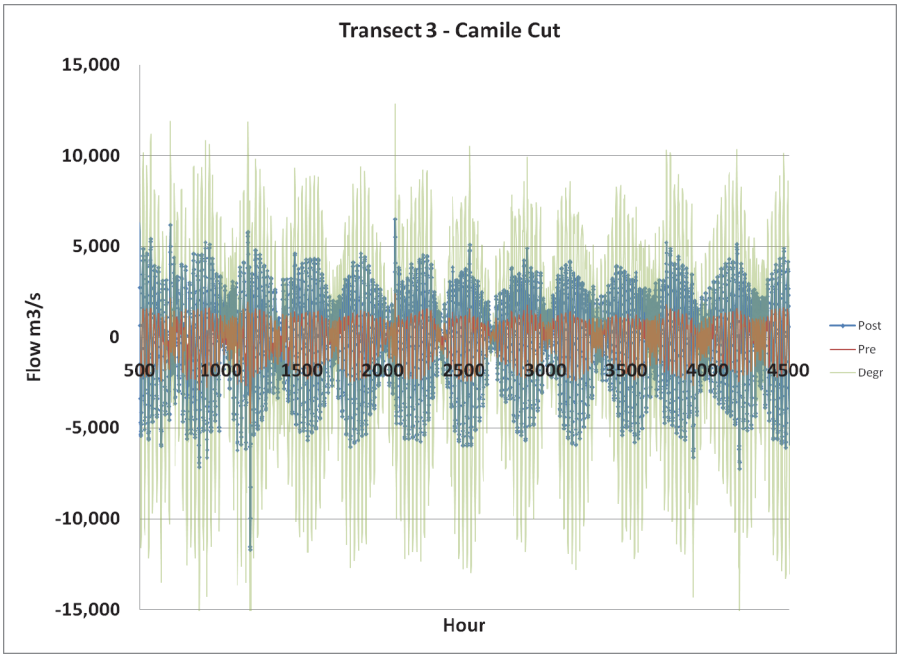

Figure 5-11. Scenario flows, Ship Island to Horn.

Figure 5-12. Scenario flows, Horn Island to Channel Island.

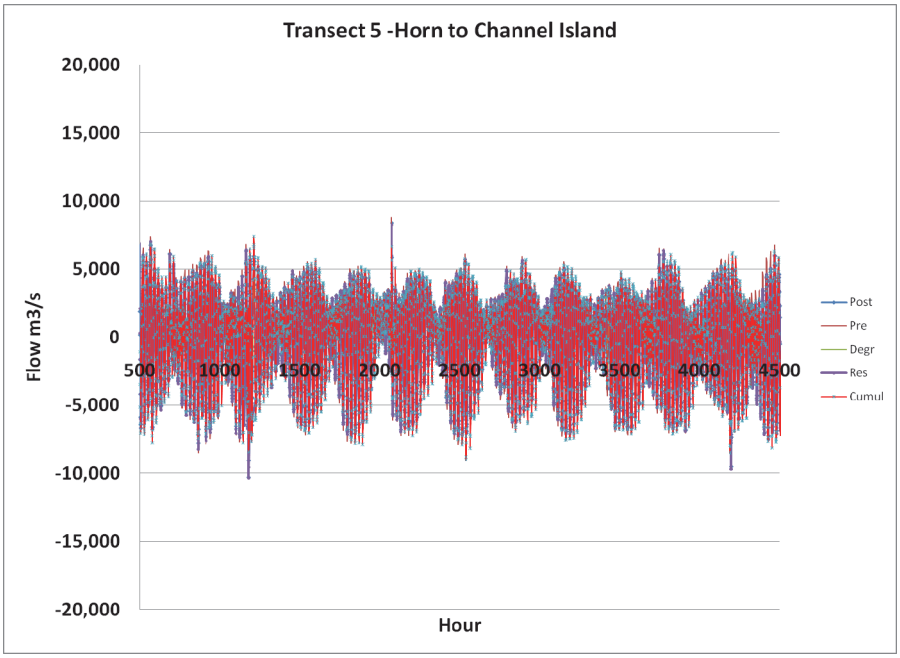

Figure 5-13. Scenario flows, Channel Island to Petit Bois.

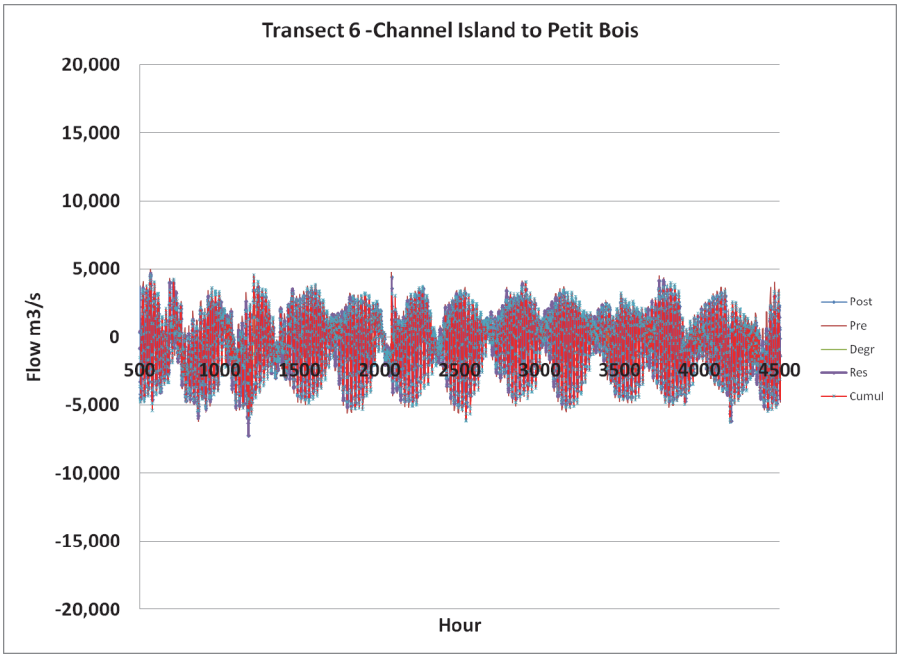

Figure 5-14. Scenario flows, Petit Bois to Dauphin Island.

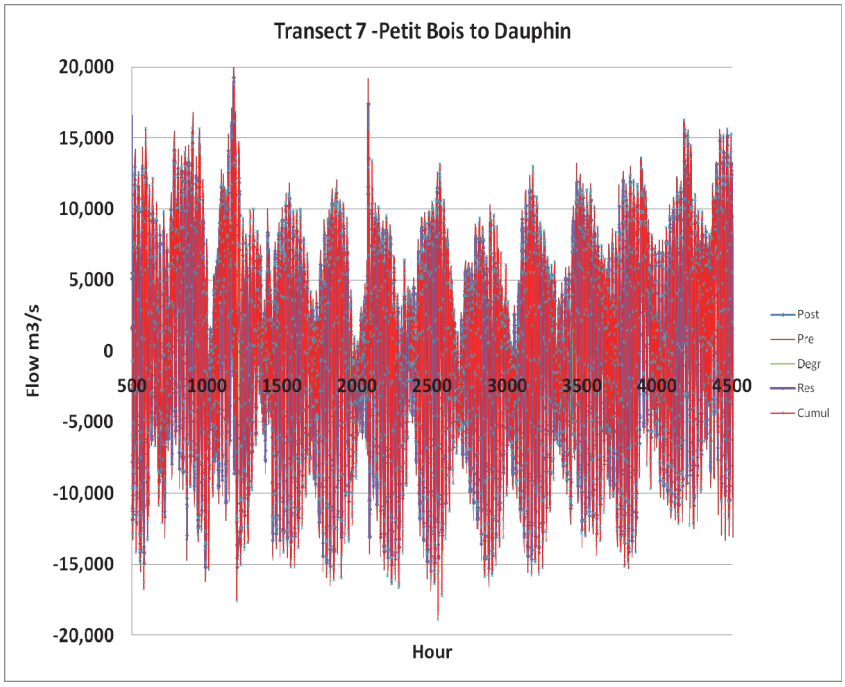

Figure 5-15. Scenario flows, Dauphin Island to Shore (East).

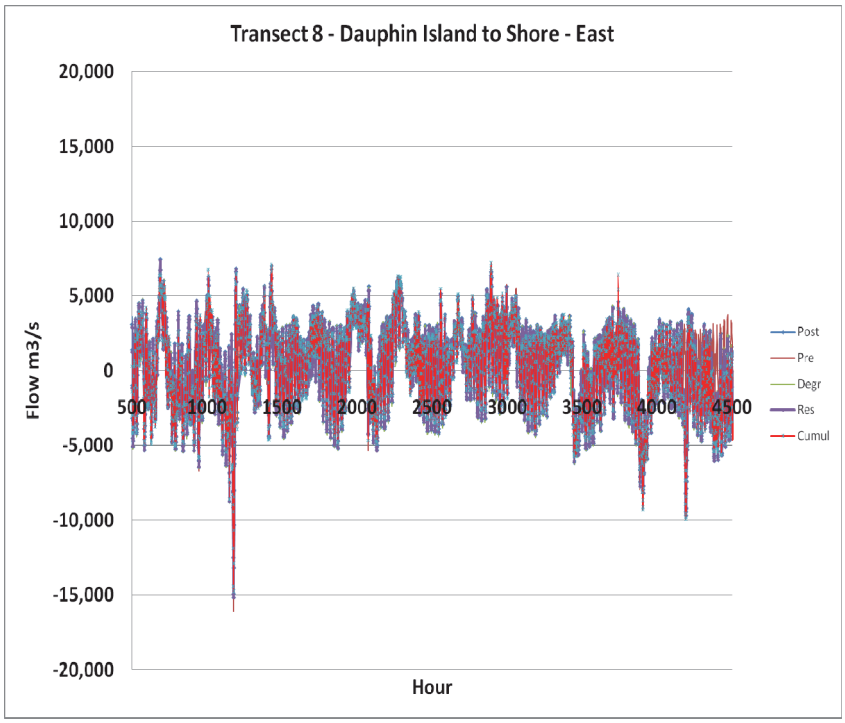

similar. Table 5-15 contains average flows at these locations for the duration of the calibration period and scenario simulation. Positive and negative values are an indication of the flow direction in the model grid. Generally positive values are for flows to the east and north while negative flows

indicate the flow is to the west or south. Some differences are observed in the averages. However, it should be noted that these averages are two orders of magnitude less than the peak flood and ebb flows across these locations. This is an indication of two things. First, MS Sound north and west of Ship Island has relatively little flushing and net transport through the system. Second, the effects of Ship Island degradation or restoration do not have major effects upon system wide circulation and therefore should not have major effects on system wide water quality conditions. The condition of Ship Island does have localized effects on circulation. Note that the average flows in Transects 2 and 4, the west and east sides of Ship Island respectively, increased in comparison to the Pre-Katrina case. The average flow across Camille Cut on Ship Island actually decreased. For the Post-Katrina case, the name Camille Cut was used to identify the entire breach in Ship Island. This should not be taken as an indication that there was less flow at any given time across this opening, see Figure 5-9, instead it is an indication that the magnitude of the flows going "in" and "out" of this opening were more equally distributed.

Table 5-15. Calibration period average flows (m^3/sec).

Locations	Scenarios				
	Pre-Katrina	Post-Katrina	Fully Degraded	Restored	Cumulative
Transect 1 Shore to Cat Island	692	731	719	724	773
Transect 2 Cat Island to Ship Island	-191	-383	-94	-583	-555
Transect 3 Camille Cut Ship Island	-124	-55	-293	Na	Na
Transect 4 Ship Island to Horn Island	-234	-511	-565	-362	-357
Transect 5 Horn Island to DA 10/Sand Island	179	105	97	78	103
Transect 6 DA10/Sand Island to Petit Bois	-344	-391	35-4533	-418	-353
Transect 7 Petit Bois Island to Dauphin Island	292	353	282	365	421
Transect 8 Dauphin Island to Shore (East)	452	266	231	230	200
Transect 9 Dauphin Island to Shore (West)	153	-326	-407	-389	-242

Locations	Scenarios				
	Pre-Katrina	Post-Katrina	Fully Degraded	Restored	Cumulative
Transect 10 Katrina Cut Dauphin Island	Na	232	Na	246	Na
Transect 11 Bay St. Louis Mouth	-9.7	-12	-12	-12	-12
Transect 12 Biloxi Bay Entrance (West)	-5.6	-15	-12	-22	-20
Transect 13 Biloxi Bay Entrance (East)	-2.1	-11	-8	-19	-17

5.8.2 Tracer simulations

Two sets of tracer simulations were performed to assess the potential impact of different scenarios on circulation and flushing immediately behind Ship Island. These tests are referred to as Parallel and Perpendicular tests based upon the orientation of the tracer loading to Ship Island. In these tests, salt was used as a neutrally buoyant, conservative tracer. In the Parallel test (Figures 5-16 and 5-17), a row of cells parallel to the north side of Ship Island was loaded with an initial concentration of 1.0 mg/L of tracer. Only surface cells were loaded. In the Perpendicular test (Figure 5-18), two rows of cells beginning on the north side of Ship Island and extending 1.0 km to the north were loaded with initial concentrations of 1.0 mg/L of tracer. The locations of the two rows for the Perpendicular tests were selected so that the cells would correspond to portions of Ship Island that are in both the Pre- and Post-Katrina grids. Results of both Parallel and Perpendicular tracer tests were evaluated using surface concentration plots. Results for the first 18 to 24 hours of the Pre-Katrina scenario, for both Parallel and Perpendicular tests, along with the first 24 hours of Parallel tests for the Restored scenario, are presented in this report. Tracer results for the full simulation period of all scenarios are available and can be supplied if requested.

In the Parallel test, results for all scenarios indicated that all evidence of the tracer was gone within five days. Tidal activity continued to move the tracer along and around Ship Island until levels fell below 1.0 percent of the initial concentration. Flushing was adequate in the Pre-Katrina case to move the tracer around the ends of Ship Island and through Camille Cut within 12 hours (Figure 5-16). After 24 hours, only low levels of tracer remained next to Ship Island in the Pre-Katrina case. The tracer next to the island was the remnant of an eddy that formed on the east end of Ship Island and then

Figure 5-16. Initial parallel tracer distribution every 3 hours for 24 hours (Pre-Katrina case). (Sheet 1 of 5).

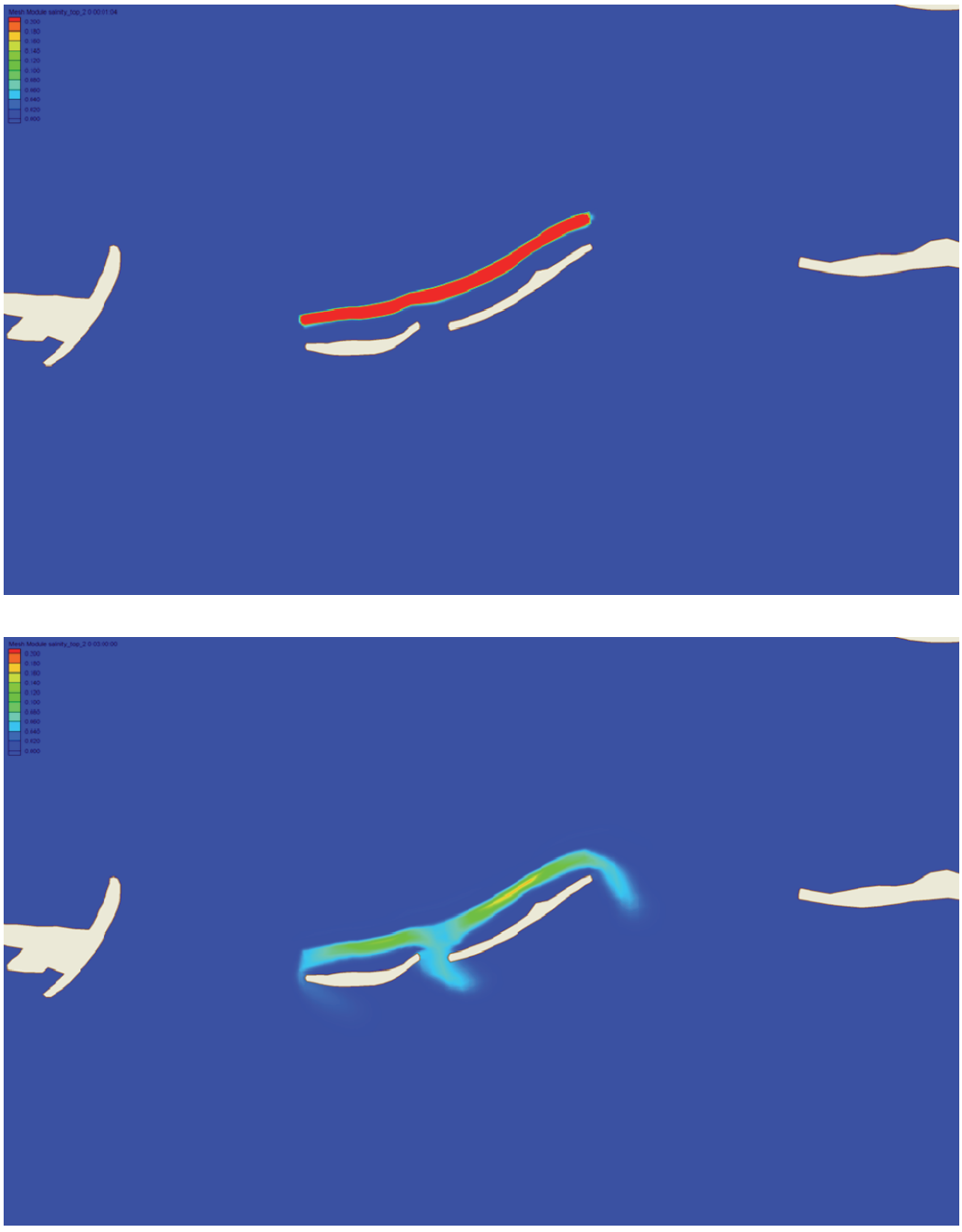

Figure 5-16. (Sheet 2 of 5).

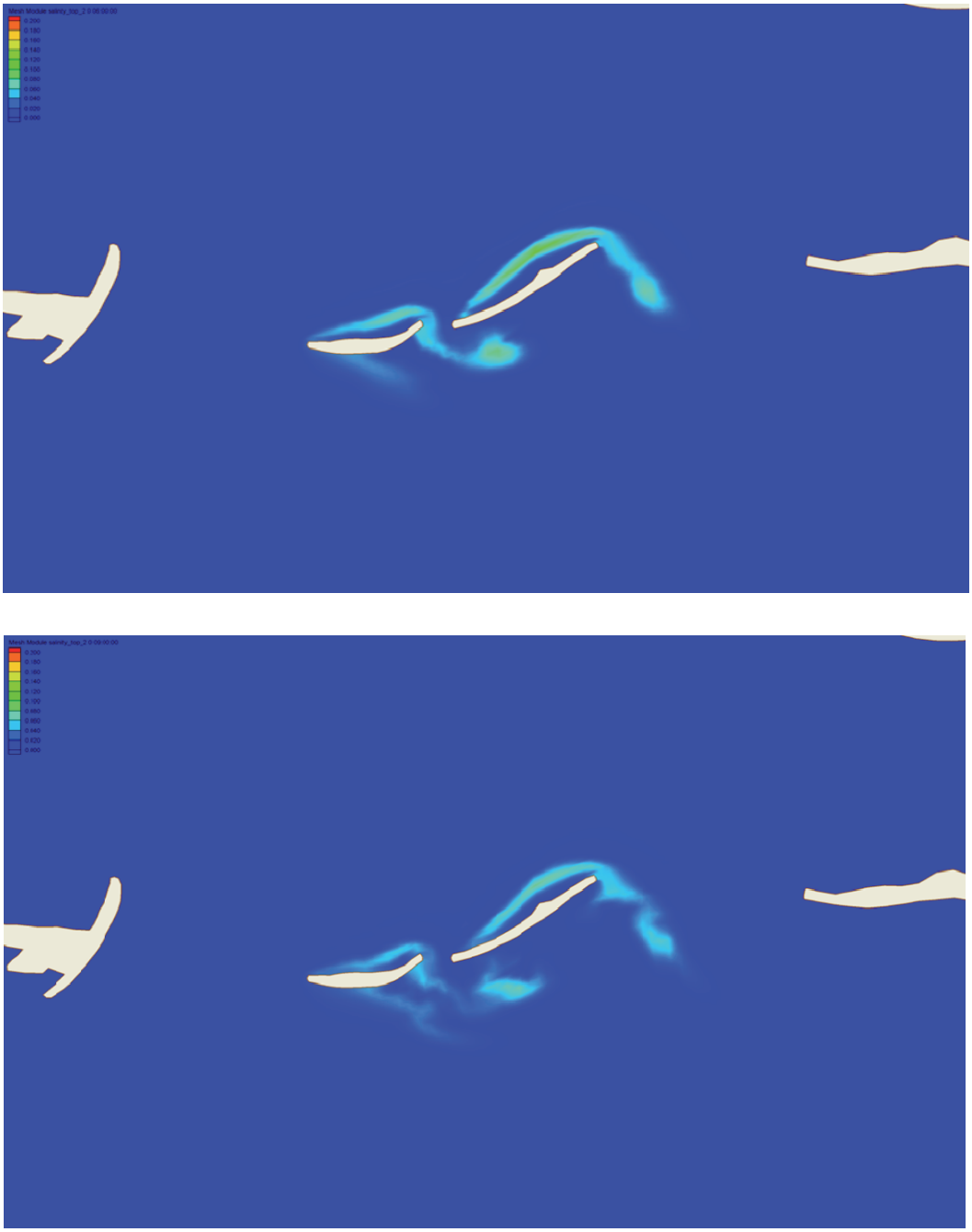

Figure 5-16. (Sheet 3 of 5).

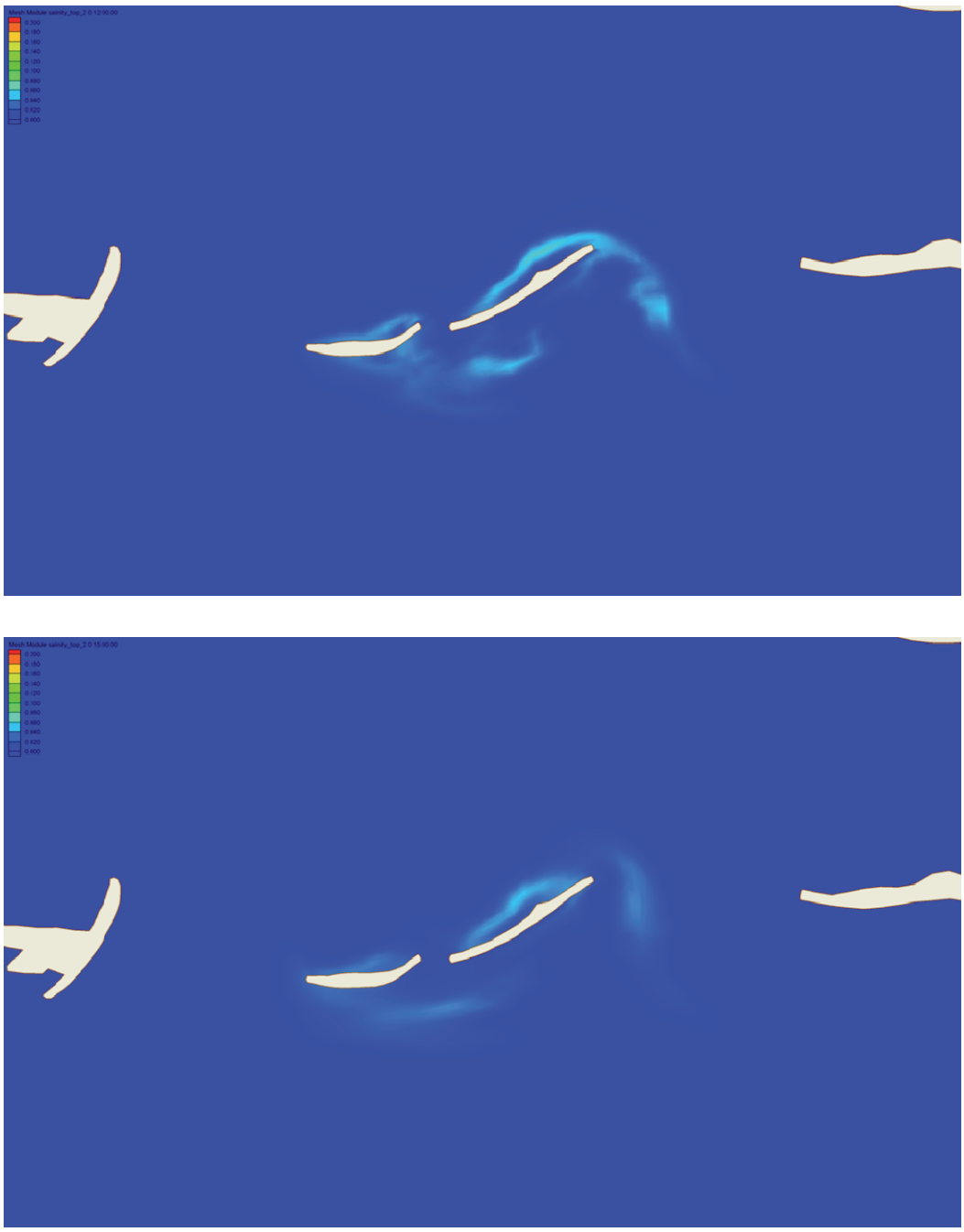

Figure 5-16. (Sheet 4 of 5).

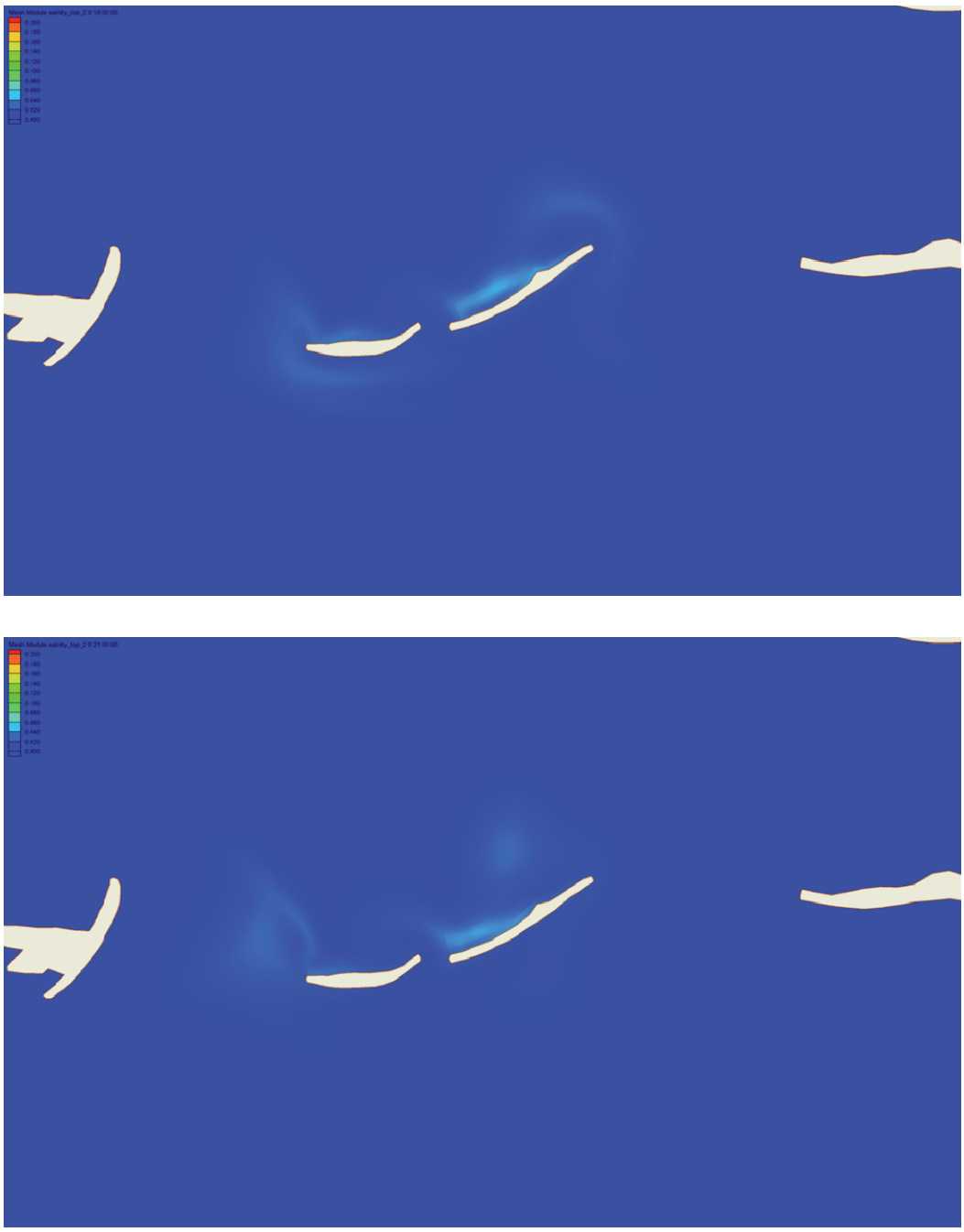

Figure 5-16. (Sheet 5 of 5).

rolled back to the west. Tracer levels in the Post-Katrina case are slightly higher, 12 hours after release in the vicinity of Ship Island. The degree of increase is not significant and is likely due to the tracer plume passing through the gap in Ship Island and not being sheared off as it rounded the eastern end of Ship Island.

Results for tracer simulations for the Restored case are shown in Figure 5-17. The behavior is similar to that of the Pre- and Post-Katrina cases except that the absence of the opening in the middle of the island allows for slightly more tracer to remain on the north side of the island. The levels of remaining tracer after 24 hours are low and similar to those of the Pre- and Post-Katrina scenarios at the same simulation time. The difference is that in the restored case the tracer is closer to the shore.

Twelve hours into the Parallel test for the Restored case, more tracer remains on the northern side of Ship Island than for either the Pre- or Post-Katrina cases (Figure 5-17). This is due to the loss of the conveyance through the middle of Ship Island. The ultimate end result is the same in that the tracer does eventually move around Ship Island.

One point of interest is that although the circulation was adequate to rapidly disperse the tracer from its original loading location, it did not fully remove it from the vicinity of Ship Island immediately. Instead, tracer plumes

Figure 5-17. Initial parallel tracer distribution every 3 hours for 24 hours (Restored case). (Sheet 1 of 5)

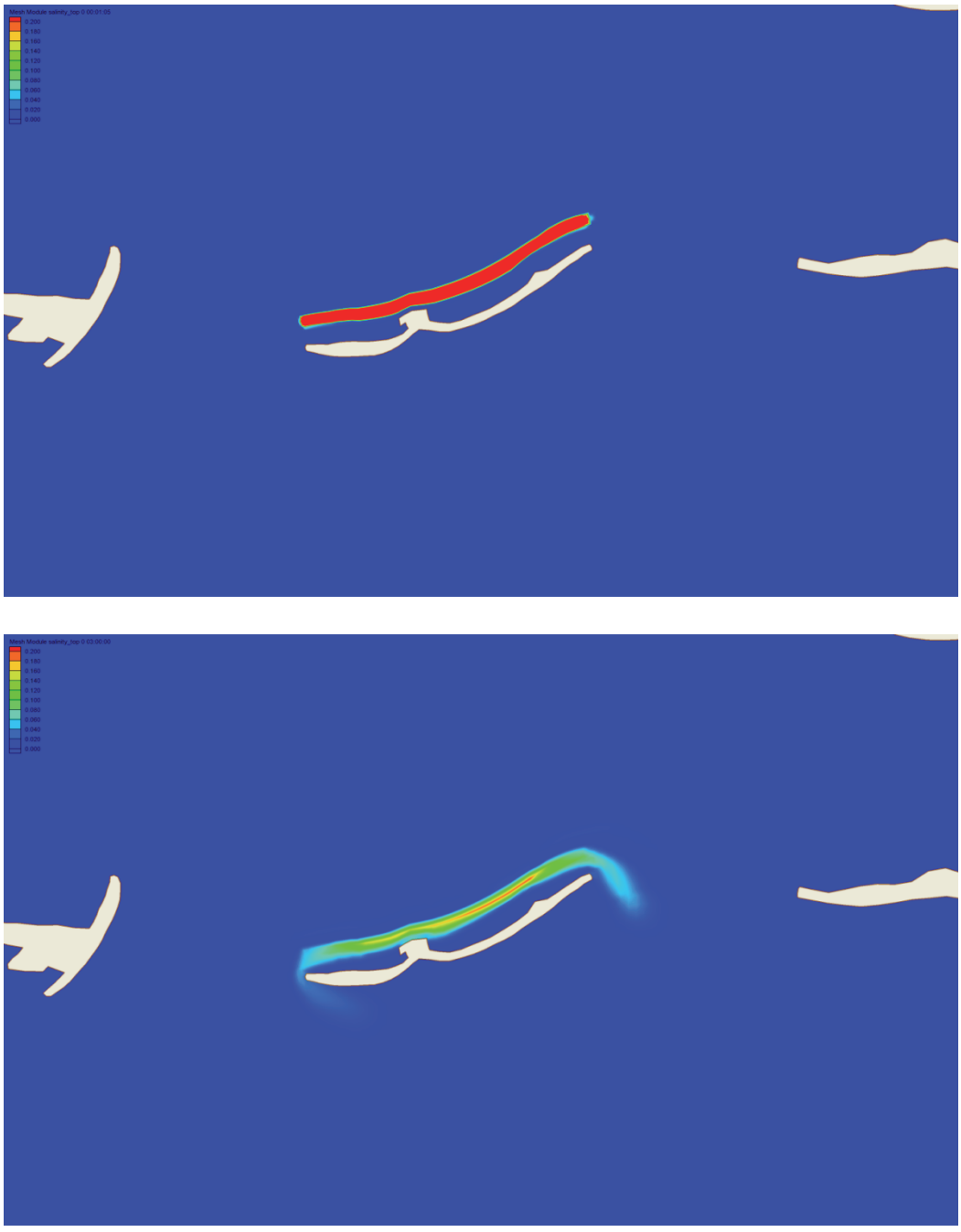

Figure 5-17. (Sheet 2 of 5).

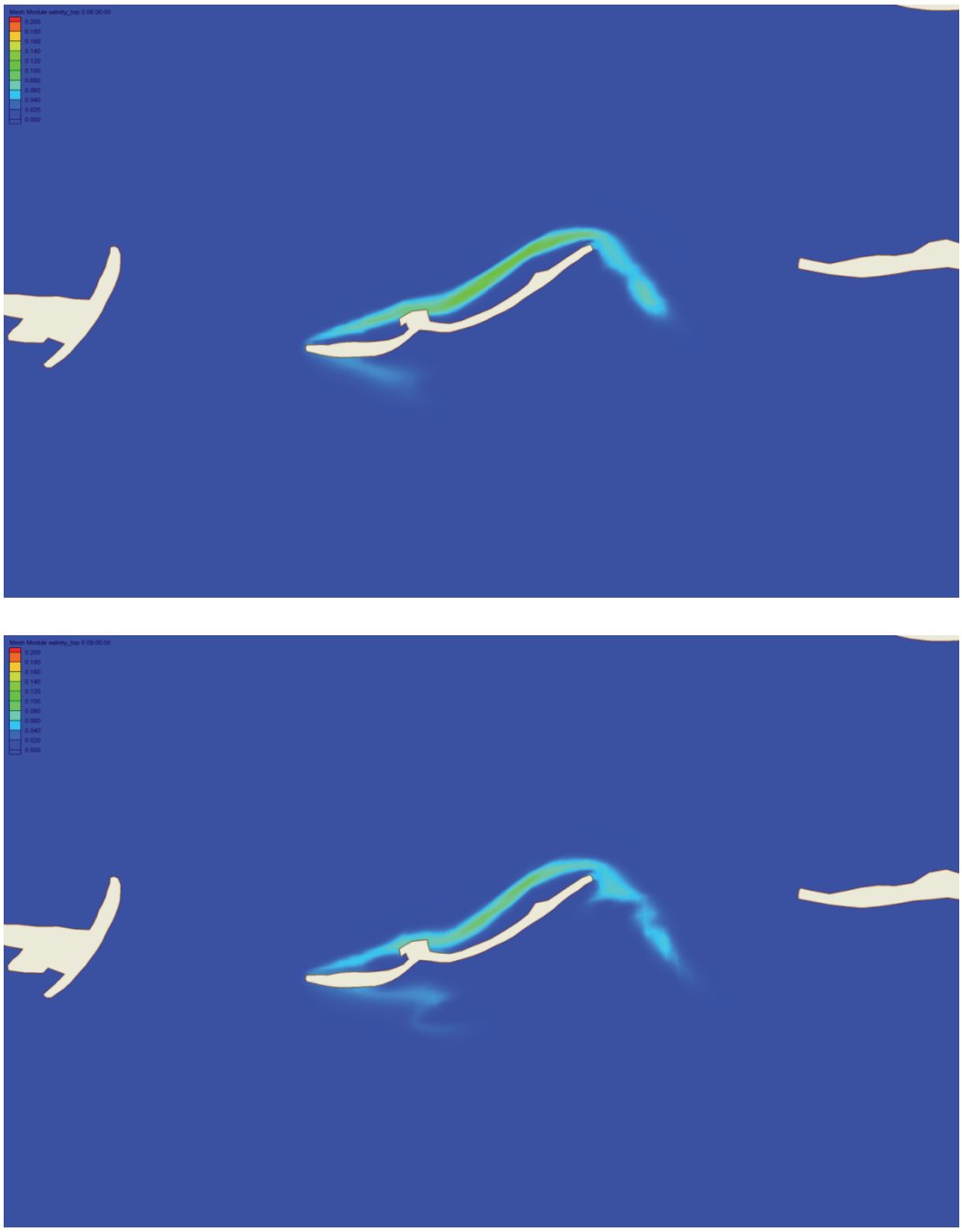

Figure 5-17. (Sheet 3 of 5).

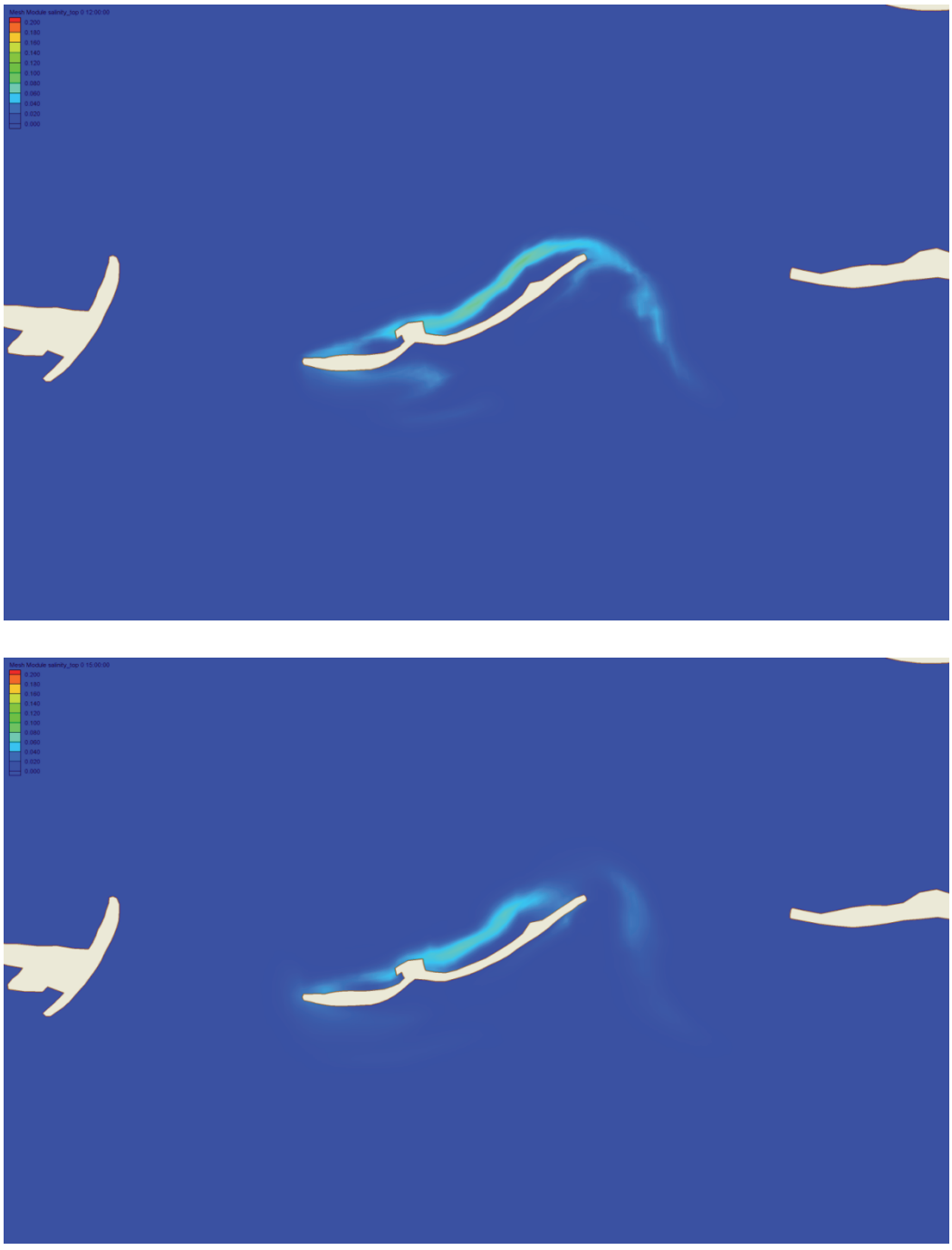

Figure 5-17. (Sheet 4 of 5).

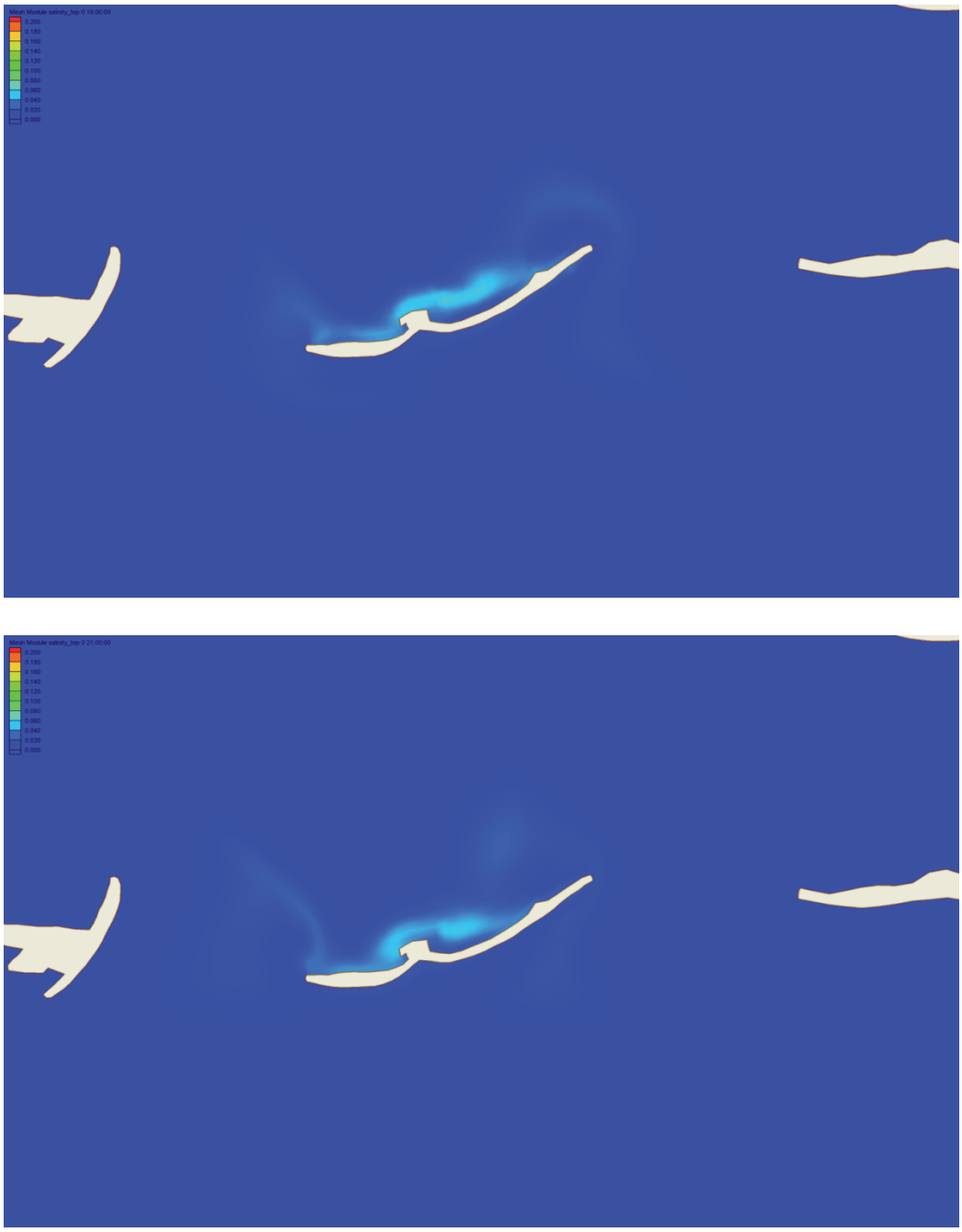

Figure 5-17. (Sheet 5 of 5).

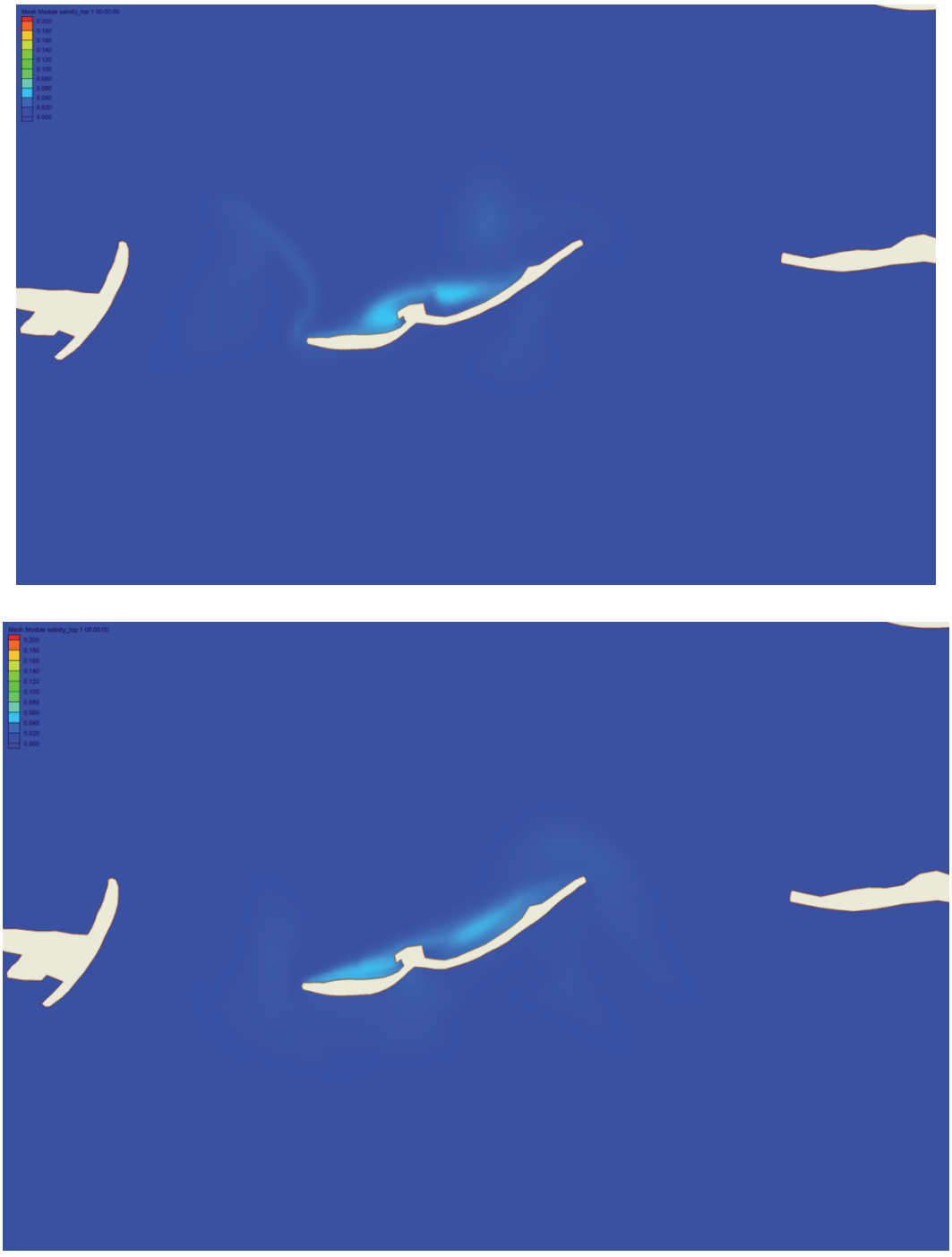

formed and moved around Ship Island and then back again. This is why very low levels of tracer were still evident days after the initial release. Such behavior indicates that the sloshing behavior seen between Ship Island and the coast also occurs south of the island. In other words, circulation is adequate to quickly displace material and move it around but does not always completely remove it from the vicinity of Ship Island.

Figure 5-18. Initial perpendicular tracer distribution every 3 hours for 18 hours.
(Sheet 1 of 4)

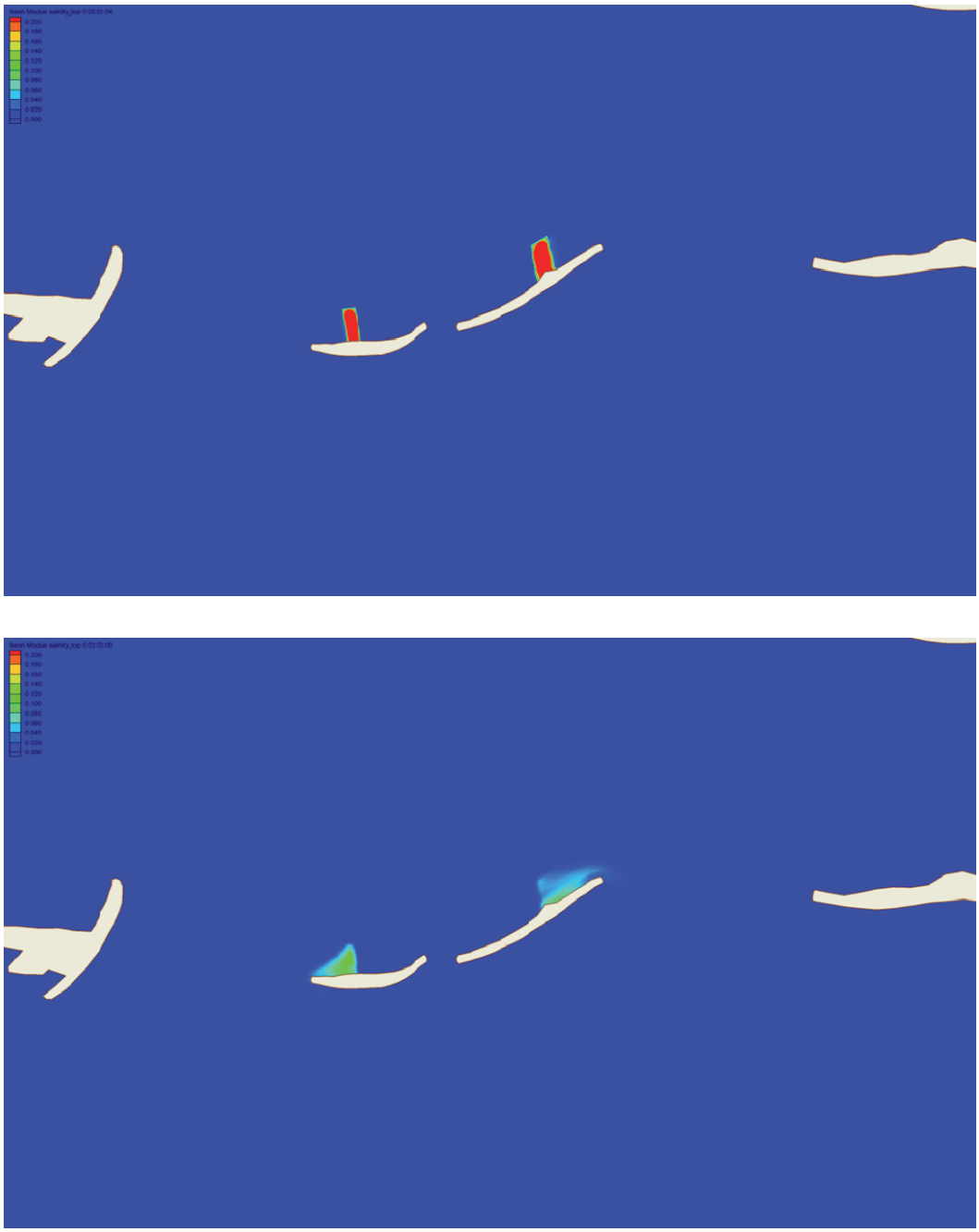

Figure 5-18. (Sheet 2 of 4).

Figure 5-18. (Sheet 3 of 4).

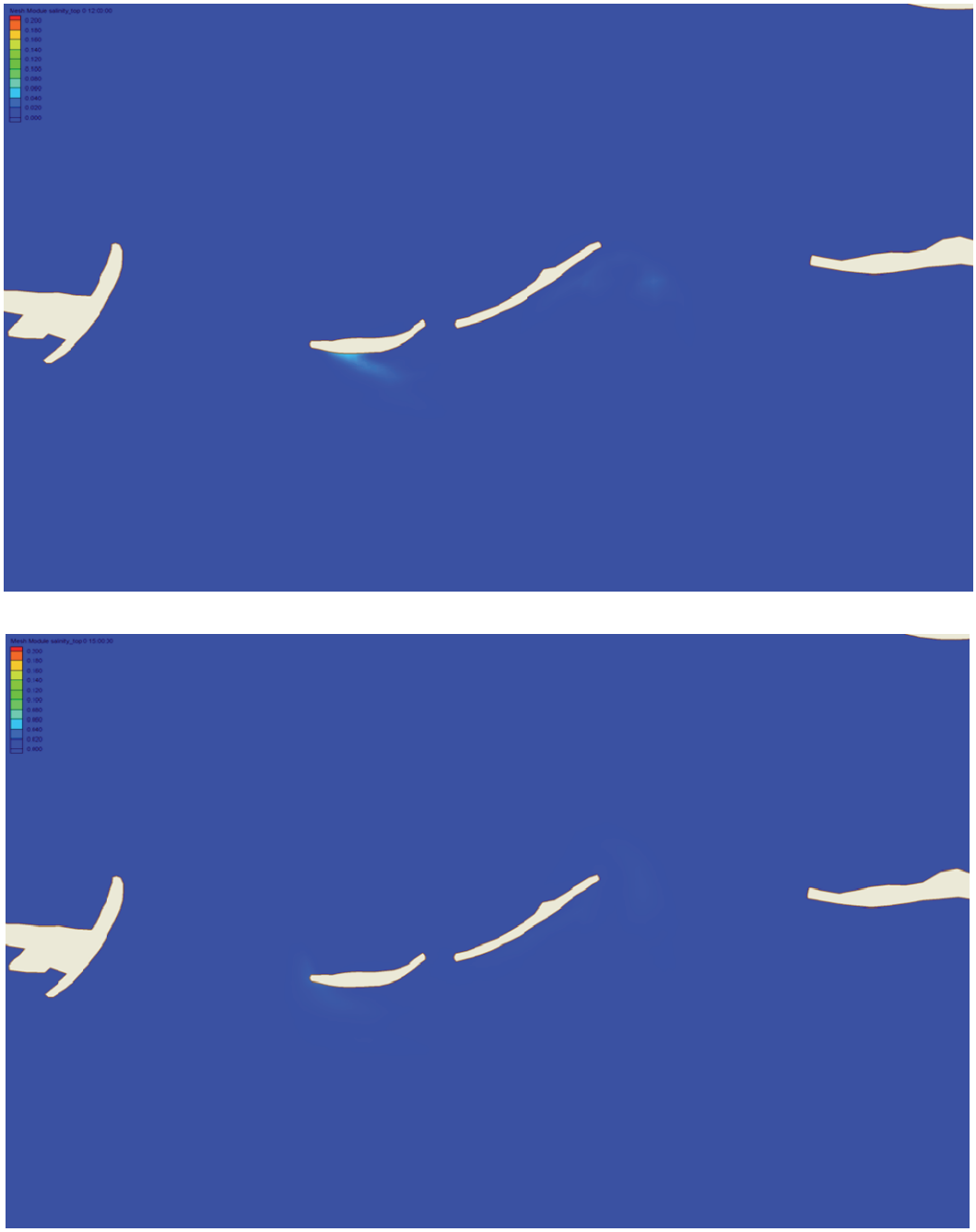

Figure 5-18. (Sheet 4 of 4).

Perpendicular tracer test results for all scenarios were similar (Figure 5-18). Tracer concentrations decreased to less that 1.0 percent of initial loading concentrations within 1 day. The reason that only 1 day was required for this to happen in this test, versus 5 days in the Parallel test, is that fewer cells were loaded and they were smaller than the cells loaded in the parallel tests. Not surprisingly, the same back and forth movement is seen in tracer released at these locations as was seen in the Parallel test.

5.9 Water quality summary and conclusions

The ERDC conducted a water quality model study of Mississippi Sound to determine potential impacts from proposed actions in the Ship Island area. The focus of the water quality effort of this study was to understand the existing water quality within the Mississippi Sound and to quantify relative changes in water quality and flushing capacity. Two numerical models, one hydrodynamic (CH3D) and one water quality model (CE-QUAL-ICM), were applied to the study area to simulate hydrodynamics and water quality in the Mississippi Sound.

In addition to the calibration/base grid (present conditions), there were a total of four configurations modeled. They included Base conditions (Pre-Katrina), Post-Katrina, Restored, Without Project (Degraded), and Cumulative (With Project, Katrina Cut Closure and authorized Federal Navigation channel dimensions).

The water quality model, CE-QUAL-ICM was calibrated for the period of April 1, 1998 through September 15, 1998 using observed data provided by the MS DEQ and appropriate kinetic rates determined in calibration. Sediment Oxygen Demand (SOD) is specified as a constant rate in the ocean and river inflows. Final calibration results compared favorably to observed data given the limited amount of comparison and boundary data available to evaluate and drive the model, respectively.

Changes in DO, salinity, and chlorophyll *a* were an indicator of changes to water quality. Conclusions from comparing alternative runs are as follows:

- Comparison of Pre- and Post-Katrina results to the other scenario results showed changes in water quality for all scenarios to some degree. Of the scenarios, "Cumulative" showed the most deviation from Pre-Katrina, especially at Stations 5 and 10 (Figure 5-2) when comparing results at all locations considered during calibration. Of the stations in the area of the proposed Ship Island restoration (Figure 5-7), most station results were comparable to results at Stations 5 and 10. Station 7 located north of Dauphin Island where Katrina cut is located showed the greatest deviation from base (Pre-Katrina). Changes at Station 7 are the direct result of the breech caused by Hurricane Katrina at Dauphin Island and were not the result of any proposed actions at Ship Island. Although water quality changes were noted, all were within the state standard for constituents of interest for ocean's waters.
- Total net flows show averages are two orders of magnitude less than the peak flood and ebb flows across locations analyzed in the area of Ship Island. This is an indication of two things. First, MS Sound in the vicinity of Ship Island has relatively little flushing and net transport through the system. Second, the effects of Ship Island degradation or restoration do not have major effects upon system wide circulation and therefore, should not have major effects on system wide water quality conditions. The condition of Ship Island does; however, appear to have localized effects on circulation.
- Two sets of tracer simulations were performed to assess the impact of different scenarios on circulation and flushing immediately behind Ship Island. Tracer concentrations were released instantaneously and allowed to disperse. These tests are referred to as the Parallel and Perpendicular tests based upon the orientation of the tracer loading to Ship Island. In the Parallel test, results for all scenarios indicated that all evidence of the tracer was gone within five days. One point of interest is that although

the circulation was adequate to rapidly disperse the tracer from its original loading location, it did not fully remove it from the vicinity of Ship Island immediately. Circulation is adequate to quickly displace material and move it around but does not always completely remove it from the vicinity of Ship Island. Perpendicular tracer test results for all scenarios were similar. Tracer concentrations decreased to less that 1.0 percent of initial loading concentrations within one day. It took less time to disperse in this test because less tracer concentration was released over a smaller area. The same back and forth movement is seen in tracer released at locations in both tests.

Overall, comparison of results from all alternative runs showed changes in circulation but this caused minor effects to water quality concentrations in the area of proposed restoration. The “Cumulative” scenario showed the greatest impacts to water quality. However, it is concluded from these results that none of the scenarios simulated would likely have system wide detrimental water quality impacts. Water quality benefits of a restored Ship Island are possible in two ways. First is that water quality behind the island would be similar to Pre-Katrina conditions. This may be more desirable from a sheltered habitat standpoint than open water of a degraded island. Second, north of Ship Island in the Restored or Cumulative case there is greater potential for Submerged Aquatic Vegetation colonization and growth in the protected waters.

6 Storm Wave Sensitivity[1]

The purpose of this chapter is to examine the wave changes which result from a degraded and restored Ship Island, when compared to the existing Post-Katrina Ship Island condition. The reduction of storm wave energy at the mainland Mississippi coast as a result of closing Camille Cut and restoring Ship Island to a "Pre-Hurricane Camille" condition was evaluated. Similarly, the increase in storm wave energy at the mainland Mississippi coast as a result of Ship Island degradation was evaluated. The relative changes resulting from the barrier island restoration and degradation are quantified through the application of an integrated coastal storm modeling system.

6.1 Introduction

After Hurricane Katrina, it became widely accepted by the public that if the Mississippi barrier islands had been in a "Pre-Hurricane Camille" condition, there would have been much less storm damage during Hurricane Katrina. The US Army Corps of Engineers, Mobile District (SAM) provided the "Pre-Hurricane Camille" restoration template, which includes the closure of Camille Cut as well as two regions of nearshore sediment placement at +0.3048 m and -0.3048 m (referenced to NAVD88 2004.65) to the east of Camille Cut as shown in Figure 6-1.

Figure 6-1. Ship Island restoration template shown with ADCIRC mesh nodes. Note: Geodetic elevations are referenced to NAVD88 2004.65.

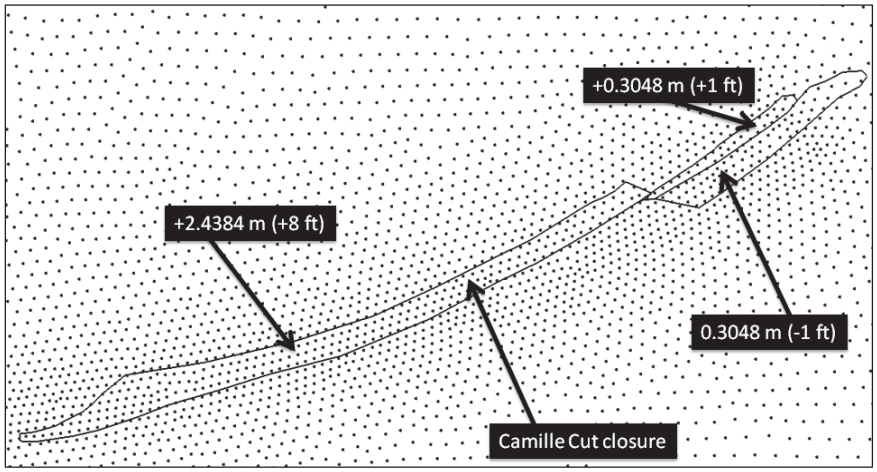

[1] Written by Alison Sleath Grzegorzewski, Coastal and Hydraulics Laboratory, US Army Engineer Research and Development Center, Vicksburg, MS.

In addition to the Ship Island restoration, SAM provided data for two borrow areas on the Gulf of Mexico side of Ship Island as shown in Figure 6-2. The borrow areas described in this chapter represent a preliminary plan of borrow areas considered. Additional borrow area configurations were evaluated and further analyses have been conducted to determine the final borrow area configuration for Ship Island (described in Chapter 8). The landward edge of the Ship Island borrow areas are positioned approximately 1.6 km (1.0 mile) offshore of the restored Ship Island shoreline and the borrow area cut depths range from -1.83 m (-6.0 ft) to -3.66 m (-12 ft).

Figure 6-2. Ship Island borrow areas and cut depths shown with ADCIRC mesh nodes.

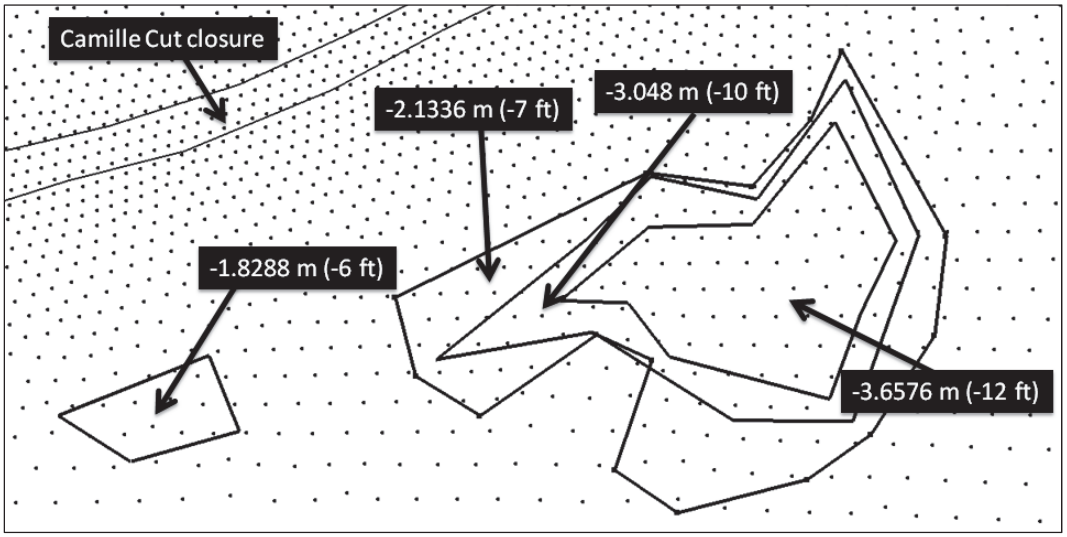

The US Army Corps of Engineers Mobile District (SAM) also provided the degradation template, which included the degradation of East and West Ship Island to subaqueous shoals at an elevation of approximately -1.0 m (referenced to NAVD88 2004.65). The bathymetry/topography for all three Ship Island modeling scenarios is shown in Figure 6-3.

To simulate the barrier island restoration scenario in the integrated coastal storm modeling system, the ADCIRC mesh was modified to include the restoration template and borrow site data. The full-plane STWAVE domain was then created by interpolation from the restored ADCIRC mesh scenario. The full-plane STWAVE bathymetry/ topography for the SE domain is shown in Figure 6-4. The domain includes over ½ million cells with 200 m square cell resolution. The spatial extent of the full-plane STWAVE grid is 140 km by 150 km.

Figure 6-3. Bathymetry/topography for the three Ship Island modeling scenarios: 1) Existing Pre-Katrina, 2) Restored, and 3) Degraded.

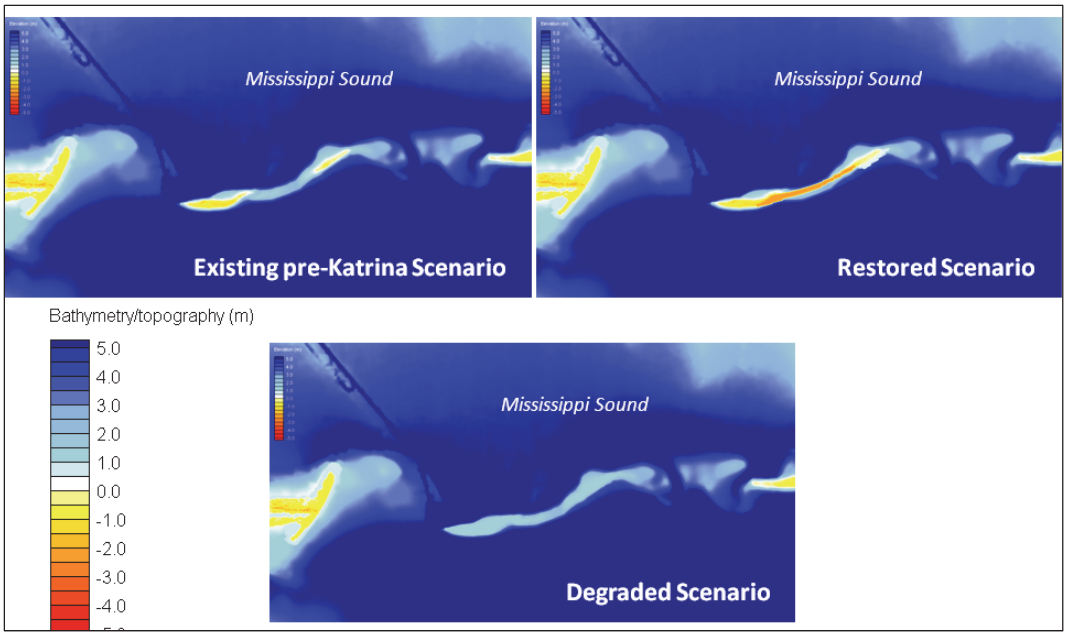

Figure 6-4. Full-plane STWAVE bathymetry/topography for the SE domain.

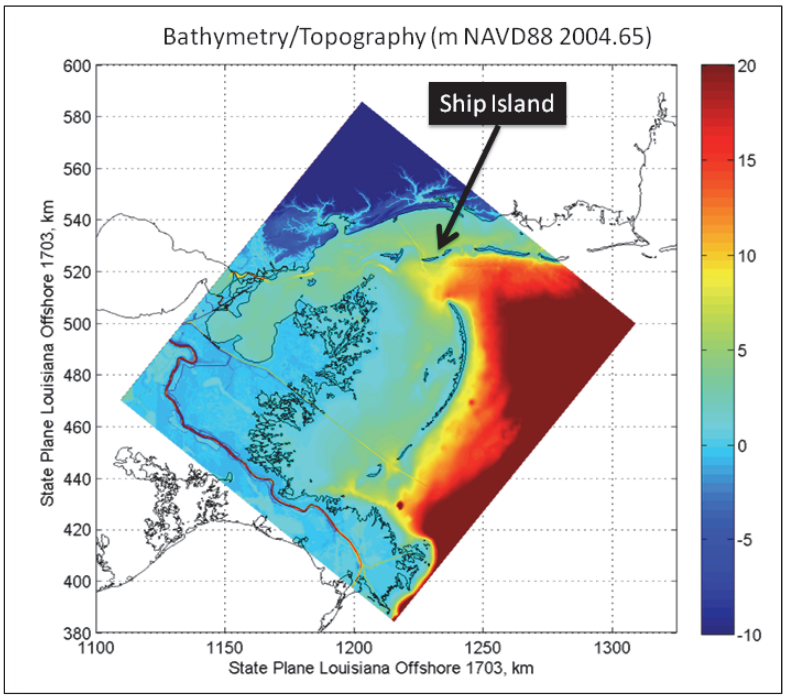

6.2 Storm suite

A synthetic storm suite consisting of 15 storms was selected for this study to include a range of high, moderate, and low surge potential storms. The

synthetic storms traverse five trajectories across Mississippi Sound and Lake Borgne, Louisiana to the west as shown in Figure 6-5. The simulated maximum surge envelopes for each synthetic storm are provided in Appendix F.

Figure 6-5. Five trajectories for the synthetic storm suite.

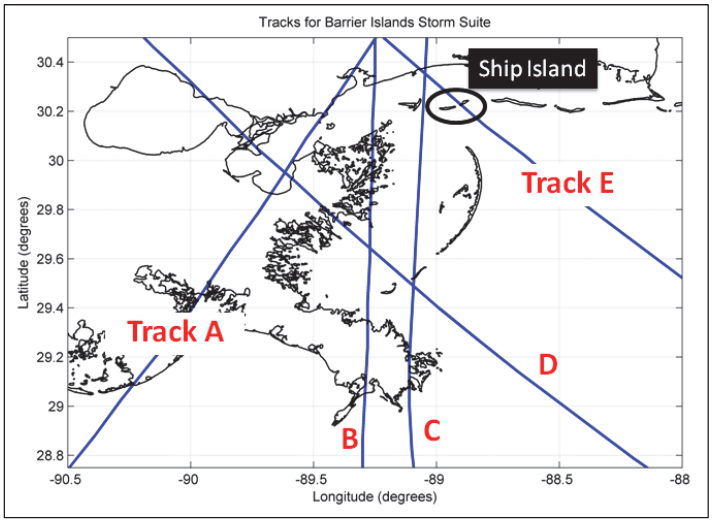

The forward speeds of the synthetic storms range from 3.1 m/sec to 8.7 m/sec, as shown in Table 6-1. The minimum central pressures and radii to maximum winds range from 90 to 96 kPa and 11.1 to 45.6 km, respectively (Table 6-1).

Table 6-1. Synthetic storm suite parameters.

Storm #	Central Pressure (kPa)	Radius to Maximum Winds (km)	Forward Velocity (m/sec)	Track
28	96	20.4	5.7	B
32	93	32.8	5.7	B
34	90	11.1	5.7	B
59	96	45.6	5.7	D
60	90	23.2	5.7	D
88	96	32.8	3.1	B
89	90	32.8	3.1	B
104	93	32.8	8.7	B
133	96	32.8	5.7	A
134	90	32.8	5.7	A
823	96	38.9	5.7	C

Storm #	Central Pressure (kPa)	Radius to Maximum Winds (km)	Forward Velocity (m/sec)	Track
825	93	32.8	5.7	C
827	90	27.6	5.7	C
851	96	45.6	3.1	E
852	90	23.2	3.1	E

6.3 Overview of the integrated coastal storm modeling system

The integrated coastal storm modeling system applied for this study is consistent with that applied by Wamsley et al. (2009), Ebersole et al. (2010), and Grzegorzewski et al. (2011) and was developed following Hurricanes Katrina and Rita in 2005 by a team of engineers and scientists in the respective fields of coastal hydrodynamics, meteorology, statistics, and computer science. Their collaborative effort produced a modeling system methodology to better estimate inundation due to storm surge in the northern Gulf of Mexico (IPET 2008; Westerink et al. 2008). The modeling system was validated for Hurricanes Katrina and Rita (Bunya et al. 2010; Dietrich et al. 2010) through comparison of high water marks on land and continuous water levels in open water areas. The extent of inland inundation for these storms was extreme, allowing for a unique opportunity to validate inundation algorithms for initially dry land, resistance of flow over topography, and subsequent decrease in wind magnitude over land and during landfall.

The integrated coastal storm modeling system includes models for simulating hurricane wind fields, wave generation and transformation, and storm surge. For a given synthetic storm, application of the TC96 Planetary Boundary Layer (PBL) model (Cardone et al. 1992; Thompson and Cardone 1996) generates a time-series of wind and atmospheric pressure fields which are used to drive the offshore wave model, WAM (Komen et al. 1994) and storm surge model ADCIRC (Kolar et al. 1994; Atkinson et al. 2004; Luettich and Westerink 2004; Dawson et al. 2006; Tanaka et al. 2010). The large-domain, discrete, time-dependent spectral wave model WAM is run to calculate directional wave spectra that serve as offshore boundary conditions for the local-domain, nearshore spectral wave generation and transformation model STWAVE (Smith et al. 2001). The WAM model was calibrated using wave growth data derived for fetch-limited conditions, and was verified through hindcasting various North Atlantic storms and Gulf of Mexico hurricanes (WAMDI Group 1988). In

parallel with WAM runs, the unstructured two-dimensional coastal ocean circulation model ADCIRC is used to simulate pressure- and wind-driven water surface elevation (storm surge) and is coupled with the nearshore wave model STWAVE. The input for each STWAVE simulation includes the bathymetry, surge, and wind fields, all interpolated from the ADCIRC domain. The STWAVE simulations are also forced with wave spectra interpolated on the offshore boundary from the WAM model. The wind and surge applied in STWAVE are spatially and temporally variable. STWAVE is run at 30-minute intervals for approximately one day prior to and following storm landfall. This procedure is repeated for each storm in the synthetic storm suite.

The circulation model ADCIRC covers a large domain including the entire Gulf of Mexico and the Atlantic Ocean eastward to the 60 degrees West longitude line. To model the storm surge in the complex regions of interest, all significant flow processes that define the physical system must be included. Waves and surge are influenced by both basin-scale and local-scale geometric features and flow gradients. The complexity of the entire system must be accurately defined and computationally resolved in the numerical models for the growth, propagation, and attenuation of waves, surge, and riverine flows to be modeled correctly. Hence, the ADCIRC mesh has over two million nodes with the majority concentrated in coastal Louisiana and Mississippi. The PBL and WAM models use a structured grid with domains that cover the entire Gulf of Mexico. The nearshore wave model, STWAVE, is nested within the other models includes the local generation and transformation of waves within the nearshore zone.

6.4 Restored versus existing condition

The maximum wave height reduction at the mainland Mississippi coast as a result of the closure of Camille Cut and Ship Island restoration ranges from 0.2 m to 1.25 m. The wave height reduction potential was found to be controlled by the storm characteristics (Table 6-1), with minimum central pressure (maximum wind speed), radius to maximum winds, forward speed, and trajectory being the controlling agents. For reference, the incident significant wave height was extracted at the peak of each synthetic storm at a location approximately 5.4 km from the Ship Island shoreline in the Gulf of Mexico, as shown in Figure 6-6.

Figure 6-6. Map for the location of incident wave conditions. The incident significant wave height was extracted at the peak of each synthetic storm at a location approximately 5.4 km from the Ship Island shoreline in the Gulf of Mexico.

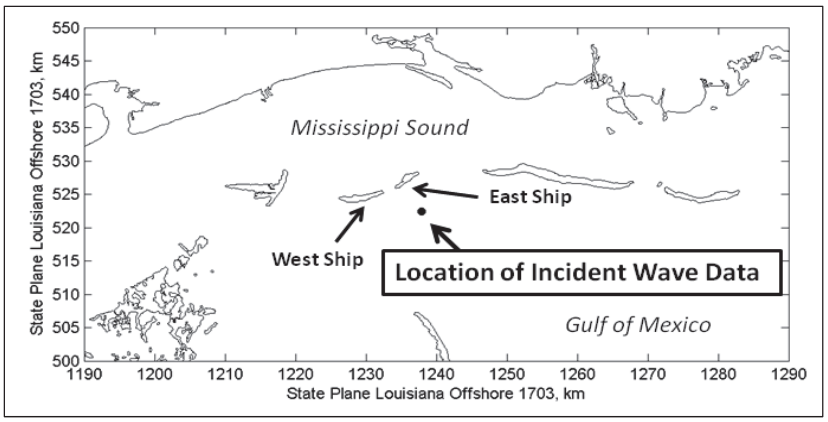

Three ranges of maximum wave reduction potential were defined to categorize the wave height results when comparing the existing Post-Katrina scenario to the Restored scenario at the mainland Mississippi coast. A "low" wave reduction potential indicates that the restoration scenario reduced wave heights at the mainland Mississippi coast by as much as 0.2 m to 0.4 m. A "medium" wave reduction potential indicates that the Restored scenario reduced wave heights at the mainland Mississippi coast by 0.4 m to 0.6 m. A "high" wave reduction potential indicates that the Restored scenario reduced wave heights at the mainland Mississippi coast by more than 0.6 m. The greatest decrease in wave heights observed at the mainland Mississippi coast for this storm suite was 1.25 m for Storm 825 (Figure 6-7).

For Track A, both low and high wave reduction potentials were observed based on the difference in minimum central pressure (maximum wind speed), as shown in Table 6-2.

Storms which traverse Track A travel from the southwest to the northeast before making landfall near Bay St. Louis, MS. Figure 6-8 show snapshots of wind speed when the storm eyes pass to the north of Biloxi Marsh and the greatest offshore-onshore directed winds encompass Ship Island. The only difference between storm characteristics for Storm 133 and Storm 134 along Track A is the minimum central pressure. Note that, Storm 134 has a lower central pressure and produces a higher wind speed (35 m/sec to 40 m/sec) when compared to Storm 133 (25 m/sec to 30 m/sec). The higher wind speeds generate larger waves and the Restored scenario blocks a substantial amount of the energy from penetrating through Camille Cut into Mississippi Sound.

Figure 6-7. Significant wave heights (m) (top left and top right) and wave height differences (bottom) during Storm 825. The existing Post-Katrina scenario wave heights are shown in the top left panel and the Restored scenario wave heights are shown in the top right panel. The difference (Restored minus Existing) in wave heights is shown in the bottom panel. Note that the cool colors indicate wave height decrease.

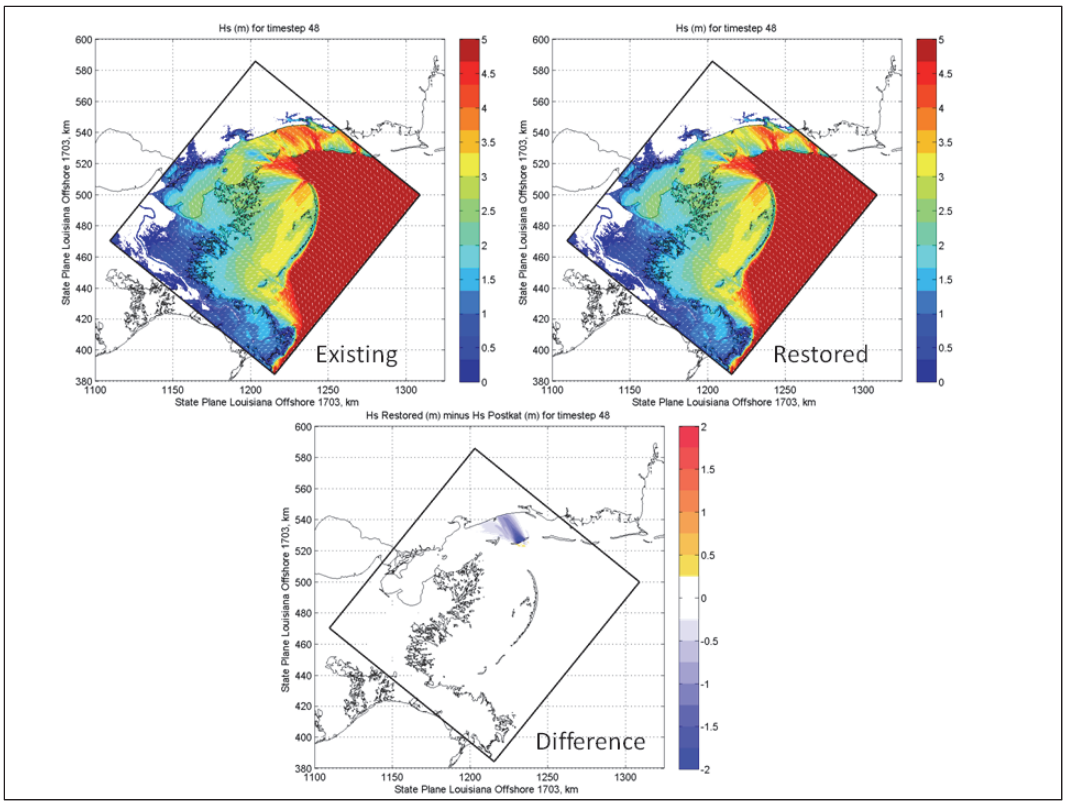

Table 6-2. Synthetic storm suite parameters and wave reduction potential at the mainland Mississippi coast for Track A.

Storm #	Central Pressure (kPa)	Radius to Max Wind (km)	Forward Velocity (m/sec)	Incident Wave Height (m)	Wave Reduction Potential at mainland MS coast
133	96	32.8	5.7	3.8	Low
134	90	32.8	5.7	5.5	High

For Track B, a range of wave reduction potentials were observed based on the dominant controlling factors of minimum central pressure (maximum wind speed), radius to maximum winds, and forward speed (Table 6-3).

Storms which traverse Track B travel from the south to the north to the west of Cat Island before making landfall just east of Bay St. Louis, MS. Figure 6-9 show snapshots of wind speed when the greatest offshore-onshore directed winds encompass Ship Island for Storm 028, Storm 032, and Storm 034. All three of these storms have the same forward velocity

Figure 6-8. Wind speed during the storm peaks for Track A.

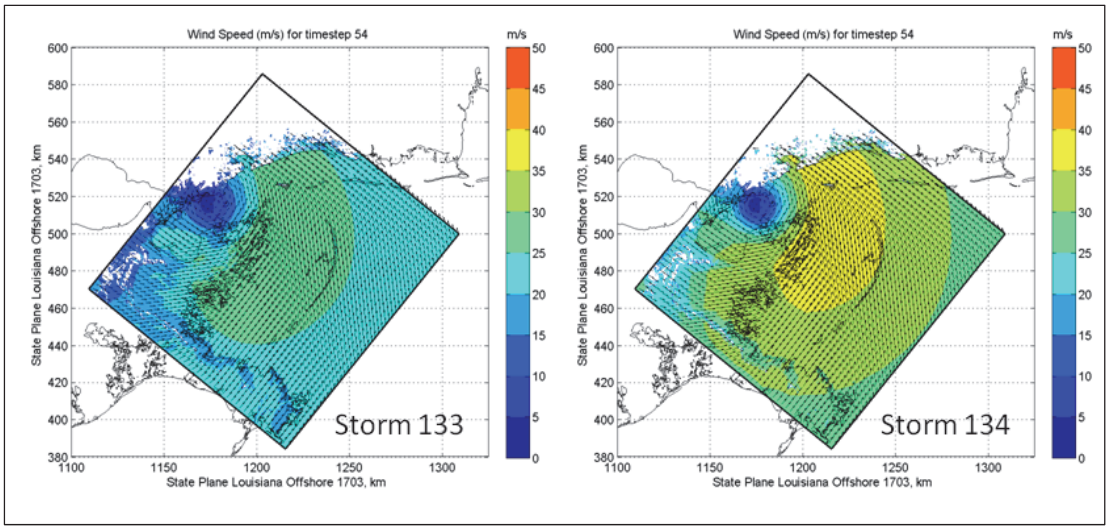

Table 6-3. Synthetic storm suite parameters and wave reduction potential at the mainland Mississippi coast for Track B.

Storm #	Central Pressure (kPa)	Radius to Max Wind (km)	Forward Velocity (m/sec)	Incident Wave Height (m)	Wave Reduction Potential at mainland MS coast
28	96	20.4	5.7	3.9	Low
32	93	32.8	5.7	5.7	Medium
34	90	11.1	5.7	3.8	Low
88	96	32.8	3.1	3.5	Low
89	90	32.8	3.1	4.9	High
104	93	32.8	8.7	6.4	High

and differ by central pressure and radius to maximum wind parameters. While Storm 034 has the lowest central pressure and the largest associated wind speeds (40 m/sec to 45 m/sec) of these three storms, the smaller radius to maximum winds means that the spiral bands of the largest winds for this storm do not encompass Ship Island. Conversely, Storm 032 has the largest radius and the spiral bands of the largest winds encompass Ship Island, as shown in Figure 6-9. Hence, Storm 032 yields larger incident waves and a greater wave reduction potential when compared to Storm 028 and Storm 034.

Figure 6-10 shows snapshots of wind speed when the greatest offshore-onshore directed winds encompass Ship Island for Storm 088 and Storm 089. The only difference between Storm 088 and Storm 089 along Track B is the minimum central pressure. Storm 089 has a lower central pressure

and produces higher wind speeds (30 m/sec to 35 m/sec) when compared to Storm 088 (20 m/sec to 25 m/sec). The higher wind speeds generate larger waves and the Restored scenario blocks a substantial amount of the energy from penetrating through Camille Cut into Mississippi Sound.

Figure 6-9. Wind speed during the storm peaks for Track B, Storms 028, 032, and 034.

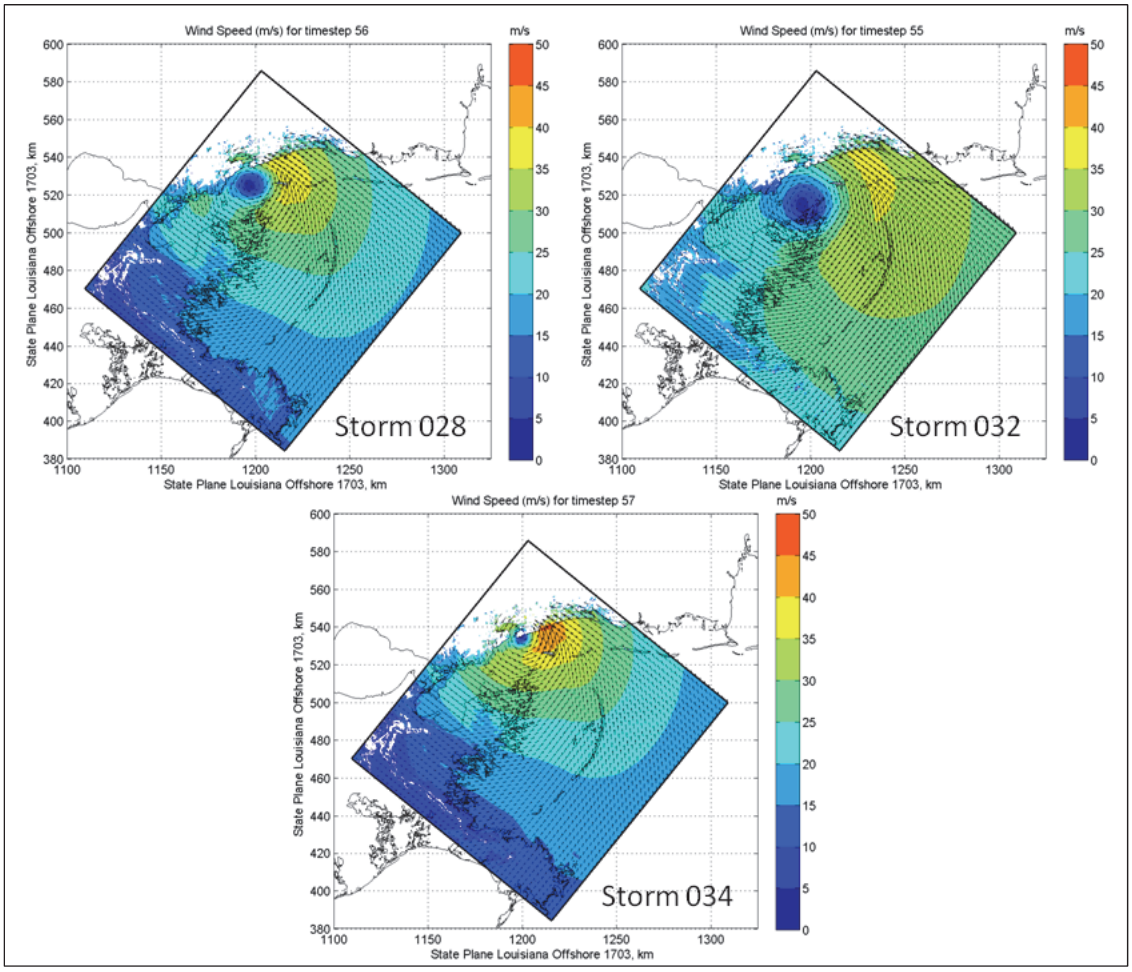

Figure 6-10. Wind speed during the storm peak for Track B, Storm 088 and Storm 089.

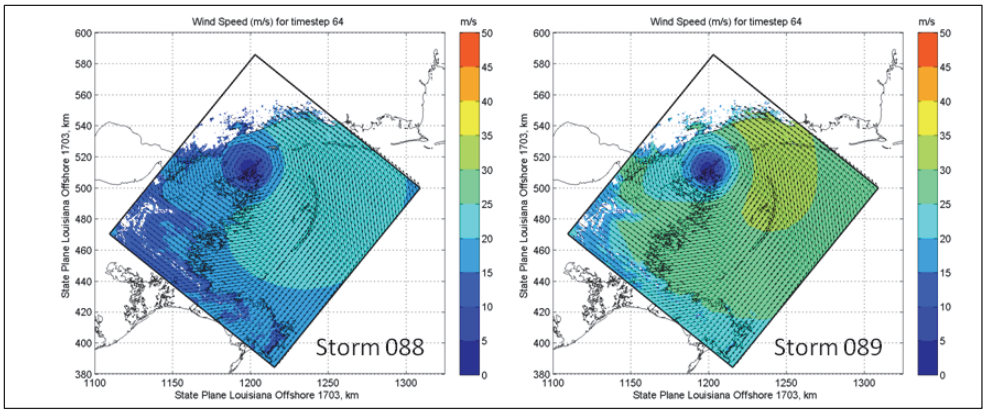

Both the forward speed and minimum central pressure are factors that affect the wave reduction potential at the mainland Mississippi coast when comparing Storm 089 to Storm 032 along Track B. Both Storm 089 and Storm 032 have the same radii to maximum winds. While Storm 089 has a lower central pressure when compared to Storm 032, Storm 032 (Figure 6-9) has greater offshore-onshore directed winds that encompass Ship Island when compared to Storm 089 (Figure 6-10). The explanation for this is that there is a time lag of 4.5 hours between the snapshot shown in Figure 6-9 and the snapshot shown in Figure 6-10. In other words, Run 089 is a slower-moving storm with a lower minimum central pressure and does indeed produce larger peak winds as shown in Figure 6-11. However, major hurricanes decay offshore before making landfall (Resio 2007), so by the time the greatest offshore-onshore directed winds encompass Ship Island, the maximum peak wind values have been reduced from 45-50 m/sec (Figure 6-11 left-panel) to 30-35 m/sec (Figure 6-11 right panel). The storm wave field represents the integrated effects of storm winds over the duration of hours, so the fact that Storm 089 is a slower-moving storm when compared to Storm 032 means that there is more time for wind energy transfer to the waves. Therefore, the greater storm reduction potential is observed for Storm 089 as the Restored scenario diminishes the incoming waves from penetrating into Mississippi Sound.

Figure 6-11. Wind speed during Storm 089 at two different snapshots in time as the storm travels from south to north before making landfall just east of Bay St. Louis, MS. The left-side panel shows the wind speeds 10.5 hours prior to the wind speeds shown on the right-side panel.

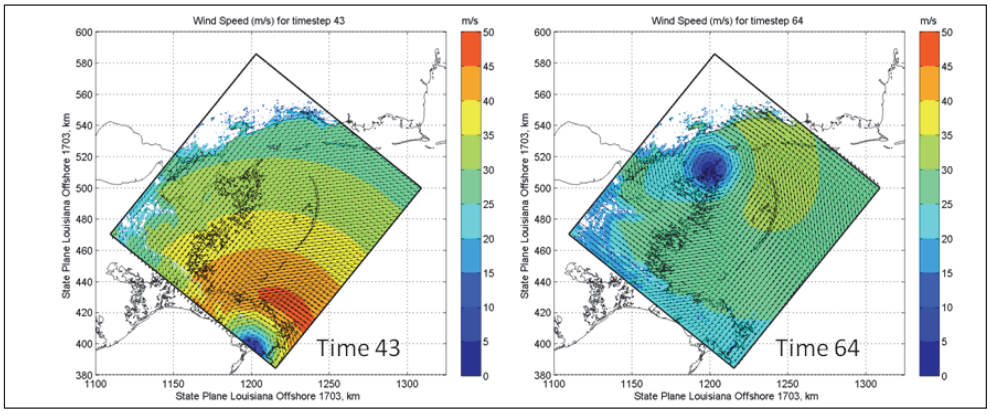

Figure 6-12 shows a snapshot of wind speed when the greatest offshore-onshore directed winds encompass Ship Island for Storm 104. Forward speed affects wave reduction potential at the mainland Mississippi coast as seen through comparison of Storm 032 to Storm 104. The only difference in

storm characteristics between Storm 032 and Storm 104 along Track B is forward speed. Storm 032 is a slower-moving storm. Therefore, by the time the greatest offshore-onshore directed winds encompass Ship Island, the storm has decayed and the maximum peak wind values have been reduced to 35 m/sec to 40 m/sec. The spiral band of maximum wind speeds encompasses a smaller spatial extent in the vicinity of Ship Island for Storm 032 when compared than Storm 104. In addition to the pre-landfall decay of storms associated with the forward speed, storms with increased forward speeds contribute to higher wind speeds in the hurricane PBL model (Resio 2007). Therefore, it follows that Storm 032 yields smaller waves and wave reduction potential at the mainland Mississippi coast when compared to Storm 104.

Figure 6-12. Wind speed during the storm peak for Track B, Storm 104.

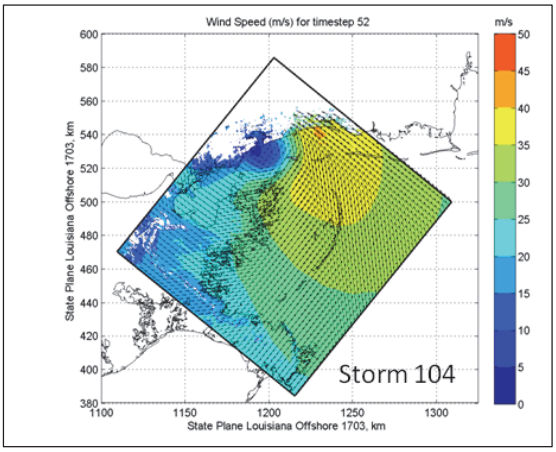

For Track C, a high wave reduction potential is observed for all three synthetic storms which follow this trajectory (Table 6-4). The dominant controlling factor for these storms is trajectory.

Table 6-4. Synthetic storm suite parameters and wave reduction potential at the mainland Mississippi coast for Track C.

Storm #	Central Pressure (kPa)	Radius to Max Wind (km)	Forward Velocity (m/sec)	Incident Wave Height (m)	Wave Reduction Potential at mainland MS coast
823	96	38.9	5.7	4.1	High
825	93	32.8	5.7	5.6	High
827	90	27.6	5.7	6.6	High

Figure 6-13 shows snapshots of wind speed when the greatest offshore-onshore directed winds encompass Ship Island for the three storms that follow Track C. Storms which traverse Track C travel from south to north to west and bisect Ship Island Pass (the tidal inlet between Cat Island and West Ship Island) before making landfall near Gulfport, MS. Hence, the alignment of this trajectory (i.e. angle of approach) provides the longest duration of offshore-onshore directed winds as the storm passes to the west of Ship Island and most time for the wind field to transfer energy to the wave field when compared to the other trajectories modeled for this study. The restoration of Camille Cut blocks wave energy from penetrating into Mississippi Sound. Therefore, even though a large range of maximum wind speeds that encompass Ship Island exist for these storms (10 m/sec up to 45 m/sec), all three storms have a high wave reduction potential based on the primary controlling factor of their trajectory alignment and sustained periods of offshore-onshore directed winds.

Figure 6-13. Wind speed during the storm peaks for Track C, Storm 823, 825, and 827.

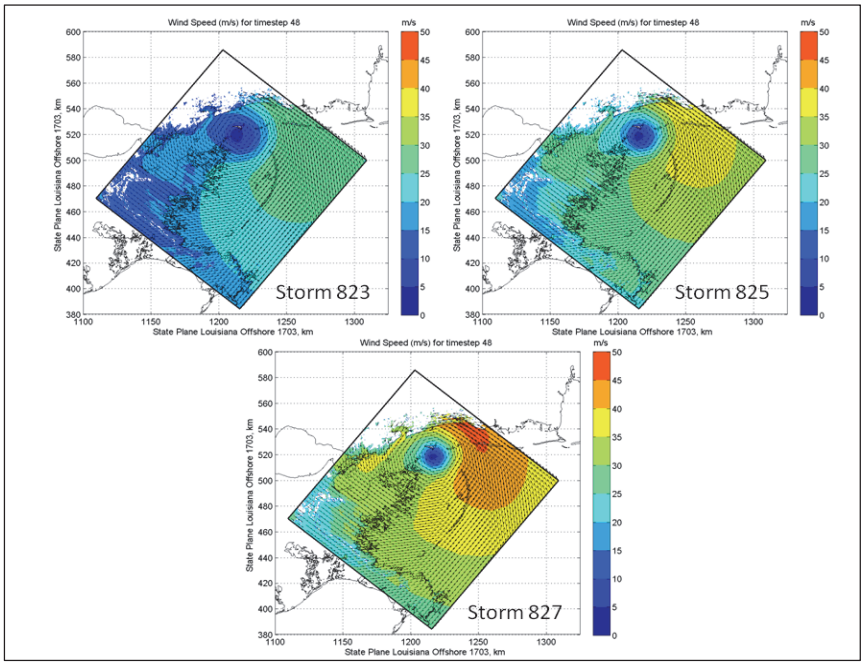

For Track D, a medium wave reduction potential is observed for both synthetic storms which follow this trajectory (Table 6-5). Trajectory is a dominant controlling factor because even though Storm 060 has a very low minimum pressure (high maximum winds), the resulting wave reduction potential at the mainland Mississippi coast is restricted by the alignment of the trajectory and limited sustained period of offshore-onshore directed winds.

Table 6-5. Synthetic storm suite parameters and wave reduction potential at the mainland Mississippi coast for Track D.

Storm #	Central Pressure (kPa)	Radius to Max Wind (km)	Forward Velocity (m/sec)	Incident Wave Height (m)	Wave Reduction Potential at mainland MS coast
59	96	45.6	5.7	3.6	Medium
60	90	23.2	5.7	3.5	Medium

Figure 6-14 shows snapshots of wind speed when the greatest offshore-onshore directed winds encompass Ship Island for the two storms that follow Track D. Storms which traverse Track D travel from the southeast to the northwest crossing over Biloxi Marsh and Lake Borgne before making landfall in Louisiana.

Figure 6-14. Wind speed during the storm peak for Track C, Storm 059 and 060.

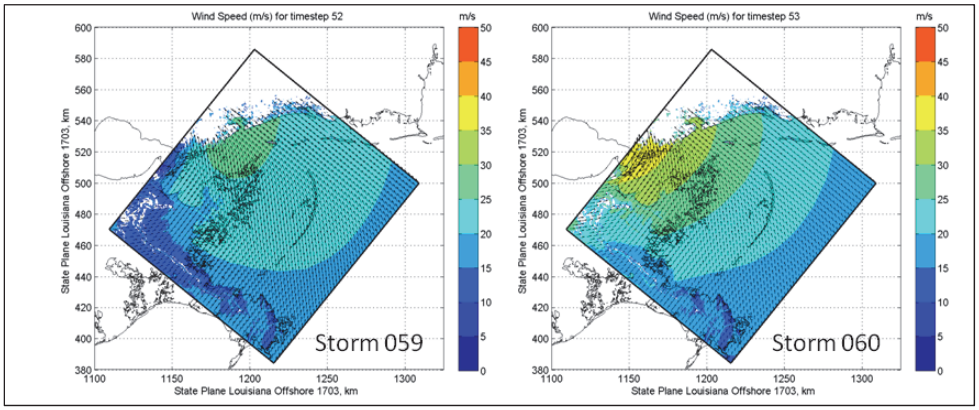

Even though Storm 060 produced very high maximum winds in excess of 45 m/sec (as shown in Figure 6-15 left panel), these largest wind speeds are directed from east to west across Mississippi Sound when the eye crosses Breton Sound due to the storm trajectory (angle of approach). Therefore, the restoration scenario does not have an impact during this time as waves are not being directed onshore into Mississippi Sound. By the time the winds change direction and are oriented perpendicular to Ship Island and the offshore-onshore winds encompass the island, the storm has already decayed and made landfall (Figure 6-15 right panel) and the offshore-onshore directed winds have been reduced to 25 m/sec to 30 m/sec for Storm 060.

For Track E, a medium wave reduction potential is observed for the two synthetic storms which follow this trajectory (Table 6-6). Storms which follow this trajectory bisect Ship Island from the southeast to the

northwest before making landfall near Gulfport, MS. The controlling factors for the storms along Track E are the minimum central pressures (maximum wind speed) and the radii to maximum winds.

Figure 6-15. Wind speed during Storm 060 at two different snapshots in time. The left-side panel shows the wind speeds 4.5 hours prior to the wind speeds shown on the right-side panel.

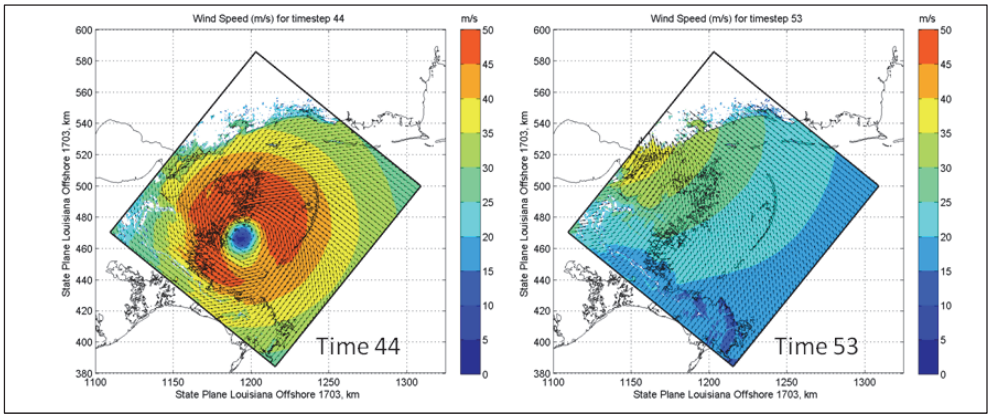

Table 6-6. Synthetic storm suite parameters and wave reduction potential at the mainland Mississippi coast for Track E.

Storm #	Central Pressure (kPa)	Radius to Max Wind (km)	Forward Velocity (m/sec)	Incident Wave Height (m)	Wave Reduction Potential at mainland MS coast
851	96	45.6	2.9	2.6	Medium
852	90	23.2	2.9	4.4	Medium

Figure 6-16 shows snapshots of wind speed when the greatest offshore-onshore directed winds encompass Ship Island for the two storms that follow Track E. Storm 852 along Track E has a lower central pressure and produces a higher wind speed (40 m/sec to 45 m/sec) when compared to Storm 851 (5 m/sec to 10 m/sec). Higher wind speeds associated with Storm 852 generate larger waves and the restoration scenario blocks a substantial amount of the energy from penetrating through Camille Cut into Mississippi Sound.

However, even if Storm 851 had a lower central pressure (and higher associated wind speeds), the large radius to maximum winds and the fact that the storm passes directly over and bisects Ship Island means the island is located within the quiescent eyewall of the storm and the wave reduction potential would still be less than the reduction potential associated with Run 852 (low pressure, but small radius storm) as the spiral bands of larger

wind speeds are located to the east of Ship Island. Therefore, in addition to central pressure, radius to maximum wind speed is also a controlling factor for this trajectory.

Figure 6-16. Wind speed during the storm peak for Track E, Storm 851 and 852.

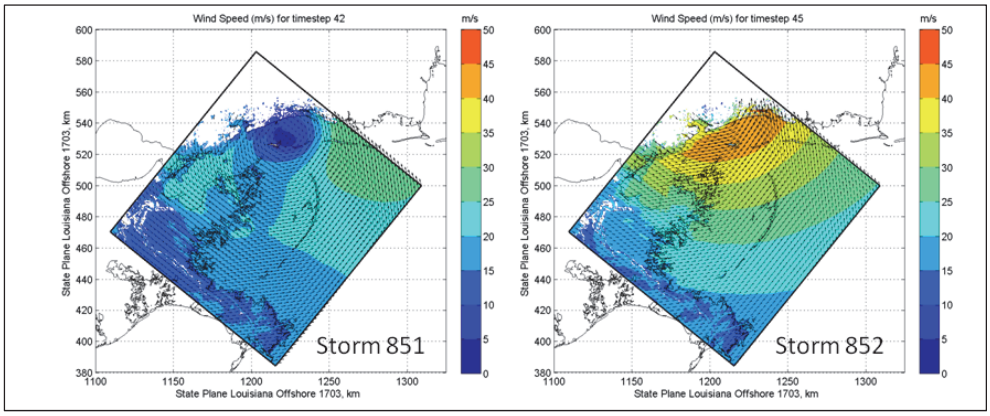

6.5 Degraded versus existing condition

The maximum wave height increase at the mainland Mississippi coast, as a result of barrier island degradation, ranges from 0.2 m to 0.4 m. Thirteen of the 15 synthetic storms experience a maximum wave height increase of 0.2 m at the mainland Mississippi coast. The remaining two synthetic storms, Storm 089 and Storm 825, experienced a maximum wave height increase of 0.4 m at the mainland Mississippi coast as shown in Figures 6-17 and 6-18.

The maximum wave change potential at the mainland Mississippi coast is smaller for the Degraded scenario than for the Restored scenario because wave energy can penetrate from the Gulf of Mexico into Mississippi Sound for both the existing Post-Katrina and Degraded scenarios. On the other hand, the Restored scenario has the potential to block a significant portion of wave energy from penetrating into the Mississippi Sound; hence the maximum wave change potential is larger.

Figure 6-19 shows the subaerial footprint of East and West Ship Island before and after Hurricane Katrina. As shown in Figure 6-19, Hurricane Katrina significantly widened Camille Cut, and this widened tidal inlet is represented in the existing Post-Katrina integrated coastal storm models. For the Degraded scenario, East and West Ship Island were degraded to subaqueous shoals approximately 1 m below NAVD88 2004.65. Therefore, the largest areas of wave height increase are in the leeward areas behind East and West Ship Island (as shown in Figures 6-17 and 6-18).

Figure 6-17. Significant wave heights (m) (top left and top right) and wave height differences (bottom) during Storm 089. The existing Post-Katrina scenario wave heights are shown in the top left panel and the Degraded scenario wave heights are shown in the top right panel. The difference (Degraded minus Existing) in wave heights is shown in the bottom panel. Note that the warm colors indicate wave height increase.

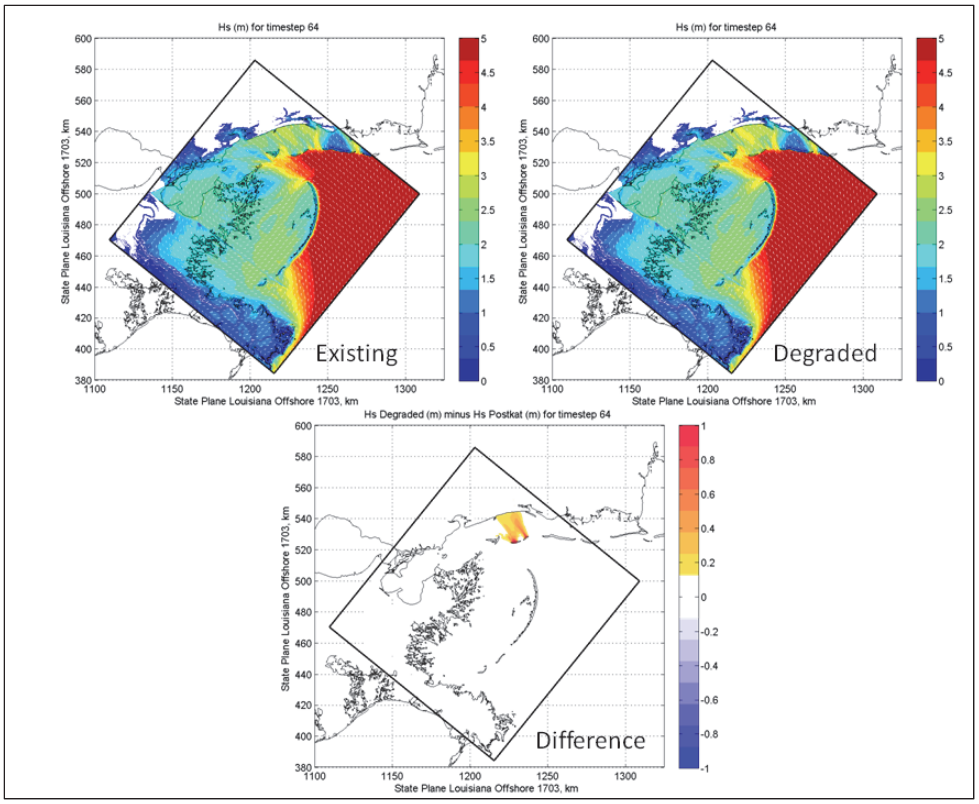

In addition to producing a larger maximum wave change potential, the Restored scenario also contributes to a prolonged duration of wave change potential along the mainland Mississippi coast when compared to the degraded condition. For Restored vs existing Post-Katrina conditions, the mainland Mississippi coast experiences a wave height decrease of 0.2 m or greater for 13 hours to 32 hours during each storm event, with an average duration of 24 hours for the 15 storm suite. In other words, the wave heights are reduced by 0.2 m or more for an average duration of 24 hours at the mainland Mississippi coast for a given storm event. In contrast, the duration of wave change potential is much less dramatic for the Degraded vs existing Post-Katrina condition. For Degraded vs existing Post-Katrina conditions, the mainland Mississippi coast experiences a wave height increase of 0.2 m or greater for 0.5 hours to 4.5 hours during each storm event, with an average duration of 2,0 hours for the 15 storm suite. In other waves, the wave heights are increased by 0.2 m or more for an average duration of 2.0 hours at the mainland Mississippi coast for a given storm event.

Figure 6-18. Significant wave heights (m) (top left and top right) and wave height differences (bottom) during Storm 825. The existing Post-Katrina scenario wave heights are shown in the top left panel and the Degraded scenario wave heights are shown in the top right panel. The difference (Degraded minus Existing) in wave heights is shown in the bottom panel. Note that the warm colors indicate wave height increase.

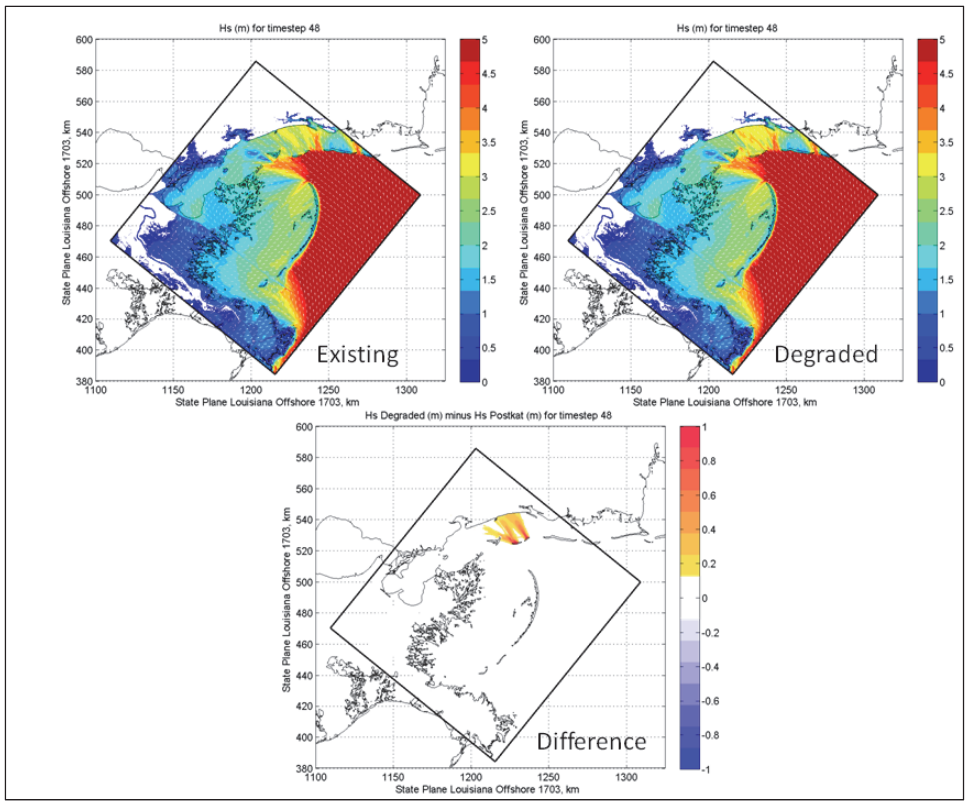

Figure 6-19. Ship Island before (top) and after (below) Hurricane Katrina. Note the significant widening of Camille Cut as a result of Katrina (source: http://soundwaves.usgs.gov/2009/03/).

As previously discussed, the Restored scenario has the potential to block a significant portion of wave energy from penetrating into the Mississippi Sound while wave energy is permitted to penetrate into the Mississippi

Sound for both the Degraded and existing Post-Katrina conditions; hence, the most dramatic effects experienced at the mainland Mississippi coast are a result of the Restoration scenario.

6.6 Storm waves and the offshore borrow areas

The effects of offshore borrow areas on storm waves were quantified through cross-shore progression of significant wave heights along three parallel transects in the vicinity of the borrow areas. The three cross-shore transects are oriented in the direction of primary offshore-onshore wave energy propagation. Transect A-A' traverses the region between two offshore borrow areas, Transect B-B' is located 2.0 km from Transect A-A' and bisects the larger, eastern offshore borrow area, and Transect C-C' is located approximately 4.5 km from Transect A-A' and traverses the area to the east of the larger borrow area (Figure 6-20). The origin Transect B-B' is located at a position 5.4 km offshore from Ship Island in the Gulf of Mexico (the incident wave location shown in Figure 6-6) and extends to the restored Ship Island shoreface, bisecting the larger, eastern offshore borrow area. The bottom position or elevation below 0 m NAVD88 2004.65, along the cross-shore Transect B-B' is shown in Figure 6-21. The cross-shore distance of 0 m corresponds with the incident wave location shown in Figure 6-6. The bottom position for the existing Post-Katrina scenario monotonically increases from -9.5 m offshore to -2.0 m nearshore. The bottom position for the Restored scenario deviates from the existing Post-Katrina scenario starting at the cross-shore distance of 600 m and re-aligns with the existing Post-Katrina scenario again starting at the cross-shore distance of 4200 m.

Figure 6-20. The effects of the offshore borrow areas on storm waves were quantified through the cross-shore progression of significant wave heights along three transects (A-A', B-B', and C-C') in the vicinity of the borrow sites. Transect B-B' extends 5.4 km from offshore of Ship Island in the Gulf of Mexico to the restored Ship Island shoreface, bisecting the larger, eastern offshore borrow area.

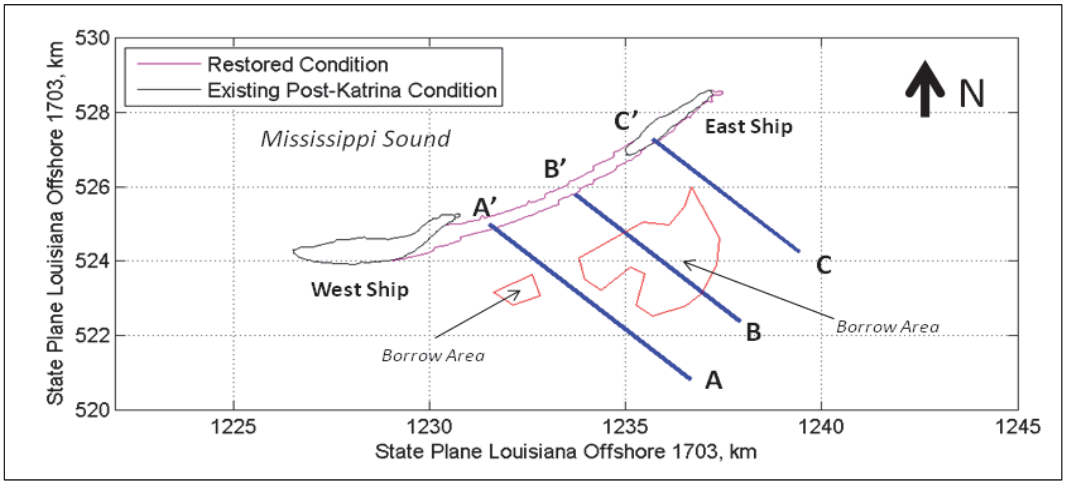

Figure 6-21. Bottom position (referenced to m NAVD88 2004.65) along Transect B-B'. Note that the cross-shore distance of 0 m corresponds with the incident wave location shown in Figure 6-6.

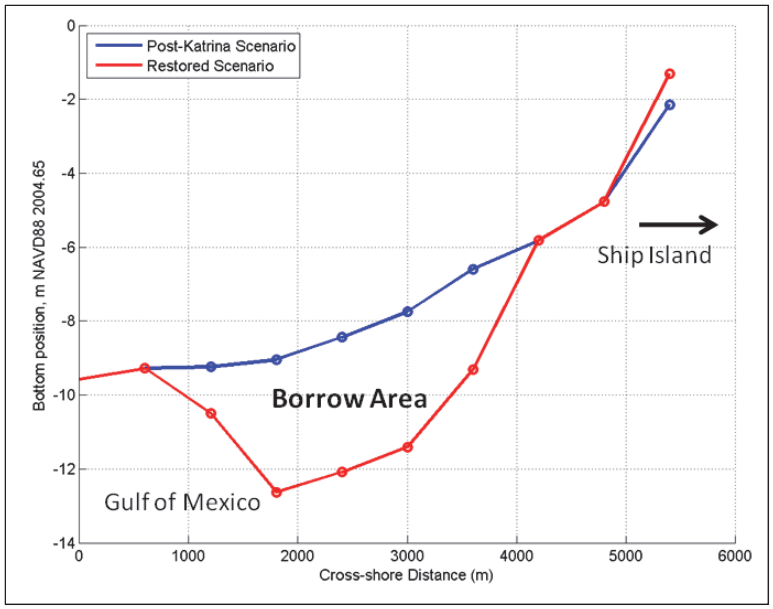

The borrow areas produce a local reduction in wave energy, i.e. a divergence of wave rays, for the Restored (Dredged) scenario when compared to the existing Post-Katrina scenario. For all of the synthetic storms, de-focusing of wave energy and de-shoaling effects are observed along Transect B-B' such that the Restored (Dredged) scenario results in lower significant wave heights across this transect. Figure 6-22 shows an example of the cross-shore progression of significant wave height during a synthetic storm peak and the divergence of wave energy observed over the borrow areas.

Because wave energy flux is conserved and the borrow areas produce a local divergence of wave rays for the Restored (Dredged) scenario, an increase in wave energy (i.e. a convergence of wave rays) is observed at the fringes of the borrow areas when compared to the existing Post-Katrina scenario. For all of the synthetic storms, focusing of wave energy and refraction effects are observed along Transect A-A' and Transect C-C' such that the Restored (Dredged) scenario results in larger significant wave heights across these transects. Figures 6-23 and 6-24 show an example of the cross-shore progression of significant wave height during a synthetic storm peak and the convergence of wave energy observed at the fringes of the borrow areas.

Figure 6-22. Significant wave height (m) versus cross-shore distance along Transect B-B' during synthetic storm peak. Divergence of wave energy is observed over the borrow areas.

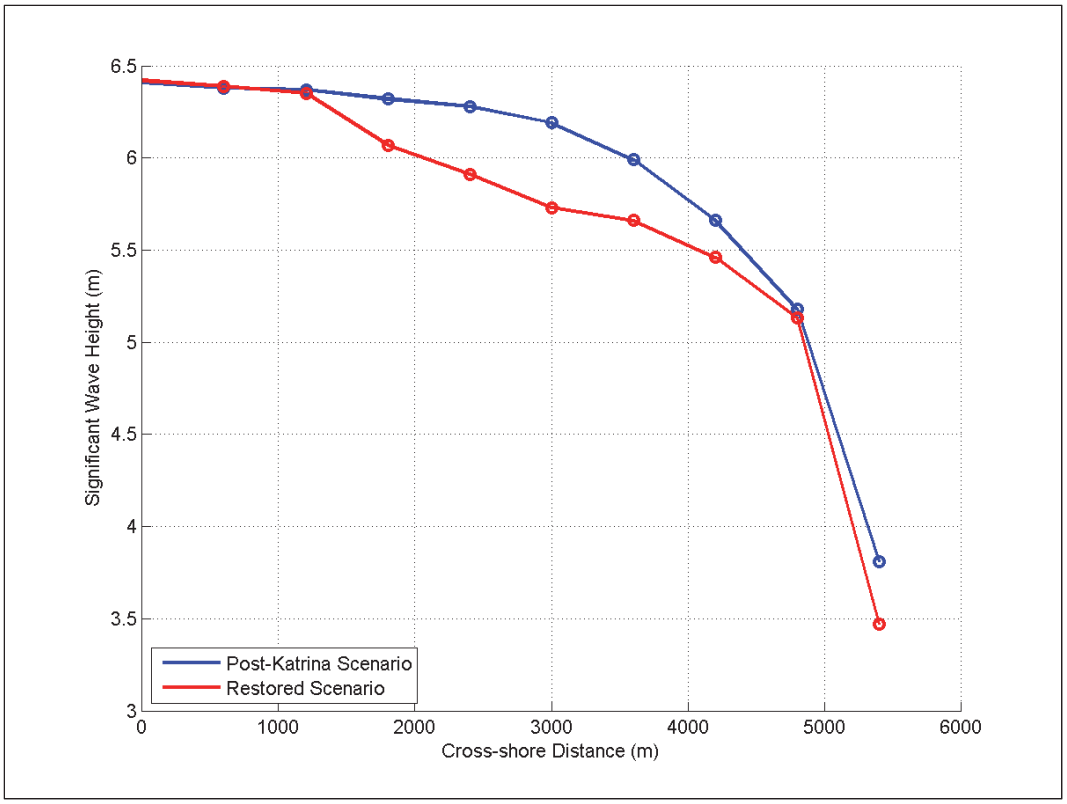

Figure 6-23. Significant wave height (m) versus cross-shore distance along Transect A-A' during synthetic storm peak. Convergence of wave energy is observed at the fringes of the borrow areas.

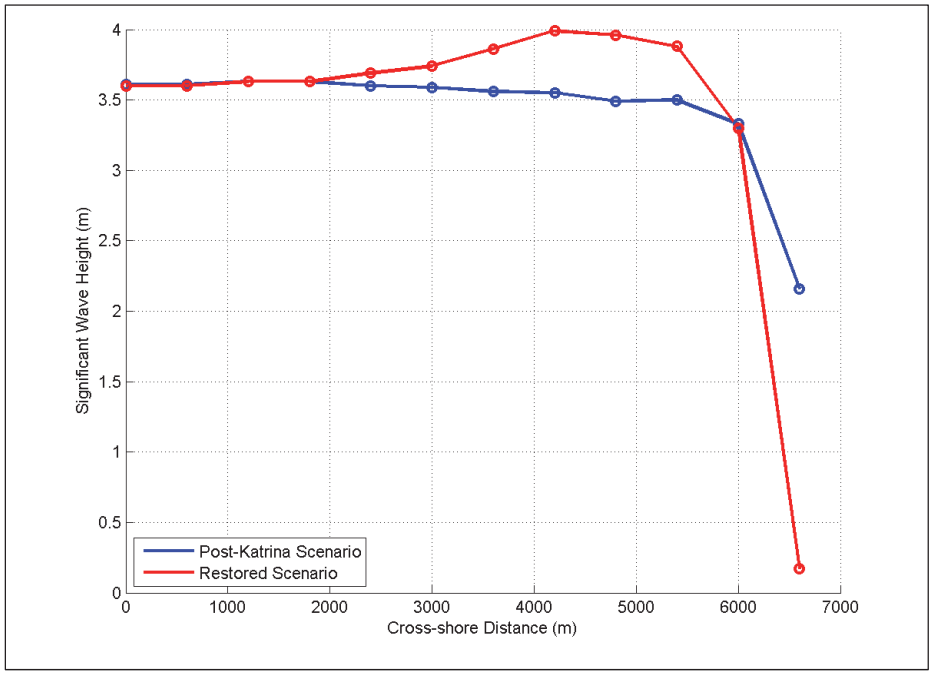

Figure 6-24. Significant wave height (m) versus cross-shore distance along Transect C-C' during synthetic storm peak. Convergence of wave energy is observed at the fringes of the borrow areas.

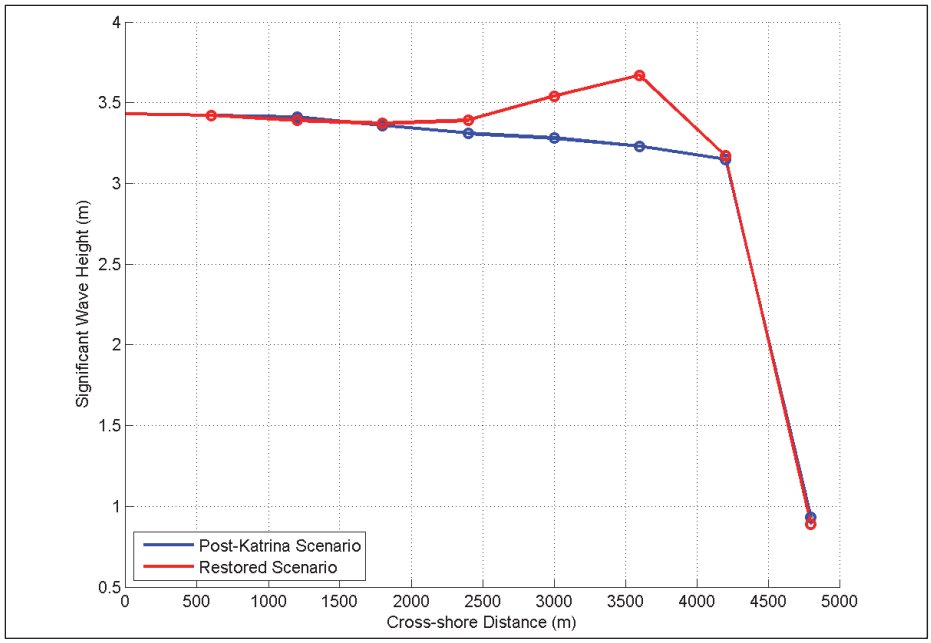

6.7 Conclusions

The purpose of this chapter was to examine the wave changes which result from a degraded and restored Ship Island, when compared to the existing Post-Katrina Ship Island scenario. Relative changes resulting from the barrier island restoration and degradation are quantified through the application of an integrated coastal storm modeling system.

Results indicate that closure of Camille Cut and Ship Island restoration does have the potential to reduce storm waves at the mainland coast. Maximum wave height reduction at the mainland Mississippi coast ranges from 0.2 m to 1.25 m relative to the existing condition. The magnitude of wave height reduction was found to be controlled by the storm characteristics, primarily minimum central pressure (maximum wind speed), radius to maximum winds, forward speed, and trajectory. Barrier island restoration reduced waves by as much as 0.2 m to 0.4 m for four of the 15 synthetic storms, 0.4 m to 0.6 m for five of the 15 synthetic storms, and by greater than 0.6 m for six of the 15 synthetic storms. The greatest decrease in wave heights observed at the mainland Mississippi coast for this storm suite was 1.25 m for Storm 825.

The maximum wave height increase at the mainland Mississippi coast as a result of East and West Ship Island degradation ranges from 0.2 m to 0.4 m, with the majority (13 of 15) of the synthetic storms experiencing a maximum wave height increase of 0.2 m. The largest areas of wave height increase are in the leeward areas behind East and West Ship Island, which were degraded to subaqueous shoals. Maximum wave change potential at the mainland Mississippi coast is smaller for the Degraded scenario than for the Restored scenario because wave energy can penetrate from the Gulf of Mexico into Mississippi Sound for both the existing Post-Katrina and degraded scenarios.

The restored scenario has the potential to block a significant portion of wave energy from penetrating into the Mississippi Sound. Table 6-7 provides a summary of maximum wave height reduction (ΔH) for the restored vs existing Post-Katrina conditions and the Restored vs Degraded conditions at the mainland Mississippi coast. Wave height reductions vary from 0.2 m to 1.7 m at the mainland Mississippi coast for the suite of storms simulated for this study.

Table 6-7. Summary of maximum wave height decrease at the mainland Mississippi coast for the Restored vs Existing and Restored vs Degraded conditions. Note that the storm tracks are shown in Figure 6-5 and the associated storm characteristics are listed in Table 6-1. The incident wave condition location is shown in Figure 6-6.

Storm #	Track	Incident Wave Height (m)	Δ H (m) for Restored minus Existing Conditions	Δ H (m) for Restored minus Degraded Conditions
028	B	3.9	0.2	0.4
032	B	5.7	0.6	0.8
034	B	3.8	0.2	0.4
059	D	3.6	0.4	0.6
060	D	3.5	0.6	0.8
088	B	3.5	0.2	0.4
089	B	4.9	0.8	1.2
104	B	6.4	0.8	1.0
133	A	3.8	0.2	0.4
134	A	5.5	0.8	1.0
823	C	4.1	0.9	1.1
825	C	5.6	1.3	1.7
827	C	6.6	1.0	1.2
851	E	2.6	0.4	0.6
852	E	4.4	0.5	0.7

The effects of the offshore borrow areas on storm waves were quantified through the cross-shore progression of significant wave heights along three parallel transects in the vicinity of the borrow areas. The borrow areas produce a local reduction in wave energy along this transect, i.e. a divergence of wave rays, for the Restored (Dredged) scenario when compared to the existing Post-Katrina scenario. For all of the synthetic storms, de-focusing of wave energy and de-shoaling effects are observed along the transect that bisects the borrow area such that the Restored (Dredged) scenario results in lower significant wave heights across this transect. Because wave energy flux is conserved and the borrow areas produce a local divergence of wave rays for the Restored (Dredged) scenario, an increase in wave energy (i.e. a convergence of wave rays) is observed at the fringes of the borrow areas when compared to the existing Post-Katrina scenario. For all of the synthetic storms, focusing of wave energy and refraction effects are observed along the fringes of the borrow areas such that the Restored (Dredged) scenario results in larger significant wave heights across these transects. Again, it should be noted that the borrow areas described in this chapter represent a preliminary plan of borrow areas considered. Additional borrow area configurations were evaluated and further analyses have been conducted to determine the final borrow area configuration for Ship Island (described in Chapter 8).

7 Nearshore Sediment Transport Modeling[1]

7.1 Introduction

The Ship Island restoration plan includes direct sand placement in Camille Cut, increasing the island footprint, and additional sand placed into the local littoral zone. A numerical model prediction of morphological response and sand fate can assist in determining volumes and nearshore placement of sand. Beach replenishment is commonly used on long stretches of mainland coast, and these cases are well treated with a class of one-dimensional models. However, these simplified models are not appropriate for the Ship Island case with complex geometry and hydrodynamics. This chapter focuses on development and calibration of a 2D-H nearshore morphology model used in the evaluation of restoration alternatives. C2SHORE model formulation is presented with emphasis on the model framework and nearshore sediment transport predictions. The modeling system relies on separation of the coastal morphology domain from basin-scale models where the detailed nearshore hydrodynamic and sediment transport model is forced at boundaries by a basin-scale model. Verification of the methodology, as well as the circulation model, is presented herein with a comparison of field data measurements detailed in Chapter 2. The predictive capability of C2SHORE is demonstrated through an application at Ship Island for Hurricane Katrina. Finally, the performance of various restoration alternatives is assessed, including sensitivity to grain size for sediment placement and local offshore borrow sites.

7.2 Model formulation

The one-dimensional numerical model, CSHORE, has been under development for the past several years. The model predicts beach profile evolution over the nearshore region, and a full description of the model development is available in Kobayashi et al. (2009). A majority of the effort has been with sediment transport algorithms for a nearshore breaking wave environment. The model CSHORE was developed for cases with long straight coasts where gradients in longshore directed transport are negligible and waves constitute the principal generation mechanism for sediment suspension. This simplification is appropriate for the model developmental phase as the

[1] Written by Bradley D. Johnson, Coastal and Hydraulics Laboratory, US Army Engineer Research and Development Center, Vicksburg, MS.

great majority of laboratory tests are conducted in a flume, but is inappropriate for many practical applications such as the case of Ship Island. The extension of the one-dimensional sediment transport to a 2D-H framework in C2SHORE is outlined herein. The model application to Hurricane Katrina with strong overtopping currents and large waves constitutes a case that is substantially more energetic than any previous exercise.

From a computational perspective, the new 2D-H model differs substantially when compared to the one-dimensional technology. The profile evolution model, CSHORE, is a monolithic source code where waves, currents and sediment transport are computed simultaneously through an iterative landward-marching procedure. Alternatively, the C2SHORE model is comprised of a loosely coupled system of waves, hydrodynamics, and transport as depicted in Figure 7-1. C2SHORE, therefore, accommodates a greater choice of component models for circulation and wave prediction. However, the wave and current interaction is reliant on sequential execution of the independent models.

Figure 7-1. C2SHORE model coupling.

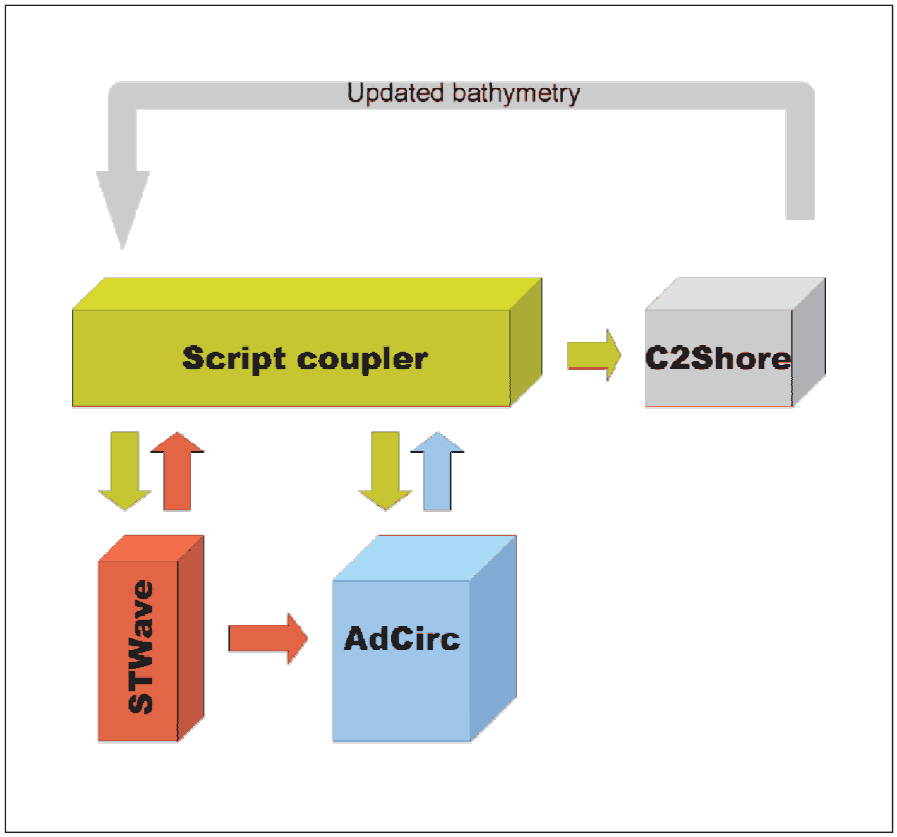

7.2.1 Wave predictions

The Ship Island effort detailed herein was completed using the STWAVE model for predictions of the nearshore wave field. STWAVE is a steady-state model for nearshore wind-wave evolution and propagation. The model numerically solves the steady-state conservation of spectral action balance along backward-traced wave rays using finite difference methods. STWAVE is applied routinely on coastal projects involving sediment transport and navigation to estimate the directional wave spectra and to predict wave height, period, and direction. Additionally, STWAVE can be used to predict wave generated radiation stresses in shoaling and breaking regions. The processes represented in STWAVE include refraction, shoaling, wave-current interaction, wave breaking, and wind wave generation. Input to the model includes bathymetry, offshore spectra, water levels, wind, and currents. Assumptions made in STWAVE include mild bottom slope; steady waves, currents, and winds; refraction and shoaling according to linear theory; depth uniform current; and radiation stresses given according to linear theory. Further details are provided by Smith et al. (2001).

7.2.2 Nearshore circulation

Nearshore circulation acts both to entrain sand and to advect suspended sediments and an accurate prediction of currents is required for predicting coastal morphology. Given the wide application and acceptance, the C2SHORE system used the ADCIRC model as a suitable two-dimensional finite-element-based horizontal (2DH) hydrodynamic solution of the shallow water equations. The governing mass continuity and momentum equations are combined into a single generalized wave continuity equation (GWCE) that is solved numerically in conjunction with the primitive momentum equations. The solution involves finite differencing in time and a continuous-Galerkin basis finite-element method in space. ADCIRC has the capability of solving for the vertical structure of the currents; to be consistent with the sediment transport formulation, however, the vertical variation is neglected and the depth integrated equations are solved. Details of the ADCIRC model are provided in Westerink et al. (1994). The continuous-Galerkin version of ADCIRC based on the GWCE is known to suffer inaccuracies in local mass conservation in shallow water. However, as explained subsequently, this effort utilizes a finite-difference sediment transport and morphology grid, and mass conservation is ensured.

7.2.3 Nearshore sediment transport

Sediment transport rates are predicted based on the computed wave and hydrodynamics from the component models as previously described. Following the methods of Kobayashi et al. (2009), the instantaneous velocity, *UT*, associated with the random wave is assumed to follow a Gaussian distribution with a zero mean and standard deviation σT. The probability density function of a random variable is prescribed as follows:

$$f(r) = \frac{1}{\sqrt{2\pi}} exp\left(-\frac{r^2}{2}\right) \tag{7.1}$$

Where, $r = U_T/\sigma_T$. Assuming a relationship between the free-surface oscillation and utilization of the linear long wave theory permits the expression of the standard deviation of wave-orbital velocity in terms of the wave model predictions:

$$\sigma_T = \frac{\sigma_n c}{h} = \frac{\sqrt{8} H_{rms} c}{h} \tag{7.2}$$

Where, σ_η is the standard deviation of the free surface position and H_{rms} is the root-mean square wave heights as predicted by STWAVE, *c* is the linear wave phase speed, and *h* is the phase-averaged water depth.

7.2.4 Bedload transport

Sediment is assumed to be characterized by a single grain size, d_{50}, with a fall velocity *wf* and sediment specific gravity *s*. The initiation of bed sediment transport is predicted to occur for conditions with an instantaneous bottom shear stress in excess of a critical shear, given in terms of the critical Shields parameter ψc and expressed as follows:

$$\tau_c = pg(s-1)d_{50}\psi_c \tag{7.3}$$

Where, ρ is the unit weight of water, *g* is gravitational acceleration. In the following work, the critical Shields parameter ψ_c is assumed constant and equal to 0.05. The instantaneous bottom shear stress τ'_b is expressed according to the standard quadratic formulation:

$$\tau_b = p\frac{f_b}{2}U_a^2 \tag{7.4}$$

Where, f_b is a wave friction factor and U_a is the total instantaneous velocity including current and wave orbital components. The expressions above can be combined with the distribution of the wave orbital velocities (Equation 7.1) to compute the probability of bedload sediment movement, P_b. Recognizing that the probability of sediment movement is equal to the probability of the exceedance of the critical shear leads to the following:

$$P_b = \int_{-\infty}^{+\infty} f(r) H\left(\tau_b(r) > \tau_c\right) dr \tag{7.5}$$

Where, H is Heaviside step function whose value is zero for negative argument and one otherwise. The expression in (7-5) is integrated numerically to compute P_b. Previous works detailing the one-dimensional model CSHORE (e.g. Kobayashi et al. 2008; 2009) have assumed currents were small relative to the wave orbital velocities and expressed the bedload as a function of the wave height. To permit a more general computation, the existing CSHORE formulations are extended to include current-dominated cases, extending application to cases including overwash and strong tidally generated currents, for instance. As in Kobayashi et al. (2009), the assumption of the classic velocity-cubed bedload model is made $\bar{q} = B\overline{|\overline{U_a}|^2 \overline{U_a}}$ where B is an empirical parameter. Substitution of the total velocity with the vector component of the currents and wave orbital velocity and averaging over the probability space in (Equaiton 7.1) yields, for instance, the bedload transport in x:

$$q_{bx} = B\left(U^3 + U\sigma_T^2 + UV^2 + 2\sigma_T^2\left(U\cos^2\alpha + V\cos\alpha\sin\alpha\right)\right) = BF_U \tag{7.6}$$

Where, U,V are the components of the steady current in the x and y direction, and α is the angle of wave propagation as computed by STWAVE. The previous one-dimensional efforts have resulted in a simple formula for the bedload that implicitly accounts for wave asymmetry by prescribing a bedload transport aligned with the direction of the wave propagation $q_{bx} = [bP_b\sigma_T^3]/[g(s-1)]$ where b is an empirical factor taken as 0.001 in this work. In an effort to maintain compatibility with the vast work done in the calibration of this expression for wave-dominated beaches, the following recombination is proposed:

$$\left(q_{bx}, q_{by}\right) = \frac{P_b}{g(s-1)}\left[b\sigma_T^3(\cos\alpha, \sin\alpha) + \left(\frac{f_{wc}}{2}\right)^{3/2}\gamma\left(F_U, F_V\right)\right] \tag{7.7}$$

Where, B is expressed in terms of the empiric current related factor $\gamma \sim 8$ and the wave-current friction factor f_{wc}, and:

$$F_V = \left(V^3 + V\sigma_T^2 + VU^2 + 2\sigma_T^2\left(V\sin^2\alpha + U\cos\alpha\sin\alpha\right)\right) \tag{7.8}$$

7.2.5 Suspended transport

Following Kobayashi et al. (2009), the degree of sediment suspension is estimated using an empirical expression of the instantaneous turbulent energy dissipation due to bottom friction. It is assumed that the probability of sediment suspension is given by the probability that a near-bed turbulent velocity given by $k = \left(f_b/2\right)^{1/3}|U_a|$ exceeds the sediment fall velocity, w_f. Analogous to the previously shown expression for P_b, the probability of sediment suspension is computed as follows:

$$P_s = \int_{-\infty}^{+\infty} f(r)H\left(k(r) > w_f\right)dr \tag{7.9}$$

Which is numerically integrated, and the volume of suspended sediment per unit area, V_s, is computed as a simple empirical function of the dissipation as introduced in Kobayashi and Johnson (2001):

$$V_s = P_s \frac{e_B D_B + e_f D_f}{pg(s-1)w_f}\sqrt{1 + S_x^2 + S_y^2} \tag{7.10}$$

Where, e_B and e_f are empirical suspension efficiencies for the energy dissipation rates D_B and D_f due to wave breaking and near-bed frictional dissipation respectively, and S_x and S_y are the bottom slope in the x and y directions. Without regard to the source or details of estimation in the nearshore wave field, the total dissipation rate $D = D_B + D_f$ is determined from the bulk energy balance from the wave model, written as follows:

$$-D = \frac{\partial E_{fx}}{\partial x} + \frac{\partial E_{fy}}{\partial y} \tag{7.11}$$

Where, E_{fx}, E_{fy} are the wave energy flux in the x, y directions respectively. The energy fluxes are computed directly from the STWAVE predictions for wave height, H_{rms}, and propagation angle α:

$$\left(E_{fx}, E_{fy}\right) = \tfrac{1}{8} pgH_{rms}^2 C_g \left(\cos\alpha, \sin\alpha\right) \tag{7.12}$$

The time-averaged near-bed frictional dissipation D_f is computed with the previously assumed wave orbital velocity probability density function and makes use of quadratic friction:

$$D_f = \frac{1}{2} p f_b \overline{U_a^3} = \int_{-\infty}^{+\infty} \left[\left(\bar{U} + r\sigma_T \sin\alpha \right)^2 + \left(V + r\sigma_T \cos\alpha \right)^2 \right]^{3/2} f(r)dr \tag{7.13}$$

Where, (Equation 7.13) is numerically integrated. Suspended sand transport is driven by the depth-averaged currents as predicted by the ADCIRC model with specific consideration for the effect of the waves on net sediment drift. The return current due to the mass flux of the waves, for instance, can generate an off-shore directed transport within the surf zone that is responsible for erosion during storm conditions and the components of velocity are expressed in a general way with linear long wave theory as follows:

$$U_R, V_R = -g\sigma_T \frac{H_{rms}}{\sqrt{8}c} \left(\cos\alpha, \sin\alpha\right) \tag{7.14}$$

This relation, in effect, dictates that any wave-generated mass flux is balanced locally by a current below trough level directed anti-parallel with the wave vector. The accuracy of such an assumption is not fully understood and this contribution must be included cautiously. It is not expected, for instance, to have the effect of a return current in the longshore direction for the case of obliquely incident waves over a cylindrical coast. Nevertheless, it is likely that the mass-flux contribution will be small relative to the pressure driven or radiation stress driven flows developed within the circulation model. For instance, in a moderate wave climate with obliquely incident waves, longshore currents may be O(1 m/sec) while the wave-generated mass flux distributed over depth is typically O(0.1 m/sec). Therefore, violations of the local balance assumption may contribute a small error and will not manifest as unreasonable predictions of suspended sediment transport.

Alternatively, the phase-coupling of the time-dependent wave-orbital velocities and sand concentrations can result in a transport aligned with the direction of wave propagation. Based on laboratory measurements detailed in Kobayashi et al. (2005), the magnitude of the wave-related transport was found to scale with the undertow. The proposed expression including the 2DH current field, return current and wave-related transport can therefore be expressed simply as follows:

$$q_{sx} = V_s\left(\overline{U} + a\overline{U}_R\right); q_{sy} = V_s\left(\overline{V} + a\overline{V}_R\right) \tag{7.15}$$

Where, a is an empiric factor less than one considering the opposing return current and wave-related transport directions and a value of a=0.5 is used throughout this study.

7.3 Model validation

The C2SHORE system applies the ADCIRC model as a suitable two-dimensional horizontal (2DH) hydrodynamic solution of the shallow water equations. Within the nearshore region, where significant sediment transport occurs, circulation originates from pressure gradients such as tidal and rivers flow, and through an applied shear stress from wind and variations in the wave height. As previously mentioned, wave height variations due to breaking are a primary driver of coastal circulation. Any accurate hydrodynamic solution of the surf zone, therefore, must resolve the breaking region well. Grid spacing must be sufficiently refined, enough to have approximately ten grid cells or elements in the surf zone in the cross-shore direction. This greater or increased resolution is required for both the wave model and circulation models. Considering the Courant limitation for model stability and the dependence on grid spacing, it is necessary to separate the coastal morphology domain from the basin-scale model domains. The typical C2SHORE coupled model system domain is several km in length, and so flows deriving from pressure gradients are developed in the model through the application of appropriate boundary conditions. For instance, storm surge can inundate and/or overwash a barrier island during a storm or hurricane event. The surge growth takes place over thousands of kilometers, which is much larger than the C2SHORE domain. The effects of surge can be modeled, nonetheless, with the careful application of water level and volume flux boundary conditions. With careful prescription of hydrodynamics at the seaward and bay boundary conditions, model circulation can be developed to entrain and advect sediment.

7.3.1 Nearshore hydrodynamics

Accurate nearshore morphology modeling is dependent on reliable and skillful estimates of nearshore waves and currents. As a provisional step in the estimation of morphology response, the circulation model was compared with the recently collected field data detailed in Chapter 2. To develop boundary conditions for the highly resolved nearshore domain, the ADCIRC model was run at the basin scale with a coarse grid with a domain width of approximately 300 km, spanning the Mississippi Sound. The Mississippi Sound ADCIRC grid is discussed in Chapter 3. Non-physical initial transients are generated from the cold start model initiation, and 30 days of model run are computed, allowing friction to attenuate the effects. The Mississippi Sound grid has been applied for other numerical modeling efforts and has demonstrated accurate predictions of water level and depth-averaged velocity. A comparison of tide level prediction compared with data measured at the two station locations depicted in Figure 7-2 is shown in Figures 7-3a and 7-3b.

The basin-scale hydrodynamics were computed without the effect of waves considering that radiation stresses are only important near the shoreline and do not affect the large-scale solution. However, the effect of wave breaking and radiation stresses are included in the prediction of the detailed nearshore currents.

Figure 7-2. Location map showing the two 2010 ERDC wave gauge deployment locations near Ship Island (from Chapter 4).

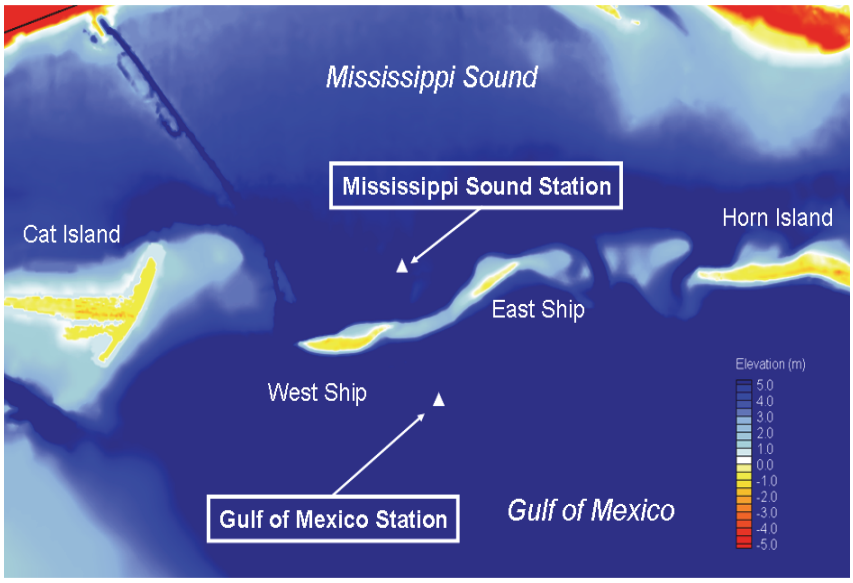

Figure 7-3a. Water level modeled (red) and measured (black), at the Gulf of Mexico wave gauge (30.1854 N, 88.9137 W).

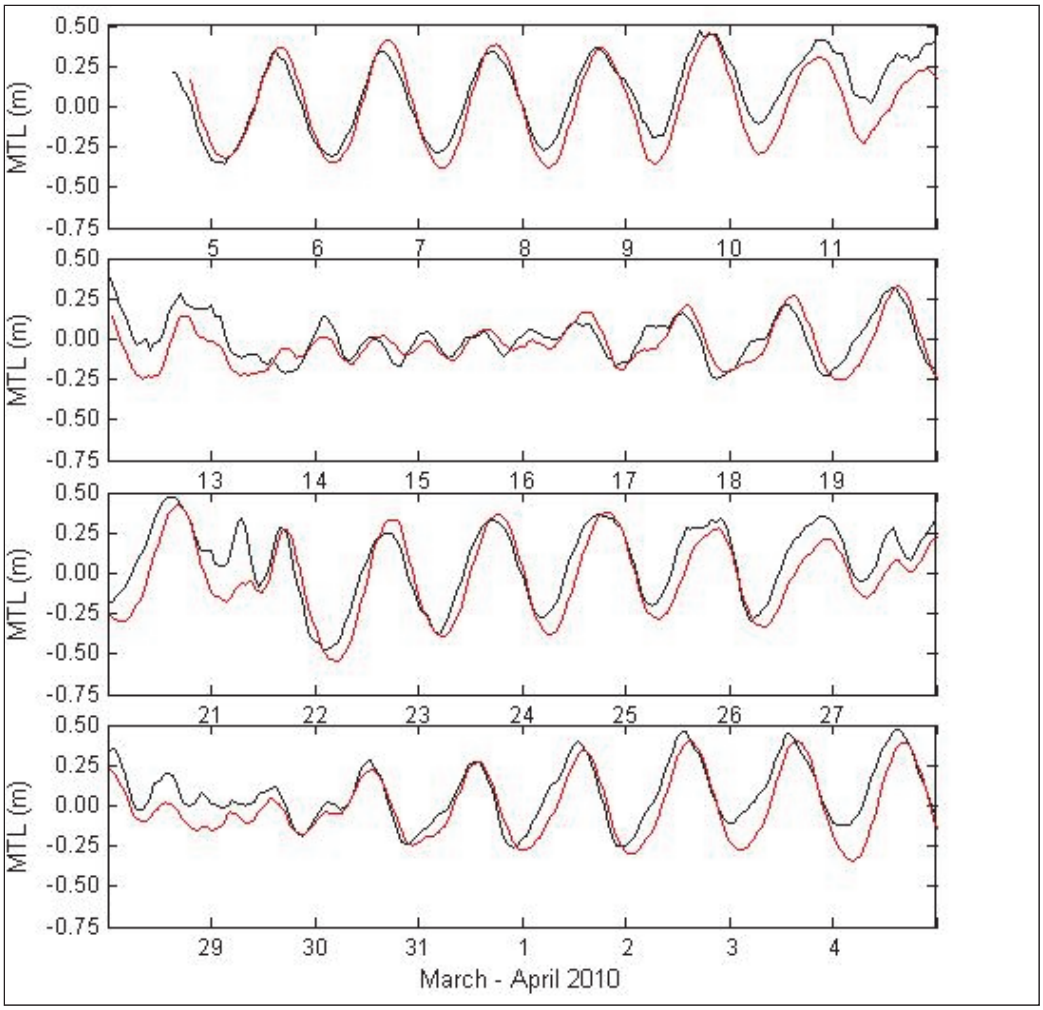

The previous results demonstrate a satisfactory comparison of the measured water levels and the ADCIRC computations on the Mississippi Sound grid (refer to Figures 7-3a and 7-3b). The C2SHORE model, generally, is appropriate for a smaller nearshore domain and is reliant on accurate boundary conditions to faithfully replicate currents and water levels associated with basin-scale forcing, such as tides or storm surge. To validate the methodology of inset model coupling for Ship Island, a smaller detailed domain that uses boundary conditions developed from the larger domain Mississippi Sound computations are compared to measured velocity data herein. As detailed in Chapter 2, a total of 13 transects of ADCP data in Camille Cut were collected on 31 March 2010 and 01 April 2010. The C2SHORE model domain used to predict the primarily tidally-driven flow is depicted in Figure 7-4, spanning approximately 400 square kilometers.

Figure 7-3b. Water level modeled (red) and measured (black), at the Mississippi Sound wave gauge (30.2466 N, 88.9332 W).

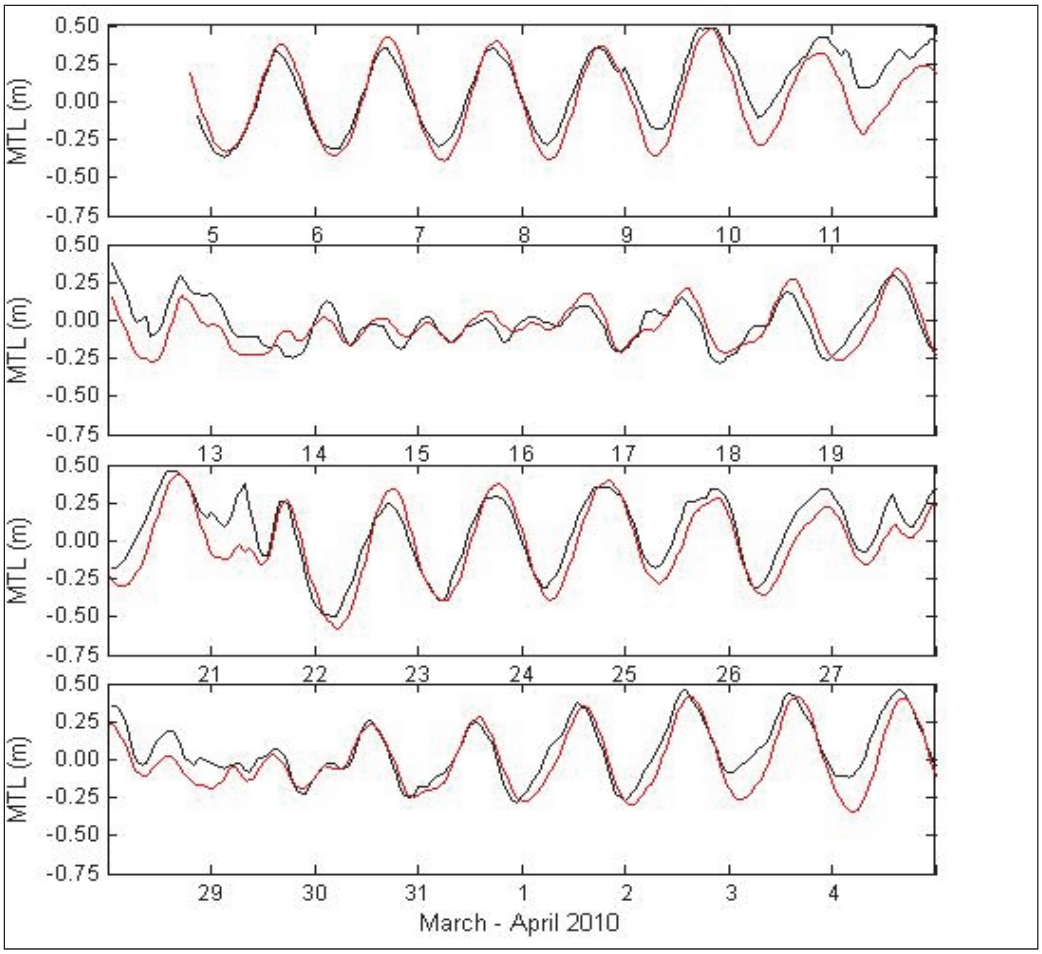

The resolution of the smaller nearshore domain ranges from 200-m in offshore deep water to 50-m through Camille cut. A combination of flux and water level boundary conditions were implemented on the nearshore domain. To properly model surge inundation, the south and east boundaries are prescribed fluxes, and the model is properly specified with water levels forcing on the north and west boundaries. The time-variation of the free surface position or flux is interpolated from the ADCIRC Mississippi Sound solution and specified at each node of the C2SHORE boundary. For simplicity, only the time-series of the average boundary forcing is depicted in Figure 7-5, where the given water level is the mean of the free surface position of all boundary nodes on the north and west. Data used in this hydrodynamic validation was collected from approximately 15:00 31 March 2010 to 0:00 01 April 2010, as described in more detail in Chapter 2. Moderate tidal amplitude of 0.2 m is evident during the period of validation, where the first data were collected during the flood tide and the last data were collected during the ebb tide conditions.

Figure 7-4. Nearshore C2SHORE model domain for hydrodynamic validation against 2010 measured data.

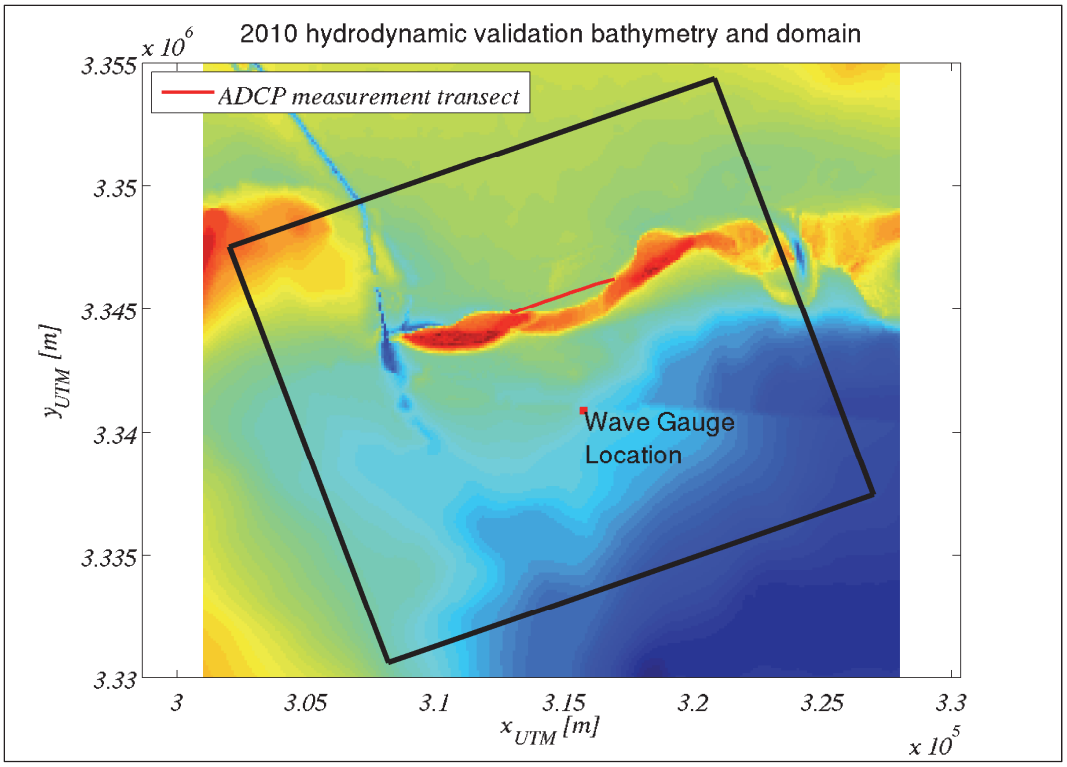

Figure 7-5. Time-variation of boundary conditions for hydrodynamic validation against 2010 measured data.

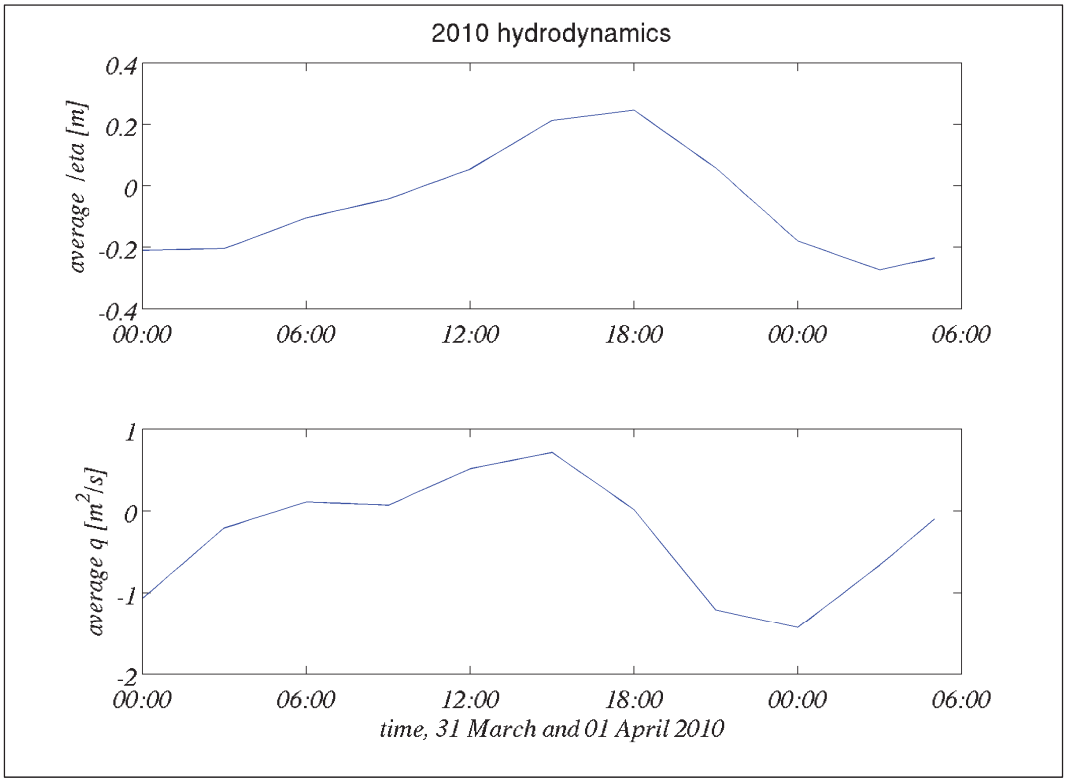

The study region is relatively shallow, and effects of wind stress are therefore included in the hydrodynamic computations. Figure 7-6 shows the time variation of wind magnitude and direction for the validation study period. With a peak wind of 7.0 m/sec, the stress was small in magnitude during 31 May 2010, but it has been included as an additional ADCIRC forcing for completeness.

Figure 7-6. Time-series of measured wind data.

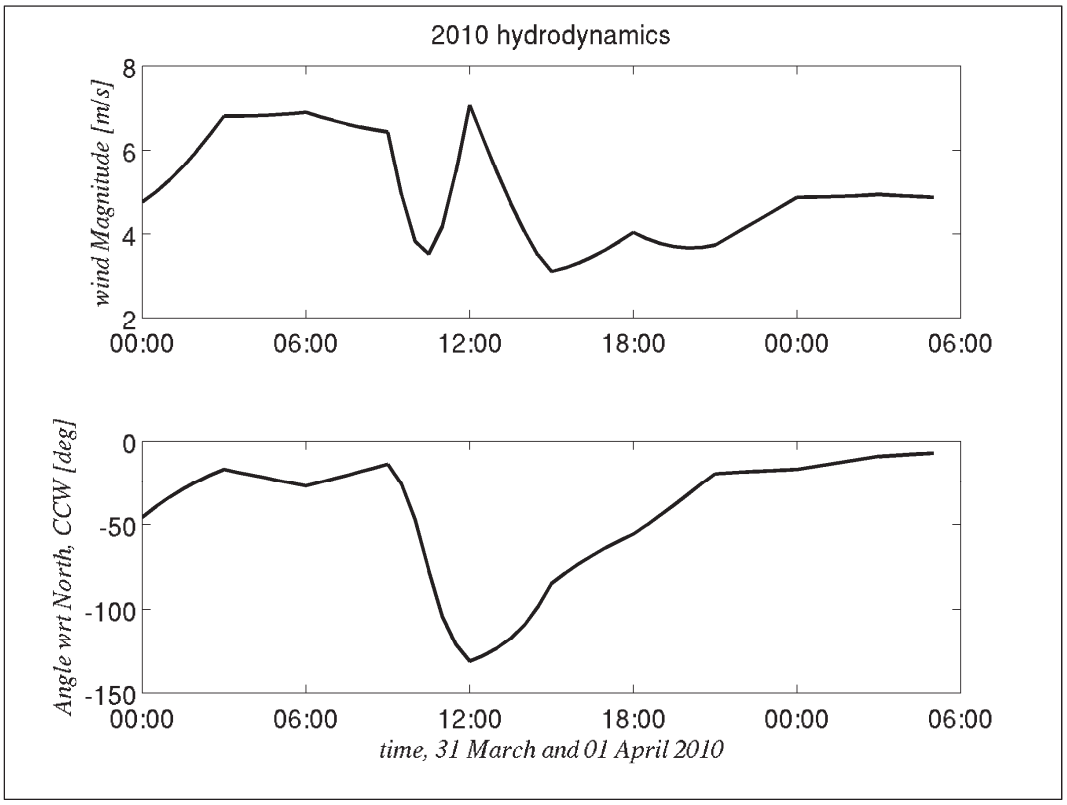

In conjunction with the collection of ADCP data, wave gauges were deployed near Ship Island, as shown in Figure 7-2. The data from the Gulf of Mexico gauge (also depicted in Figure 7-4) can be used as an offshore boundary condition for the STWAVE model. Strictly speaking, the measured data should be transformed in height and angle for use on the seaward boundary. However, the waves were small during the period of validation and shoaling and refraction changes were considered insignificant. A simple energy flux conservation and application of Snell's Law indicates that the differences in the wave parameters are less than 2.0 percent with the transformation. Therefore, for simplicity, the measured wave parameters were applied at the boundary without modification.

The variation of offshore wave parameters is shown in Figure 7-7. Low energy conditions were measured at the wave gauge during the time of data collection, spanning from 15:00 to 00:00, and it is expected that the wave stress contribution was minor. Nevertheless the wave stress is included in the following comparison for completeness.

Figure 7-7. Time-series of measured wave data at the South gauge.

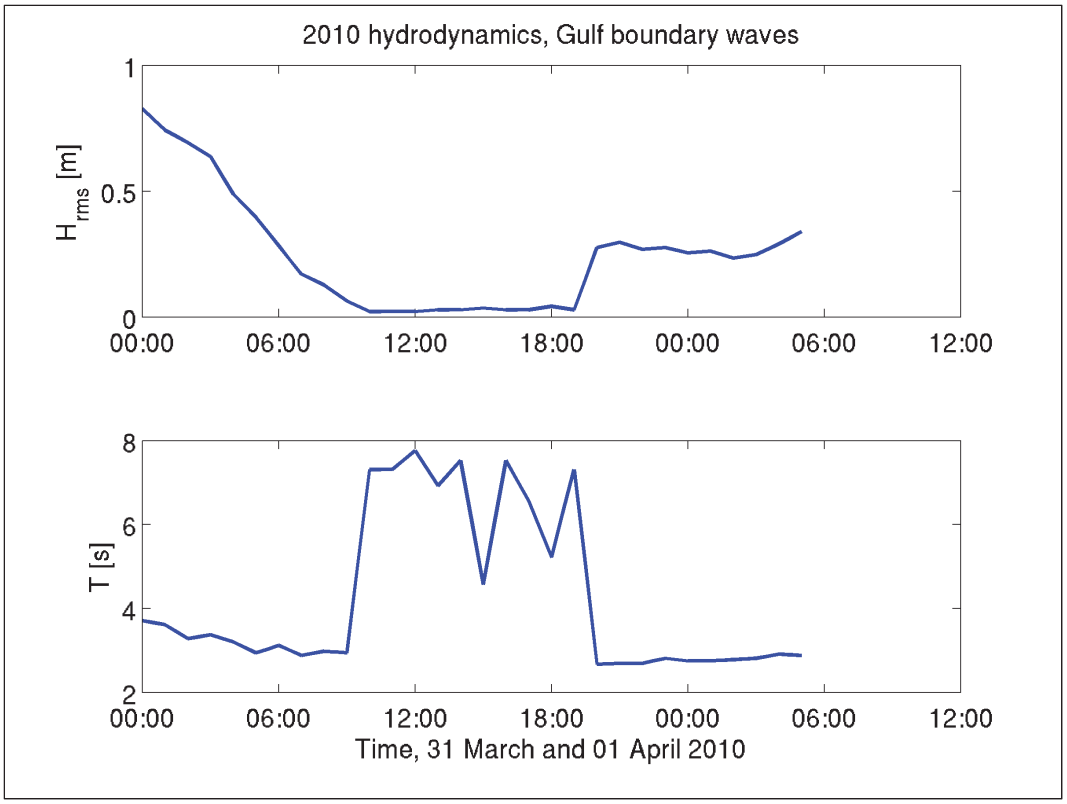

ADCP data collected at 15:30, near the peak flood tide, have been depth-averaged and are shown in Figure 7-8. To provide a sense of the degree of scatter in the data, all depth-averaged currents from the measurement transect are depicted as light grey arrows. The bin-averaged velocities are less prone to random error and are shown as red arrows. Measured flood velocities have substantial cross-channel variation with small magnitudes on the shallow edges and the largest velocity of approximately 20 cm/sec in the deepest part of Camille Cut. ADCIRC-computed velocities also are shown for comparison in Figure 7-8 as green arrows. In general, the computed velocities across the transect have less variability. It should be noted that the model domain bathymetry is based in part on an USGS interim product data from June 2008-June 2009 (Version 3). Bathymetry over which more recent measurements were taken or newly processed data may be substantially different from the ADCIRC depths in the existing

ADCIRC model domain. The degree to which this bathymetry inconsistency may affect the comparison of the computed results and measured data is unknown.

Figure 7-8. Computed and measured depth-averaged velocities during flood tide.

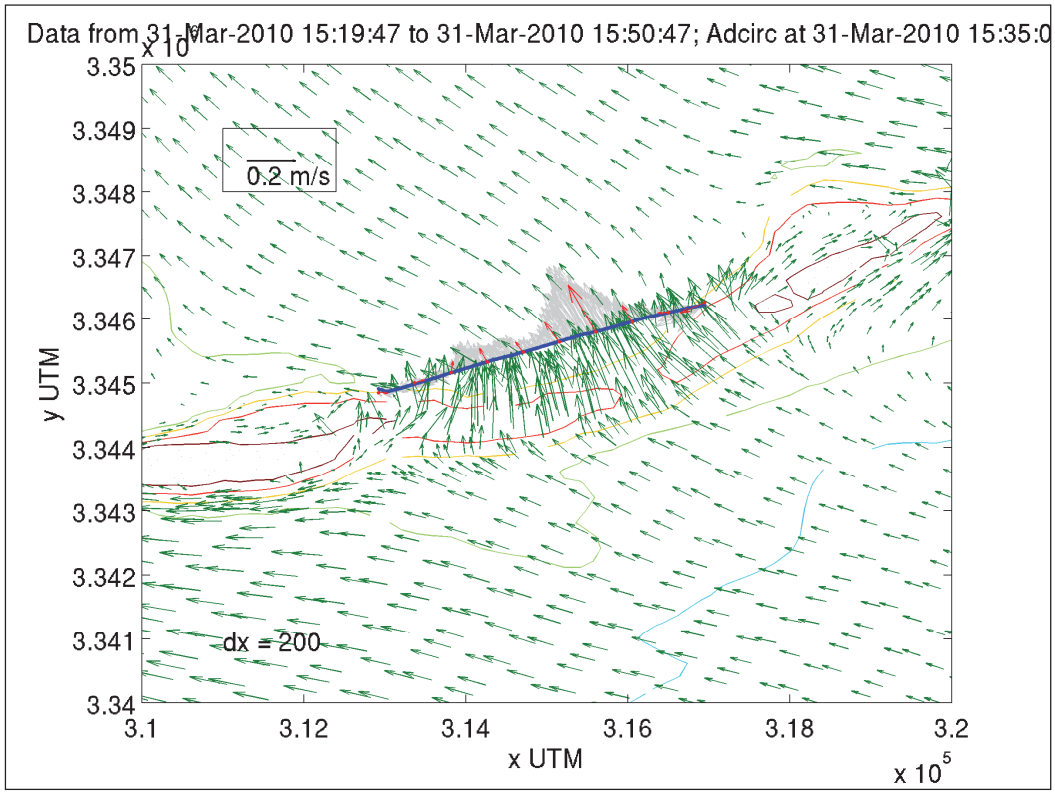

Measured and computed data for the ebb tide condition is shown in Figure 7-9. The arrow colors shown in Figure 7-9 are consistent with the colors in Figure 7-8, i.e. measurements are depicted as light grey arrows, bin-averaged measured velocities are shown as red arrows, and the ADCIRC-computed velocity field is shown as green arrows. For this comparison, the velocities associated with flood are smaller than the ebb currents. This asymmetry derives from the basin-scale model ADCIRC application and affects the small nearshore domain through the applied boundary conditions. It should be noted that this one tidal cycle may not be representative of the circulation in general. The measured flows for this ebb tide have less cross-channel variation and compare better with model computed velocities, as opposed to the comparisons with the flood stage shown in Figure 7-8. In general, the ADCIRC-computed velocities are in agreement with the measurements, both in terms of magnitude and direction.

Figure 7-9. Computed and measured depth-averaged velocities during ebb tide.

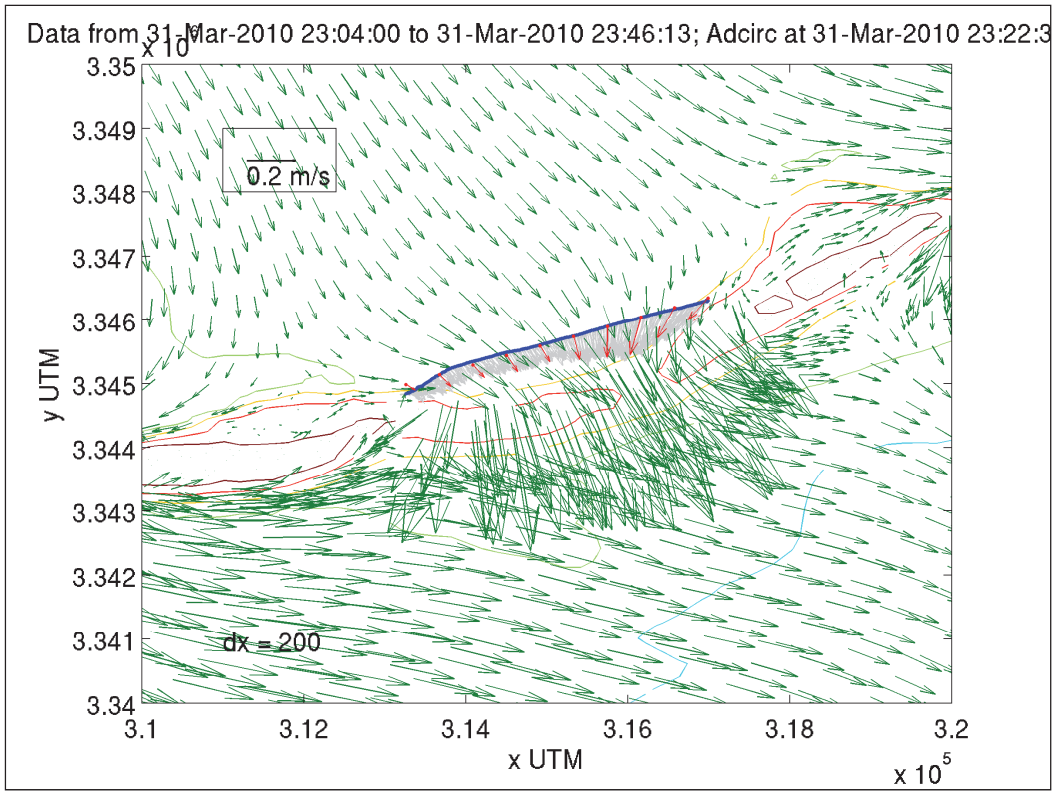

The C2SHORE model is ultimately used to predict channel morphology, and an accurate prediction of currents is therefore necessary. To ascertain the accuracy of the time-variation of currents through Camille Cut, the average velocity was computed from the measured data at 13 measurement intervals and compared with the model results. It is common in river flow, for instance to compare the total flux of water rather than the average velocity. In this case, velocity is a more reasonable metric considering the likely differences between present channel configuration and model domain bathymetry. In both cases, the average velocity is comprised of line integrals across ADCP measurement transects of length L, and computed as follows:

$$V = \frac{\int_L d\bar{u} \bullet \hat{n}\, ds}{\int_L d\, ds} \int \tag{7.16}$$

Where, d is the depth, $\bar{u}$ is the depth-averaged velocity vector, and $\hat{n}$ is the unit normal vector, defined positive to the northwest. Figure 7-10 shows the time-variation of measured and computed averaged velocity through Camille Cut. The measurements span a time period of eight hours, about

one half of a diurnal tidal signal. The ADCIRC model predictions agree well with the measured values, but exhibit an over-prediction of approximately 20 percent for both flood and ebb flows.

Figure 7-10. Computed and measured channel-averaged velocities.

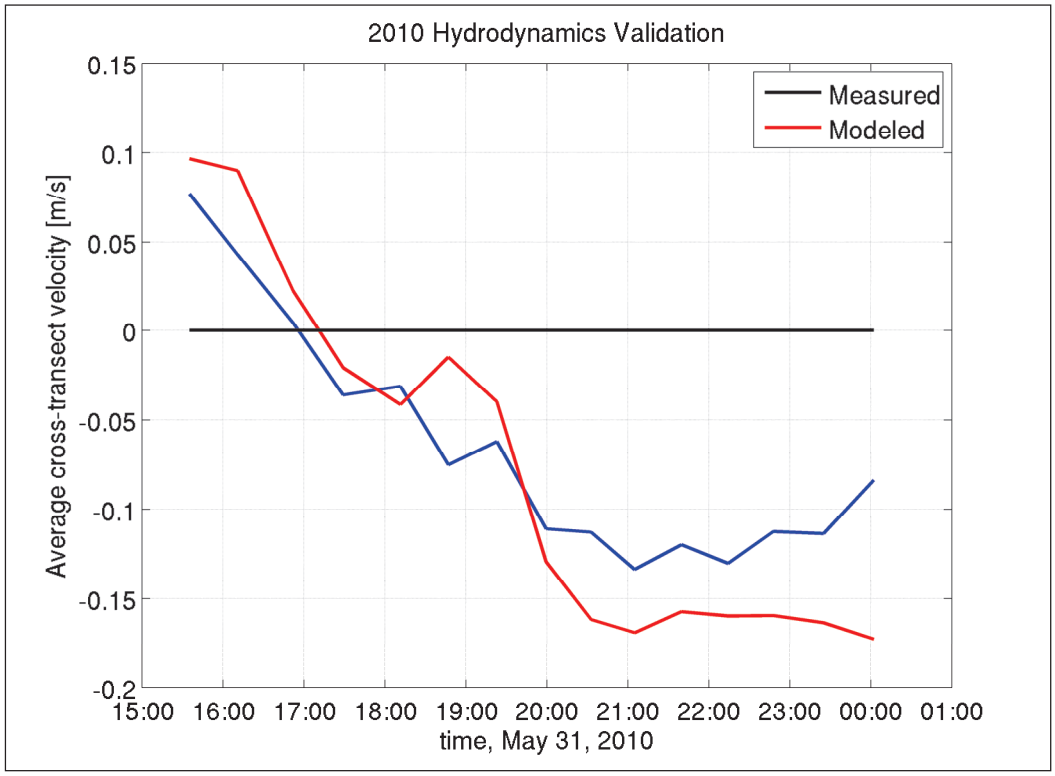

In summary, the C2SHORE model domain, including ADCIRC and STWAVE model components, has been set up for Ship Island and used measured velocity data to verify the computed hydrodynamics. For the period of measurements, both the winds and waves were small, and the primary mechanism in driving nearshore circulation is expressed through boundary forcing conditions. Model computations compare well with measured currents for flood and ebb tide, although some details of the current field are poorly predicted. The model domain may differ substantially from the recent bathymetry, however, and may affect the comparison. The channel-averaged velocity, on the other hand, may be less dependent on the channel shape and the model results compare well with the measurements.

7.3.2 Morphology

To build confidence in the developed model and to validate the selection of empirical parameters, the C2SHORE morphology model was applied at

Ship Island for Hurricane Katrina and compared to measured data. With pre- and post-storm bathymetry and topography available, this numerical investigation provides an opportunity to assess the new model.

The large and destructive Hurricane Katrina crossed the Mississippi Sound on August 29, 2005 with the center tracking 50 km to the west of Ship Island. Measurements and recent numerical model studies indicate that the wind and wave driven surge completely inundated the island and sustained hurricane force winds generated wave heights in deep water of more than 15 m (IPET 2008). Pronounced morphological changes were recorded with several meters of lowering and several hundred meters of shoreline recession on the Gulf side of the barrier islands. Camille Cut, the channel between East and West Ship islands, was stable and less than 1.0 km wide prior to Hurricane Katrina in 2005. Large waves and currents associated with Hurricane Katrina widened Camille Cut to approximately 3.0 km, and the significant change is depicted in Figure 7-11.

Figure 7-11. Ship Island before (top) and after (bottom) Hurricane Katrina. Note the significant widening of Camille Cut as a result of Katrina; Source: http://soundwaves.usgs.gov/2009/03/.

The Ship Island domain used in this nearshore sediment transport study is 20 km by 20 km, sized to maintain a reasonable computational burden and is shown in Figure 7-12 (as a red outline in the aerial photo) and in Figure 7-13 (the initial topobathy used for the Hurricane Katrina validation).

The half-plane version of STWAVE was used in this study; therefore, the domain was rotated 20 degrees counterclockwise from North to approximately align with the primary incident wave direction. The finite element

model ADCIRC uses an unstructured grid, and the element sizes ranged from 300-m to 100-m. STWAVE and the nearshore transport computations in C2SHORE utilize a coincident grid in this exercise with square cells of 100-m size.

Figure 7-12. Outline of 20 km x 20 km C2SHORE domain.

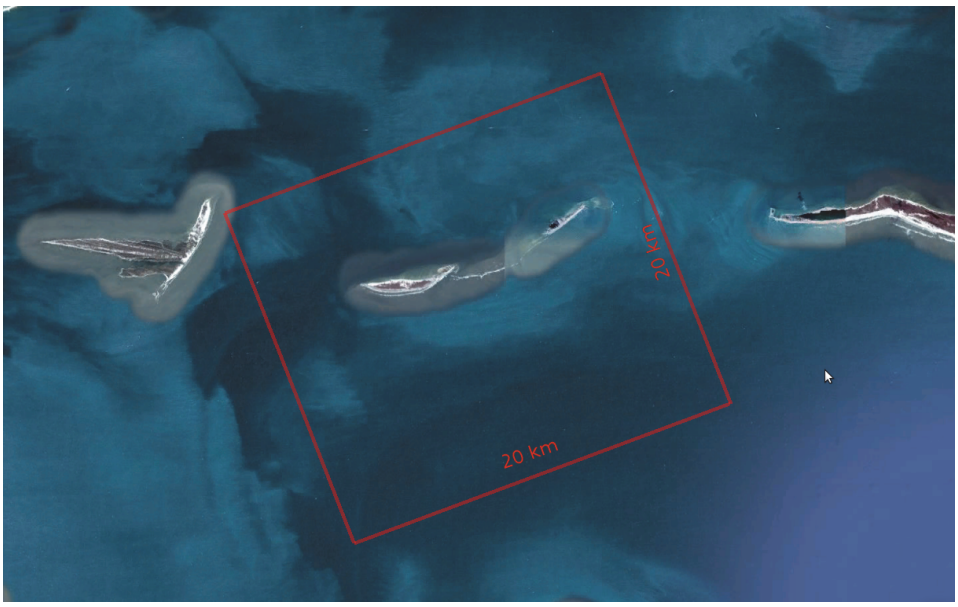

Figure 7-13. C2SHORE domain showing the initial condition (time = 0) topobathy for the Hurricane Katrina validation.

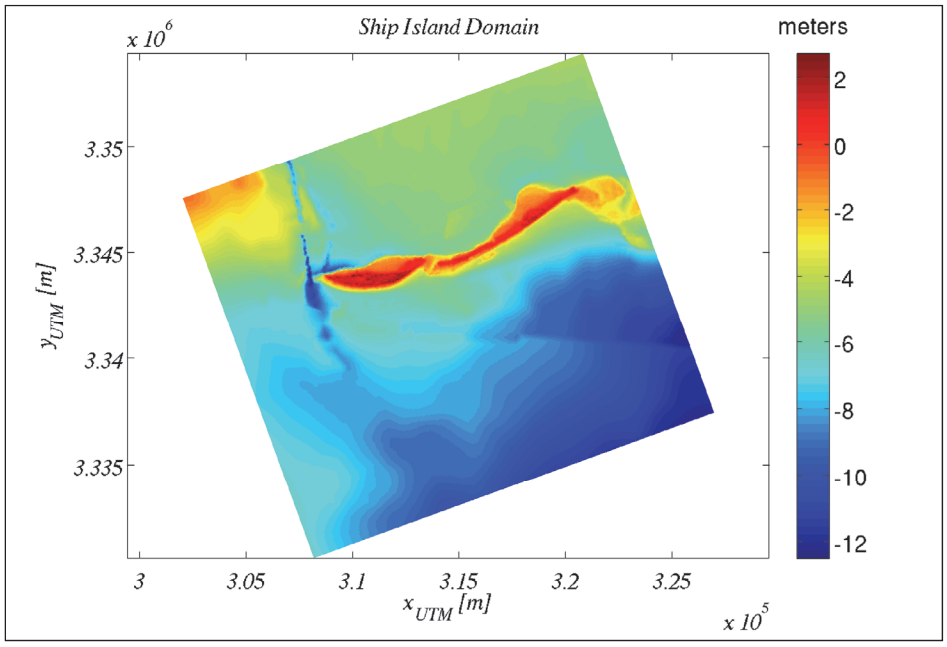

To impose the basin-scale currents within this smaller domain, a combination of forcing boundary conditions was employed. Conditions at

each boundary node are uniquely prescribed with flux conditions given on the southeast and northeast boundaries while water levels are given at the southwest and northwest boundaries.

The model exercise consisted of a 45-hour simulation beginning on August 28, 12:00 UTC, approximately one day prior to the peak of the incident wave conditions. An abridged set of boundary conditions is shown in Figure 7-14 where the largest wave height (top panel) of 4.5-m occurs at hour 25 (August 29, 13:00 UTC) and the largest surge of approximately 6-m [NAVD] lags by 2 or 3 hr. All of the 126 boundary node surge levels are depicted in Figure 7-14 (bottom panel) and demonstrate the degree of variation in water level over the 20 km C2SHORE domain.

Figure 7-14. An abridged set of boundary conditions for the Hurricane Katrina validation; Wave height is shown in the top panel and all 126 boundary node surge levels are shown in the bottom panel.

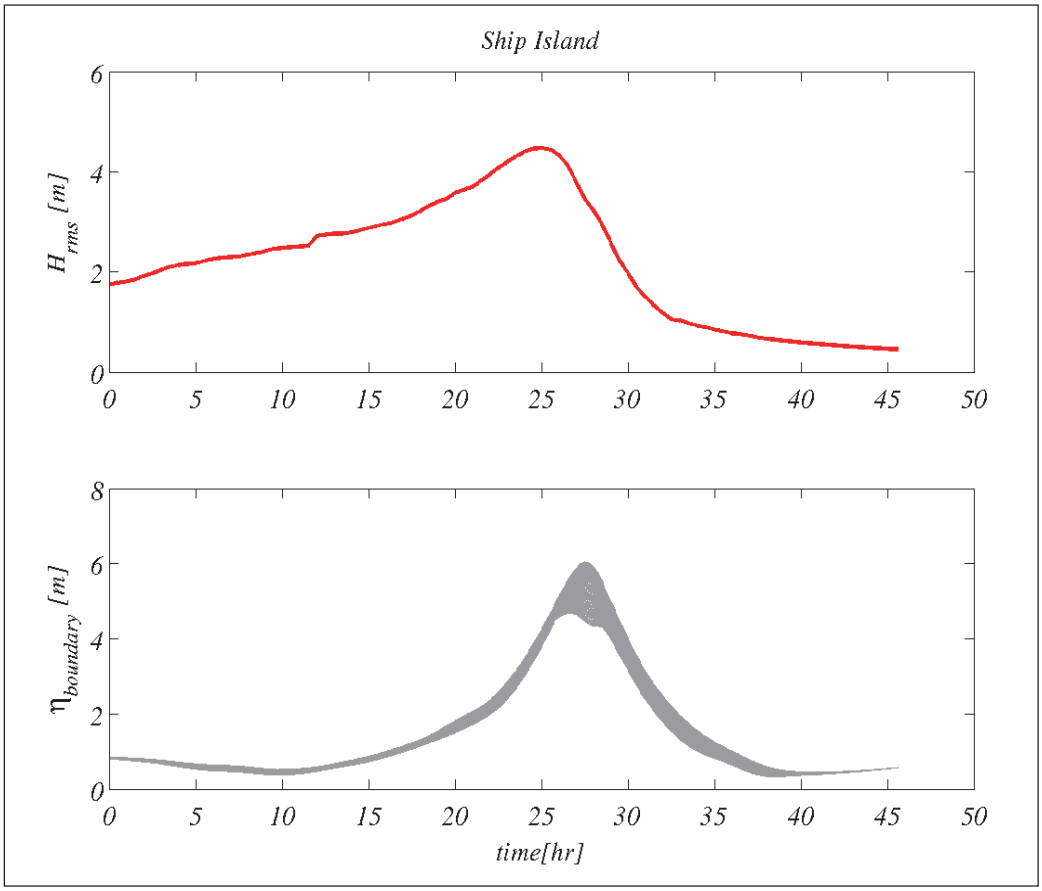

The wave field as computed by STWAVE at the peak of the storm is shown in Figure 7-15, where the large waves are nearly normally incident to the rotated domain. Depth limited breaking conditions are predicted for a

broad surf zone extending approximately 1 km from the barrier island crest. Figure 7-15 also shows the less energetic wave climate in the shadow of the island (Mississippi Sound side of Ship Island) where less sediment transport is expected.

Figure 7-15. Wave field modeled during the peak of the Hurricane Katrina validation.

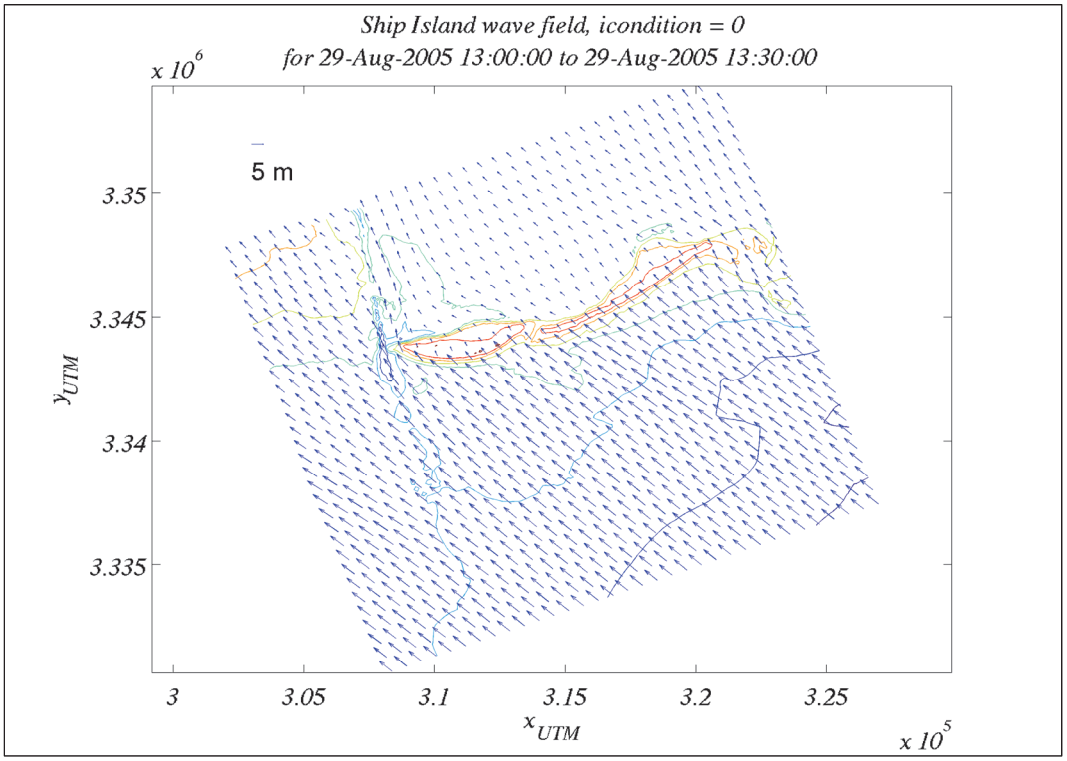

Steady currents as predicted by ADCIRC during the time of peak wave heights are shown in Figure 7-16. The surge level of approximately 4.5-m continues to increase at a rate of 1.0-m/hr with large onshore-directed currents. The largest current magnitudes are predicted over the island and through Camille Cut with velocities in excess of 4.0-m/sec.

Sediment transport modeling was completed using a single representative median d_{50} = 0.3 mm, although the actual median sand sizes ranges from 0.2-0.4 mm over the domain. Volumetric concentration of suspended sediment is shown in Figure 7-17 and is predicted according to Equation 7.10 making use of efficiencies e_B 0.05 and e_f = 0.01. These empiric parameters are in agreement with the previously calibrated values used in other laboratory and field studies (Johnson et al. 2012, Kobayashi et al. 2009). The concentration values are shown in Figure 7-17, where the largest concentrations are in excess of 0.1 percent [m^3/m^3] during the peak of the storm.

Figure 7-16. Current field modeled during the peak wave conditions of the Hurricane Katrina validation. Note: The largest current magnitudes are predicted over the island and through Camille Cut with velocities in excess of 4.0 m/sec.

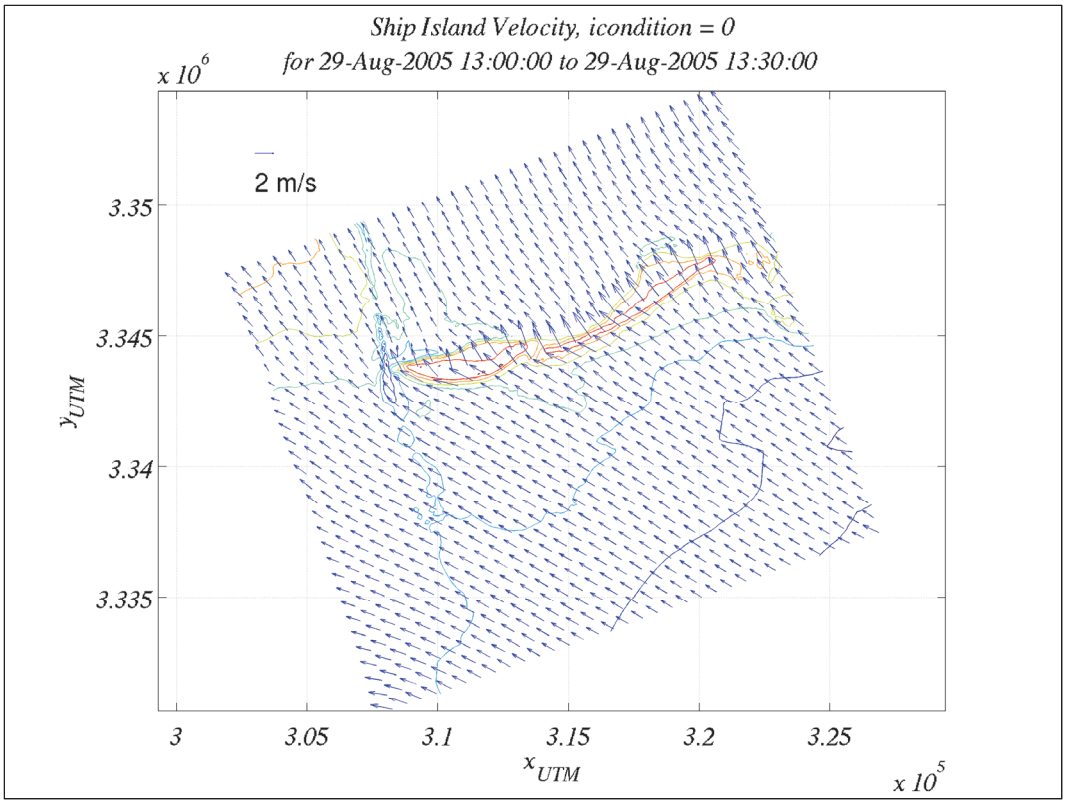

Figure 7-17. Volumetric concentration of suspended sediment modeled during the peak of Hurricane Katrina. Note: The largest concentrations are in excess of 0.1 percent [m³/m³].

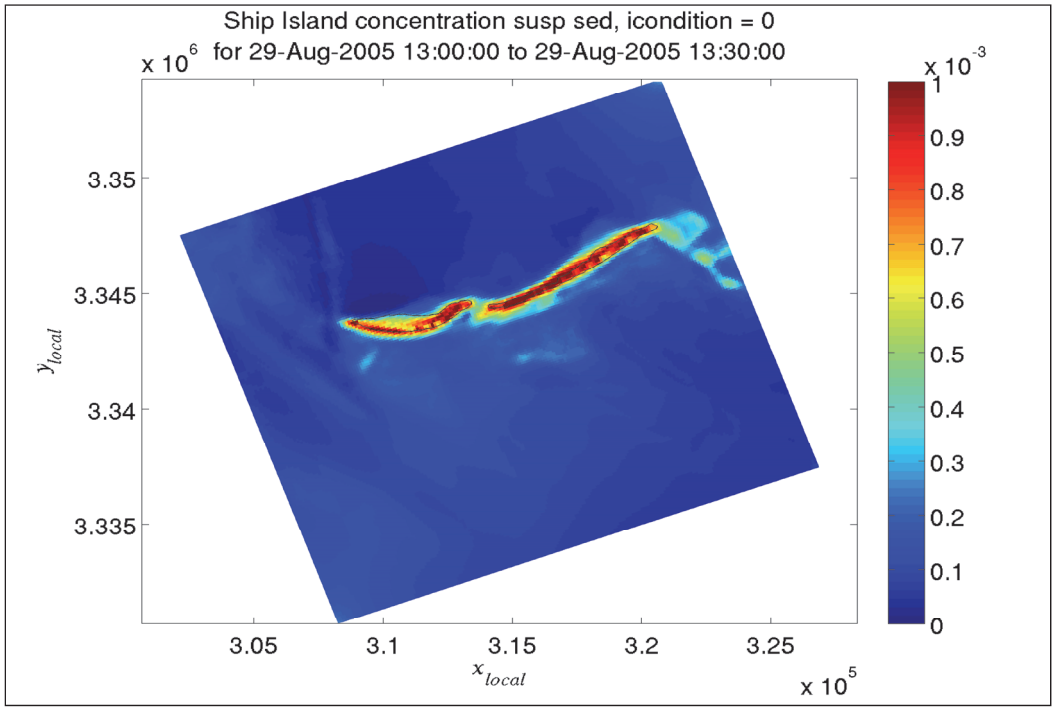

The associated flood stage currents of the surge result in a large onshore transport of sediment. A snapshot of suspended sediment transport is depicted in Figure 7-18, where the largest values occur directly over the submerged island with intense wave breaking and strong currents. The bedload transport in the energetic storm environment, provided in Figure 7-19, is smaller in contrast. The computations are computed according to Equation 7.7 with $b = 0.001$ and $\gamma = 8$, both in agreement with the previous efforts and recommended values (Kobayashi et al. 2009, Ribberink 1998).

While suspended transport has large variation and distinct peaks within the surf zone, bedload is more spatially homogenous with less dependence on wave breaking dissipation.

The best available bathymetric surveys and lidar were used to develop the Pre- and Post-Katrina morphology for comparison to the C2SHORE model results. The far-field conditions were taken from the sl15v3 ADCIRC mesh (IPET 2008) and include additional unpublished pre-storm data provided by the Joint Airborne Bathymetry Technical Center of Expertise (JALBTCX) and the CHARTS system collected during the period April 24, 2004 to May 5, 2004. Regarding the IPET (2008) bathymetry data, the combination of data sources for that project resulted in a hybrid set that includes an abrupt transition seen in Figure 7-13 to the south of Ship Island around 9.0-m depth. This unnatural feature is due to either differing measurement data or differences in datum. Although the break is not realistic, it is in relatively deep water and is not expected to affect the results in a significant way. Detailed Post-Katrina bathymetry were derived from USGS data taken June 2008 and June 2009 and combined with EAARL lidar (Brock et al. 2007). Unfortunately, the available Pre-Katrina nearshore bathymetry data may be in significant error. Initially, the nearshore sl15v3 ADCIRC mesh data were combined with Pre-Katrina lidar for a complete pre-storm bottom condition. These data were compared to the USGS data after the storm and indicated a shoreface recession of approximately 1.0 km on West Ship Island. This large apparent erosion is not supported by photos and is an order of magnitude larger than any credible account of the beach recession found in a literature review (Morton 2010; Otvos and Carter 2008; Fritz et al. 2007). Because the sl15v3 ADCIRC mesh is likely to be in significant error for the nearshore bathymetry in 2005, the present study makes use of the 2008 USGS survey data combined with the Pre-Katrina lidar. Because of this inaccuracy in initial conditions, only the post-storm lidar data

Figure 7-18. Suspended sediment transport modeled during the peak of Hurricane Katrina.

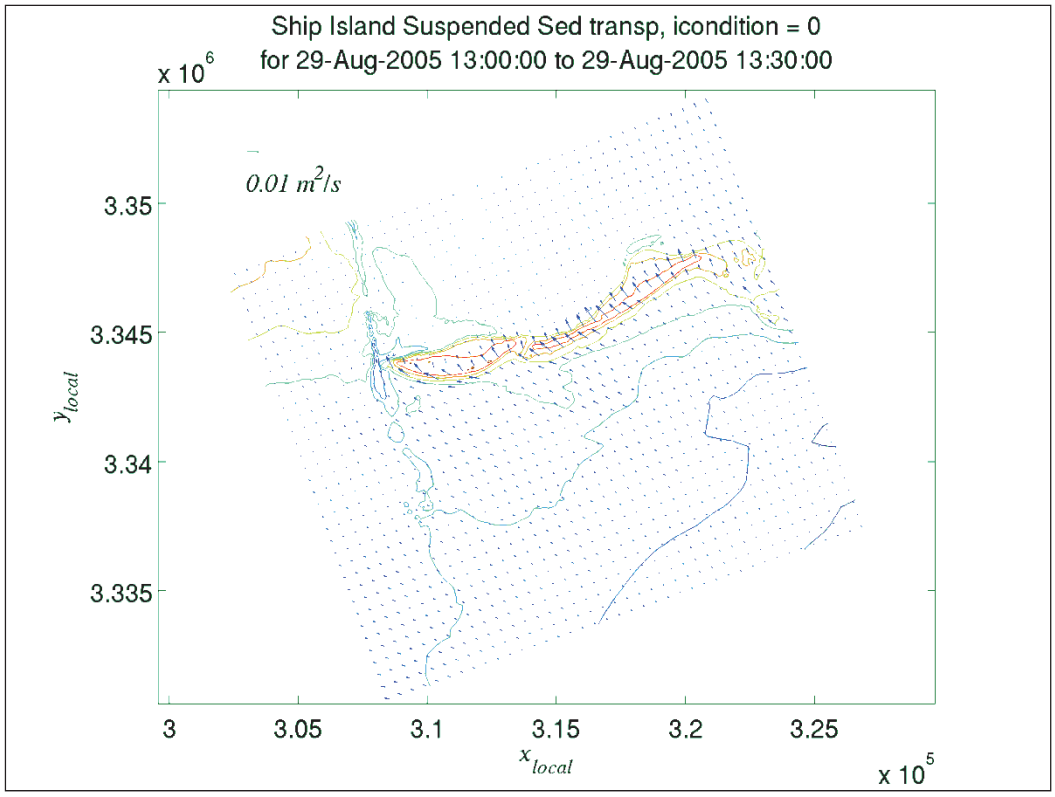

Figure 7-19. Bedload sediment transport modeled during the peak of Hurricane Katrina.

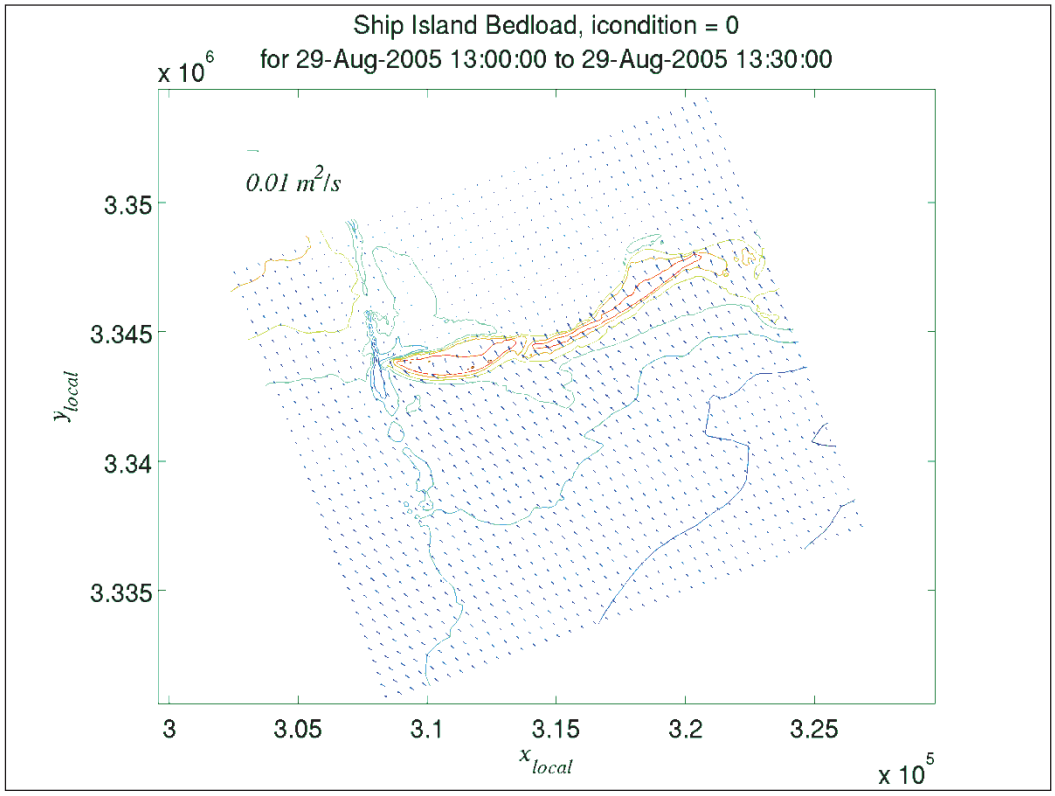

are compared with model predictions. Pre-storm morphology and post-storm topography are provided in Figures 7-20 and 7-21, respectively. A single contour near the MSL (z = 0.2 m NAVD) for each condition is provided as a solid black line.

Additionally, a series of nine transects crossing the island are depicted in Figures 7-20, 7-21, and 7-23 that will be used subsequently to show detailed morphology changes. A comparison of the pre- and post-storm island conditions shows that the portion of island with the highest elevation, such as most of West Ship Island, undergoes relatively small change. The low-lying and narrow sand spit spanning most of Camille Cut is eroded significantly to a level below mean sea level.

Given the lack of quality subaqueous data, the model to data comparison is limited to the relatively small emergent regions. Figure 7-22 shows the change in bottom position predicted by the C2SHORE model as a result of Hurricane Katrina.

Figure 7-20. Pre-storm topobathy.

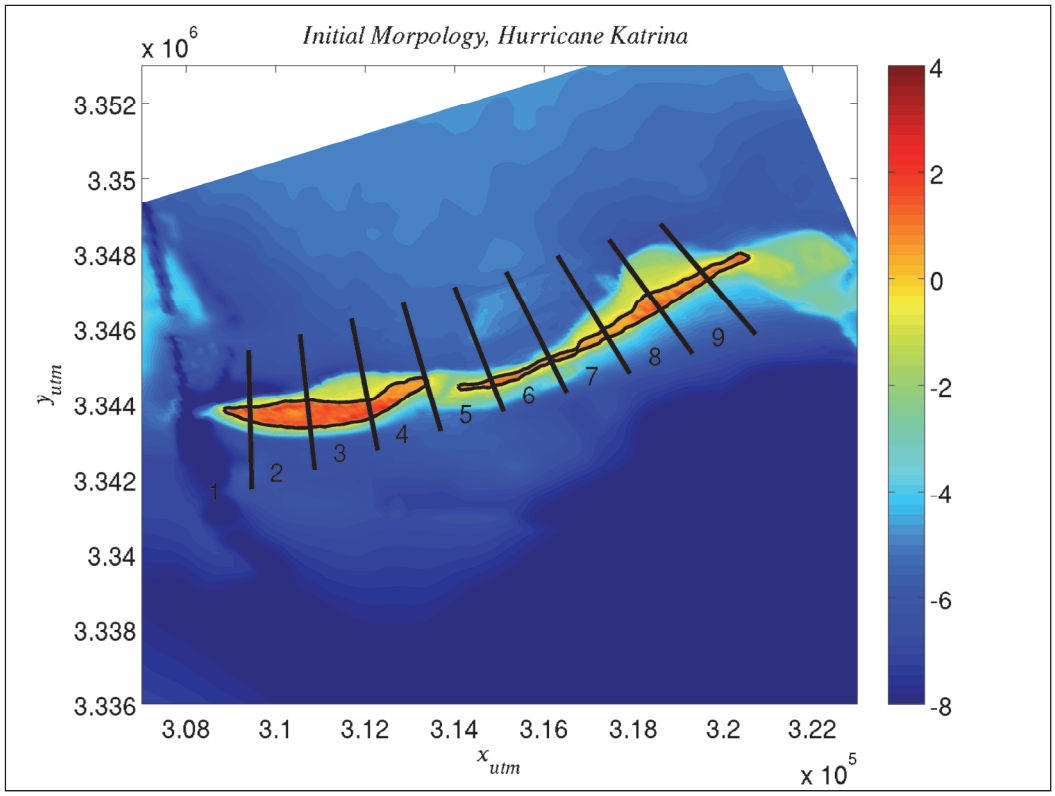

Figure 7-21. Post-storm topography.

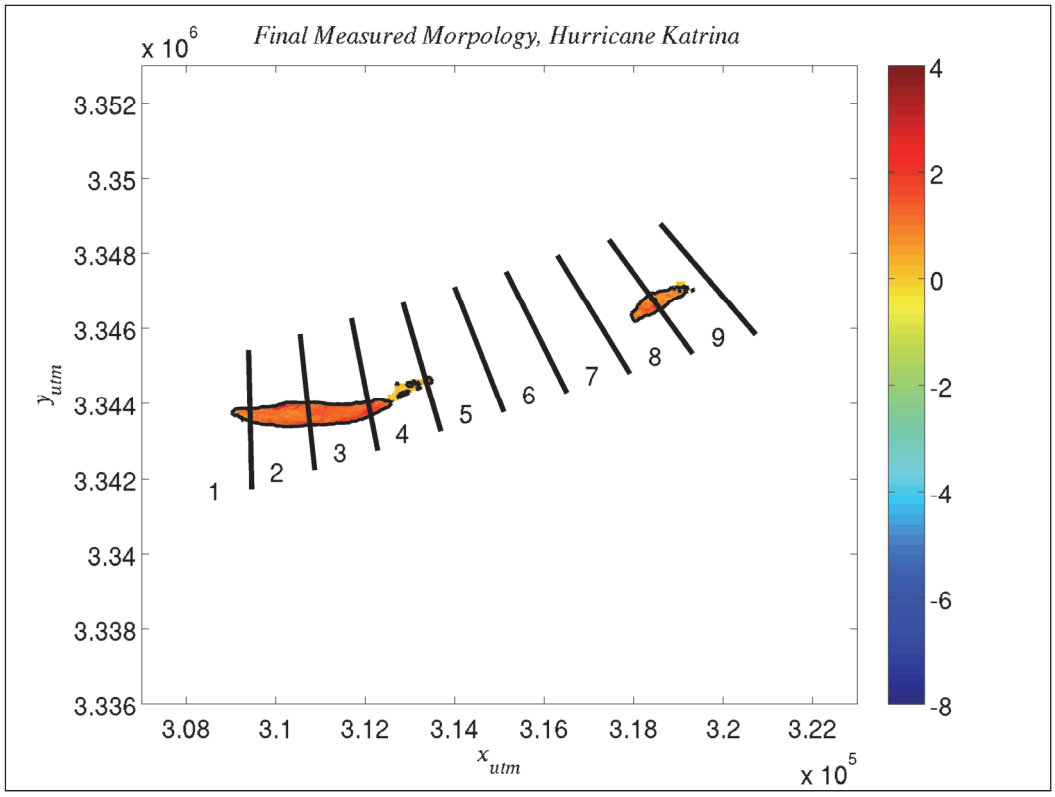

Figure 7-22. C2SHORE-modeled change in bottom position as a result of Hurricane Katrina. Note: Warm/red colors indicate erosion and cool/blue colors indicate accretion.

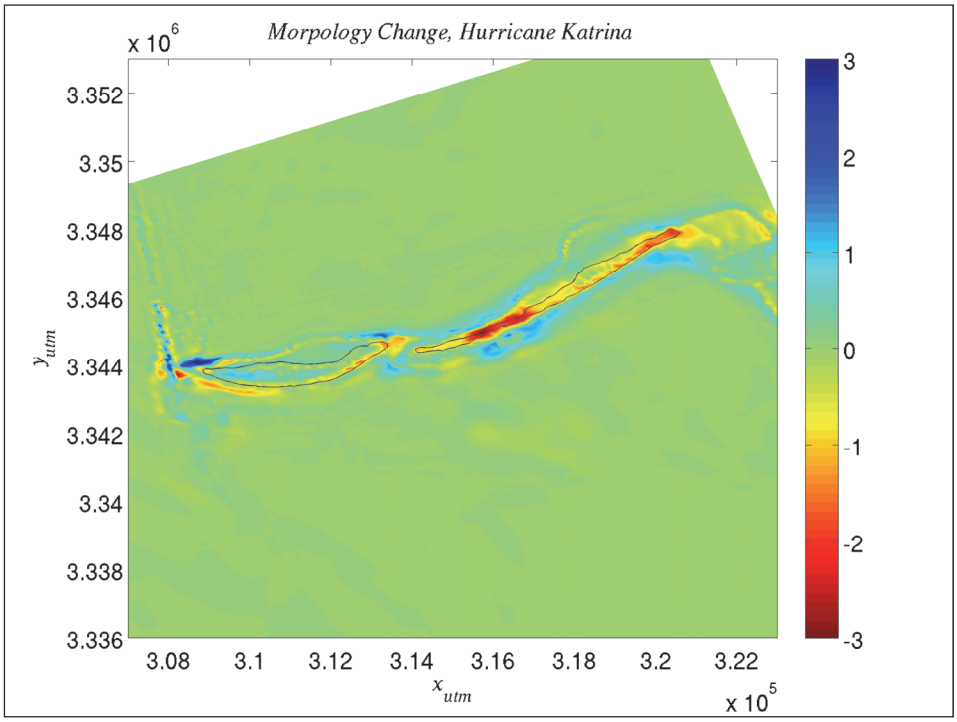

Figure 7-23. C2SHORE-modeled final predicted bathymetry during the Hurricane Katrina validation.

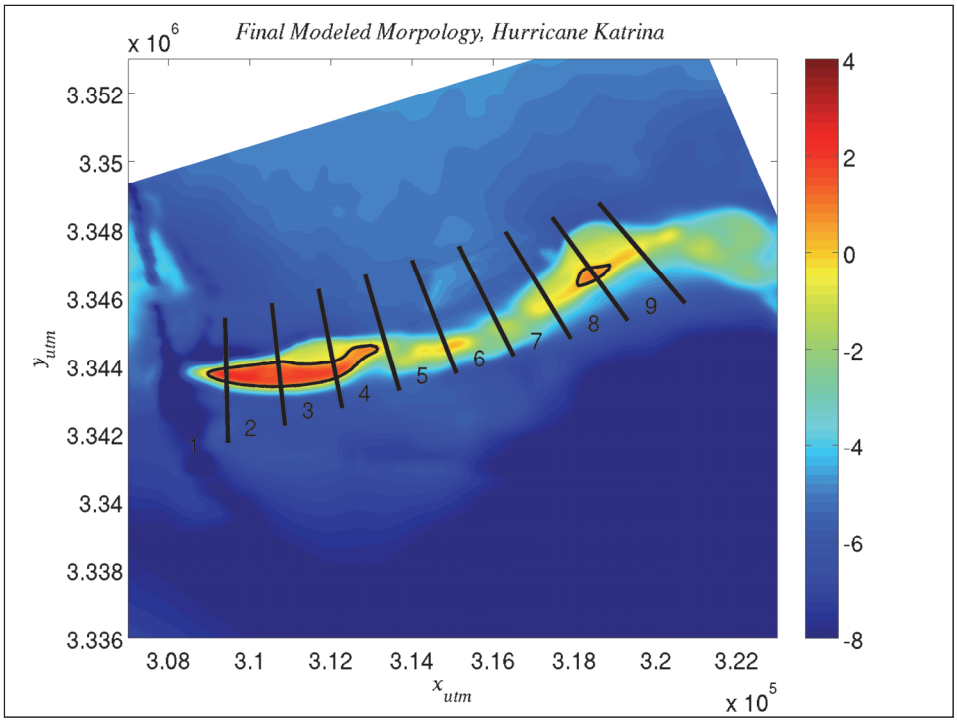

The regions of greatest sediment loss are within Camille Cut, where erosion of up to 3.0 vertical meters of the thin sand spit is predicted. Corresponding areas of deposition are apparent on both the Gulf and Sound sides of the Camille Cut. The regions of the island that have a higher initial elevation exhibit less dramatic erosion of the shoreface. The final predicted bathymetry is provided in Figure 7-23. The most prominent development is the notable loss of the thin sand spit across most of Camille Cut and a significant loss of emergent land mass on East Ship Island. The predicted and modeled evolution of the contour near mean sea level (z = 0.2 m NAVD) is shown in Figure 7-24.

Using the default parameters for the sediment transport model previously discussed, the retreat of the 0.2-m NAVD contour is slightly over-predicted. In general, however, the model predictions show consistency when compared with lidar measurements with the widening of Camille Cut and the large reduction in the emergent land mass along East Ship Island. To examine these limited data in greater detail, the measured morphological changes along the nine transects crossing the island are compared with the modeled results. These nine transects are shown in Figures 7-20, 7-21, and 7-23 and are numerically ordered 1-9 beginning with #1 on the west side and concluding with #9 on the east side. The transect results are shown in

Figure 7-24. Comparison of the predicted and C2SHORE-modeled evolution of the contour near mean sea level (z = 0.2 m NAVD) during the Hurricane Katrina validation.

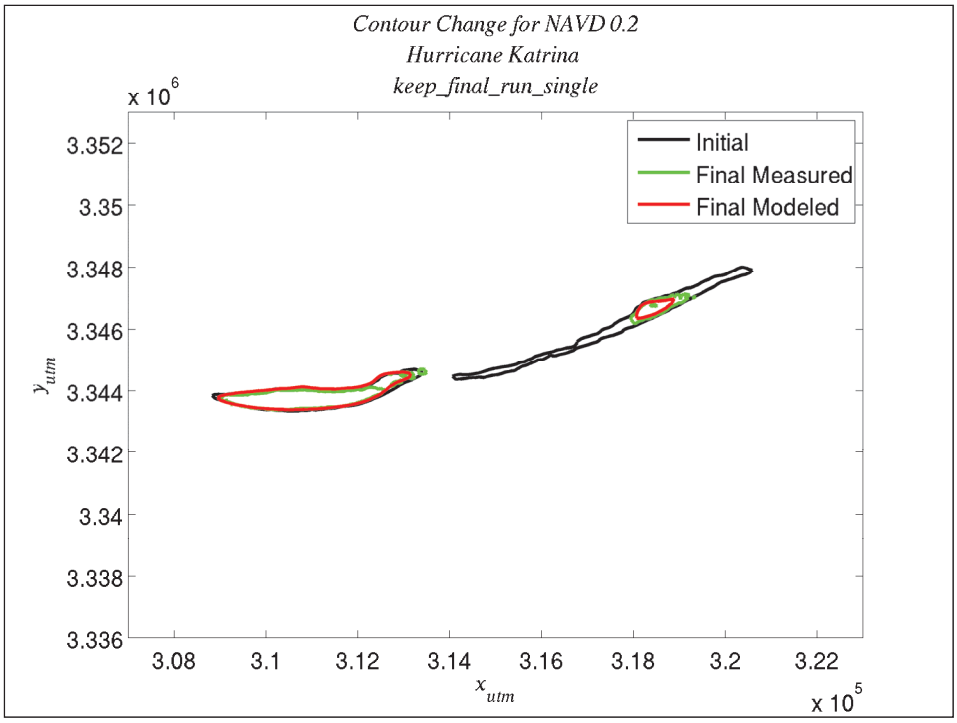

Figure 7-25 with initial and final profiles. There is only a small subaerial region for model and data comparisons and the large subaqueous regions lack data. The measured data from the first transect on the west indicates little change due to the storm inundation. The C2SHORE predictions, on the other hand show considerable accumulation of sand. The general direction of net sediment transport modeled during this storm is from east to west. An example of this large conveyance of sand is indicated in the sediment transport Figures 7-18 and 7-19. As previously noted, the applied wave model in this case was the half-plane version of STWAVE. This simple wave model is appropriate for predicting the wave-driven currents and sediment transport for the island coast facing the Gulf of Mexico and the regions of greatest morphology change. For instance, the wave field on the exposed Camille Cut Gulf beach is well-modeled with the half-plane version of STWAVE. Waves on the west end of the island, however, are poorly treated with a half-plane wave model as the hurricane trajectory is to the north with counter-clockwise wind fields. As Hurricane Katrina makes landfall, the east end of the island is exposed to large waves with short periods. The large energy dissipation associated with wave breaking results in hindering deposition, or in other words, the resuspension of sand. Modeled accretion along Transect 1, therefore, is likely due to a wave field that is poorly represented as this particular hurricane passes to the west of

Ship Island. Transect 4 on the other hand, indicates an over-prediction of erosion with a removal of the emergent island that is not supported by the data. Model and data comparisons were reasonable for the remainder of the available lidar. The transects within Camille Cut show a transport north to the Mississippi Sound side and south to the Gulf side of the island. It should again be noted that the pre-storm conditions are taken, in part, from a 2008 interim product USGS bathymetric survey data and may contribute to inaccuracies in the modeled results.

Figure 7-25. Initial and final profile transects for the Hurricane Katrina validation. Note: Transects are shown in Figures 7-20, 7-21, and 7-23 and are numbered 1-9 beginning with #1 on the west side.

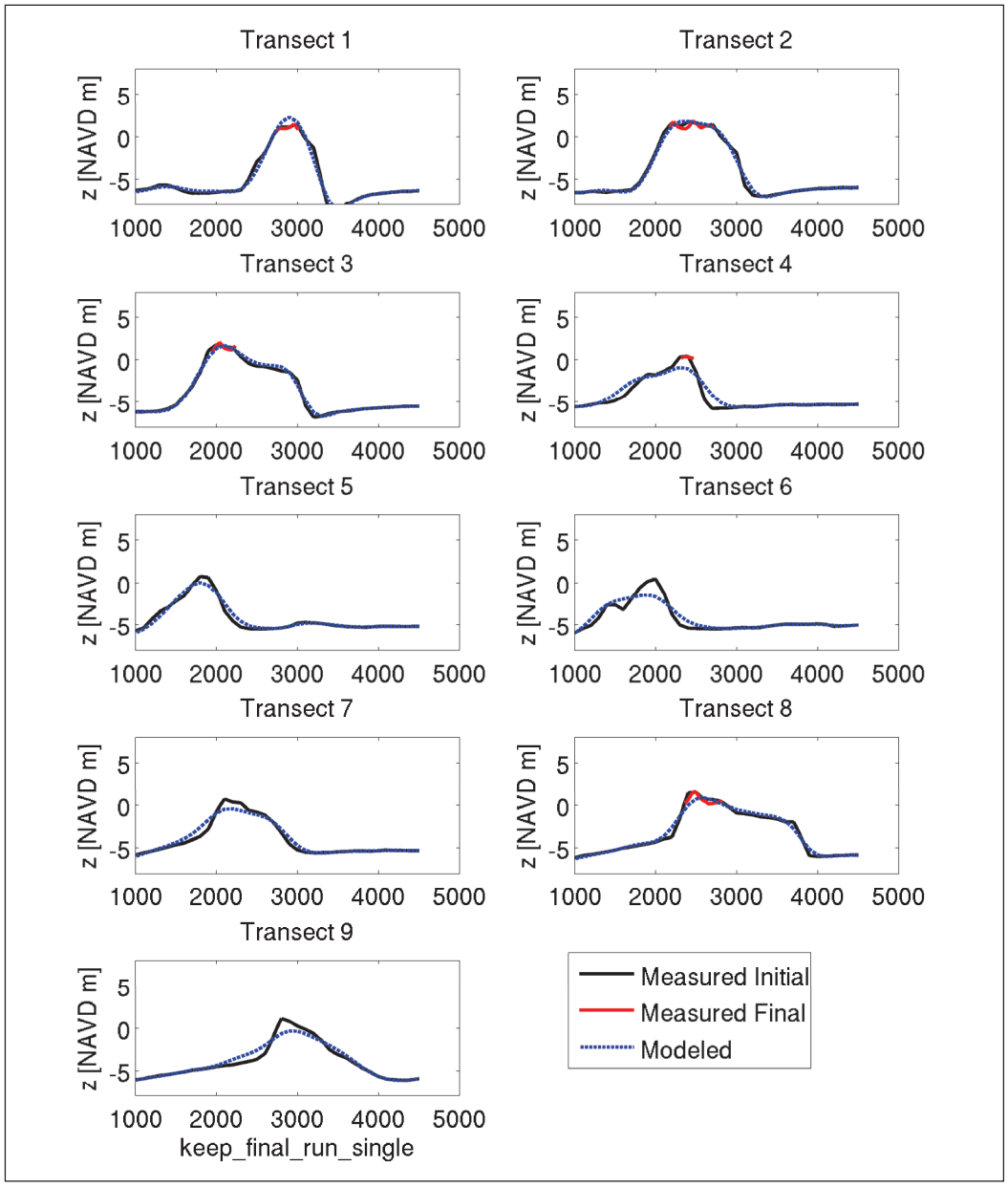

7.4 Sensitivity

The objective of the MSCIP project includes restoring sediment to crucial areas of the barrier island system including Camille Cut at Ship Island and along East Ship Island. Although this intention is clear, the directive can be satisfied using varied design scenarios. Indeed, the intention is to develop an economical and resilient restoration for Ship Island. To this end, the C2SHORE nearshore morphology change model, as previously introduced and calibrated, is applied to several design scenarios defined below. Initially, the storm effect on the existing conditions is provided and acts as a baseline for further comparison to the various scenarios. The proposed Camille Cut fill affects the local wave and current conditions, and the new sediment transport environment is examined. Native sand for Ship Island has a median grain size of 0.3 mm. Some of the available candidate replenishment sand from borrow sites, however, is smaller in diameter. To ascertain the effect of the smaller grain size, three scenarios of varied grain size also are explored. Additionally, one of the scenarios for sand supply has a borrow region within 2.0 km of the Ship Island shore face, and the potential impact of this change in bathymetry is explored.

7.4.1 Hypothetical storm selection

Three storm events were modeled for the Ship Island restoration scenarios. Two hypothetical tropical storms that produce approximately a 1-year (Storm #1) and 10-year (Storm #2) surge elevation near Ship Island were selected from the storm database developed in the first phase of the MsCIP. Storm surge hydrograph for both storms are plotted in Figure 7-26. A snapshot of the wind field for each storm is plotted in Figures 7-27 and 7-28. The third storm event (Storm #3) is based on the historical Hurricane Katrina storm characteristics, and was also included in the storm suite database. Table 7-1 summarizes the three storm events modeled for the Camille Cut restoration scenarios.

7.4.2 Existing conditions

Existing conditions bathymetry/topography are shown in Figure 7-29 for the +/-3m contours. To establish a baseline for sediment transport and morphology change, the three hypothetical storm conditions were applied to the existing island. Figures 7-30, 7-31, and 7-32 show the net bathymetric change predicted for the existing conditions and the three synthetic storms, and the different scales of coloration should be noted. The island footprint

Figure 7-26. Storm surge (approx. +/- 1 day of landfall) for Storm #1 (blue) and Storm #2 (green) at -88.910004, 30.17087; Depth = approx. 8.2 m (27 ft).

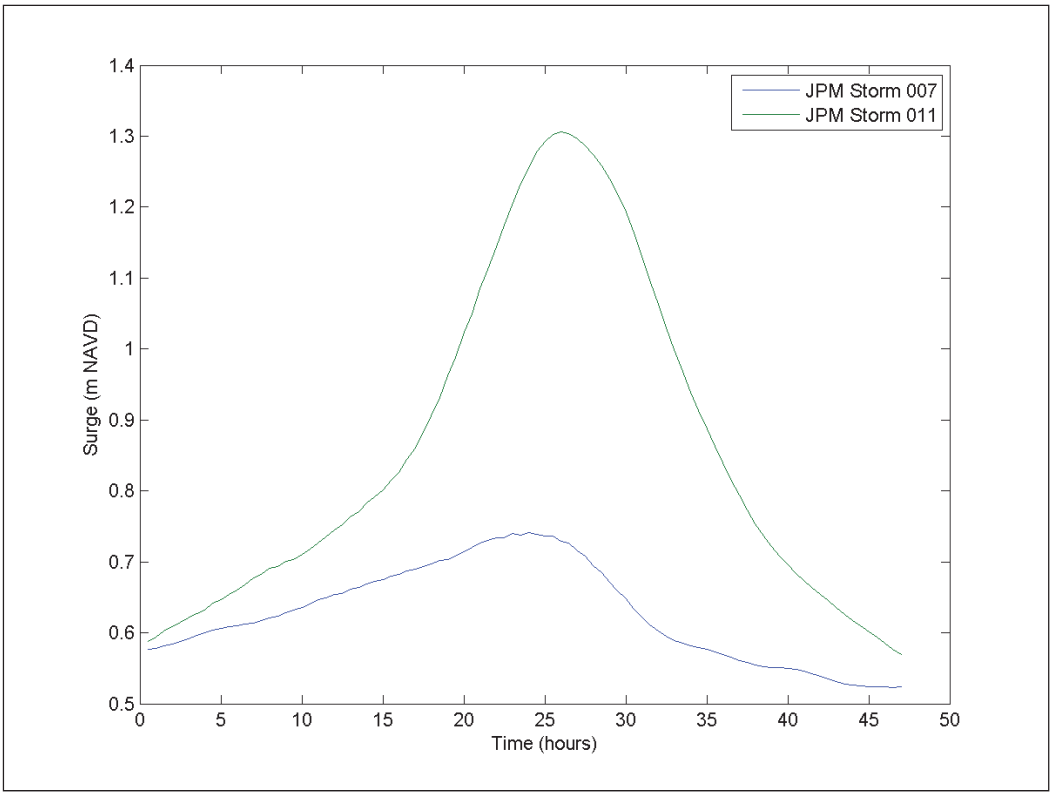

Figure 7-27. Landfall winds for Storm #1.

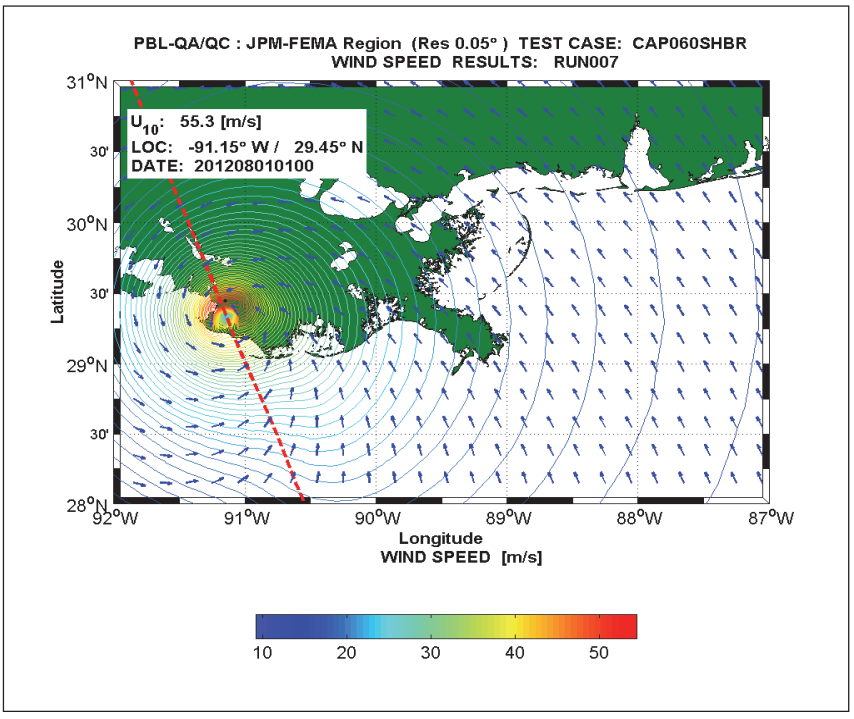

Figure 7-28. Landfall winds for Storm #2.

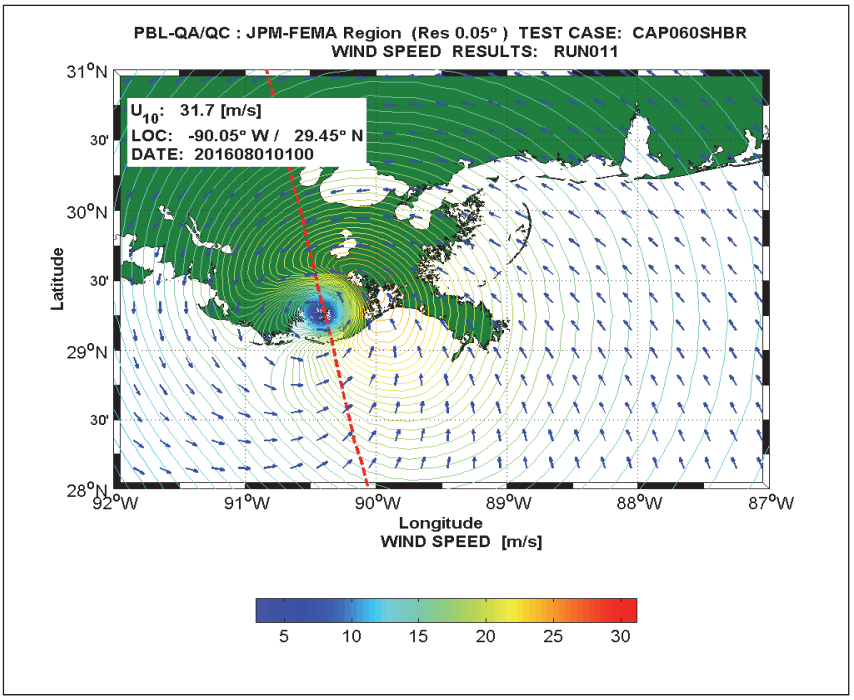

Table 7-1. Storm suite for Ship Island modeling alternatives.

Storm #	Selection criteria	Approx. Return Period (years)
1	Maximum storm surge	~1
2	Maximum storm surge	~10
3	N/A	~500

Figure 7-29. Bathymetry/topography for the existing Post-Katrina Ship Island modeling scenario.

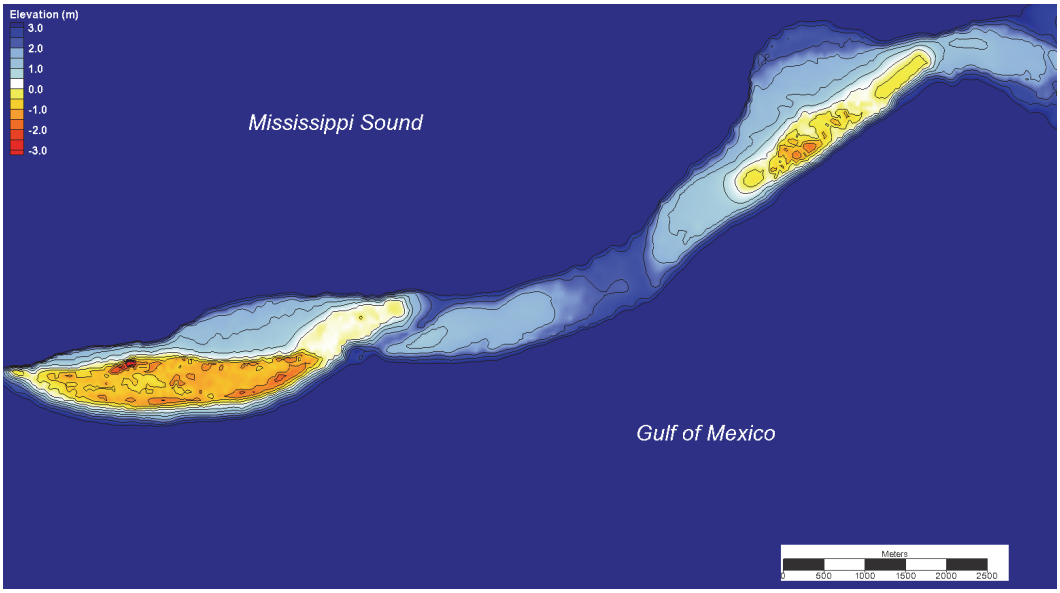

Figure 7-30. Morphology change using existing bathymetry for Storm #1.

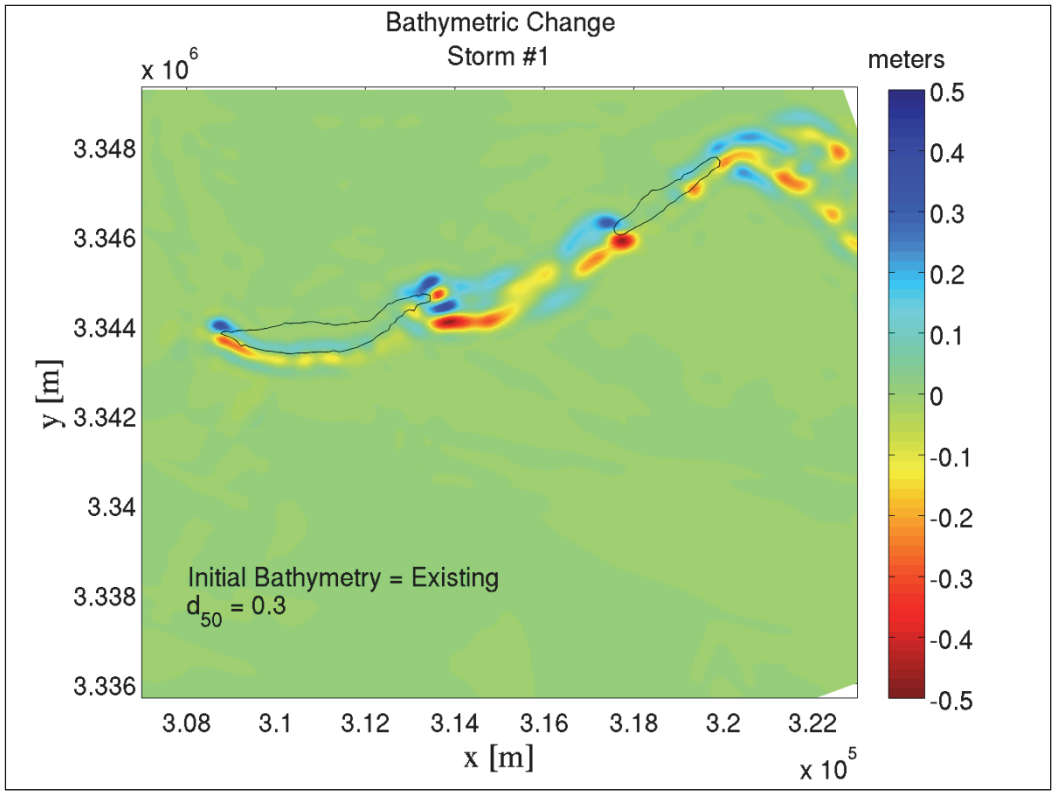

Figure 7-31. Morphology change using existing bathymetry for Storm #2.

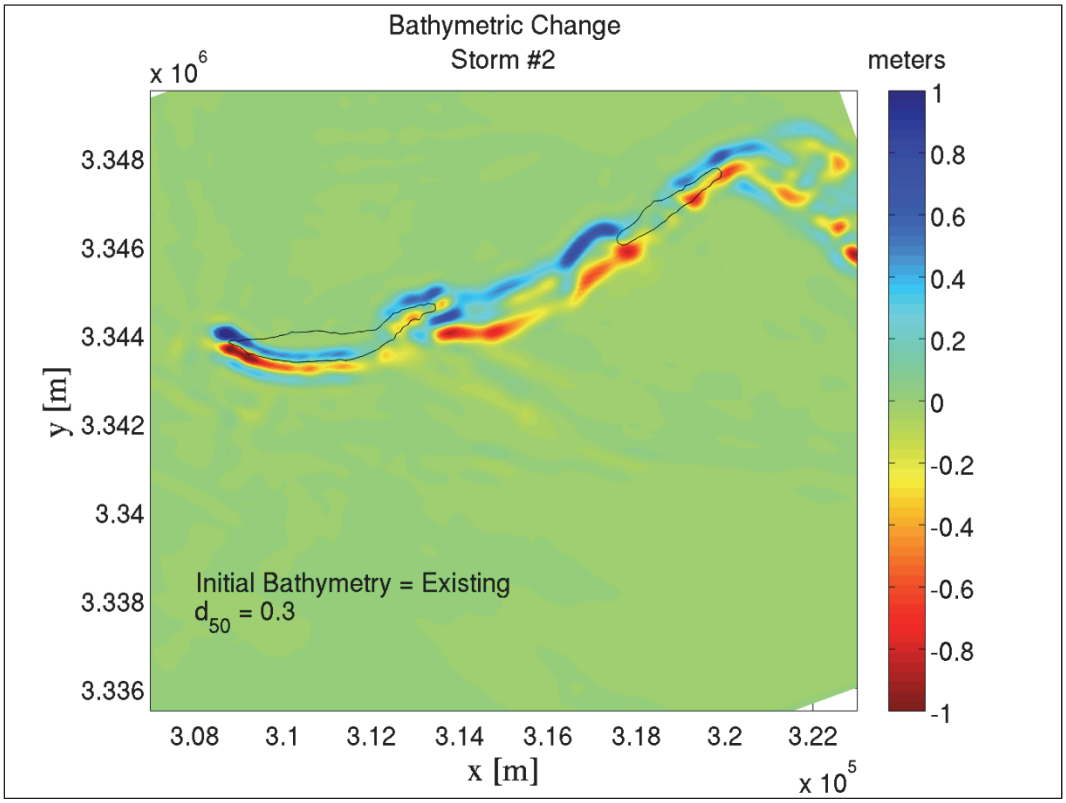

Figure 7-32. Morphology change using existing bathymetry for Storm #3.

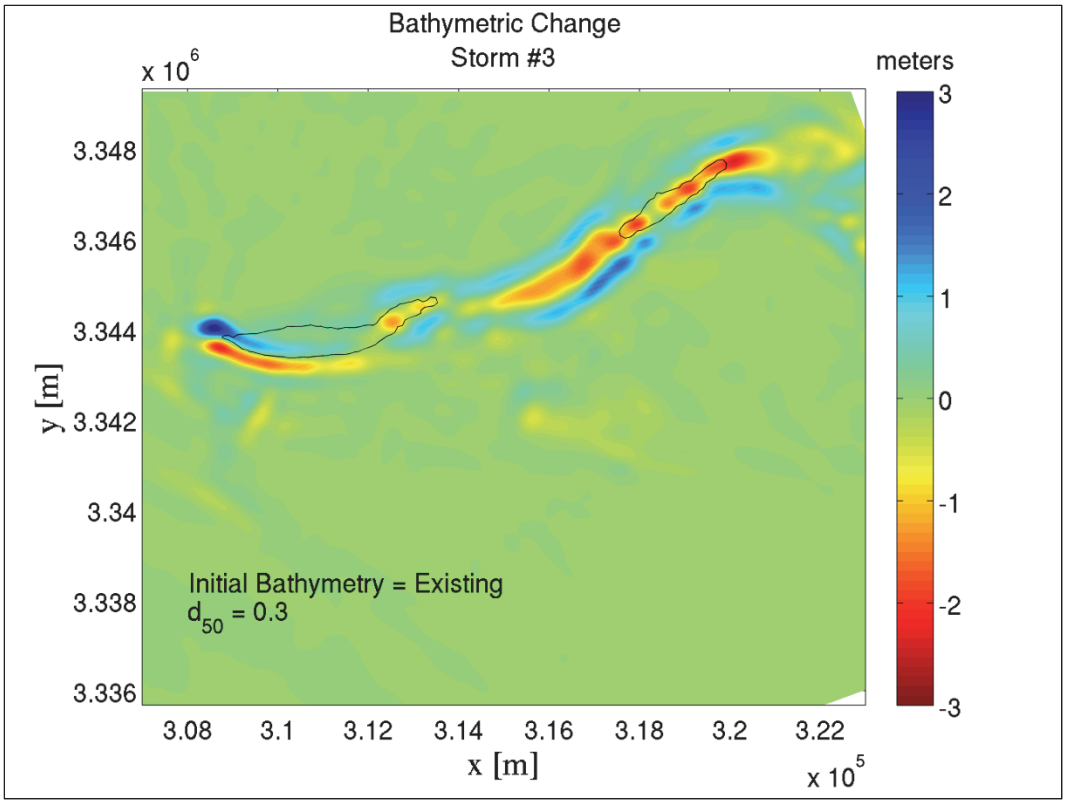

(NAVD = 0 m) contour is also depicted for reference. In general, the large currents and wave breaking on the east and west island ends result in large bathymetric changes for each storm. At the west end of Ship Island, for instance, a region within the surf zone was lowered by 0.5, 1.0 and 3.0 m for the three storms, respectively. Additional deepening of Camille Cut is also predicted with a lowering of the bed level by 3.0 vertical meters for the energetic Storm #3.

In general, the sediment movement during the rising storm surge is characterized by transport to the west and to the north around the islands. In general, the subsequent falling surge produces a smaller flux in opposetion, directed to the east and south. The final bathymetry for the baseline conditions and each of the three modeled storms is shown in Figures 7-33, 7-34 and 7-35. Additionally, net transport generated across eleven transects is provided. Transport is integrated over each transect for each time step, and the rate is provided numerically in the figures with units of millions of cubic meters and millions of cubic yards. To present positive values for longshore transport in the prevailing direction, the convention for provided values is positive for westerly and southerly transport for the black lines depicted. In other words, it should be noted that the sign convention is

Figure 7-33. Morphology and transport using existing bathymetry for Storm #1.

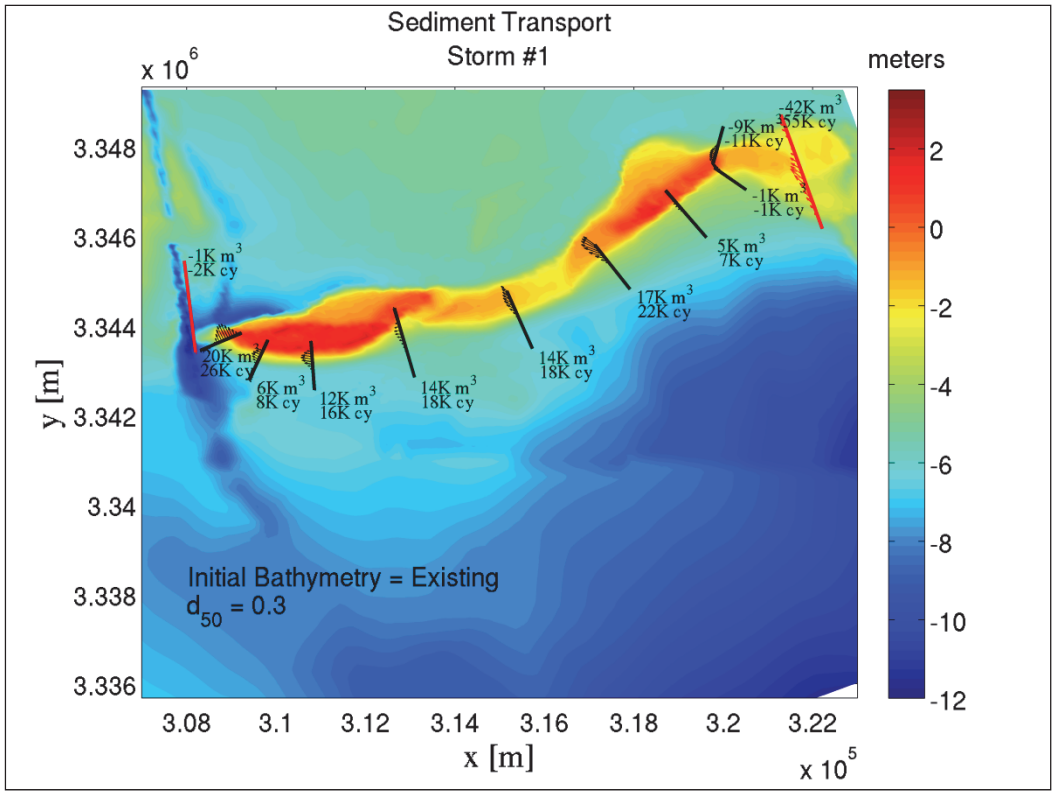

Figure 7-34. Morphology and transport using existing bathymetry for Storm #2.

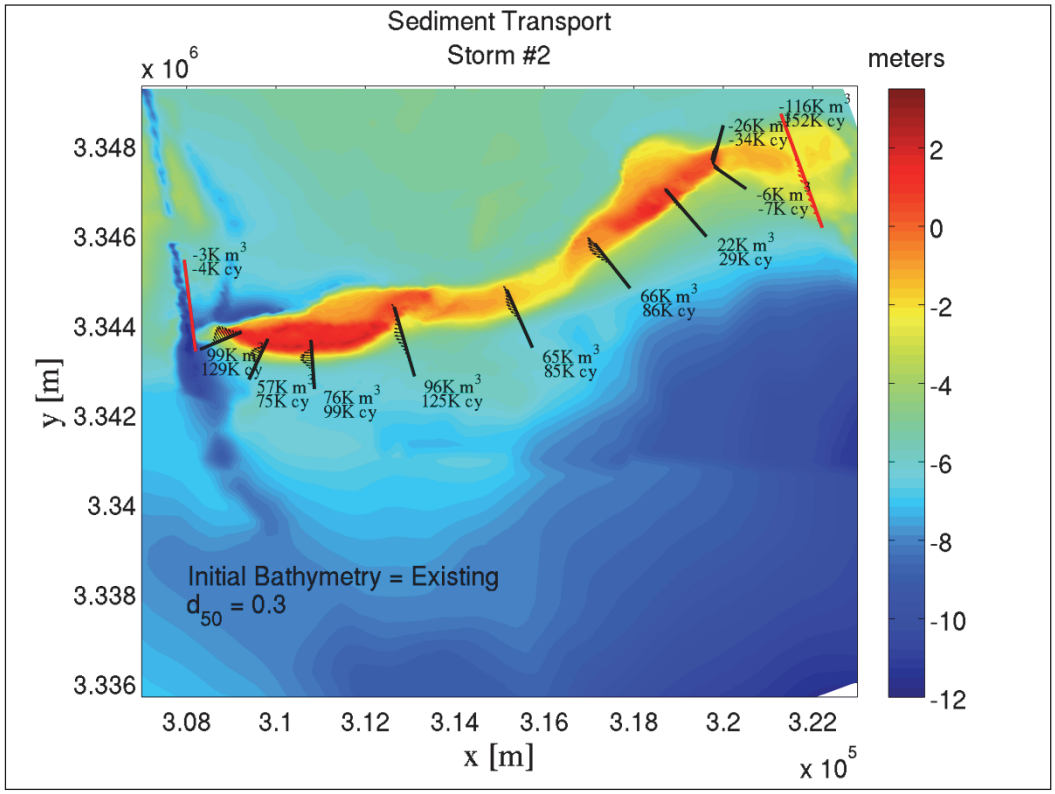

Figure 7-35. Morphology and transport using existing bathymetry for Storm #3.

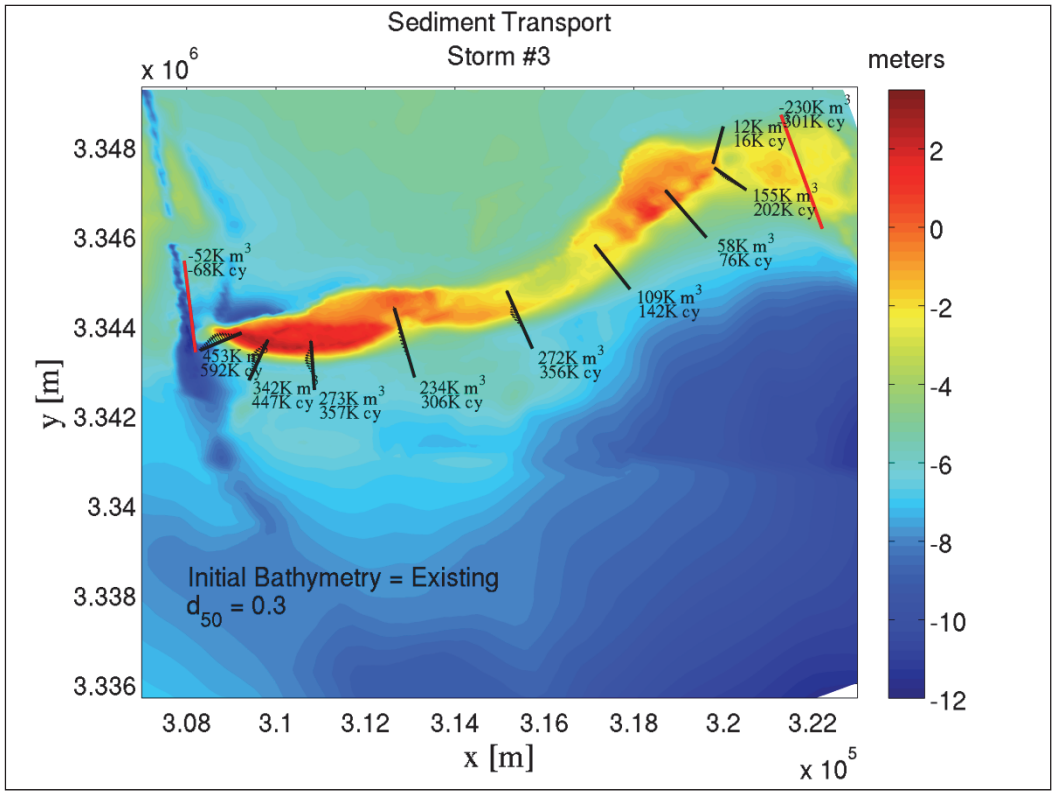

positive for flux clockwise around the island for the black lines. However, for the red lines depicted east and west of the island (which do not radiate from Ship Island), the convention for the provided values is Cartesian, with easterly and northerly values representing positive sediment transport. As expected, transport is primarily within the region of intensive wave breaking, and the resultant sand transport is to the west for the simulated storm events. Storm #1, with an approximate 1-yr return period, generates average storm transport rates on the order of 20,000 cubic meters of sand, as indicated in Figure 7-33. Sand originating at the east end of the island is transported into the Sound or carried by longshore currents along the Gulf shore face. Note that the resultant transport in Camille Cut has a north-directed component, indicating a conveyance of sand through the gap and into the Sound.

The transport environment of larger Storm #2, with an approximate 10-yr return period, is shown in Figure 7-34, and the patterns are similar to the smaller storm. The larger surge and waves, however, results in larger transport rates of 50,000 to 100,000 cubic meters. The predicted transport rates are approximately five times larger when compared with Storm #1. The total transport for the largest event, depicted in Figure 7-35, is

approximately 100,000 to 400,000 cubic meters. This large event, designed with the hydrodynamics of Katrina, results in relatively small transport on the east side of the island. The values increase and peak at the west side as sand is transported north into the Sound.

7.4.3 Restoration alternatives

The US Army Corps of Engineers Mobile District (SAM) developed the restoration templates, which include the closure of Camille Cut as well as an attached feeder berm along the Gulf side of East Ship Island (east of Camille Cut). The restored bathymetry/topography and the outline of the fill regions are shown in Figure 7-36 for Alternative #1.

Figure 7-36. Bathymetry/topography for the restored Ship Island modeling scenario which includes: 1) northshore placement of fill along West Ship Island, 2) Camille Cut closure, 3) Emergent feeder berm along East Ship Island, and 4) Submerged feeder berm.

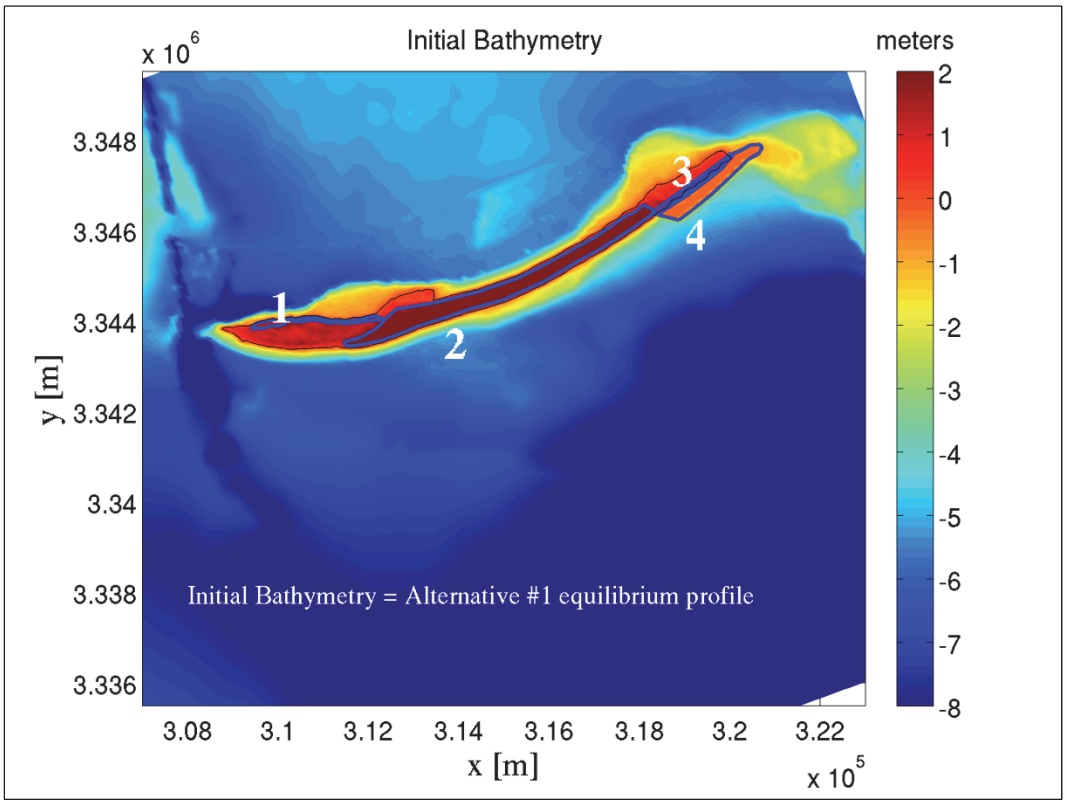

Alternative #1 includes filling the cut between East and West Ship Islands and the nearshore region of East Ship Island with upwards of 22 million cubic yards of sandy material with a median grain size ranging between 0.2 mm to 0.3 mm. The fill template for Camille Cut breach closure consists of an averaged approximate 1,000 foot equilibrated island width at an

elevation of approximately 2.4 m NAVD88. The feeder berm template along East Ship consists of fill placed between elevations of approximately +0.3 to -4.6 m NAVD88. Restoration scenarios also include a north shore (Mississippi Sound) placement of fill along West Ship Island, east and west of Fort Massachusetts, with a fill volume of approximately 428,000 m^3 (560,000 yd^3).

7.4.4 Sensitivity to sediment grain size for Alternative #1

The native sediment may differ from the candidate borrow sites, and some variation of transport is expected for varied grain sizes. To ascertain the resilience of the restoration project, transport predictions with a fine 0.2 mm sand, an intermediate grain size of 0.26 mm, and a relatively coarse 0.3 mm sand corresponding to the native sand have been conducted for Alternative #1. A presentation and discussion of an abridged set of scenarios is presented here, but a complete set of nine transport environments for three storms and three grain classes is provided in Appendix G. While the Camille Cut restoration island elevation of about 2.4 m (8.0 ft) and width platform of approximately 305 m (1000 ft) are maintained for Alternative #1 scenarios, the equilibrium slope varies based on the median sediment grain diameter (d_{50}), as outlined in Table 7-2. Note that the attached feeder berm along the Gulf side of East Ship Island and the north shore fill placement along West Ship Island are held uniform in volume and geometry for all restoration alternatives presented herein. Figures 7-37 and 7-38 depict the final modeled morphology along with the net sediment transport for the fine and coarse grain sizes (Alternative #1 templates A and C, respectively) with Storm #1. Naturally, transport patterns for the two scenarios are similar with movement of sediment to the North around the island and a westerly longshore transport. As expected, fine-grained sand is associated with larger transport where magnitudes are increased by 10-20 percent. It should be noted that a comparison of Figures 7-37 and 7-38 indicate that the restoration results in a small increase in transport around the island when compared with existing base condition. The loss of the hydraulic connection between the Gulf and Sound through Camille Cut generates a larger velocity on the ends of the contiguous island, and an increased transport on the ends is therefore expected. The conclusions of the grain size dependence for the larger Storm #2 are similar with a general increase in the transport of 10-20 percent for the finer grain material (see Appendix G).

Table 7-2. Camille Cut restoration template parameters for Alternative #1.

Template	d50 (mm)	Offshore Slope	Island Elevation (m)	Island Width (m)
A	0.20	1:75	2.4384	305
B	0.26	1:60	2.4384	305
C	0.30	1:55	2.4384	305

Figure 7-37. Restored conditions for Storm #1; d_{50} = 0.20 mm (Template A).

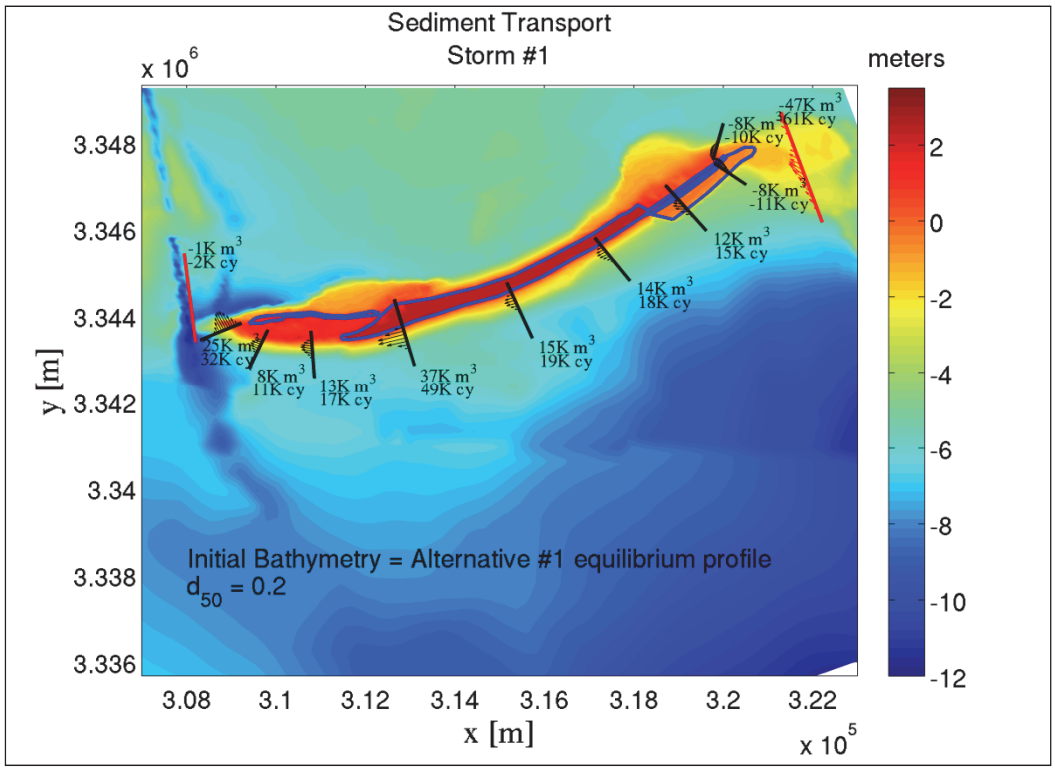

Figures 7-39 and 7-40 depict the final modeled morphology along with net sediment transport for fine and coarse grain sizes with the Storm #3. The large storm surge completely inundates the restored island and Camille Cut is once again breached during this energetic event. It is worth noting that the breaching occurs for both grain sizes, although erosion is reduced for the coarse grain scenario. Grain size dependence is more dramatic in this case with the fine-sand transport increased by 20-40 percent when compared to the native sand case.

7.4.5 Sensitivity to local borrow sites for Alternative #1

One possible source of sand is shown in Figure 7-41, where the borrow sites are shown as a deeper bathymetric region to the southeast of the island. This large depression may affect change in the local wave and current field

Figure 7-38. Restored conditions for Storm #1; d_{50} = 0.30 mm (Template C).

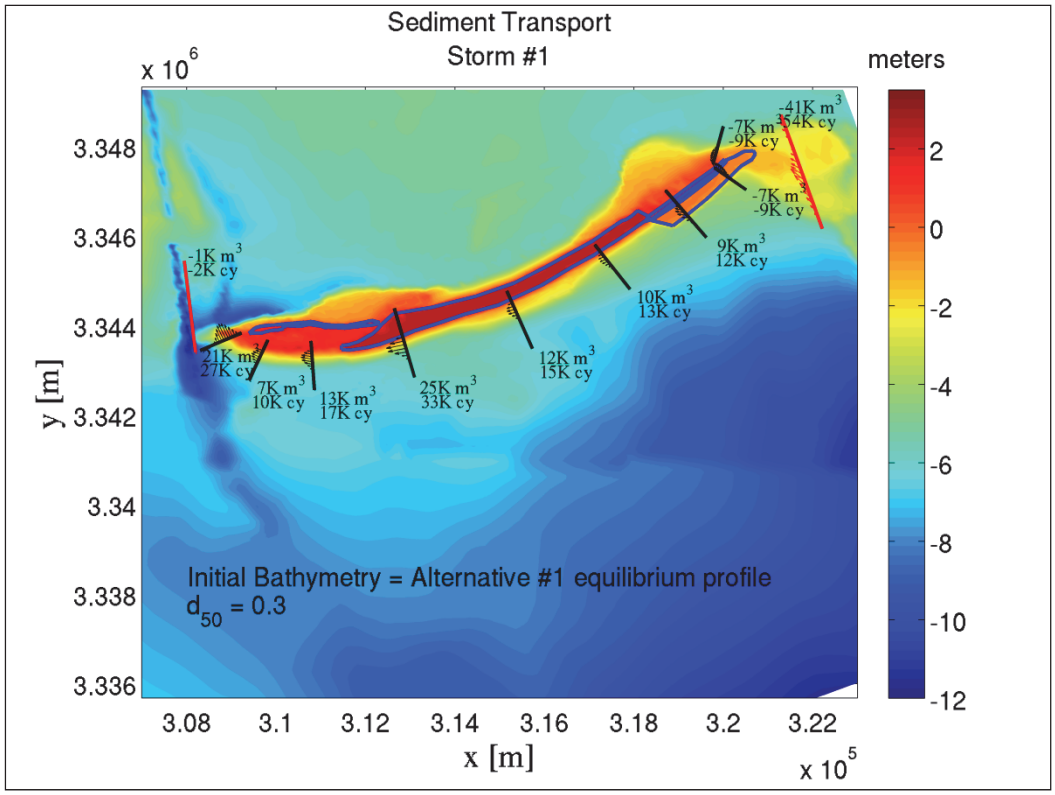

Figure 7-39. Restored conditions for Storm #3; d_{50} = 0.20 mm (Template A).

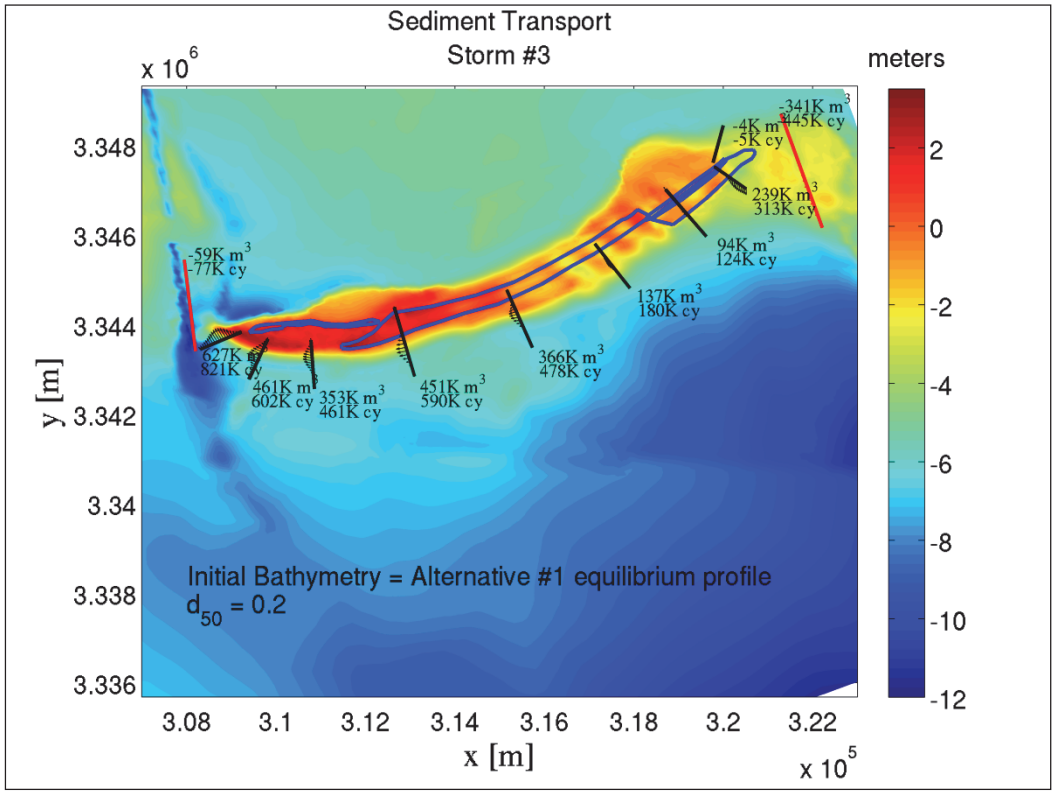

Figure 7-40. Restored conditions for Storm #1; d_{50} = 0.30 mm (Template C).

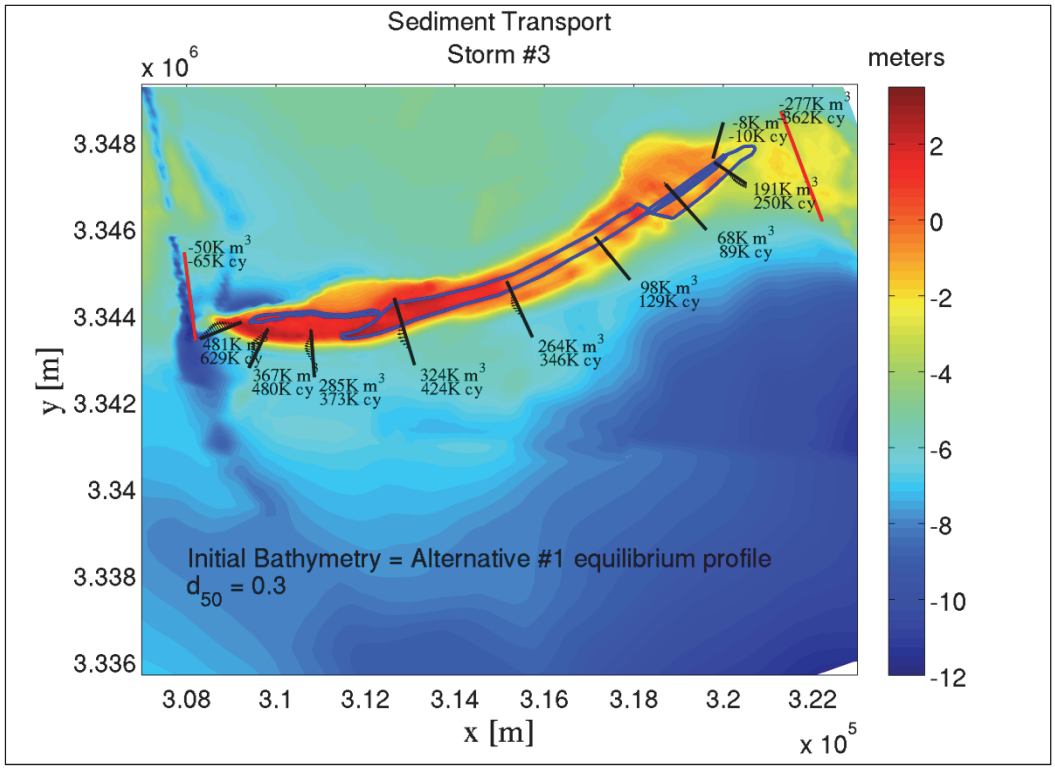

Figure 7-41. The borrow site is shown as a deeper bathymetric region to the southeast of Ship Island. The plans indicate a maximum cut depth of 12 feet within the Eastern borrow pit and a 6.0 foot cut in the smaller site located to the West.

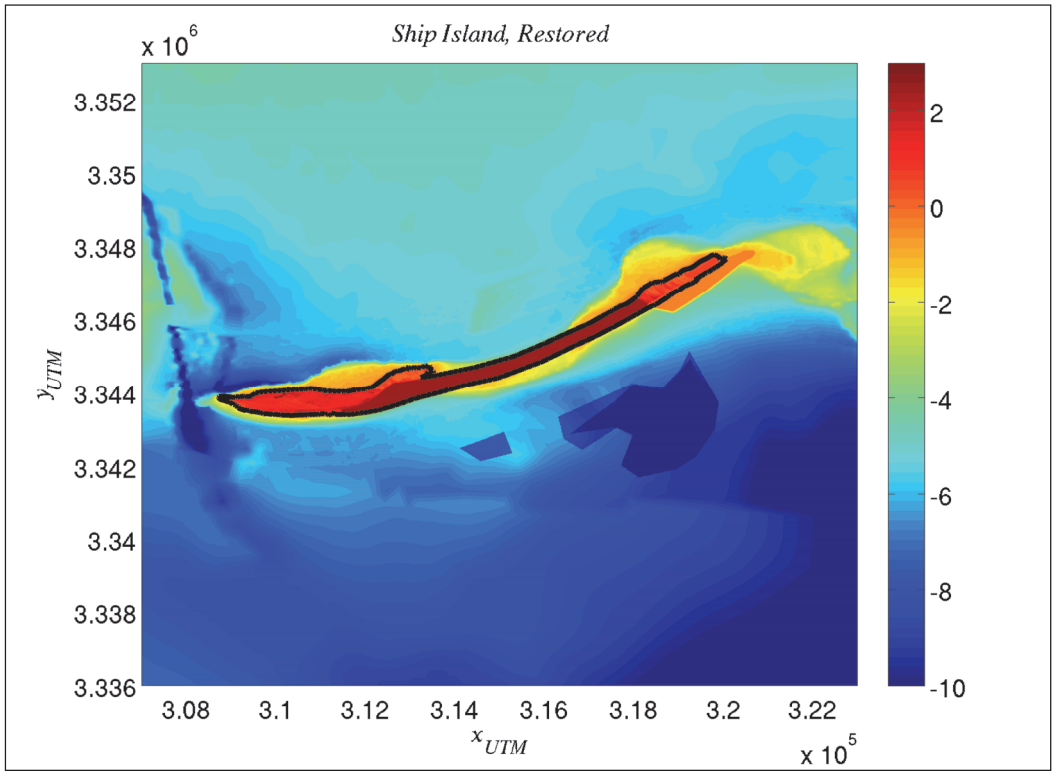

near Ship Island and the potential impact on storm transport is explored herein. The analysis presented in this chapter assesses the sensitivity of the sediment transport associated with the borrow areas on the storm event time scale. The reader is referred to Chapter 8 for a detailed discussion of the longer-term impacts of the borrow areas on shoreline processes. For the following sensitivity analysis, the anthropogenic feature is within 1.5 km of the restored shoreline, and measures nearly 3.0 km across the larger of the two borrow sites. Plans indicate a maximum cut depth of 12 feet within the eastern borrow pit and a 6.0 foot cut in the smaller site located to the West, with a total borrow volume of approximately 22 million cubic yards from these two local borrow sites. Excavated material from this nearby site is finer than the native sand with a d_{50} = 0.2 mm. Model predictions to determine the effect of the pits, therefore, are limited to use of only this single fine grain size.

To determine the impact of the borrow sites properly; the three hypothetical storms were completed with the restored Alternative #1 bathymetry and the fine grain sand. Example computations for these control runs is provide for Storm #2 in the following figures (see Appendix G for the full suite of results). Figure 7-42 shows the final morphology and net sediment transport for the conditions without the pits. The model results for the contrasting conditions with the local borrow site are provided in Figure 7-43. It is clear that the far-field results for the two cases are similar. Significant differences do occur in the vicinity of the pits, however. Transects along the Camille Cut fill, for instance, show a dramatic decrease in longshore transport and are associated with a deposition. A large depression in close proximity to the shoreline is expected to affect the local wave conditions as the wave rays refract over the borrow feature. The resulting redistribution of energy creates relatively small regions of low wave action. The limited breaking within these areas impedes the longshore transport and may explain the reduced sediment transport evident in Figure 7-42.

The morphology change induced by Storm #2 for the Alternative #1 restored Ship Island without and with a local borrow site are shown in Figures 7-44 and 7-45.

Overall storm morphology change is larger than the differences in the modeled change, and the figures appear similar. To better discern the effect of the local borrow site, the difference in the morphology change for Alternative #1 is depicted in Figure 7-46. The most obvious feature is the

Figure 7-42. The final morphology and net sediment transport for sediment transport for Alternative #1 *without* the borrow pits (Storm #2).

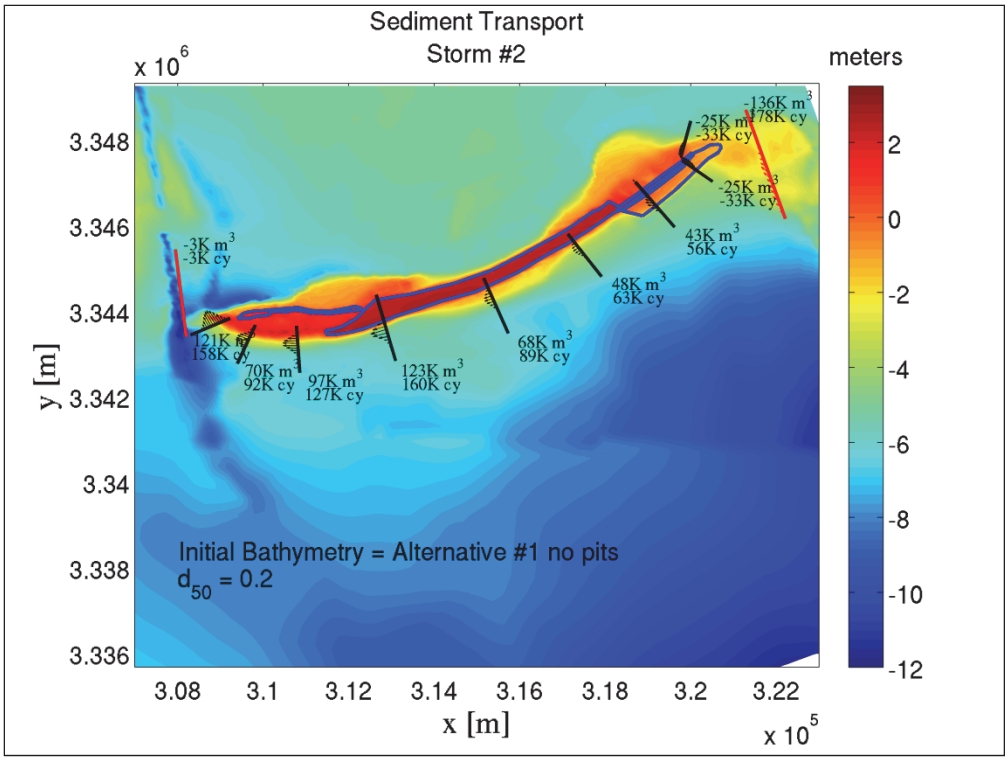

Figure 7-43. The final morphology and net sediment transport for sediment transport for Alternative #1 *with* the borrow pits (Storm #2).

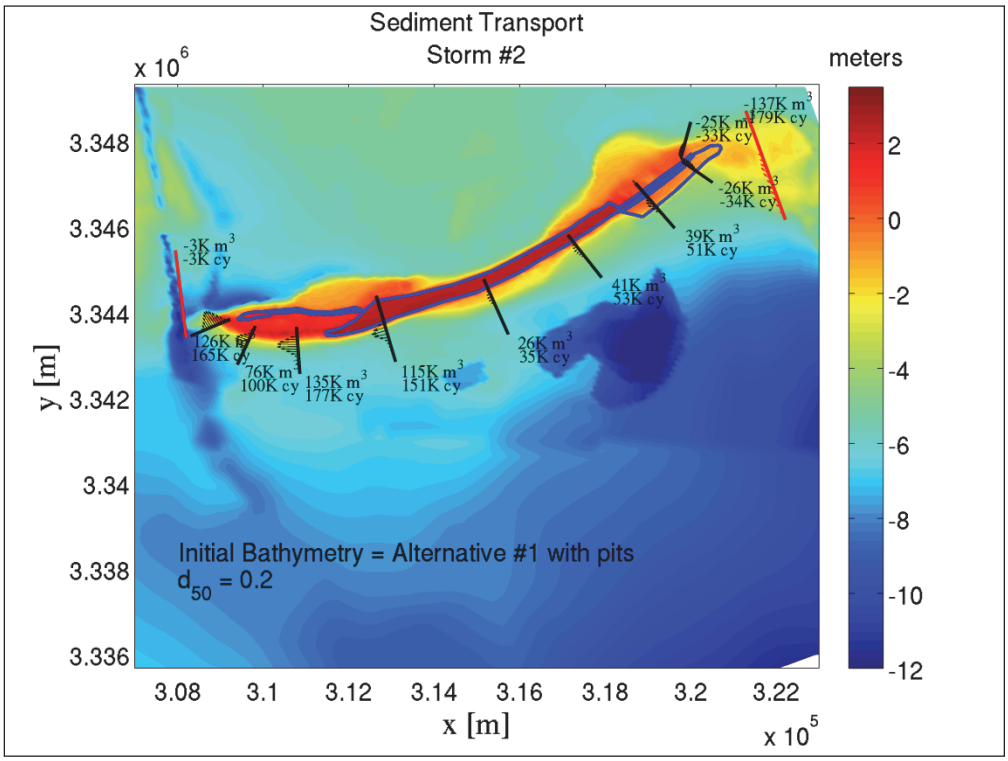

Figure 7-44. The morphology change for Alternative #1 without the pits (Storm #2).

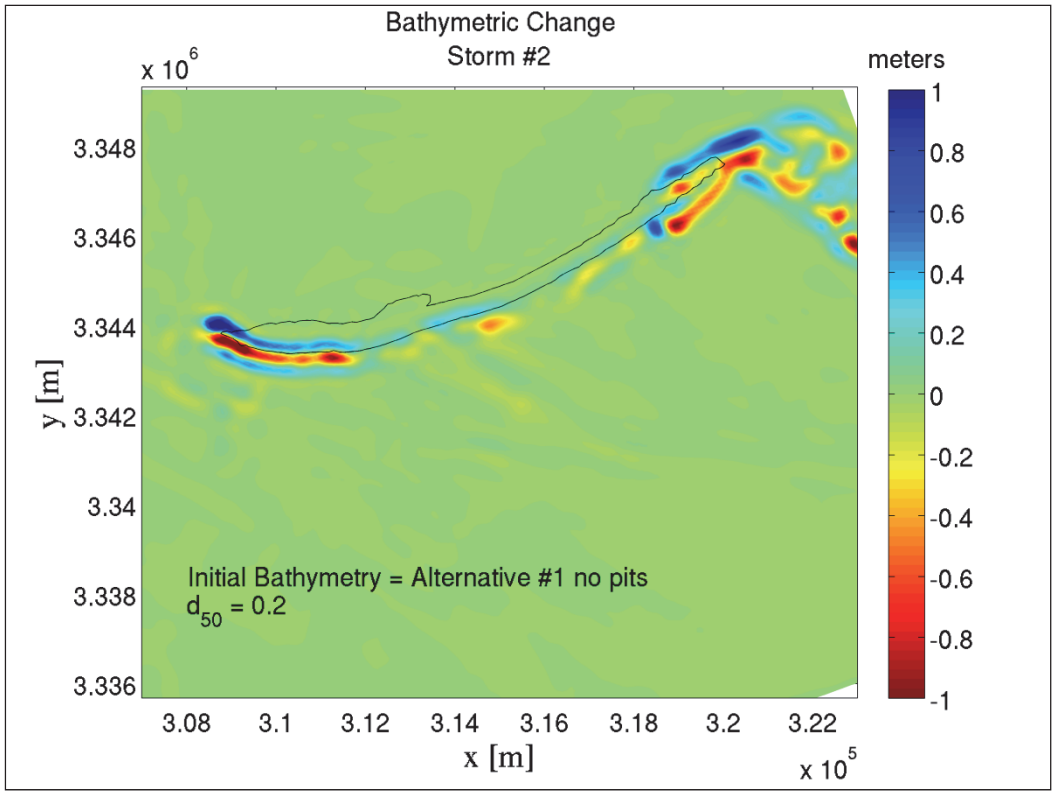

Figure 7-45. The morphology change for Alternative #1 with the pits (Storm #2).

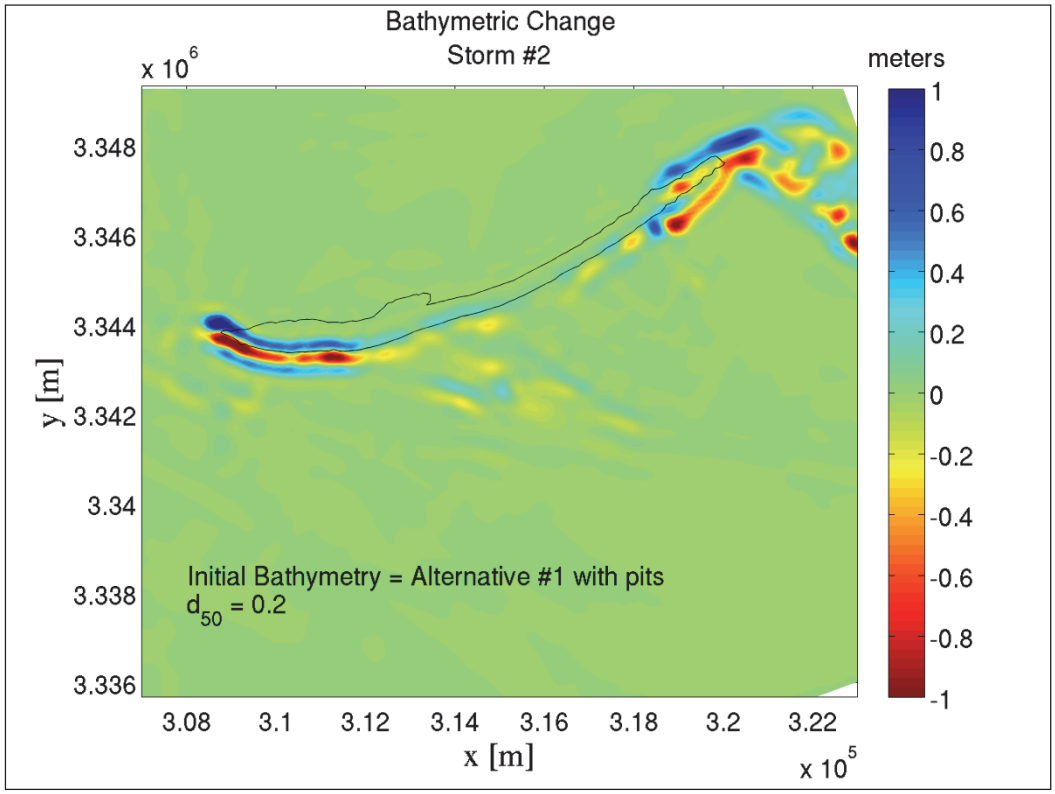

Figure 7-46. The effect of the borrow site on morphology change (Storm #2).

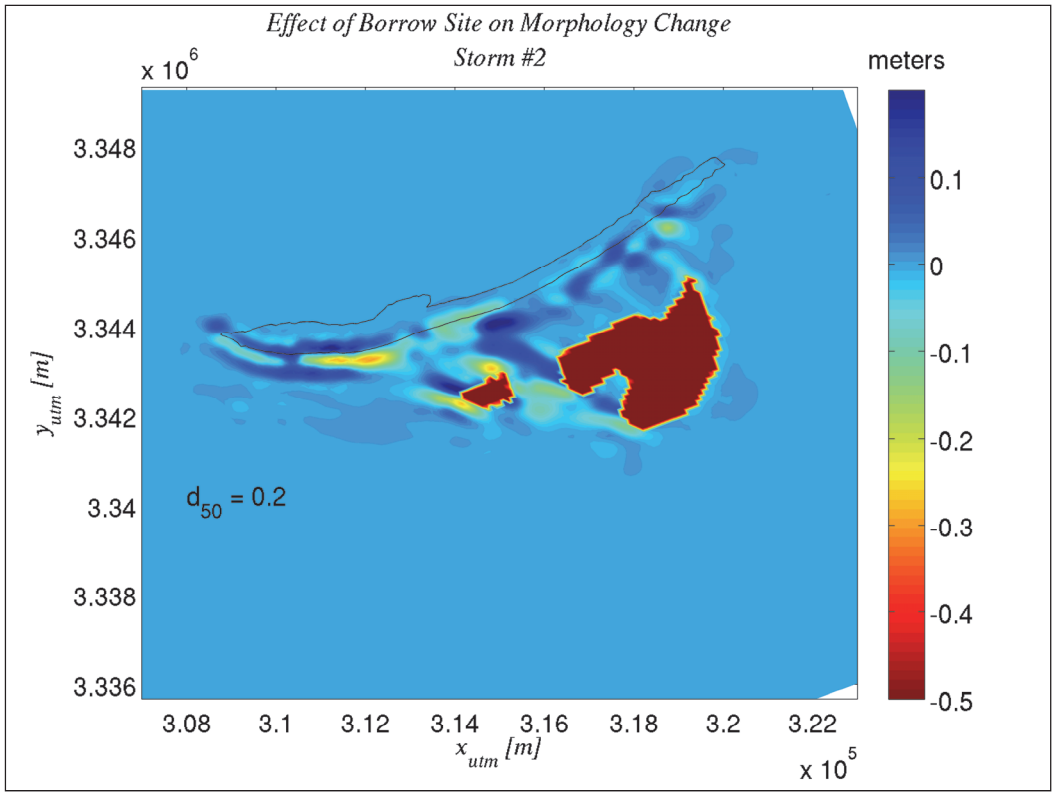

presence of the larger pits, which, of course is a difference in initial conditions for the two cases. The effect on storm morphology is limited to small regions with an increased erosion or deposition. In general the differences are on the order of 10 cm. There are, however, limited regions corresponding to the fringes of the pits with an additional 30 cm of predicted erosion. Also, it is noted that the region directly behind the depression is largely unchanged. The reader is referred to Appendix G for the complete set of results.

The effects of the pit for Storm #1 and Storm #3 are depicted below in Figures 7-47 and 7-48, respectively. For the most part, the local borrow site induces a change in morphology for Storm #1 that is similar to the results detailed for Storm #2, with increased erosion in the fringes of the pits. The results for Storm #3, however, are fundamentally different. Because the largest storm (Storm #3) completely overtops the island and waves break over the entire nearshore region, the pattern of erosion and deposition is more chaotic. It is interesting to note, also, that the magnitude of the pit effect is similar to the intermediate storm, despite the markedly different energies.

Figure 7-47. The effect of the borrow site on morphology change (Storm #1).

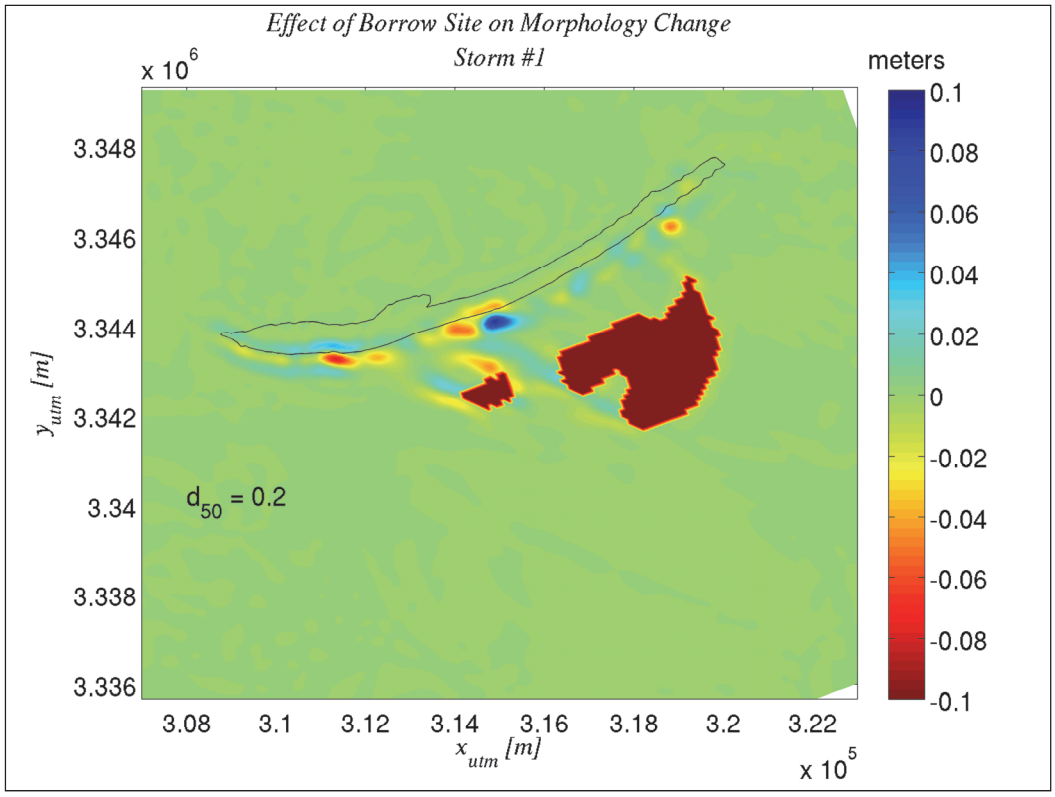

Figure 7-48. The effect of the borrow site on morphology change (Storm #3).

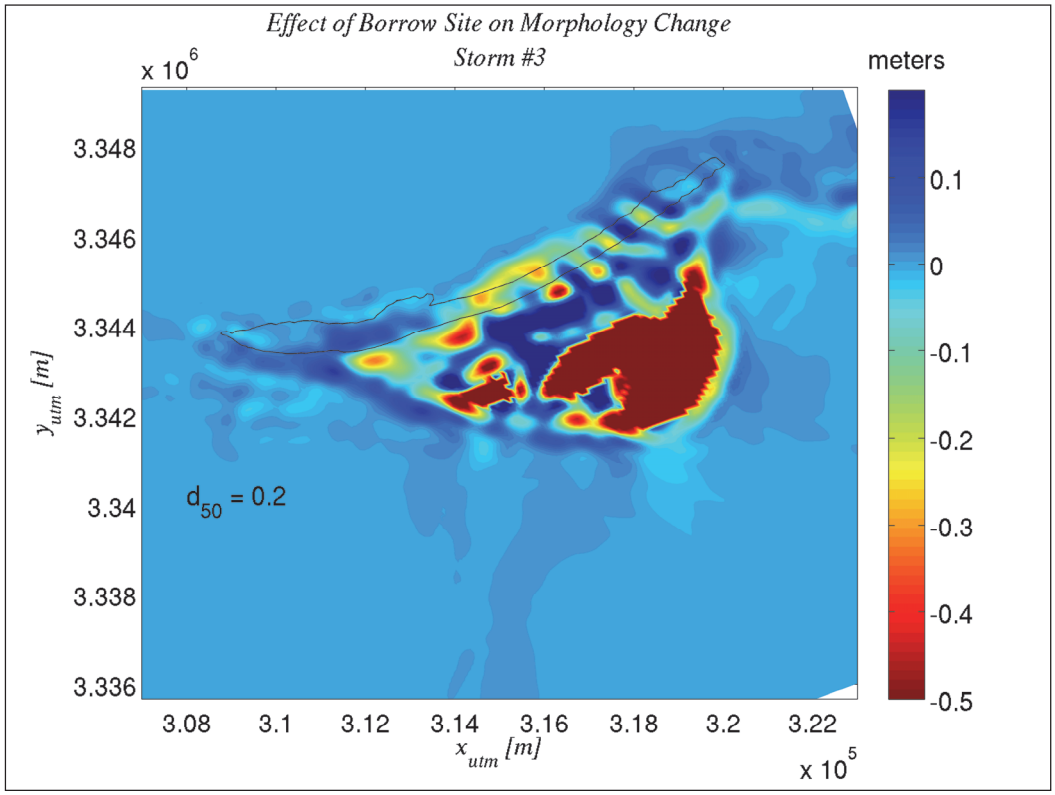

7.4.6 Sensitivity results for Alternative #2

Alternative #2 includes filling the cut between East and West Ship Islands and the nearshore region of East Ship Island with upwards of 17 million cubic yards of sandy material with a median grain size of approximately 0.32 mm. Sand sources for the fill consists of a number of potential sources including beneficial use of dredged material from the Pascagoula Federal Navigation Channel, offshore sources, and potential beneficial uses of dredged material from the Alabama and Lower Tombigbee waterways located within the State of Alabama. The fill template for Camille Cut breach closure consists of an averaged approximate 700 foot equilibrated island width at an elevation of approximately 2.1 m NAVD88. The feeder berm template along East Ship consists of an average approximate 1,000 foot equilibrated berm width at elevation of approximately 1.8 m. Alternative #2 includes a proposed 1.0 mcy borrow area located between 1.0 and 1.5 miles south of Ship Island in ambient water depths of approximately 10 m. The area is roughly 180 m wide (north-south direction) and 1800 m long (east-west direction) with an average cut depth of approximately 2.5 m. This moderately sized borrow pit is not expected to have a significant effect on the morphology, and no effort was made to isolate the effect of the borrow site. Restoration alternative #2 is depicted in Figure 7-50 where the borrow site is shown and the 1.8 m and 2.1 m berm outlines are provided as dashed and solid lines respectively. A comparison of Figures 7-49 and 7-50 indicates that restoration results in a small increase in transport around the island when compared to the existing base condition. The loss of the hydraulic connection between the Gulf and Sound through Camille Cut generates a larger velocity on the ends of the contiguous island, and an increased transport on the ends is therefore expected. Similar results are noted with Storm #2 (see full results in Appendix G).

Figures 7-51 and 7-52 depict the final modeled morphology along with the net sediment transport for Storm #3. The large storm surge completely inundates the restored island and Camille Cut is once again breached during this energetic event. It is worth noting that while breaching does indeed occur for the restoration scenario, the net sediment transport characteristics may differ significantly, especially at and near the fringes of the restoration template (shown as a solid blue line in Figure 7-52). In some areas near the restoration template fringes, the erosion is significantly increased due to the newly replenished volume of sand available for transport along with the altered hydrodynamics. The reader is referred to Appendix G for the complete set of results, including the morphology change induced by each of the three storms for the Alternative #2 Restoration.

Figure 7-49. The net sediment transport and final morphology for the existing conditions for Storm #1.

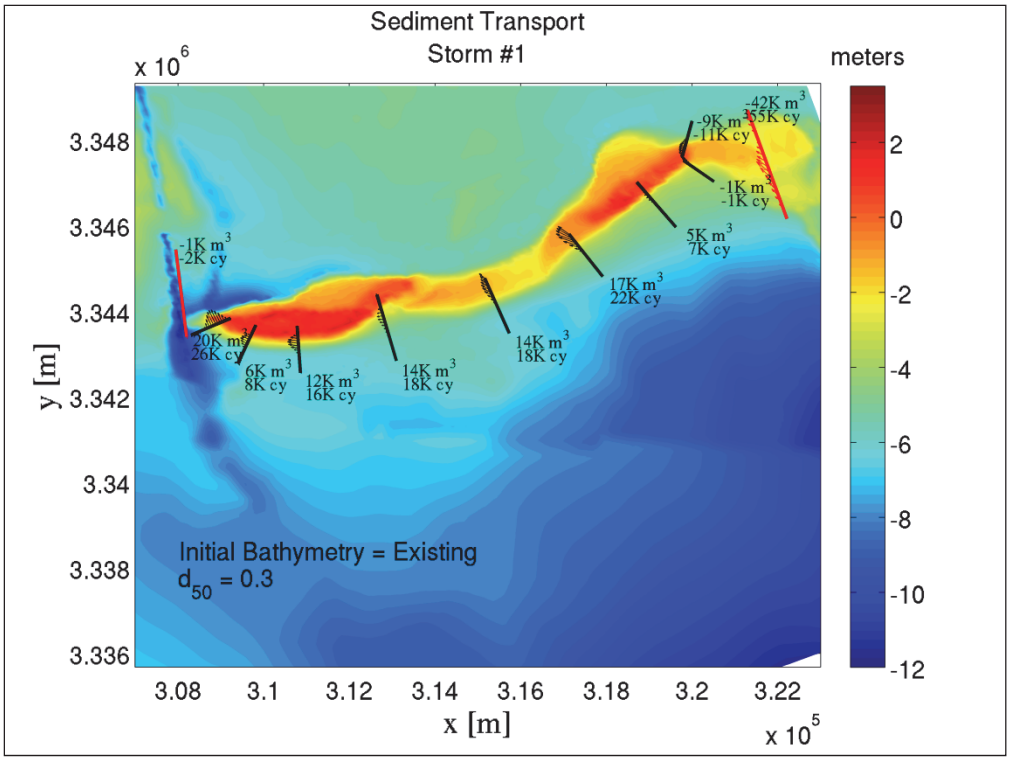

Figure 7-50. The net sediment transport and final morphology for the Alternative #2 Restored scenario for Storm #1.

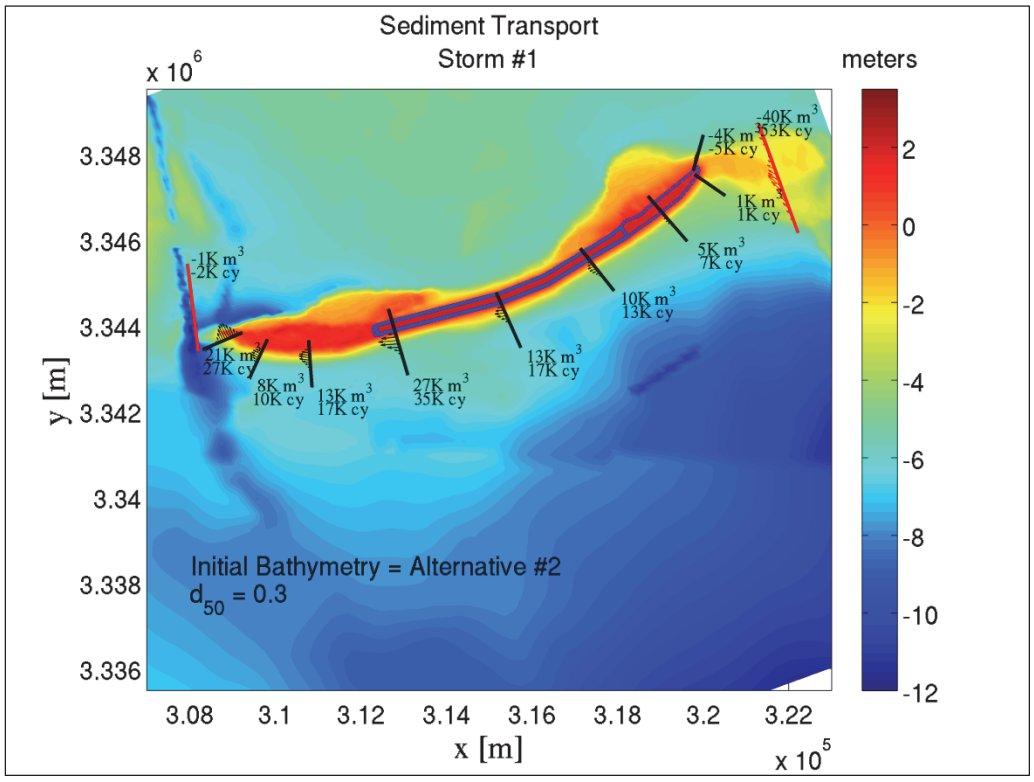

Figure 7-51. The net sediment transport and final morphology for the existing conditions for Storm #3.

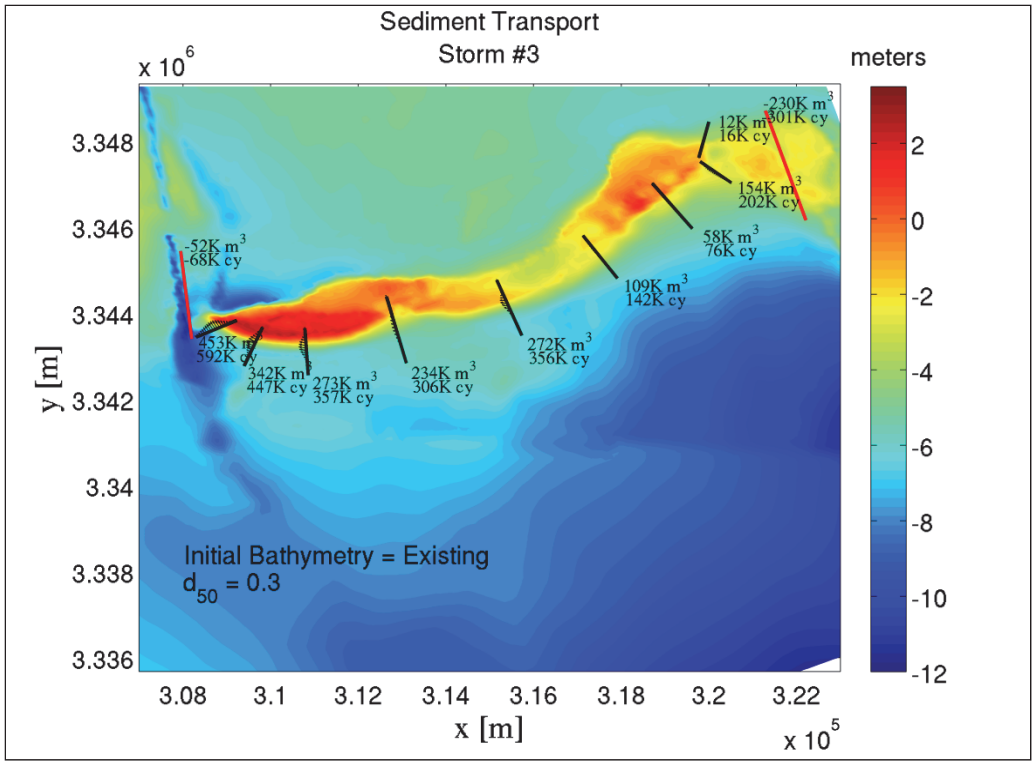

Figure 7-52. The net sediment transport and final morphology for the Alternative #2 restored scenario for Storm #3.

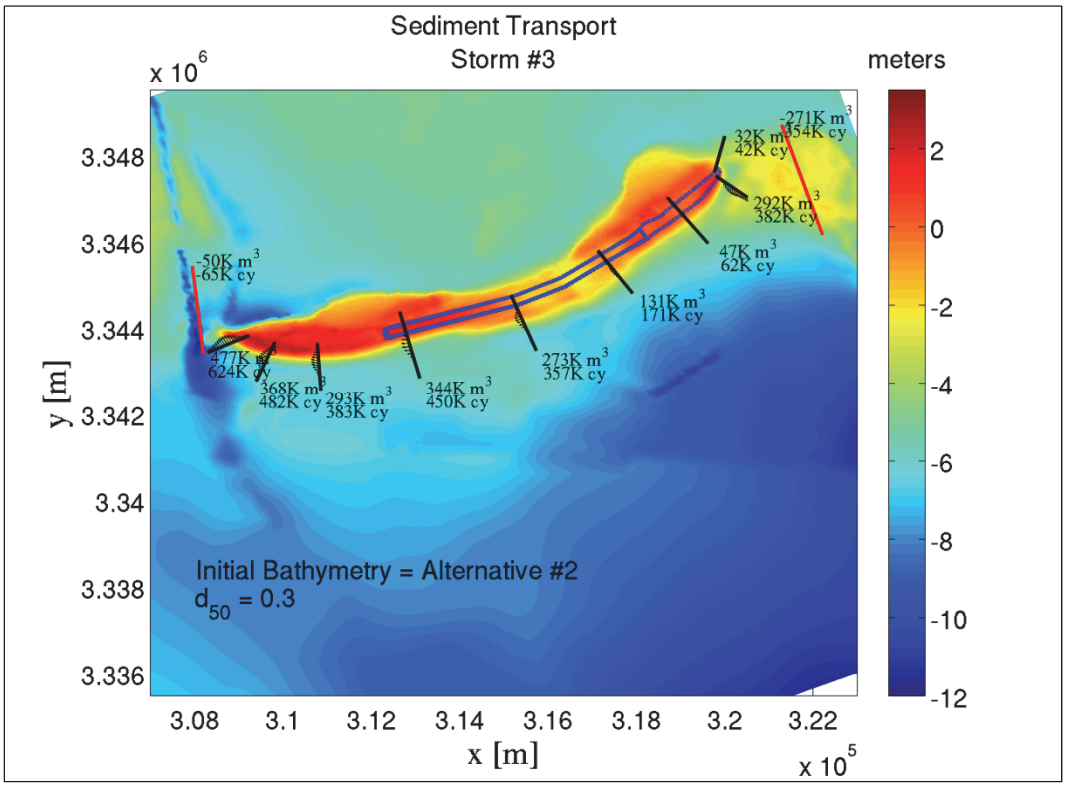

It is worth noting the gradients in transport and associated implications for the proposed restoration alternatives. For example, there is an increase in transport as you move westward from the center of East Ship Island to the center of the Camille Cut fill as seen in Figures 7-50 and 7-52. This is indicative of an erosive condition for this area. Conversely, the gradients between transects indicate depositional conditions along central and eastern West Ship Island. The western tip of West ship Island is always erosional for scenarios both with and without sand fill. Generally, these findings are in agreement with the island history where the more erosive conditions exist along the eastern part of Ship Island and the more stable conditions exist along the western part. This is also evident in the baseline conditions modeled results (shown herein) as well as during energetic historical storm breaching events, such as during Hurricane Katrina (modeled and shown herein) and the Ship Island breaching between West and East Ship Island in the present location of Camille Cut in response to the 1852 "Great Mobile" hurricane that made landfall near Horn Island that is described in Sullivan (2009) and Byrnes et al. (2011).

Also, modeled morphology results indicate that sand infills the navigation channel (indicated by a solid red lines in Figures 7-51 and 7-52) for extreme events (Storm #3). However, the volume of sand is similar for existing and restoration conditions (for both Alternative #1 and Alternative #2). This may indicate that on the west end of Ship Island, near-full transport potential is being realized. It should again be noted that the half-plane version of STWAVE was used in this analysis. An improvement with the analysis may be obtained with the full-plane, fully-direction version of STWAVE, especially with hurricanes which pass close to the island.

7.5 Summary

The recently developed C2SHORE morphology model is an extension of the one-dimensional CSHORE model. Building on a strong foundation in surf zone processes, the 2DH generalization allows arbitrary gradients and shoreline orientations. The previous wave-dominated limitation is eliminated with the introduction of a current formulation and numerical integration of the wave averaging procedure. The C2SHORE model, with numerically intensive nearshore computations, has a relatively small domain size. The effects of basin-scale hydrodynamics such as storm surge are included in the domain through the appropriate application of boundary conditions.

Implementation of the model coupling with large scale models to C2SHORE is examined by comparing predicted hydrodynamics with the field measurements presented in Chapter 2. Because differences in the existing bathymetry and the model domain may be significant, the flow velocity averaged over Camille Cut is used as a basis for comparison. For tidally driven flow, the model phase results were well predicted, but the amplitude was somewhat larger than the measured values during both flood and ebb tides.

To ascertain the C2SHORE performance for storm morphology change, Hurricane Katrina was modeled and compared with measured data. Unfortunately, Pre-Katrina subaqueous data in the nearshore region is sparse. Therefore, a pre-storm model domain was implemented from several available data sets, including a 2008 survey. Due to these limitations in the data, model-to-measurement comparisons were limited to lidar surveys of the emergent island. The modeled evolution in a contour near mean sea level agrees well with observations; with a general loss of land and a significant widening of Camille Cut. Likewise, the comparison of details of morphology change on emergent regions is reasonably well predicted with the exception of the west end of the island. Observed differences between model and measurements on the west end of Ship Island may be due to the use of the half-plane version of the STWAVE model, where energetic waves approach at angle outside of the model limits as the hurricane passes nearby to the west of Ship Island.

Finally, results are provided that examine the effect of the proposed restoration scenarios on the sediment transport environment. Three hypothetical storms are presented, with approximate return periods of 1.0, 10, and 500 years, and the transport environment is examined within the framework of these events for the Alternative #1 and Alternative #2 restoration scenarios. Initially, existing morphology is modeled to establish baseline conditions, which indicate a transport to the north around the ends of the island and a westerly longshore transport. With restoration and the fill of Camille Cut, loss of a hydraulic pathway between the separated island results in larger flow around the east and west ends of the contiguous island. Results indicate that the Camille Cut restoration fill survives higher-frequency storms (such as the 1-yr and 10-yr events), but is breached during the low-frequency 500-yr event modeled herein. Gradients in transport along the island indicate a more erosive condition to the east of Camille Cut and a more stable condition to the west of

Camille Cut, and these findings are in agreement with island history. To the west of Ship Island, sand infills the navigation channel, but only for the extreme event modeled (500-yrs), and the volume of infill is similar for existing conditions and the restoration scenarios (Alternative #1 and Alternative #2). To the east of Ship Island, modeled transport values indicate that the subaqueous region off the east end (Little Dog Keys Pass) will accumulate sediment, and this is in agreement with the Mississippi sediment budget.

Several choices exist for restoration sand depending on the material source, and the grain size effect is explored by modeling Alternative #1 storm morphology with a fine 0.2 mm, an intermediate 0.26 mm, and relatively coarse 0.3 mm sand. For smaller storms, fine-grain sand transport was 20 percent larger when compared with the 0.3 mm sand. A more dramatic difference is modeled in transport for Storm #3, where the increase in sand transport was approximately 40 percent. Additional model results for Alternative #1 scenarios indicate the effect of a possible sand borrow site located less than 1.5 km from the shoreline of the restored island. The large feature has the effect of redistributing wave energy along the island coast and generating local regions of increased or decreased wave action. For the smaller events, the effect of this variation is to significantly suppress the longshore transport. An additional effect of the pits is revealed for the smaller two events which show localized regions of increased erosion on the fringes of the pits, due, presumably, to wave focusing.

8 Borrow Area Analysis[1]

Planning of a restoration effort to the Mississippi Barrier Islands includes direct sand placement in the breach between East and West Ship Island, increasing the island footprint, and additional sand placed into the local littoral zone. The plan being considered, calls for placement of approximately 17 to 22 mcy of material in Camille Cut and along East Ship Island. Proposed borrow areas have been identified off the coasts of Ship, Dauphin, and Horn Islands. This chapter documents an analysis of relative changes with and without project conditions to examine the influence of the potential dredged borrow areas on sediment transport and shoreline changes along each island.

8.1 Modeling approach

Shoreline and littoral transport impacts induced by the excavation of proposed borrow areas were examined with the spectral near shore wave transformation model STWAVE (Smith et al. 1999) and the shoreline change model GENESIS (Hanson and Kraus 1989). The condition simulated the pre- and post dredging bathymetry for each proposed borrow area. The analysis involved simulating the transformation of offshore wave conditions gathered from offshore WIS stations. The transformed wave information corresponds to the offshore boundary of the STWAVE grid. Nearshore wave conditions generated by STWAVE provide necessary input to GENESIS, which estimates longshore sand transport rates and shoreline change along the Gulf of Mexico shorelines of the barrier islands.

8.2 Ship Island

A proposed source of material for the Ship Island restoration is located approximately 1.0 mile south of Ship Island in an ambient water depth of approximately 30 ft. Multiple borrow area configurations were considered off Ship Island. The borrow area SI1 is 1.0 mile wide (north-south direction) and 2.0 miles long (east-west direction) and has a maximum cut depth of 11.5 ft. Borrow area SI2 is located within SI1 with a maximum cut depth of 8.0 ft. Borrow area SI3 is also located within SI1 and has a maximum cut

[1] Written by Rusty L. Permenter, David B. King, and Mark B. Gravens, Coastal and Hydraulics Laboratory, US Army Engineer Research and Development Center, Vicksburg, MS.

depth of 5.0 ft. Borrow area SI4 is in the same vicinity as SI3 with a maximum cut depth of 10.4 ft. Borrow area SI5 is located on the offshore end of SI4 with a maximum cut depth of 8.8 ft. The proposed borrow areas are located in relatively shallow water depths and positioned in proximity to the new breach closure shoreline, creating potential for adverse shoreline impacts due to wave refraction over excavated borrow pits. The condition simulated for each borrow area represents the bathymetry following dredging and restoration of Ship Island. The restored shoreline, location of the SI1 borrows pits, and the model domains are illustrated in Figure 8-1. Proposed borrow areas SI2, SI3, SI4 and SI5 are located within the limits of the east pit of borrow area SI1.

Figure 8-1. STWAVE and GENESIS model domains.

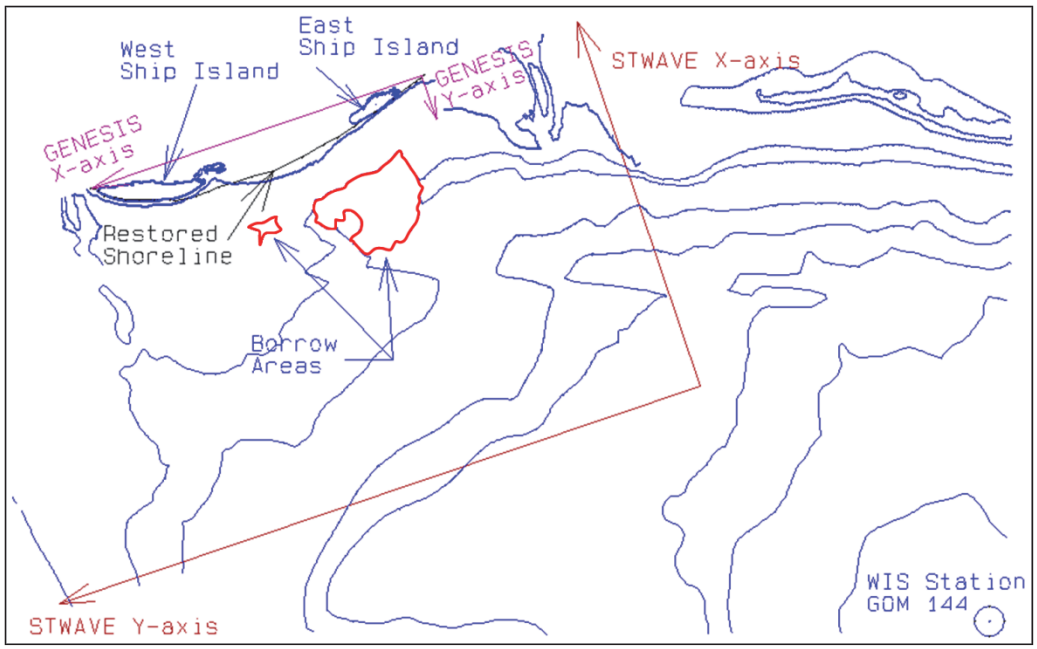

8.2.1 Model setup

Analysis for Ship Island involved simulating the transformation of offshore wave conditions derived from WIS Station GOM 144 (southeast corner of Figure 8-1) from the 15-m contour to the 12-m contour with the WIS Phase III transformation technique. The transformed wave information corresponds to the offshore boundary of the STWAVE grid. The grid domain for STWAVE simulations is shown in Figure 8-1.

The STWAVE X-axis is directed onshore, the *Y*-axis is directed alongshore and is aligned parallel with the Ship Island shoreline. Resolution of the STWAVE computational grid is 25 m in both the *x* and *y* directions.

Nearshore wave conditions generated by STWAVE along the nominal 5.0-m contour for both the Existing and Dredged condition provided necessary input to GENESIS, which estimates longshore sand transport rates and shoreline change along the restored Gulf of Mexico shoreline of Ship Island.

The GENESIS *X*-axis runs parallel to the Ship Island shoreline from the East Ship Island to West Ship Island and is comprised of 475 shoreline cells at 25 m intervals. Because detailed calibration data are not available for this study, the calibration coefficients were assigned typical values of $K1 = 0.4$ and $K2 = 0.2$, which result in a reasonable longshore sand transport regime compatible with developed sediment budgets in the region (Byrnes et al. 2011). These calibration values are typical of those applied in previous studies that employed WIS hindcast wave information as input, for example the Northern Gulf of Mexico Regional Sediment Management demonstration project (Lillycrop and Parson 2000), and produced longshore sand transport rates that are in general agreement with the Ship Island sediment budget. Because this study is a relative analysis between with and without excavated borrow areas, aimed at estimating the potential shoreline impacts of proposed dredging of the nearshore borrow area, the importance of a detailed calibration is diminished.

Dredged bathymetry for SI1 is shown in Figure 8-2 and bathymetry change between with and without borrow area is plotted in Figures 8-3 to 8-7 for all three proposed borrow areas to highlight the borrow configuration. The nearshore wave reference line (where the STWAVE information is stored and transferred to the GENESIS model) is represented by the thick black line. The landward edge of the borrow areas is approximately 1.6 km (1.0 mile) offshore of the restored Ship Island shoreline and the maximum increased depth in the borrow areas approaches 3.5 m (11.5 ft).

8.2.2 Wave transformation analysis

Nearshore wave transformation simulations were performed for 46 representative wave conditions identified through analysis of WIS hindcast station GOM 144 located in 15 m water depth offshore of Ship Island (Figure 8-1). Figure 8-8 shows the distribution of representative wave conditions by incident wave angle and period. The incident wave angle is measured clockwise from shore normal. The value in each block represents the number of occurrences for a specific wave condition in the 20-year WIS hindcast spanning the interval 1980 through 1999. For each representative wave condition an idealized TMA wave spectrum with an H_{mo} of 1.0 m was

Figure 8-2. Dredged bathymetry for SI1.

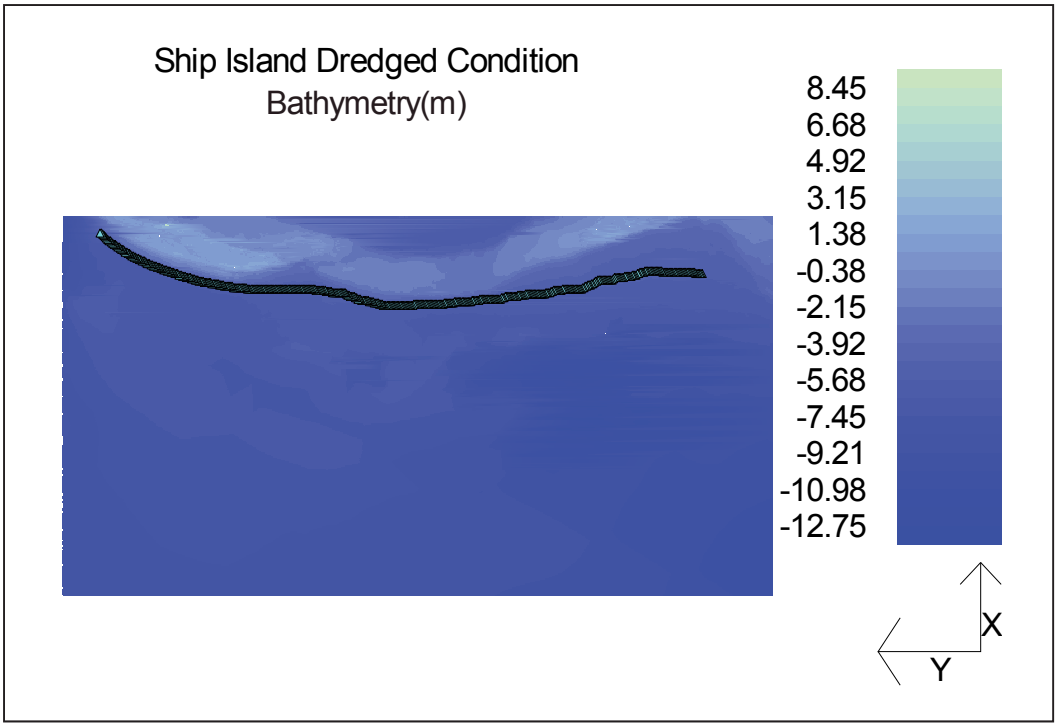

Figure 8-3. Existing condition bathymetry minus SI1 Dredged condition bathymetry.

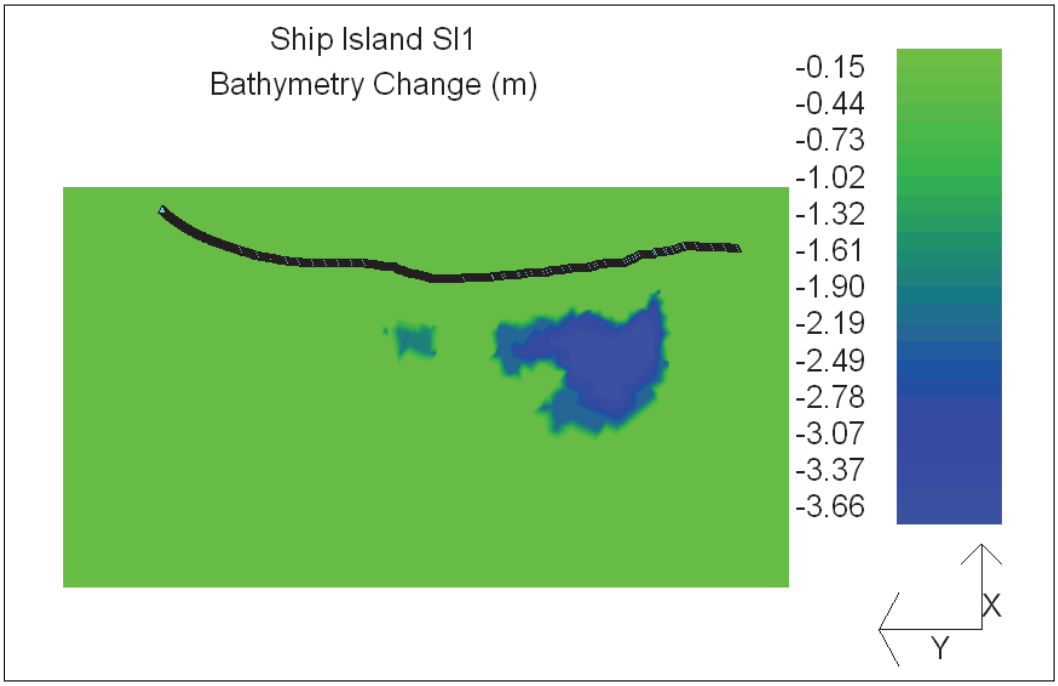

Figure 8-4. Existing Condition bathymetry minus SI2 Dredged condition bathymetry.

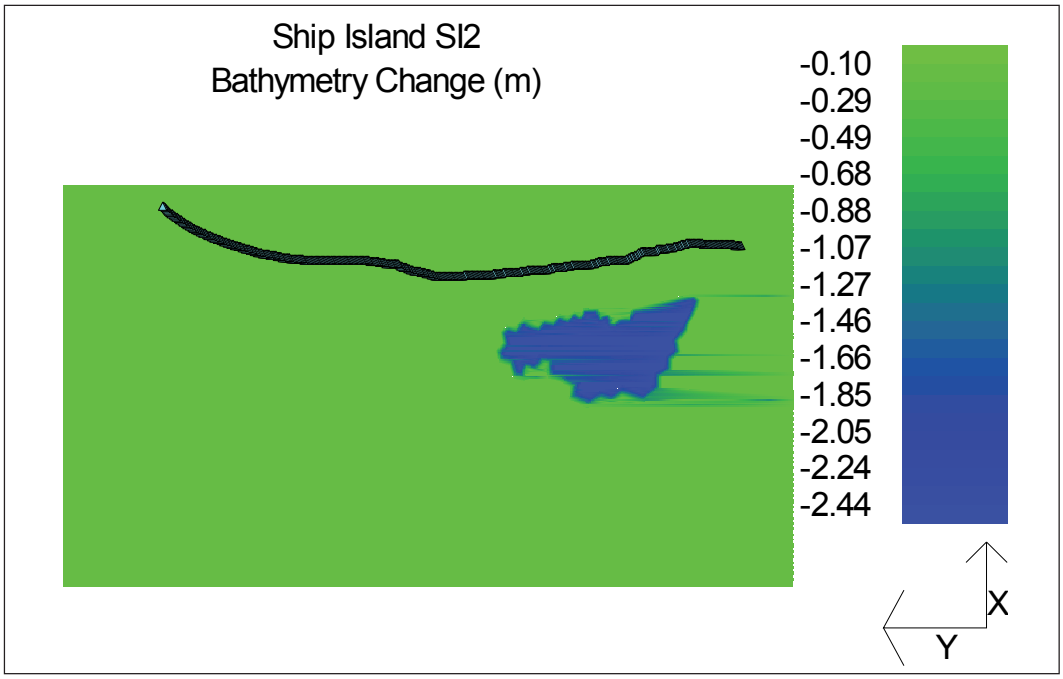

Figure 8-5. Existing Condition bathymetry minus SI3 Dredged condition bathymetry.

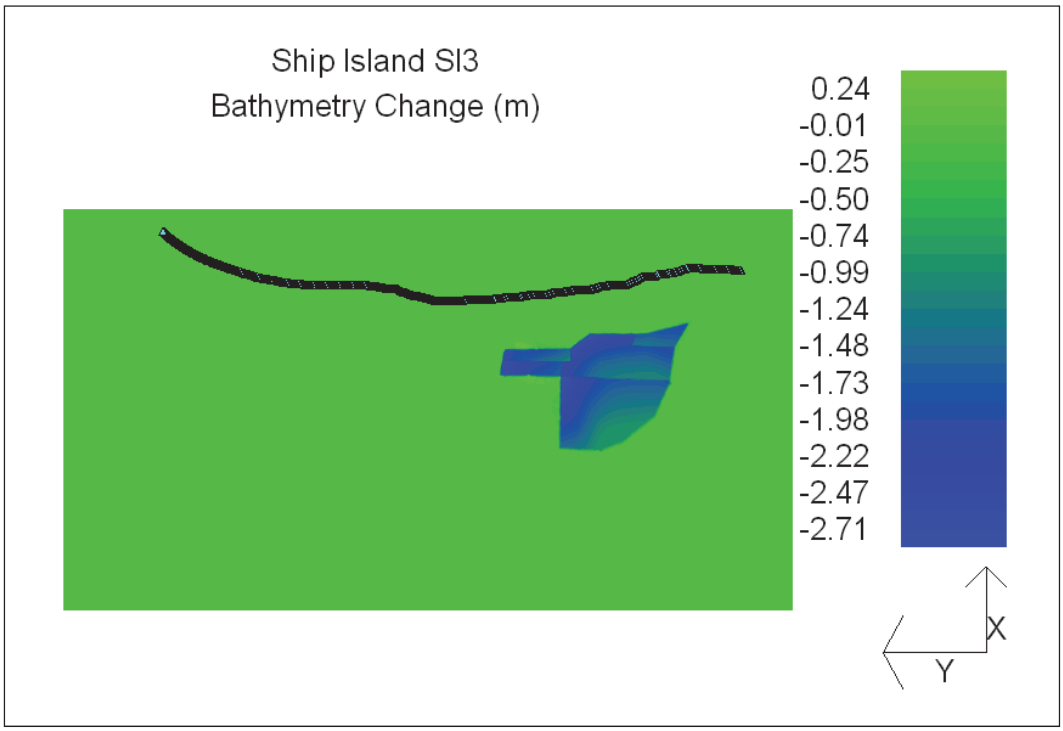

Figure 8-6. Existing Condition bathymetry minus SI4 Dredged condition bathymetry.

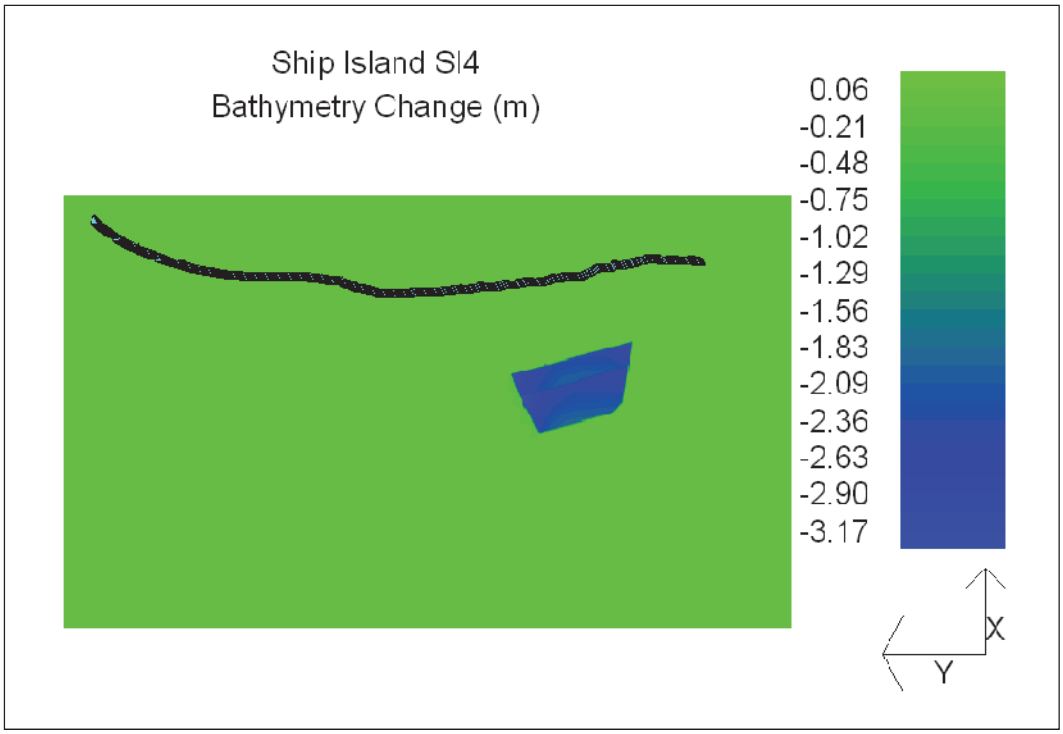

Figure 8-7. Existing Condition bathymetry minus SI5 Dredged condition bathymetry.

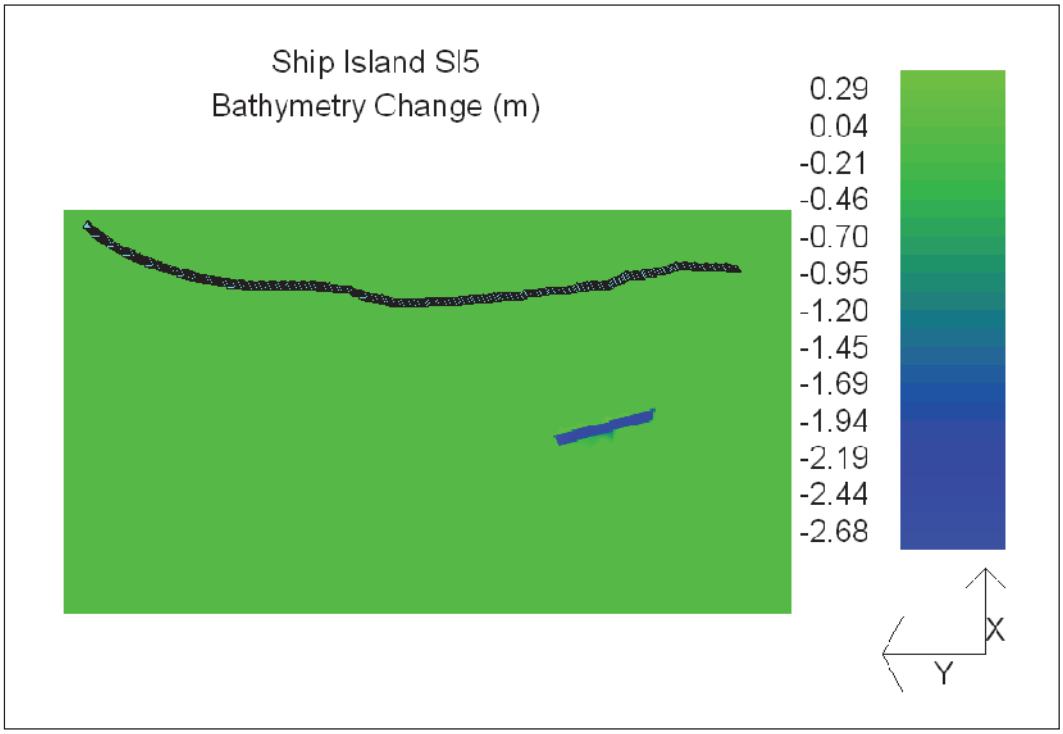

Figure 8-8. Distribution of the representative wave conditions by incident wave angle and period.

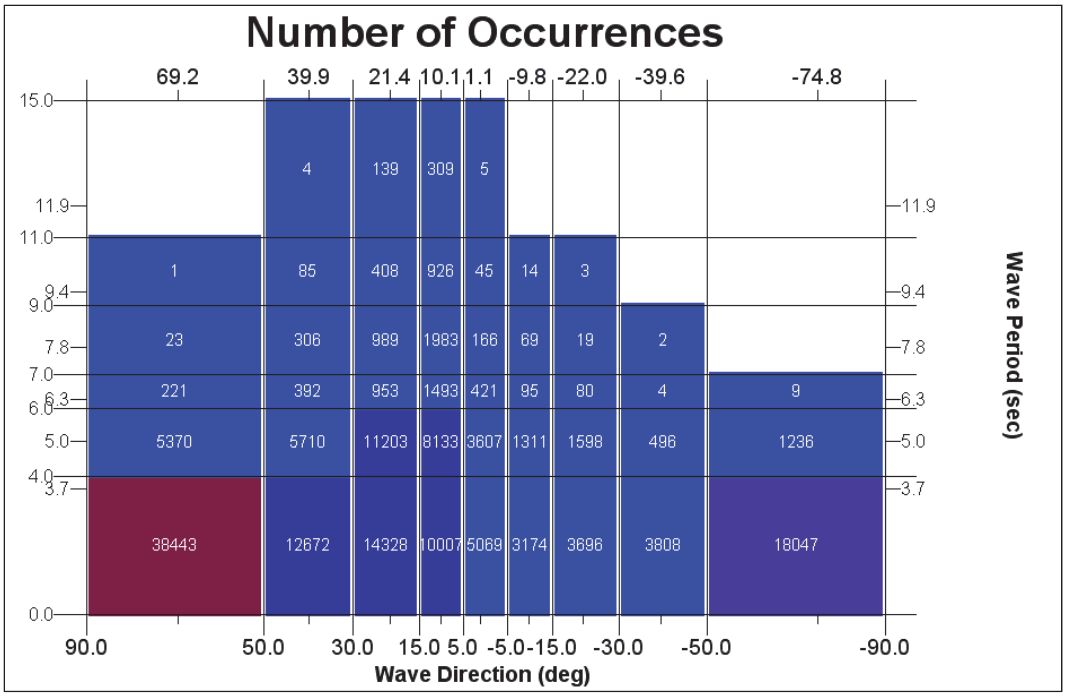

generated and applied as the input to STWAVE. Because wave transformation in intermediate water depths is independent of wave height prior to breaking, the transformation of a unit wave height produces a wave height transformation coefficient that is used by GENESIS to estimate nearshore waves heights by multiplying the time varying offshore wave height by the STWAVE estimated wave height transformation coefficient. This technique allows for complete characterization of nearshore wave conditions through the transformation of a limited number of representative offshore wave conditions.

STWAVE simulations were performed to compute wave transformation across irregular offshore bathymetry from approximately the 12-m contour to the 5.0-m contour. Two sets of STWAVE simulations were performed to estimate nearshore wave conditions for both the existing and Dredged (Restored) conditions for SI1, SI2, SI3, SI4, and SI5. Changes in significant wave height and direction resulting from excavation of the proposed borrow areas were determined by subtracting existing condition STWAVE results from Dredged condition STWAVE results. Figure 8-9 is a plot of wave heights over the STWAVE computational domain for existing bathymetry for an event with a period of 5.0 sec and an approach angle of 10.11 degrees. Figures 8-10 through 8-15 illustrate estimated significant wave height changes induced by excavation of proposed borrow areas SI1, SI2, SI3, SI4,

Figure 8-9. Existing Condition wave heights for incident wave of *H* = 1.0 m, *T* = 5.0 sec and *Theta* = 10.11 deg.

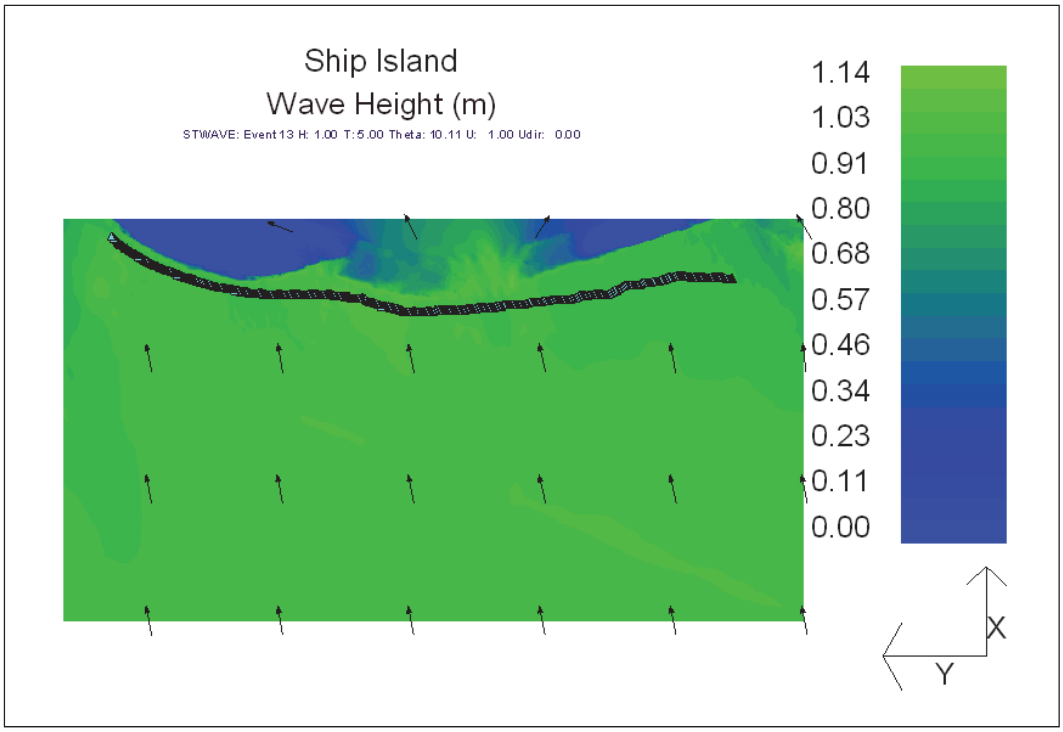

and SI5 offshore of Ship Island for select characteristic wave conditions. Wave conditions selected represent the four most frequent and the two most severe wave conditions.

These changes are calculated by subtracting wave heights found for the Existing condition from wave heights for the Dredged condition for each wave state. Figures 8-10 through 8-13 correspond to typical 5.0 sec waves approaching Ship Island from east-southeast through south-southeast, respectively. Figures 8-14 and 8-15 correspond to 11 sec waves approaching Ship Island from the south-southeast sector. For all potential borrow configurations wave height decreases in the lee of the borrow area as the waves pass over the borrow areas. Wave heights tend to increase along the sides of the potential borrow areas in the down-wave direction. Borrow areas SI2, SI3, SI4, and SI5 cause less focusing on the restoration area than does borrow area SI1 due and the absence of the smaller western pit. SI2 has slightly larger changes due to SI3's lesser depth and the smaller footprint of SI4 and SI5. SI5 minimizes effects of the borrow area due to a minimal footprint. The restored Ship Island shoreline is indicated by the top black line in each figure.

Figure 8-10. Wave height change (Dredged – Existing) for incident wave of *H* = 1.0 m, *T* = 5.0 sec and *Theta* = 10.11 deg. (Continued)

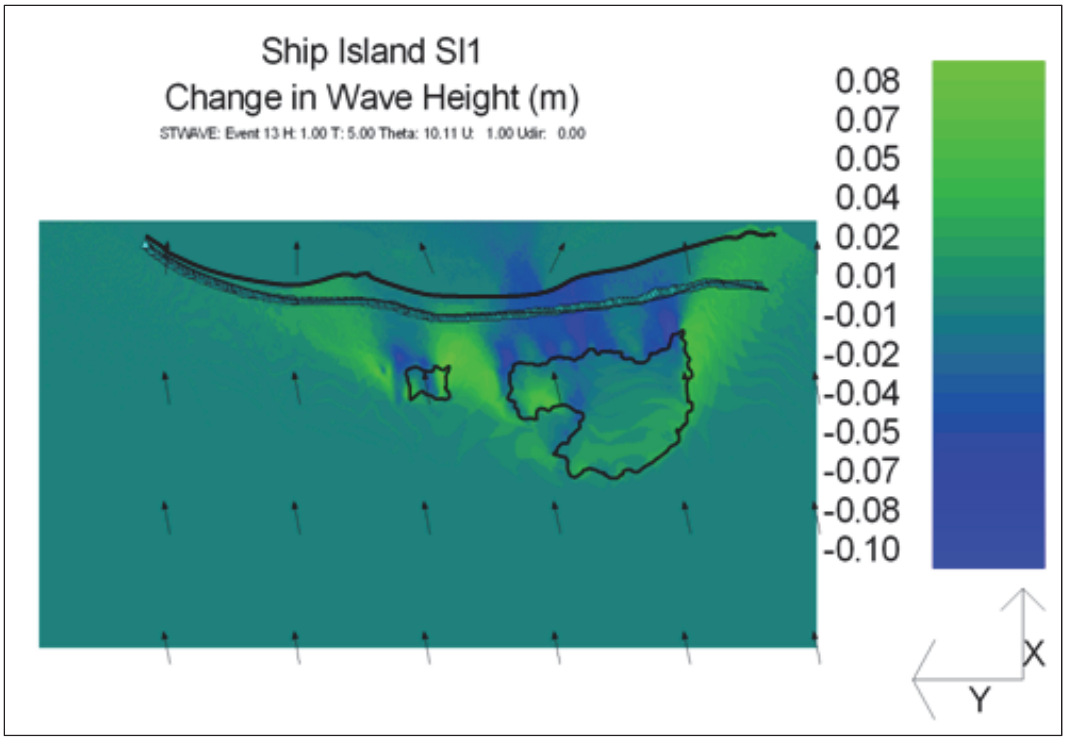

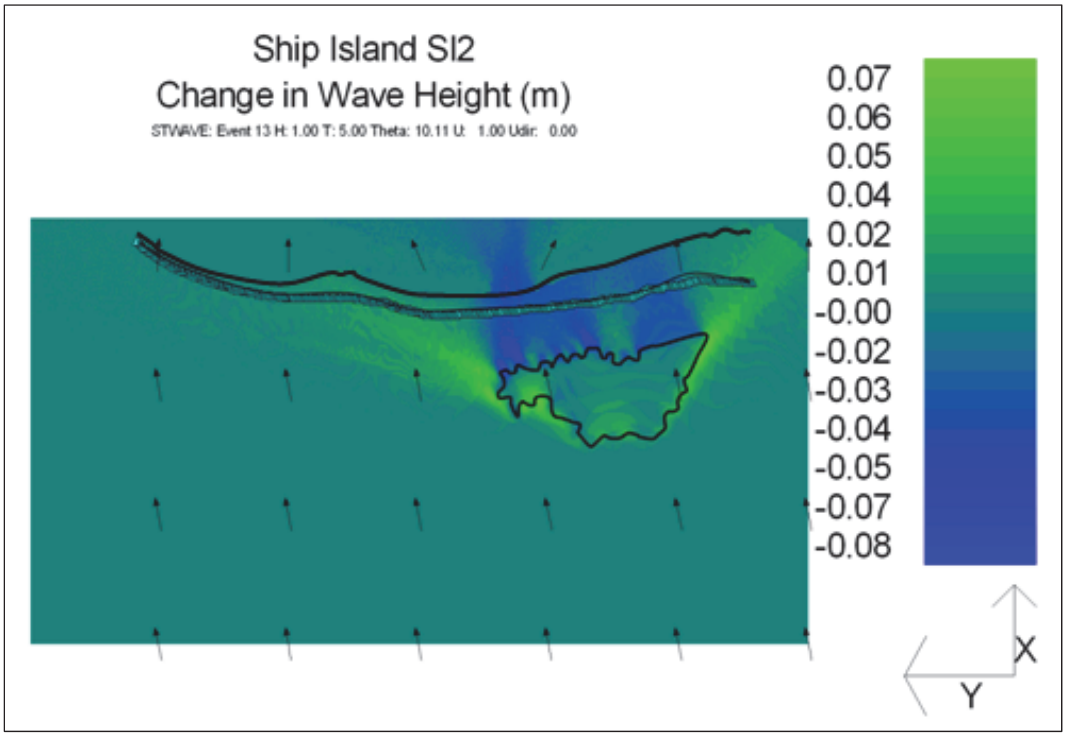

Figure 8-10. (Continued).

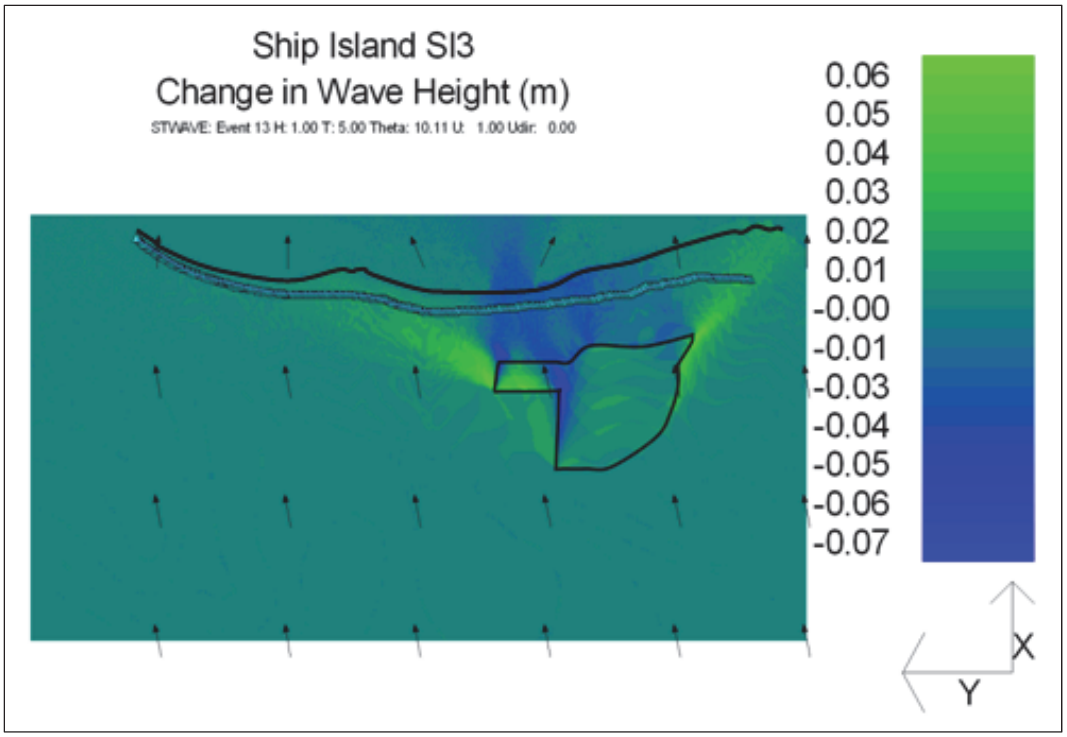

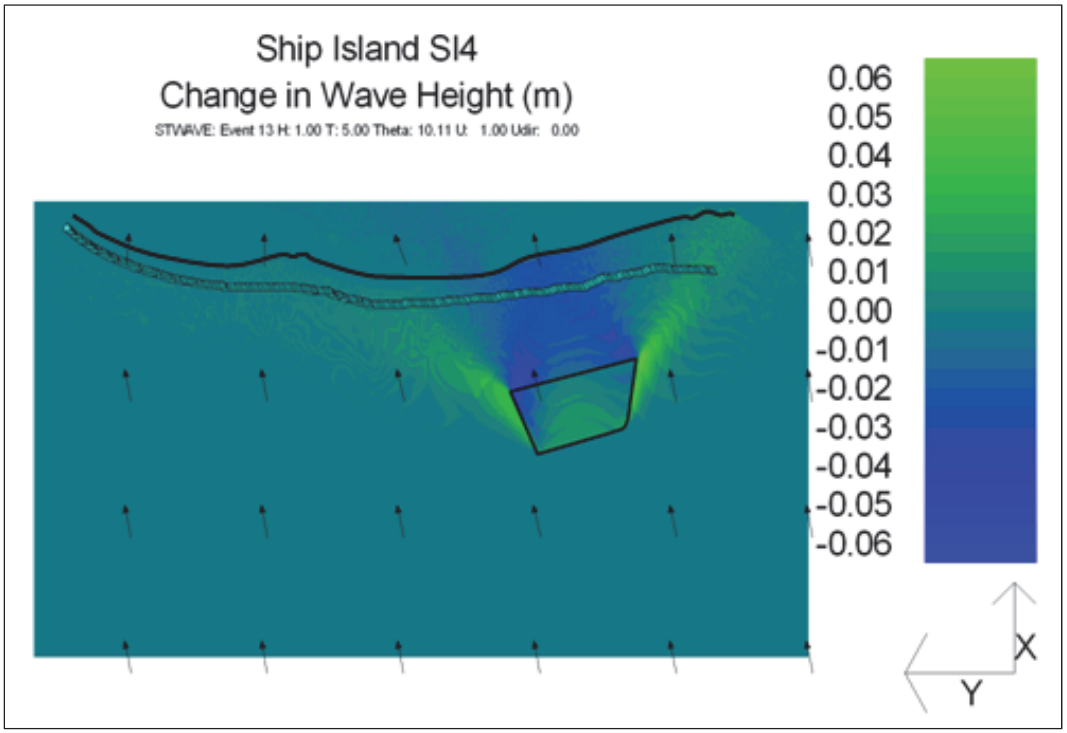

Figure 8-10. (Concluded).

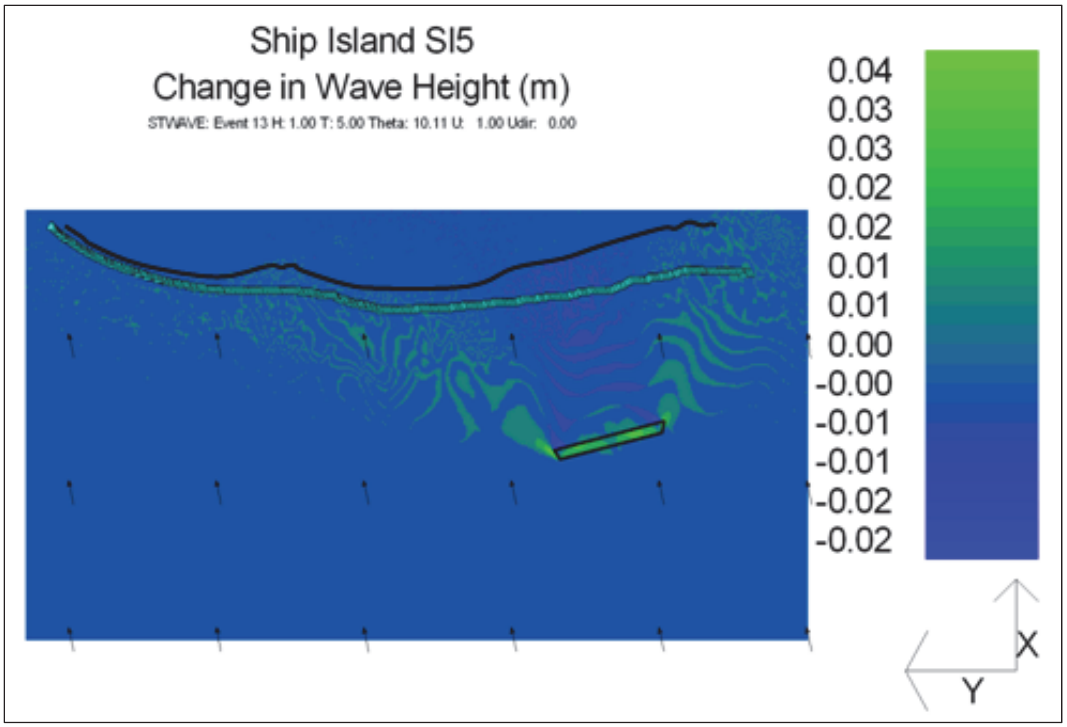

Figure 8-11. Wave height change (Dredged – Existing) for incident wave of *H* = 1.0 m, *T* = 5.0 sec and *Theta* = 21.34 deg. (Continued)

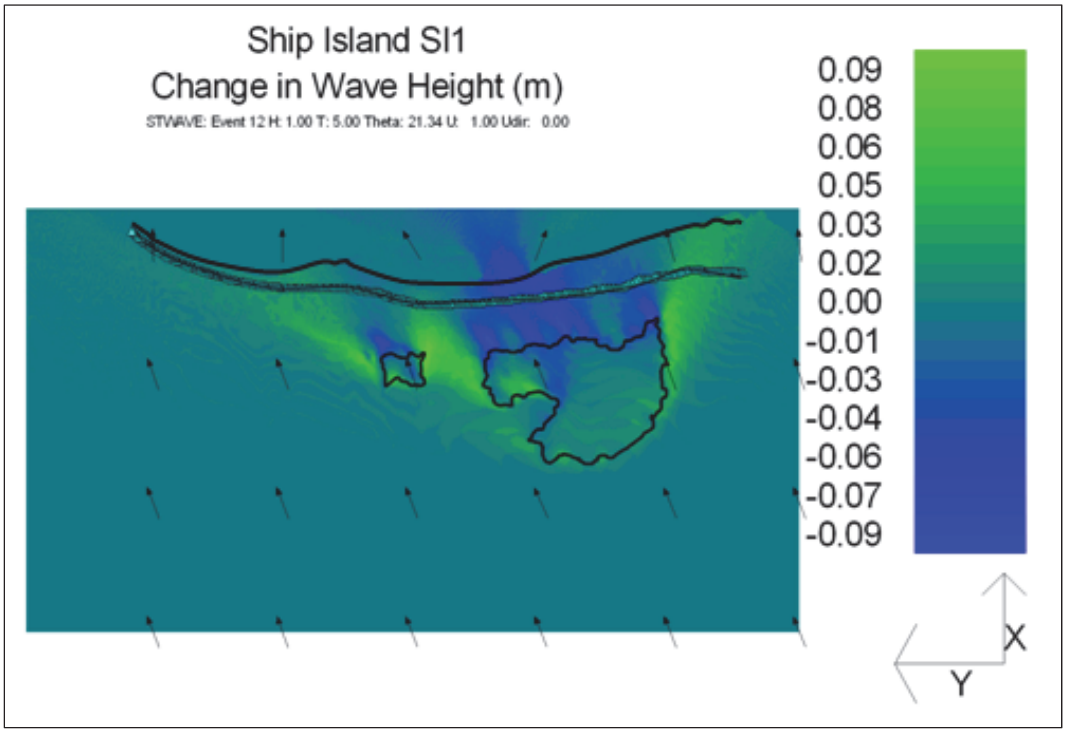

Figure 8-11. (Continued).

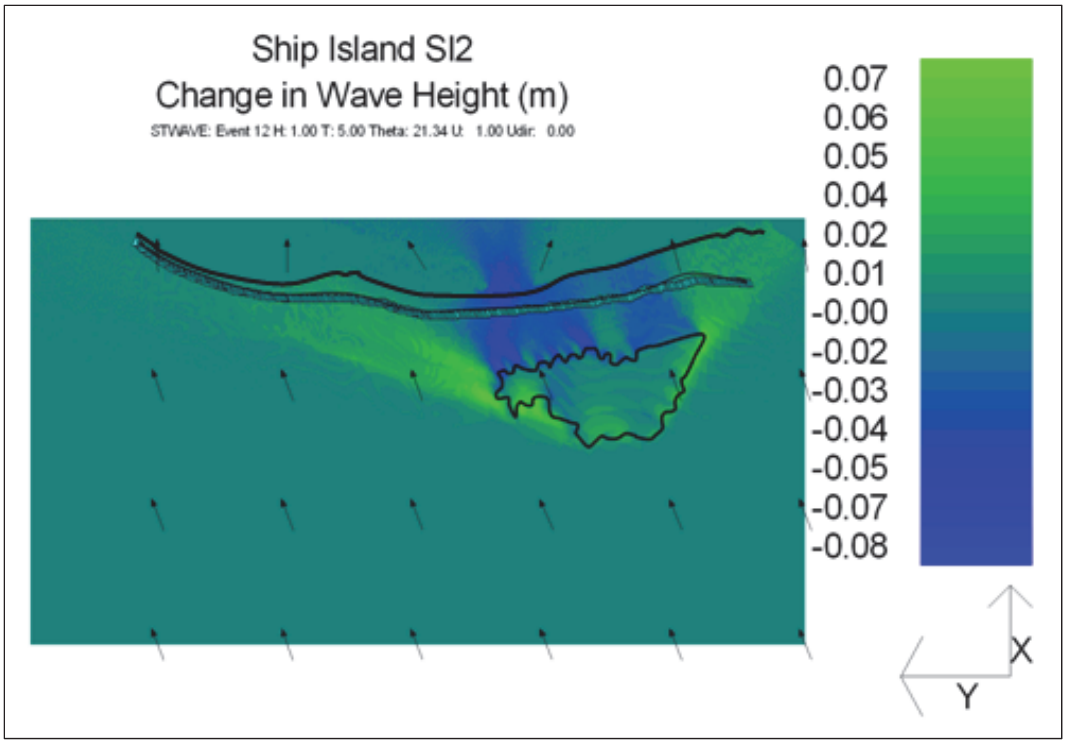

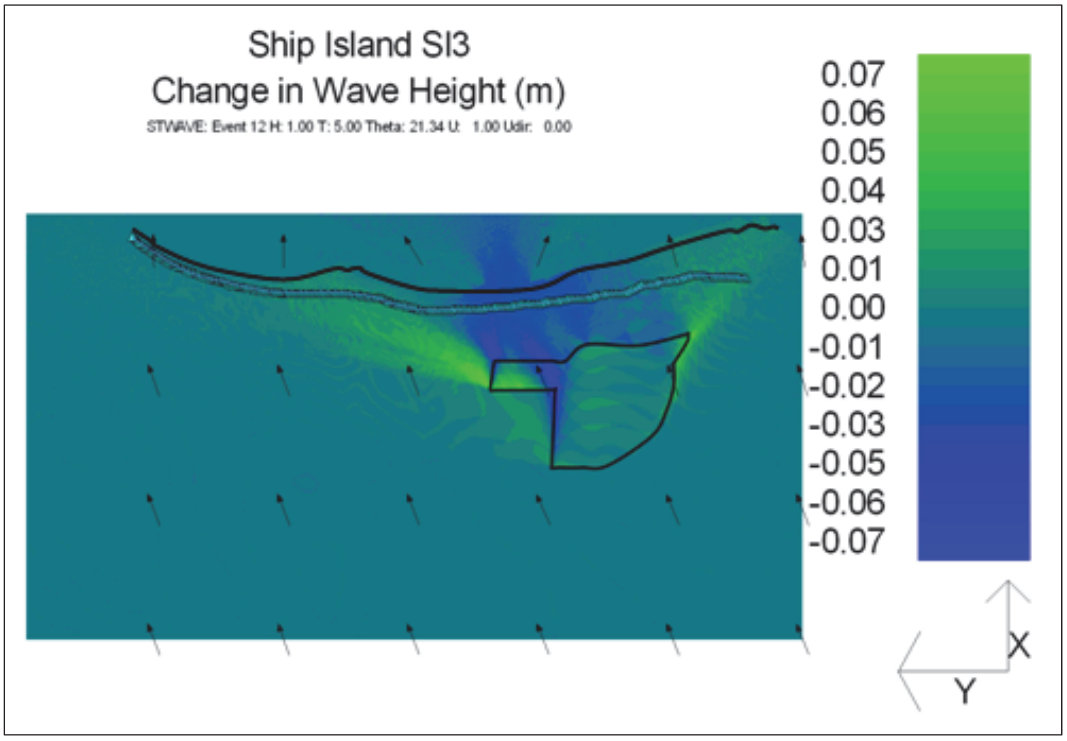

Figure 8-11. (Concluded).

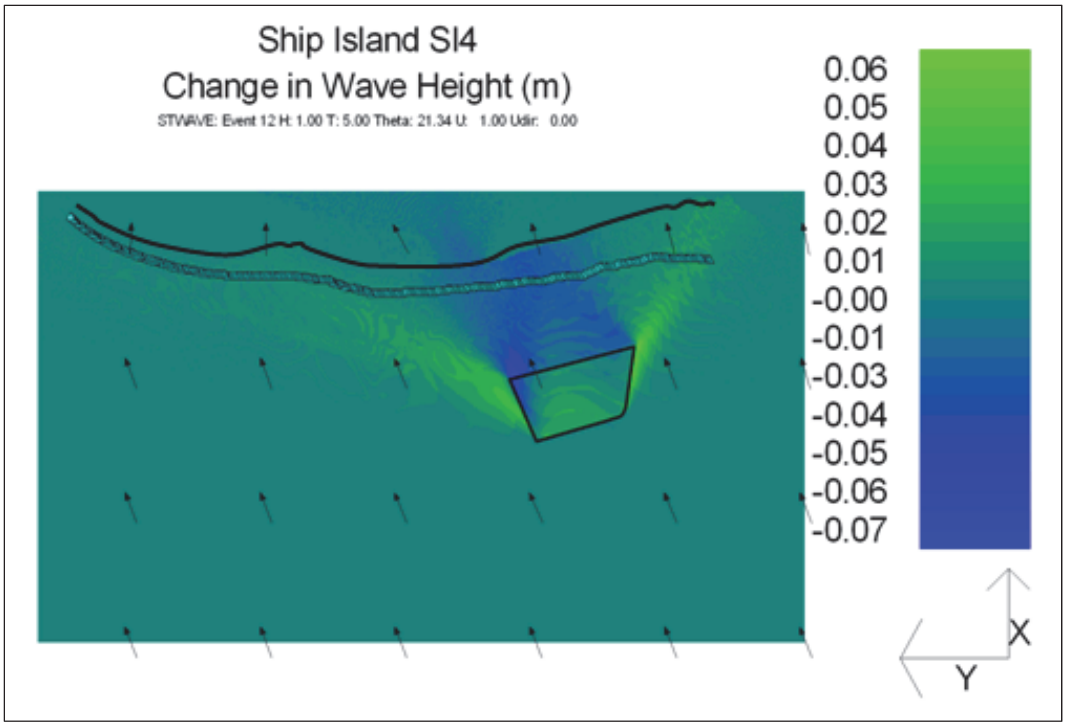

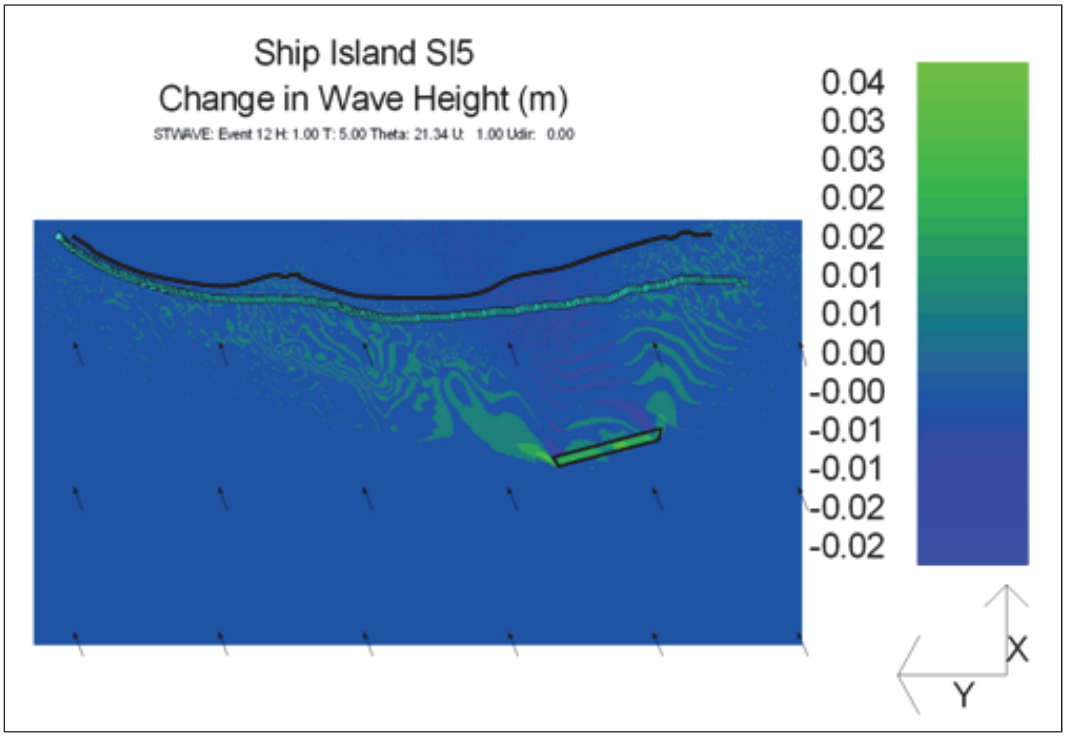

Figure 8-12. Wave height change (Dredged – Existing) for incident wave of *H* =1.0 m, *T* = 5.0 sec and *Theta* = 38.38 deg. (Continued)

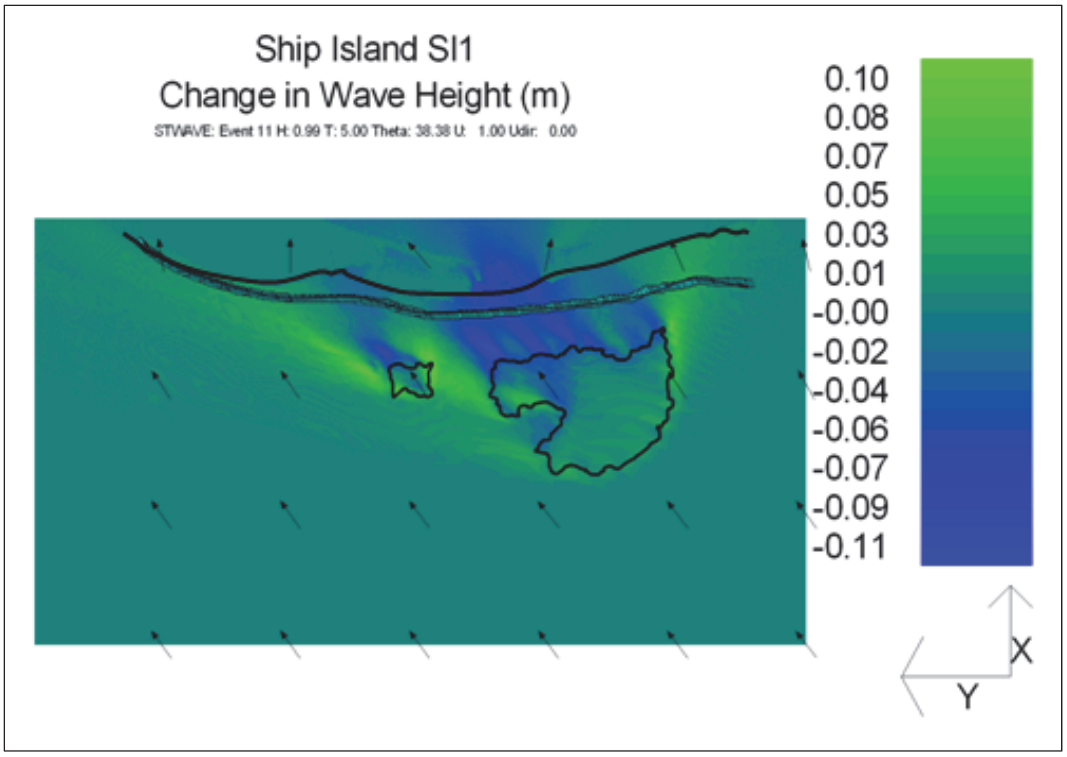

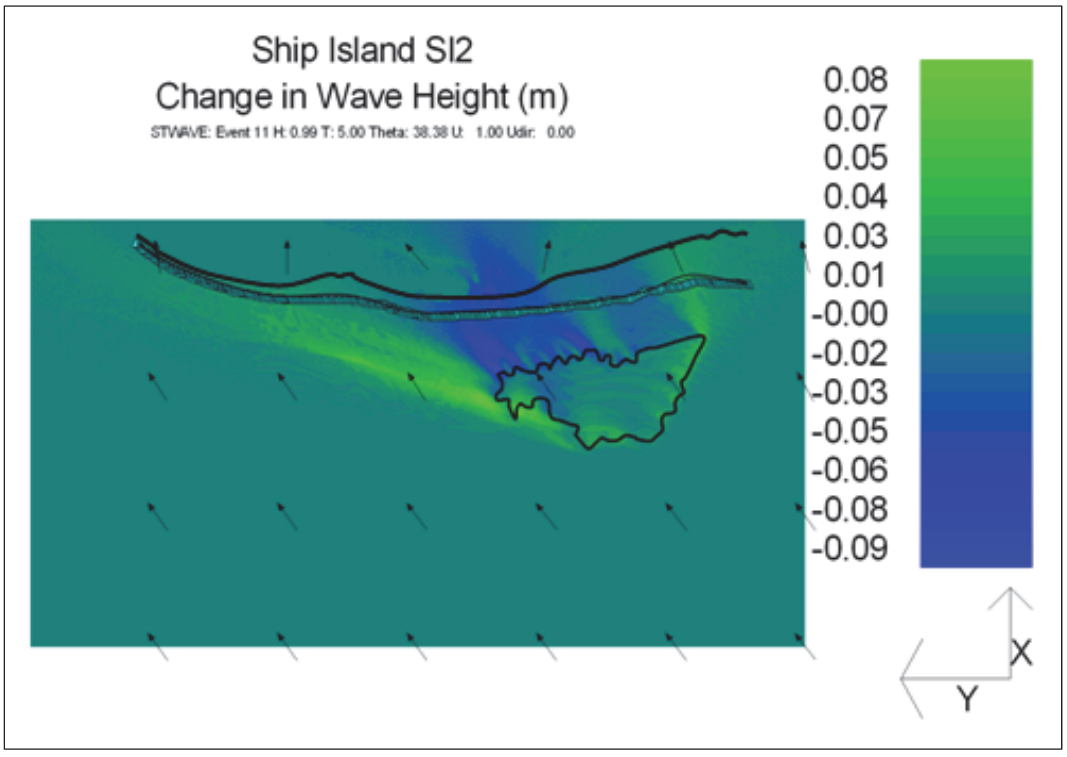

Figure 8-12. (Continued).

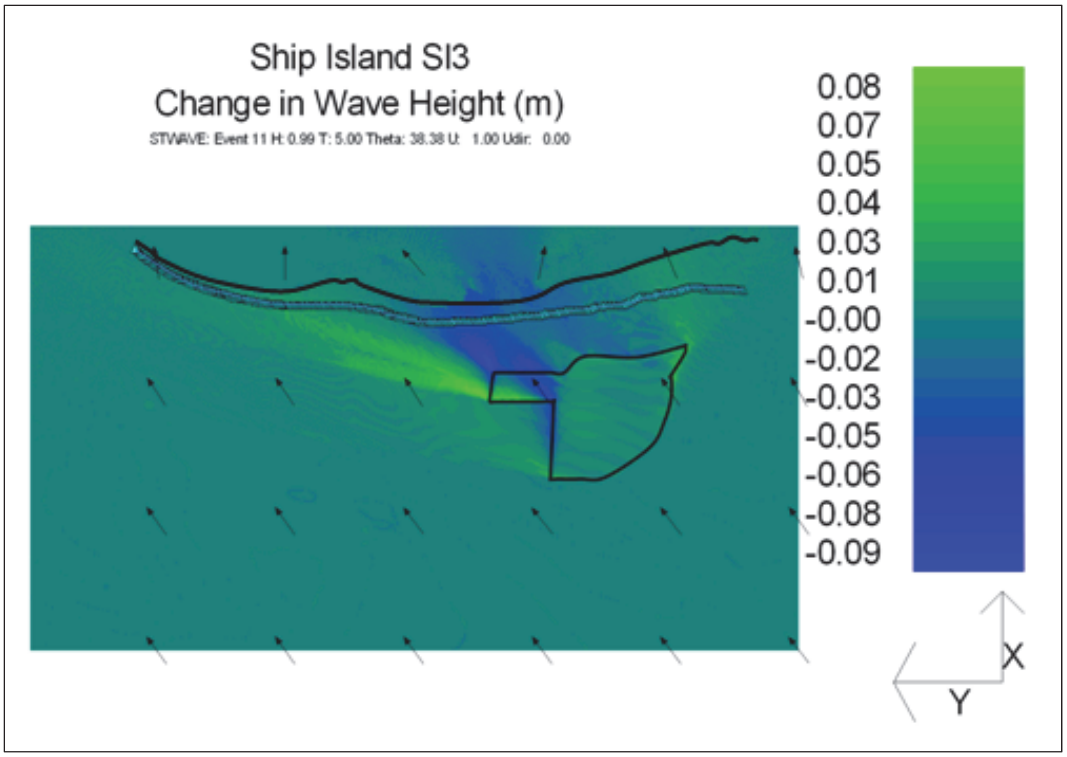

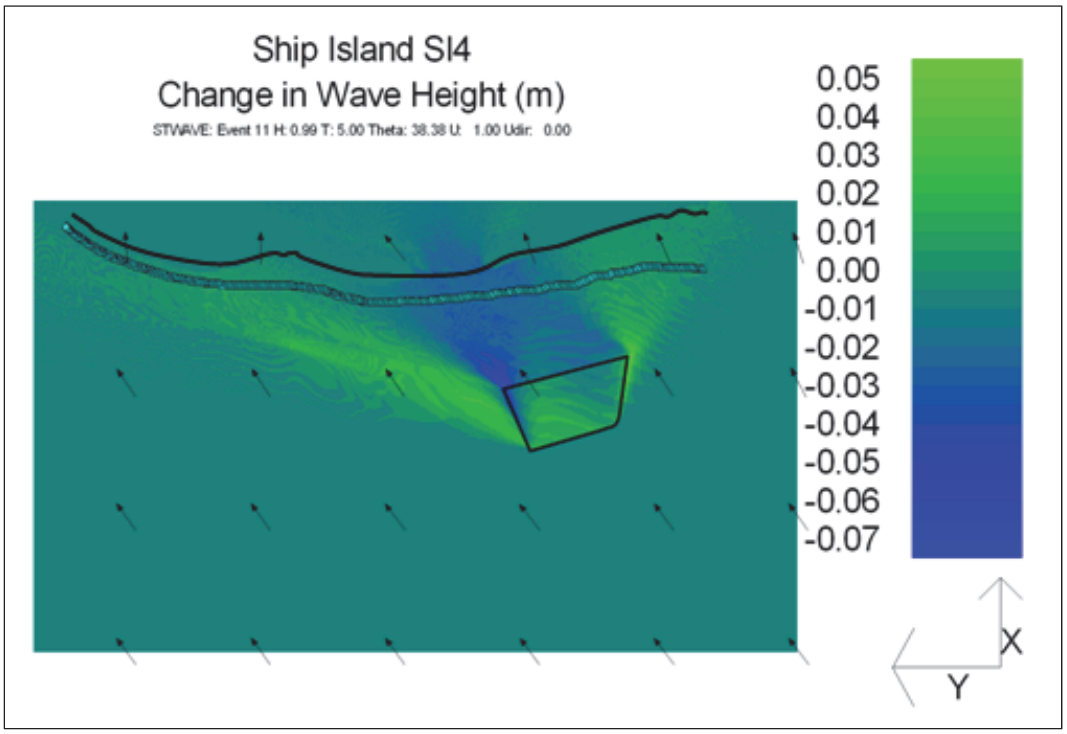

Figure 8-12. (Concluded).

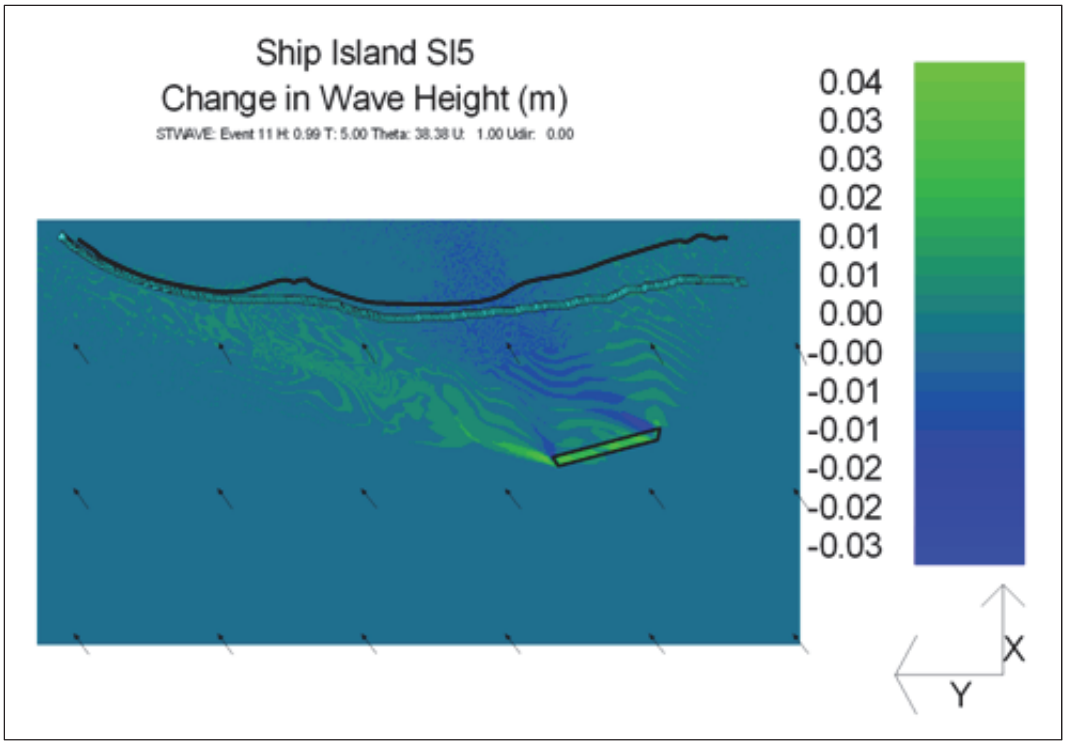

Figure 8-13. Wave height change (Dredged – Existing) for incident wave of *H* = 1.0 m, *T* = 5.0 sec and *Theta* = 58.65 deg. (Continued)

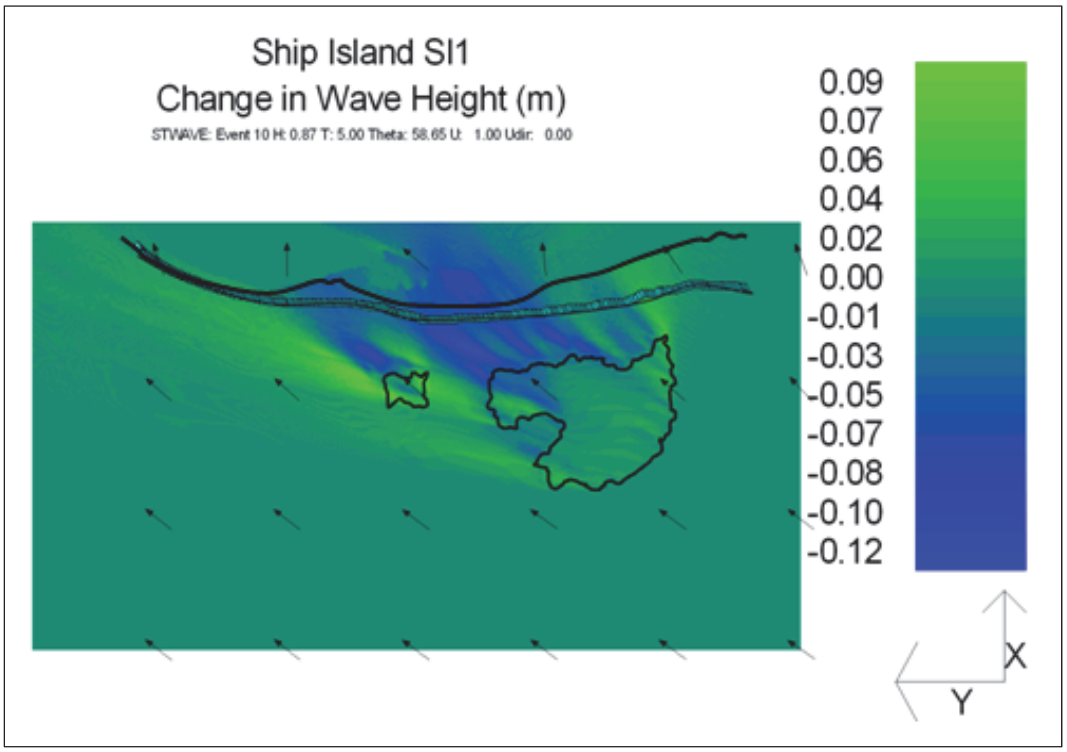

Figure 8-13. (Continued).

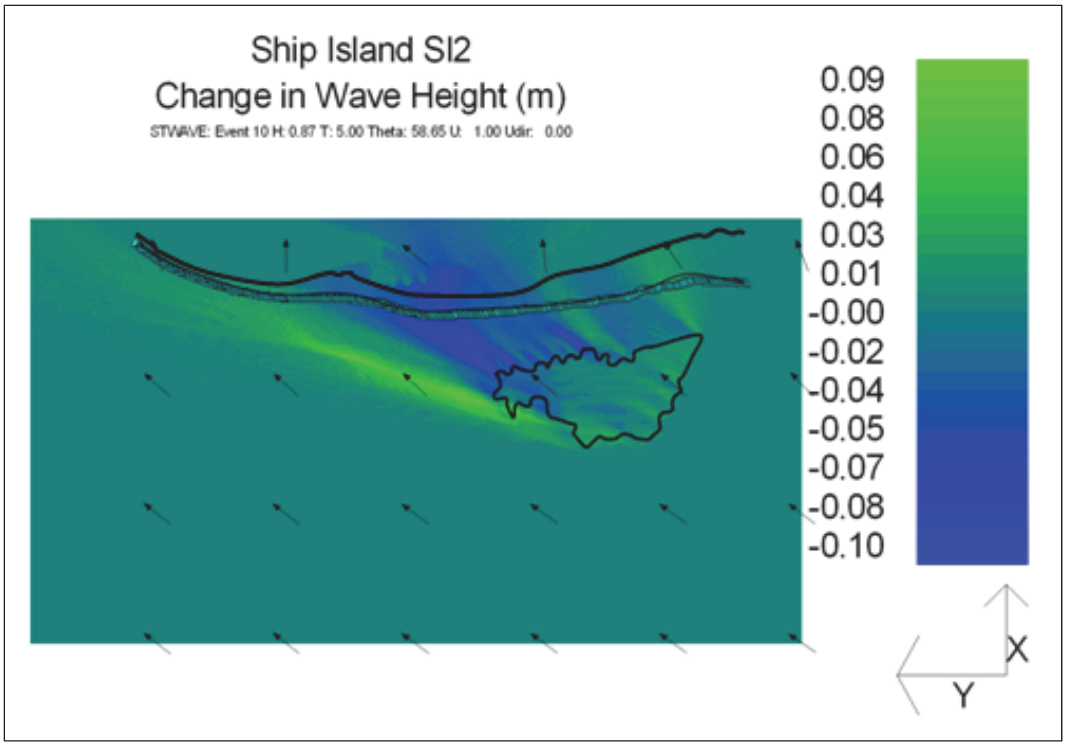

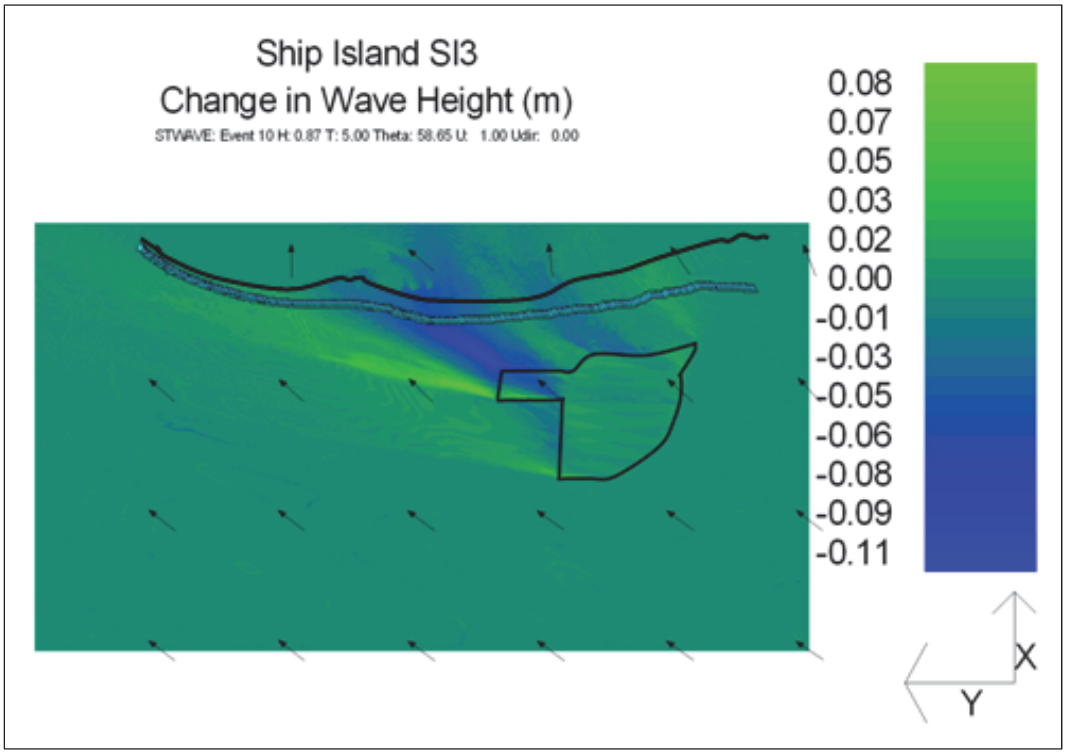

Figure 8-13. (Concluded).

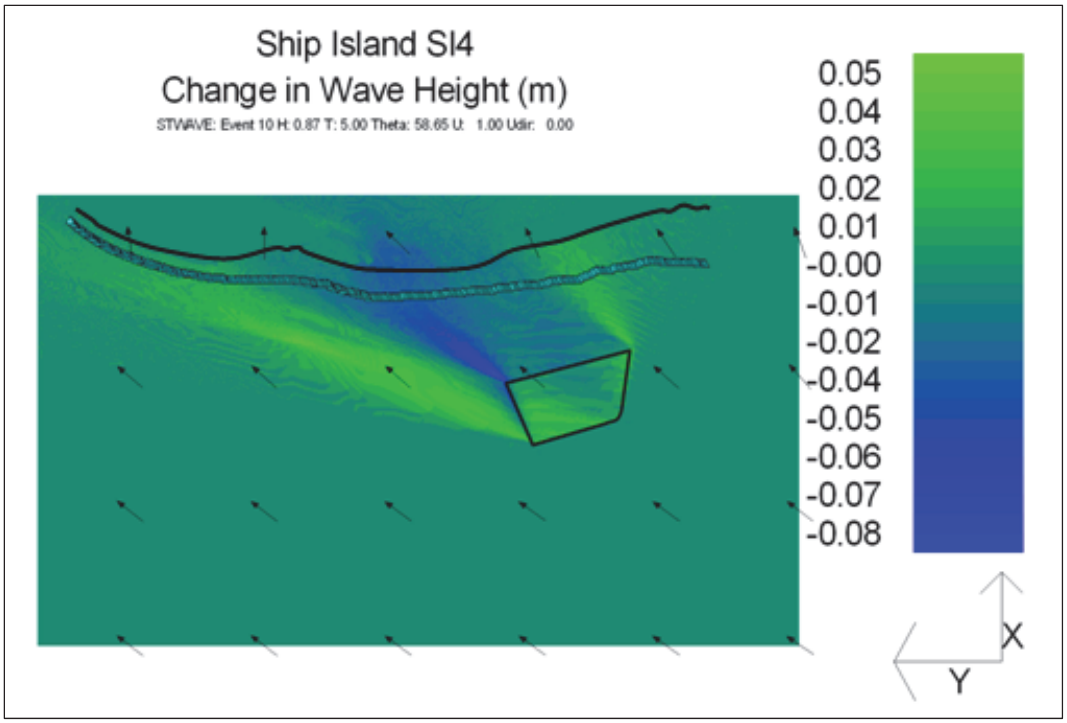

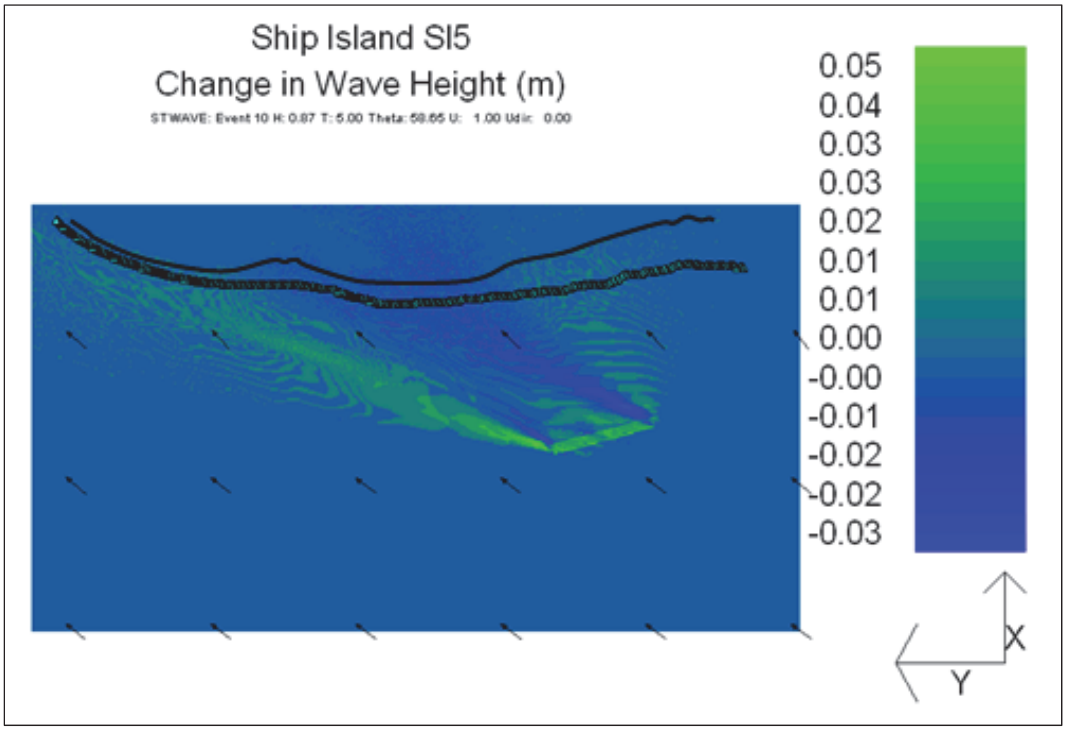

Figure 8-14. Wave height change (Dredged – Existing) for incident wave of *H* = 1.0 m, *T* = 11.11 sec and *Theta* = 1.09 deg. (Continued)

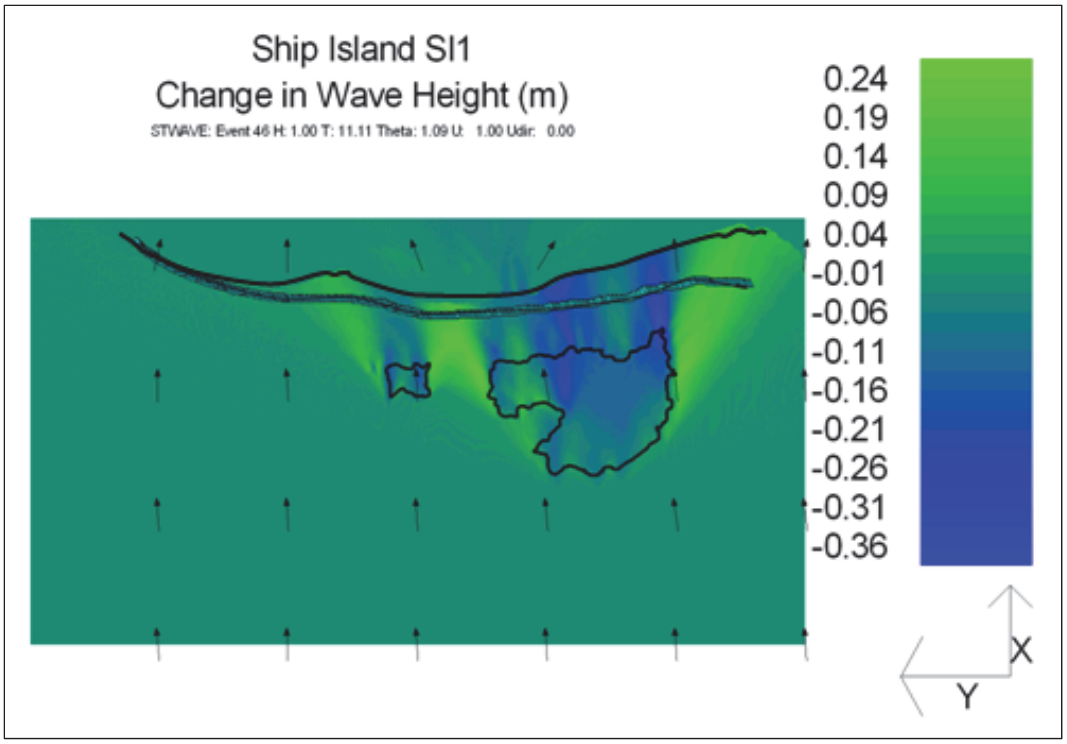

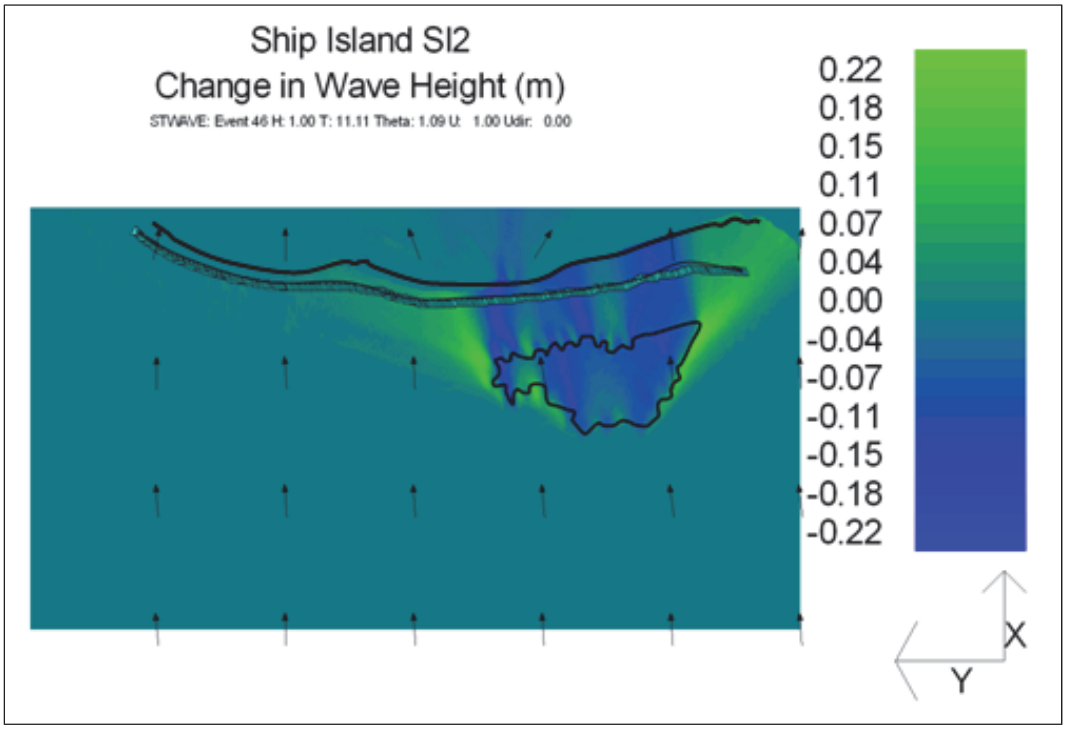

Figure 8-14. (Continued).

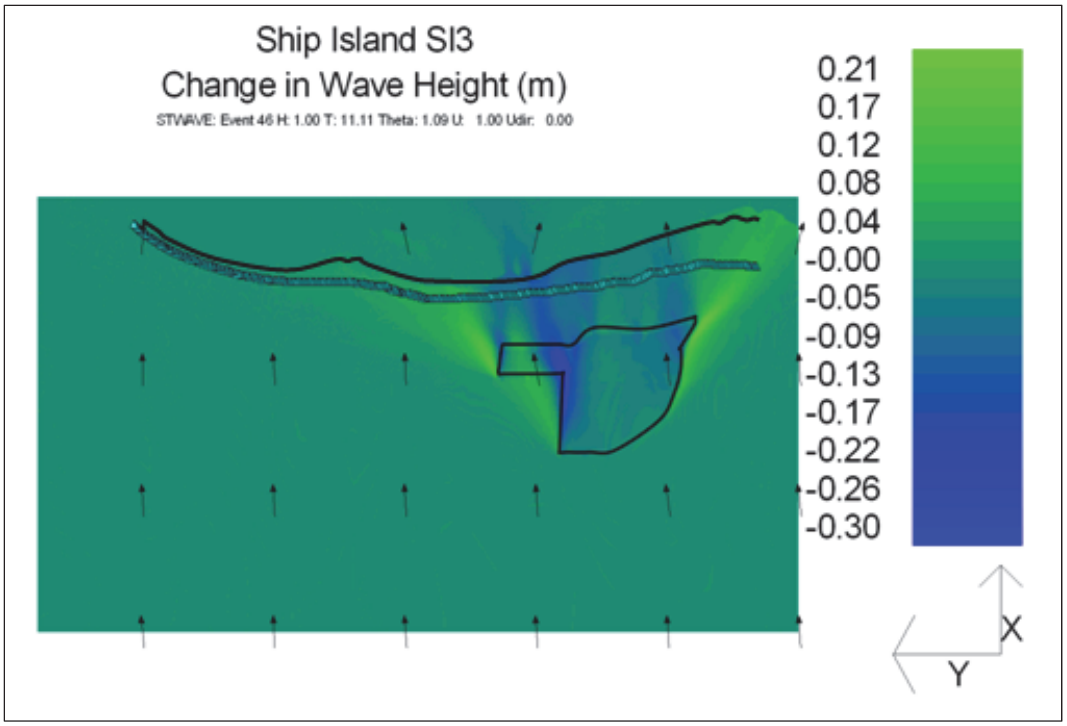

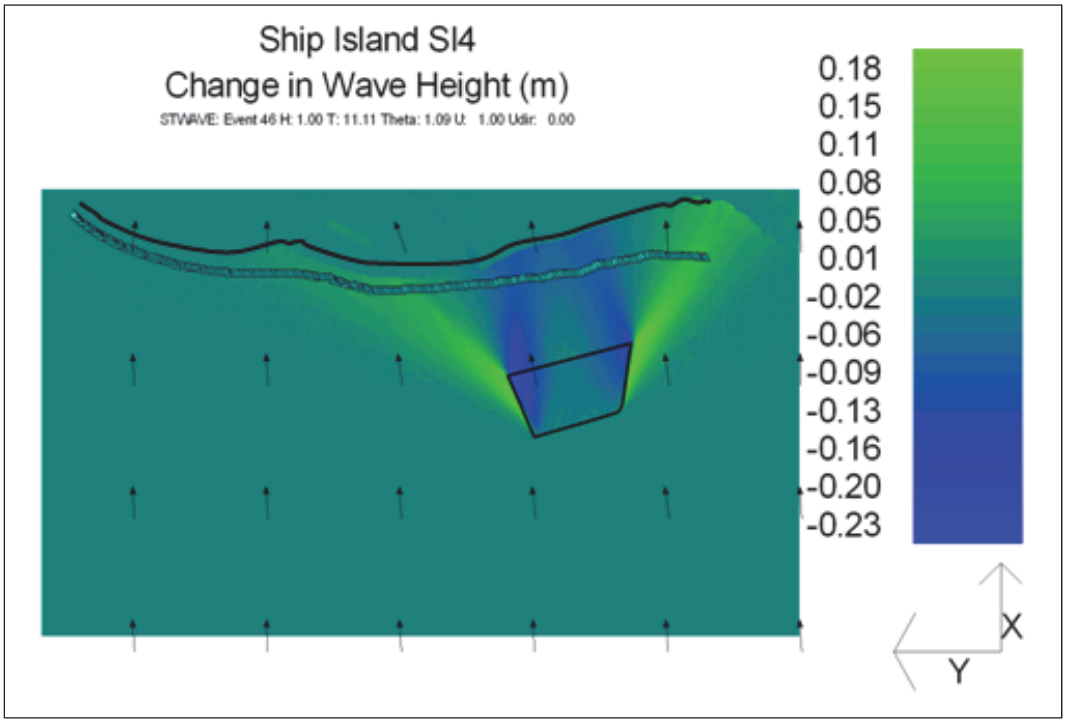

Figure 8-14. (Concluded).

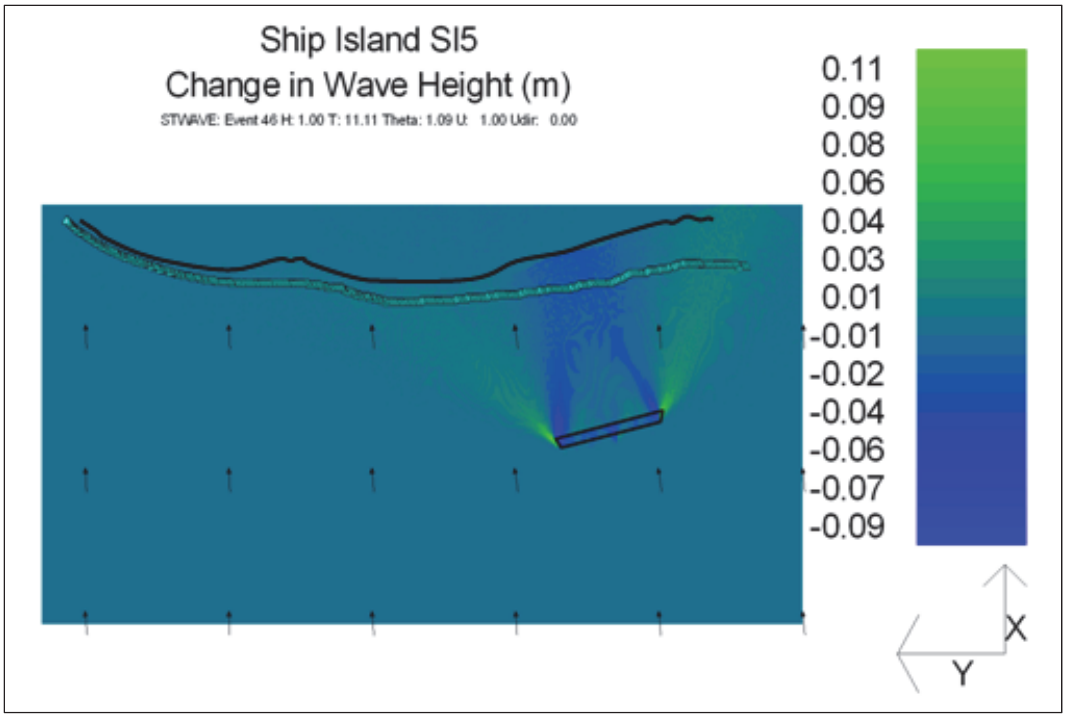

Figure 8-15. Wave height change (Dredged-Existing) for incident wave of *H* = 1.0 m, *T* = 11.11 sec and *Theta* = 10.11deg. (Continued)

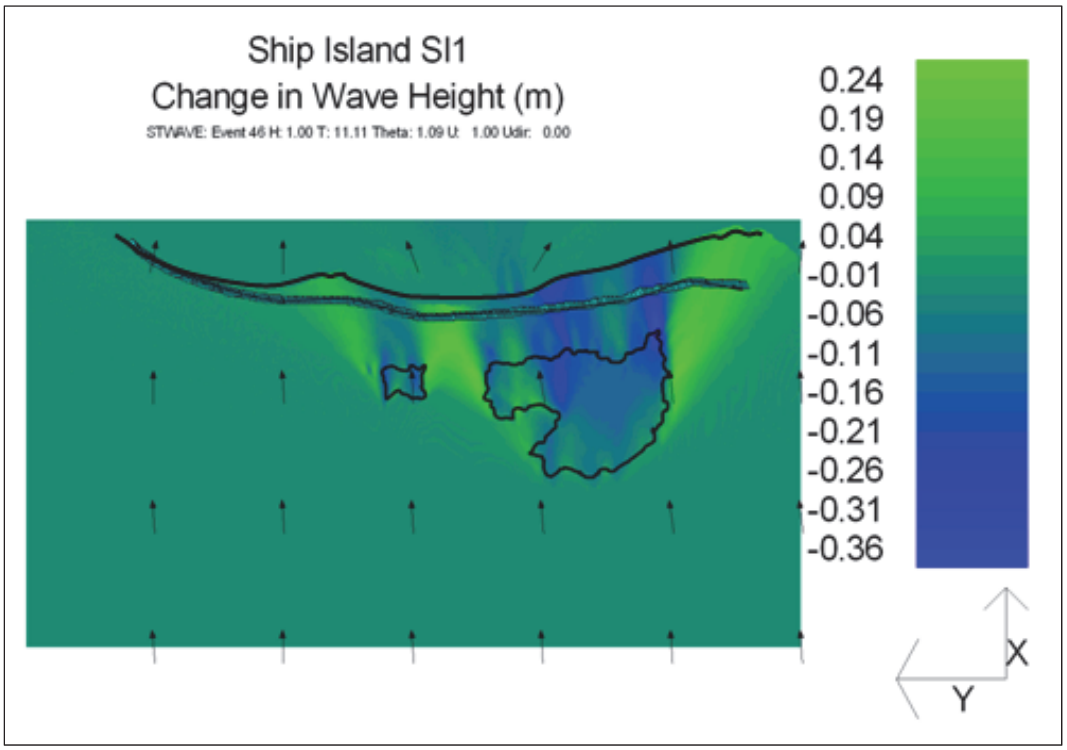

Figure 8-15. (Continued).

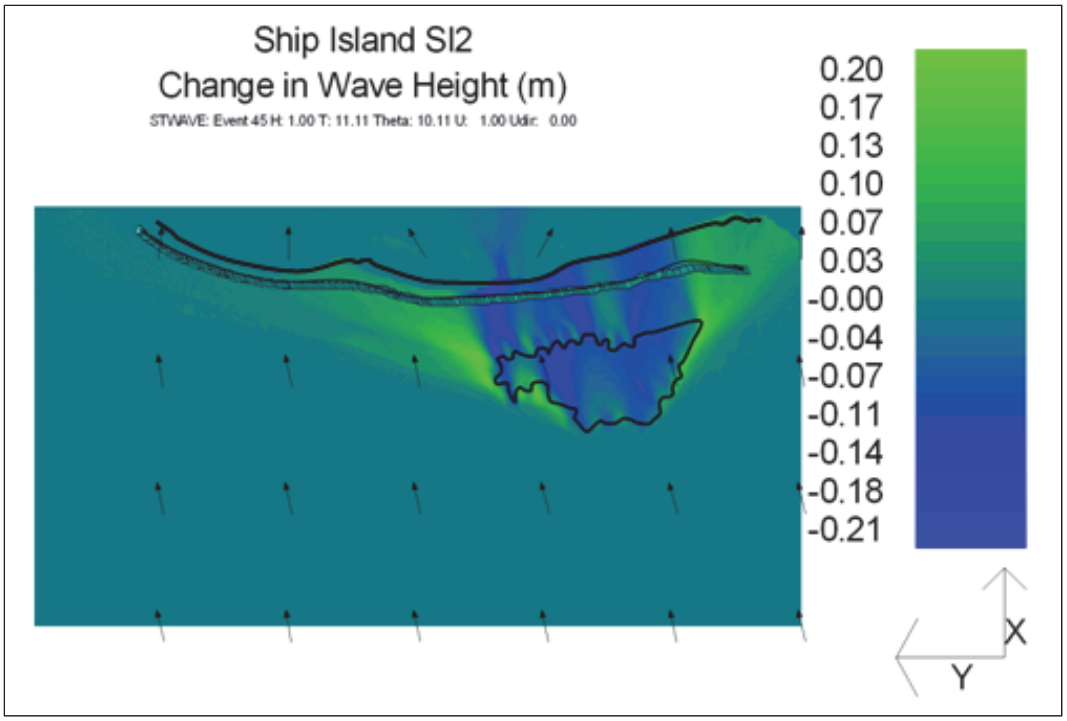

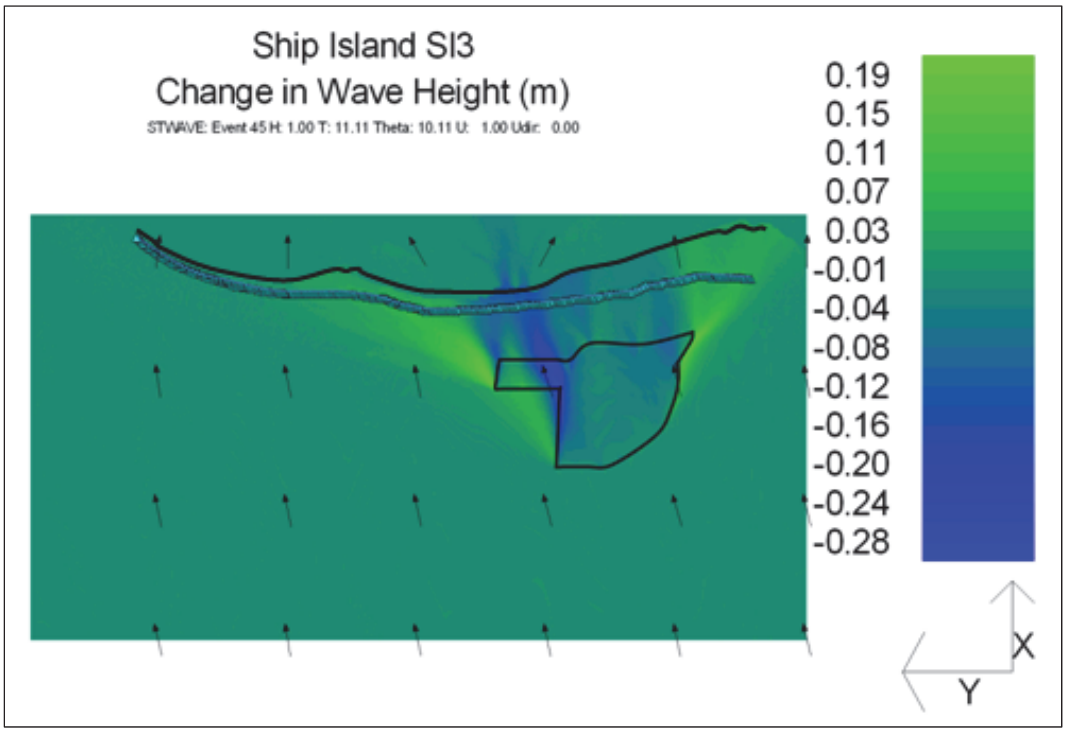

Figure 8-15. (Concluded).

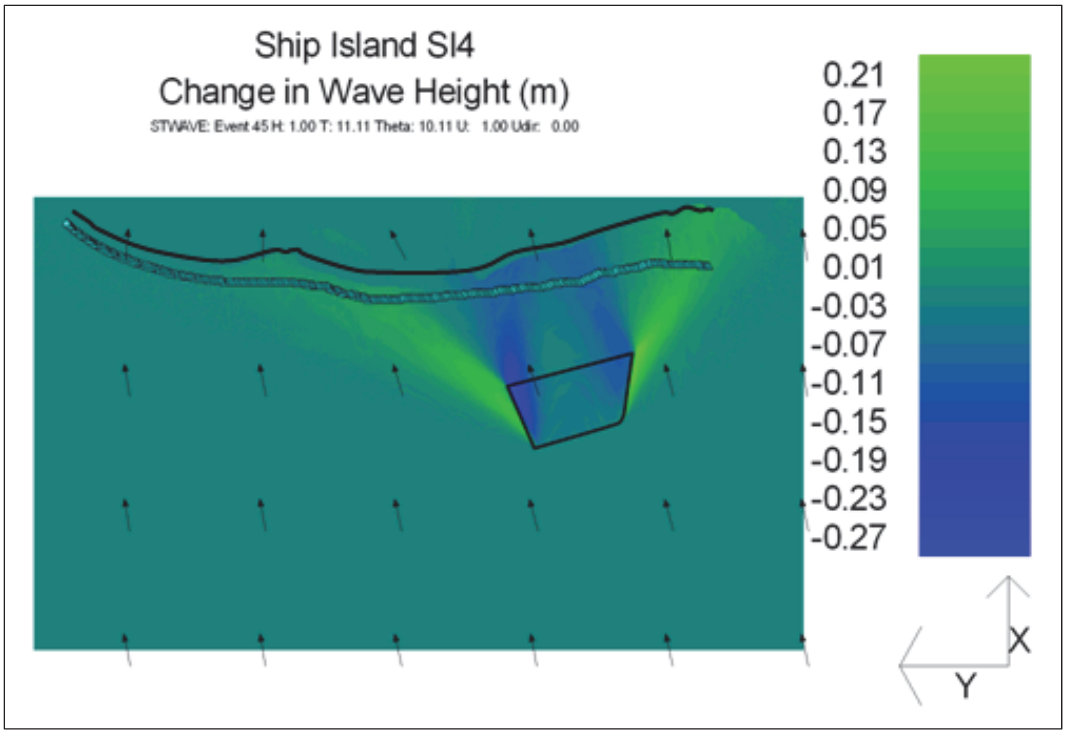

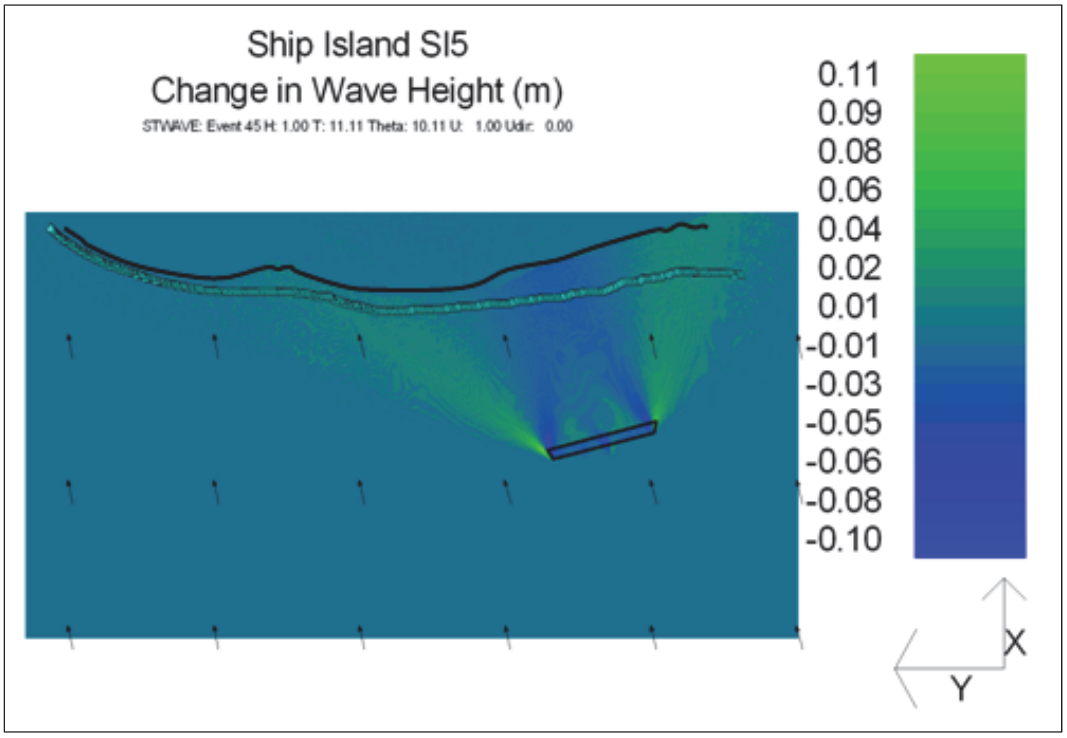

Figure 8-16 plots the change in wave height for each potential borrow area alternative along GENESIS nearshore wave reference line landward of the borrow areas where wave information is passed from STWAVE to GENESIS. The *X*-axis of the plot goes from east on the left to west on the right. Note that change in wave height is limited to approximately plus or minus five percent for the 5.0 sec waves whereas for the 11 sec waves the wave height change approaches 10 percent for SI2, SI3, and SI4 compared to almost 20 percent for the SI1. The increase in SI5 is negligible. Of concern for SI1 is the apparent focusing of wave energy between the two borrow areas which align with the restored shoreline that will result from the closure of Camille Cut. Wave heights are reduced in the lee of the borrow areas due to refraction of waves towards each side of the pit. The combination of the two segments of SI1 causes a focusing of refracted wave energy on the restored shoreline, particularly in shore normal wave cases. For SI2, SI3, SI4 and SI5 there is also an increase in wave energy along the sides of the borrow area. Absence of the small western segment of the proposed borrow in SI1 reduces focusing of wave energy around Camille Cut for the other potential borrow area configuration, but there is still up to approximately a 10 percent increase in wave height along East Ship Island for SI1, an 8.0 percent increase for SI3, and 6.0 percent increase for SI4. SI5 shows a maximum of 2.0 percent increase in wave height over the modeling domain. For each potential borrow area alternative, wave heights are reduced in the lee of the dredged areas due to refraction of the waves towards each side of the borrow area. The more oblique angles tend to focus energy towards the northwest due to their approach angle. For longer period waves, the effects of the borrow areas are the most apparent.

8.2.3 Sediment transport and shoreline change

A GENESIS model domain was generated for examining the potential influence of the borrow areas on shoreline processes along the restored Ship Island shoreline. The model domain is 11.85 km (7.36 miles) long and the initial shoreline position was developed from the existing Gulf shorelines of East and West Ship Islands connected by the estimated post-restoration shoreline. The Camille Cut segment of shoreline is approximately 4.5 km (2.79 miles) in length and extends between approximate GENESIS alongshore positions 2800-m and 7300-m.

Wave conditions determined through STWAVE simulations for the potential borrow area alternatives and existing condition were applied as input to GENESIS to estimate longshore sand transport rates and shoreline

Figure 8-16. Percent change in wave height at nearshore reference line.

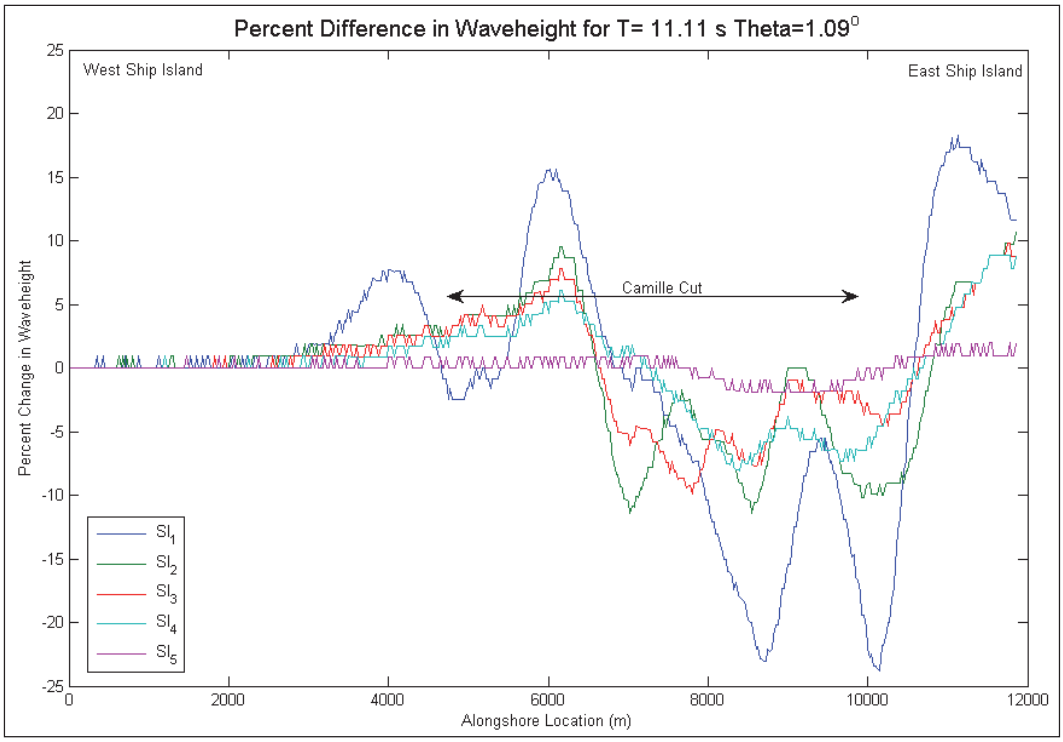

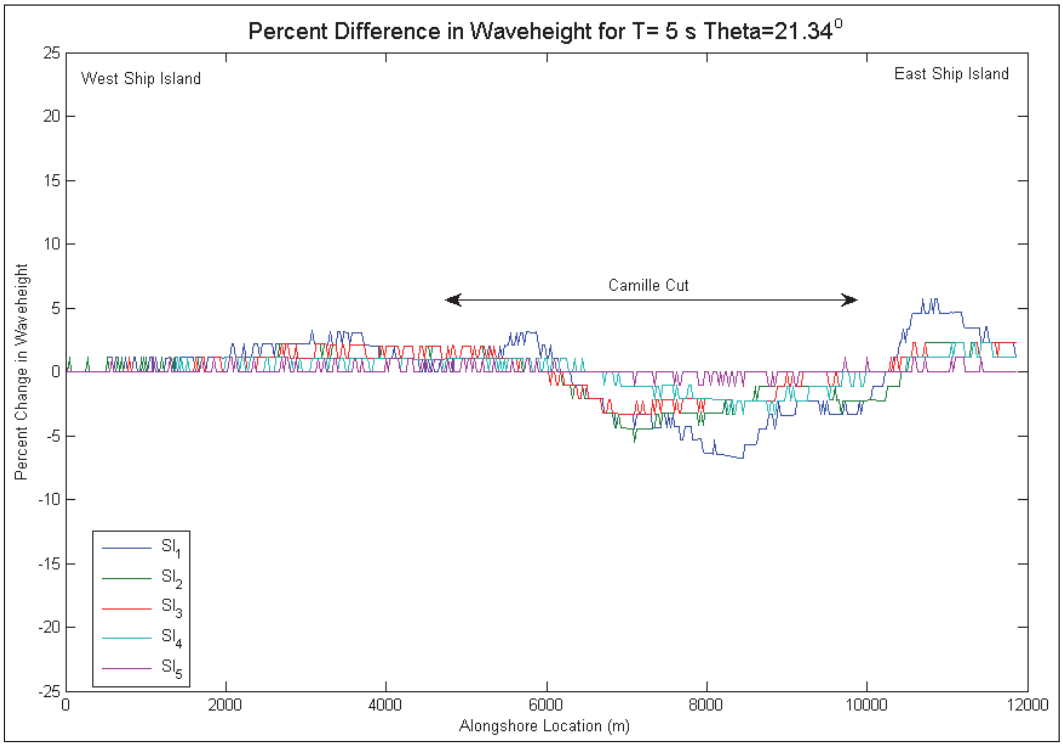

change. GENESIS simulations were run for the 20-year WIS hindcast offshore wave time-series (1980-1999). Figure 8-17 displays the estimated final shoreline position for both existing and three dredged conditions (restored condition) as well as the initial shoreline position. Potential borrow area dredged conditions show an increase in erosion over the 20-year simulation interval as compared to existing condition for borrow area SI1, SI2, SI3, SI4, and SI5 bathymetries. Increased erosion associated with the dredged bathymetries is observed primarily between GENESIS alongshore position 4500-m and 8000-m which corresponds to much of the Camille Cut restored shoreline area. The SI2, SI3, SI4, and SI5 borrow areas have a smaller impact, but still cause increased erosion. Figure 8-18 plots shoreline change rate for these conditions. Negative values indicate erosion and positive values indicate accretion. Figure 8-19 plots the difference, or change, in estimated shoreline change rates between existing and dredged conditions for each point on the GENESIS-axis. Borrow areas SI2 and SI3 decrease the erosion rate by approximately one third when compared to SI1. SI4 decreases the erosion rate by 60 percent in the vicinity of Camille Cut compared to SI1. SI5 reduces the erosion rate of SI1 by 90 percent. However, SI2 does cause a 25-m increase in erosion for Ship Island compared to the existing condition over the 20-yr period. SI3 shows a similar increase in erosion over the same period. SI4 increases the erosion by 28-m around Camille Cut. SI5 causes a minimal 5.0-m increase of erosion over 20 years. Figure 8-19 indicates that SI1 will induce accelerated shoreline erosion along eastern end of East Ship Island (alongshore positions 0- to 2000- m) and along the restored shoreline in the vicinity of Camille Cut (alongshore positions 4500- to 8000- m). Borrow area SI2 minimizes the effects on East Ship Island and reduces the induced erosion in the vicinity of Camille Cut. Borrow area SI3 slightly increases the erosion on East Ship Island compared to SI2. The increased shoreline recession rate associated with SI1 is estimated to approach 3.5-m/year in the vicinity of alongshore position 6000-m which represents an increase in shoreline erosion from approximately 2.5-m/year for the existing condition bathymetry to nearly 6.0-m/year in this region. Borrow areas SI2 and SI3 result in an increase in shoreline recession of approximately 2-m/year in the vicinity of Camille Cut. Borrow area SI4 results in an increase of shoreline recession of about 1.4-m/year in this region. Borrow area SI5 increases erosion by about 0.3-m/year in this location. Relative accretion occurs on West Ship Island for all five borrow areas. SI1, SI2, and SI4 cause accretion of about 7.0-m for East Ship Island, while SI3 causes 3.0-m and SI5 actually causes erosion of about 2.0-m over the 20 yr simulation period. West Ship Island accretes 27-m for SI1, 21-m for SI2, 24-m for SI3, 14-m for SI4, and 3.0-m for SI5.

Figure 8-17. Comparison of existing and potential Dredged borrow area condition estimated final shoreline for a 20-year simulation.

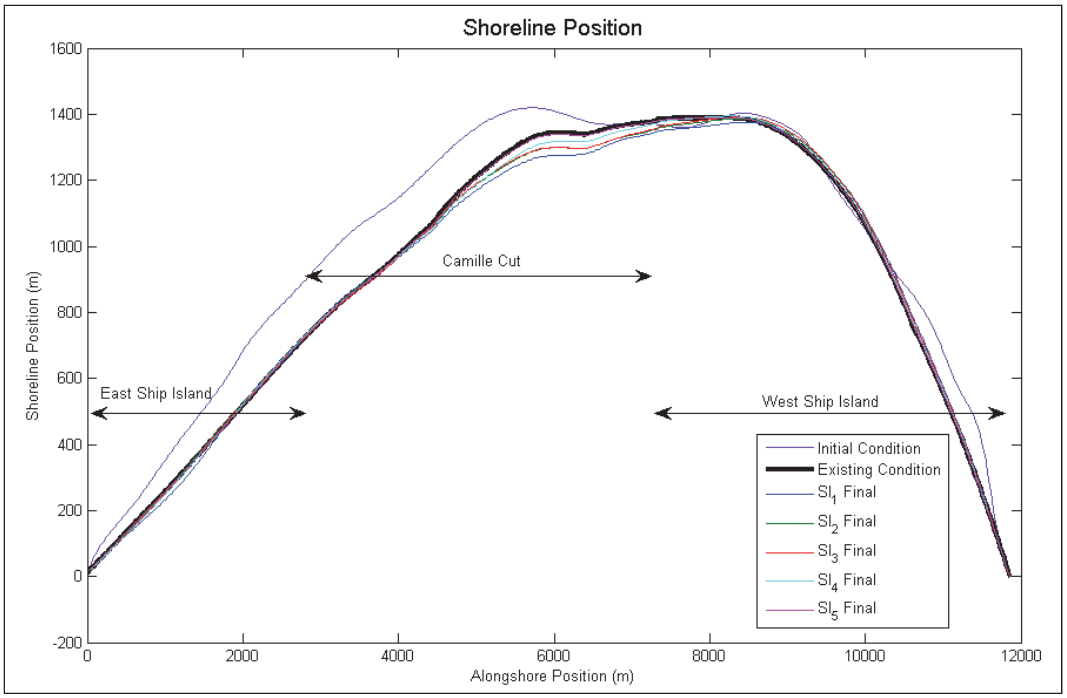

Figure 8-18. Comparison of existing and potential Dredged borrow area condition shoreline change rate.

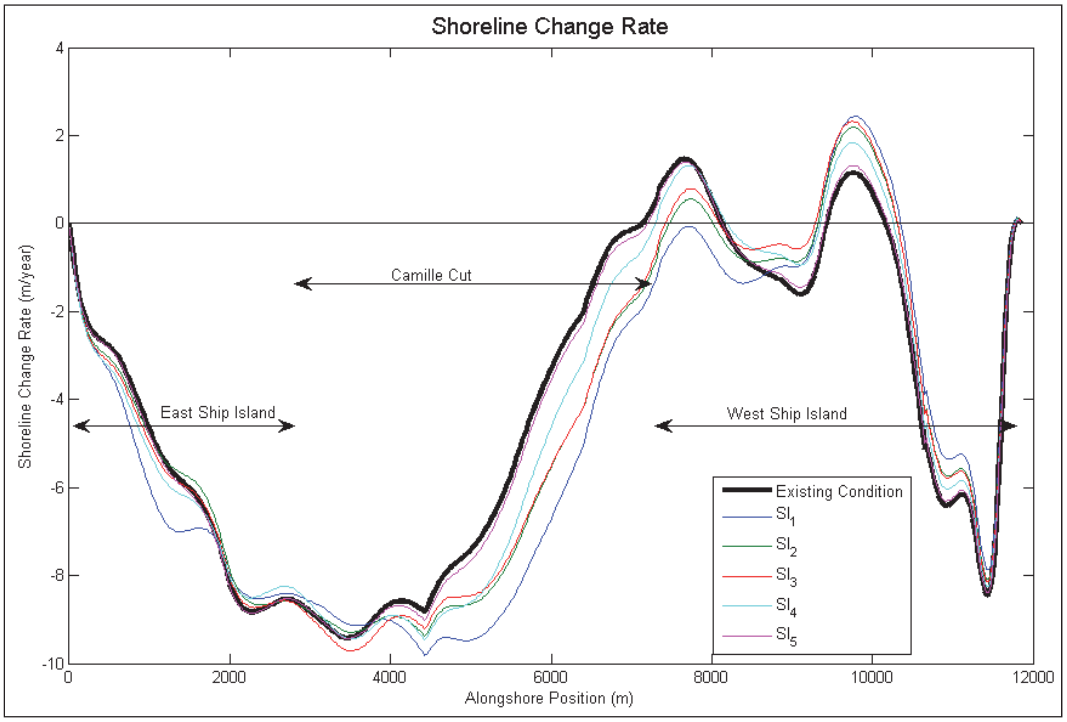

Figure 8-19. Potential borrow area dredging induced change in shoreline change rate.

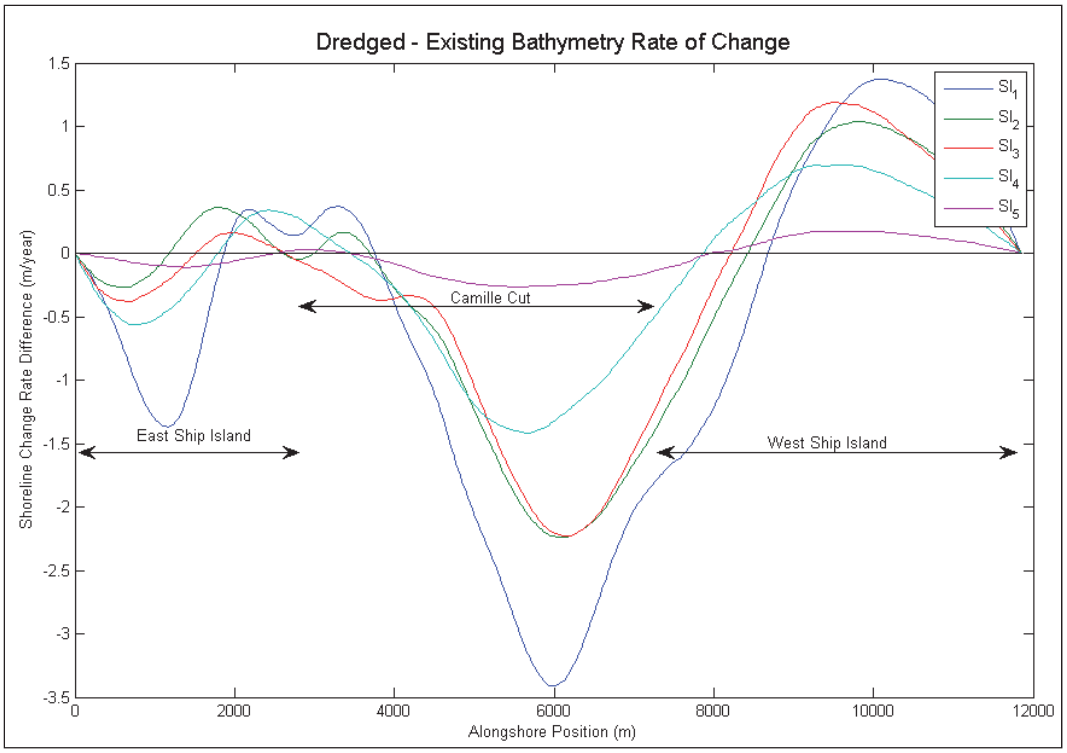

Estimated average annual longshore sand transport rate for both existing and potential borrow area Dredged conditions is plotted in Figure 8-20. Recall that positive values indicate transport to the right on the plot (east to west transport). This leads to a positive slope in the longshore sand transport rate indicating erosion; whereas, a negative slope indicates shoreline accretion. The steeper the slope the higher the predicted shoreline rate of change. A stable shoreline is associated with a constant longshore sand transport rate. Estimated average annual longshore sand transport rates for potential borrow area Dredged conditions vary from approximately -50,000 m^3/year (east-directed) at the eastern end of East Ship Island to nearly 318,000 m^3/year (west-directed) at the western end of West Ship Island for borrow area SI1 and -30,000 m^3/year to approximately 310,000 m^3/year for SI2 , SI3, and SI4. SI5 spans from approximately -20,000 m^3/year to 300,000 m^3/year. To isolate the influence of potential excavated borrow areas on longshore sand transport rates, the change in estimated transport rates between the existing and dredged condition are plotted in Figure 8-21. The change in estimated sand transport rates ranges from about -32,000 m^3/year to 33,000 m^3/year for SI1, and -15,000 m^3/year to 25,000 m^3/year for SI2 and SI3. SI4 ranges from -10,000 m^3/year to 10,000 m^3/year, while SI5 ranges from -2,000 m^3/year to 4,000 m^3/year. The transport rate difference is most significant towards the center of the island at the Camille

Cut closure area. In general, all borrow area alternatives appear to increase erosion in the area being restored, with borrow area SI5 having the least potential impact.

Figure 8-20. Mean alongshore transport rate.

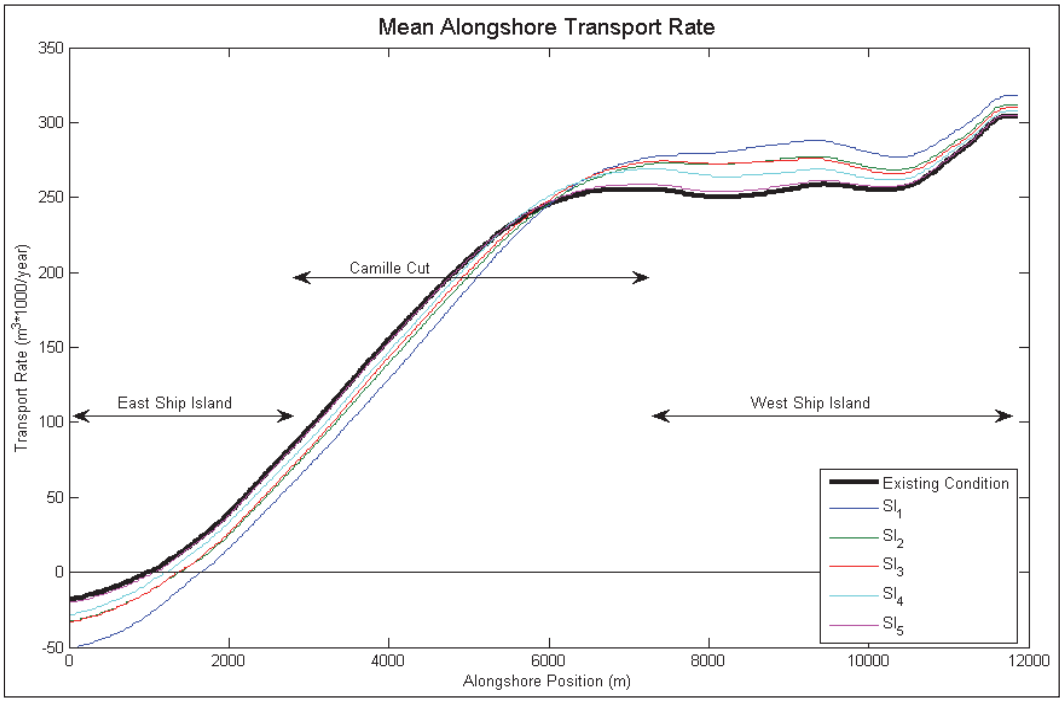

Figure 8-21. Change in average annual longshore transport.

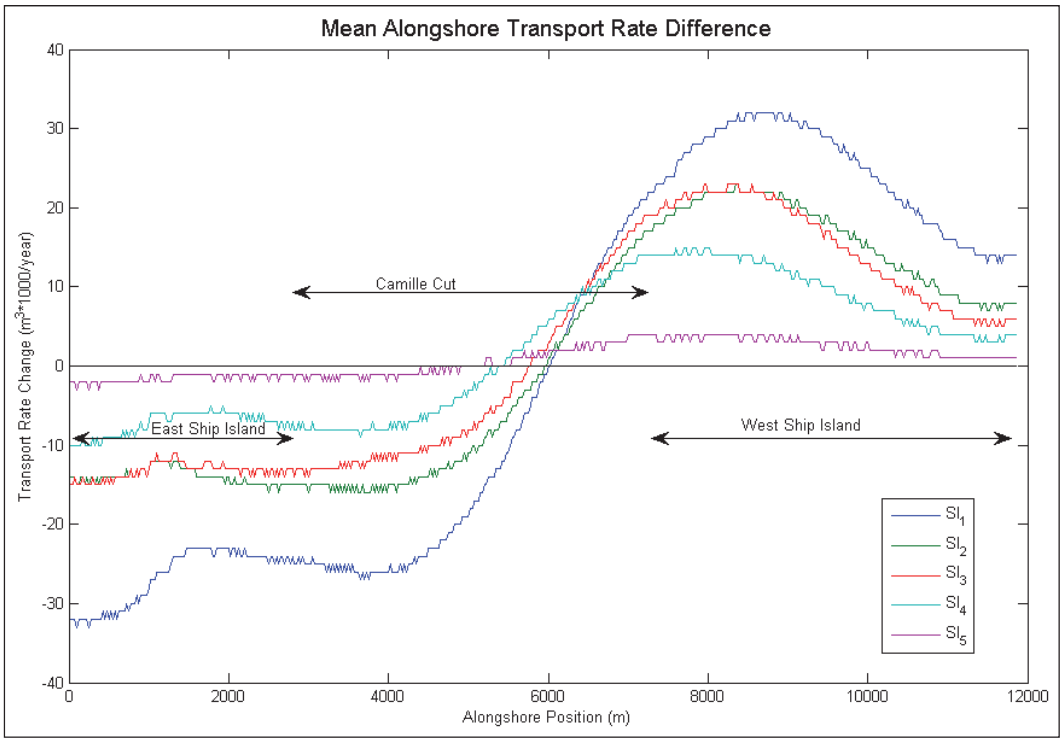

8.2.4 Summary

Potential impacts of excavation of nearshore borrow areas for the proposed restoration projects on Ship Island were assessed with spectral nearshore wave transformation model STWAVE and shoreline change model GENESIS. Wave conditions from WIS hindcast database for WIS Station GOM 144 were transformed from the 15-m contour to the 12-m contour to provide wave data for the offshore portion of the STWAVE grid using a WIS Phase III transformation. STWAVE simulations were performed for both Existing and Dredged condition to obtain estimates of nearshore wave conditions landward of the borrow areas and to enable a comparative analysis aimed at quantifying potential borrow area impacts on shoreline processes along the restored Ship Island shoreline. Potential effects of the proposed borrow areas SI1, SI2, SI3, SI4, and SI5 on nearshore wave conditions were quantified by examination of the change in nearshore wave height and direction landward of each potential borrow area alternative. STWAVE results show an increase in wave heights in the area of the Camille Cut closure due to refraction caused by the borrow areas focusing wave energy. The wave height increase was within ten percent for the short period waves but for longer period waves the focusing caused increased wave heights of over 10 percent for SI2, SI3, and SI4 compared to 20 percent for SI1. SI5 minimized the wave height increase to about 2.0 percent. The STWAVE results were applied as input to GENESIS to quantify the influence of the borrow areas on shoreline processes. Longshore sand transport rates were calibrated with typical values for K1 and K2 of 0.4 and 0.2, respectively and to produce transport rates consistent with sediment budget estimates (Byrnes et al. 2011). The borrow areas were shown to increase erosion over much of the Camille Cut closure area. The magnitude of the increased erosion reaches 68-m for SI1, 48-m around the Camille Cut over the 20-year period of analysis for the SI2 and SI3, 28-m for SI4, and 5.0-m for SI5. The western portion of West Ship Island is expected to prograde compared to the existing condition for SI1-SI4 with a maximum increase of 27-m with SI1, 21-m with SI2, 24-m with SI3, and 14-m with SI3. SI5 causes increased erosion of about 2-m.

8.3 Horn Island

A proposed borrow area for the Ship Island restoration is located to the southeast of Horn Island in an ambient water depth of 12-m. The borrow area reaches a cut depth of 10-m spanning an area 1300-m wide by 1600-m long. The proposed area's proximity to Horn Island creates potential

adverse affects on the shoreline of Horn Island due to the wave refraction over the excavated pit. This chapter details an analysis conducted to quantify the potential impacts of the borrow area excavation (for beach nourishment) on sediment transport and shoreline change at Cat Island.

8.3.1 Model setup

The STWAVE grid domain and the location of the borrow pit relative to Horn Island is shown in Figure 8-22. The analysis involved simulating the transformation of offshore wave conditions gathered from WIS Station 144 from the 16-m contour to the 14-m contour with the WISPH III transformation technique. The transformed wave information corresponds to the offshore boundary of the STWAVE grid with the *X*-axis directed onshore, and the *Y*-axis parallel with the Horn shoreline. The resolution of the STWAVE grid is 25 m in both the *x* and the *y* directions. Nearshore wave conditions generated by STWAVE along the nominal 5.0-m contour for both the Existing and Dredged condition provided necessary input to GENESIS, which estimates longshore sand transport rates and shoreline change along the shoreline of Horn Island.

Figure 8-22. STWAVE grid domain with location of borrow area.

The GENESIS *X*-axis runs parallel to the Gulf shoreline of Horn Island from east to west and is comprised of 391 shoreline cells at 25-m intervals. Because detailed calibration data are not available for this study, the calibration coefficients were assigned typical values of K1=0.10 and K2=0.05. These calibration values are typical of those applied in previous studies that employed WIS hindcast wave information as input and produced longshore sand transport rates that are in general agreement with

the Horn Island sediment budget.(Byrnes et al. 2011) Because this study is a relative analysis between with and without an excavated borrow area, aimed at estimating the potential shoreline impacts of proposed dredging of the near shore borrow area, the importance of a detailed calibration is diminished. The existing bathymetry is shown in Figure 8-23 and bathymetry change between with and without the borrow pit is plotted in Figure 8-24 to highlight the borrow pit configuration. The near shore wave reference line (where the STWAVE information is stored and transferred to the GENESIS model) is represented by a thick black line in both figures.

8.3.2 Wave transformation analysis

Near shore wave transformation simulations were performed for 162 representative wave conditions identified through analysis of WIS hindcast station GOM 144 located in 15 m water depth offshore of Cat Island. Figure 8-25 shows the distribution of the wave conditions by incident wave angle and period. The incident wave angle is measured clockwise from shore normal. The value in each block is the number of occurrences of that wave condition in the 20-yr WIS hindcast spanning the interval 1980 through 1999. For each representative wave condition an idealized TMA wave spectrum was generated and applied as the input to STWAVE.

Figure 8-23. Existing bathymetry.

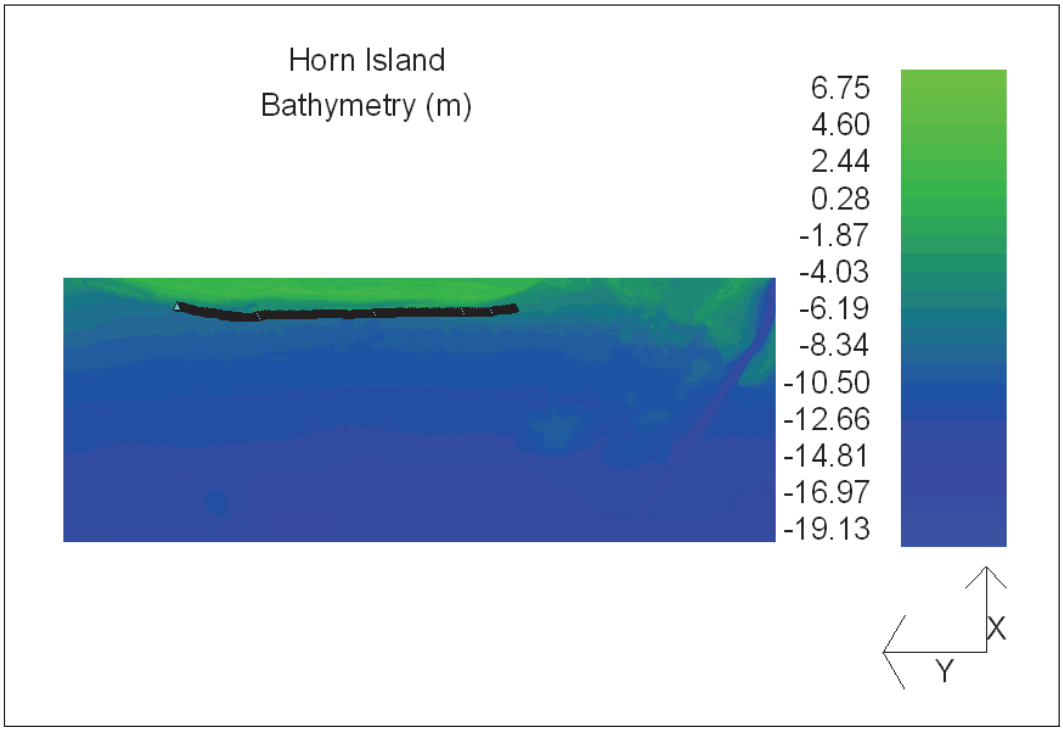

Figure 8-24. Existing condition bathymetry minus dredged condition bathymetry.

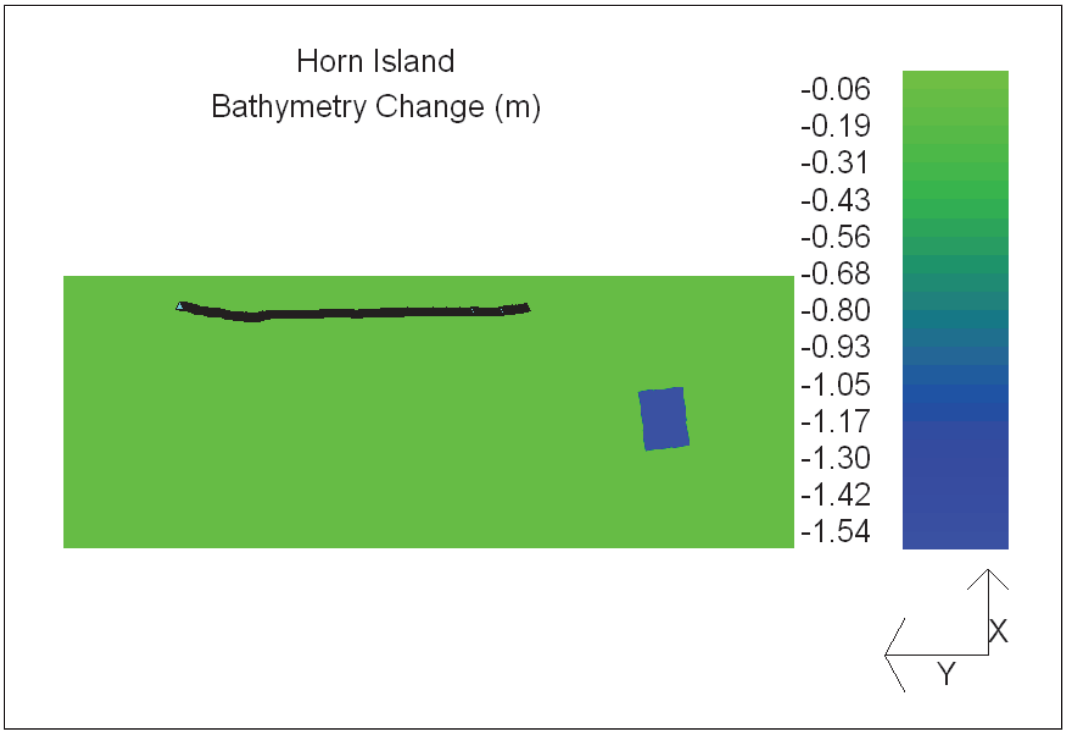

Figure 8-25. Distribution of the representative wave conditions by incident wave angle and period.

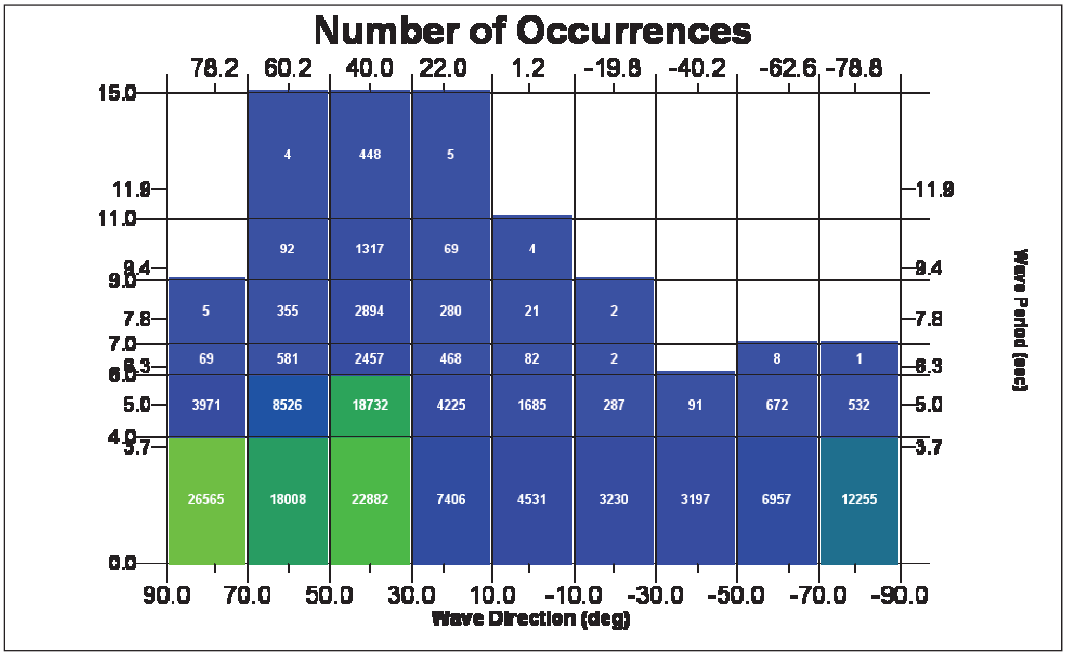

STWAVE simulations were performed to compute wave transformation across the irregular offshore bathymetry from approximately the 14-m contour to the 5.0-m contour. Two sets of STWAVE simulations were performed to estimate near shore wave conditions for both the existing and

dredged conditions. The change in significant wave height and direction resulting from excavation of the proposed borrow area was determined through subtracting the existing condition STWAVE results from the dredged condition STWAVE results. Figures 8-26 through 8-29 are the estimated significant wave height changes induced by excavation of the borrow area offshore of Horn Island for select characteristic wave conditions. These changes are calculated by subtracting the wave heights found for the existing condition from the wave heights for the dredged condition for each wave state. Figure 8-24 corresponds to typical 3.70 second waves approaching Horn Island from the southeast. Figures 8-27 through 8-29 correspond to long period waves approaching Horn Island from the south-southeast sector. For the longer period waves, wave heights decrease in the lee of the borrow area as the waves pass over the borrow areas. Wave heights tend to increase along the sides of the borrow areas in the down-wave direction for longer period wave events but breaking occurs before the waves reach the GENESIS save stations. Figure 8-30 demonstrates the percentage change in wave heights at the save stations. For both short and long period waves, minimal impact is felt along the GENESIS save stations. For short wave period events, the depth of the borrow area decreases its impact to the point that the wave conditions are virtually identical before and after dredging.

Figure 8-26. Wave height change (dredged – existing) for incident wave of *H* = 1.22 m, *T* = 3.70 sec and *Theta* = 21.92 deg.

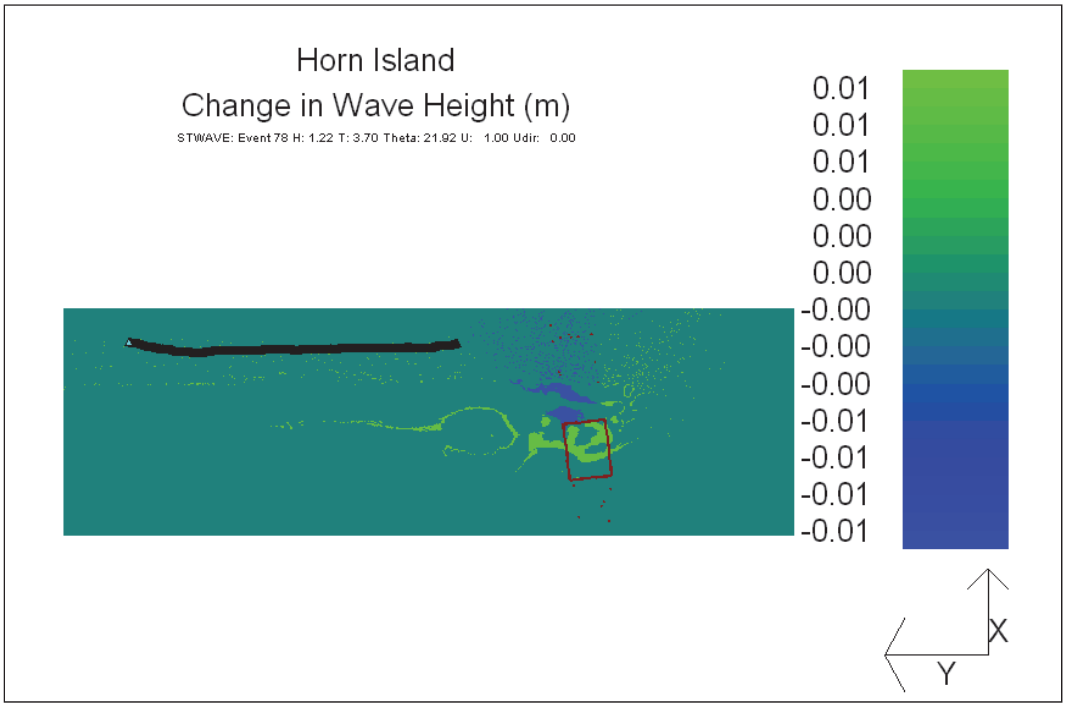

Figure 8-27. Wave height change (dredged – existing) for incident wave of *H* = 2.91 m, *T* = 7.69 ecs and *Theta* = 38.50 deg.

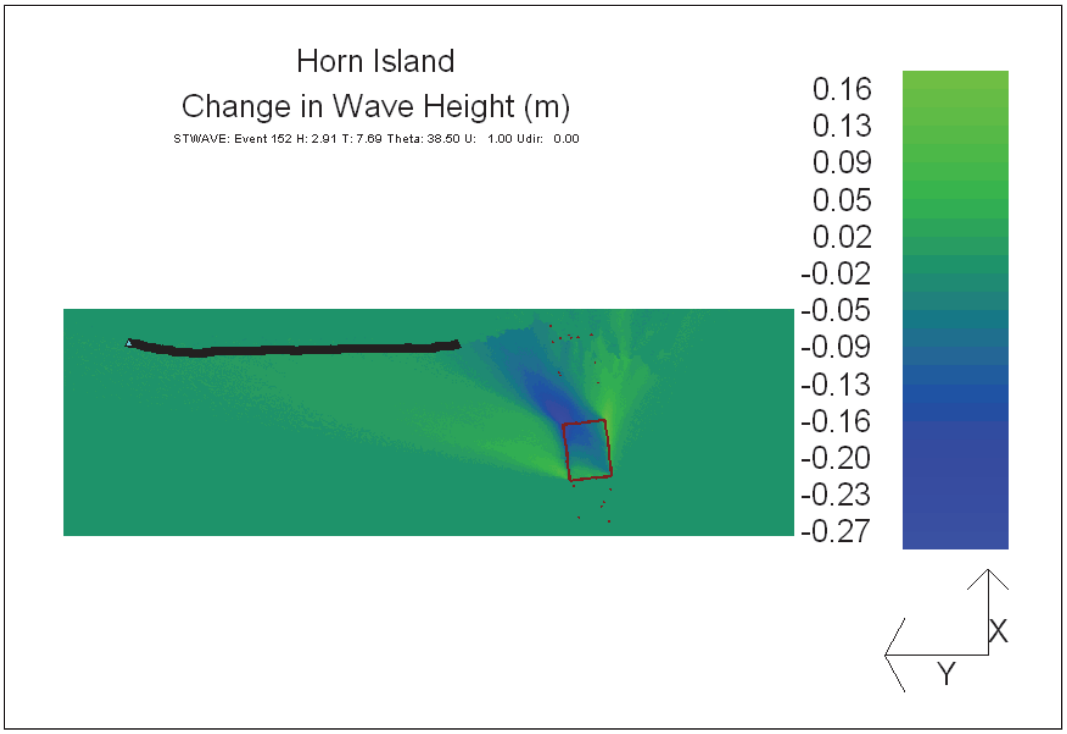

Figure 8-28. Wave height change (dredged – existing) for incident wave of *H* = 2.72 m, *T* = 9.09 sec and *Theta* = 53.43 deg.

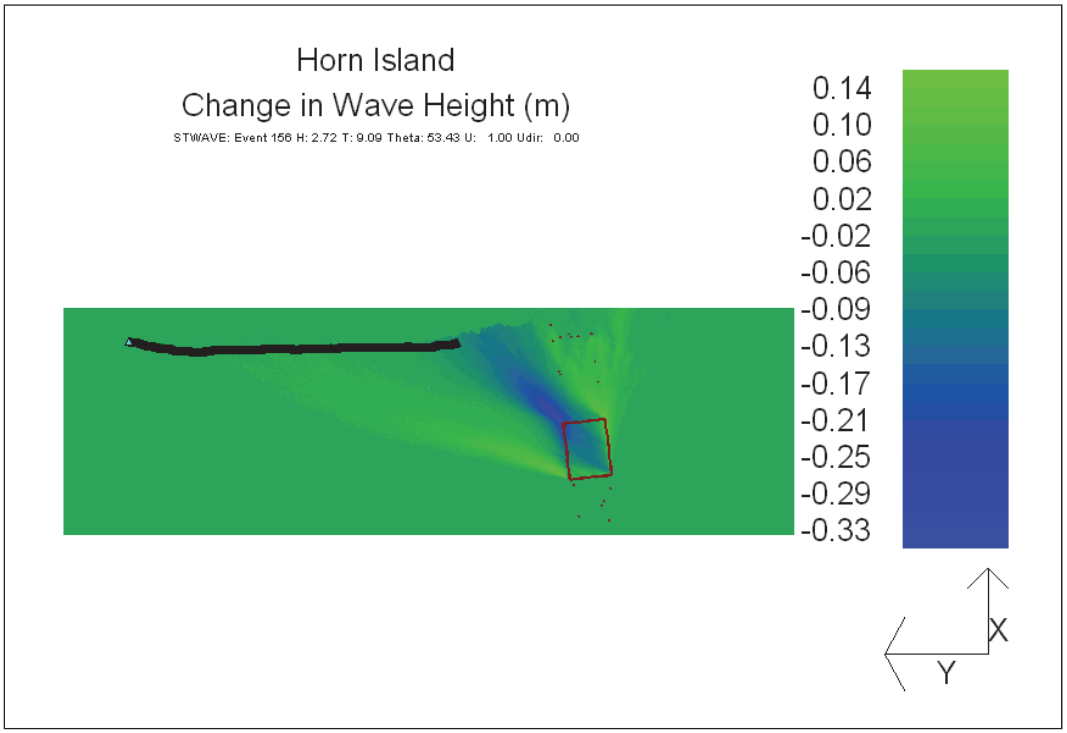

Figure 8-29. Wave height change (dredged – existing) for incident wave of *H* = 4.91 m, *T* = 11.11 sec and *Theta* = 39.94 deg.

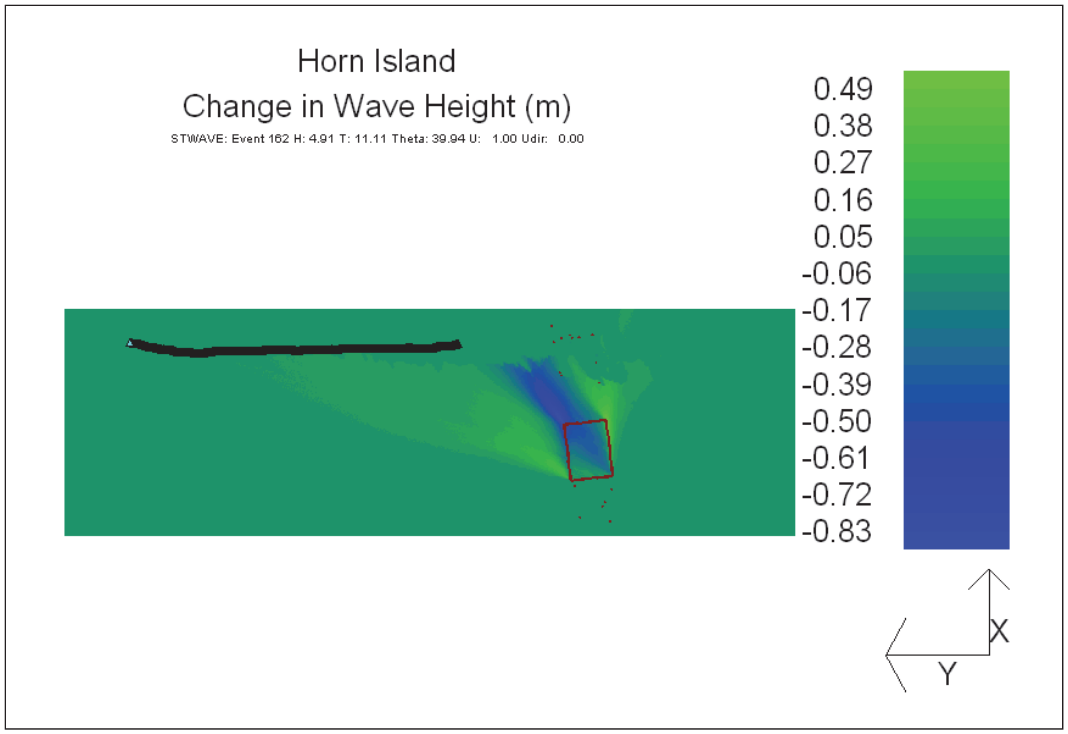

Figure 8-30. Percent wave height change at GENESIS stations.

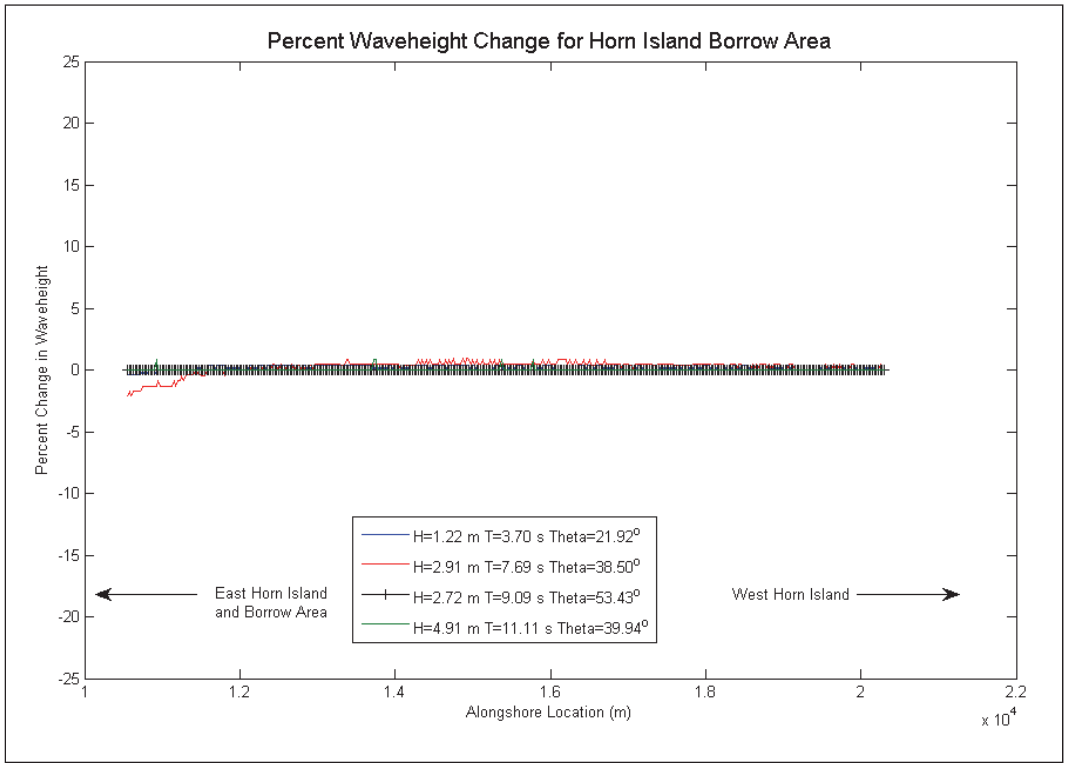

8.3.3 Sediment transport and shoreline change

A GENESIS model domain was generated for examining the influence of the borrow area on shoreline processes along the Horn Island shoreline. The model domain is 4.25 km (2.64 miles) long and the initial shoreline position was developed from the existing Gulf shorelines of Horn Island.

The wave conditions determined through the STWAVE simulations for both the dredged and existing condition were applied as input to GENESIS to estimate longshore sand transport rates and shoreline change. The GENESIS simulations were run for the 20-year WIS hindcast offshore wave time-series (1980-1999). Figure 8-30 displays the estimated final shoreline position for both the existing and dredged condition as well as the initial shoreline position. The dredged condition shows negligible change in erosion over the 20-year simulation interval as compared to the existing condition. The final shoreline show negligible difference between the dredged and existing cases. Figure 8-31 plots the shoreline change over 20 years for both conditions. Negative values indicate erosion and positive values indicate accretion. Figure 8-32 plots the difference, or change, in the estimated shoreline change rates between the existing and dredged condition for each point on the GENESIS axis. This plot indicates that the dredged bathymetry causes minimal changes in shoreline change rates over the 20 year period. The greatest difference in the shoreline change rates is a reduction in predicted shoreline advance by approximately 0.1 m per year (Figure 8-33). Estimated increases in predicted shoreline recession are less than 0.05 m per year.

8.3.4 Summary

The impacts of excavating a borrow area offshore of Horn Island for the proposed restoration project at Ship Island were assessed with the spectral near shore wave transformation model STWAVE and the shoreline change model GENESIS. Wave conditions from the WIS hindcast database for WIS Station GOM 144 were transformed from the 16 m contour to the 14 m contour to provide wave data for the offshore portion of the STWAVE grid using a WIS Phase III transformation. STWAVE simulations were performed for both the existing and dredged condition to obtain estimates of nearshore wave conditions landward of the borrow area and to enable a comparative analysis aimed at quantifying the borrow area impacts on shoreline processes along the Horn Island Gulf shoreline. The effects of the proposed borrow areas on nearshore wave conditions were quantified by

Figure 8-31. Comparison of existing and dredged condition estimated final shoreline after 20 years.

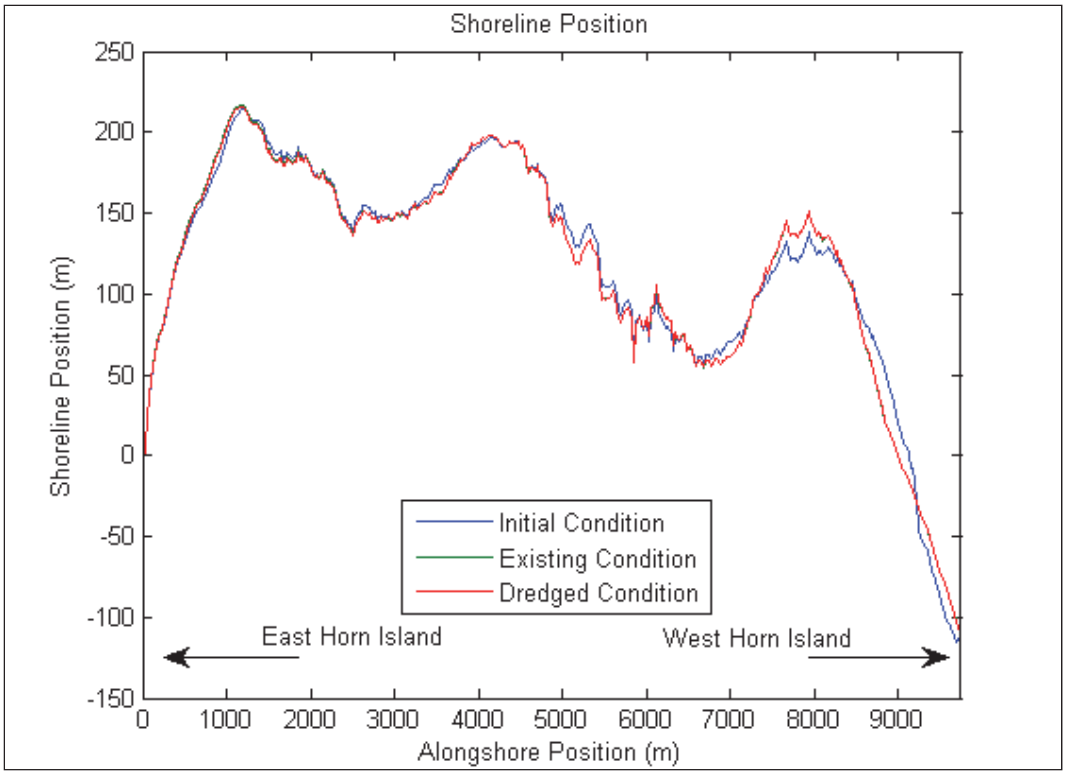

Figure 8-32. Comparison of existing and dredged condition shoreline change for the 20-year simulation period.

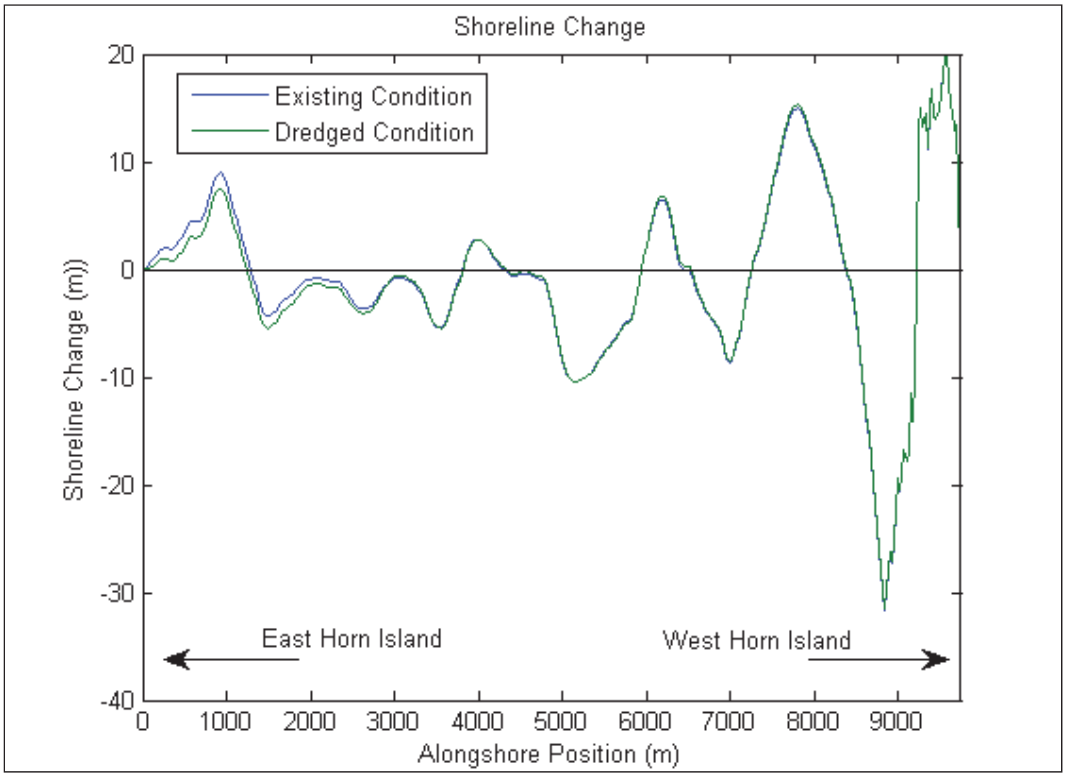

examination of the change in nearshore wave height and direction landward of the borrow area. The STWAVE results show minimal increases in wave heights surrounding the borrow area with little affect on the GENESIS save stations. The STWAVE results were applied as input to GENESIS to quantify the influence of the borrow areas on shoreline processes. A sensitivity analysis was conducted, comparing results for both the existing and dredged (restored) conditions. Longshore sand transport rates were calibrated with typical values for K1 and K2 of 0.10 and 0.05, respectively, and produced transport rates consistent with sediment budget estimates. The proposed borrow area was shown to have minimal impact on shoreline change rates over the entirety of Horn Island. The maximum magnitude of change reduces predicted shoreline advance by about 1.5 m for the 20-year period of analysis. The greatest increase in erosion is approximately 1.0 m over 20 years. The western portion of Horn Island is expected to slightly prograde as a result of the project.

Figure 8-33. Dredging induced change in shoreline change rate.

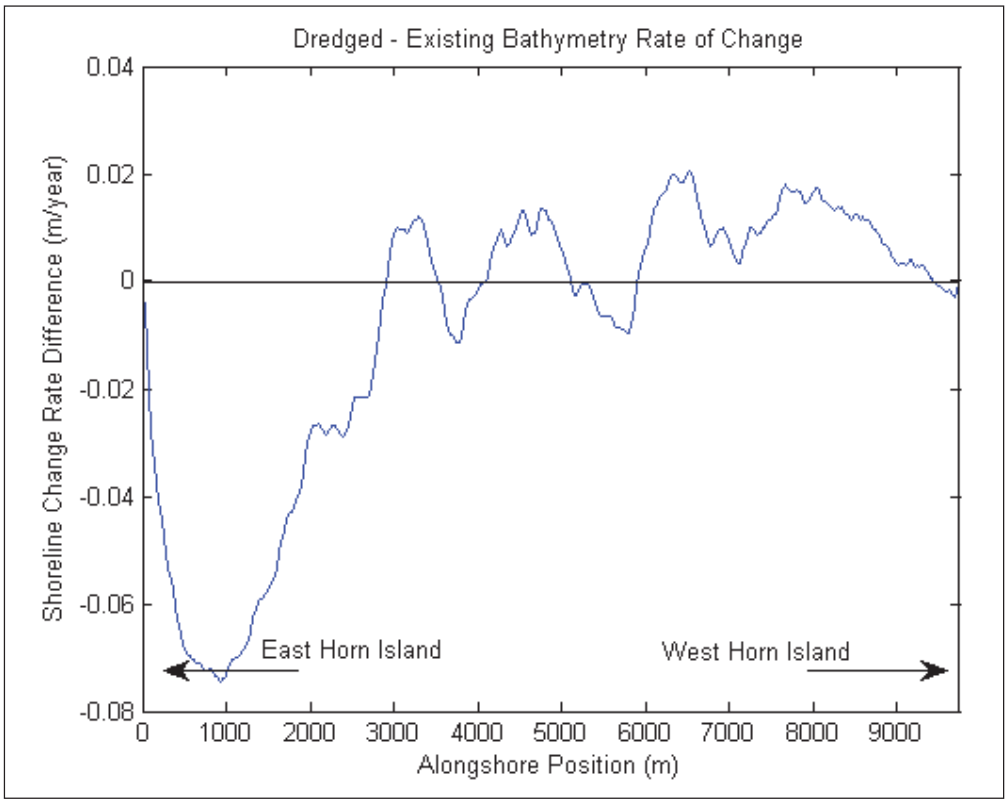

8.4 Petit Bois borrow area analysis

This chapter discusses two configurations for a proposed borrow site located on the seaward side of Petit Bois Inlet, which is between Petit Bois

Island and Dauphin Island in the northern Gulf of Mexico (Figure 8-1). The borrow site would supply sand for a shoreline restoration project on Ship Island. The two borrow site configurations broadly overlap, as shown in Figures 8-35a through 8-35c. Both are approximately 9000 ft (2700 m) southwest of West Dauphin Island in a nominal water depth of 30 ft (9.0 m).

The design for the first configuration calls for the removal of the top 8.0 feet of material from the site. The second configuration divides the site into 10 sub-areas, with each sub-area being dredged to a different depth, as shown in Table 8-34. Figure 8-35c shows how the first configuration (in brown) overlaps the second (multi-colored).

Because of the proposed borrow area's proximity to Dauphin Island, there is a potential for adverse shoreline impacts due to changes in wave refraction over the excavated pit. This chapter describes the analysis conducted to examine the impacts of the dredged borrow area on sediment transport and shoreline change along the west end of West Dauphin Island.

8.4.1 Model setup

The shoreline and littoral transport impacts induced by the excavation of proposed borrow areas were examined with the spectral near shore wave transformation model STWAVE (Smith et al. 1999) and the shoreline change model GENESIS (Hanson and Kraus 1989). The location of the STWAVE model domain, the borrow sites, and the hindcast WIS wave station are illustrated in Figures 8-35a and 8-35b. Figures 8-36a and 8-36b show a more detailed view of the bathymetry (north is approximately to the right in these figures), along with the West Dauphin Island shoreline (orange), the western portion of West Dauphin Island (yellow), the STWAVE save station line (light blue), and the line of the GENESIS grid (black) along the right edge of the figure. The borrow areas are shown incised into the bathymetry.

The analysis involved simulating the transformation of hindcast offshore wave conditions at WIS Station 73150 (Figures 8-35a and 8-35b) from the 20-m contour to the 19.5-m contour using the WIS Phase III transformation technique. The transformed wave information corresponds to the offshore boundary of the STWAVE grid. The area shown in Figures 8-36 is the model domain used for the STWAVE simulations. The STWAVE *X*-axis is directed onshore (357 deg); the *Y*-axis is directed alongshore and is aligned roughly

Figure 8-34. Location map in northern Gulf of Mexico.

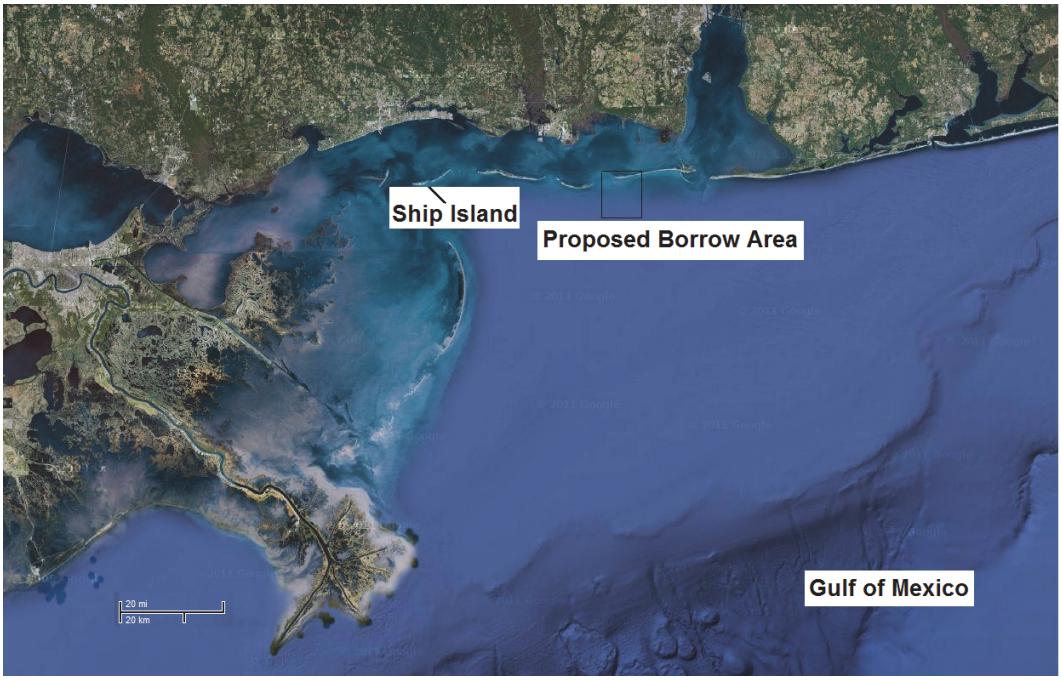

Figure 8-35a. STWAVE grid and borrow site Configuration 1.

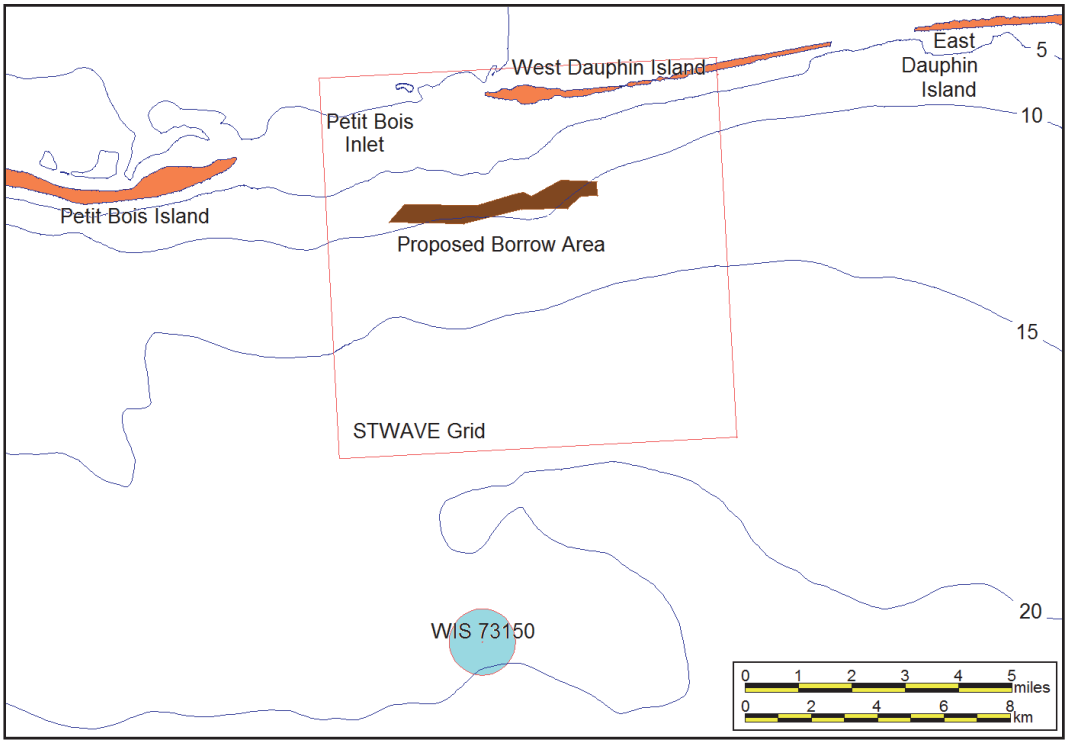

Figure 8-35b. STWAVE grid and borrow site Configuration 2.

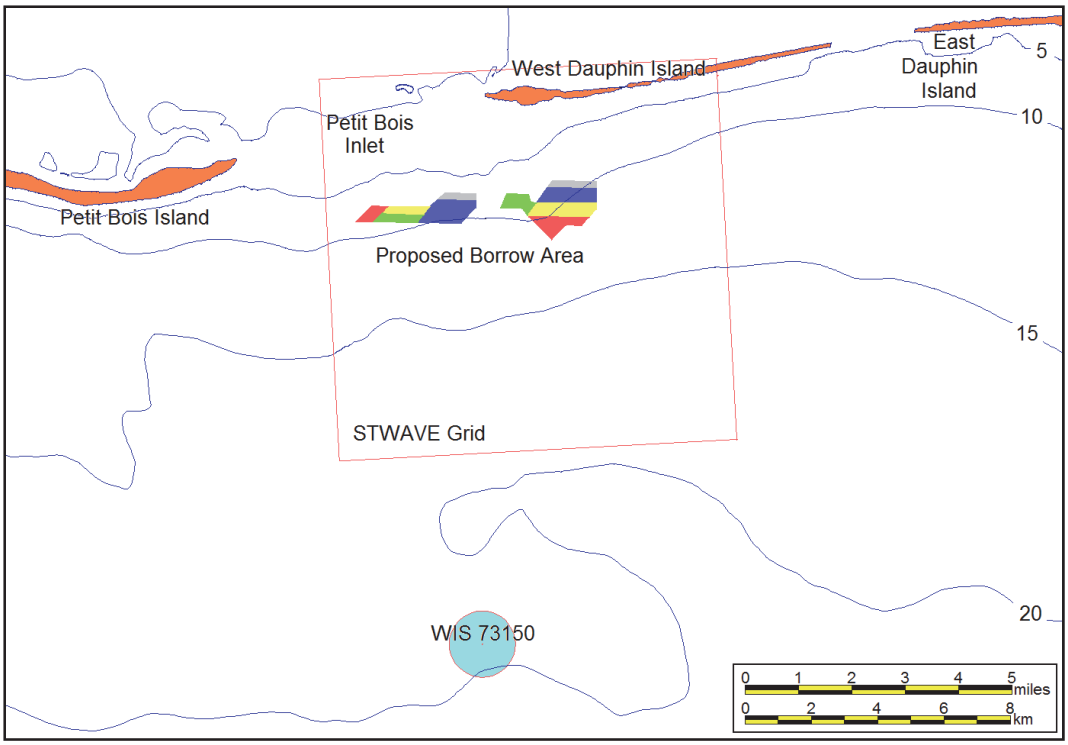

Figure 8-35c. Comparison of borrow site Configurations 1 and 2.

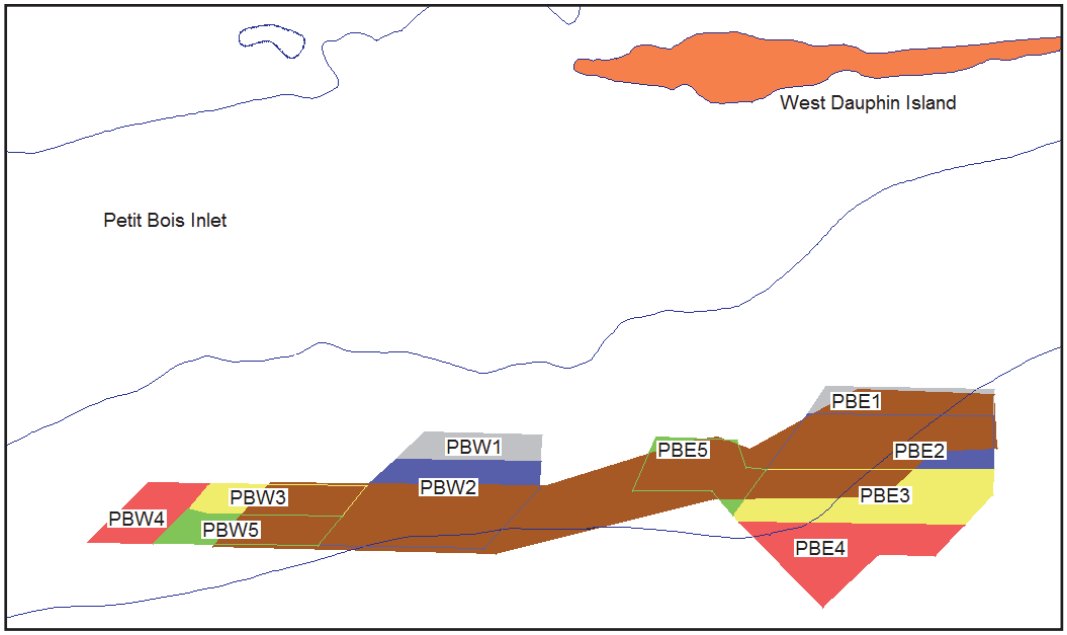

Figure 8-36a. Configuration 1 dredged bathymetry. Depth in meters.

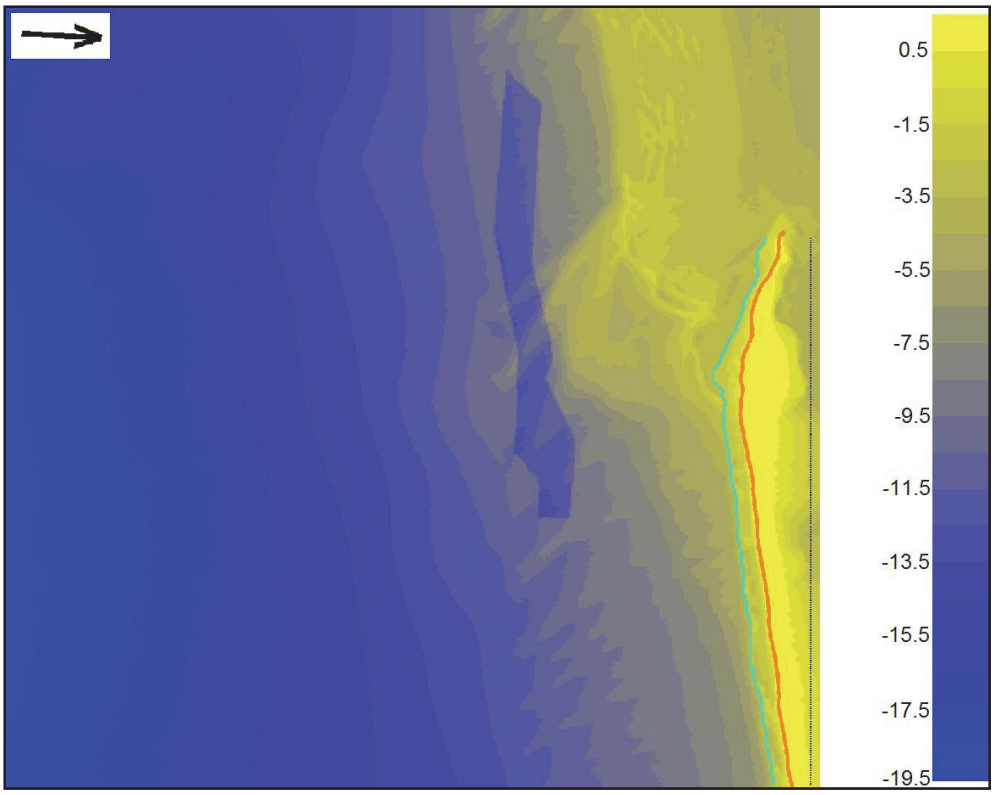

Figure 8-36b. Configuration 2 dredged bathymetry. Depth in meters.

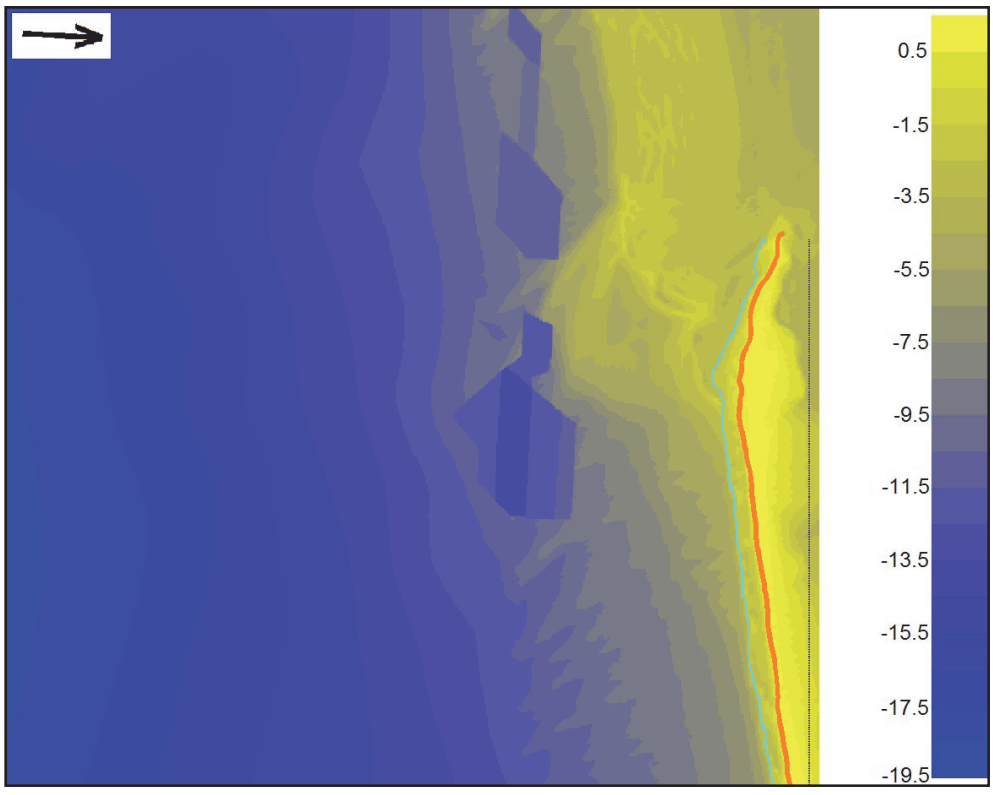

Table 8-1. Borrow site dredge depths.

Configuration 1		
Figure 8-2 color: Brown		
Dredge elevation: 8 ft below ambient.		
Configuration 2		
Sub-area	Figure 8-2 color	Dredge elevation (ft)
PBE1	Gray	-37
PB32	Blue	-42
PBE3	Yellow	-48
PBE4	Red	-42
PBE5	Green	-40
PBW1	Gray	-33
PBW2	Blue	-38
PBW3	Yellow	-34
PBW4	Red	-37
PBW5	Green	-32

parallel with the West Dauphin Island shoreline. The resolution of the STWAVE computational grid is 25 m in both the *X* and *Y* directions. Estimates of nearshore wave conditions generated by STWAVE along the nominal 3.1-m contour for both the existing and dredged condition provided necessary input to GENESIS, which estimates longshore sand transport rates and shoreline change along the western portion of the Gulf of Mexico shoreline of West Dauphin Island.

The GENESIS *X*-axis runs parallel to the West Dauphin Island shoreline and is comprised of 309 shoreline cells at 25 m intervals. Because detailed calibration data are not available for this study, the GENESIS calibration coefficients were assigned default values of K1 = 0.4 and K2 = 0.2. These calibration values are typical of those applied in other studies discussed in this report and produced longshore sand transport rates that are in general agreement with the Dauphin Island sediment budget. Because this study is a relative analysis between with and without excavated borrow areas, aimed at estimating the potential shoreline impacts of proposed dredging of the nearshore borrow area, the importance of a detailed calibration is diminished.

8.4.2 Wave transformation analysis

Wave data were obtained from WIS station 73150, whose location is shown in Figures 8-35a and 8-35b. The predominant direction of wave approach at this site is from the southeast, as seen in the Figure 8-37 wave rose. (This figure shows the compass direction that the waves are coming from.) As seen from Figure 8-34, land masses block all waves, except low energy, locally generated waves, from most other directions. Nearshore wave transformation simulations were performed for 213 representative wave conditions identified through analysis of the WIS hindcast data. Figure 8-38 shows the distribution of representative wave conditions by incident wave angle and height. The incident wave angle is measured clockwise from shore normal. Wave direction data in this figure are referenced to the local shore normal direction of 177 deg azimuth. Positive wave angles are those approaching the coast from the southeast (from the left for a person standing on the beach looking offshore). The value in each block is the number of occurrences of that wave condition in the 20-year WIS hindcast spanning the interval 1980 through 1999. Figure 8-39 shows the distribution of wave conditions by height and period, and Figure 8-40, by angle and period. Figure 8-41 shows a histogram of heights, periods, and directions. For each of the 213 representative wave conditions, an idealized TMA wave spectrum was generated and applied as the input to STWAVE.

STWAVE simulations were performed to compute wave transformation across the irregular offshore bathymetry from approximately the 19.5-m contour to the 3.1-m contour. Three simulations were run. The first employed existing bathymetry and the second and third used the bathymetry that would result from the two post-dredging configurations.

Figure 8-42 is a plot of wave heights over the STWAVE computational domain for the existing bathymetry for a 5.0 sec wave with an offshore height of 0.8 m and an angle of 40 degrees. In this figure, wave heights are shown by colors from blue to yellow and wave directions by black arrows. Also, West Dauphin Island is in gold, with its shoreline in orange, offshore contours are in brown, the STWAVE save stations are the blue-green line near the shoreline, and the GENESIS baseline is the black line across the top (right) of the figure. Note the complex changes in wave height over the large shoal area near the western tip of the island.

Figure 8-37. WIS Station 73150 wave rose.

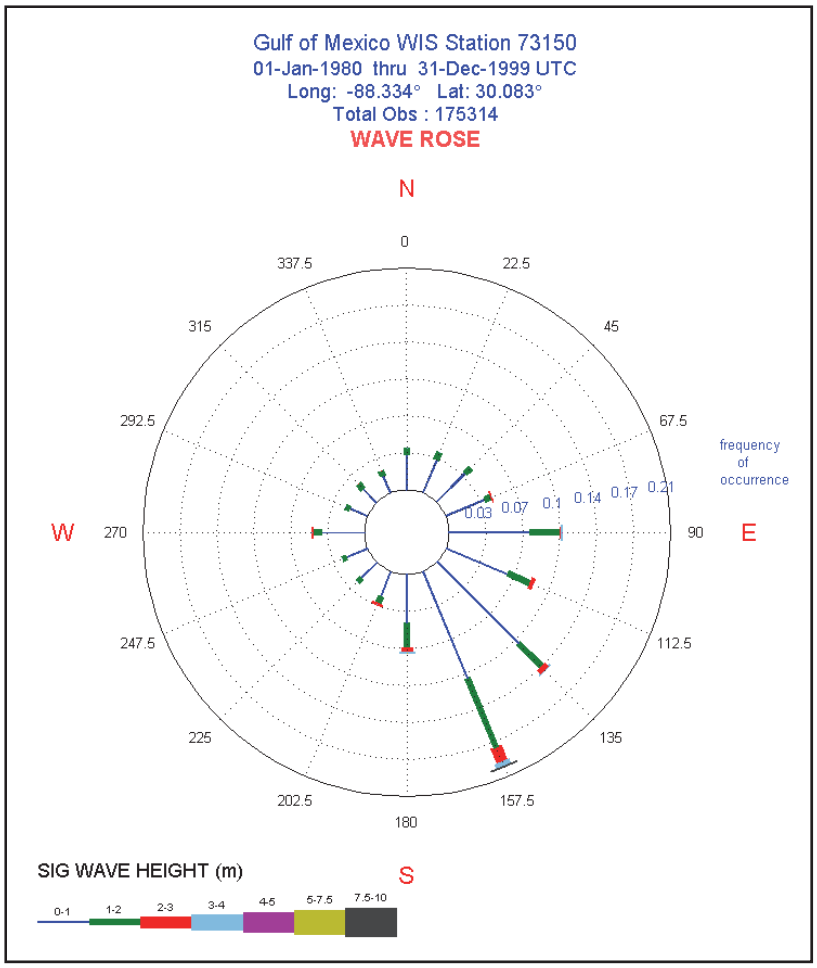

Figure 8-38. Distribution of the representative wave conditions by incident wave angle and height.

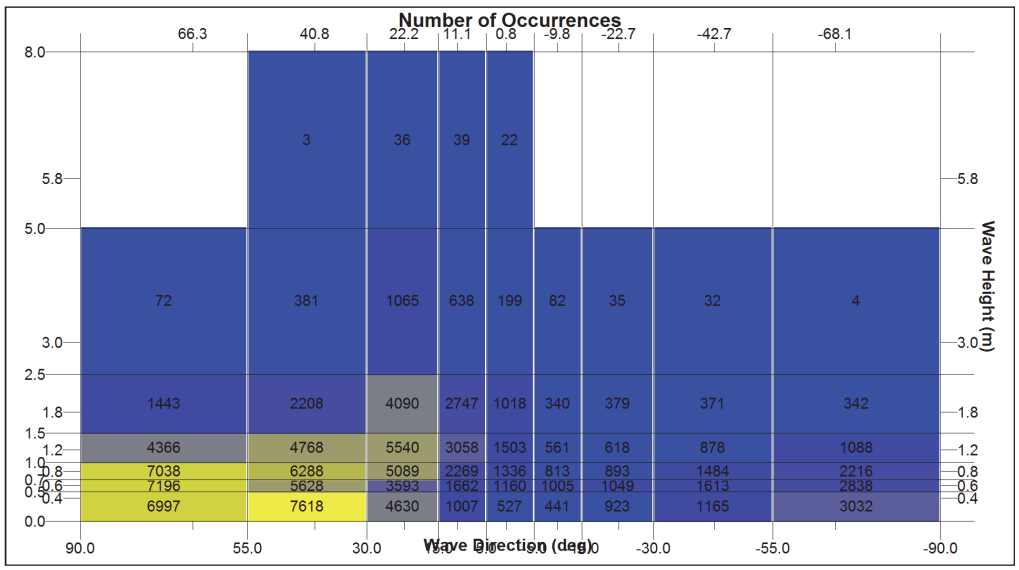

Figure 8-39. Distribution of the representative wave conditions by incident wave height and period.

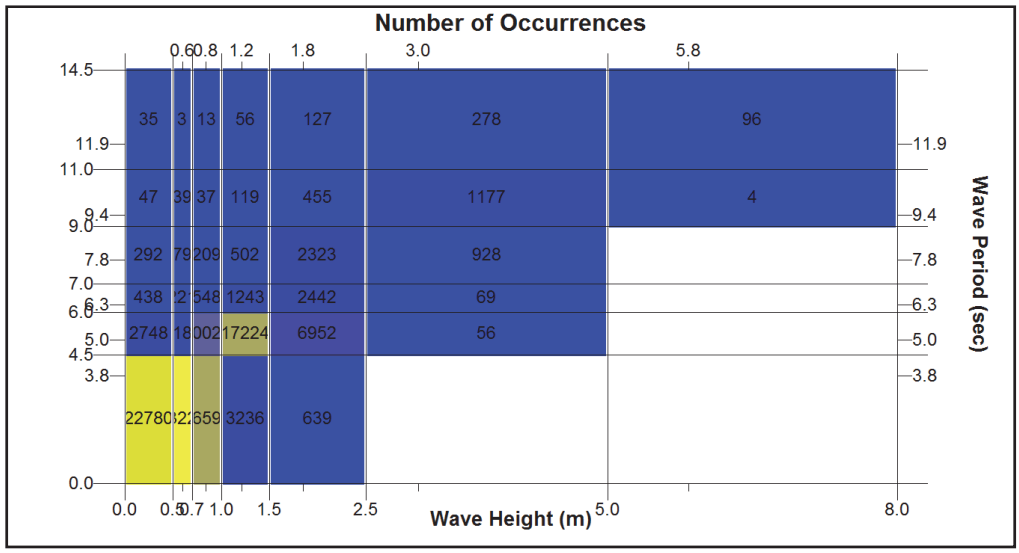

Figure 8-40. Distribution of the representative wave conditions by incident wave angle and period.

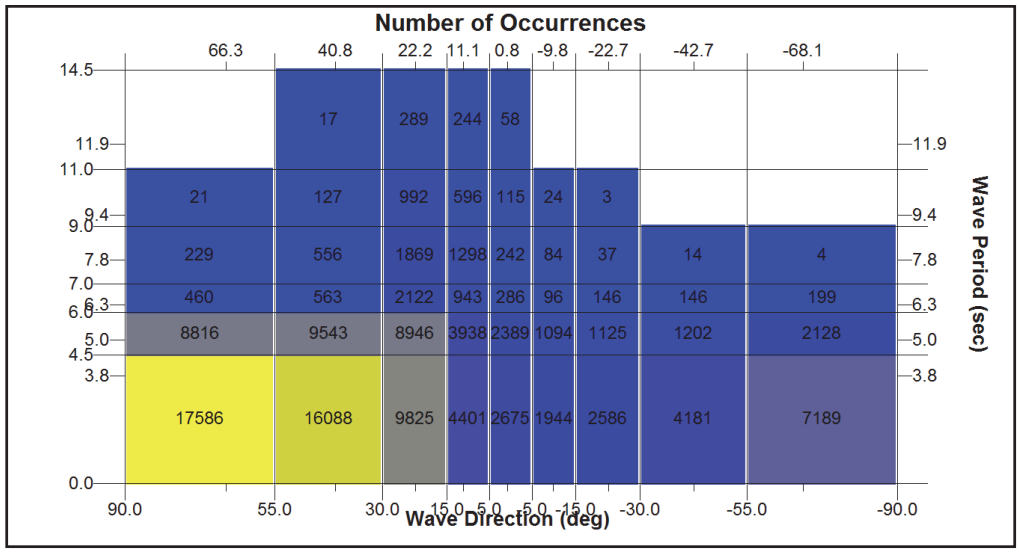

Figures 8-43 through 8-57 illustrate the effects of wave refraction over the first configuration borrow site using five example wave conditions. Figure 8-43 shows estimated significant wave height changes induced by excavation of the borrow area for a 0.8 m, 5.0 sec incident wave for three incident wave angles. The wave height changes are calculated by subtracting the existing condition wave heights from the first configuration dredged condition wave heights. The portion of the borrow area seaward of the dredged site is not shown in these figures as no differences occur there. Figure 8-43, Panel A shows height differences for the same wave condition

illustrated in Figure 8-42. As discussed above, the 20-year wave record was divided into 213 wave height-wave period-wave angle bins. The three bins shown in Figure 8-10 are representative of wave conditions that occur 1.23, 0.26, and 0.08 percent of the time, respectively.

Figure 8-41. Histogram of wave heights, periods, and directions.

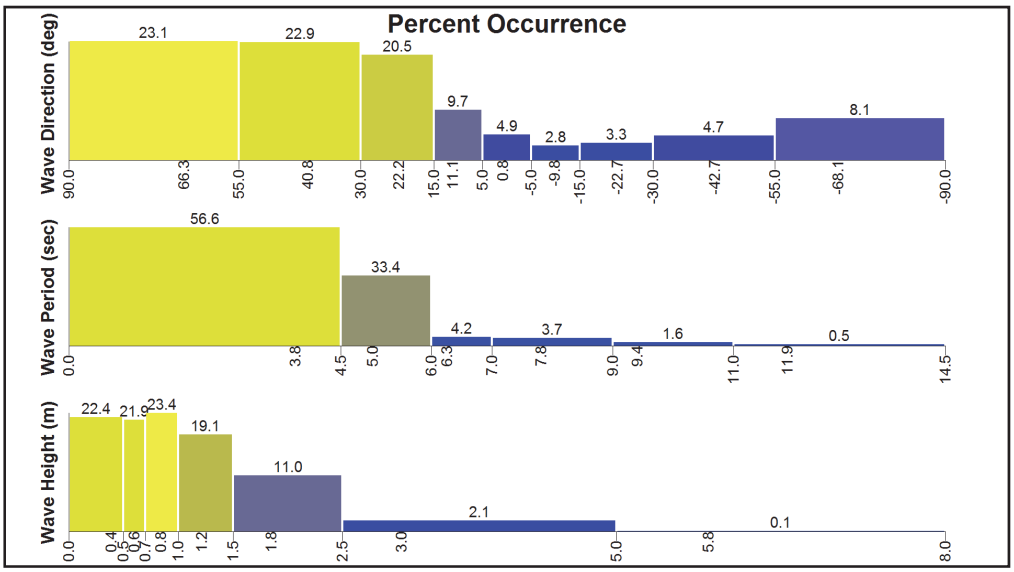

Figure 8-42. Existing condition wave heights for incident wave of *H* = 0.83 m, *T* = 5 sec and *Theta* = 40 deg.

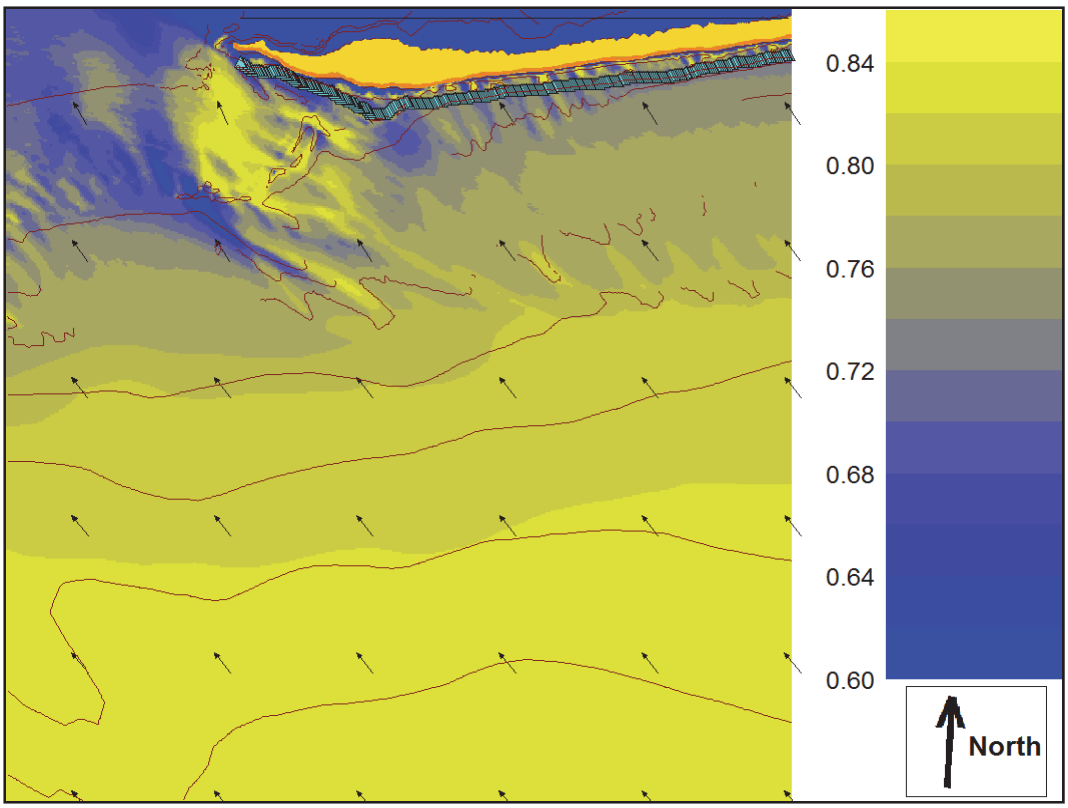

Figure 8-43. Wave height change (dredged – existing) for incident wave of H = 0.8 m, T = 5.0 sec.

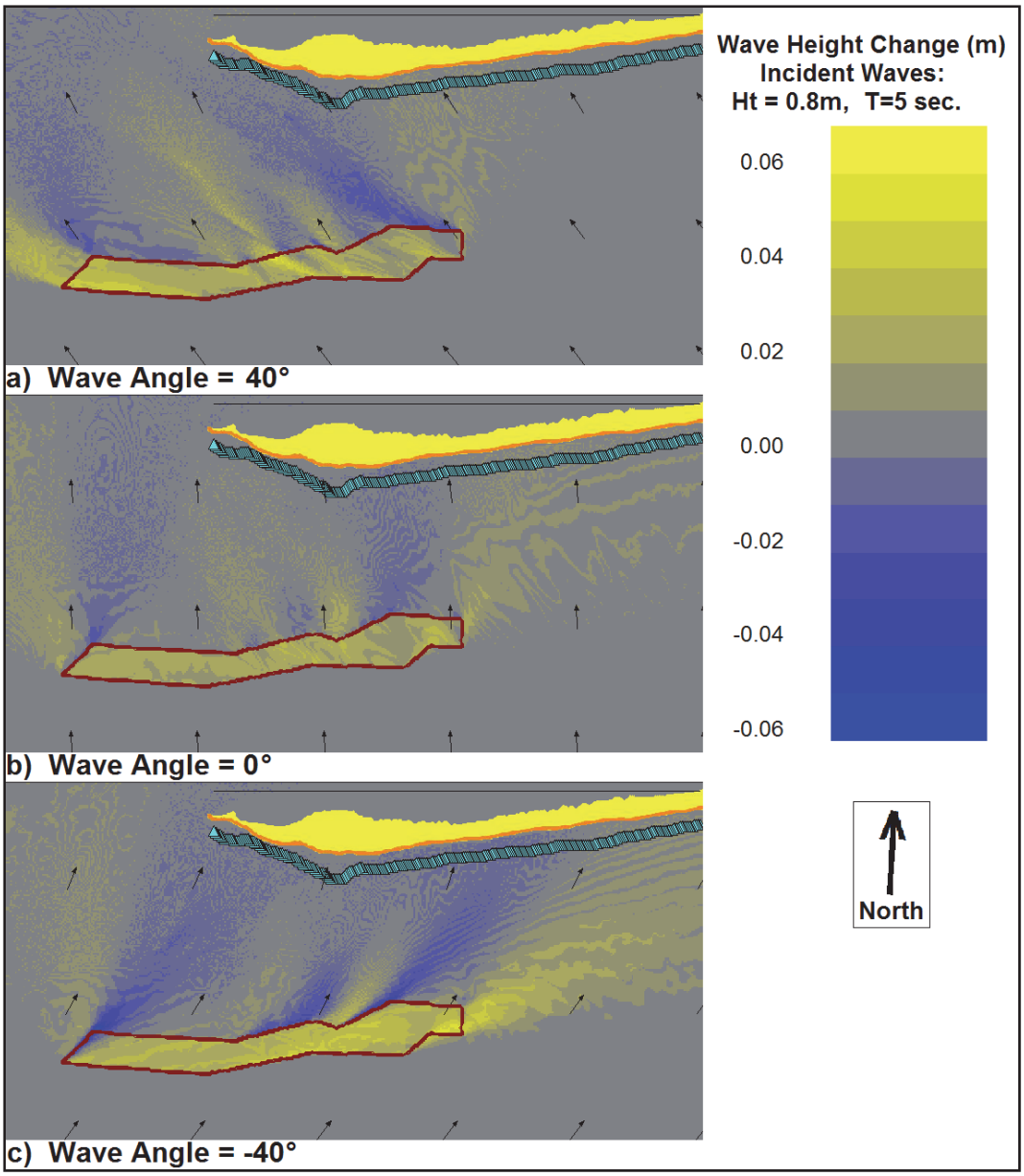

Figure 8-44 shows height differences for larger 3.0 m, 11 sec waves. These rarer conditions occurred 0.003 and 0.010 percent of the time in the wave record, respectively. The 20-year wave record contained no events for waves of this height and period approaching from a minus 40 degree angle (comparable to Figure 8-43, Panel C). Because these larger waves break on the shoal off the tip of Dauphin Island, at this location they are depth limited and their heights become equal.

Figure 8-44. Wave height change (dredged – existing) for incident wave of H = 3.0 m, T = 11 sec.

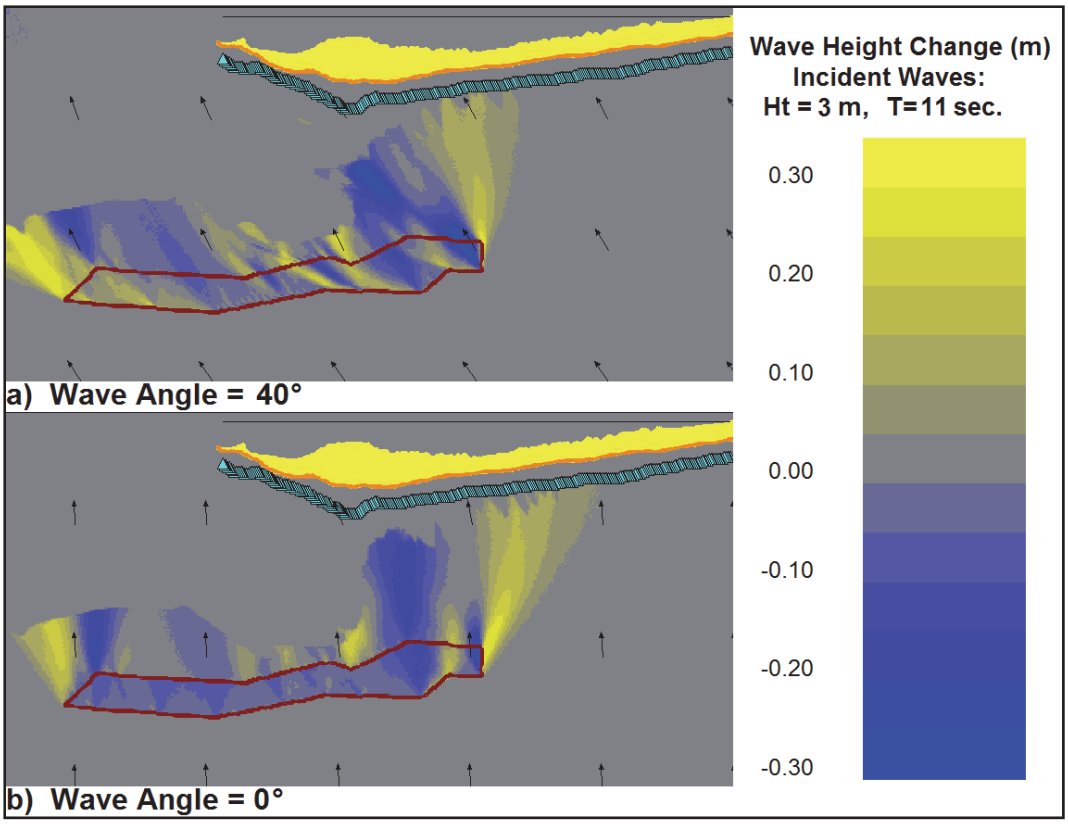

Figures 8-45 and 8-46 show wave angle differences for the same wave conditions illustrated in Figures 8-43 and 8-44. Yellow colors represent a clockwise rotation of the wave angle in the dredged condition relative to the existing condition, while blue represents a counter-clockwise rotation. The black arrows on the figures show the wave directions for the existing conditions.

Figures 8-47 through 8-50 show how the second borrow site configuration impacts the wave refraction. The explanation for these figures is the same as for Figures 8-43 through 8-46, respectively.

Figure 8-51a shows the first configuration percent difference in wave heights at the STWAVE save stations for the five wave cases shown in Figures 8-43 through 8-46. The locations of the STWAVE save stations are shown as the line of blue-green triangles offshore of Dauphin Island in Figures 8-43 through 8-50. The vertical axis in Figure 8-51a has been scaled for easy comparison with similar plots from other borrow sites. Figure 8-51b shows the same information for the second borrow site configuration. As shown in these figures, for these five cases, at no location along Dauphin Island does the wave height difference exceed 1.25 percent.

Figure 8-45. Wave angle change (dredged – existing) for incident wave of H = 0.8 m, T = 5.0 sec.

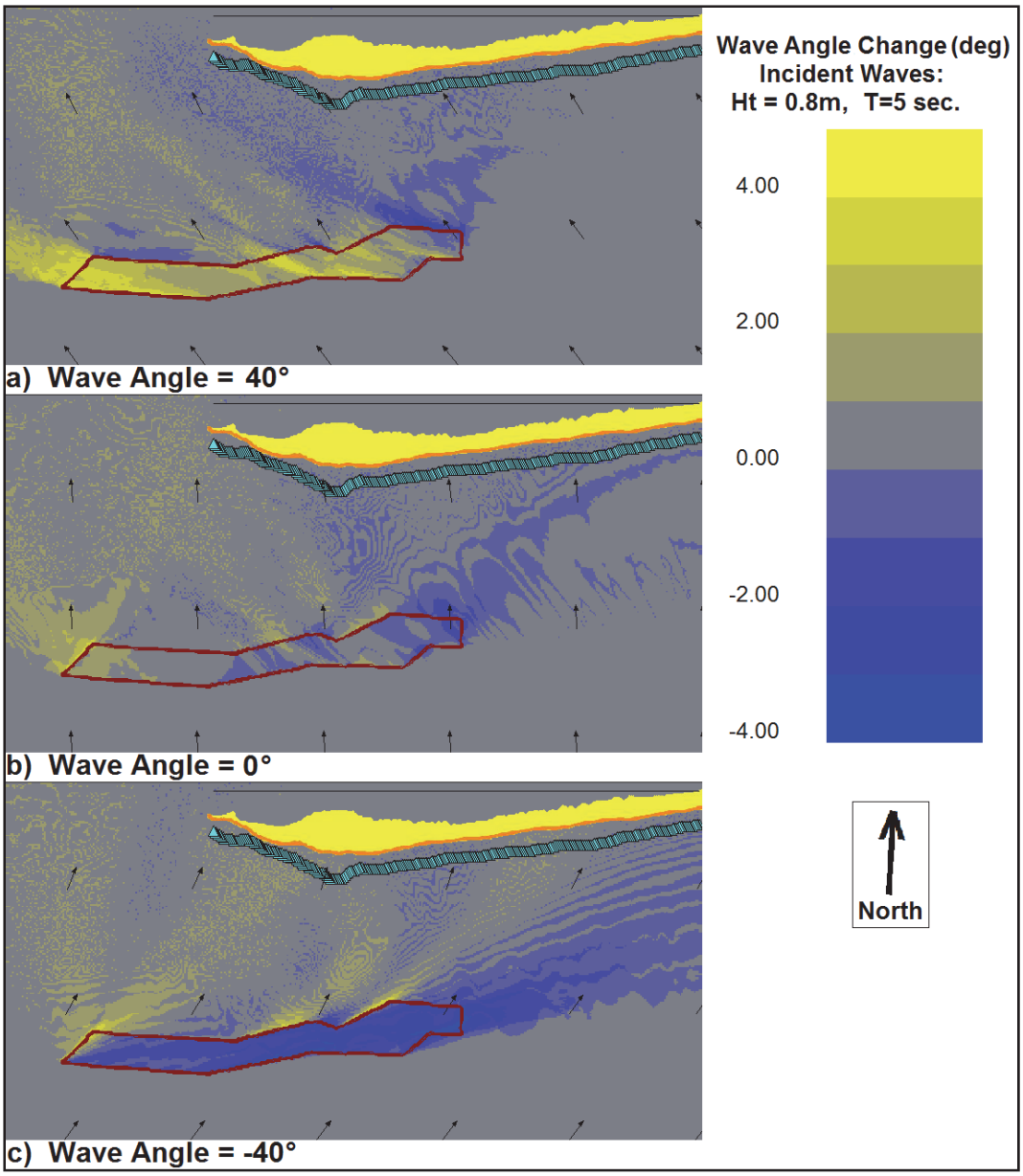

8.4.3 Sediment transport and shoreline change

A GENESIS model domain was generated for examining the influence of the borrow areas on shoreline processes along the westernmost 7700-m (4.8 miles) of West Dauphin Island. STWAVE generated near-shore wave conditions for both dredged and existing condition were applied as input to GENESIS to estimate longshore sand transport rates and shoreline change. The GENESIS simulations were run for the 20-year WIS hindcast offshore wave time-series (1980-1999).

Figure 8-46. Wave angle change (dredged – existing) for incident wave of H = 3.0 m, T = 11 sec.

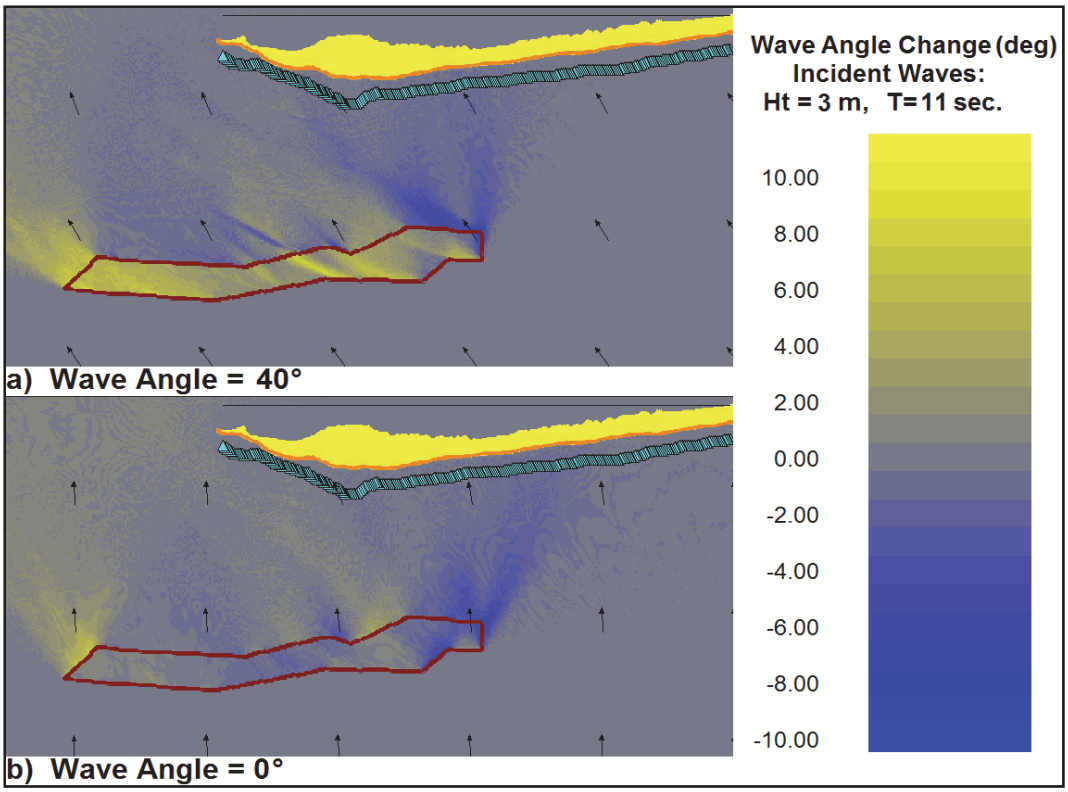

Figure 8-52 shows the GENESIS grid for the western portion of West Dauphin Island. The scale is in meters. The offshore direction in this figure is 177 degrees (nearly due south). The graphs that follow Figure 8-52 show GENESIS results referenced to this horizontal axis. That is, these graphs should be visualized as facing nearly due south, making the western tip of the island on the right. Also, in these figures, results for the first configuration are labeled BA1 (Borrow Area1), and the second, BA2.

Figure 8-53 displays the initial shoreline position along with three estimated final (20 yr) shoreline positions (existing bathymetry and both dredged configurations). In this figure there is approximately a 7:1 distortion in offshore to along shore distances.

Figure 8-54 plots the shoreline change rate for the three simulations. Negative values indicate erosion and positive values indicate accretion. Figure 8-55 plots the difference, or change, in the estimated shoreline change rates between the existing and dredged condition for each point on the GENESIS axis. Comparing Figures 8-54 and 8-55, it is seen that the dredged-induced impacts to the shoreline change rate are anticipated to be in the range of 2-4 percent of the existing rate.

Figure 8-47. Wave height change, H = 0.8 m, T = 5.0 sec, 2nd configuration.

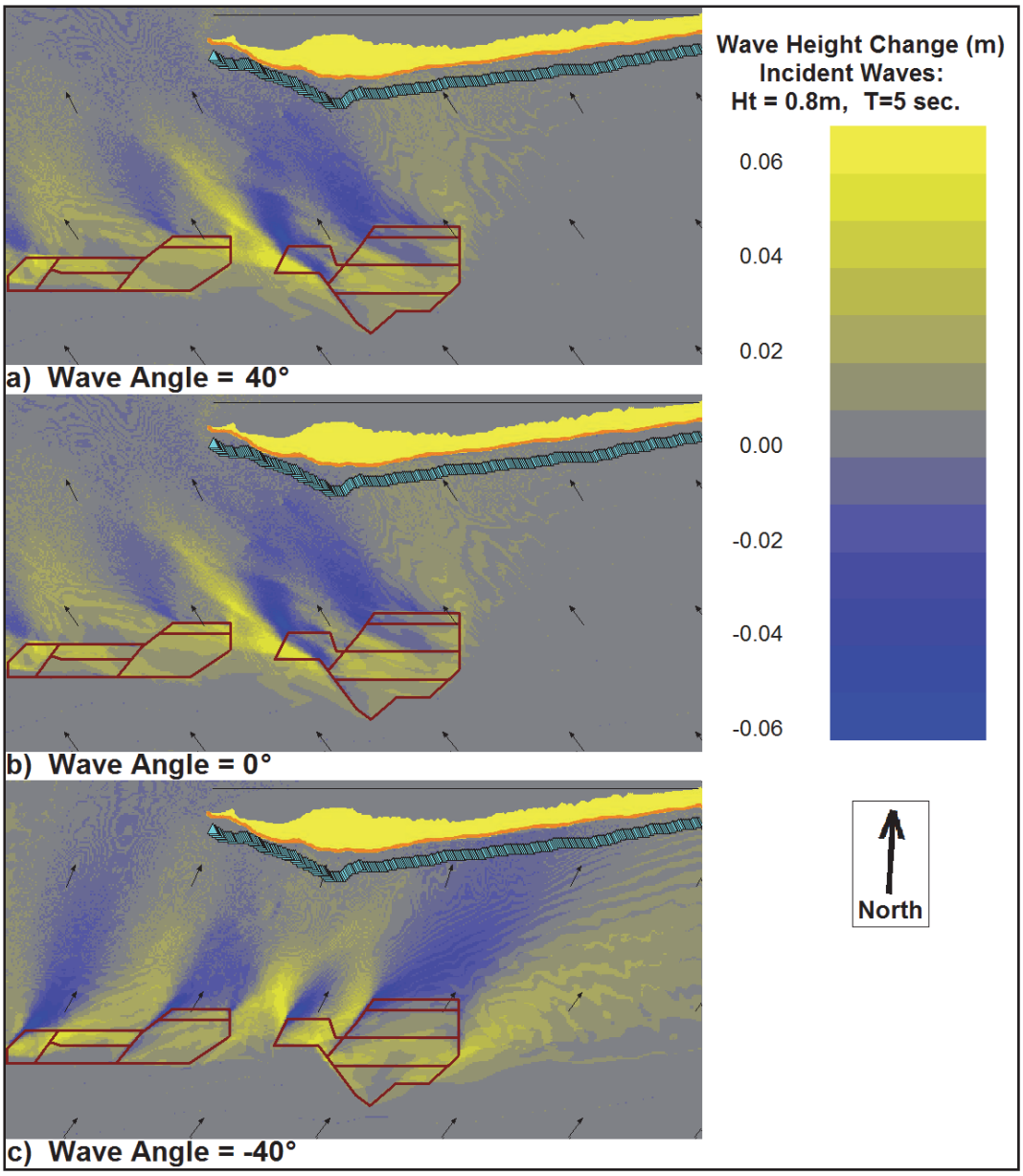

The estimated average net annual longshore sand transport rates for the existing and the two dredged conditions are plotted in Figure 8-56. Positive values indicate transport to the right on the plot (i.e., the net transport is to the west all along this portion of coastline). This leads to a positive slope in the longshore sand transport rate indicating erosion whereas a negative slope indicates shoreline accretion. The steeper the slope the higher the predicted shoreline rate of change. A stable shoreline is associated with a constant longshore sand transport rate, which would be a flat line in this figure. The estimated average annual longshore sand transport rates for the current and the two dredged conditions vary between approximately

Figure 8-48. Wave height change, H = 3.0 m, T = 11 sec, 2nd configuration.

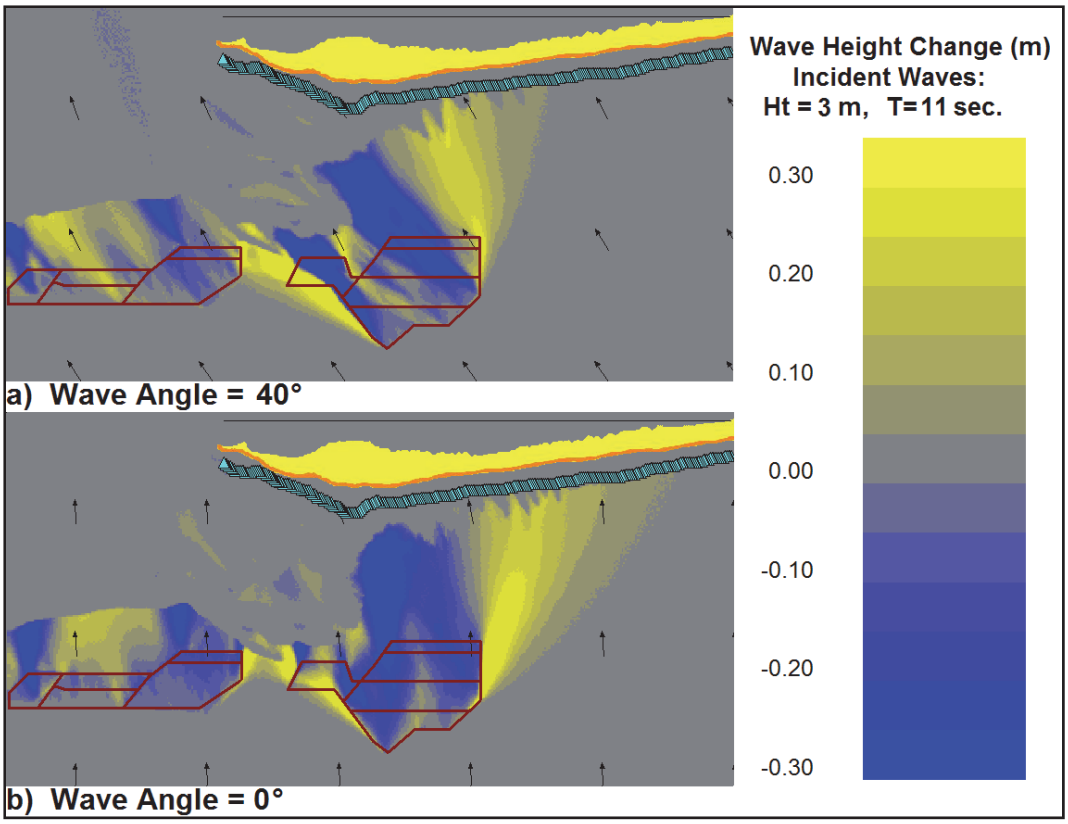

100,000 and 225,000 m³/year (west-directed). The change in estimated transport rates between the existing and dredged condition is less than 3 percent.

To isolate the influence of the excavated borrow areas on longshore sand transport rates, the change in estimated transport rates between the existing and dredged condition are plotted in Figure 8-57. The vertical axis in Figure 8-57 has been scaled for easy comparison with similar plots from other borrow sites. As shown in this figure, the modeling predicts that at no location along Dauphin Island will the net longshore sediment transport rates change by more than 4,000 m³/yr.

8.4.4 Summary

The expected refraction-induced shoreline impacts to West Dauphin Island are similar for either borrow site configuration and generally only change the naturally occurring processes by a few percent. The dredged-induced impacts to the shoreline change rate are anticipated to be in the range of 2-4 percent of the existing rate. In addition, the changes will be largely stabilizing. That is, over most of the shoreline, the small dredge

Figure 8-49. Wave angle change H = 0.8 m, T = 5.0 sec, 2nd configuration.

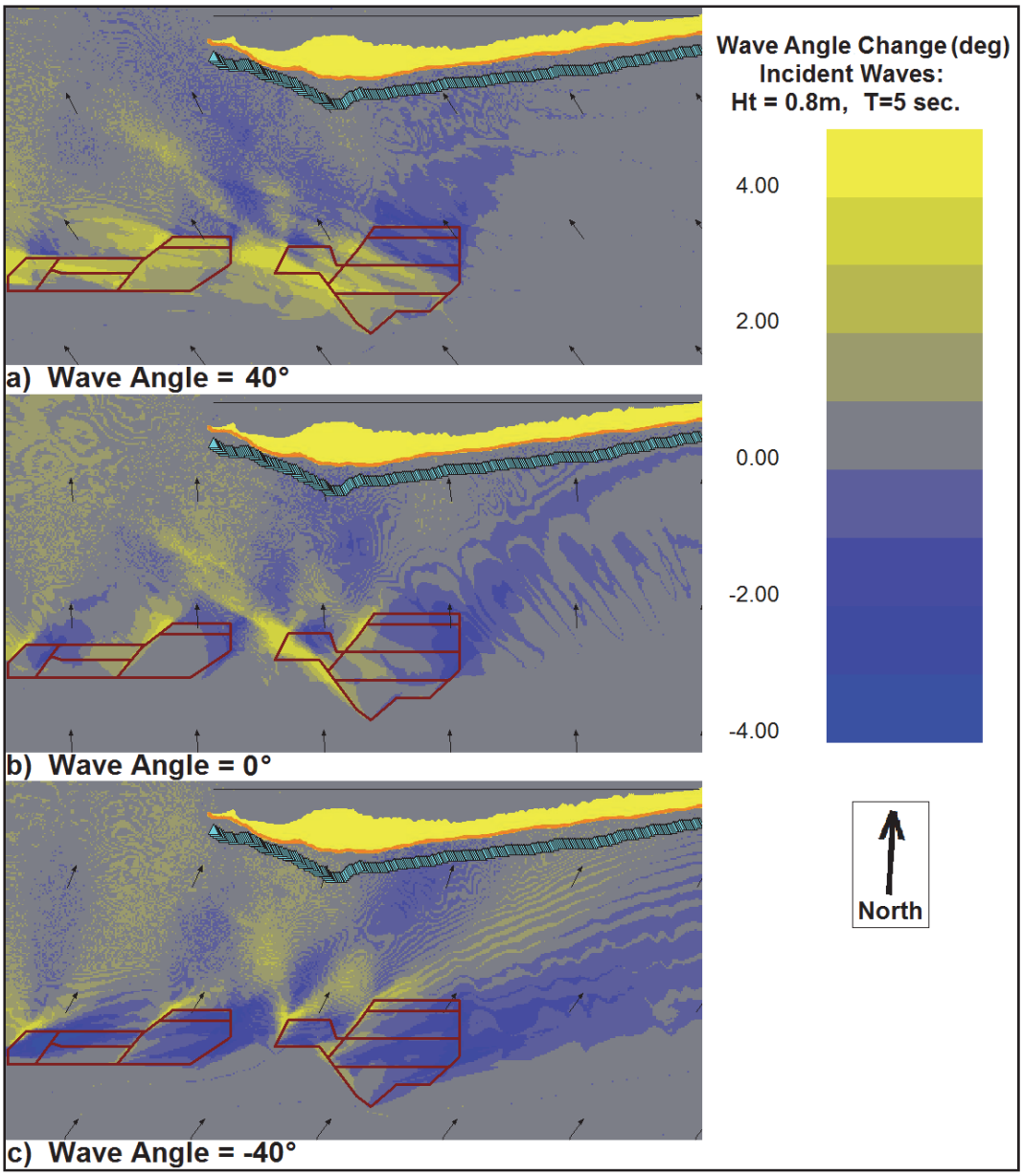

induced changes will decrease both the erosion and the accretion in the areas where they occur. A comparison of Figures 8-55 and 8-56 shows that mining either borrow area will decrease the net alongshore sediment transport rate by less than about 3 percent of its current value.

The large shallow shoal between the borrow area and Dauphin Island substantially rectifies the waves and produces wave breaking for most incident wave conditions for both the dredged and existing cases. Thus, this shoal area largely shields Dauphin Island from any bathymetry-change effects at the borrow sites. In addition, the dominant incident wave

direction is from the SSE-SE sectors (Figure 8-4) which results in down-wave impacts of the borrow area occurring generally in the region of Petit Bois Inlet rather than along the Dauphin Island shoreline. The conclusion that offshore dredging will have a minimal shoreline impact is in good general agreement with the results of Byrnes et al. (2004) who used a different procedure to analyze the potential from mining offshore sand bodies along the Alabama Gulf coast.

Figure 8-50. Wave angle change, H = 3.0 m, T = 11 sec, 2nd configuration.

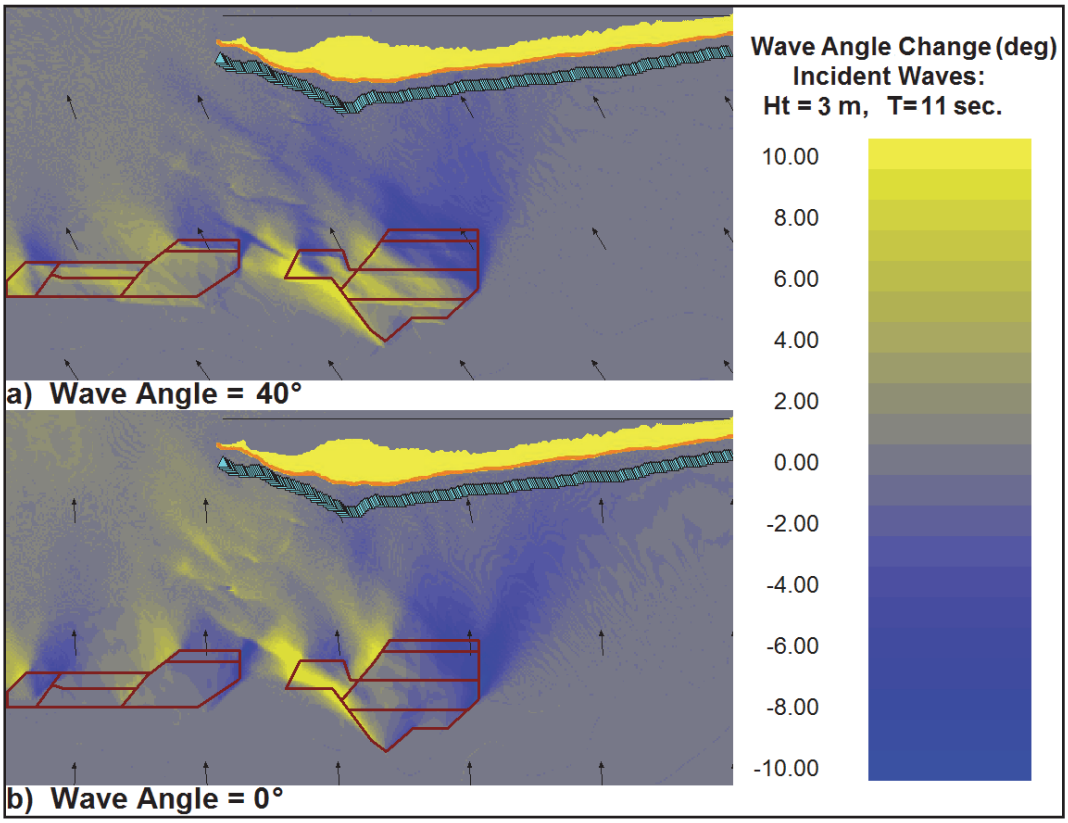

Figure 8-51a. Percent change in wave height at nearshore reference line.

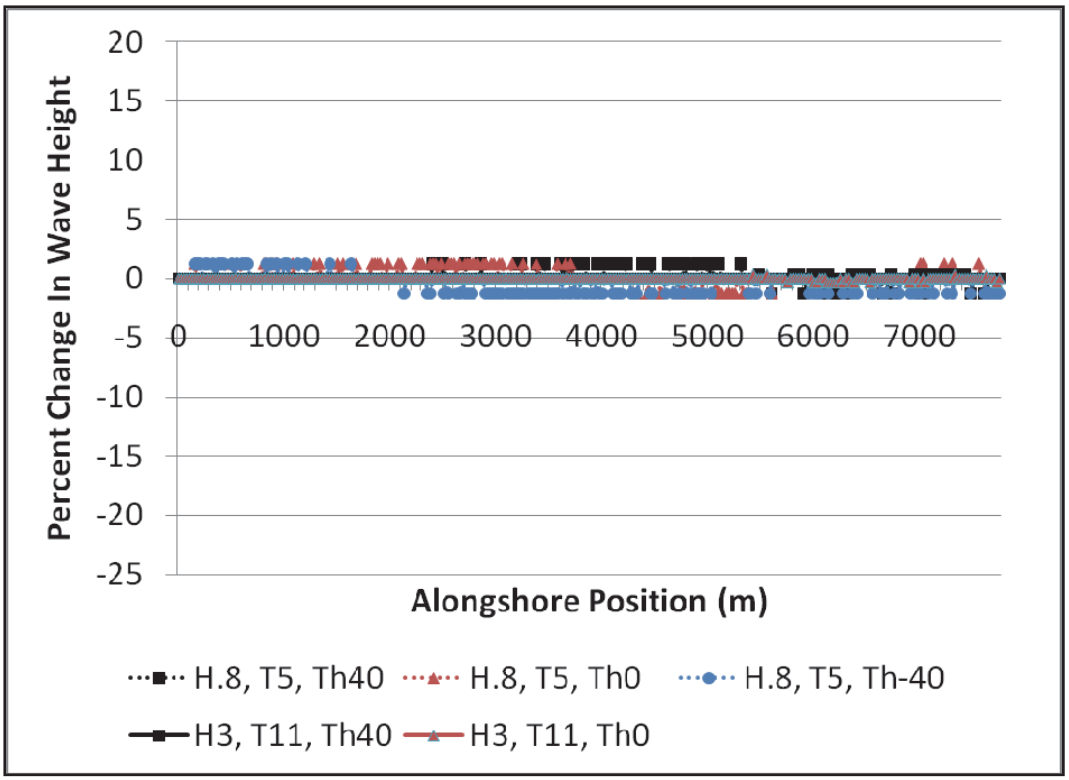

Figure 8-51b. Percent change in wave height at nearshore reference line for second borrow area configuration.

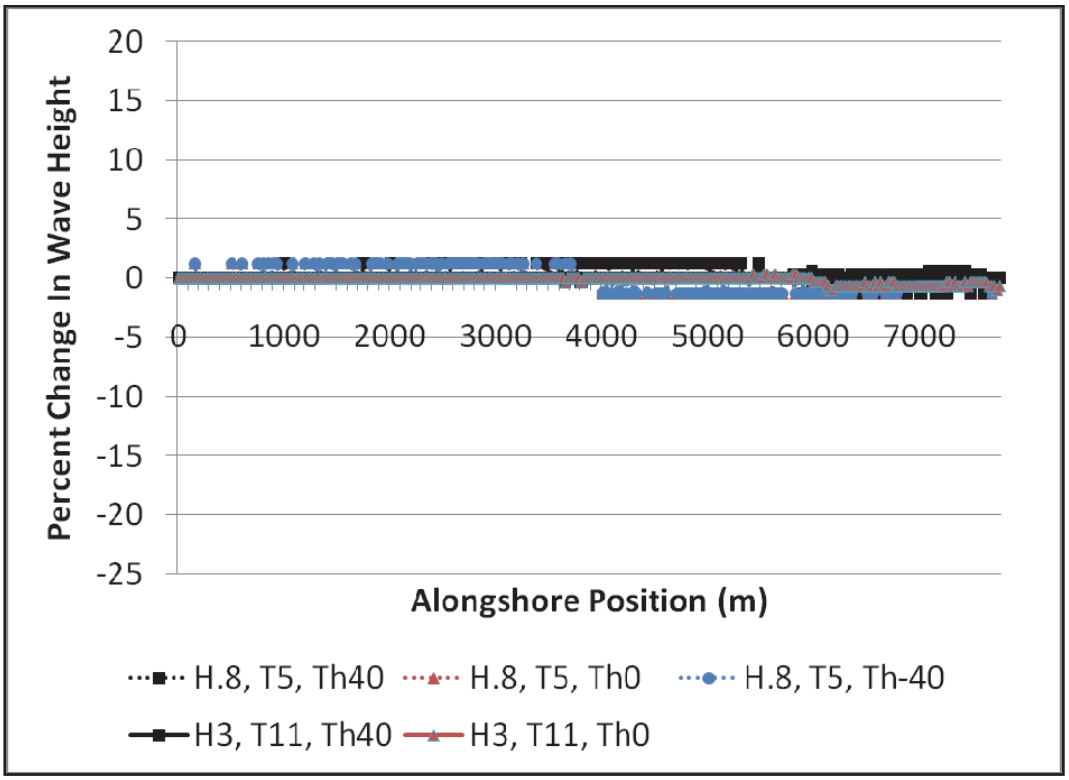

Figure 8-52. GENESIS grid for West Dauphin Island.

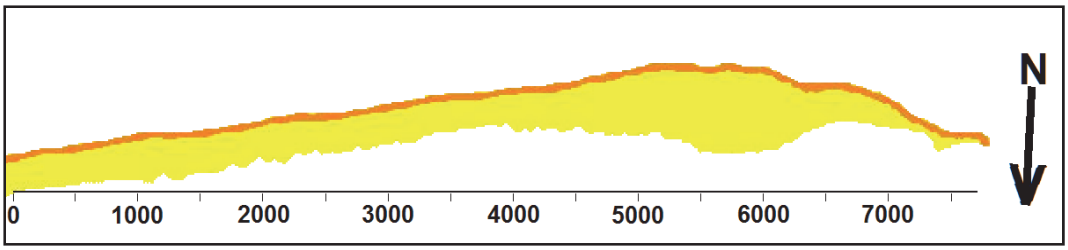

Figure 8-53. Comparison of existing and dredged condition estimated final shoreline.

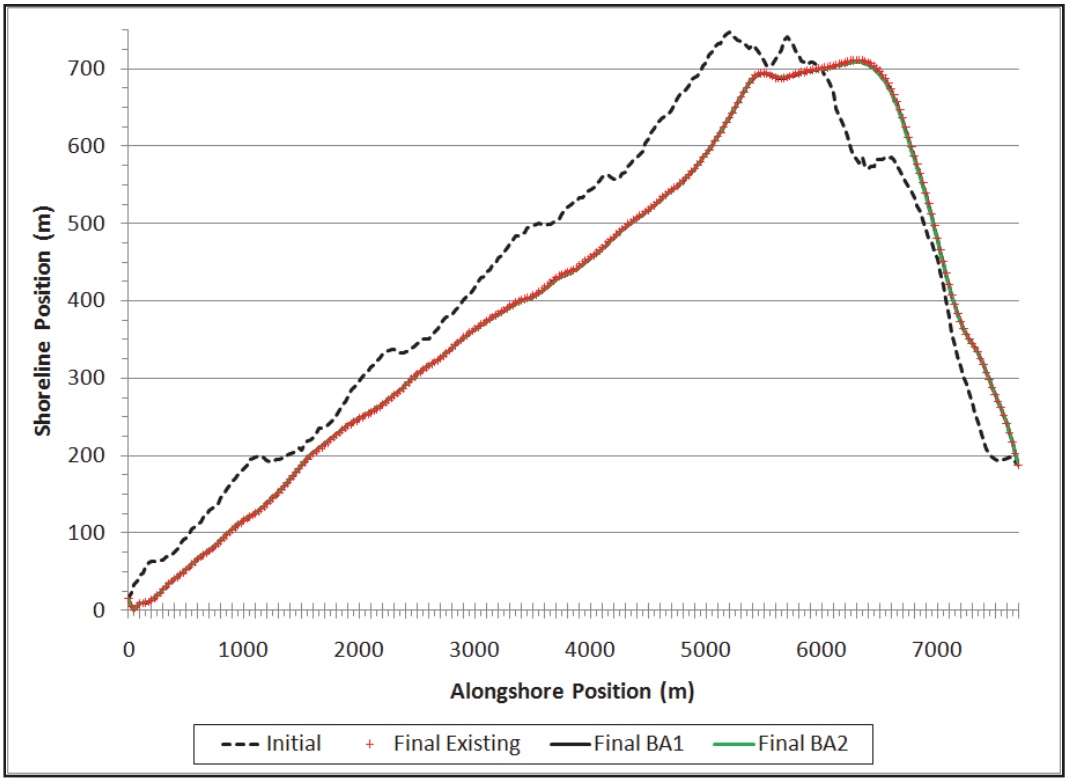

Figure 8-54. Comparison of existing and dredged condition shoreline change rate.

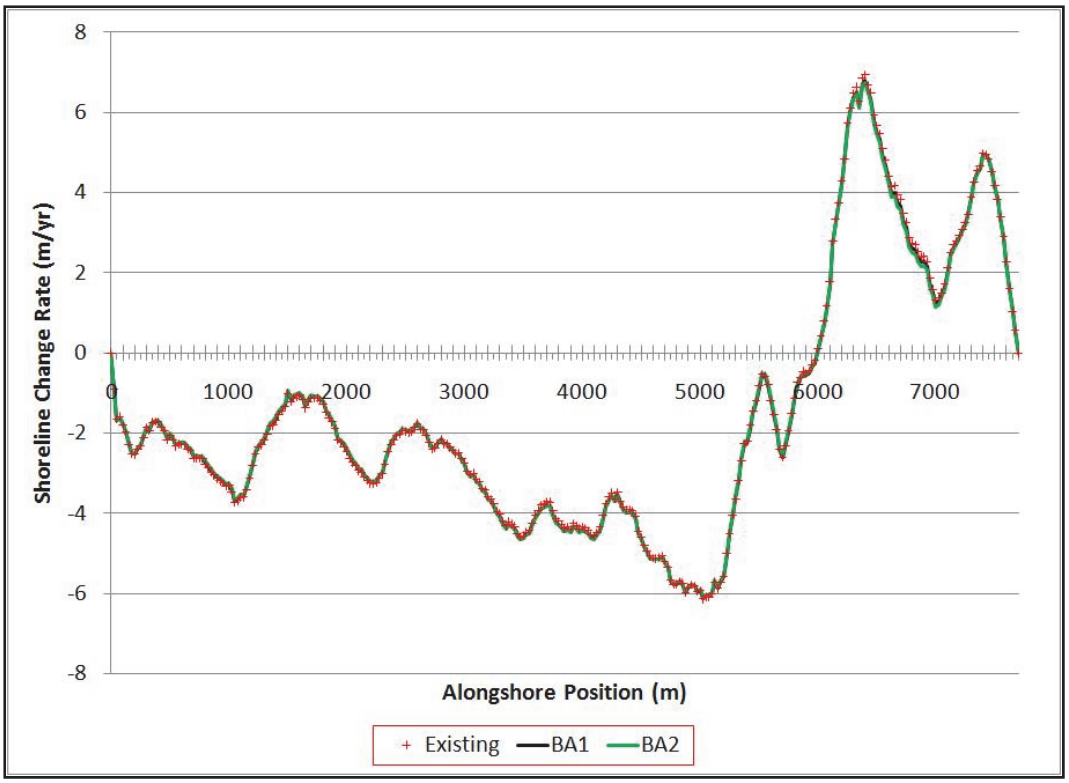

Figure 8-55. Dredging induced change in shoreline change rate.

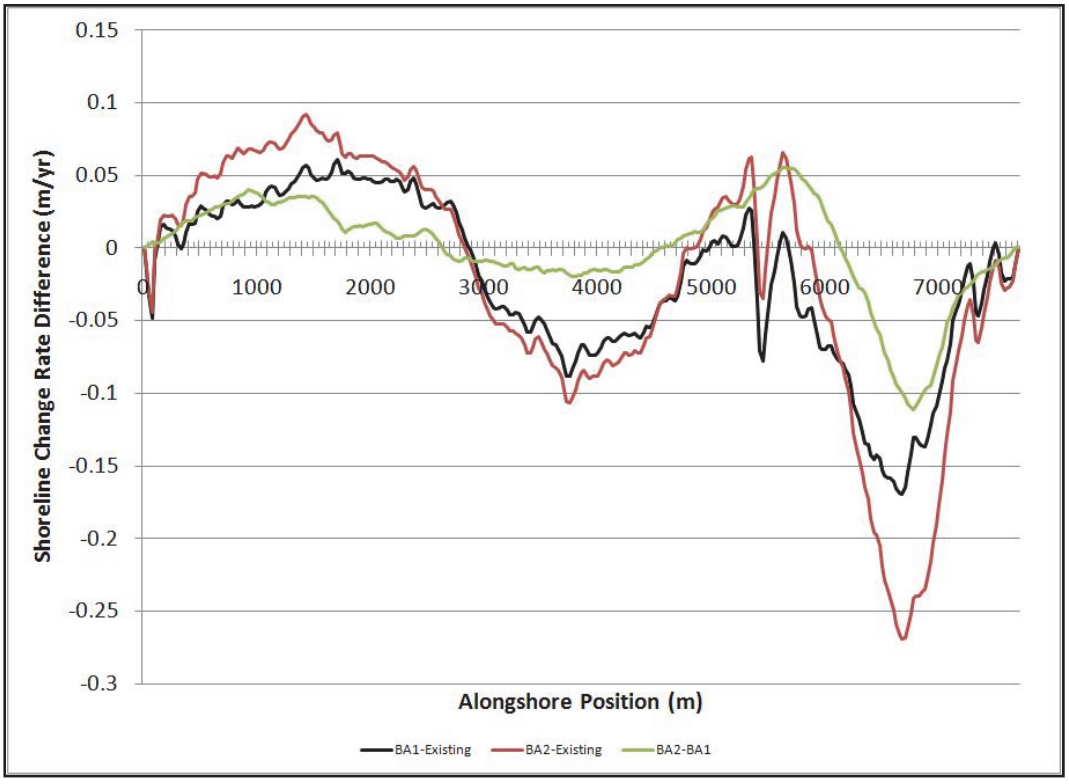

Figure 8-56. Mean alongshore transport rate.

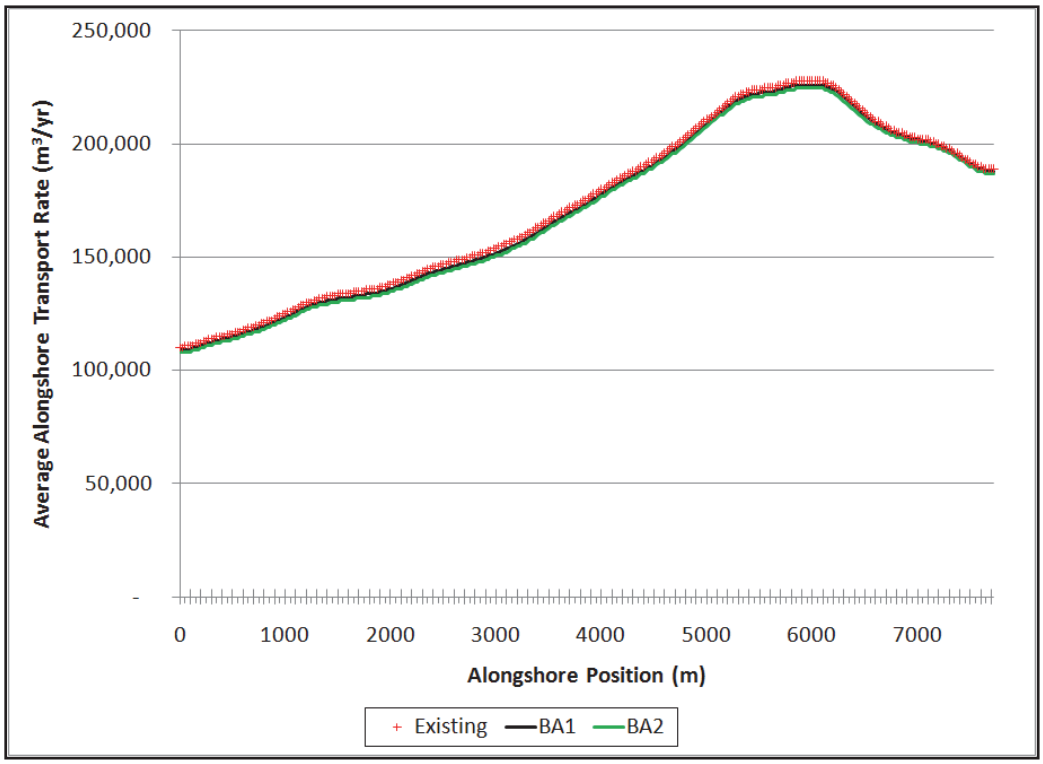

Figure 8-57. Change in the average net longshore transport rate.

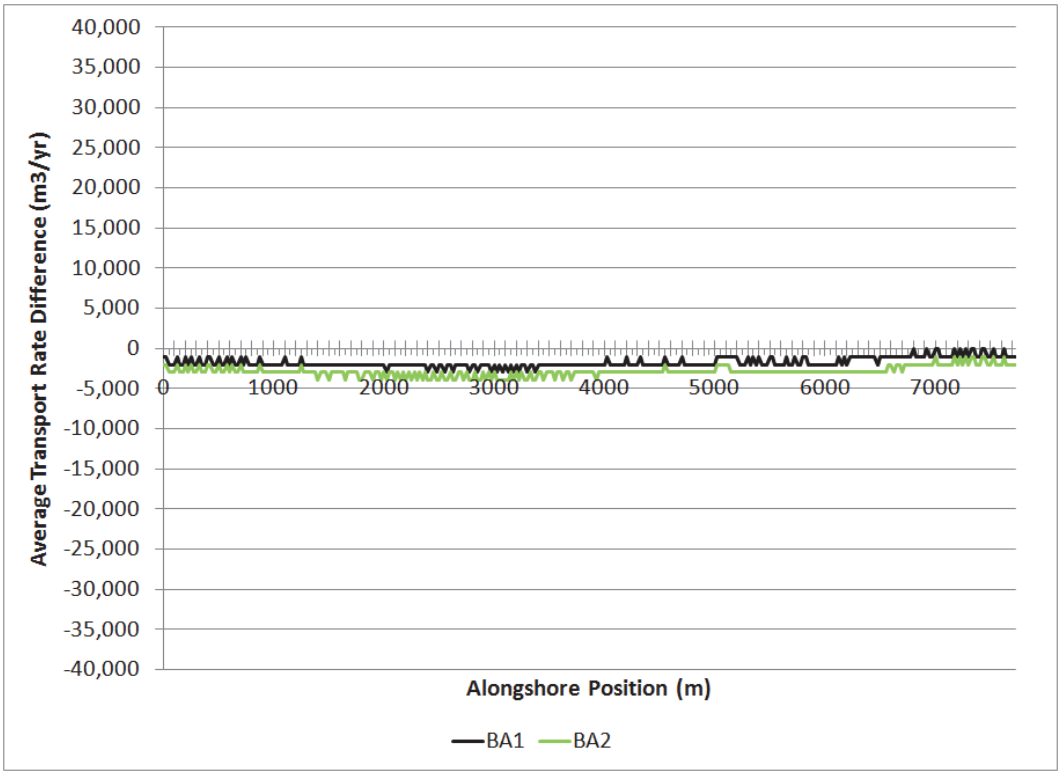

9 Summary

Hydrodynamic, wave, sediment transport, and water quality numerical modeling was conducted to support engineering and design as well as the development of a Supplemental Environmental Impact Statement for the restoration of Ship Island. The purpose of this report was to evaluate the effect of Camille Cut closure on circulation and water quality of Mississippi Sound; the combined effect of Camille Cut and Katrina Cut closures on circulation and water quality of Mississippi Sound; reduction of storm wave energy at the mainland Mississippi coast as a result of closing Camille Cut; and optimization of nearshore placement of sand in the littoral zone.

Field data was collected to support numerical modeling efforts and to provide baseline data so that changes resulting from the reconstruction of Ship Island could be quantified during project monitoring. Data collected include waves on both the seaward and sound side of Ship Island, current velocities and flow through the cuts and passes around Ship and Dauphin Islands, and water quality information at strategic locations.

The circulation, water quality, and storm wave energy was evaluated through comparison of results for four alternative conditions including a Base condition (Post-Hurricane Katrina), With-project (Camille Cut closed), Degraded (Ship Island lowered to below mean sea level across the entire island footprint), and a Cumulative condition which includes Camille Cut closed, Katrina Cut closed, and navigation channels deepened to authorized depths.

The relative changes in circulation within Mississippi Sound resulting from proposed Ship Island restoration alternative configurations were estimated through application of a combination of the two dimensional ADCIRC hydrodynamic model and the three dimensional CH3D model. These models were applied to provide hydrodynamic input to the water quality model CE-QUAL-ICM. Nearshore wave modeling was conducted with STWAVE to provide radiation stress gradients for CH3D and to estimate the reduction of storm wave energy at the mainland Mississippi coast as a result of closing Camille Cut.

STWAVE performance was evaluated through comparison to the field data collected during March-July 2010 at two stations near Ship Island, one station in the Gulf of Mexico, and one station in Mississippi Sound. In addition, STWAVE has been validated during Hurricane Gustav in 2008. Overall, the STWAVE model results compared with good agreement to the measurements. The wave model also predicted the attenuation in wave heights across Ship Island rather well, from the exposed waves at the Gulf of Mexico station to the more sheltered waves at the Mississippi Sound station. The average wave height reduction factor predicted by the model is 0.67, whereas the average wave height reduction factor observed in the measured data is 0.64, where the wave height reduction factor is defined as the ratio of wave height at the Gulf of Mexico station to the wave height at the Mississippi Sound station.

A water quality model study of Mississippi Sound was conducted to determine potential impacts from proposed actions in the Ship Island area. The focus of the water quality effort was to understand the existing water quality within the Mississippi Sound and to quantify relative changes in water quality and flushing for the four alternative configurations. CH3D and CE-QUAL-ICM were applied to the study area to simulate hydrodynamics and water quality in the Mississippi Sound. The STWAVE model was applied for the period March-September 1998 so that the resulting radiation stress gradients could be applied within CH3D. The water quality model, CE-QUAL-ICM, was calibrated for the period of April 1, 1998 - September 15, 1998, using observed data provided by the Mississippi Department of Environmental Quality and appropriate kinetic rates determined in calibration. Sediment Oxygen Demand (SOD) is specified as a constant rate in the ocean and river inflows. Final calibration results compared favorably to observed data given the limited amount of comparison and boundary data available to evaluate and drive the model, respectively.

Changes in dissolved oxygen, salinity, and chlorophyll were an indicator of changes to water quality. Comparison of Pre- and Post-Katrina results to the other alternative results showed changes in water quality for all alternatives to some degree. Although water quality changes were noted, all were within the State standard for constituents of interest for ocean waters. Total net flows show averages are two orders of magnitude less than the peak flood and ebb flows across locations analyzed in the area of Ship Island. This is an indication of two things. First, Mississippi Sound in the vicinity of Ship Island has relatively little flushing and net transport

through the system. Second, the effects of Ship Island degradation or restoration do not have major effects upon system-wide circulation and, therefore, should not have major effects on system-wide water quality conditions. The condition of Ship Island does have localized effects on circulation. Two sets of tracer simulations were performed to assess the impact of different alternatives on circulation and flushing immediately behind Ship Island. Tracer concentrations were released instantaneously and allowed to disperse. Circulation is adequate to quickly displace material and move it around but does not always completely remove it from the vicinity of Ship Island.

Overall, comparison of results from all alternative runs showed changes in circulation, but this caused only minor changes to water quality concentrations in the area of proposed restoration. It is concluded from these results that none of the alternatives simulated would likely have system-wide detrimental water quality impacts. Water quality benefits of a restored Ship Island are possible in two ways. First, water quality behind the island would be similar to Pre-Katrina conditions. This may be more desirable from a sheltered habitat standpoint than open water of a degraded island. Second, there is greater potential for submerged aquatic vegetation colonization and growth in the protected waters north of Ship Island in a restored condition.

The reduction of storm wave energy at the mainland Mississippi coast as a result of closing Camille Cut and restoring Ship Island to a Pre-Hurricane Camille condition was also evaluated. Similarly, the increase in storm wave energy at the mainland Mississippi coast as a result of Ship Island degradation was evaluated. The relative changes resulting from the barrier island restoration and degradation are quantified through the application of an integrated coastal storm modeling system. Results indicate that closure of Camille Cut and Ship Island restorations does have the potential to reduce storm waves at the mainland coast. Maximum wave height reduction at the mainland Mississippi coast ranges from 0.2 m to 1.25 m relative to the existing Post-Katrina condition. The magnitude of wave height reduction was found to be controlled by the storm characteristics, primarily minimum central pressure (maximum wind speed), radius to maximum winds, forward speed, and trajectory. Barrier island restoration reduced waves by as much as 0.2 m to 0.4 m for 4 of the 15 synthetic storms simulated, 0.4 m to 0.6 m for 5 of the 15 synthetic storms simulated, and by greater than 0.6 m for 6 of the 15 synthetic storms

simulated. The greatest decrease in wave heights observed at the mainland Mississippi coast for the storm suite simulated was 1.25 m.

The maximum wave height increase at the mainland Mississippi coast as a result of East and West Ship Island degradation ranges from 0.2 m to 0.4 m, with the majority (13 of 15) of the synthetic storms experiencing a maximum wave height increase of 0.2 m. The largest areas of wave height increase are in the leeward areas behind East and West Ship Island, which were degraded to subaqueous shoals. Maximum wave change potential at the mainland Mississippi coast is smaller for the degraded scenario than for the restored scenario because wave energy can penetrate from the Gulf of Mexico into Mississippi Sound for both the existing Post-Katrina and degraded scenarios.

The effects of the offshore borrow areas on storm waves were quantified through the cross-shore progression of significant wave heights along three parallel transects in the vicinity of the borrow areas. The borrow areas produce a local reduction in wave energy, i.e., a divergence of wave rays, for the restored (dredged) scenario when compared to the existing Post-Katrina scenario. For all of the synthetic storms simulated, de-focusing of wave energy and de-shoaling effects are observed along the transect that bisects the borrow area such that the restored (dredged) scenario results in lower significant wave heights across this transect. Because wave energy flux is conserved and the borrow areas produce a local divergence of wave rays for the restored (dredged) scenario, an increase in wave energy (i.e., a convergence of wave rays) is observed at the fringes of the borrow areas when compared to the existing Post-Katrina scenario. For all of the synthetic storms simulated, focusing of wave energy and refraction effects are observed along the fringes of the borrow areas such that the restored (dredged) scenario results in larger significant wave heights across these transects.

The borrow areas evaluated in the storm wave sensitivity represented a preliminary borrow area plan offshore of Ship Island. Additional borrow area configurations were evaluated, and further analyses were conducted to support final borrow area configuration selection. Proposed borrow areas were identified not only off the coast of Ship Island but also offshore of Dauphin and Horn Islands. Potential impacts of excavation of nearshore borrow areas for the proposed restoration projects were assessed with the spectral nearshore wave transformation model STWAVE and shoreline

change model GENESIS. STWAVE simulations were performed for both existing and restored (dredged) condition to obtain estimates of nearshore wave conditions landward of the borrow areas and to enable a comparative analysis aimed at quantifying potential borrow area impacts on shoreline processes along nearby island shorelines.

For Ship Island, potential effects of the proposed borrow areas SI1, SI2, SI3, SI4, and SI5 on nearshore wave conditions were quantified by examination of the change in nearshore wave height and direction landward of each potential borrow area alternative. STWAVE results show an increase in wave heights in the area of the Camille Cut closure due to refraction caused by the borrow areas focusing wave energy. The wave height increase was within 10 percent for the short period waves. However, for longer period waves, the focusing caused increased wave heights of over 10 percent for SI2, SI3, and SI4 compared to 20 percent for SI1. SI5 minimized the wave height increase to approximately 2 percent. The STWAVE results were applied as input conditions to GENESIS to quantify the influence of the borrow areas on shoreline processes. Longshore sand transport rates were calibrated with typical values for K1 and K2 of 0.4 and 0.2, respectively, and to produce transport rates consistent with sediment budget estimates (Byrnes et al. 2011). The borrow areas were shown to increase erosion over much of the Camille Cut closure area. The magnitude of the increased erosion over the 20-year period of analysis reaches 68 m for SI1, 48 m around the Camille Cut for SI2 and SI3, 28 m for SI4, and 5.0 m for SI5. The western portion of West Ship Island is expected to prograde compared to the existing condition for SI1-SI4 with a maximum increase of 27 m with SI1, 21 m with SI2, 24 m with SI3, and 14 m with SI3. SI5 causes increased erosion of approximately 2.0 m.

The impacts of excavating a borrow area offshore of Horn Island were also quantified by examination of the change in nearshore wave height and direction landward of the borrow area. The STWAVE results show minimal increases in wave heights surrounding the borrow area with little effect on the GENESIS save stations. The STWAVE results were applied as input conditions to GENESIS to quantify the influence of the borrow area on shoreline processes. A sensitivity analysis was conducted, comparing results for both the existing and dredged conditions. Longshore sand transport rates were calibrated with typical values for K1 and K2 of 0.10 and 0.05, respectively, and produced transport rates consistent with sediment budget estimates. The proposed borrow area was shown to have minimal impact on

shoreline change rates over the entirety of Horn Island. The maximum magnitude of change reduces predicted shoreline advance by approximately 1.5 m for the 20-year period of analysis. The greatest increase in erosion is approximately 1.0 m over 20 years. The western portion of Horn Island is expected to slightly prograde as a result of the project.

The expected refraction-induced shoreline impacts to West Dauphin Island are similar for the borrow site configurations evaluated and generally only change the naturally occurring processes by a relatively small percentage. The dredged-induced impacts to the shoreline change rate are anticipated to be in the range of 2.0-4.0 percent of the existing rate. In addition, the changes will be largely stabilizing. That is, over most of the shoreline, the small dredged-induced changes will decrease both the erosion and the accretion in the areas where they occur. The large shallow shoal between the borrow area and Dauphin Island substantially rectifies the waves and produces wave breaking for most incident wave conditions for both the dredged and existing cases. Thus, this shoal area largely shields Dauphin Island from any bathymetry-change effects at the borrow sites. In addition, the dominant incident wave direction is from the SSE-SE sectors which results in down-wave impacts of the borrow area occurring generally in the region of Petit Bois Inlet rather than along the Dauphin Island shoreline. The conclusion that offshore dredging will have a minimal shoreline impact is in good general agreement with the results of Byrnes et al. (2004) who used a different procedure to analyze the potential from mining offshore sand bodies along the Alabama Gulf Coast.

The Ship Island restoration plan includes direct sand placement in Camille Cut, increasing the island footprint, and additional sand placed into the local littoral zone. A numerical model prediction of morphological response and sand fate can assist in determining volumes and nearshore placement of sand. Beach replenishment is commonly used on long stretches of main-land coast, and these cases are well treated with a class of one-dimensional models. However, these simplified models are not appropriate for the Ship Island case with complex geometry and hydrodynamics. The C2SHORE model was applied to evaluate the performance of several restoration alternatives, including sensitivity to grain size for sediment placement and local offshore borrow sites. The C2SHORE model, with numerically intensive nearshore computations, has a relatively small domain size. The effects of basin-scale hydrodynamics such as storm surge are included in the domain through the appropriate application of boundary conditions.

Implementation of the model coupling with large scale models to C2SHORE was examined by comparing predicted hydrodynamics with the field measurements collected for this study. Because differences in the existing bathymetry and the model domain may be significant, the flow velocity averaged over Camille Cut is used as a basis for comparison. For tidally-driven flow, the model phase results were well-predicted, but the amplitude was somewhat larger than the measured values during both flood and ebb tides. To ascertain the C2SHORE performance for storm morphology change, Hurricane Katrina was modeled and compared with measured data. Unfortunately, pre-Katrina subaqueous data in the nearshore region is sparse. Therefore, a pre-storm model domain was implemented from several available data sets, including a 2008 survey. Due to these limitations in the data, model-to-measurement comparisons were limited to lidar surveys of the emergent island. The modeled evolution in a contour near mean sea level agrees well with observations, with a general loss of land and a significant widening of Camille Cut. Likewise, the comparison of details of morphology change on emergent regions is reasonably well-predicted with the exception of the west end of the island.

Three hypothetical storms were simulated, with approximate return periods of 1.0, 10, and 500 years, to examine the effect of the proposed restoration scenarios on the sediment transport environment. Initially, existing morphology is modeled to establish baseline conditions, which indicate a transport to the north around the ends of the island and a westerly long-shore transport. With restoration and the fill of Camille Cut, loss of a hydraulic pathway between the separated island results in larger flow around the east and west ends of the contiguous island. Results indicate that the Camille Cut restoration fill survives higher-frequency storms (such as the 1.0-yr and 10-yr events), but is breached during the low-frequency 500-yr event modeled herein. Gradients in transport along the island indicate a more erosive condition to the east of Camille Cut and a more stable condition to the west of Camille Cut, and these findings are in agreement with island history. To the west of Ship Island, sand infills the navigation channel, but only for the extreme event modeled (500-yrs), and the volume of infill is similar for existing conditions and the restoration scenarios. To the east of Ship Island, modeled transport values indicate that the subaqueous region off the east end (Little Dog Keys Pass) will accumulate sediment, and this is in agreement with the Mississippi sediment budget.

Several choices exist for restoration sand depending on the material source, and the grain size effect is explored by modeling storm morphology with a fine 0.2 mm, an intermediate 0.26 mm, and relatively coarse 0.3 mm sand. For smaller storms, fine-grain sand transport was 20 percent larger when compared with the 0.3 mm sand. A more dramatic difference is modeled in transport for more intense storms, where the increase in sand transport was approximately 40 percent. Additional model results indicate the effect of a possible sand borrow site located less than 1.5 km from the shoreline of the restored Ship Island. The large borrow feature modeled has the effect of redistributing wave energy along the island coast and generating localized regions of increased or decreased wave action. For the smaller events, the effect of this variation is to significantly suppress the longshore transport. An additional effect of the modeled borrow pits is revealed for the smaller two events, which shows localized regions of increased erosion along the fringes of the modeled borrow pits due to wave focusing.

References

Amante, C., and B. W. Eakins. 2009. ETOPO1 1 Arc-Minute Global Relief Model: Procedures, Data Sources and Analysis. NOAA Technical Memorandum NESDID NGDC-24, 19 pp.

Atkinson, J. H., J. J. Westerink, and J. M. Hervouet. 2004. Similarities between the Quasi-Bubble and the Generalized Wave Continuity Equation Solutions to the Shallow Water Equations. *International Journal for Numerical Methods in Fluids*, 45:689-714.

Brock, J., W. Wright, A. Nayegandhi, M. Patterson, I. Wilson, and L. Travers. 2007. EAARL Topography-Gulf Islands National Seashore-Mississippi. USGS Open File Report 2007-1377.

Bunch, B., C. Cerco, M. Dortch, B. Johnson, and K. Kim. 2000. *Hydrodynamic and water quality model study of San Juan Bay and Estuary*. ERDC TR-00-1. Vicksburg, MS: US Army Engineer Research and Development Center.

Bunch, B. W., M. Channel, W. D. Corson, B. A. Ebersole, L. Lin, D. J. Mark, J. P. McKinney, S. A. Pranger, P. R. Schroeder, S. J. Smith, D. H. Tillman, B. A. Tracy, M. W. Tubman, and T. L. Welp. 2003. *Evaluation of island and nearshore confined disposal facility alternatives, Pascagoula River Harbor Dredged Material Management Plan*. ERDC TR-03-3. Vicksburg, MS: US Army Engineer Research and Development Center.

Bunch, B. W., D. H. Tillman, and D. J. Mark. 2003a. *Sensitivity analysis of winds and bathymetry on the Port of Los Angeles (POLA) main channel*. Letter Report. Vicksburg, MS: US Army Engineer Research and Development Center.

Bunch, B. W., D. H. Tillman, and D. J. Mark. 2003b. *Sensitivity analysis of wind and bathymetry on the Port of Los Angeles Pier 300 expansion and Dominguez Channel studies*. Letter Report. Vicksburg, MS: US Army Engineer Research and Development Center.

Bunch, B. W., W. D. Corson, B. A. Ebersole, D. J. Mark, J. P. McKinney, D. H. Tillman, and M. W. Tubman. 2005. *Evaluation of Gulfport Navigation Channel Alternatives, Gulfport Reevaluation Report (GRR)*. Draft Report. Vicksburg, MS: US Army Engineer Research and Development Center, Waterways Experiment Station.

Bunya, S., J. C. Dietrich, J. J. Westerink, B. A. Ebersole, J. M. Smith, J. H. Atkinson, R. Jensen, D. T. Resio, R. A. Leuttich, C. Dawson, V. J. Cardone, A. T. Cox, M. D. Powell, H. J. Westerink, and H. J. Roberts. 2010. A high-resolution coupled riverine flow, tide, wind, wind wave, and storm surge model for southern Louisiana and Mississippi. Part I – Model development and validation. Monthly Weather Review, 138:345-377.

Buster, N. A., and R. A. Morton. 2011. Historical bathymetry and bathymetric change in the Mississippi-Alabama coastal region, 1847–2009: U.S. Geological Survey Scientific Investigations Map 3154, 13 p. pamphlet.

Byrnes, M. R., R. M. Hammer, T. D. Thibaut, and D. B. Snyder. 2004. Physical and biological effects of sand mining offshore Alabama, USA. *J. Coastal Res.*, 20(1):6–24.

Byrnes, M., J. Rosati, and S. Griffee. 2011. Sediment Budget: Mississippi Sound Barrier Islands. In *Proceedings, Coastal Sediments '11*. American Society of Civil Engineers.

Cardone, V. J., C. V. Greenwood, and J. A. Greenwood. 1992. *Unified program for the specification of hurricane boundary layer winds over surfaces of specified roughness*. Contract Report CERC-92-1. Vicksburg, MS: US Army Corps of Engineers.

Cerco, C., and T. Cole. 1994. *Three-dimensional eutrophication model of Chesapeake Bay*. Technical Report EL-94-4. Vicksburg, MS: US Army Engineer Waterways Experiment Station.

Cerco, C., B. Bunch, M. Cialone, and H. Wang. 1994. *Hydrodynamic and eutrophication model study of Indian River and Rehoboth Bay, Delaware*. Technical Report EL-94-5. Vicksburg, MS: US Army Engineer Waterways Experiment Station.

Cerco, C., and B. Bunch. 1997. *Passaic River tunnel diversion model study, Report 5, water quality modeling*. Technical Report HL-96-2. Vicksburg, MS: US Army Engineer Waterways Experiment Station.

Cerco, C. F., B. W. Bunch, A. M. Teeter, and M. S. Dortch. 2000. *Water quality model of Florida Bay*. ERDC/EL TR-00-10. Vicksburg, MS: US Army Engineer Research and Development Center.

Cerco, C., and M. Noel. 2004. The 2002 Chesapeake Bay eutrophication model. EPA 903-R-04-004. Annapolis, MD: Chesapeake Bay Program Office, US Environmental Protection Agency.

Chapman, R. S., B. H. Johnson, and S. R. Vemulakonda. 1996. *Users guide for the sigma stretched version of CH3D-WES; A three-dimensional numerical hydrodynamic, salinity and temperature model*. Technical Report HL-96-21. Vicksburg, MS: US Army EngineerWaterways Experiment Station.

Chapman, R. S., P. V. Luong, and M. W. Tubman. 2006. Mississippi sound hydrodynamic and salinity sensitivity modeling. Final Report prepared for US Army District, Mobile, Mobile, AL.

Cox, A. T., and V. J. Cardone. 2007. Workstation assisted specification of tropical cyclone parameters from archived or real time meteorological measurements. 10th International Workshop on Wave Hindcasting and Forecasting and Coastal Hazard Symposium, North Shore, Hawaii, November 11-16, 2007.

Dawson, C., J. J. Westerink, J. C. Feyen, and D. Pothina. 2006. Continuous, discontinuous and coupled discontinuous-continuous galerkin finite element methods for the shallow water equations. *International Journal for Numerical Methods in Fluids* 52:63-88.

Dietrich, J. C., S. Bunya, J. J. Westerink, B. A. Ebersole, J. M. Smith, J. H. Atkinson, R. Jensen, D. T. Resio, R. A. Leuttich, C. Dawson, V. J. Cardone, A. T. Cox, M. D. Powell, H. J. Westerink, and H. J. Roberts. 2010. A high resolution coupled riverine flow, tide, wind, wind wave and storm surge model for southern Louisiana and Mississippi. Part II - Synoptic Description and Analyses of Hurricanes Katrina and Rita. Monthly Weather Review 138:378-404.

Dortch, M. S., M. Zakikhani, M. Noel, and S. C. Kim. 2007. *Application of a water quality model to Mississippi sound to evaluate impacts of freshwater diversions*. ERDC/EL TR-07-20. Vicksburg, MS: US Army Engineer Research and Development Center.

Ebersole, B. A., J. J. Westerink, S. Bunya, J. C. Dietrich, and M. A. Cialone. 2010. Development of storm surge which led to flooding in St. Bernard Polder during Hurricane Katrina. *Ocean Engineering* 37:91-103.

Eiker, E. E. 1977. Heat exchange programs, Thermal simulation of lakes, User's manual. Baltimore, MD: US Army Engineer District, Baltimore.

Fritz, H. M., C. Blount, R. Sokoloski, J. Singleton, A. Fuggle, B. G. McAdoo, A. Moore, C. Grass, and B. Tate. 2007. Hurricane Katrina storm surge distribution and field observations on the Mississippi barrier islands, Estuarine, Coastal, and Shelf. *Science* 74:12-20.

Grzegorzewski, A. S., M. A. Cialone, and T. V. Wamsley. 2011. Interaction of barrier islands and storms: implications for flood risk reduction in Louisiana and Mississippi. *Journal of Coastal Research*.

Hanson, H., and N. C. Kraus. 1989. *GENESIS: Generalized model for simulating shoreline change, Report 1, Technical reference*. Technical Report CERC-89-19. Vicksburg, MS: US Army Engineer Waterways Experiment Station, Coastal Engineering Research Center.

Interagency Performance Evaluation Task Force (IPET). 2008. Performance evaluation of the New Orleans and southeast Louisiana hurricane protection system, Final Report of the Interagency Performance Evaluation Task Force, Volume IV, The Storm.' USACE, Washington, DC http://ipet.wes.army.mil.

Johnson, B., R. Heath, B. Hsieh, K. Kim, and L. Butler. 1991. *Development and verification of a three-dimensional numerical hydrodynamic, salinity, and temperature model of Chesapeake Bay*. HL-91-7. Vicksburg, MS: US Army Engineer Waterways Experiment Station.

Johnson, B. D., N. Kobayashi, and M. B. Gravens. 2012. *Cross-shore numerical model CSHORE for waves, currents, sediment transport and beach profile evolution*. ERDC/CHL TR-12-22. Vicksburg, MS: US Army Engineer and Research Development Center.

Kobayashi, N., and B. D. Johnson. 2001. Sand suspension, storage, advection and settling in surf and swash zones. *Journal of Geophysical Research* 106(C5): 9363-9376.

Kobayashi, N., H. Zhao, and Y. Tega. 2005. Suspended sand transport in surf zones. *J. Geophys. Res.*, 110, C12009, doi:10.1029/2004JC002853.

Kobayashi, N., A. Payo, and L. Schmied. 2008. Cross-Shore Suspended Sand and Bedload Transport on Beaches. *Journal of Geophysical Research* 113,C07001, doi:10.1029/2007JC004203.

Kobayashi, N., A. Payo, and B. D. Johnson. 2009. Suspended sand and bedload transport on beaches. Handbook of Coastal and Ocean Engineering. *World Scientific.* (28):807-823.

Kolar, R. L., J. J. Westerink, M. F. Cantekin, and C. A. Blain. 1994. Aspects of nonlinear simulations using shallow water models based on the wave continuity equation. *Computers and Fluids* 23(3):523-538.

Komen, G. J., L. Cavaleri, M. Donelan, K. Hasselmann, S. Hasselmann, and P. A. E. M. Janssen. 1994. Dynamics and modelling of ocean waves. Cambridge, UK: Cambridge University Press.

Leonard, B. 1979. A stable and accurate convection modelling procedure based on quadratic upstream interpolation. *Computer Methods in Applied Mechanics and Engineering* 19:59-98

Lick, W., J. Gailani, C. Jones, E. Hayter, L. Burkhard, and J. McNeil, 2005. The 28 transport of sediments and contaminants in surface waters. short course 29 Notes, University of California, Santa Barbara.

Lillycrop, L. S., and L. Parson. 2000. The Mobile District regional sediment management demonstration program. In *Proceedings, Florida Shore and Beach Preservation Association Annual Meeting*. Captive Island, FL, 13-15 September.

Luettich, R. A., Jr., J. J. Westerink, and N. W. Scheffner. 1992. *ADCIRC: An advanced three-dimensional circulation model for shelves, coasts, and estuaries*. Technical Report DRP-92-6. Vicksburg, MS: US Army Engineer Waterways Experiment Station.

Luettich, R. A., and J. J. Westerink. 2004. Formulation and numerical implementation of the 2D/3D ADCIRC finite element model version 44.XX; http://adcirc.org/adcirc_theory_2004_12_08.pdf

Martin, K., D. H. Tillman, W. C. Seabergh, R. McAdory, B. W. Bunch, M. J. Briggs, H. Acuff, and F. C. Carson. 2008. *Port of Los Angeles: Inner Cabrillo Beach, water quality improvement project*. ERDC/CHL TR-08-3. Vicksburg, MS: US Army Engineer Research and Development Center.

Morton, R. A. 2010. First-order controls of extreme-storm impacts on the Mississippi-Alabama barrier-island chain. *Journal of Coastal Research* 26:635-648.

Mukai, A. Y., J. J. Westerink, R. A. Luettich, and D. Mark. 2002. Eastcoast 2001, *A tidal constituent database for Western North Atlantic, Gulf of Mexico, and Carribean Sea*. ERDC/CHL TR-02-24. Vicksburg, MS: US Army Corps of Engineers Engineer Research and Development Center.

National Oceanic and Atmospheric Administration (NOAA). 2008. National Geophysical Data Center, NGDC Coastal Relief Model, Retrieved 01 December 2008, http://www.ngdc.noaa.gov/mgg/coastal/coastal.html

Otvos, E., and G. Carter. 2008. Beach aggradation following hurricane landfall: Impact comparisons from two contrasting hurricanes, northern Gulf of Mexico. *Journal of Coastal Research* 24(2):463-478.

Resio, D. T. 2007. White paper on estimating hurricane inundation probabilities. Vicksburg, MS: US Army Corps of Engineers, Engineer Research and Development Center.

Ribberink, J. S. 1998. Bed-load transport for steady flows and unsteady oscillatory flows. *Journal of Coastal Engineering* 34(1-2)59-82, 1998. DOI: 10.1016/S0378-3839(98)00013-1.

Ris, R. C., L. J. Holthuijsen, and N. J. Booij. 1999. A third generation wave model for coastal regions 2. Verification. *Geophys. Res.* 104(C4)7667–7681.

Romeiser, R. 1993. Global validation of the wave model WAM over a 1-year period using Geosat wave height data. *J. Geophys. Res.* 98:4713–4726.

Schmid, K., and B. Yassin, 2004. Mississippi coastal data node and value added GIS data products [abs]: Mississippi Academy of Sciences, v. 49, 1, p. 59.

Smith, J. M., D. T. Resio, and A. K. Zundel. 1999. *STWAVE: Steady-State spectral wave model; Report 1: User's manual for STWAVE version 2.0*. Instructional Report CHL-99-1. Vicksburg, MS: US Army Engineer Research and Development Center.

Smith, J. M., A. R. Sherlock, and D. T. Resio. 2001. *STWAVE: Steady-state spectral wave model user's manual for STWAVE, Version 3.0*. ERDC/CHL SR-01-1. Vicksburg, MS: US Army Engineer Research and Development Center.

Smith, J. M. 2001. *Modeling nearshore transformation with STWAVE*. Coastal and Hydraulics Engineering Technical Note CHETN I-64. Vicksburg, MS: US Army Engineer Research and Development Center.

Smith, J. M. 2007. *Full-Plane STWAVE II: Model Overview*. ERDC CHETN-I-75. Vicksburg, MS: US Army Engineer Research and Development Center.

Smith, J. M., R. E. Jensen, A. B. Kennedy, C. J. Dietrich, and J. J. Westerink. 2010. Waves in Wetlands: Hurricane Gustav. In *Proceedings from the 32nd International Conference on Coastal Engineering*. Shanghai, China, June 30-July 5, 2010.

Sullivan, C. L. 2009. Hurricanes of the Mississippi Gulf Coast: Three centuries of destruction. Perkinston, MS: Mississippi Gulf Coast Community College Press.

Tanaka, S., S. Bunya, J. J. Westerink, C. Dawson, R. A. Luettich. 2010. Scalability of an unstructured grid continuous galerkin based hurricane storm surge model. *Journal of Scientific Computing*.

Thompson, E. F., and V. J. Cardone. 1996. Practical modeling of hurricane surface wind fields. *J. Waterway, Port, Coastal Engr.* 122(4):195-205.

Tillman, D., C. Cerco, M. Noel, J. Martin, and J. Hamrick. 2004. *Three-dimensional eutrophication model of the lower St. Johns River, Florida*. ERDC TR-04-13. Vicksburg, MS: US Army Engineer Research and Development Center.

Tillman, D. H. , R. McAdory, B. W. Bunch, S. K. Martin, M. J. Briggs, F. C. Carson, G. Savant, and N. K. Raphelt. 2008. *Circulation and water quality modeling in support of deepening the port of Los Angeles: Alternative disposal sites*. ERDC/CHL TR-08-6. Vicksburg, MS: US Army Engineer Research and Development Center.

US Army Corps of Engineers (USACE). 2009. Mississippi coastal improvements program, Hancock, Harrison, and Jackson Counties, Mississippi, comprehensive plan and integrated programmatic environmental impact statement. Mobile, AL: US Army Engineer District; Mobile.

WAMDI Group. 1988. The WAM Model – A third generation ocean wave prediction model. *Journal of Physical Oceanography* 18:1775-1810.

Wamsley, T. V., M. A. Cialone, J. M. Smith, B. A. Ebersole, and A. S. Grzegorzewski. 2009. Influence of landscape restoration and degradation on storm surge and waves in southern Louisiana. *Journal of Natural Hazards*, doi:10.1007/s11069-009-9378-z.

Westerink, J. J., C. A. Blain, R. A. Luettich, and N. W. Scheffner. 1994. *ADCIRC: an advanced three-dimensional circulation model for shelves, coasts, and estuaries*. Technical Report DRP-92-6. Vicksburg, MS: US Army Engineer Research and Development Center.

Westerink, J. J., R. A. Luettich, J. C. Feyen, J. H. Atkinson, C. Dawson, H. J. Roberts, M. D. Powell, J. P. Dunion, E. J. Kubatko, and H. Pourtaheri. 2008. A basin-to-channel-scale unstructured grid hurricane storm surge model applied to southern Louisiana. *Monthly Weather Review* 136:833-864.

Zambreski, L. 1989. A verification study of the global WAM model, December 1987–November 1988, Tech. Rep. 63, Eur. Cent. for Medium-Range Weather Forecasts, Reading, England.

Zambreski, L. 1991. An evaluation of two WAM hindcasts for LEWEX, in Directional Ocean Wave Spectra, edited by R. C. Beal, pp. 167–172. Baltimore, MD: Johns Hopkins Univ. Press.

Appendix A: Wave Measurements Results

Figure A-1. Wave direction (direction waves are coming from at the spectral peak), H_{mo}, and wave period (at the spectral peak), for the gauge in the Mississippi Sound (top) and for the gauge in the Gulf of Mexico (bottom) from March 4 through 11, 2010.

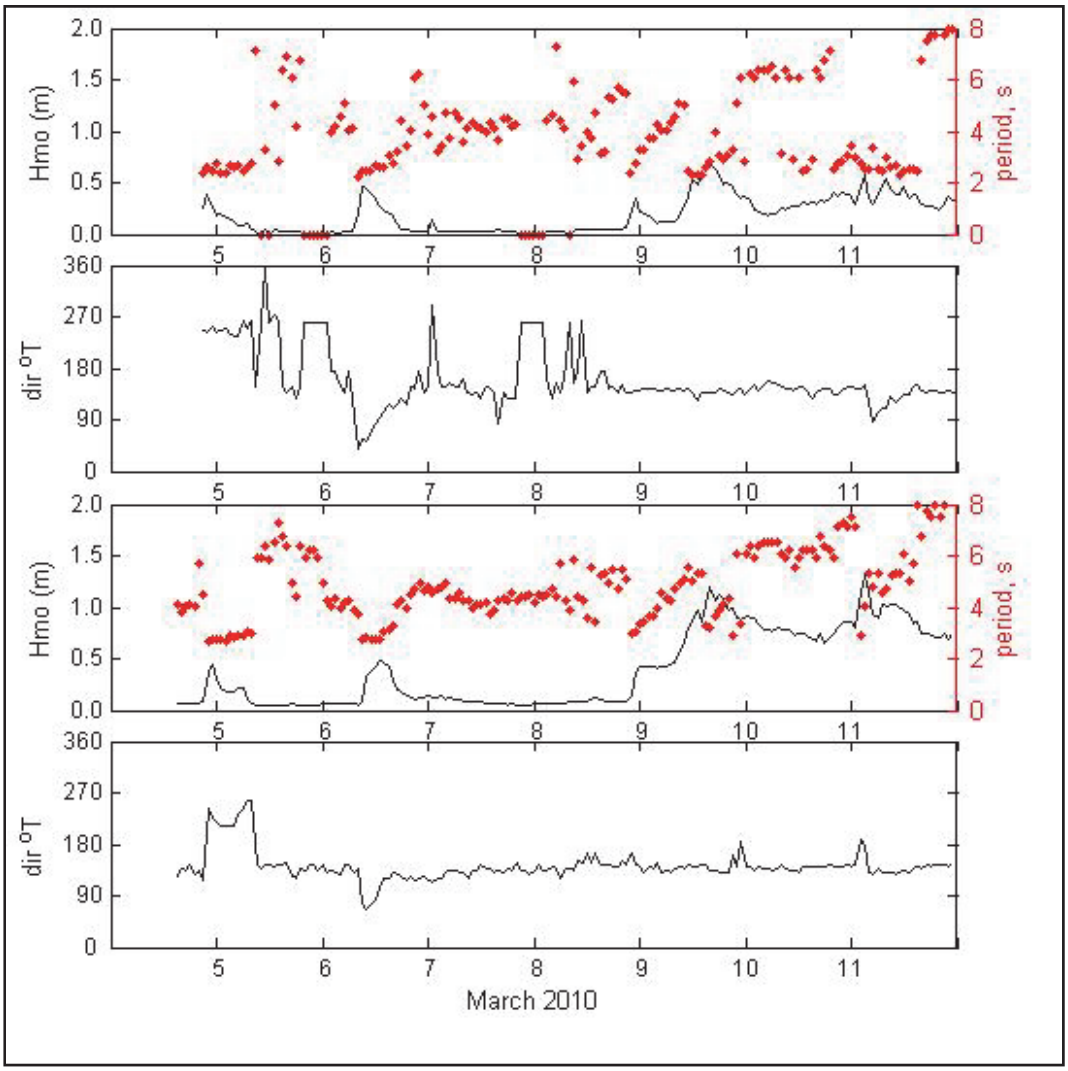

Figure A-2. Wave direction (direction waves are coming from at the spectral peak), H_{mo}, and wave period (at the spectral peak), for the gauge in the Mississippi Sound (top) and for the gauge in the Gulf of Mexico (bottom) from March 12 through 19, 2010.

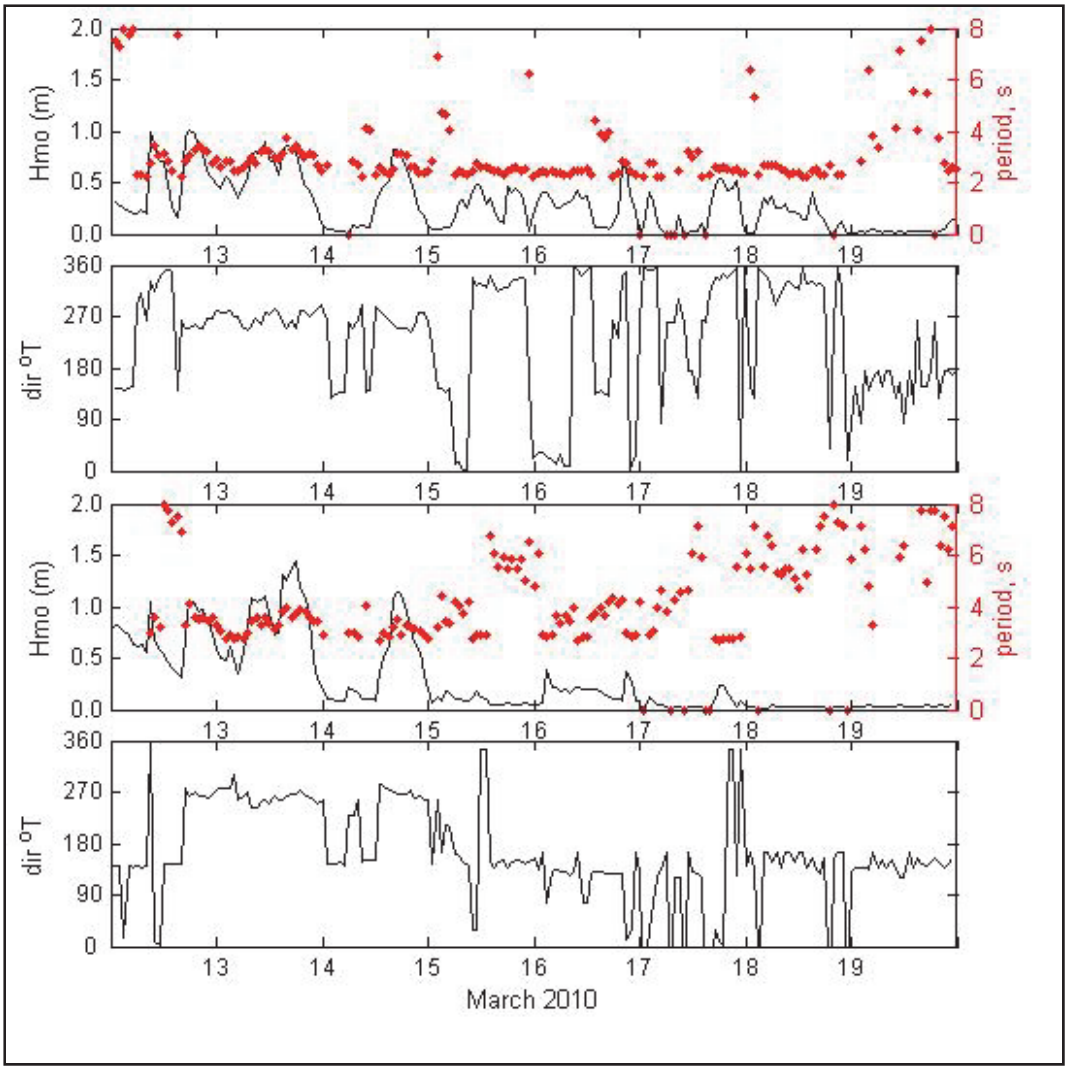

Figure A-3. Wave direction (direction waves are coming from at the spectral peak), H_{mo}, and wave period (at the spectral peak), for the gauge in the Mississippi Sound (top) and for the gauge in the Gulf of Mexico (bottom) from March 20 through 27, 2010.

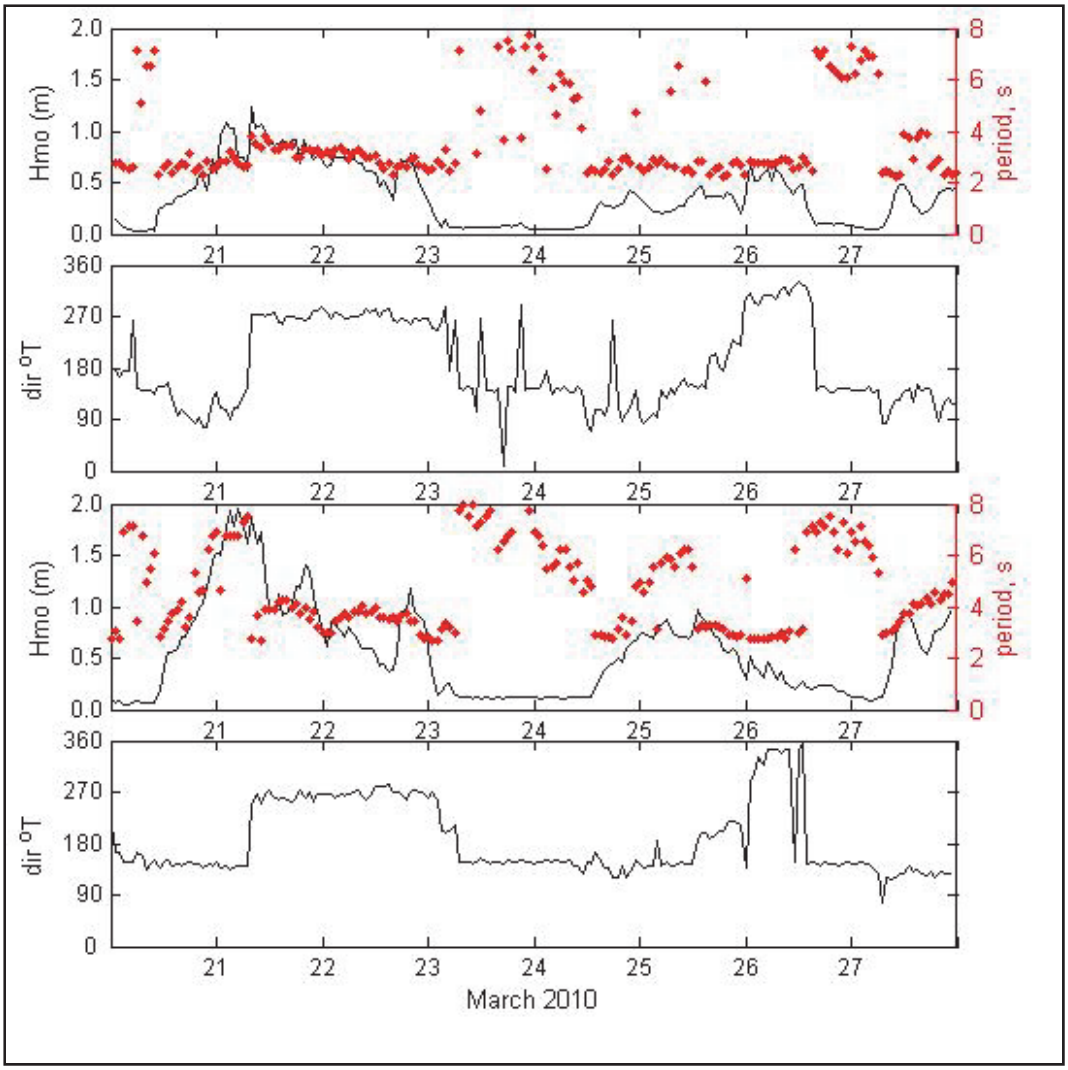

Figure A-4. Wave direction (direction waves are coming from at the spectral peak), H_{mo}, and wave period (at the spectral peak), for the gauge in the Mississippi Sound (top) and for the gauge in the Gulf of Mexico (bottom) from March 28 through April 4, 2010.

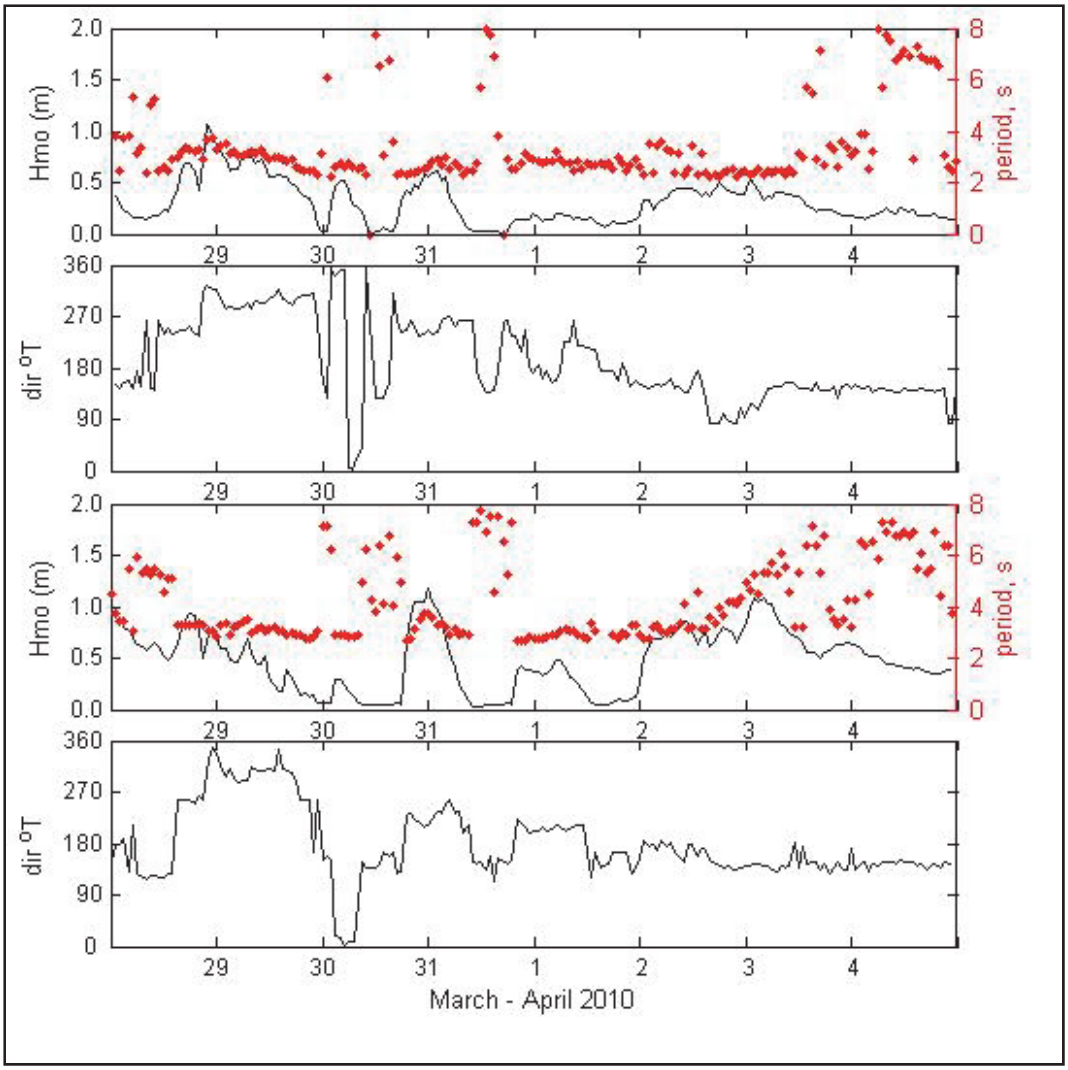

Figure A-5. Wave direction (direction waves are coming from at the spectral peak), H_{mo}, and wave period (at the spectral peak), for the gauge in the Mississippi Sound (top) and for the gauge in the Gulf of Mexico (bottom) from April 5 through 12, 2010.

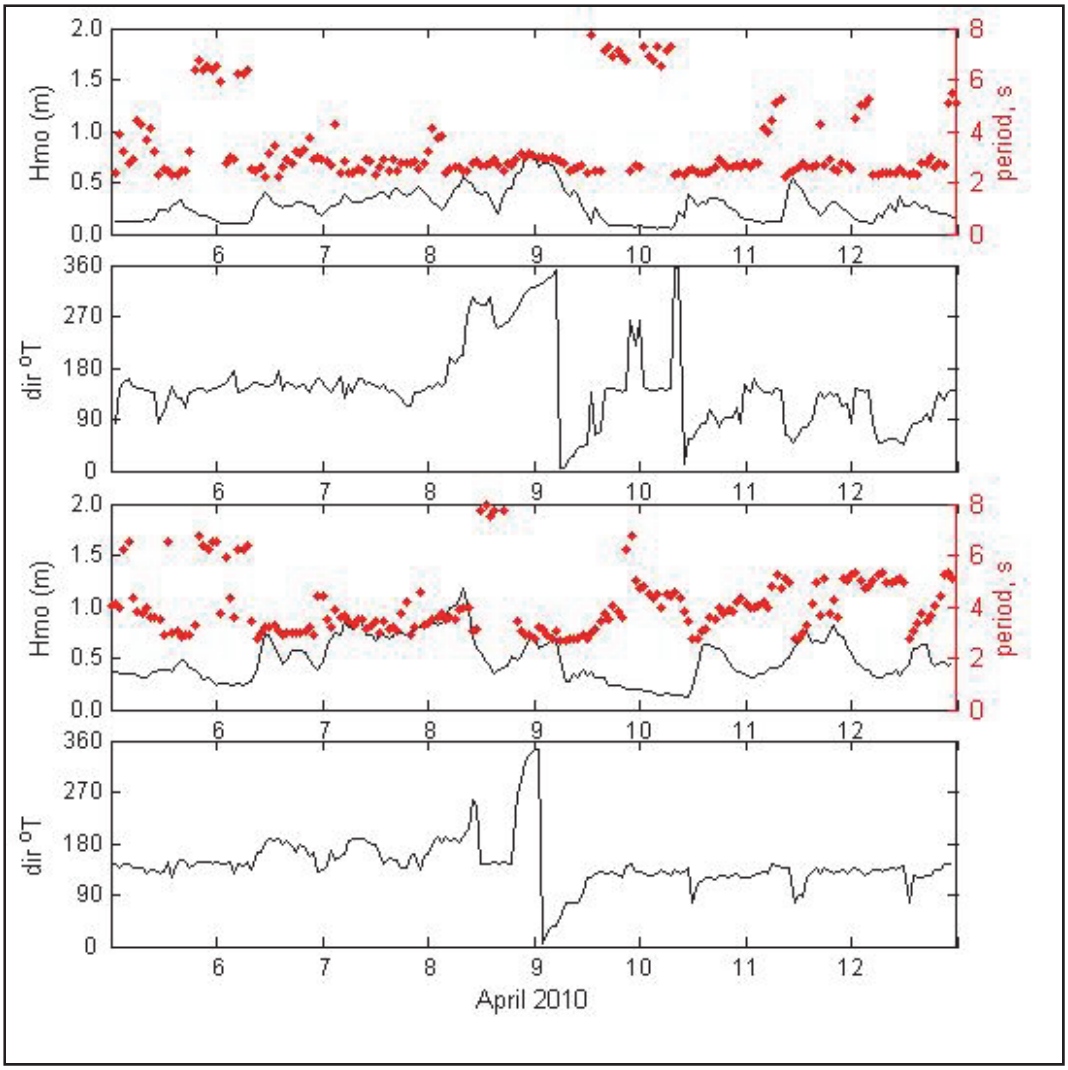

Figure A-6. Wave direction (direction waves are coming from at the spectral peak), H_{mo}, and wave period (at the spectral peak), for the gauge in the Mississippi Sound (top) and for the gauge in the Gulf of Mexico (bottom) from April 13 through 20, 2010.

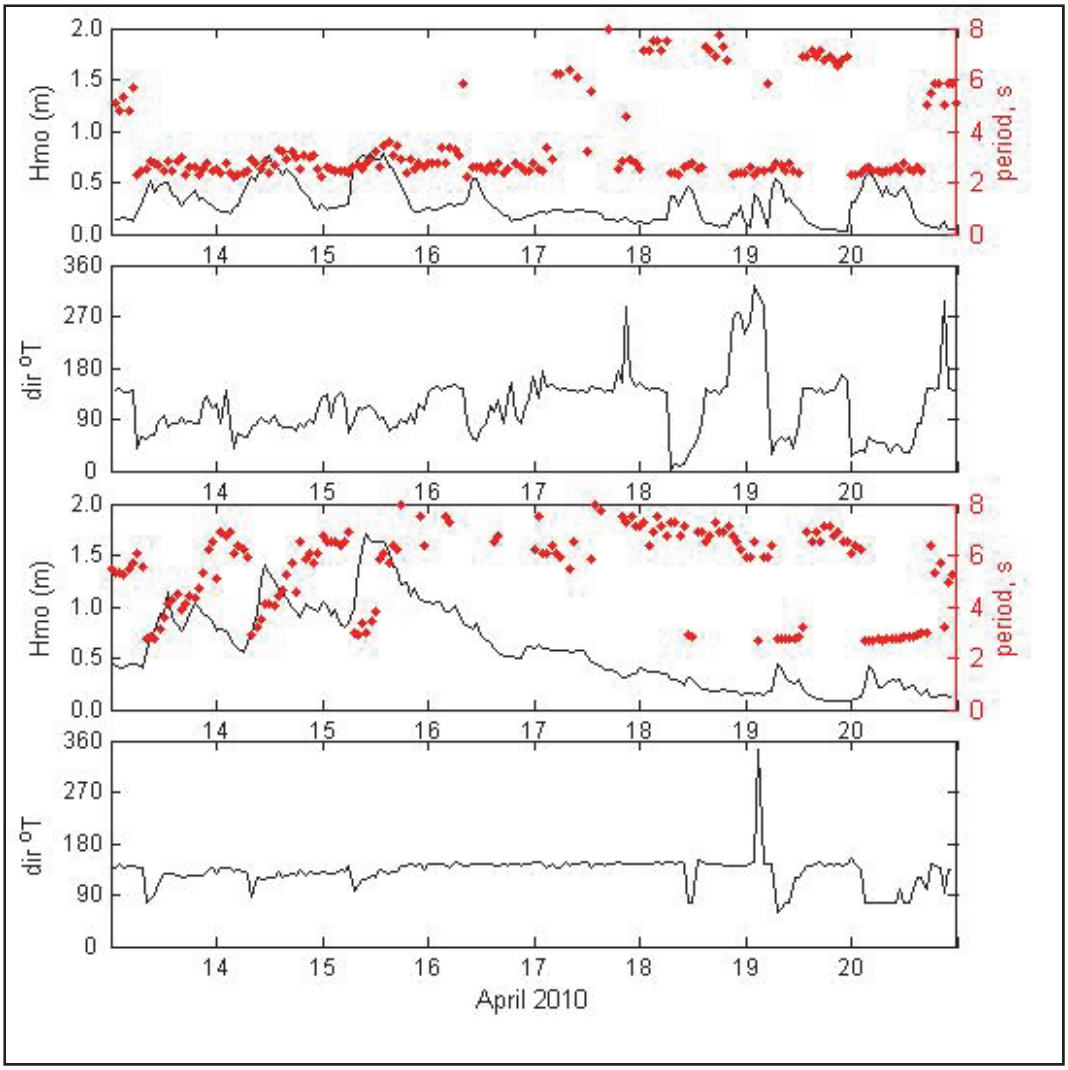

Figure A-7. Wave direction (direction waves are coming from at the spectral peak), H_{mo}, and wave period (at the spectral peak), for the gauge in the Mississippi Sound (top) and for the gauge in the Gulf of Mexico (bottom) from April 21 through 28, 2010.

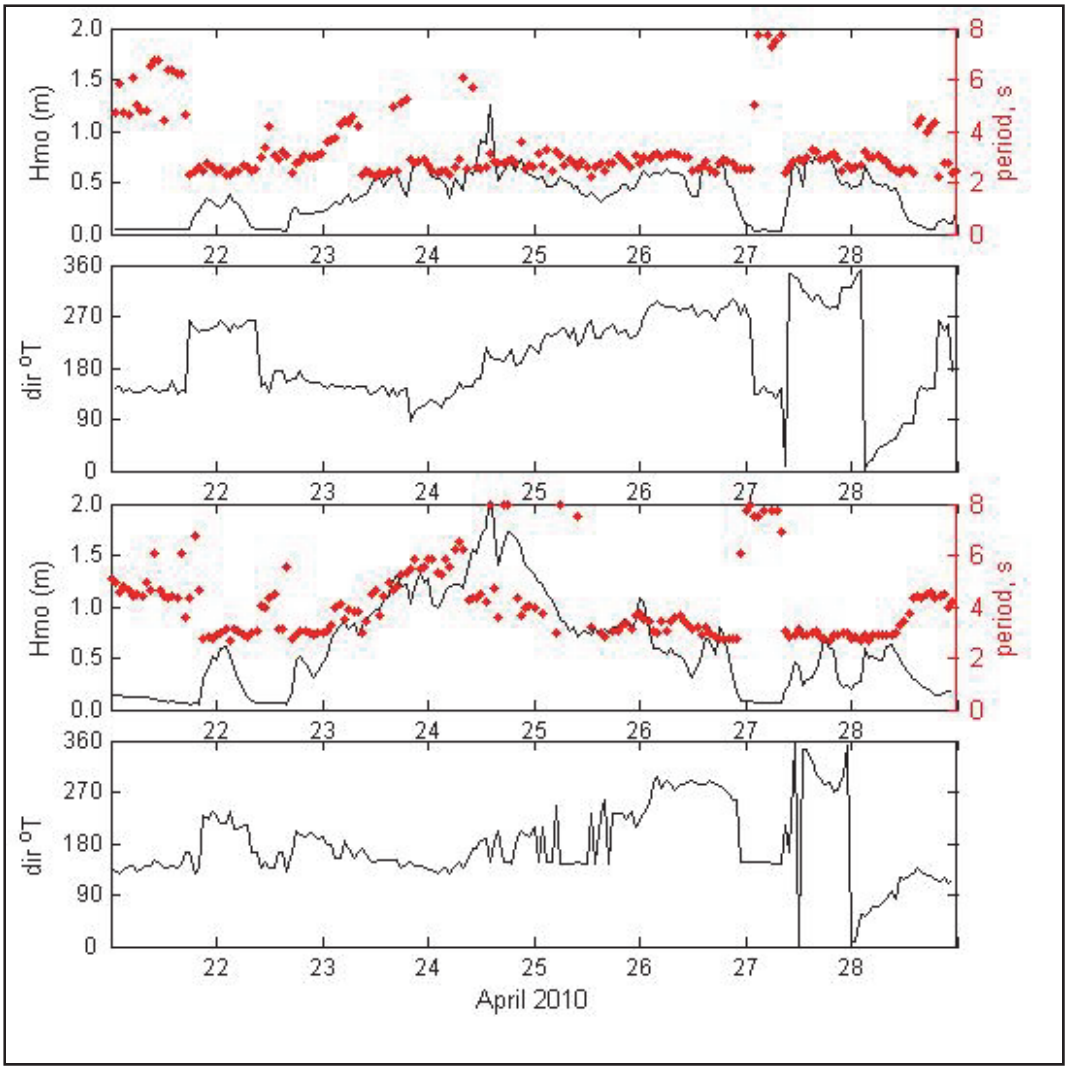

Figure A-8. Wave direction (direction waves are coming from at the spectral peak), H_{mo}, and wave period (at the spectral peak), for the gauge in the Mississippi Sound (top)) from April 29 through May 6, 2010, and for the gauge in the Gulf of Mexico (bottom) from April 29 until it stopped recording valid data on April 30, 2010.

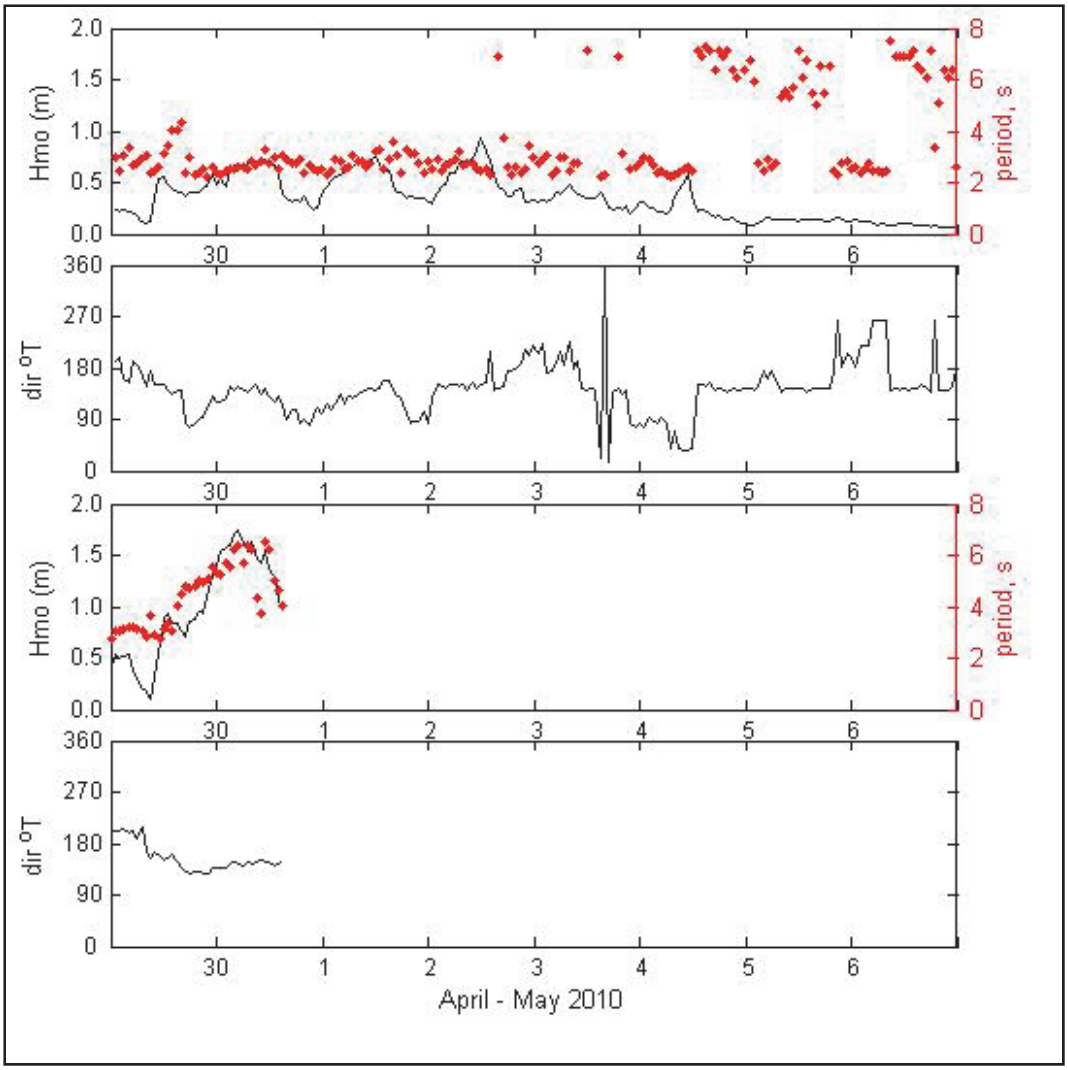

Figure A-9. Wave direction (direction waves are coming from at the spectral peak), H_{mo}, and wave period (at the spectral peak), for the gauge in the Mississippi Sound from May 7 through 22, 2010.

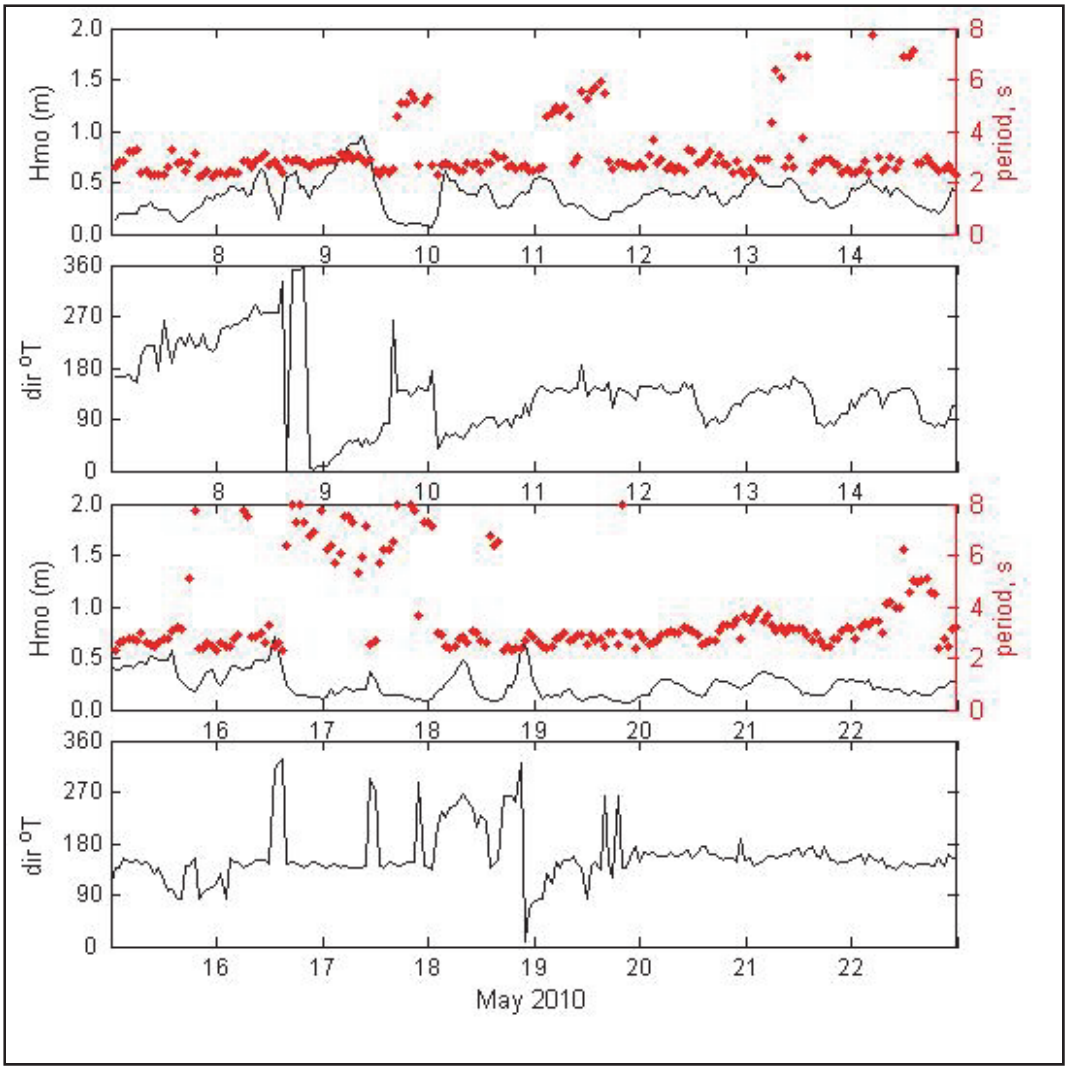

Figure A-10. Wave direction (direction waves are coming from at the spectral peak), H_{mo}, and wave period (at the spectral peak), for the gauge in the Mississippi Sound from May 23 through June 7, 2010.

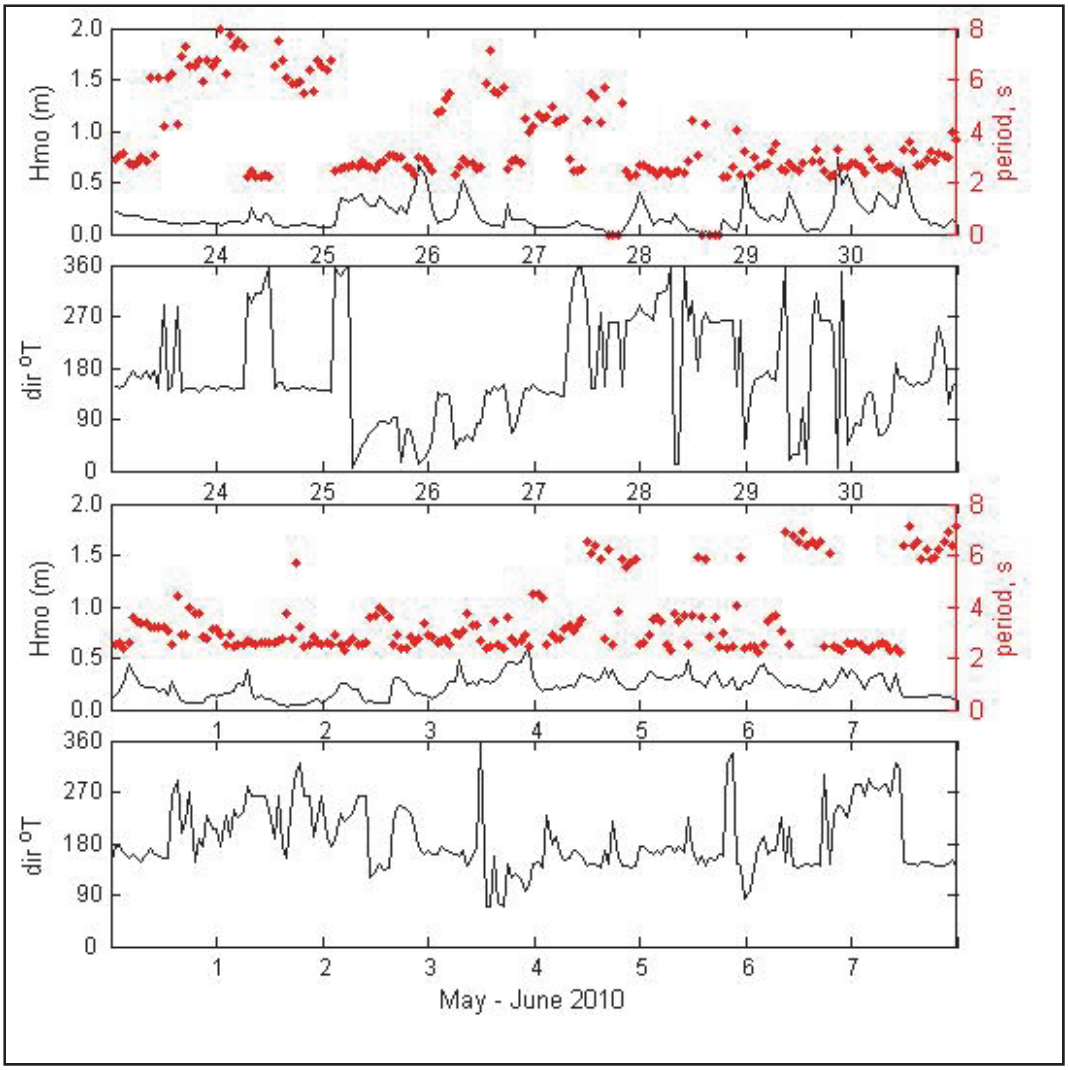

Figure A-11. Wave direction (direction waves are coming from at the spectral peak), H_{mo}, and wave period (at the spectral peak), for the gauge in the Mississippi Sound from June 8 through 23, 2010.

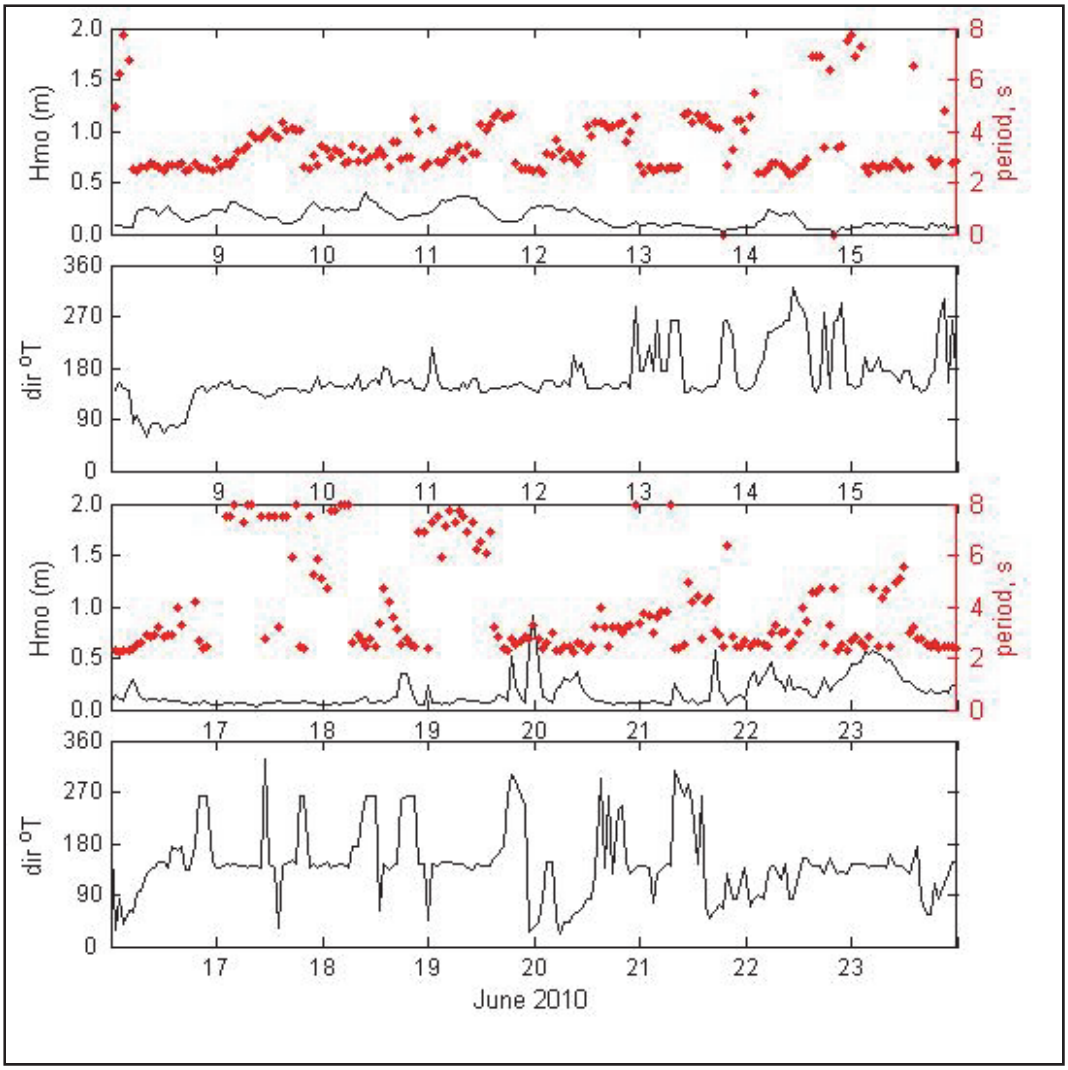

Figure A-12. Wave direction (direction waves are coming from at the spectral peak), H_{mo}, and wave period (at the spectral peak), for the gauge in the Mississippi Sound from June 24 through July 9, 2010.

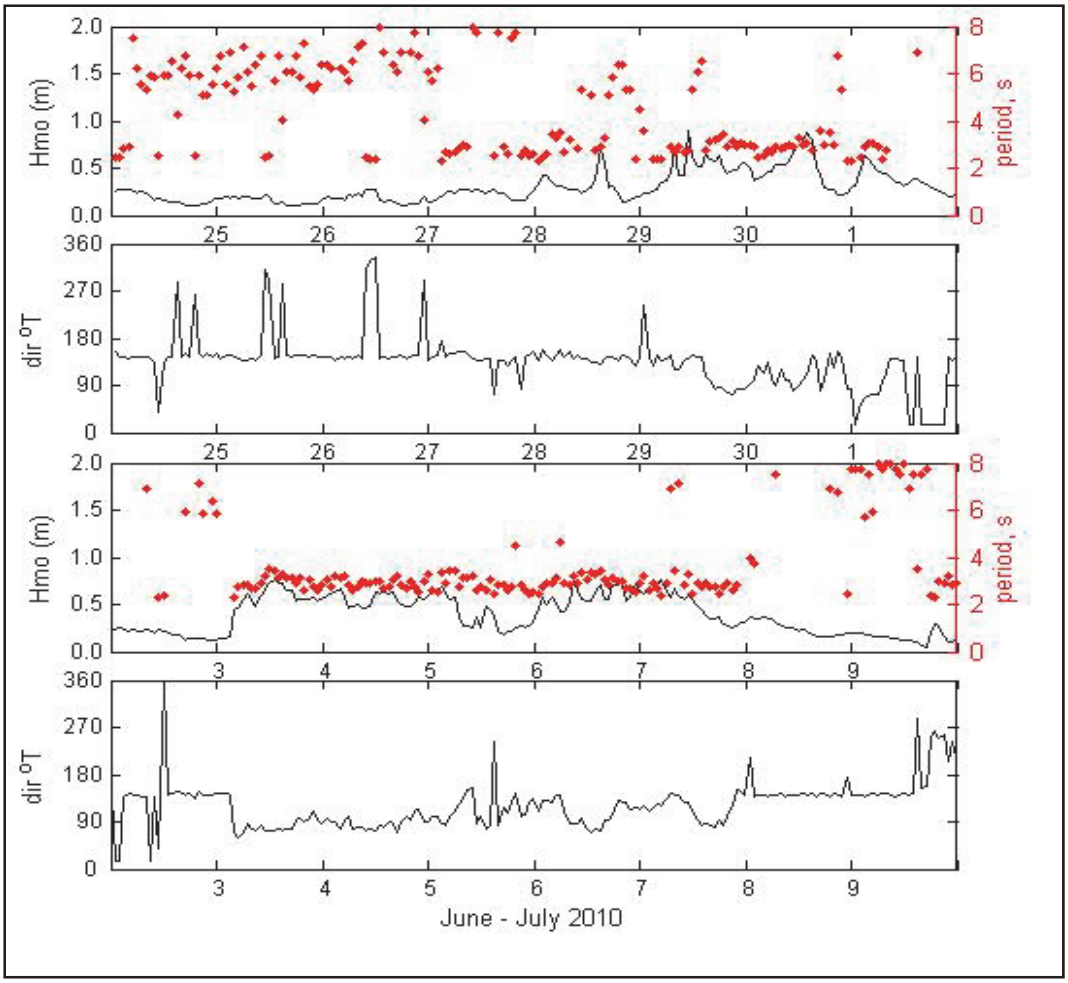

Figure A-13. Wave direction (direction waves are coming from at the spectral peak), H_{mo}, and wave period (at the spectral peak), for the gauge in the Mississippi Sound from July 10 until it was recovered on July 15, 2010.

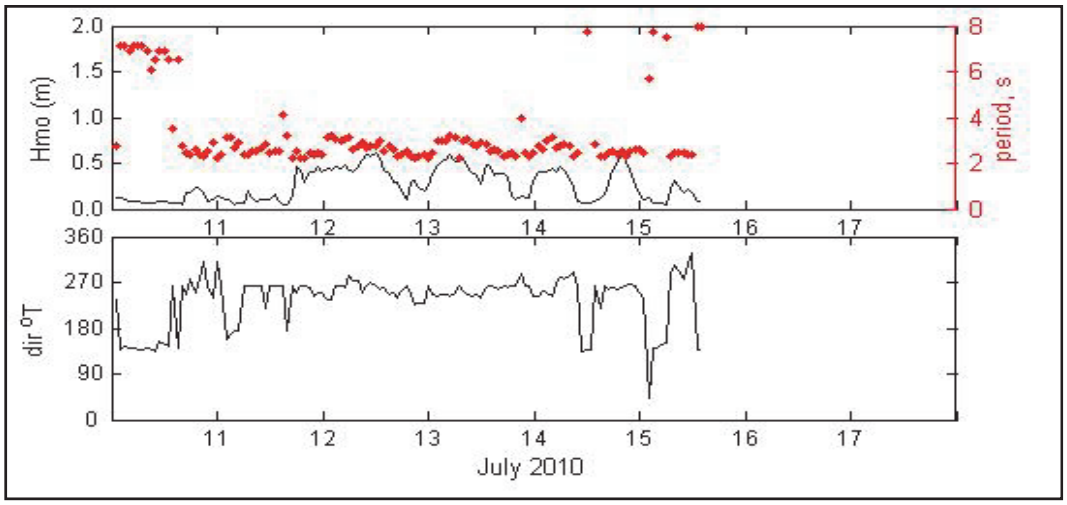

Appendix B: Water Level Measurements

Figure B-1. Mean water levels at the Sound wave gauge (black line) and at the Gulf gauge (red line) for March 4 through April 4, 2010.

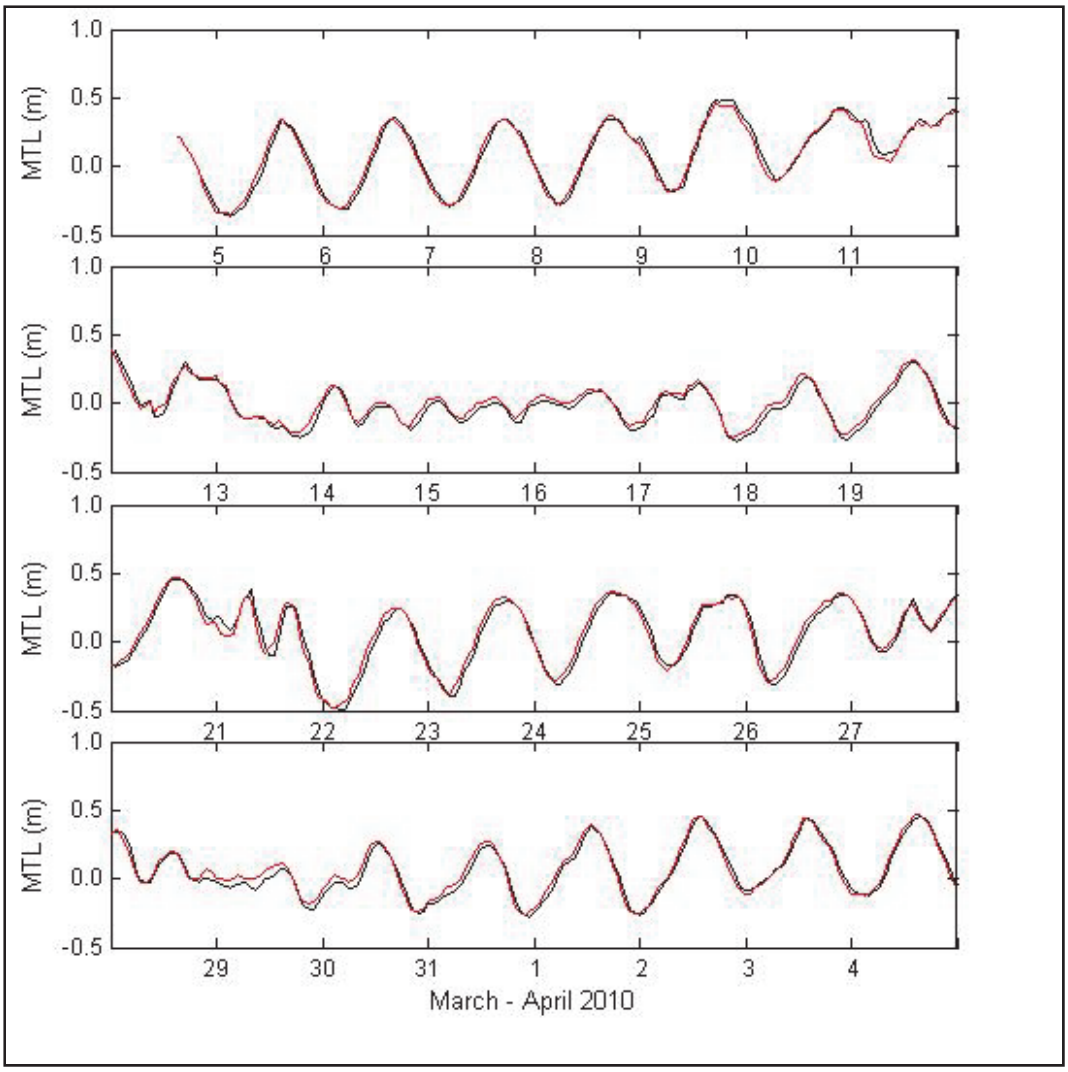

Figure B-2. Mean water levels at the Sound wave gauge (black line) for April 5 through May 6, 2010, and at the Gulf gauge (red line) for April 5 to April 30, 2010.

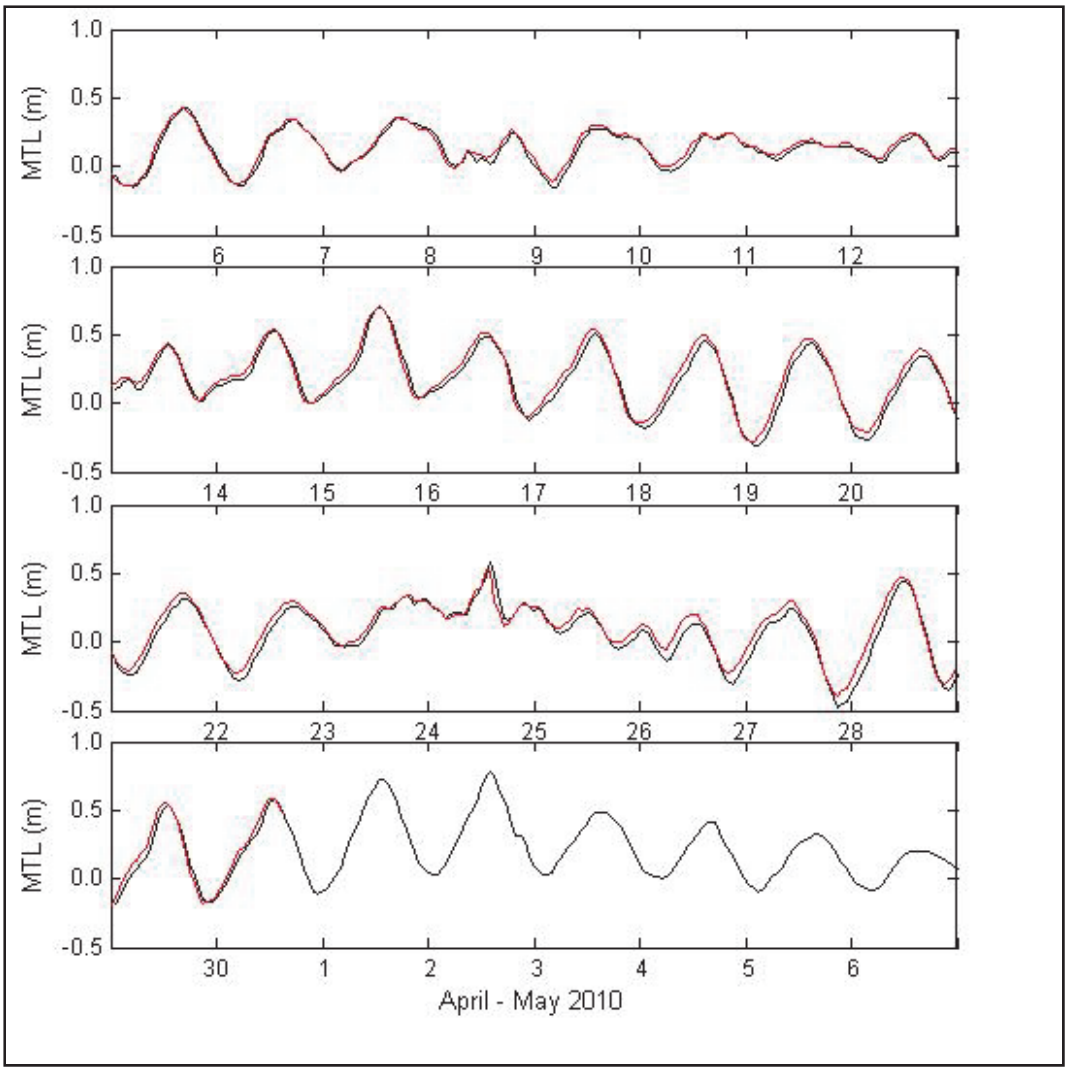

Figure B-3. Mean water levels at the Sound wave gauge for May 7 through June 7, 2010.

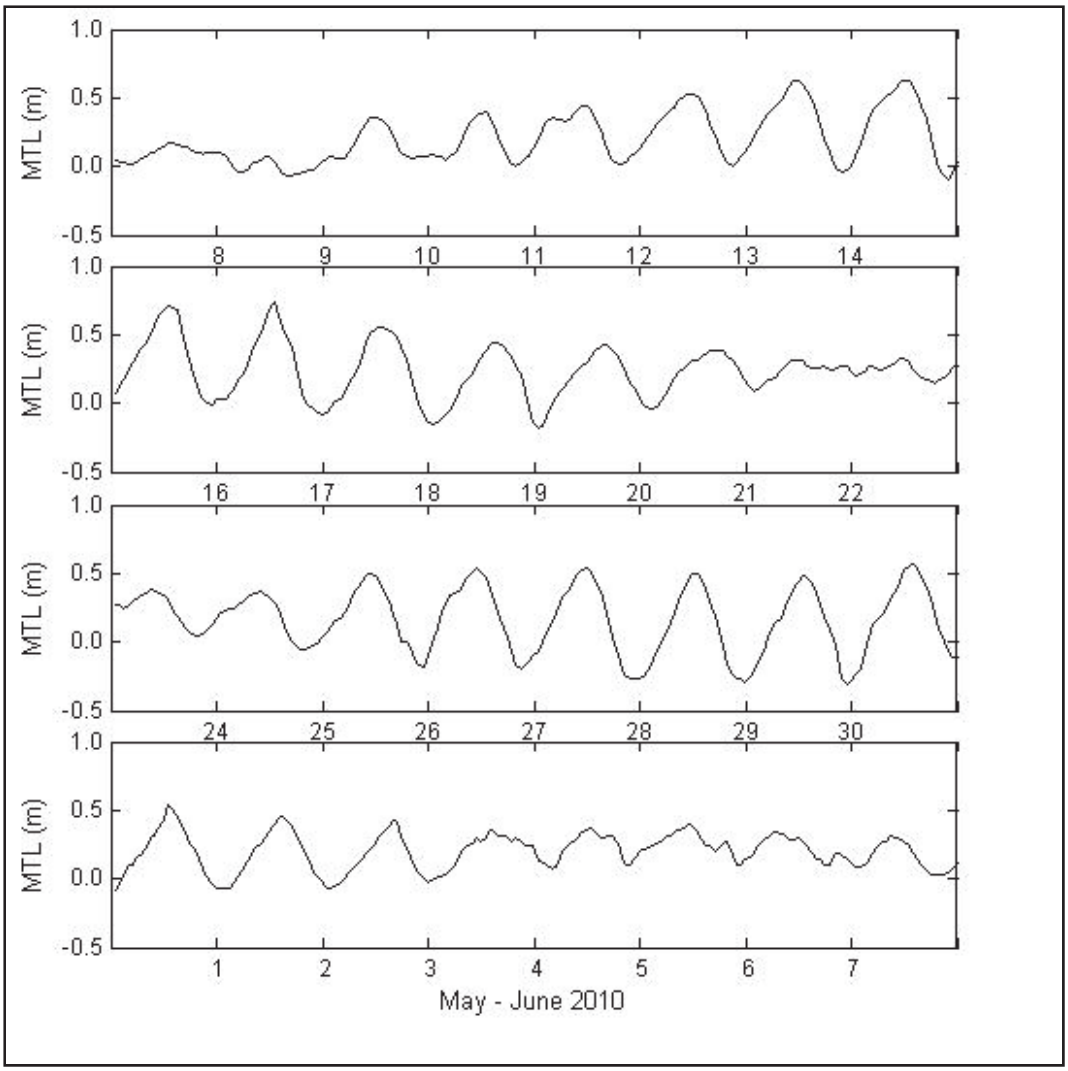

Figure B-4. Mean water levels at the Sound wave gauge for June 8 through July 9, 2010.

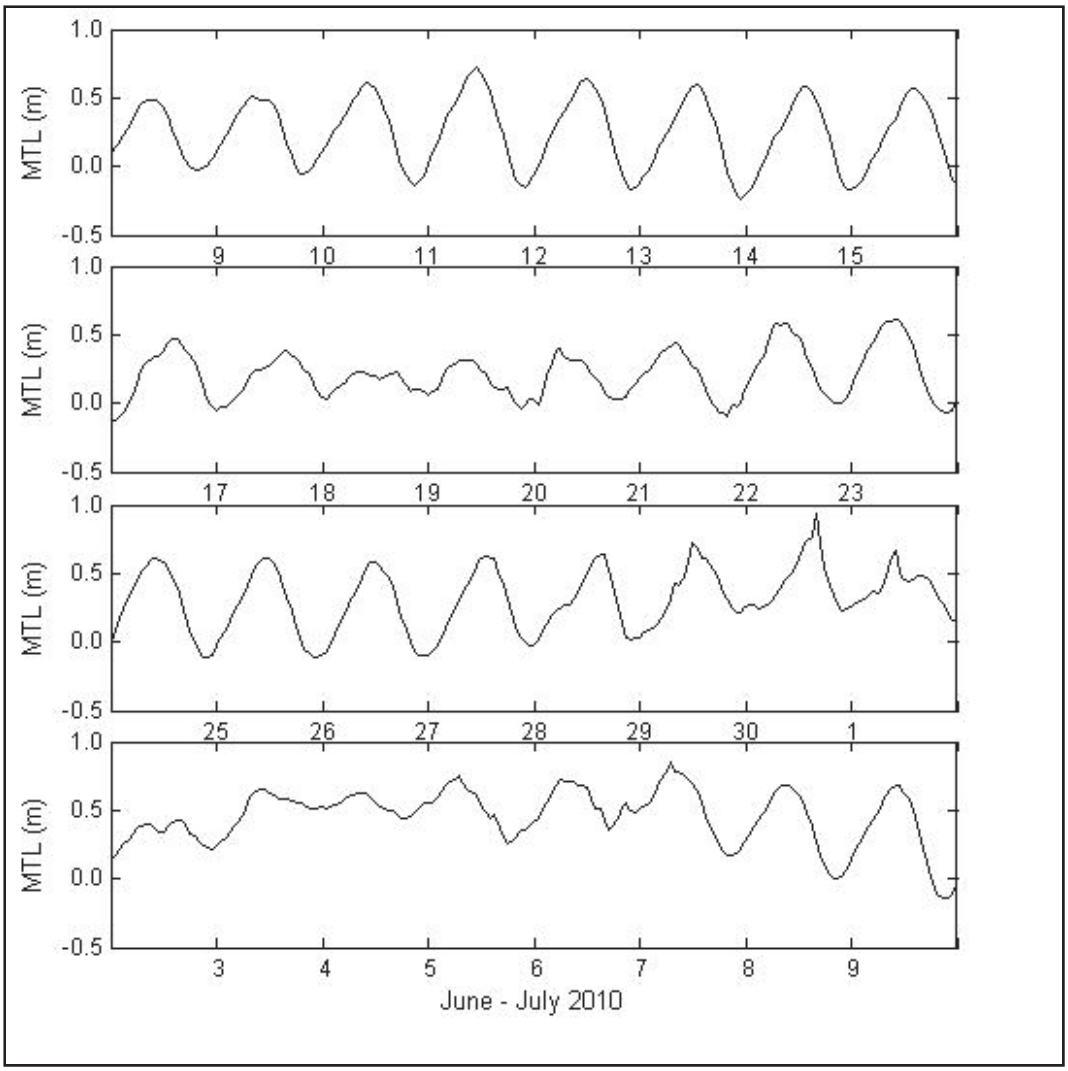

Figure B-5. Mean water levels at the Sound wave gauge for July 10 to July 15, 2010.

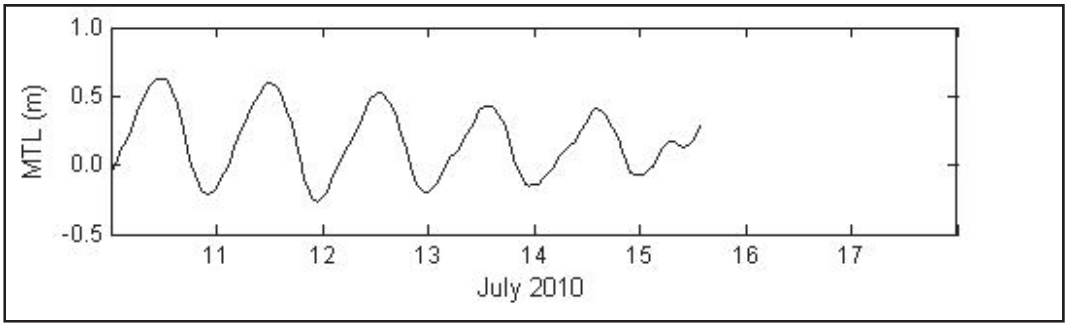

Appendix C: Current Measurements Results

Ship Island Pass

Figure C-1. Ship Island Pass Transect 1. Shown east (left side) to west (right side).

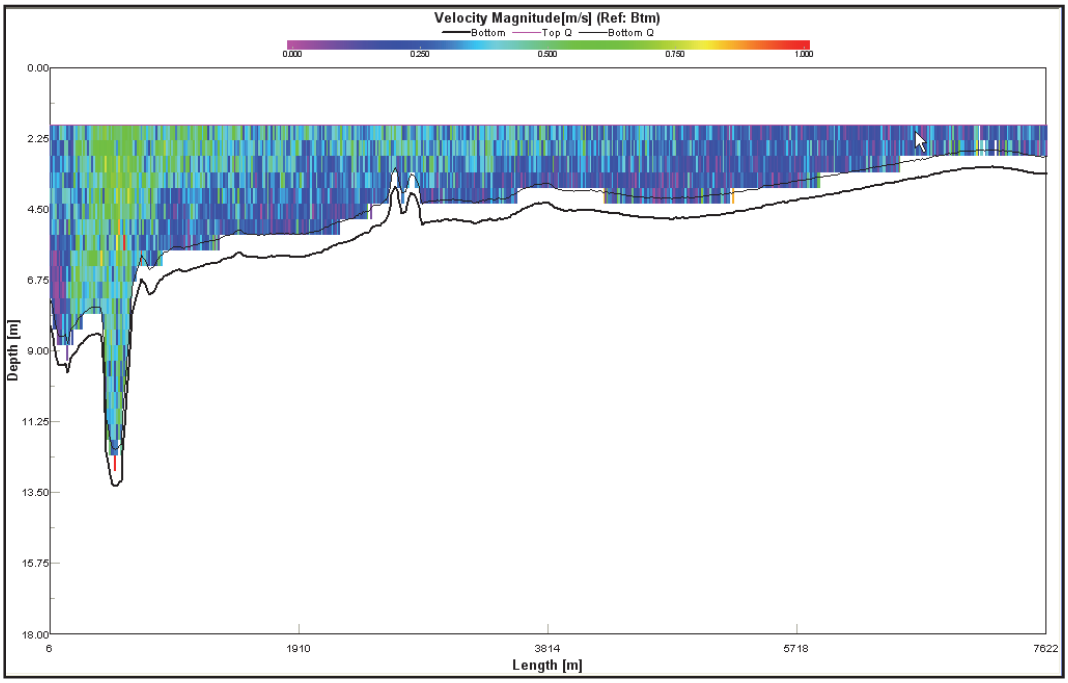

Figure C-2. Ship Island Pass Transect 2. Shown east (left side) to west (right side).

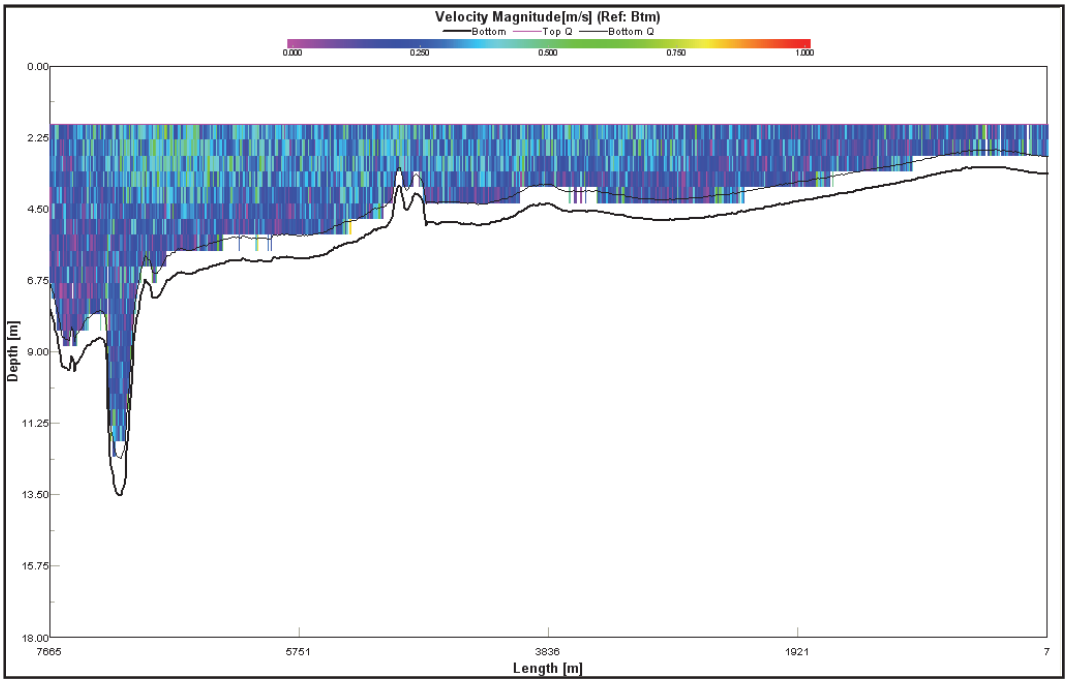

Figure C-3. Ship Island Pass Transect 3. Shown east (left side) to west (right side).

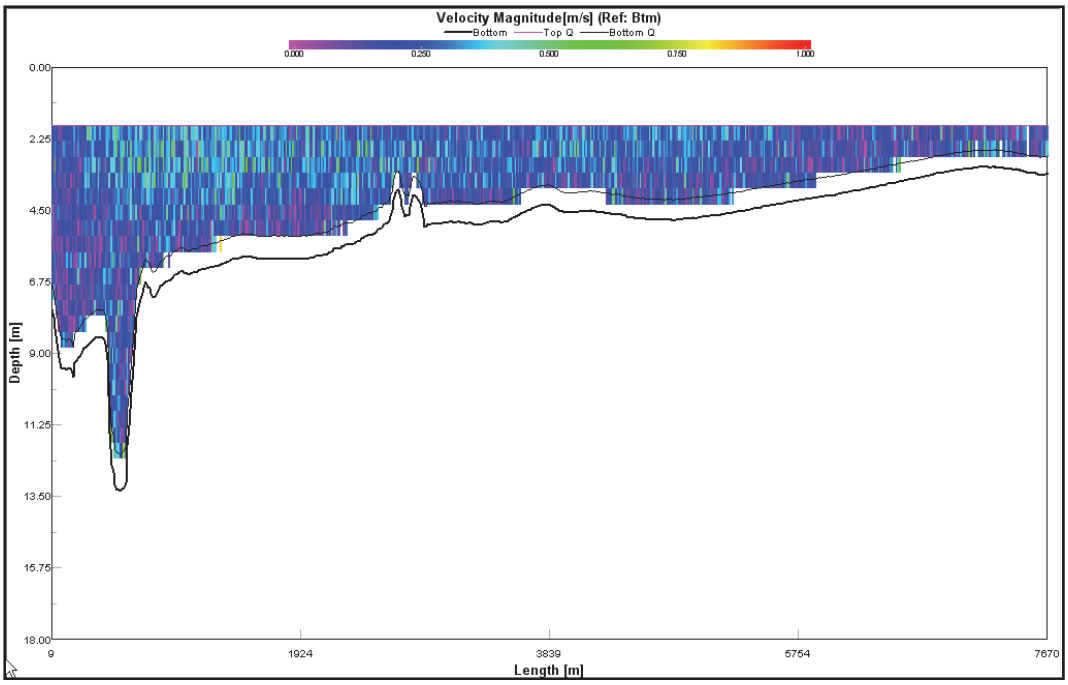

Figure C-4. Ship Island Pass Transect 4. Shown east (left side) to west (right side).

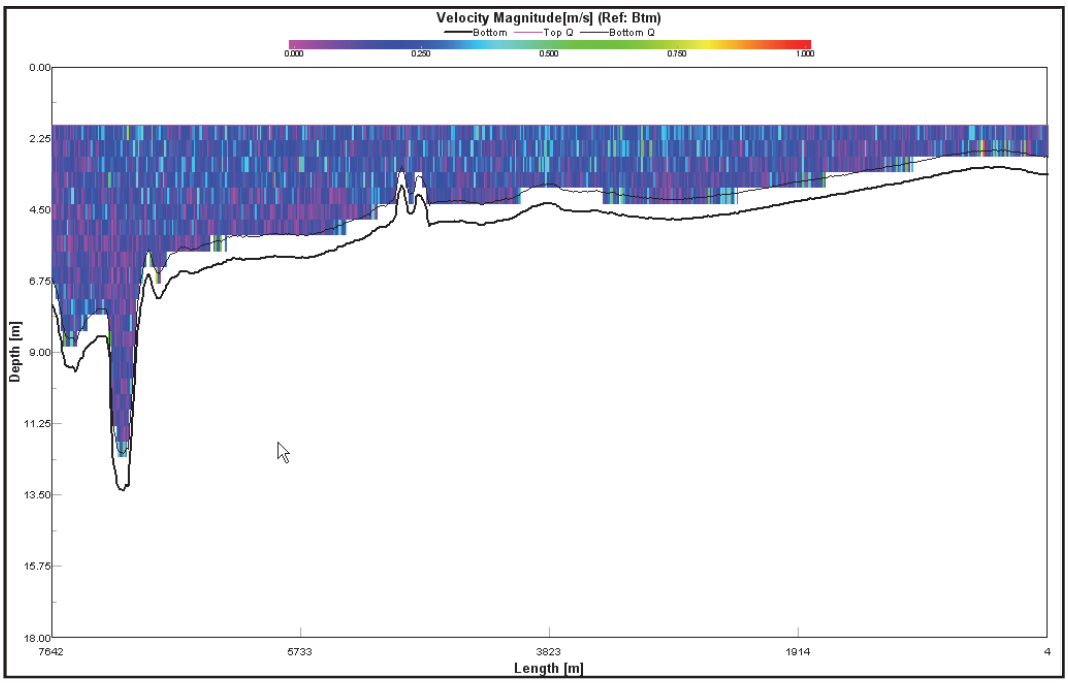

Figure C-5. Ship Island Pass Transect 5. Shown east (left side) to west (right side).

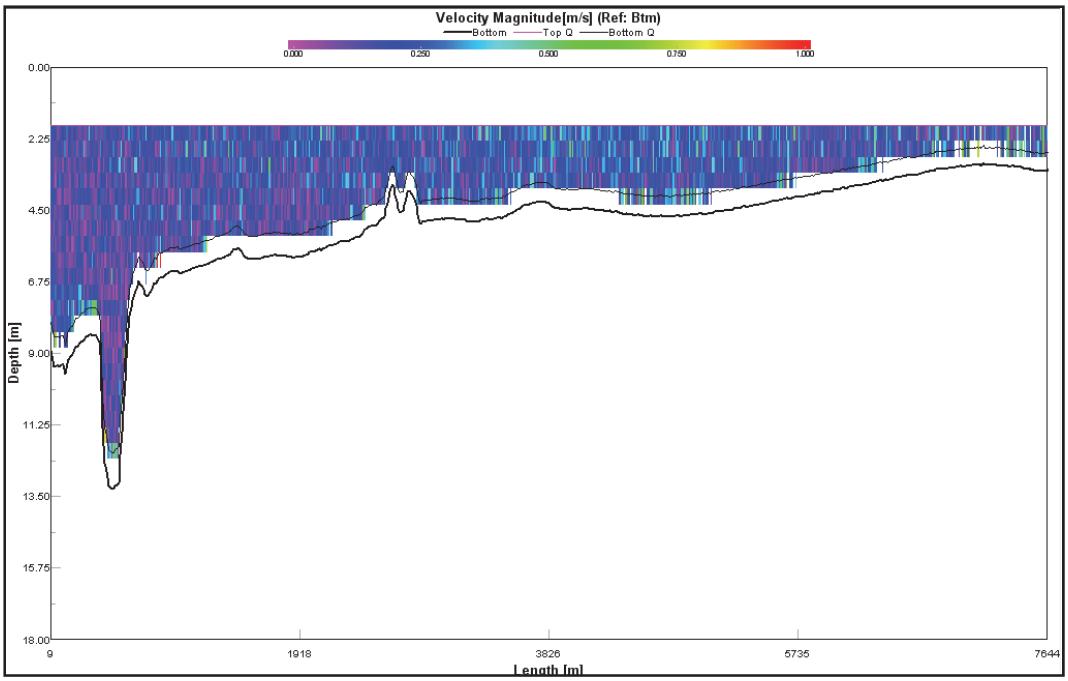

Figure C-6. Ship Island Pass Transect 6. Shown east (left side) to west (right side).

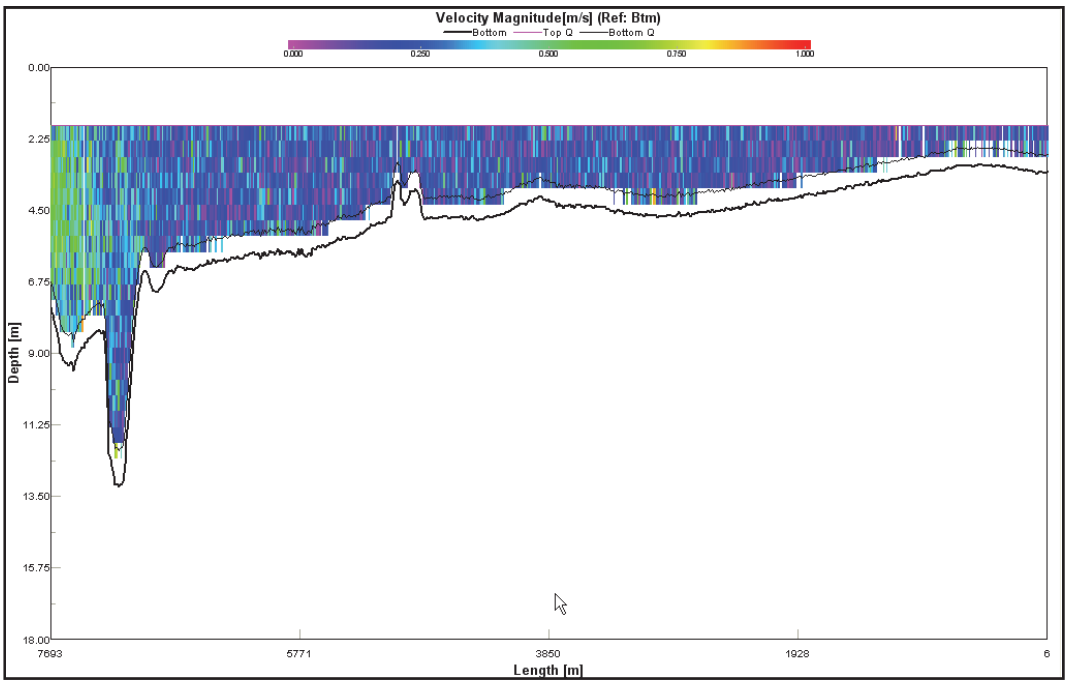

Figure C-7. Ship Island Pass Transect 7. Shown east (left side) to west (right side).

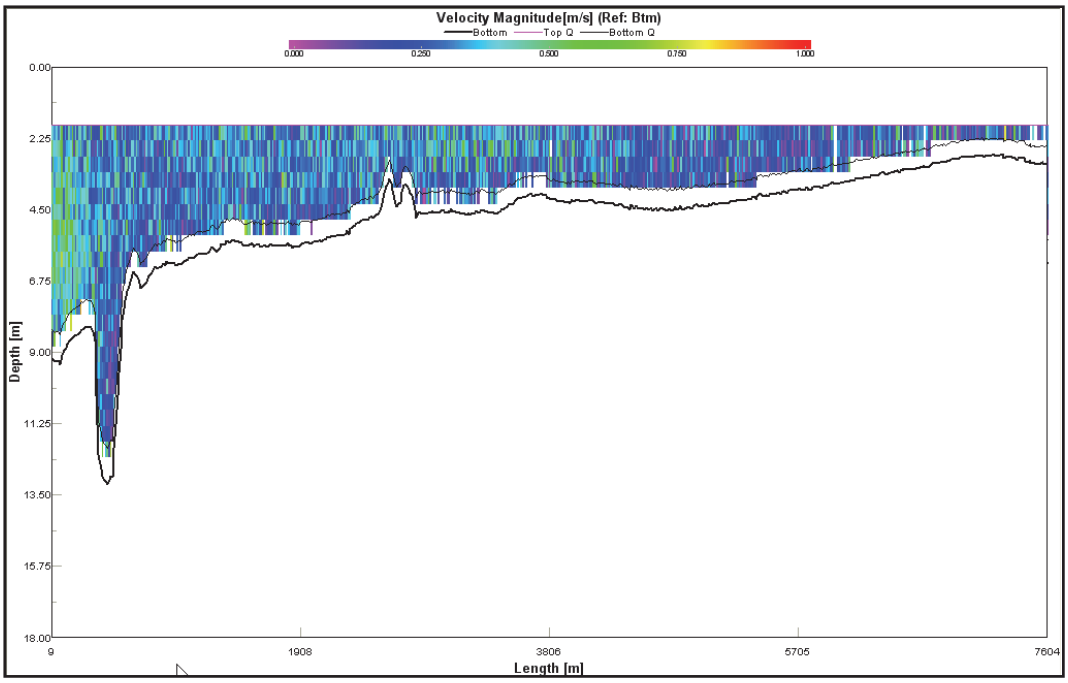

Figure C-8. Ship Island Pass Transect 8. Shown east (left side) to west (right side).

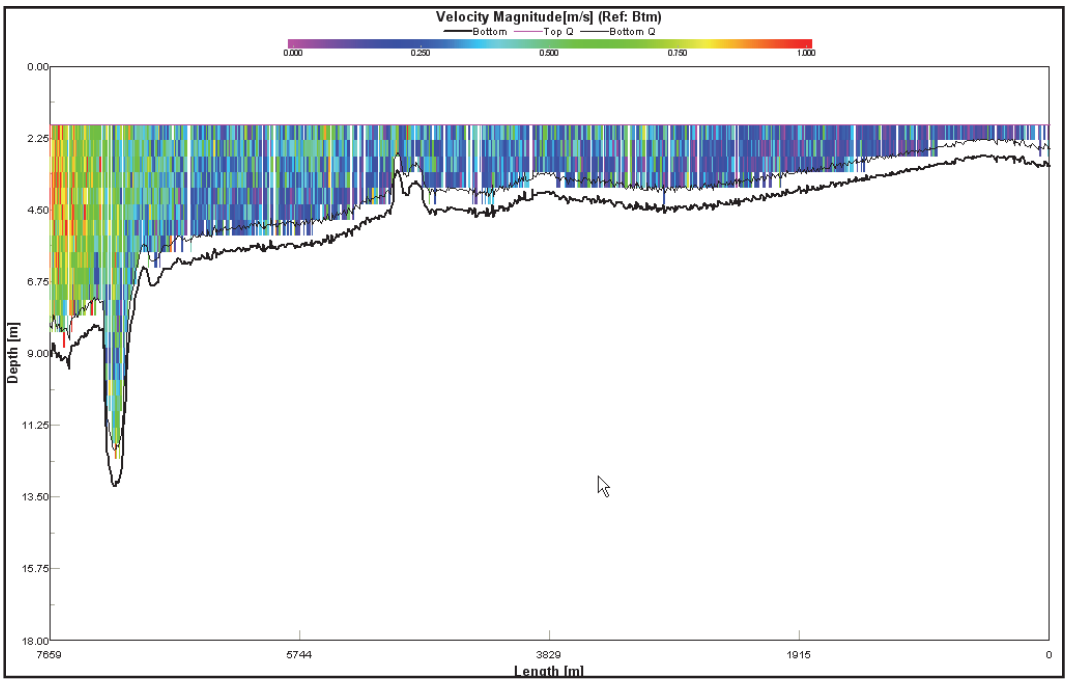

Dog Keys Passes

Figure C-9. Dog Keys Passes Transect 1. Shown west (left side) to east (right side).

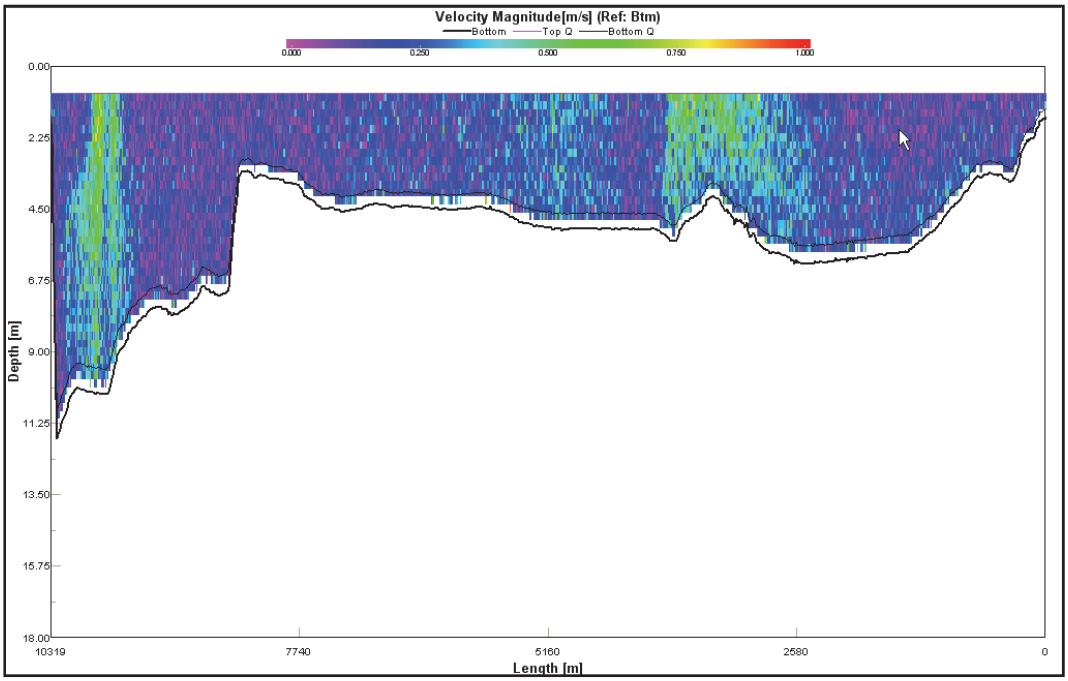

Figure C-10. Dog Keys Passes Transect 2. Shown west (left side) to east (right side).

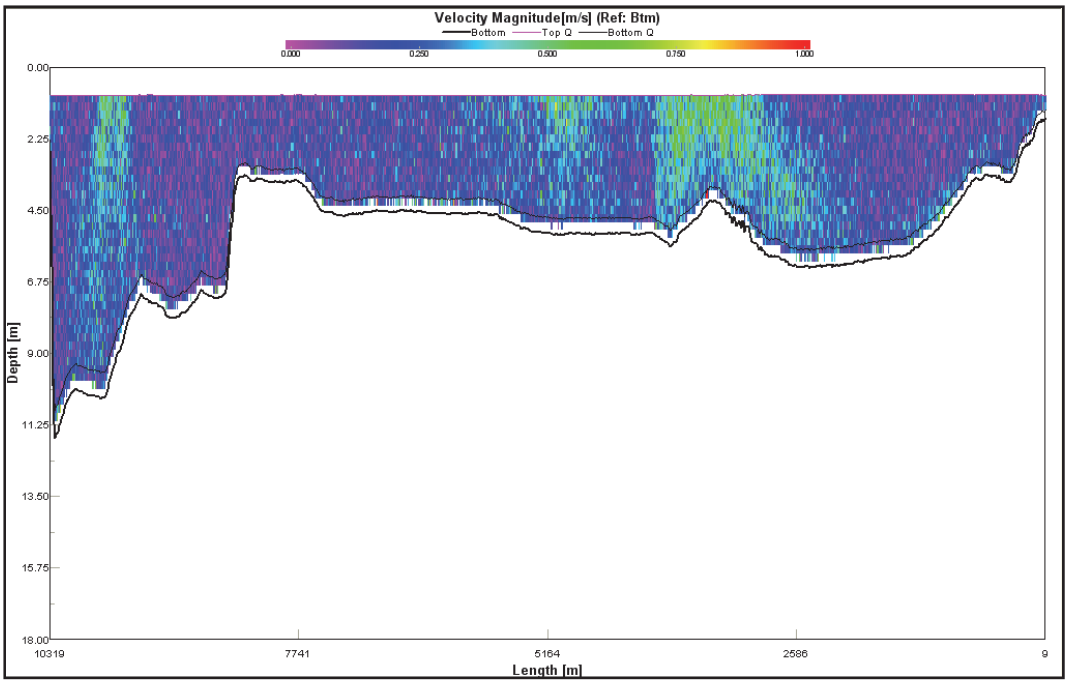

Figure C-11. Dog Keys Passes Transect 3. Shown west (left side) to east (right side).

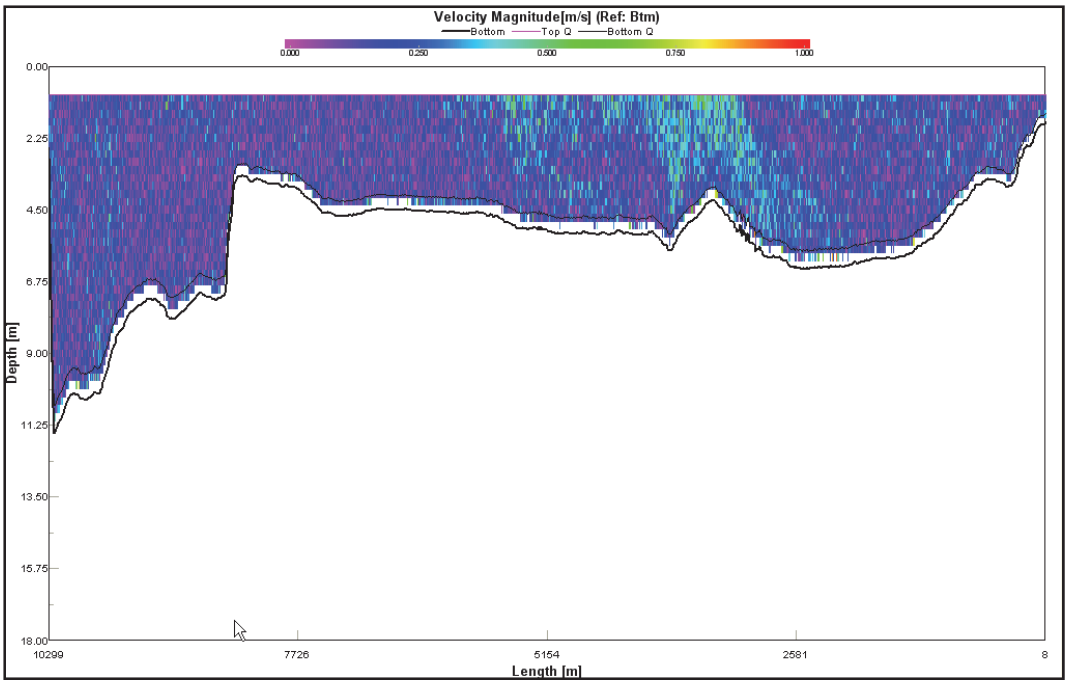

Figure C-12. Dog Keys Passes Transect 4. Shown west (left side) to east (right side).

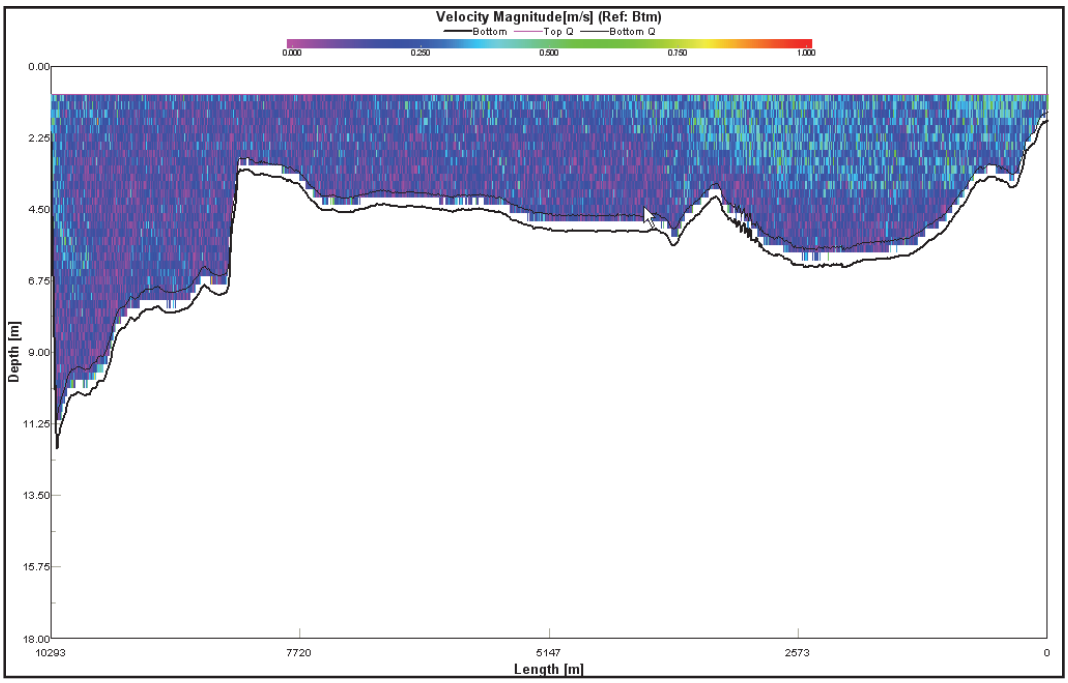

Figure C-13. Dog Keys Passes Transect 5. Shown west (left side) to east (right side).

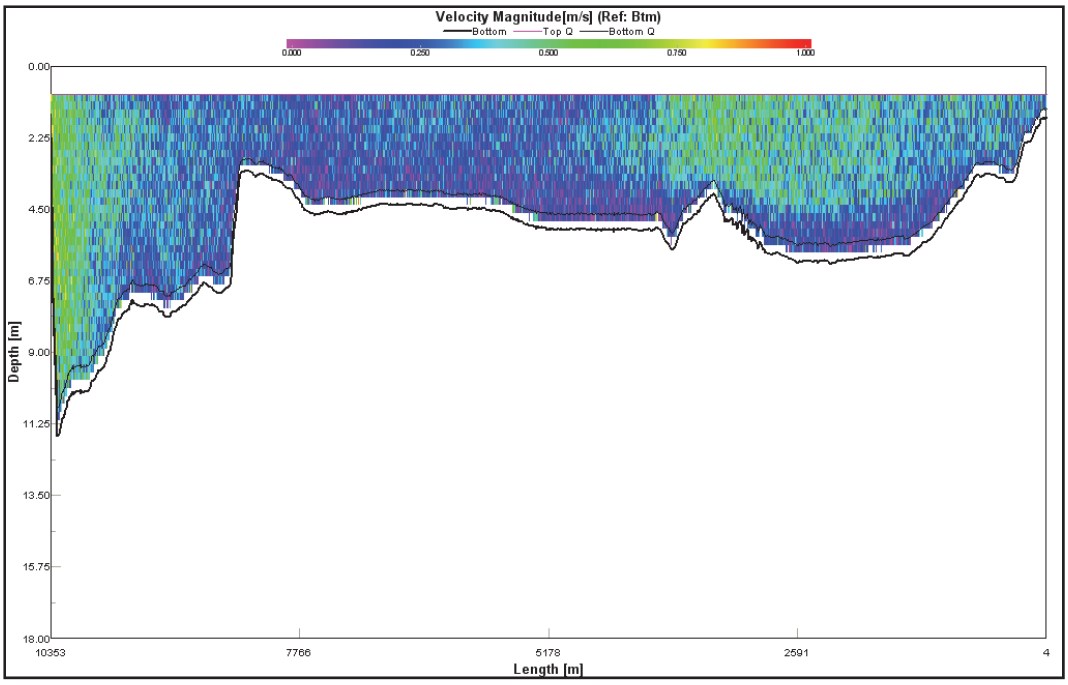

Figure C-14. Dog Keys Passes Transect 6. Shown west (left side) to east (right side).

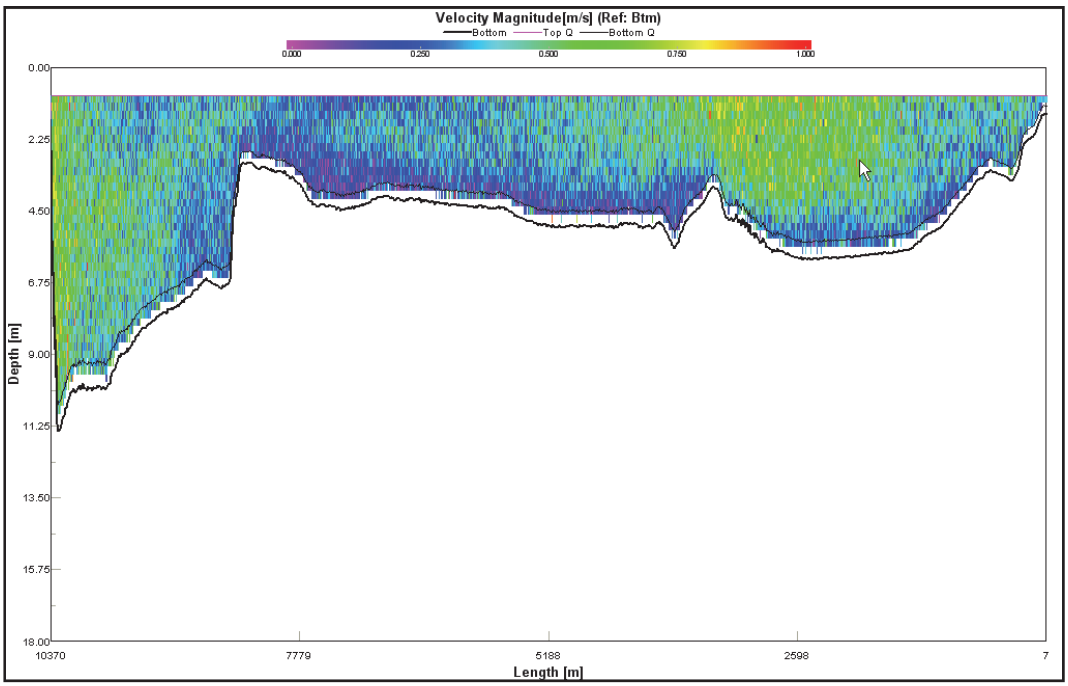

Figure C-15. Dog Keys Passes Transect 7. Shown west (left side) to east (right side).

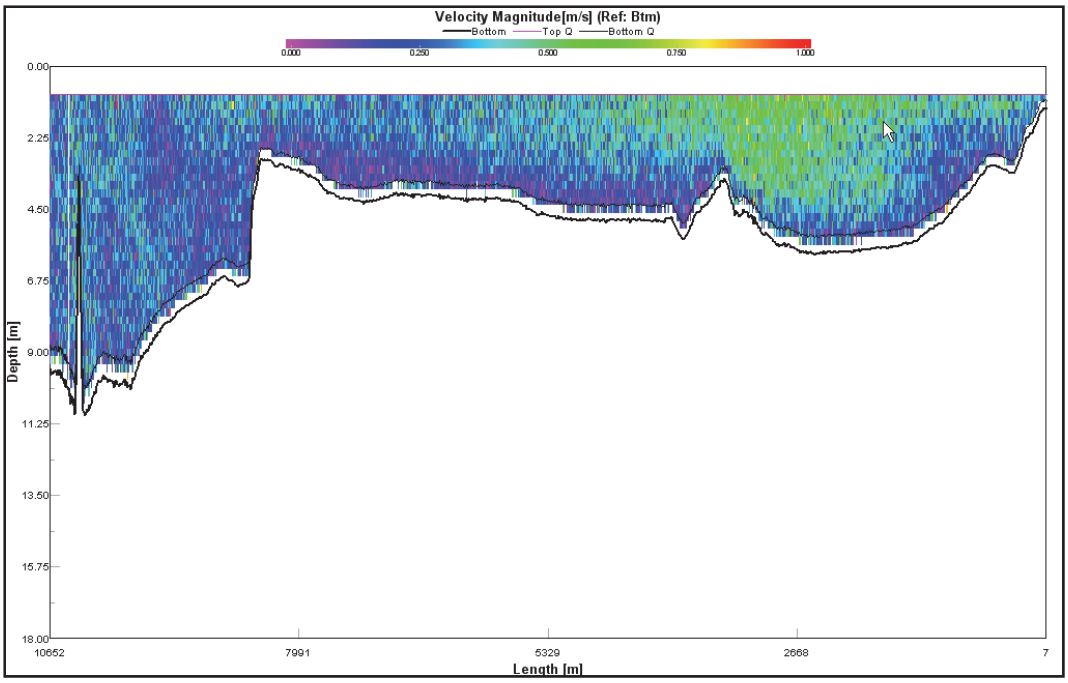

Petit Bois Pass

Figure C-16. Petit Bois Pass Transect 1. Shown west (left side) to east (right side).

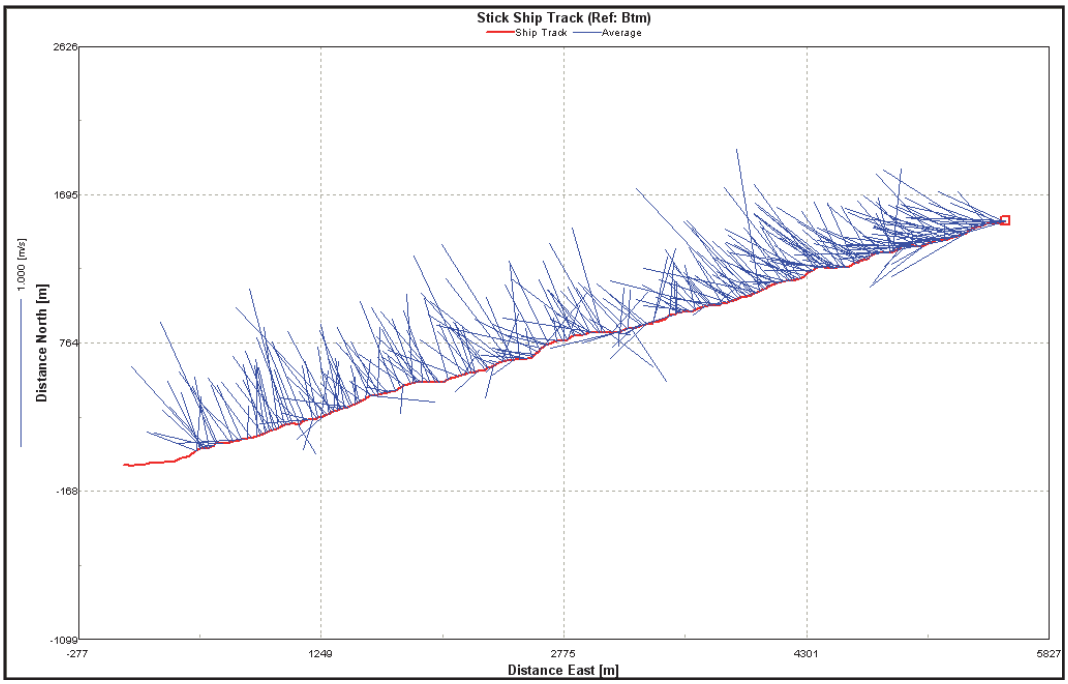

Figure C-17. Petit Bois Pass Transect 2. Shown west (left side) to east (right side).

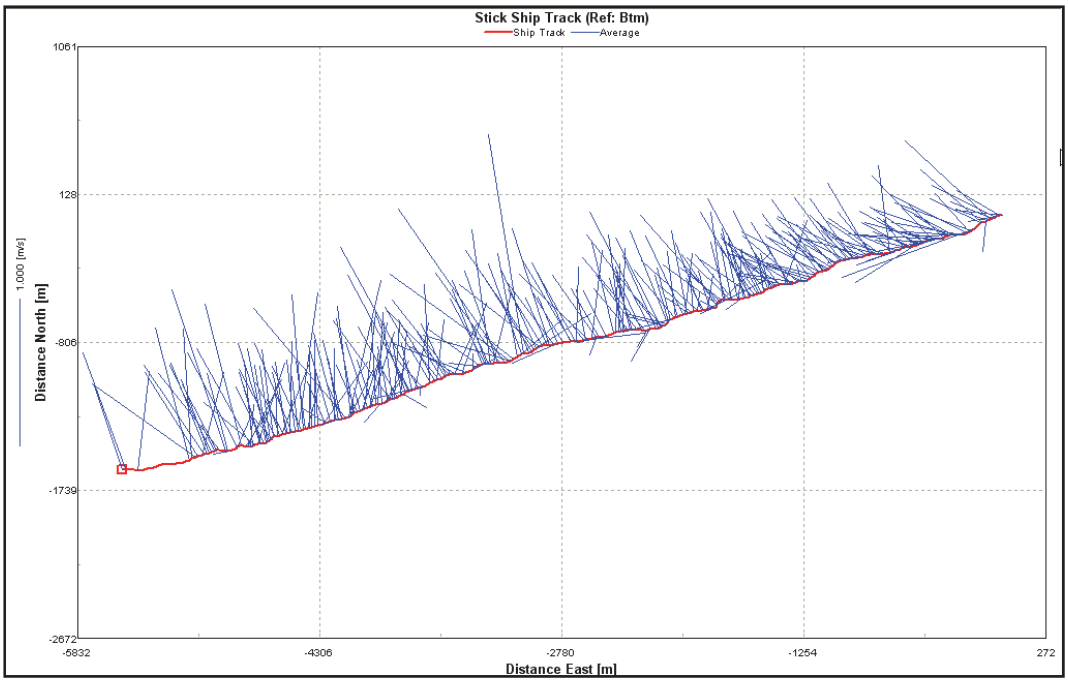

Figure C-18. Petit Bois Pass Transect 3. Shown west (left side) to east (right side).

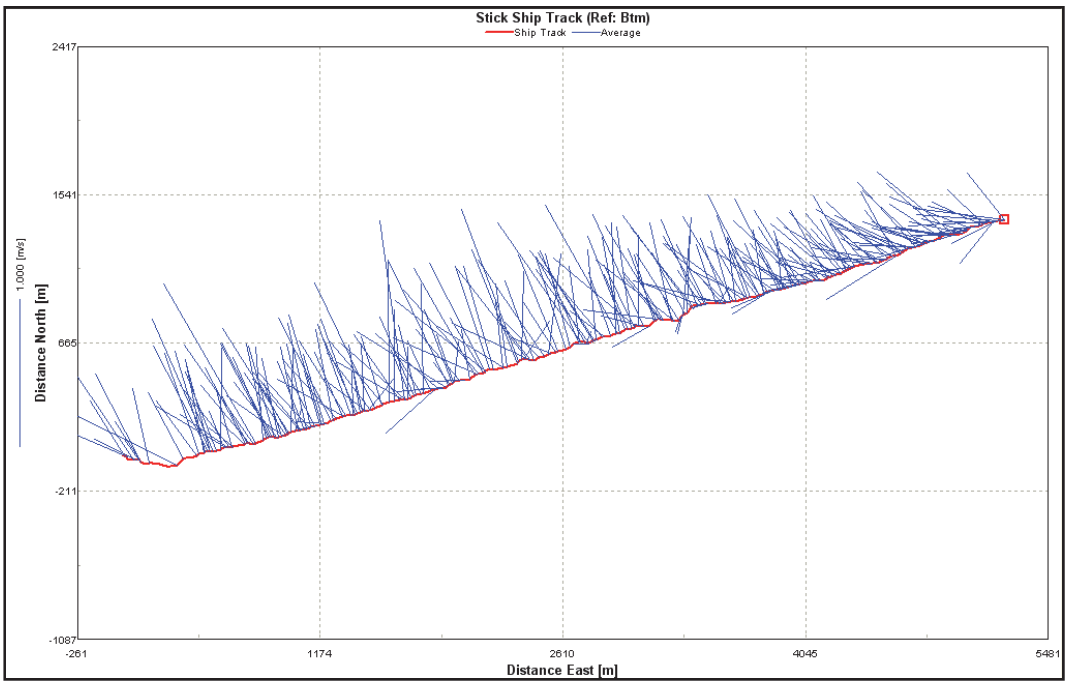

Figure C-19. Petit Bois Pass Transect 4. Shown west (left side) to east (right side).

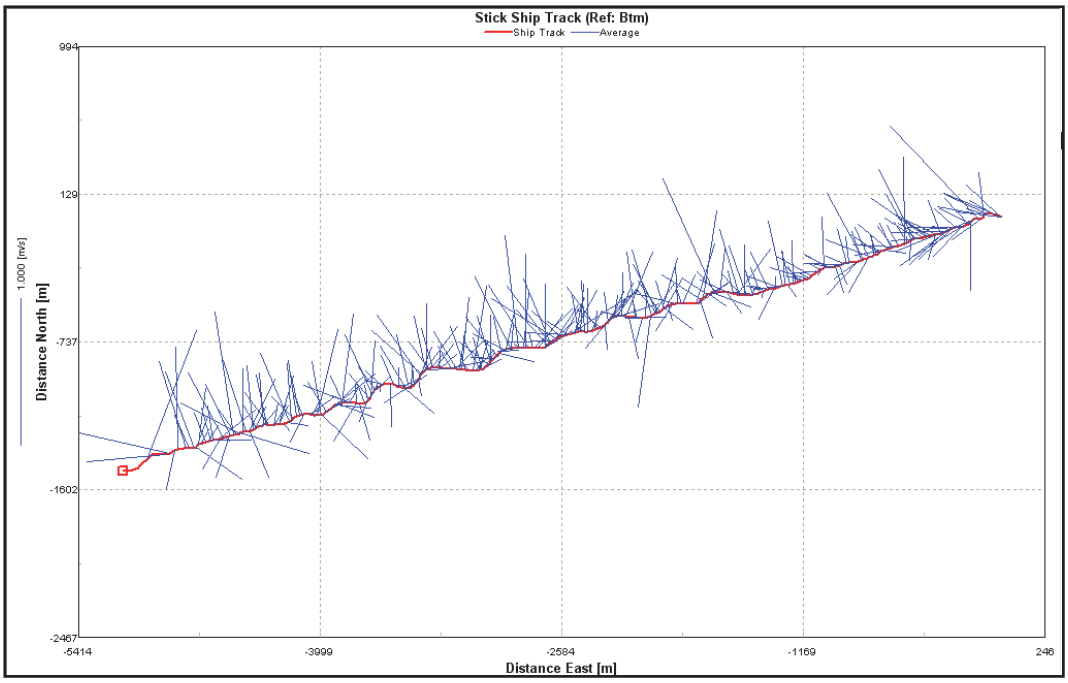

Figure C-20. Petit Bois Pass Transect 5. Shown west (left side) to east (right side).

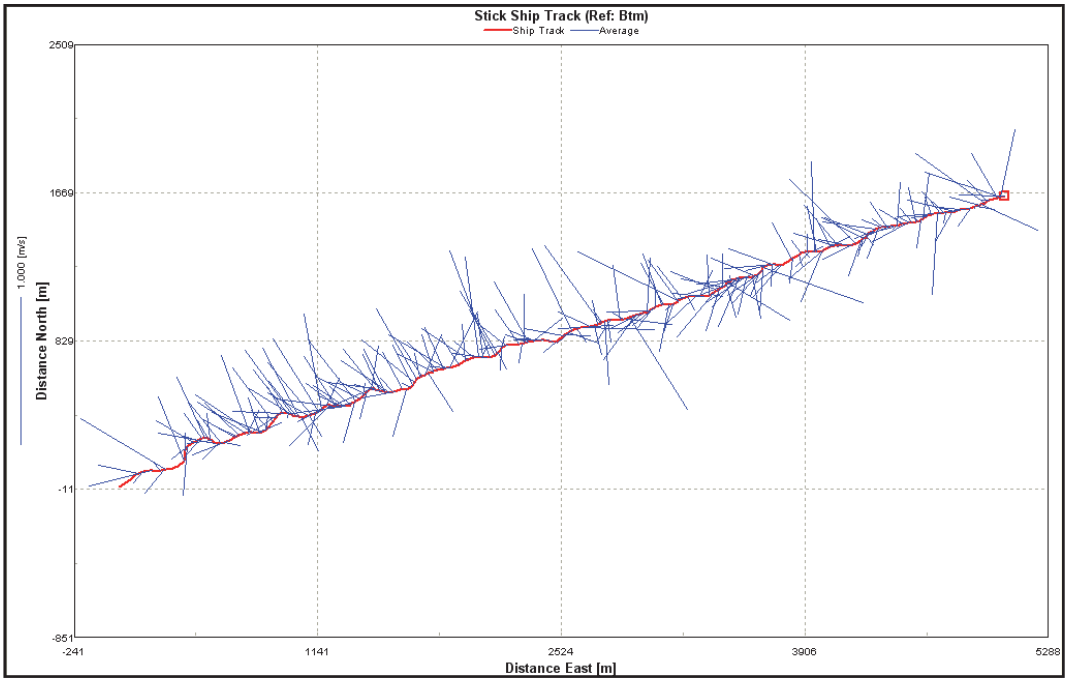

Figure C-21. Petit Bois Pass Transect 6. Shown west (left side) to east (right side).

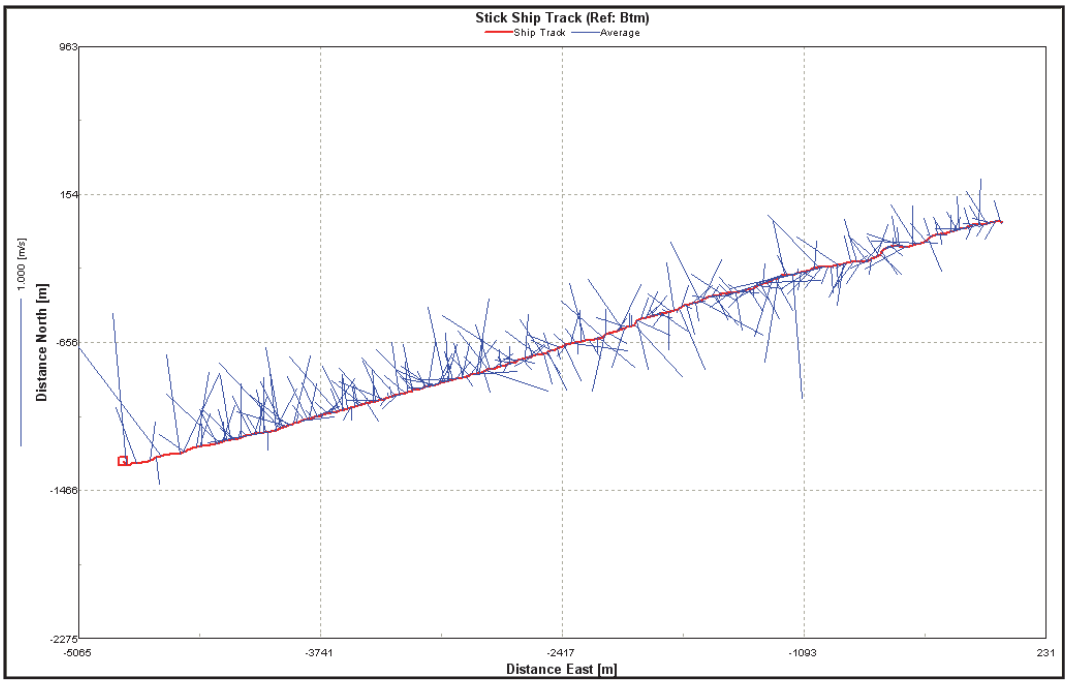

Figure C-22. Petit Bois Pass Transect 7. Shown west (left side) to east (right side).

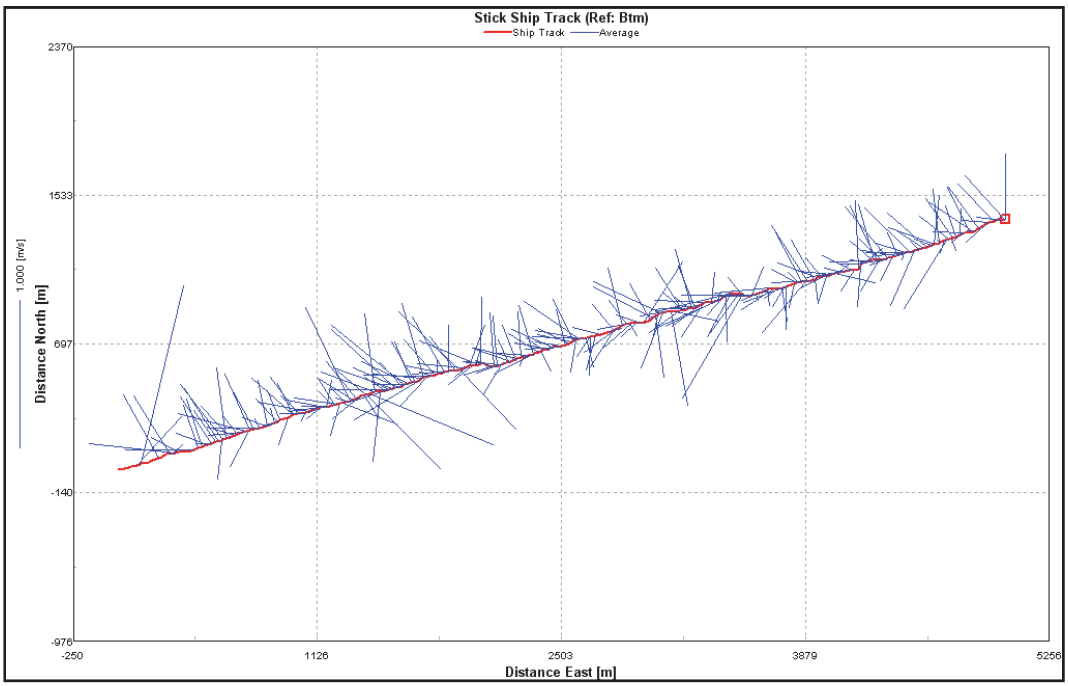

Figure C-23. Petit Bois Pass Transect 8. Shown west (left side) to east (right side).

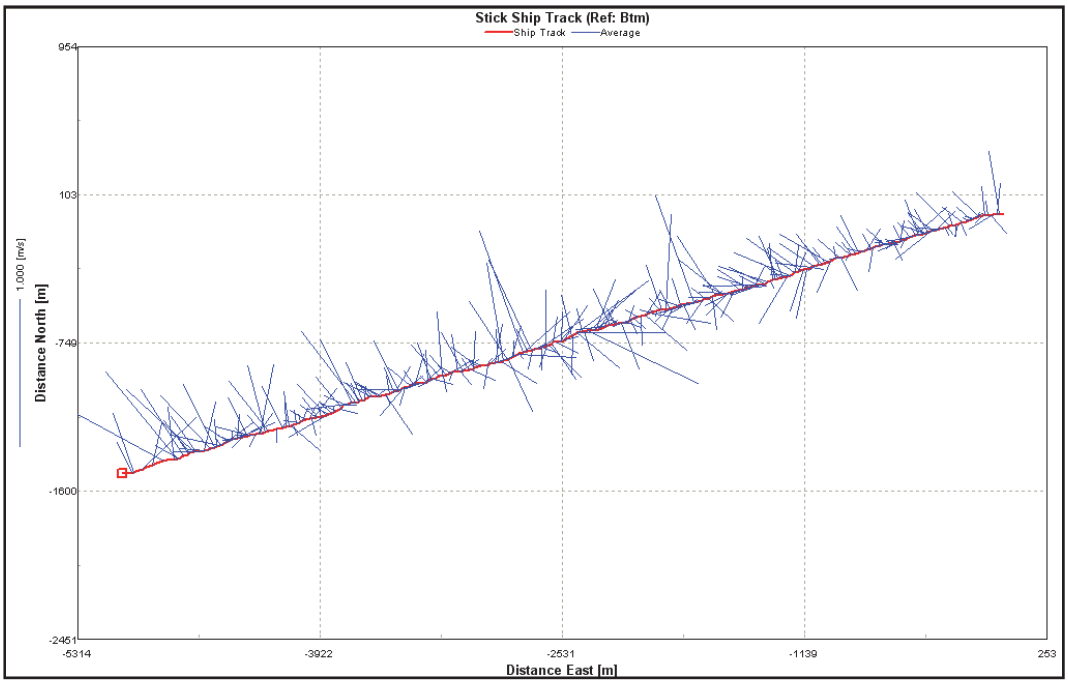

Figure C-24. Petit Bois Pass Transect 9. Shown west (left side) to east (right side).

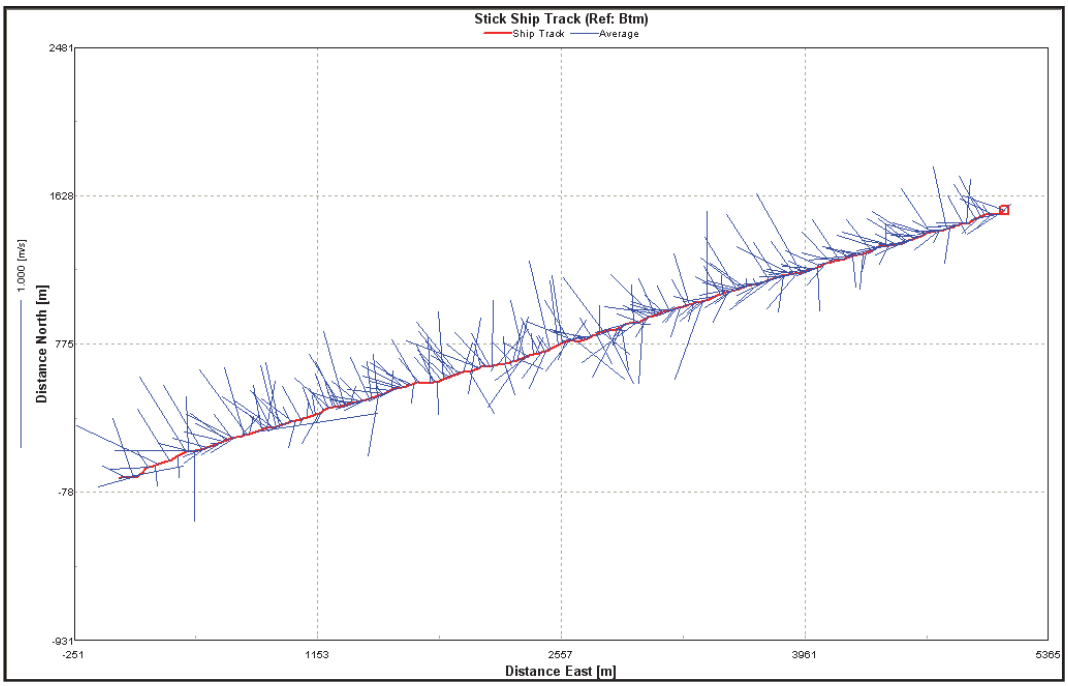

Figure C-25. Petit Bois Pass Transect 10. Shown west (left side) to east (right side).

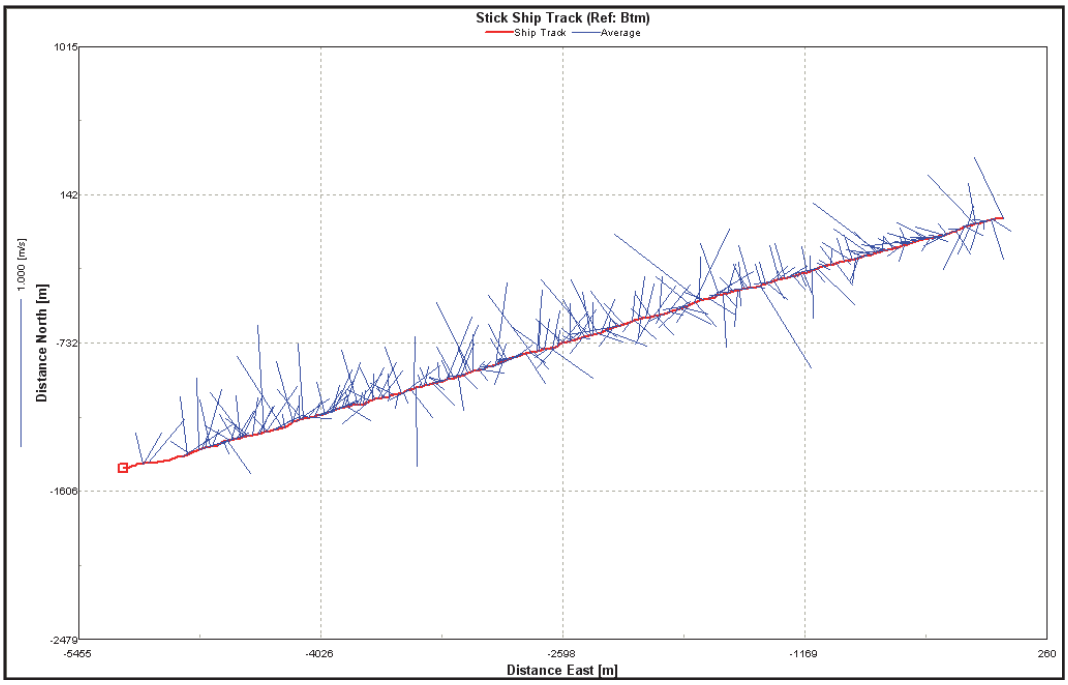

Figure C-26. Petit Bois Pass Transect 11. Shown west (left side) to east (right side).

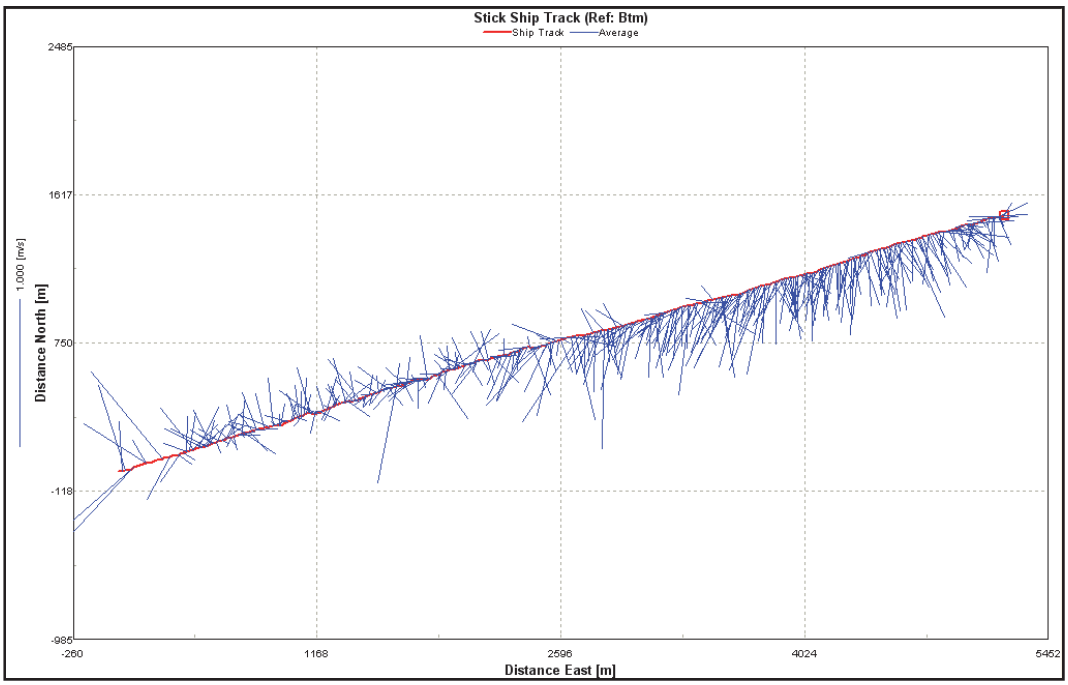

Pass Aux Herons

Figure C-27. Pass Aux Herons Transect 1. Shown northwest (top) to southeast (bottom).

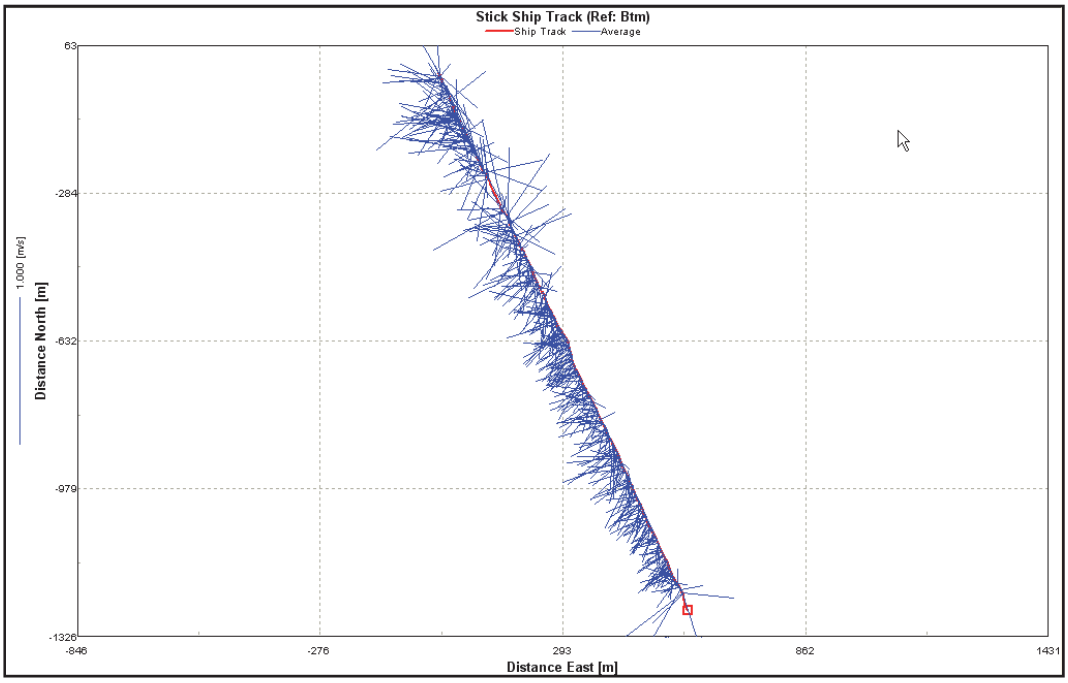

Figure C-28. Pass Aux Herons Transect 2. Shown northwest (top) to southeast (bottom).

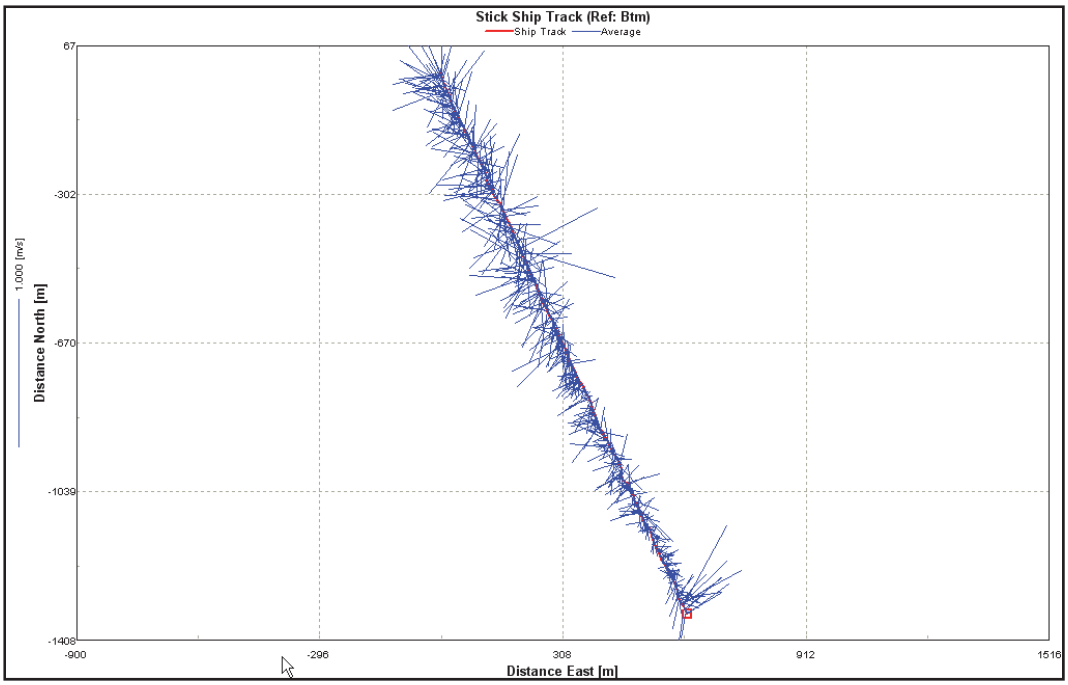

Figure C-29. Pass Aux Herons Transect 3. Shown northwest (top) to southeast (bottom).

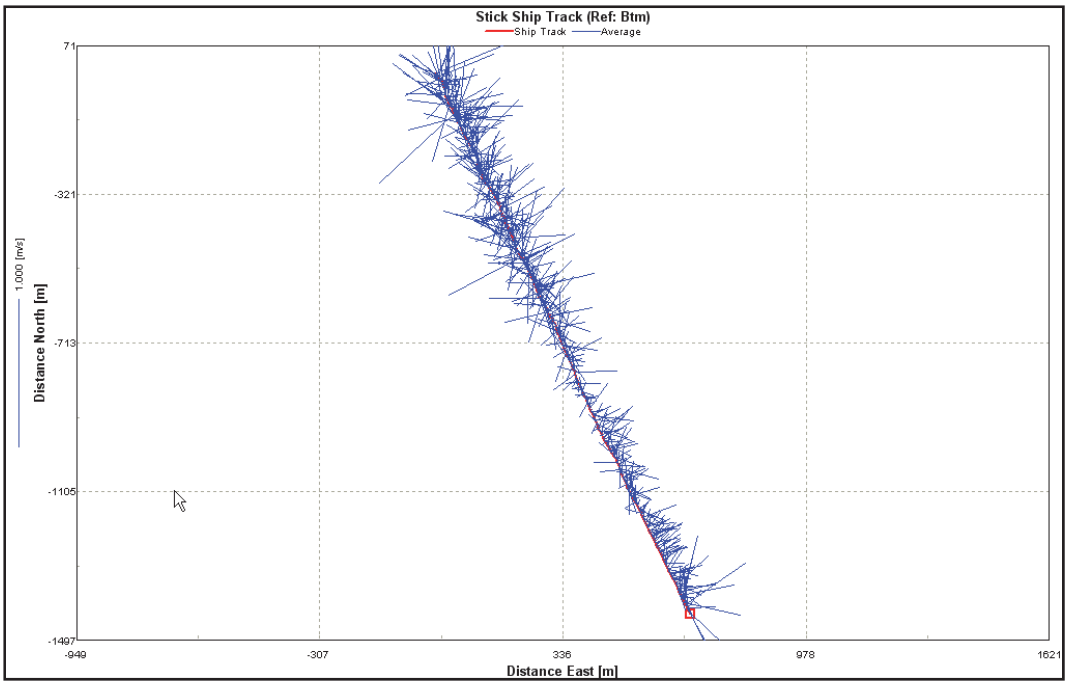

Figure C-30. Pass Aux Herons Transect 4. Shown northwest (top) to southeast (bottom).

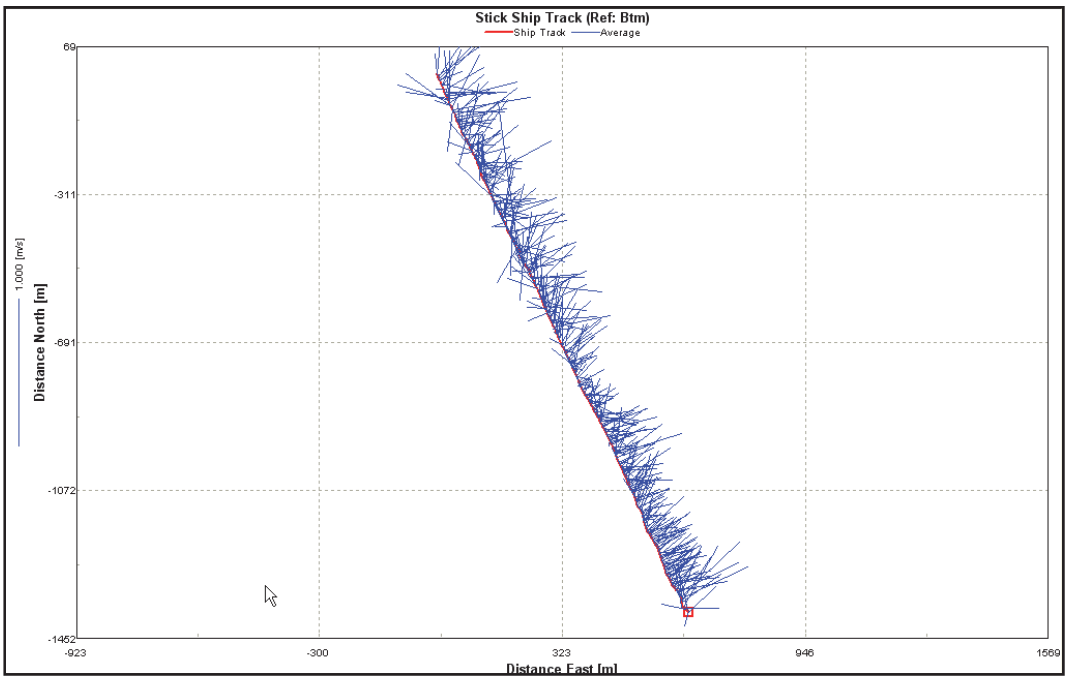

Figure C-31. Pass Aux Herons Transect 5. Shown northwest (top) to southeast (bottom).

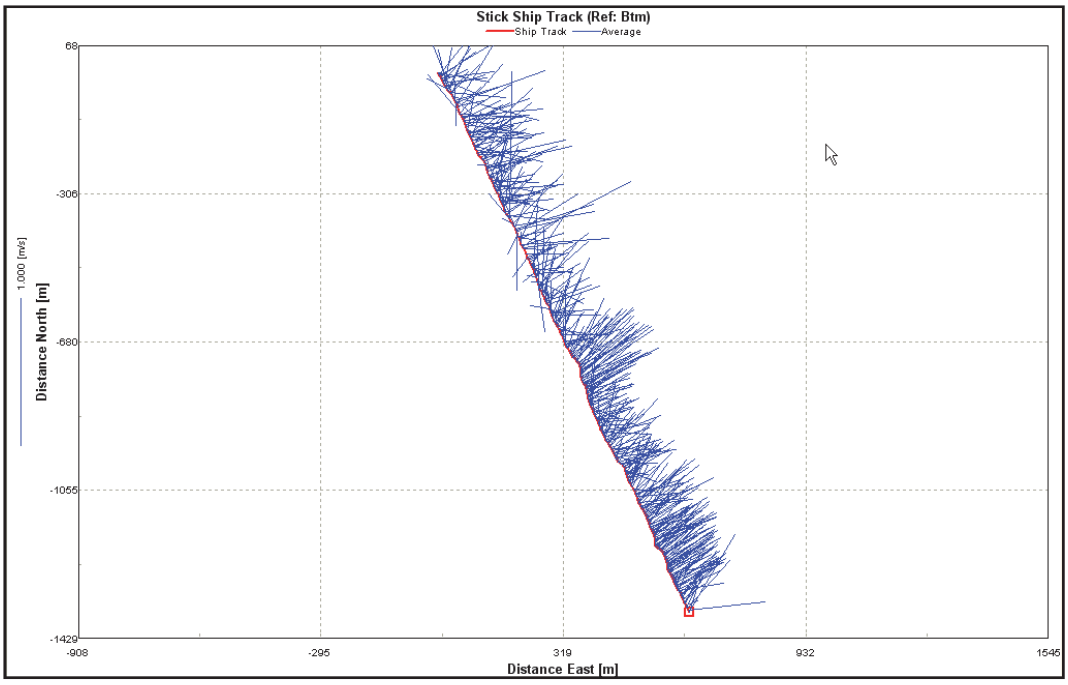

Figure C-32. Pass Aux Herons Transect 6. Shown northwest (top) to southeast (bottom).

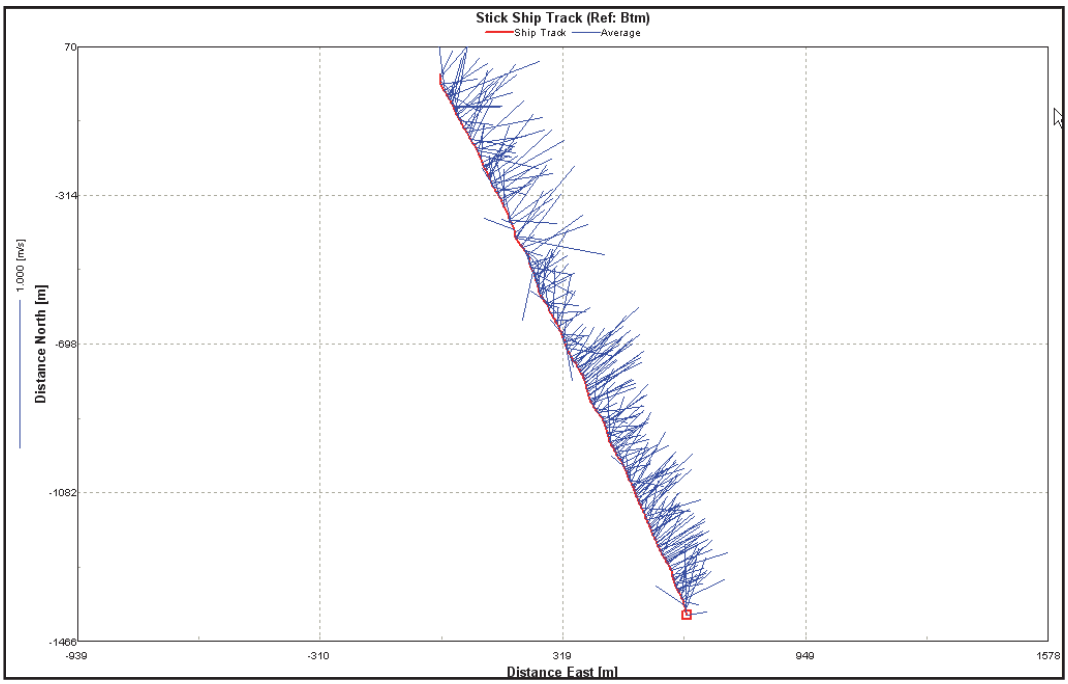

Figure C-33. Pass Aux Herons Transect 7. Shown northwest (top) to southeast (bottom).

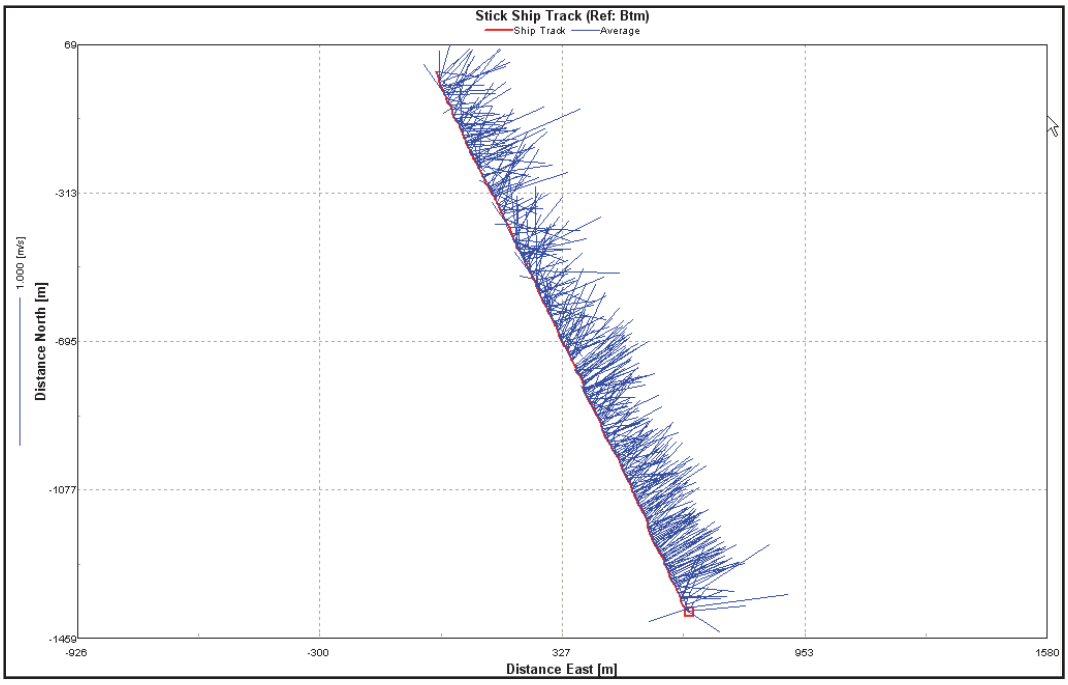

Figure C-34. Pass Aux Herons Transect 8. Shown northwest (top) to southeast (bottom).

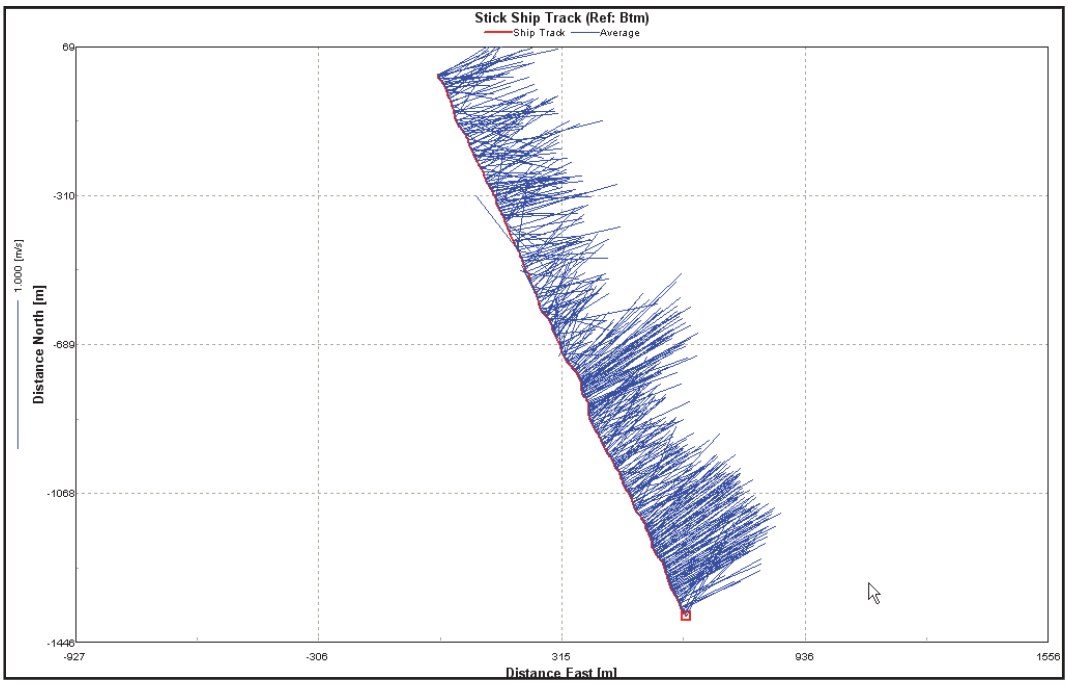

Figure C-35. Pass Aux Herons Transect 9. Shown northwest (top) to southeast (bottom).

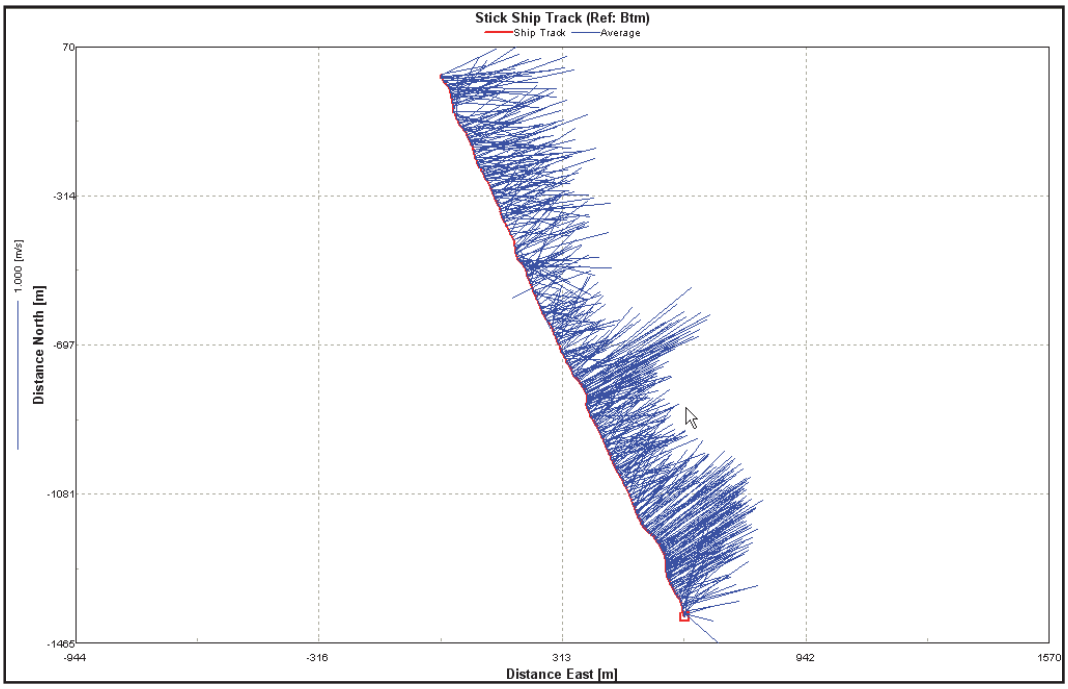

Figure C-36. Pass Aux Herons Transect 10. Shown northwest (top) to southeast (bottom).

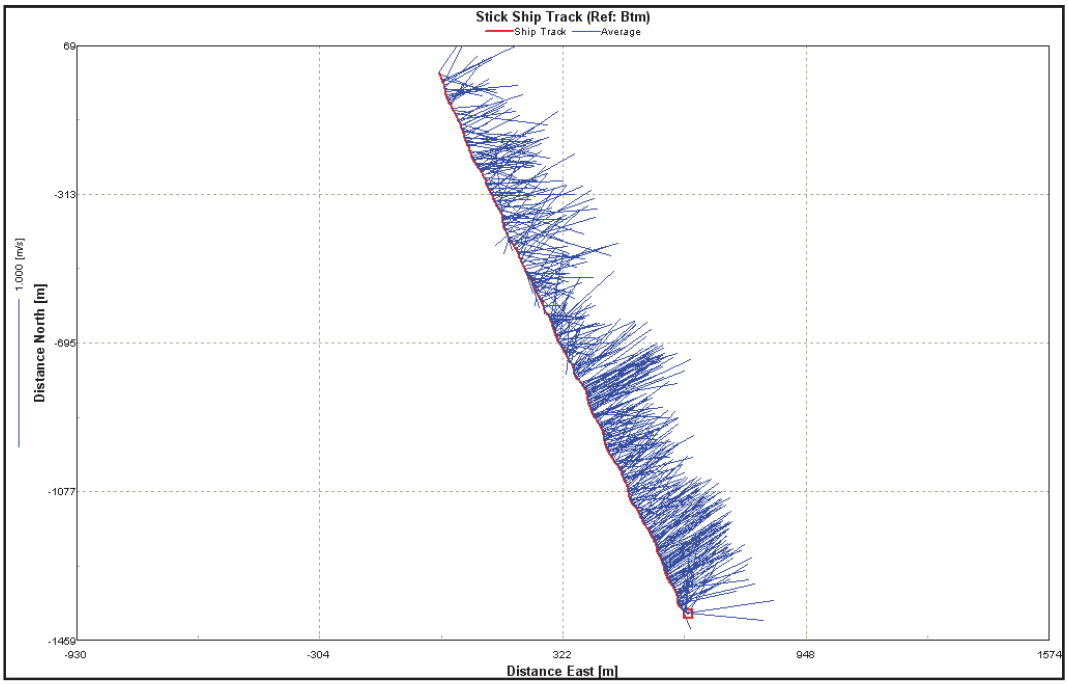

Figure C-37. Pass Aux Herons Transect 11. Shown northwest (top) to southeast (bottom).

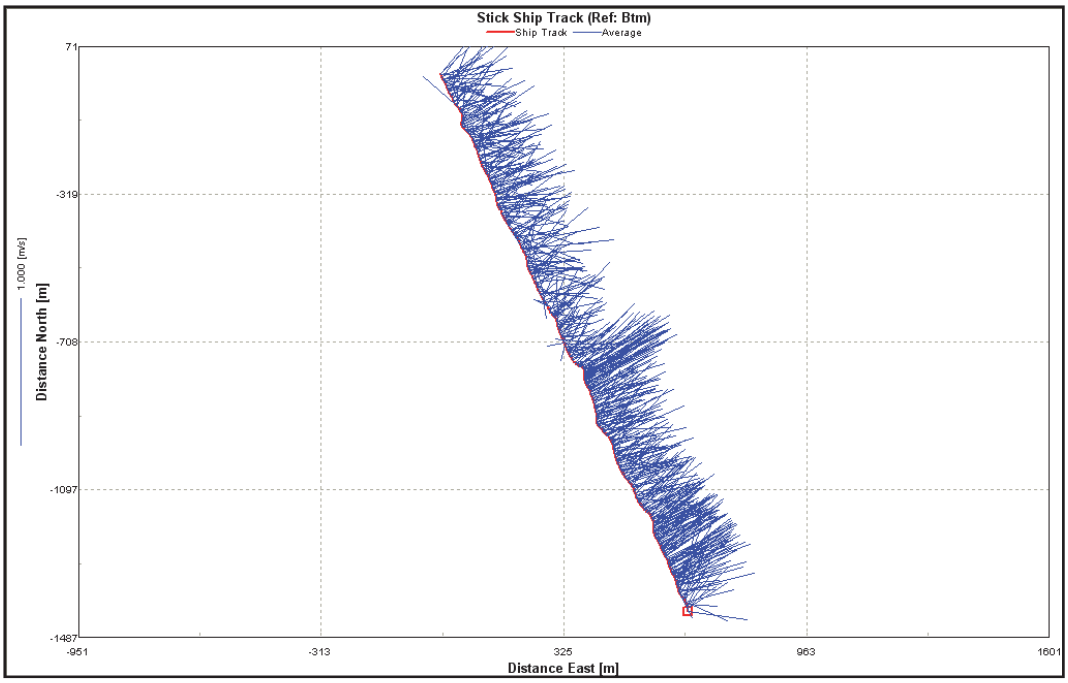

Figure C-38. Pass Aux Herons Transect 12. Shown northwest (top) to southeast (bottom).

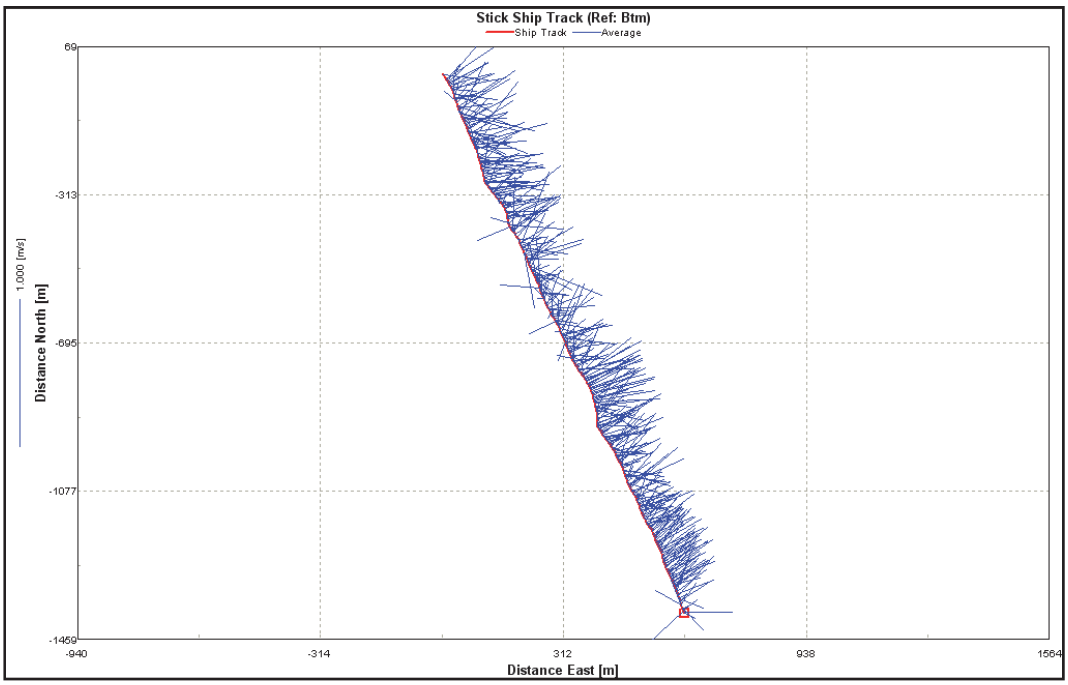

Figure C-39. Pass Aux Herons Transect 13. Shown northwest (top) to southeast (bottom).

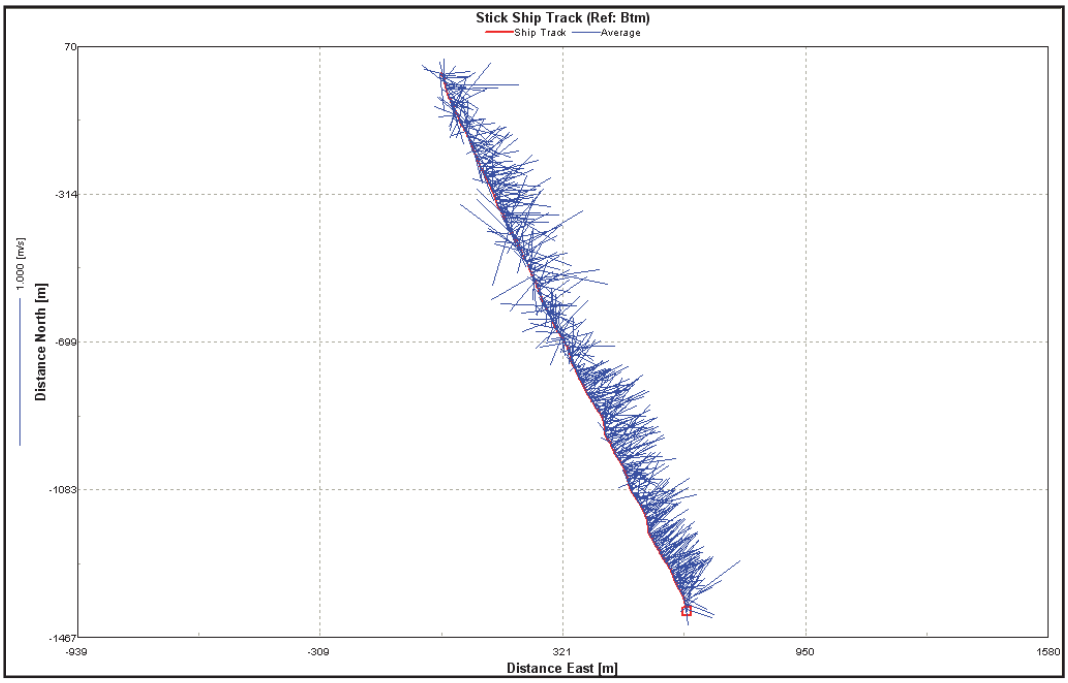

Figure C-40. Pass Aux Herons Transect 14. Shown northwest (top) to southeast (bottom).

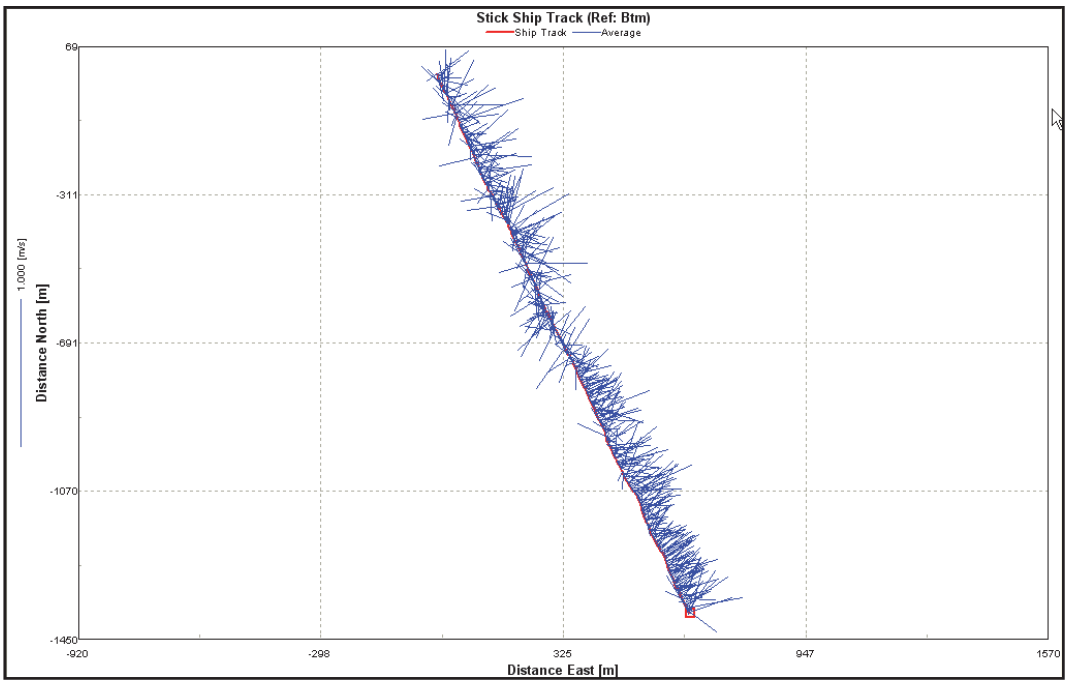

Figure C-41. Pass Aux Herons Transect 15. Shown northwest (top) to southeast (bottom).

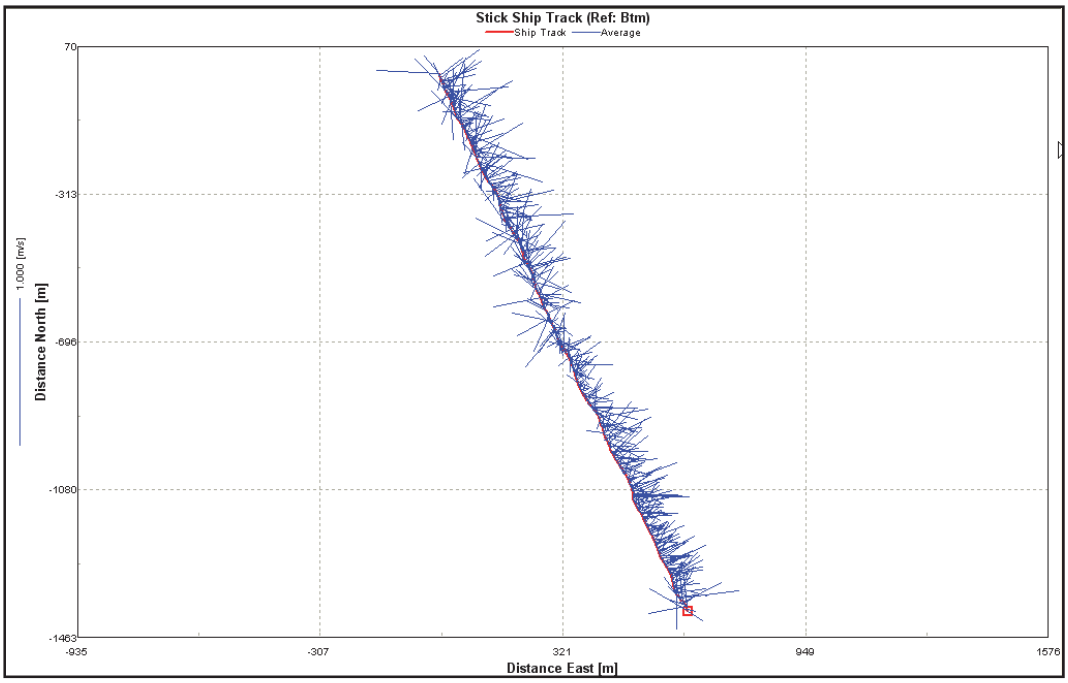

Figure C-42. Pass Aux Herons Transect 16. Shown northwest (top) to southeast (bottom).

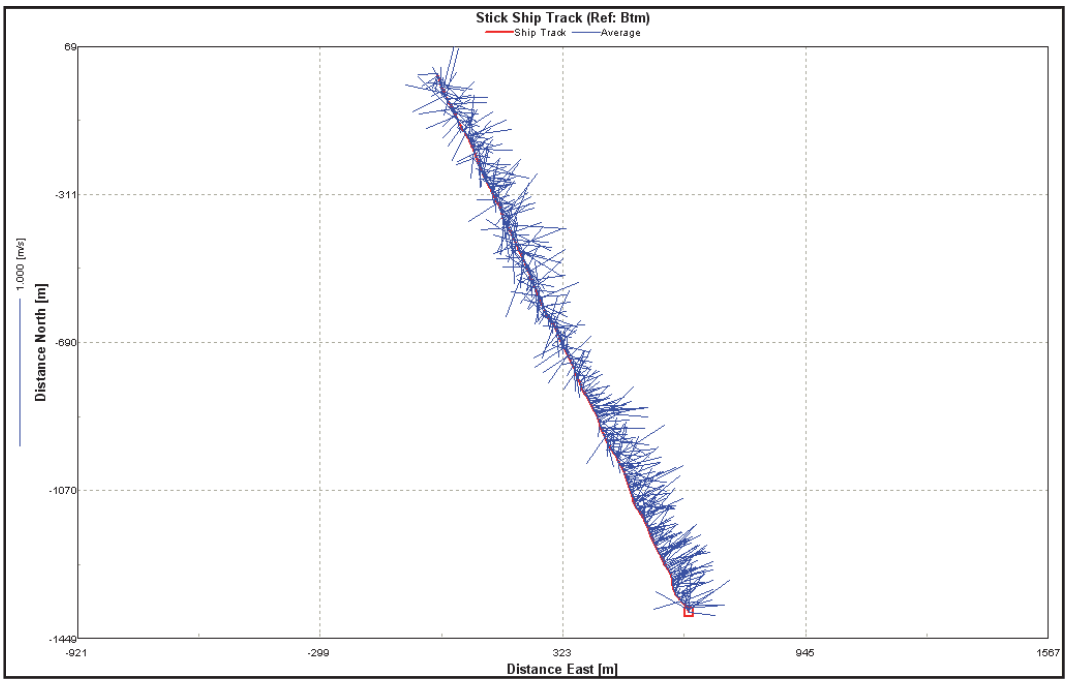

Figure C-43. Pass Aux Herons Transect 17. Shown northwest (top) to southeast (bottom).

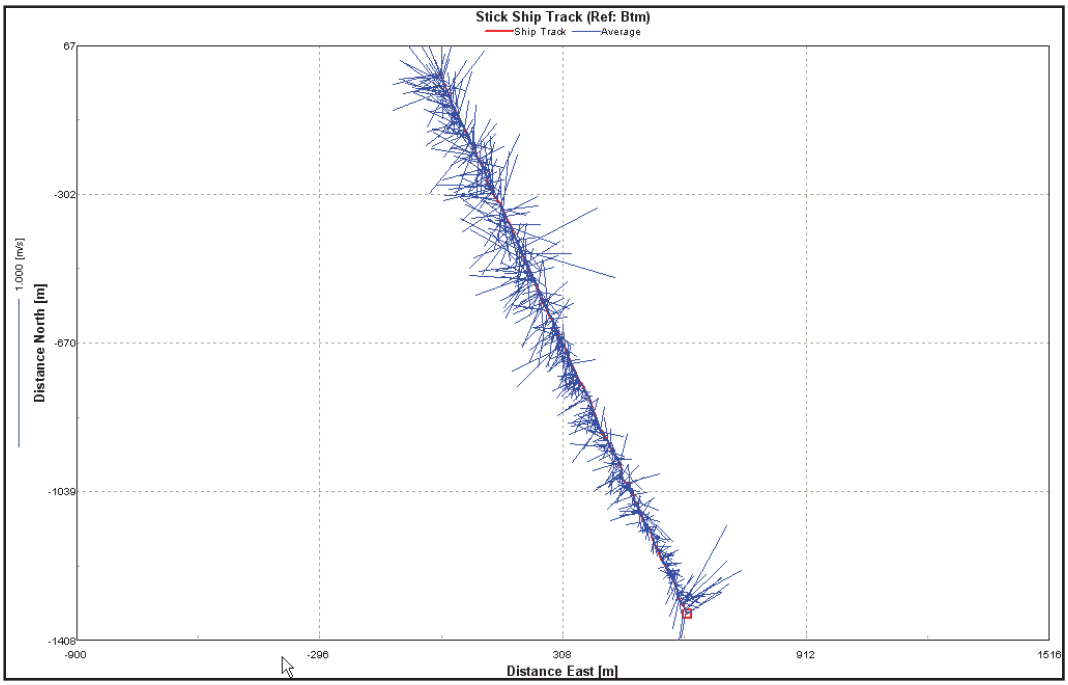

Figure C-44. Pass Aux Herons Transect 18. Shown northwest (top) to southeast (bottom).

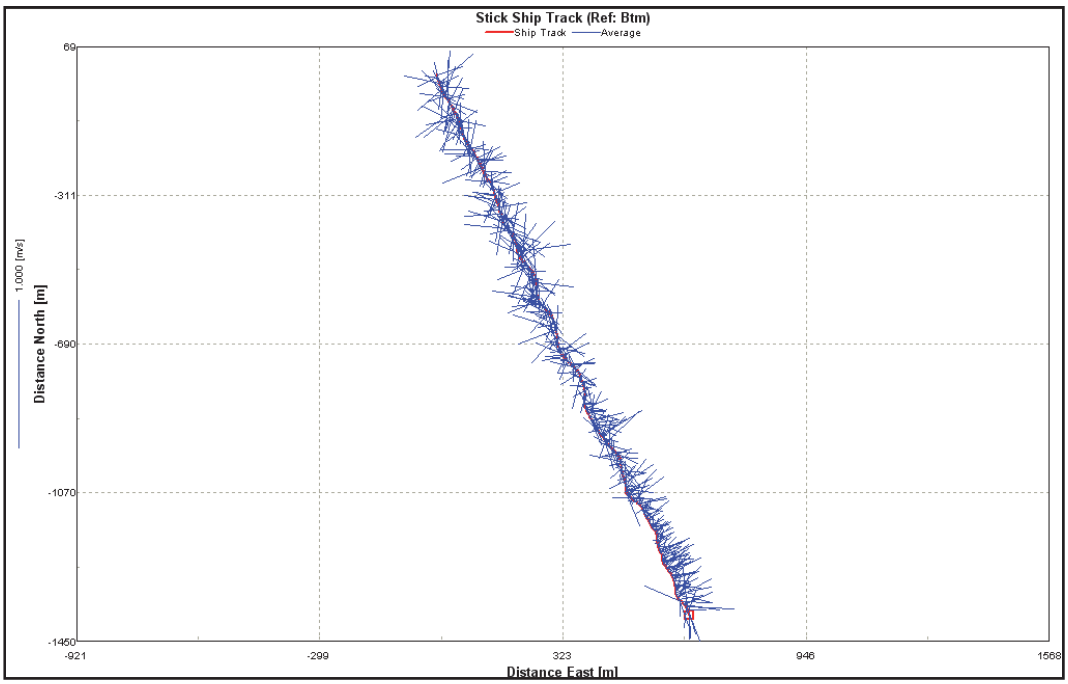

Appendix D: ICM Control and Input Files for Calibration

Control file for WQM

```
TITLE C ……TITLE……
Apply St. John's parallel code to Ship Island pre- Katrina
Code provided by MN in GOLD_STANDARD Jan 17, 2010
Terry's vertical code installed by CFC in terrys_code_FGS Jan 23, 2006
This code brought up from aquarius /disk2/new_ches_bay/Jan_27_06
Run on Jade: Run102910 052610 hydro - added atm loads : Pre-Katrina
102910; SEDNO3 = .05

GEOM DEFINE NB NSB NQF NHQF NSHQF NL
 196820 39364 544951 387495 77499 5

TIME CON TMSTRT TMEND
 0.0 163.5

# DLT NDLT
 1

DLT DAY DLTD DLTD DLTD DLTD DLTD DLTD DLTD DLTD DLTD
 0.0

DLT VAL DLTVAL DLTVAL DLTVAL DLTVAL DLTVAL DLTVAL DLTVAL DLTVAL
 3600.

DLT MAX DLTMAX DLTMAX DLTMAX DLTMAX DLTMAX DLTMAX DLTMAX DLTMAX
 3600.

DLT FTN DLTFTN DLTFTN DLTFTN DLTFTN DLTFTN DLTFTN DLTFTN DLTFTN
 0.70

HM DLT AHMDLT FILGTH
 3600.0 30.0

SNAPSHOT SNPC NSNP
 ON 1

SNAP DAY SNPD SNPD SNPD SNPD SNPD SNPD SNPD SNPD SNPD
 0.0

SNAP FRQ SNPF SNPF SNPF SNPF SNPF SNPF SNPF SNPF SNPF
 5.0

PLOT PLTC QPLTC SPLTC SAVPLTC NPLT
 ON ON OFF OFF 1

PLOT DAY PLTD PLTD PLTD PLTD PLTD PLTD PLTD PLTD PLTD
 0.5

PLOT FREQ PLTF PLTF PLTF PLTF PLTF PLTF PLTF PLTF PLTF
 1.0

AV PLOT APLTC NAPL
 ON 1
```

```
AVPLT DAY APLTD APLTD APLTD APLTD APLTD APLTD APLTD APLTD
 0.0

AVPLT FREQ APLF APLF APLF APLF APLF APLF APLF APLF APLF
 0.125

TRAN FLUX HTFLC VTFLC STFLC NTFL
 OFF OFF OFF 1

FLUX DAY TFLD TFLD TFLD TFLD TFLD TFLD TFLD TFLD TFLD
 0.0

FLUX FREQ TFLF TFLF TFLF TFLF TFLF TFLF TFLF TFLF TFLF
 30.41

KIN FLUX KFLC NKFL
 ON 7

FLUX DAY KFLD KFLD KFLD KFLD KFLD KFLD KFLD KFLD KFLD
 0.0 30.0 60.0 90.0 120.0 150.0 170.0

FLUX FREQ KFLF KFLF KFLF KFLF KFLF KFLF KFLF KFLF KFLF
 365.25 365.25 365.25 365.25 365.25 365.25 365.25

OXY PLOT OPLC NOPL NOINT
 ON 1 4

OXY INT OINT OINT OINT OINT OINT OINT OINT OINT OINT
 -10.0 0.211 2.11 5.11

OXY DAY OPLD OPLD OPLD OPLD OPLD OPLD OPLD OPLD OPLD
 .0208333

OXY FREQ OPLF OPLF OPLF OPLF OPLF OPLF OPLF OPLF OPLF
 .0416667

MASS BAL MBLC NMBL
 OFF 1

MBL DAY MBLD MBLD MBLD MBLD MBLD MBLD MBLD MBLD MBLD
 0.0

MBL FREQ MBLF MBLF MBLF MBLF MBLF MBLF MBLF MBLF MBLF
 365.0

DIAGNSTCS DIAC NDIA
 ON 1

DIA DAY DIAD DIAD DIAD DIAD DIAD DIAD DIAD DIAD DIAD
 0.

DIA FREQ DIAF DIAF DIAF DIAF DIAF DIAF DIAF DIAF DIAF
 1.00

RESTART RSOC NRSO RSIC
 OFF 1 OFF

RST DAY RSOD RSOD RSOD RSOD RSOD RSOD RSOD RSOD RSOD
 360.0

HYD MODEL HYDC
 BINARY
```

```
HYD SOLTN SLC CONSC TH MINSTEP
 QUICKEST MASS 0.55 5.0

CONTROLS SEDC AUTOC VBC BFOC STLC ICIC ICOC SAVMC
 OFF ON ON OFF ON UNIFORM ON OFF

CONTROLS SUSFDC DEPFDC KEIMC SEDKIN
 OFF OFF P_ABS SSI

DEAD SEA FLC XYDFC ZDFC
 ON ON ON

HDIFF XYDF ZDFMUL
 1.0 1.00

CST INPUT S1C S2C S3C BFC ATMC SAVLC SEDTR ROMS
 OFF OFF OFF ON ON OFF OFF OFF

NUTR RED REDS1C REDS1N REDS1P REDS2C REDS2N REDS2P REDS3C REDS3N REDS3P
 1.0 1.0 1.0 1.0 1.0 1.0 1.0 1.0 1.0

NUTR RED REDCBC REDCBN REDCBP
 1.0 1.0 1.0

BOUNDARY BNDTC
 INTERP

ACT CST ACC ACC ACC ACC ACC ACC ACC ACC ACC
 ON ON ON OFF OFF ON OFF OFF ON
 OFF ON OFF ON ON OFF ON OFF ON
 OFF ON ON OFF ON OFF OFF OFF ON
 OFF ON OFF OFF OFF OFF OFF OFF OFF

# FILES NHYDF NTVDF
 7 2

MAP FILE.....MAPFN.....
 map_pre_shipisland10.npt

GEO FILE.....GEOFN.....
 wqmgeo_pre_shipisland10.npt

ICI FILE.....ICIFN.....
 wqm_ici_shipisland10.uni

AGR FILE.....AGRFN.....
 wqm_agr_shipisland10.npt

ZOO FILE.....ZOOFN.....
 wqm_zoo.run156

SUS FILE.....SUSFN.....
 wqm_sfi.run367

STL FILE.....STLFN.....
 wqm_stl_shipisland10.npt

MRL FILE.....MRLFN.....
 wqm_mrl_shipisland.npt

EXT FILE.....EXTFN.....
 wqm_kei_shipisland10.npt
```

HYD FILE.....HYDFN.....
hydro.dat-0498Pre
hydro.dat-0598Pre
hydro.dat-0698Pre
hydro.dat-0798Pre
hydro.dat-0898Pre
hydro.dat-0998Pre
hydro.dat-0998Pre

MET FILE.....METFN.....
mobile_98_shipisland10.npt
mobile_98_shipisland10.npt

S1 FILE.....S1FN.....
wqm_ptsrc.91_Phase51
wqm_ptsrc.92_Phase51

S2 FILE.....S2FN.....
wqm_nps.91_run341
wqm_nps.92_run341

S3 FILE.....S3FN.....
wqm_atm_s3.npt
wqm_atm_s3.npt

ATM FILE.....ATMFN.....
wqm_atm.npt
wqm_atm.npt

SVI FILE.....ATMFN.....
wqm_sav.run399
wqm_sav.run399

CBC FILE.....CBCFN.....
wq_shipisland10_bc_090710.npt
wq_shipisland10_bc_090710.npt

BFI FILE.....BFIFN.....
wqm_bfi_shipisland10_pre_101510.npt
wqm_bfi_shipisland10_pre_101510.npt

ICO FILE.....ICOFN.....
wqm_ico_shipisland10_090210.npt

SNP FILE.....SNPFN.....
wqm_snp_shipisland10_pre_run102910_f.opt

RSO FILE.....RSOFN.....
wqm_rso_shipisland10_pre_run102910_f.opt

PLT FILE.....PLTFN.....
wqm_plt_shipisland10_pre_run102910_f.opt

APL FILE.....APLFN.....
wqm_apl_shipisland10_pre_run102910_f.opt

DIA FILE.....DIAFN.....
wqm_dia_shipisland10_pre_run102910_f.opt

TFL FILE.....TFLFN.....
wqm_tfl_shipisland10_pre_run102910_f.opt

KFL FILE.....KFLFN.....
wqm_kfl_shipisland10_pre_run102910_f.opt

OPL FILE.....OPLFN.....
wqm_opl_shipisland10_pre_run102910_f.opt

MBL FILE.....MBLFN.....
wqm_mbl_shipisland10_pre_run102910_f.opt

ALO FILE.....ALOFN.....
wqm_alo_shipisland10_pre_run102910_f.opt

ZFO FILE.....ZFOFN.....
wqm_zfo_shipisland10_pre_run102910_f.opt

BFO FILE.....BFOFN.....
wqm_bfo_shipisland10_pre_run102910_f.opt

SVO FILE.....BFOFN.....
wqm_svo_shipisland10_pre_run102910_f.opt

SUD FILE.....BFOFN.....
wqm_sfo_shipisland10_pre_run102910_f.opt

Nov 3, 2010.
Ship Island Algal parameters from Gulfport study.
Title line
Title line
Title line
Title line

PREDATN TRPR KTPR
20.0 0.0320

FRACTN N FNIP FNUP FLNDP FNRDP FNLP FNRP
0.40 0.30 0.30 0.00 0.300 0.000

FRACTN P FPIP FPLDP FPRDP FPLP FPRP
0.50 0.00 0.00 0.200 0.000

FRACTN C FDOP FCLDP FCRDP FCLP FCRP
0.00 0.000 0.00 0.750 0.000

FRACTN SI FSAP
0.0

GROUP 1 1 ANC1 APC1 ASC1 STF1
0.167 0.0125 0.000 0.30

GROUP 1 CCHLC1
30.

GROUP 1 2 KHN1 KHNH41 KHP1 KHS1 KHR1 KHST1
0.01 0.001 0.00250 0.00 0.50 0.5

GROUP 1 3 ALPHMN PRSP1 PRPWR
3.15 0.25 2.0

GROUP 1 4 TMP1 TR1
29.0 20.00

GROUP 1 5 KTG11 KTG12 KTB1

```
 0.0050 0.0040 0.0322

GROUP 1 6 FNI1 FNLD1 FNRD1 FNLP1 FNRP1
 0.55 0.20 0.00 0.200 0.050

GROUP 1 7 FPI1 FPLD1 FPRD1 FPLP1 FPRP1
 0.75 0.25 0.00 0.000 0.000

GROUP 1 8 FCLD1 FCRD1 FCLP1 FCRP1
 0.000 0.000 0.000 0.00

GROUP 2 1 ANC2 APC2 ASC2 STF2
 0.167 0.0125 0.300 0.1

GROUP 2 CCHLC2
 75.0

GROUP 2 2 KHN2 KHNH42 KHP2 KHS2 KHR2 KHST2
 0.025 0.001 0.0025 0.03 0.5 2.0

GROUP 2 3 ALPHMN PRSP2 PRPWR
 8.00 0.25 2.0

GROUP 2 4 TMP2 TR2
 16.0 20.00

GROUP 2 5 KTG21 KTG22 KTB2
 0.0018 0.0060 0.0322

GROUP 2 6 FNI2 FNLD2 FNRD2 FNLP2 FNRP2
 0.55 0.20 0.00 0.200 0.050

GROUP 2 7 FPI2 FPLD2 FPRD2 FPLP2 FPRP2
 0.75 0.25 0.00 0.000 0.000

GROUP 2 8 FCLD2 FCRD2 FCLP2 FCRP2
 0.100 0.00 0.100 0.000

GROUP 3 1 ANC3 APC3 ASC3 STF3
 0.175 0.0175 0.100 0.00

GROUP 3 CCHLC3
 100.

GROUP 3 2 KHN3 KHNH43 KHP3 KHS3 KHR3 KHST3
 0.050 0.100 0.0050 0.001 0.50 35.0

GROUP 3 3 ALPHMN PRSP3 PRPWR
 8.00 0.25 2.0

GROUP 3 4 TMP3 TR3
 30.0 20.00

GROUP 3 5 KTG31 KTG32 KTB3
 0.00350 0.01000 0.0320

GROUP 3 6 FNI3 FNLD3 FNRD3 FNLP3 FNRP3
 0.70 0.20 0.00 0.300 0.000

GROUP 3 7 FPI3 FPLD3 FPRD3 FPLP3 FPRP3
 0.60 0.20 0.00 0.200 0.000

GROUP 3 8 FCLD3 FCRD3 FCLP3 FCRP3
```

```
 0.000 0.000 0.000 0.00

GROUP 1 SPVAR1 PRINT1
 CONSTANT NO

 BOX PM1 BMR1 BPR1
 1 0.0 0.030 0.000

GROUP 2 SPVAR2 PRINT2
 CONSTANT NO

 BOX PM2 BMR2 BPR2
 1 0.0 0.010 0.215

GROUP 3 SPVAR3 PRINT3
 CONSTANT NO

 BOX PM3 BMR3 BPR3
 1 150.0 0.030 0.220

PREDATN TPVAR PRINT
 CONSTANT ALL

 DAY TVPR
 1 1.000

GROUP 2 TB2GR PRINT
 CONSTANT ALL

 DAY TB2G2
 1 1.00


Ship Island Uniform Initial Conditions for Large grid
No sediment model 11-04-10

INIT CONC CIC CIC CIC CIC CIC CIC CIC CIC CIC
 18.4 10.0 0.0 0.0 0.0 0.02 0.00 0.0 7.00
 0.0 0.0 0.00 0.12 0.02 0.0 0.0 .0000 0.0
 0.0 0.16 0.0045 0.0005 0.0 0.0 0.0050 0.0 8.3
 0.0 0.0 0.0 0.0 0.0 0.0 0.0 0.0 0.0


Linear model ke = a + b TSS. March 7, 2002
KE a linear function of chlorophyll

 INTKE INITKE KECHL
 0.5 0.1 0.02

 SPVARKE PRINTKE
 CONSTANT NO

 CELL KE KEISS KEDOC
 1 1.0000 0.0800 0.0000


Ship Island using Gulfport values
Direct PO4 settling 1 m/d.

HALF SAT KHONT KHNNT KHOCOD KHODOC KHNDN
 3.0 1.0 0.500 0.5 0.1
```

```
RATIOS AOCR AONT
 2.67 4.33

REF T RESP TRCOD TRMNL TRHDR TRSUA
 23.0 20.0 20.0 20.0

TEMP EFF KTCOD KTMNL KTHDR KTSUA
 0.041 0.069 0.069 0.092

NITRIF T KTNT1 KTNT2 TMNT
 0.090 0.090 30.0

SORPTION KADPO4 KADSA JBSPO4 JESPO4
 0.0 0.0 255.0 285.0

MISC AANOX ANDC
 0.5 0.933

REAER AREAR BREAR CREAR
 0.156 1.5 1.5

 SPVAR PRINT
 CONSTANT NO

 KLDC
 0.0100

 SPVAR PRINT
 CONSTANT NO

 KRDC
 0.000

 SPVAR PRINT
 CONSTANT NO

 KLPC
 0.020

 SPVAR PRINT
 CONSTANT NO

 KRPC
 0.005

 SPVAR PRINT
 CONSTANT NO

 KLDN
 0.052

 SPVAR PRINT
 CONSTANT NO

 KRDN
 0.000

 SPVAR PRINT
 CONSTANT NO

 KLPN
 0.150
```

SPVAR PRINT
CONSTANT NO

KRPN
0.000

SPVAR PRINT
CONSTANT NO

KLDP
0.100

SPVAR PRINT
CONSTANT NO

KRDP
0.000

SPVAR PRINT
CONSTANT NO

KLPP
0.100

SPVAR PRINT
CONSTANT NO

KRPP
0.000 0.000 0.005 0.000 0.000 0.000 0.000 0.000 0.000

SPVAR PRINT
CONSTANT NO

KSUA
0.030 0.100 0.100 0.000 0.000 0.000 0.000 0.000 0.000

SPVAR PRINT
CONSTANT NO

KCOD
20.000 20.000 20.000 0.000 0.000 0.000 0.000 0.000 0.000

SPVAR PRINT
CONSTANT NO

KDCALG
0.000

SPVAR PRINT
CONSTANT NO

KLCALG
0.000

SPVAR PRINT
CONSTANT NO

KDNALG
0.000

SPVAR PRINT
CONSTANT NO

KLNALG
0.000

SPVAR PRINT
CONSTANT NO

KDPALG
0.400 0.400 0.400 0.000 0.000 0.000 0.000 0.000 0.000

SPVAR PRINT
CONSTANT NO

KLPALG
0.000 0.000 0.000 0.000 0.000 0.000 0.000 0.000 0.000

SPVAR PRINT
CONSTANT NO

NTMAX
0.040 0.040 0.040 0.000 0.000 0.000 0.000 0.000 0.000

Settling Rates
Ship Island values are from Gulfport study (2004)

SPVARM PRINTM
CONSTANT NO

BOX WSS WSLAB WSREF WSC WSD WSG WSPBS WSPO4
1 0.100 0.050 0.000 0.000 0.000 0.050 1.000 0.000

Mobile-Keesler meteorological data comparison

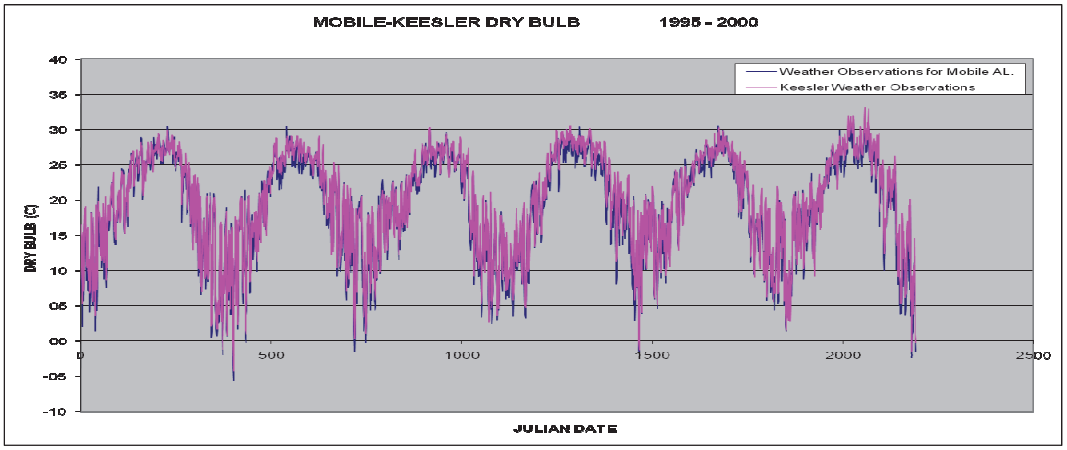

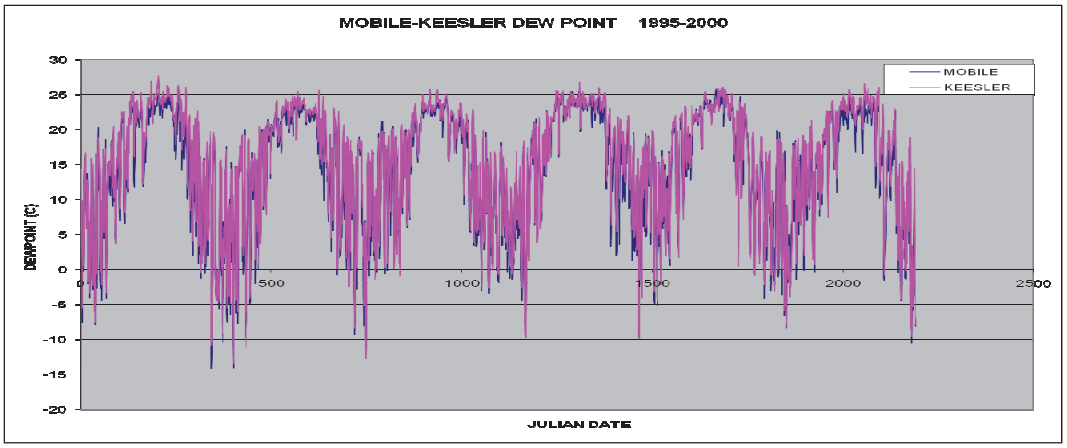

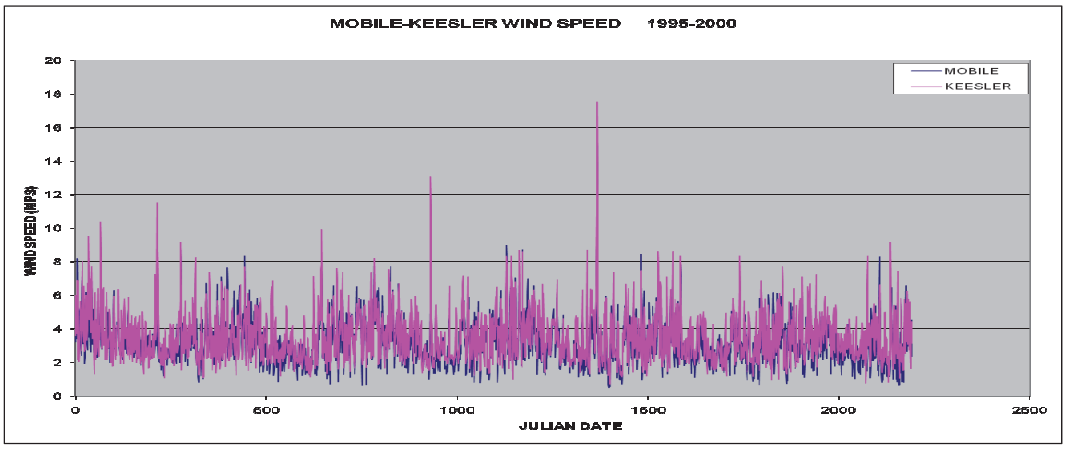

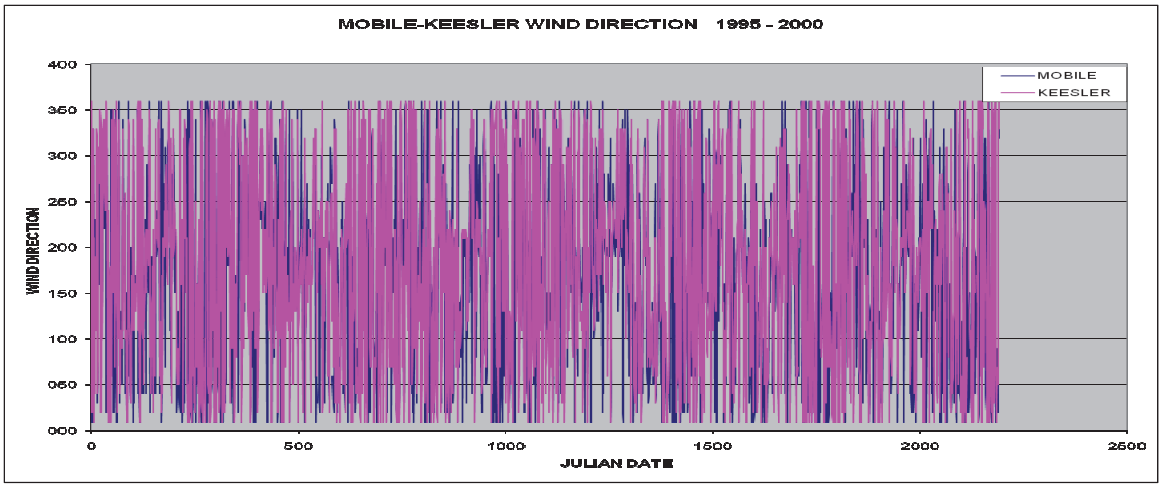
MOBILE-KEESLER WIND DIRECTION 1995 - 2000
MOBILE
KEESLER
WIND DIRECTION
400
350
300
250
200
150
100
050
000
0
500
1000
1500
2000
2500
JULIAN DATE

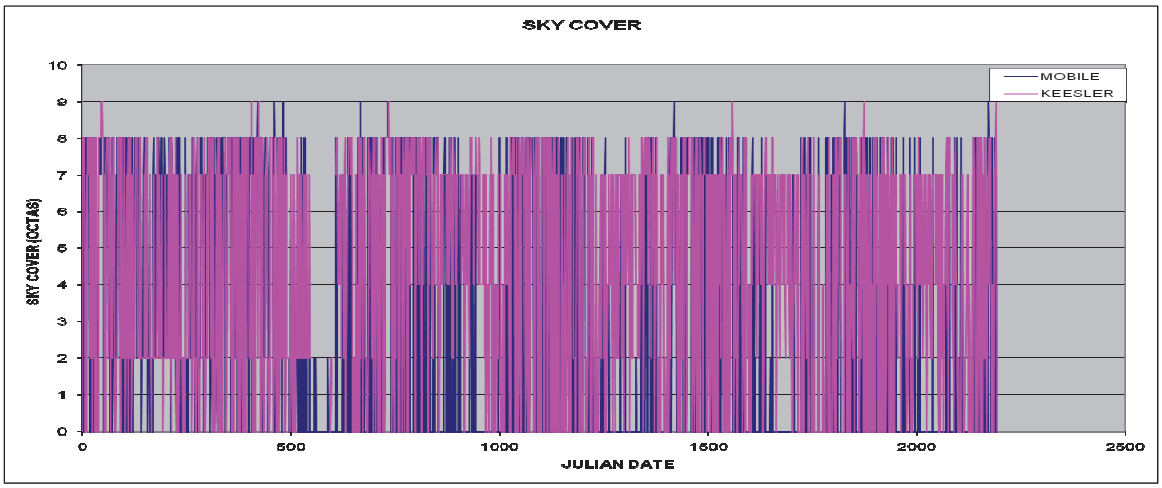
SKY COVER
MOBILE
KEESLER
SKY COVER (OCTAS)
10
9
8
7
6
5
4
3
2
1
0
0
500
1000
1500
2000
2500
JULIAN DATE

Appendix E: Calibration and Scenario Time-Series Results

Figure E-1. Calibration results for temperature at Station 1 for surface layer (upper) and bottom layer (lower).

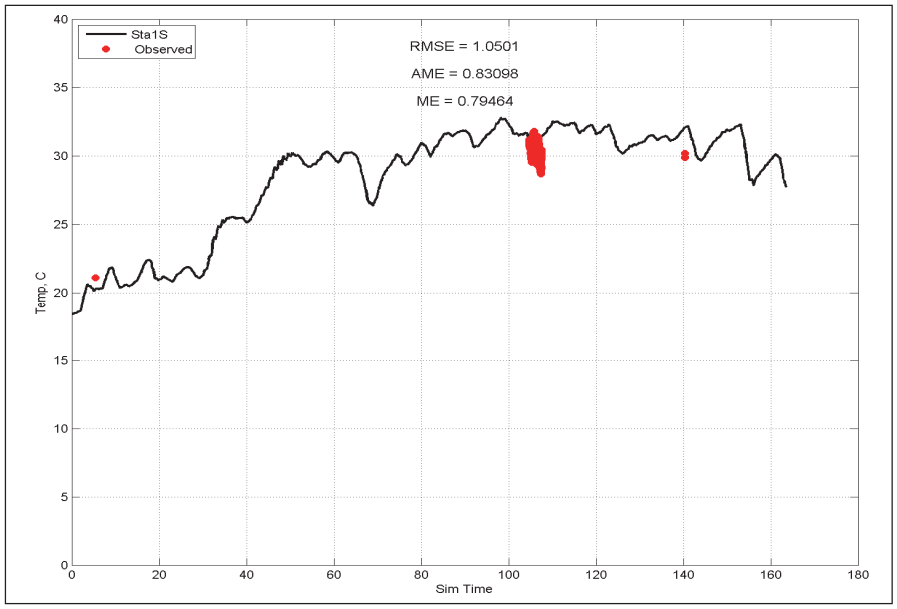

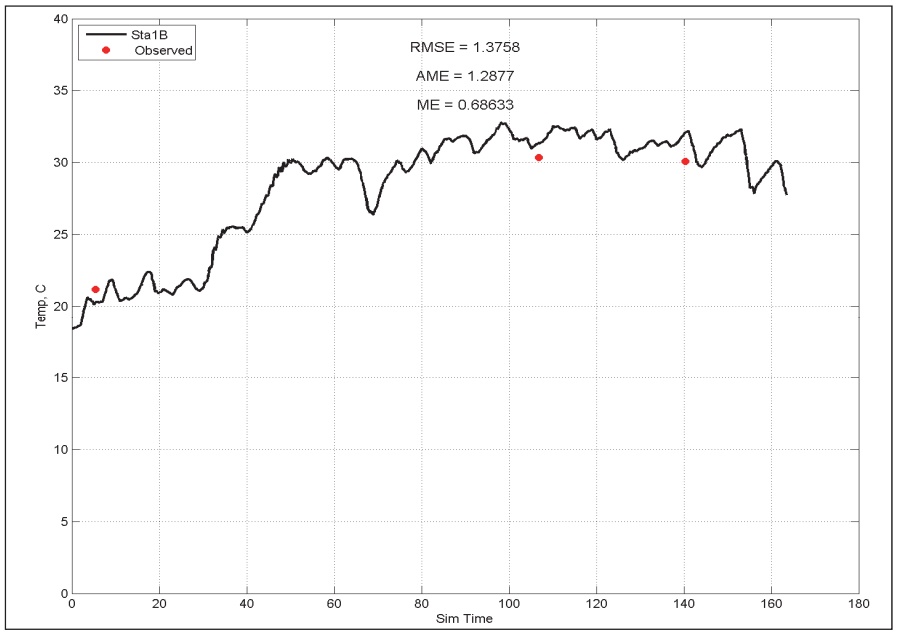

Figure E-2. Calibration results for salinity at Station 1 for surface layer upper) and bottom layer (lower).

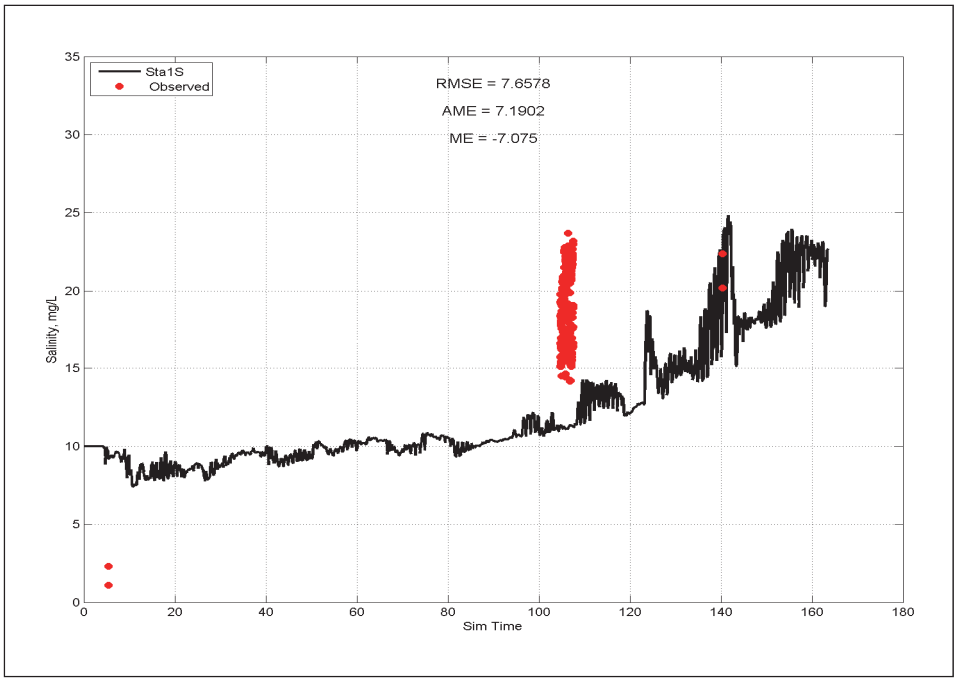

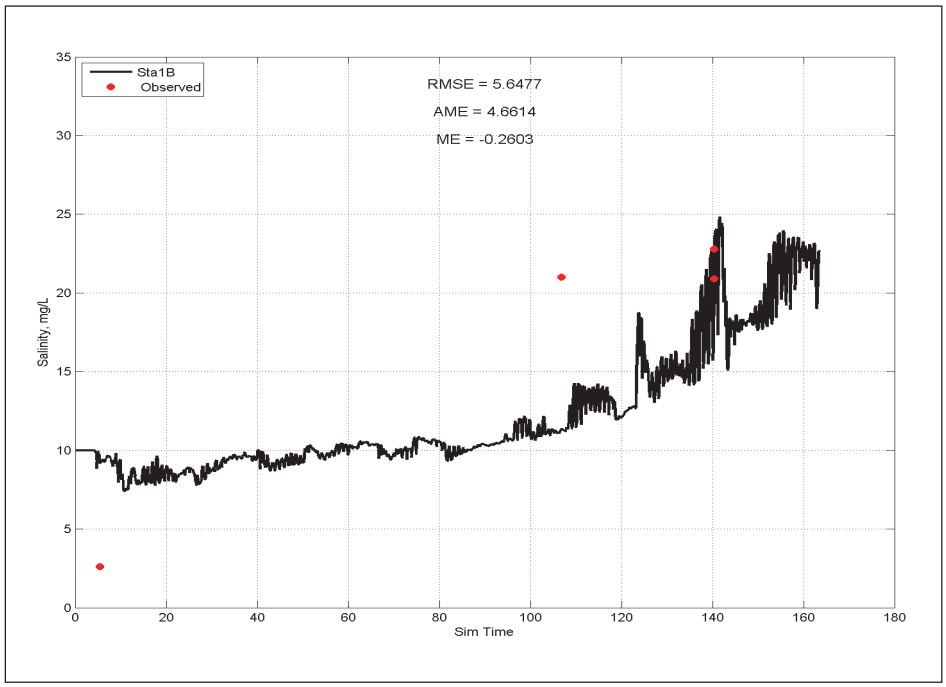

Figure E-3. Calibration results for DO at Station 1 for surface layer (upper) and bottom layer (lower).

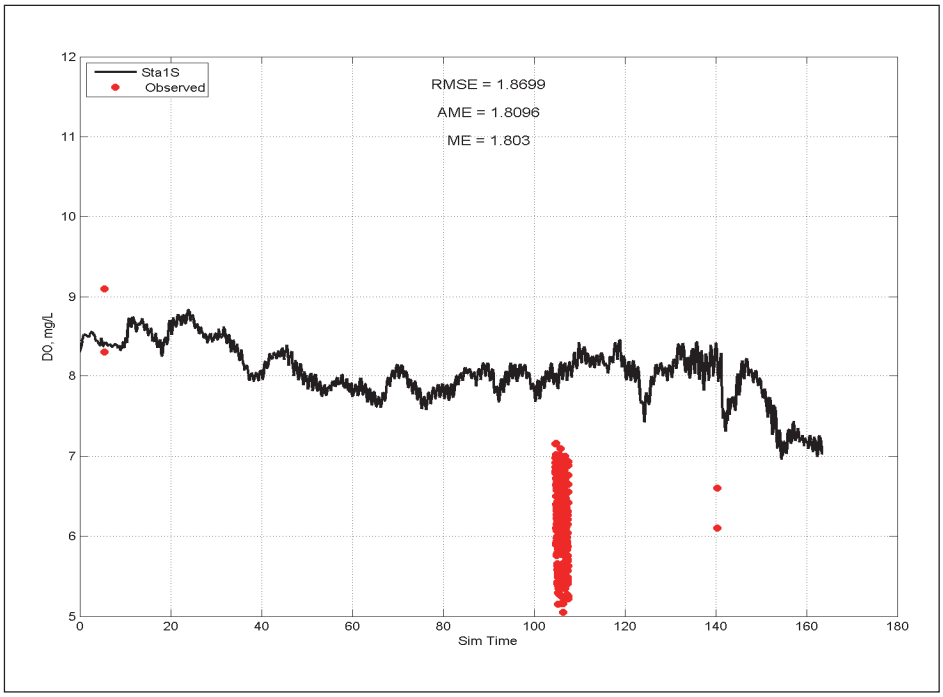

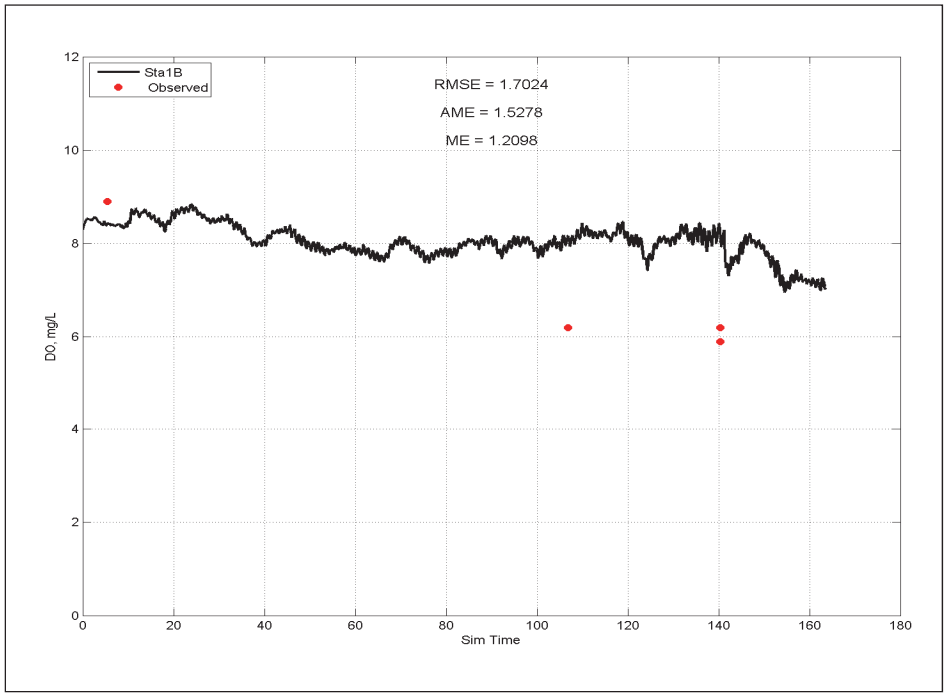

Figure E-4. Calibration results for NH_4 at Station 1 for surface layer upper) and bottom layer (lower).

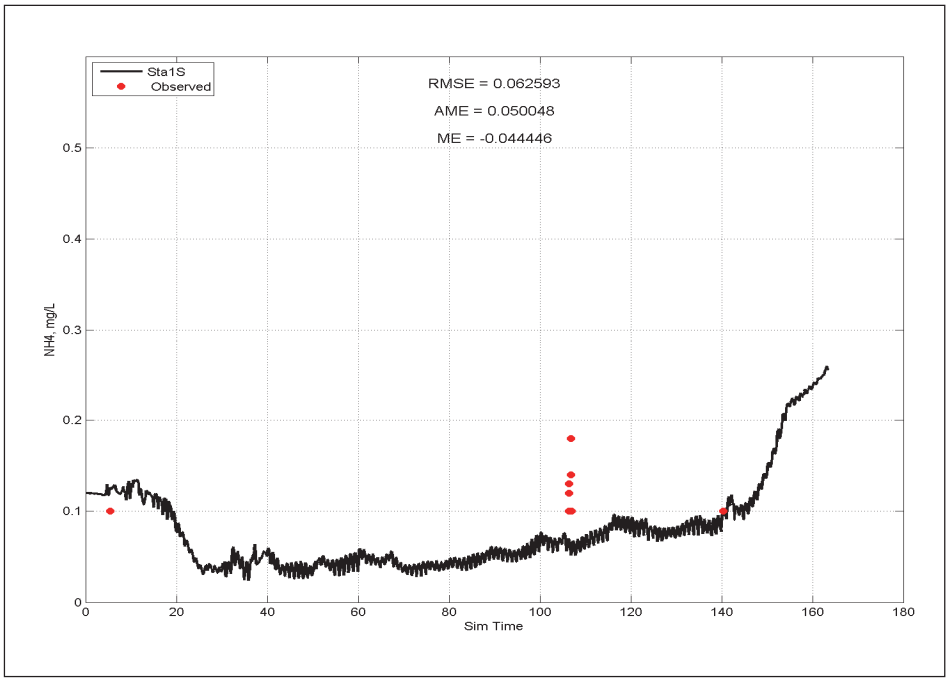

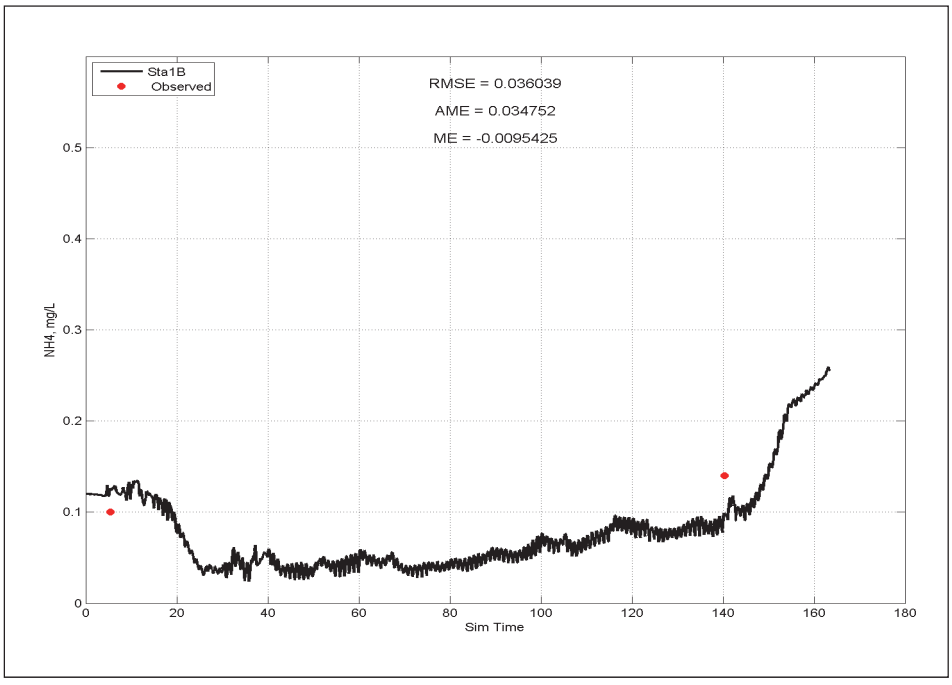

Figure E-5. Calibration results for NO_3 at Station 1 for surface layer (upper) and bottom layer (lower).

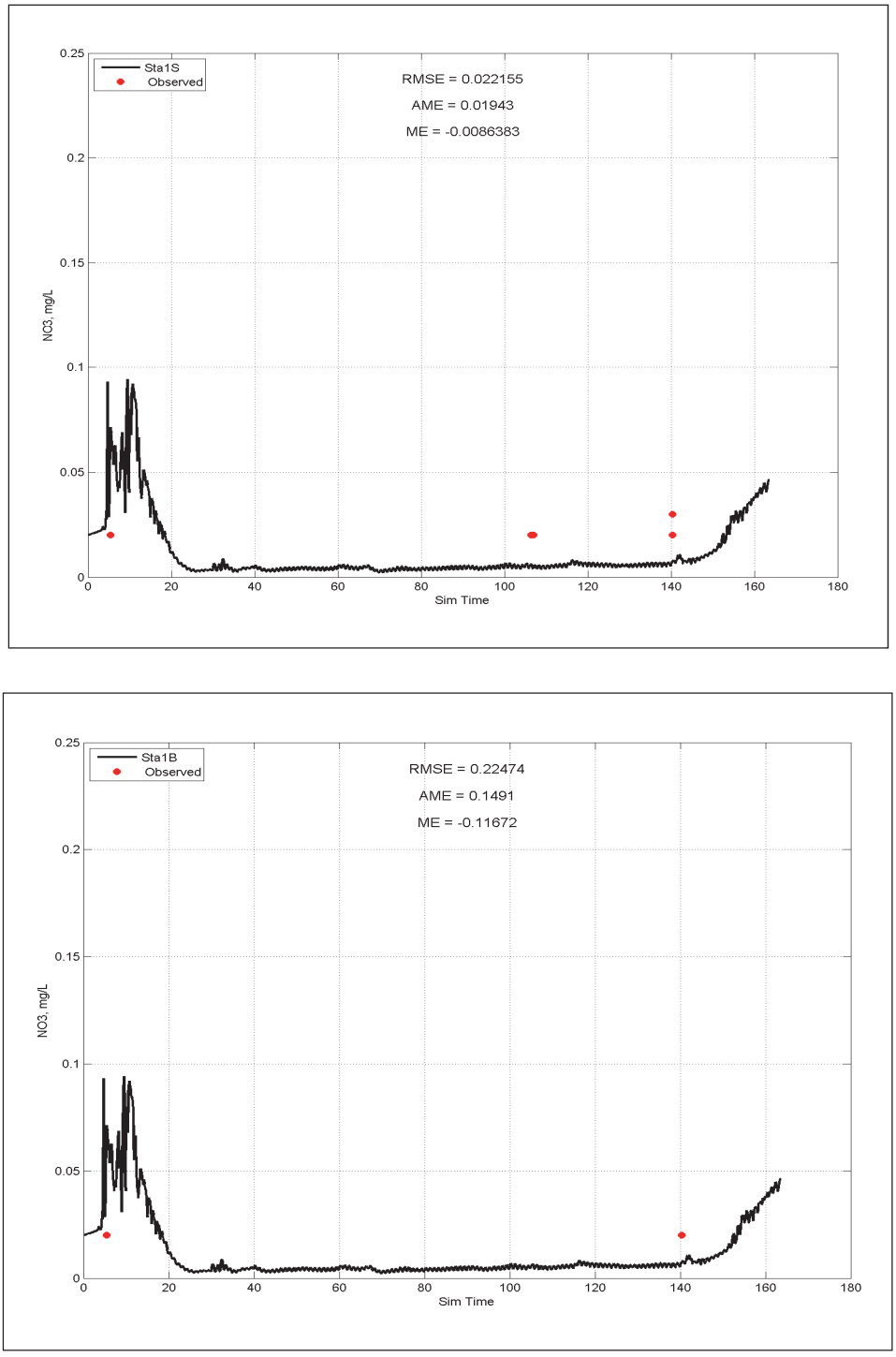

Figure E-6. Calibration results for *Tp* at Station 1 for surface layer (upper) and bottom layer (lower).

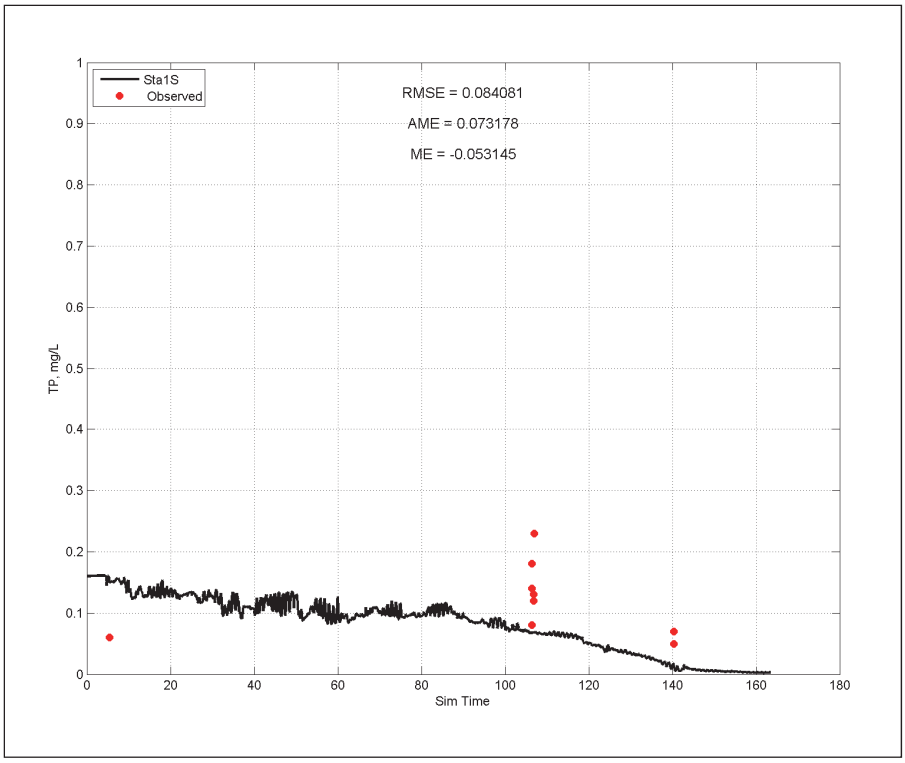

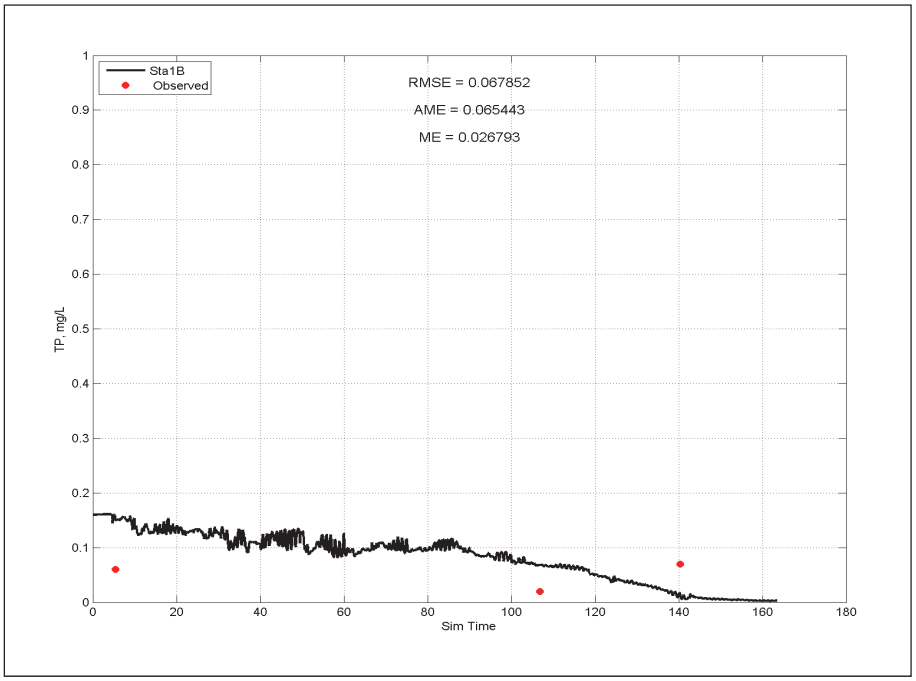

Figure E-7. Calibration results for temperature at Station 2 for surface layer (upper) and bottom layer (lower).

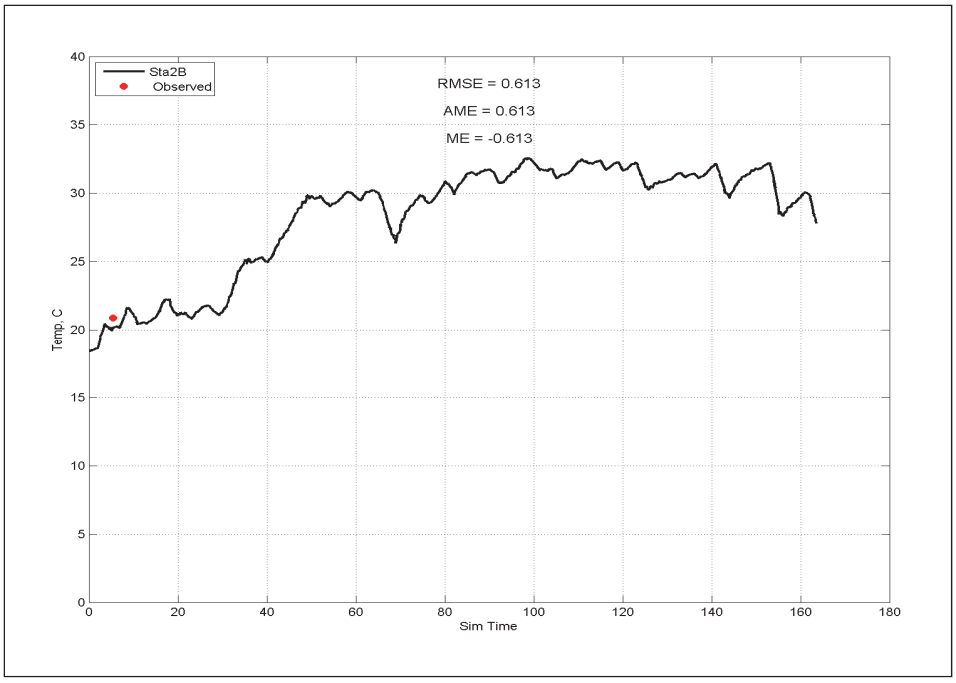

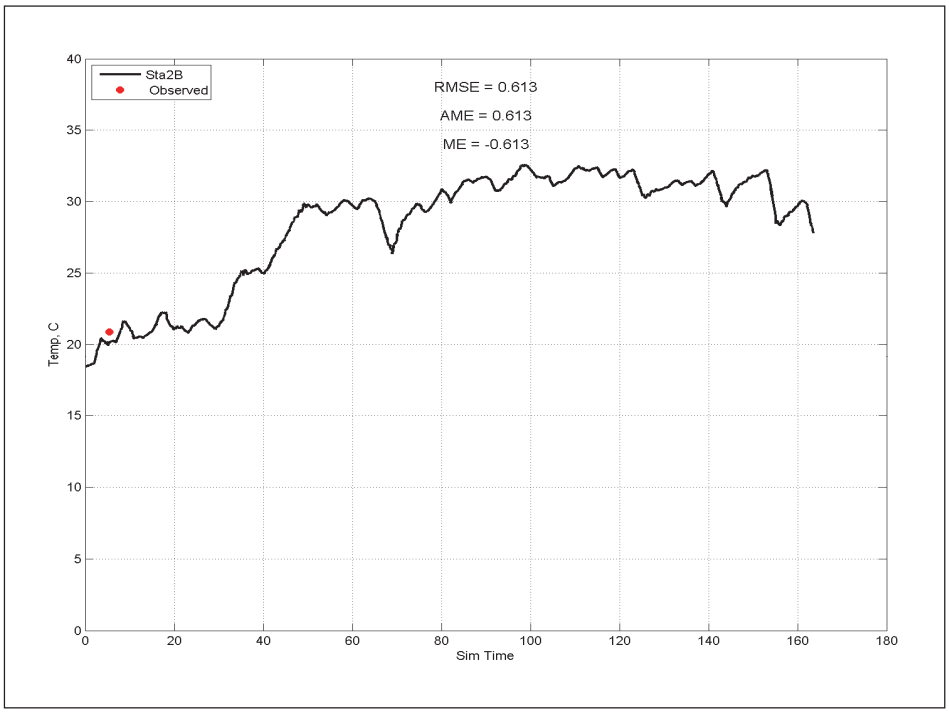

Figure E-8. Calibration results for salinity at Station 2 for surface layer (upper) and bottom layer (lower).

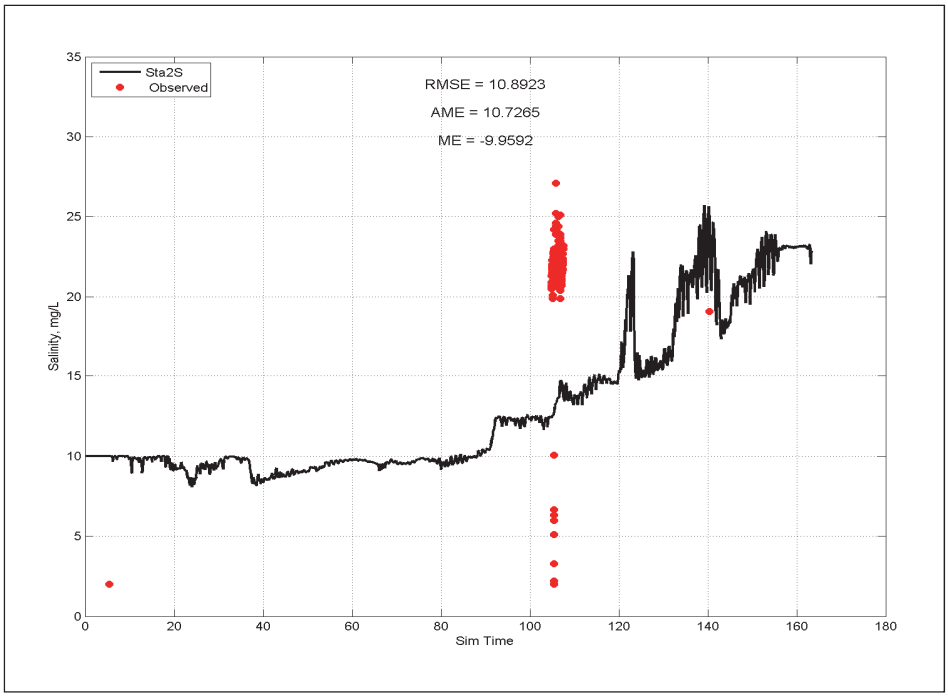

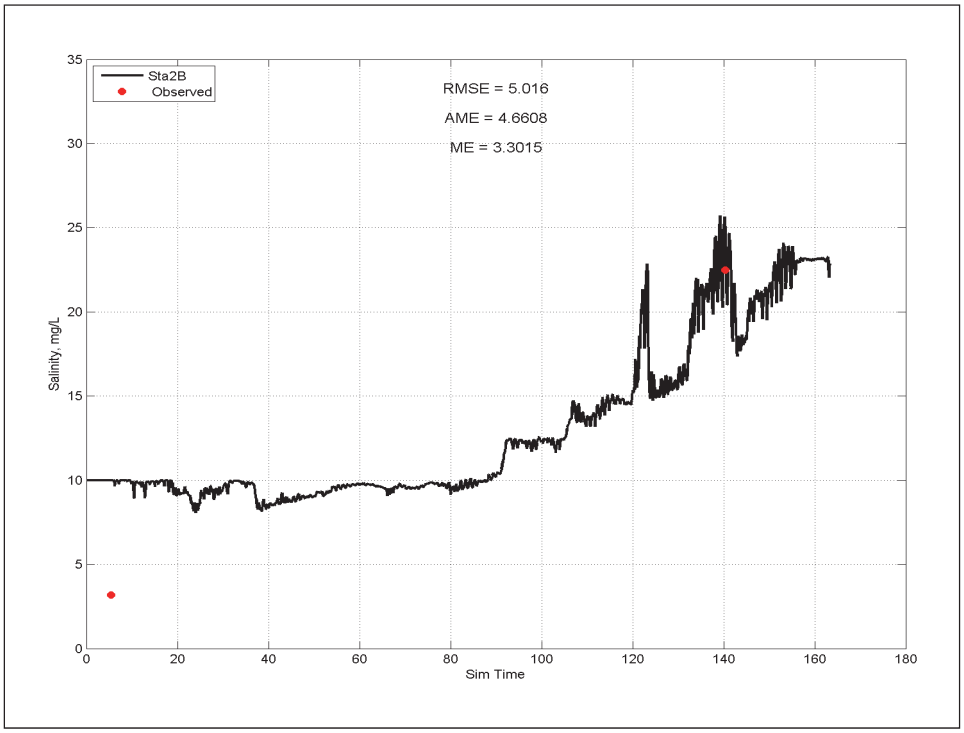

Figure E-9. Calibration results for DO at Station 2 for surface layer (upper) and bottom layer (lower).

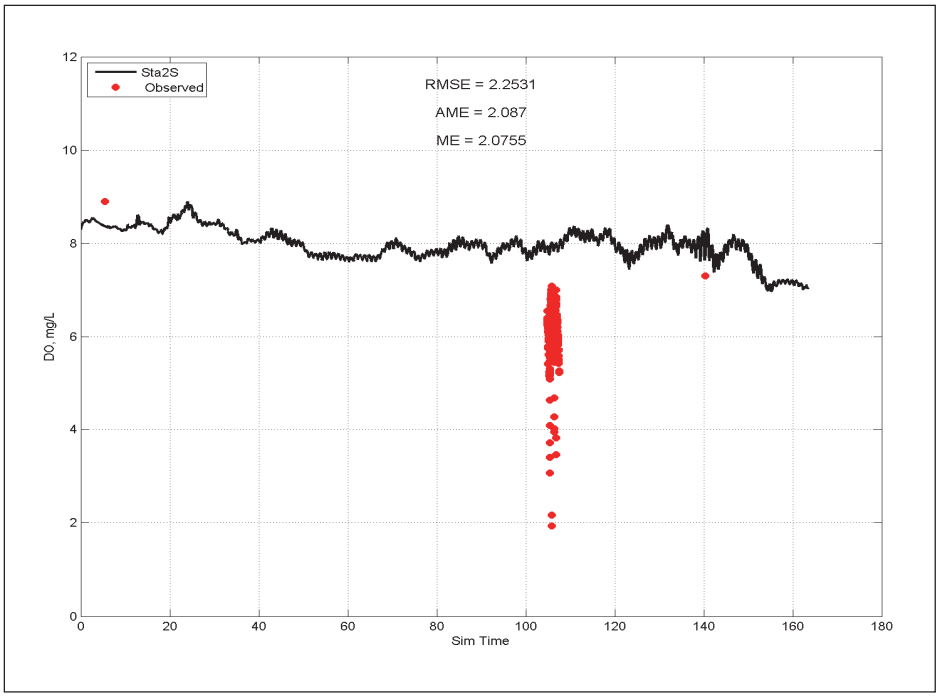

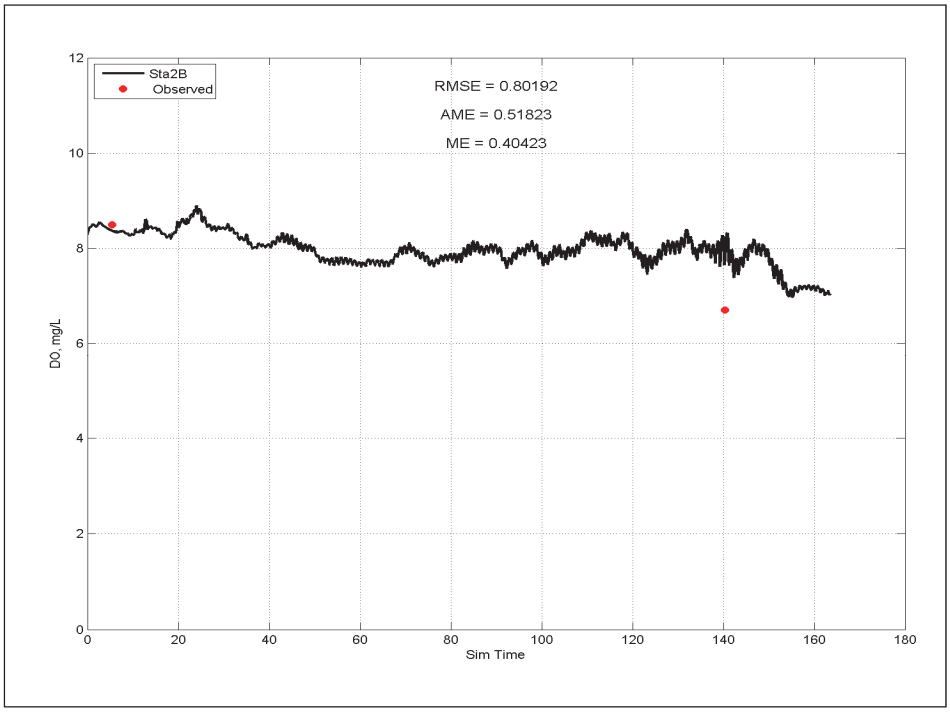

Figure E-10. Calibration results for NH_4 at Station 2 for surface layer (upper) and bottom layer (lower).

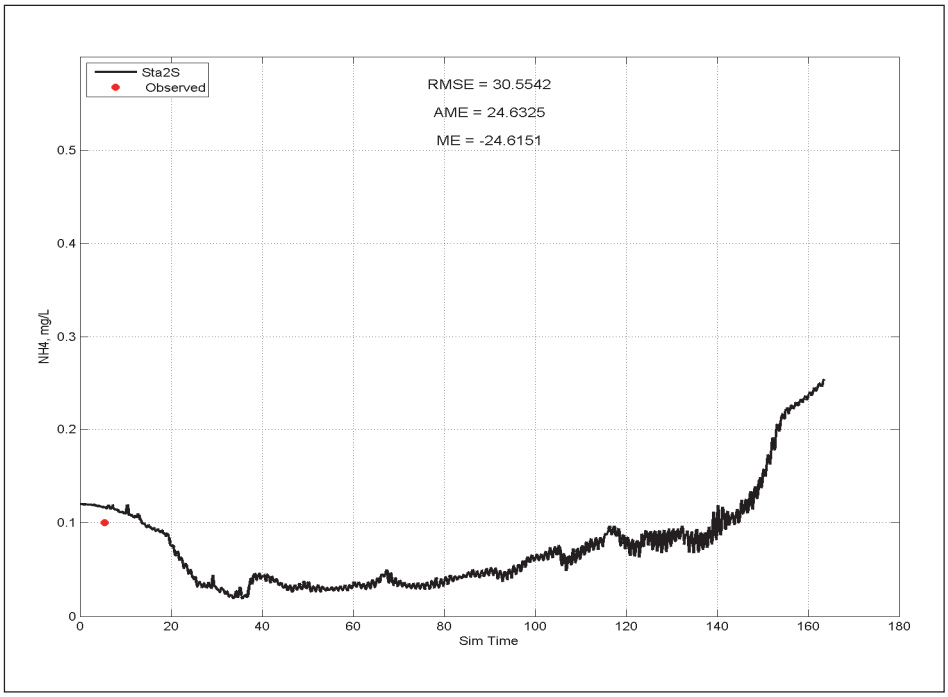

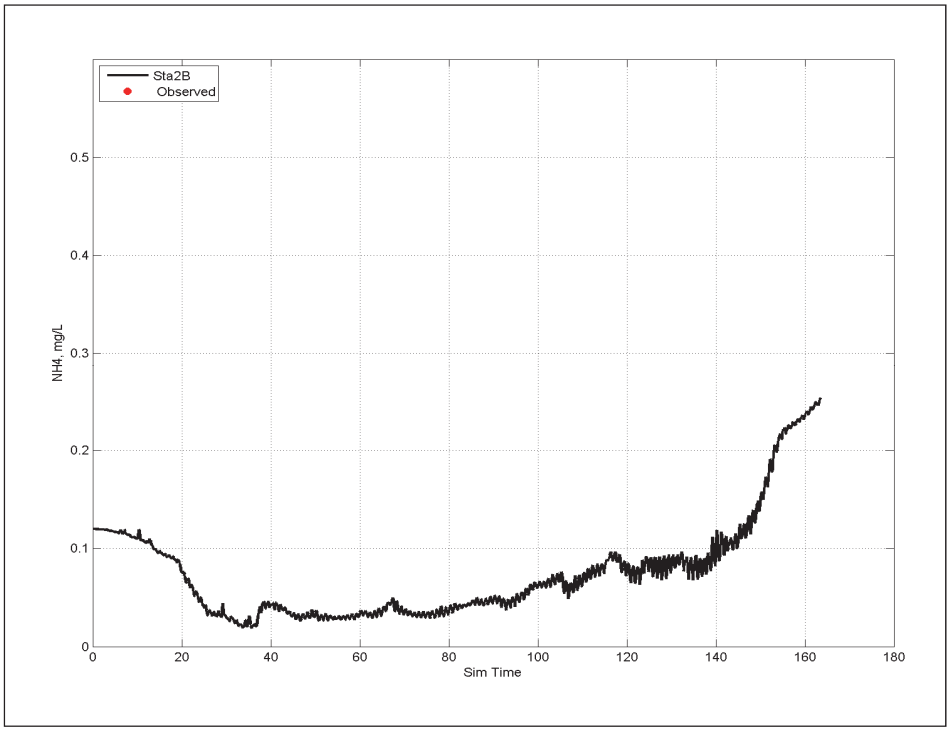

Figure E-11 Calibration results for NO_3 at Station 2 for surface layer (upper) and bottom layer (lower).

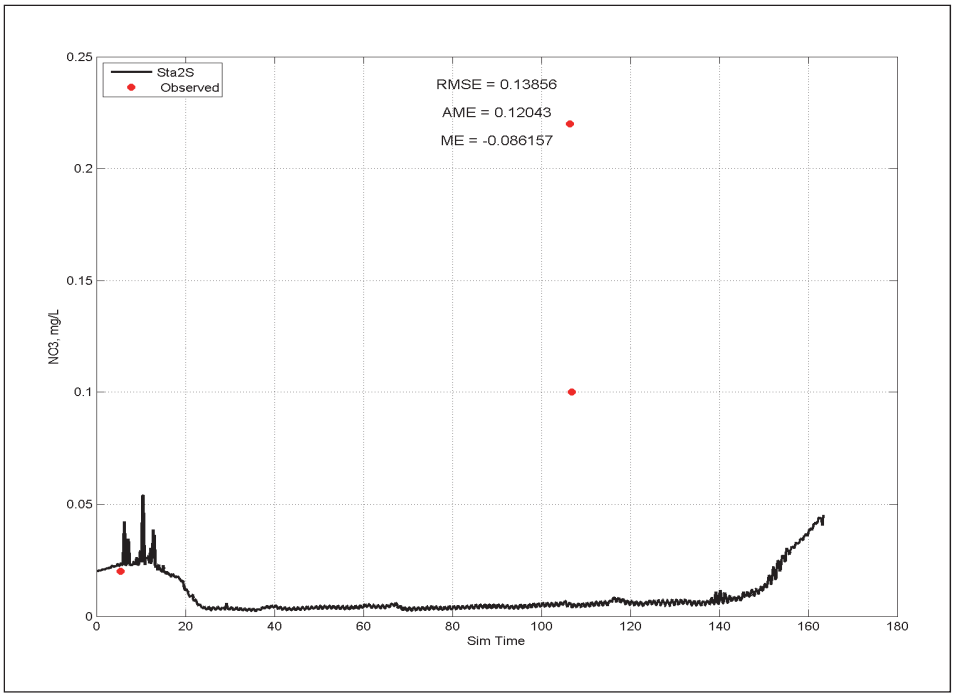

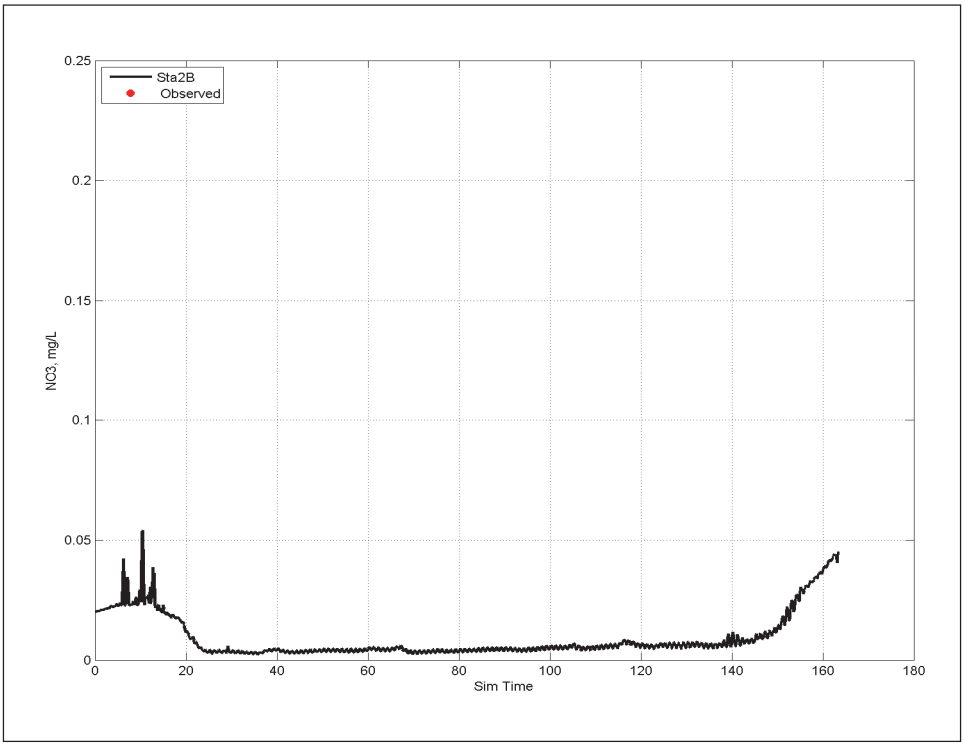

Figure E-12. Calibration results for *Tp* at Station 2 for surface layer (upper) and bottom layer (lower).

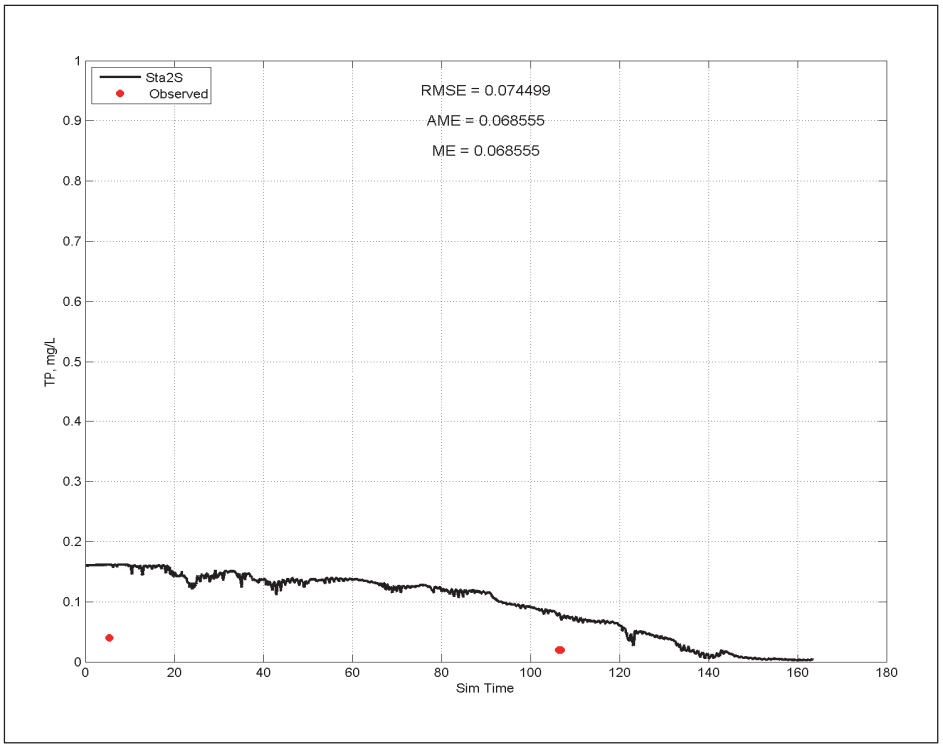

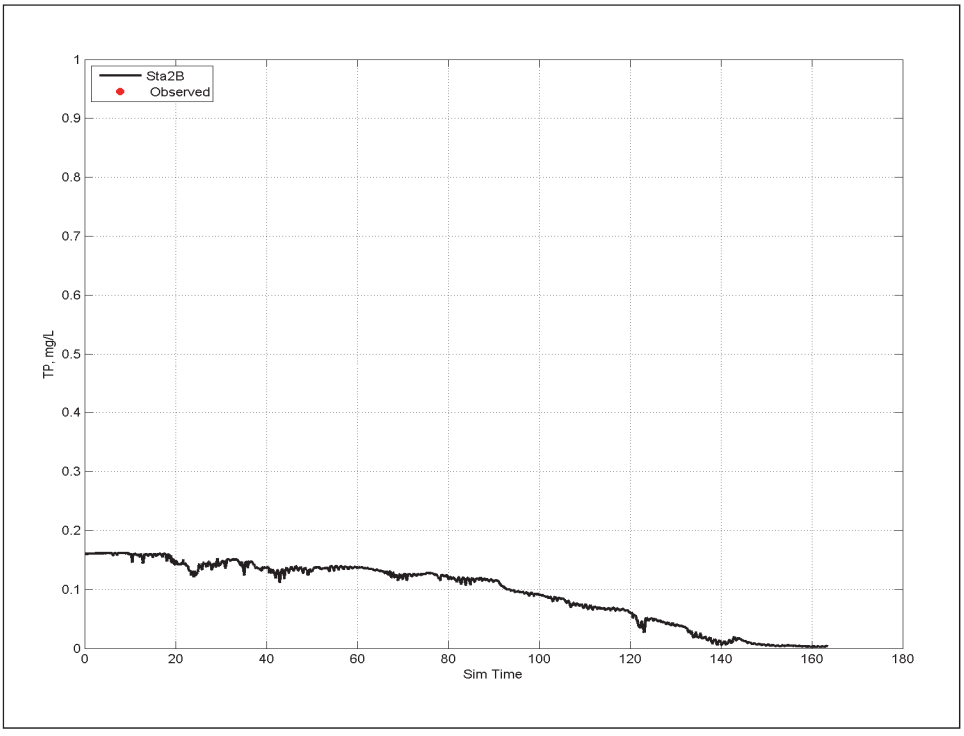

Figure E-13. Calibration results for temperature at Station 3 for surface layer (upper) and bottom layer (lower).

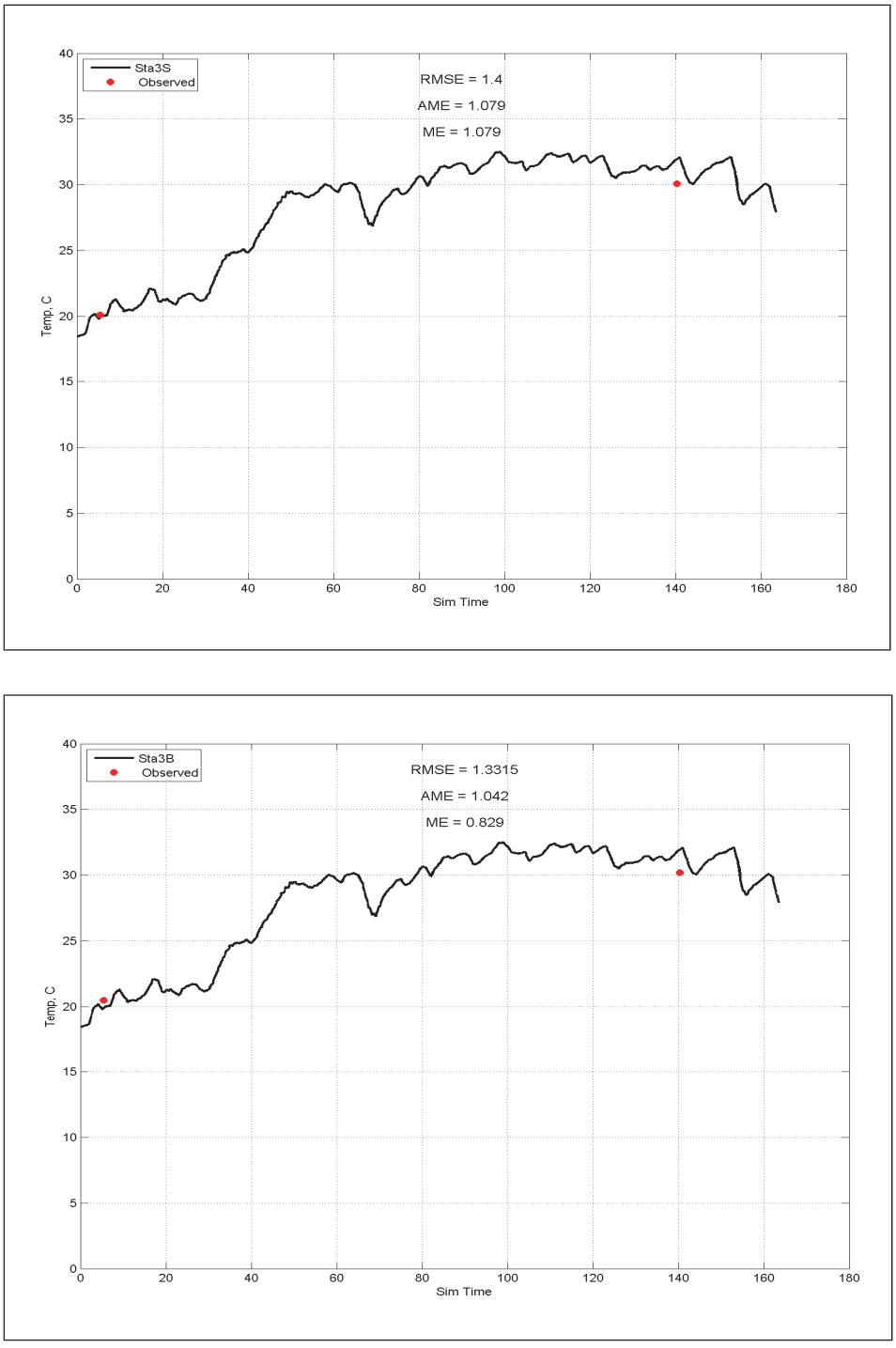

Figure E-14. Calibration results for salinity at Station 3 for surface layer (upper) and bottom layer (lower).

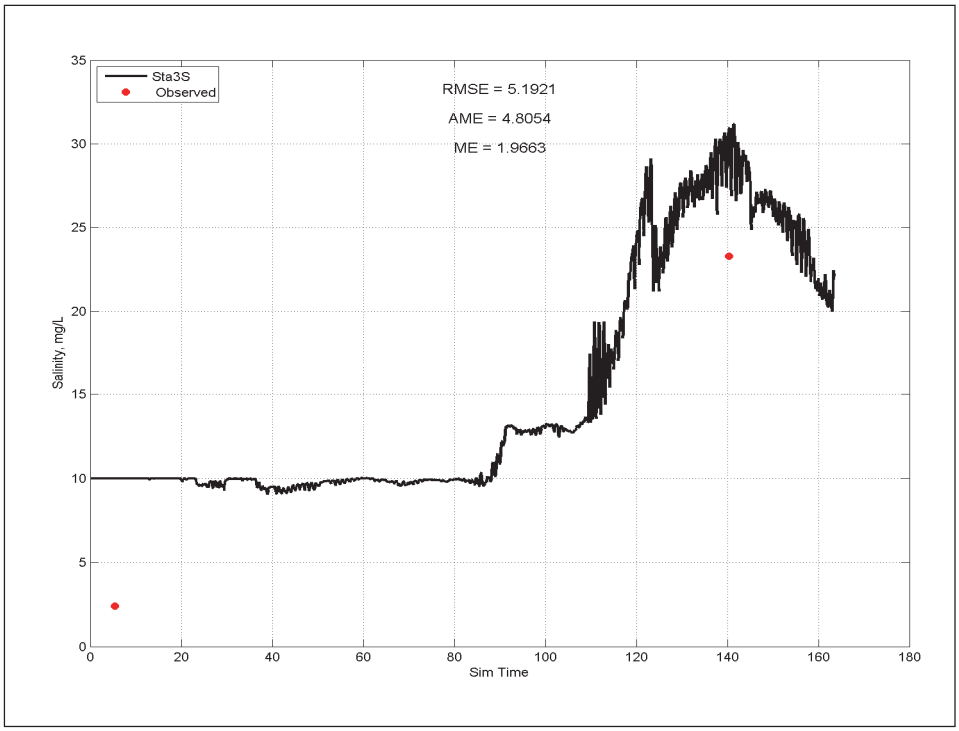

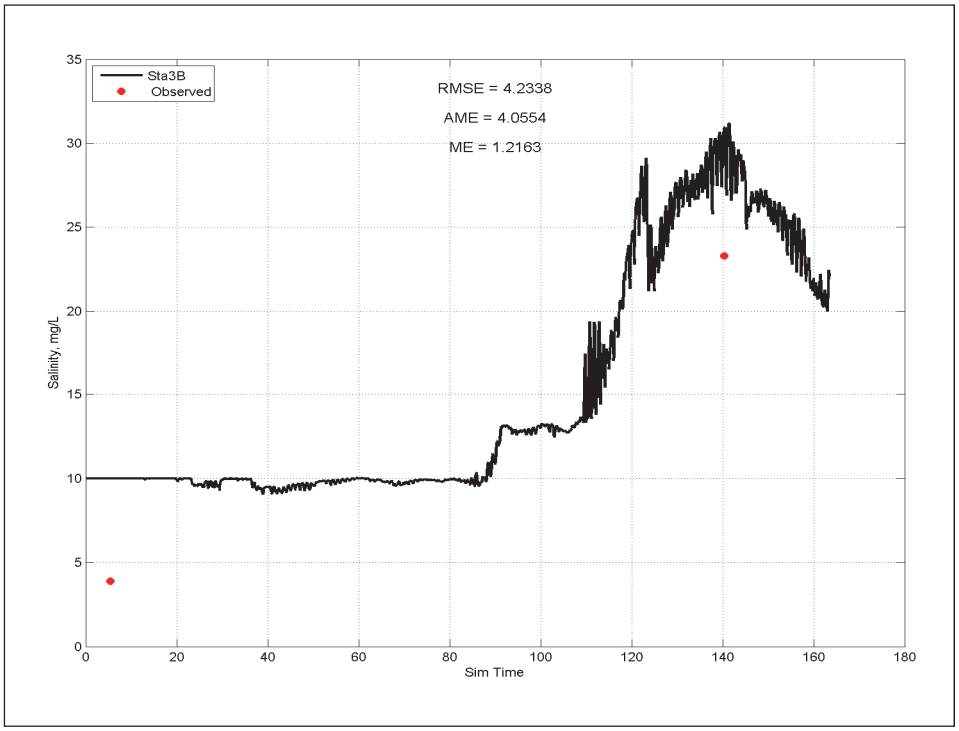

Figure E-15. Calibration results for DO at Station 3 for surface layer (upper) and bottom layer (lower).

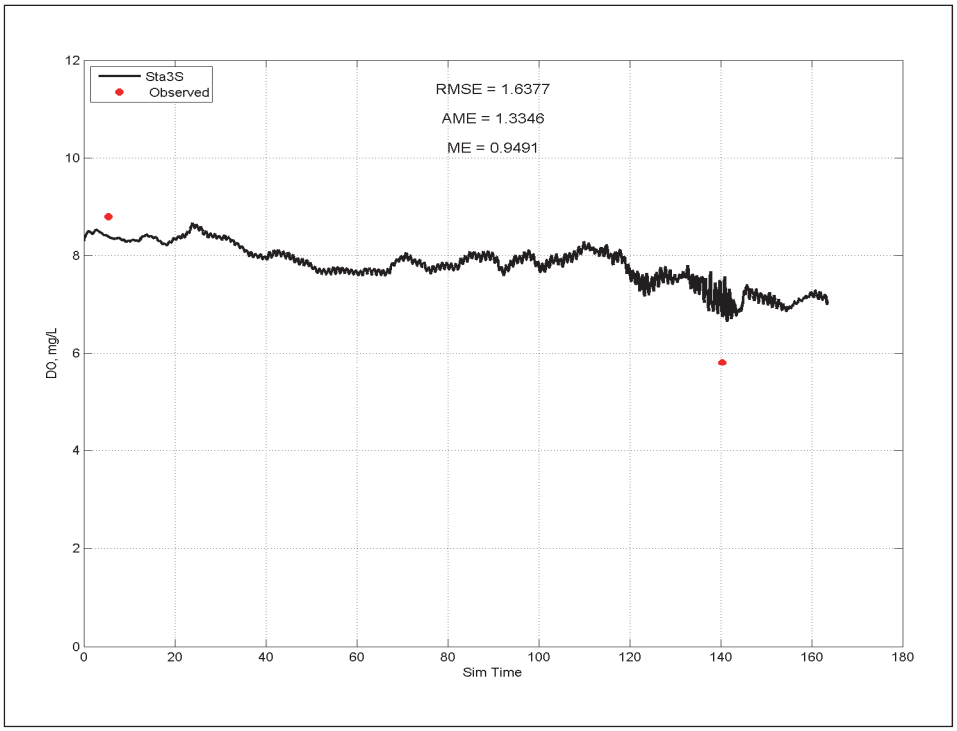

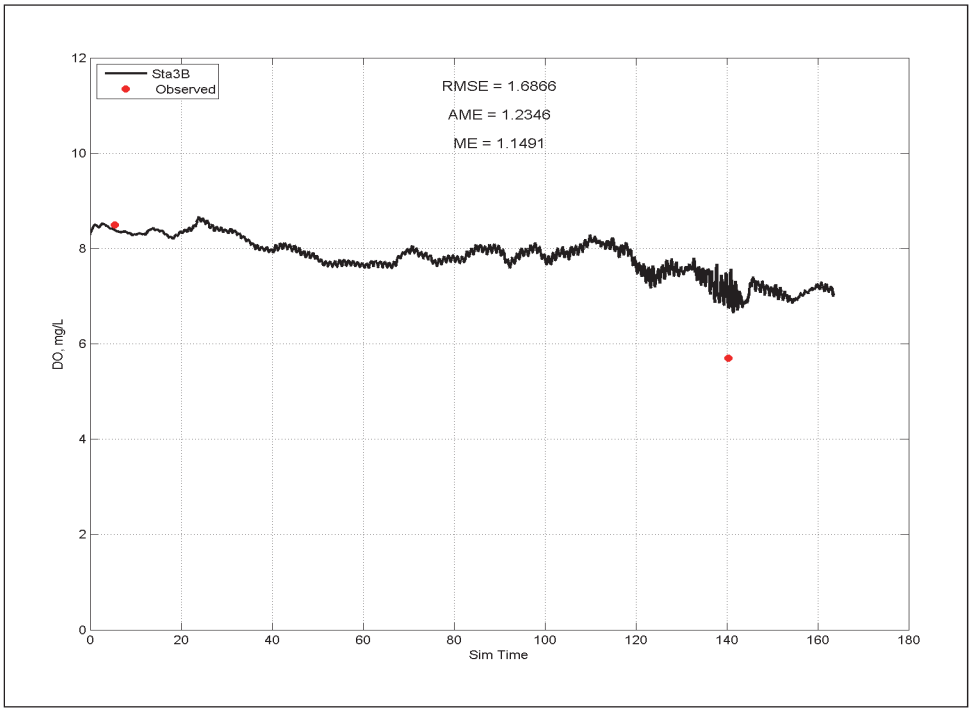

Figure E-16. Calibration results for NH_4 at Station 3 for surface layer (upper) and bottom layer (lower).

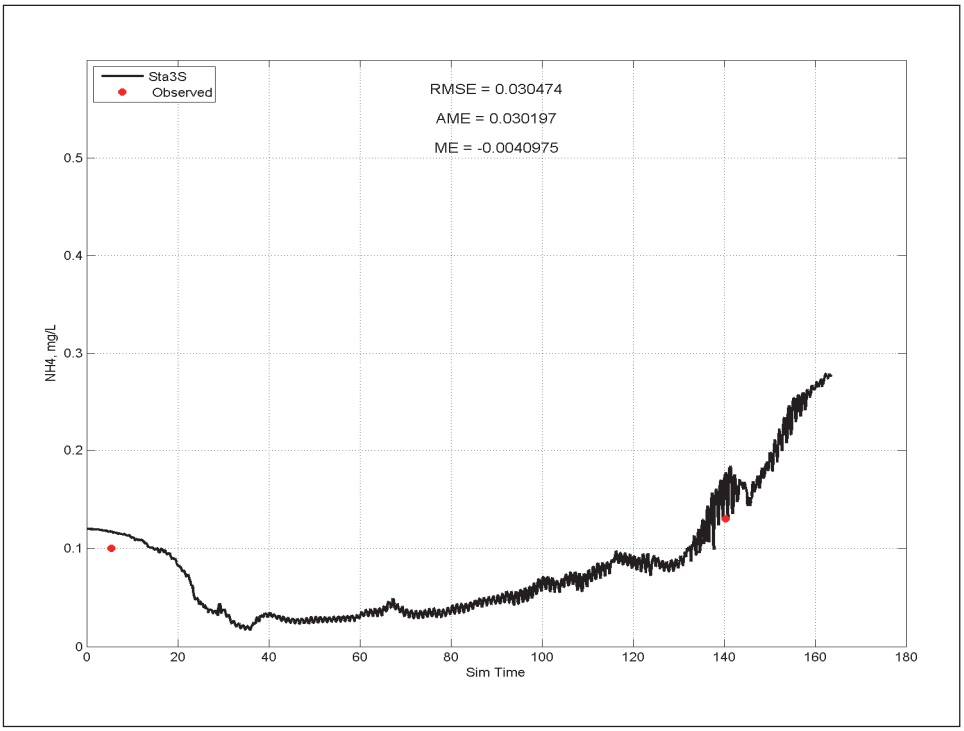

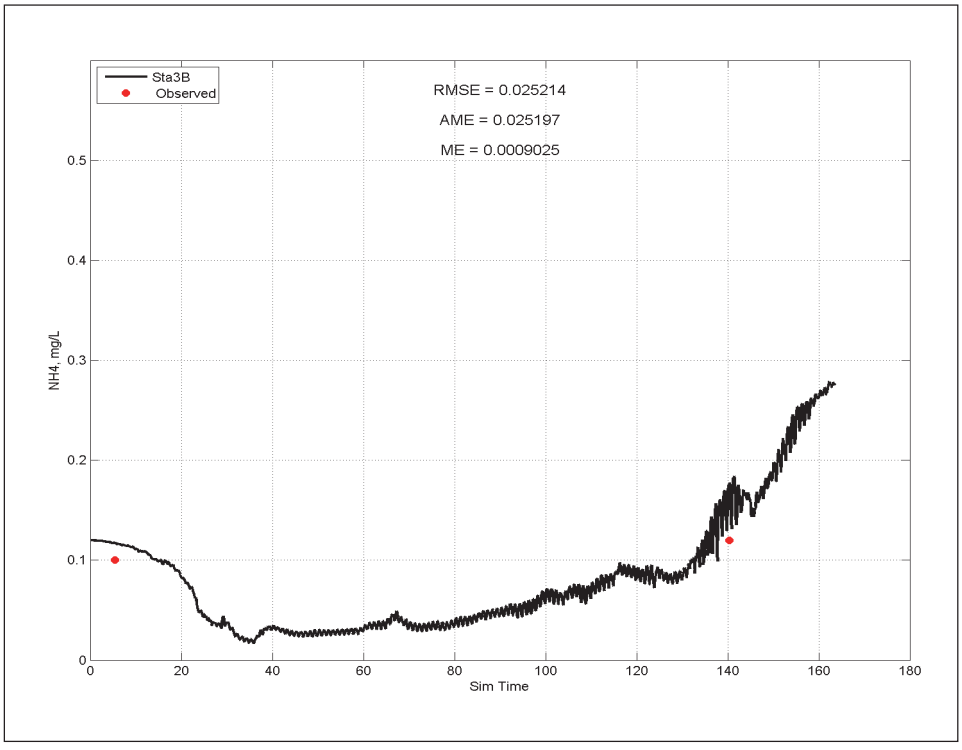

Figure E-17 Calibration results for NO_3 at Station 3 for surface layer (upper) and bottom layer (lower).

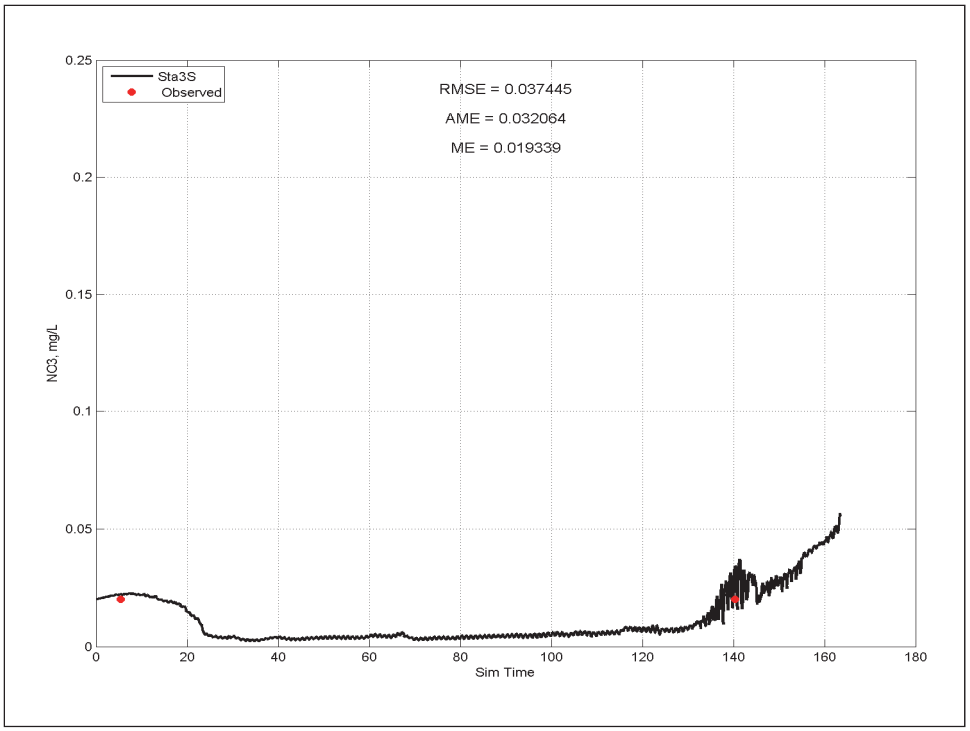

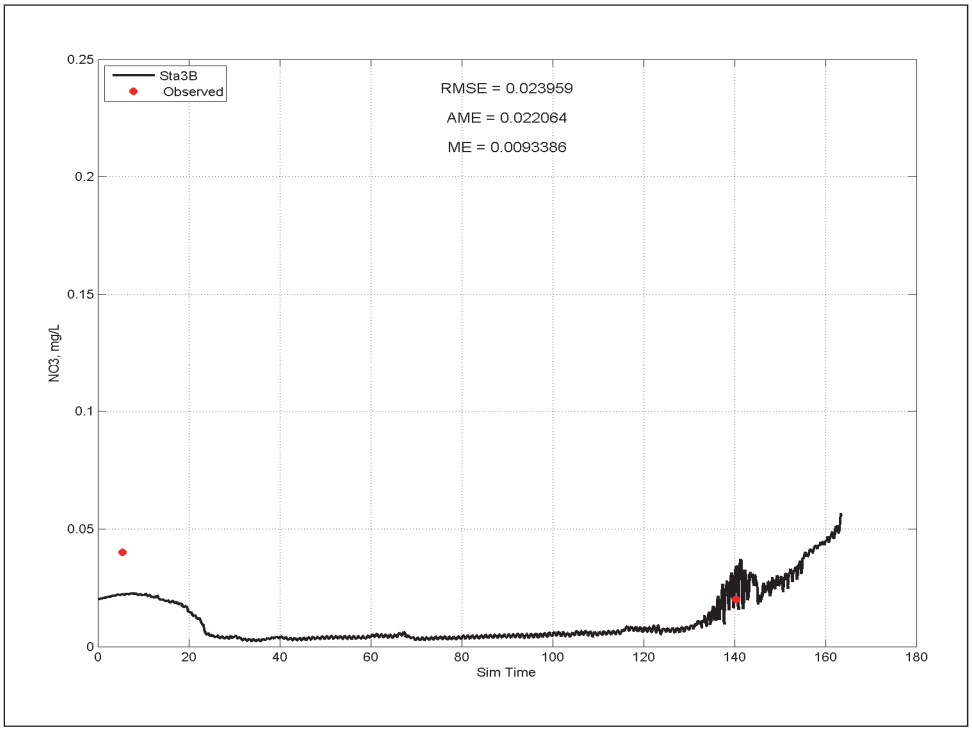

Figure E-18. Calibration results for *Tp* at Station 3 for surface layer (upper) and bottom layer (lower).

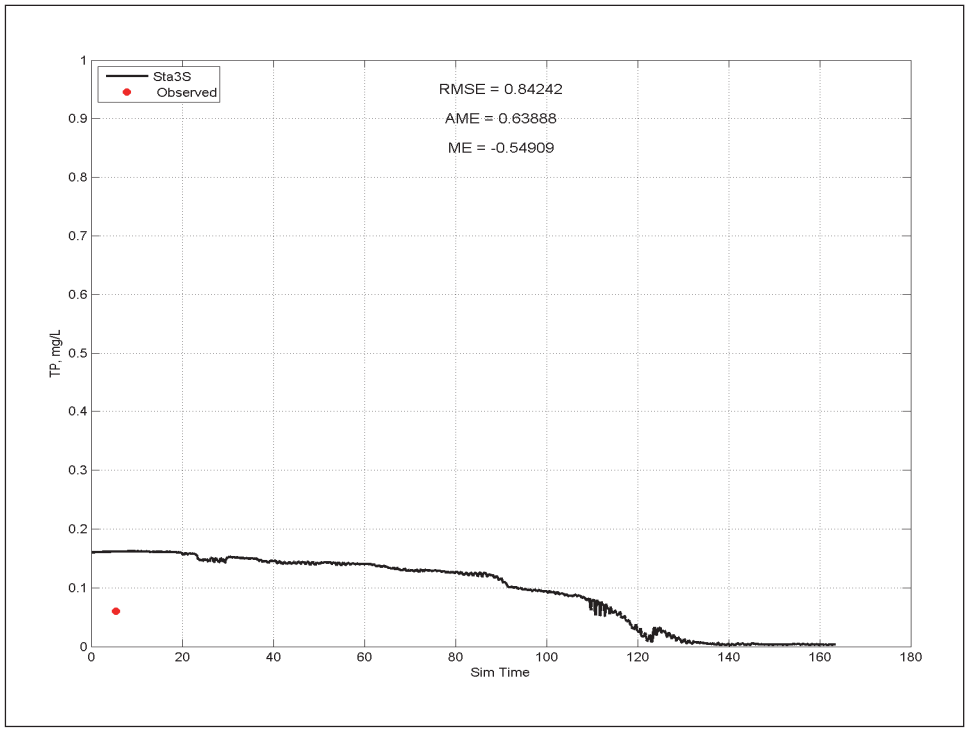

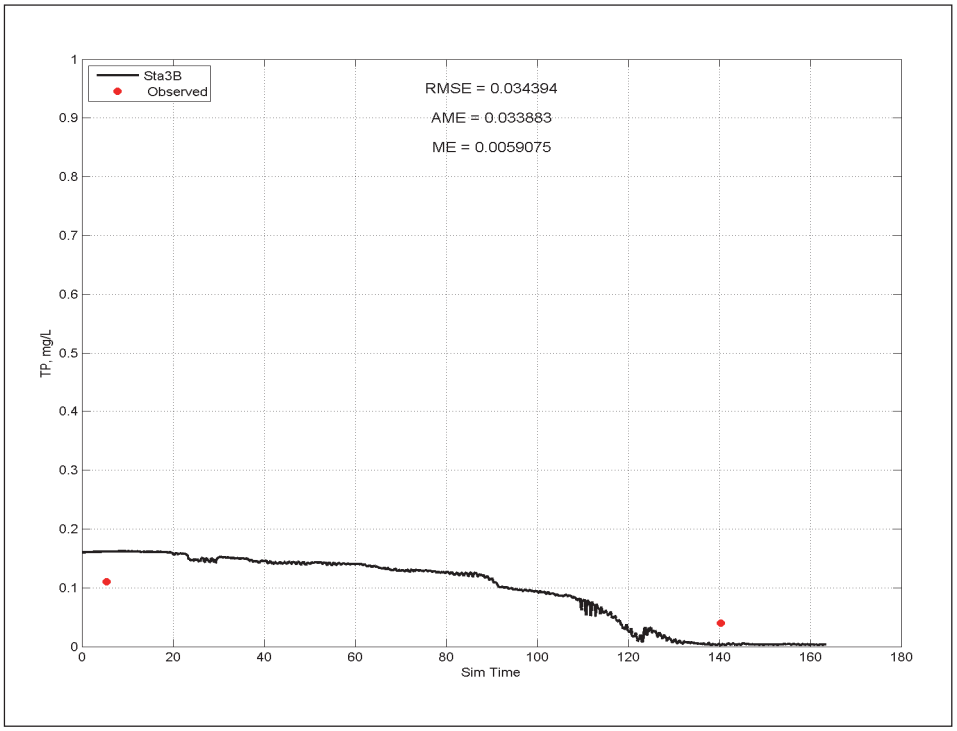

Figure E-19. Calibration results for temperature at Station 4 for surface layer (upper) and bottom layer (lower).

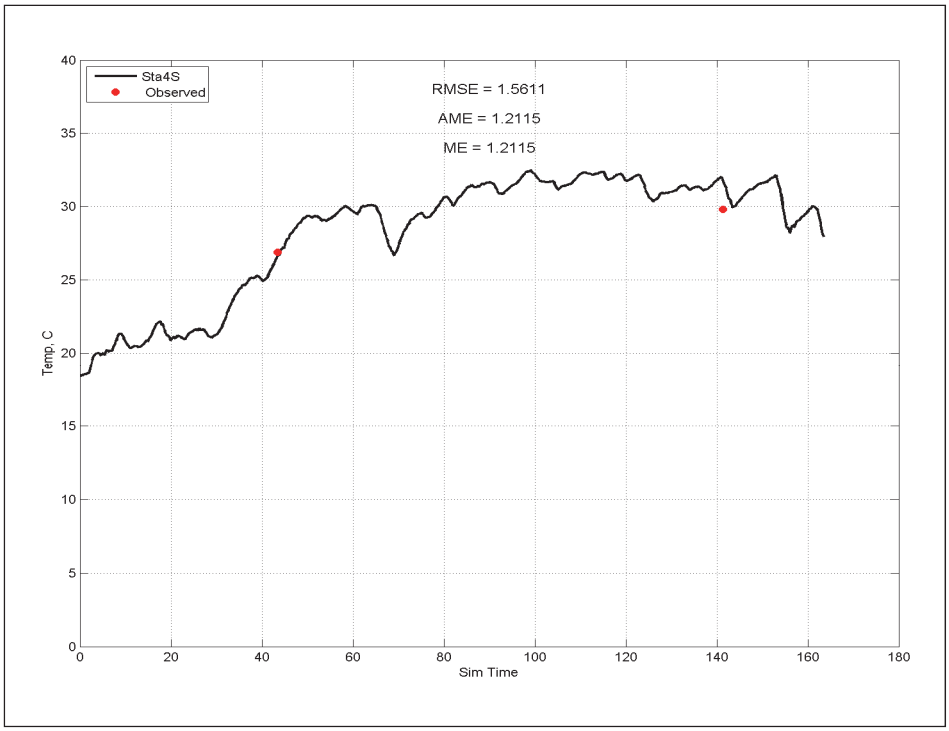

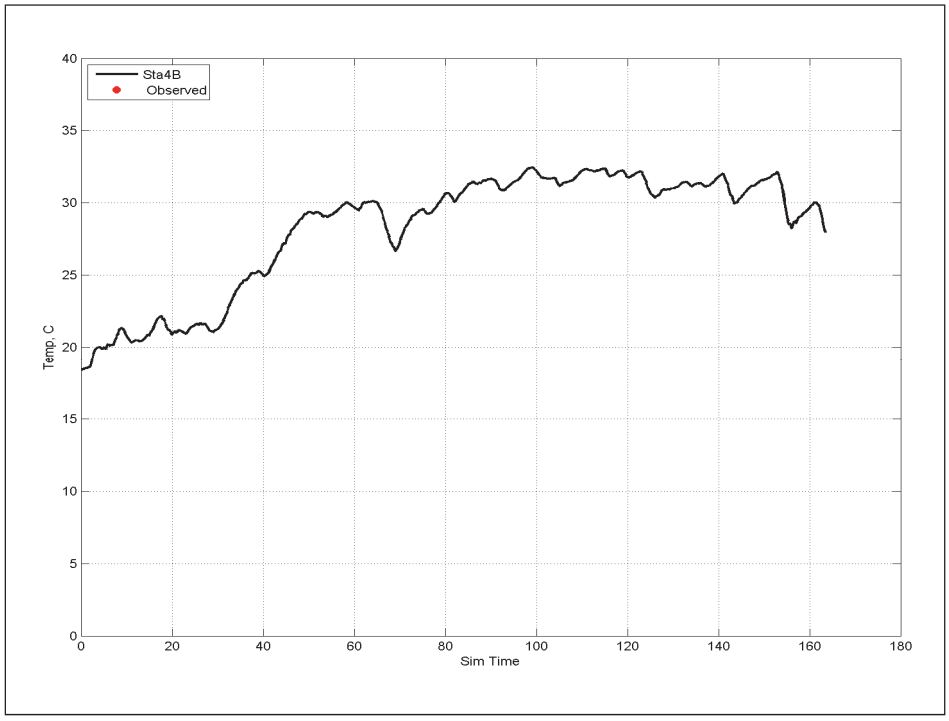

Figure E-20. Calibration results for salinity at Station 4 for surface layer (upper) and bottom layer (lower).

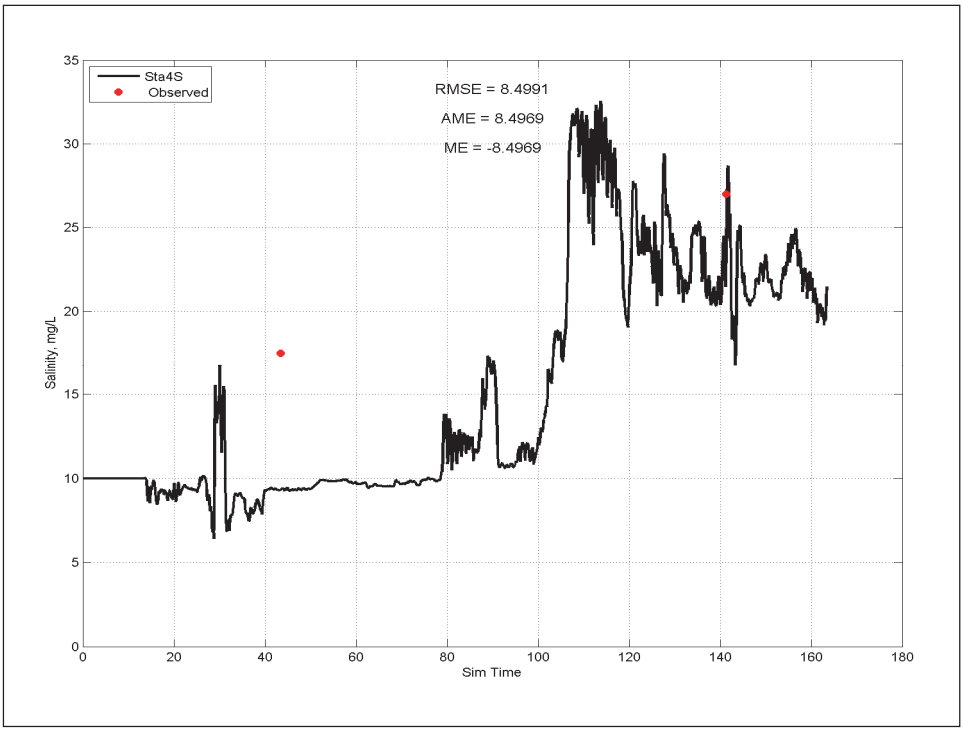

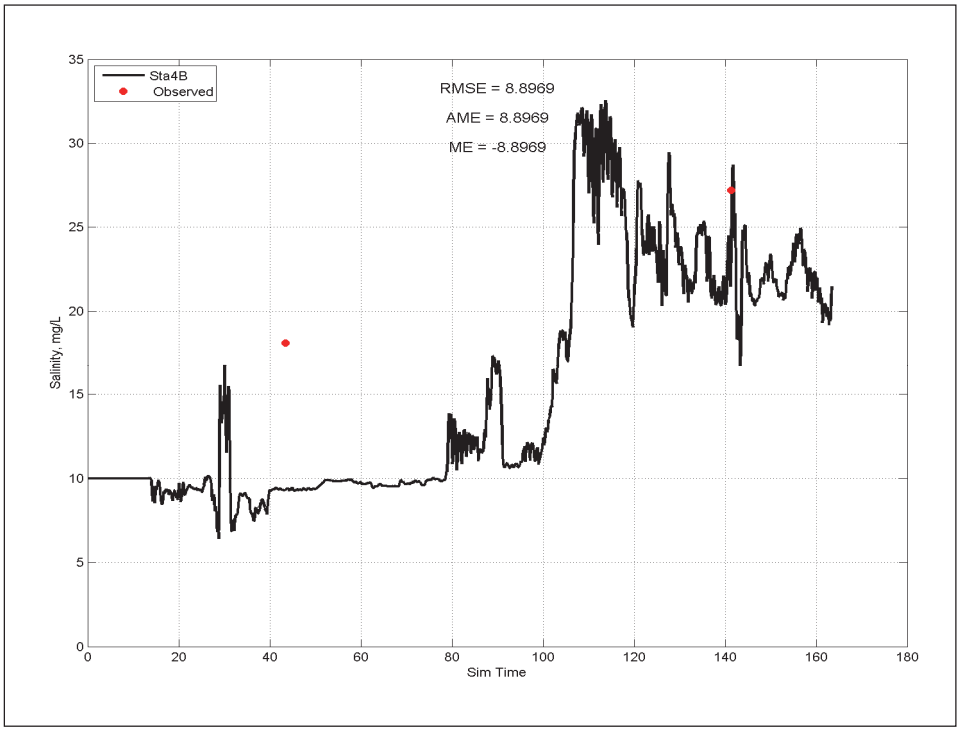

Figure E-21. Calibration results for DO at Station 4 for surface layer (upper) and bottom layer (lower).

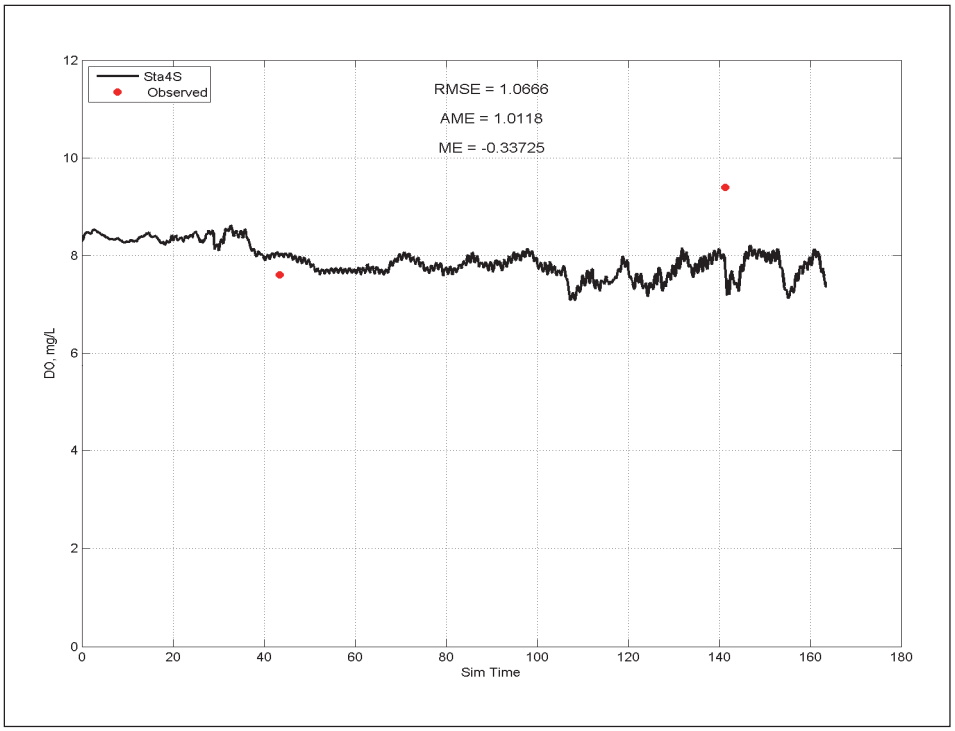

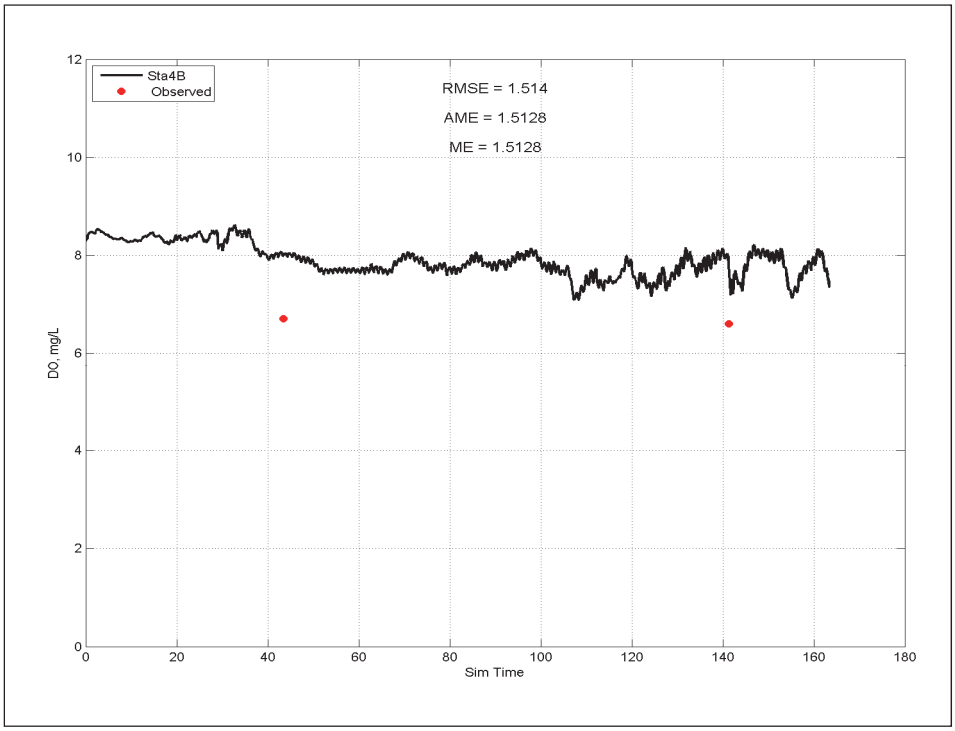

Figure E-22. Calibration results for NH_4 at Station 4 for surface layer (upper) and bottom layer (lower).

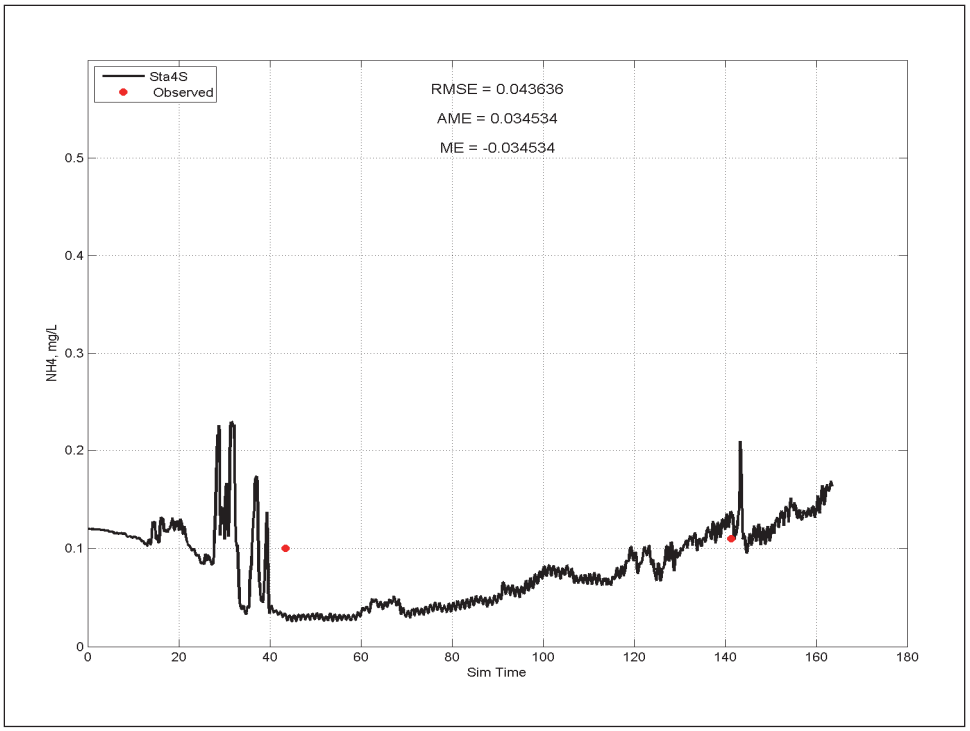

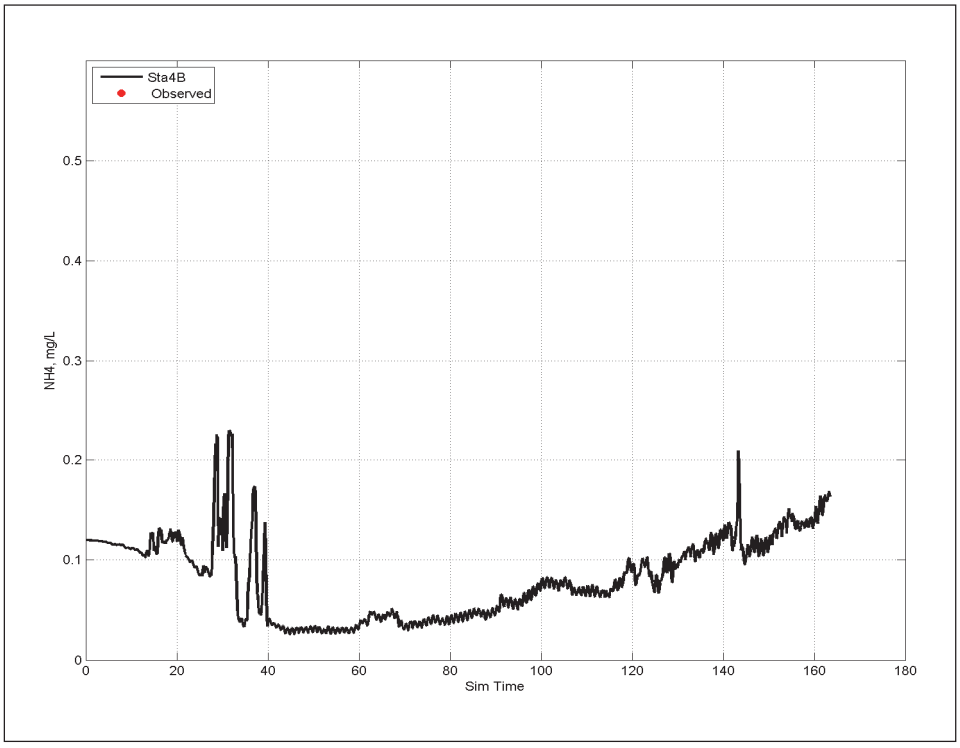

Figure E-23 Calibration results for NO_3 at Station 4 for surface layer (upper) and bottom layer (lower).

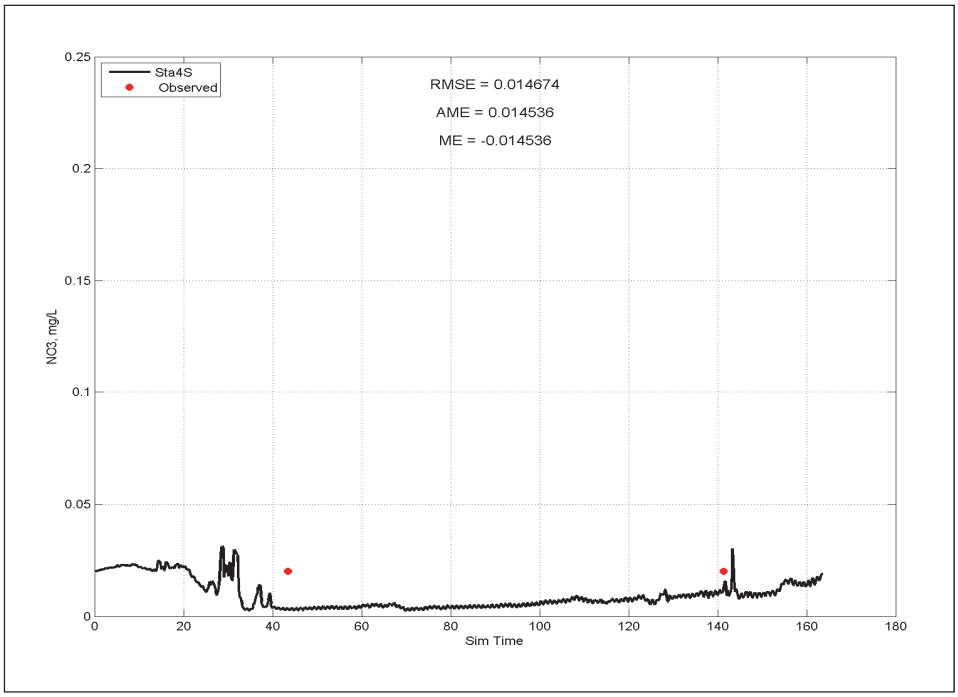

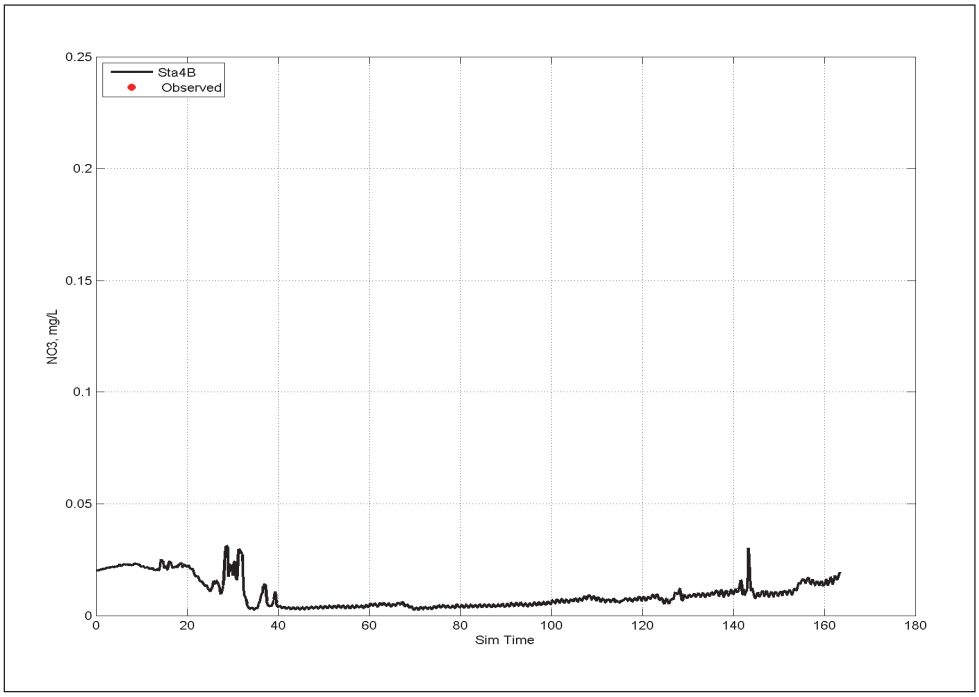

Figure E-24. Calibration results for *Tp* at Station 4 for surface layer (upper) and bottom layer (lower).

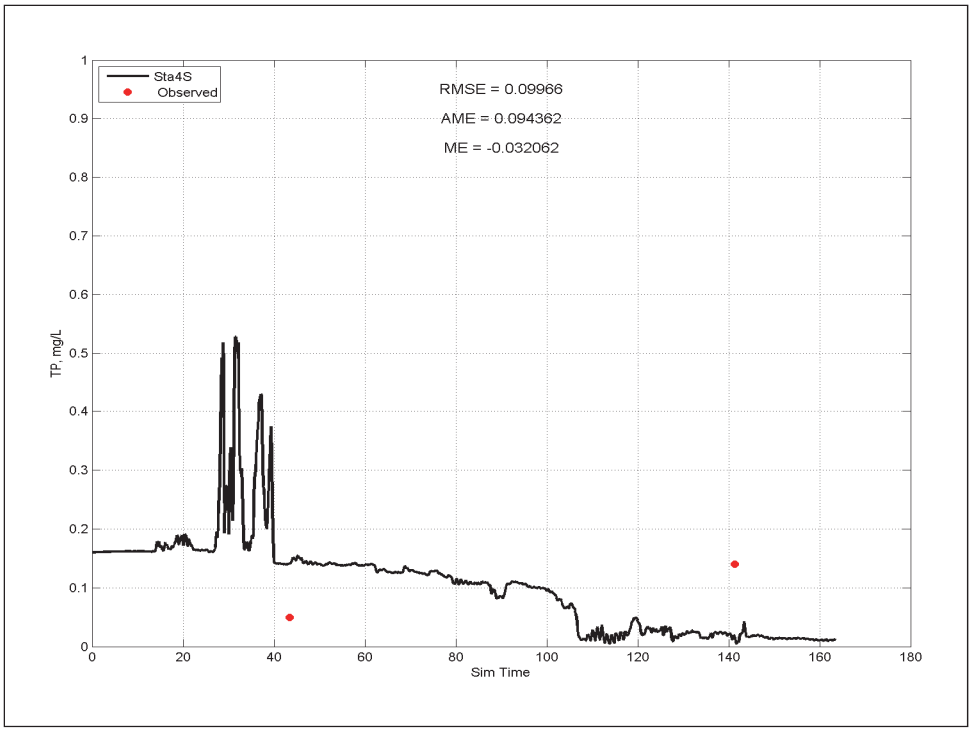

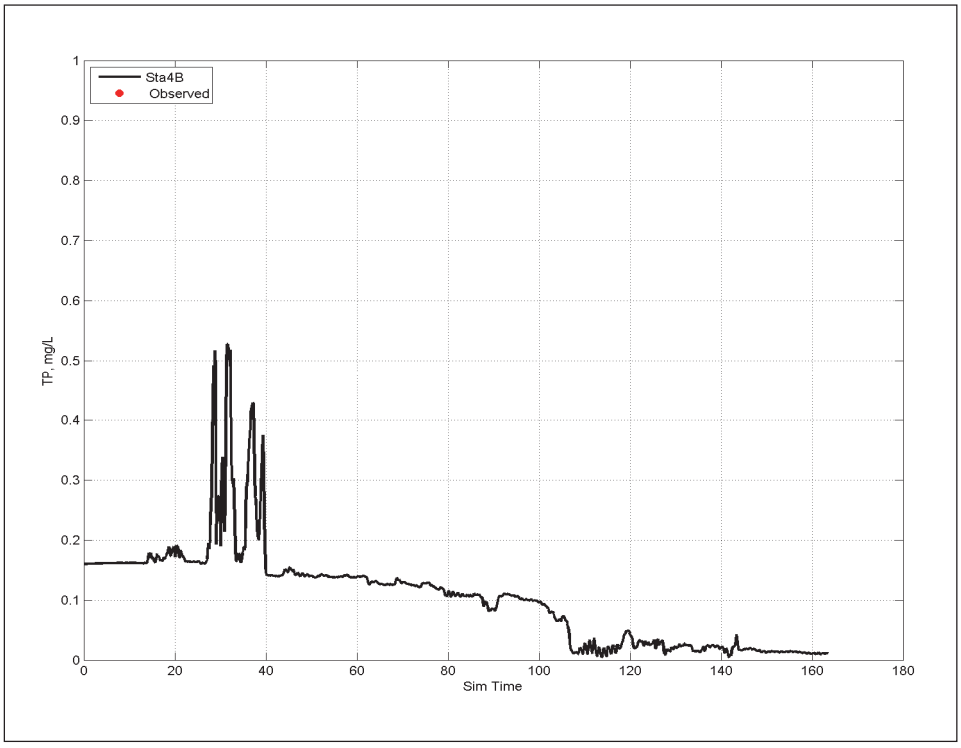

Figure E-25. Calibration results for temperature at Station 5 for surface layer (upper) and bottom layer (lower).

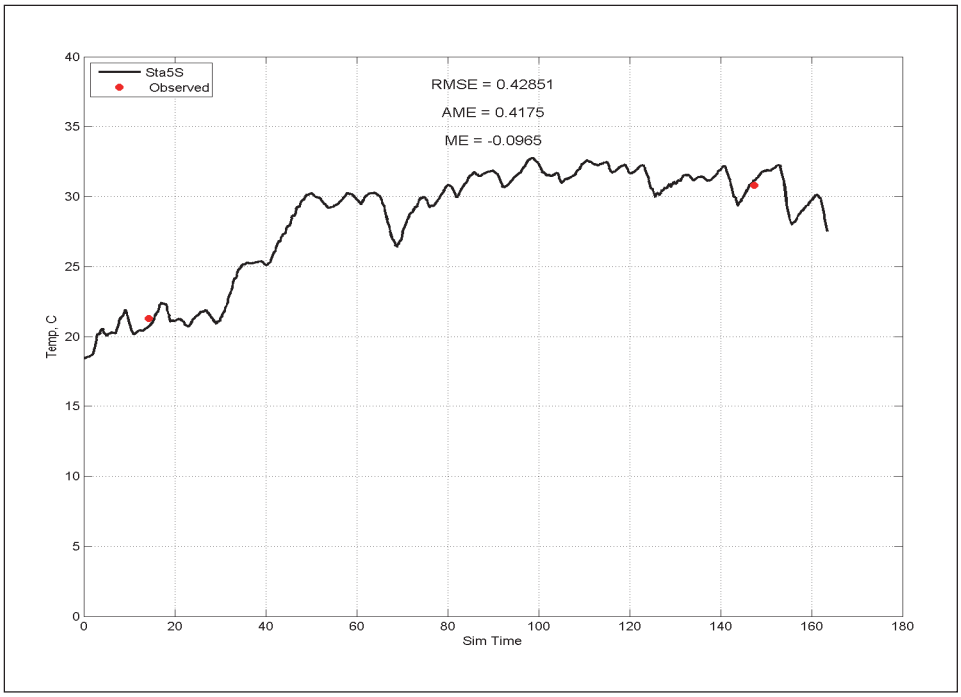

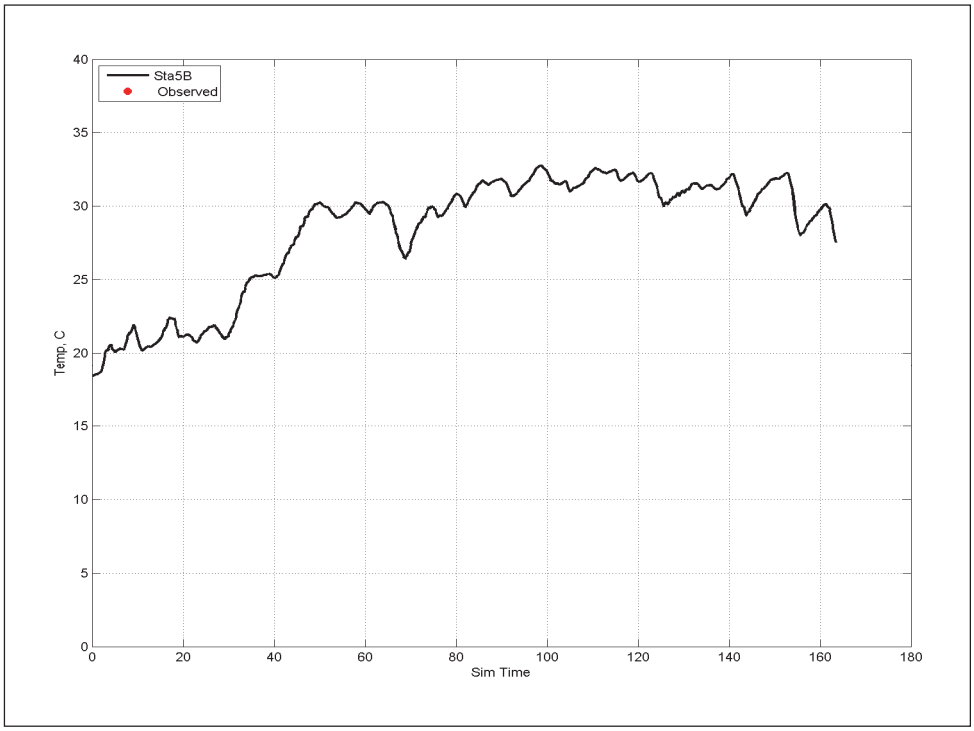

Figure E-26. Calibration results for salinity at Station 5 for surface layer (upper) and bottom layer (lower).

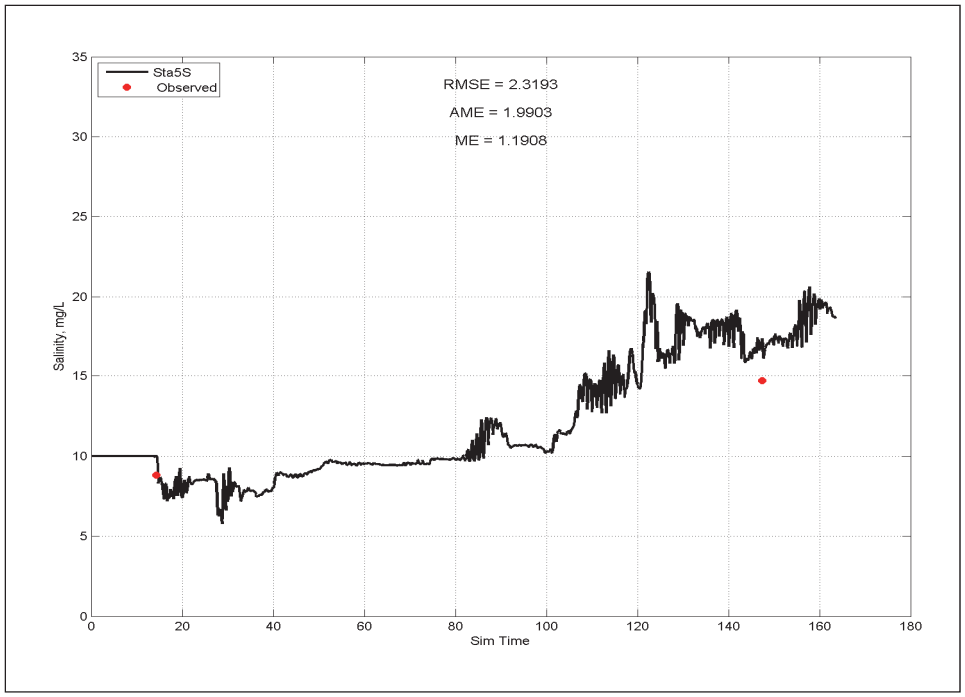

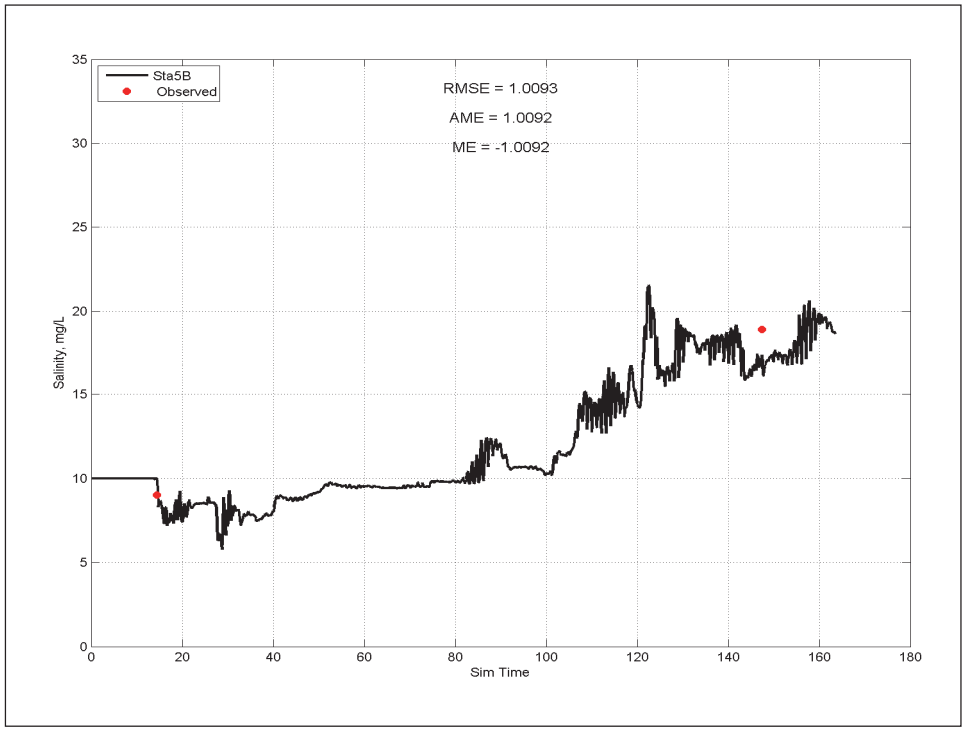

Figure E-27. Calibration results for DO at Station 5 for surface layer (upper) and bottom layer (lower).

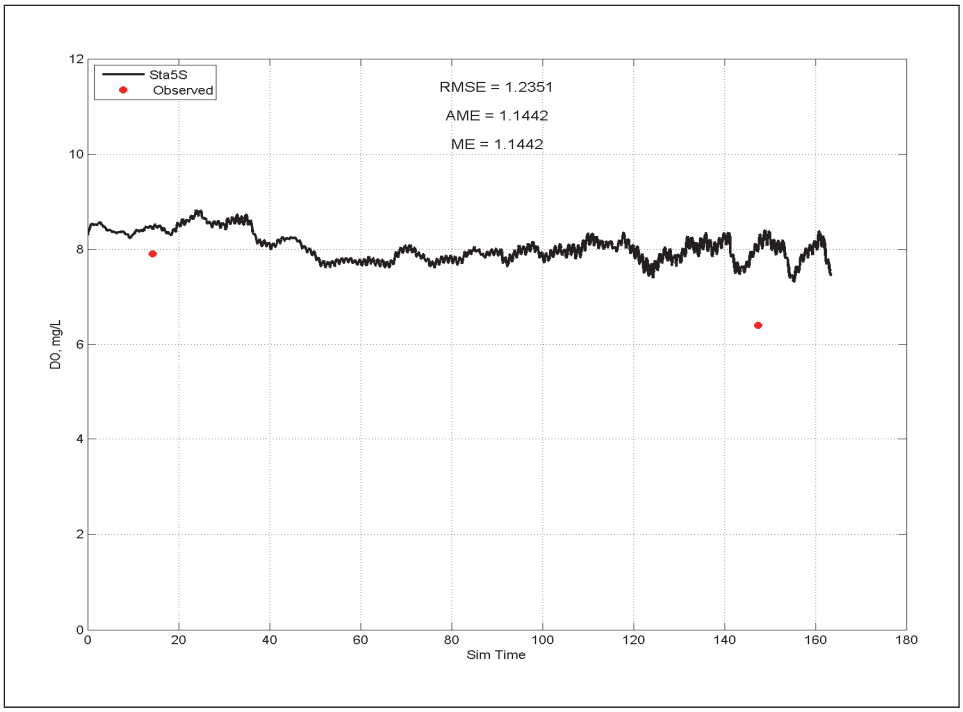

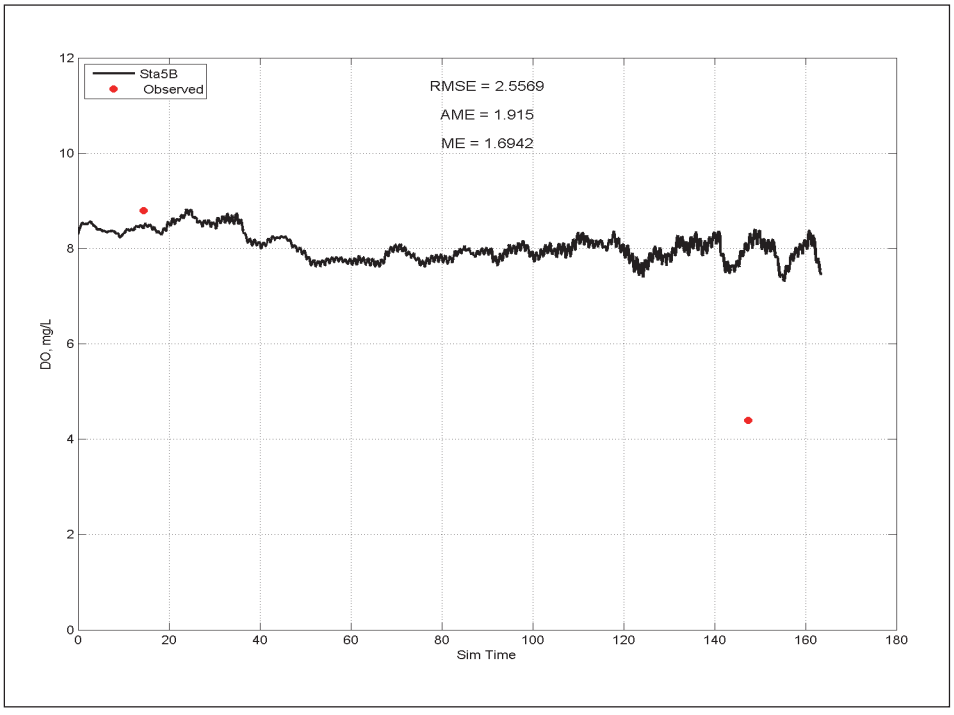

Figure E-28. Calibration results for NH_4 at Station 5 for surface layer (upper) and bottom layer (lower).

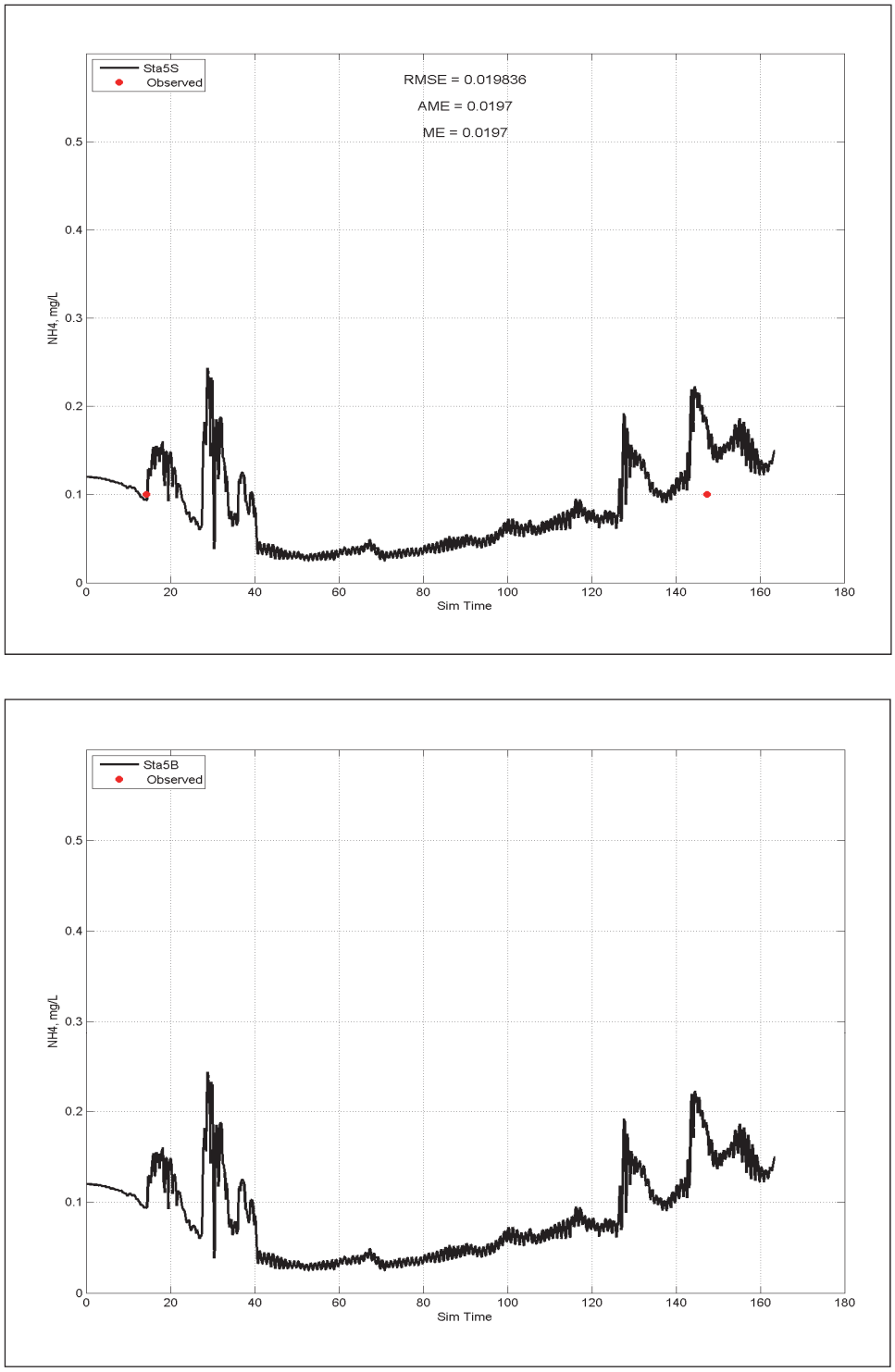

Figure E-29 Calibration results for NO_3 at Station 5 for surface layer (upper) and bottom layer (lower).

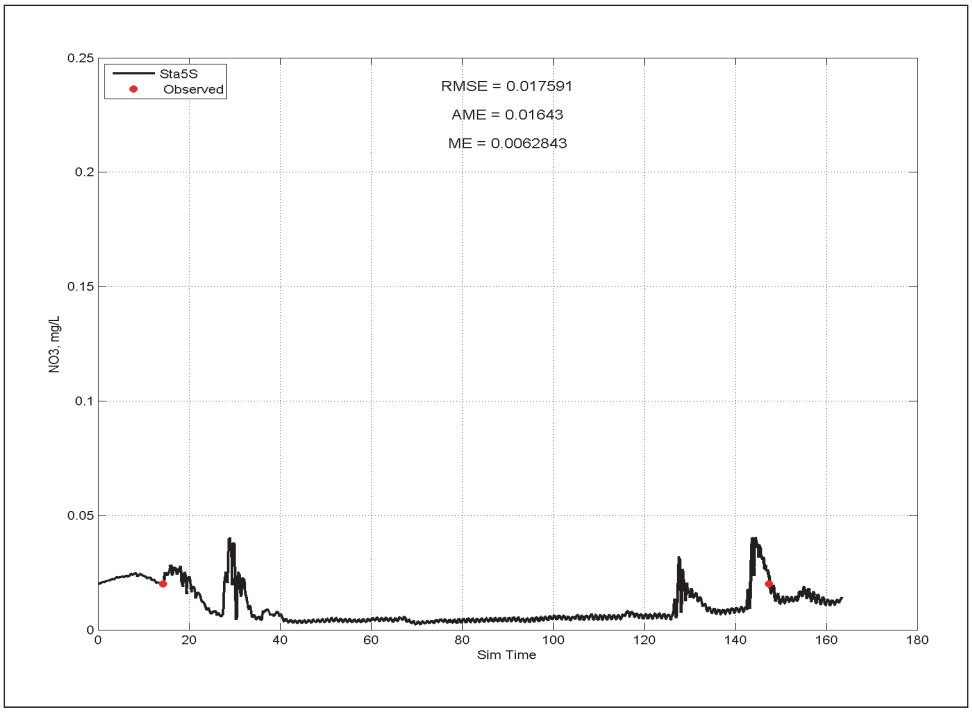

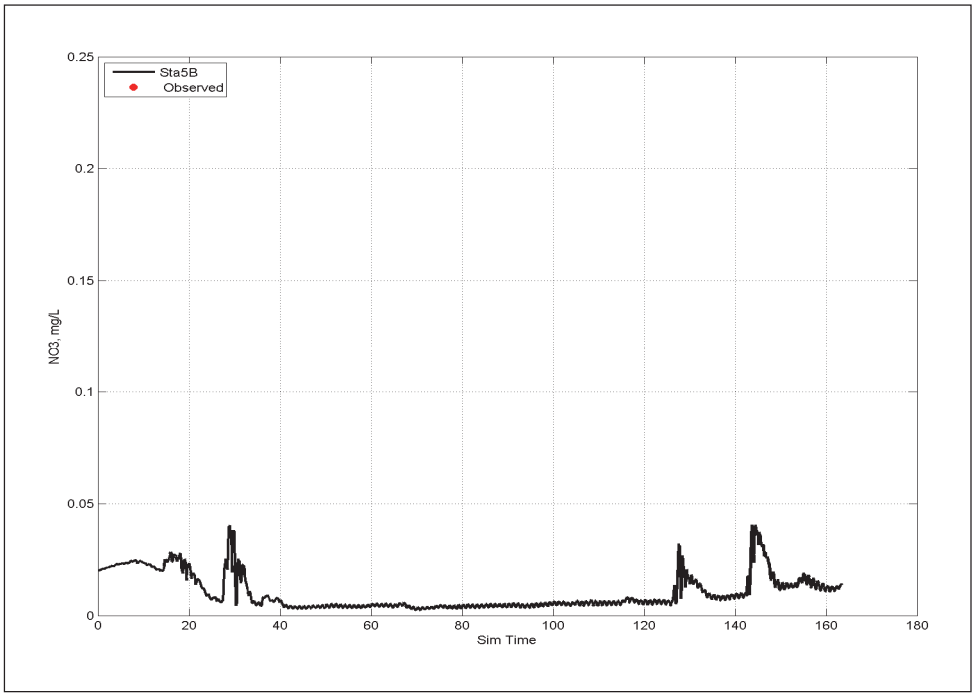

Figure E-30. Calibration results for *Tp* at Station 5 for surface layer (upper) and bottom layer (lower).

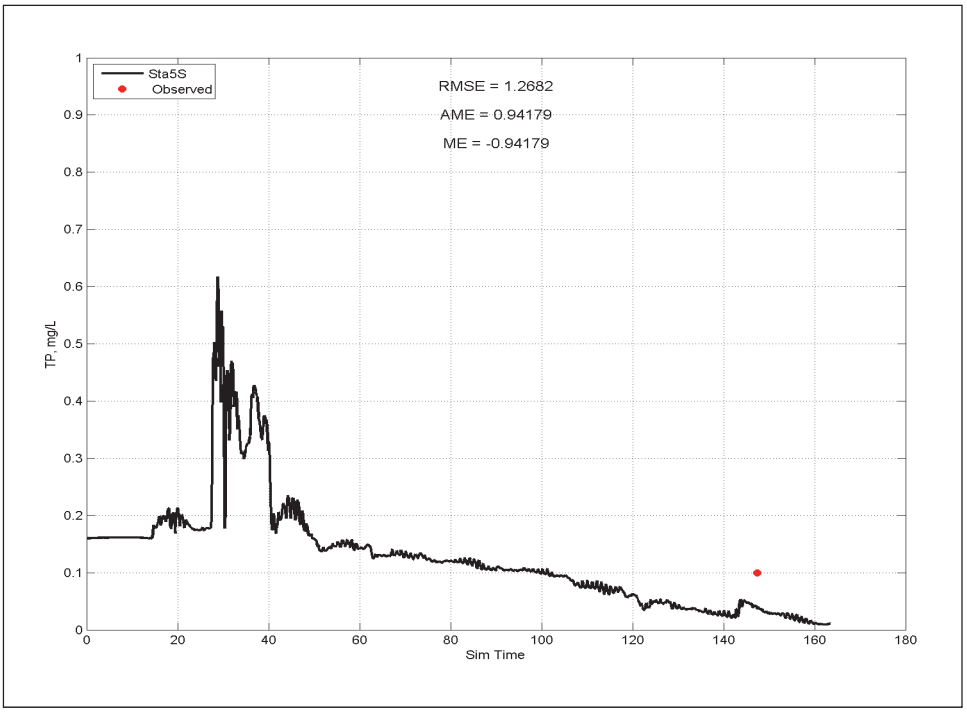

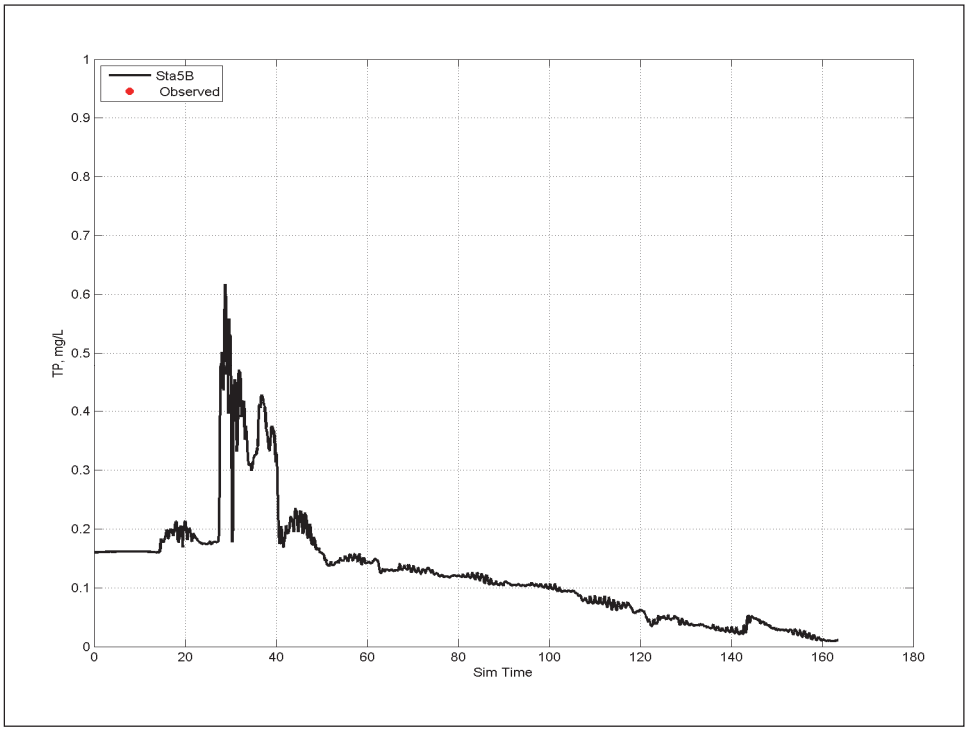

Figure E-31. Calibration results for temperature at Station 6 for surface layer (upper) and bottom layer (lower).

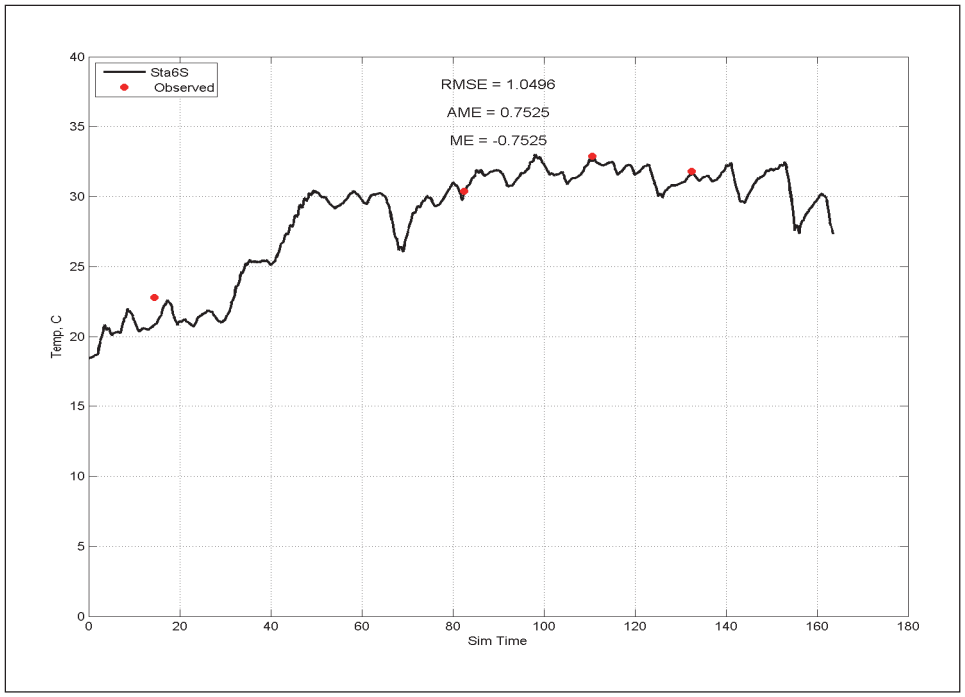

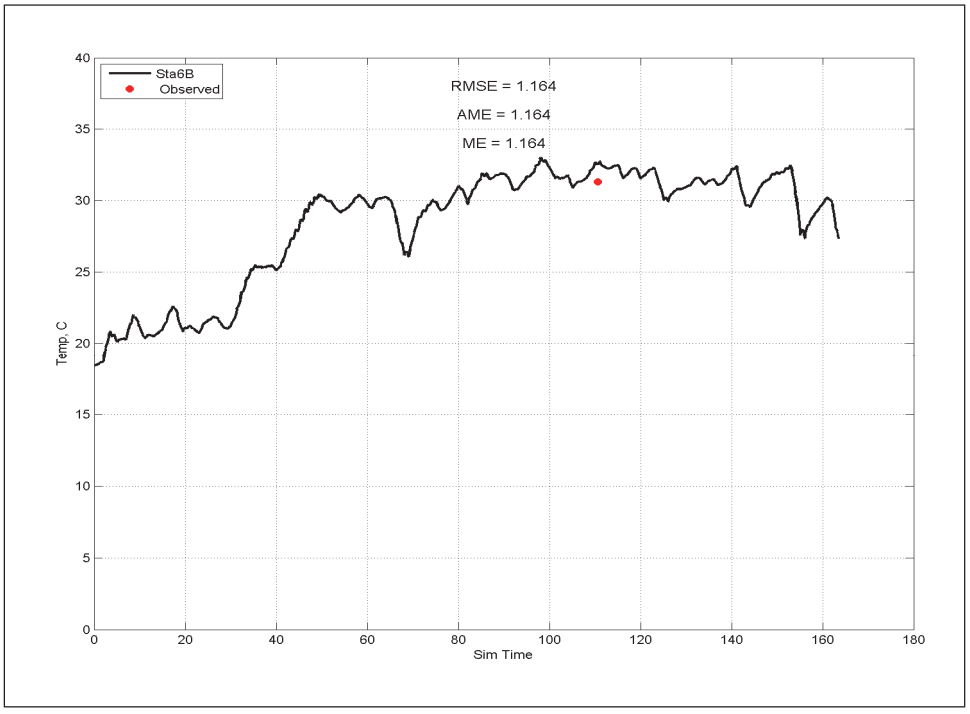

Figure E-32. Calibration results for salinity at Station 6 for surface layer (upper) and bottom layer (lower).

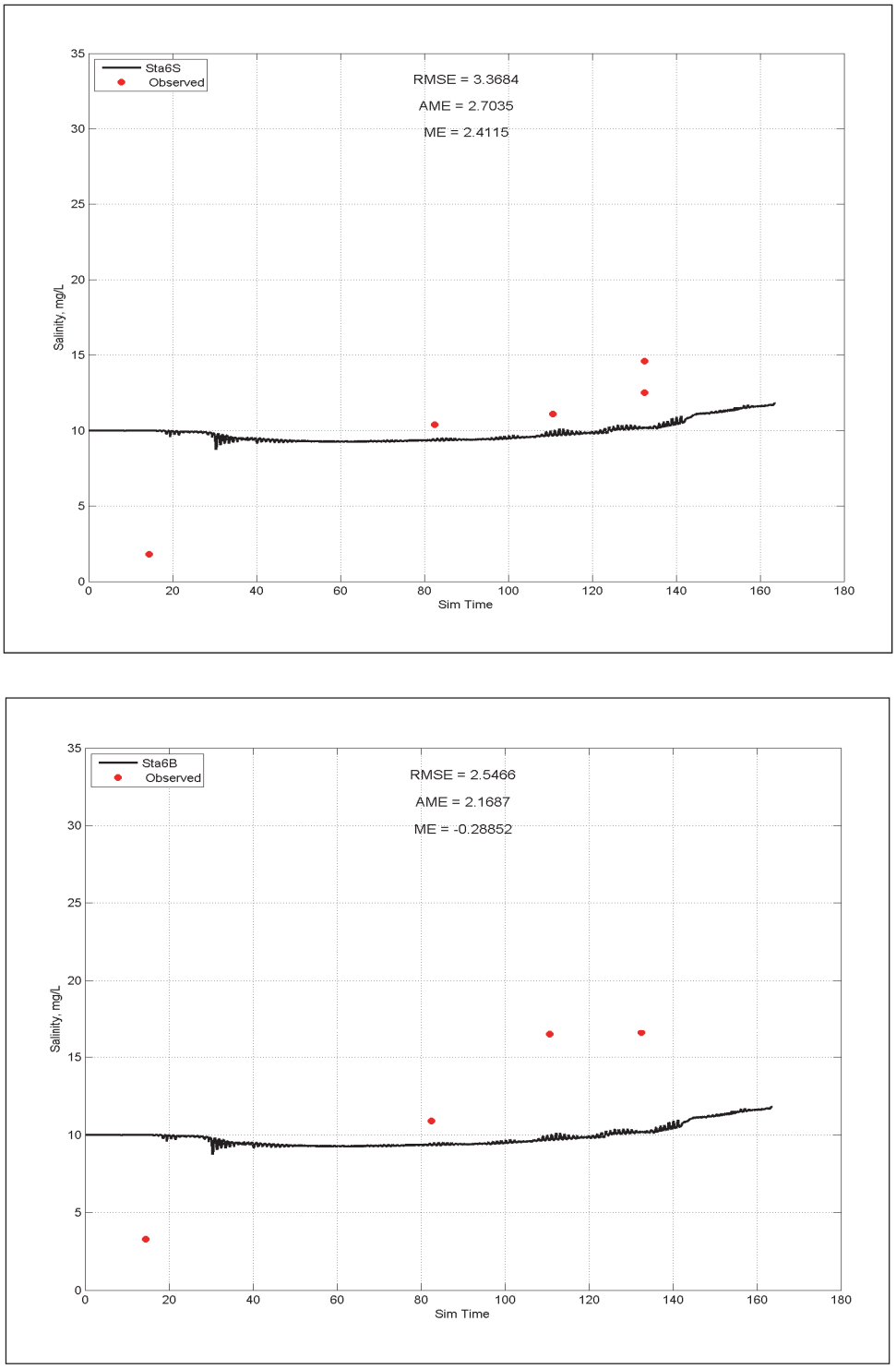

Figure E-33. Calibration results for DO at Station 6 for surface layer (upper) and bottom layer (lower).

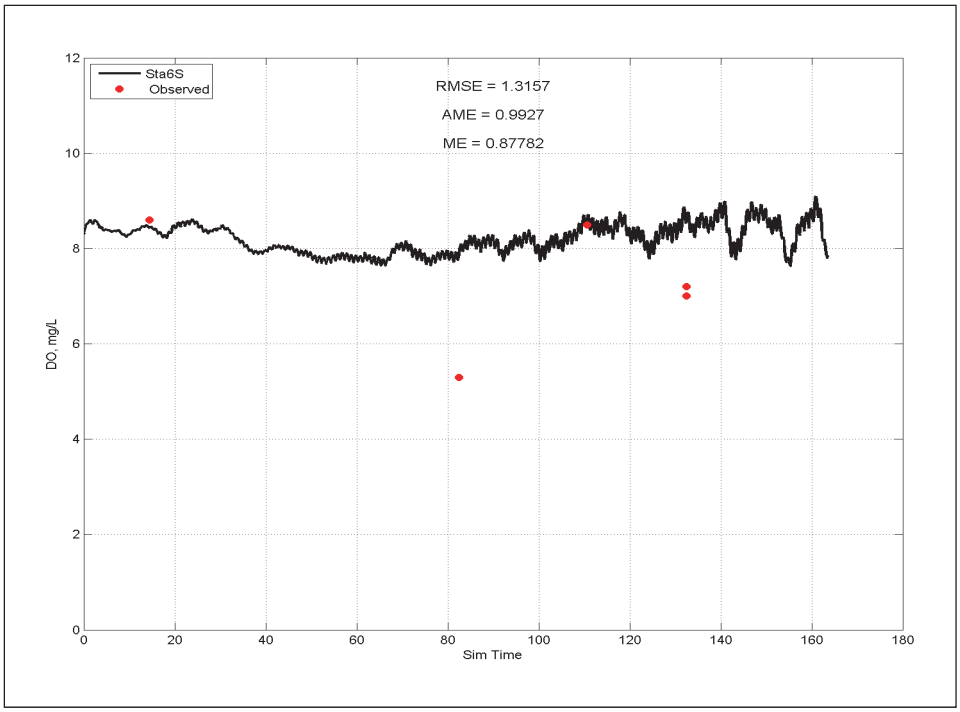

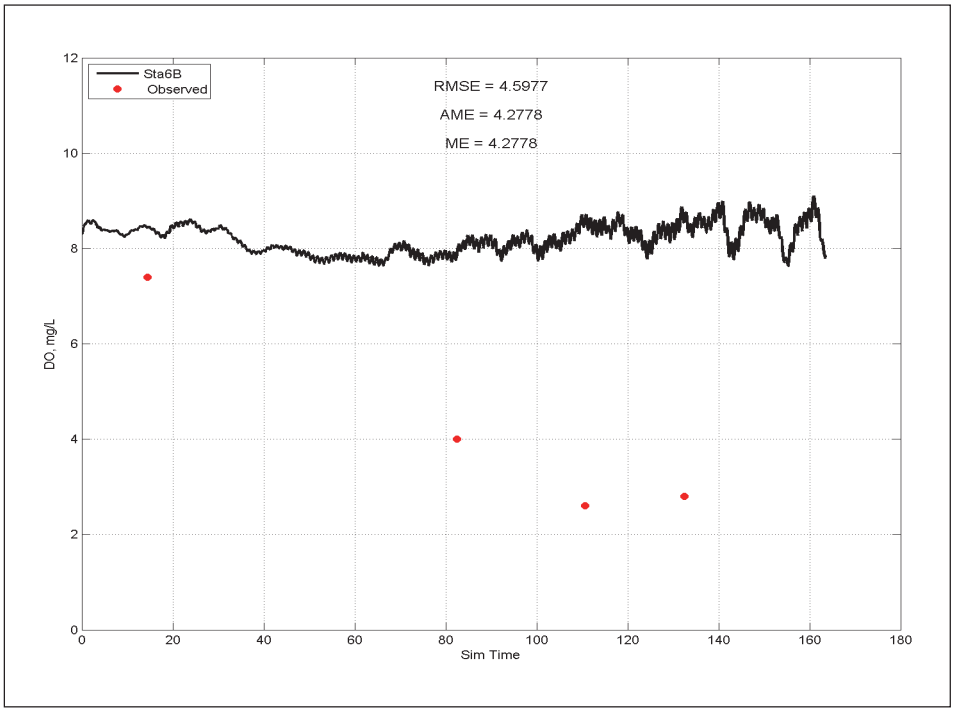

Figure E-34. Calibration results for NH_4 at Station 6 for surface layer (upper) and bottom layer (lower).

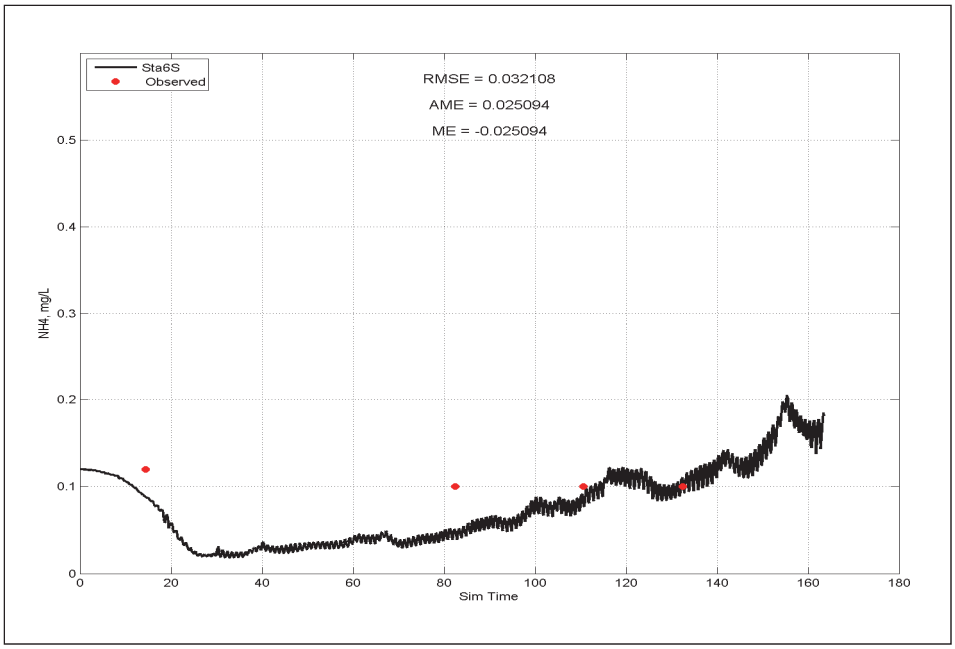

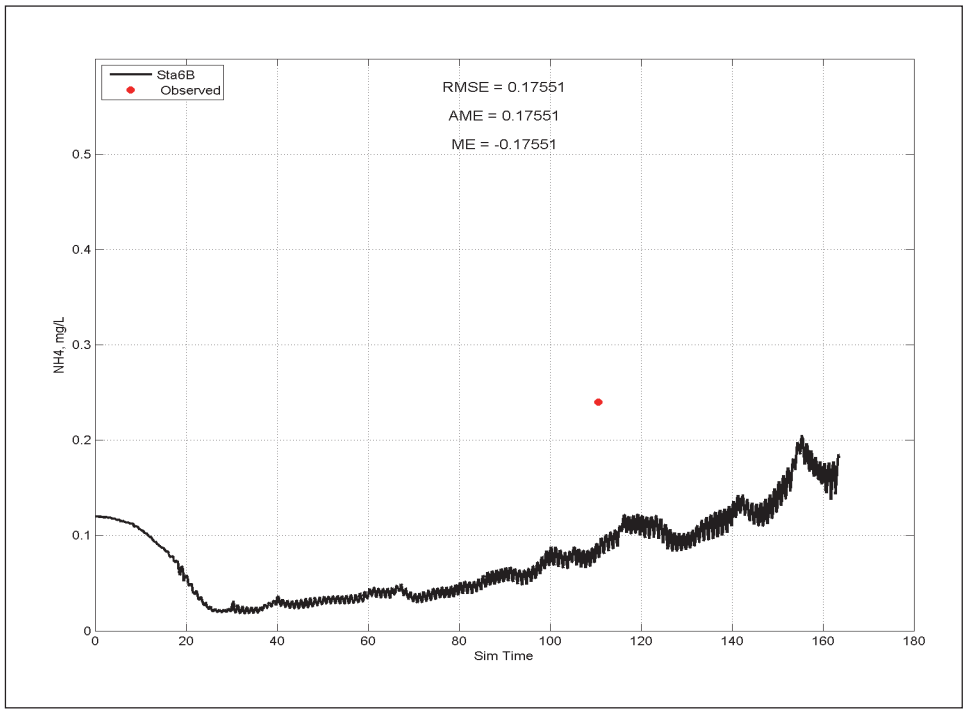

Figure E-35. Calibration results for NO_3 at Station 6 for surface layer (upper) and bottom layer (lower).

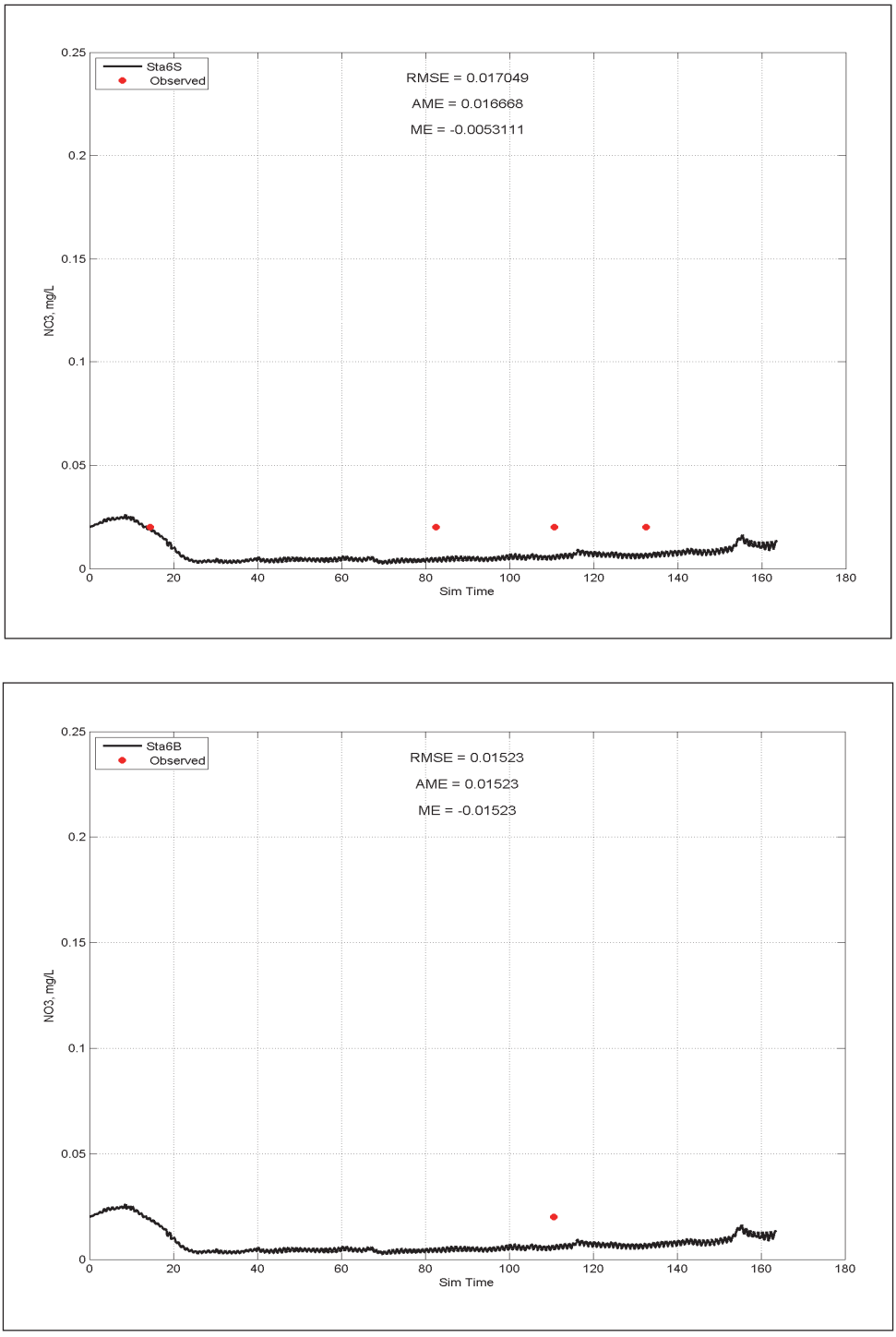

Figure E-36. Calibration results for *Tp* at Station 6 for surface layer (upper) and bottom layer (lower).

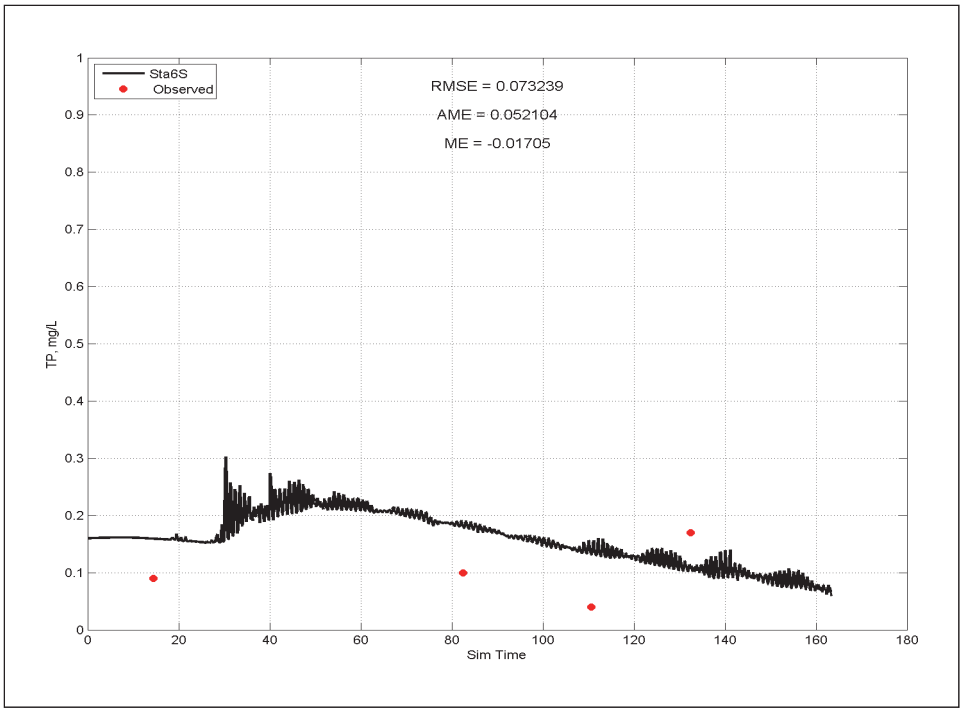

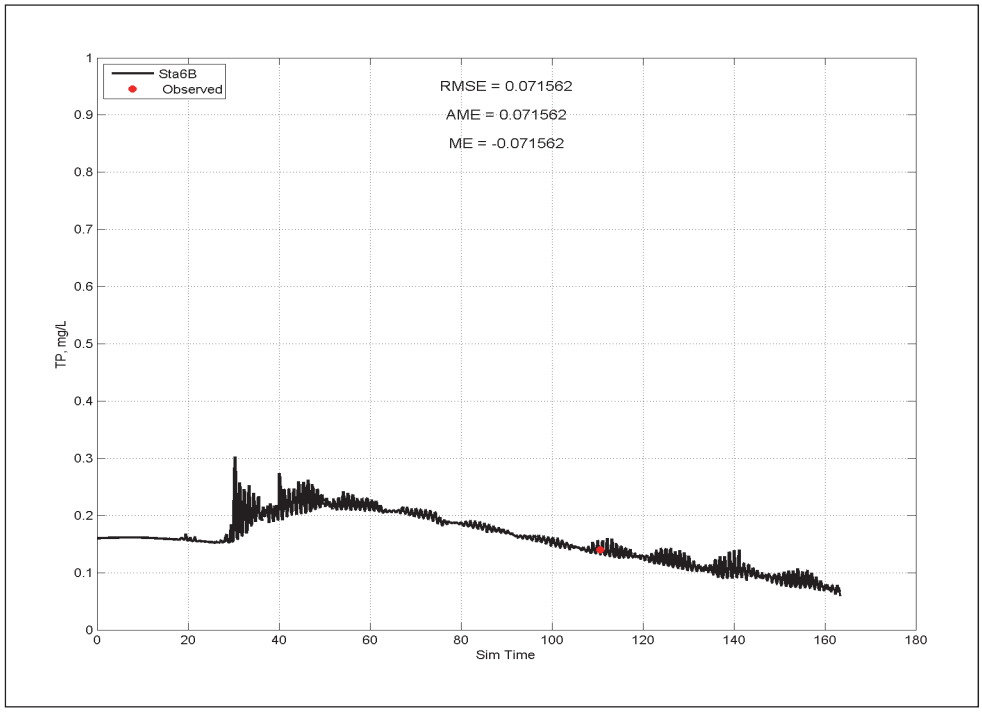

Figure E-37. Calibration results for temperature at Station 7 for surface layer (upper) and bottom layer (lower).

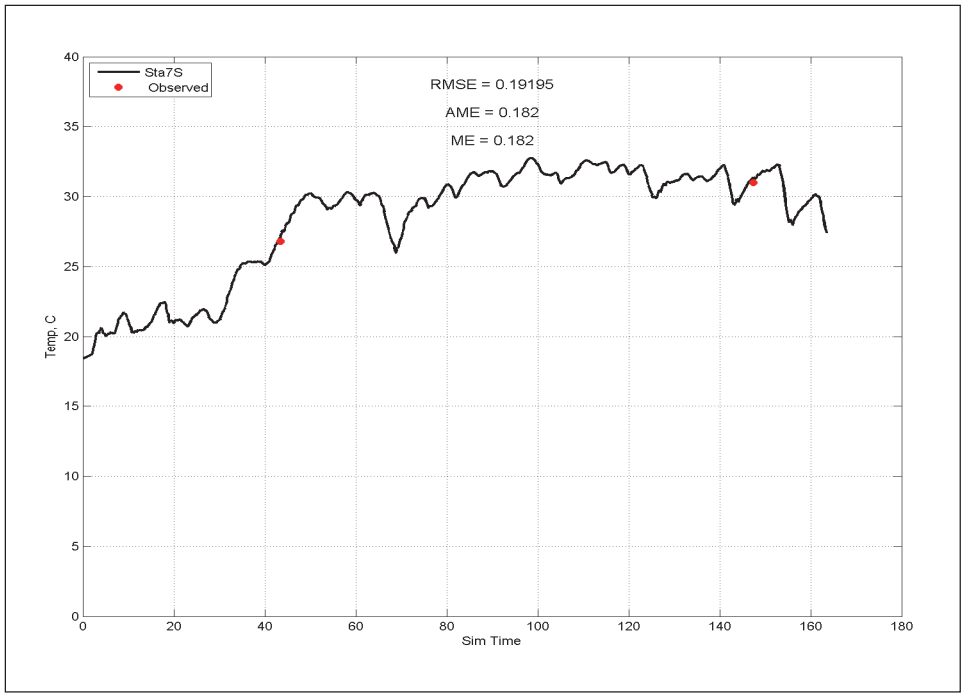

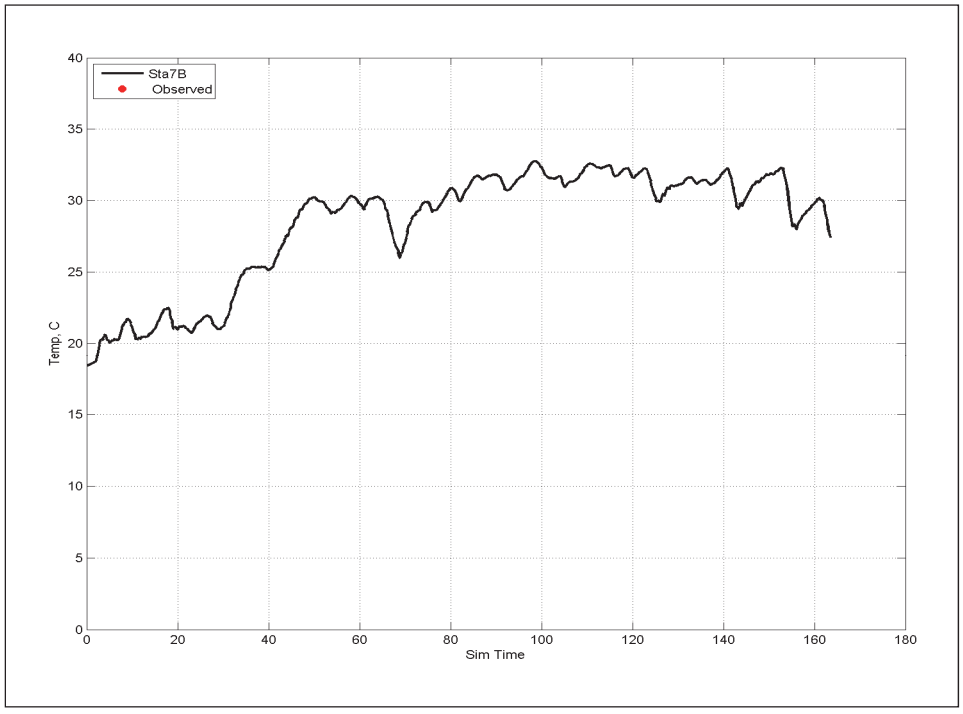

Figure E-38. Calibration results for salinity at Station 7 for surface layer (upper) and bottom layer (lower).

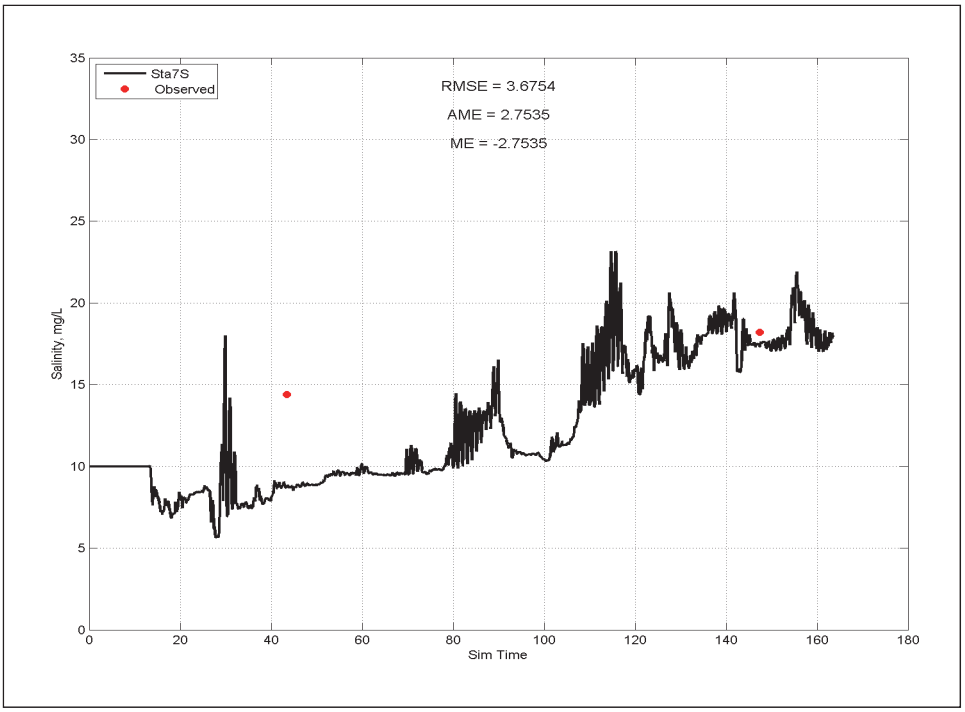

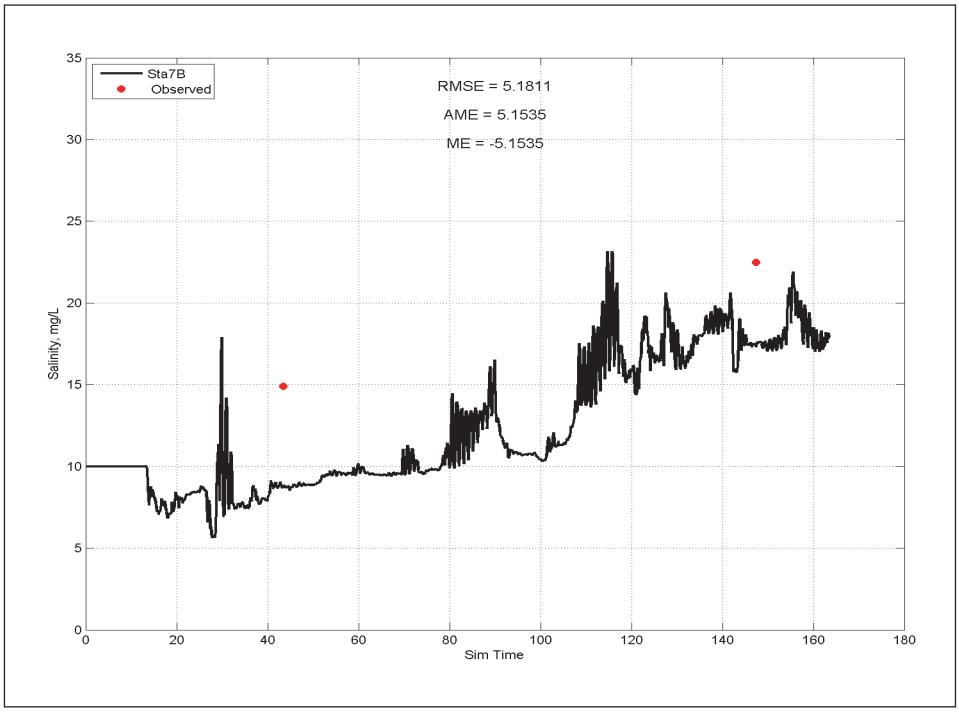

Figure E-39. Calibration results for DO at Station 7 for surface layer (upper) and bottom layer (lower).

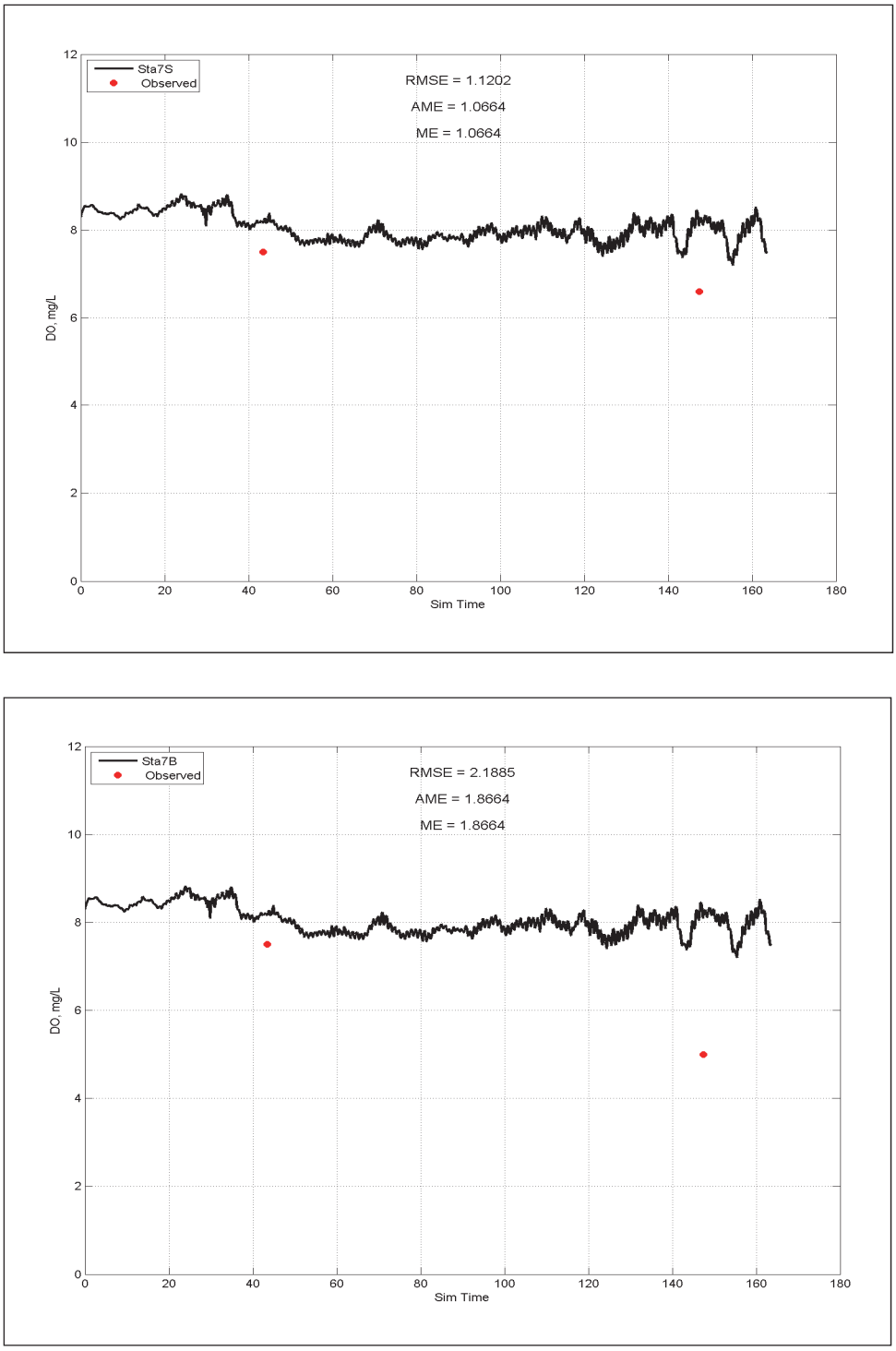

Figure E-40. Calibration results for NH_4 at Station 7 for surface layer (upper) and bottom layer (lower).

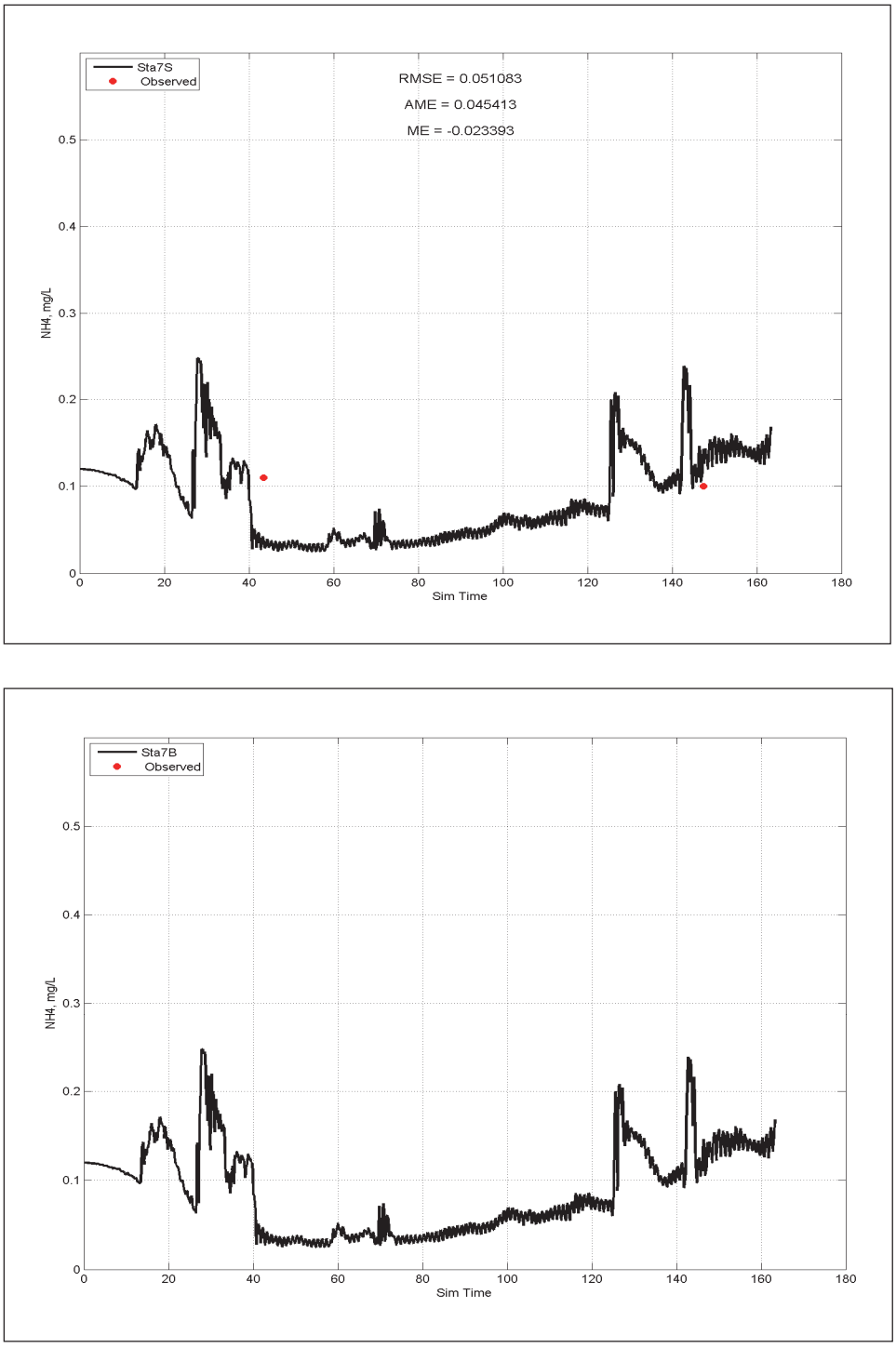

Figure E-41 Calibration results for NO_3 at Station 7 for surface layer (upper) and bottom layer (lower).

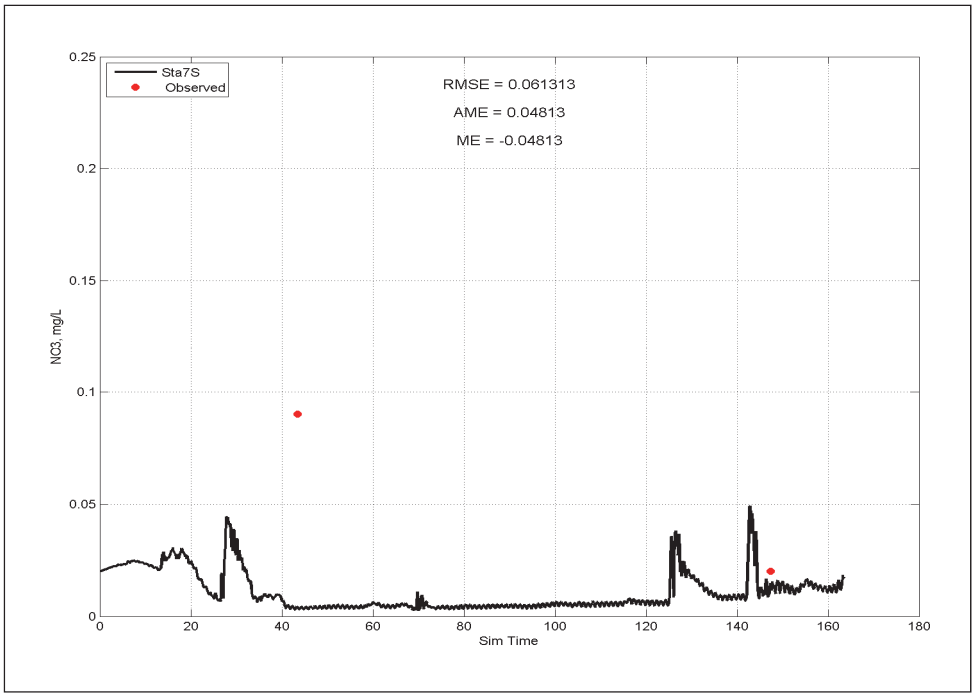

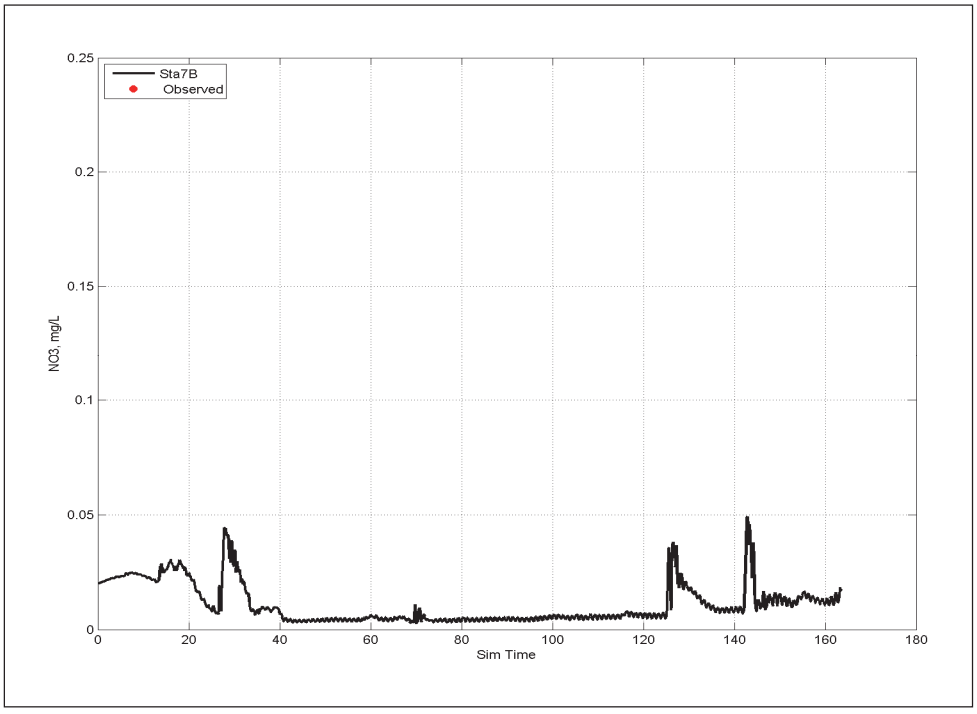

Figure E-42. Calibration results for *Tp* at Station 7 for surface layer (upper) and bottom layer (lower).

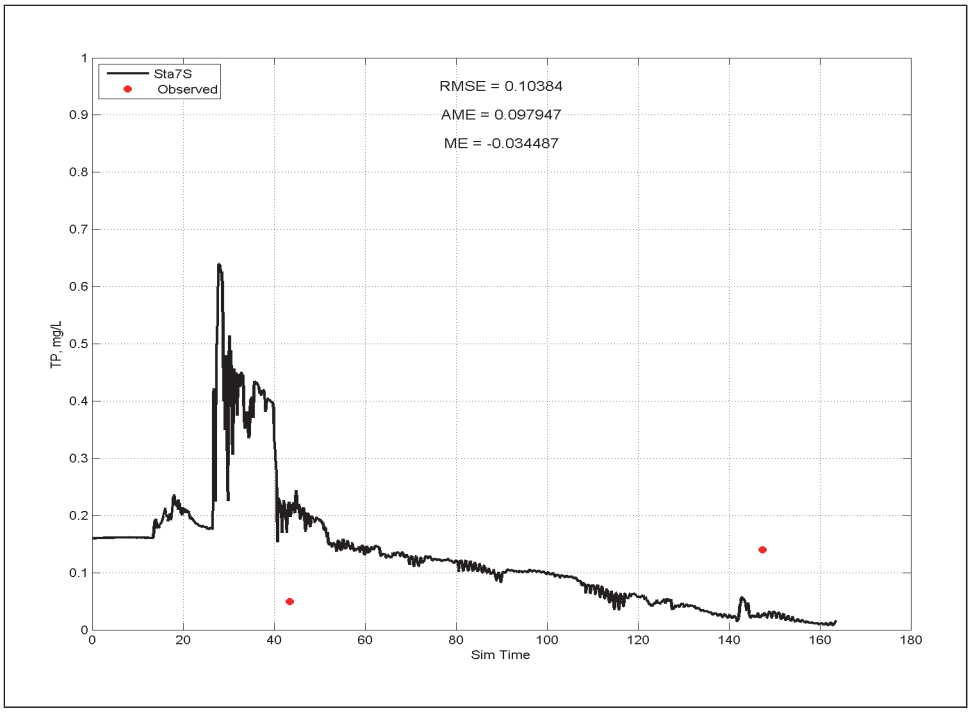

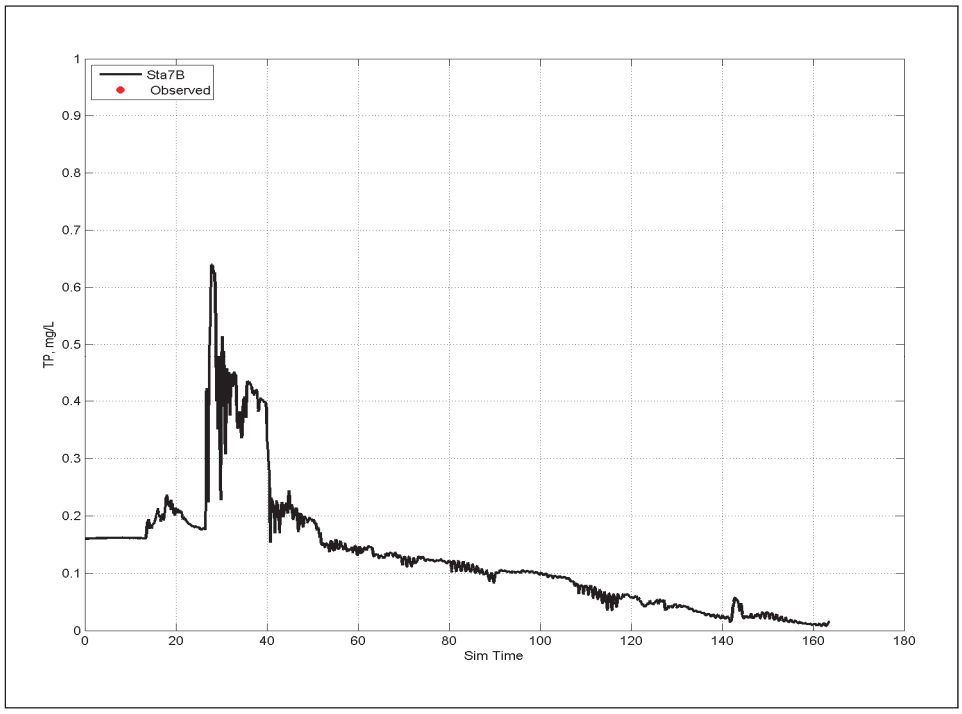

Figure E-43. Calibration results for temperature at Station 8 for surface layer (upper) and bottom layer (lower).

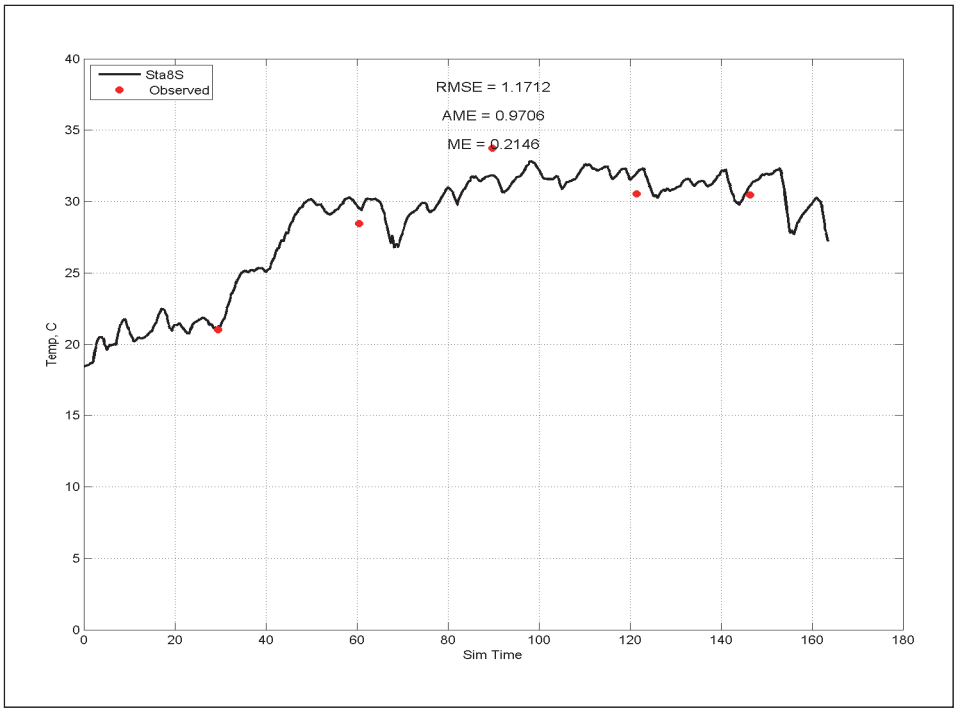

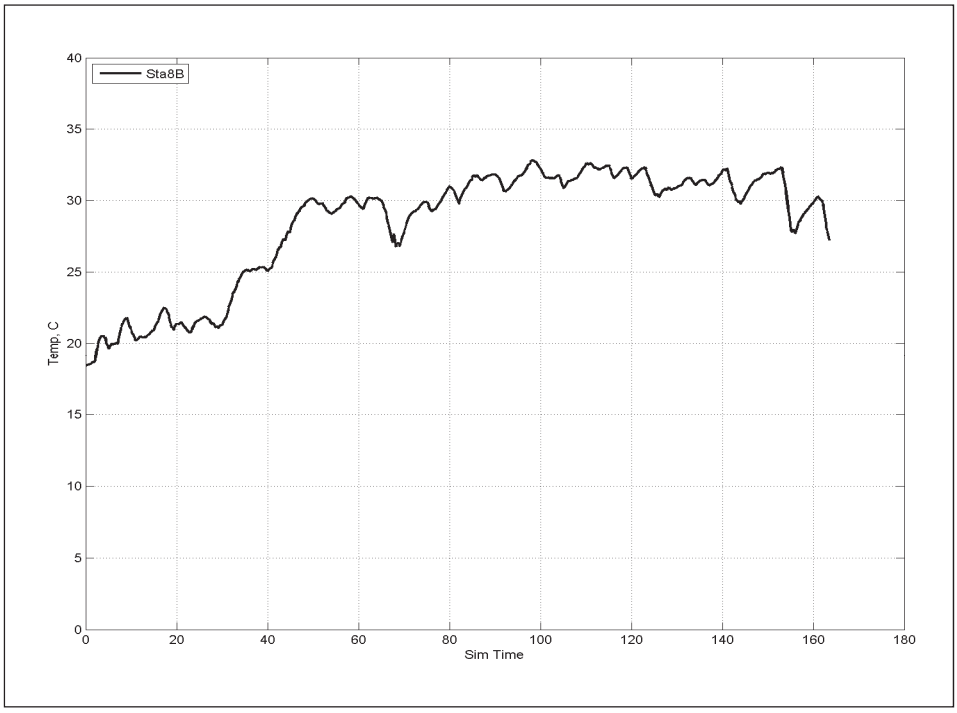

Figure E-44. Calibration results for salinity at Station 8 for surface layer (upper) and bottom layer (lower).

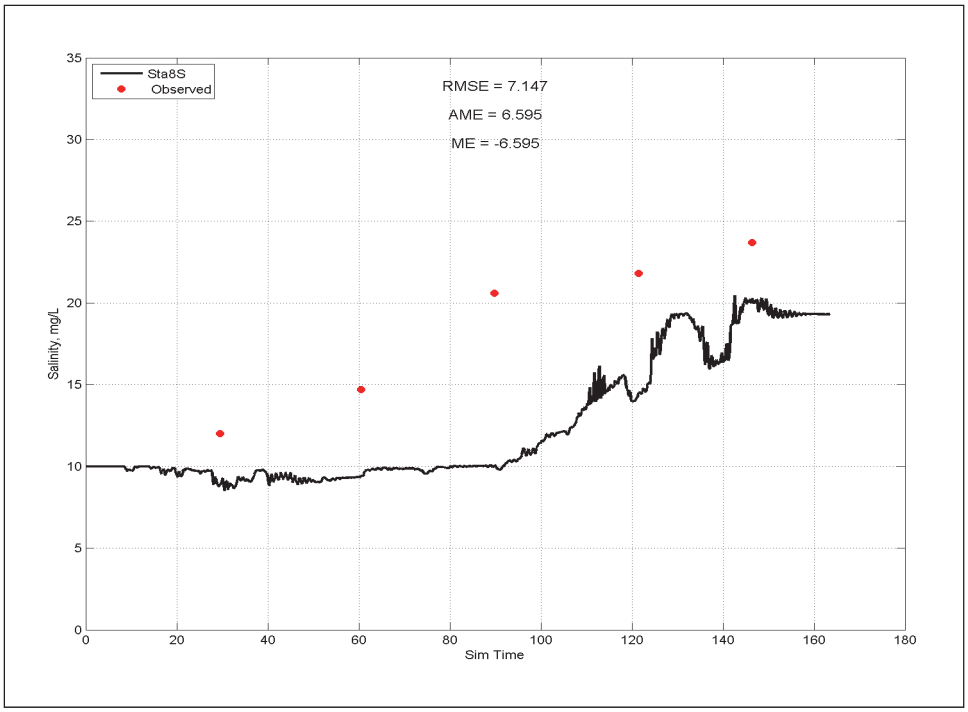

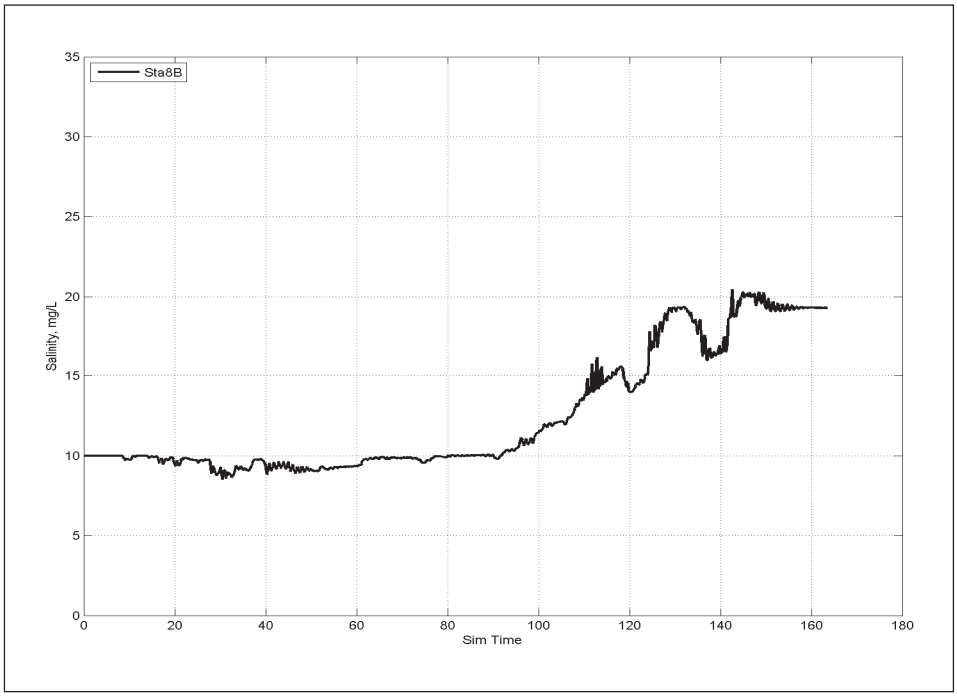

Figure E-45. Calibration results for DO at Station 8 for surface layer (upper) and bottom layer lower).

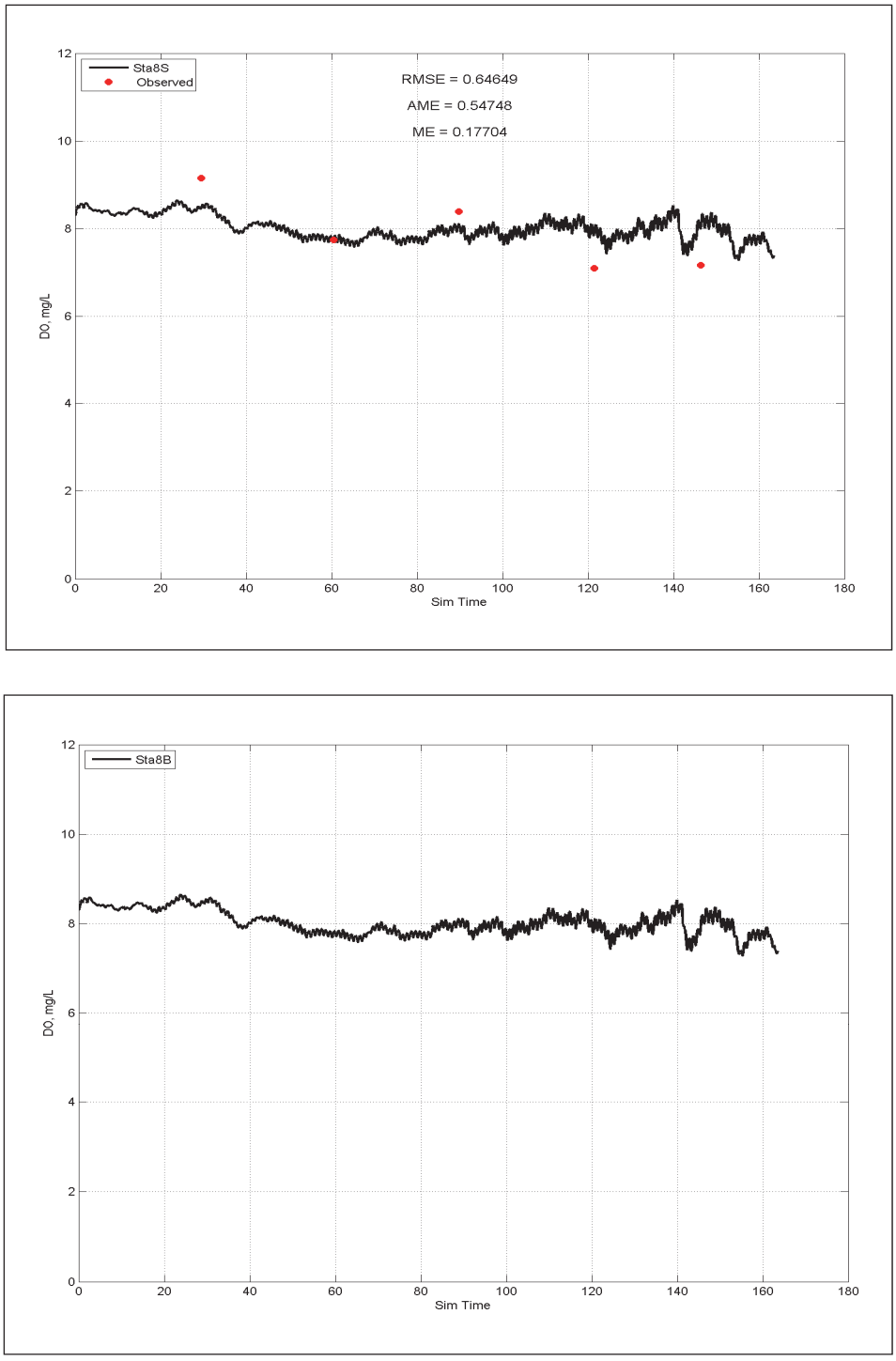

Figure E-46. Calibration results for NH_4 at Station 8 for surface layer (upper) and bottom layer (lower).

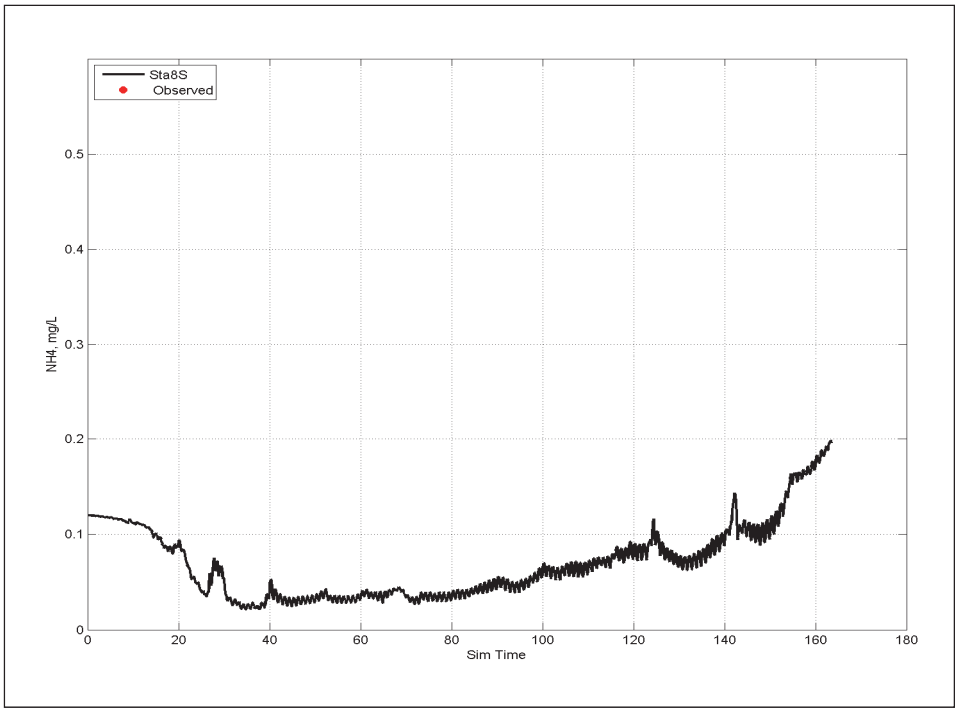

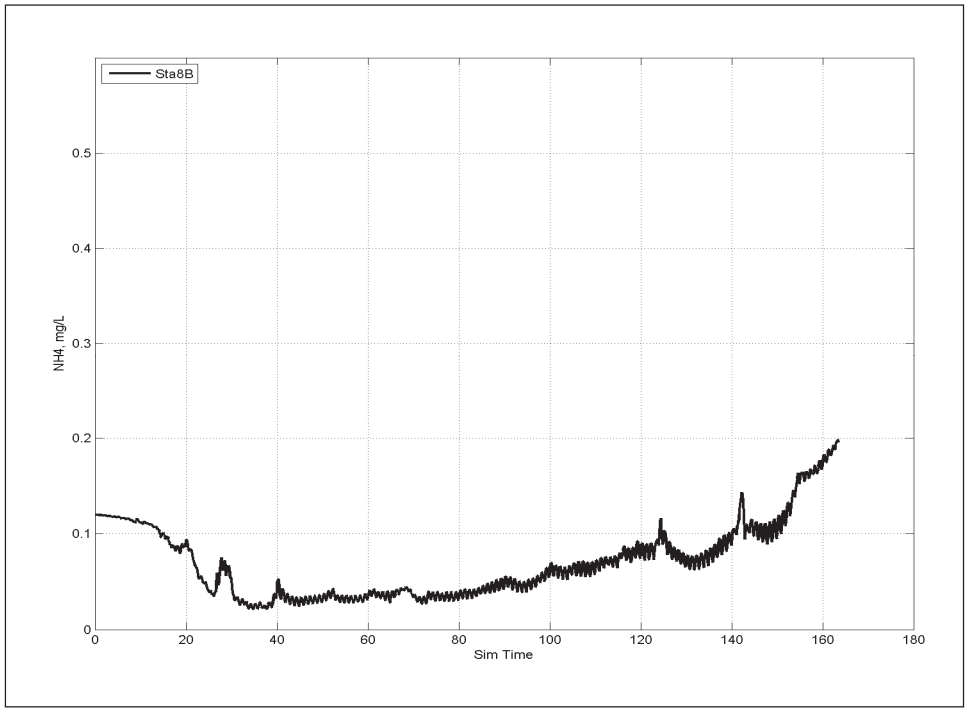

Figure E-47 Calibration results for NO_3 at Station 8 for surface layer (upper) and bottom layer (lower).

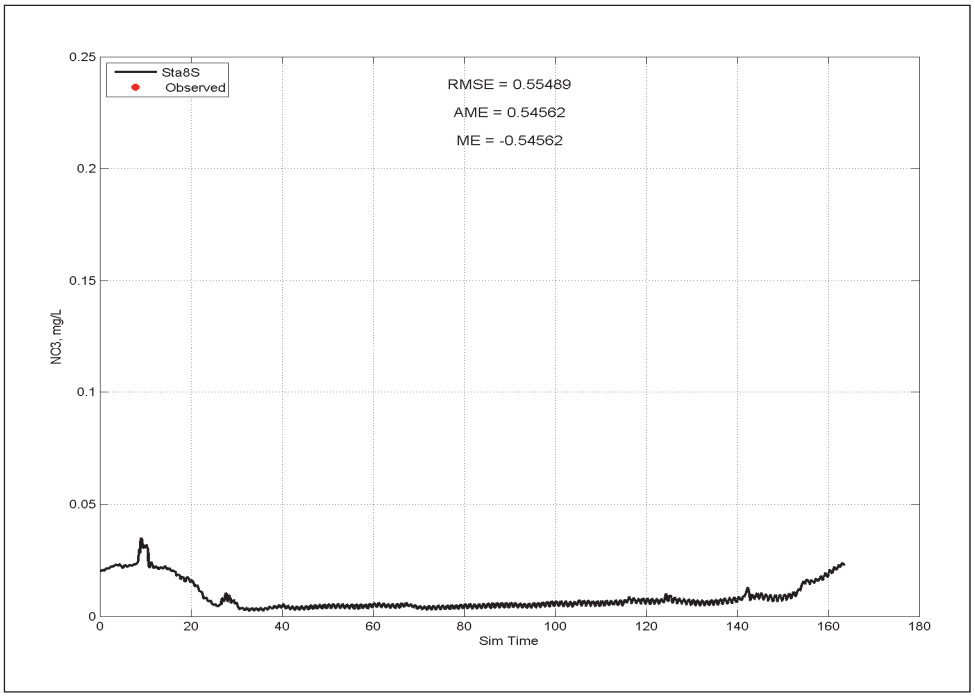

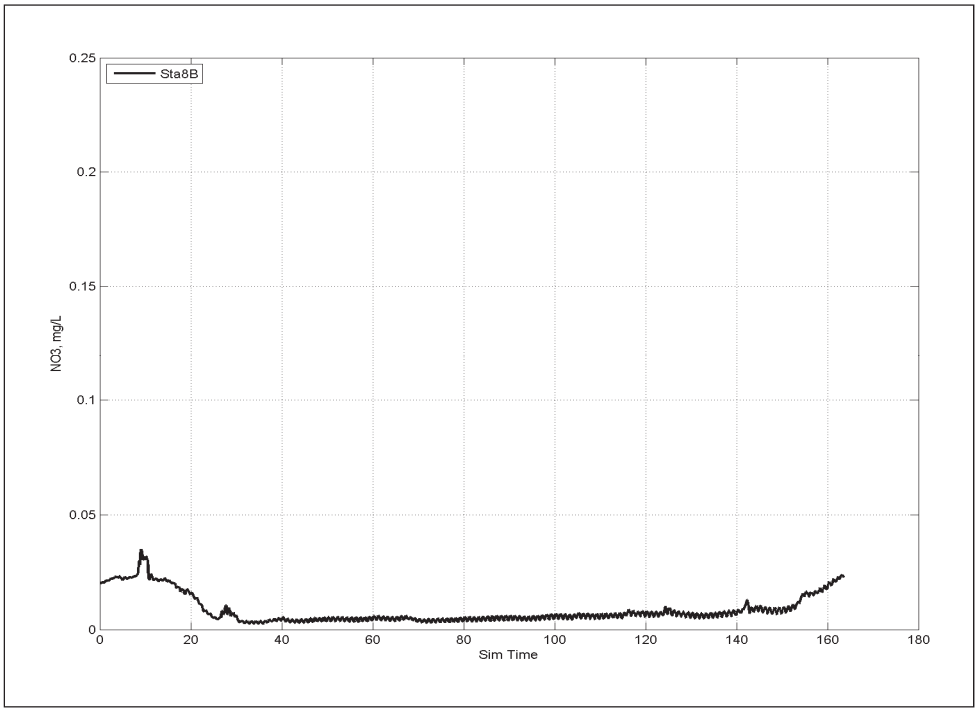

Figure E-48. Calibration results for *Tp* at Station 8 for surface layer (upper) and bottom layer lower).

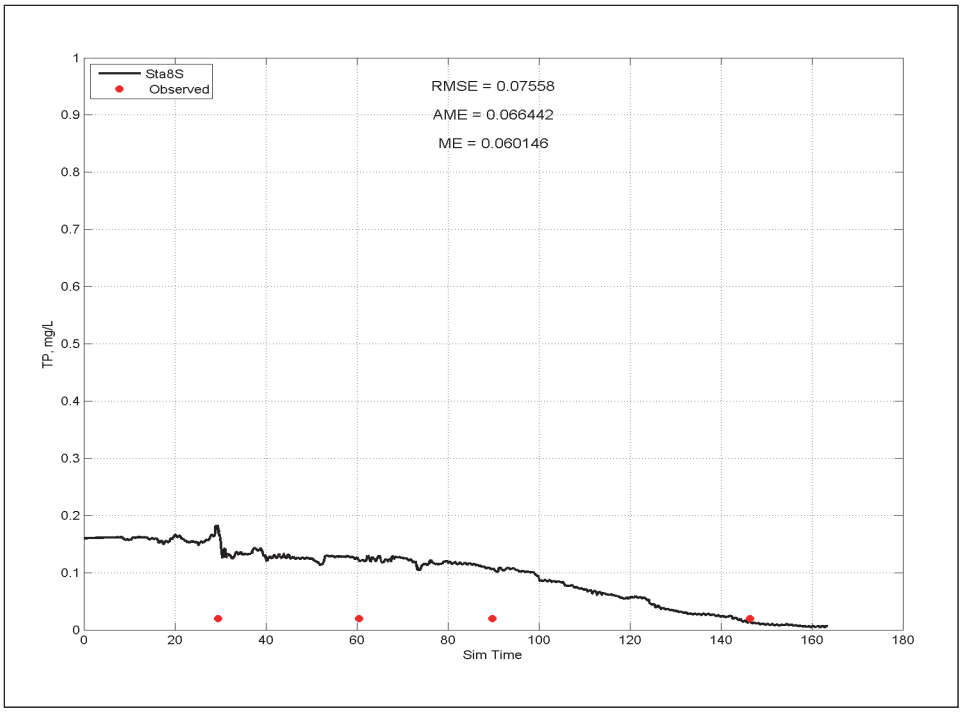

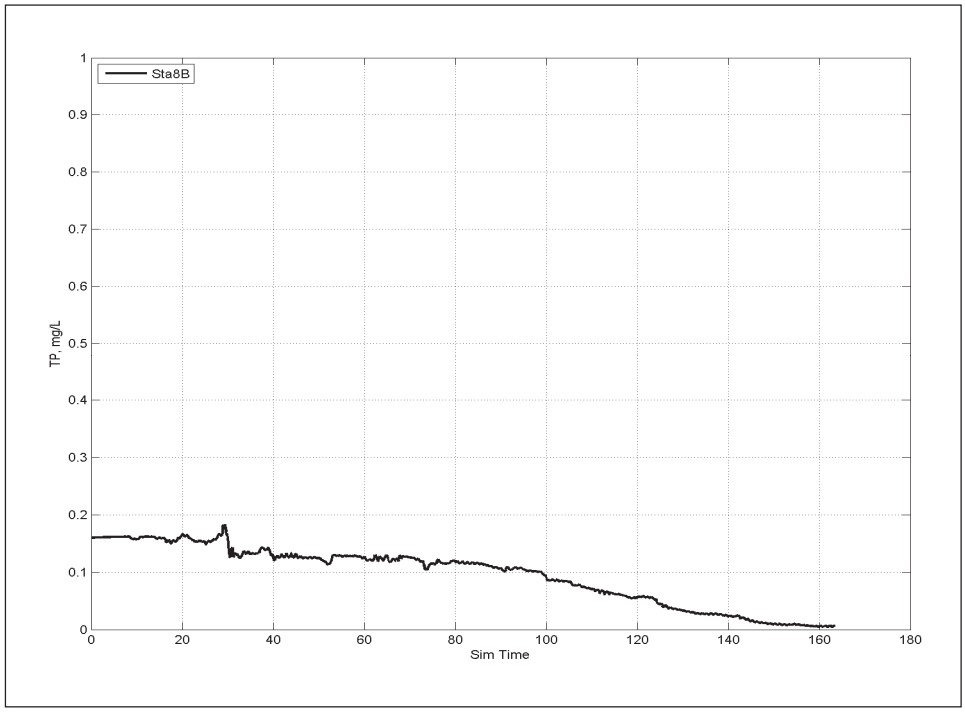

Figure E-49. Calibration results for temperature at Station 9 for surface layer (upper) and layer (lower).

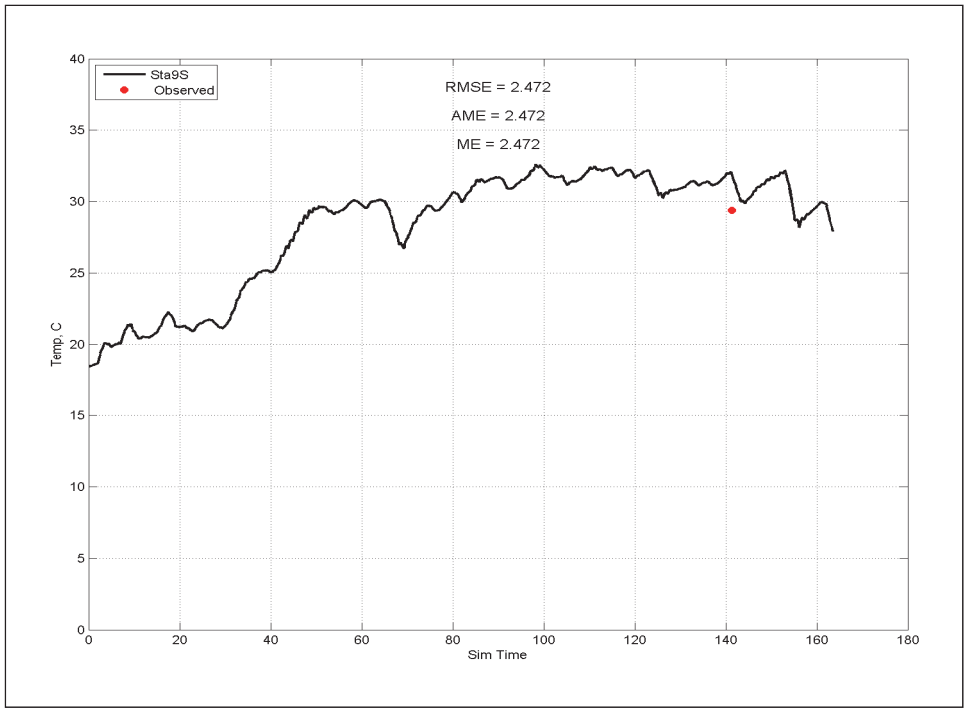

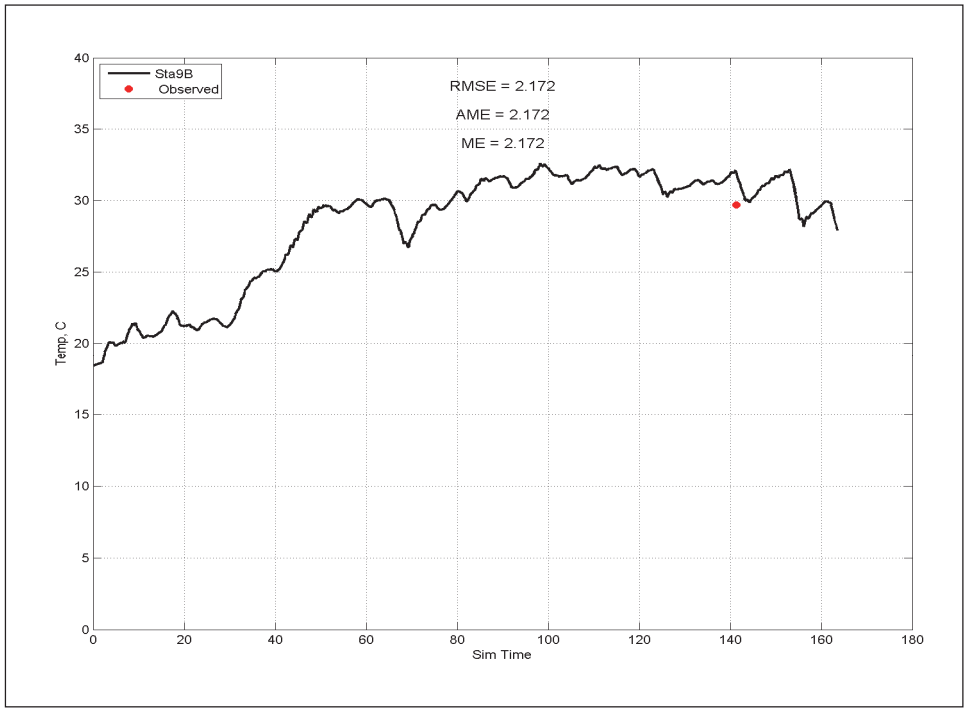

Figure E-50. Calibration results for salinity at Station 9 for surface layer (upper) and bottom layer (lower).

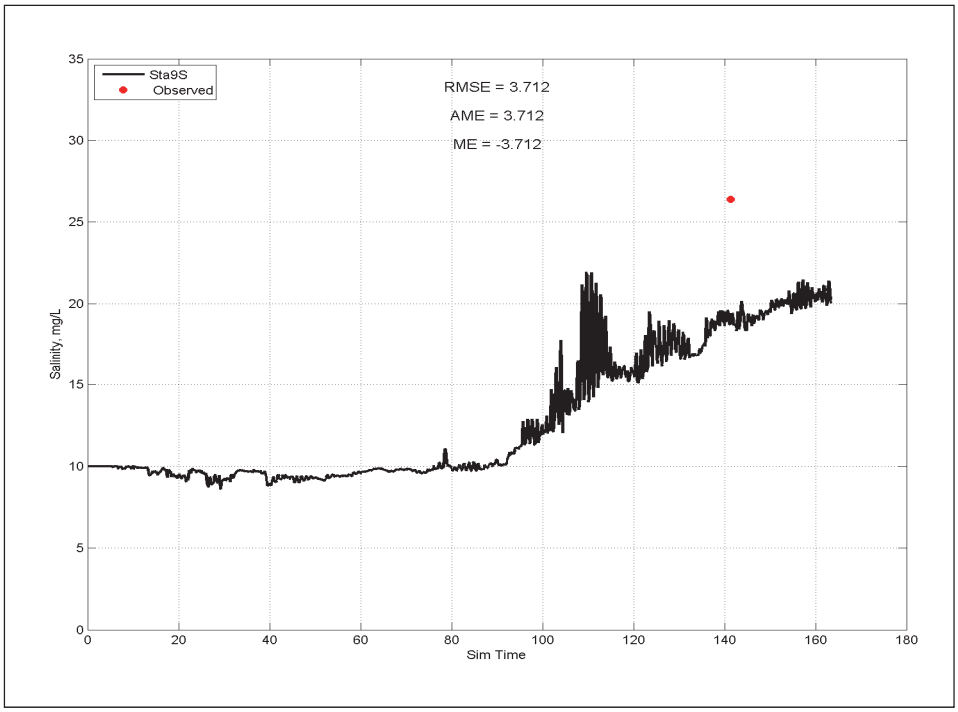

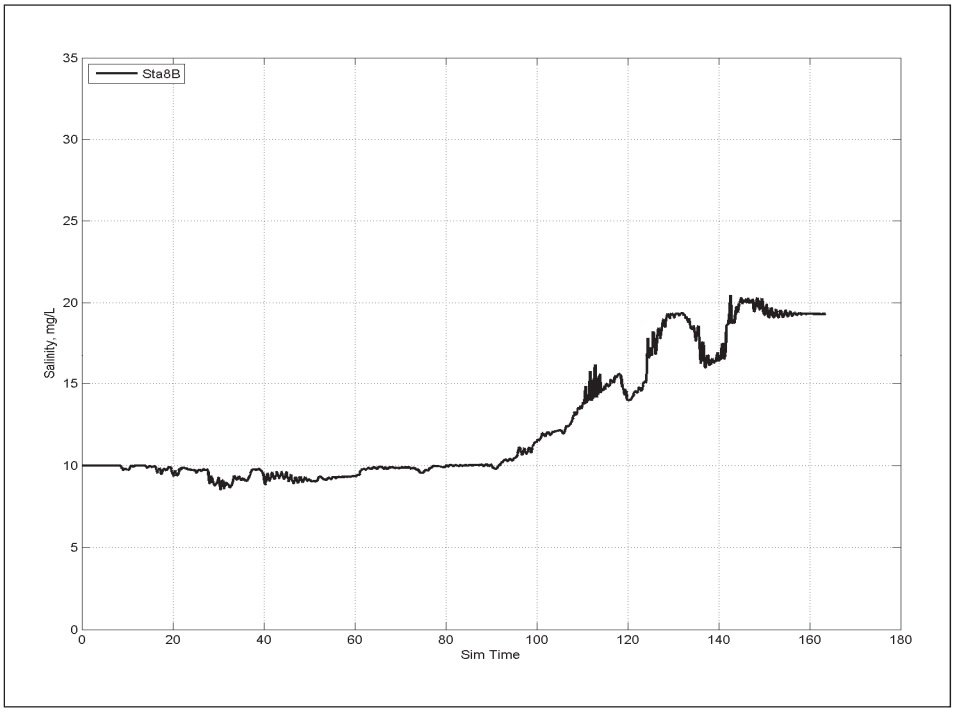

Figure E-51. Calibration results for DO at Station 9 for surface layer (upper) and bottom layer lower).

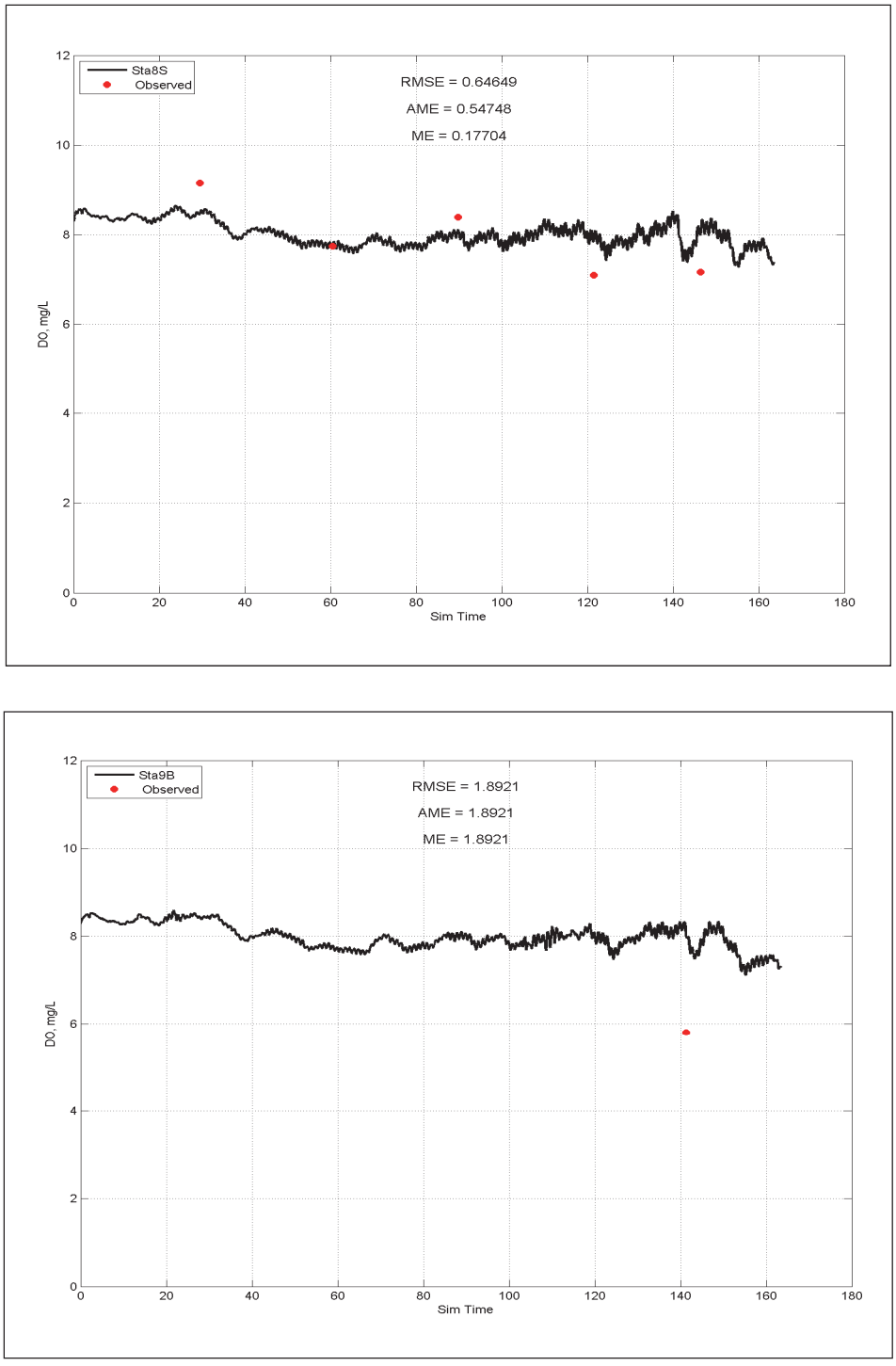

Figure E-52. Calibration results for NH_4 at Station 9 for surface layer (upper) and bottom layer (lower).

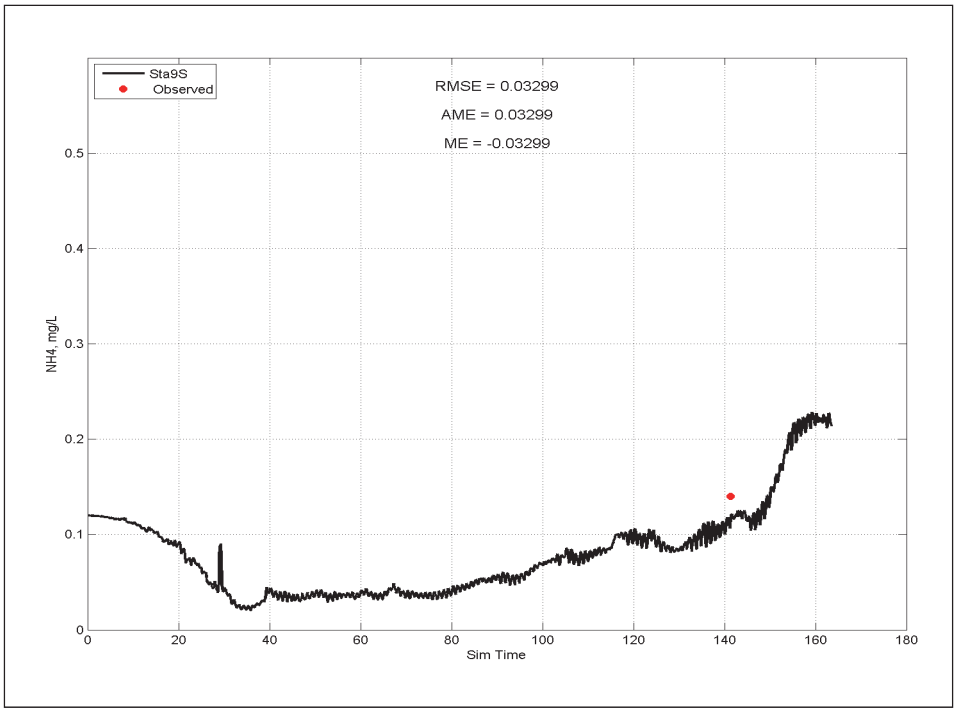

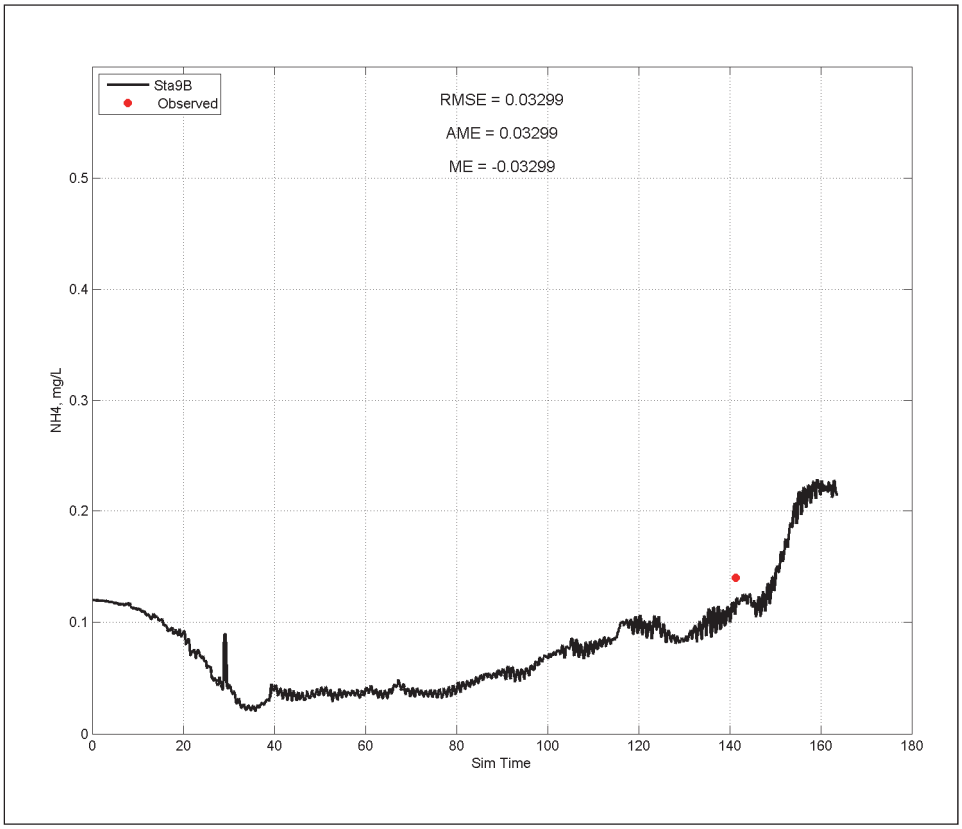

Figure E-53. Calibration results for NO_3 at Station 9 for surface layer (upper) and bottom layer (lower).

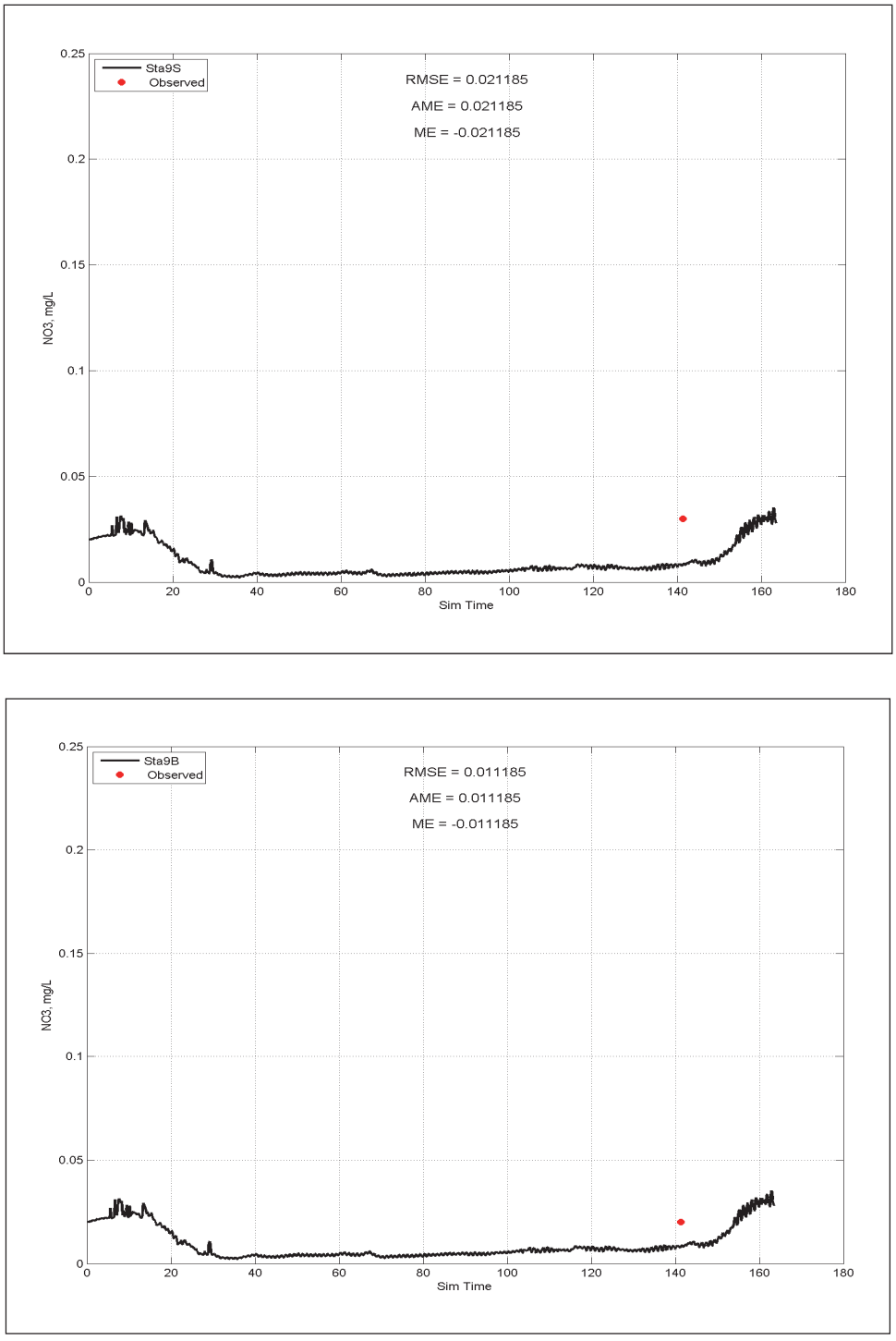

Figure E-54. Calibration results for *Tp* at Station 9 for surface layer (upper) and bottom layer (lower).

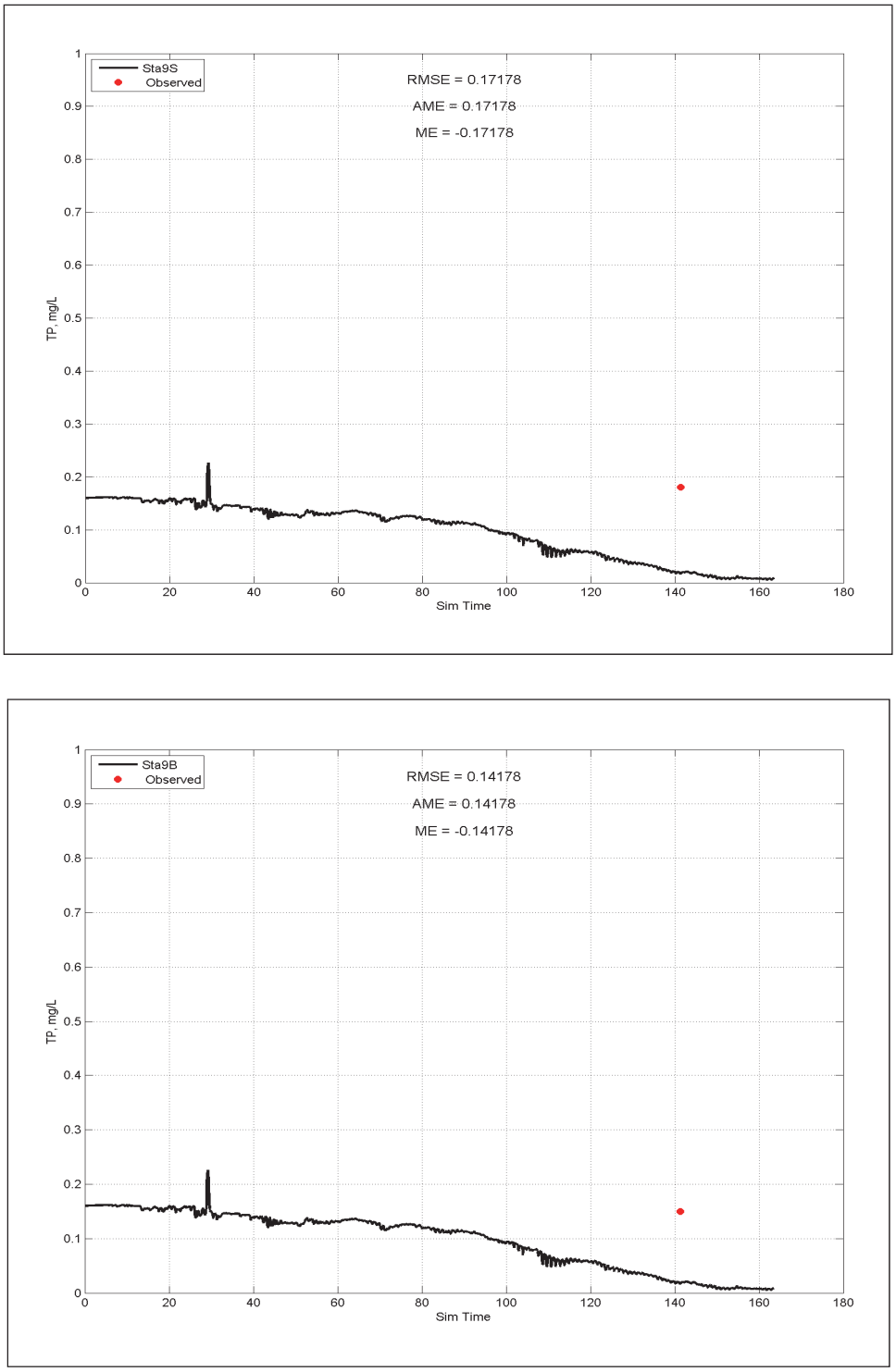

Figure E-55. Calibration results for temperature at Station 10 for surface layer (upper) and bottom layer (lower).

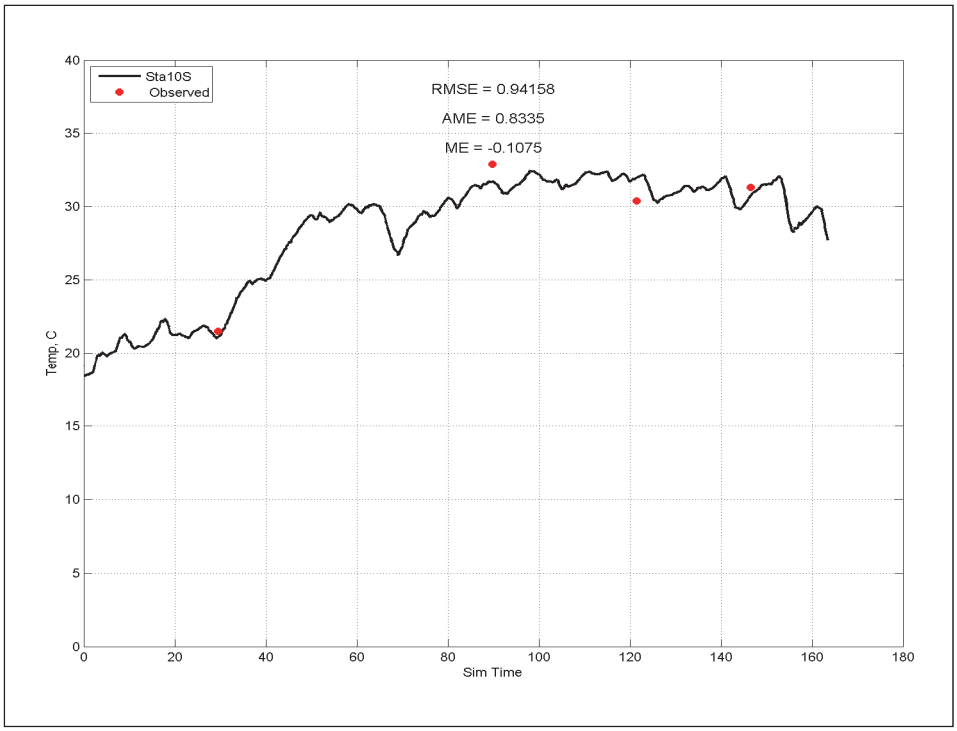

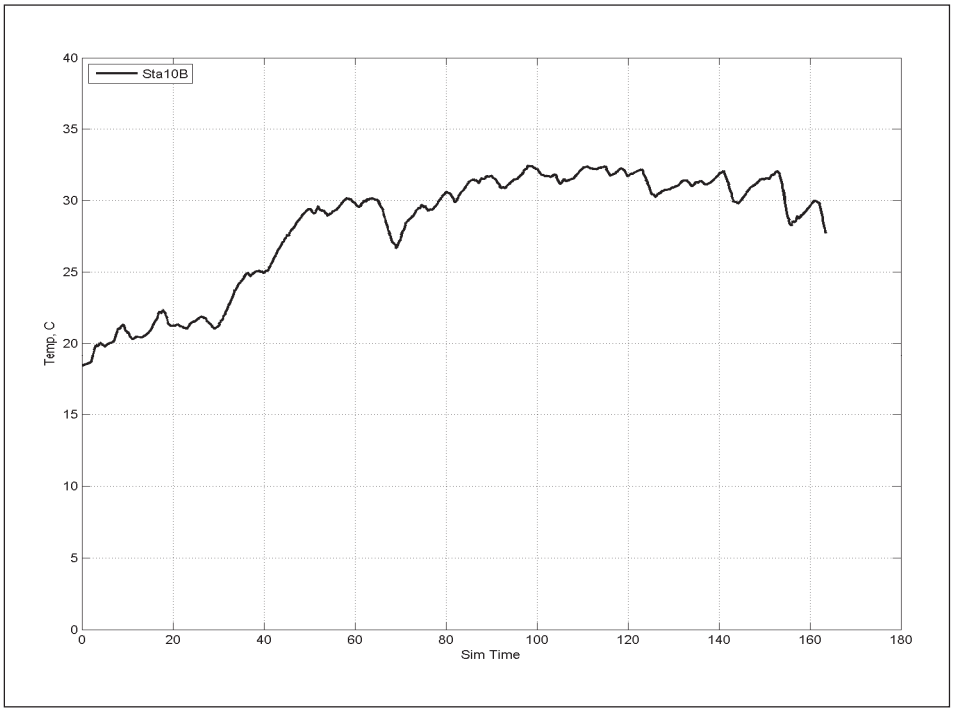

Figure E-56 Calibration results for salinity at Station 10 for surface layer (upper) and bottom layer (lower).

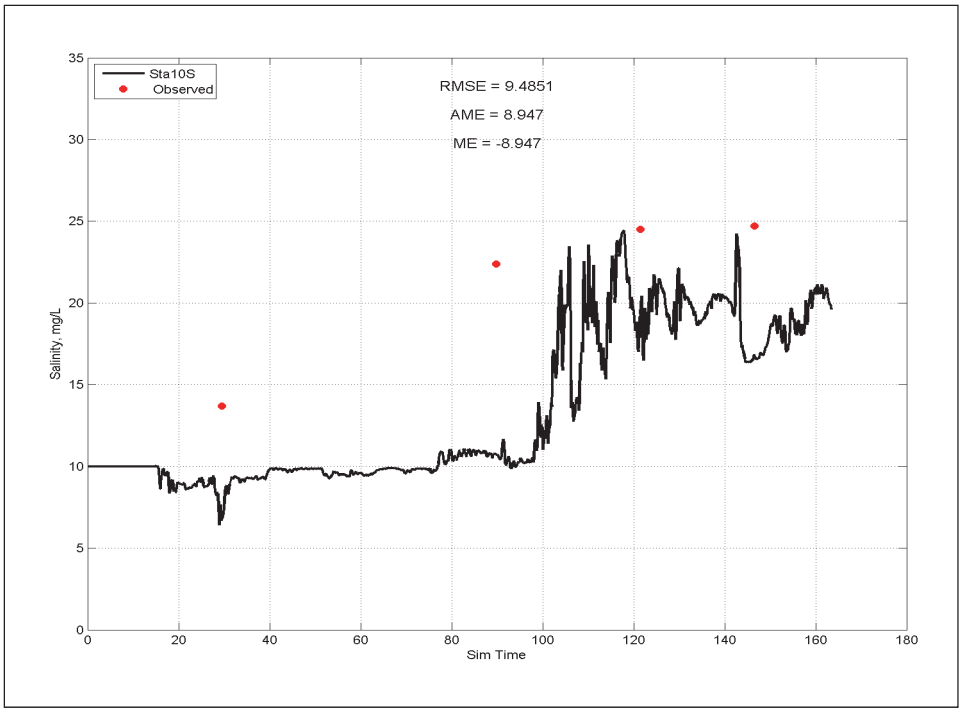

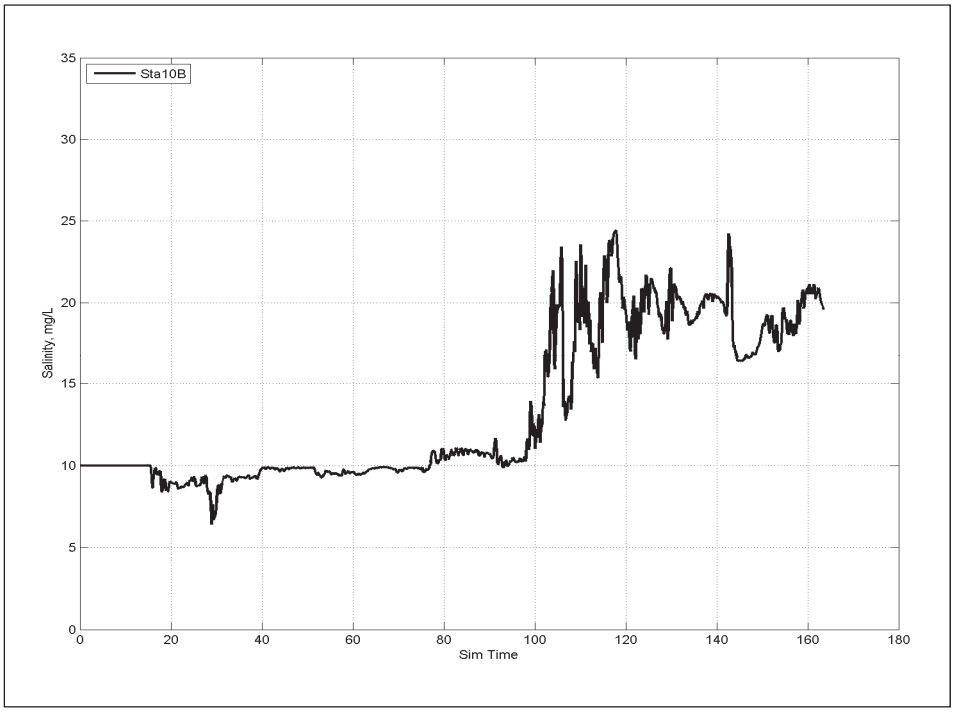

Figure E-57. Calibration results for DO at Station 10 for surface layer (upper) and bottom layer (lower).

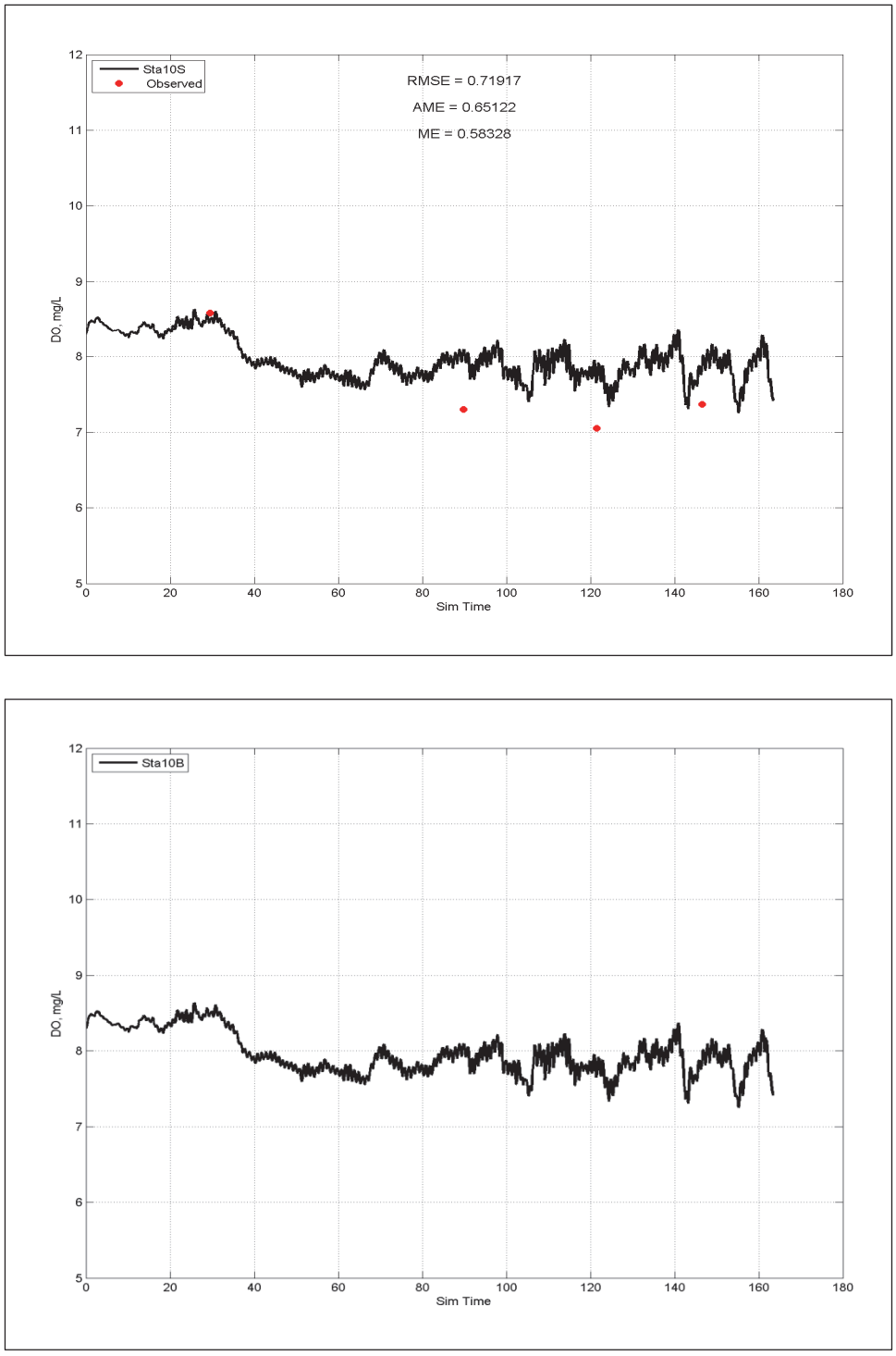

Figure E-58. Calibration results for NH_4 at Station 10 for surface layer (upper) and bottom layer (lower).

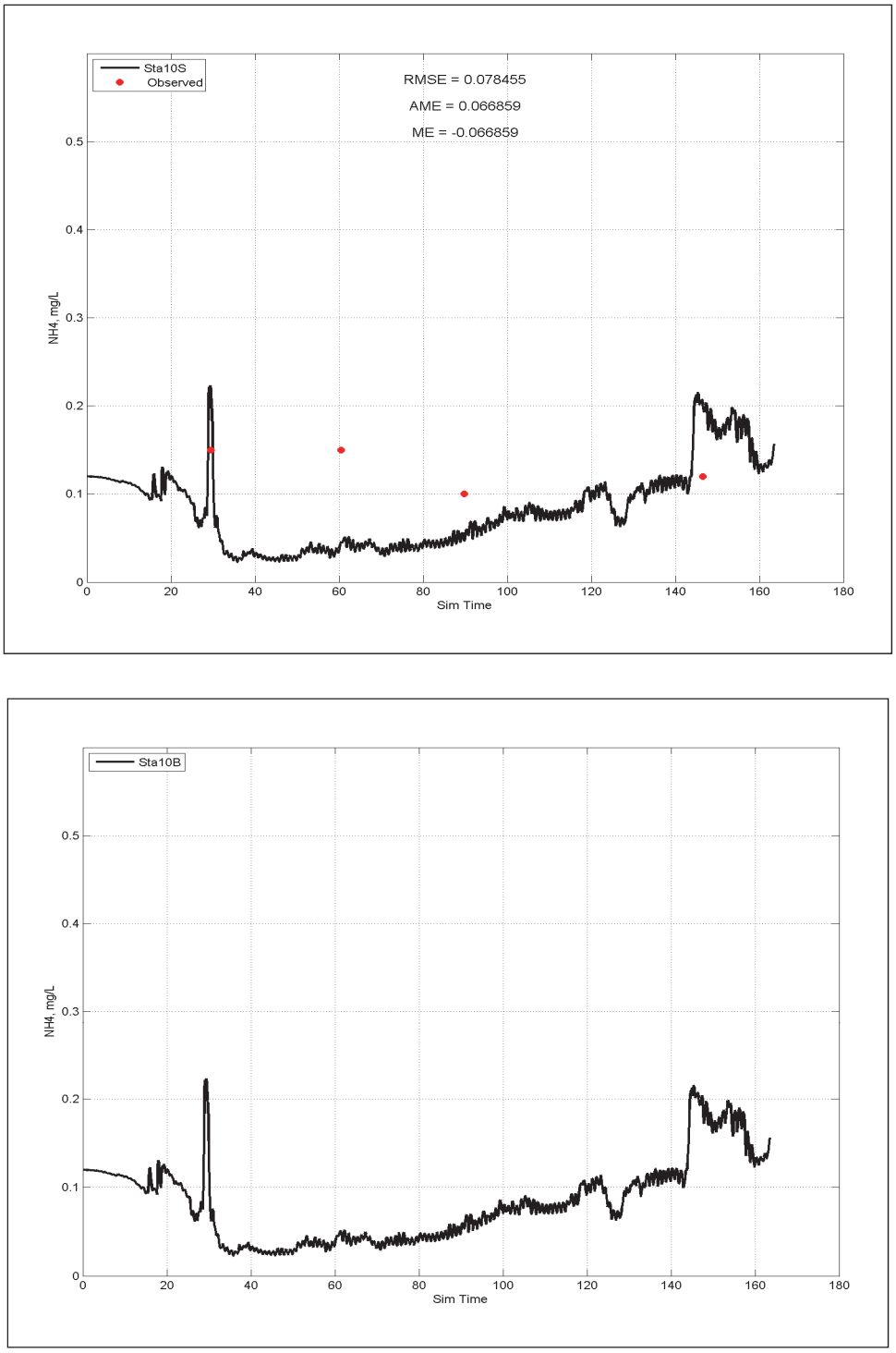

Figure E-59. Calibration results for NO_3 at Station 10 for surface layer (upper) and bottom layer (lower).

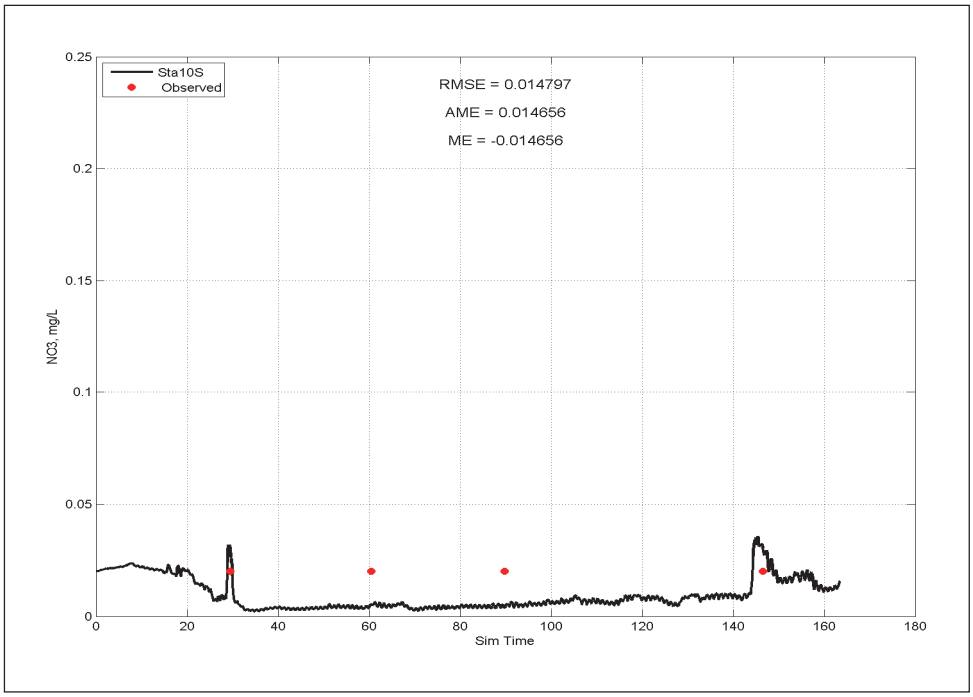

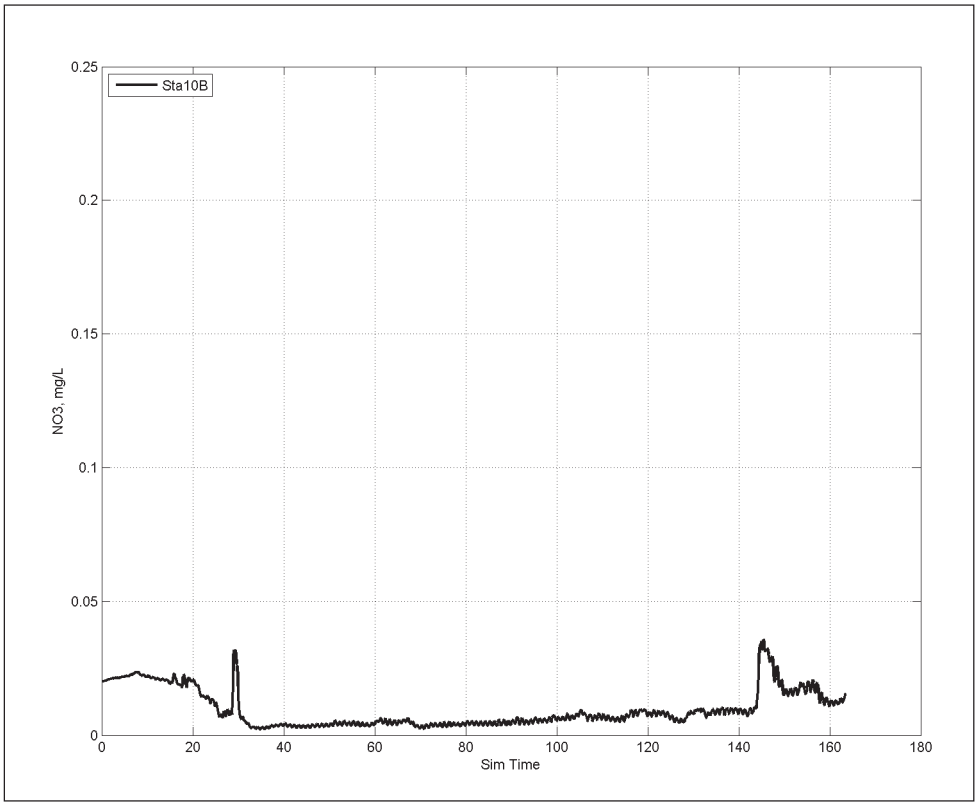

Figure E-60. Calibration results for *Tp* at Station 10 for surface layer (upper) and bottom layer (lower).

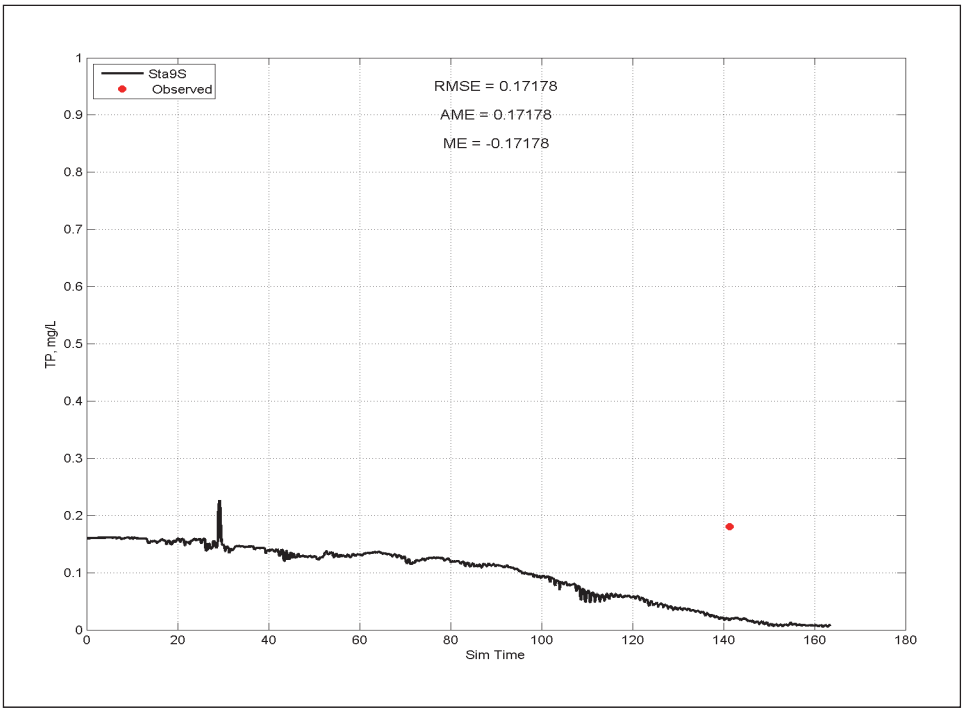

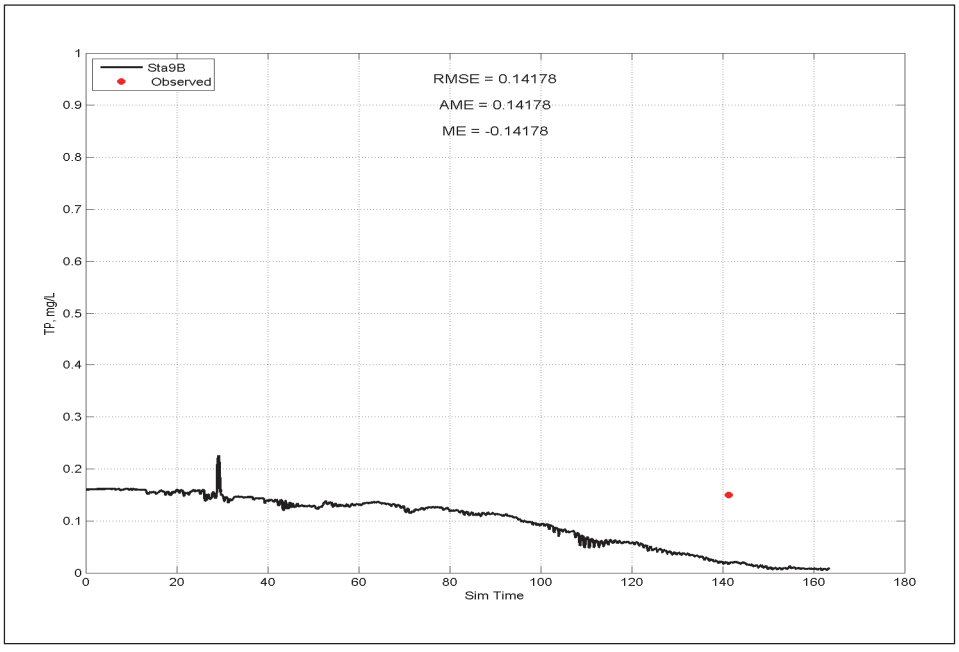

Figure E-61. Comparison of DO, Chlororphyll, and Salinity at Station 1 (Figure 5-2) for results from simulations representing Pre, Post, Restored, Degraded, and Cumulative conditions (continued).

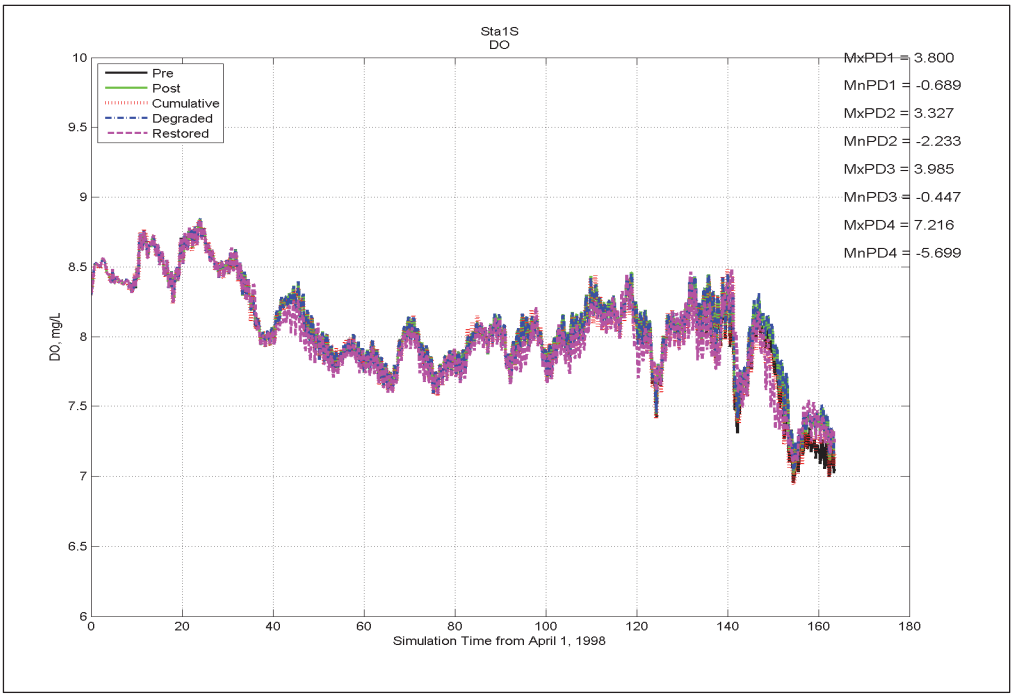

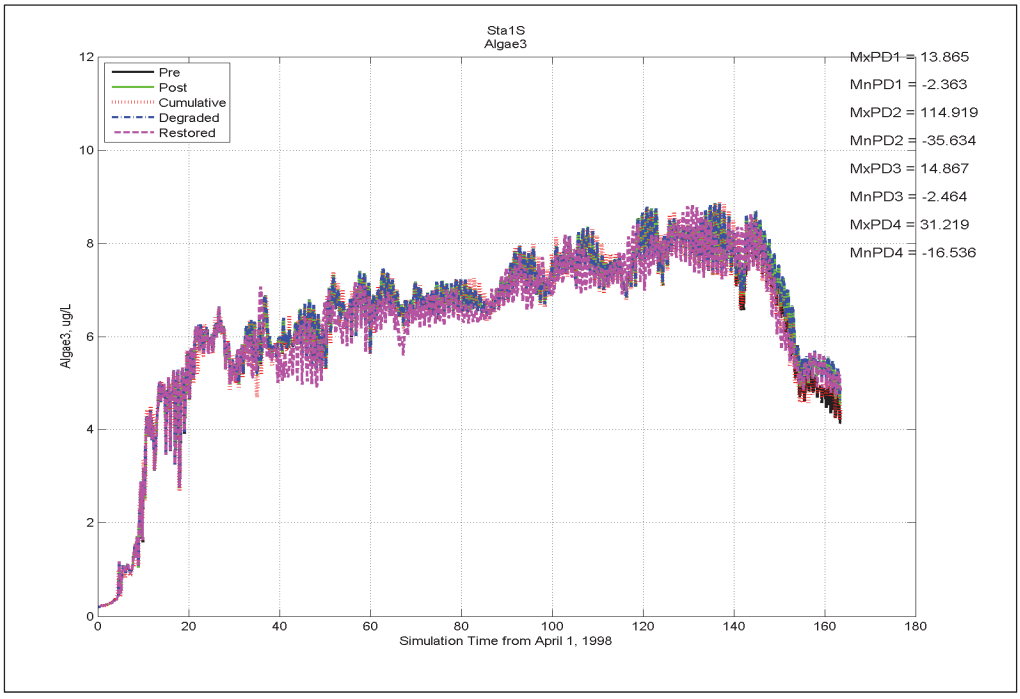

Figure B-61. Concluded.

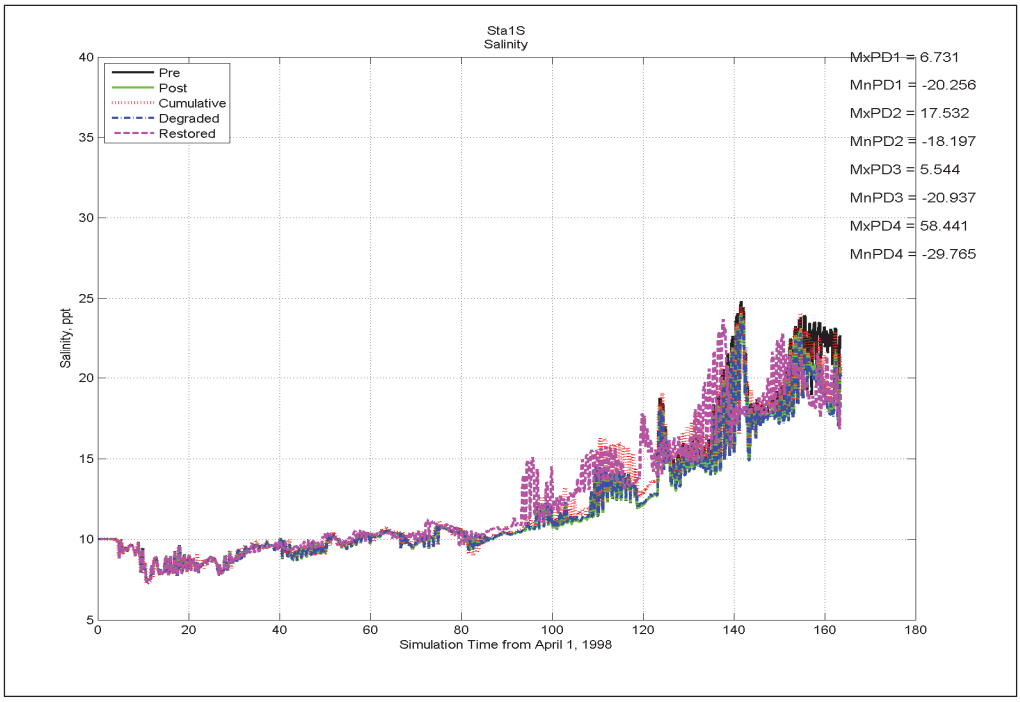

Figure E-62. Comparison of DO, Chlororphyll, and Salinity at Station 3 (Figure 5-2) for results from simulations representing Pre, Post, Restored, Degraded, and Cumulative conditions (continued).

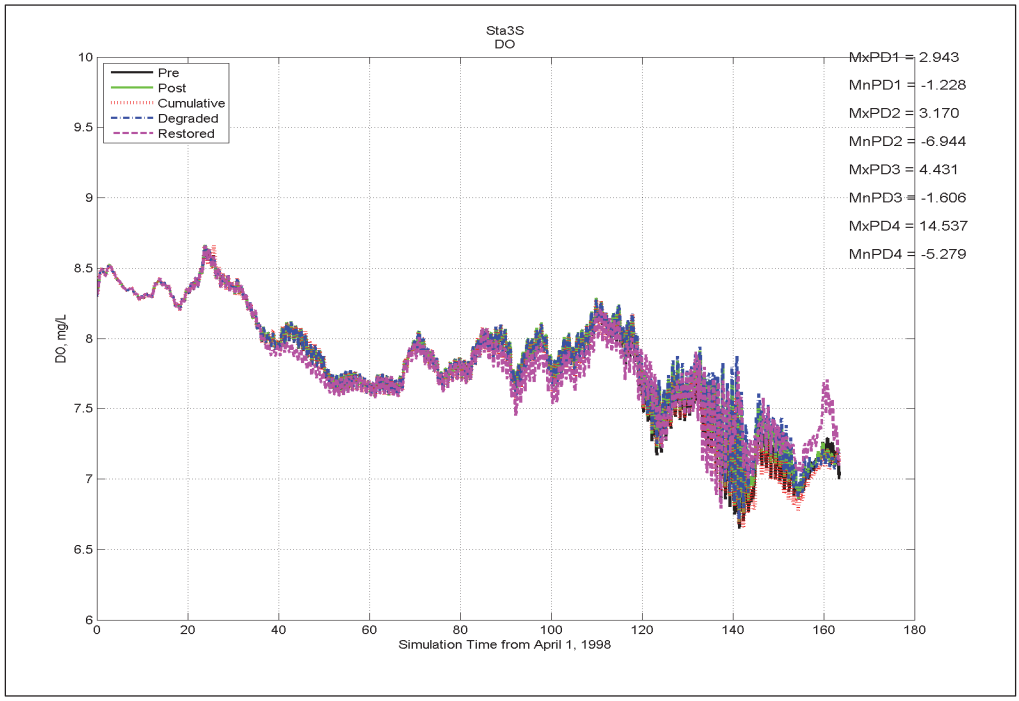

Figure E-62. Concluded.

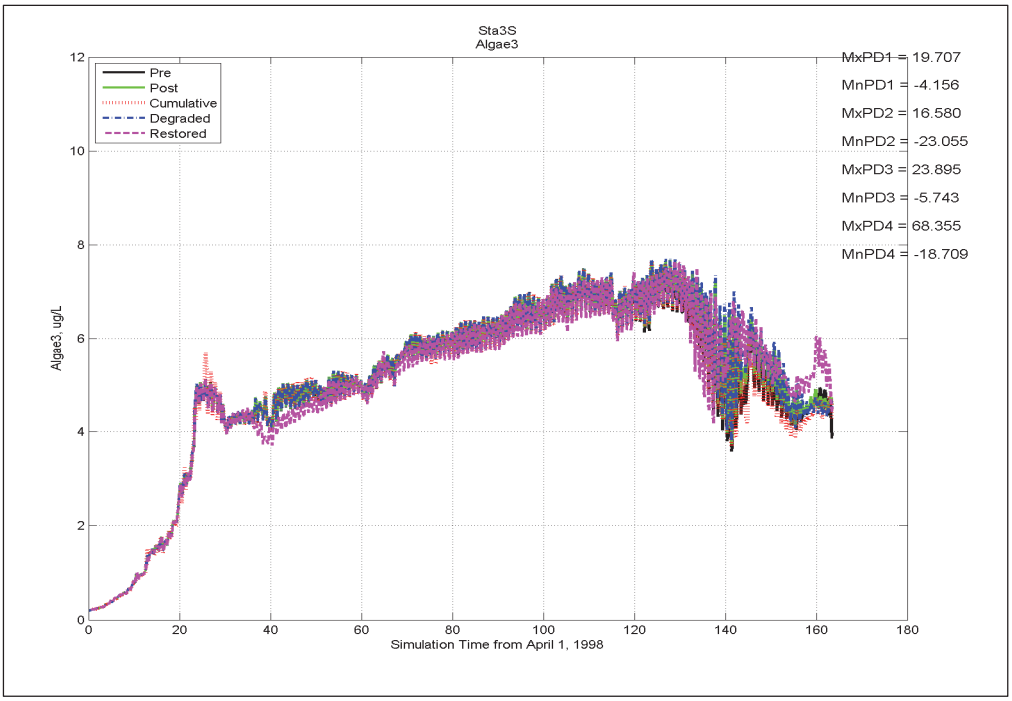

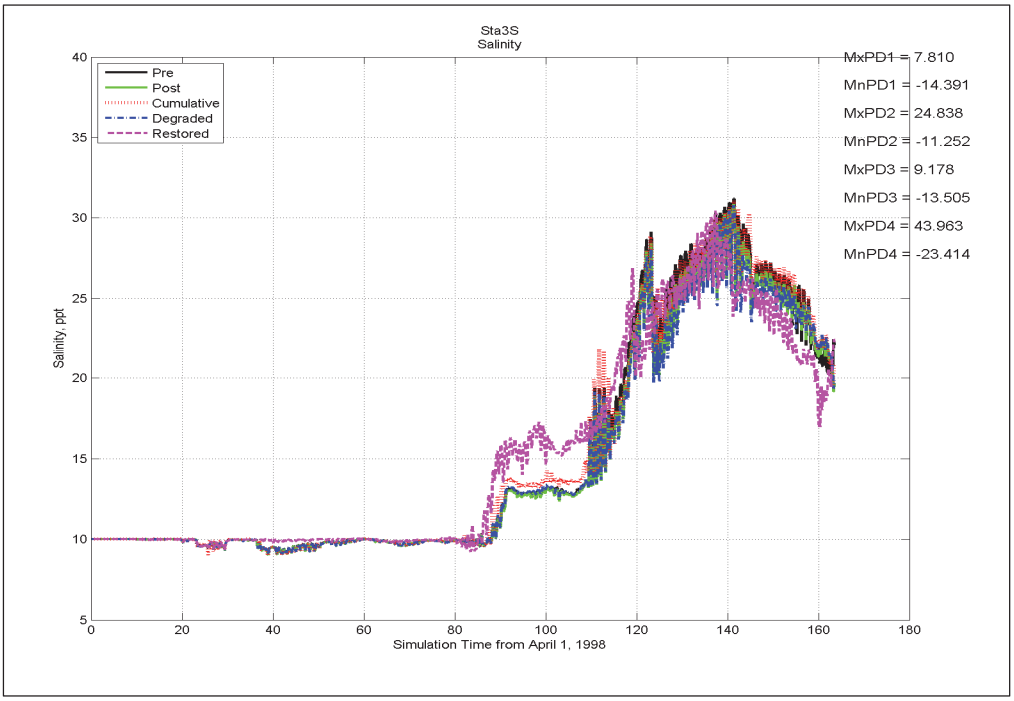

Figure E-63. Comparison of DO, Chlororphyll, and Salinity at Station 4 (Figure 5-2) for results from simulations representing Pre, Post, Restored, Degraded, and Cumulative conditions (continued).

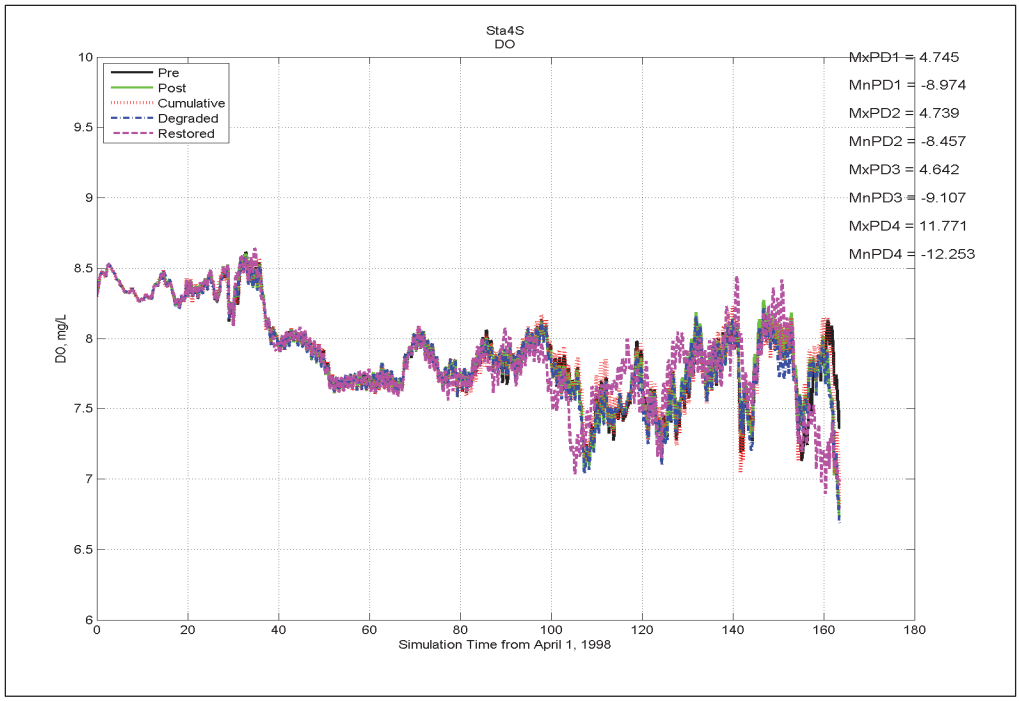

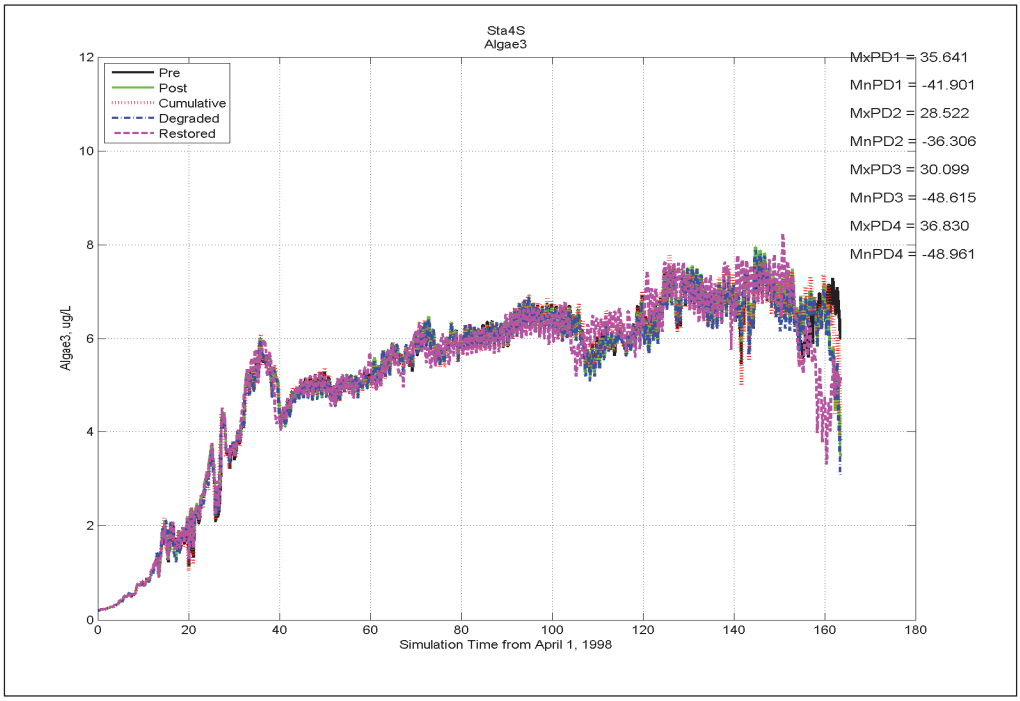

Figure E-63. Concluded.

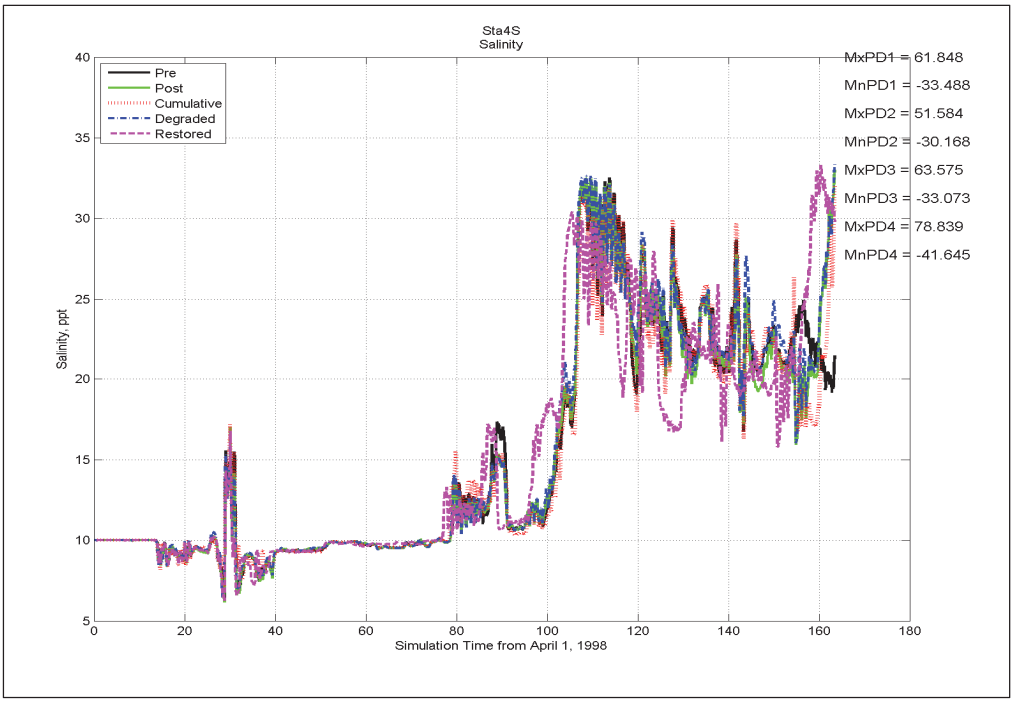

Figure E-64. Comparison of DO, Chlororphyll, and Salinity at Station 6 (Figure 5-2) for results from simulations representing Pre, Post, Restored, Degraded, and Cumulative conditions (continued).

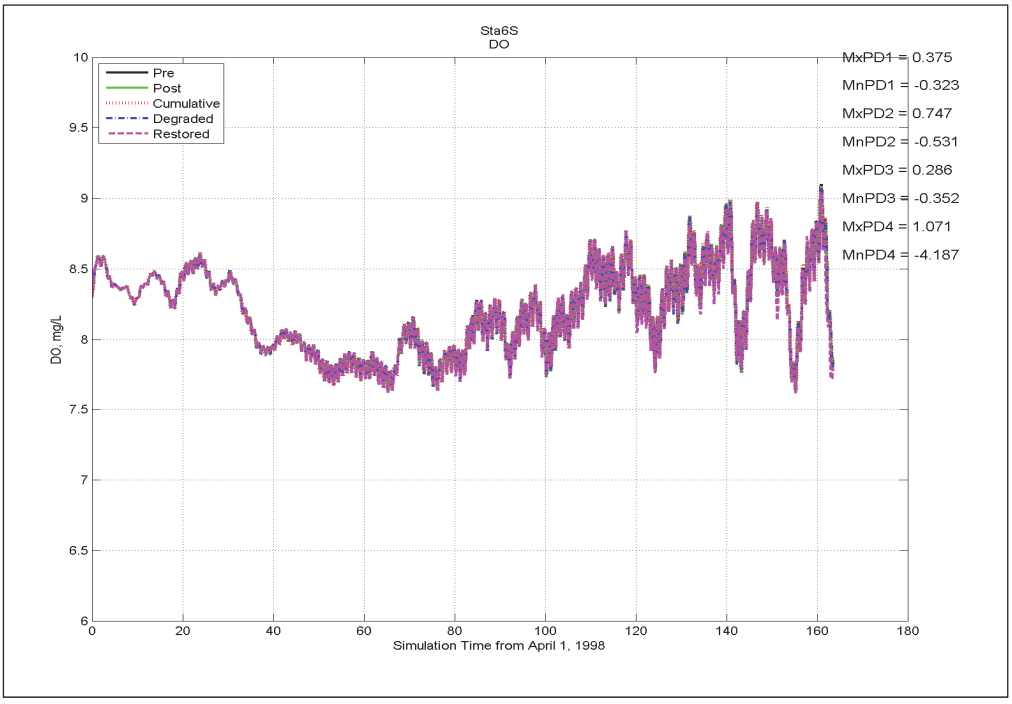

Figure E-64. Concluded.

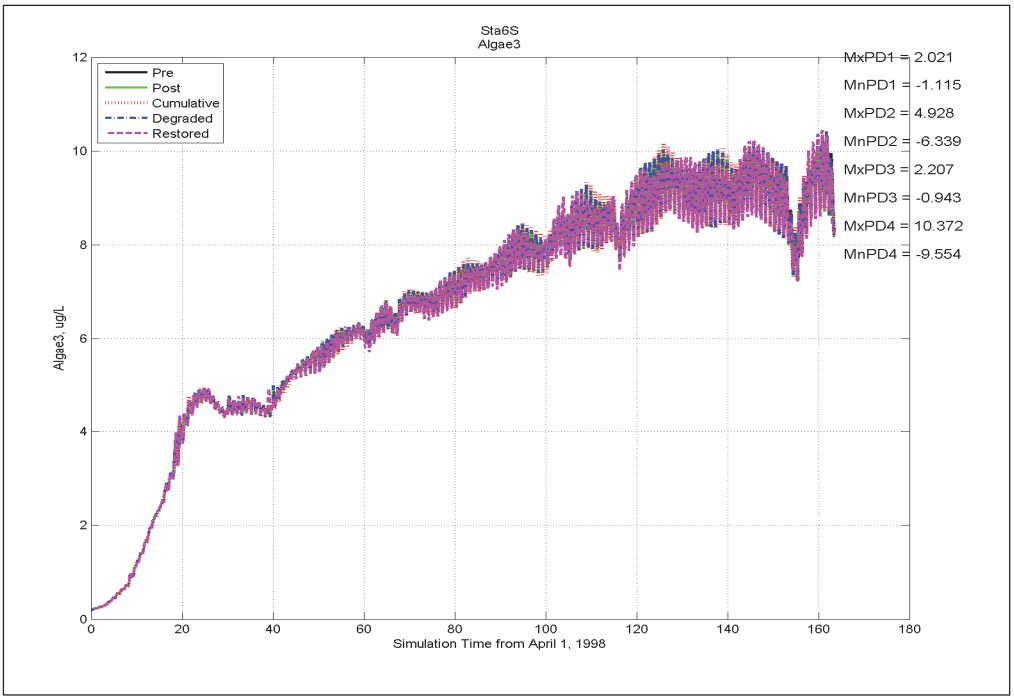

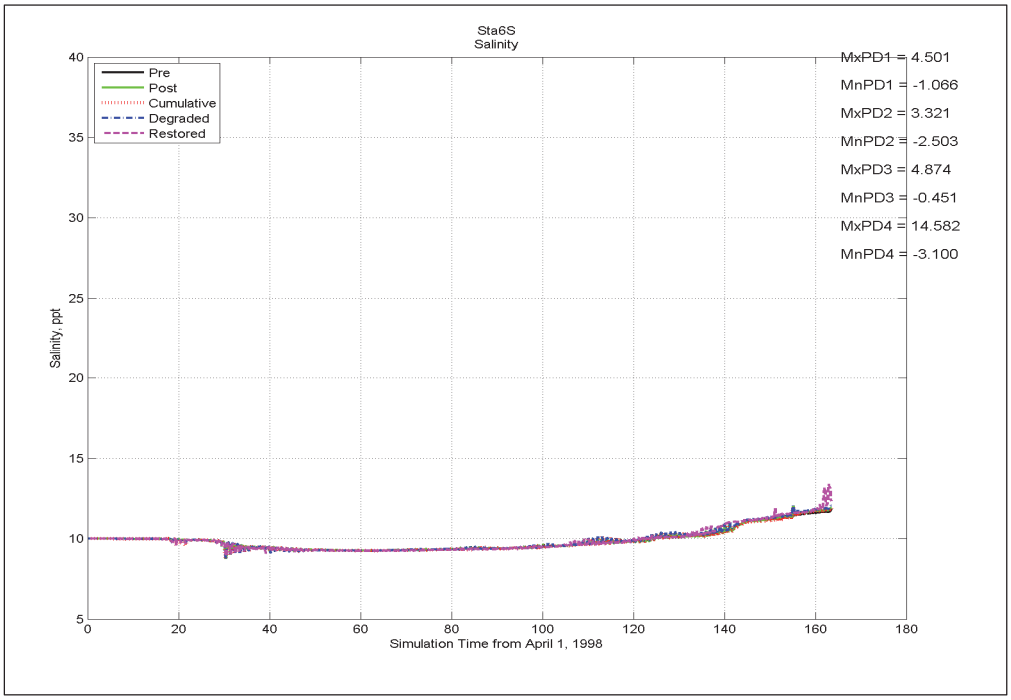

Figure E-65. Comparison of DO, Chlororphyll, and Salinity at Station 7 (Figure 5-2) for results from simulations representing Pre, Post, Restored, Degraded, and Cumulative conditions (continued).

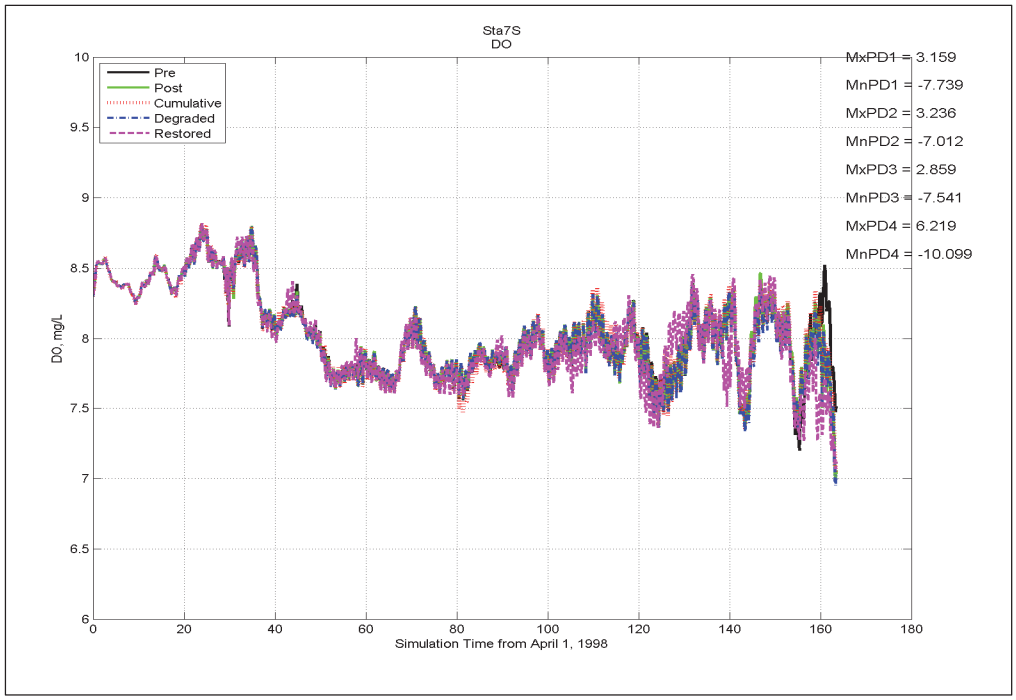

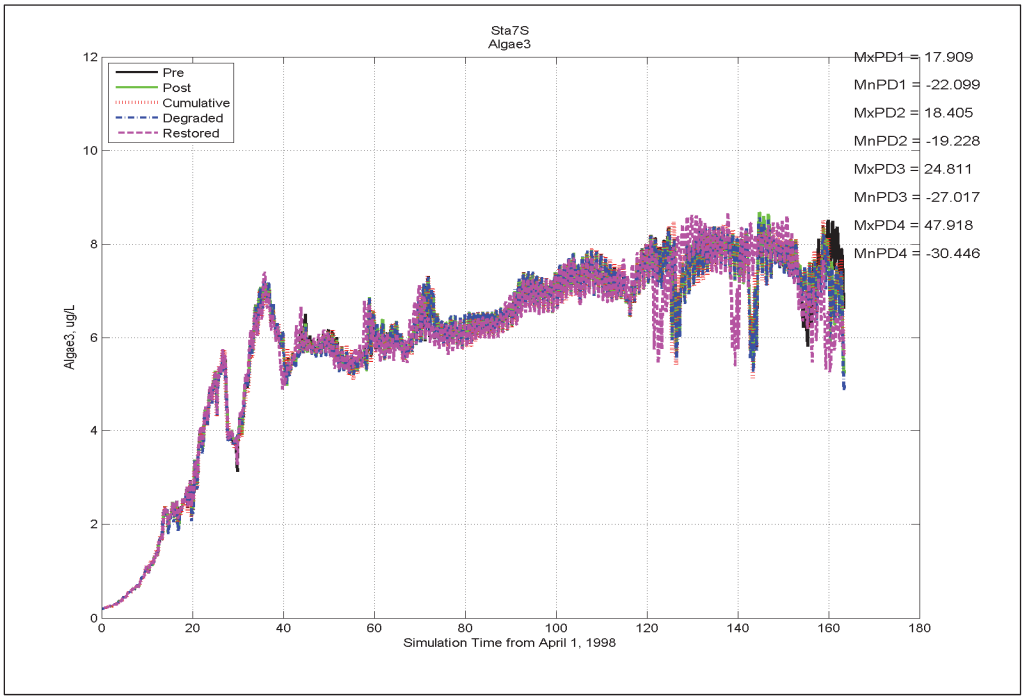

Figure E-65. Concluded.

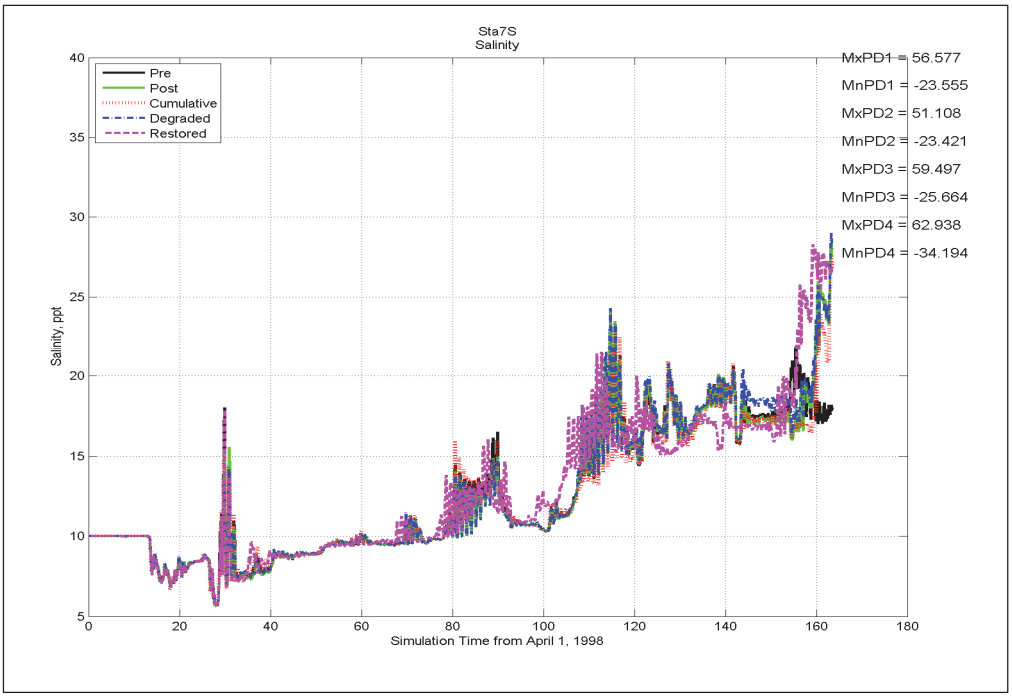

Figure E-66. Comparison of DO, Chlororphyll, and Salinity at Station 8 (Figure 5-2) for results from simulations representing Pre, Post, Restored, Degraded, and Cumulative conditions (continued).

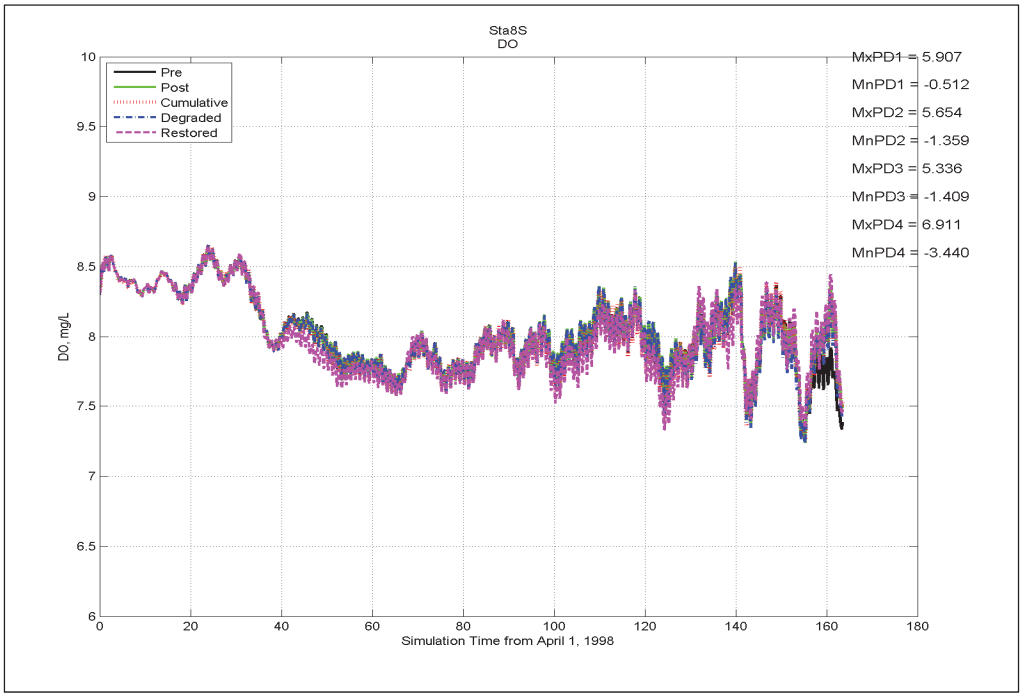

Figure E-66. Concluded.

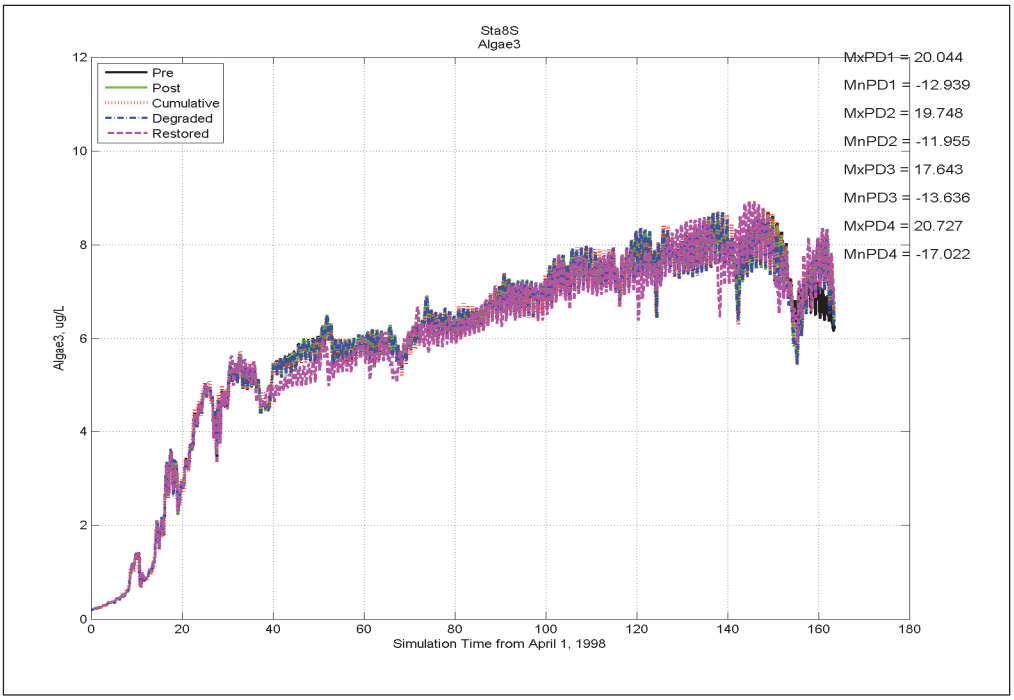

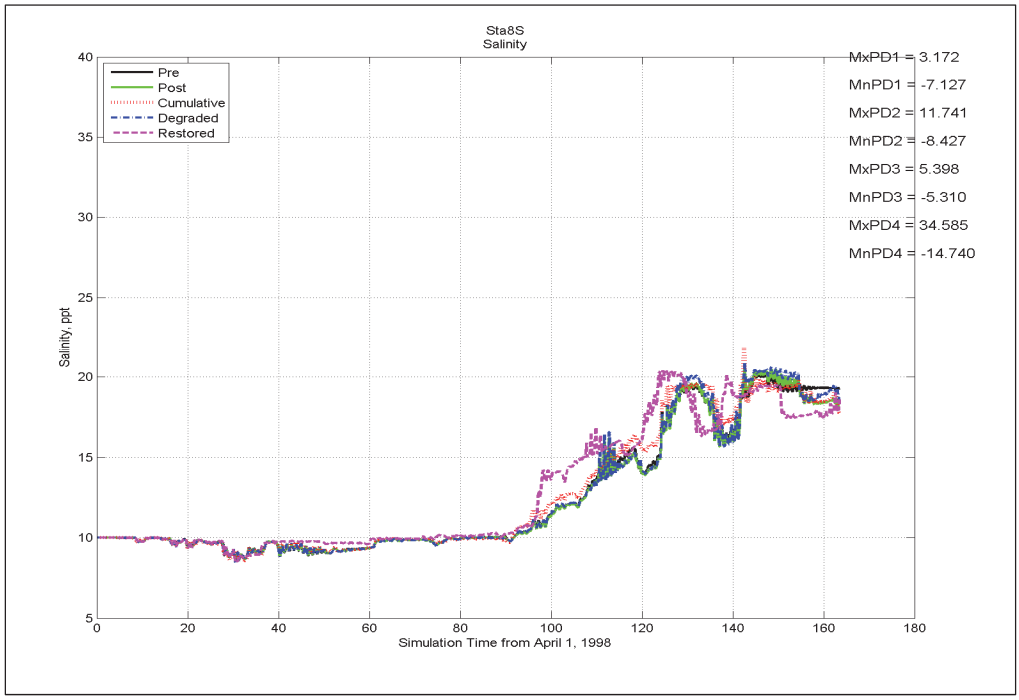

Figure E-67. Comparison of DO, Chlororphyll, and Salinity at Station 9 (Figure 5-2) for results from simulations representing Pre, Post, Restored, Degraded, and Cumulative conditions (continued).

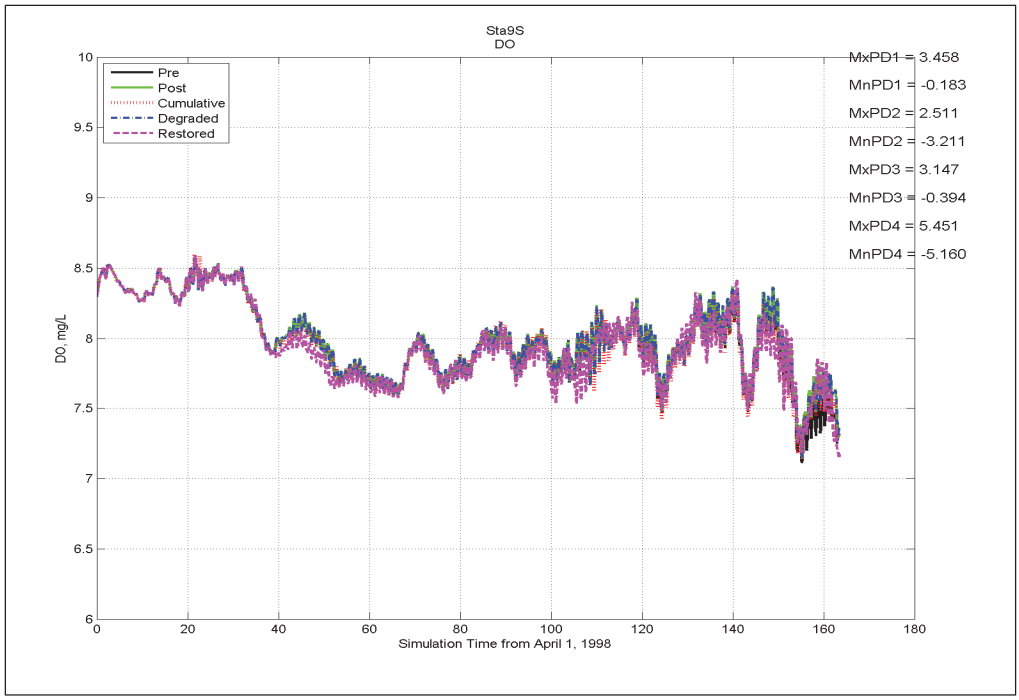

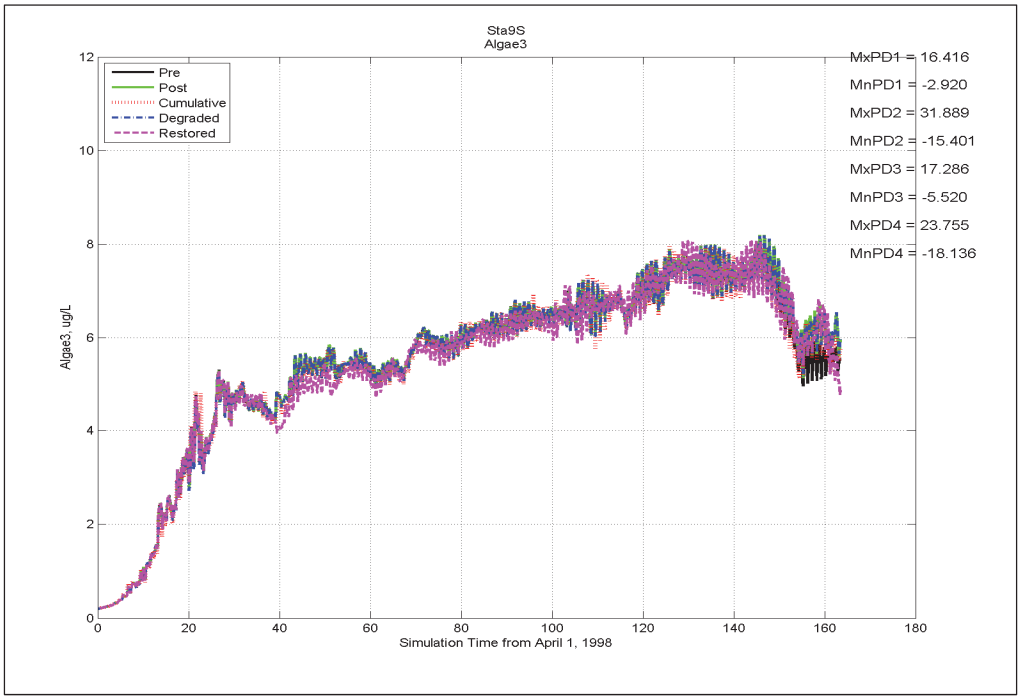

Figure E-67. Concluded.

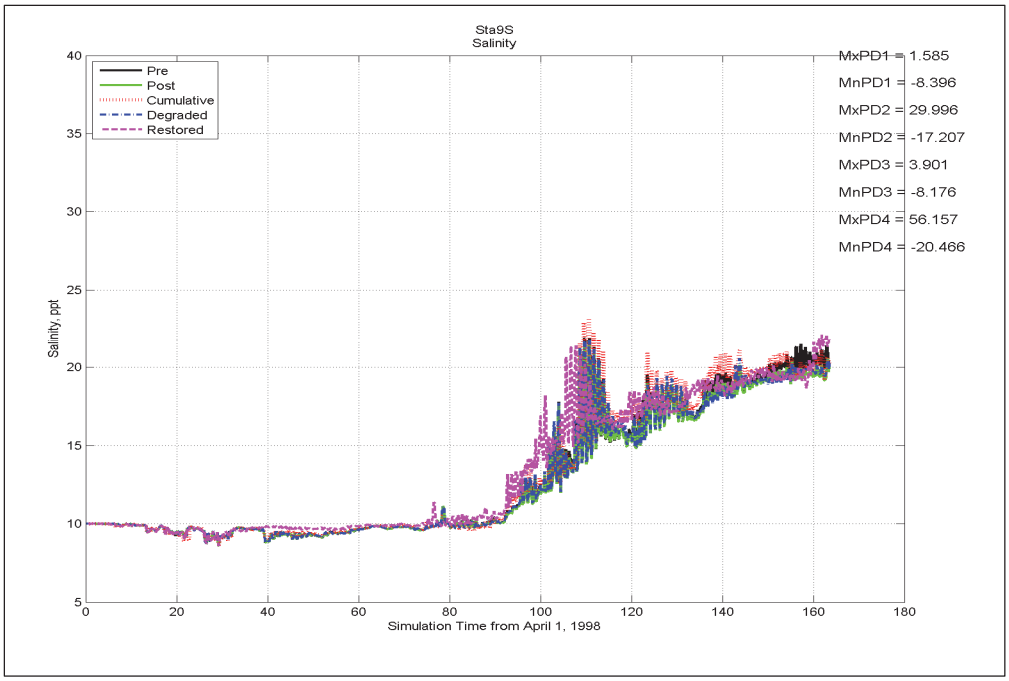

Figure E-68. Comparison of DO, Chlororphyll, and Salinity at Station 11 (Figure 5-8) for results from simulations representing Pre, Post, Restored, Degraded, and Cumulative conditions (continued).

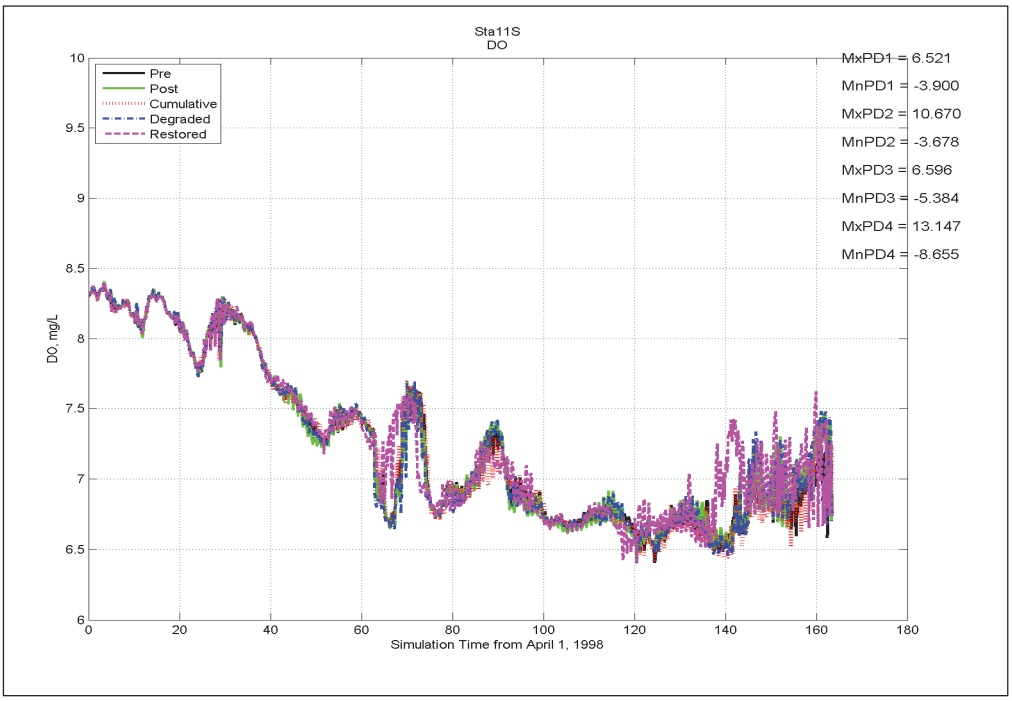

Figure E-68 Concluded.

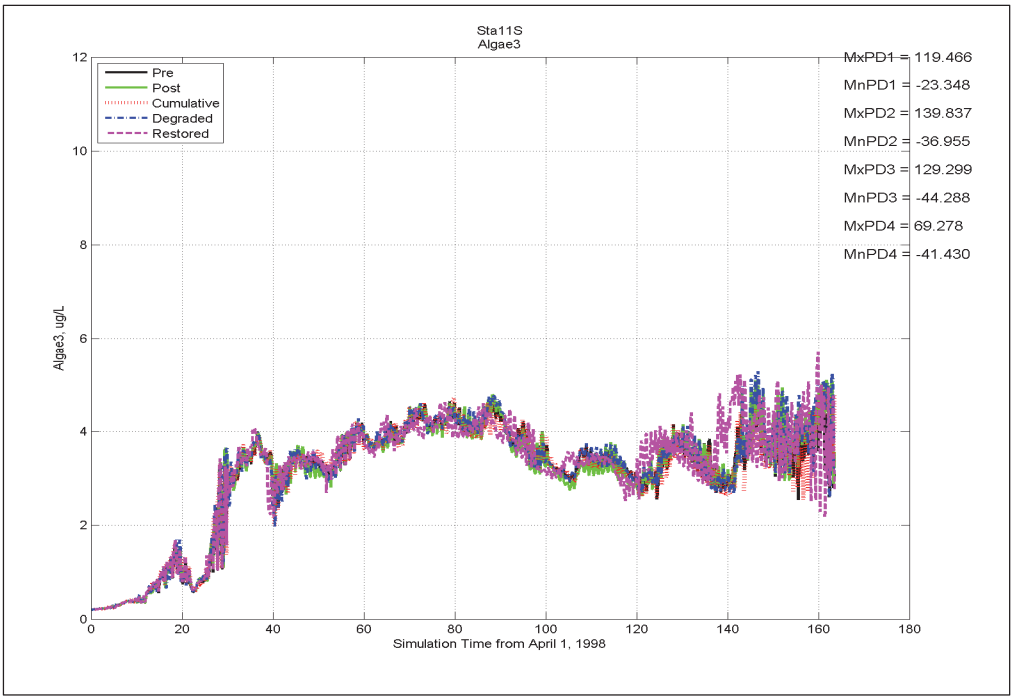

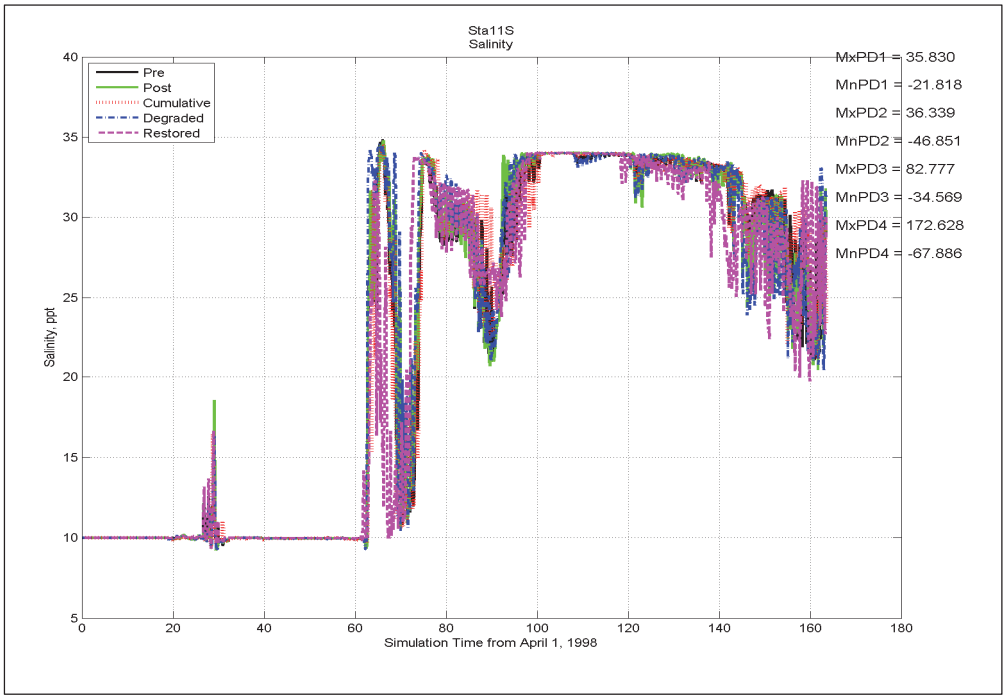

Figure E-69. Comparison of DO, Chlorophyll, and Salinity at Station 12 (Figure 5-8) for results from simulations representing Pre, Post, Restored, Degraded, and Cumulative conditions (continued).

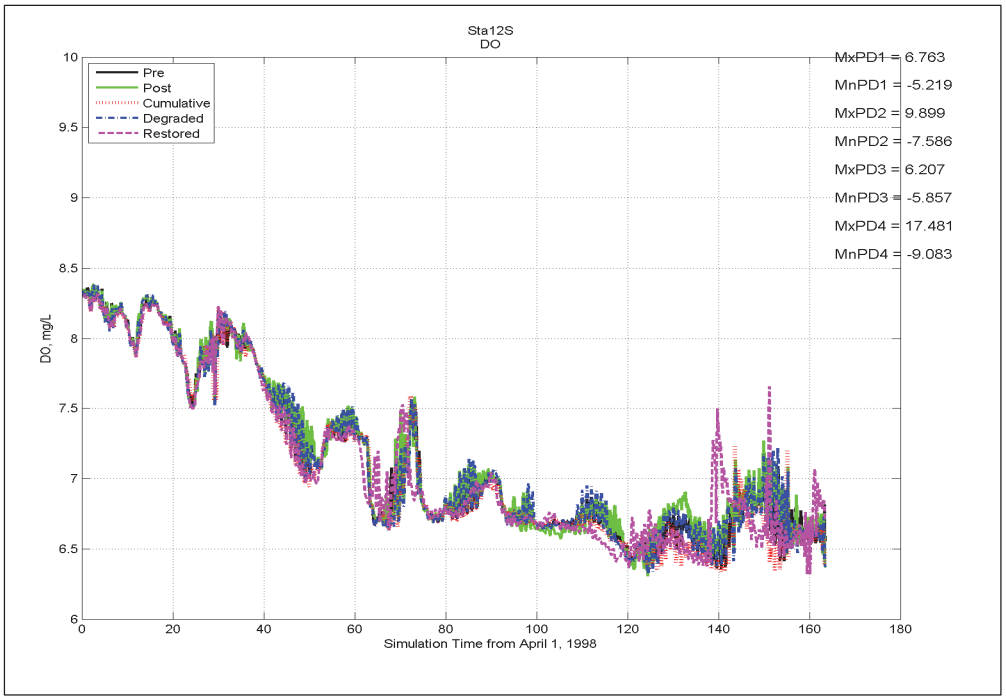

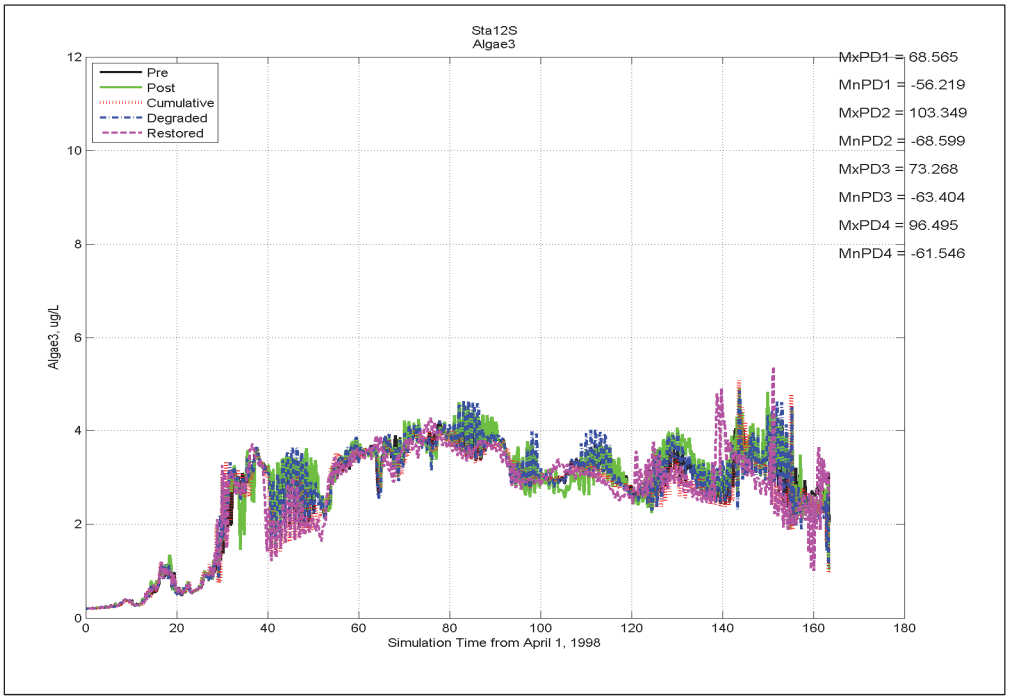

Figure E-69. Concluded.

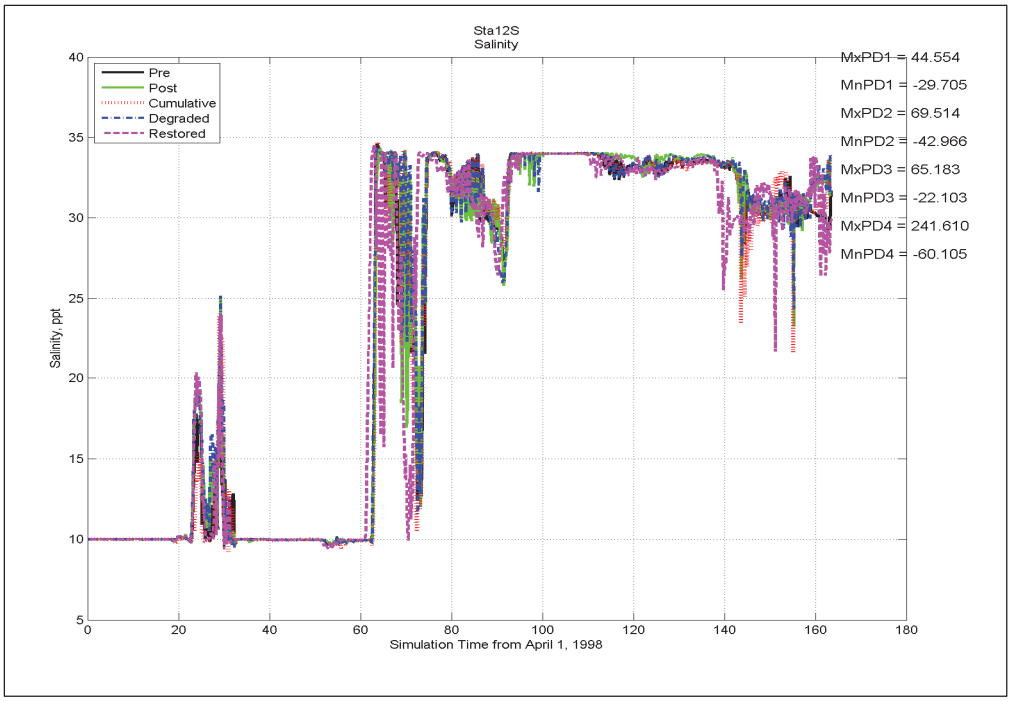

Figure E-70. Comparison of DO, Chlororphyll, and Salinity at Station 13 (Figure 5-8) for results from simulations representing Pre, Post, Restored, Degraded, and Cumulative conditions (continued).

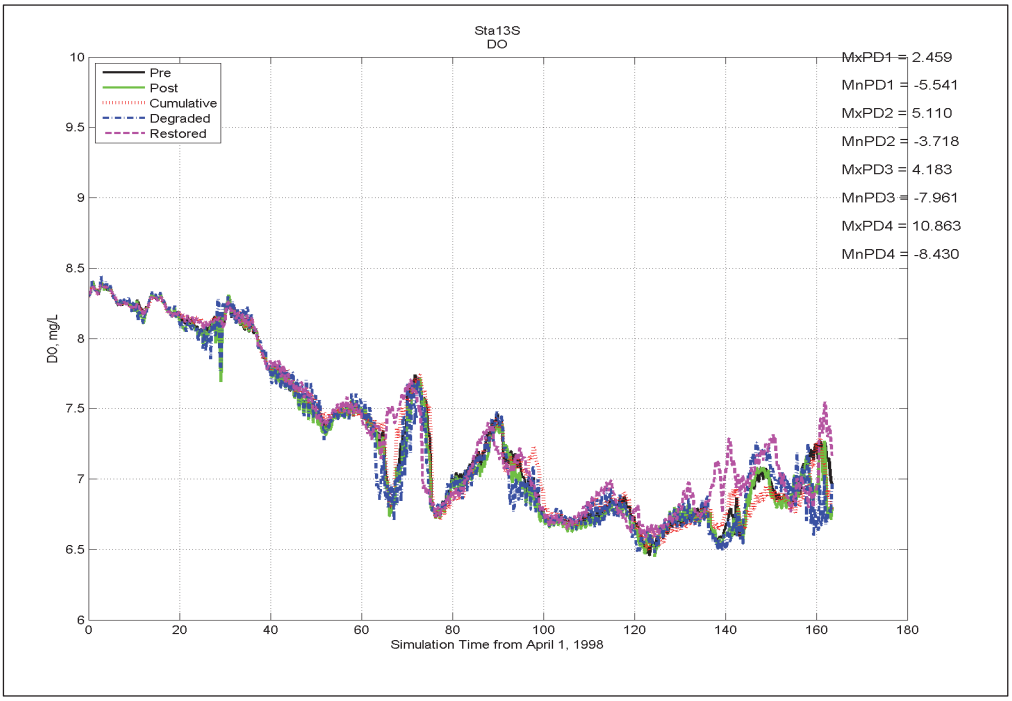

Figure E-70 Concluded.

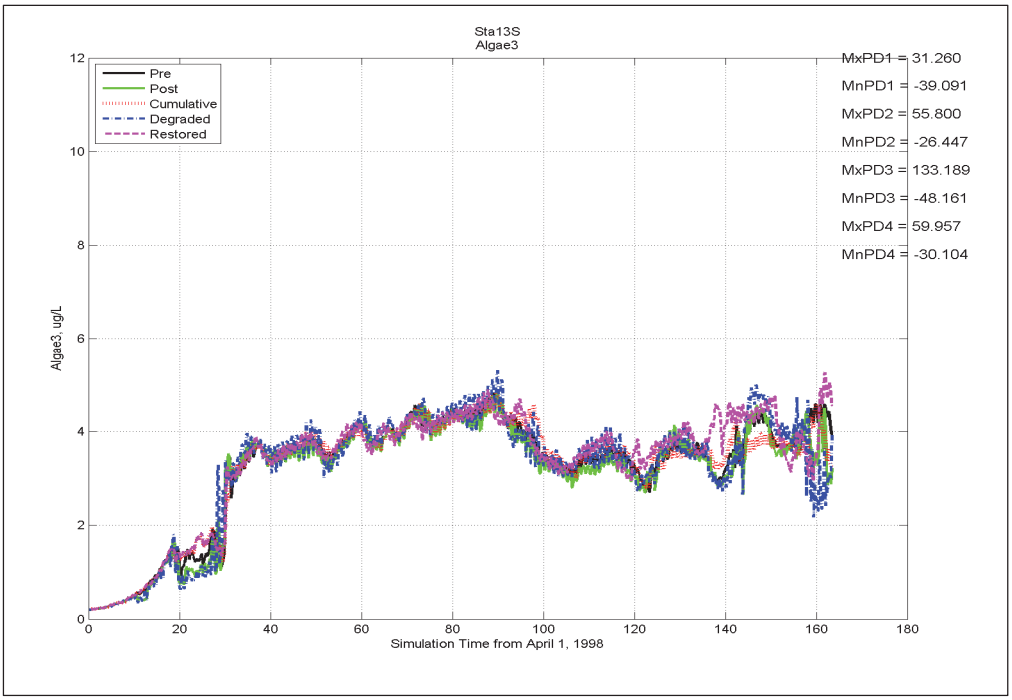

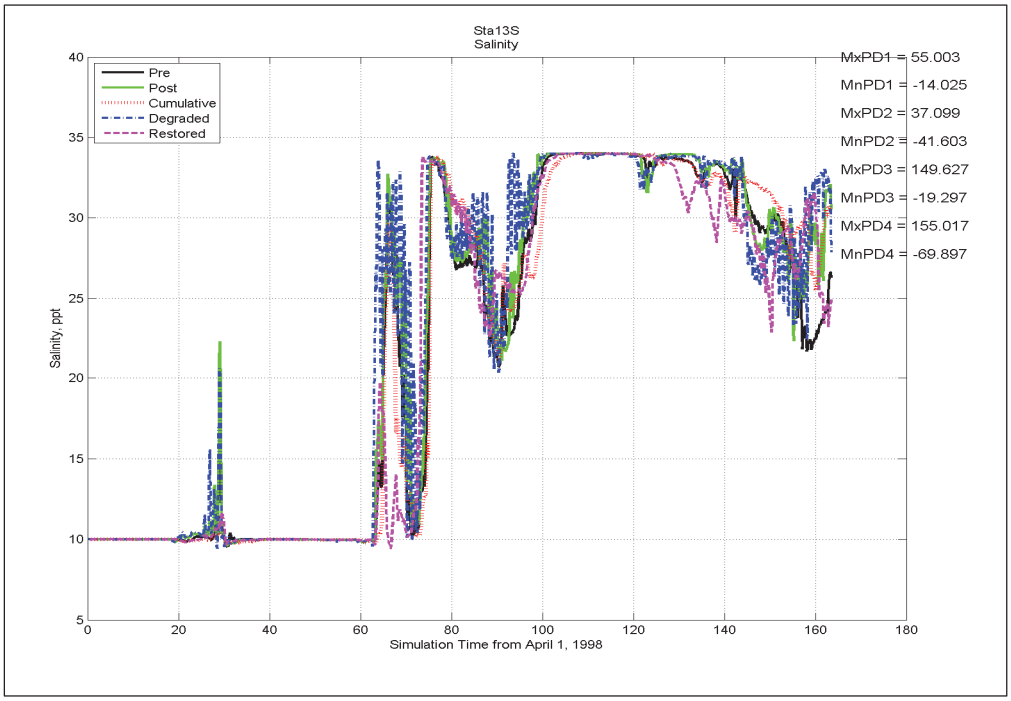

Figure E-71. Comparison of DO, Chlororphyll, and Salinity at Station 14 (Figure 5-8) for results from simulations representing Pre, Post, Restored, Degraded, and Cumulative conditions (continued).

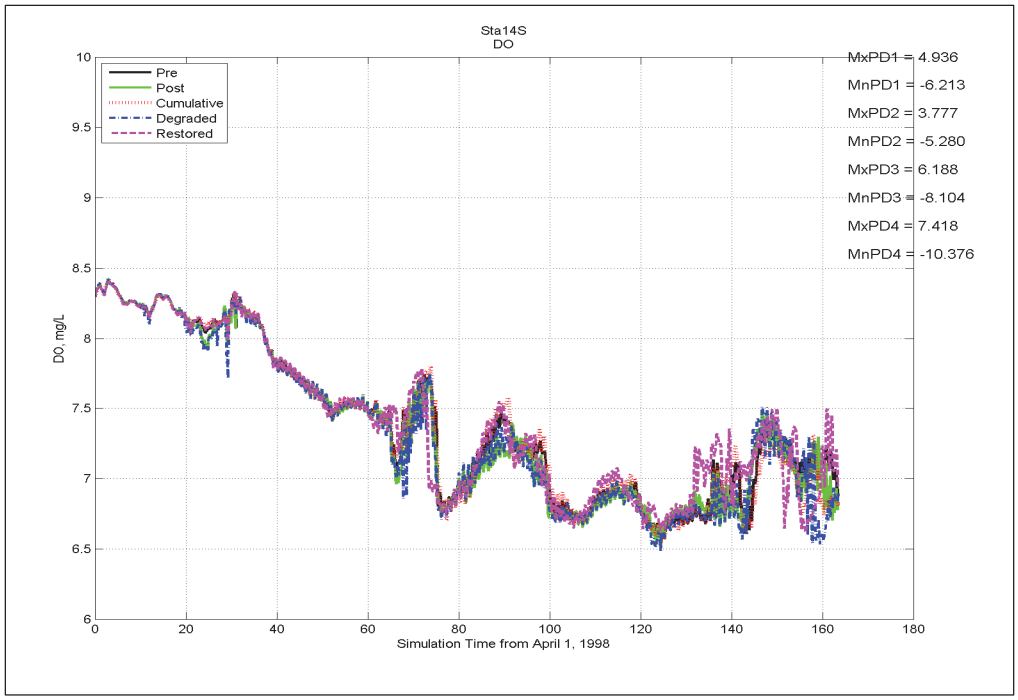

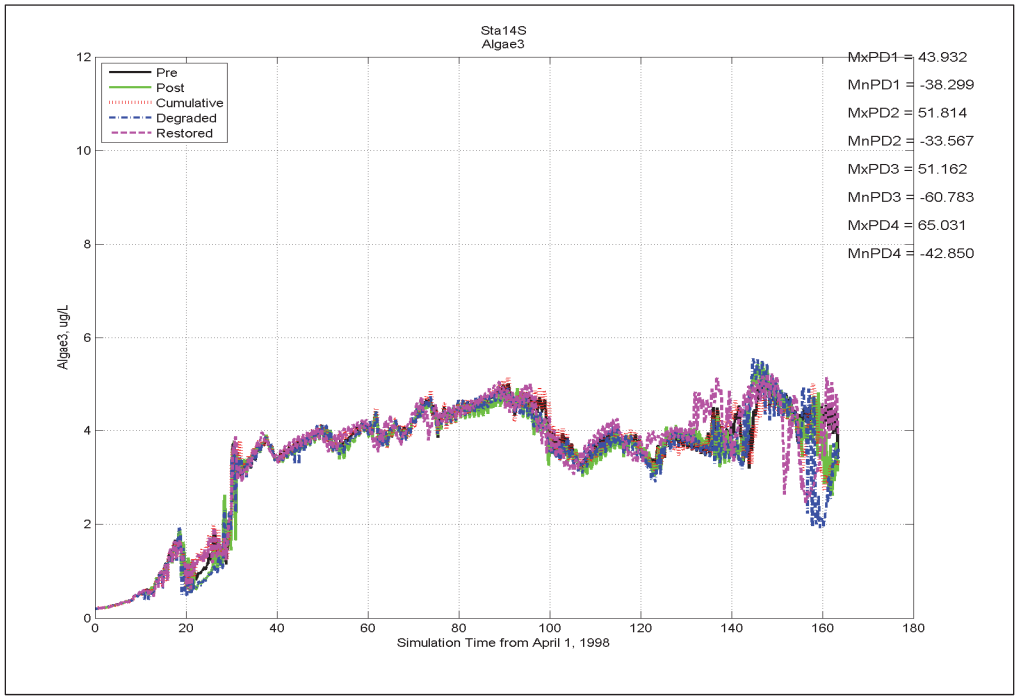

Figure E-71. Concluded.

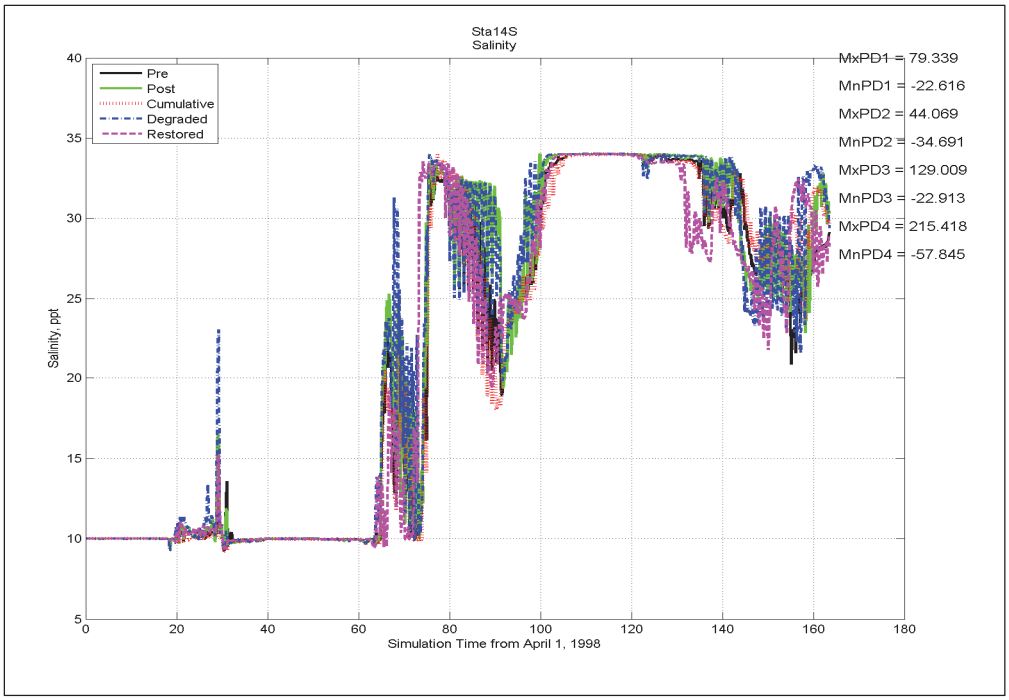

Figure E-72. Comparison of DO, Chlororphyll, and Salinity at Station 15 (Figure 5-8) for results from simulations representing Pre, Post, Restored, Degraded, and Cumulative conditions (continued).

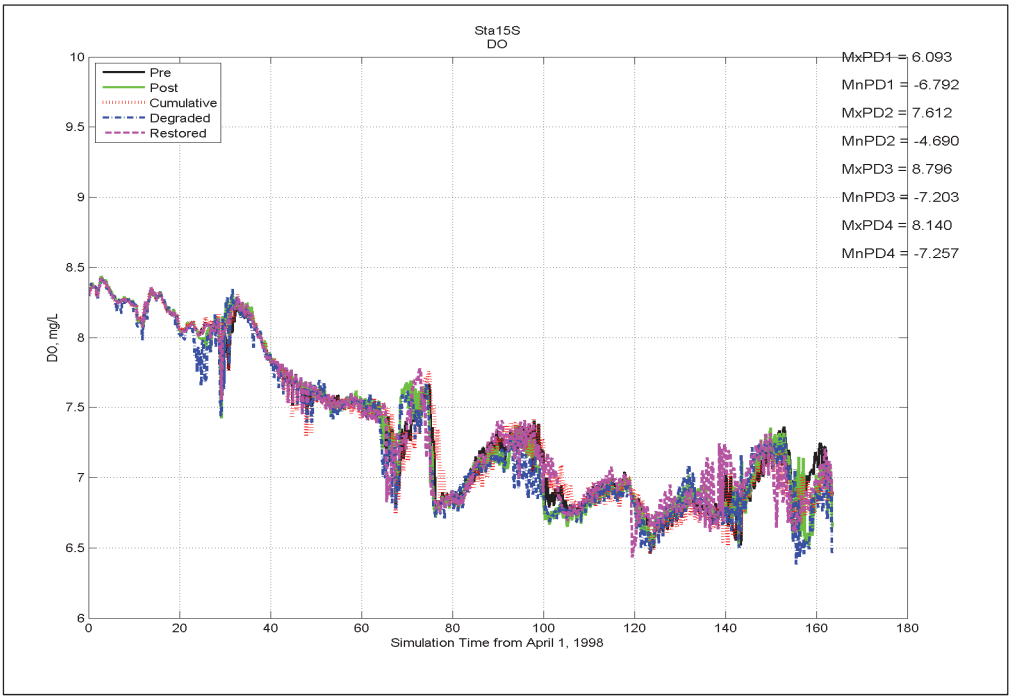

Figure E-72. Concluded.

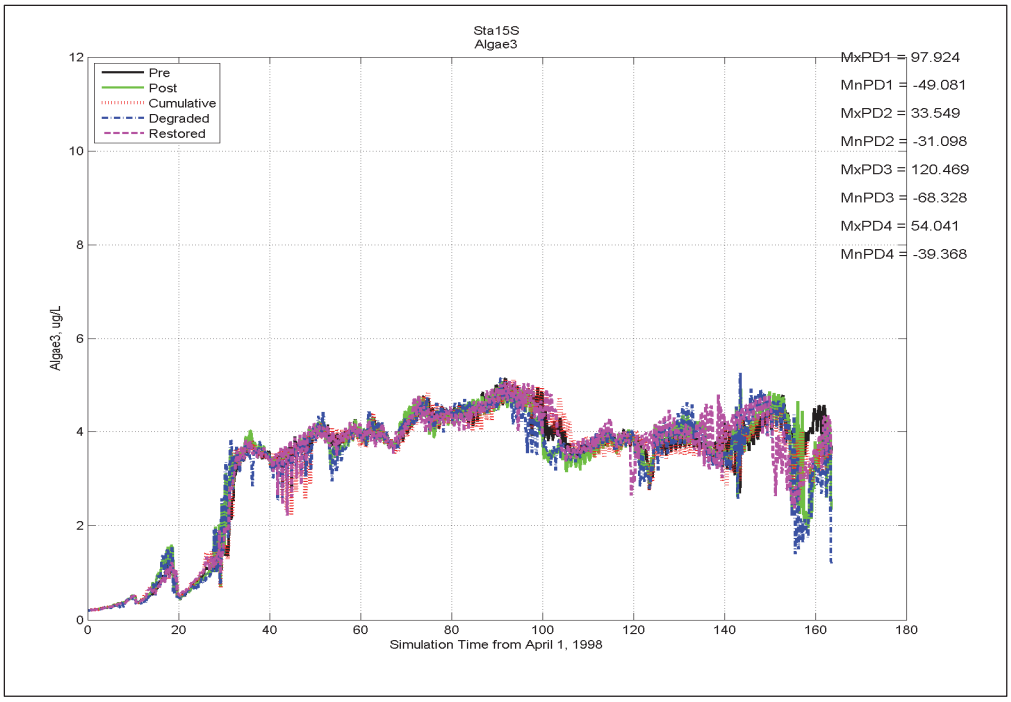

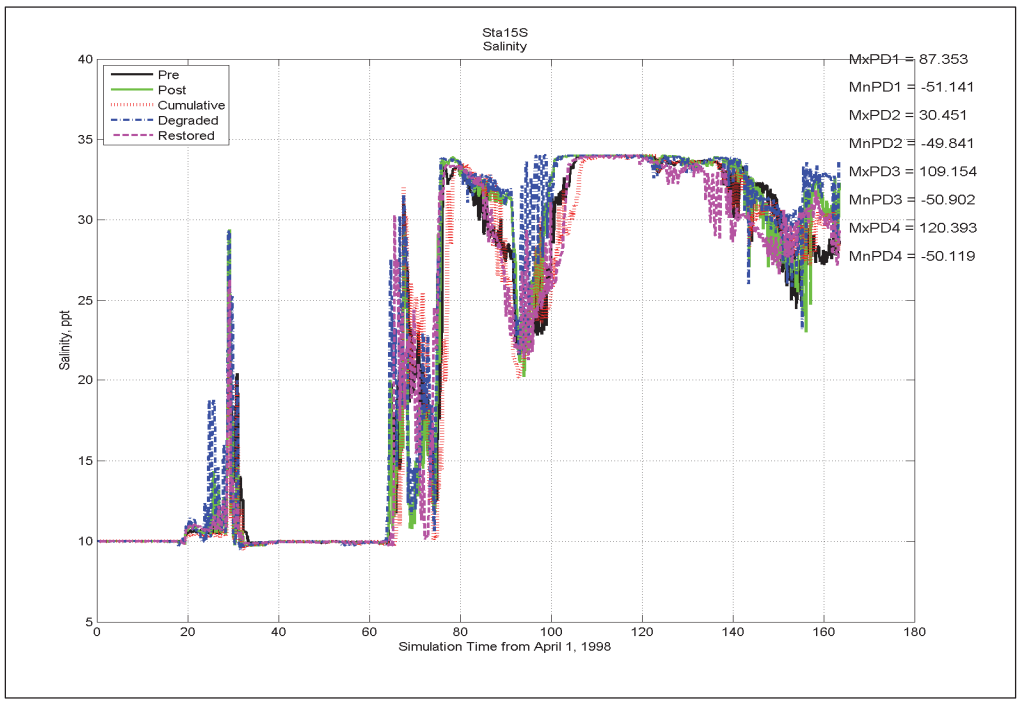

Figure E-73. Comparison of DO, Chlorophyll, and Salinity at Station 16 (Figure 5-8) for results from simulations representing Pre, Post, Restored, Degraded, and Cumulative conditions (continued).

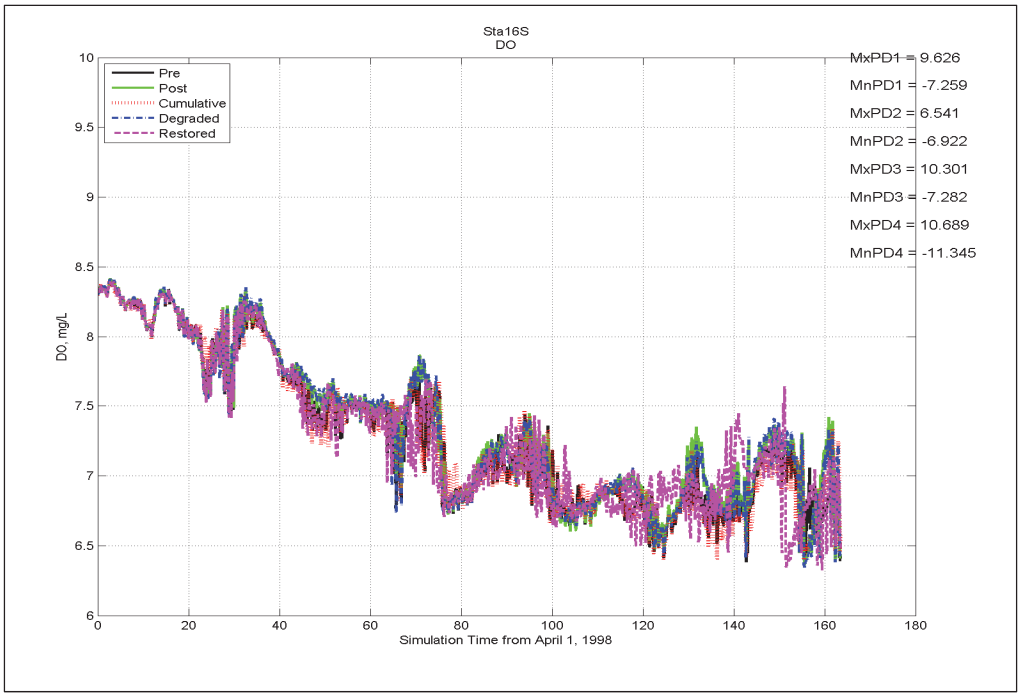

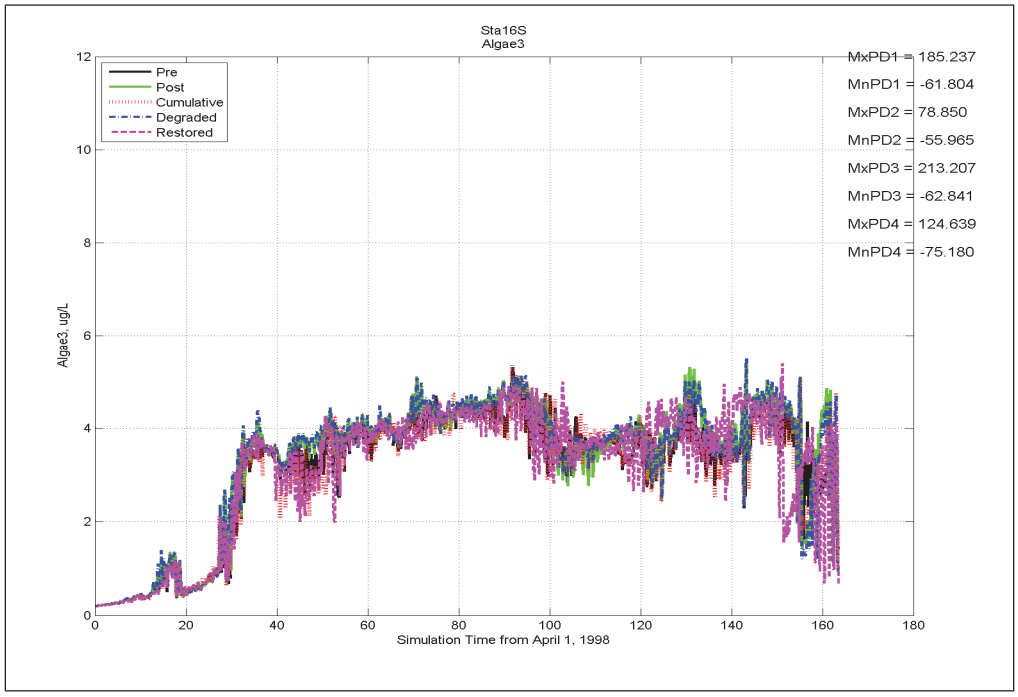

Figure E-73. Concluded.

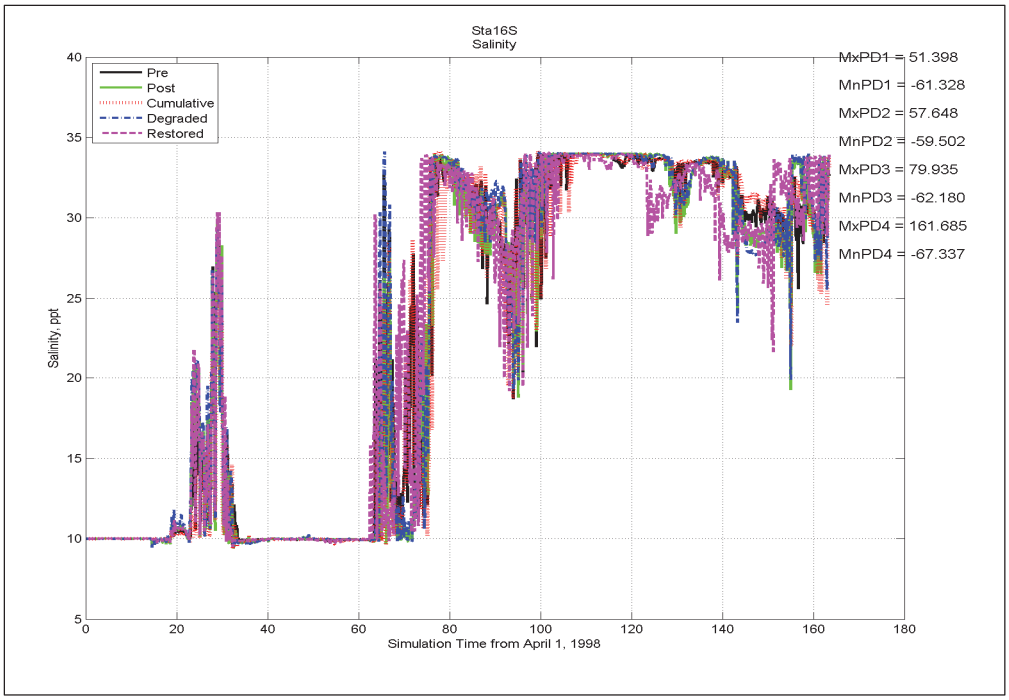

Appendix F: ADCIRC-Simulated Maximum Surge Envelopes

Figure F-1. Maximum surge envelope for Storm 028, Post-Katrina condition.

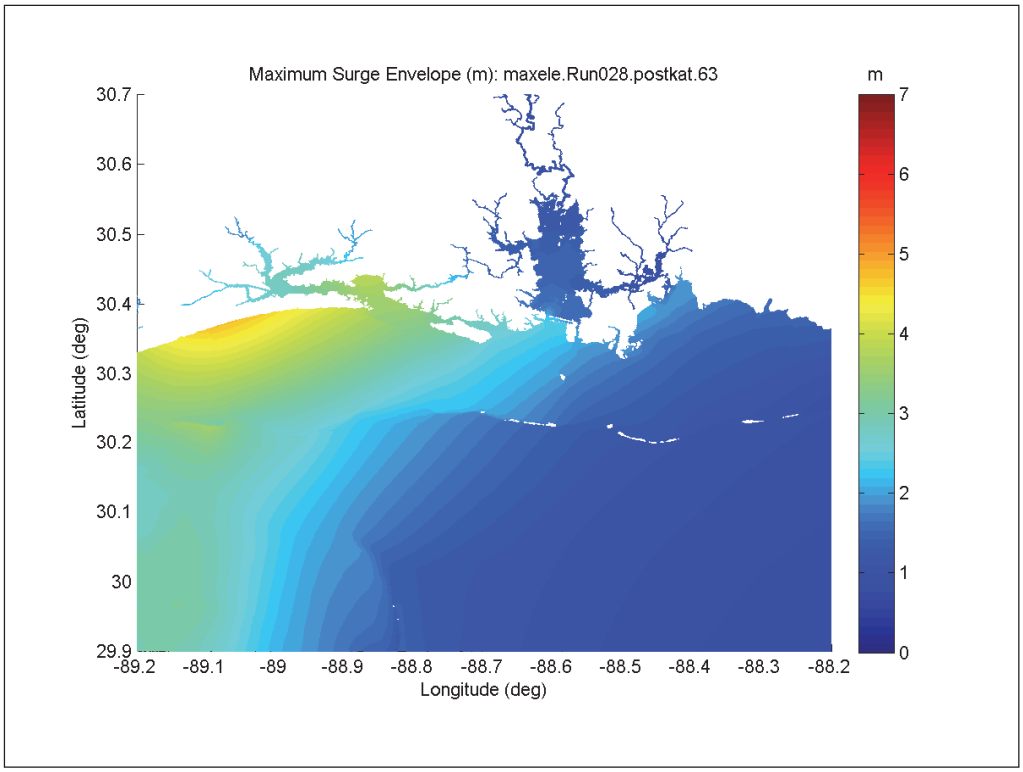

Figure F-2. Maximum surge envelope for Storm 028, Degraded condition.

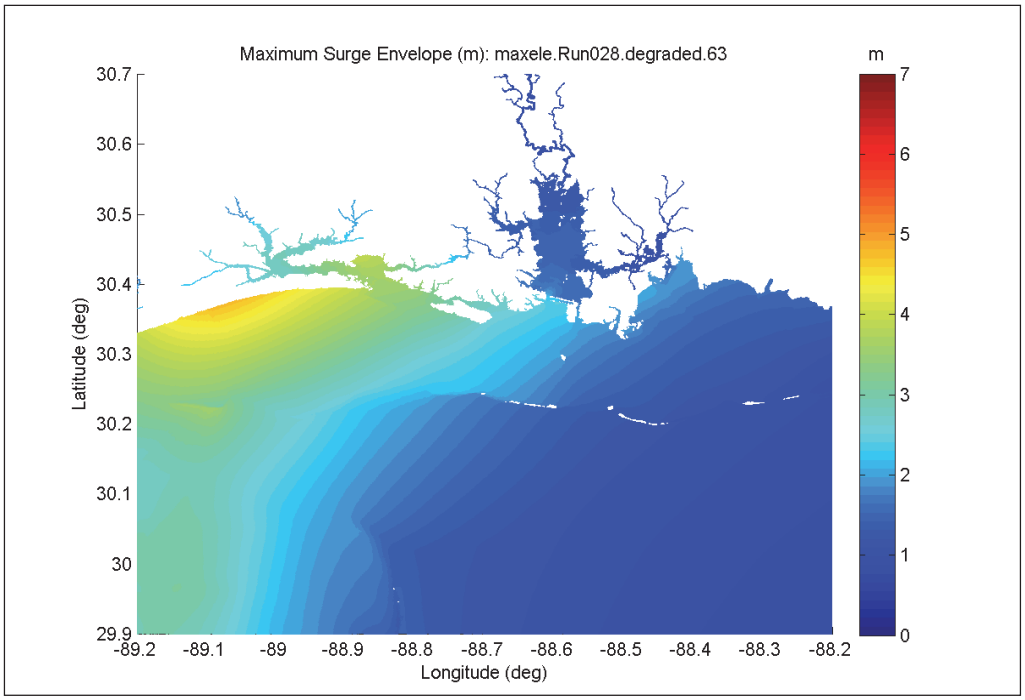

Figure F-3. Maximum surge envelope for Storm 028, Restored condition.

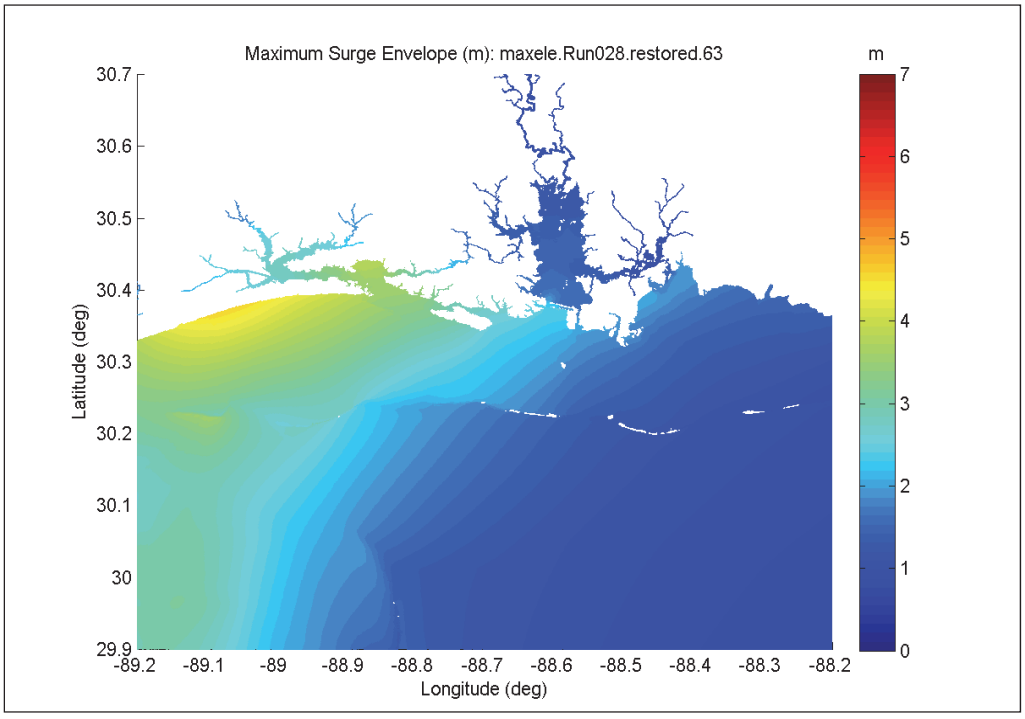

Figure F-4. Maximum surge envelope for Storm 028, Cumulative condition.

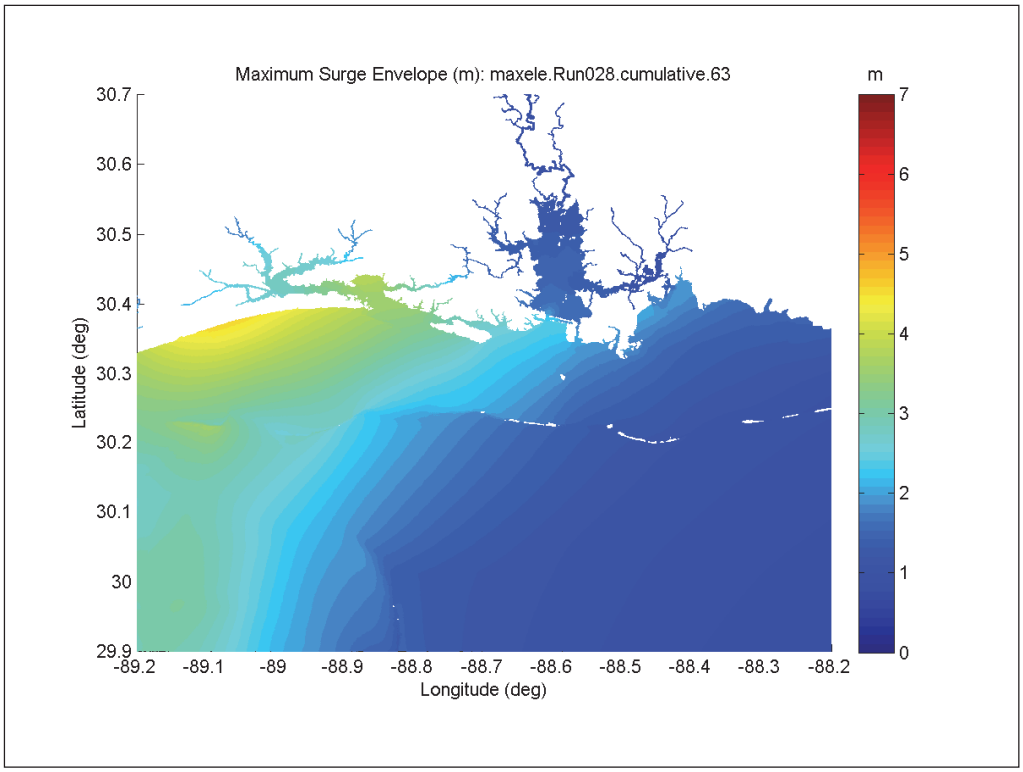

Figure F-5. Maximum surge envelope for Storm 032, Post-Katrina condition.

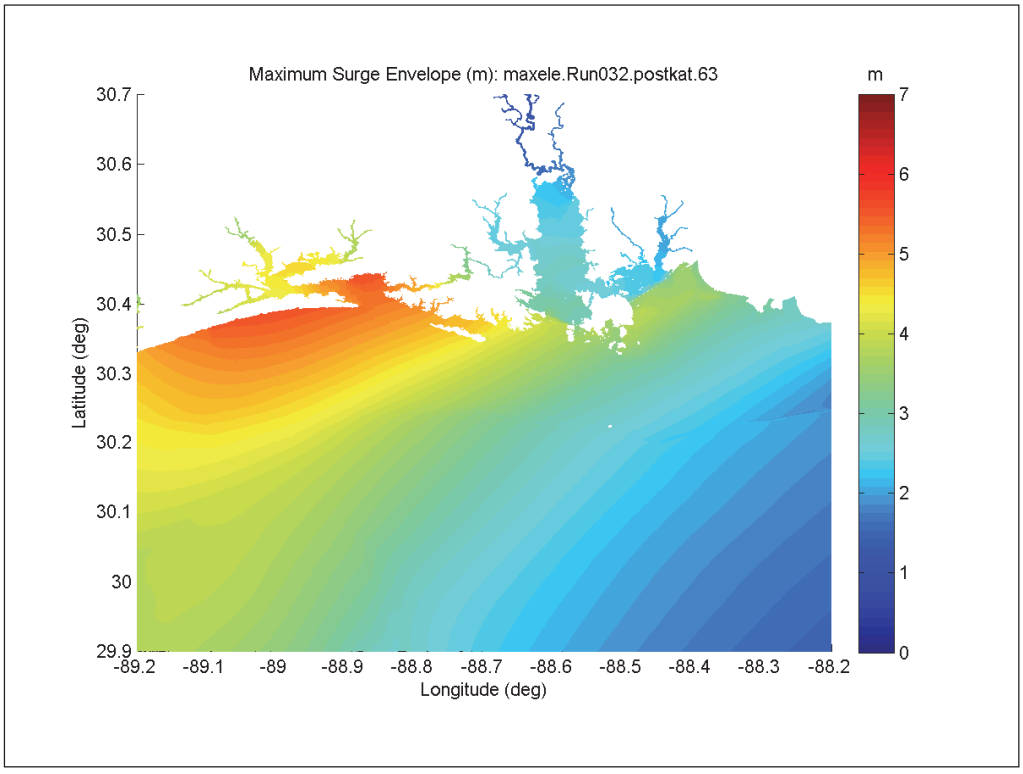

Figure F-6. Maximum surge envelope for Storm 032, Degraded condition.

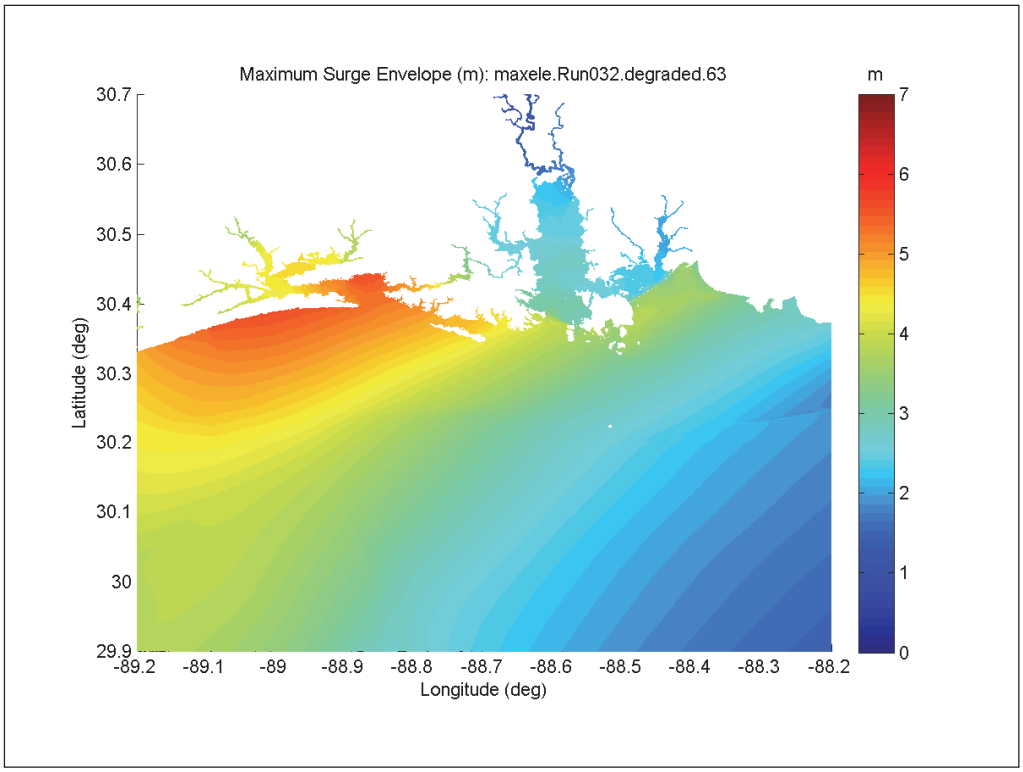

Figure F-7. Maximum surge envelope for Storm 032, Restored condition.

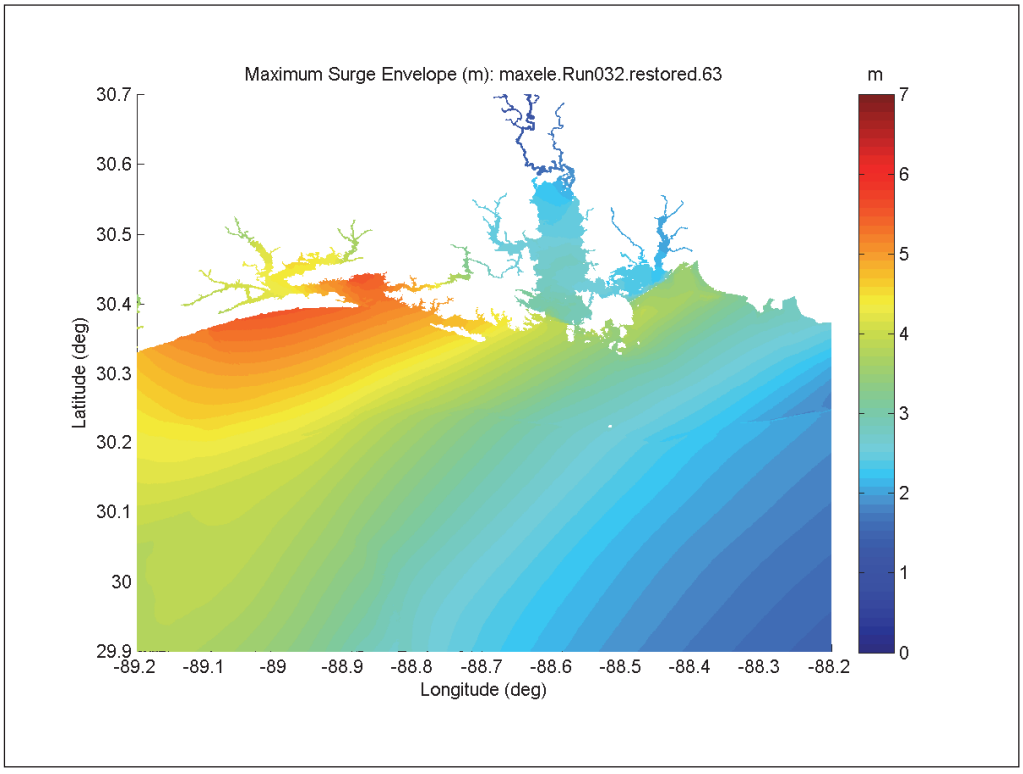

Figure F-8. Maximum surge envelope for Storm 032, Cumulative condition.

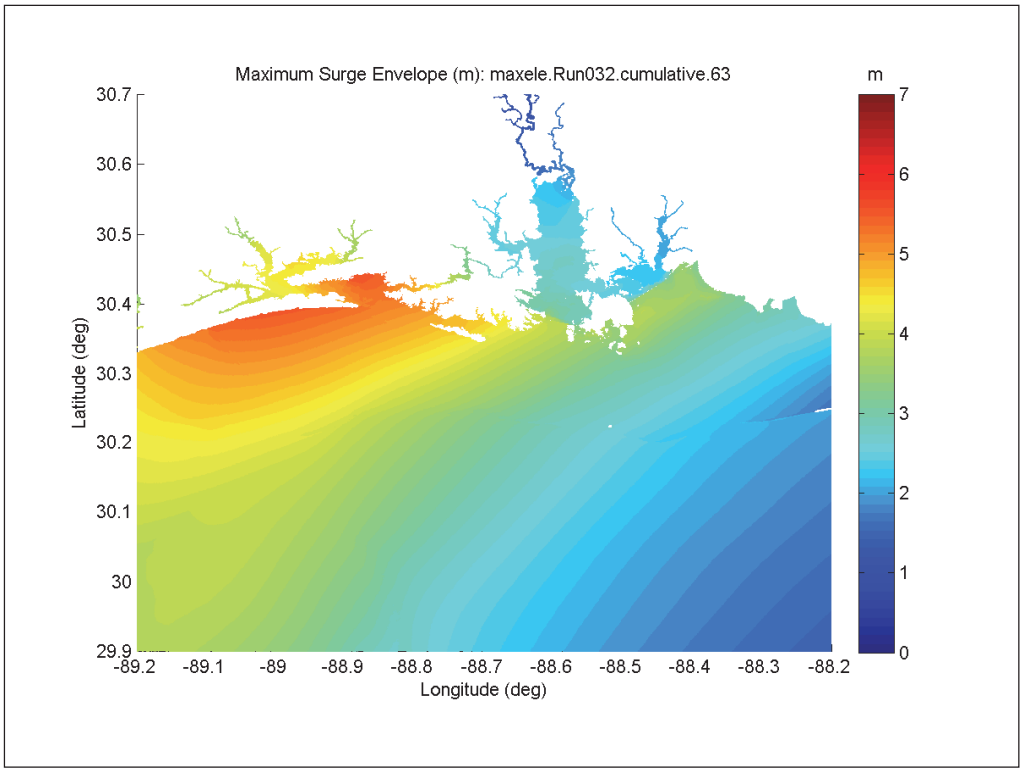

Figure F-9. Maximum surge envelope for Storm 034, Post-Katrina condition.

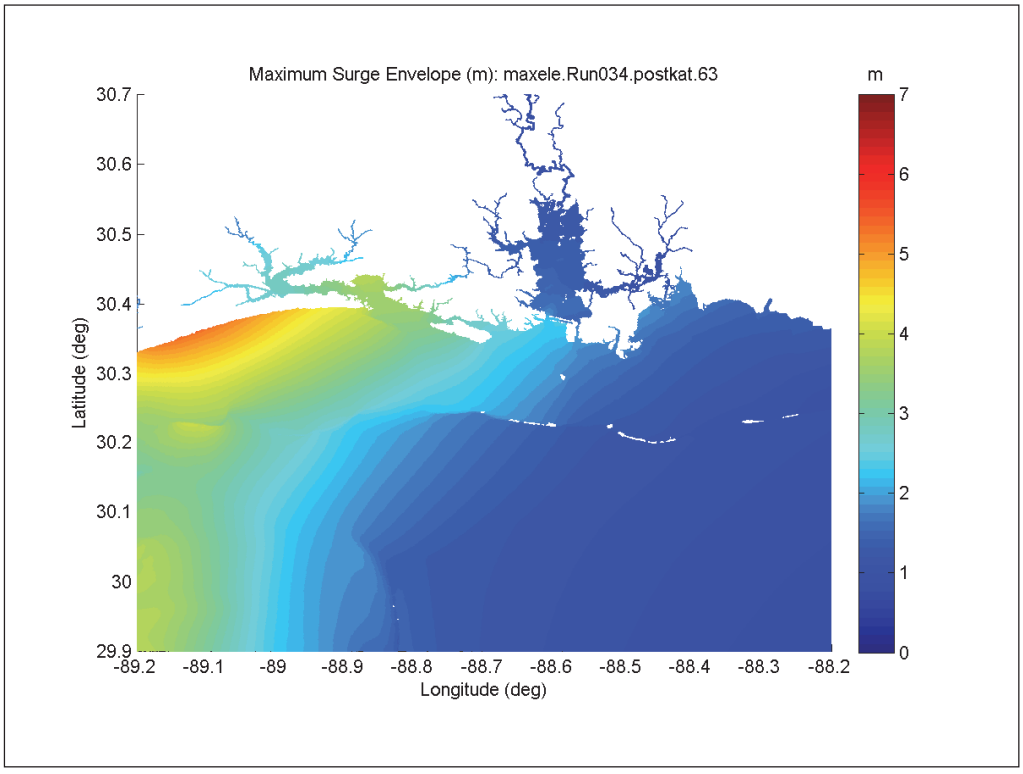

Figure F-10. Maximum surge envelope for Storm 034, Degraded condition.

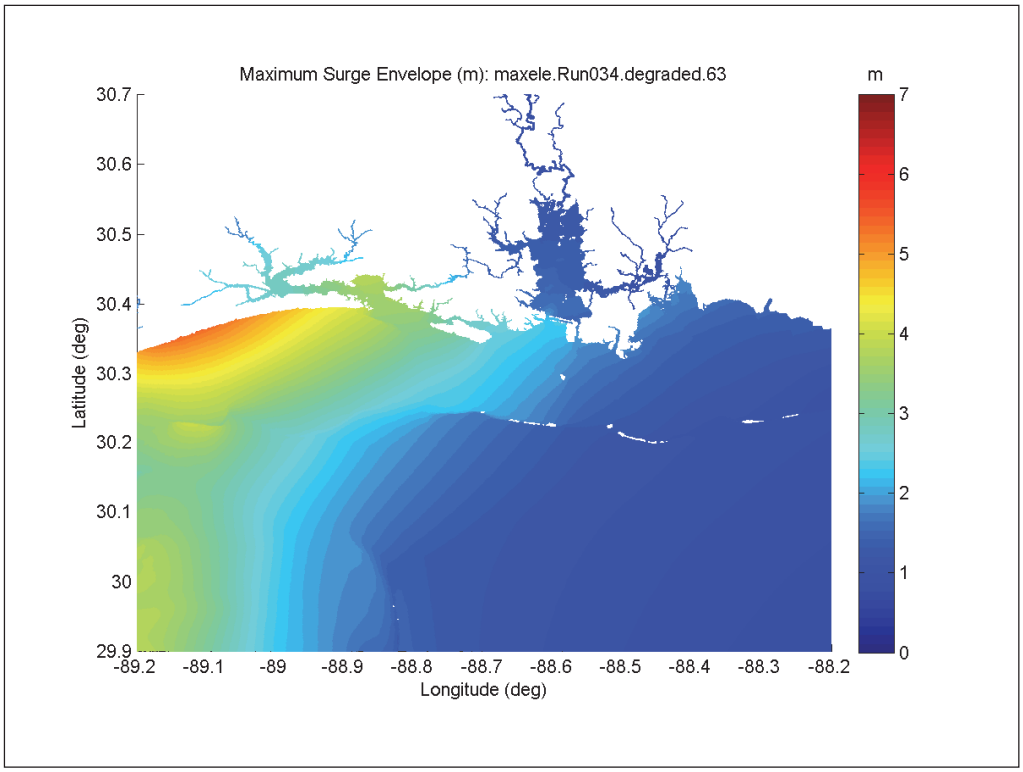

Figure F-11. Maximum surge envelope for Storm 034, Restored condition.

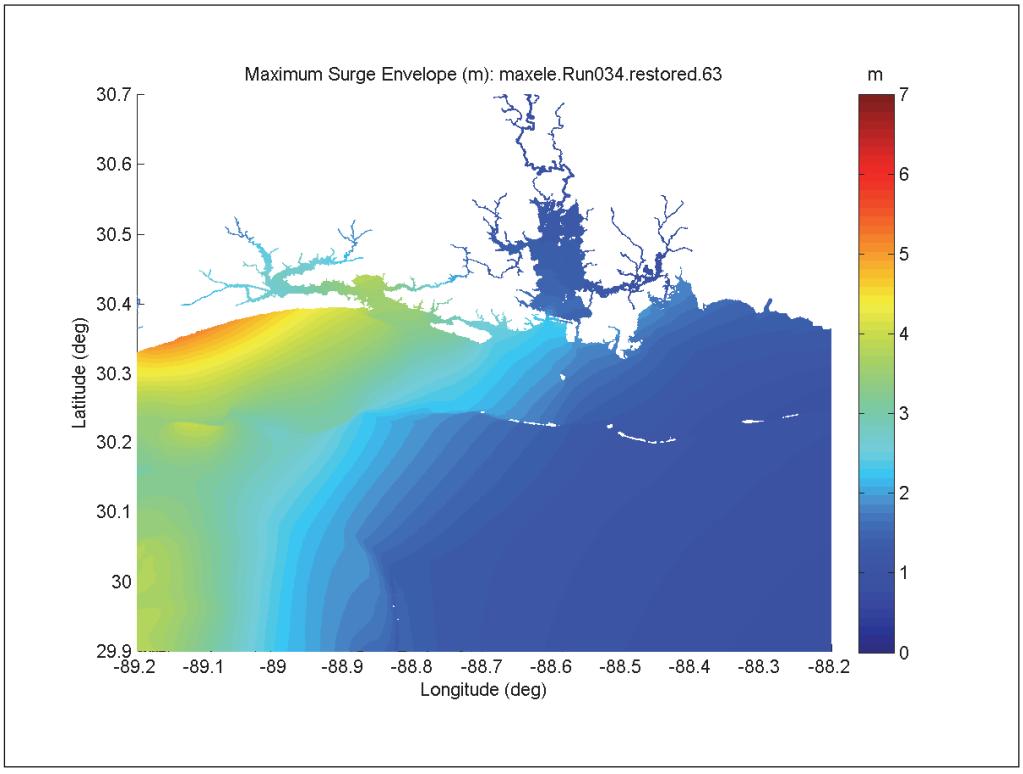

Figure F-12. Maximum surge envelope for Storm 034, Cumulative condition.

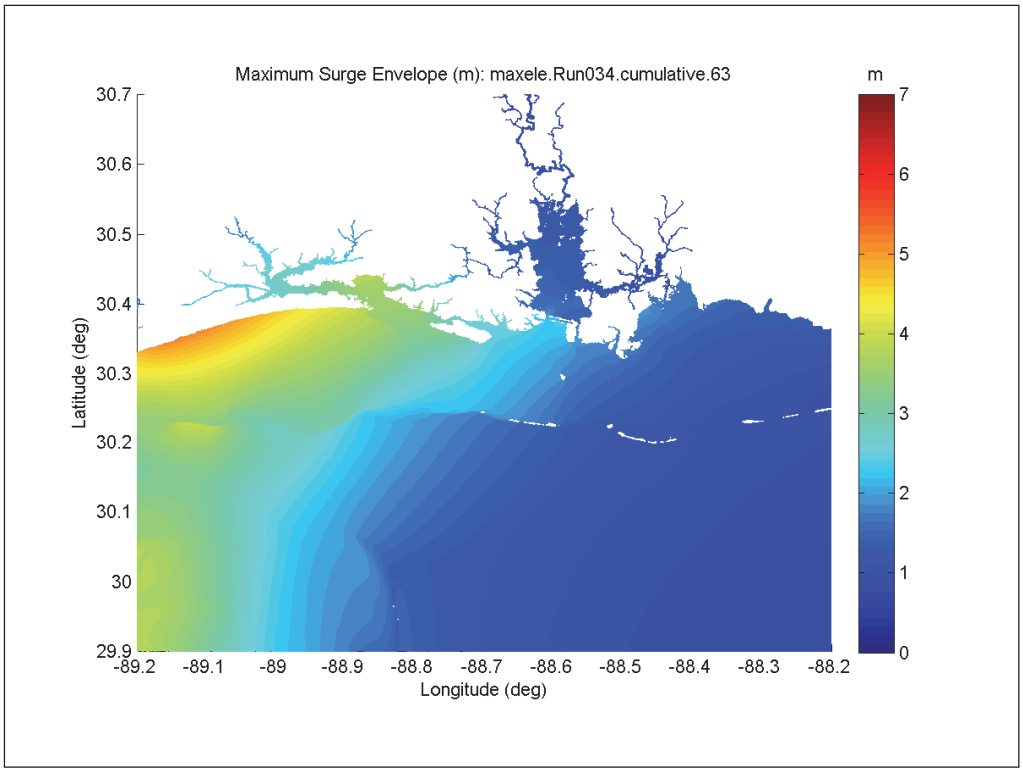

Figure F-13. Maximum surge envelope for Storm 059, Post-Katrina condition.

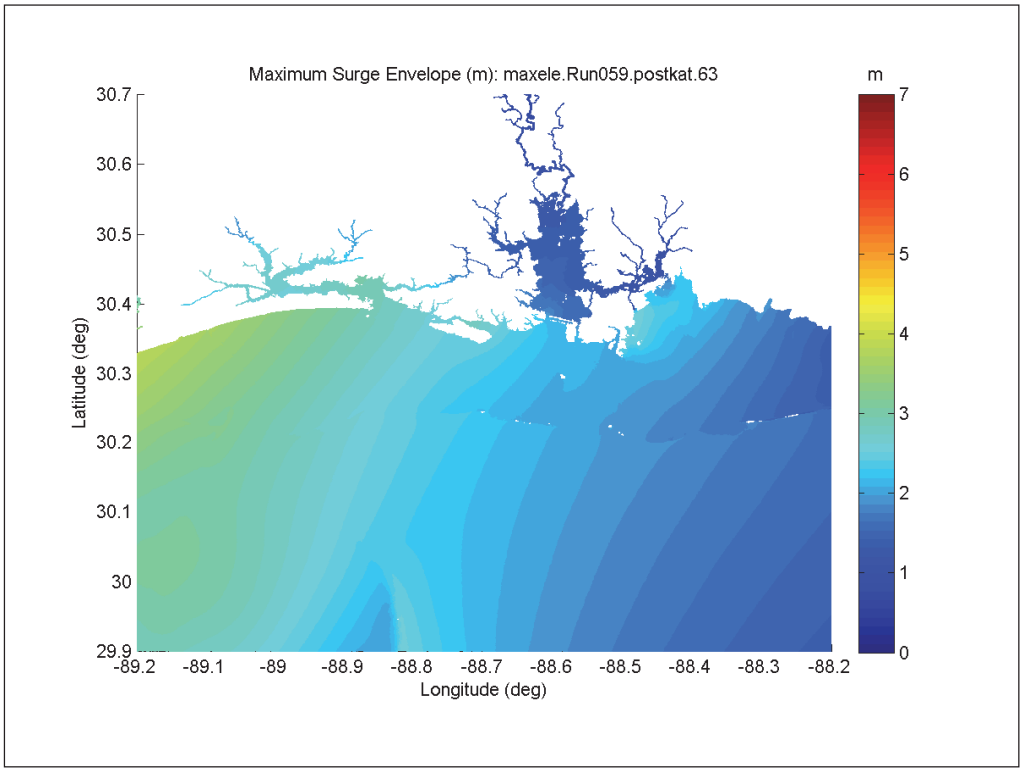

Figure F-14. Maximum surge envelope for Storm 059, Degraded condition.

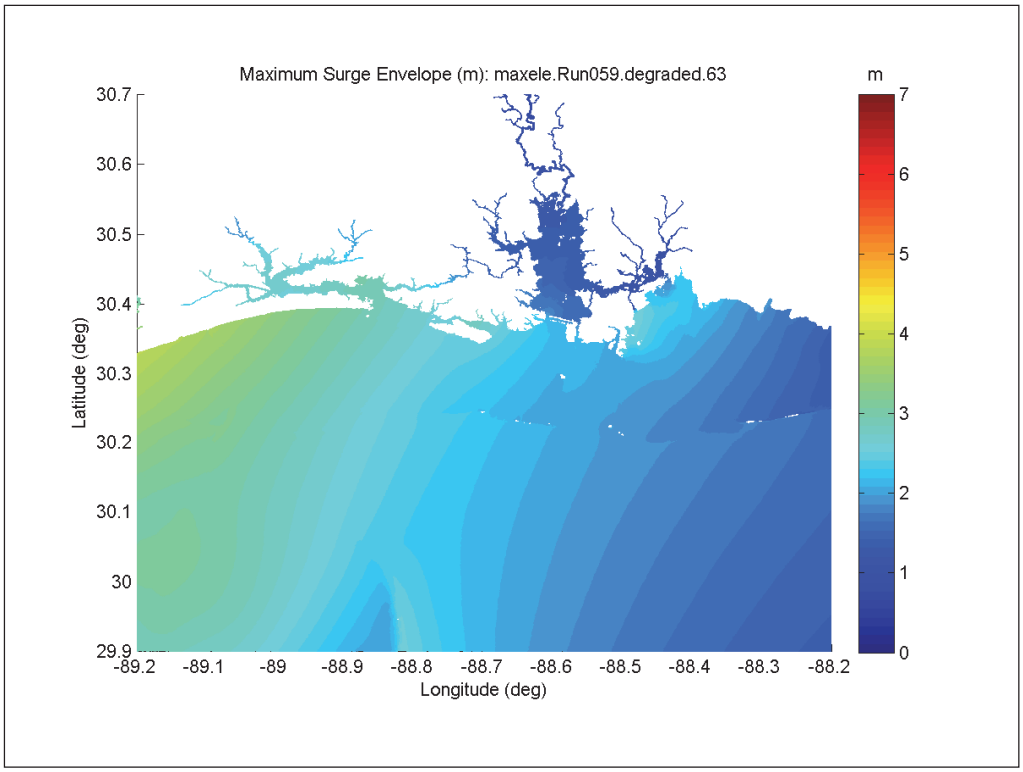

Figure F-15. Maximum surge Envelope for Storm 059, Restored condition.

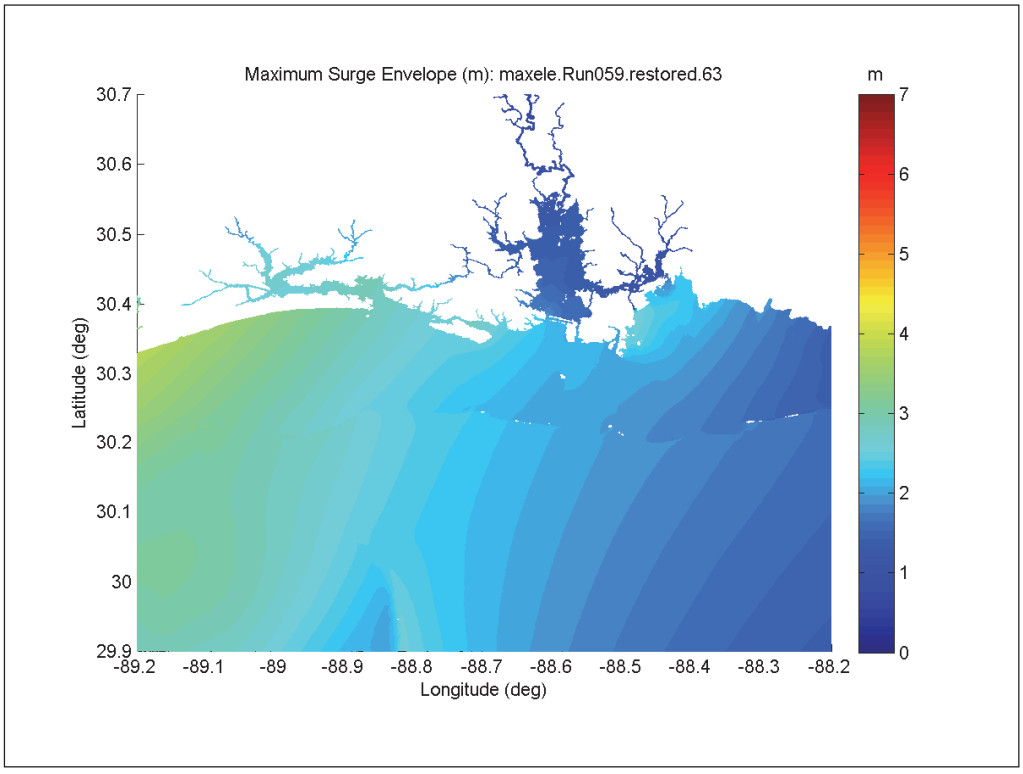

Figure F-16. Maximum surge envelope for Storm 059, Cumulative condition.

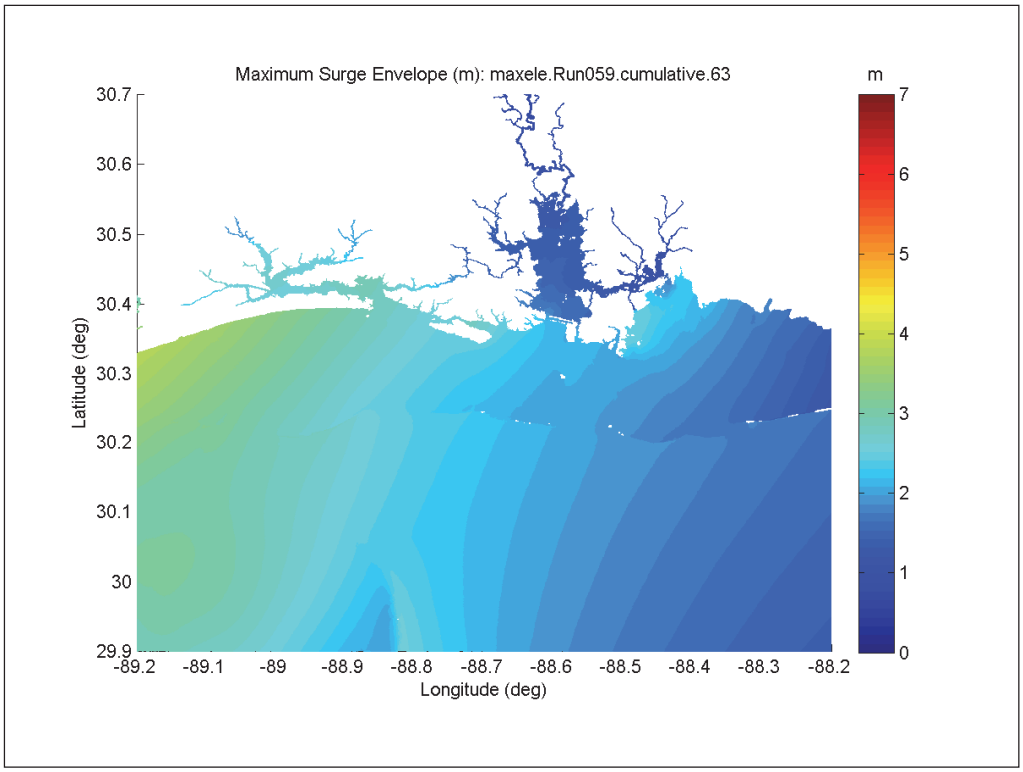

Figure F-17. Maximum surge envelope for Storm 060, Post-Katrina condition.

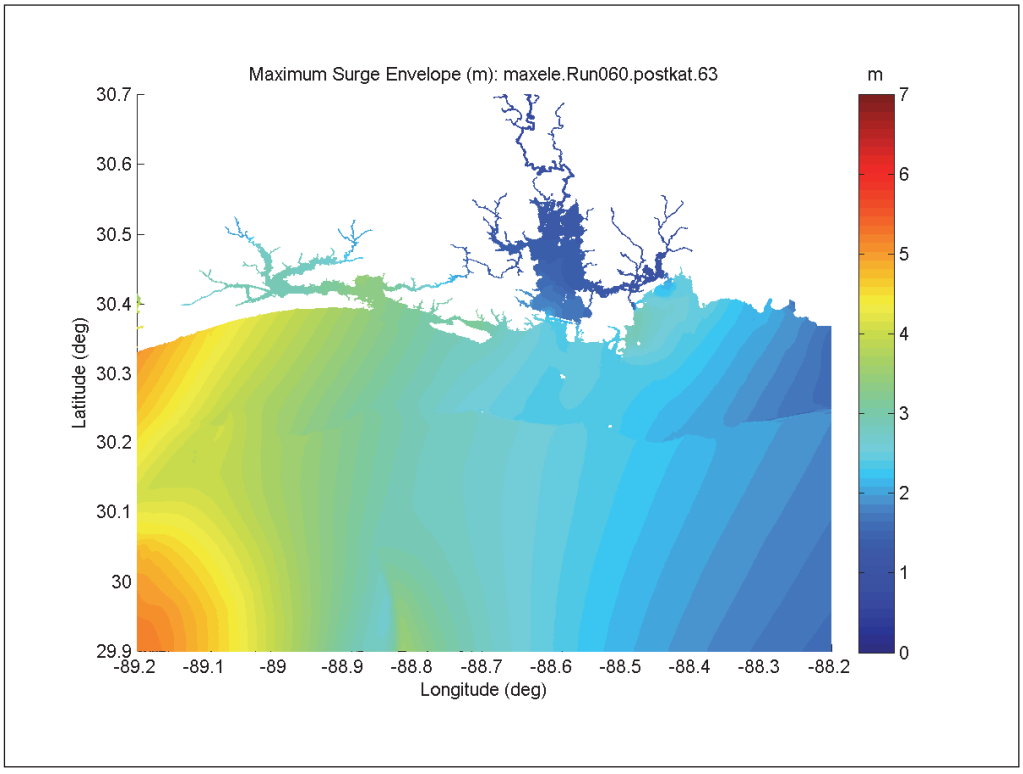

Figure F-18. Maximum surge envelope for Storm 060, Degraded condition.

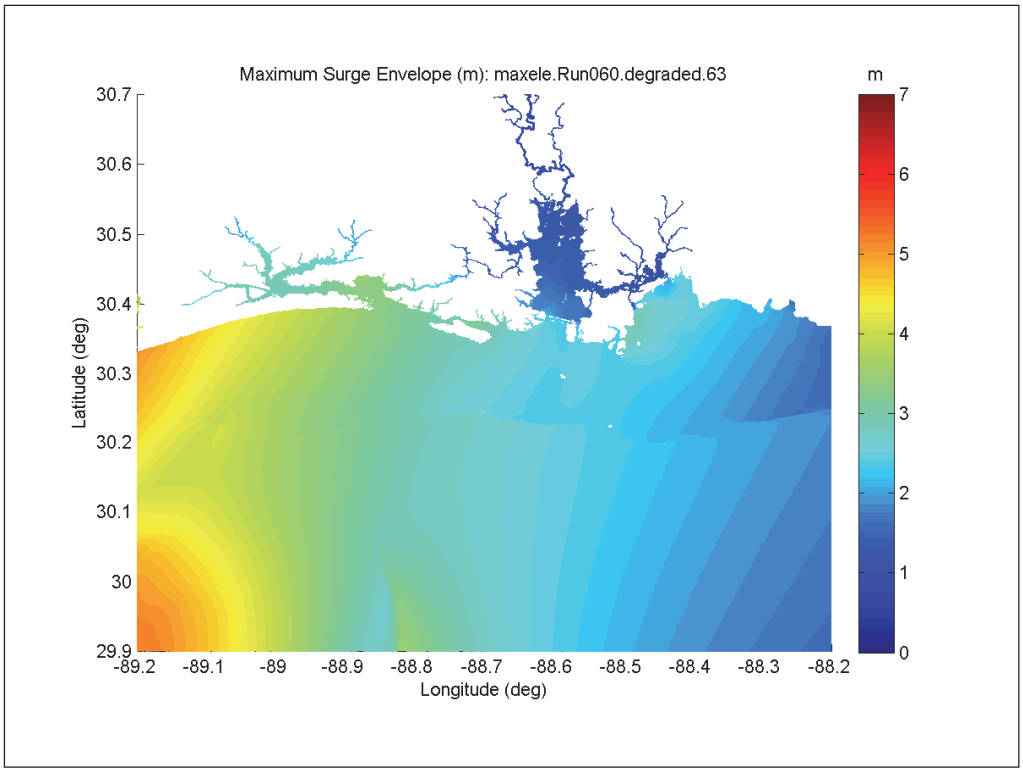

Figure F-19. Maximum surge envelope for Storm 060, Restored condition.

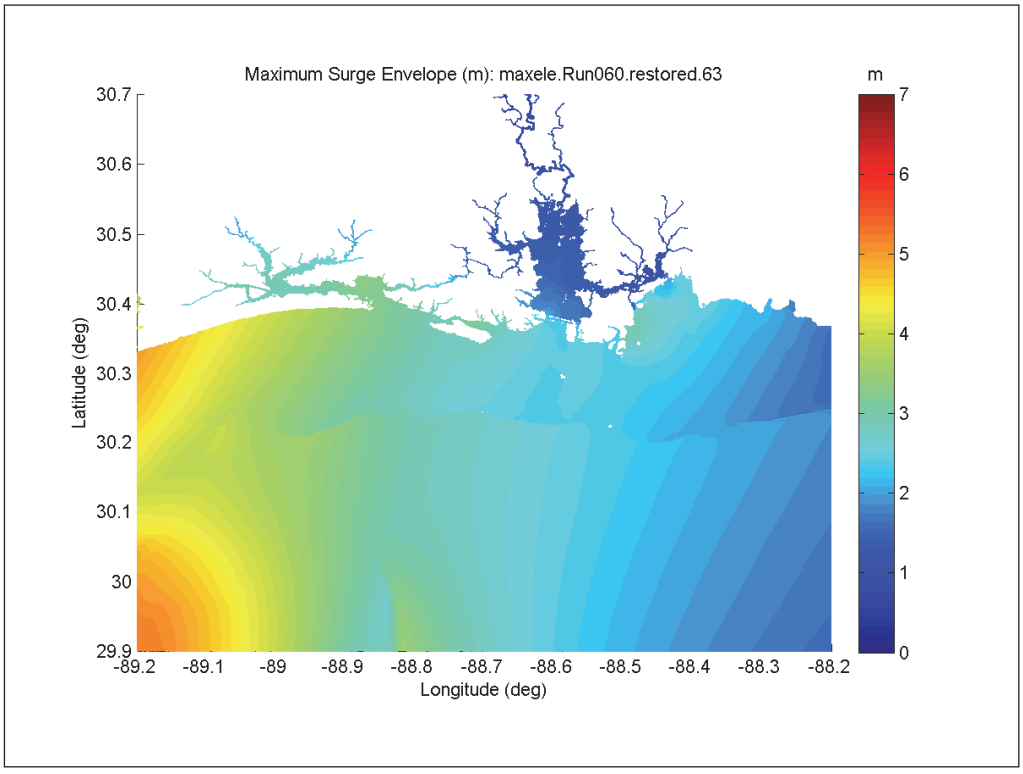

Figure F-20. Maximum surge envelope for Storm 060, Cumulative condition.

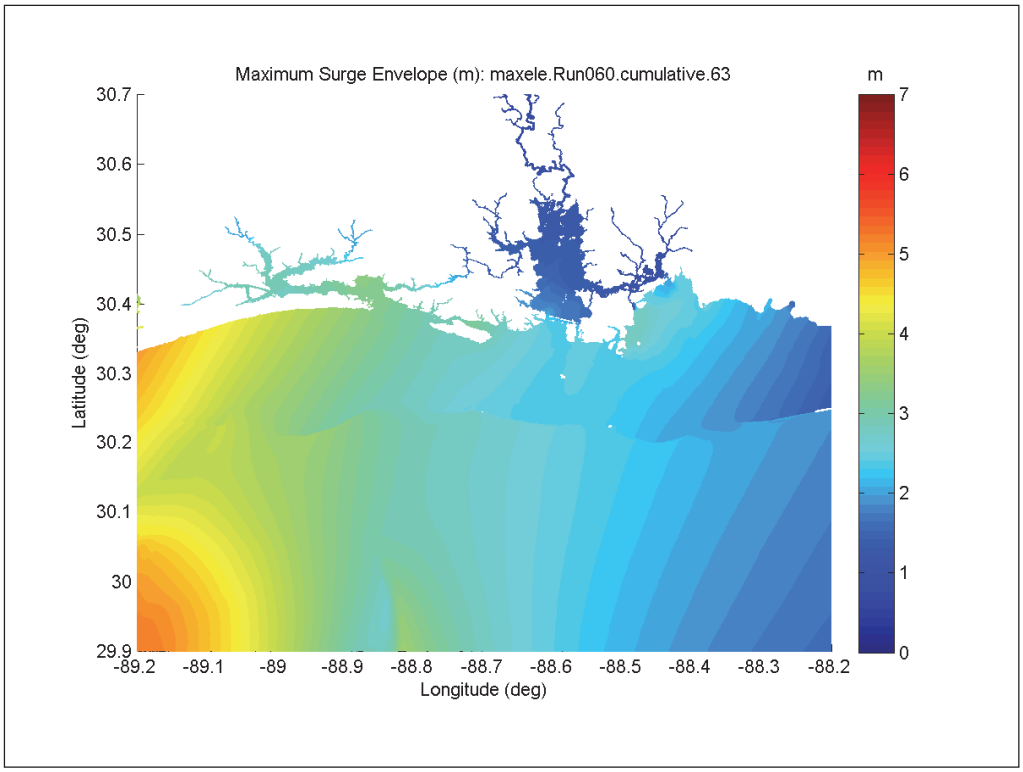

Figure F-21. Maximum surge envelope for Storm 088, Post-Katrina condition.

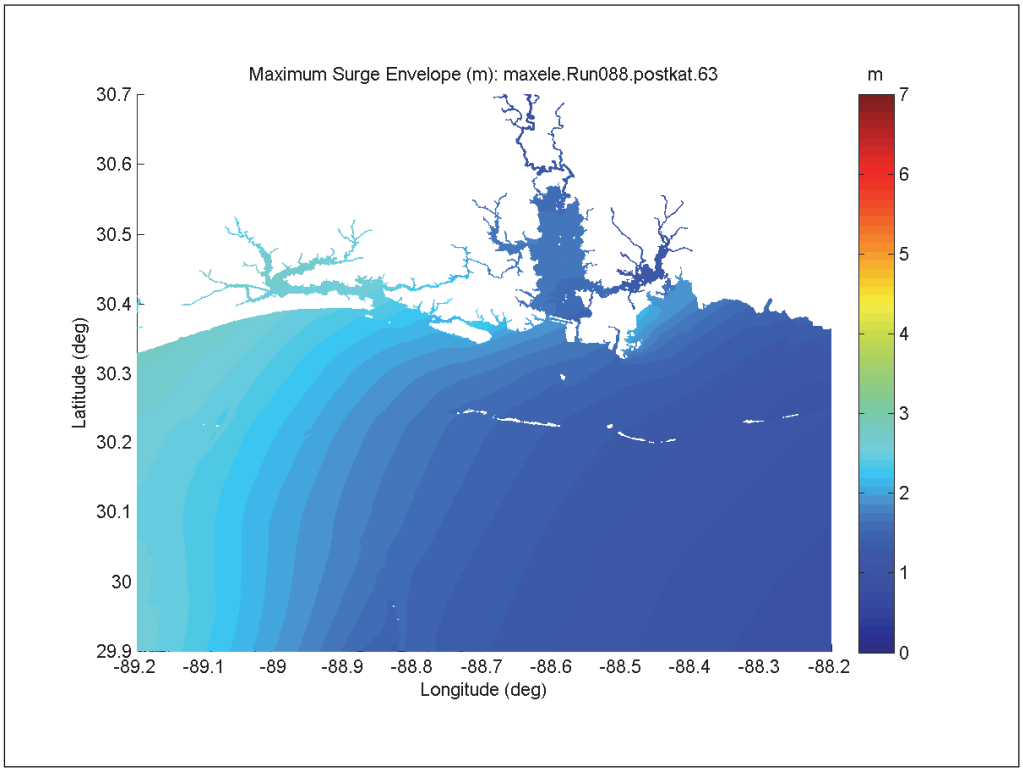

Figure F-22. Maximum surge envelope for Storm 088, Degraded condition.

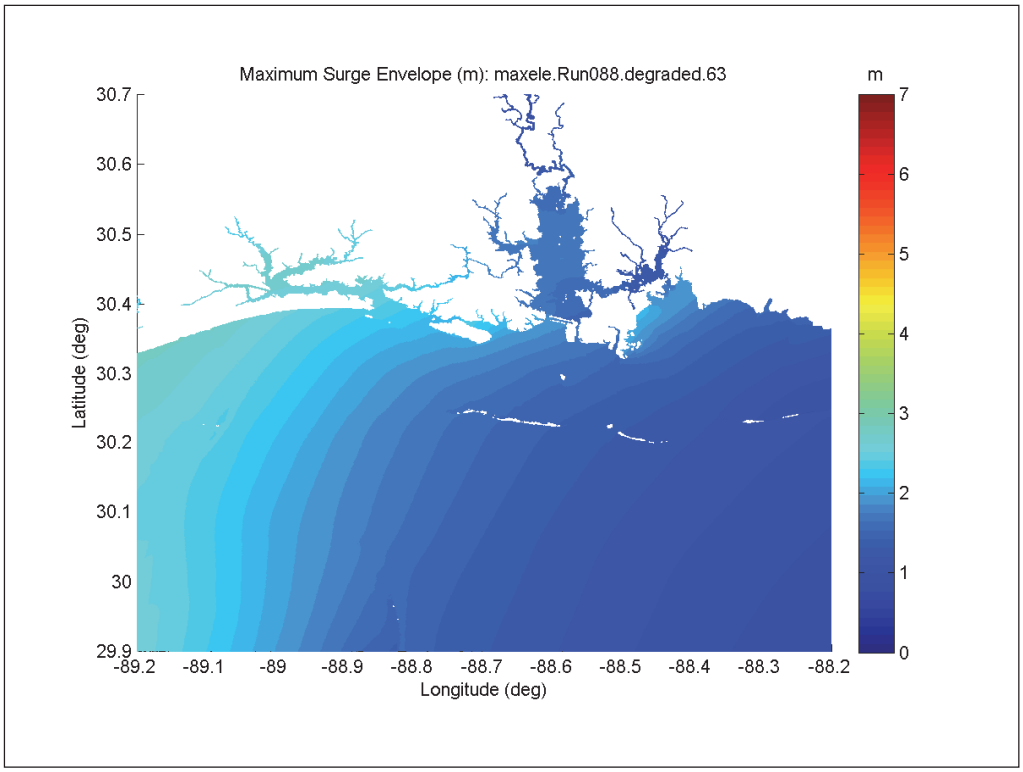

Figure F-23. Maximum surge envelope for Storm 088, Restored condition.

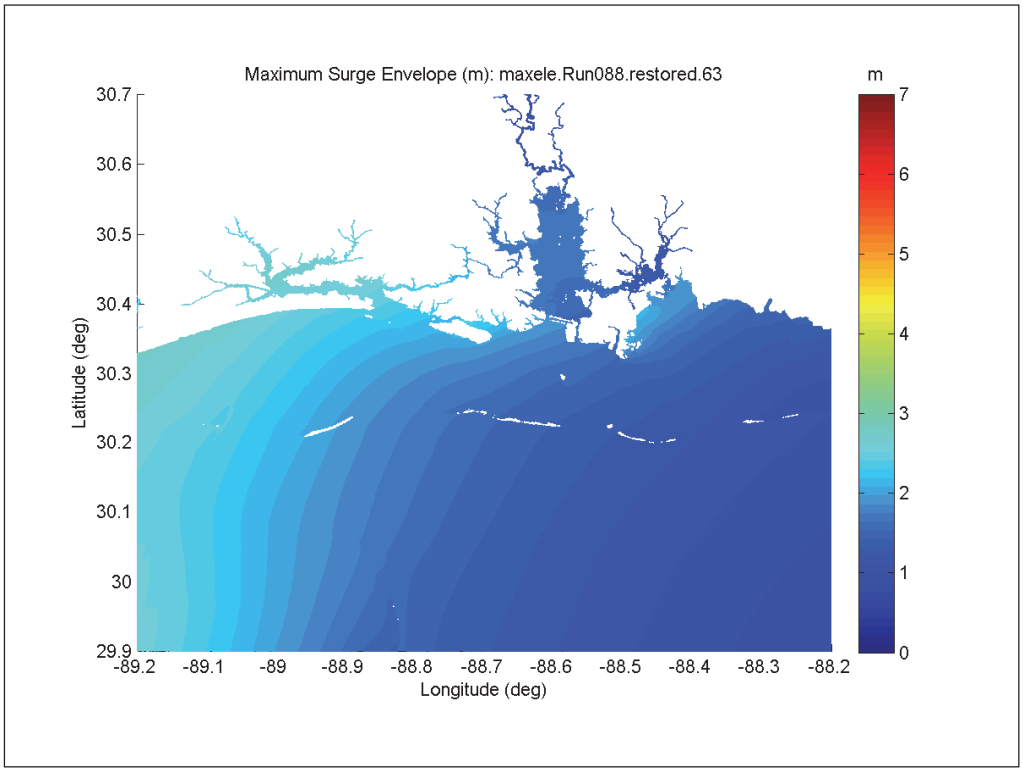

Figure F-24. Maximum surge envelope for Storm 088, Cumulative condition.

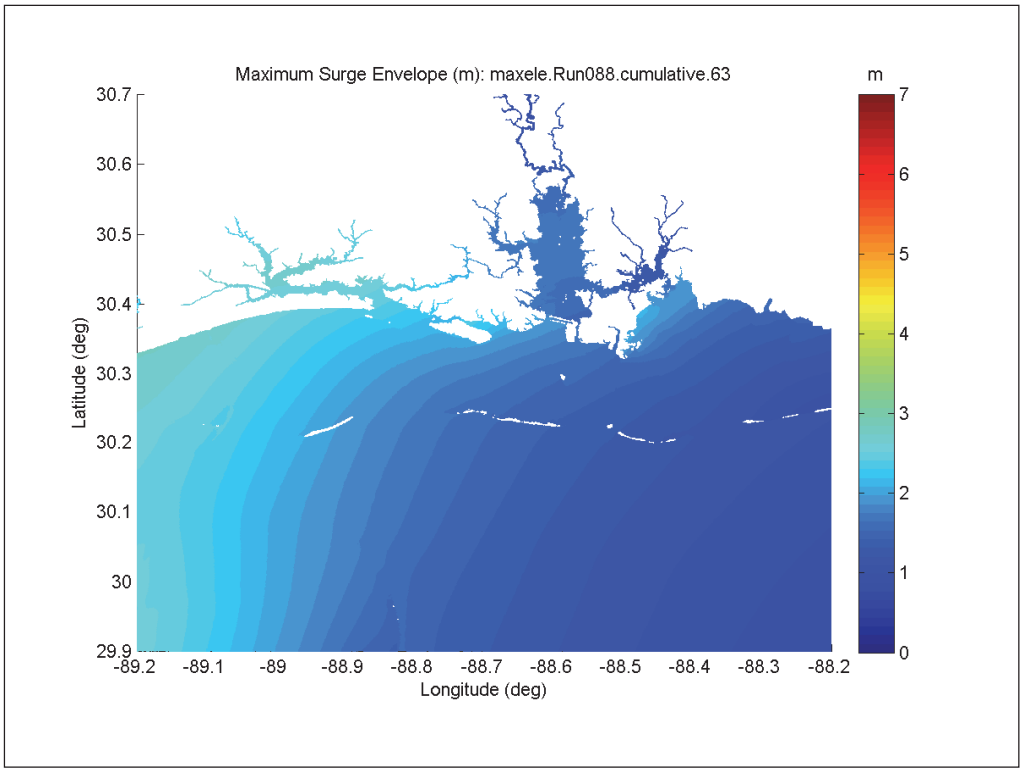

Figure F-25. Maximum surge envelope for Storm 089, Post-Katrina condition.

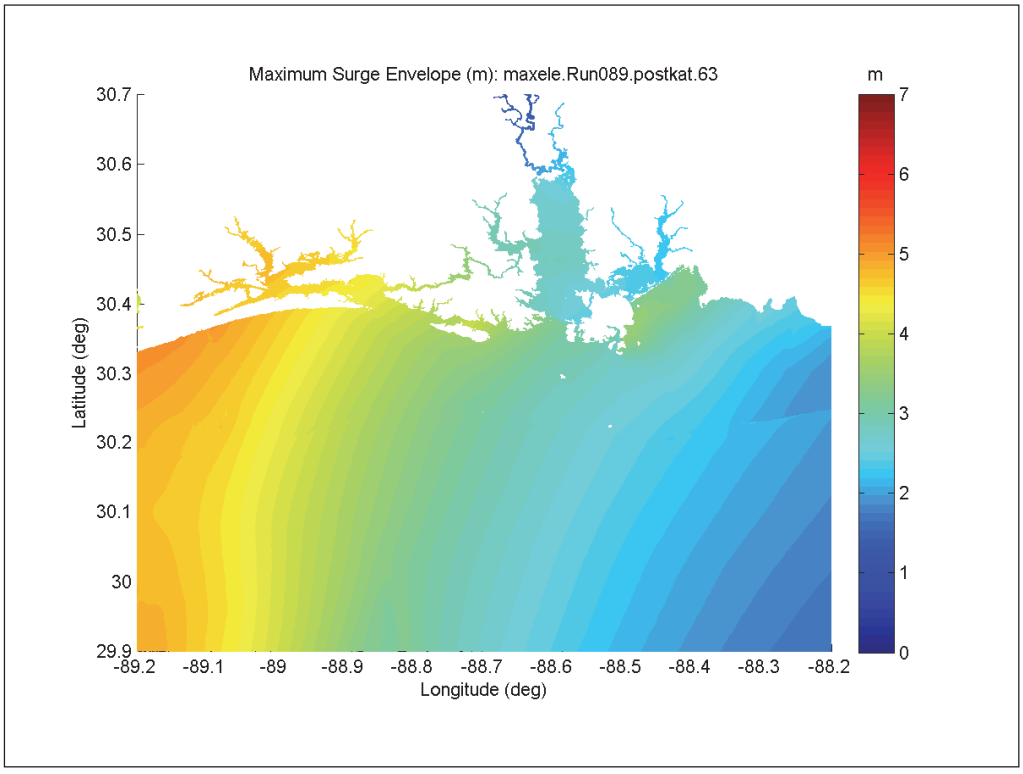

Figure F-26. Maximum surge envelope for Storm 089, Degraded condition.

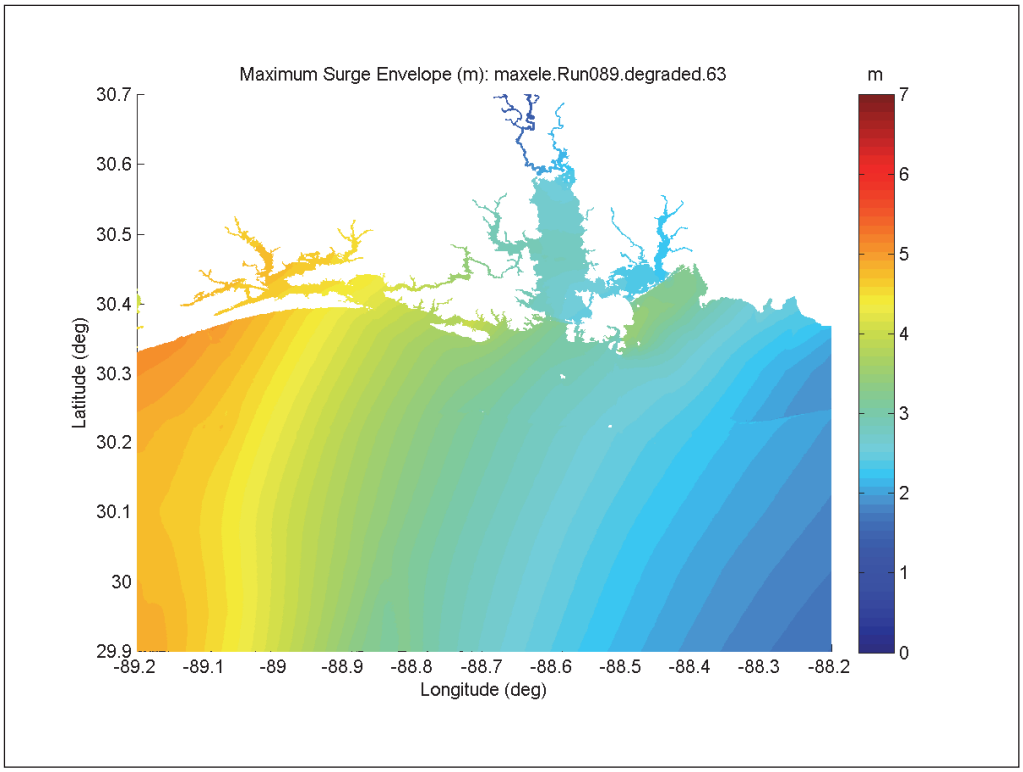

Figure F-27. Maximum surge envelope for Storm 089, Restored condition.

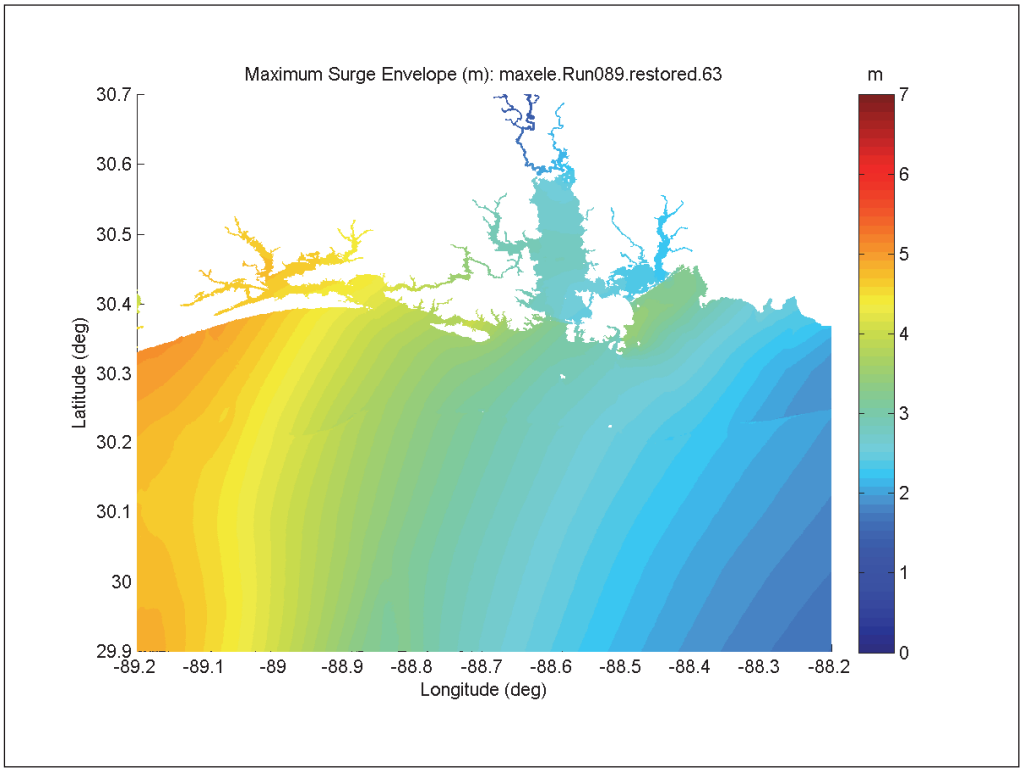

Figure F-28. Maximum surge envelope for Storm 089, Cumulative condition.

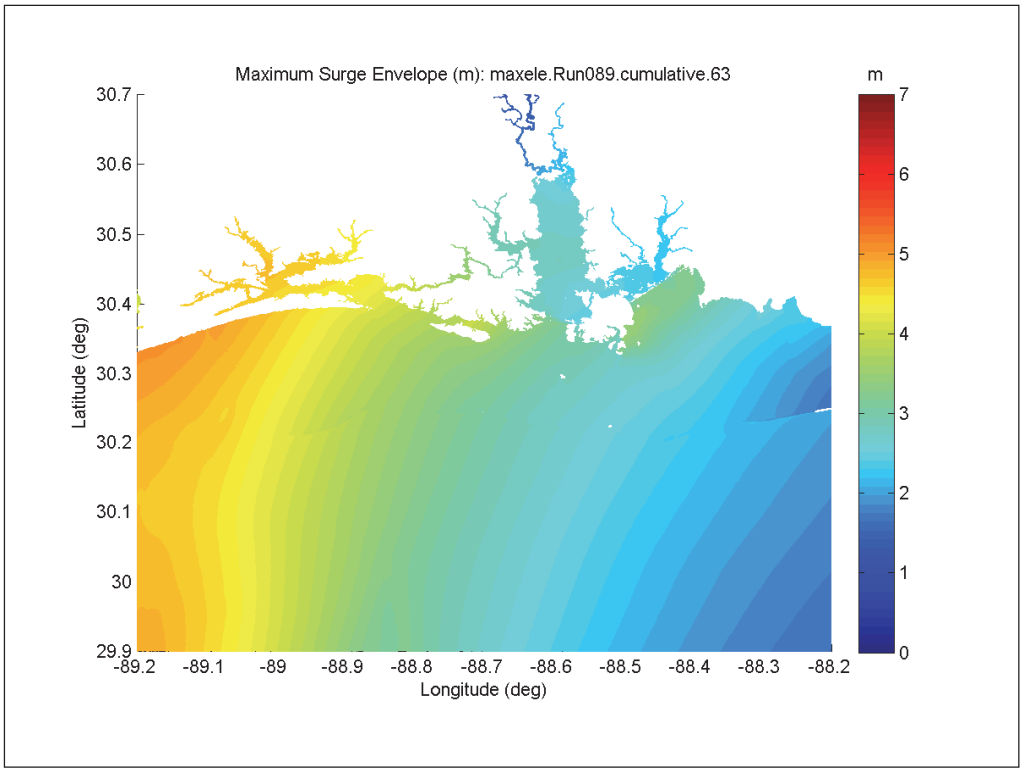

Figure F-29. Maximum surge envelope for Storm 104, Post-Katrina condition.

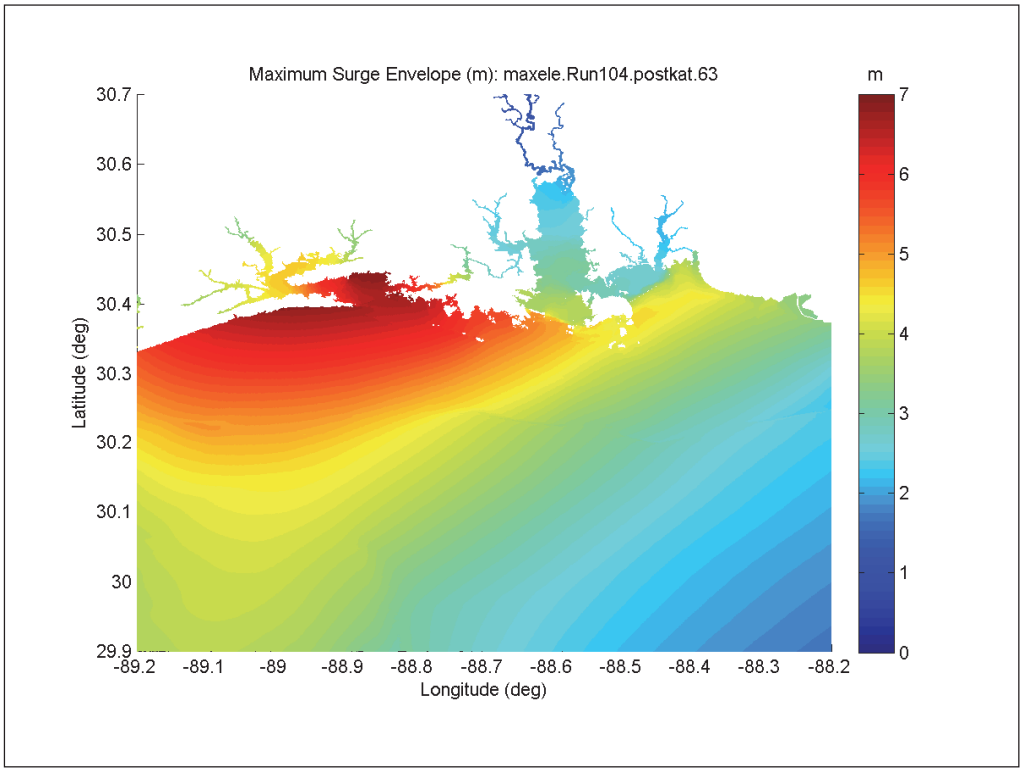

Figure F-30. Maximum surge envelope for Storm 104, Degraded condition.

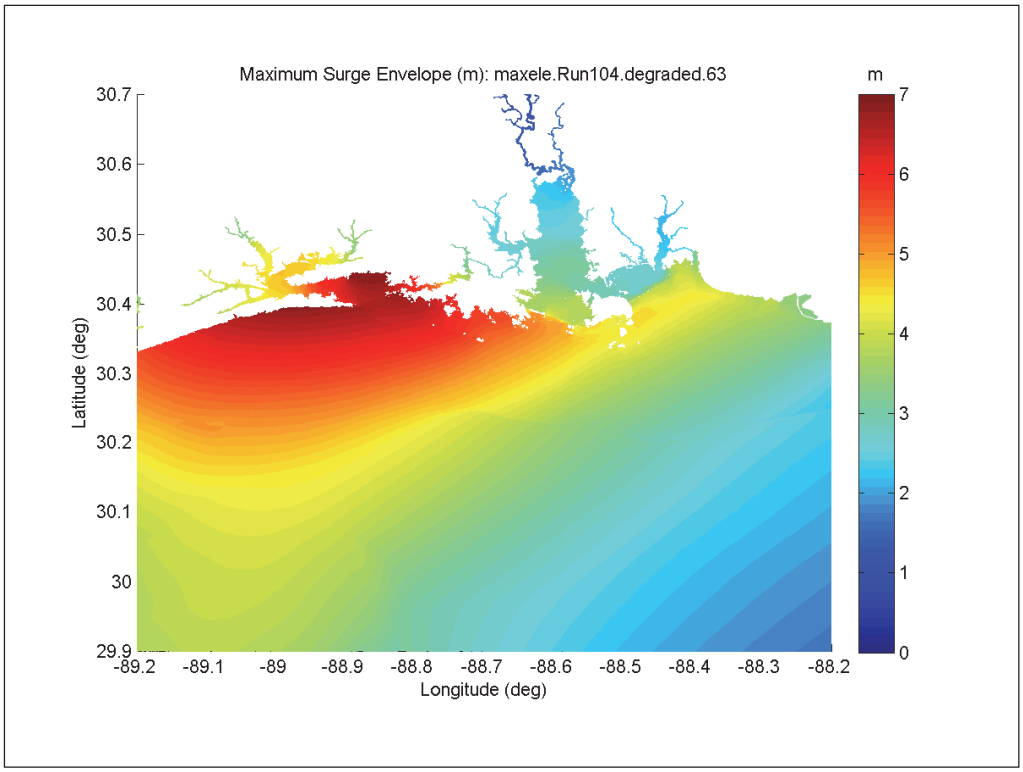

Figure F-31. Maximum surge envelope for Storm 104, Restored condition.

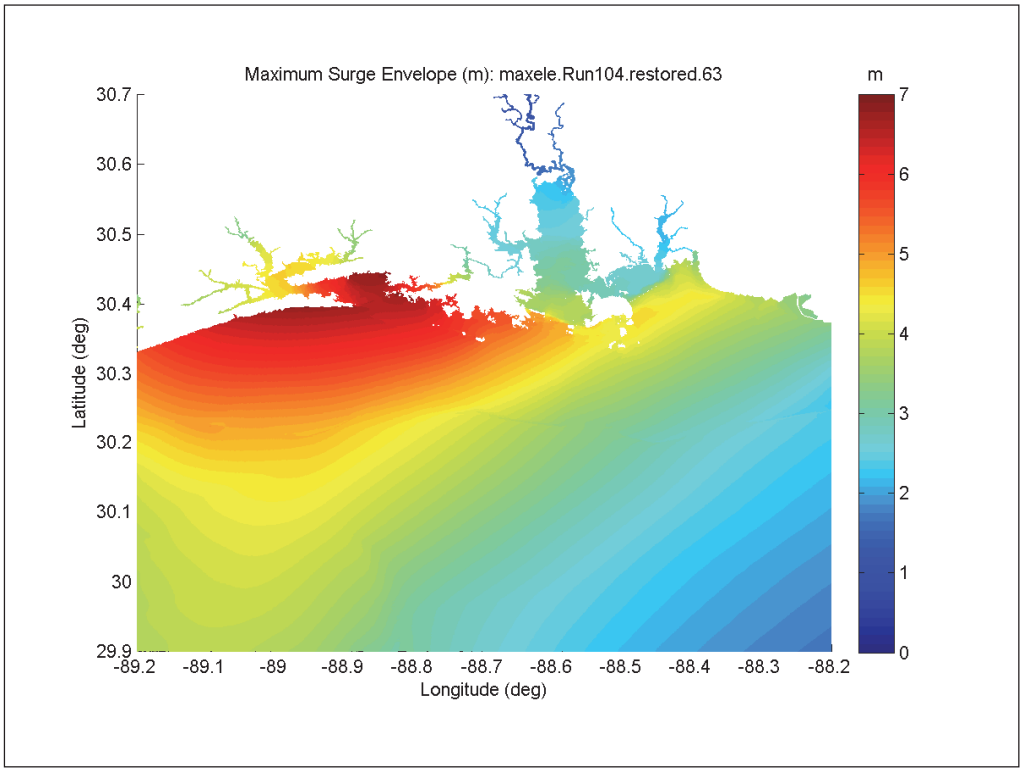

Figure F-32. Maximum surge envelope for Storm 104, Cumulative condition.

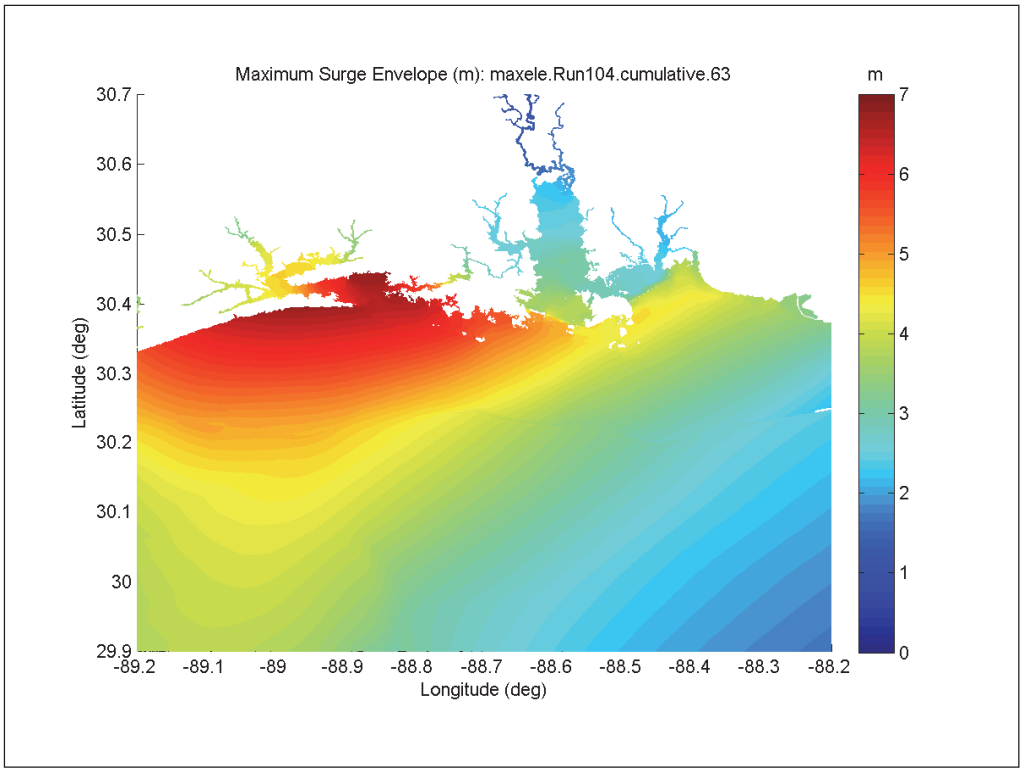

Figure F-33. Maximum surge envelope for Storm 133, Post-Katrina condition.

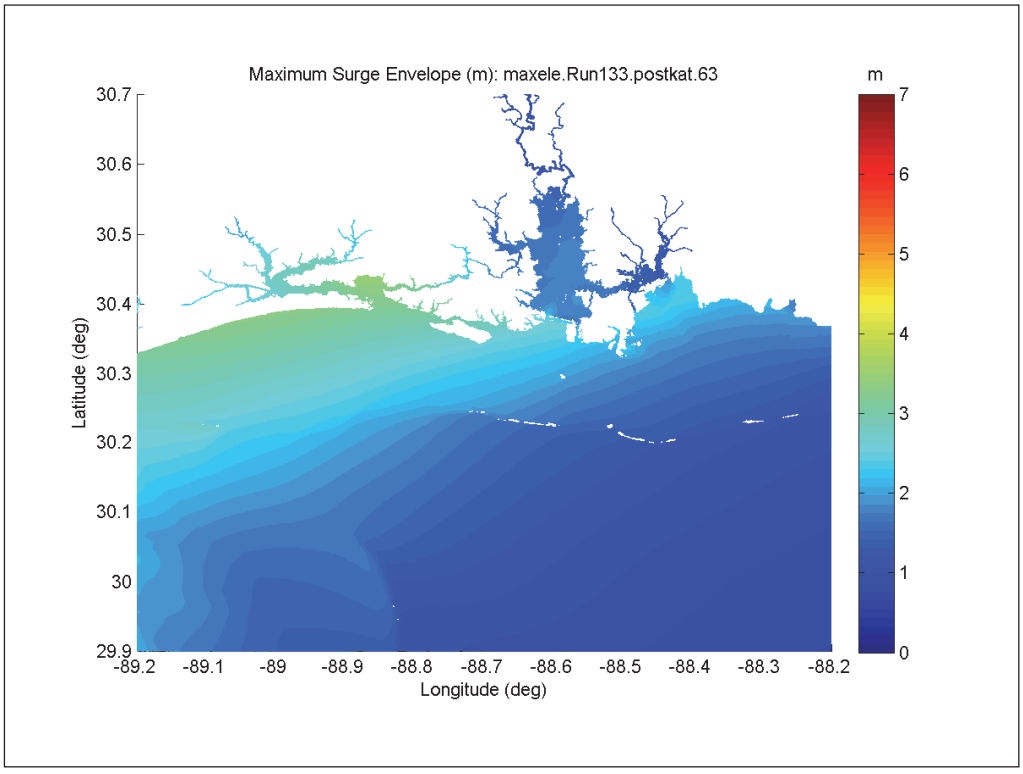

Figure F-34. Maximum surge envelope for Storm 133, Degraded condition.

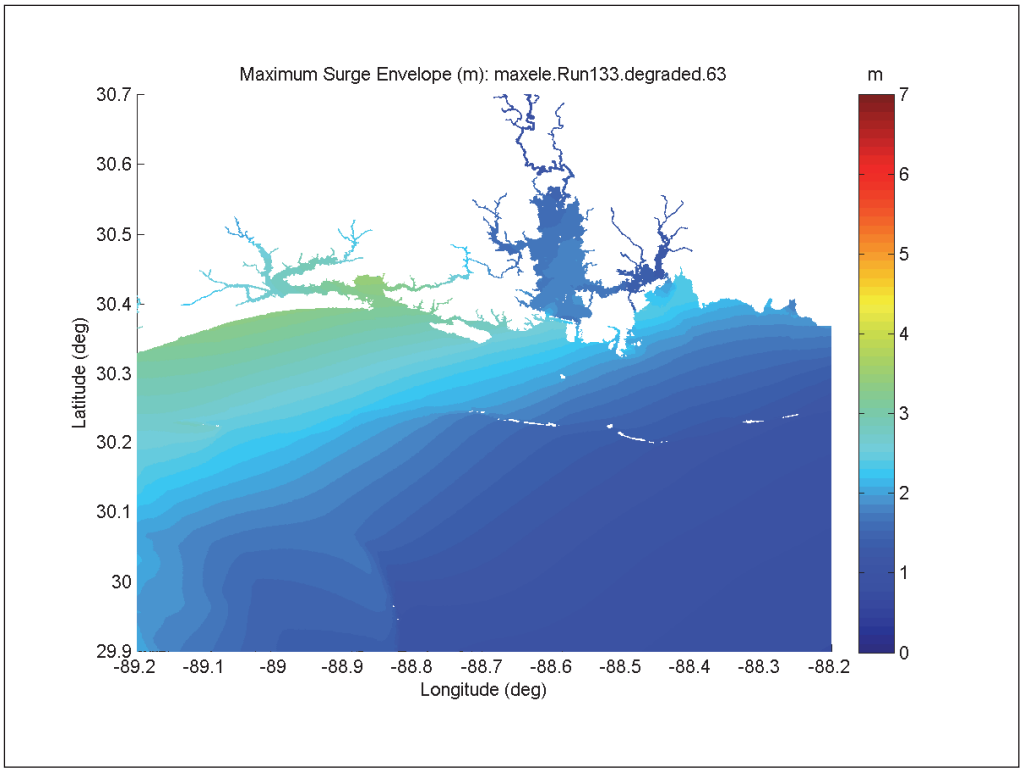

Figure F-35. Maximum surge envelope for Storm 133, Restored condition.

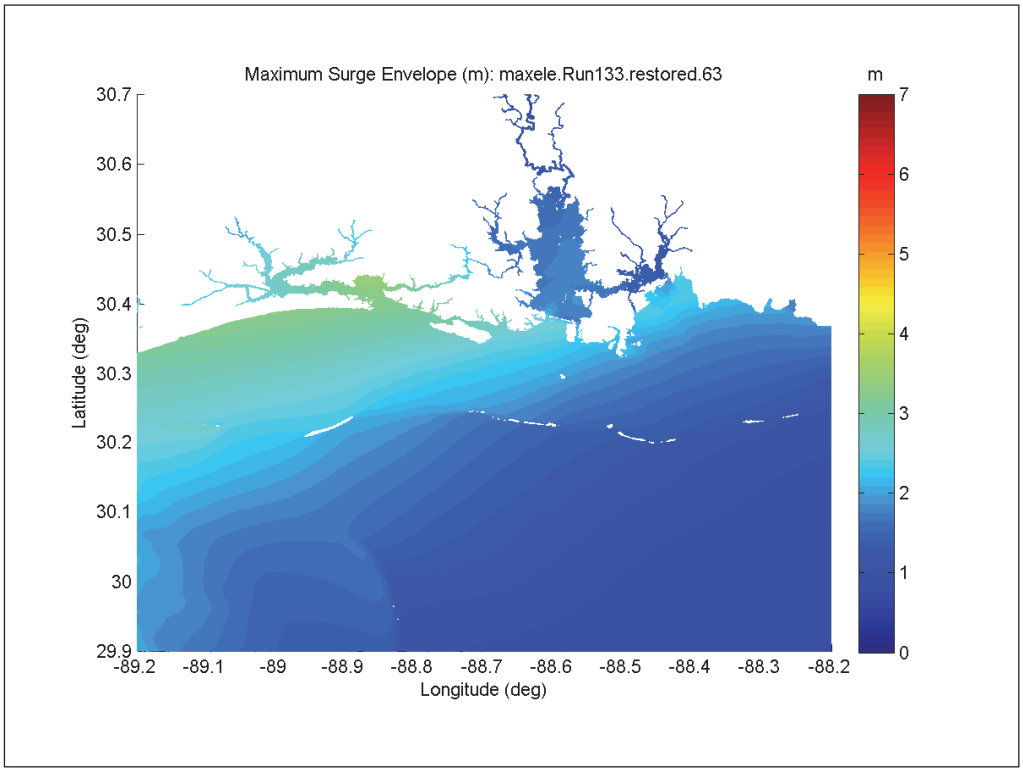

Figure F-36. Maximum surge envelope for Storm 133, Cumulative condition.

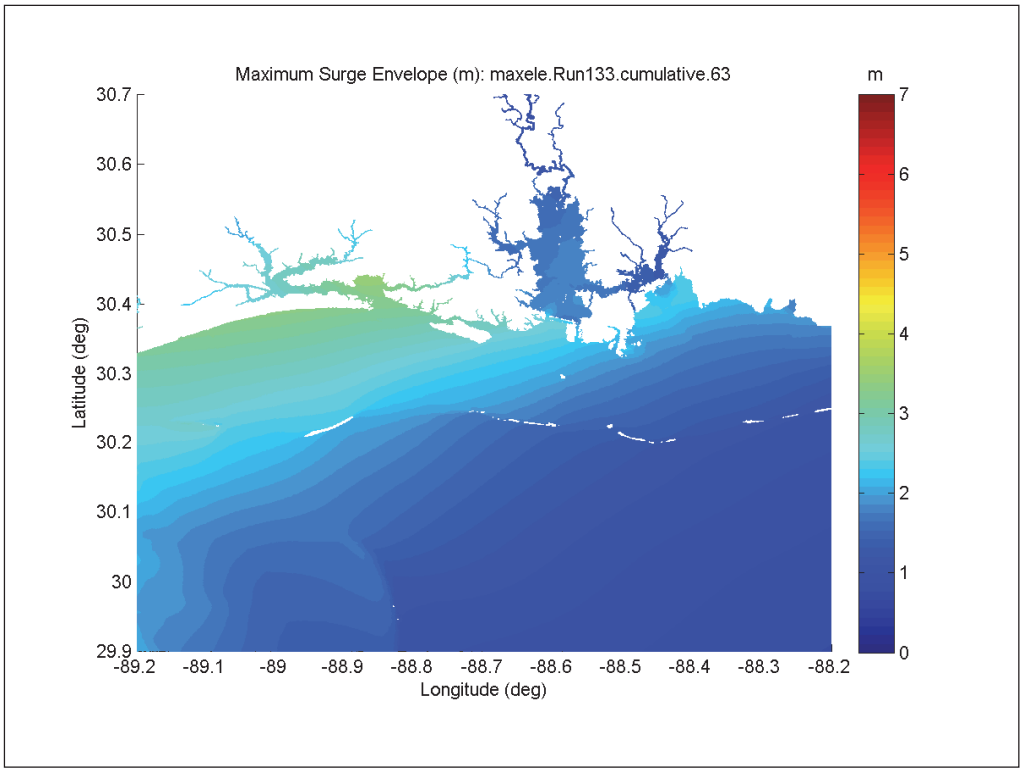

Figure F-37. Maximum surge envelope for Storm 134, Post-Katrina condition.

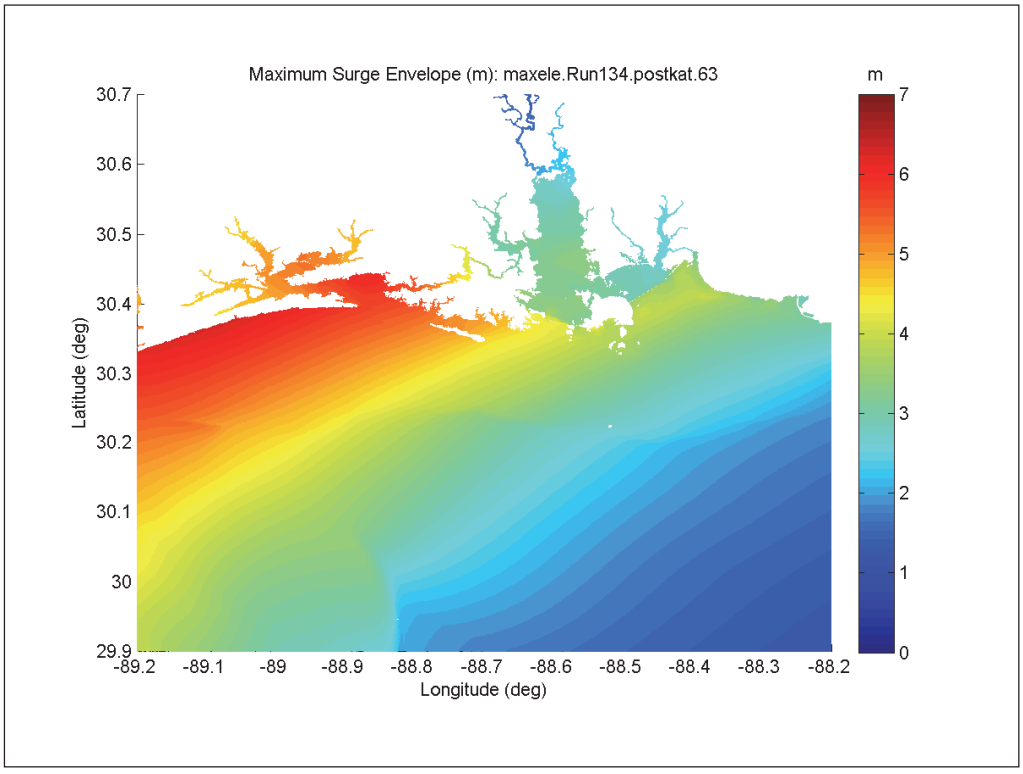

Figure F-38. Maximum surge envelope for Storm 134, Degraded condition.

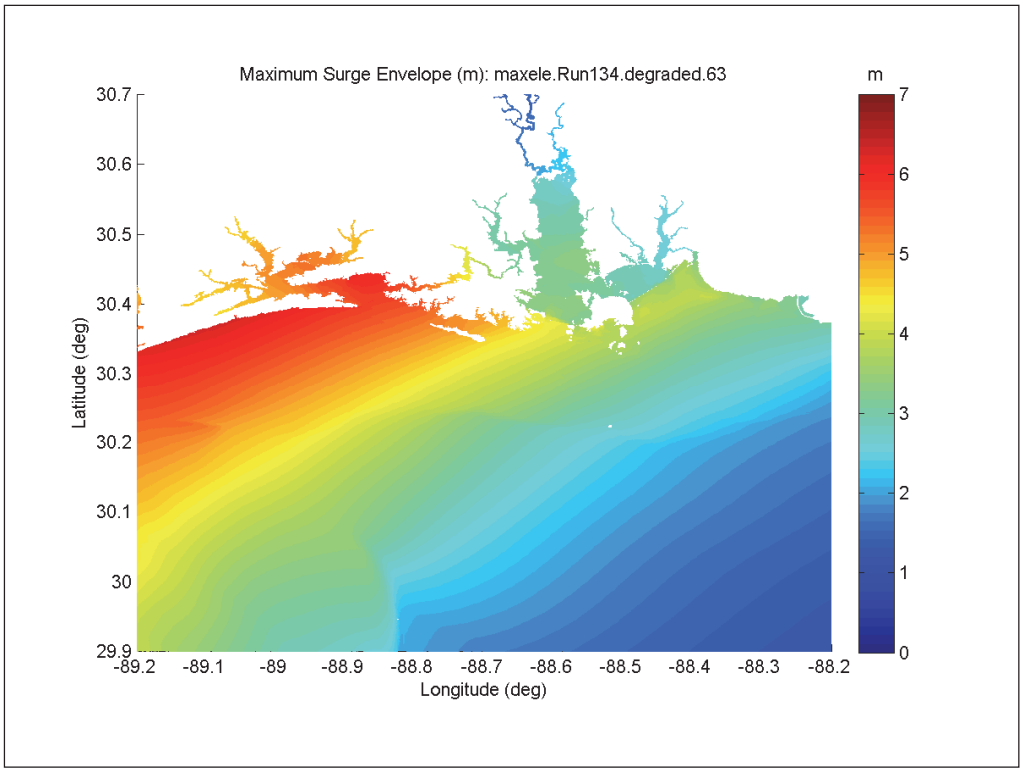

Figure F-39. Maximum surge envelope for Storm 134, Restored condition.

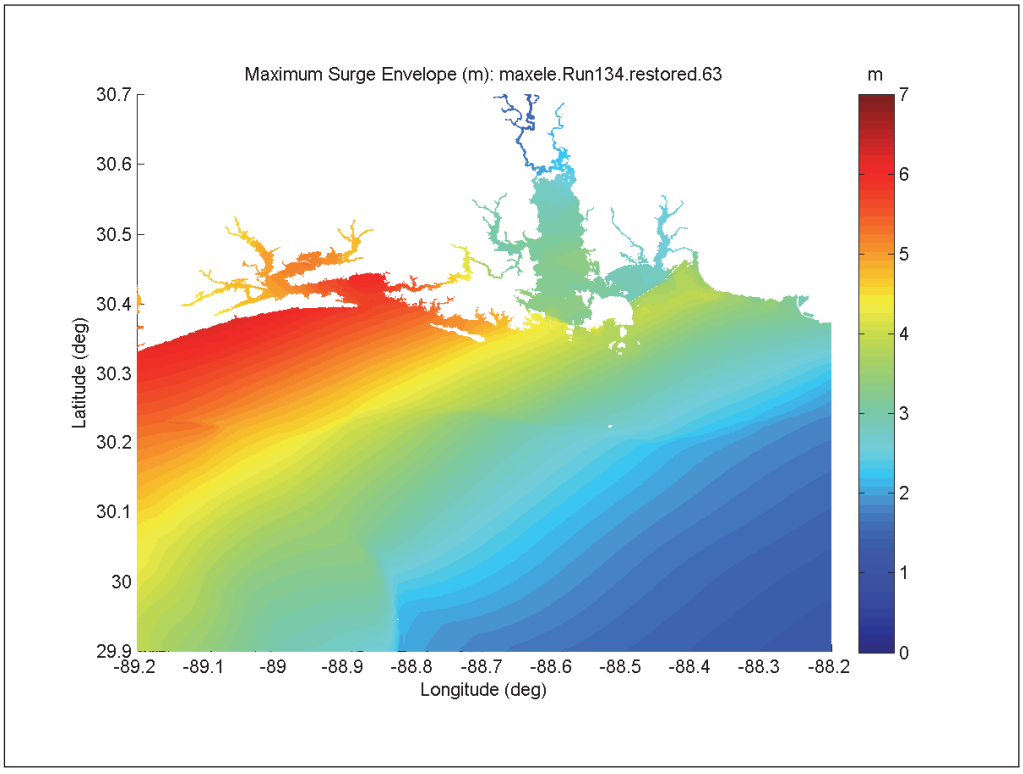

Figure F-40. Maximum surge envelope for Storm 134, Cumulative condition.

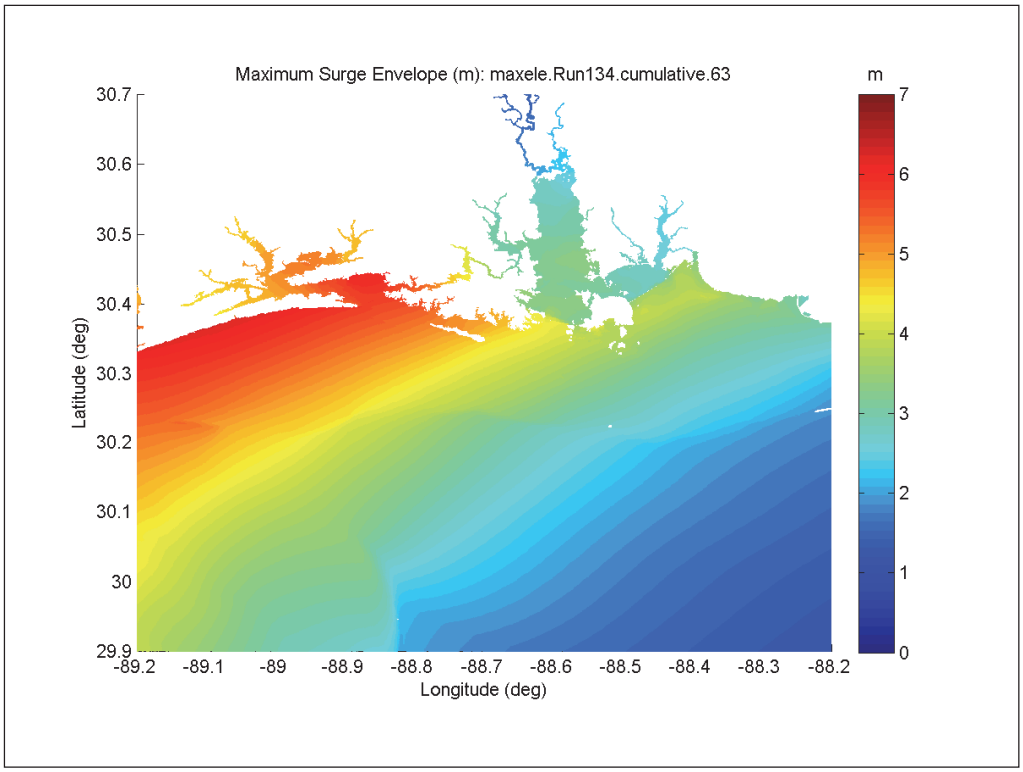

Figure F-41. Maximum surge envelope for Storm 823, Post-Katrina condition.

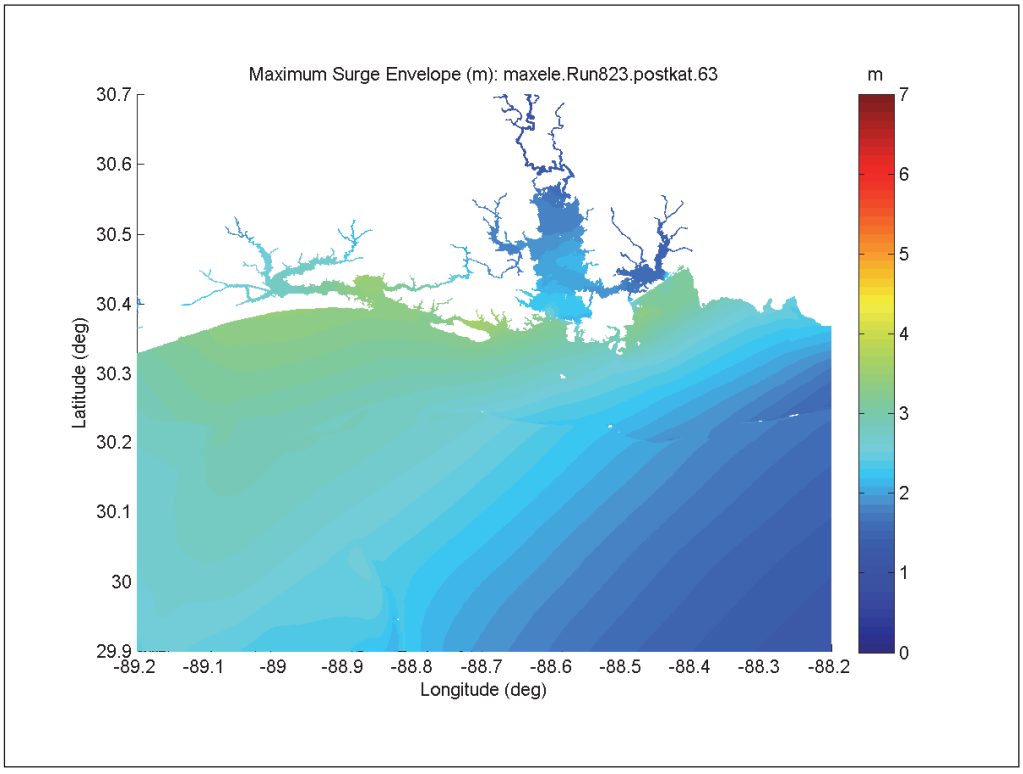

Figure F-42. Maximum surge envelope for Storm 823, Degraded condition.

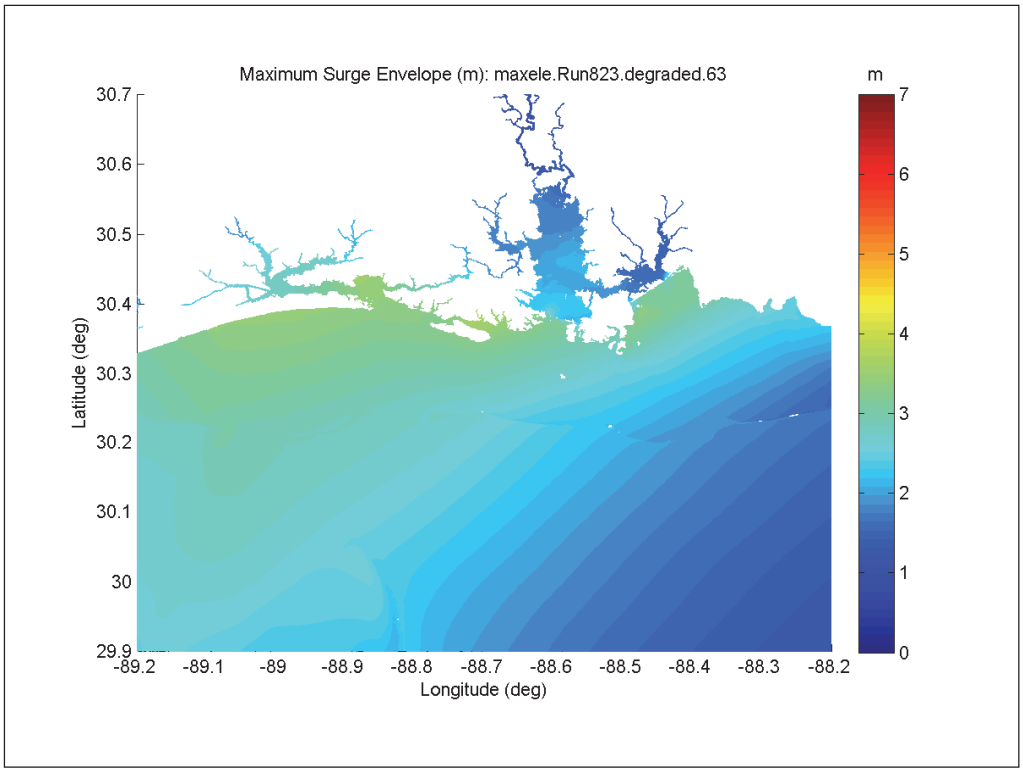

Figure F-43. Maximum surge envelope for Storm 823, Restored condition.

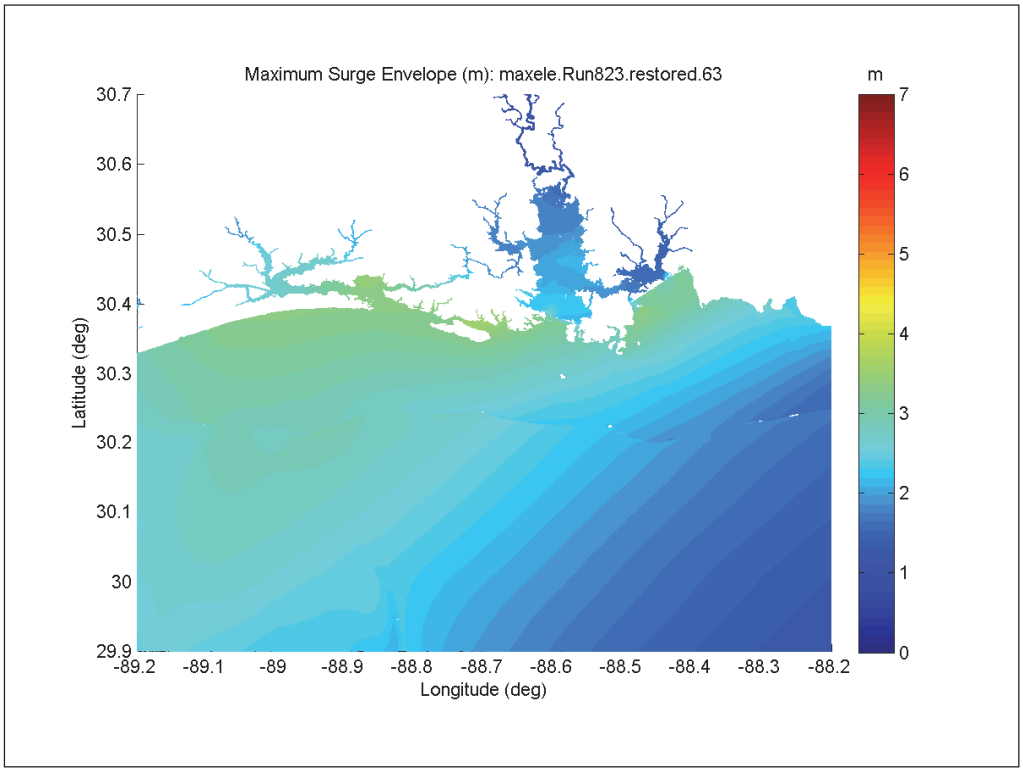

Figure F-44. Maximum surge envelope for Storm 823, Cumulative condition.

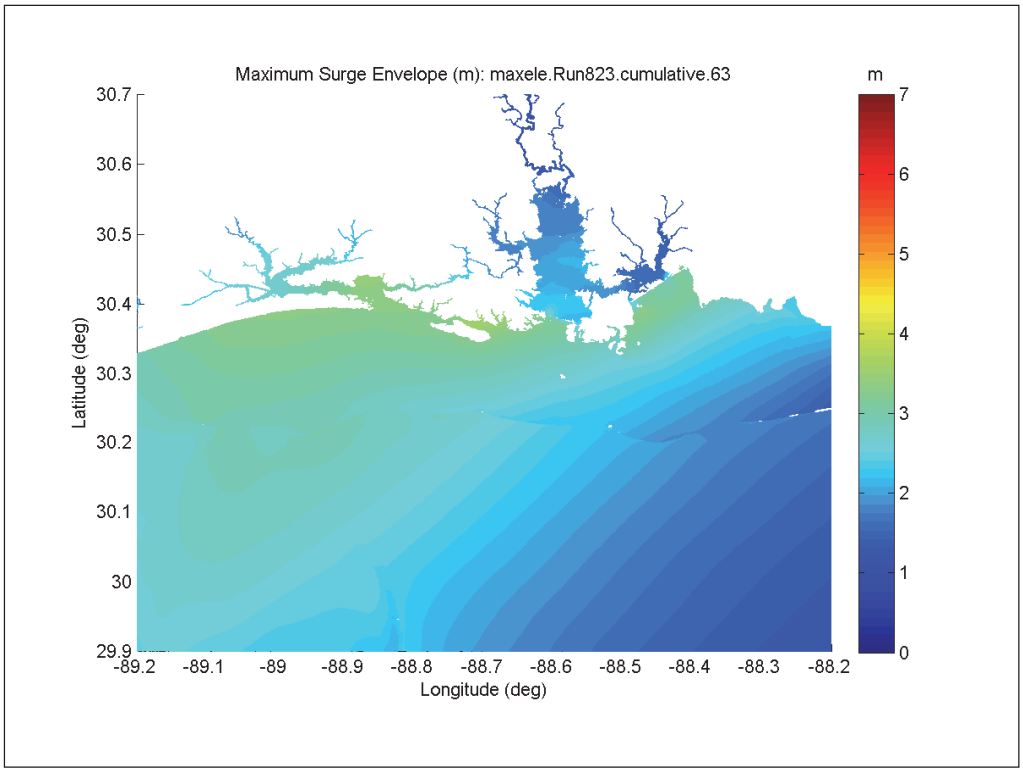

Figure F-45. Maximum surge envelope for Storm 825, Post-Katrina condition.

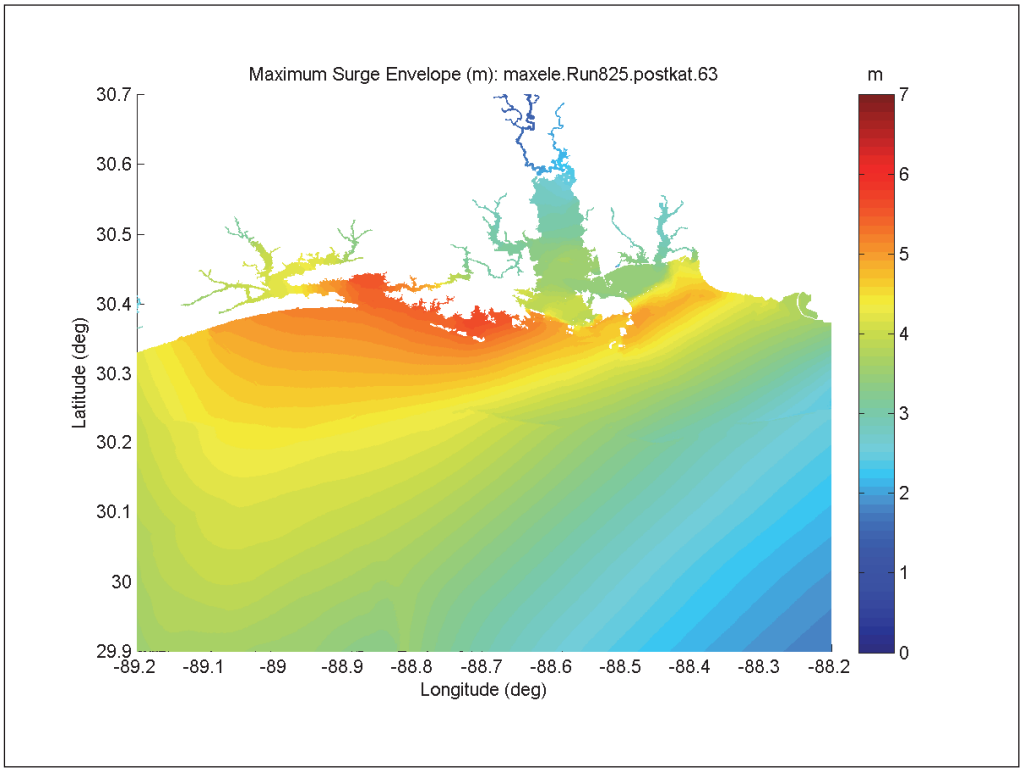

Figure F-46. Maximum surge envelope for Storm 825, Degraded condition.

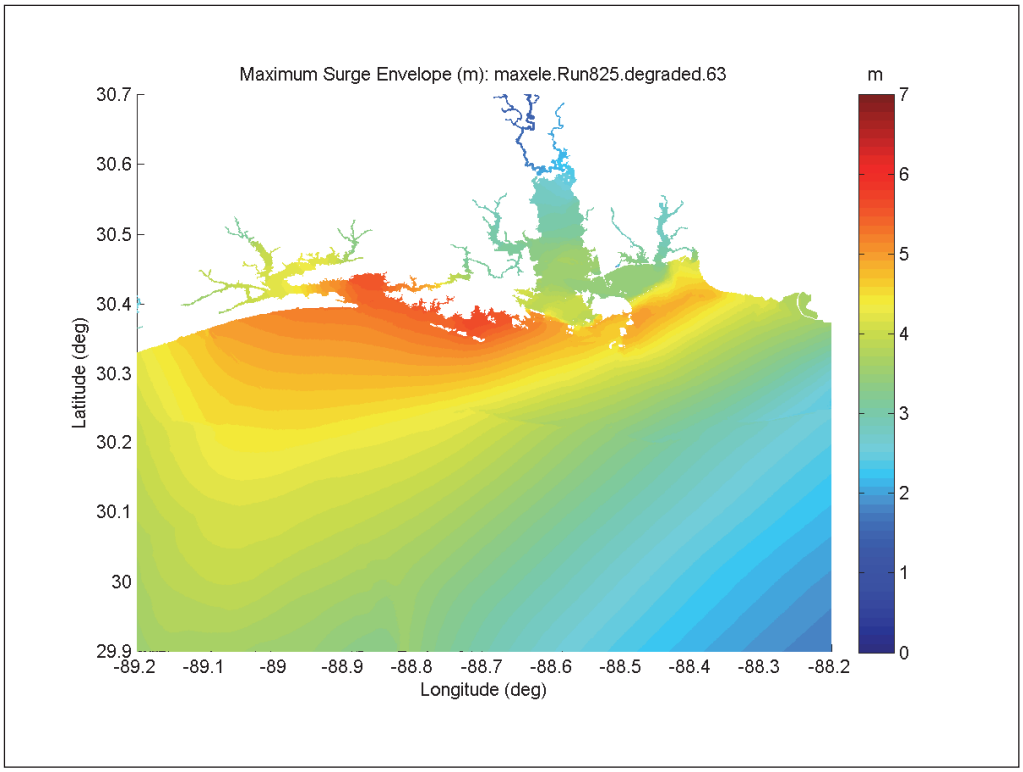

Figure F-47. Maximum surge envelope for Storm 825, Restored condition.

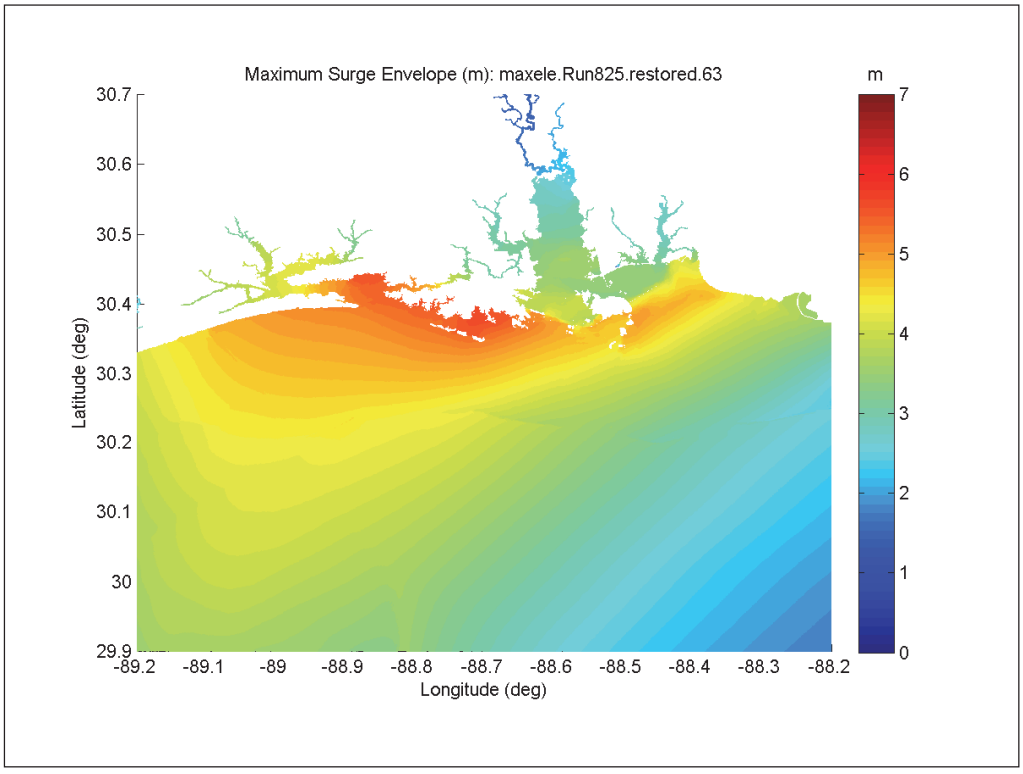

Figure F-48. Maximum surge envelope for Storm 825, Cumulative condition.

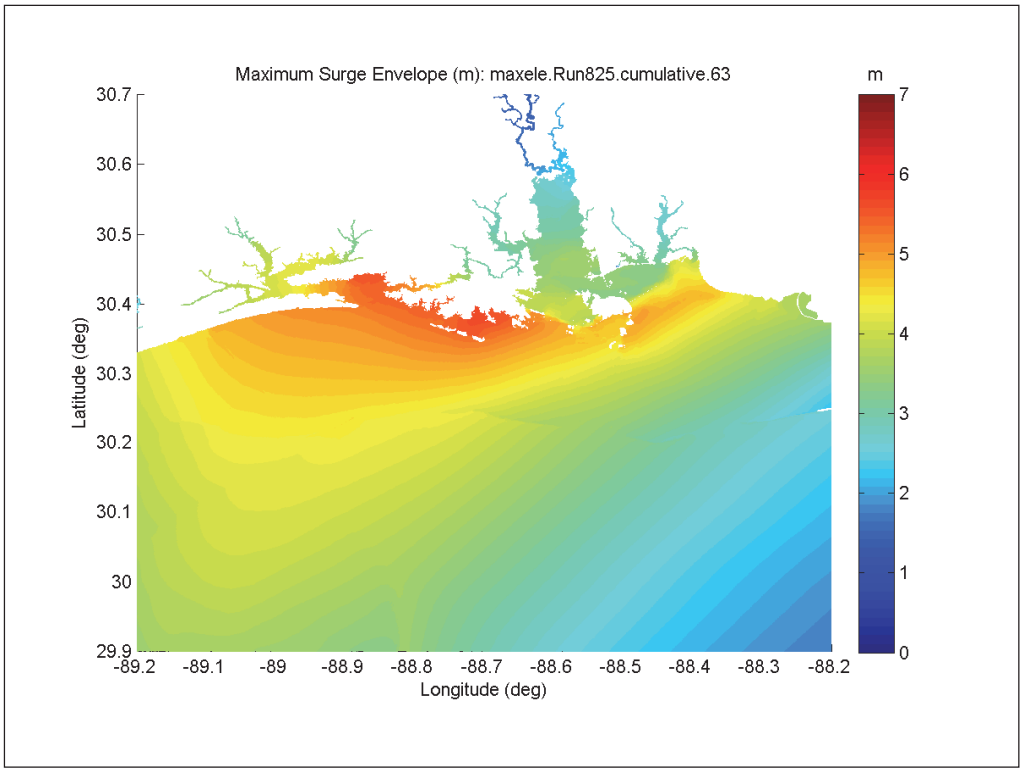

Figure F-49. Maximum surge envelope for Storm 827, Post-Katrina condition.

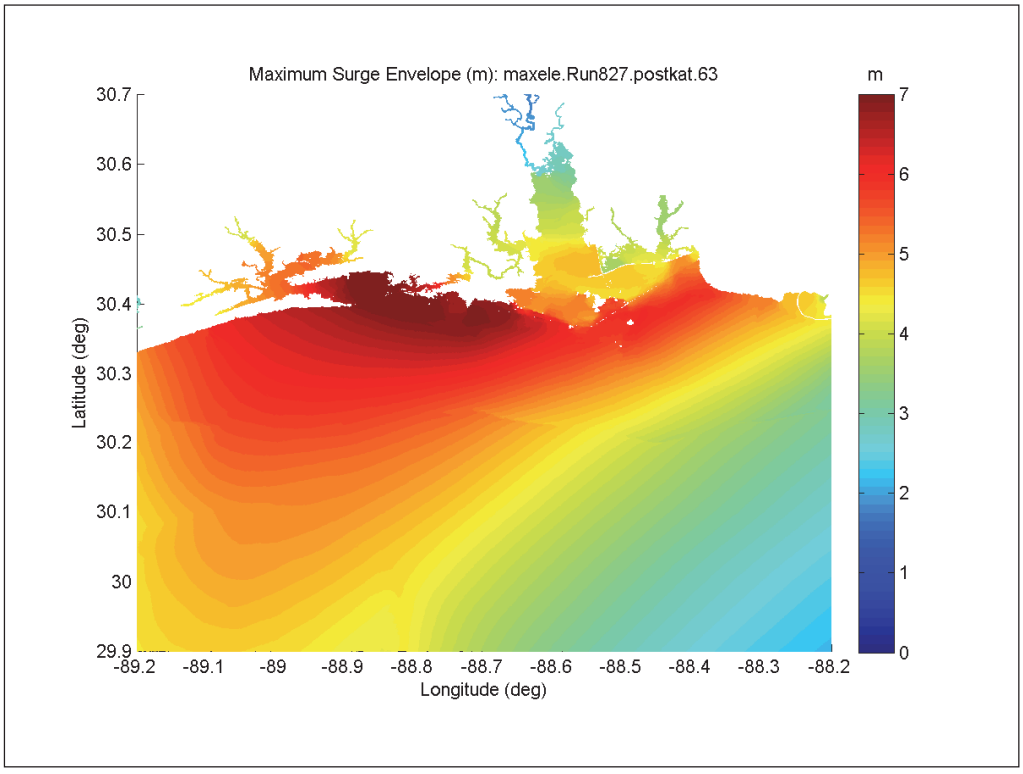

Figure F-50. Maximum surge envelope for Storm 827, Degraded condition.

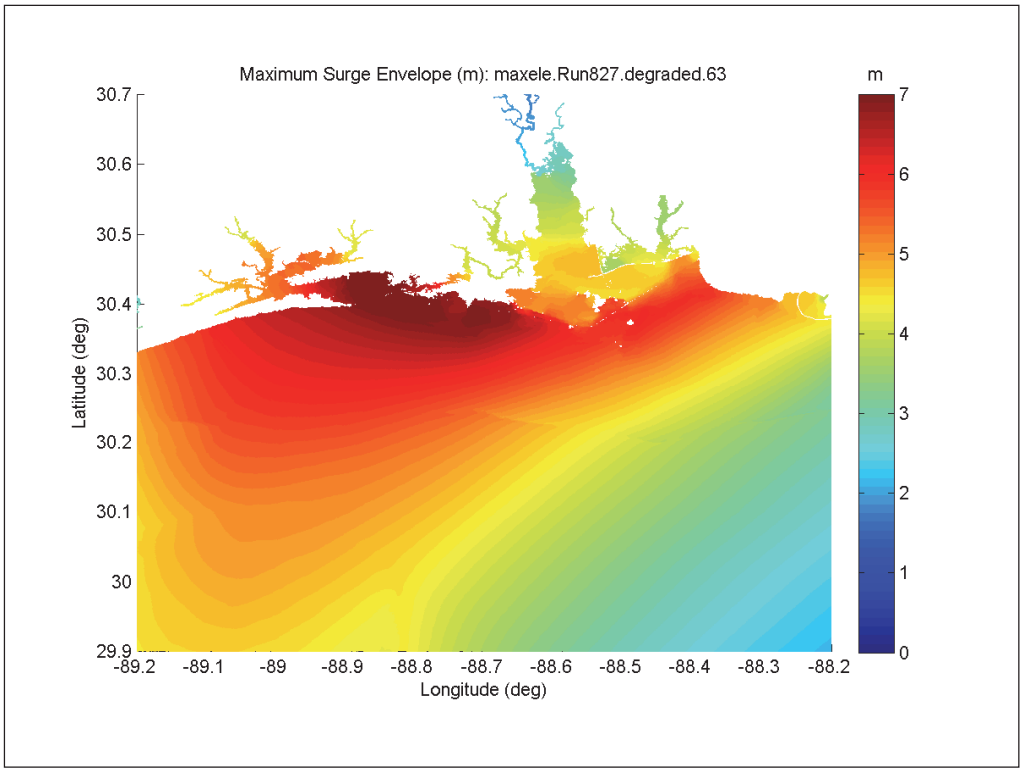

Figure F-51. Maximum surge envelope for Storm 827, Restored condition.

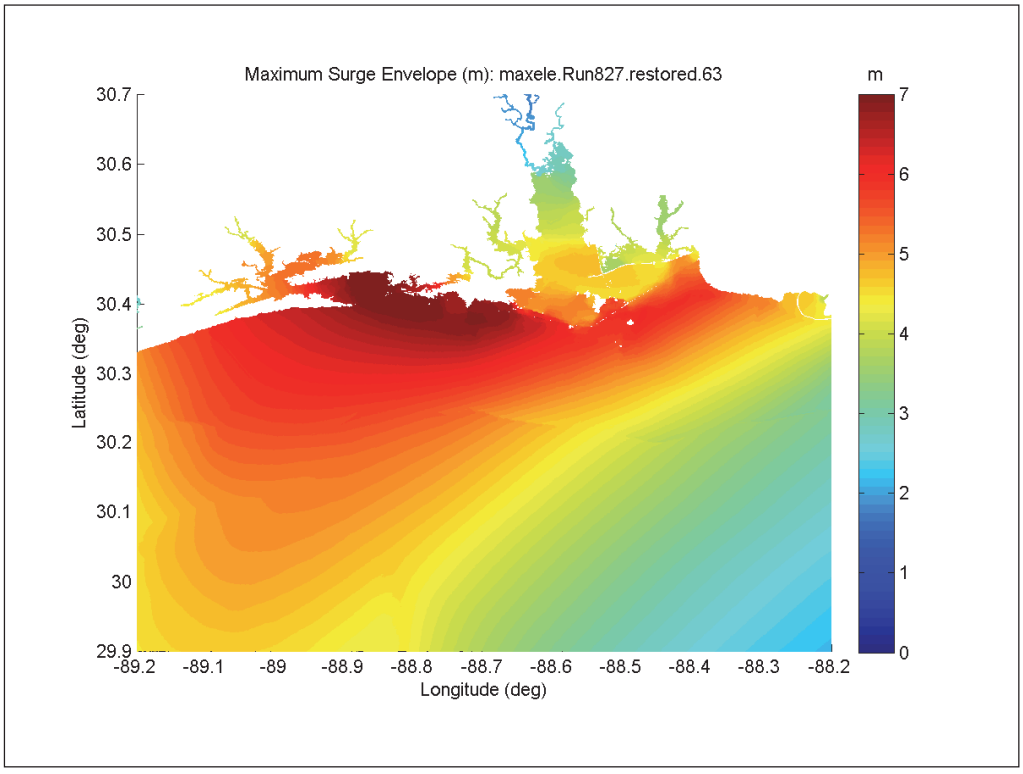

Figure F-52. Maximum surge envelope for Storm 827, Cumulative condition.

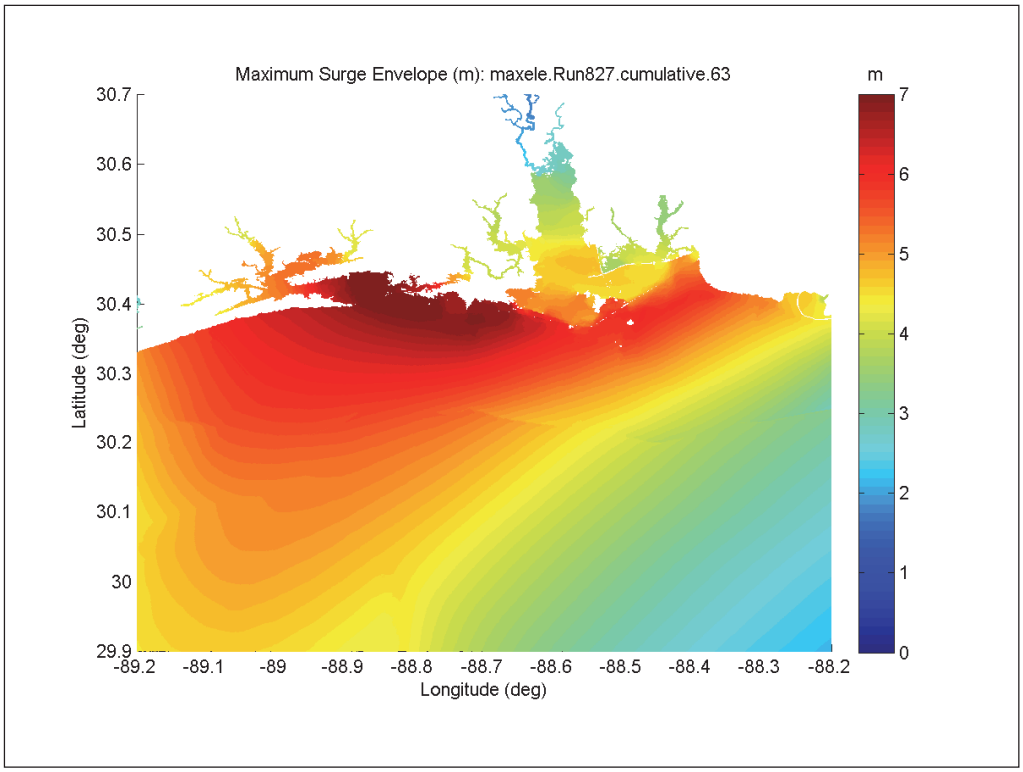

Figure F-53. Maximum surge envelope for Storm 851, Post-Katrina condition.

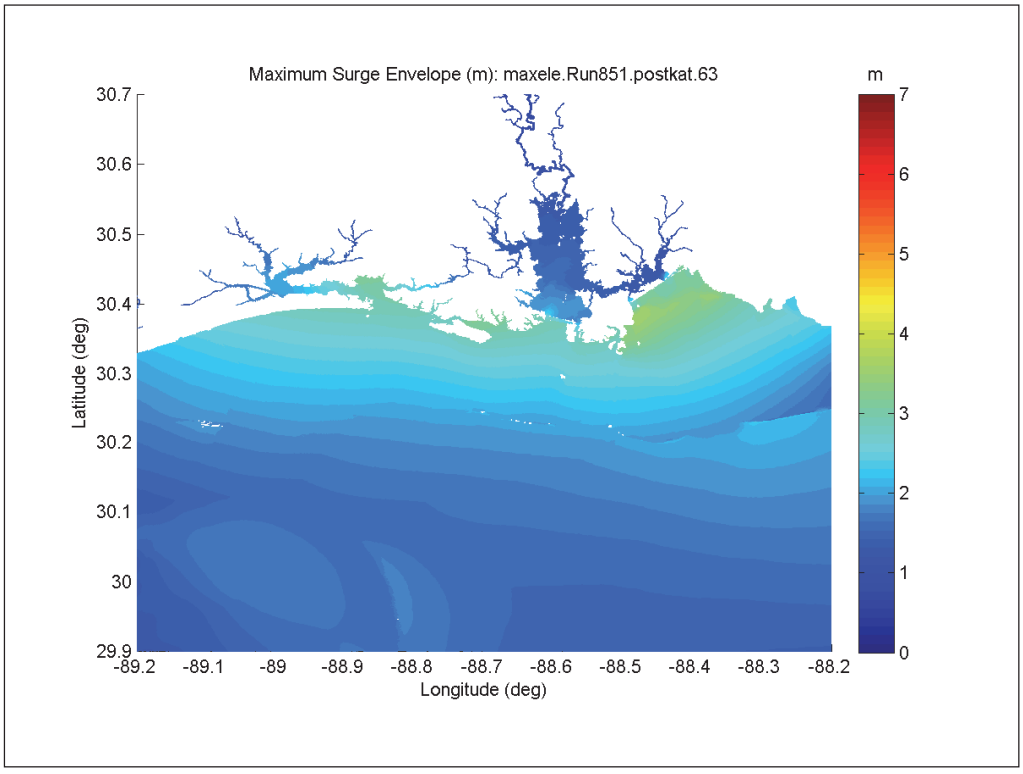

Figure F-54. Maximum surge envelope for Storm 851, Degraded condition.

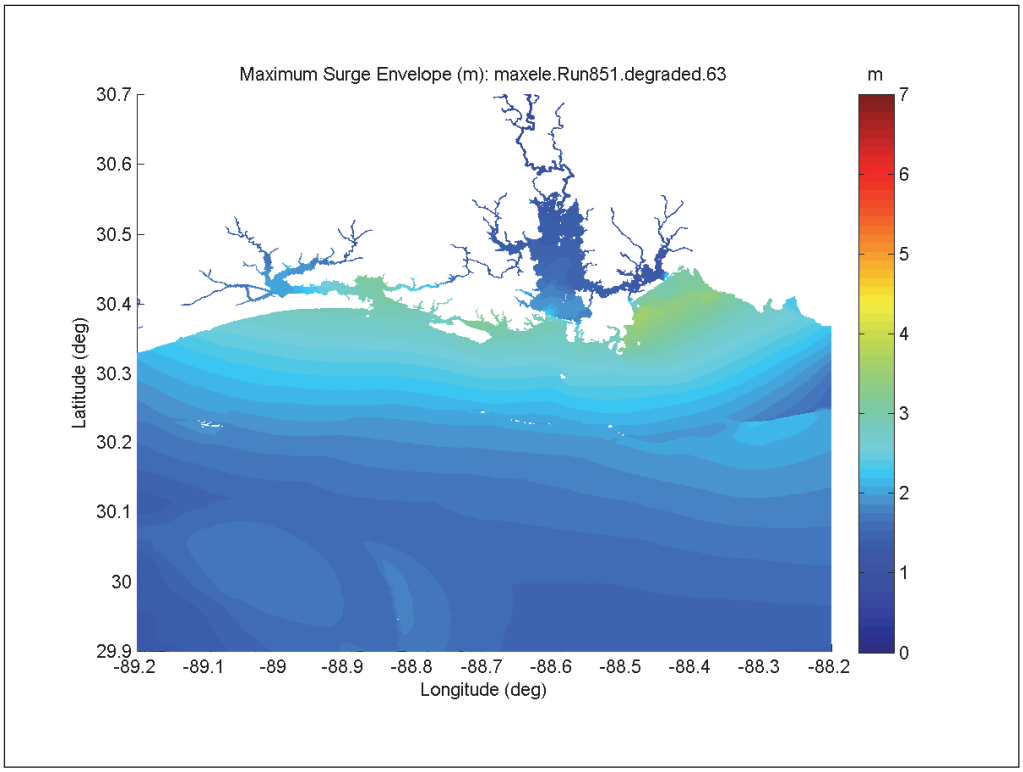

Figure F-55. Maximum surge envelope for Storm 851, Restored condition.

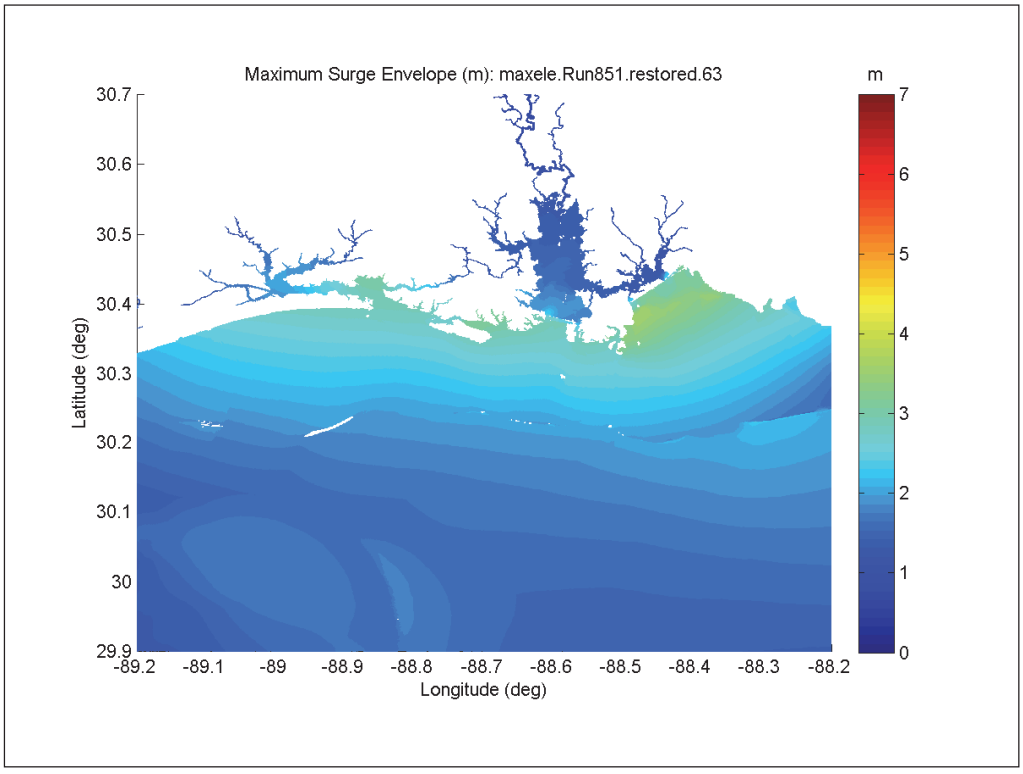

Figure F-56. Maximum surge envelope for Storm 851, Cumulative condition.

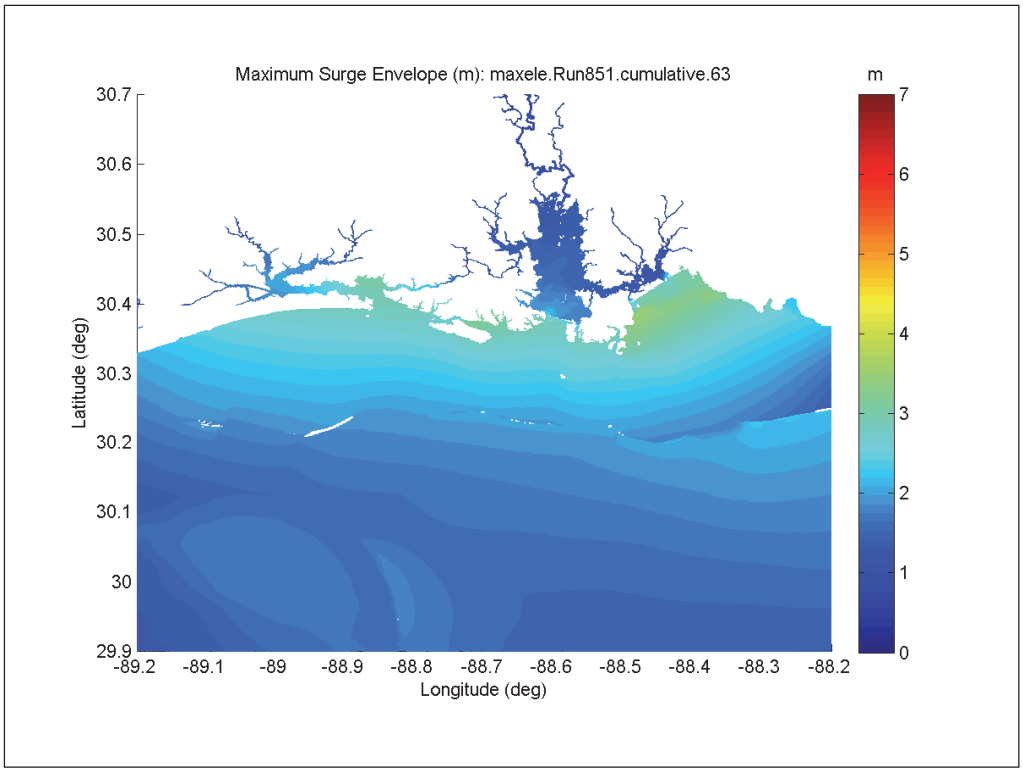

Figure F-57. Maximum surge envelope for Storm 852, Post-Katrina condition.

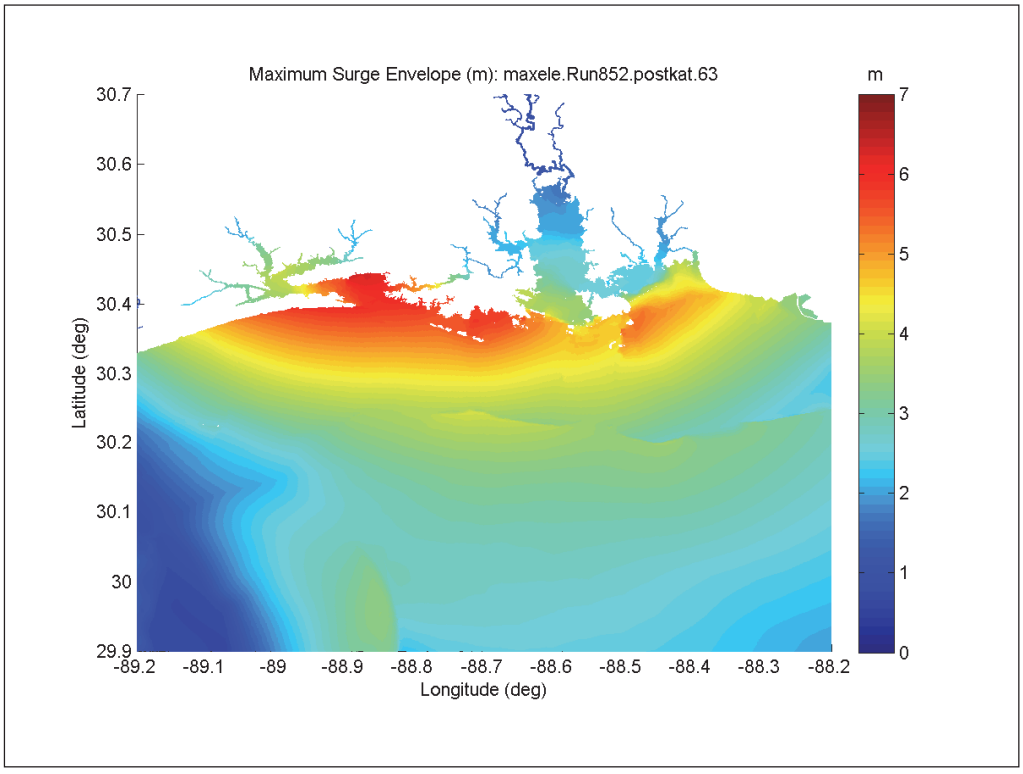

Figure F-58. Maximum surge envelope for Storm 852, Degraded condition.

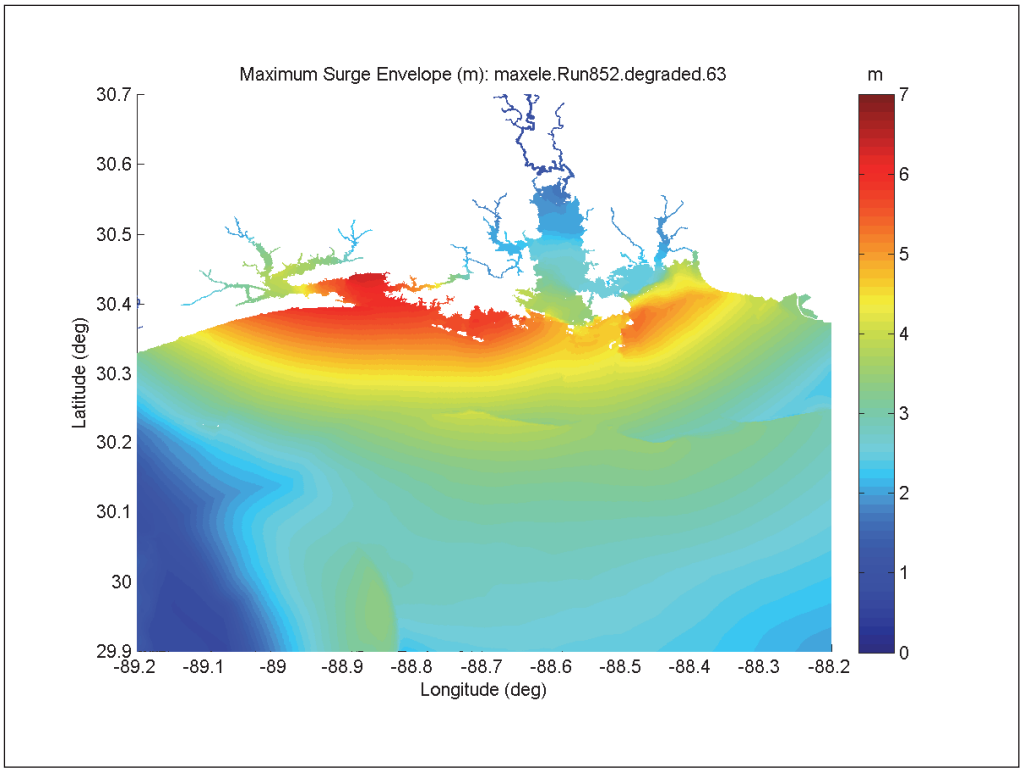

Figure F-59. Maximum surge envelope for Storm 852, Restored condition.

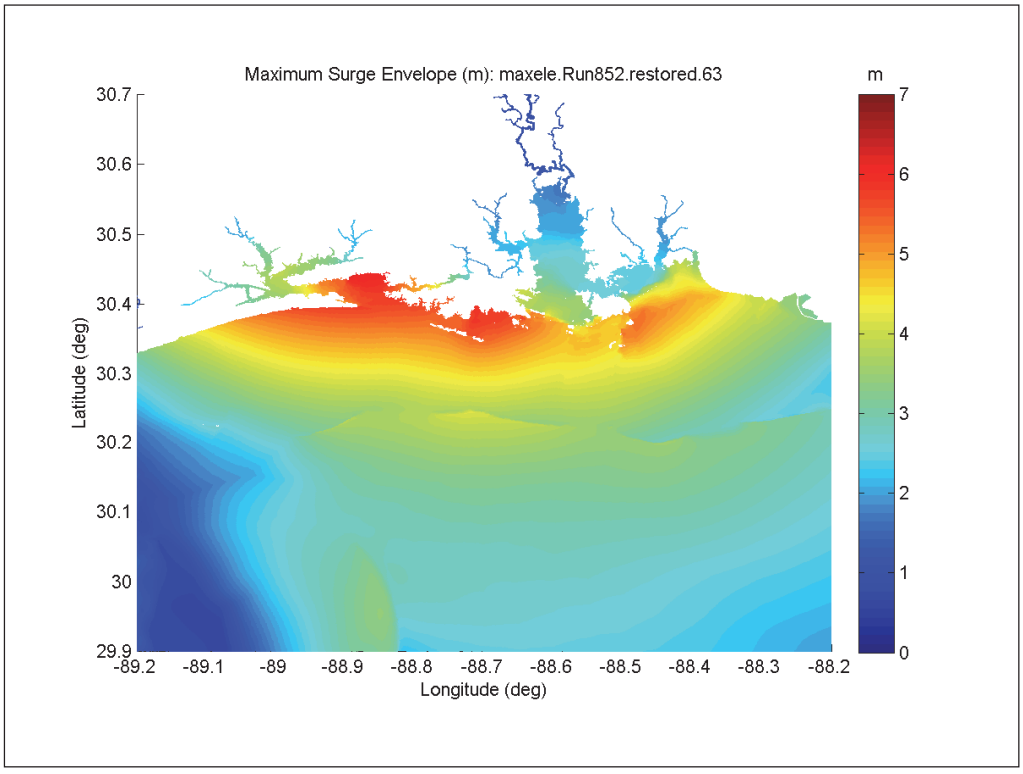

Figure F-60. Maximum surge envelope for Storm 852, Cumulative condition.

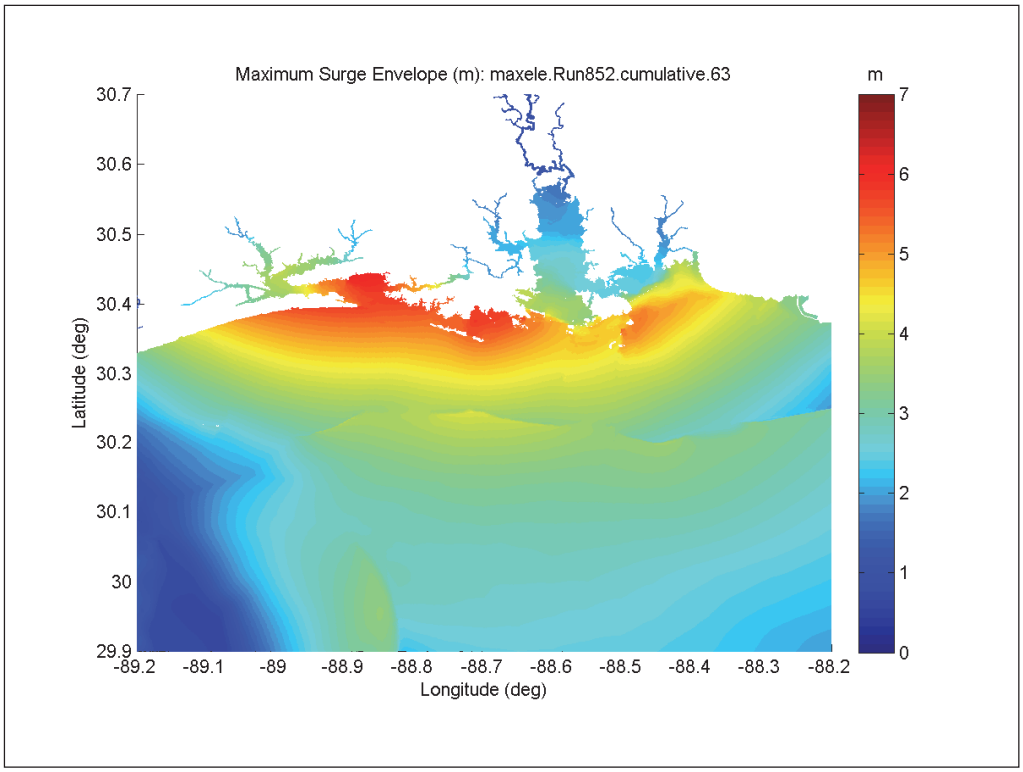

Appendix G: Nearshore Sediment Transport and Bathymetric Change Results for Existing Conditions and Restoration Scenarios

Notes

- There is no fill placement for the existing conditions, but the fill regions are indicated with dashed blue lines to facilitate comparison with the restoration scenarios (Figures G-1, G-8, and G-15 for the Alternative #1 Restoration scenarios and Figures G-43, G-45, and G-47 for the Alternative #2 Restoration).
- The fill regions for the restoration scenarios are indicated with solid blue lines to facilitate comparison (Figures G-2 through G-7, G-9 through G-14, and G-16 through G-21 for the Alternative #1 Restoration scenarios and Figures G-44, G-46, and G-48 for the Alternative #2 Restoration).
- The post-storm island footprint (NAVD = 0 m) contour is depicted as a black outline for reference for the existing conditions and the Alternative #1 Restoration scenarios (Figures G-22 through G-41), as well as the Alternative #2 Restoration (Figures G-49 through G-51).

Figure G-1. Existing conditions for Storm #1.

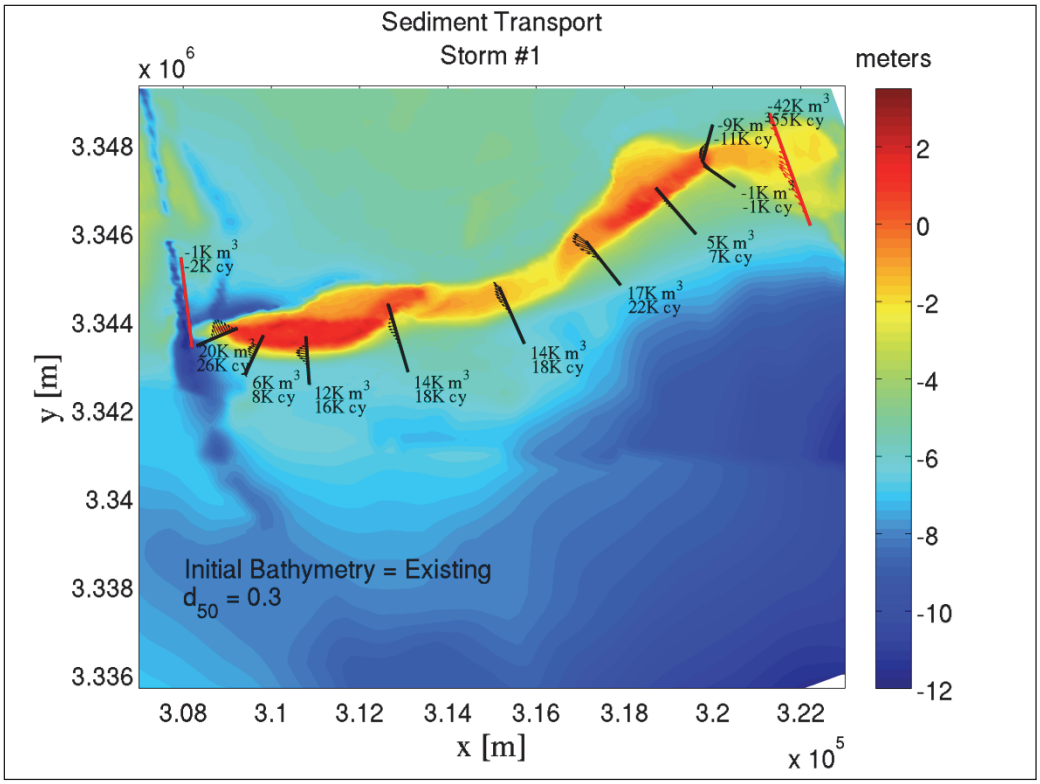

Figure G-2. Alternative #1 Restored conditions for Storm #1; Template A; With borrow pits.

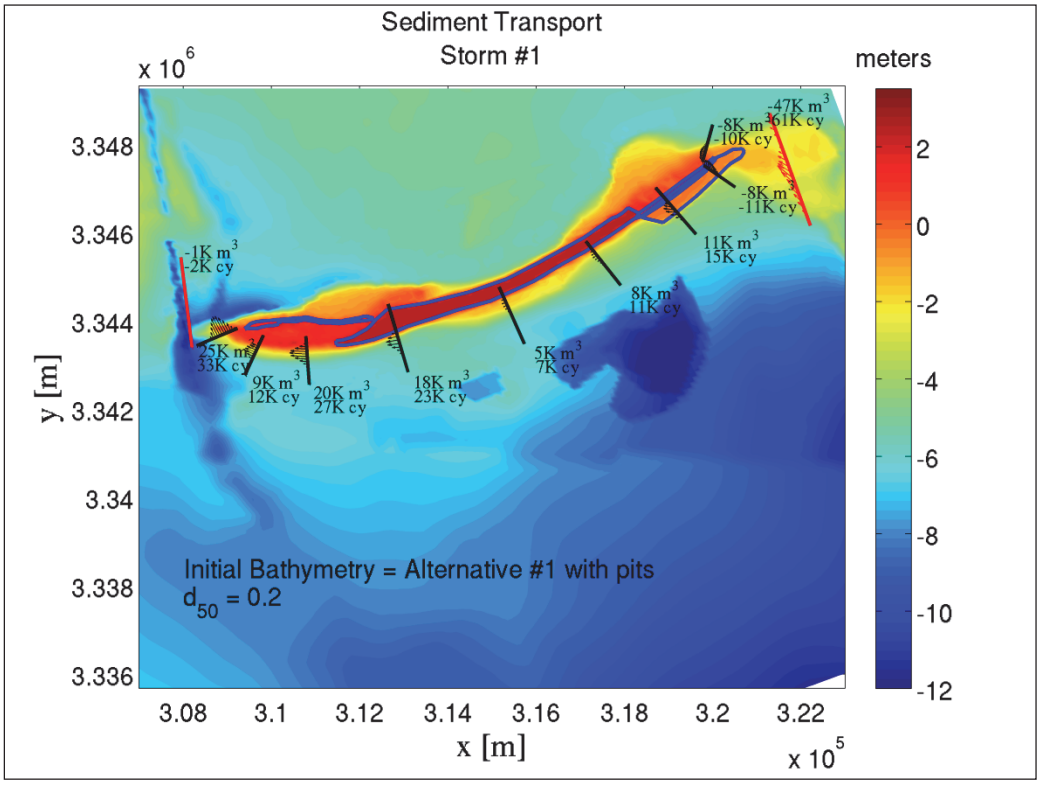

Figure G-3. Alternative #1 Restored conditions for Storm #1; Template B; With borrow pits.

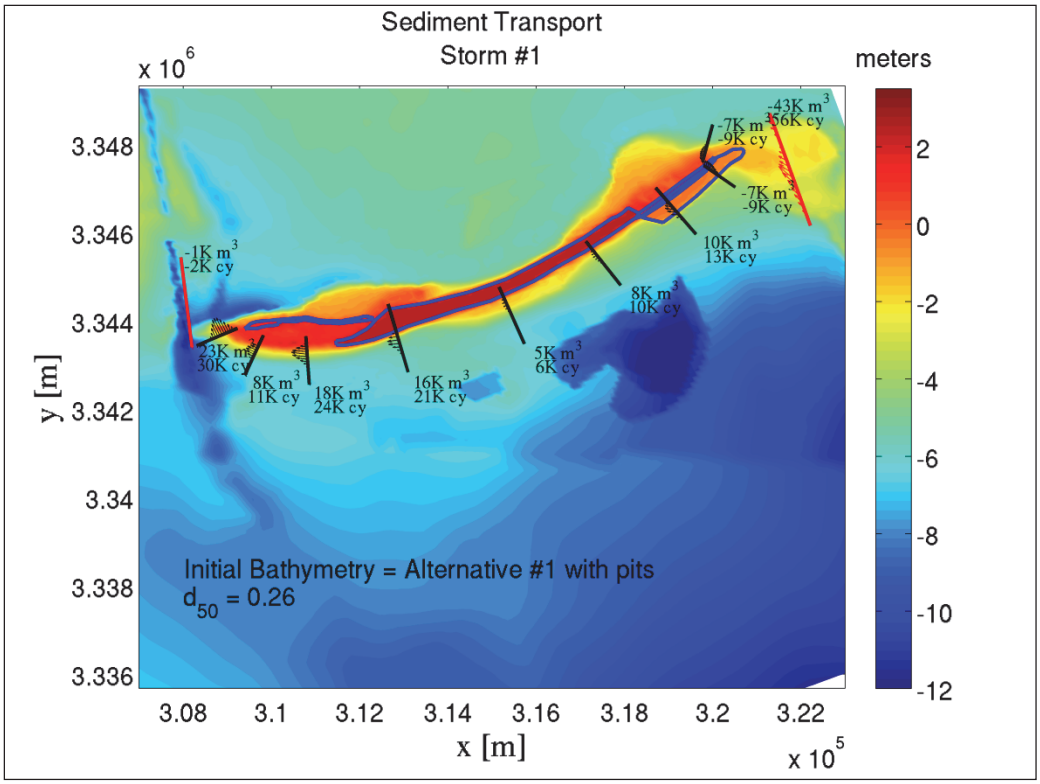

Figure G-4. Alternative #1 Restored conditions for Storm #1; Template C; With borrow pits.

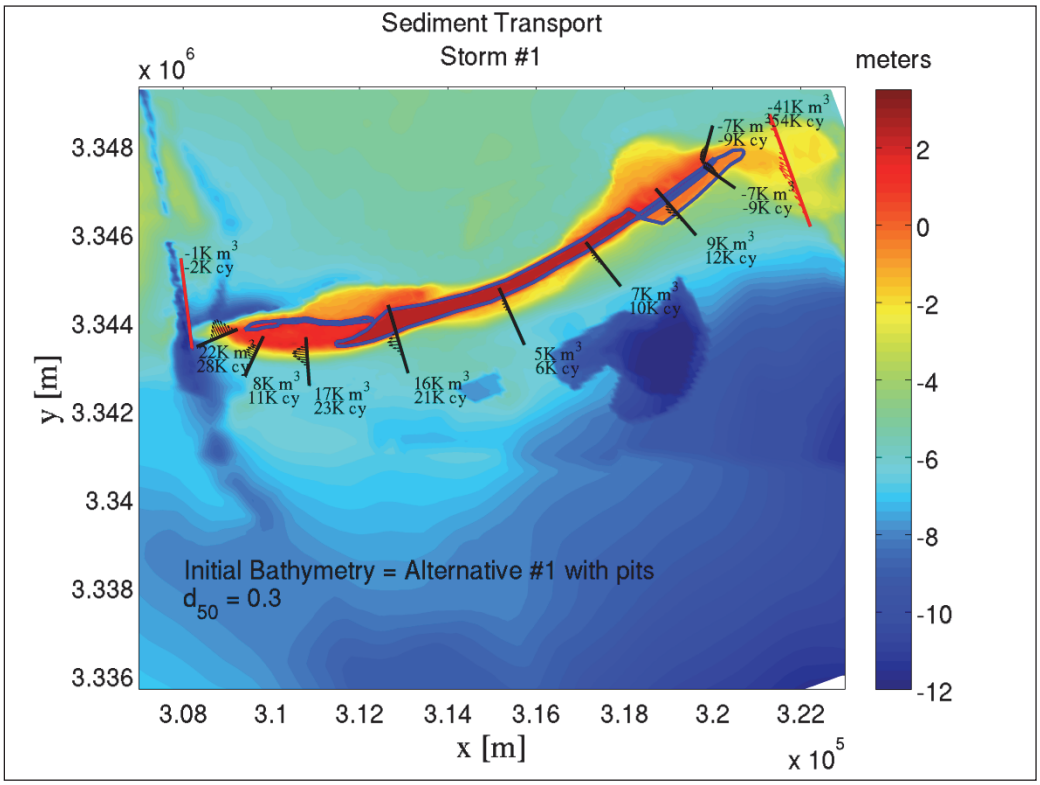

Figure G-5. Alternative #1 Restored conditions for Storm #1; Template A; Without borrow pits.

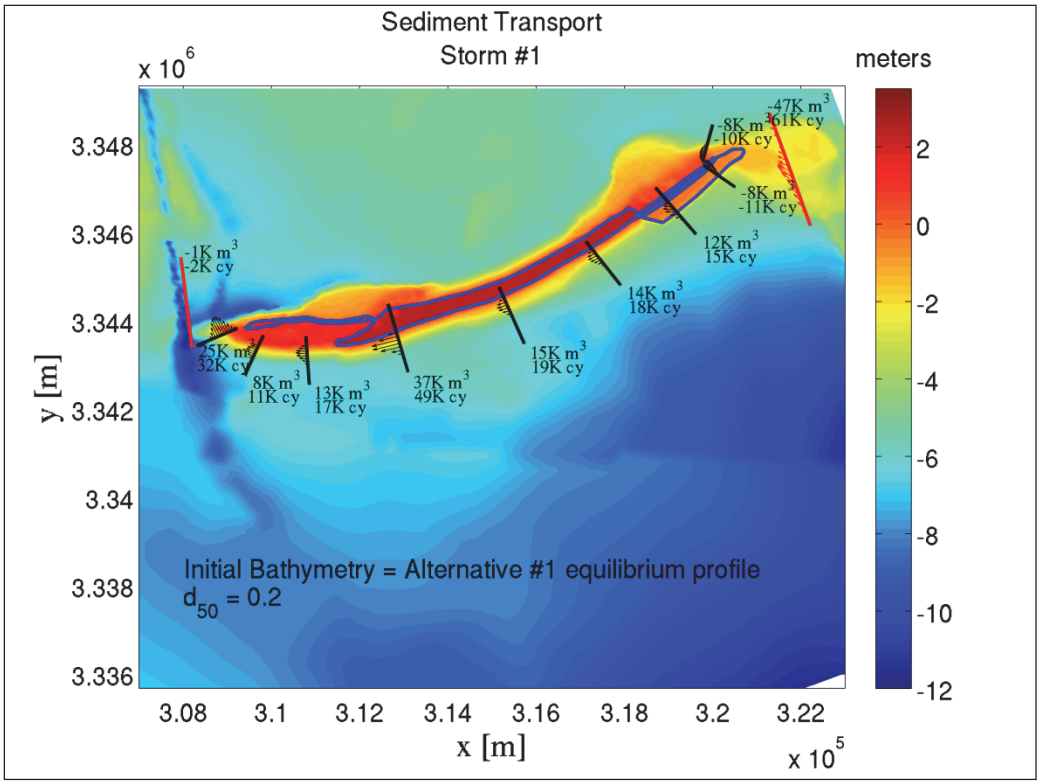

Figure G-6. Alternative #1 Restored conditions for Storm #1; Template B; Without borrow pits.

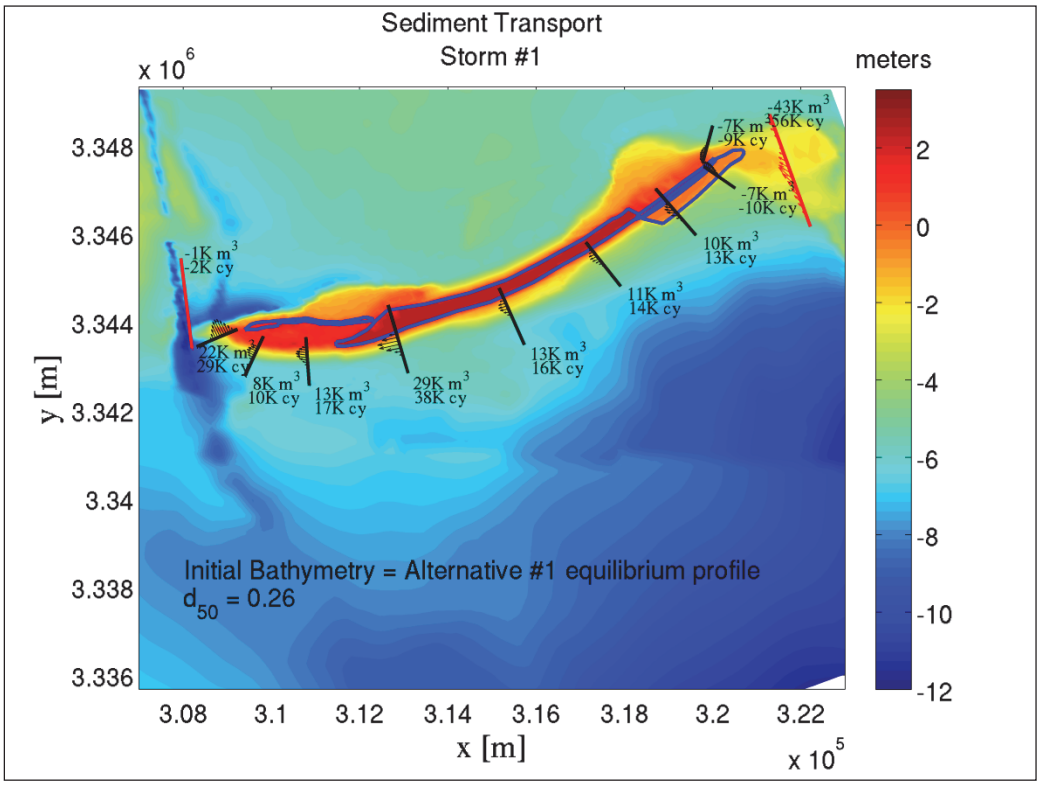

Figure G-7. Alternative #1 Restored conditions for Storm #1; Template C; Without borrow pits.

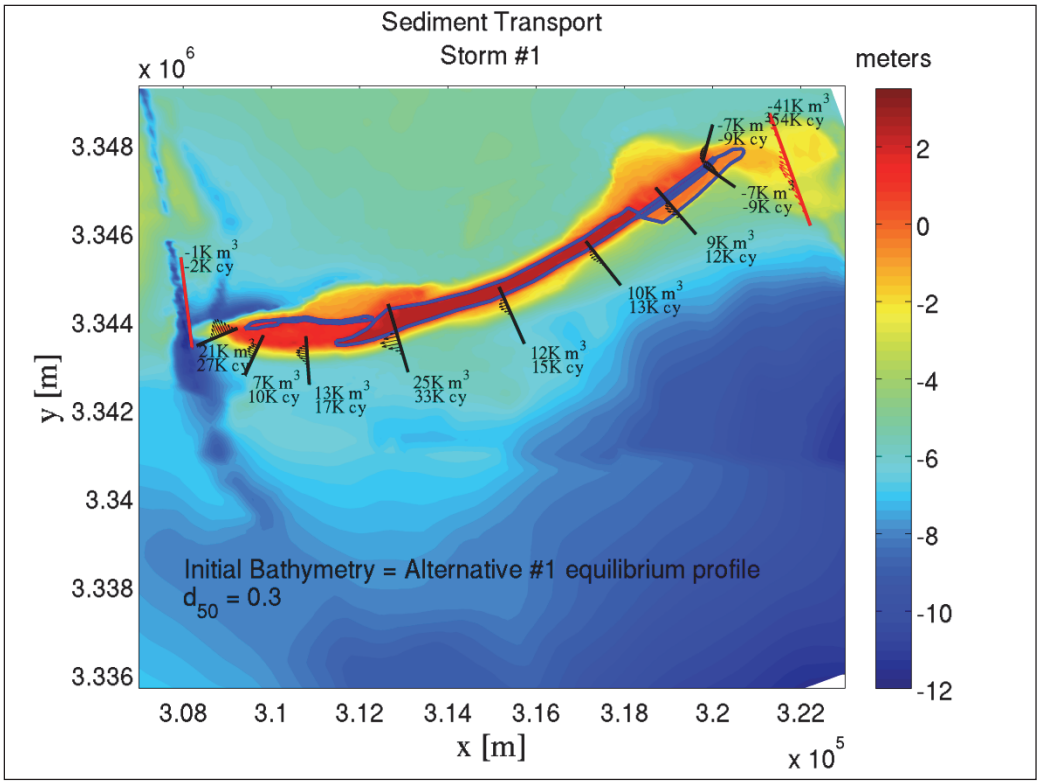

Figure G-8. Existing conditions for Storm #2.

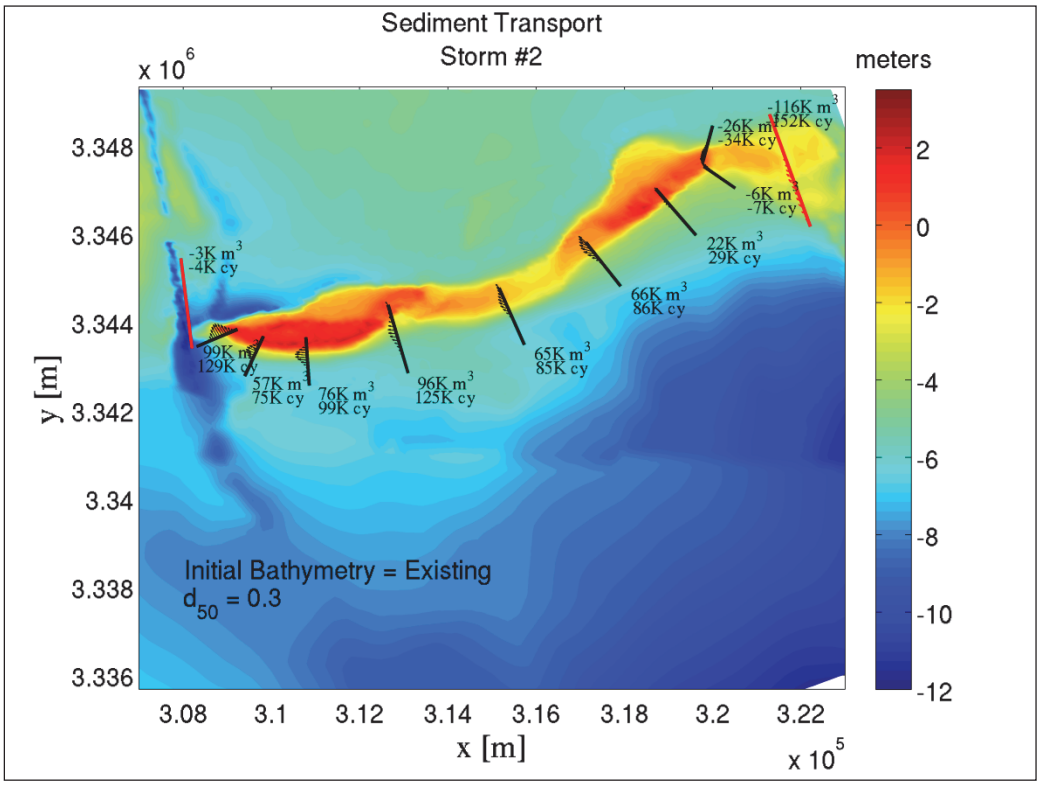

Figure G-9. Alternative #1 Restored conditions for Storm #2; Template A; With borrow pits.

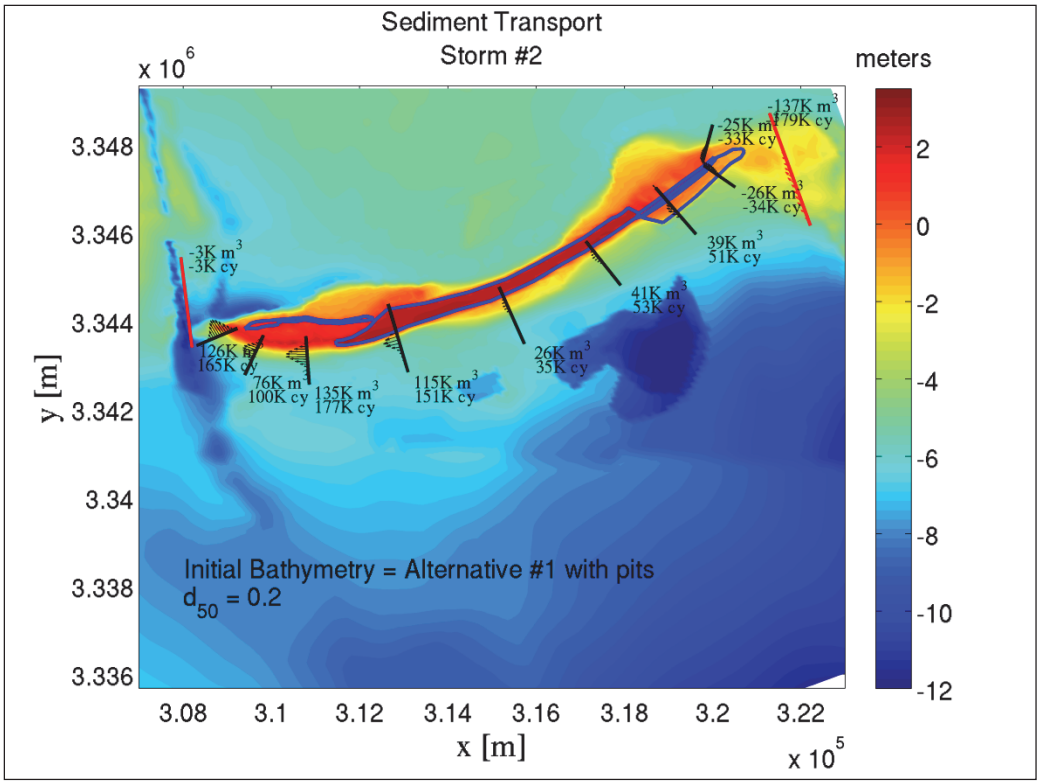

Figure G-10. Alternative #1 Restored conditions for Storm #2; Template B; With borrow pits.

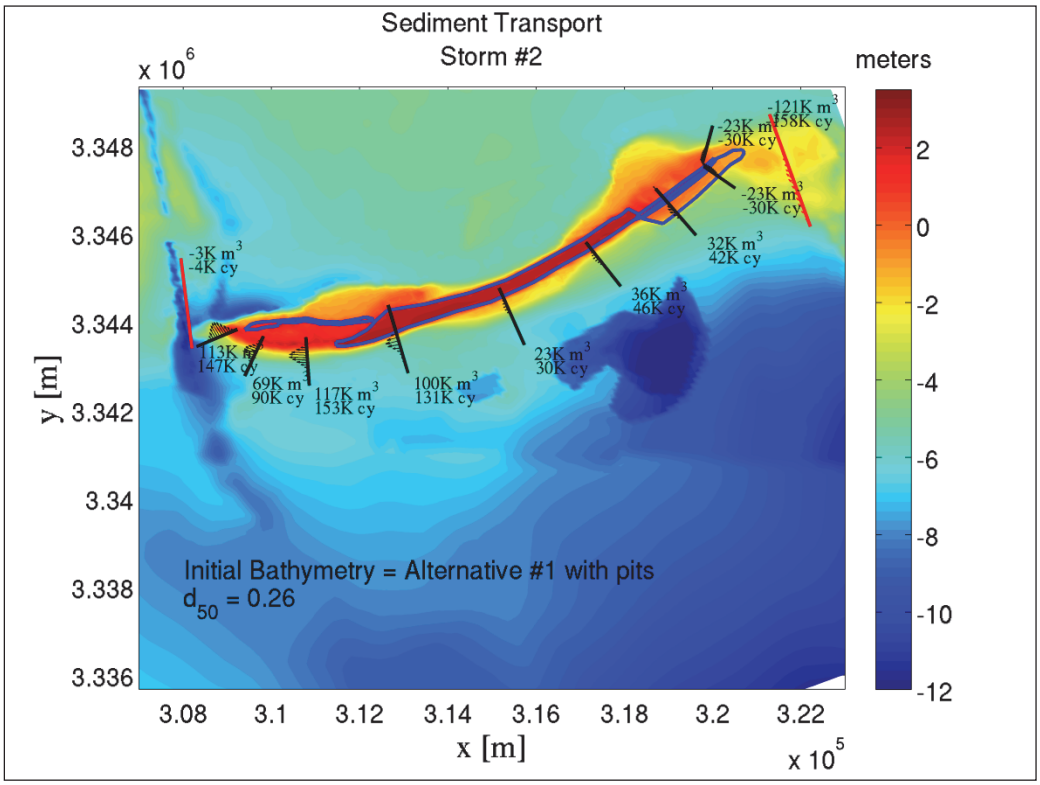

Figure G-11. Alternative #1 Restored conditions for Storm #2; Template C; With borrow pits.

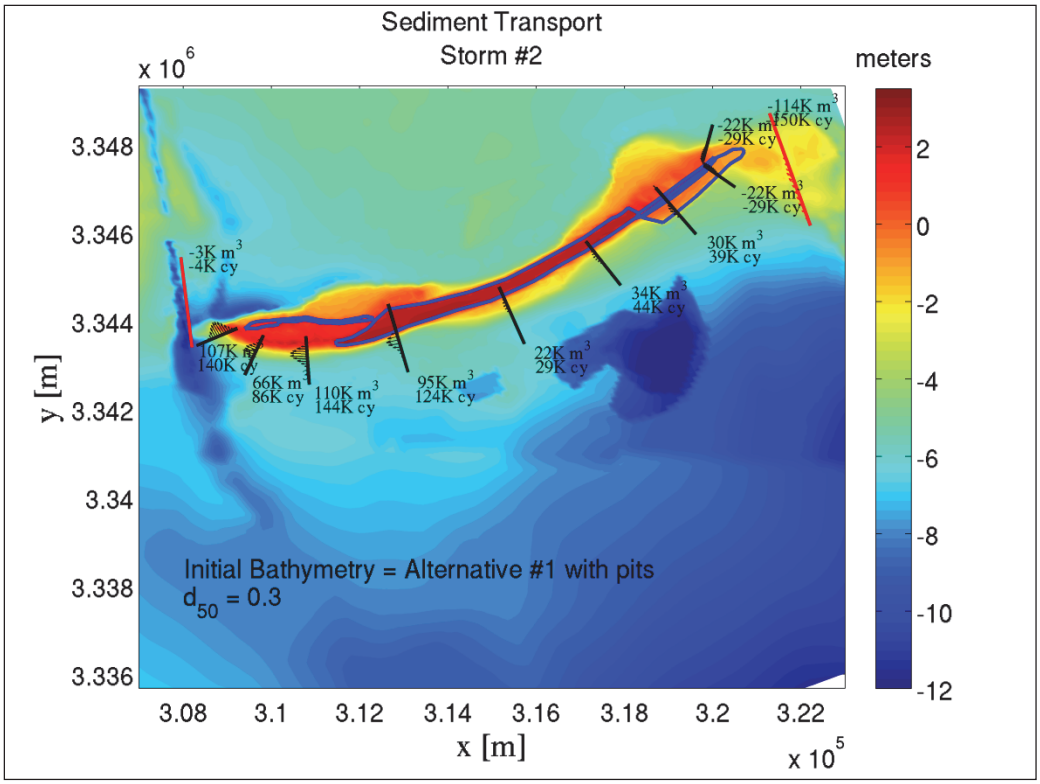

Figure G-12. Alternative #1 Restored conditions for Storm #2; Template A; Without borrow pits.

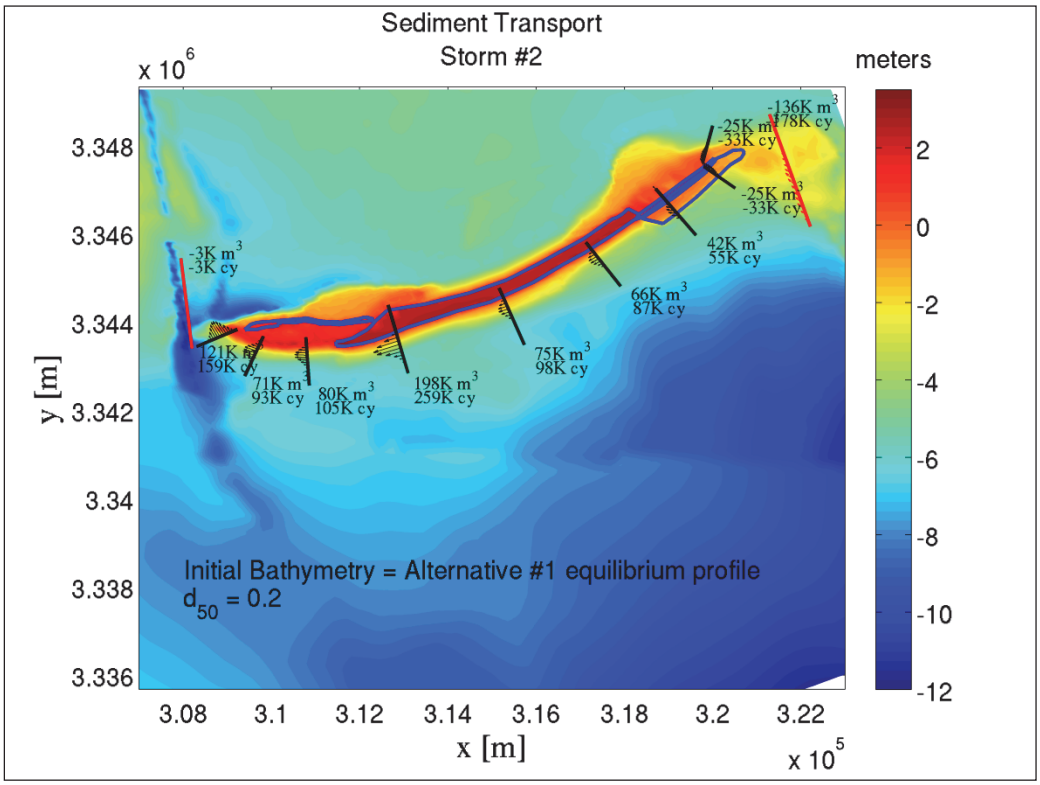

Figure G-13. Alternative #1 Restored conditions for Storm #2; Template B; Without borrow pits.

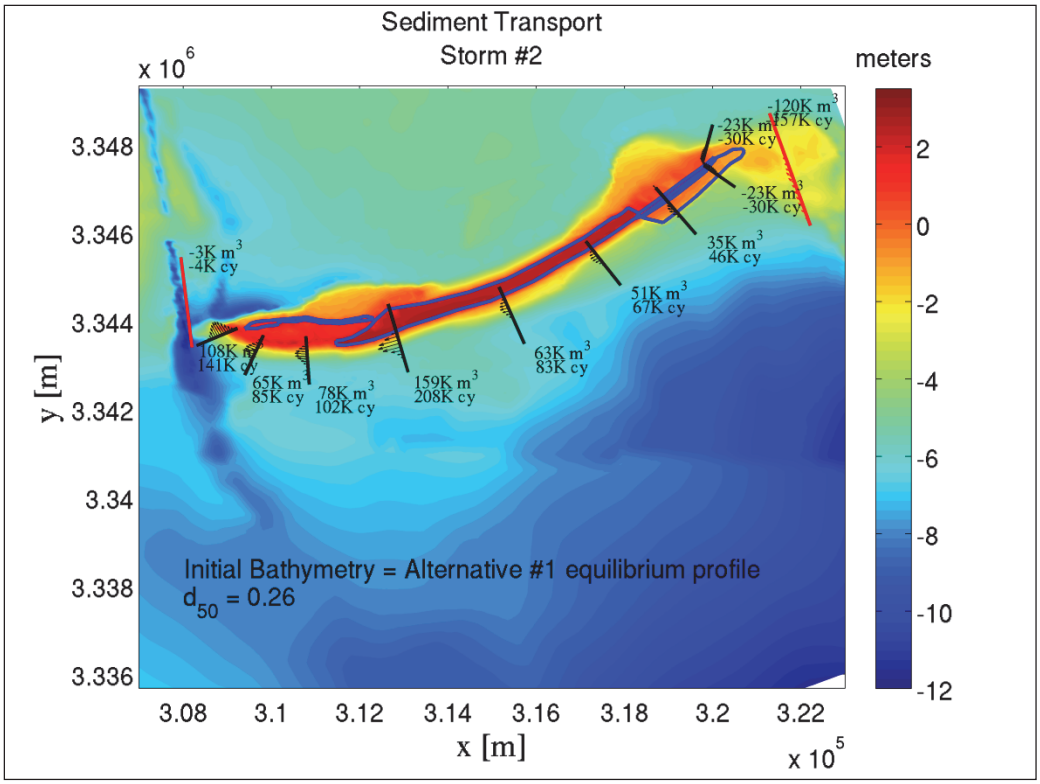

Figure G-14. Alternative #1 Restored conditions for Storm #2; Template C; Without borrow pits.

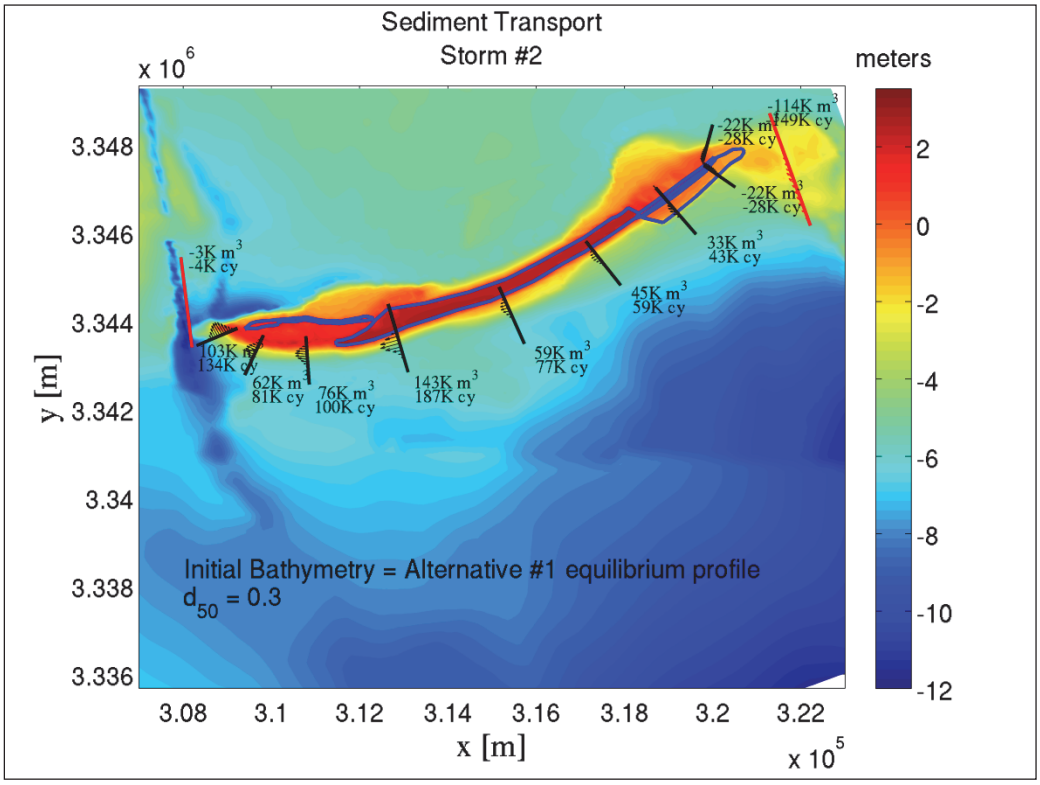

Figure G-15. Existing conditions for Storm #3.

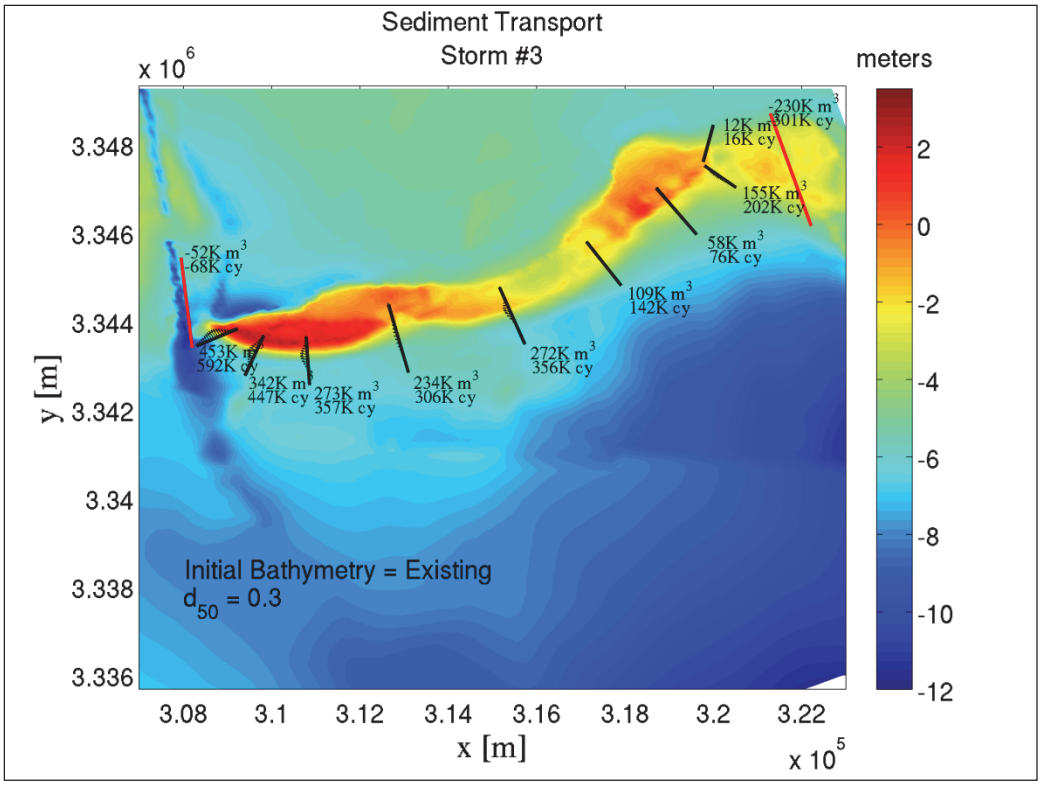

Figure G-16. Alternative #1 Restored conditions for Storm #3; Template A; With borrow pits.

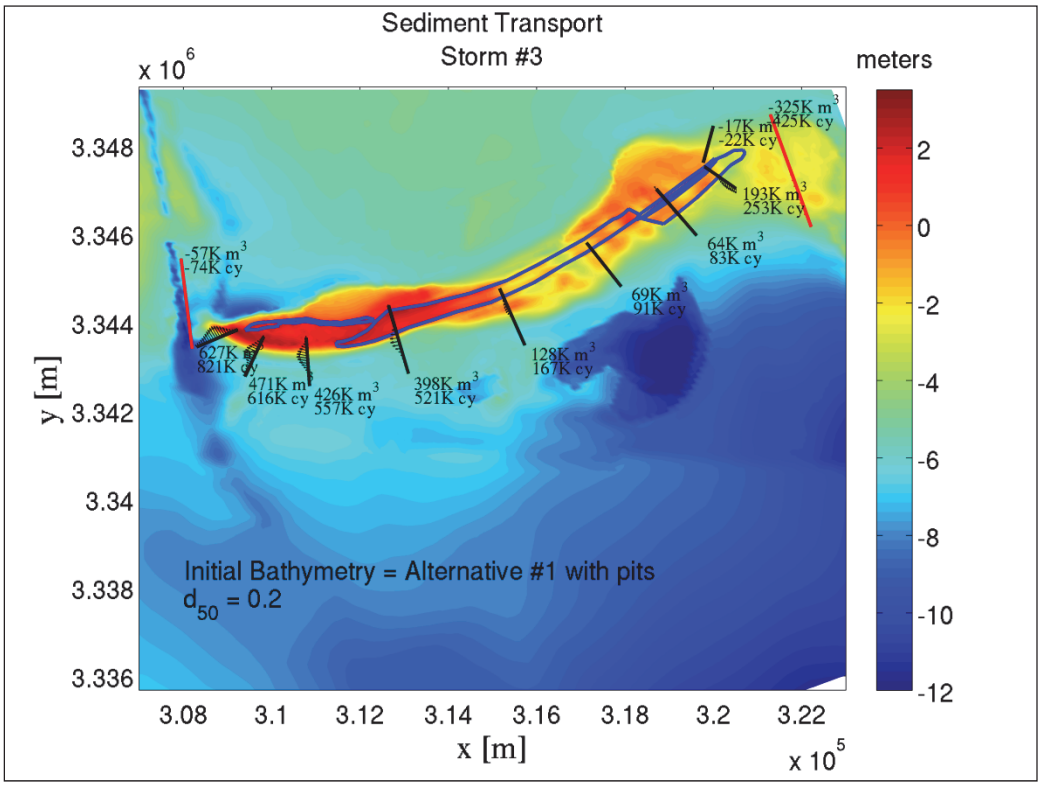

Figure G-17. Alternative #1 Restored conditions for Storm #3; Template B; With borrow pits.

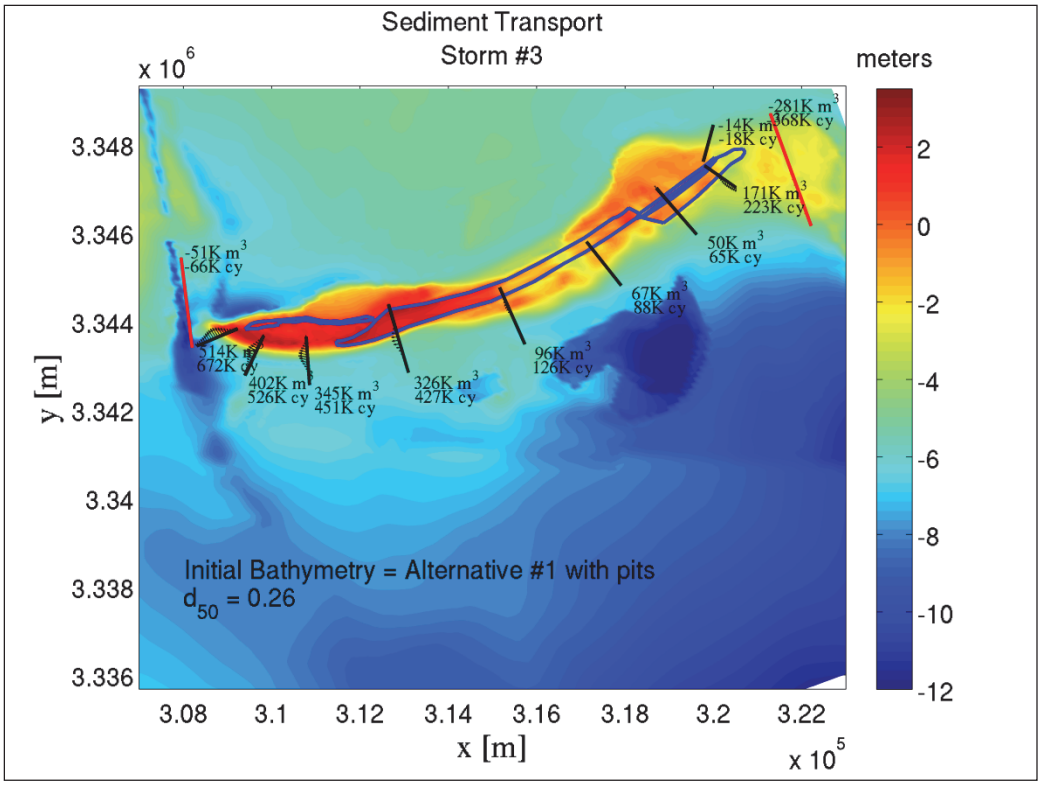

Figure G-18. Alternative #1 Restored conditions for Storm #3; Template C; With borrow pits.

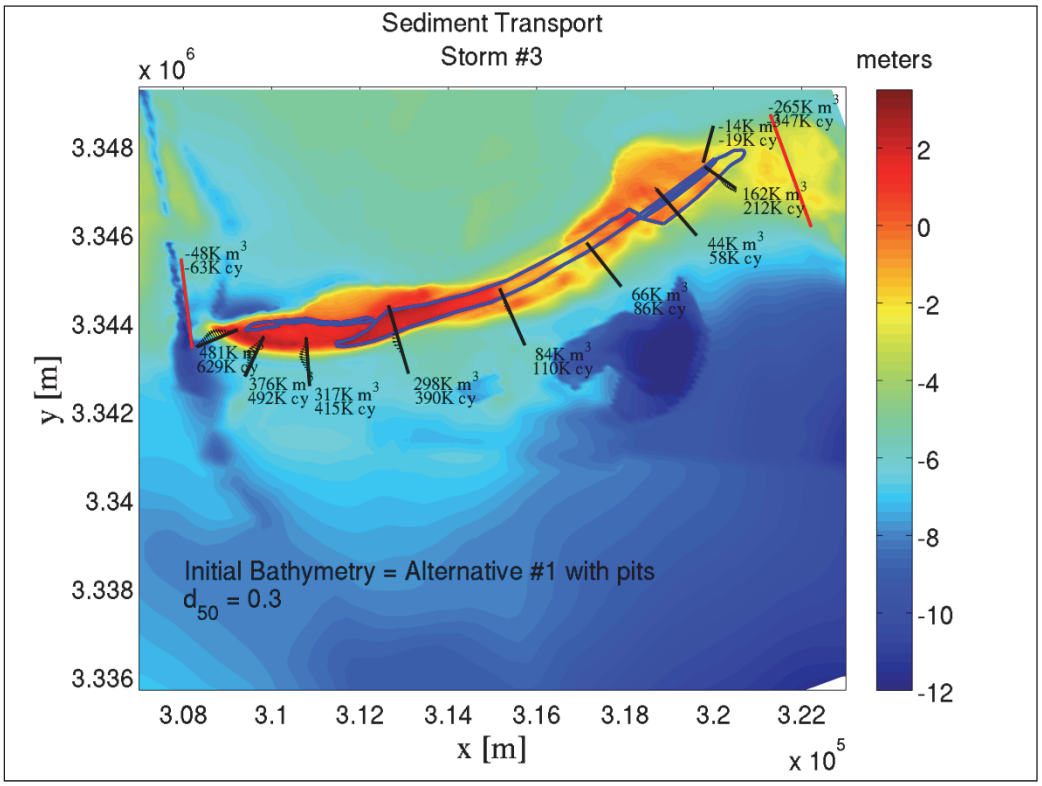

Figure G-19. Alternative #1 Restored conditions for Storm #3; Template A; Without borrow pits.

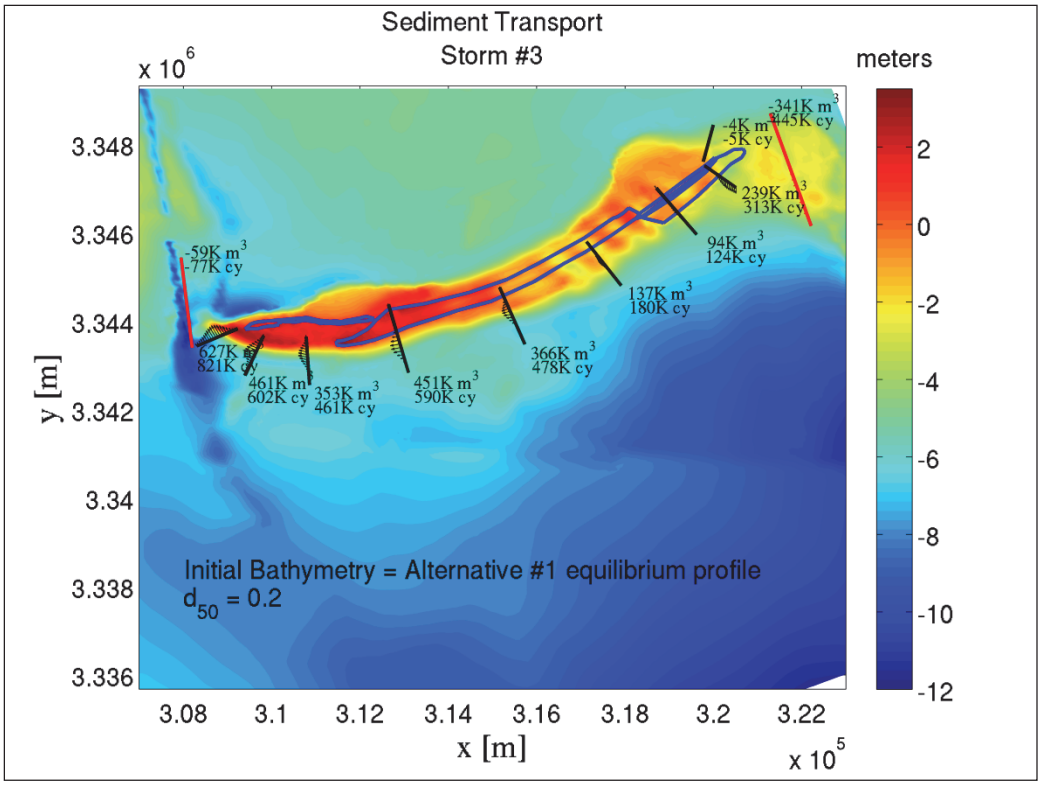

Figure G-20. Alternative #1 Restored conditions for Storm #3; Template B; Without borrow pits.

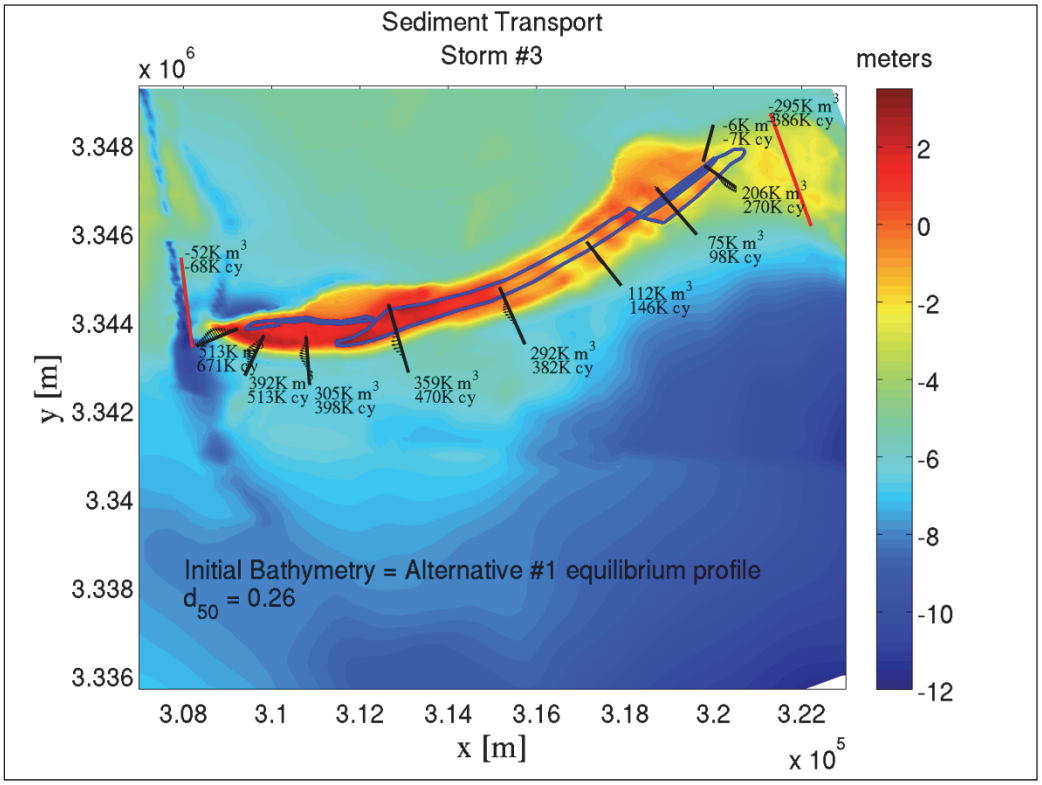

Figure G-21. Alternative #1 Restored conditions for Storm #3; Template C; Without borrow pits.

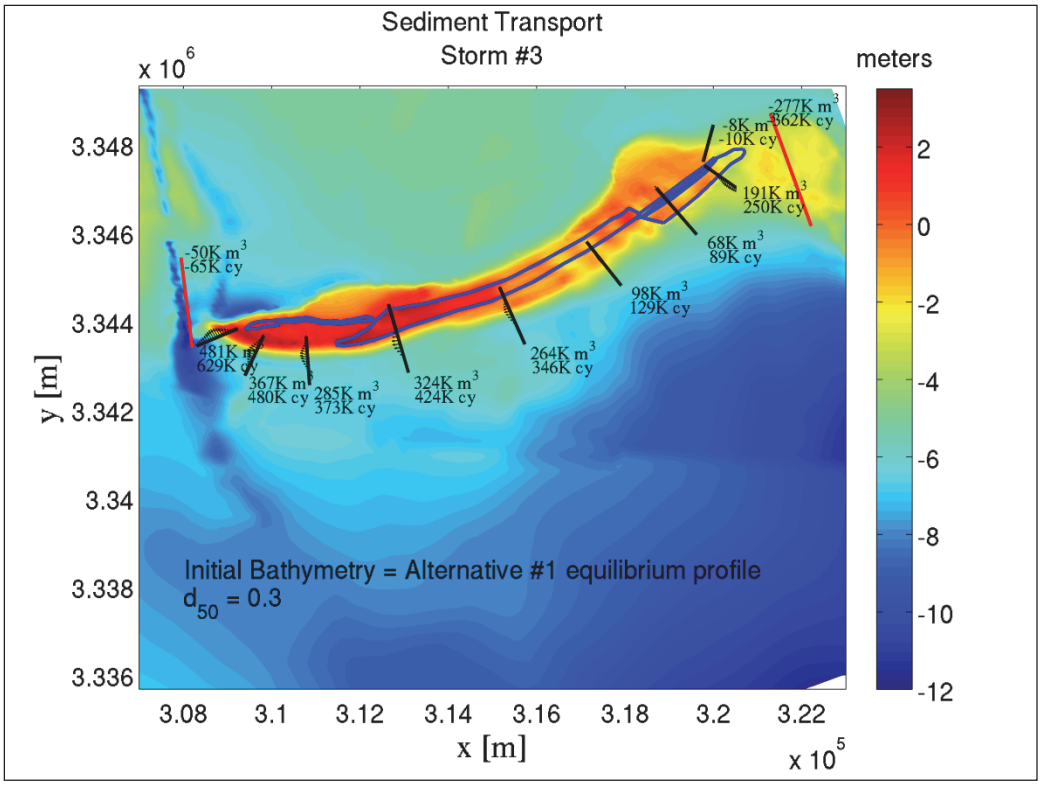

Figure G-22. Existing conditions for Storm #1.

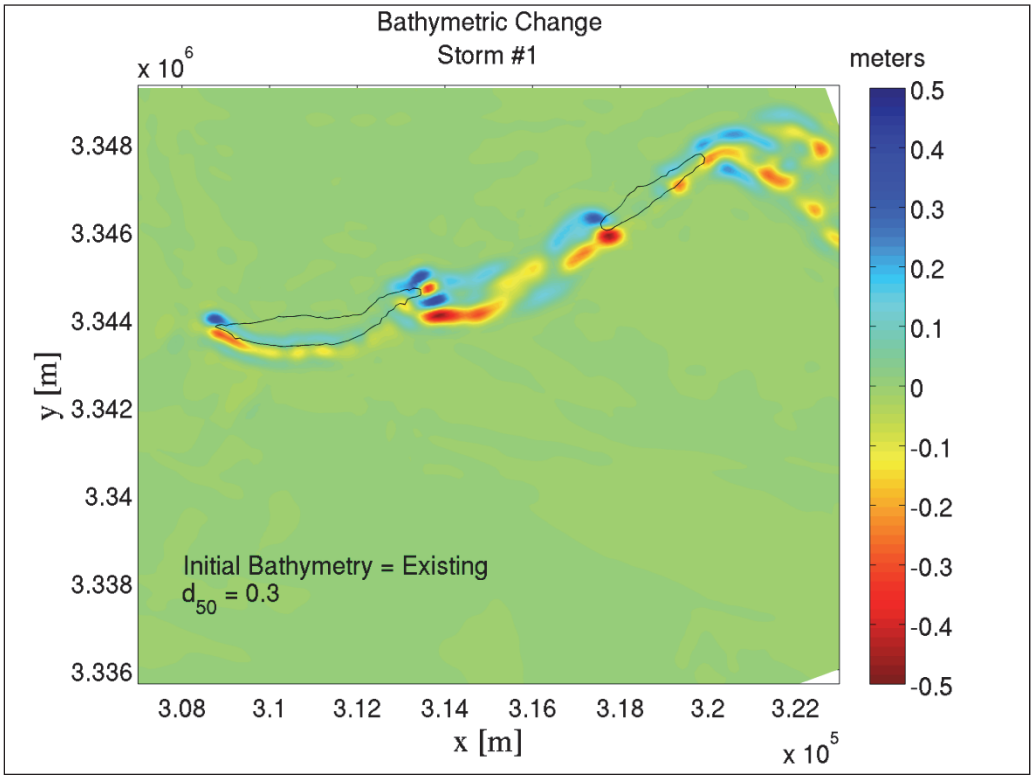

Figure G-23. Alternative #1 Restored conditions for Storm #1; Template A; With borrow pits.

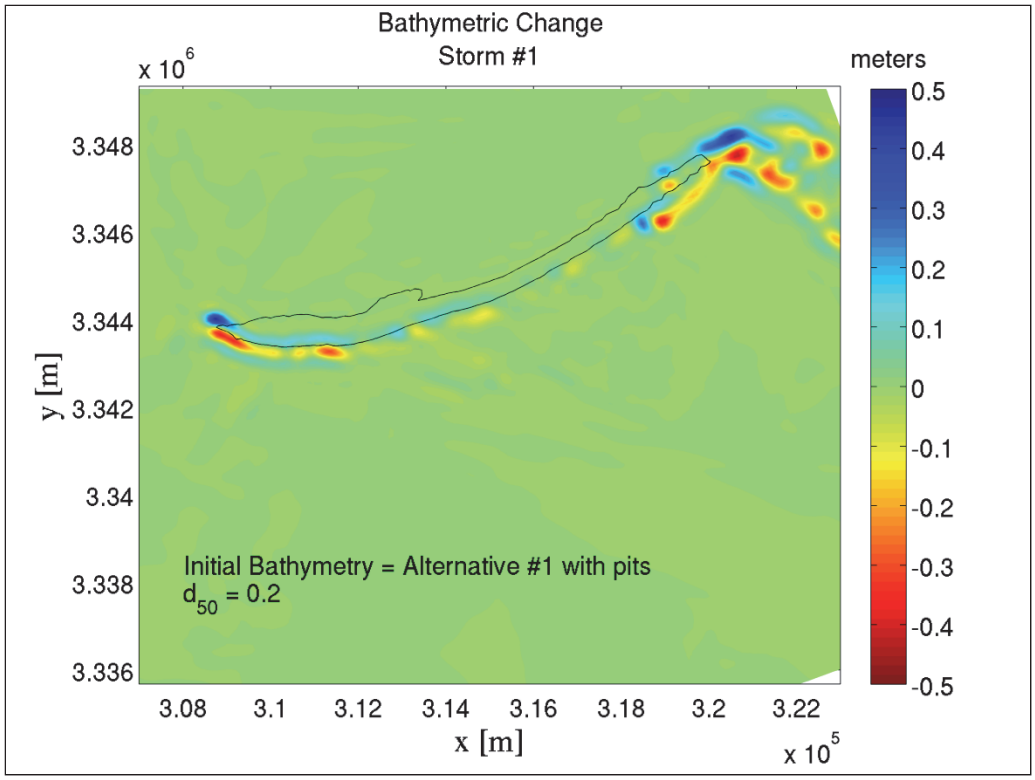

Figure G-24. Alternative #1 Restored conditions for Storm #1; Template B; With borrow pits.

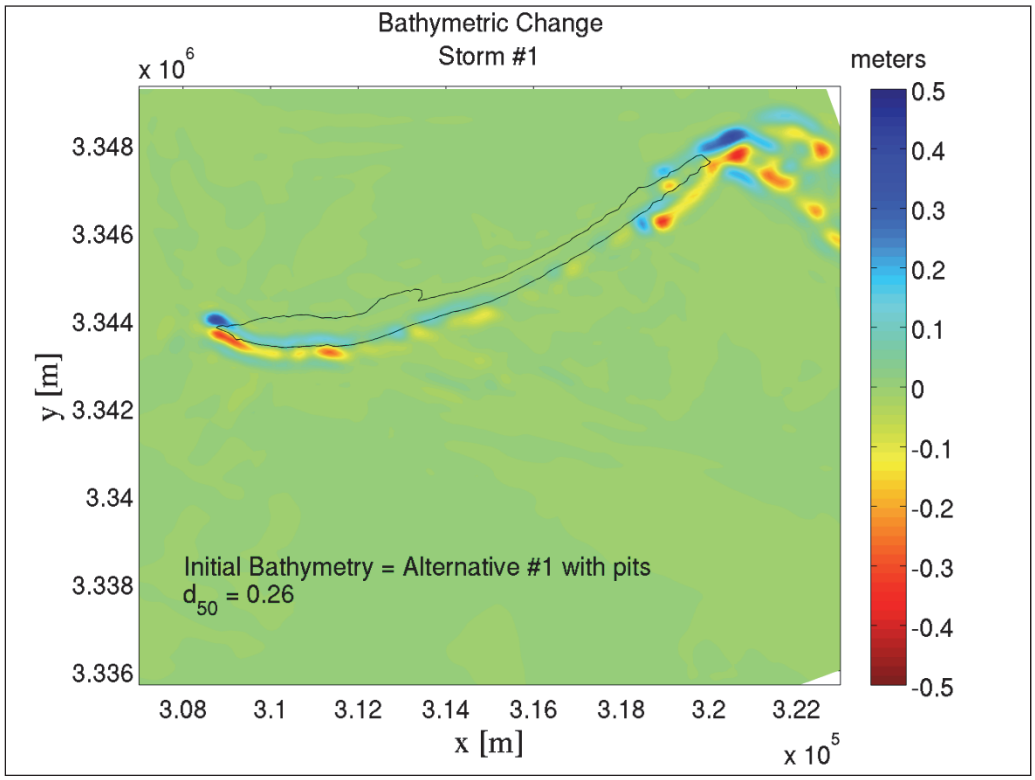

Figure G-25. Alternative #1 Restored conditions for Storm #1; Template C; With borrow pits.

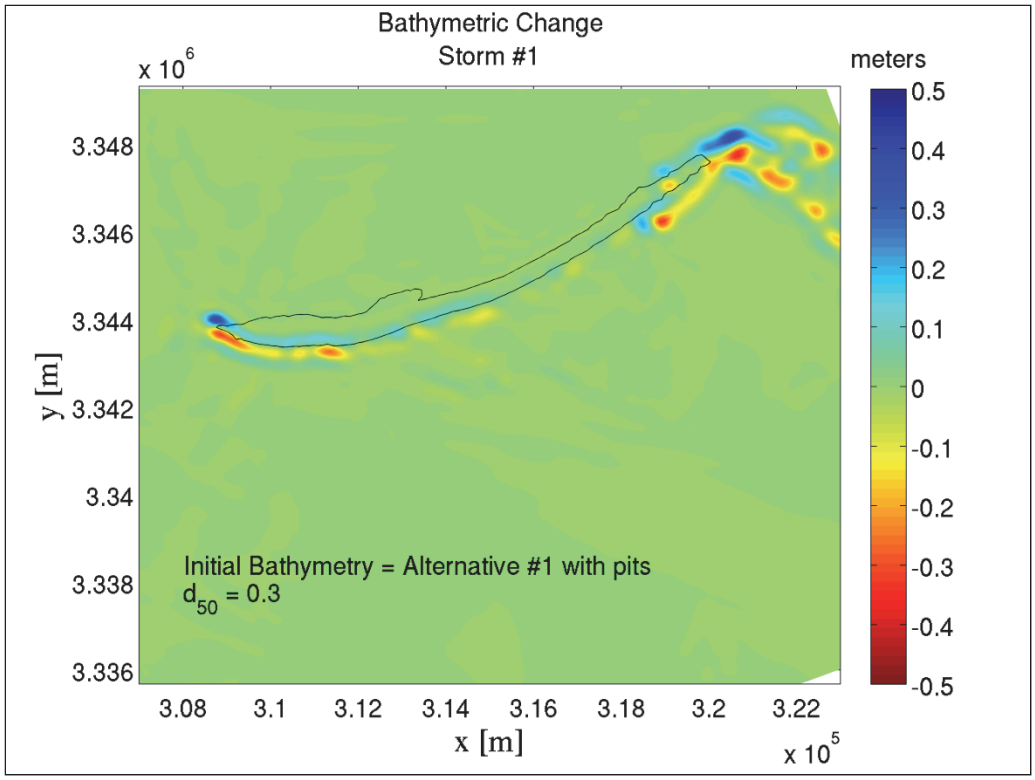

Figure G-26. Alternative #1 Restored conditions for Storm #1; Template A; Without borrow pits.

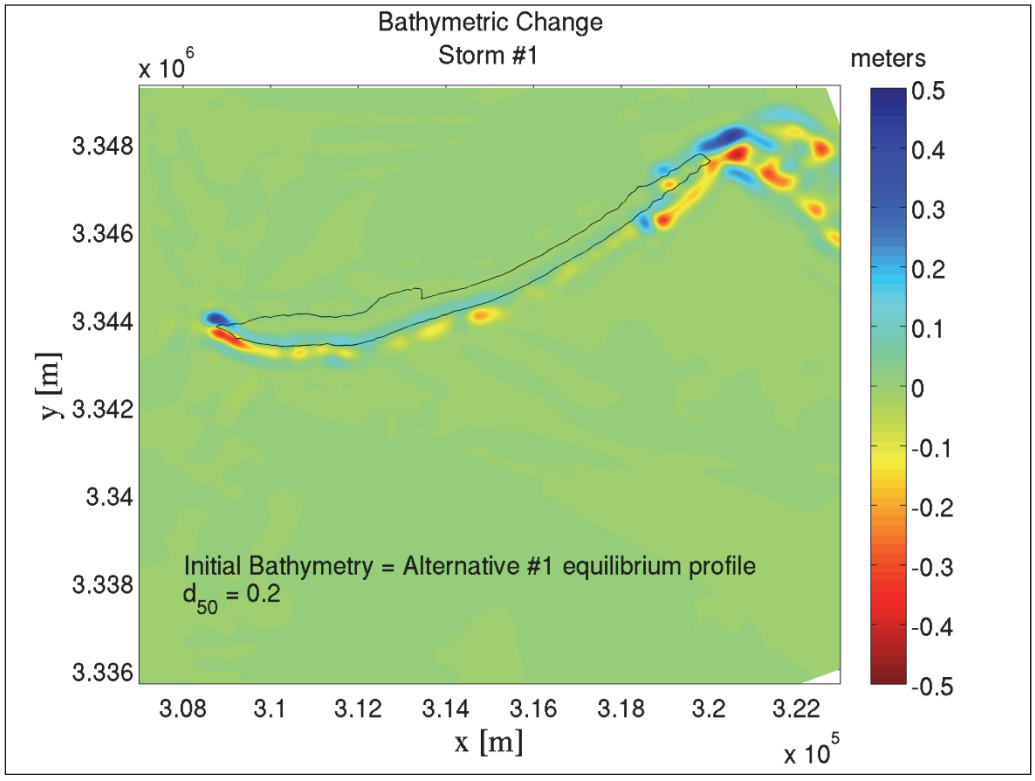

Figure G-27. Alternative #1 Restored conditions for Storm #1; Template B; Without borrow pits.

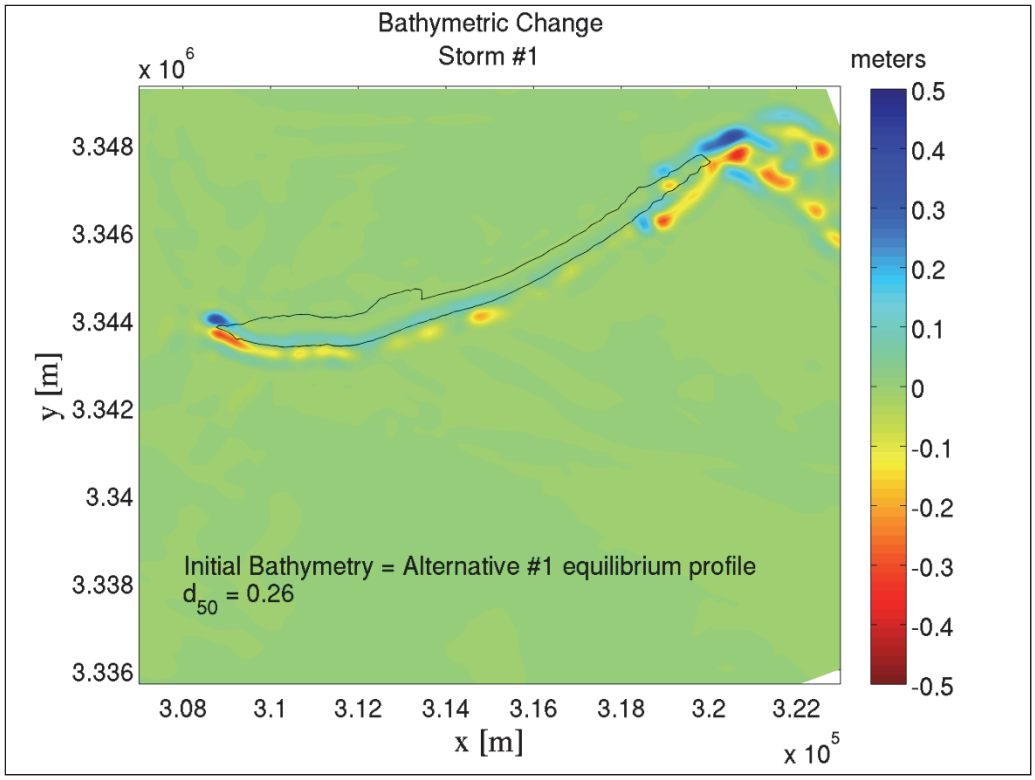

Figure G-28. Alternative #1 Restored conditions for Storm #1; Template C; Without borrow pits.

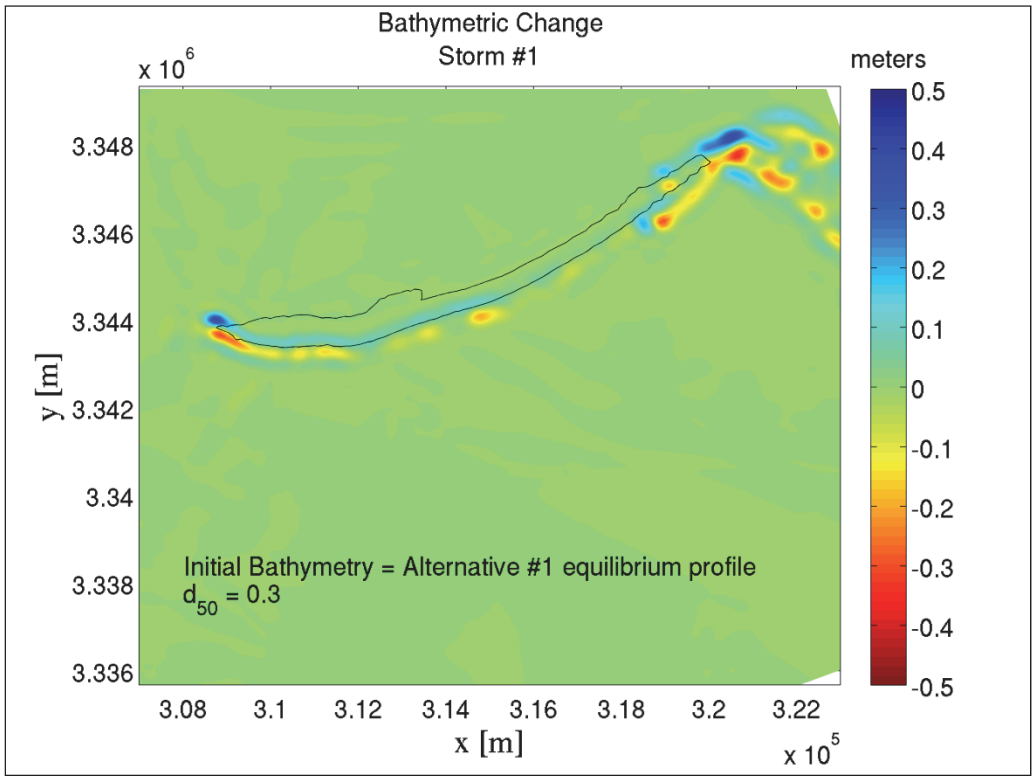

Figure G-29. Existing conditions for Storm #2.

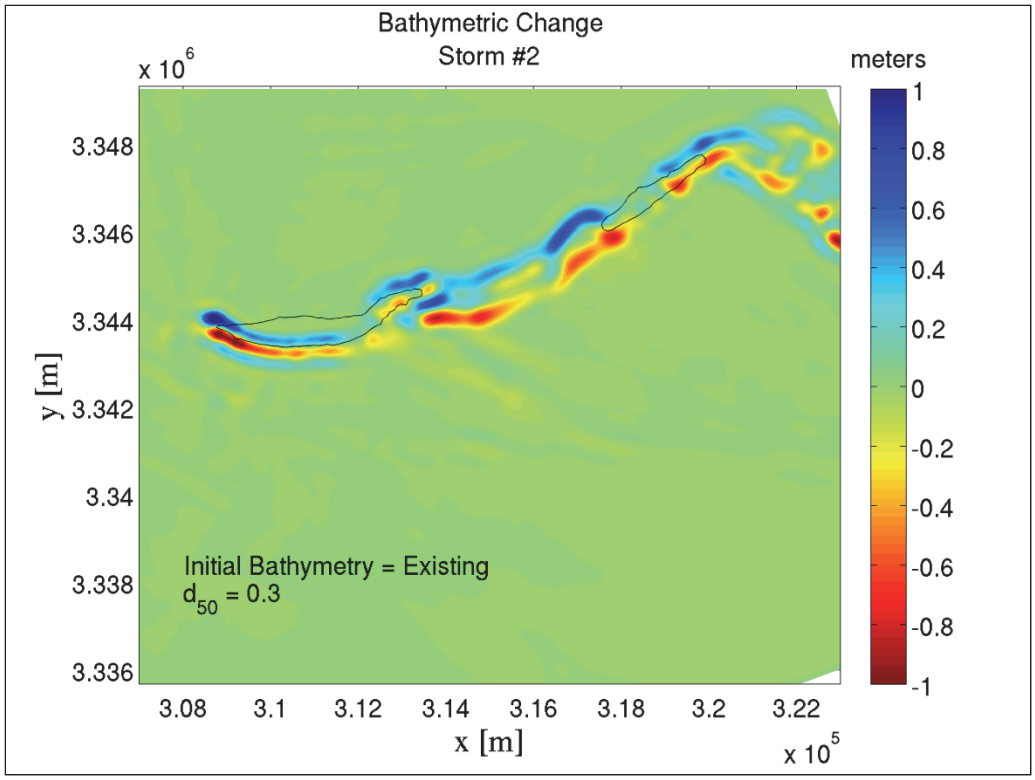

Figure G-30. Alternative #1 Restored conditions for Storm #2; Template A; With borrow pits.

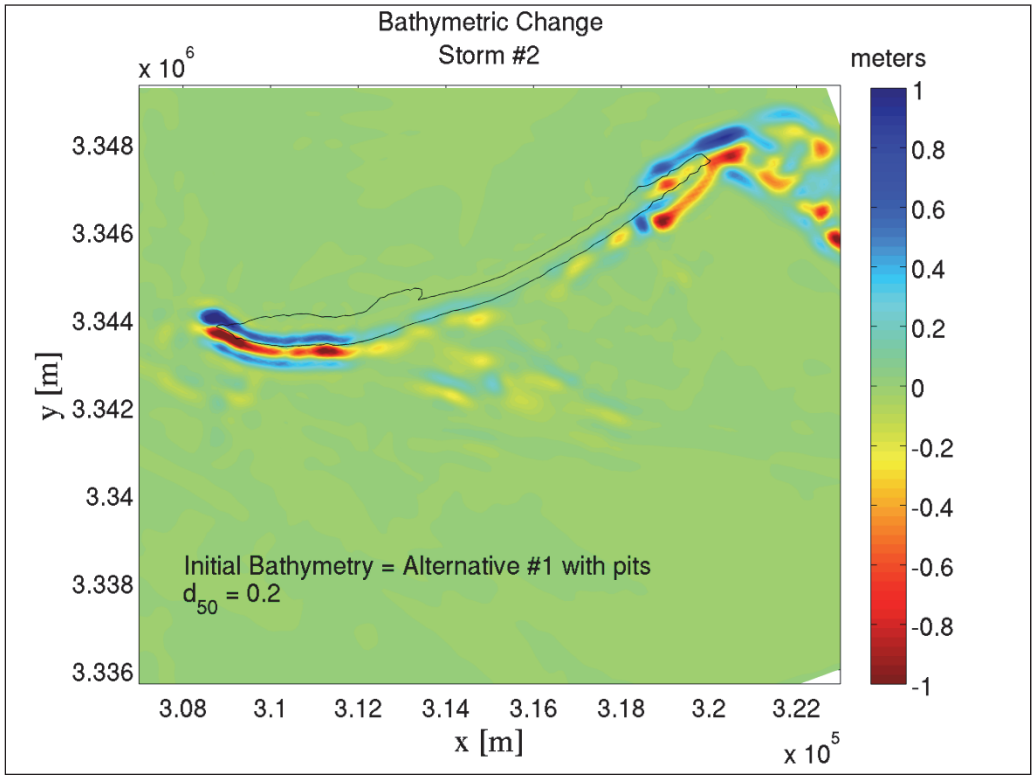

Figure G-31. Alternative #1 Restored conditions for Storm #2; Template B; With borrow pits.

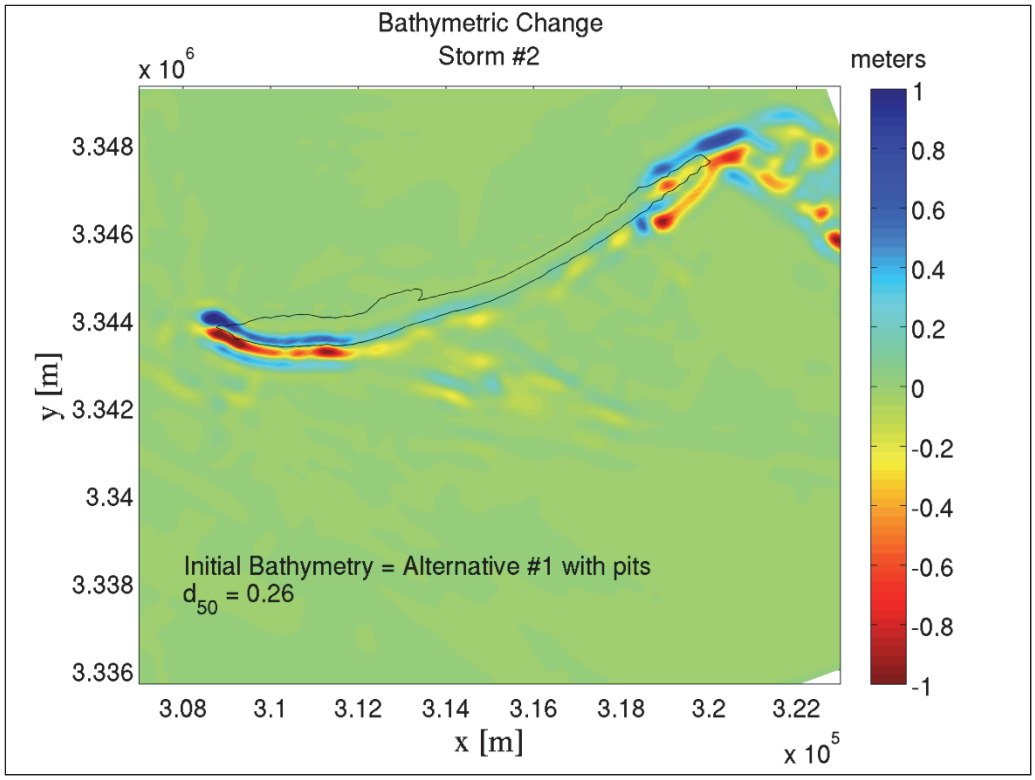

Figure G-32. Alternative #1 Restored conditions for Storm #2; Template C; With borrow pits.

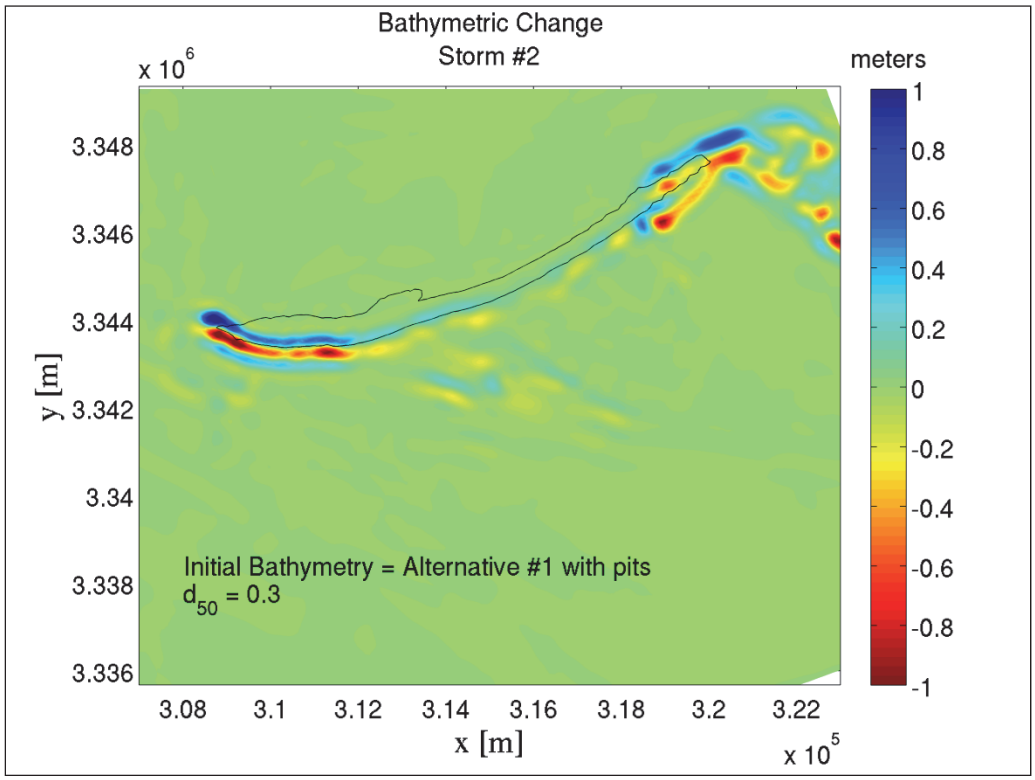

Figure G-33. Alternative #1 Restored conditions for Storm #2; Template A; Without borrow pits.

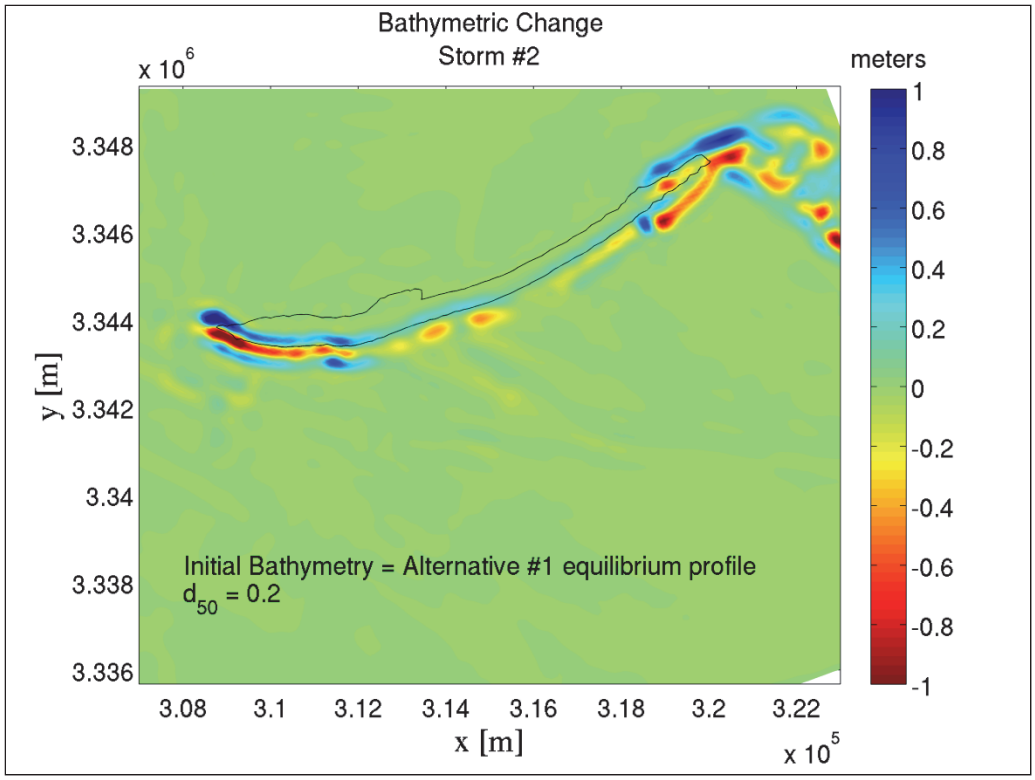

Figure G-34. Alternative #1 Restored conditions for Storm #2; Template B; Without borrow pits.

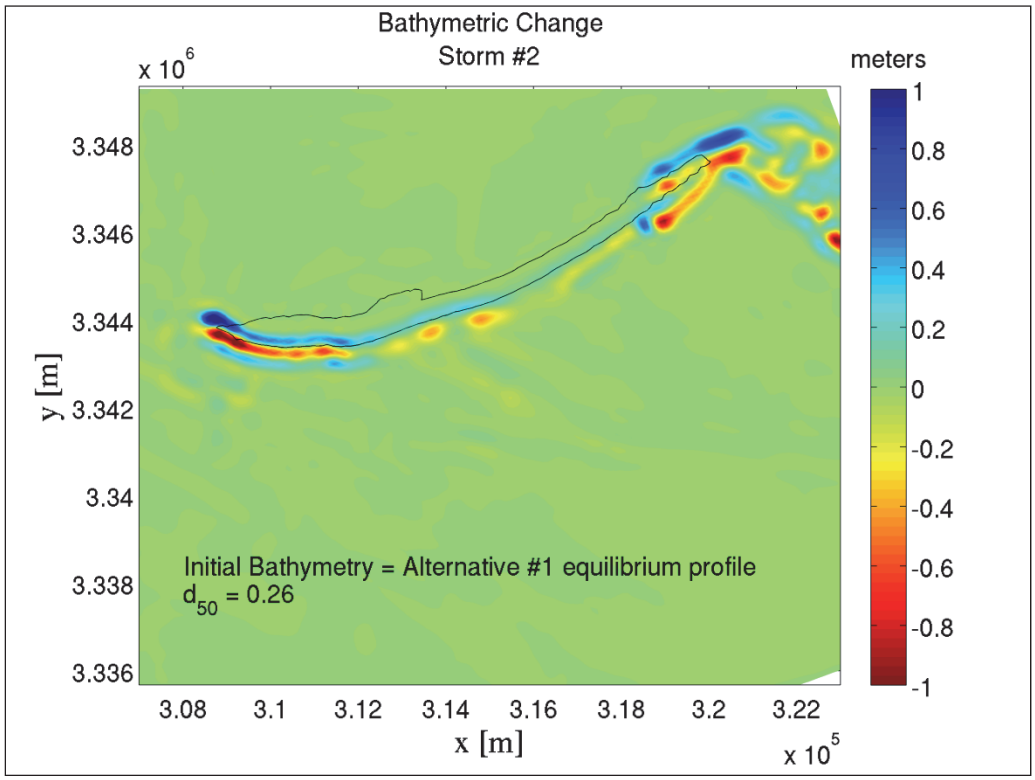

Figure G-35. Alternative #1 Restored conditions for Storm #2; Template C; Without borrow pits.

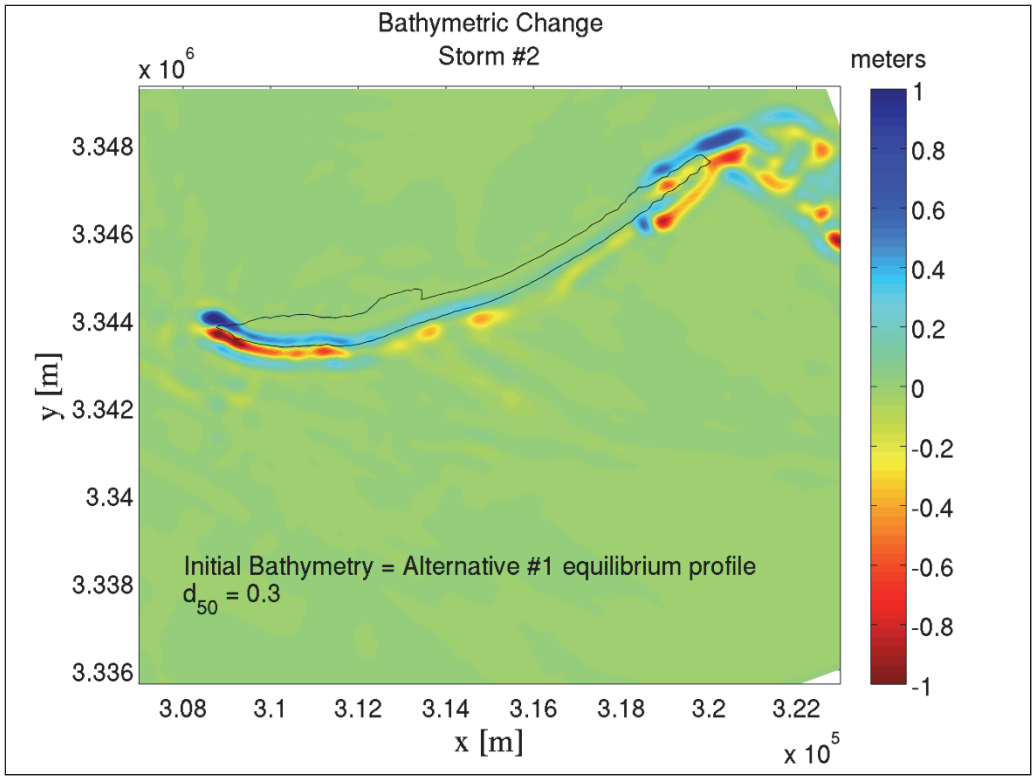

Figure G-36. Existing conditions for Storm #3.

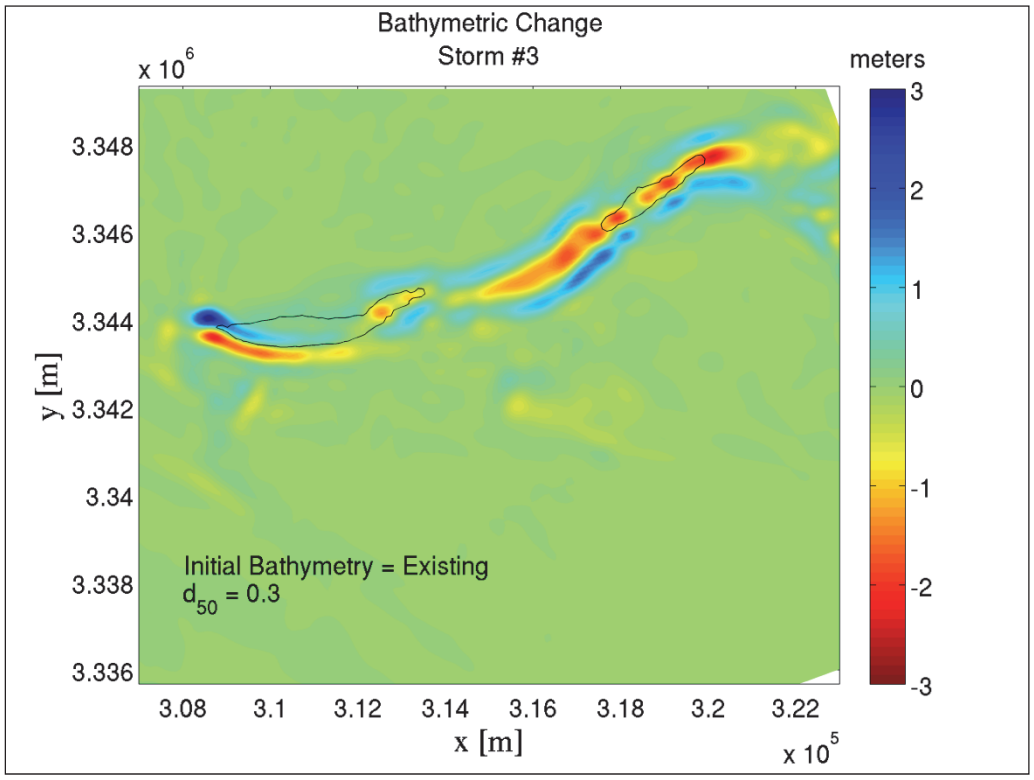

Figure G-37. Alternative #1 Restored conditions for Storm #3; Template A; With borrow pits.

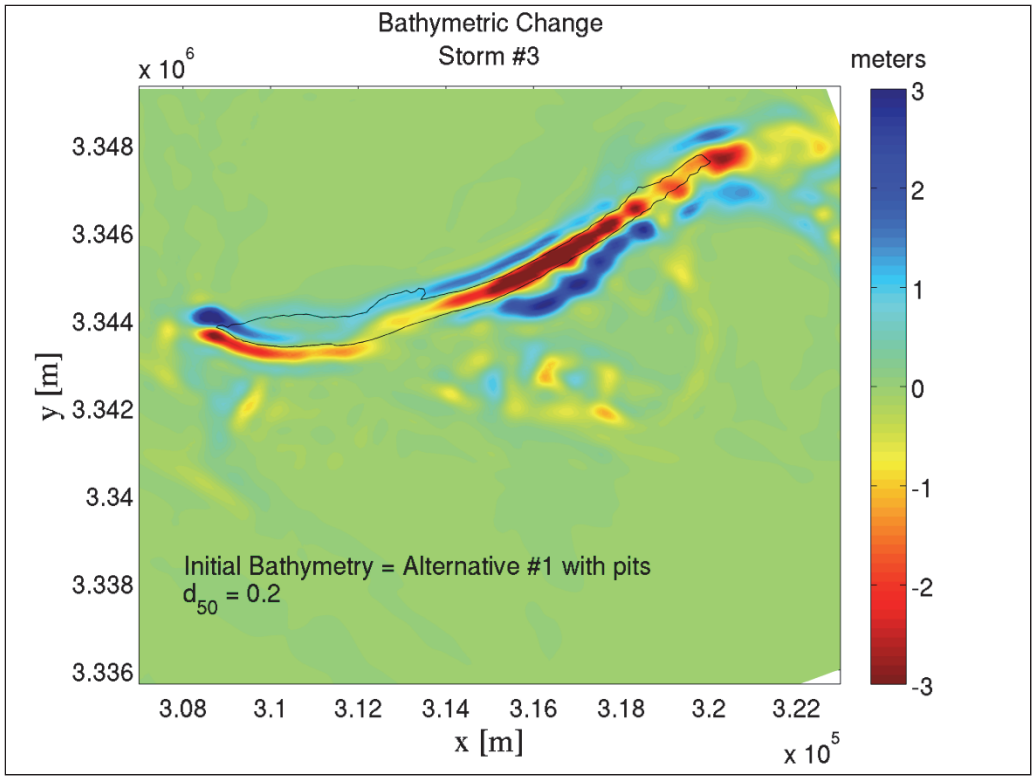

Figure G-38. Alternative #1 Restored conditions for Storm #3; Template B; With borrow pits.

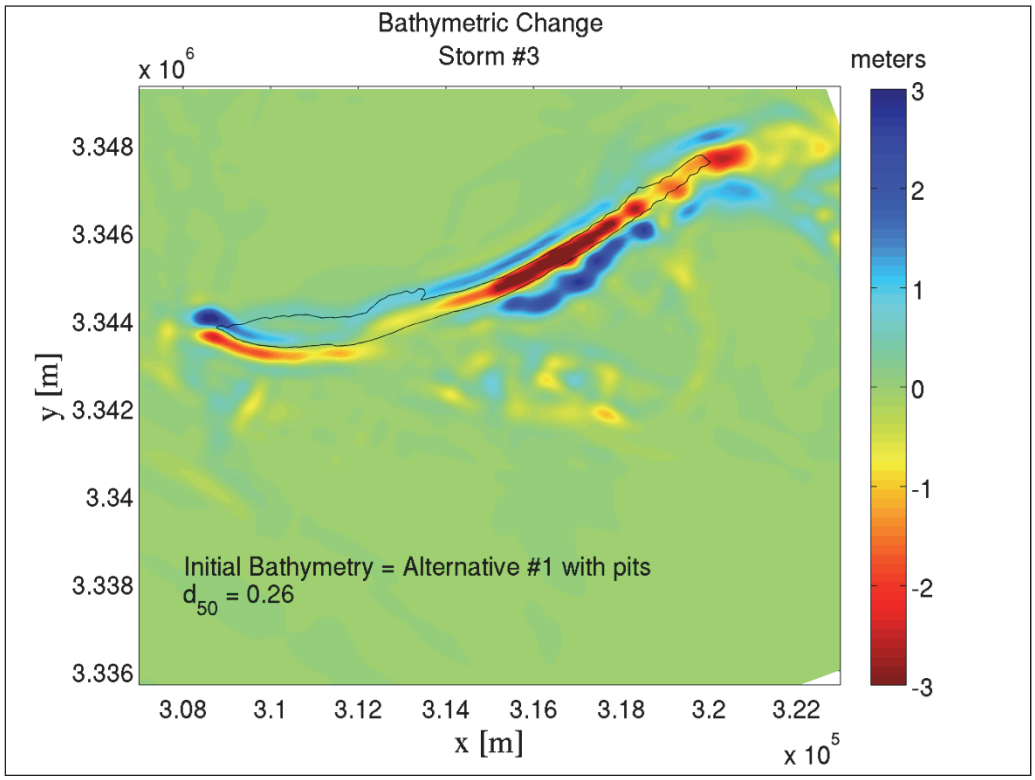

Figure G-39. Alternative #1 Restored conditions for Storm #3; Template C; With borrow pits.

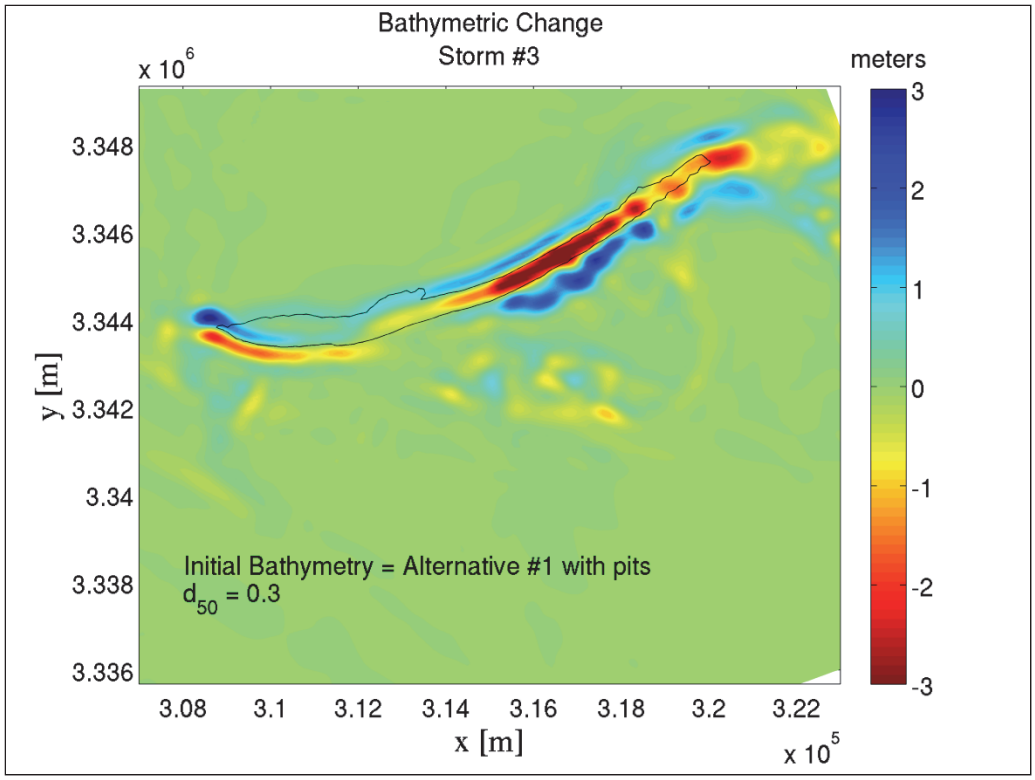

Figure G-40. Alternative #1 Restored conditions for Storm #3; Template A; Without borrow pits.

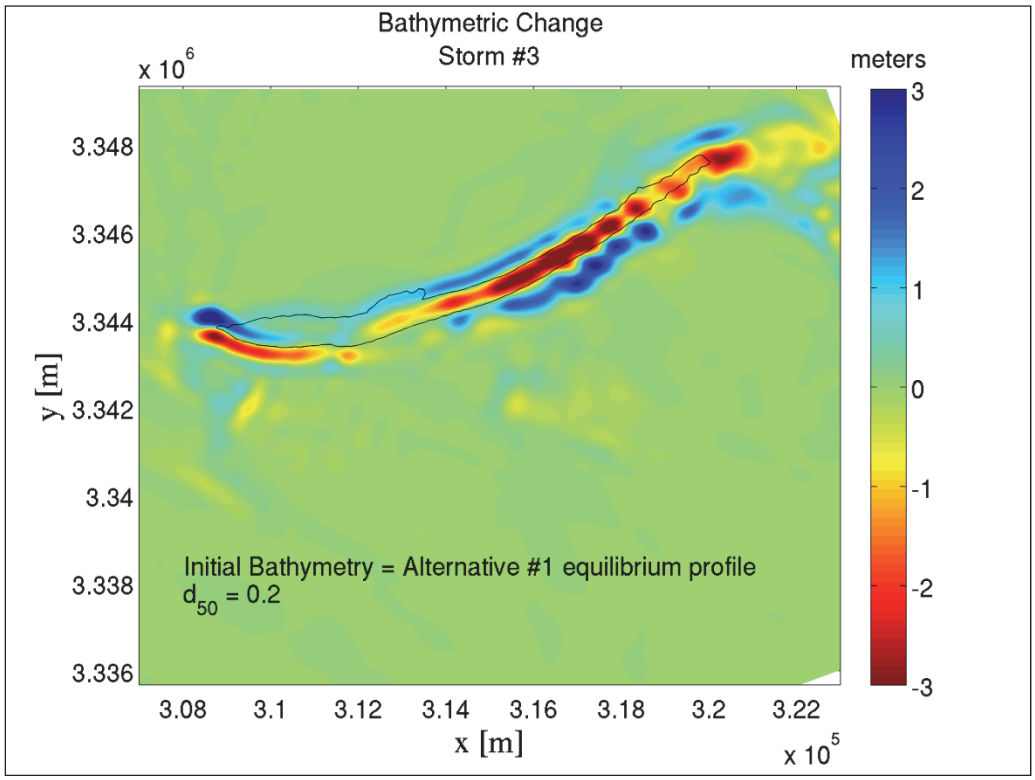

Figure G-41. Alternative #1 Restored conditions for Storm #3; Template B; Without borrow pits.

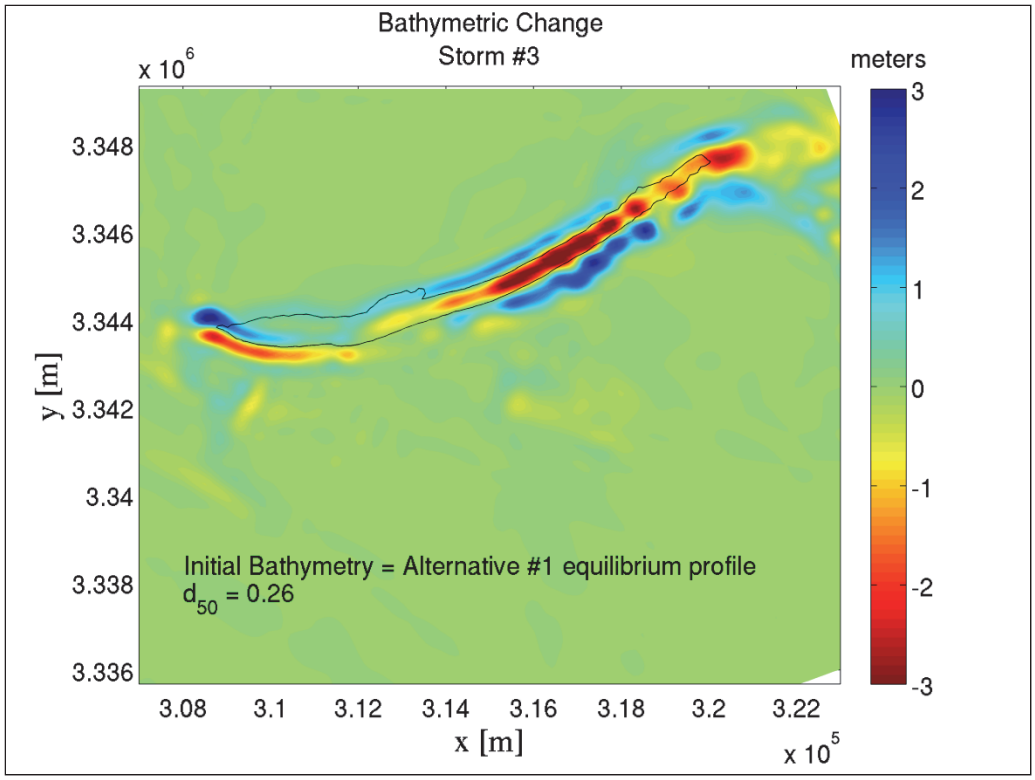

Figure G-42. Alternative #1 Restored conditions for Storm #3; Template C; Without borrow pits.

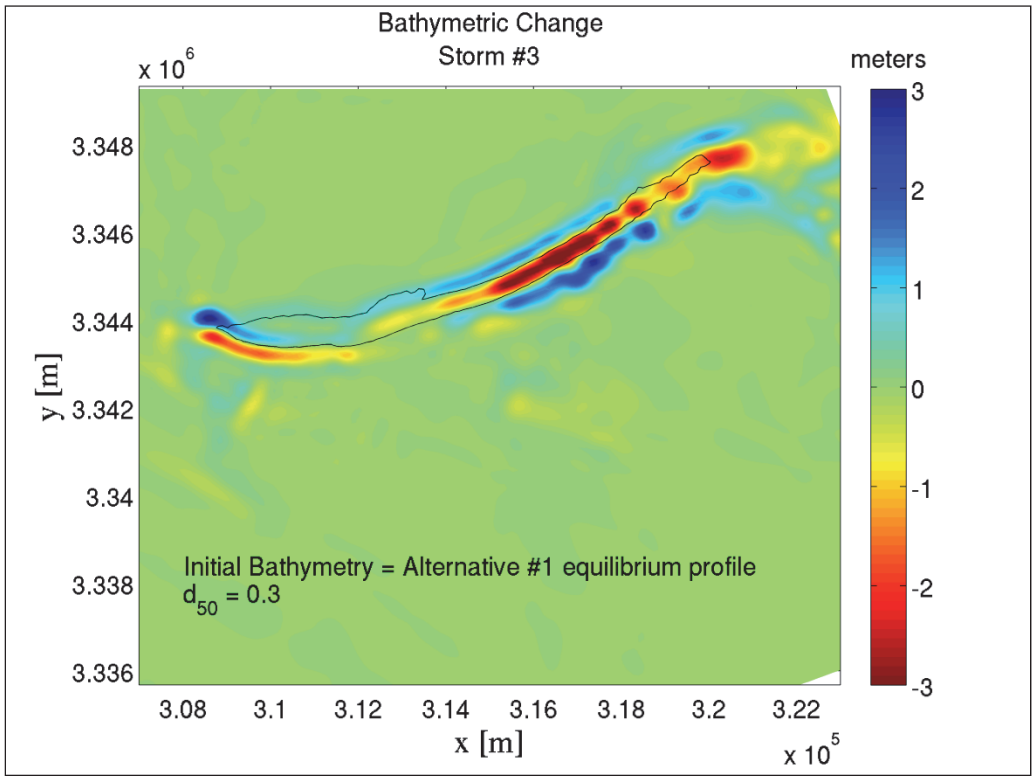

Figure G-43. Existing conditions for Storm #1.

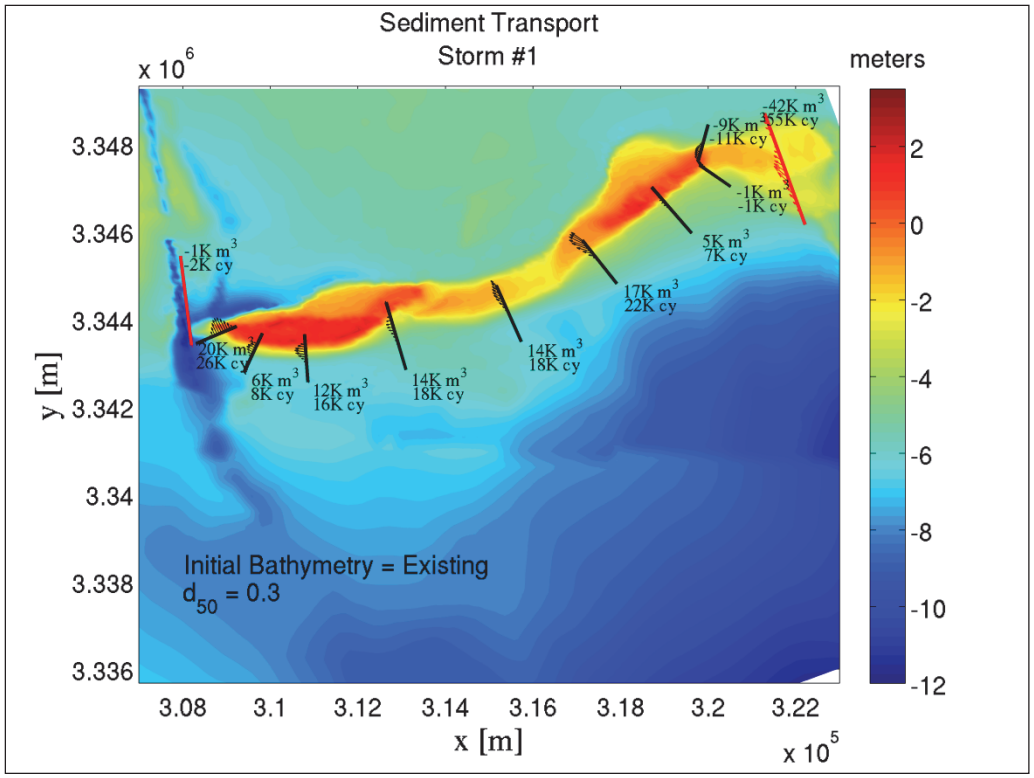

Figure G-44. Alternative #2 Restored conditions for Storm #1.

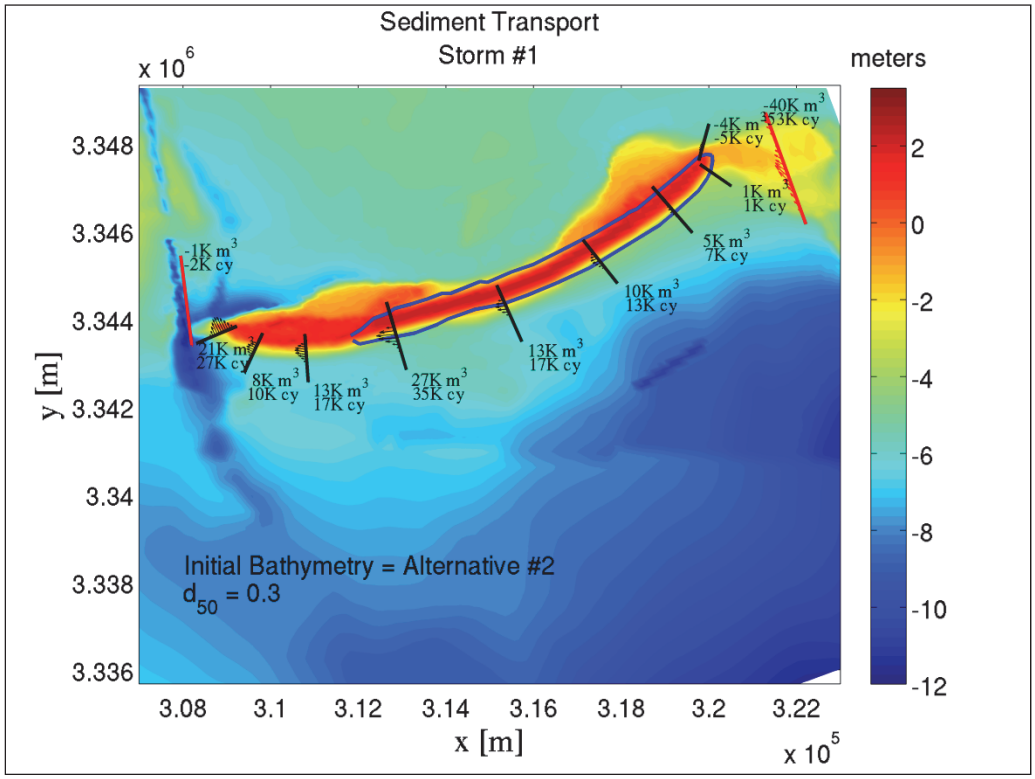

Figure G-45. Existing conditions for Storm #2.

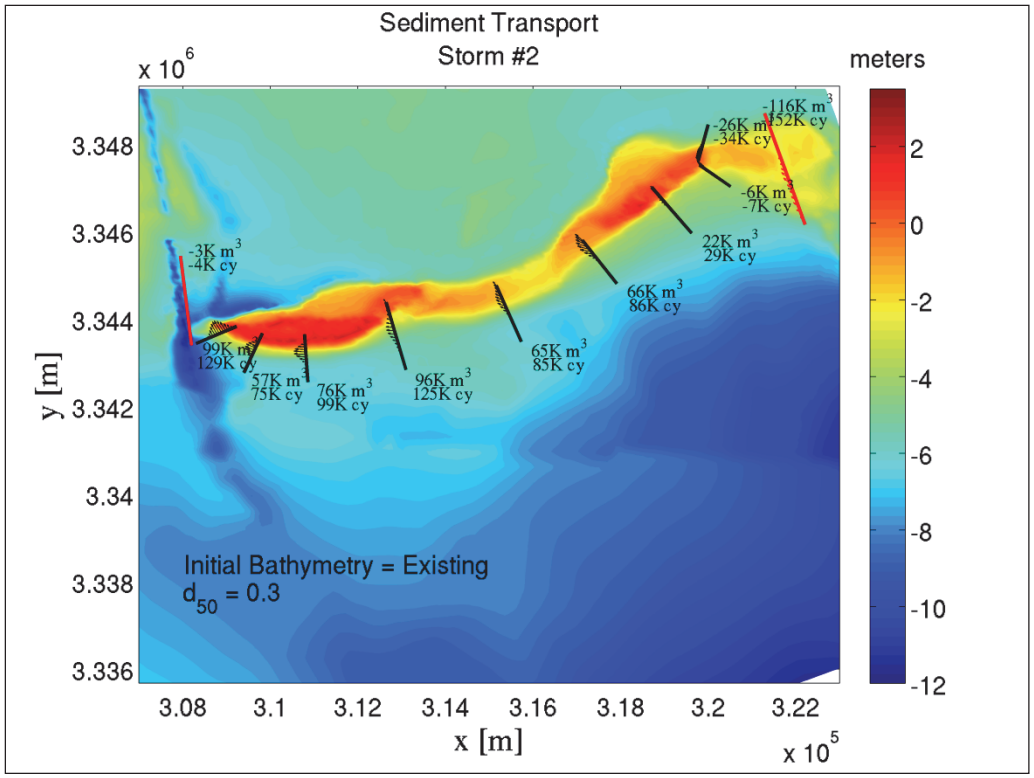

Figure G-46. Alternative #2 Restored conditions for Storm #2.

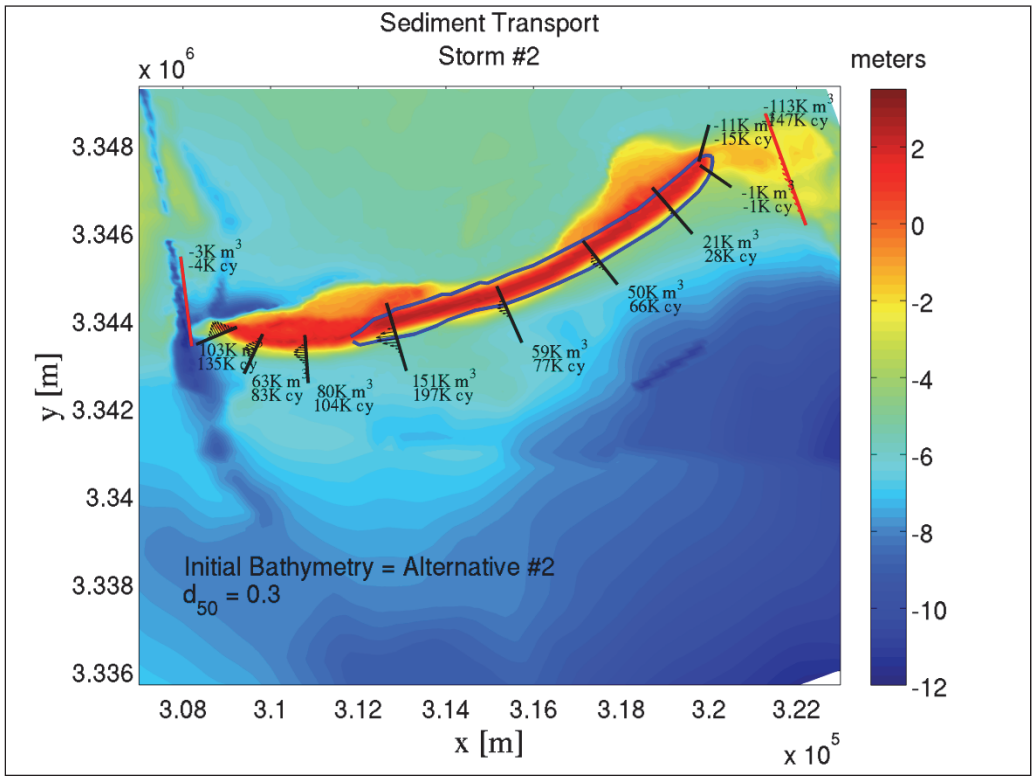

Figure G-47. Existing conditions for Storm #3.

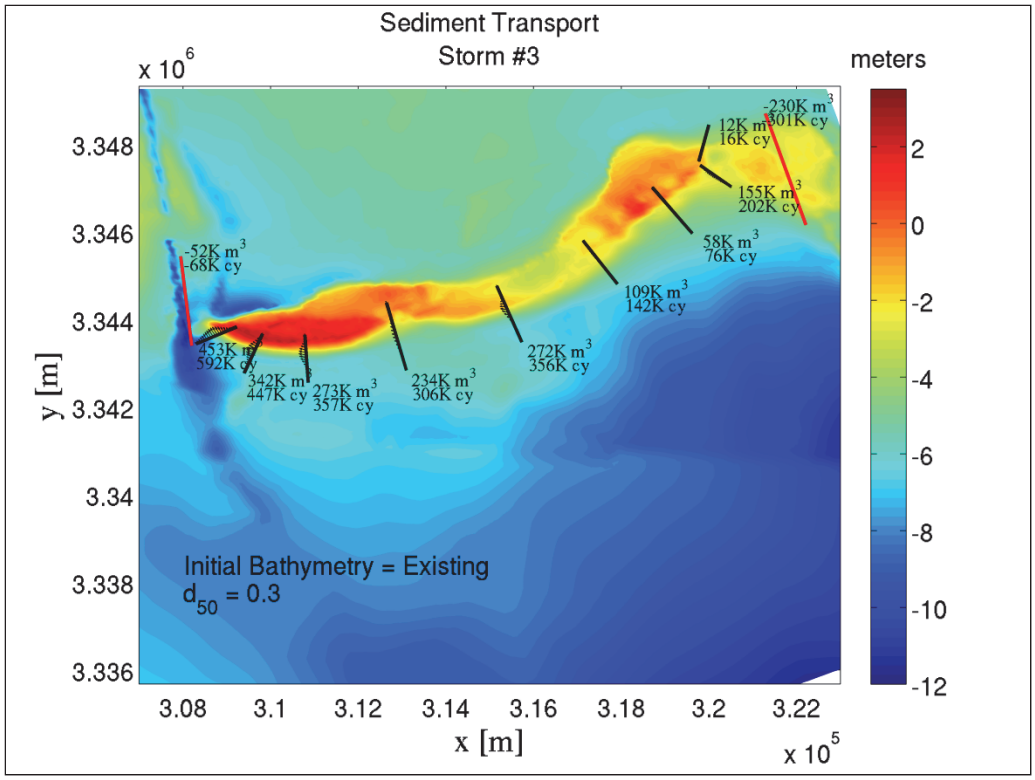

Figure G-48. Alternative #2 Restored conditions for Storm #3.

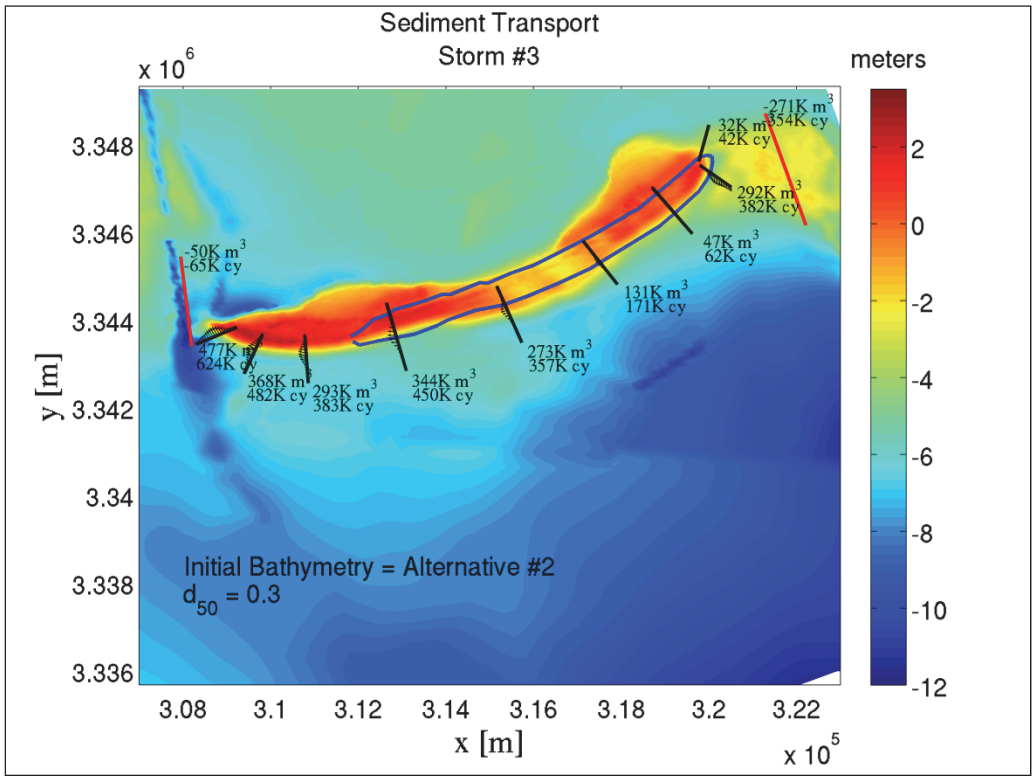

Figure G-49. Alternative #2 Restored conditions for Storm #1.

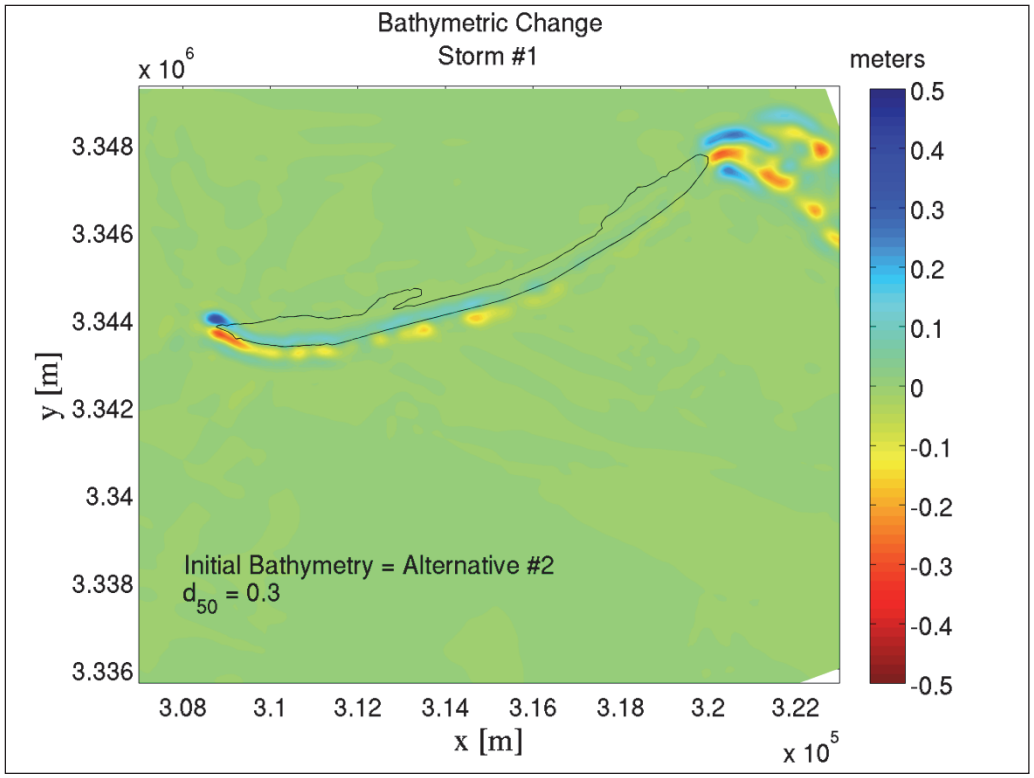

Figure G-50. Alternative #2 Restored conditions for Storm #2.

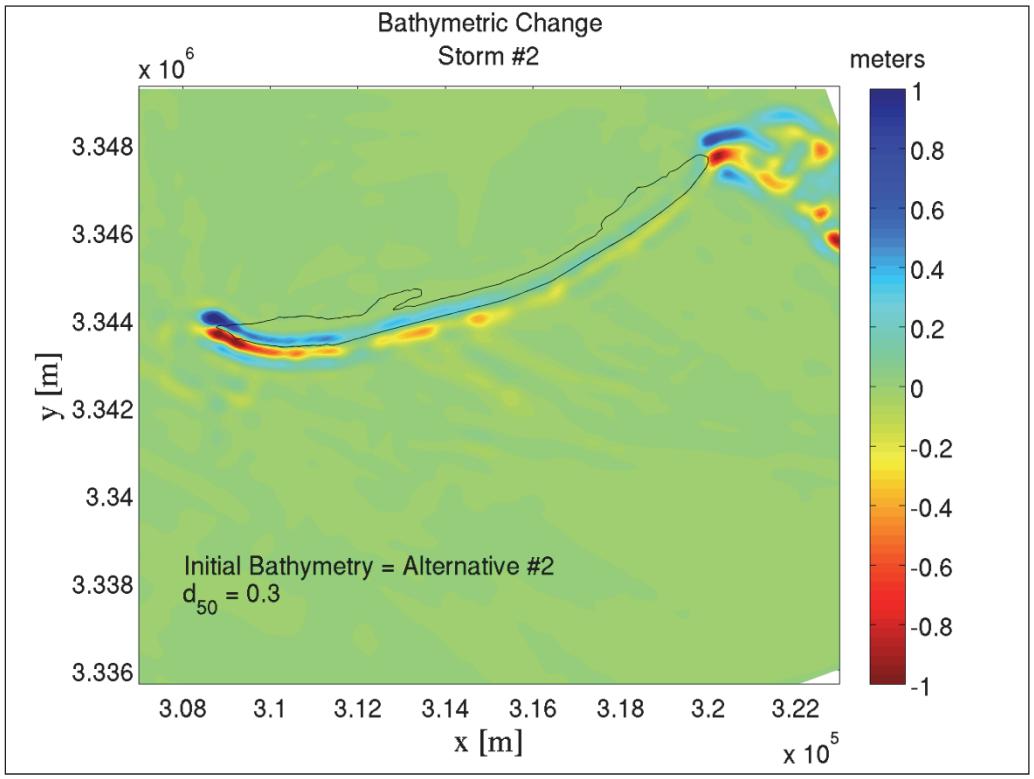

Figure G-51. Alternative #2 Restored conditions for Storm #3.

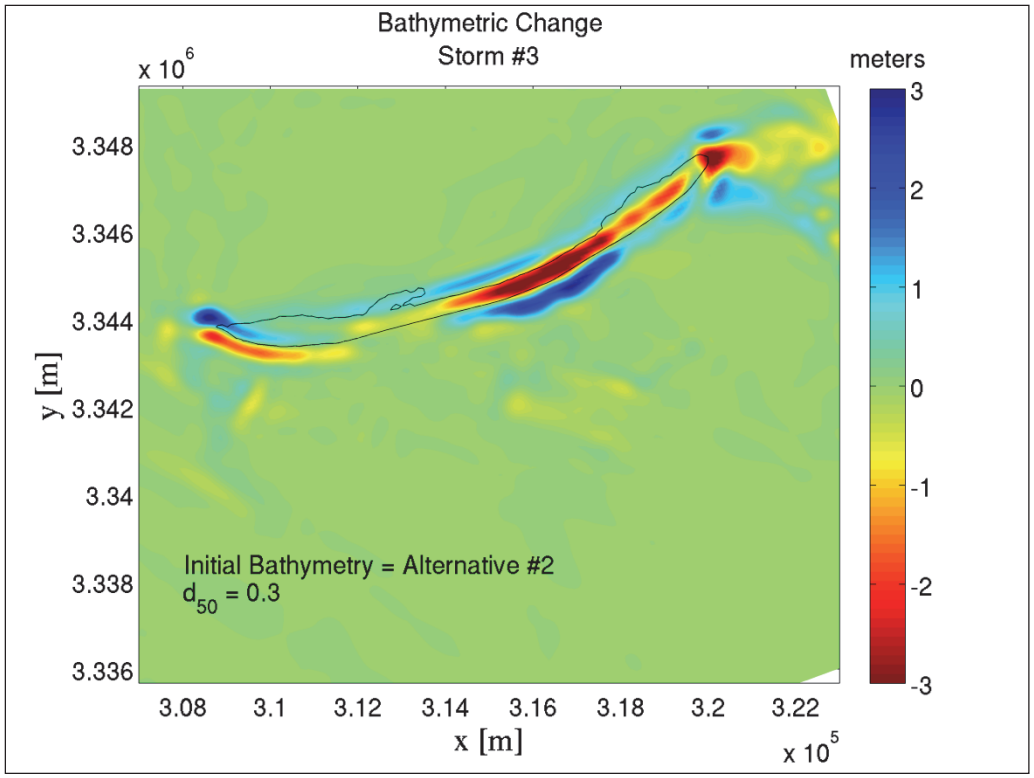

Appendix H: Nearshore Bathymetric Change Modeled Results for Existing Conditions and Restoration Scenarios

Note: The island footprint (NAVD = 0) contour is depicted as a black outline for reference.

Figure H-1. Existing conditions for Storm #1; d_{50} = 0.30 mm.

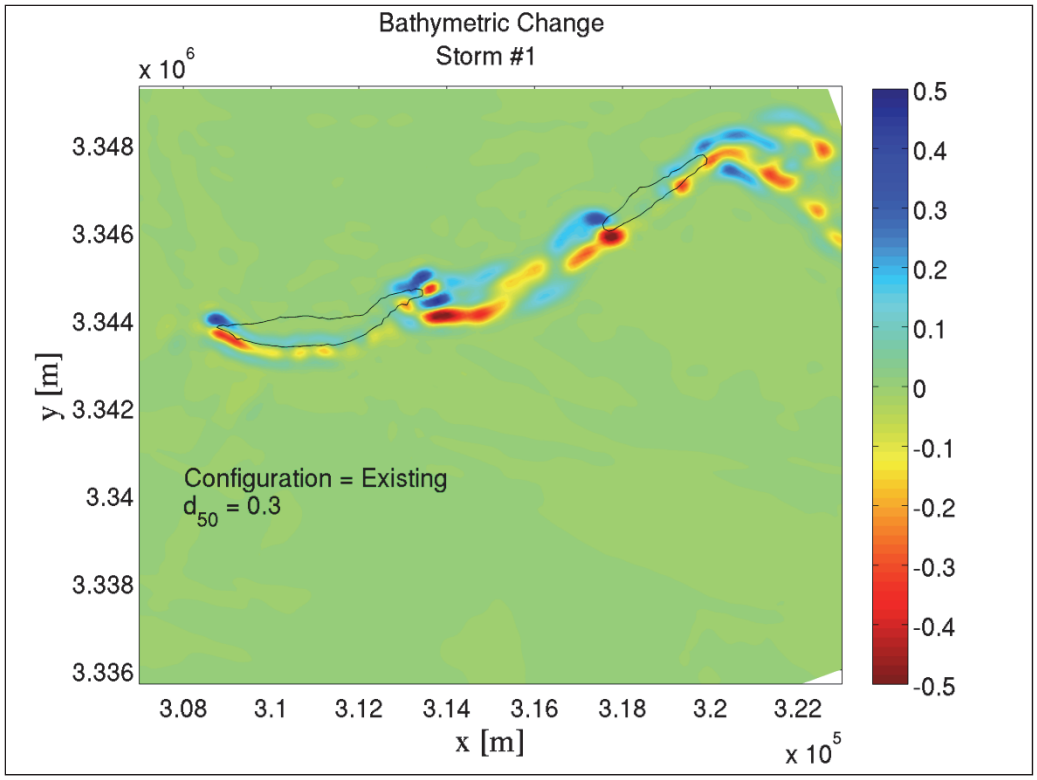

Figure H-2. Restored conditions for Storm #1; d_{50} = 0.20 mm (Template #1); With borrow pits.

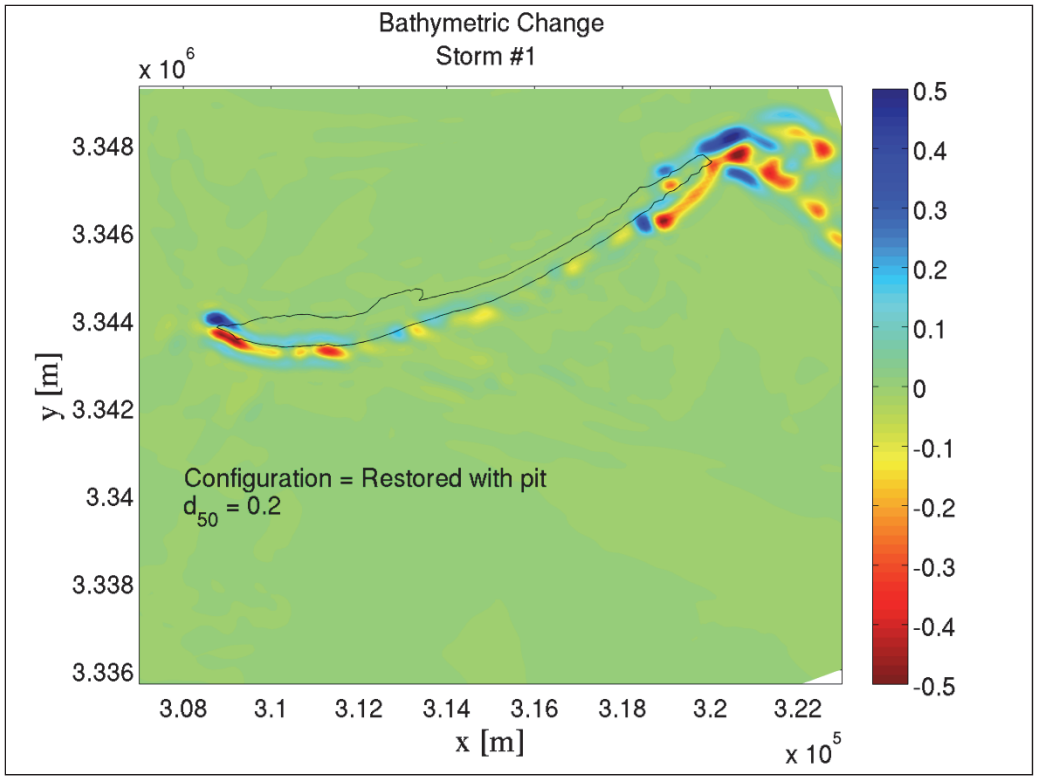

Figure H-3. Restored conditions for Storm #1; d50 = 0.26 mm (Template #2); With borrow pits.

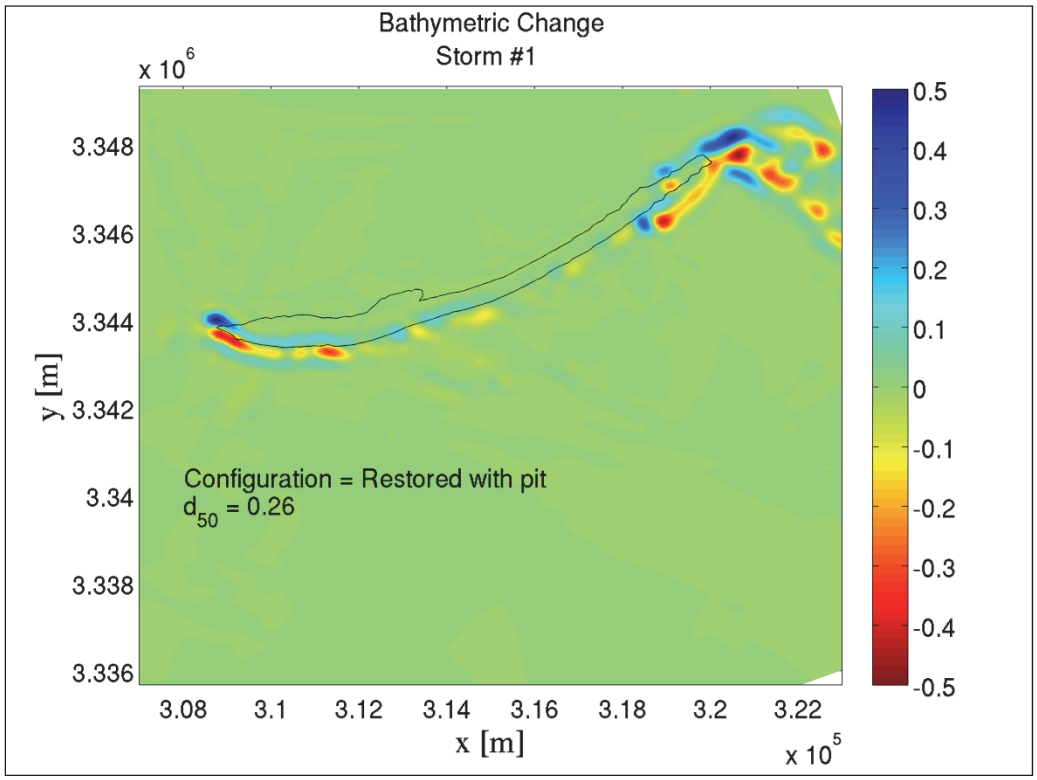

Figure H-4. Restored conditions for Storm #1; d_{50} = 0.30 mm (Template #3); With borrow pits.

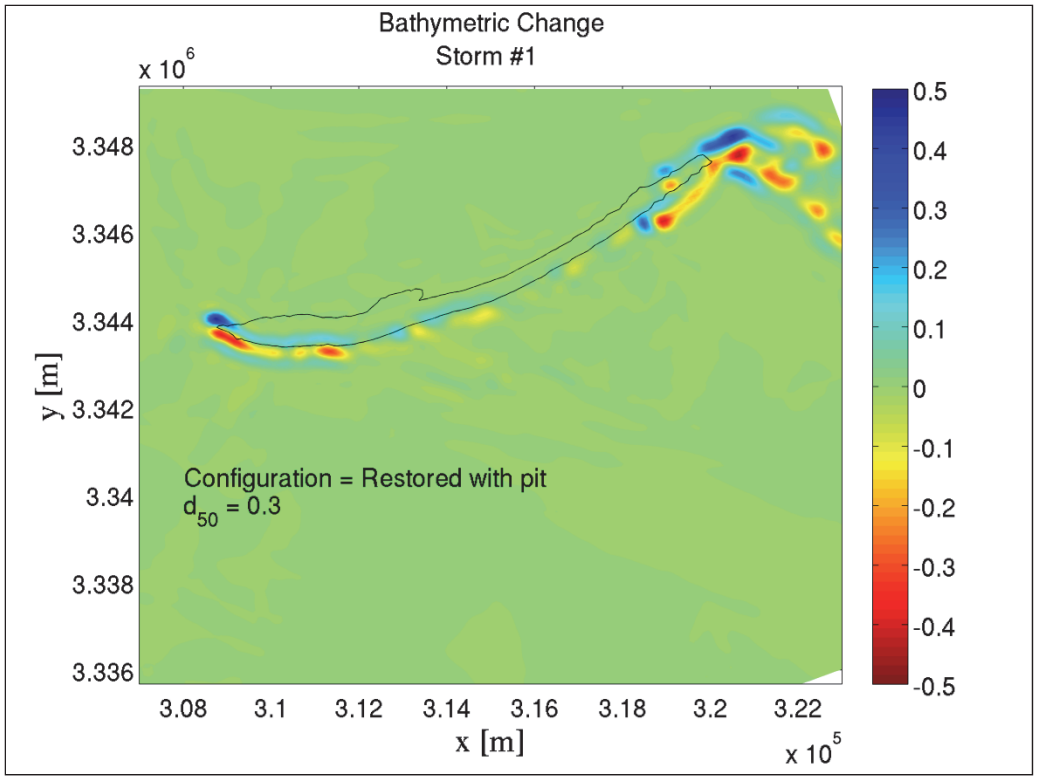

Figure H-5. Restored conditions for Storm #1; d_{50} = 0.20 mm (Template #1); Without borrow pits.

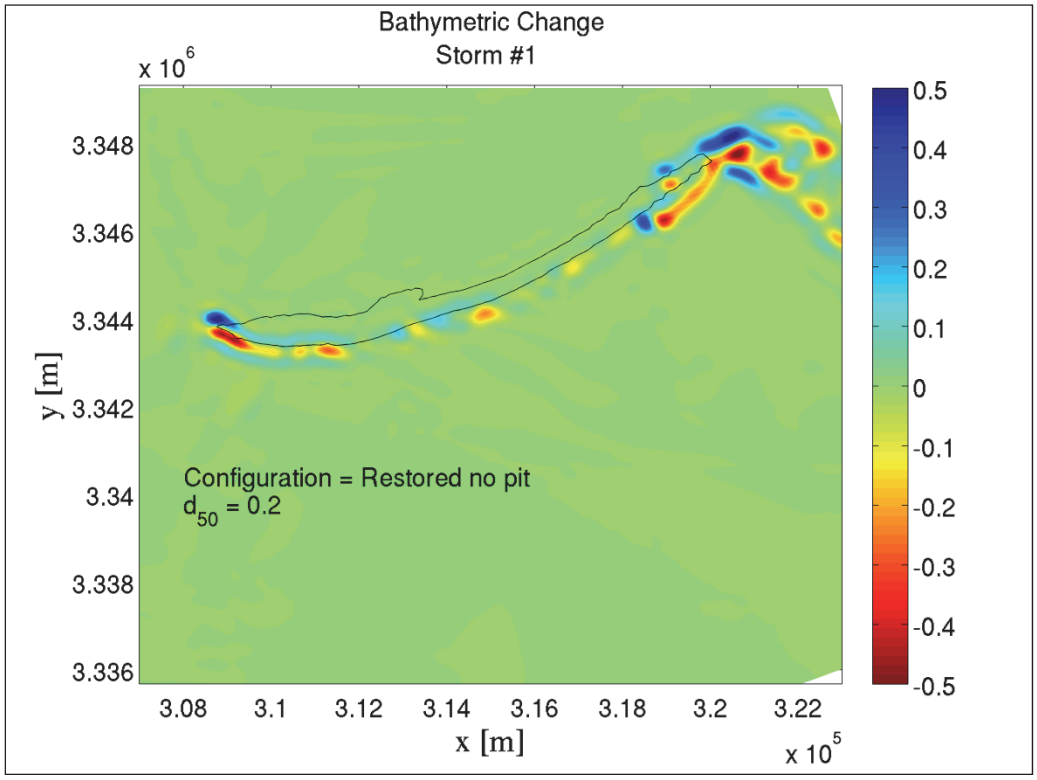

Figure H-6. Restored conditions for Storm #1; d_{50} = 0.26 mm (Template #2); Without borrow pits.

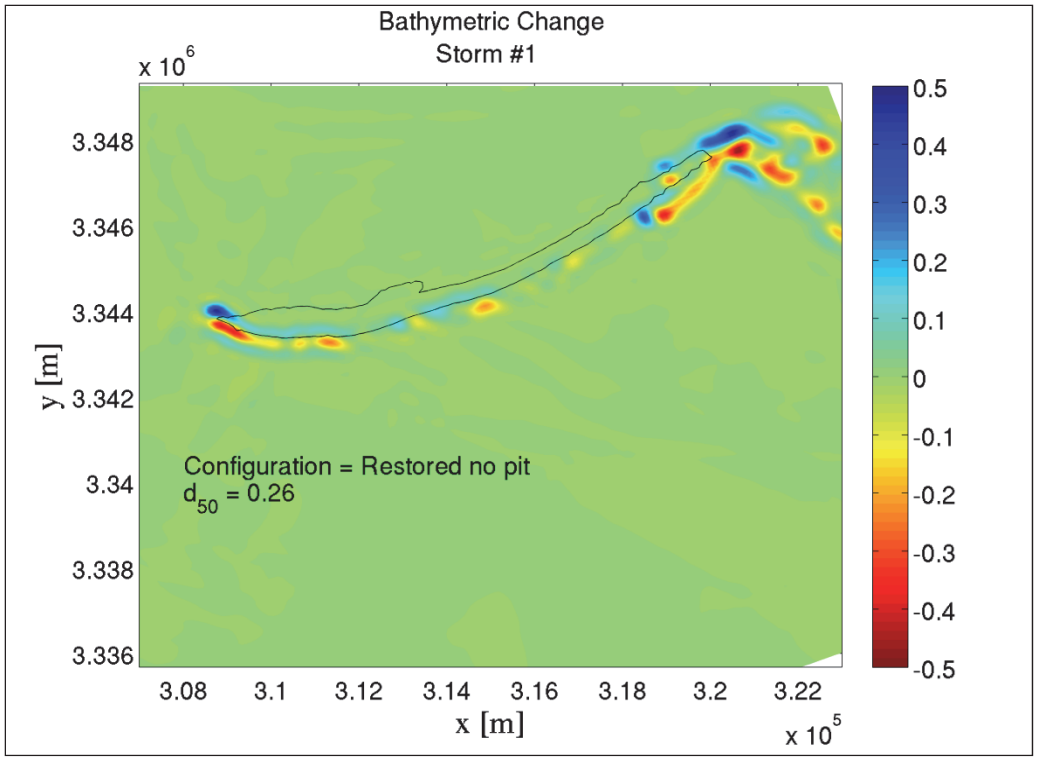

Figure H-7. Restored conditions for Storm #1; d_{50} = 0.30 mm (Template #3); Without borrow pits.

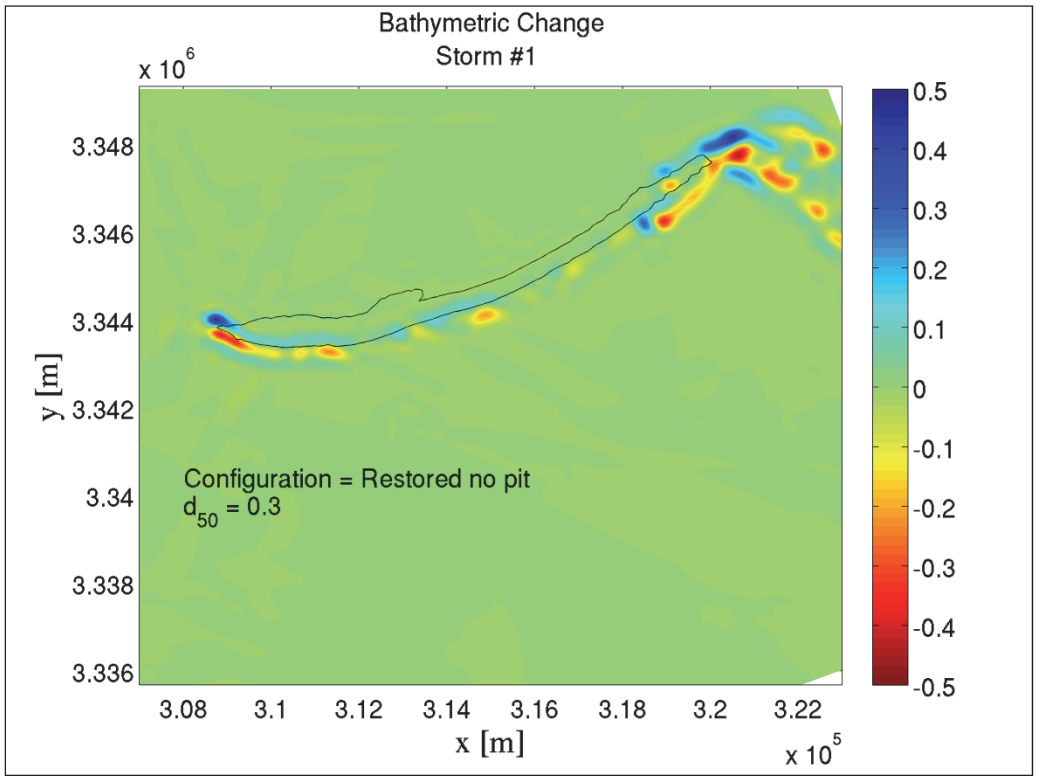

Figure H-8. Existing conditions for Storm #2; d_{50} = 0.30 mm.

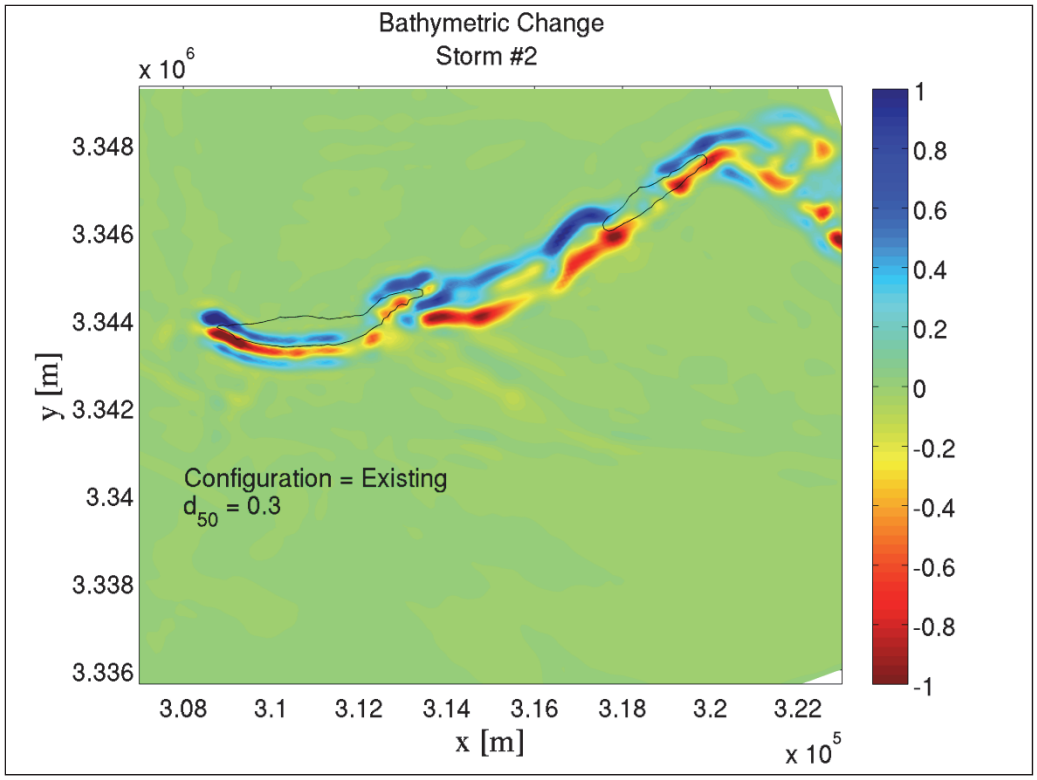

Figure H-9. Restored conditions for Storm #2; d_{50} = 0.20 mm (Template #1); With borrow pits.

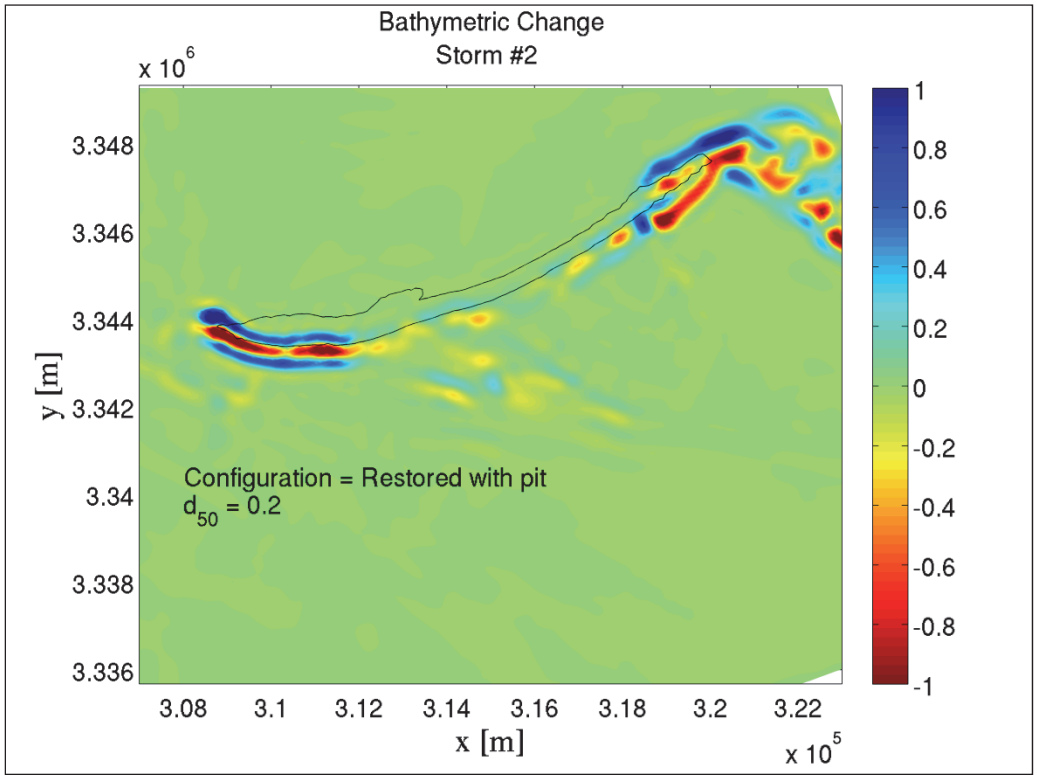

Figure H-10. Restored conditions for Storm #2; d_{50} = 0.26 mm (Template #2); With borrow pits.

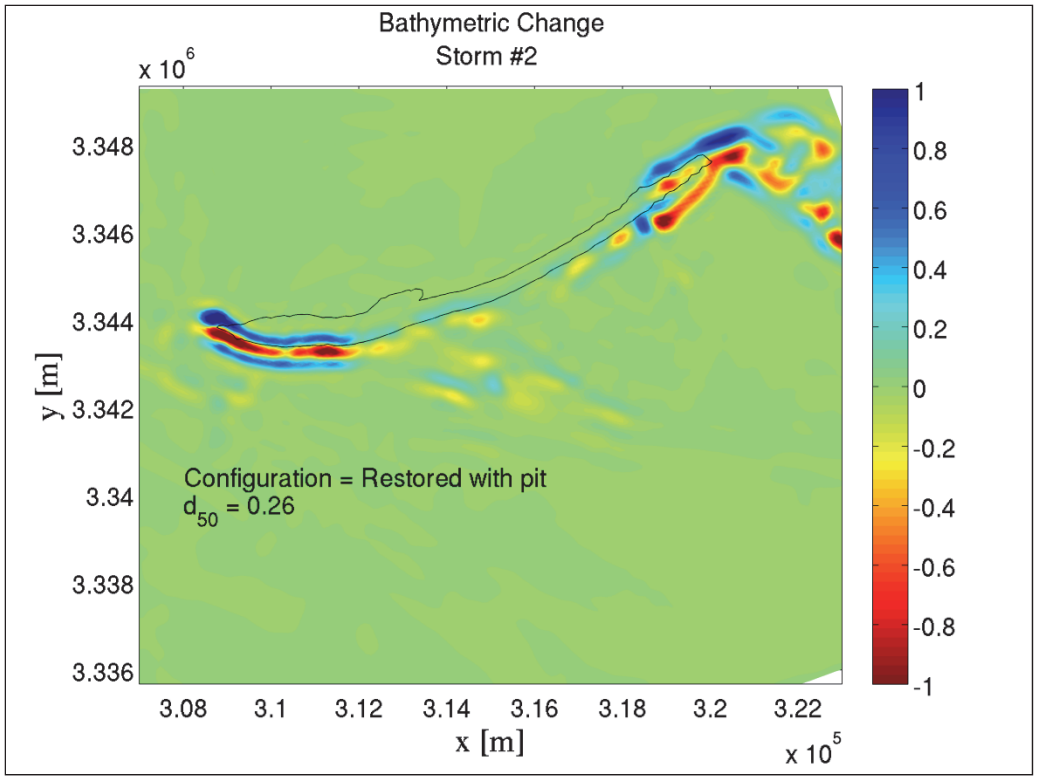

Figure H-11. Restored conditions for Storm #2; d_{50} = 0.30 mm (Template #3); With borrow pits.

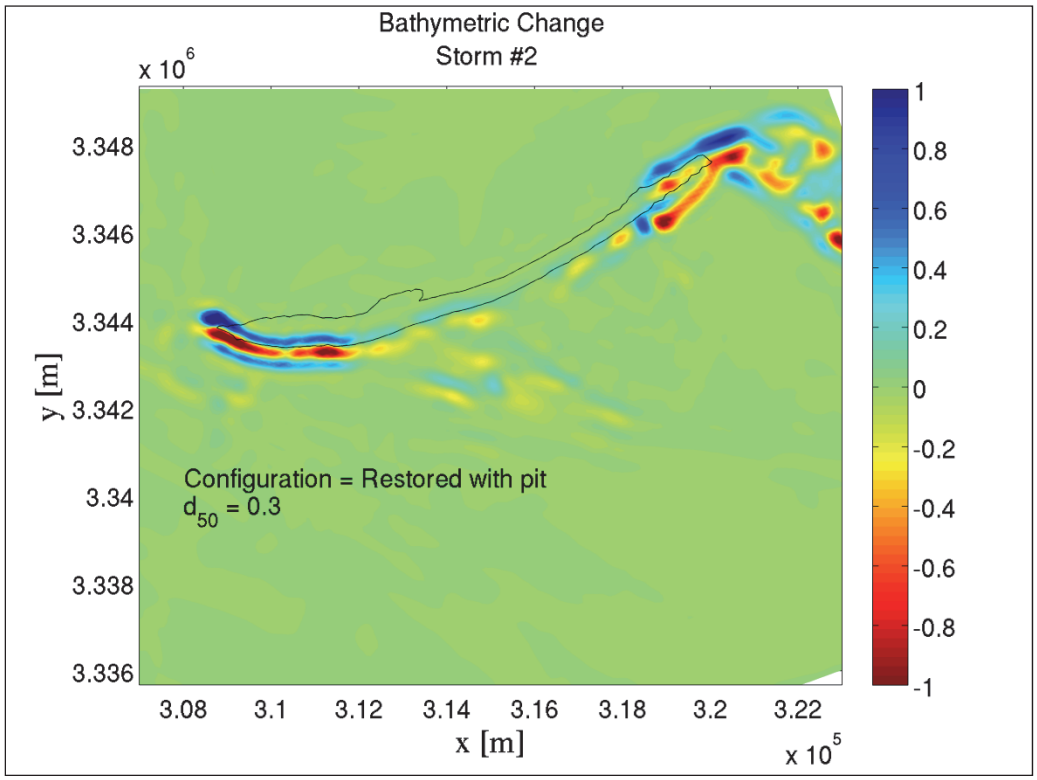

Figure H-12. Restored conditions for Storm #2; d_{50} = 0.20 mm (Template #1); Without borrow pits.

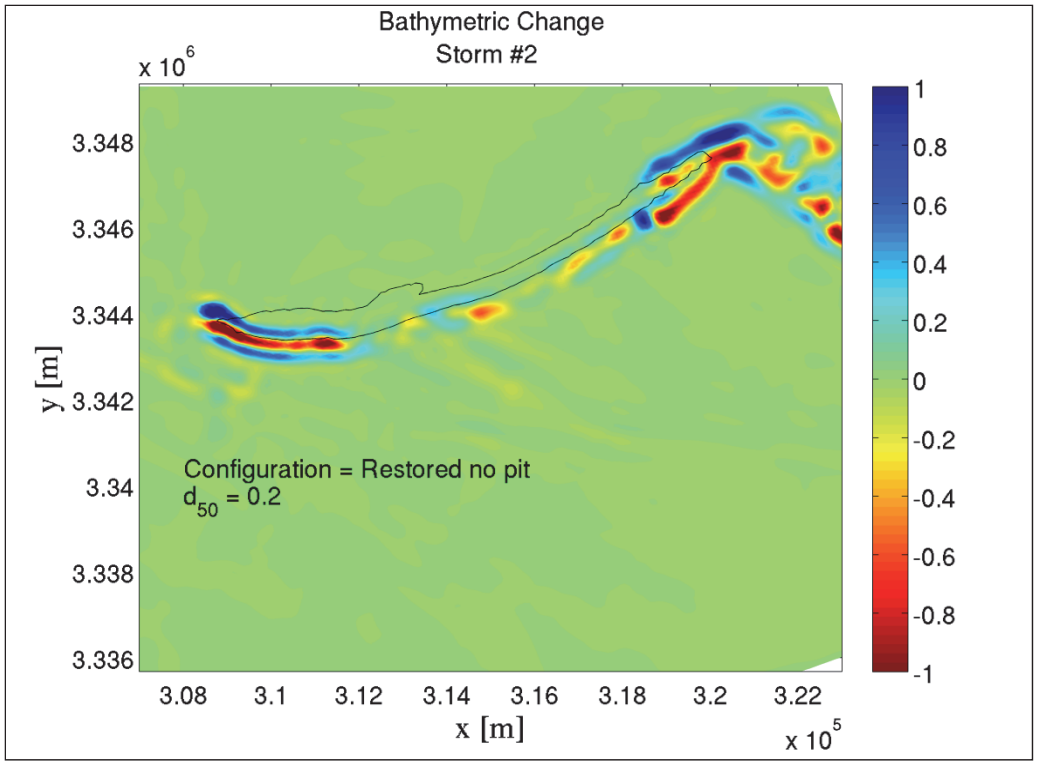

Figure H-13. Restored conditions for Storm #2; d_{50} = 0.26 mm (Template #2); Without borrow pits.

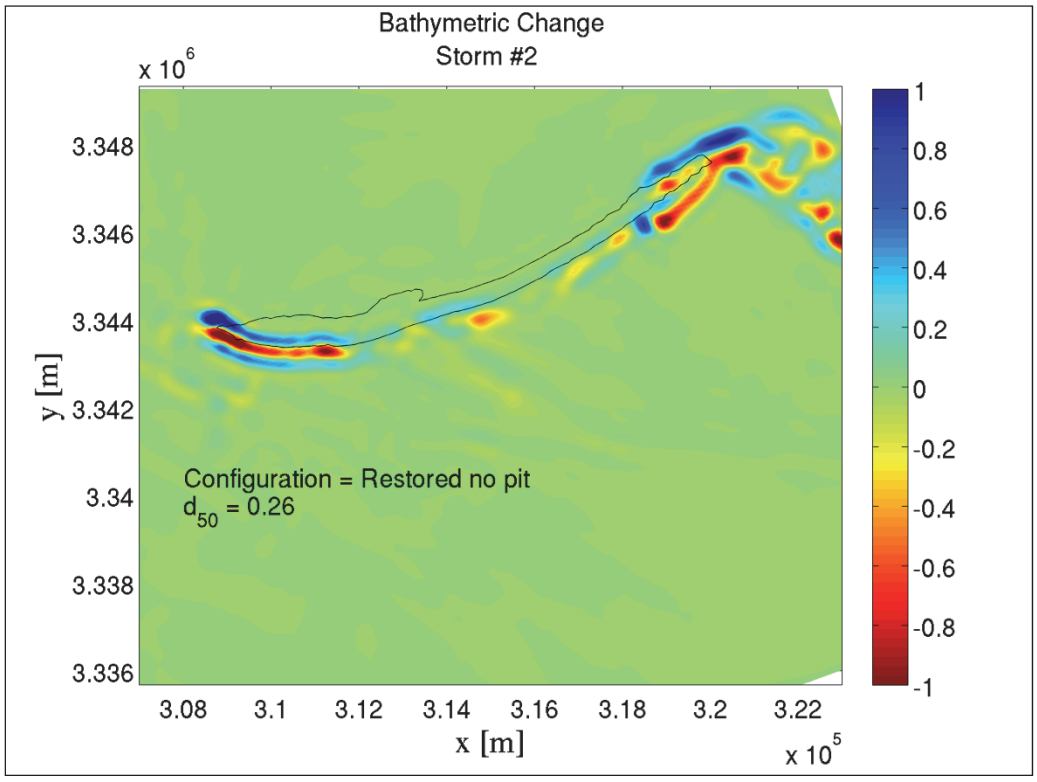

Figure H-14. Restored conditions for Storm #2; d_{50} = 0.30 mm (Template #3); Without borrow pits.

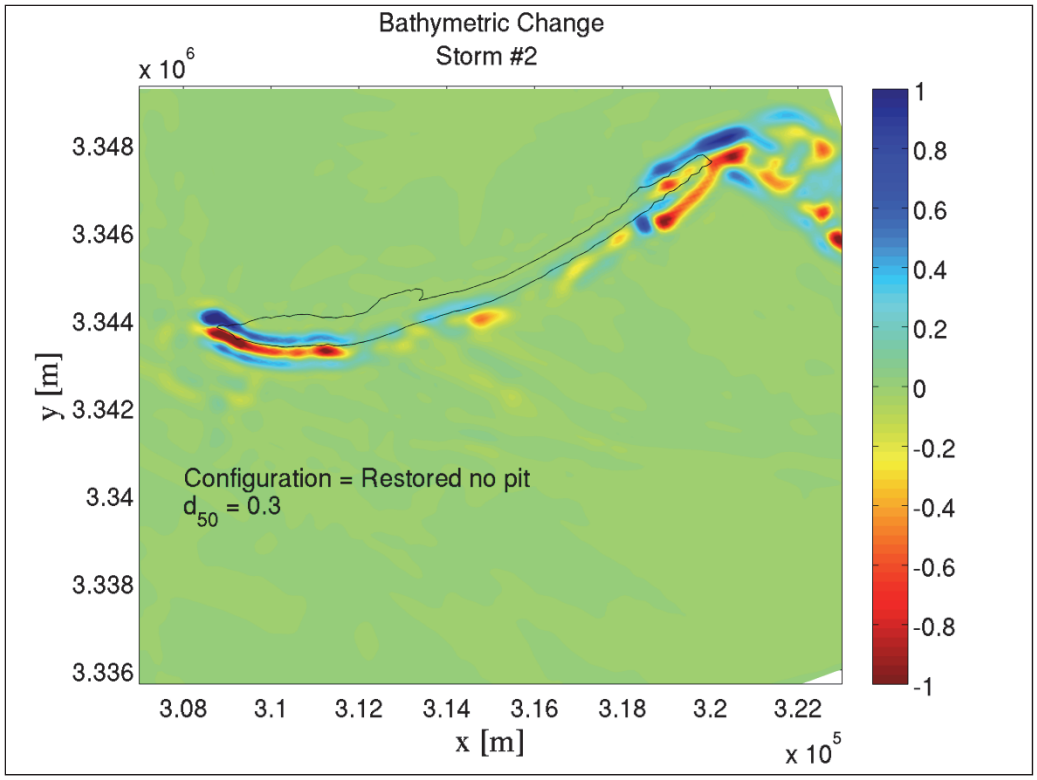

Appendix I: Nearshore Sediment Transport Modeled Results for Existing Conditions and Restoration Scenarios

Figure I-1. Existing conditions for Katrina; d_{50} = 0.30 mm.

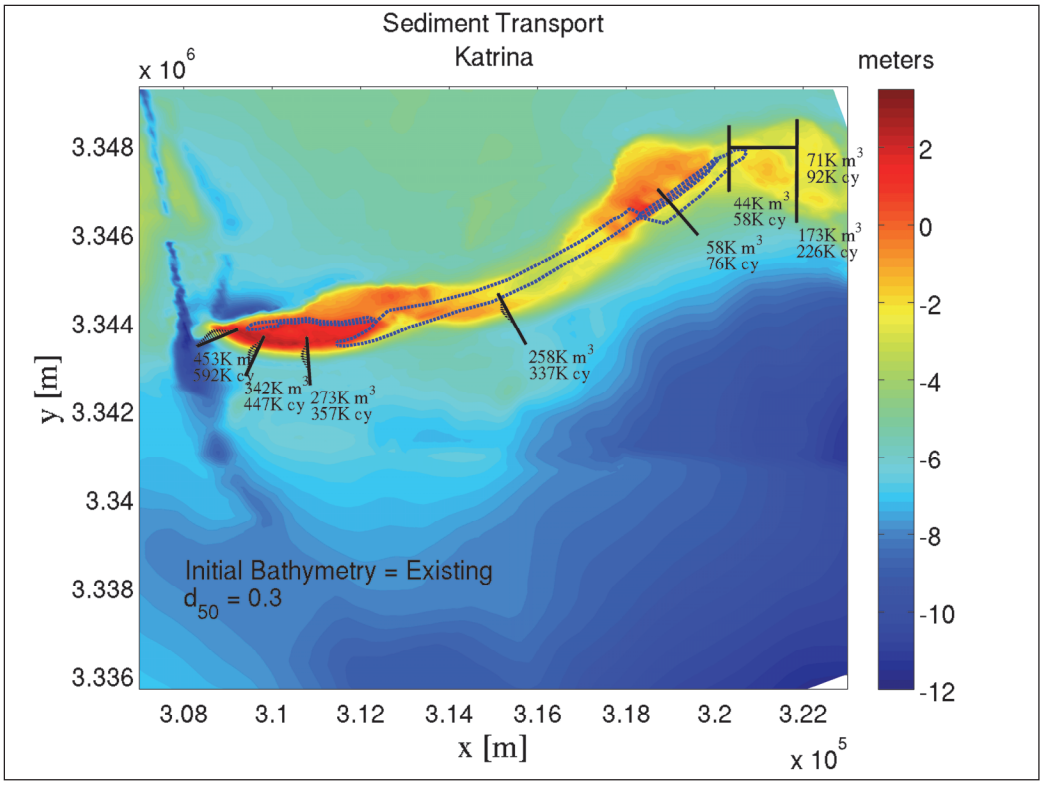

Figure I-2. Restored conditions for Katrina; d_{50} = 0.20 mm (Template #1); With borrow pits.

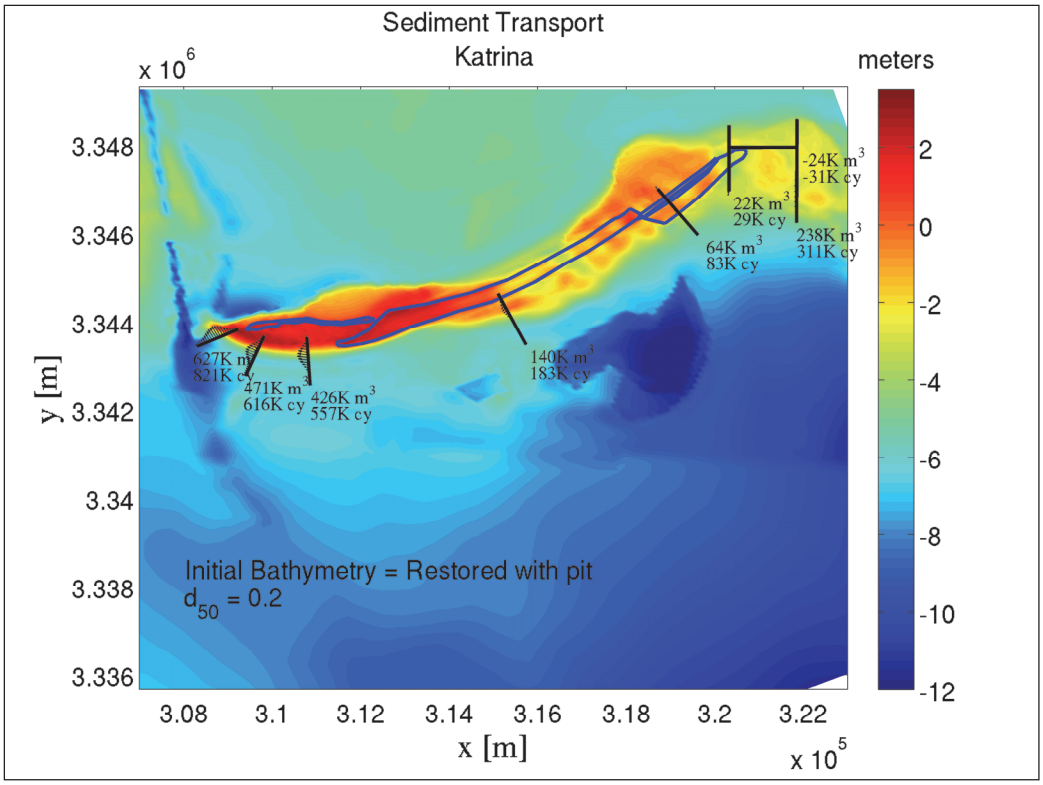

Figure I-3. Restored conditions for Katrina; d_{50} = 0.26 mm (Template #2); With borrow pits.

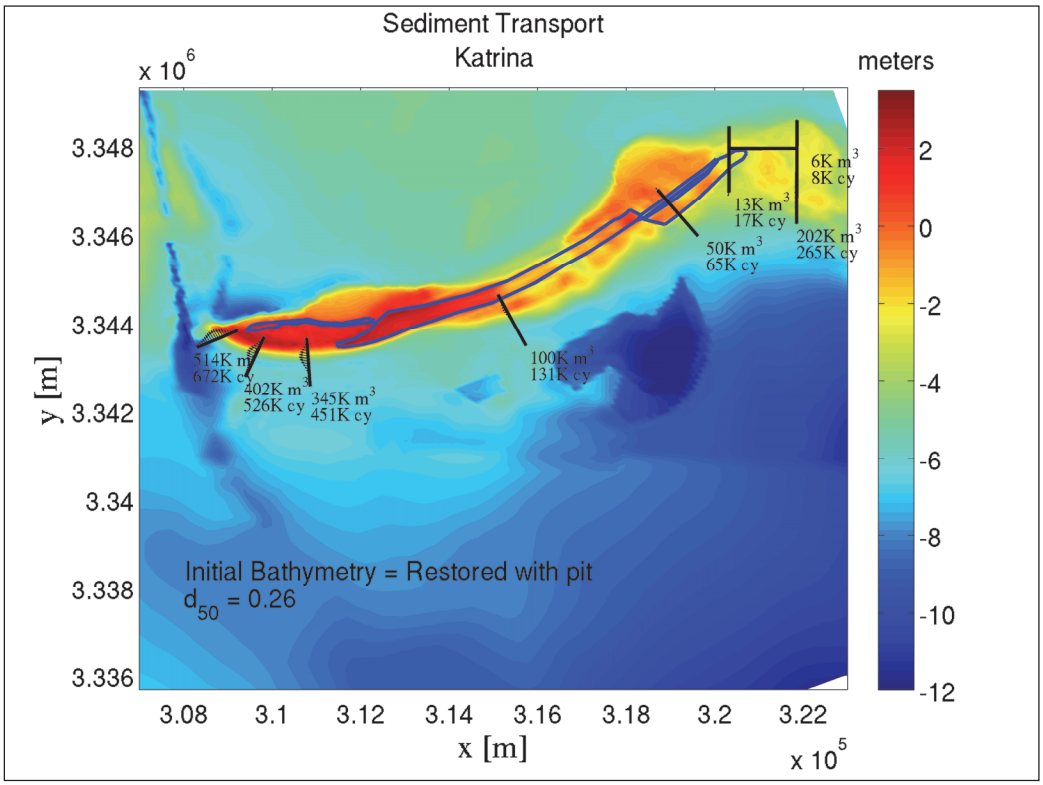

Figure I-4. Restored conditions for Katrina; d_{50} = 0.30 mm (Template #3); With borrow pits.

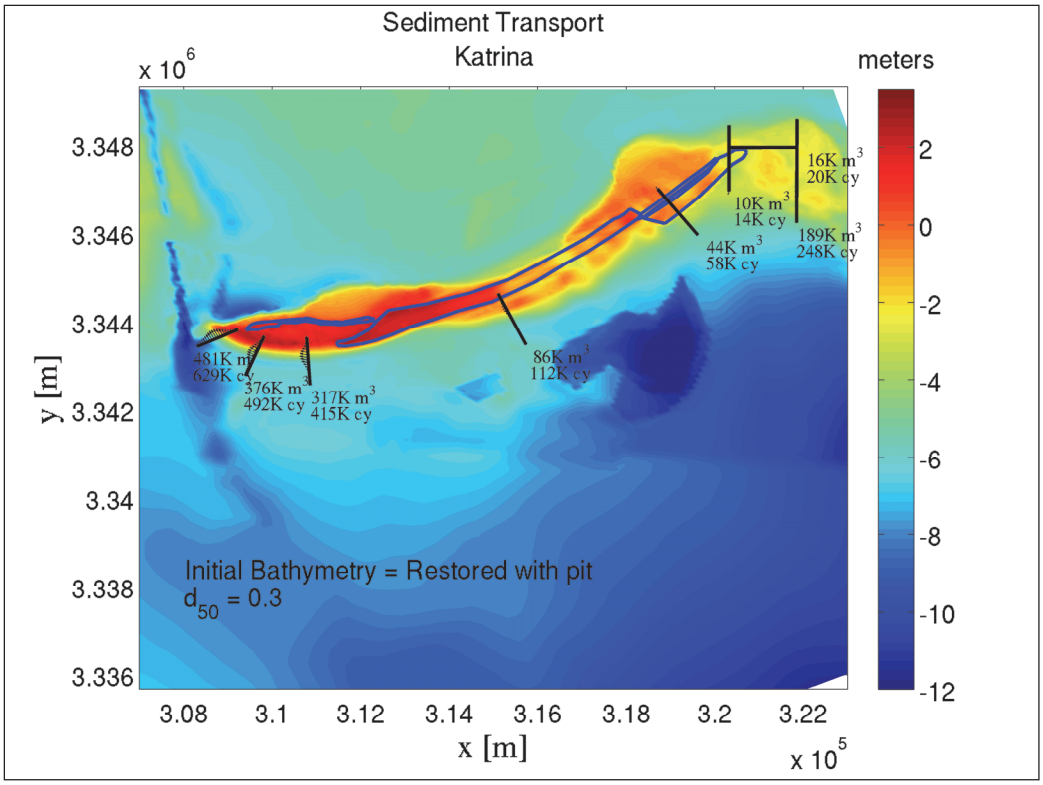

Figure I-5. Restored conditions for Katrina; d_{50} = 0.20 mm (Template #1); Without borrow pits.

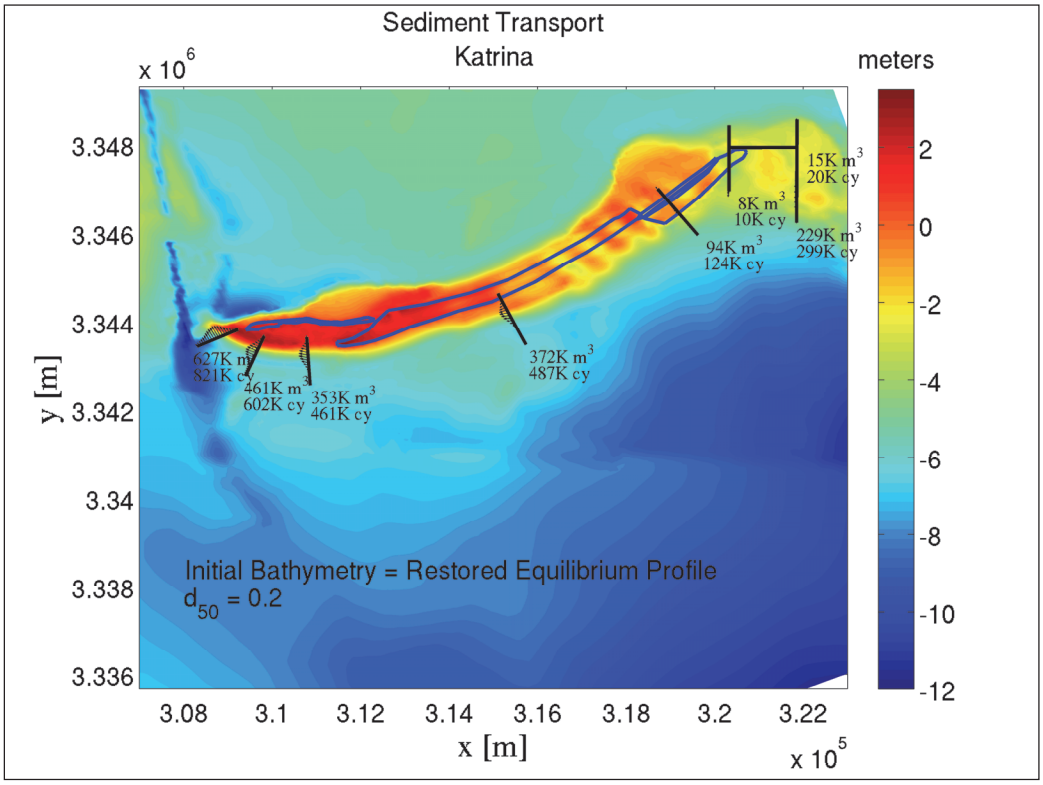

Figure I-6. Restored conditions for Katrina; d_{50} = 0.26 mm (Template #2); Without borrow pits.

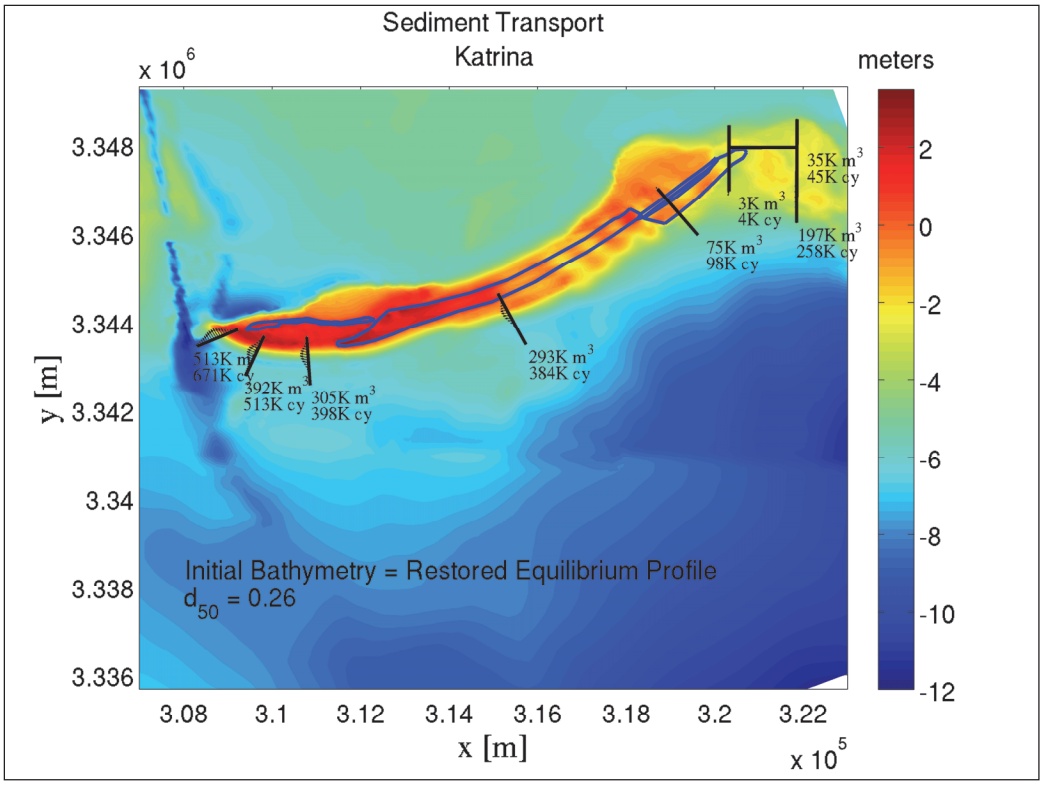

Figure I-7. Restored conditions for Katrina; d_{50} = 0.30 mm (Template #3); Without borrow pits.

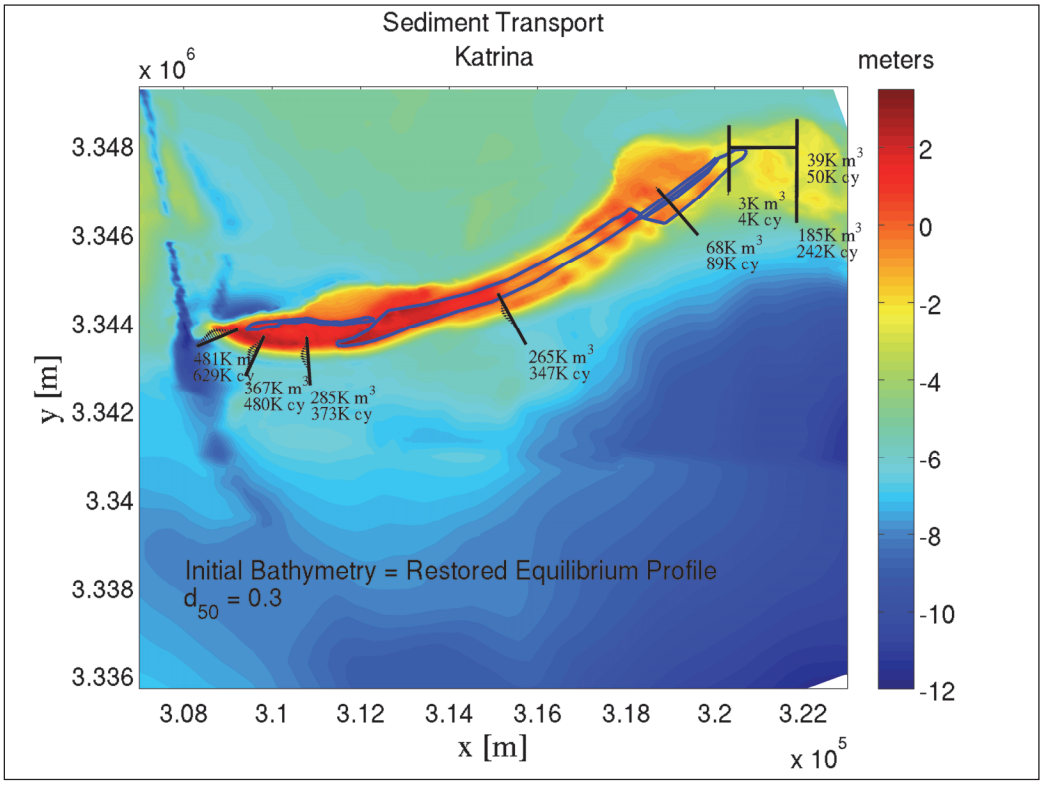

Appendix J: Nearshore Sediment Transport and Bathymetric Change Modeled Results for Existing Conditions and Alternative 3 Restoration Scenario

Note: The island footprint (NAVD = 0) contour is depicted as a black outline for reference in Figures J-7 through J-12.

Figure J-1. Existing conditions for Storm #1; d_{50} = 0.30 mm.

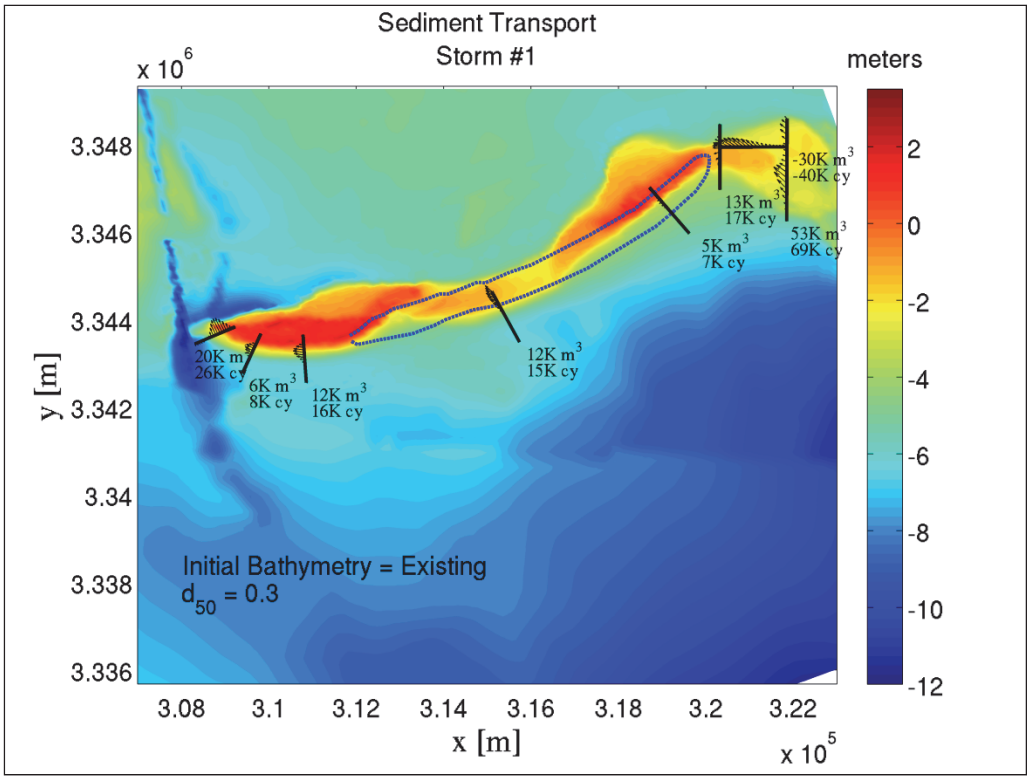

Figure J-2. Alternative 3 Restored conditions for Storm #1; d_{50} = 0.30 mm; With borrow pit.

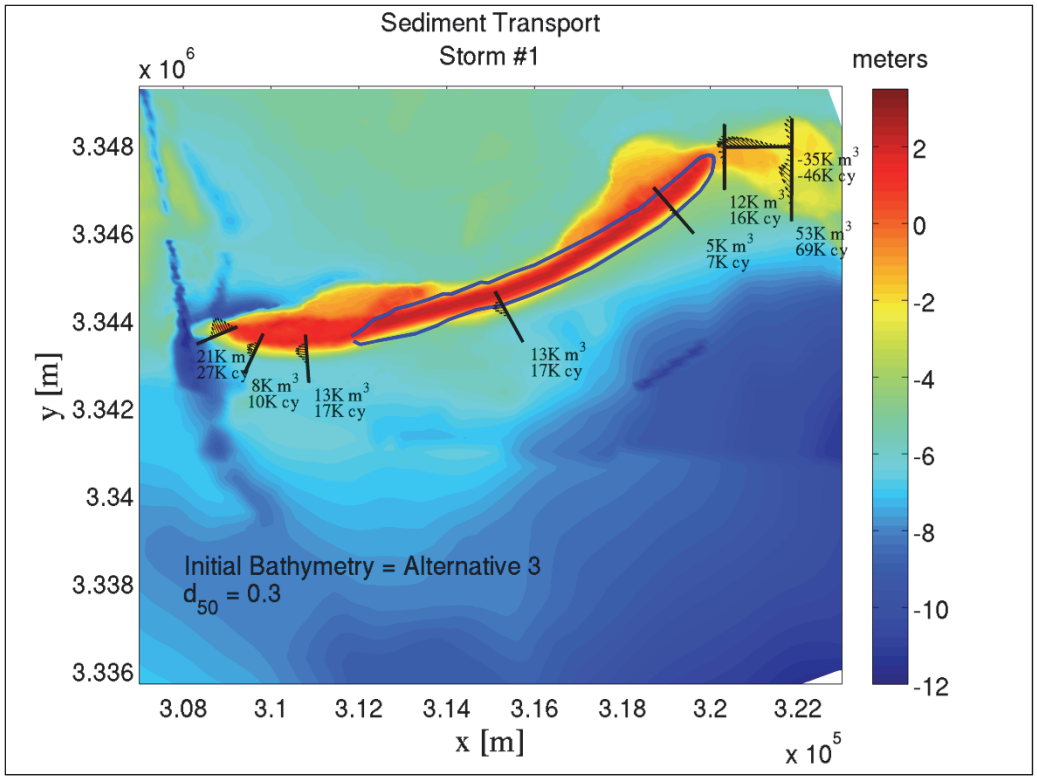

Figure J-3. Existing conditions for Storm #2; d_{50} = 0.30 mm.

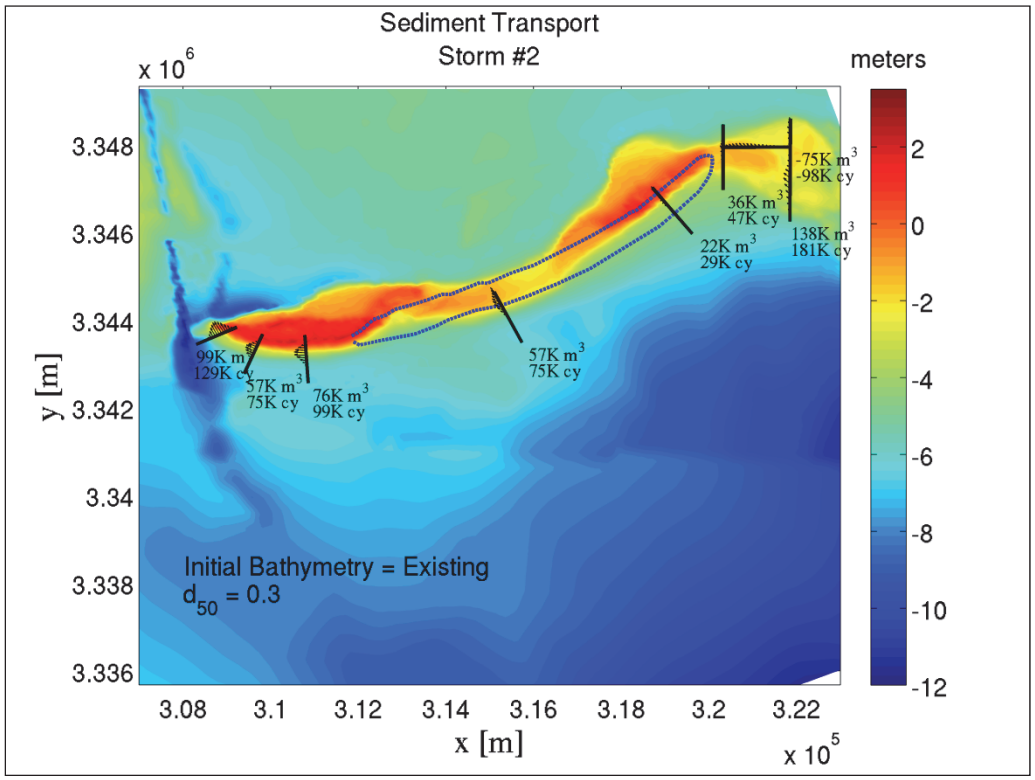

Figure J-4. Alternative 3 Restored conditions for Storm #2; d_{50} = 0.30 mm; With borrow pit.

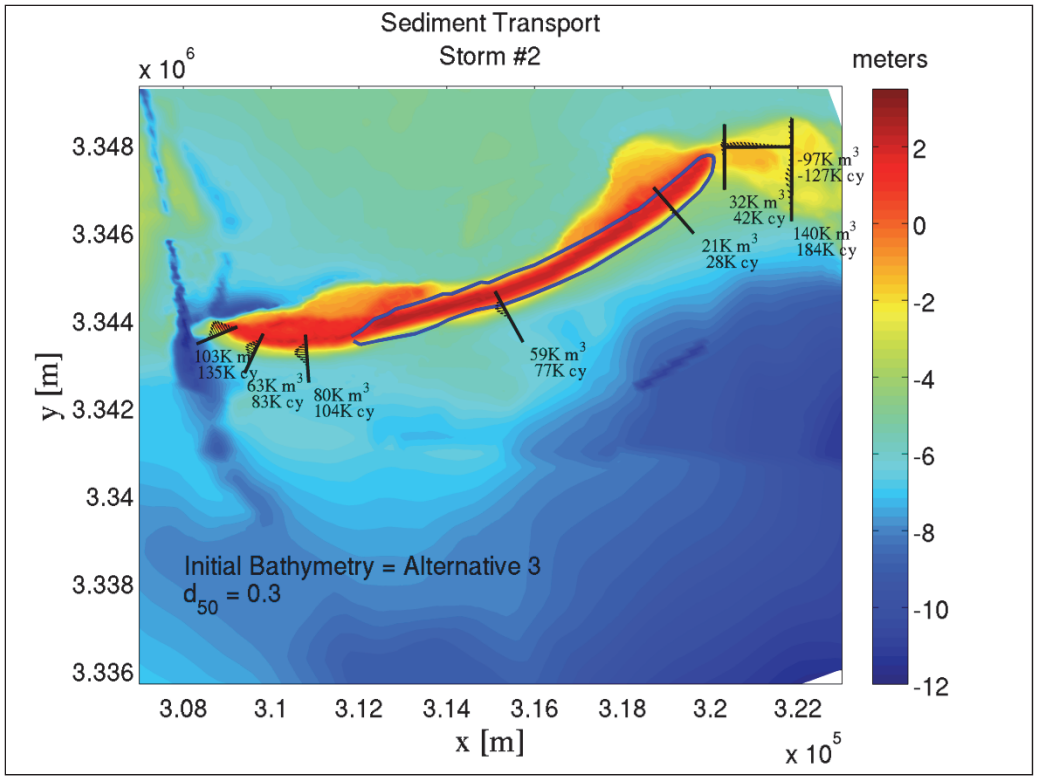

Figure J-5. Existing conditions for Storm #3; d_{50} = 0.30 mm.

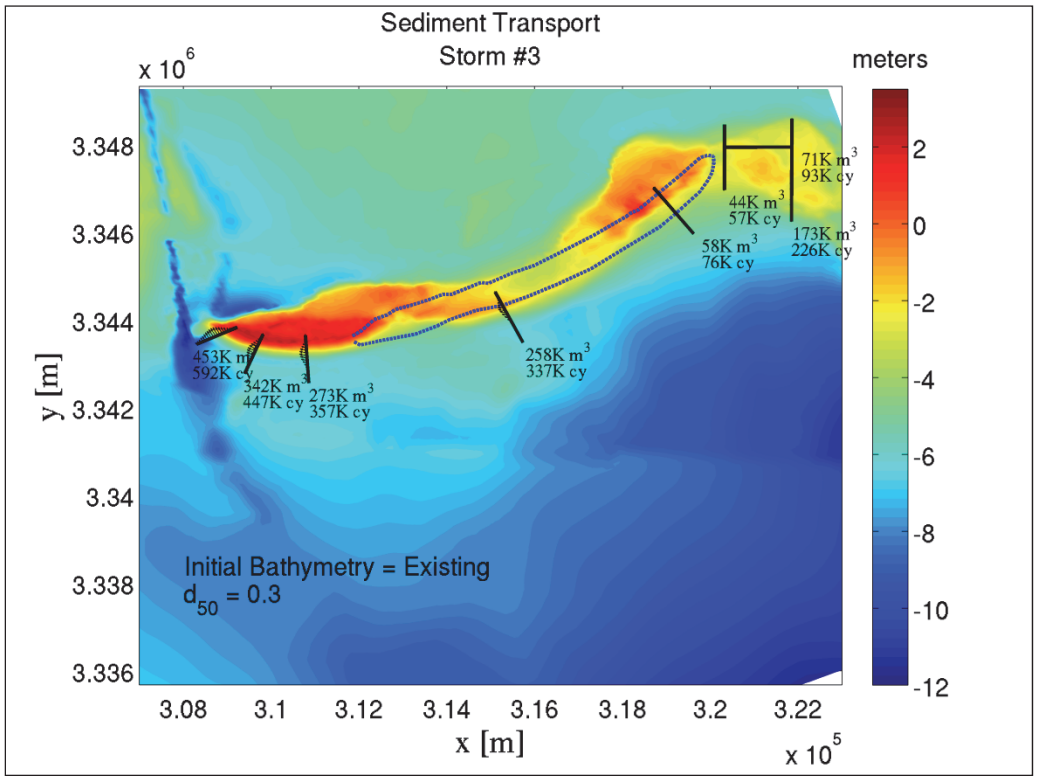

Figure J-6. Alternative 3 Restored conditions for Storm #3; d_{50} = 0.30 mm; With borrow pit.

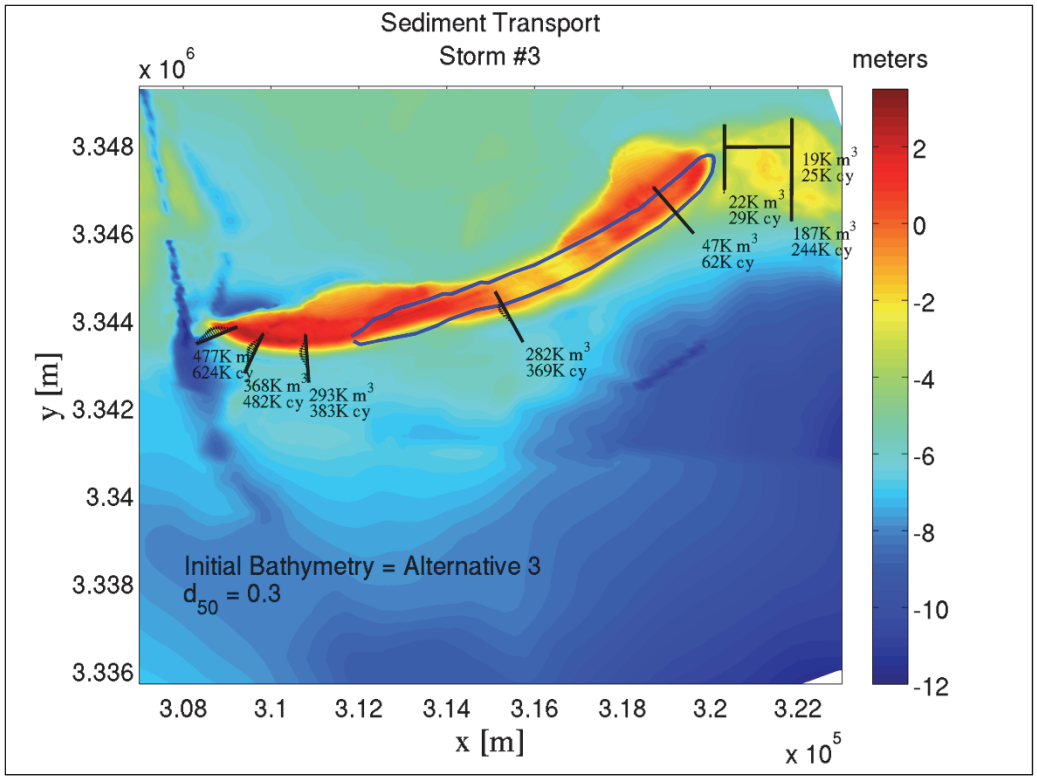

Figure J-7. Existing conditions for Storm #1; d_{50} = 0.30 mm.

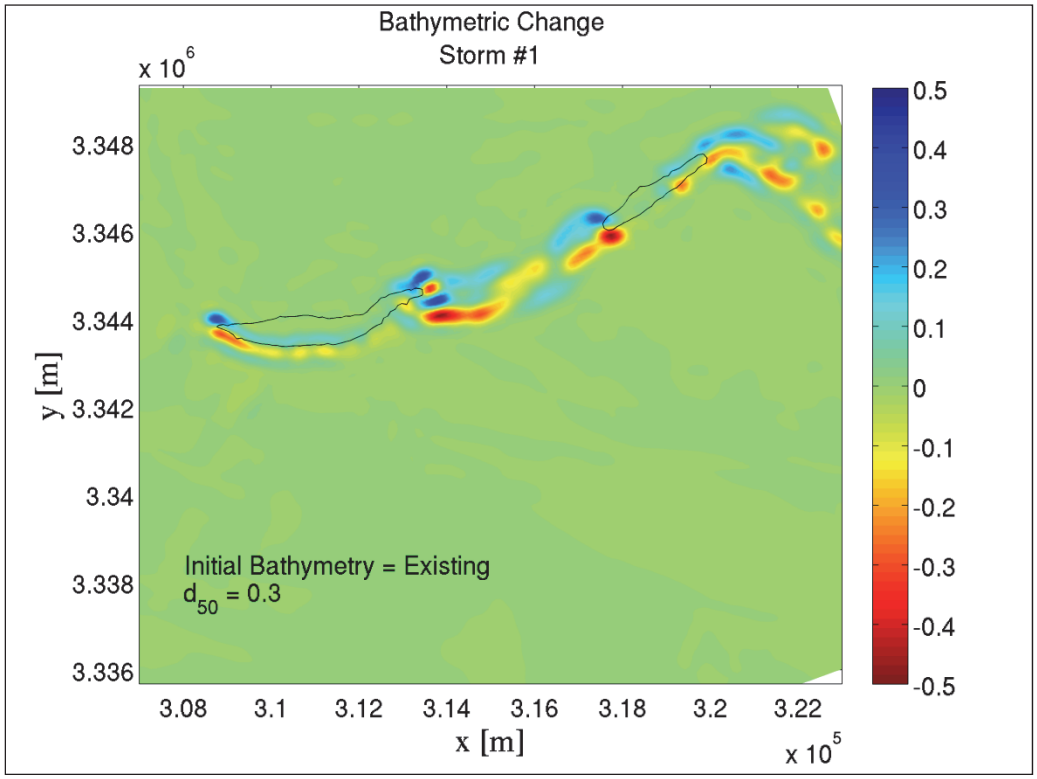

Figure J-8. Alternative 3 Restored conditions for Storm #1; d_{50} = 0.30 mm; With borrow pit.

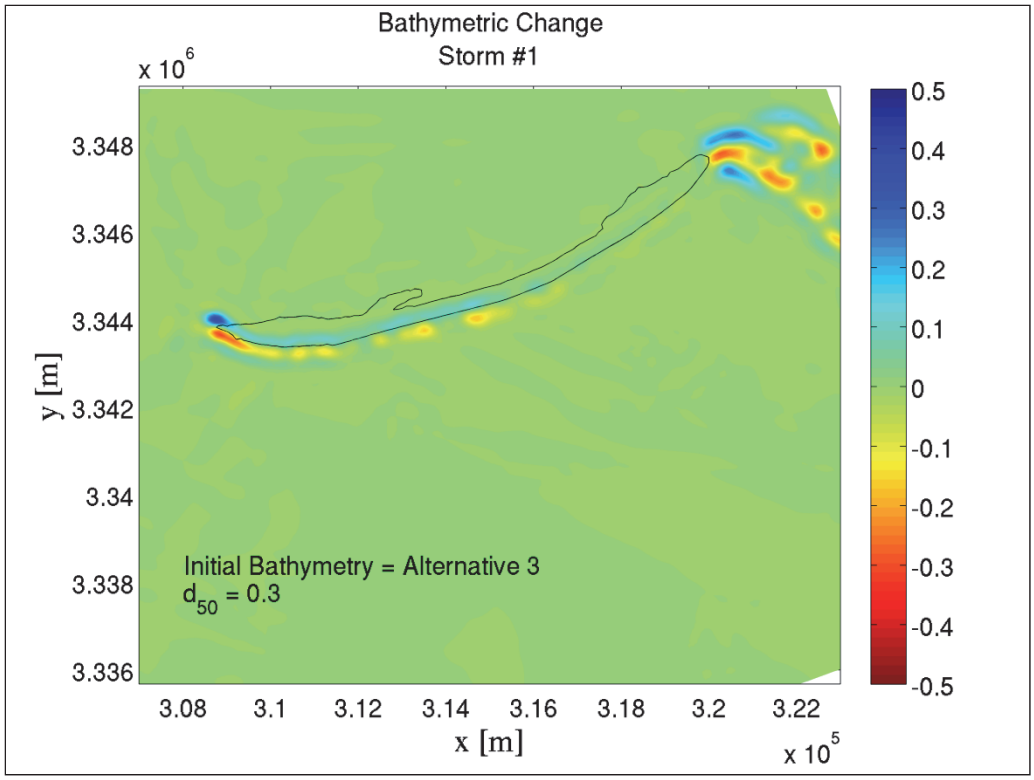

Figure J-9. Existing conditions for Storm #2; d_{50} = 0.30 mm.

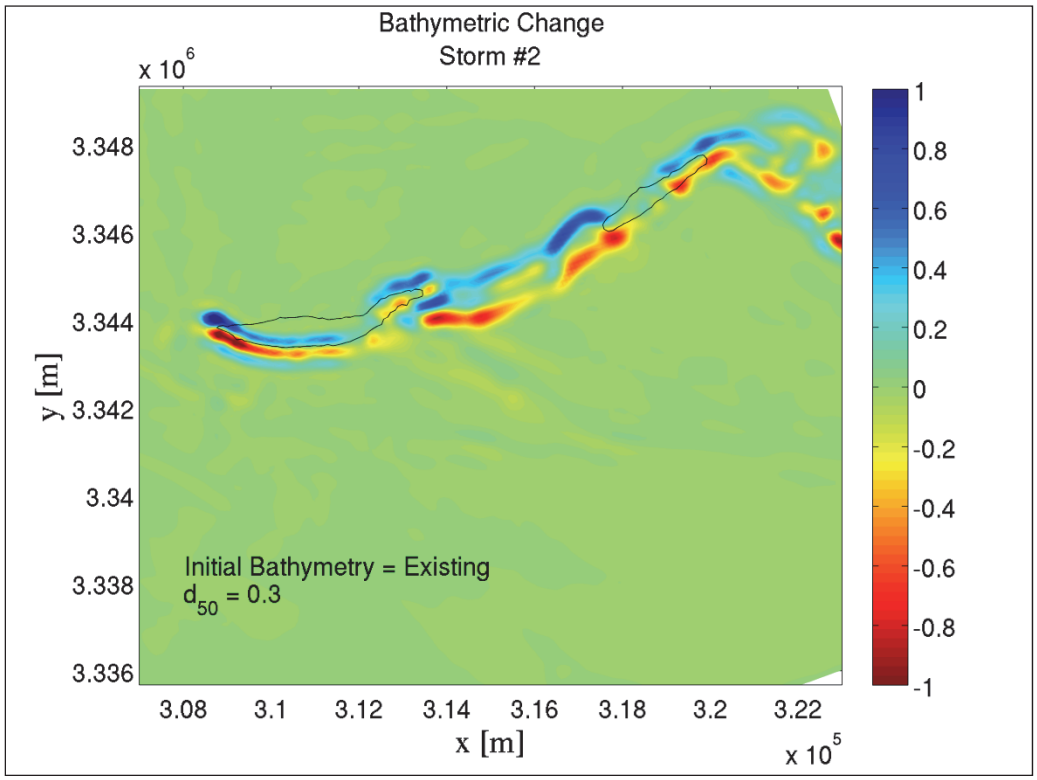

Figure J-10. Alternative 3 Restored conditions for Storm #2; d_{50} = 0.30 mm; With borrow pit.

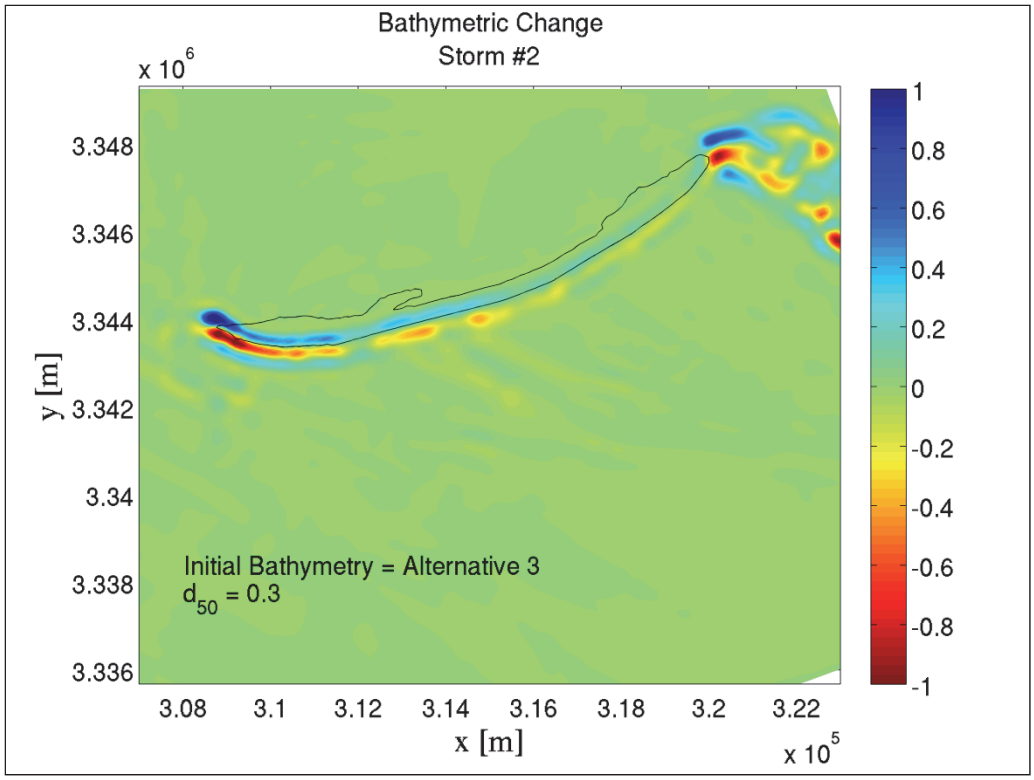

Figure J-11. Existing conditions for Storm #3; d_{50} = 0.30 mm.

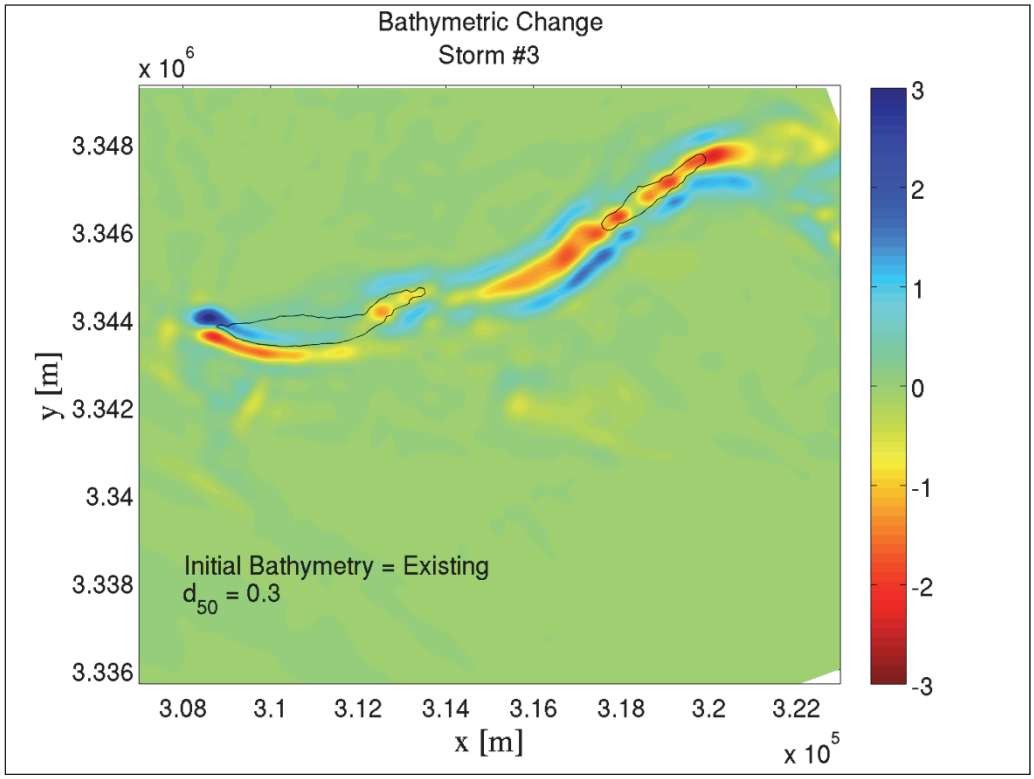

Figure J-12. Alternative 3 Restored conditions for Storm #3; d_{50} = 0.30 mm; With borrow pit.

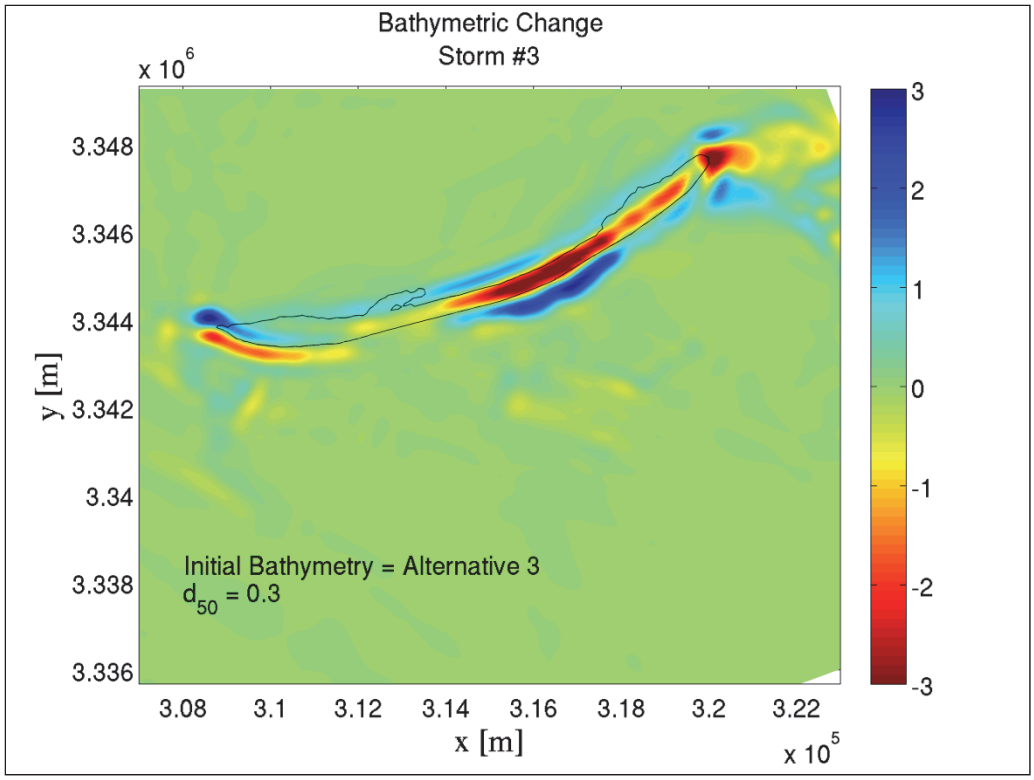

REPORT DOCUMENTATION PAGE

Form Approved
OMB No. 0704-0188

1. REPORT DATE *(DD-MM-YYYY)*	2. REPORT TYPE	3. DATES COVERED *(From - To)*
May 2013	Final Report (TR)	

4. TITLE AND SUBTITLE

Mississippi Coastal Improvements Program; Evaluation of Barrier Island Restoration Efforts

5a. CONTRACT NUMBER

5b. GRANT NUMBER

5c. PROGRAM ELEMENT NUMBER

6. AUTHOR(S)

Ty V. Wamsley, Elizabeth S. Godsey, Barry W. Bunch, Raymond S. Chapman, Mark B. Gravens, Alison S. Grzegorzewski, Bradley D. Johnson, David B. King, Rusty L. Permenter, Dorothy H. Tillman, and Michael W. Tubman

5d. PROJECT NUMBER

5e. TASK NUMBER

5f. WORK UNIT NUMBER

7. PERFORMING ORGANIZATION NAME(S) AND ADDRESS(ES)

Coastal and Hydraulics Laboratory
US Army Engineer Research and Development Center
3909 Halls Ferry Road
Vicksburg, MS 39180

8. PERFORMING ORGANIZATION REPORT NUMBER

ERDC TR-13-12

9. SPONSORING / MONITORING AGENCY NAME(S) AND ADDRESS(ES)

US Army Corps of Engineer District, Mobile
109 Saint Joseph Street, Mobile Alabama 36602

10. SPONSOR/MONITOR'S ACRONYM(S)

11. SPONSOR/MONITOR'S REPORT NUMBER(S)

12. DISTRIBUTION / AVAILABILITY STATEMENT

Approved for public release; distribution is unlimited.

13. SUPPLEMENTARY NOTES

14. ABSTRACT

A comprehensive numerical modeling study was undertaken to support the barrier island restoration plan as part of the Mississippi Coastal Improvements Program. Hydrodynamic, wave, sediment transport, and water quality numerical modeling was conducted to evaluate the effect of Camille Cut closure on circulation and water quality of Mississippi Sound; the combined effect of Camille Cut and Katrina Cut closures on circulation and water quality of Mississippi Sound; reduction of storm wave energy at the mainland Mississippi coast as a result of closing Camille Cut; and optimization of nearshore placement of sand in the littoral zone. Water quality modeling of Mississippi Sound was conducted to determine potential impacts from proposed actions in the Ship Island area using the Curvilinear Hydrodynamic 3D model (CH3D) and the water quality model (CE-QUAL-ICM). Although water quality changes were observed for the alternatives modeled, the impact of Ship Island degradation or restoration does not significantly alter system wide circulation and water quality conditions. However, the condition of Ship Island has localized effects on circulation and water quality. The changes in storm wave energy at the mainland Mississippi coast as a result of Ship Island degradation and restoration were quantified through the application of an integrated coastal storm modeling system. Results indicate that the closure of Camille Cut and Ship Island restoration have the potential to reduce storm waves at the mainland coast. The C2SHORE model was applied to numerically predict the morphological response and sand fate for a selection of proposed alternatives. Results indicate that the Camille Cut restoration fill survives higher-frequency storms (such as the 1-yr and 10-yr events), but is breached during the lower-frequency 500-yr event modeled. Potential impacts of nearshore borrow areas were assessed with the spectral nearshore wave transformation model STWAVE and shoreline change model GENESIS. Scenarios included borrow areas offshore of Ship Island, Horn Island, and West Dauphin Island and were evaluated over a period of 20-years. The expected shoreline impacts are site-specific, with both prograding and eroding shoreline areas predicted.

15. SUBJECT TERMS

Borrow areas
Breach
Coastal Morphology
Hurricane
Water quality
Mississippi Sound
Shoreline erosion
Storm waves

16. SECURITY CLASSIFICATION OF:			17. LIMITATION OF ABSTRACT	18. NUMBER OF PAGES	19a. NAME OF RESPONSIBLE PERSON Ty V. Wamsley
a. REPORT	b. ABSTRACT	c. THIS PAGE			19b. TELEPHONE NUMBER *(include area code)*
Unclassified	Unclassified	Unclassified		515	601-634-2099